

Qingfeng Li · David Aili
Hans Aage Hjuler · Jens Oluf Jensen
Editors

High Temperature Polymer Electrolyte Membrane Fuel Cells

Approaches, Status, and Perspectives

High Temperature Polymer Electrolyte Membrane Fuel Cells

Qingfeng Li • David Aili
Hans Aage Hjuler •
Jens Oluf Jensen
Editors

High Temperature Polymer Electrolyte Membrane Fuel Cells

Approaches, Status,
and Perspectives

 Springer

Editors

Qingfeng Li
Department of Energy Conversion
and Storage
Technical University of Denmark
Lyngby, Denmark

Hans Aage Hjuler
Danish Power Systems
Kvistgård, Denmark

David Aili
Department of Energy Conversion
and Storage
Technical University of Denmark
Lyngby, Denmark

Jens Oluf Jensen
Department of Energy Conversion
and Storage
Technical University of Denmark
Lyngby, Denmark

ISBN 978-3-319-17081-7 ISBN 978-3-319-17082-4 (eBook)
DOI 10.1007/978-3-319-17082-4
Springer Cham Heidelberg New York Dordrecht London

Library of Congress Control Number: 2015948948

© Springer International Publishing Switzerland 2016

This work is subject to copyright. All rights are reserved by the Publisher, whether the whole or part of the material is concerned, specifically the rights of translation, reprinting, reuse of illustrations, recitation, broadcasting, reproduction on microfilms or in any other physical way, and transmission or information storage and retrieval, electronic adaptation, computer software, or by similar or dissimilar methodology now known or hereafter developed.

The use of general descriptive names, registered names, trademarks, service marks, etc. in this publication does not imply, even in the absence of a specific statement, that such names are exempt from the relevant protective laws and regulations and therefore free for general use.

The publisher, the authors and the editors are safe to assume that the advice and information in this book are believed to be true and accurate at the date of publication. Neither the publisher nor the authors or the editors give a warranty, express or implied, with respect to the material contained herein or for any errors or omissions that may have been made.

Printed on acid-free paper

Springer International Publishing AG Switzerland is part of Springer Science+Business Media
(www.springer.com)

Contents

1	Introduction	1
	Jens Oluf Jensen, Hans Aage Hjuler, David Aili, and Qingfeng Li	
2	Modifications of Sulfonic Acid-Based Membranes	5
	Antonino S. Aricò, Vincenzo Baglio, Francesco Lufrano, Alessandro Stassi, Irene Gatto, Vincenzo Antonucci, and Luca Merlo	
3	Acid–Base Chemistry and Proton Conductivity	37
	Qingfeng Li, David Aili, Robert F. Savinell, and Jens Oluf Jensen	
4	Applications of Acid–Base Blend Concepts to Intermediate Temperature Membranes	59
	Jochen Kerres	
5	Pyridine Containing Aromatic Polyether Membranes	91
	Joannis K. Kallitsis, Aikaterini K. Andreopoulou, Maria Daletou, and Stylianos Neophytides	
6	Techniques for PBI Membrane Characterization	127
	Dirk Henkensmeier and David Aili	
7	Synthesis of Polybenzimidazoles	151
	Jingshuai Yang, Ronghuan He, and David Aili	
8	Phosphoric Acid and its Interactions with Polybenzimidazole-Type Polymers	169
	Carsten Korte, Fosca Conti, Jürgen Wackerl, and Werner Lehnert	
9	Polybenzimidazole Membranes by Post Acid Doping	195
	David Aili, Jens Oluf Jensen, and Qingfeng Li	
10	PBI Membranes Via the PPA Process	217
	Kayley Fishel, Guoqing Qian, and Brian C. Benicewicz	

11 Polybenzimidazoles with Enhanced Basicity: A Chemical Approach for Durable Membranes	239
Simone Angioni, Davide Carlo Villa, Piercarlo Mustarelli, and Eliana Quartarone	
12 Polybenzimidazole/Porous Poly(tetrafluoro ethylene) Composite Membranes	251
T. Leon Yu	
13 PBI-Based Composite Membranes	275
José J. Linares, Liliane C. Battirola, and Justo Lobato	
14 Catalysts and Catalyst-Layers in HT-PEMFCs	297
Tom Engl, Lorenz Gubler, and Thomas J. Schmidt	
15 Catalyst Support Material and Electrode Fabrication	315
Marina Welsch and Markus Perchthaler	
16 Design and Optimization of HT-PEMFC MEAs	331
Jung Ock Park and Suk-Gi Hong	
17 Characterization of HT-PEM Membrane-Electrode-Assemblies	353
F. Javier Pinar, Maren Rastedt, Nadine Pilinski, and Peter Wagner	
18 Approaches for the Modeling of PBI/H₃PO₄ Based HT-PEM Fuel Cells	387
Christian Siegel, Sebastian Lang, Ed Fontes, and Peter Beckhaus	
19 Bipolar Plates and Gaskets: Different Materials and Processing Methods	425
Isabel Kundler and Thorsten Hickmann	
20 Stack Concepts for High Temperature Polymer Electrolyte Membrane Fuel Cells	441
Holger Janßen, Jen Supra, and Werner Lehnert	
21 High Temperature PEM Fuel Cell Systems, Control and Diagnostics	459
Søren Juhl Andreasen, Søren Knudsen Kær, Kristian Kjær Justesen, and Simon Lennart Sahlin	
22 Durability Issues and Status of PBI-Based Fuel Cells	487
Mark Tonny Dalsgaard Jakobsen, Jens Oluf Jensen, Lars Nilausen Cleemann, and Qingfeng Li	
23 High Temperature Polymer Electrolyte Fuel Cell Systems for Aircraft Applications	511
Wendelin Waiblinger, Josef Kallo, Johannes Schirmer, and K. Andreas Friedrich	

24 Electrochemical Hydrogen Pumping	527
Kayley Fishel, Guoqing Qian, Glenn Eisman, and Brian C. Benicewicz	
Index	541

Preface

Since the concept of high temperature polymer electrolyte membrane fuel cells (HT-PEMFC) was proposed in early 1990s, it has attracted a large interest in the fuel cell community and over time spread around the world. Hundreds of patents have been filed and thousands of research papers have been published on the subject. Both research and development activities are flourishing at research institutions as well as in industrial companies. Many new scientists and engineers have been educated in the field and more are coming. Multiple products including polymer membranes, electrodes, cells, stacks, and systems are today available on the market, though a real commercial breakthrough is yet to be seen.

Thus, we decided that it was time to review and update the knowledge about the materials and technology in a book dedicated to the HT-PEMFC. Our aim is that it will be used as a reference for the fuel cell communities in universities and companies as well as for students around the world.

Going forward, the main challenges for HT-PEMFC—as for other fuel cell technologies—are the cost, performance, and the durability issues. The use of platinum and other noble metals as well as other expensive materials is a significant barrier for the technology to enter the market on a large scale. Also the durability or the lifetime of materials, components, and systems must be enhanced. Further, there might be even more barriers for an emerging technology that need to be overcome which can be customer adaptation, concerns about pressurized hydrogen, toxic fuels, and other hazards. We hope that this book can be helpful to overcome at least some of these challenges.

We are very pleased to have received so many well-written chapters from researchers and workers of expertise in the field. We would like to thank all the authors for the many hours they have spent. We are also grateful for the good discussions we have had with the authors. The authors of the individual chapters were granted a high degree of freedom to follow their own preferences with regard to use of abbreviations and to their choice of English orthography, though attempts are made to keep technical terms consistent. We would also like to mention that the group of contributors was not put together with the aim to include all key research groups or companies involved in the PBI-based HT-PEMFC development, but merely to cover, as we see it, the most important scientific aspects of the technology without too much redundancy. This means that several leading groups are not directly

represented as authors but well referred to in the chapters. We hope for their understanding.

A special thanks goes to Kenneth Howell, Abira Sengupta, and other staff from Springer Publishing in New York. They have been extremely helpful for all practical aspects of getting this book published.

Finally, on behalf of all the authors, we would like to thank all funding agencies, universities, and companies that have made it possible to do all the work in the laboratories around the world.

Lyngby, Denmark
Lyngby, Denmark
Lyngby, Denmark
Kvistgård, Denmark

Qingfeng Li
David Aili
Jens Oluf Jensen
Hans Aage Hjuler

Contributors

David Aili Department of Energy Conversion and Storage, Technical University of Denmark, Kgs. Lyngby, Denmark

Søren Juhl Andreassen Department of Energy Technology, Aalborg University, Aalborg East, Denmark

Aikaterini K. Andreopoulou Department of Chemistry, University of Patras, Rio-Patras, Greece
Foundation for Research and Technology Hellas/Institute of Chemical Engineering Sciences (FORTH/ICE-HT), Patras, Greece

Simone Angioni Department of Chemistry and INSTM, University of Pavia, Pavia, Italy

Vincenzo Antonucci CNR-ITAE, Messina, Italy

Antonino S. Aricó CNR-ITAE, Messina, Italy

Vincenzo Baglio CNR-ITAE, Messina, Italy

Liliane C. Battirola Instituto de Química, Universidade de Campinas, Campinas, SP, Brazil

Peter Beckhaus ZBT GmbH – Zentrum für BrennstoffzellenTechnik, Duisburg, Germany

Brian C. Benicewicz Department of Chemistry and Biochemistry, University of South Carolina, Columbia, SC, USA

Lars Nilausen Cleemann Department of Energy Conversion and Storage, Technical University of Denmark, Kgs. Lyngby, Denmark

Fosca Conti Department of Chemical Sciences, University of Padova, Padova, Italy

Maria Daletou Foundation for Research and Technology Hellas/Institute of Chemical Engineering Sciences (FORTH/ICE-HT), Patras, Greece

Glenn Eisman H2Pump LLC, Latham, NY, USA

Tom Engl Electrochemistry Laboratory, Paul Scherrer Institut, Villigen PSI, Switzerland

Kayley Fishel Department of Chemistry and Biochemistry, University of South Carolina, Columbia, SC, USA

Ed Fontes COMSOL AB, Stockholm, Sweden

K. Andreas Friedrich Institute of Engineering Thermodynamics, German Aerospace Center, Stuttgart, Germany

Irene Gatto CNR-ITAE, Messina, Italy

Lorenz Gubler Electrochemistry Laboratory, Paul Scherrer Institut, Villigen PSI, Switzerland

Ronghuan He Department of Chemistry, College of Sciences, Northeastern University, Shenyang, China

Dirk Henkensmeier Fuel Cell Research Center, Korea Institute of Science and Technology, Seongbukgu, Seoul, South Korea

Thorsten Hickmann Eisenhuth GmbH & Co. KG, Osterode am Harz, Germany

Hans Aage Hjuler Danish Power Systems, Kvistgård, Denmark

Suk-Gi Hong Samsung Advanced Institute of Technology, Samsung Electronics, Co. Ltd, Seoul, South Korea

Mark Tonny Dalsgaard Jakobsen Department of Energy Conversion and Storage, Technical University of Denmark, Kgs. Lyngby, Denmark

Holger Janßen Forschungszentrum Jülich GmbH, Jülich, Germany

Jens Oluf Jensen Department of Energy Conversion and Storage, Technical University of Denmark, Kgs. Lyngby, Denmark

Kristian Kjær Justesen Department of Energy Technology, Aalborg University, Aalborg East, Denmark

Joannis K. Kallitsis Department of Chemistry, University of Patras, Rio-Patras, Greece

Foundation for Research and Technology Hellas/Institute of Chemical Engineering Sciences (FORTH/ICE-HT), Patras, Greece

Josef Kallo Institute of Engineering Thermodynamics, German Aerospace Center, Stuttgart, Germany

Jochen Kerres Institute of Chemical Process Engineering, University of Stuttgart, Stuttgart, Germany

Carsten Korte Institute for Energy and Climate Research, Electrochemical Process Engineering (IEK-3), Jülich, Germany

Isabel Kundler Eisenhuth GmbH & Co. KG, Osterode am Harz, Germany

Søren Knudsen Kær Department of Energy Technology, Aalborg University, Aalborg East, Denmark

Sebastian Lang Technische Universität Darmstadt, Fachgebiet Thermische Verfahrenstechnik, Darmstadt, Germany

Werner Lehnert Institute of Energy and Climate Research, Electrochemical Process Engineering (IEK-3), Forschungszentrum Jülich GmbH, Jülich, Germany

Qingfeng Li Department of Energy Conversion and Storage, Technical University of Denmark, Kgs. Lyngby, Denmark

José J. Linares Instituto de Química, Universidade de Brasília, Brasília, DF, Brazil

Justo Lobato Chemical Engineering Department, Universidad de Castilla-La Mancha, Ciudad Real, Spain

Francesco Lufrano CNR-ITAE, Messina, Italy

Luca Merlo Solvay Specialty Polymers, Bollate (MI), Italy

Piercarlo Mustarelli Department of Chemistry and INSTM, University of Pavia, Pavia, Italy

Stylianos Neophytides Foundation for Research and Technology Hellas/ Institute of Chemical Engineering Sciences (FORTH/ICE-HT), Patras, Greece

Jung Ock Park Samsung Advanced Institute of Technology, Samsung Electronics, Co. Ltd, Seoul, South Korea

Markus Perchthaler Elcomax GmbH, Munich, Germany

Nadine Pilinski NEXT ENERGY, EWE Research Centre for Energy Technology, Oldenburg, Germany

F. Javier Pinar NEXT ENERGY, EWE Research Centre for Energy Technology, Oldenburg, Germany

Guoqing Qian Department of Chemistry and Biochemistry, University of South Carolina, Columbia, SC, USA

Eliana Quartarone Department of Chemistry and INSTM, University of Pavia, Pavia, Italy

Maren Rastedt NEXT ENERGY, EWE Research Centre for Energy Technology, Oldenburg, Germany

Simon Lennart Sahlin Department of Energy Technology, Aalborg University, Aalborg East, Denmark

Robert F. Savinell Department of Chemical Engineering, Case Western Reserve University, Cleveland, OH, USA

Johannes Schirmer Institute of Engineering Thermodynamics, German Aerospace Center, Stuttgart, Germany

Thomas J. Schmidt Electrochemistry Laboratory, Paul Scherrer Institut, Villigen PSI, Switzerland

Laboratory of Physical Chemistry, ETH Zürich, Zürich, Switzerland

Christian Siegel Siegel Schleimer Ingénieurs-conseils SARL, Belvaux, Luxembourg

Alessandro Stassi CNR-ITAE, Messina, Italy

Jen Supra Forschungszentrum Jülich GmbH, Jülich, Germany

Davide Carlo Villa Department of Chemistry and INSTM, University of Pavia, Pavia, Italy

Jürgen Wackerl Institute for Energy and Climate Research, Electrochemical Process Engineering (IEK-3), Jülich, Germany

Peter Wagner NEXT ENERGY, EWE Research Centre for Energy Technology, Oldenburg, Germany

Wendelin Waiblinger Institute of Engineering Thermodynamics, German Aerospace Center, Stuttgart, Germany

Jesse S. Wainright Case Western Reserve University, Cleveland, OH, USA

Marina Welsch Elcomax GmbH, Munich, Germany

Jingshuai Yang Department of Chemistry, College of Sciences, Northeastern University, Shenyang, China

T. Leon Yu Department of Chemical Engineering and Materials Science, Fuel Cell Center, Yuan Ze University, Chung-Li, Taoyuan, Taiwan

About the Editors

David Aili obtained his M.Sc. degree in Organic Chemistry in 2007 from the Institute of Technology at Linköping University after a diploma project at the Arrhenius Laboratory, Stockholm University. He subsequently moved to Technical University of Denmark to pursue a Ph.D. in the field of proton conducting membranes for electrochemical energy conversion technologies under the supervision of Professor Niels J. Bjerrum at the Department of Chemistry. After obtaining his Ph.D. degree in 2011 and after a shorter period as a development engineer in the phenolic resin business, he joined the newly formed Department of Energy Conversion and Storage at Technical University of Denmark in 2012 as a Postdoctoral Research Fellow. His current research covers fundamental and application-oriented aspects of ion conducting materials with special emphasis on polymer-based membranes.



Hans Aage Hjuler was educated as M.Sc. (Chemistry) at Technical University of Denmark in 1980. In 1983, he obtained his Ph.D. degree in Advanced Rechargeable Batteries at Technical University of Denmark. As postdoc, he formed a significant research group in batteries (from 1983) and fuel cells R&D (from 1988). He has worked with PAFC, MCFC, SOFC, and PEM-based fuel cell systems and materials. He worked as laboratory manager with superconducting materials (high T_c) at NKT Research Center from 1991 to 1994. He was director in Novo Nordisk from 1998 to 2009. He was one of the founders of Danish Power Systems in 1994 and chairman from

1994 to 2010. He was appointed Managing Director, CEO in 2010. H.A.H. is vice-chair of the Board of Directors of the Danish Partnership for Hydrogen and Fuel Cells, member of Annex 22, International Energy Agency (IEA) Implementing Agreement on Advanced Fuel Cells. He is member of the Scientific Committee of Fuel Cell and Hydrogen Joint Undertaking (FCH-JU), European Commission, Brussels, Belgium.



Jens Oluf Jensen is a full Professor at Technical University of Denmark, where he is heading the section named Proton Conductors (ca. 25 people) at Department of Energy Conversion and Storage. He is the coordinator of the technology tracks for PEM fuel cells and for low temperature electrolyzers at the department. In 1997, he received his Ph.D. for a study on metal hydrides for batteries. Today, his research fields include high temperature PEM fuel cells and alkaline electrolyzers. The approach is experimental and focused on materials like electrolytes, catalysts, and electrode structures. He has initiated and coordinated numerous national and international research projects, mostly in collaboration with industry, and arranged a number of symposia/workshops. Lately, he chaired the third International Carisma Conference in Copenhagen 2012 and the Danish Korean PEM Fuel cell workshop in Seoul 2013. He is a board member of the Partnership for



Hydrogen and Fuel cells in Denmark. At DTU, he has taught at numerous courses and is at present involved in teaching hydrogen energy and fuel cells as well as thermodynamics.

Qingfeng Li is a full professor at Department of Energy Conversion and Storage, Technical University of Denmark. His research areas include proton conducting electrolytes, electrocatalysts, and the related technologies particularly fuel cells and electrolyzers. He received his Ph.D. in electrochemistry from Northeastern University, China, in 1990 and was awarded Doctor Degree of Technics at DTU in 2006. As a postdoc, he started in the middle of 1990s the research on high temperature polymer electrolyte membrane fuel cells at DTU. He has participated/coordinated more than 20 EU and Nordic research projects within the fuel cell area and is currently the leader of 4M Centre devoted to fundamental research on mechanisms, materials, manufacturing, and management of high temperature polymer electrolyte membrane fuel cells, funded by Innovation Fund Denmark. He is an active member of, among other, the Electrochemical Society and the International Society of Electrochemistry (and currently the region representative of Denmark 2012-now). Prof. Li has been involved in teaching at all DTU levels including a lecturing and an experimental course on Hydrogen Energy and Fuel cells.



Overture: The Early History of PBI/Phosphoric Acid Membranes

Robert F. Savinell and Jesse S. Wainright

The two of us, Robert F. Savinell (R.F.S.) and Jesse S. Wainright (J.S.W.), have collaborated on the development of PBI/PA membranes for fuel cells at CWRU from the very early days, and are pleased to tell this story about the early history of the PBI/PA high temperature membrane for fuel cells.

It was in the late 1980s time period when R.F.S. was the Associate Director of the Case Center for Electrochemical Sciences (now the Yeager Center for Electrochemical Sciences at Case Western Reserve University) working with Professor Ernest B Yeager (see Fig. 1).

Robert F. Savinell (✉) • Jesse S. Wainright
Department of Chemical Engineering, A.W. Smith
Building, Case Western reserve University,
Cleveland, Ohio 44106, USA
e-mail: Robert.savinell@case.edu



Fig. 1. Robert F. Savinell on far left and Professor Yeager on right of plaque at the celebration of the renaming of the Case Center of Electrochemical Sciences to the Yeager Center for Electrochemical Sciences with CWRU administrators and Dorothy Hummel Hovorka, wife of Frank Hovorka, Professor Yeager's Ph.D. advisor

At that time, Professor Yeager's group was interested in enhancing the electrokinetics of oxygen reduction reaction in a phosphoric acid electrolyte. One approach he took was to add perfluorinated surfactants to a phosphoric acid electrolyte so as to enrich the oxygen activity near the electrocatalyst surface. Indeed, this worked to some extent and enhanced oxygen reduction polarization curves were demonstrated. It was this work that stimulated our thinking about fuel cells and the idea of using a high temperature membrane.

In early 1991, Professor Yeager and R.F.S. met with colleagues on a weekly basis to discuss research strategies to address the development of a high performance direct methanol fuel cell. These meetings explored many different aspects of improving methanol fuel cell performance from electrocatalysts and membrane materials to cell designs. A number of times we would go down a strategic path in great detail, but only to throw out the approach after weeks of deep discussion. After about 6 months of weekly discussions and as we rapidly drew near a proposal submission deadline, we concluded that if a proton conducting polymer membrane can be developed that operates at ~ 200 °C, then there would be "opportunities to overcome the catalyst's activity and stability problems." The thought was that the right membrane could lead to high performance direct methanol fuel cells.



Fig. 2. Professor Morton Litt examining an early sample of a cast PBI membrane (from *Case Alumnus*, Spring 1997)

We then set out to propose a research program with its principle objective being the development of a high proton conducting solid polymer electrolyte membrane which is chemically stable under the oxidizing and reducing conditions existing in a direct methanol fuel cell and operates at temperatures of 200 °C. Two approaches that were proposed involved new polymers with superacid functional groups such as the perfluorinated sulfonimides and the perfluorinated phosphonic acid materials, with the thought that they would retain water even at higher temperatures. Looking for alternative approaches, Professor Morton Litt of CWRU (see Fig. 2) brought to our attention the 1977 work of Hoel and Grunwald [*J. Phys. Chem.*, 81 2135 (1977)] which reported evidence of proton conductivity in films of polybenzimidazole, although the conductivities were quite low (10^{-4} S cm⁻¹). Professor Litt suggested we explore poly(benzimidazoles) and poly(quinolones) by doping films with acid and even trying to functionalize the films with acid groups.

These polymers were known to be stable at elevated temperatures. As the PI for the research program, R.F.S. decided to include this idea to broaden our membrane approaches. The proposal was submitted to the US Defense Advanced Research Projects Agency (DARPA) on July 11, 1991, and included the three polymer approaches mentioned above, as well as new electrocatalysts for operating in these polymeric environments, and a variety of fundamental measurements. We also proposed integrating these new materials in a laboratory scale “microfuel cell” to demonstrate actual operating performance. The program was selected for funding and a contract awarded in 1992. This is when J.S.W., just completing his Ph.D. studies, joined R.F.S. and the team to pursue this research program (see Fig. 3).

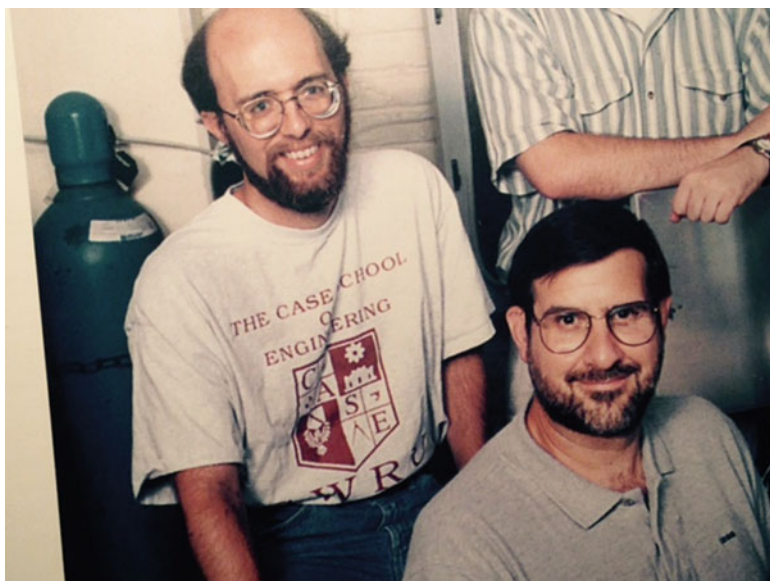


Fig. 3. Jesse S. Wainright and Robert F. Savinell in the early days of PBI/PA research (from *Case Alumnus*, Spring 1997)

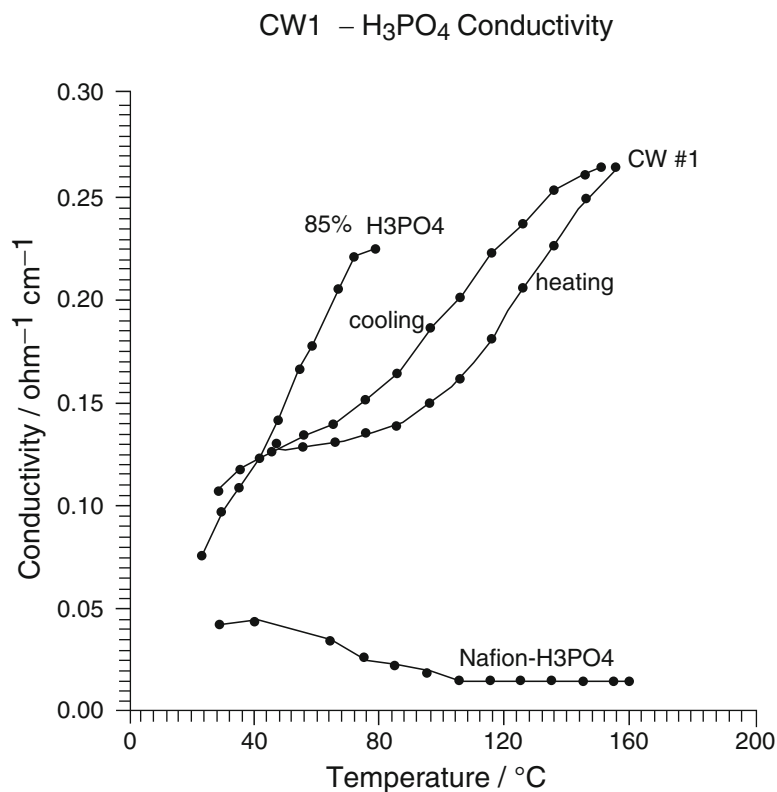


Fig. 4. Four-point conductivity measurements for Nafion 117 and polybenzimidazole films infused with phosphoric acid. Conductivity cell measurements of phosphoric acid shown for comparison. Figure 3 of the first quarter (ending September 1992) project report of the CWRU DARPA methanol fuel cell project

The CWRU DARPA program pursued all three polymer approaches simultaneously. Eventually, we learned that the superacid perfluorinated polymer strategy produced some very intriguing membrane films, but none performed any better at elevated temperatures than the state-of-the-art Nafion product of DuPont. Here, we will summarize of our early quarterly progress reports of the CWRU DARPA program that give some insight on our early thinking and contain much unpublished data and results. During the first quarter of the project, sulfuric acid and phosphoric acid sorption in PBI films studies were initiated. It was demonstrated that with a $\text{H}_2\text{SO}_4/\text{PBI}$ molar ratio of 0.2, the PBI unit interacted so strongly with the acid that the acid could not be extracted from the polymer with water. The first conductivity measurements were made on acid-doped PBI, and the first quarterly project report for the period ending September 1992 stated: "The third set of results is for the CWRU undoped polybenzimidazole sample which has been given the designation CW1. As received, this material exhibited a very low conductivity, ca. $10^{-4} \text{ S cm}^{-1}$. Doped films are expected to have much higher proton conductivity. We pretreated the undoped film in H_3PO_4 for 1 h at 150°C and the conductivity was found to be very high, as shown in Figure 3 (Fig. 4 of this article). This data was obtained in dry air. The conductivity of the CW1 sample is much greater than that of the hydrated Nafion sample and approaches the conductivity of the liquid phosphoric acid. It would appear that the CW1 sample is acting as an acid support."

During the second quarter, ending December 1992, it was shown that phosphoric acid-doped PBI was more thermally stable than undoped PBI films. Studies also measured sulfuric acid and phosphoric acid permeation through PBI films in order to predict doping times. More controlled experiments of conductivity as a function of acid doping took place during this quarter, with phosphoric acid doping levels of 25, 33, and 42 mol%, all showing relatively low conductivities.

In the third quarter of this program, ending March 1993, we demonstrated that as phosphoric acid doping levels increased from 40 to 170–190 mol% (mole acid to PBI repeat unit X100), the conductivity also improved substantially. J.S.W. was the persistent researcher in the lab who recognized the increasing conductivity trend with acid doping level and continued the studies to explore the effects on conductivity at even higher acid doping levels. We also showed that doping with excess sulfuric acid increased conductivity, and 250 mol% sulfuric acid-doped PBI at 160°C had about a quarter of the conductivity of Nafion at 80°C fully hydrated. But, high doping levels with sulfuric acid at temperatures of 350°C for a few minutes sulfonated PBI, which decreased conductivity. During that quarter, we also

began to appreciate the importance of phosphoric acid dehydration and polymerization in low humidity conditions so we initiated experiments controlling the relative humidity during conductivity measurements. It was shortly after this quarter we discontinued using sulfuric acid, and focused attention on phosphoric acid doping of PBI. During the third quarter, we also started measuring oxygen and methanol permeation rates through a PBI/acid-doped film and compared the measured permeability with those of Nafion and acid-doped/Nafion films.

During the fourth quarter, ending June 1993, we started exploring various PBI-type structures. Also during the first year of the program, we studied the Nafion/PA system as well and used its conductivity, stability, and permeability characteristics as a basis for comparison with PBI/PA or PBI/SA results.

The research performed during the fifth quarter of the program, ending September 1993, was especially significant. We became fully aware of the importance of high molecular weight PBI polymers for film strength. We demonstrated high conductivity with PA doping levels of 350 mol%, approaching 0.02 S cm^{-1} at 190°C . Doping levels would later be increased to over 500 mol% in our labs, and even higher by other researchers. We demonstrated methanol vapor cross over permeation rates an order of magnitude below that of the hydrated Nafion in direct liquid methanol fuel cells. The polarization curve and the operating stability under constant voltage and constant current load were demonstrated in a PBI/PA fuel cell. Some of these original data graphs are shown in Figure 5 (Figs. 6.5.1b, 6.5.1c, 6.5.1d of the September 1993 Progress Report). The efforts of two of our Ph.D. students, Jiang-Tao Wang and Dacong Weng, were particularly instrumental in obtaining these key early results. We learned that a Nafion/PA membrane in a fuel cell, although having high ac conductivity, could not sustain high dc current densities. This result bothered us and suggested that there were fundamental differences in the transport mechanism as compared to a PBI/PA membrane. It was shortly into the second year of the program that we stopped much of our work on the Nafion/PA system, with the exception of using it for evaluating electrocatalyst performance under elevated temperature conditions. Recently, we collaborated with the DTU group to investigate the Nafion/PA system and repeated some of the observations we made earlier at CWRU. Although not fully understood, there are clearly some significant differences in proton conduction between the Nafion/PA and PBI/PA systems. As a colleague recently commented to one of us, "you may have just been lucky to stumble upon the PBI/PA system."

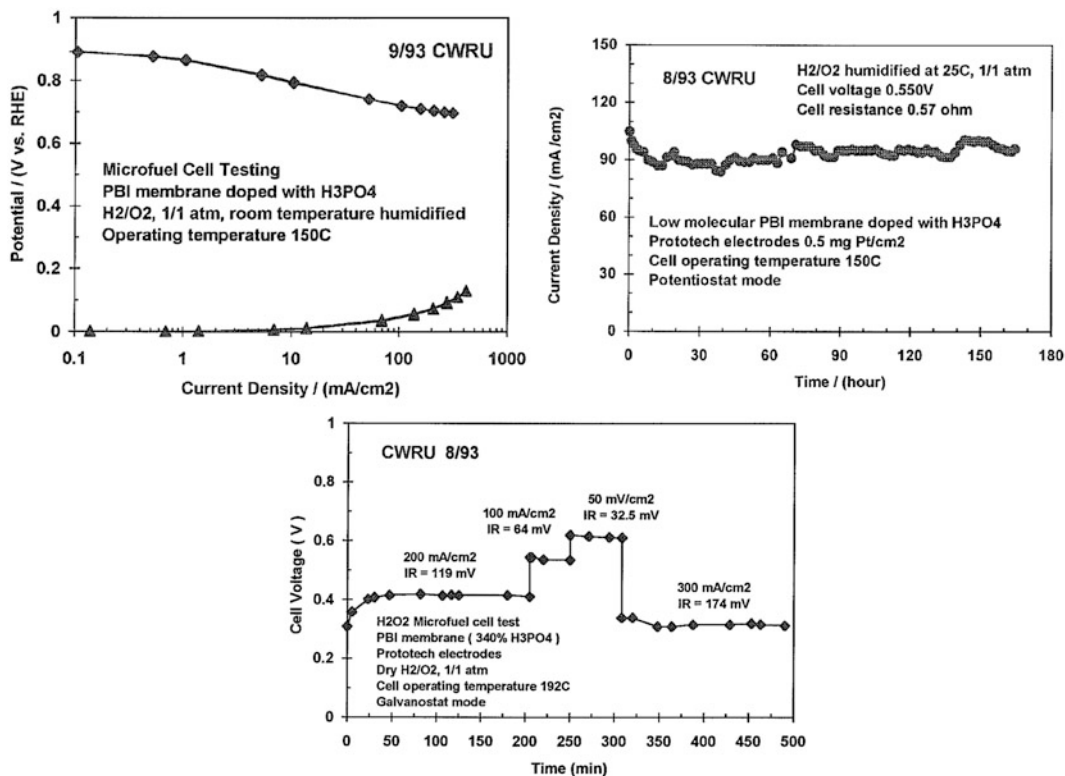


Fig. 5. These figures are taken from the fifth quarter progress report of the CWRU DARPA Direct Methanol Fuel Cell Program, dated September 1993. They show the first results of fuel cell testing with PBI/PA in a fuel cell

The DARPA program continued for another 3 years. During this period, Professor Litt and his students developed a way to cast doped films in one step that increased both the doping levels possible and the consistency of the acid content. We explored operating a PBI/PA membrane fuel cell with various fuels, fuel purities, and measured temperature effects. We began to appreciate the relevancy of the technology for fuel cells operating on reformed fuels. Our studies with PBI/PA evolved to become more thorough and under better controlled conditions, and our understanding of the conductivity mechanism became deeper by studying water drag and performing NMR studies. In addition to the electrolyte work, we developed new oxygen reduction reaction electrocatalysts, including methanol-tolerant high performance non-precious metal C–N ligands.

The CWRU patents were licensed to several companies, and our publications (>15 papers from 1995 to 1998) on PBI/PA fuel cell membranes garnered more attention in the USA and worldwide. These licensee companies as well as other corporate and university researchers from around the world further explored the PBI/PA approach to improve mechanical and proton conducting properties and to evaluate the membranes in operating fuel cells and electrolyzers at elevated temperatures.

So what will be the long-lasting significance of the PBI/PA system, if any? Well, the system does not represent the best environment for electrochemical reactions such as oxygen reduction, and it certainly cannot be used at lower temperatures with liquid water present. But we are sure PBI/PA and similar polymers and approaches will continue to find applications in electrochemistry. Phosphoric acid is a highly conductive electrolyte rich in fascination because of its fundamental mechanisms for proton transport. But other doping acids might also be explored as well. In our view, the most significant feature of the PBI/PA membrane discovery is that it opened the door to our thinking about high temperature proton conducting membranes in general, and stimulated global research to find a better approach. As a result, many researchers have been cross-trained in electrochemistry and polymer/materials science through their work on this technology. These cross-trained scientists and engineers are those who will likely find better solutions in the future for efficient and cost-effective energy conversion technologies. On a personal level, our work on this system has led to close collaboration and friendship with colleagues and students at CWRU, and especially between the two coauthors of this article. It also led to many fruitful and rewarding collaborations and friends from around the world. This is what we value the most.



Robert F. Savinell
Distinguished University Professor and George
S. Dively Professor of Engineering
Case Western Reserve University



Jesse S. Wainright
Research Professor
Case Western Reserve University

Jens Oluf Jensen, Hans Aage Hjuler, David Aili,
and Qingfeng Li

High temperature polymer electrolyte membrane fuel cells (HT-PEMFC) have been an active field of research and development over more than two decades. The term *high temperature* used in this book refers to a temperature range from 100 to 200 °C, relative to the well-developed PEMFC technology typically operating at 80 °C. It should be stressed that fuel cells working at temperatures up to 200 °C still belong to the overall class of *low temperature fuel cells*, in contrast to *high temperature fuel cells* which are molten carbonate fuel cells (MCFC) and solid oxide fuel cells (SOFC) all working at above 600 °C.

The temperature range from 100 to 200 °C does not sound very high in any engineering sense; however, a significant effort is indeed behind the development of high temperature polymer electrolyte membranes and their cells, from both materials science and technological points of view. Obviously, elevated temperatures tend to challenge thermal, chemical, and mechanical stability of polymer materials, but besides that, obtaining sufficient proton conductivity in

a stable and practical way, most preferably under ambient pressure, is far from trivial. One might think that a proton, a positive hydrogen ion, being orders of magnitude smaller than any other ion will have the ability to travel easily through many materials simply due to its tiny size. The contrary is true. The extremely small size makes the charge density very high, and the protons are always associated to other species. In a liquid electrolyte, this is not a problem since other mobile molecules carry the proton as a charged species and establish a net movement of the protons. The first fuel cells were developed around liquid electrolytes, but from a construction and handling point of view and in order to make the electrolyte as thin as possible to minimize internal resistance, solid electrolytes are very attractive and the electrolyte of interest here is the proton-conducting polymer. The cells are referred to as polymer fuel cells, polymer electrolyte fuel cells (PEFC), or polymer electrolyte membrane fuel cells/proton exchange membrane fuel cells (PEMFC).

In traditional PEMFC (based on polyperfluorosulfonic acid, PFSA), water is used as such a proton shuttle and the polymer membrane must be highly humidified in order to maintain proton conductivity. An increase in operating temperature from 80 to 150 °C leads to an increase of the water vapor pressure from 0.47 to 4.8 bar (ten times) and the membrane will dry out and lose conductivity unless the fuel cell is

J.O. Jensen (✉) • D. Aili • Q. Li
Department of Energy Conversion and Storage,
Kemitorvet 207, 2800 Lyngby, Denmark
e-mail: jojen@dtu.dk; larda@dtu.dk; qfi@dtu.dk

H.A. Hjuler
Danish Power Systems ApS, Egeskovvej 6C, 3490
Kvistgård, Denmark
e-mail: hah@daposy.dk

operated under a correspondingly increased pressure, which is impractical in most cases. At 200 °C, the water vapor pressure is as high as 15 bar. Additionally, softening of PFSA membranes is mechanically limiting the operation at elevated temperatures.

The question is then: why increase the working temperature of a PEMFC? This fuel cell has been very successful and one of the key advantages is the low working temperature. Startup is easy, the gases need not to be preheated, the selection of construction materials is wide (including elastomers for sealing), and degradation processes are generally slower at lower temperatures. All this is true, but there are yet a number of advantages of a higher temperature.

Key drivers for the development have been (1) increased tolerance to fuel impurities (in particular, carbon monoxide) of the platinum catalyst, (2) easier water management or even no water management at all (when conduction is not depending on water), (3) easier thermal management (cooling) due to higher temperature difference to the surroundings, and (4) a higher quality of the waste heat.

The fact that the tolerance to carbon monoxide increases with increasing temperature is well known from phosphoric acid fuel cells (PAFC), which also apply platinum as electrocatalysts. The carbon monoxide tolerance is critical if the fuel is hydrogen obtained via reforming (chemical conversion) of carbon containing fuels. In this process, the carbonaceous fuel is converted into hydrogen and carbon dioxide, but traces of carbon monoxide are always present as a by-product. Carbon monoxide adsorbs strongly to platinum surfaces and blocks the access of hydrogen. At 80 °C, a carbon monoxide content as low as 20 ppm (0.002 %) in the fuel stream results in a significant loss in cell performance, but at 160 °C, even 0.5–1 % carbon monoxide has only a minor effect. Therefore, very pure hydrogen or a complicated cleaning system is mandatory for the low temperature PEMFC, but not for high temperature PEMFC. Cells can thus be easily operated on abundant fuels like methanol, natural gas (methane), or liquefied petroleum

gas (LPG) through reforming when a hydrogen infrastructure is missing.

In a conventional low temperature PEMFC, a careful management of the water balance (water management) to maintain a high degree of hydration of the membrane is a delicate matter. It is crucial for maintaining high conductivity and is done by humidification of the gas flows into the fuel cell. Water is also produced in the cell and if the net content gets above saturation water condenses and blocks gas channels and porosities leading to a severe performance drop. The water management is further complicated by a high electroosmotic drag of water, i.e., water transport along with the protons, in PFSA membranes. At temperatures above the boiling point of water at the actual operating pressure, condensation cannot take place. This is indeed the case in a high temperature PEMFC. Moreover, if conduction is based on another proton carrier than water, then water management should be much less intensive or even needless.

Easier cooling of PEMFC is a wish of the automotive industry because even though fuel cells produce less heat than small internal combustion engines (ICE), heat removal is more challenging with a low temperature fuel cell. While the ICE rejects most of its heat through the exhaust and a smaller part through the cooler, the fuel cell does so mostly via the coolant loop and a radiator. Besides, the temperature difference between the coolant and the surrounding is smaller in case of an 80 °C fuel cell than of the ICE. The transfer of more heat by means of a smaller temperature difference calls for a much larger radiator, which is not convenient for the auto developers. A fuel cell working temperature of 120–130 °C should be enough to compensate for this effect. Similarly, if a high temperature PEMFC is air cooled, the air flow needed is much smaller because it carries more heat per volume and a smaller and less energy-intensive blower can be applied. Finally, as about half of the energy of the fuel is converted into heat in a fuel cell, it would be most desirable if this heat could be better utilized. The number of uses for this heat rises with temperature.

The doing away with CO purification, water management, and extensive coolers allows for a simpler and possibly less costly system architecture. The saying of the fuel cell company, Serenergy, encompasses this fact: “The power of simplicity.”

There are two ways to a higher operating temperature of PEMFCs. One is to pursue more efficient humidification at high temperatures either by increasing pressure or by enhancing water retention or self-humidification by produced water. The other way is to use less volatile proton carriers in the membrane. Different approaches to better water retention at high temperature have been explored. Alternative PFSA membranes with shorter side chains and higher crystallinity and particularly their composites with inorganic fillers have shown some feasibility, often in association with a slightly higher pressure, as described in Chap. 2. In the search for alternative proton carriers, inorganic proton-conducting materials in the forms of oxyacid salts (e.g., phosphates and pyrophosphates) and solid acids (e.g., CsHSO_4 and CsH_2PO_4) have been extensively explored. Fuel cell electrolytes made of such solid inorganic proton conductors as the main constituent are however rather ceramic than polymer electrolytes and not included in this book. Interesting is also the significant amount of work on organic–inorganic composites, of which only selected work in connection to polybenzimidazole (PBI) is presented. The most successful nonvolatile proton carrier to replace water in the membrane is phosphoric acid (H_3PO_4).

Phosphoric acid is unique with respect to its high thermal stability and proton conductivity at high concentrations. Based on concentrated phosphoric acid (85–100 wt%) as electrolyte, the phosphoric acid fuel cell technology operates at temperatures up to 210 °C. The use of concentrated acid substantially minimizes the water vapor pressure. Significant dehydration of phosphoric acid takes place at above 200 °C under limited atmospheric humidity, resulting in the formation of condensed strong acids, which are relatively stable and possess reasonable conductivity. Consequently, the electrolyte is

able to operate at very low water activity without significant loss of the proton conductivity. The combination of very low volatility and nearly anhydrous conductivity in a wide temperature range allows for an easy control of airflow, humidity, and stack temperature, compared with the PFSA-based PEM fuel cells. The stack temperature can be in a wide range, say, from 150 to 210 °C. This wide temperature range of operation, in turn, allows for a combination of the dynamic load and easy cooling by either process air, a liquid, or by evaporation. The conventional phosphoric acid fuel cells use a brittle ceramic matrix layer of silicon carbide in which the electrolyte is confined. It must be free from pinholes, cracks, and un-wetted areas in order to prevent the gas crossover. For the same reason, it should have a high bubble breakthrough resistance and it should have significant mechanical strength. Consequently, such electrolyte layers typically have a thickness of 100–200 μm . A strong, flexible, and elastic polymer matrix is highly desirable for phosphoric acid-based fuel cells.

Having found the proton carrier, the next step is to find a suitable host polymer that possesses the appropriate thermal stability and compatibility with phosphoric acid in the desired temperature range. Using a basic polymer is a general practice via acid–base interactions with the acid. For this, the most successful polymers are PBIs, a large family of heterocyclic polymers with excellent thermal, chemical, and mechanical stabilities. PBI variants, their blends as well as analogues such as pyridine containing aromatic polymers are chosen as the focal point of this book.

It has often been debated whether the fuel cell built around a phosphoric acid containing polymer is a PEM fuel cell or a phosphoric acid fuel cell in a polymeric disguise. The most correct understanding is probably that it is a hybrid between the two.

From a materials science point of view, the acid–base chemistry plays a key role in the acid doping and resulted in essentially one-phase solid membranes with good homogeneity. The membranes may contain up to about 90 wt%

phosphoric acid networked by the polymer. In a molar ratio, this corresponds to a wide range from 10 to 40 molecules of phosphoric acid per polymer repeat unit and the membranes still possess sufficient mechanical strength for handling and processing without the need for a support. From a practical point of view, the electrolyte thus behaves like a membrane and is handled as such. Its gas tightness does not depend on the acid as it does in the matrix of a phosphoric acid fuel cell, and it can be processed into almost as thin sheets as one might like. The small thickness compensates the reduced proton conductivity compared to the liquid acid. It is flexible and elastic. The membrane in a typical thickness of a few to over a 100 μm is the support for the catalysts or electrodes in the fuel cell assemblies. Beyond the periphery of active electrodes the membrane is self-standing, allowing for easy seal and stacking of the cells. Such a membrane can

tolerate a pressure difference of at least 2–3 bars, convenient for the fuel cell construction and operation. Compared to fuel cells with liquid acid electrolytes, no reservoir, little management, and much less creeping of the electrolyte occurs. On the other hand, proton conduction is brought about by phosphoric acid which is a fundamental property shared with the phosphoric acid fuel cell, as discussed above.

Should we finally return to the argument whether the fuel cell based on an acid-doped polymer is a PEMFC or a PAFC, we notice that it is common and exclusive practice within the community developing the technology to name it a high temperature PEM fuel cell, and the title of this book reflects that. One could argue slightly sarcastically that if the fuel cell addressed in this book is claimed not a polymer fuel cell but rather a phosphoric acid fuel cell, then the conventional PEMFC is not a polymer fuel cell either, but rather a water fuel cell.☺

Antonino S. Aricò, Vincenzo Baglio, Francesco Lufrano, Alessandro Stassi, Irene Gatto, Vincenzo Antonucci, and Luca Merlo

2.1 Introduction

Hydrogen is the candidate fuel for future fuel cell-based electrical vehicles. It can be produced in a sustainable way from renewable energies [1]. Overcapacities in electricity production from renewable energy sources can be suitably addressed by converting the surplus of electrical energy into hydrogen [1]. Proton exchange membrane (PEM) electrolyzers can thus be combined with renewable energy sources for peak shaving in integrated systems or for grid independent operating conditions. Hydrogen generated through electrolysis is stored and optionally used to refill fuel cell-based cars.

Due to the intermittent character of renewable power sources, it may be necessary for short time periods to sustain a power input significantly larger than that conventionally managed by the PEM electrolyser. This issue is also occurring in the case of fuel cell application in the automotive field [2]. Under some circumstances, the electrochemical device operates at an efficiency lower than that designed for normal operating

conditions and there is a significant heat release in the device causing considerable increase in temperature. This problem should be in principle managed at the materials level without increasing the complexity of the system (balance of plant), e.g., by adding cumbersome and expensive cooling devices. As well known, the polymer membrane is the material that mainly suffers from this problem due to the low glass transition temperature of most of the commercial membranes and their dehydration characteristics causing loss of mechanical properties and ionic conductivity at intermediate temperature [2]. Accordingly, there is the need to develop membranes with higher glass transition temperature, a higher fraction of crystallinity and capability of water retention at high temperature in order to keep suitable ion conduction [2]. Perfluorinated sulfonic acid membranes combine suitable properties for rapid startup of electrochemical systems, excellent performance (high conductivity and stability), capability to sustain duty cycles, and therefore a good candidate to be properly modified for high temperature operation.

For portable and assisted power units, the use of organic liquid fuels is characterized by high energy density and easy handling appears promising [3]. The electromotive force associated to the electrochemical oxidation of methanol or ethanol to CO_2 is comparable to that of hydrogen oxidation to water. Both

A.S. Aricò (✉) • V. Baglio • F. Lufrano • A. Stassi
I. Gatto • V. Antonucci
CNR-ITAE, Via Salita S. Lucia sopra Contesse 5,
Messina 98126, Italy
e-mail: arico@itae.cnr.it

L. Merlo
Solvay Specialty Polymers, Viale Lombardia 20,
Bollate (MI) 20021, Italy

methanol and ethanol have promising characteristics in terms of reactivity at low temperatures, storage, and handling. However, despite these practical system benefits, direct alcohol fuel cells are characterized by a significantly lower power density and lower efficiency than a PEM fuel cell operating with hydrogen. This is due to the slow oxidation kinetics of methanol/ethanol and the fuel cross-over from the anode to the cathode [3].

The strong activation control of the methanol and ethanol oxidation reactions indicates that the high temperature operation is the most useful strategy to increase the performance [3]. High temperature operation allows to achieve high current densities with consequent fast methanol/ethanol consumption at the anode/electrolyte interface. This effect reduces the concentration gradient allowing to decrease the methanol cross-over [3]. Accordingly, the low reaction rate can be efficiently improved by increasing the operating temperature from the conventional 60–80 °C to 120–150 °C; however, this also requires the development of membranes characterized by suitable characteristics for intermediate temperature operation such as suitable proton conductivity, proper stability, and moderate cross-over. Composite membranes containing inorganic fillers have shown suitable properties for intermediate temperature operation and reduced methanol cross-over as consequence of a suitable water retention and an increased tortuosity factor caused by the presence of the filler particles inside the membrane [4].

This chapter reviews characteristics and performance of modified sulfonic acid-based membranes, particularly composite membranes including inorganic fillers and short-side chain perfluorosulfonic membranes for intermediate temperature applications. The characteristics of these systems for operation in direct alcohol fuel cells, in polymer membrane (PEM) electrolyser and automotive PEM fuel cells are analyzed.

2.2 Composites Membranes Containing Inorganic Fillers

2.2.1 Composite Perfluorosulfonic Acid Membranes for Direct Methanol Fuel Cells

A low cost and high temperature membrane, with suitable ionic conductivity and stability from ambient temperature up to 150 °C, would be a potential solution to some of the drawbacks presently affecting PEM direct methanol and ethanol fuel cells (DMFCs, DEFCs) [3]. Fuel cell operation at elevated temperatures can limit the effects of electrode poisoning by adsorbed CO molecules, increase both methanol oxidation and oxygen reduction kinetics, and simplify water and thermal management. Furthermore, high temperature operation can reduce the complexity of the reforming reactor employed for PEMFCs [5], the temperature range from 130 to 150 °C is ideal for application of these systems in electric vehicles and for distributed power generation.

Various proton-conducting polymer electrolyte materials have been investigated for high temperature operation. Two categories of membranes have been proposed, depending on whether water is required for proton conduction or not [6]. Polymer electrolytes involving water molecules in the proton mobility mechanism (e.g., perfluorosulfonic membranes) need humidification to maintain suitable conductivity characteristics [7]. The amount of humidification may vary depending on the operating temperature and membrane properties; it influences the size and complexity of the device. Some other electrolytes do not necessarily involve water molecules in the mechanism of proton conduction, e.g., polybenzimidazole(PBI)/H₃PO₄ [8], blends of PBI and polysulfone [9], hybrids of polymers and proton-conducting inorganic compounds such as Zr(HPO₄)₂ [10], etc.). The acid-doped PBI membranes are the major subject of this book and will be well described in the

other chapters. Here the discussion is focused on composite perfluorosulfonic membranes containing different types of inorganic fillers such as hygroscopic oxides [4], surface modified oxides [7, 11], zeolites [12], inorganic proton conductors [13], and so on have shown an increased conductivity with respect to the bare perfluorosulfonic membranes at high temperatures and DMFC operation up to about 150 °C has been demonstrated (Fig. 2.1).

The mechanism enhancing proton conduction at such temperatures is still subject of debate [6]. There is evidence that such an effect is mainly due to the water retention capability of the filler [6]. In fact, some of these compounds, for example, silica, zeolites, and so on are

frequently used as desiccant materials in storage systems. In this application, after some time, saturation by the environment humidity occurs. The desiccant materials are “re-activated” by desorbing the condensed water at temperatures around 120–150 °C [6]. This fact indicates that such materials may physically adsorb and retain water on the surface at temperatures close to those ideal for PEMFC/DMFC operation in automotive applications [2]. In the adsorption process, the first layer involves a chemical interaction between the surface sites of the filler and water. Generally, this causes a water displacement on the surface with formation of a chemical bond between water residues and filler functional groups [14].

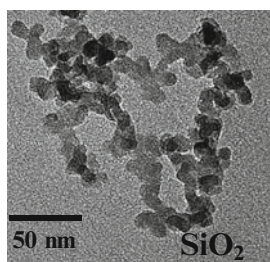
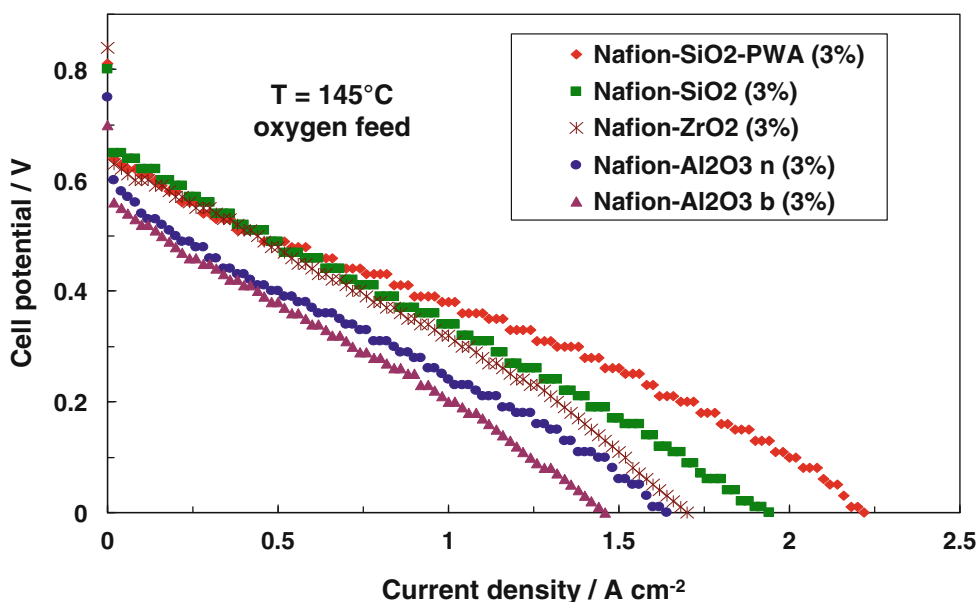


Fig. 2.1 Direct methanol fuel cell polarization curves at 145 °C for MEAs containing different inorganic fillers (*top*). Methanol feed 2 M, 2.5 atm (gauge pressure); oxygen

feed 2.5 atm (gauge pressure). Pt loading $2 \pm 0.1 \text{ mg cm}^{-2}$. A typical filler morphology is shown (*bottom*). Reproduced from [7] with permission of Elsevier

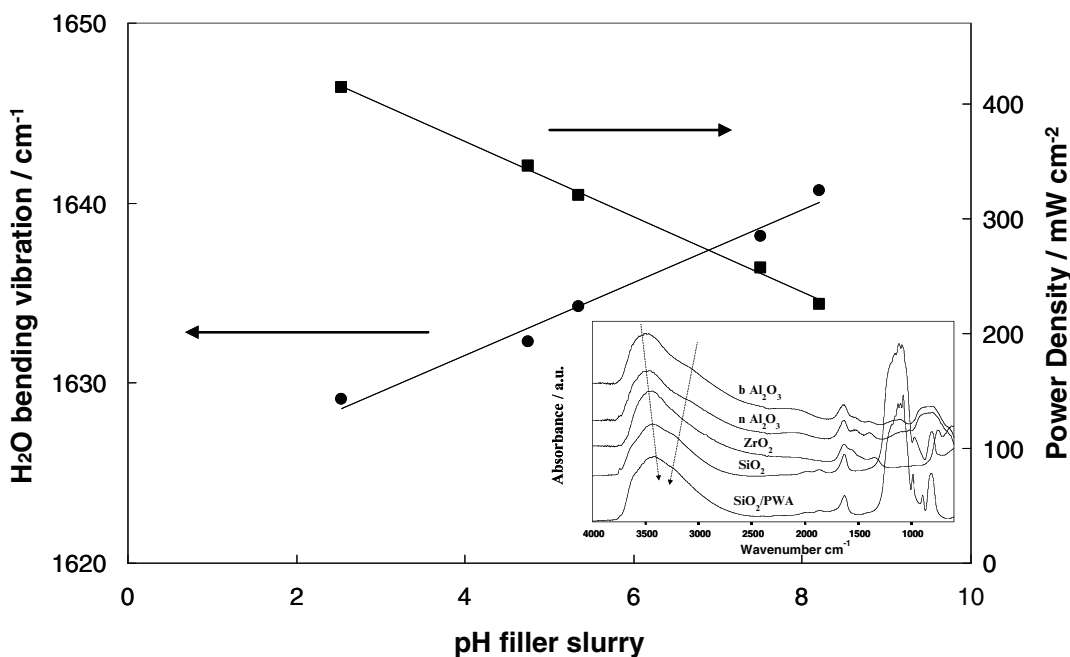


Fig. 2.2 Variation of O–H bending vibration frequencies of physically adsorbed water and DMFC maximum power density vs. the pH of slurry of the fillers. The *inset* shows

the FT-IR spectra. Reproduced from [14] with permission of Elsevier

Figure 2.2 shows the correlation between the characteristics of adsorbed water on the filler surface and the DMFC power density at high temperatures. Multiple layers of adsorbed water may form subsequently by physical interaction involving Van der Waals bonds. In this case, no displacement of water should occur. Such bonds become weaker as the distance of the physically adsorbed water from the surface increases. Whereas, chemically adsorbed water can involve up to a monolayer, physical adsorption and water condensation in the pores may build up a shell of water molecules surrounding the primary particles and agglomerates of the inorganic filler [14].

Most of these inorganic materials used as fillers have intrinsically low proton conduction up to 150 °C. It has been observed that they can be loaded with a proper dispersion in amounts up to 3–5 % inside the membrane without affecting significantly the conductivity at or below 90 °C [7]. However an increase in the operating temperature is possible in the presence of the filler [6]. A proper distribution of the nanoparticle filler in the membrane water channels can

maximize the effect of water retention in the conduction path at high temperatures. The presence of hygroscopic inorganic oxides inside the composite membrane, besides extending the operation of perfluorosulfonic membranes (e.g., Nafion) in the high temperature range, reduces the cross-over effects by increasing the “tortuosity factor” in the permeation path [11]. Such effects are of particular significance at high temperatures in DMFC systems. Presently, these membranes appear to operate better at moderate pressures since this allows one to maintain a suitable content of liquid water inside the assembly or to facilitate water condensation in the pores. In DMFC devices, cathode operation at high pressures reduces the system efficiency because of power consumption by the air compressor [2]; whereas, the power loss for the liquid pump at the anode is less remarkable. Although, significant progress has been achieved in the last few years on the development of composite membrane-based systems [6], the moderate pressure requirement (at least 0.5 bar gauge pressure), is actually the main feature limiting

large-scale applications of such composite electrolytes at temperatures above 100 °C.

Significant efforts have been made to address technical aspects concerning composite membranes development; fewer attempts have been devoted to an in-depth analysis of the basic mechanism of operation of such materials. A better understanding of the effects enhancing the proton conductivity at 150 °C in hybrid-membrane systems could allow one to identify new routes to enhance conductivity and reduce high pressure. In this regard, a wide range analysis of the filler and composite membrane properties is mandatory for a basic understanding. It appeared that an appropriate tailoring of the surface chemistry in these nanoparticles is a key step towards enhancing water retention at high temperatures [15].

A rational analysis of filler effects on structural, proton transport properties and electrochemical characteristics of composite perfluorosulfonic membranes for Direct Methanol Fuel Cells (DMFCs) was reported [7]. It has been observed that a proper tailoring of the surface acid–base properties of the inorganic filler for application in composite Nafion membranes allows appropriate DMFC operation at high temperatures and with reduced pressures [7]. An increase in both strength and amount of acidic surface functional groups in the fillers would enhance the water retention inside the composite membranes through an electrostatic interaction, in the presence of humidification constraints, in the same way as for the adsorption of hydroxyl ions in solution [7].

It was observed that the surface acidity of the fillers influences the bending and stretching vibrational frequencies of the water physically adsorbed on the filler surface [6, 14]. The conductivity of composite membranes and maximum power density of DMFCs at 145 °C appear to be related to the characteristics of the water adsorbed on the filler particles [6, 14]. Inorganic fillers characterized by acidic properties undergo a strong interaction with water and enhance the DMFC performance at high temperatures. The self-diffusion coefficients of water and methanol have been determined over

a wide temperature range by PFGSE ^1H NMR method [6]. The transport mechanism appears to be influenced by the surface properties of the inorganic fillers. It was observed that acidic fillers, such as silica, promote proton transport in the composite membrane with respect to basic fillers, e.g., alumina [6]. An interaction of the silica surface with methanol molecules is also envisaged from the analysis of proton self-diffusion coefficients of methanol.

Thus, acid–base properties of inorganic fillers play a key role in the water uptake of composite Nafion-based membranes at temperatures close to 150 °C by influencing the proton conductivity of the electrolyte. The presence of acidic OH groups on the particle surface facilitates water coordination which acts as a vehicle molecule for proton migration. Physically adsorbed water, forming a multilayer shell around the filler nanoparticles, is desorbed from the inorganic fillers surface at around 130 °C, causing an inversion in the conductivity vs. temperature behavior. This determines a minimum in the value of cell resistance around this temperature (Fig. 2.3).

DMFC performances of various MEAs based on composite membranes, containing fillers with different acid–base characteristics are found to increase as the pH of the slurry of the inorganic filler decreases (Fig. 2.4). These results indicate that the ionic conductivity of the composite membranes and their range of operation may be increased by an appropriate tailoring of the surface characteristics of the ceramic oxides inside the membrane. For materials characterized by the same type of surface functional groups, the effect of the filler surface area becomes prevailing in determining the water retention properties of the composite membranes at high temperatures. This effect appears to be associated with the larger number of water-adsorbing acidic sites on the filler surface. As expected, the surface properties play a more important role than the crystalline structure of the filler, since the water molecules acting as promoters towards the proton migration are effectively coordinated by the surface groups.

The conductivity and performance of composite perfluorosulfonic membranes in DMFCs are

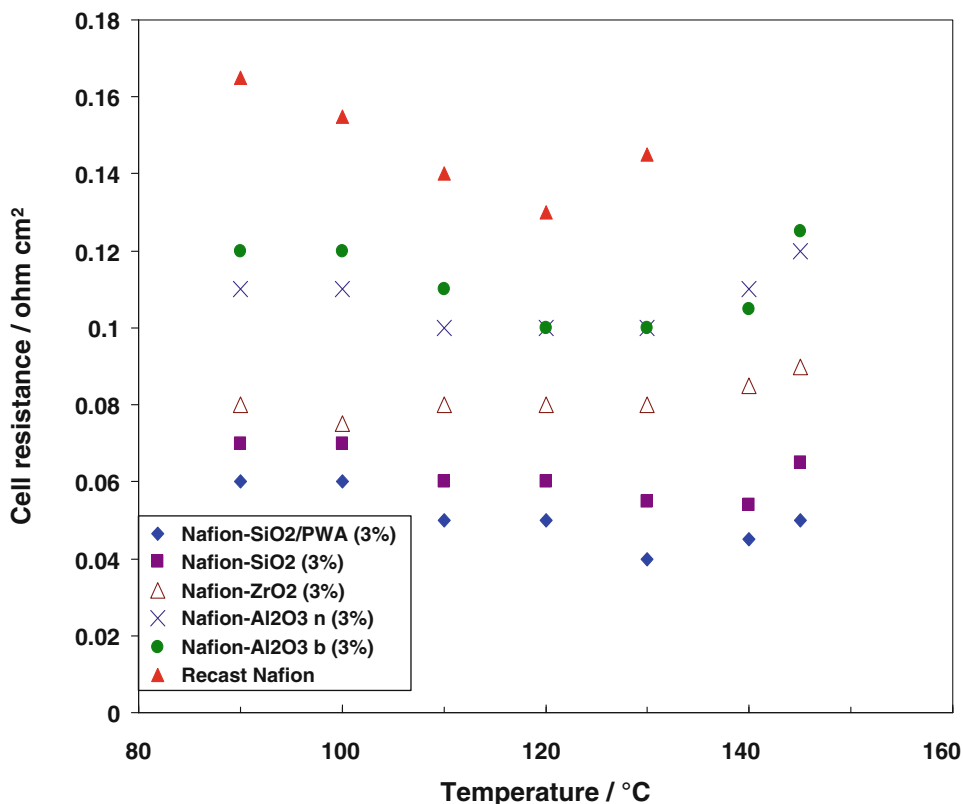


Fig. 2.3 Variation of cell resistance as a function of temperature in DMFCs equipped with composite membranes containing inorganic fillers. Reproduced with from [7] with permission of Elsevier

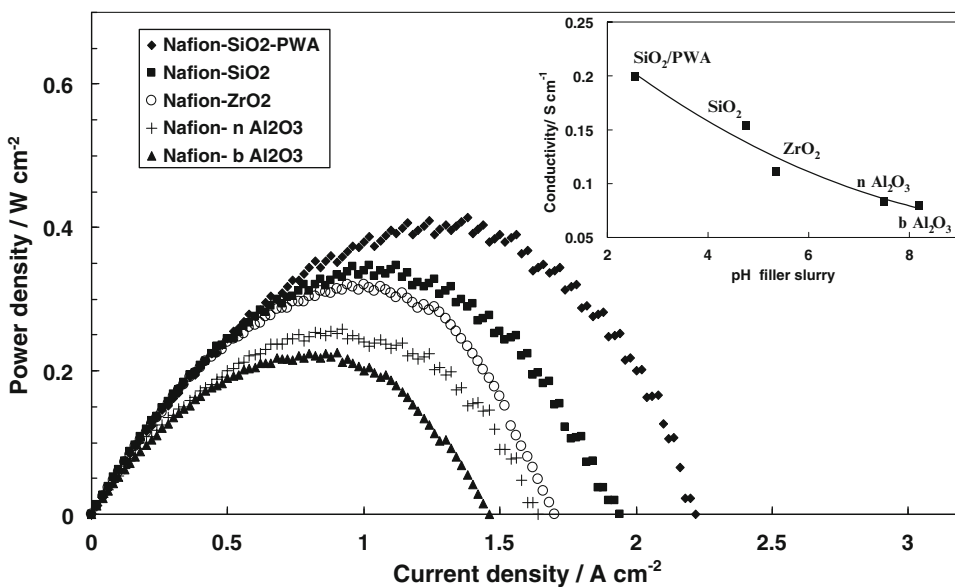


Fig. 2.4 DMFC power density curves at 145 °C for MEAs containing different inorganic fillers. Methanol feed 2 M, 2.5 atm (gauge pressure); oxygen feed 2.5 atm (gauge pressure). Pt loading $2 \pm 0.1 \text{ mg cm}^{-2}$. The inset

shows the variation of membrane conductivity at 145 °C as a function of the pH of slurry of the filler. Reproduced [6] with permission of Wiley

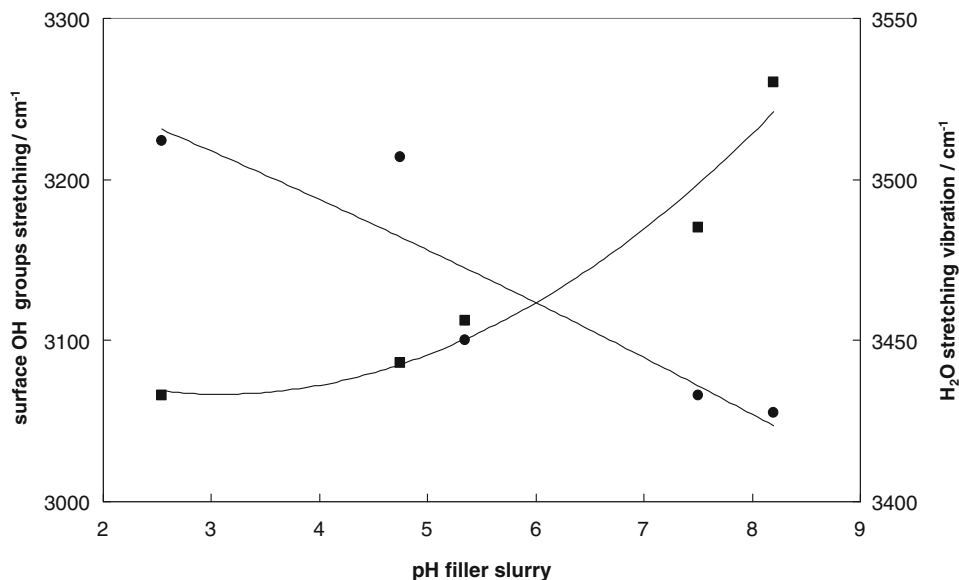


Fig. 2.5 Variation of O–H stretching vibration frequencies for surface OH functionalities and physically adsorbed water vs. the pH of slurry of the fillers. Reproduced from [14] with permission of Elsevier

strongly related to the surface acidity, which in turn influences the characteristics of the water physically adsorbed on the inorganic filler surface. It has been observed that the more acidic the filler surface is the larger the capability to undergo a strong interaction with water through the formation of hydrogen bonds. This latter effect produces a decrease in the O–H stretching and bending frequencies in the physically adsorbed water (Fig. 2.5). Furthermore, an increase in the water uptake in the composite membrane and an enhancement of the proton conductivity are observed in the presence of acidic fillers [7]. The proton migration inside the membrane appears to be assisted by the water molecules on the surface of the nanofiller particles and could also be promoted by the formation and breaking of hydrogen bonds [6].

Operation at low pressure causes a decrease of performance but it does not appear to introduce significant technical limitation for the hydration/conductivity characteristics of composite membranes in high temperature DMFCs (Fig. 2.6). Reduction of the applied pressure causes a reduction of the fraction of liquid water inside the system and, to some extent, the water retention ability. However, the lower

consumption of electrical power needed for the auxiliaries passing from a compressor to an air blower would probably more than compensate for the power output losses due to the small increase in resistance.

On the other hand, in the absence of methanol-tolerant oxygen reduction catalysts, high oxygen partial pressures are needed for proper cathode operation in the presence of methanol cross-over.

2.2.2 Composite Hydrocarbon Membranes for DMFCs

The composite membrane approach can also be used for membranes alternative to Nafion such as sulfonated polyetherketones and polysulfones. Sulfonated polysulfone is one of the most promising polymers for PEMs due to its low cost, commercial availability, and easy processability. Composite polysulfone-based membranes based on silica have been prepared and characterized for DMFC to extend the operating temperature up to 120 °C [16]. As an example, the following describes the preparation and characterization of a

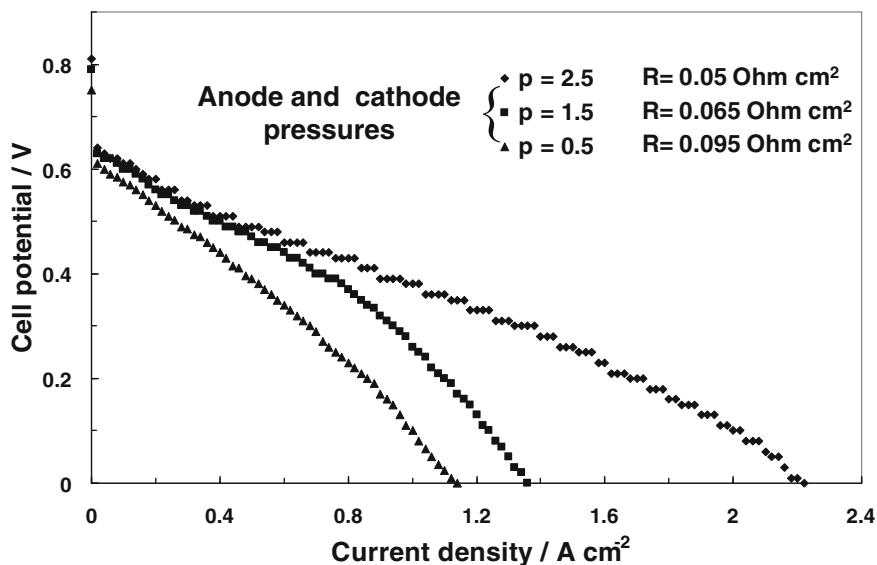


Fig. 2.6 DMFC polarization behavior for the hybrid Nafion–PWA–SiO₂ membrane at 145 °C at different operating pressures. Reproduced from [7] with permission of Elsevier

composite polysulfone-based hydrocarbon membrane for DMFC.

The synthesis of sulfonated polysulfone has been performed by a post sulfonation method using trimethyl silyl chlorosulfonate as a mild sulfonating agent [16]. Bare polysulfone membranes were prepared with different sulfonation levels (e.g., 60 %, SPSf-60 and 70 %, SPSf-70), whereas a composite membrane of SPSf-60 was prepared with 5 wt% silica filler (SPSf-60-SiO₂).

Figure 2.7 shows the different steps of the synthesis procedure. The commercial polysulfone Udel (Amoco) was dissolved in chloroform at a temperature of 25 °C and subsequently treated with trimethylsilyl chlorosulfonate (Aldrich) to produce a silyl sulfonate polysulfone. The amount of the intermediate product was controlled by the molar ratio of the sulfonating agent to the polymer repeating unit and varied from 2 to 2.3. The reaction time was 24 h at a temperature of 25 ± 0.1 °C. The obtained silyl sulfonate polysulfone polymer was then treated with a 30 wt% sodium methoxide/methanol solution (2.26 mmol g⁻¹ of polysulfone) at 25 °C for 1 h, which was used to cleave the silyl sulfonate moieties, yielding the sodium

sulfonated polysulfone. The polymer was recovered by precipitation with ethanol. The precipitate was separated from the mother liquor by filtration, vigorously washed with ethanol, and rinsed several times with distilled water. Finally, the sulfonated polysulfone powders were dried in an oven for at least 48 h at 110 °C for complete removal of solvents. The obtained SPSfNa polymer powders were dissolved in (0.5–1 g) 5–10 mL of *N,N*-dimethylacetamide (DMAc) at ambient temperature to form a homogeneous solution. The membrane was afterwards prepared by casting the SPSfNa solution on a glass plate and the solvent was slowly evaporated at a temperature of 50 °C for at least 15 h. Subsequently, the membrane was peeled out from the glass with aid of distilled water, and then dried in oven at 80 °C under vacuum for at least 24 h. The membranes had thicknesses of about 80 μm in dry state. For some specific purposes, membranes of 150 μm were also prepared. Finally, the membranes were converted into acid form by treatment with 1 M HCl solution at 50–60 °C for 15 h and subsequently rinsed with water several times. Composite membranes with a silica content of 5 wt% in SPSf-60 were prepared by using the following procedure. SPSfNa (0.5 g)

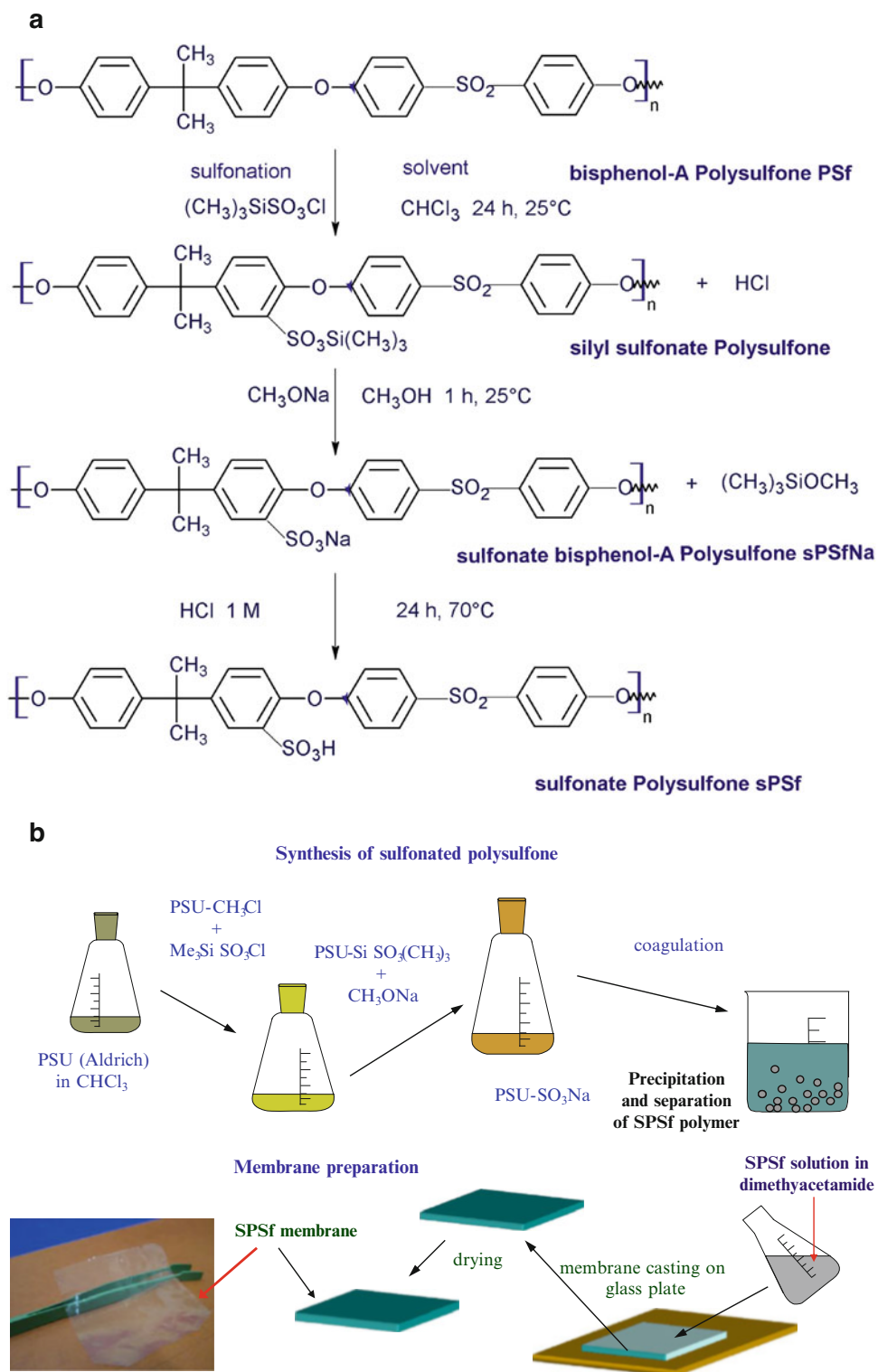


Fig. 2.7 (a) Synthesis of sulfonated polysulfone membranes. (b) Preparation of sulfonated polysulfone membranes. Reproduced from [16] with permission from Elsevier

was dissolved in 5 mL DMAc; silica (0.025 g of Cab-O-Sil, EH-5, particle size = 7 nm, by Cabot Corporation, Boston USA) was added to the solution, which was treated in an ultrasonic bath for 20 min. This solution was cast on a glass plate by a film applicator. The membranes, peeled out from glass, were dried at 80 °C under vacuum to remove traces of the solvent. The thickness of membranes was about 70–80 µm. The composite membranes were treated with HCl 1 M and then washed with distilled water.

The ion-exchange capacity (IEC) as well as their water and methanol uptake/swelling, measured at 25 and 80 °C, for these hydrocarbon membranes are reported in Table 2.1.

As can be observed from the table, the degree of sulfonation for the studied samples varied from 60 to 70 wt% as calculated by the elemental analysis. The water uptake for bare sulphonated polysulfone and SiO₂-doped membrane was ranging from 24 to 29 wt% at 25 and 80 °C; whereas, a high 2 M MeOH uptake of 38 ± 1 wt% was found at 80 °C. The degree of swelling was found to be significantly smaller than that of the solution uptake for all membranes. It was varied from 4 to 6 % at 25 °C; whereas these values rose up to 10 % upon the swelling in 2 M MeOH at 80 °C (Table 2.1).

Figure 2.8 shows the thermal properties for the bare polysulfone and for a sulfonated polysulfone sample. The DSC curves (inset in Fig. 2.8) show an increase in glass transition temperature from 187 °C for the bare polysulfone to about 205 °C for the sulfonated polysulfone. Moreover, it is observed an increase in glass transition temperature (T_g) with the increasing degree of sulfonation of the polymer. The upper limit of thermal stability of these materials, as shown by TGA curves, should be up to 220–250 °C after which the desulfonation process starts. From the inset of Fig. 2.8, it is also found that the desulfonation peak for the composite membrane compared to bare membranes is increased from 234 to 242 °C. This is attributed to the interaction of silica particles with the polymer matrix producing a slight increase of its thermal stability. The temperature of about

200 °C represents the onset of desulfonation for this type of ionomeric polymer. However, such phenomena could appear at temperatures slightly different than 200 °C, independent of the polymer structure and/or the presence in the bare polymer of side groups. These can mask the starting process of desulfonation or even accelerate it, as a function of the environment (type of gas, heating rate, etc.) in which it occurs. Therefore, with a reasonably good approximation, a practical fuel cell temperature up to 150–160 °C for this type of ionomeric polymers could be possible. As discussed, the performance of the membranes in H₂/air and methanol/air fuel cells depends on the mechanical, chemical, and electrochemical stability, as well as their capability to maintain high proton conductivity and good lifetime for DMFC performance under temperatures higher than 100 °C.

The surface morphology of the sulfonated polysulfone membranes was investigated by scanning electron microscopy (SEM), as shown in Fig. 2.9. The composite membrane shows a relatively uniform distribution of silica particles in the polymer matrix (see Fig. 2.9c and d). However, agglomeration of silica particles with dimensions in the range of 20–50 nm is also observed.

Variation of cell resistance values for MEAs based on these membranes as a function of the temperature is shown in Fig. 2.10. At temperatures lower than 90 °C, the cell resistance of the bare membrane is lower than that of the composite one, whereas at $T > 100$ °C there is an inversion and the composite membrane became less resistive. The water retention and ionic conductivity of the composite membrane at higher temperature ($T > 100$ °C) are greater than those of bare membranes. The behavior of the proton conductivity for the studied membranes is typical of thermally activated process. The recorded activation energy was 17 and 21.6 kJ mol⁻¹ for bare and composite membranes, respectively. Cell resistance values as low as ~0.1 Ω cm² (corresponding to a conductivity better than 7.5×10^{-2} S cm⁻¹) under operating temperatures of 100–120 °C can be achieved (Fig. 2.10).

Table 2.1 Characteristics of sulfonated polysulfone polymer membranes

Sample	X ^a	Level of sulfonation	IEC by titration (meq g ⁻¹)	Water uptake (%)	2 M CH ₃ OH uptake (%)			Swelling ratio in water (%)		Swelling ratio in 2 M CH ₃ OH (%)	
					80 °C	25 °C	80 °C	25 °C	80 °C		25 °C
SPSf-60	2.0	60	1.41	24.3	29.1	25.7	38.7	4.6	5.9	4.9	10.4
SPSf-70	2.3	70	1.42	32.5	–	31.9	–	6.3	–	6.2	–
^b SPSf-60-SiO ₂	2.0	60	1.35	24.3	28.9	25.3	38.2	4.8	6.2	5.1	10.6

^aMolar ratio of sulfonating agent to polymer repeating unit; reaction time 24 h at 25 °C^bSPSf-60 + 5 wt% SiO₂

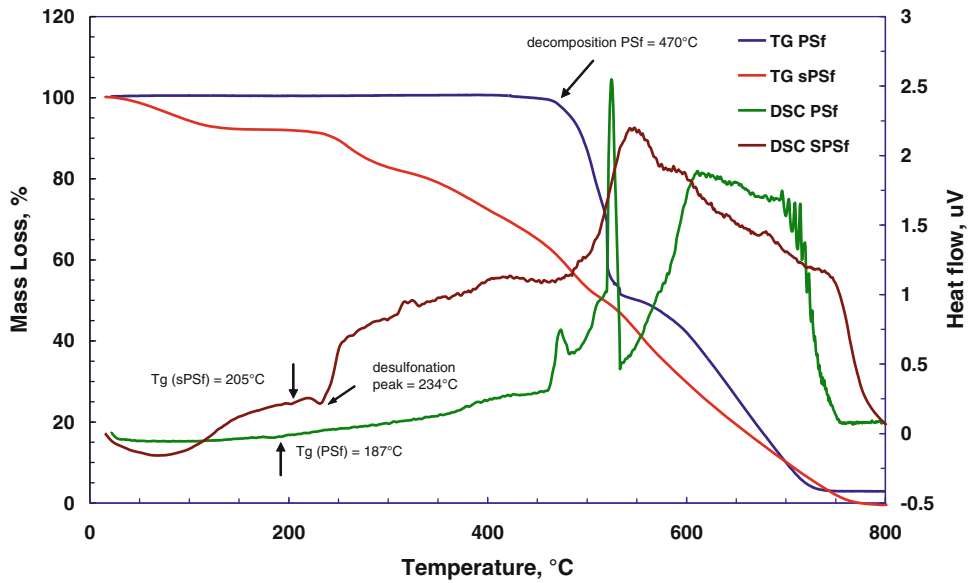


Fig. 2.8 TGA and DSC thermograms of polysulfone membranes. Reproduced from [16] with permission of Elsevier

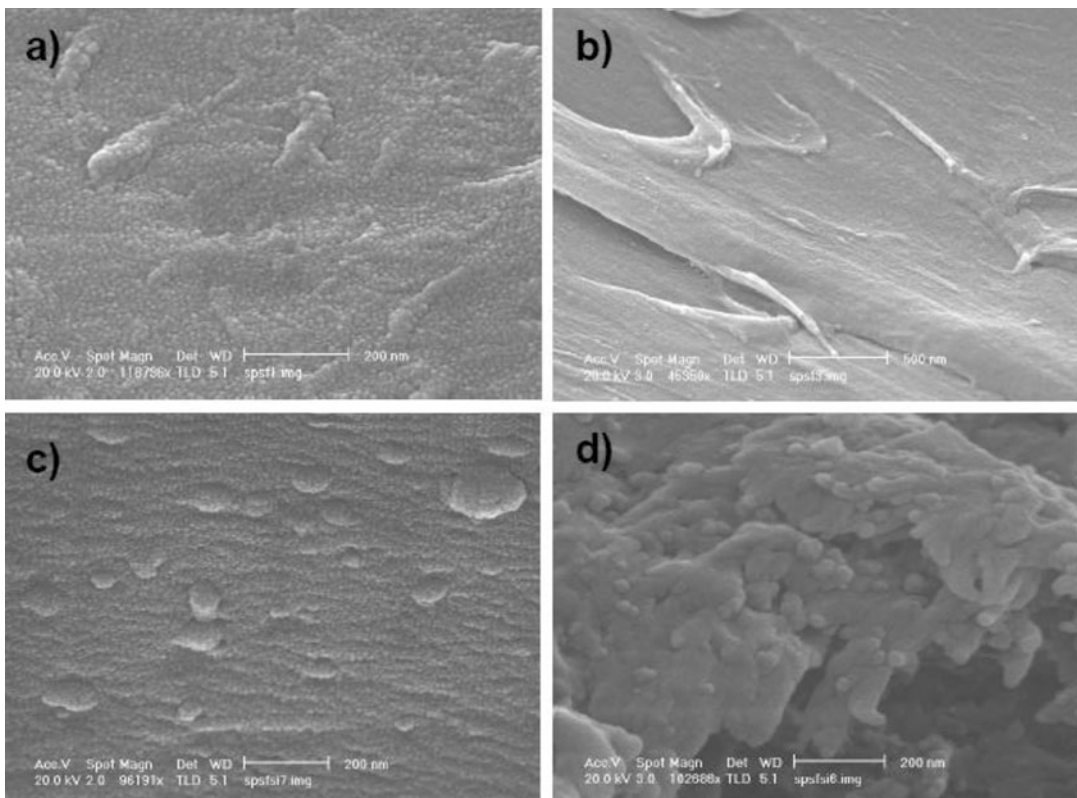


Fig. 2.9 Surface morphology of bare (a, b) and composite with silica filler nanoparticles (c, d) sulfonated polysulfone membrane

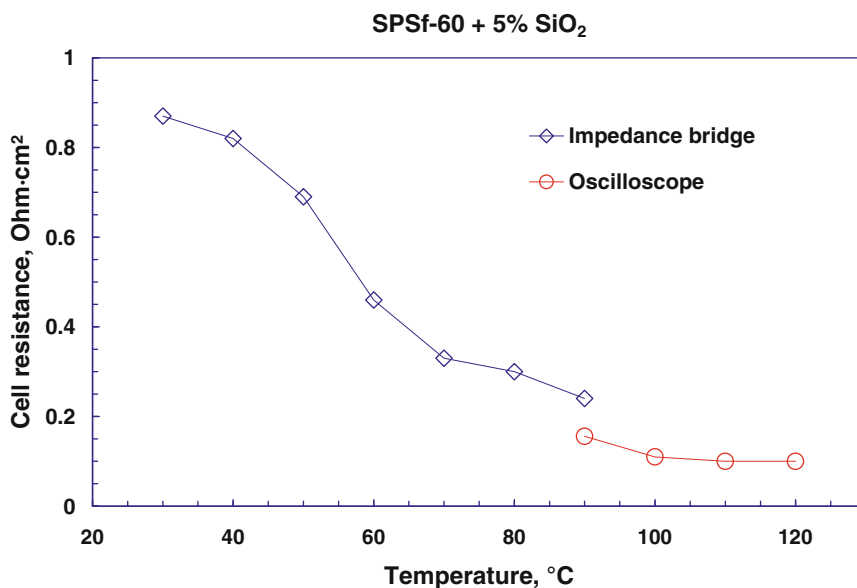


Fig. 2.10 Cell resistance and proton conductivity of composite silica-sulfonated polysulfone membrane as a function of the temperature. The measurement was carried out at open circuit voltage up to 90 °C and under operation with a load of 200 mA cm⁻² from 90 to 120 °C

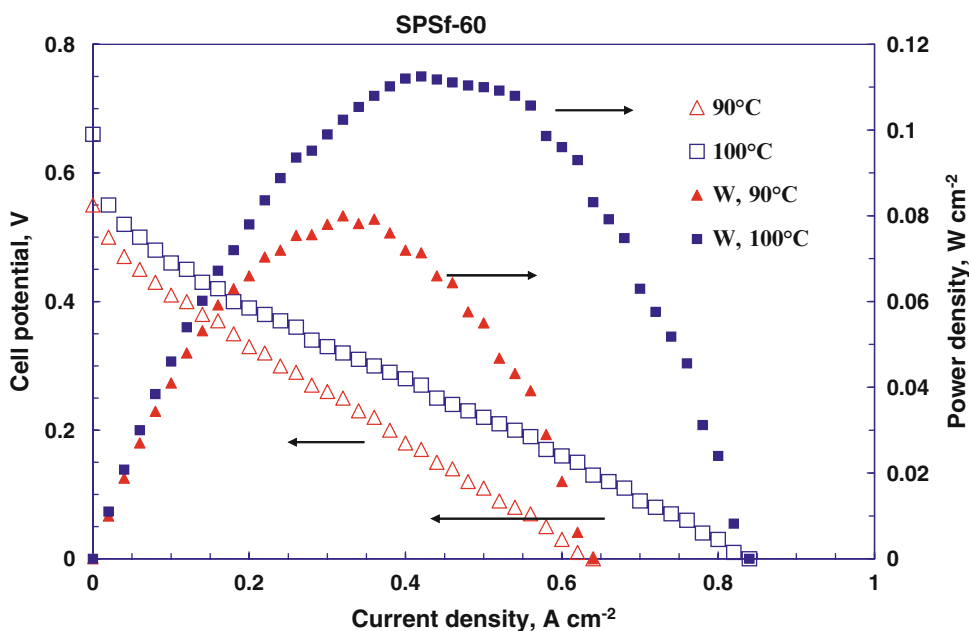


Fig. 2.11 Polarization and power density curves for a cell equipped with sulfonated polysulfone, SPSf-60, at 90 and 100 °C in 2 M MeOH/O₂. Reproduced from [16] with permission of Elsevier

These sulfonated polysulfone membranes have been investigated in DMFCs operating at high temperatures (100–120 °C). Figure 2.11 shows the DMFC performances at 90 and

100 °C for the cell equipped with sulfonated polysulfone membrane. The fuel cell performance at 100 °C compared to 90 °C shows a lower open circuit voltage (OCV) (0.77

vs. 0.85 V) but higher power density (~140 vs. ~120 mW cm⁻²). A further increase in cell temperature produced a decrease in cell performance and an unstable behavior for the bare membrane, due to strong dehydration under these conditions. The composite membrane presents better water retention at temperatures above 100 °C [3]. When the fuel cell temperature is raised, there is also an enhancement of the methanol electro-oxidation kinetics. The fuel cross-over decreases the OCV due to the presence of a mixed potential at the cathode, whereas the improved electro-kinetics is generally associated with higher power densities. Thus, the negative effect of increased methanol cross-over is counterbalanced by a decrease of the activation energy of the methanol electro-oxidation reaction.

DMFC polarization curves for the cell equipped with the composite membrane in a wide temperature range are reported in Fig. 2.12. The performance increases significantly with the cell temperature. The maximum power density for the cell with the composite membrane at 120 °C is 180 mW cm⁻² which is a performance of relevant interest for DMFCs being achieved with a hydrocarbon membrane [16].

A direct comparison of the present results with those obtained with other non-perfluorinated ionomer membranes on the basis of the current literature is not easy, since generally the physicochemical and electrochemical characteristics of the sulfonated ionomers are different. Moreover, it is difficult to compare fuel cell performance, when different kinds of catalysts (supported or unsupported) and various noble metal loadings (mg/cm²) are used as well as when the DMFC measurements are performed at different pressures and temperatures. It appears that the performance of composite perfluorosulfonic acid (PFSA) membrane-based MEAs is generally better than the corresponding hydrocarbon counterpart. This is due to the effect of higher conductivity and better interface with the electrodes.

On the other hand, a general advantage of sulfonated polysulfone compared to Nafion-type

membranes is that the non-perfluorinated membranes exhibit lower methanol cross-over; this may in part compensate for the lower performance.

2.2.3 Short-Side Chain PFSA Membranes for DMFCs

Conventional ion-exchange perfluoropolymer membranes such as the well-known Nafion[®] membrane are based on long-side chain polymers (LSC). In the last decades, Solvay has developed a new short-side chain (SSC) proton-conducting perfluoropolymer membrane, i.e., Aquivion[®] (previously Hyflon[®] Ion membrane). Aquivion[®] is characterized by excellent chemical stability and equivalent weight (850 g eq⁻¹) lower than conventional Nafion 117 (1100 g eq⁻¹) [2] (Fig. 2.13). The Aquivion[®] SSC ionomer is prepared from a free radical copolymerization of the Sulfonyl Fluoride Vinyl Ether (SFVE) monomer with the tetrafluoroethylene (TFE) in aqueous media by using a fluorinated surfactant in emulsion or micro-emulsion conditions. A TFE pressure between 9 and 11 bar of TFE is typically used for obtaining a polymer with EW of 790 g eq⁻¹. The reactivity of TFE is sensitive to pressure changes. This parameter is fundamental when the molar composition needs to be controlled. The latex is stripped for removing the residual monomers and then coagulated by freezing–thawing (or eventually by addition of electrolytes). The polymer powder (with the functional groups in –SO₂F form) is then washed in water several times and dried at high temperatures. The precursor polymer powder, after drying, is pelletized and melt-extruded into films in a screw extruder at a temperature at least 30 °C above the complete melting of the polymer as determined by differential scanning calorimetry (DSC). The film is then hydrolyzed with a process comprising the first step in hot, strong bases (usually potassium hydroxide or sodium hydroxide) and the second step in strong acid.

Besides the improved conductivity related to the higher degree of sulfonation, the short-side

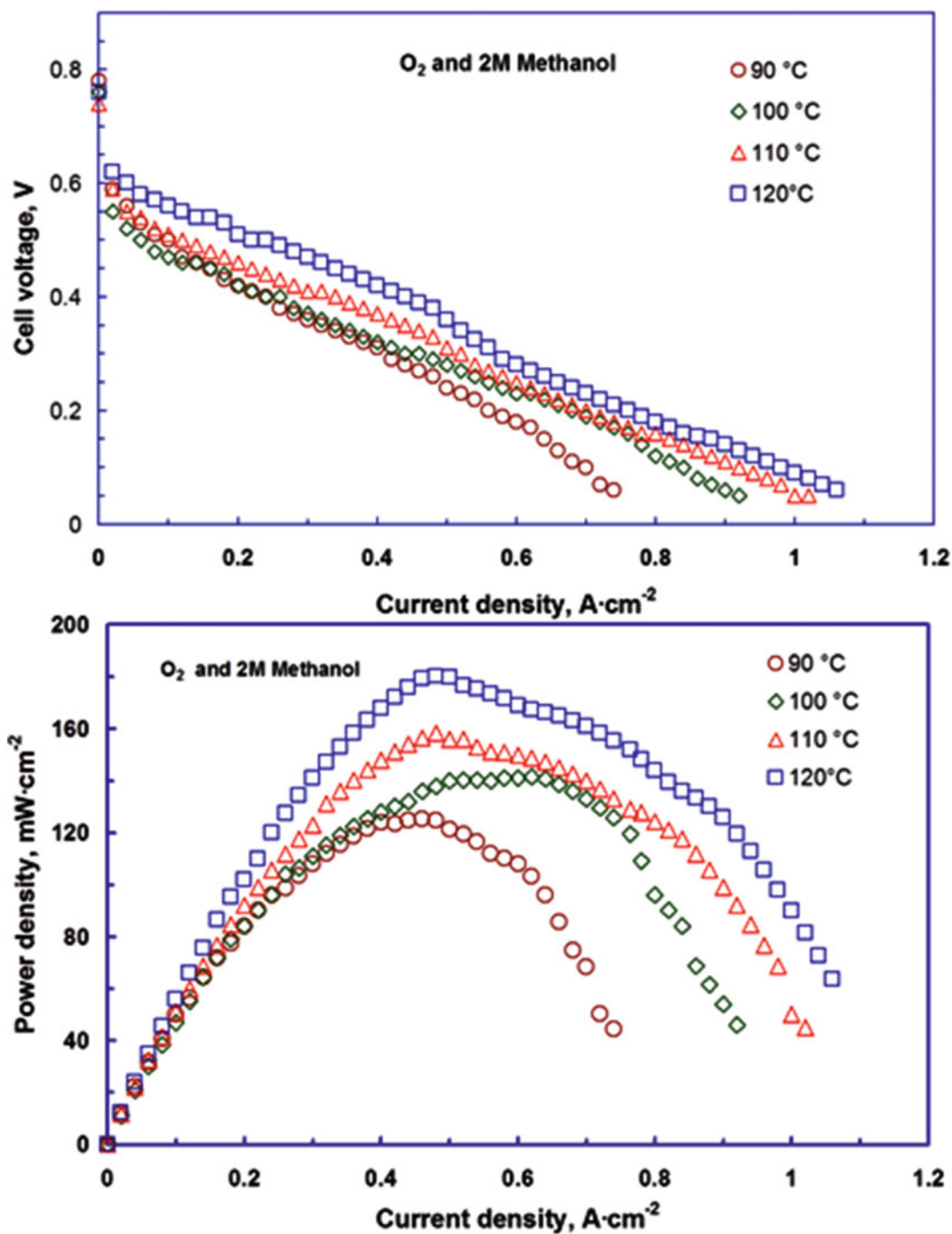


Fig. 2.12 Cell voltage and power density as a function of current density for the composite SPSf-60-SiO₂ membrane-based DMFC at different temperatures in 2 M MeOH/O₂. Reproduced from [16] with permission of Elsevier

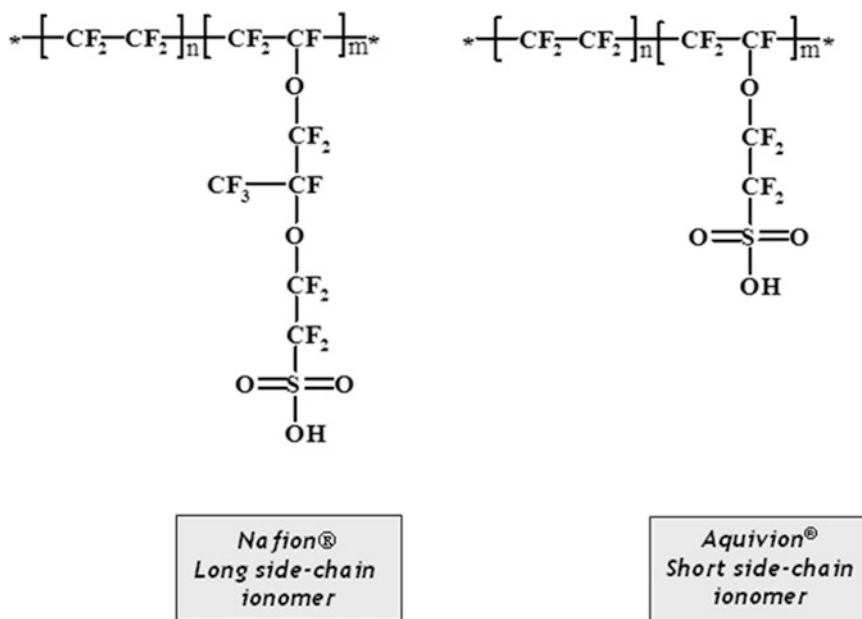


Fig. 2.13 Structure of long-side chain Nafion[®] and short-side chain Aquivion[®] polymers

chain Aquivion[®] is characterized, in the protonic form, by a primary transition at around 160 °C, whereas the conventional Nafion shows this transition at about 110 °C. Such a characteristic of the Aquivion[®] membrane ensures proper operation at high temperatures (100–150 °C) provided that sufficient amount of water is supplied to the membrane or retained inside the polymer under these conditions. In principle, the water uptake properties of sulfonic acid-based membranes may be modulated by selecting a proper concentration and distribution of sulfonic groups inside the polymer. In this regard, the Solvay Aquivion[®], due to its equivalent weight lower than conventional polymers, is favored for the high-temperature operation. Solvay Aquivion[®] (Hyflon[®] Ion) membranes have been investigated for applications in DMFCs operating between 90 and 140 °C [17]. DMFC assemblies based on these membranes showed low cell resistance and promising performances compared to conventional membranes. A peak power density of about 290 mW cm⁻² was reached at 140 °C and 3 bars abs. with 1 M methanol and air feed (Fig. 2.14). This is among the best performance reported for air-fed DMFCs.

2.3 Composite PFSA Membranes for Direct Ethanol Fuel Cells

Another suitable organic fuel candidate for fuel cells applications in portable and assisted power units is ethanol. Ethanol can be obtained from renewable energy sources, e.g., through fermentation of agricultural products and from biomasses. Although the oxidation of ethanol to carbon dioxide requires the cleavage of the C–C bond, several studies have shown an interesting electrochemical reactivity of ethanol on Pt-based catalysts, at operating temperatures above 100 °C [4]. The main bulk products in the electrochemical oxidation of ethanol on Pt are CO₂, acetaldehyde, and acetic acid. The presence of acetaldehyde and acetic acid in the reaction products determines low electrical energy yield for ethanol oxidation and poses some environmental problems. This drawback is addressed by operating the fuel cell at elevated temperatures and/or by developing highly selective catalysts. Nanostructured materials such as nanosized catalysts and nanocomposite membranes offer unique properties in terms of electrodes and

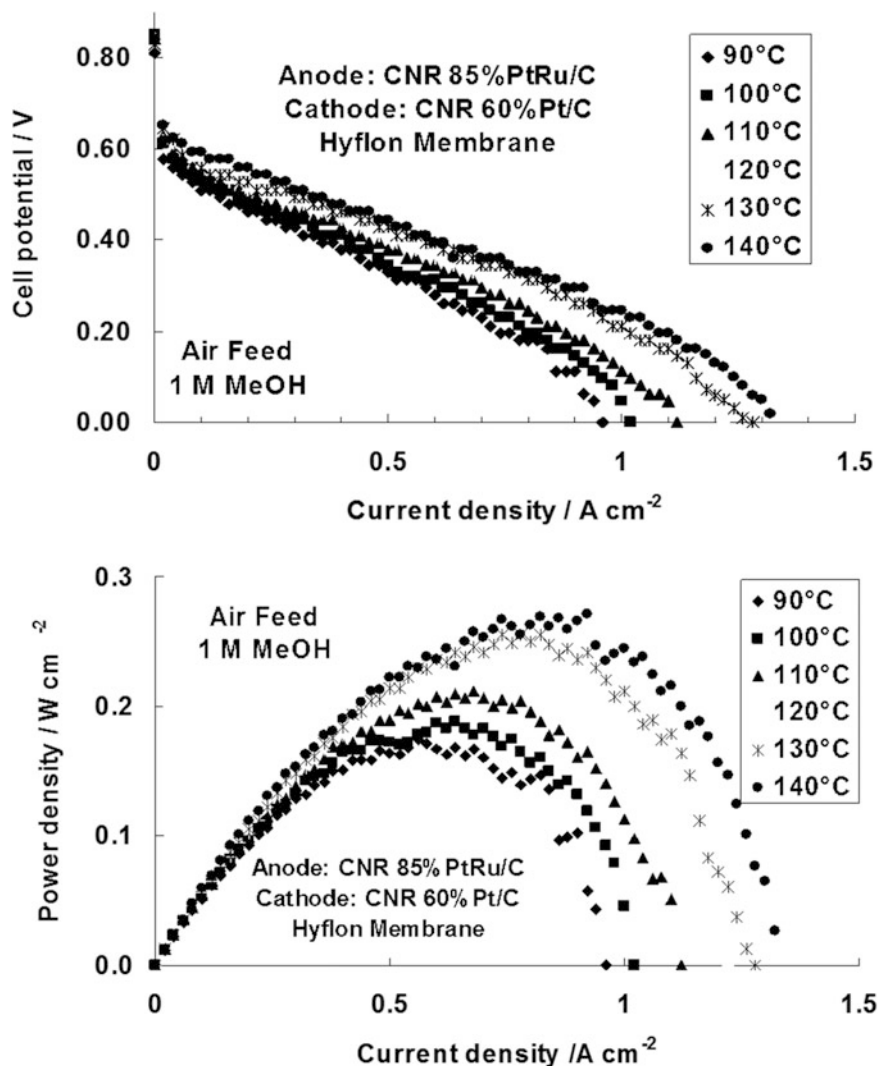


Fig. 2.14 Performance of air-fed DMFC equipped with Hyflon[®] (now Aquivion[®]) membranes at intermediate temperatures. Reproduced from [17] with permission of Elsevier

electrolytes for enhancing the electrochemical behavior of PEMFCs fed with organic fuels. As discussed above, since the state-of-the-art membranes dehydrate at temperatures above 100 °C, new membranes, capable of sustaining high temperature (150 °C), with ambient humidification are developed. There are promising evidences that this drawback can be overcome by the use of composite membranes including nanosized hygroscopic oxides dispersed in the polymeric matrix. A possible range of operating temperatures between

110 and 150 °C for direct ethanol fuel cells (DEFC) is feasible using composite membranes. For DEFC based on composite polymer electrolyte for applications in portable or distributed generation of electrical energy, relevant aspects are performance, efficiency, cross-over, and CO₂ yield. A significant increase of performance and CO₂ yield is achieved by operating the DEFC in the presence of composite membranes containing appropriate ceramic fillers [4]. Furthermore, ethanol cross-over through the membrane is reduced by the increase in tortuosity factor

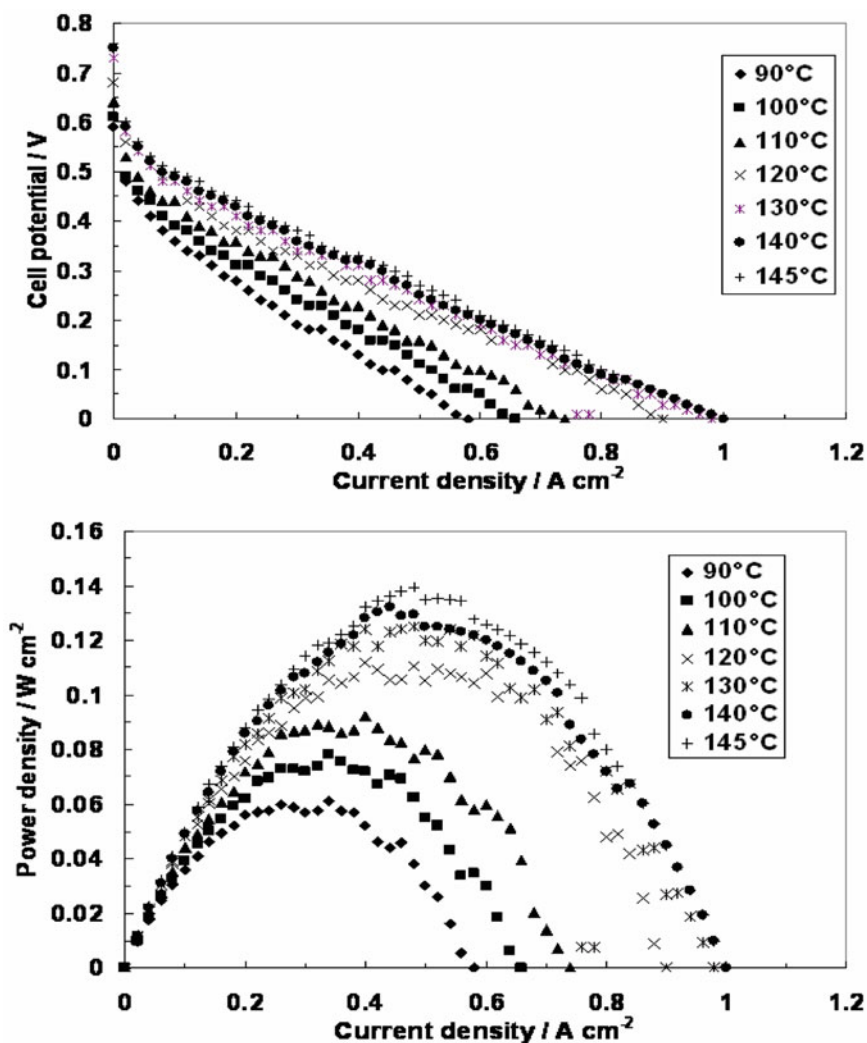


Fig. 2.15 Polarization and power density curves for a direct ethanol fuel cell equipped with a composite Nafion–SiO₂ in the temperature range from 90 to 145 °C (CNR-ITAE internal report)

caused by the filler and ethanol consumption due to enhanced reaction kinetics at the anode–electrolyte interface.

Electrochemical characterizations of DEFCs at high temperatures (90–145 °C) have been carried out on using Nafion–SiO₂ composite membrane as electrolyte and 1.5 M ethanol solution at the anode. The composite membrane composed by Nafion ionomer and silica shows advantageous water retention properties at high temperatures (90–145 °C) useful for the DEFC process.

Figure 2.15 shows the polarization and power density curves obtained for this cell from 90 to

145 °C. An enhancement of the cell performance was recorded as the temperature was increased. A maximum power density of about 140 mW cm^{-2} was obtained at 145 °C. A durability study at 0.4 V showed a low performance decay during 250 h operation at 145 °C (Fig. 2.16). The stability appears better than at lower temperatures using conventional membranes. The lower stability usually recorded at the conventional temperature is ascribed to the occurrence of strongly adsorbed ethanolic residues; this effect is less critical at high temperatures due to the lower poisoning effect

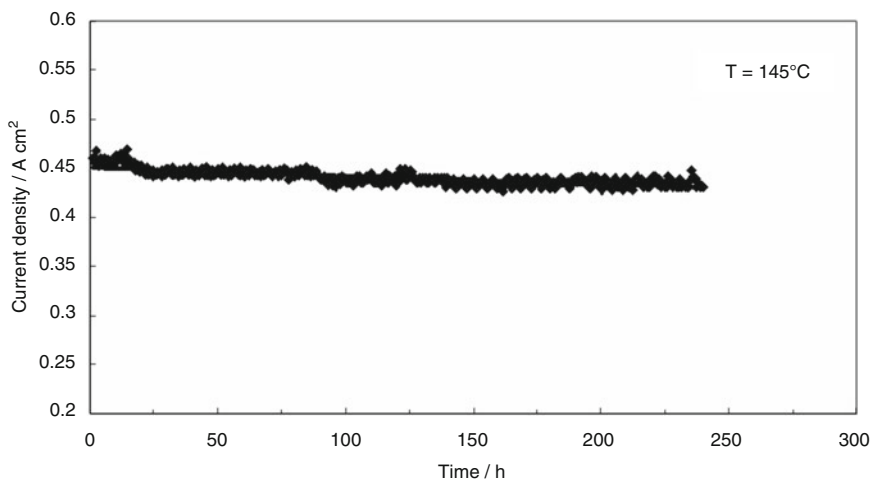


Fig. 2.16 Durability study for a direct ethanol fuel cell equipped with a composite Nafion-SiO₂ at 0.4 V and 145 °C (CNR-ITAE internal report)

of the adsorbed intermediates and the faster desorption rate.

The results registered for direct methanol and ethanol fuel cells operating at intermediate temperatures (up to about 150 °C) in combination with composite PFSA membranes with enhanced properties under these conditions indicate that this approach can provide a promising solution to increase performance by overcoming the low reaction oxidation rate of the organic fuel, enhance the desorption rate of the adsorbed organic residues thus enhancing the electrochemical stability, and may promote an increase of the CO₂ yield in the case of ethanol-fed fuel cells.

2.4 Composite and Modified PFSA Membranes for Intermediate Temperature PEM Electrolysis

2.4.1 General Aspect of PEM Electrolysis

Several processes and devices are currently developed for water electrolysis such as alkaline systems, solid oxide electrolyte, and PEM-based electrolyzers. PEM water electrolysis is considered the most promising method to produce hydrogen with a high degree of purity from renewable energy resources such as wind,

photovoltaic, and hydropower [18]. The process is characterized by high efficiencies and suitable current density. PEM electrolysis systems have a number of advantages in comparison to the traditional alkaline electrolyzers, such as ecological cleanliness, considerably smaller mass-volume characteristics, less corrosive electrolyte, low maintenance and, essentially, a high degree of gas purity [19]. There is also the opportunity to obtain compressed gases directly from the electrolyser at an increased level of safety [18].

Electrolysis is an endothermic process; it needs a proper heat supply to operate at high temperatures. An increase of temperature causes a decrease of the Gibb's free energy change and an increase of the reaction kinetics, whereas the thermoneutral voltage remains almost constant. Operation at high temperatures requires a lower amount of total energy since no heat associated with water vaporization enthalpy is needed. In general, operation of PEM electrolyzers with photovoltaic or wind energy devices is appropriate at low temperatures (e.g., <100 °C). However, there are some cases where PEM electrolyzers can take advantage of the supply of waste heat or the device need to manage a large release of heat due to the irreversible electrochemical process.

The main perspective for PEM electrolyzers is a suitable integration with renewable power

sources. However, due to the intermittent characteristics of renewable power sources, the system should also be capable of managing a high power input in short periods. This can cause significant heat release with an increase in temperature. The polymer membrane should allow operation in a wide temperature range and specific properties such as glass transition temperature, degree of crystallinity, and capability of water retention at high temperatures are of relevant interest for this application.

2.4.2 Intermediate Temperature PEM Electrolysis

An increase of the operation temperature of the electrolyser should enhance the oxygen evolution reaction rate that is the rate-determining step of the entire process allowing to obtain high current and high conversion efficiency.

An electrolysis process operating at high temperatures may also take advantage of the more favorable thermodynamic conditions for water vapor splitting. However, the conductivity of Nafion membranes decreases at temperatures $>100\text{ }^{\circ}\text{C}$ due to membrane dehydration. Alternative membranes more suitable to high temperature operation, at least in the range of $120\text{ }^{\circ}\text{C}$ with good mechanical properties and high T_g level, would be appropriate. As above discussed, composite membranes containing hygroscopic oxide fillers have been developed for high temperature fuel cells (up to $150\text{ }^{\circ}\text{C}$) [4]. The inorganic fillers enhance the water retention inside the composite

membrane allowing the system to operate at high temperatures and, moreover, they decrease the cross-over by effect of the increased tortuosity factor induced by the presence of nanoparticles inside the membrane.

Composite PSFA–silica membranes have been demonstrated for water electrolysis. Composite membrane containing 3 wt% SiO_2 (Cab-O-Sil EH5, Cabot) for water electrolysis were prepared by using a combination of recast and thermal treatment procedures. The thickness of the composite membrane was comparable to Nafion 115, i.e., $120\text{ }\mu\text{m}$. The membrane forming procedure is exemplified in Fig. 2.17.

High temperature conductivities have been recorded under pressurized conditions; the series resistance in situ recorded for a $120\text{ }\mu\text{m}$ thick membranes is determined as a function of temperature (Fig. 2.18).

Polarization curves in a wide temperature range for a PEM water electrolyser single cell based on a composite PFSA– SiO_2 membrane and Nafion 115 under pressurized operation are shown in Fig. 2.19 [20]. It is clearly observed that the composite membrane shows enhanced performance in the high temperature operating range. At high pressure, even above $100\text{ }^{\circ}\text{C}$, there is a good fraction of liquid water inside the system and the composite membranes should suffer much less from dehydration compared to Nafion. Moreover, the filler surface can be properly tailored to include recombination pathway promoters (Ce, Mn) that reduce the occurrence of hydrogen peroxide radicals generally caused by cross-over.

Composite Membrane preparation

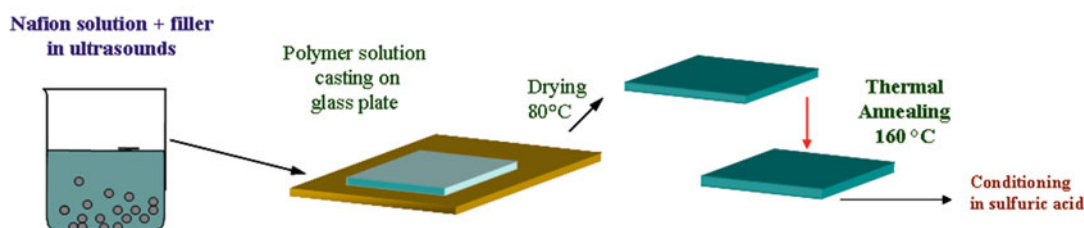


Fig. 2.17 Composite PFSA–silica membrane preparation

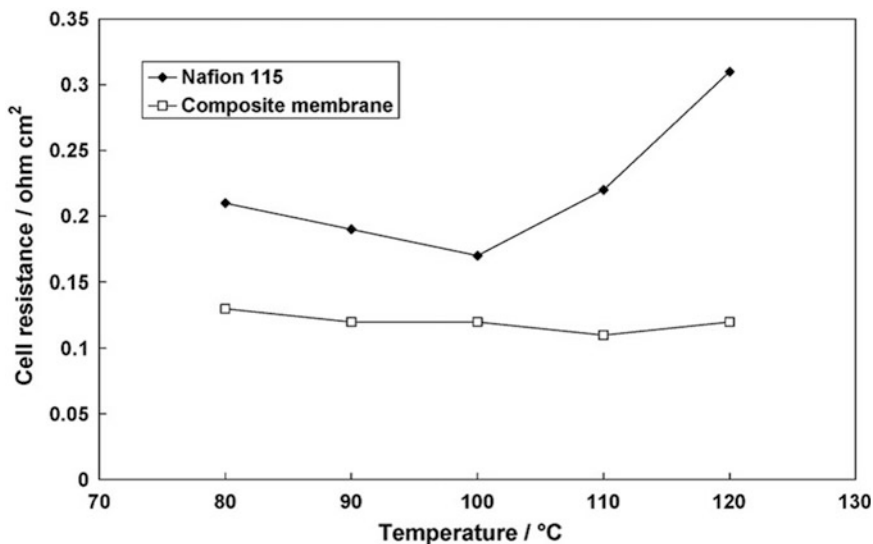


Fig. 2.18 Series resistance of Nafion (bare and composite with SiO₂ fillers) vs. temperature. The series resistance of the cell hardware is not subtracted by the contribution

of electrodes, current collector, and interfacial resistance. Reproduced from [20] with permission of Elsevier

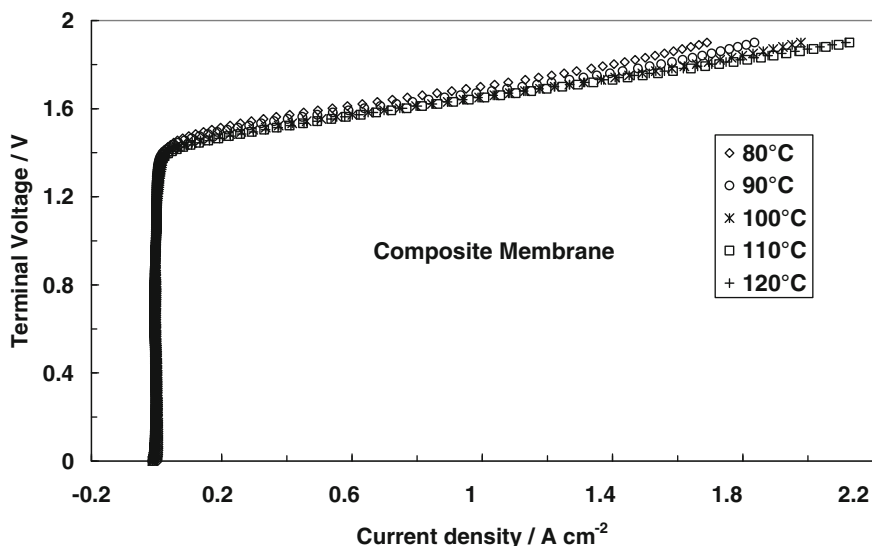


Fig. 2.19 Terminal voltage vs. current density curves for a PEM electrolyser equipped with Nafion-SiO₂ (3%) composite membrane at different temperatures

(80–120 °C) and pressurized conditions. Reproduced from [20] with permission of Elsevier

An increase of the operation temperature of an electrolyser should enhance the oxygen evolution reaction rate that is the rate-determining step of this process allowing for high current and high conversion efficiency.

The composite PFSA-SiO₂ membrane for PEM electrolysers shows promising properties for high temperature operation allowing to achieve significantly higher performances with respect to a bare commercial Nafion. This effect

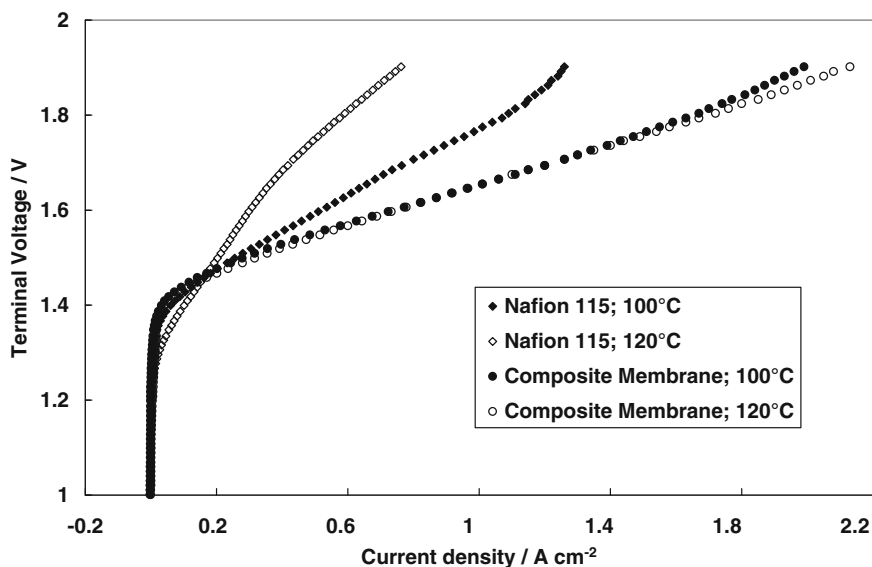


Fig. 2.20 Variation of electrolyser performance for Nafion 115 and composite membrane-based MEA as a function of the cell temperature with a water pressure of 3 bar. Reproduced from [20] with permission of Elsevier

is mainly due to a significantly better water retention than the bare perfluorosulfonic membrane and lower gas cross-over, resulting by the increased tortuosity effect produced by the inorganic filler inside the membrane. The performance of the electrolyser based on Nafion–SiO₂ membrane increases as a function of the temperature up to 120 °C and pressure. A current density of about 2.1 A cm⁻² vs. 0.7 A cm⁻² at 1.9 V, 120 °C and 3 bar abs., has been recorded for a composite membrane compared to Nafion 115 (Fig. 2.20). An increase of electrical efficiency is recorded for the high temperature electrolyser compared to conventional devices [20].

Such an improvement is due to lower activation energy for the electrochemical process related to the higher operating temperature, whereas the lower resistance of the composite membrane produces a better proton transport in the whole investigated temperature range. The water retention properties of the inorganic filler in the composite membranes also play a key role in increasing the range of operation temperature for the PEM electrolyser.

On the contrary to solid polymer electrolyte fuel cells, the increase of pressure in the PEM

electrolysers represents a technical advantage since it reduces the constraints related to the gas pressurization for storage purposes. It was discussed above that the composite Nafion–SiO₂ membrane has improved mechanical stability with respect to commercial Nafion membranes due to an enhanced crystallinity; this aspect is relevant for elevated pressure operation.

2.4.3 Short-Side Chain Membranes for PEM Water Electrolysis

In general, PFSA membranes are characterized by excellent performance, electrochemical stability, suitable mechanical properties, and allow rapid startup. However, it appears necessary to ameliorate the PFSA membranes and ionomers to improve the operating efficiency of membrane-electrode assemblies of PEM electrolysers at practical current densities useful to reduce capital costs. PFSA membranes used in electrochemical devices are essentially based on Nafion[®]; however, several alternative PSFA membranes with shorter pendant side chain have been developed by Dow, 3 M, Gore, Asahi Glass, Solvay Specialty Polymers, etc.,

especially for utilization in polymer electrolyte fuel cells [21–26].

As above discussed, Solvay Specialty Polymers has developed a short-side chain perfluorosulfonic membrane with the trade name Aquivion[®]. The polymer structure is reported in Fig. 2.13 [26]. The E87-12S SSC, chemically stabilized PFSA membrane has an equivalent weight of 870 g eq⁻¹. As previously discussed, this ionomer is characterized by both larger crystallinity and higher glass transition temperature than LSC polymers at a given equivalent weight [21–24]. In the dry form, a glass transition temperature (T_g) of 127 °C for Aquivion[®] has been observed [21–24]. Under humidified conditions, the T_g increases proportionally due to the presence of water that enhances the ionic interactions, despite its plasticizing effect [21–24]. Conductivities significantly better than Nafion[®] have been recorded for Aquivion[®] in the range of 200 mS cm⁻¹ [24]. Aquivion ionomer has been especially investigated for fuel cell applications [26], whereas research on this ionomer material for PEM electrolysis has started very recently [27, 28].

Aquivion[®] E87-12S short-side chain perfluorosulfonic acid (SSC-PFSA) membrane with equivalent weight (EW) of 870 g eq⁻¹ and 120 μm thickness produced by Solvay Specialty Polymers was tested in a polymer electrolyte membrane water electrolyser (PEMWE) and compared to a benchmark Nafion[®] N115 membrane (EW 1100 g eq⁻¹) of similar thickness [27]. Both membranes were tested in conjunction with in-house prepared unsupported IrO₂ anode and carbon-supported Pt cathode electrocatalyst. The electrocatalysts consisted of nanosized IrO₂ and Pt particles (particle size ~2–4 nm). The electrochemical tests showed better water splitting performance for the Aquivion[®] membrane and ionomer-based membrane-electrode assembly (MEA) as compared to Nafion[®] (Fig. 2.21). Lower ohmic drop constraints and smaller polarization resistance were observed for the electrocatalyst–Aquivion[®] ionomer interface indicating a better catalyst–electrolyte interface. A current density of 3.2 A cm⁻² for water

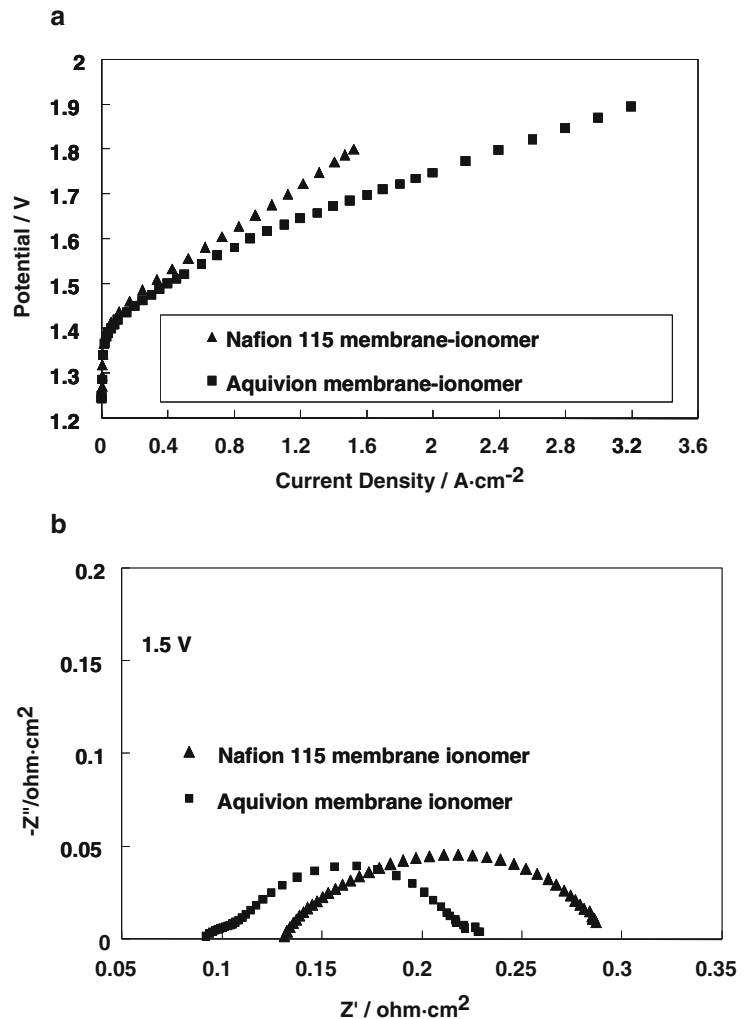
electrolysis was recorded at around 1.8 V cell voltage with the Aquivion[®]-based MEA [27]. Besides the lower ohmic resistance, a slightly lower cross-over and a significantly better electro-catalytic activity were observed for the Aquivion[®] MEA under electrolysis conditions. These enhanced properties were explained by the different chemical and structural characteristics, producing larger crystallinity, higher glass transition temperature, and lower equivalent weight for Aquivion[®] [27]. The first two properties assure better mechanical properties, whereas the latter produces higher conductivity and an enhancement of the catalyst–electrolyte characteristics. However, some decay of performance with time was recorded for the Aquivion[®] membrane-based MEA during an endurance test [27]. This effect appears essentially related to a modification of the interface properties. Such evidences indicate that a further optimization is required to improve the membrane-electrode electrolyte assembly interface in the presence of a SSC ionomer.

2.5 SSC-PFSA Membranes

One of the main challenges of PFSA ionomer-based polymer electrolyte membrane fuel cells (PEMFCs) for automotive applications is represented by the need to operate at medium or high temperatures (above 120 °C) [2, 29]. In contrast to an internal combustion engine (ICE), which rejects almost half of the heat through the exhaust, a fuel cell has to reject most of the heat through the radiator [2]. Since most of the standard PFSA-based membranes are characterized by a limiting operating temperature of 95 °C, additional cooling efforts are necessary to keep the operating temperature at a reasonable temperature level. This implies a fact that large size radiators are often not compatible with the required compactness of the car as well as an increase of the system complexity and total cost.

Increasing the operating temperature up to ~130 °C would alleviate this drawback and improve the catalyst behavior [30]. As an

Fig. 2.21 Comparison of the water electrolysis polarization behavior (a) and ac-impedance spectra (b) for Aquivion® and Nafion®-based MEAs. Reproduced from [27] with permission of Elsevier



example, high temperature operation will reduce the size of the thermal subsystem [2], improve reaction kinetics, and increase tolerance to impurities contained in the reactant stream, e.g., CO contained in the hydrogen stream produced by a reforming process, chloride impurities which may be present in water, etc. [2]. Moreover, for stationary purposes, the heat produced by a PEM fuel cell at high temperatures (i.e., 130 °C) could be used to produce hot water, as well as for ambient heating and possibly for cogeneration in order to increase the overall system efficiency [2]. Compared with phosphoric acid-doped polybenzimidazole membranes [31], PFSA membranes are characterized by excellent

performance, electrochemical stability, suitable mechanical properties, and allow rapid startup. Thus, it appears evident that the PFSA membranes can be explored to make them able to operate at higher temperatures.

Nowadays, common membranes adopted in PEM fuel cell are based on Nafion® (N212, N115, N117; etc.); however, as discussed above, several alternative PSFA membranes with shorter pendant side chain have been developed [29]. Despite the good performance under conventional operating conditions (60–80 °C), most of them are not suitable for high-temperature PEM fuel cell applications, especially if they are operated at temperatures above 100 °C. It is well

documented in the literature that at a temperature over 100 °C Nafion[®] membranes suffer from several drawbacks, including dehydration and excessive swelling. The first drawback causes a decrease of proton conductivity according to the “vehicle” mechanism for proton conduction, whereas the latter problem leads the backbone structure to collapse quickly [29].

The E79-03S SSC, chemically stabilized PFSA membrane developed by Solvay has a thickness of 30 μm (dry form) and an equivalent weight of 790 g eq⁻¹ [26]. The relevant properties of this ionomer have been discussed above. It is stressed that this ionomer is characterized by both larger crystallinity and higher glass transition temperature than LSC polymers at a given equivalent weight [24].

The Aquivion[®] membrane appears thus to be more reliable than Nafion[®] to operate at high temperatures. The performance of Aquivion[®] and Nafion[®] membranes has been compared under operation with both low pressure and relative humidity as required for automotive applications [2, 26]. It was observed that the maximum realistic operating temperature was 95 °C for Nafion[®], whereas this limit can be shifted to 110 °C for Aquivion[®], indicating a clear progress beyond the state-of-the-art of perfluorosulfonic membranes [2]. An experimental comparison of the higher temperature (130 °C) operation between Aquivion[®] and Nafion[®], as representatives of a short-side chain ionomer and long-side chain ionomer, has been made [26]. Besides the different conductivity characteristics, there are also different electrocatalytic properties arising from the presence of a different ionomer at the catalyst–electrolyte interface under such conditions. Long-side chain and short-side chain PFSA membranes were initially non-reinforced films, i.e., extruded products. Thus, the conventional Aquivion[®] PFSA membrane is generally a melt-extruded product based on the unique SSC copolymer of tetrafluoroethylene and a sulfonyl fluoride vinyl ether of low molecular weight produced by Solvay. The ionomer dispersion used for electrode manufacturing in the Aquivion-based MEA has generally the same structure/

composition of the membrane; it is in acid form and contains as solvents, 20 % water, 40 % 1-propanol, and 40 % 2-propanol. More recently, thin (10–20 μm) reinforced Aquivion membranes have been developed providing further increase of performance and stability.

It is considered that for practical catalyst–ionomer interfaces, the effects of metal–support interaction, the lack of triple-phase boundary in small micropores, the uneven distribution of the ionomer and ionomer dry-out in the catalytic layer can significantly reduce the catalyst utilization. To get information on the effect of the two different ionomers (LSC and SSC) on Pt utilization in situ cyclic voltammetry analyses have been carried out (Fig. 2.22).

The electrochemically active surface area is generally larger in the case of the interface with Aquivion[®] ionomer than in the case of Nafion[®] [26]. The gain in terms of electrochemical active surface area for the cathode in the MEA equipped with Aquivion[®] membrane was close to 30 % compared to Nafion[®]. In fact, the ECSA changed from 66 m² g⁻¹ for the cathode equipped with Nafion[®] ionomer to 84 m² g⁻¹ for that containing Aquivion[®] ionomer [26]. The increase of electrochemical active surface area has been interpreted in terms of

1. Smaller equivalent weight for Aquivion[®], increasing the triple-phase boundary region as it would be played by a liquid electrolyte.
2. A different interaction between the ionomer and the catalysts at the three-phase reaction zone.
3. A better filling of the catalyst micropores by the Aquivion[®] ionomer micelles leads to an increase of the availability of platinum sites.

Besides these aspects, it should be considered that Aquivion[®] suffers less than Nafion[®] as the ionomer dry-out is limited under harsh conditions [2]. The catalyst utilization is 60 %, in the case of Aquivion[®]-based MEA, whereas the utilization reaches 47 % for Nafion[®]-based MEA. Accordingly, the increase of Pt utilization in the presence of the SSC ionomer with respect to the LSC ionomer in each electrode is about 13 %.

Fig. 2.22 Comparison of the cyclic voltammetric behavior at the Pt electrocatalyst–solid polymer electrolyte interface, at intermediate temperatures, for Aquivion® and Nafion® membrane and ionomer-based MEAs. Reproduced from [26] with permission of Elsevier

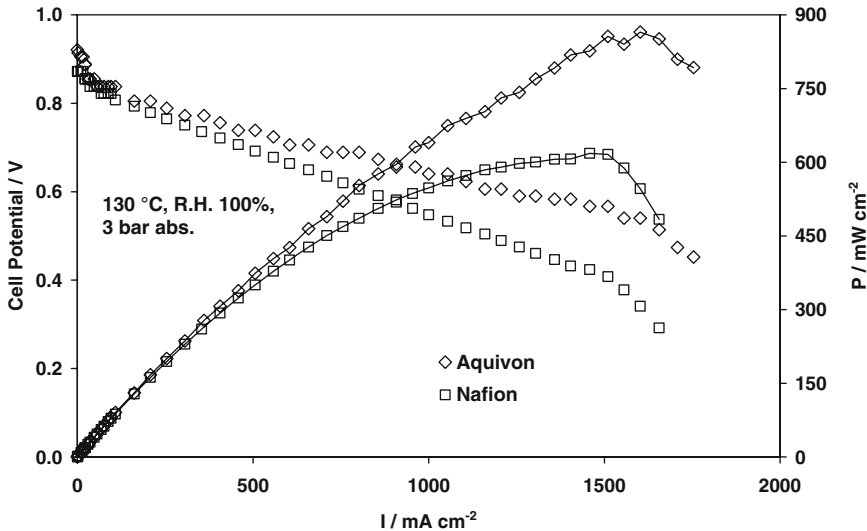
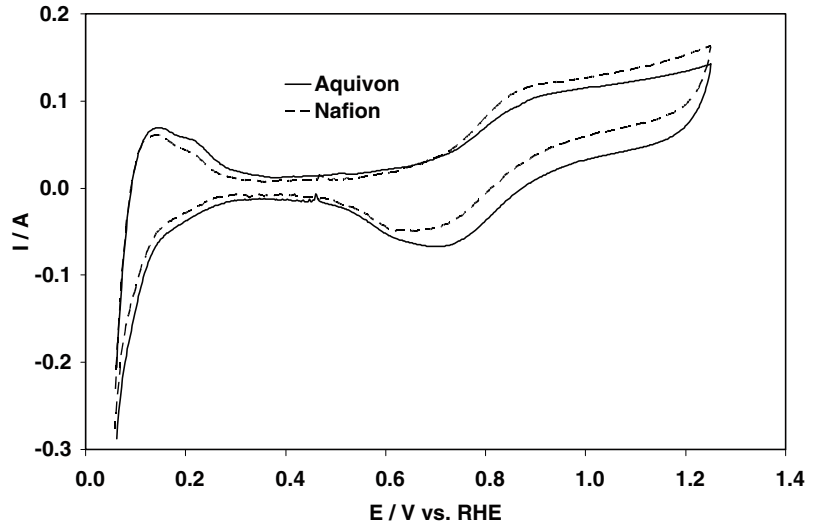
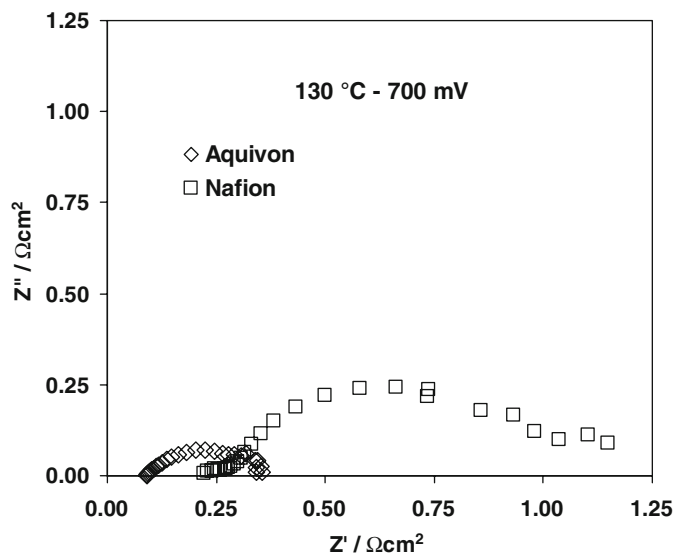


Fig. 2.23 Comparison of the polarization behavior for Aquivion® and Nafion® membrane and ionomer-based MEAs at $130\ ^\circ C$ and 3 bar abs. Reproduced from [26] with permission of Elsevier

Intermediate temperature polarization curves for two different PEM single cells equipped with the Nafion® and Aquivion® membranes under slightly pressurized conditions are reported in Fig. 2.23. Polarizations are carried out at $130\ ^\circ C$ (3 bar abs.; 100 % RH). A higher OCV is registered for the Aquivion-based MEA at this temperature than for the Nafion-based MEA. This behavior could be attributed principally to an increase of the hydrogen cross-over effect in

Nafion® at this temperature [2]. In fact, the decrease of OCV for the Nafion-based with respect to the Aquivion-based MEA could be attributed to an increase in membrane swelling at high temperatures [2]; this usually causes an increase of the hydrogen cross-over through the electrolyte and, thus, a mixed potential at the cathode. The increase of hydrogen cross-over with the temperature has been previously reported [2]. It should also be mentioned that

Fig. 2.24 Comparison of the ac-impedance behavior for Aquivion[®] and Nafion[®] membrane and ionomer-based MEAs at 130 °C and 2 bar rel. Reproduced from [26] with permission of Elsevier



Nafion[®] has a lower glass transition temperature than Aquivion[®]. The latter is also characterized by improved mechanical and crystalline properties.

A maximum power density of about 850 mW cm^{-2} was reported for Aquivion[®]-based MEAs at 130 °C. This value is significantly better compared to the power density of 600 mW cm^{-2} measured with Nafion[®] membrane under similar conditions in pressurized mode (Fig. 2.23). The voltage efficiency at the maximum power density is also larger for Aquivion[®] (0.57 V) than Nafion[®] (0.4 V). A larger electrochemical active surface area and a lower cross-over for Aquivion[®]- vs. Nafion[®]-based MEAs may provide a suitable explanation for the better performance in the first case. Moreover, the higher conductivity of Aquivion[®] vs. Nafion[®] can also account for this; the latter aspect can be mainly interpreted in terms of lower equivalent weight.

Useful information is obtained by comparing the ac-impedance spectra (Fig. 2.24) for Aquivion- and Nafion-based MEAs at an intermediate cell potential, i.e., 0.7 V, where the effect of activation control, mainly determined by the catalyst–electrolyte interface characteristics, is present. It has been observed that the series (ohmic) resistance, i.e., high frequency

intercept is only $0.11 \Omega \text{ cm}^2$ for the Aquivion[®] at 130 °C with high pressure and full humidification. In the case of Nafion, it is about twice, i.e., $0.23 \Omega \text{ cm}^2$.

Thickness is slightly different (30 vs. 50 μm) for Aquivion[®] and Nafion[®] 212. After normalization of the series resistance by the membrane thickness, resistivity values of $46 \Omega \text{ cm}$ and $36 \Omega \text{ cm}$ for the Nafion[®]- and Aquivion[®]-based MEAs, respectively, are obtained. This indicates better hydration and higher conductivity for the Aquivion[®] membrane vs. Nafion[®] on account of the smaller EW (790 vs. 1100 g eq^{-1}). This is corroborated by the fact that the extruded Solvay short-side chain ionomer of EW 790 g eq^{-1} is characterized by a larger uptake of liquid water at high temperature compared to Nafion[®] ionomer with EW 1100 g eq^{-1} . A large difference envisaged from the impedance spectra is related to the significantly lower polarization resistance for Aquivion[®] than Nafion[®]-based MEA (0.26 vs. $0.93 \Omega \text{ cm}^2$). It is considered that at 0.7 V, the polarization resistance mainly reflects the electro-catalytic properties than diffusion limitations which are predominant at high current densities and lower cell voltages. Thus, these results clearly indicate that there is not only the effect of larger ionic conductivity but also an impact on electro-catalytic properties played by

the short-side chain ionomer–catalyst interface. At high cell potential (i.e., in the region that may be of major interest to operate under suitable efficiency conditions), the electro-catalytic effect may be predominant. This evidence represents a new insight to achieve a better understanding of the behavior of PSFA membranes, especially at high temperatures. It may be envisaged that such an effect appears related to the better triple-phase boundary and the lower extent of ionomer dry-out for Aquivion[®]. Yet, in our opinion, it should not be discarded the effect of super-acidity or proton activity at the electrode–electrolyte interface. Protons are involved in the oxygen reduction reaction. Their availability at the catalyst–electrolyte interface is thus important. In the case of ionomer dry-out, clear mass transport constraints have been recorded in PEFC polarization curves [2]. Under high temperature operation, the super-acidity may compensate for a lower water availability which generally causes a decrease of proton transport towards the interface. Interestingly, the Pt-oxide reduction peak in the cyclic voltammograms is shifted towards higher potentials in the case of Pt–Aquivion[®] interface vs. Pt–Nafion[®] (Fig. 2.22) as it occurs in the case of an increase of specific activity [30].

Automotive applications of polymer electrolyte membrane fuel cells require intermediate temperature operation at pressures below

1.5 bar abs. and low relative humidity. Extruded Aquivion[®] E79-03S membrane consisting of an equivalent weight of 790 g eq⁻¹ was investigated in fuel cell at 110 °C and low pressure [32]. Figure 2.25 shows the steady-state polarization curves for a fuel cell based on this membrane at intermediate temperature and different relative humidity. The polarization curves were carried out from OCV to the maximum current densities and the potential at each current was collected when a steady-state condition was reached. At low current densities, the potential losses were small in the presence of a high relative humidity (RH 100 %); however, at high current densities, the flooding effect due to the large amount of water produced at the cathode caused an increase of potential losses in the presence of high RH (100 %). The largest peak power density of 800 mW cm⁻² was indeed obtained in the presence of 50 % RH. For what concerns the steady-state polarization curve recorded with 25 % RH (Fig. 2.25), large potential losses were observed at low current densities; however, as the MEA was internally humidified by the electrochemically produced water, the potential losses diminished and the occurrence in the polarization curves of a sudden increase of potential at certain values of current densities was envisaged (the polarization curve was recorded from OCV to the maximum current and the internal humidification spontaneously increased with the

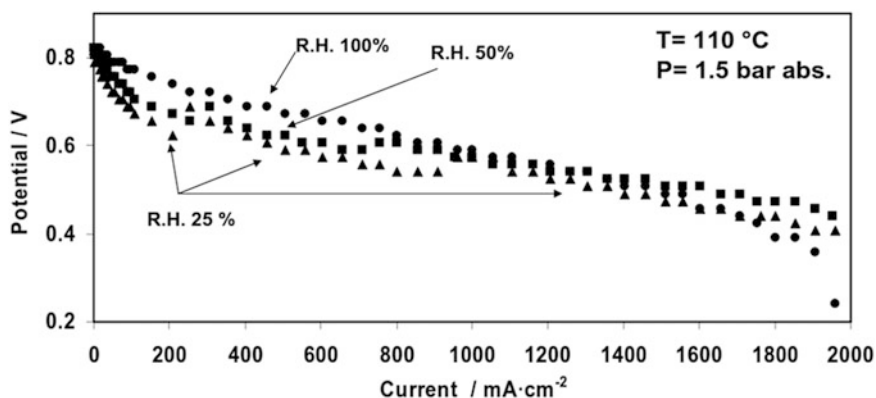


Fig. 2.25 Steady-state polarization curves at different relative humidities for high temperature polymer electrolyte fuel cell based on Aquivion[®] (Solvay) membrane and CNR-ITAE catalysts. The effect of internal

humidification is observed at high current densities and low RH. Reproduced from [32] with permission of the American Chemical Society

current). These results showed the advantage of the occurrence of internal humidification for the thin (30 μm) short-side chain Aquivion[®] membrane. The small membrane thickness promotes back-diffusion of the water produced at the cathode favoring anode humidification. The water retention and proton conductivity are also favored by the low equivalent weight resulting from the short-side chain, whereas mechanical resistance is assured by the enhanced crystalline properties of the polymer. At high current density, the obtained peak power density of 700 mW cm^{-2} at 110 $^{\circ}\text{C}$, 25 % RH, $\text{H}_2\text{-O}_2$, 1.5 bar abs. appears promising for automotive applications.

Better stability has been recorded for intermediate temperature operation of Aquivion than Nafion [26]. In the case of the Nafion[®], the low glass transition temperature and poor mechanical properties at high temperatures may cause an increase of membrane swelling with time with consequent increase of hydrogen cross-over. This leads to a mixed potential at the cathode.

Hydrogen and oxygen may react directly on the platinum cathodic sites. This reaction is extremely exothermic and it produces a local heating that, with time, can destroy the membrane backbone structure or cause a strong catalyst sintering. This latter effect, even if less dramatic, may also contribute to the catalyst sintering effect at the cathode also in the case of the Aquivion-based MEA. Although, the OCV is larger for Aquivion[®], it is lower than that recorded for the MEA based on the same membrane under conventional or less critical operating conditions indicating the occurrence of cross-over at 130 $^{\circ}\text{C}$. However, it should be mentioned that under practical operation conditions, a lower relative humidity generally mitigates such effect because the membrane swelling is not only determined by temperature but also by the water content.

Figure 2.26 shows histograms related to the peak power in the high temperature range for short stacks (10-cells) developed in the FP6 EU

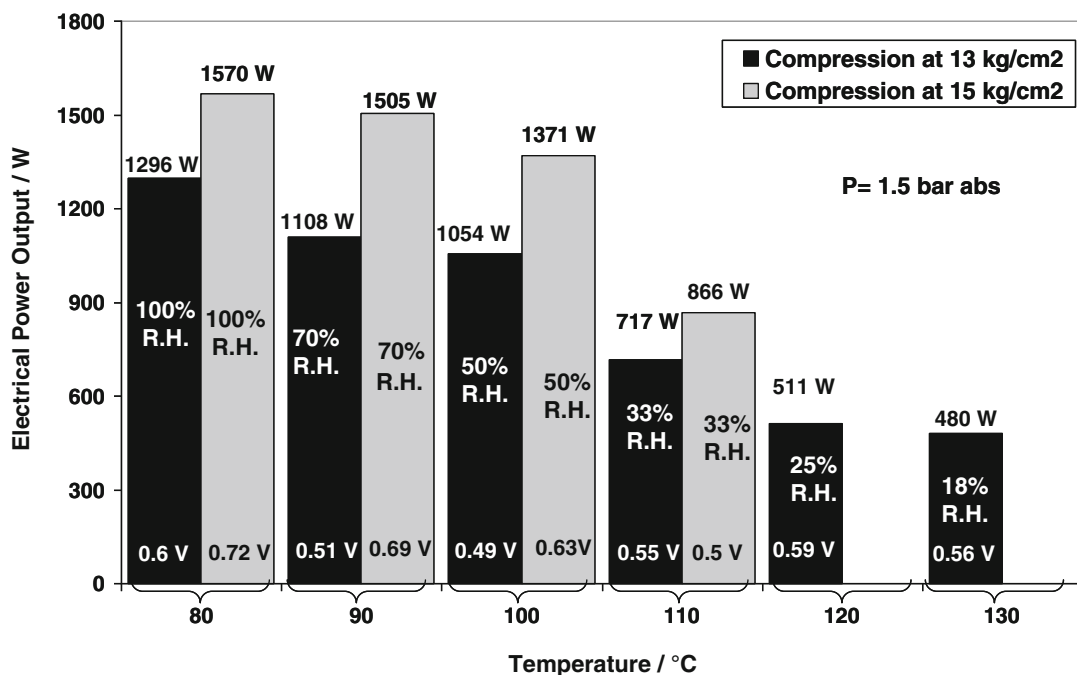


Fig. 2.26 Variation of the electrical power output as function of temperature for six-cell short stacks assembled under two different compressions with Aquivion-

based MEAs (active area 360 cm^2). Reproduced from [2] with permission of Wiley

Autobrane project and assembled with MEAs containing Aquivion[®] membranes under different compressions [2]. The stacks were operated at low pressure as appropriate for automotive operation. The effect of compression on the stack performance was also observed at the various temperatures; however, it was less relevant at 110 °C. The best performance of about 700 mW cm⁻² was achieved at 80 °C. The short stacks showed a suitable power output up to 100 °C with power densities exceeding 600 mW cm⁻² and a moderate decrease at slightly higher temperatures (110 °C). However, the performance decreased in the range 120–130 °C possibly due to strong dehydration effects as a consequence of the decrease of relative humidity. Typical cell resistances inside the stack of 0.05–0.08 Ω cm² were measured at 80 °C under optimal compression, whereas these reached the values of 0.15–0.18 Ω cm² under poor compression. These results were confirmed by cross-comparison of the data obtained from the current interrupt, ac-impedance spectroscopy, and hydrogen pumping methods. The cell resistance increased from 0.05 to about 0.2 Ω cm² on increasing temperature from 80 to 110 °C, due to the membrane dehydration. This indicated a predominant effect of the membrane (the same in the two stacks) with respect to the other MEAs components in determining the ohmic resistance.

Stack tests on Aquivion-containing MEAs have shown that only a moderate decrease in performance occurs at 110 °C, 1.5 bar abs. with 33 % RH. MEA hydration in the stack at intermediate temperature was mainly assured by the internal humidification and the back-diffusion of the water from the cathode to the anode through the thin (30 μm) low equivalent weight (790 g eq⁻¹) PFSA membrane. In the stack, the new Aquivion[®] E79-03S membrane showed high conductivity, good water retention, and mechanical properties above 100 °C as compared to the conventional PFSA membranes and appropriate characteristics for a rapid startup in a cold environment as well as suitable operation in duty cycles. These promising characteristics were supported by improved MEA structures,

with especially optimized catalyst layers. Duty cycles studies at high temperatures showed appropriate electrochemical behavior under various operating conditions [2].

2.6 Conclusions

In the last decade, considerable progress has been made on new proton-conducting membrane materials for high temperature PEMFCs. Several of these materials have also shown interesting properties for automotive applications, but few efforts have been made to assess the new materials at the stack/system level as well in the presence of duty cycles. The polymer electrolyte membrane fuel cell (PEMFC) technology for automotive applications requires operation at high working temperatures to improve efficiency, tolerance of contaminants, and to enable simplification of the thermal and water management subsystems. An evaluation of performance and stability in a practical system, over a wide temperature range from ambient to intermediate temperature, e.g., (130–150 °C), can provide a full assessment of the PEMFC components and clearly identify the progress beyond the state-of-art. Aquivion[®] short-side chain perfluorosulfonic membranes, generally characterized by an equivalent weight of 790–850 g eq⁻¹, appear as one of the most promising solid electrolytes combining rapid startup and suitable operation at intermediate temperature. Tests performed at temperatures of 110–130 °C representing the target for automotive applications have shown suitable properties. The Aquivion[®]-based MEAs appear significantly more performing under these conditions than Nafion-based MEAs. Besides the lower ohmic resistance, a lower cross-over and a better electro-catalytic activity have been observed for Aquivion[®] under intermediate temperature operation. These enhanced properties appear related to a larger crystallinity, higher glass transition temperature, and lower equivalent weight of Aquivion[®]. The first two properties assure better mechanical properties, whereas the latter produces higher conductivity and an increase of

catalyst utilization. Lower performance decay is recorded for the Aquivion[®] membrane-based MEA than conventional PFSA systems during endurance tests at intermediate temperatures. This is essentially related to the lower dry-out and cross-over effects.

Intermediate temperature operation is also very appropriate for direct alcohol fuel cells since it affects significantly the reaction kinetics at the anode. High temperature operation allows achieving high current densities with consequent fast methanol/ethanol consumption at the anode/electrolyte interface thus allowing for a decrease of the fuel cross-over. Composite PFSA membranes containing inorganic fillers have shown suitable properties for intermediate temperature operation and reduced methanol cross-over as consequence of a suitable water retention and an increased tortuosity factor caused by the presence of the filler particles inside the membrane. Various efforts have been addressed to composite membranes development and some attempts addressed to the understanding of the basic operation mechanism. An appropriate tailoring of the surface chemistry for the filler nanoparticles appears as a key step to enhance water retention and thus conductivity at intermediate temperature.

The enhanced mechanical properties and water uptake produced by the inorganic filler are of relevant interest for application in PEM electrolyzers. These operate at high pressure and thus are less affected by water dehydration issues at intermediate temperatures. The intermittent characteristics of renewable power sources require the use of suitable energy storage options. Hydrogen is considered as the future energy vector. The electrolysis system can be thus coupled to renewable power sources, but it should be capable of managing high power input in short periods. This can cause significant heat release with an increase in temperature. The polymer membrane should allow for operation in a wide temperature range and specific properties such as glass transition temperature, degree of crystallinity, and capability of water retention at high temperatures. Modified PFSA membranes such as hybrid inorganic–organic systems and short-side chain polymers have both shown enhanced

characteristics for PEM electrolysis and may provide a route to enhance efficiency and reduce the cost of such systems.

References

1. Aricò AS, Siracusano S, Briguglio N et al (2013) Polymer electrolyte membrane water electrolysis: status of technologies and potential applications in combination with renewable power sources. *J Appl Electrochem* 43:107–118
2. Aricò AS, Di Blasi A, Brunaccini G et al (2010) Investigation of proton exchange membrane fuel cell stacks for high temperature operation. *Fuel Cells* 10:1013–1023
3. Arico AS, Srinivasan S, Antonucci V (2001) DMFCs: from fundamental aspects to technology development. *Fuel Cells* 1:133–161
4. Aricò AS, Creti P, Antonucci PL et al (1998) Comparison of ethanol and methanol oxidation in a liquid-feed solid polymer electrolyte fuel cell at high temperature. *Electrochem Solid-State Lett* 1:66–68
5. Costamagna P, Srinivasan S (2001) Quantum jumps in the PEMFC science and technology from the 1960s to the year 2000: Part I. Fundamental scientific aspects. *J Power Sources* 102:242–252
6. Aricò AS, Baglio V, Antonucci V (2008) Composite membranes for high temperature direct methanol fuel cells. In: Peinemann KV, Nunes SP (eds) *Membrane for energy conversion*. Wiley-VCH Verlag GmbH & Co. KGaA, Weinheim, pp 123–168
7. Aricò AS, Baglio V, Di Blasi A et al (2003) Influence of the acid-base characteristics of inorganic fillers on the high temperature performance of composite membranes in direct methanol fuel cells. *Solid State Ionics* 161:251–265
8. Li Q, Jensen JO (2008) Membranes for HT-PEMFC based on acid doped polybenzimidazoles. In: Peinemann KV, Nunes SP (eds) *Membrane for energy conversion*. Wiley-VCH Verlag GmbH & Co. KGaA, Weinheim, pp 61–96
9. Savadogo O (1998) Emerging membranes for electrochemical systems. *J New Mater Electrochem Syst* 1:47–66
10. Alberti G, Casciola M (2003) Composite membranes for medium-temperature PEM fuel cells. *Annu Rev Mater Res* 33:129–154
11. Ruffmann B, Silva H, Schulte B (2003) Organic/inorganic composite membranes for application in DMFC. *Solid State Ionics* 162–163:269–275
12. Jung DH, Cho SY, Peck DH et al (2003) Preparation and performance of a Nafion/montmorillonite nanocomposite membrane for direct methanol fuel cell. *J Power Sources* 118:205–211
13. Yang C, Srinivasan S, Aricò AS et al (2001) Composite Nafion/zirconium phosphate membranes for direct methanol fuel cell operation at high temperature. *Electrochem Solid-State Lett* 4:A31–A34

14. Aricò AS, Baglio V, Di Blasi A et al (2003) FTIR spectroscopic investigation of inorganic fillers for composite DMFC membranes. *Electrochem Commun* 5:862–866
15. Aricò AS, Baglio V, Di Blasi A et al (2004) Surface properties of inorganic fillers for application in composite membranes-direct methanol fuel cells. *J Power Sources* 128:113–118
16. Lufrano F, Baglio V, Staiti P et al (2008) Polymer electrolytes based on sulfonated polysulfone for direct methanol fuel cells. *J Power Sources* 179:34–41
17. Aricò AS, Baglio V, Di Blasi A et al (2006) Proton exchange membranes based on the short-side-chain perfluorinated ionomer for high temperature direct methanol fuel cells. *Desalination* 199:271–273
18. Barbir F (2005) PEM electrolysis for production of hydrogen from renewable energy sources. *Sol Energy* 78:661–669
19. Millet P, Mbemba N, Grigoriev SA et al (2011) Electrochemical performances of PEM water electrolysis cells and perspectives. *Int J Hydrogen Energy* 36:4134–4142
20. Antonucci V, Di Blasi A, Baglio V et al (2008) High temperature operation of a composite membrane-based solid polymer electrolyte water electrolyser. *Electrochim Acta* 53:7350–7356
21. Arcella V, Ghielmi A, Tommasi G (2003) High performance perfluoropolymer films for membranes. *Ann N Y Acad Sci* 984:226–244
22. Ghielmi A, Vaccarone P, Troglia C et al (2005) Proton exchange membranes based on short-side chain perfluorinated ionomer. *J Power Sources* 145:108–115
23. Arcella V, Troglia C, Ghielmi A (2005) Hyflon ion membranes for fuel cells. *Ind Eng Chem Res* 44:7646–7651
24. Merlo L, Ghielmi A, Cirillo L et al (2007) Membrane electrode assemblies based on Hyflon ion for an evolving fuel cell technology. *Sep Sci Technol* 42:2891–2908
25. Peron J, Nedellec Y, Jones DJ et al (2008) The effect of dissolution, migration precipitation of platinum in Nafion[®]-based membrane electrode assemblies during fuel cell operation at high potential. *J Power Sources* 185:1209–1217
26. Stassi A, Gatto I, Passalacqua E et al (2011) Performance comparison of long and short-side chain perfluorosulfonic membranes for high temperature polymer electrolyte membrane fuel cell operation. *J Power Sources* 196:8925–8930
27. Siracusano S, Baglio V, Stassi A et al (2014) Performance analysis of short-side-chain Aquivion[®] perfluorosulfonic acid polymer for proton exchange membrane water electrolysis. *J Membr Sci* 466:1–7
28. Skulimowska A, Dupont M, Zaton M et al (2014) Proton exchange membrane water electrolysis with short-side-chain Aquivion[®] membrane and IrO₂ anode catalyst. *Int J Hydrogen Energy* 39:6307–6316
29. Chandan A, Hattenberger M et al (2013) High temperature (HT) polymer electrolyte membrane fuel cells (PEMFC)—a review. *J Power Sources* 231:264–278
30. Gasteiger HA, Kocha SS, Sompalli B et al (2005) Activity benchmarks and requirements for Pt, Pt-alloy, and non-Pt oxygen reduction catalysts for PEMFCs. *Appl Catal B Environ* 56:9–35
31. Li Q, Jensen JO, Pan C et al (2008) Partially fluorinated arylene polyethers and their ternary blends with PBI and H₃PO₄: Part II. Characterisation and fuel cell tests of the ternary membranes. *Fuel Cells* 8:188–199
32. Aricò AS, Stassi A, Gatto I et al (2010) Surface properties of Pt-based electro-catalysts and their influence on performance and degradation of high temperature polymer electrolyte fuel cells. *J Phys Chem C* 114:15823–15836

Qingfeng Li, David Aili, Robert F. Savinell,
and Jens Oluf Jensen

3.1 Introduction

Phenomena of proton conduction are of fundamental importance in many chemical reactions, biomolecular and electrochemical energy conversion processes [1–4]. Most biochemical processes in nature are sensitive to pH changes, indicating that the proton transport plays a critical role. During the past two decades, great efforts, primarily within the materials science community, have been made to understand the underlying elementary processes as well as transport phenomena of proton conduction. A major motivation is to develop new proton conducting materials for energy conversion and other technologies. Structural and dynamical information is obtained for a few material systems while other materials are still in their infancy concerning the understanding of the proton conducting mechanisms [5, 6].

A proton is a very unique ion, so unique that it is in fact not called an ion but an elementary particle in physics. When a hydrogen atom is

stripped of its electron, there is no electron shell to shield the nucleus. It is of femtometre dimension (10^{-15} m), much smaller than any other ions. A proton, with a positive charge and little steric restriction, may approach very close to a neighboring atom or ion, which is always surrounded by the negatively charged electron shell. As a result, a bare proton exists only in some very special cases such as in plasma, solar wind, or in a synchrotron ring. In condensed phases, protons interact strongly with the environment forming associated entities. In aqueous media, the proton interacts with other molecules or ions forming multinuclear proton species such as OH^- , H_3O^+ , NH_4^+ , H_4PO_4^+ , or H_2PO_4^- . The unique chemistry of protons suggests two possible mechanisms of proton conduction: the proton transfer with a carrying molecule (*vehicle mechanism*) or through a hydrogen bond chain by jumping from one site to another (*Grothuss mechanism*).

The *vehicle mechanism* involves migration of protons associated with a molecular carrier (vehicle) [7]. The transport of protons with the help of carrier molecules does not require or take advantage of an infinite hydrogen bond network and therefore follows Stokes law. With water as the most popular proton solvent, the proton conduction in aqueous media often involves migration of various hydrated proton complexes. This mechanism prevails in particular when protons are strongly associated with a base carrier such as

Q. Li (✉) • D. Aili • J.O. Jensen
Section of Proton Conductors, Department of Energy
Conversion and Storage, Technical University of
Denmark, Kemitorvet 207, 2800 Lyngby, Denmark
e-mail: qfli@dtu.dk; larda@dtu.dk; jojen@dtu.dk

R.F. Savinell
Department of Chemical Engineering, Case Western
Reserve University, Cleveland, OH 44106, USA
e-mail: rfs2@case.edu

in NH_4^+ or are completely dissociated from a very strong acid such as trifluoromethane or perfluoro sulfonic acids.

Poly(perfluorosulfonic acid) (PFSA) membranes are among a variety of proton exchange membranes (PEMs) of particular significance. A PFSA membrane consists of a perfluorinated backbone and perfluorinated ether side chains with terminal sulfonic acid functional groups. Due to the high electronegativity of fluorine, the sulfonic acid bound to the perfluorinated backbone is super strong. It absorbs water forming a continuous hydrated domain, in which protons are solvated from the immobilized anionic (R-SO_3^-) counter ions. The resultant hydrated protons (e.g., H_3O^+) are the inherent protonic charge carriers [8]. In brief, the proton conductivity of the PFSA membranes involves the vehicle mechanism and is strongly dependent on the presence of water, reaching above 0.1 S cm^{-1} under fully hydrous conditions at 80°C .

The Grotthuss mechanism, on the other hand, involves proton conduction through an infinite network of hydrogen bonds. The strength of the hydrogen bond is intermediate, typically with a bond energy of around $10\text{--}30 \text{ kJ mol}^{-1}$. This energy is higher than that of van der Waals interactions (around 1 kJ mol^{-1}) but much lower than that of covalent chemical bonds (about 400 kJ mol^{-1}) [9]. Because of this relatively low bond strength, the energetics for formation and breaking of hydrogen bonds can be triggered by, e.g., thermal energy, often resulting in a time-varying distribution of hydrogen bonds among different donor–acceptor pairs in an acid–base system. A combination of two-dimensional infrared (2DIR) spectroscopy and molecular dynamic simulations has demonstrated that a vast number of hydrogen bonds are part of a “hydrogen bonded well” of attraction in which protons are changing the hydrogen bonding partners within a time scale of 200 fs [10]. Despite this continuous dynamics, the fluctuation is quite small in terms of the total number of H-bonds, which means that an individual hydrogen atom for $85\text{--}90\%$ of the time is involved in hydrogen bonding with one or another oxygen atom [11].

The variable, temporary, forming-breaking dynamic hydrogen bonds allow for the hopping mechanism of proton conduction, a more chemical than hydrodynamic process. The hopping mechanism involves the breaking of an O–H bond in one molecule and forming the same type of bond with another through a well-established hydrogen bond chain. The net effect is a structure diffusion rather than transfer of individual protons [12]. This should be understood in a way that it is not the same proton that is transmitted along the chain. Each proton moves over a very small distance though the eventual effective movement of the charge is over a larger distance. Another characteristics for this structure diffusion process is the low activation energy of conductivity compared to that for a regular movement of the ions through a viscous medium.

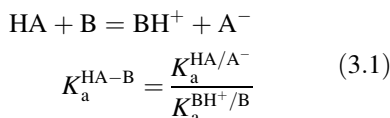
As an example, concentrated H_3PO_4 undergoes a self-dissociation to a degree of 7.4% with the formation of H_4PO_4^+ and H_2PO_4^- [13, 14]. The acid is well known to exhibit strong and polarizable hydrogen bonds, resulting in clustering of acid molecules with a viscosity of nearly two orders of magnitude higher than that of water. The high viscosity effectively hinders the Stokesian migration of ions and as a result phosphoric acid exhibits a high intrinsic proton conductivity based to a significant extent on the *Grotthuss mechanism*, with a proton transference number of $t_{\text{H}^+} \approx 0.98$ [15].

The Grotthuss mechanism of proton conductivity does not involve parasitic transport of the proton solvent, e.g., water. From technological points of view, to achieve operation of a PEM fuel cell at elevated temperatures above the boiling point of water under ambient pressure, a membrane of this type of proton conduction mechanism is desired. So far the most successful approach towards high temperature proton conducting membranes is to dope basic polymers with amphoteric acids, e.g., phosphoric acid, which is the major subject of this book. It is the acid–base interaction that is generating the protonic charge carriers. Chemically, the acidity difference ($\Delta\text{p}K_{\text{a}}$) between the conjugate acid of the base and the free acid dictates the

degree of proton transfer of the acid–base equilibria and therefore, to a great extent, the ionicity and the strength of the hydrogen bonds. It has long been invoked that the strength of the H-bond can be accounted for in terms of the ΔpK_a by thermodynamic, IR and NMR studies [16]. Though by no means straightforward [17], the pK_a method is the most promising empirical tool for quick and efficient H-bond strength prediction for design of complex H-bond interaction patterns in crystals and mesophases [16]. This chapter is first devoted to compiling information of proton conducting acid–base systems from aqueous solutions, ionic liquids, ionic solid crystals to acid–base polymer membranes. Based on the information, the hypothesis is extended such that an appropriate acidity matching of the acid and base components is assumed to play a critical role in the formation of extensive hydrogen bonding networks, which are essential to establish the Grotthuss mechanism of the proton conductivity. It should be remarked that the acid–base chemistry should only be considered as proton conductivity precursors while the structural and dynamical nature of hydrogen bonds are the key to understanding long-range proton transport in these environments [6]. This chapter, however, does not explicitly address the molecular dynamics, for which the reader is referred to the excellent work by Kreuer et al. [6, 18, 19].

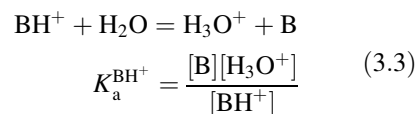
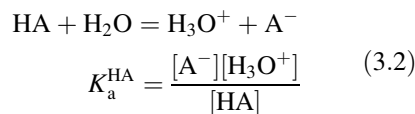
3.2 Thermodynamics of Acid–Base Chemistry

In chemistry, acids and bases can be categorized in terms of their Brønsted acidity. It relates to the ability of the Brønsted acid, HA, to donate a proton to a Brønsted base, B, which is normally the solvent (3.1).



With water as the most widely used solvent, the acidity constants of an acid and a protonated base

are expressed according to (3.2) and (3.3), respectively. Note that concentrations are used here for simplicity although a more correct procedure is to use activities.



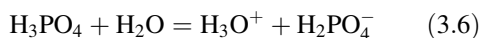
More often pK_a or $\Delta pK_a^{\text{BH}^+-\text{HA}}$ is used where the operator, p, means $-\log x$. The latter is defined as the difference of the pK_a value of the conjugate acid BH^+ of the base B and the pK_a value of the acid, HA, as shown in (3.4).

$$\Delta pK_a^{\text{BH}^+-\text{HA}} = pK_a^{\text{BH}^+} - pK_a^{\text{HA}} \quad (3.4)$$

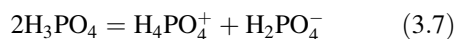
Thermodynamically, the $\Delta pK_a^{\text{BH}^+-\text{HA}}$ of an acid–base pair indicates the free energy change for the proton transfer from the acid to the base as in (3.5).

$$\Delta G^0 = -2.303RT \Delta pK_a \quad (3.5)$$

Taking phosphoric acid as an example, the acid dissociates in a dilute aqueous solution (3.6).



For $pK_a^{\text{H}_3\text{PO}_4} = 2.12$ and $pK_a^{\text{H}_3\text{O}^+} = -1.74$, the $\Delta pK_a^{\text{H}_3\text{O}^+-\text{H}_3\text{PO}_4} = -3.86$ corresponds to a free energy change of 22 kJ mol^{-1} , i.e., 0.23 eV is needed for the transfer of a proton from one phosphoric acid molecule to a water molecule. Consequently it only happens to a limited extent. In the absence of water, the self-dissociation of the acid occurs, as in (3.7).

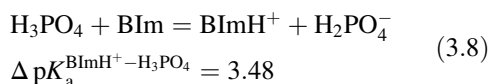


$pK_a^{\text{H}_4\text{PO}_4^+} = -3.0$ and $\Delta pK_a^{\text{H}_4\text{PO}_4^+-\text{H}_3\text{PO}_4} = -5.12$. Thus, H_4PO_4^+ is more acidic than H_3O^+ and more energy (0.30 eV) is needed for transfer of a proton from one phosphoric acid molecule to another.

It should be remarked that the pK_a is often defined for a dilute solution, typically 0.1 mol L^{-1} , with water as the proton solvent. In concentrated solutions, the water activity should be taken into account. When definitions refer to the pK_a scale in aqueous solutions it has the exact meaning only within the water autoprotolysis range ($0 \leq pK_a \leq 14$). This range can be extended by using solvents more acidic or more basic than water; however, such pK_a values are in general less accurate the farther from the water range they are [20]. As to be discussed below, in solvent-free ionic liquid, ionic solid as well as polymeric acid–base systems, the pK_a values are informative only in a qualitative way.

When a stronger base than water is used, its conjugate acid is less acidic than the hydronium ion and therefore the solvent is a stronger proton acceptor. In a phosphoric acid–benzimidazole

(BIm) mixture, for example, the benzimidazole as a proton solvent has a conjugate acid BImH^+ with $pK_a^{\text{BImH}^+} = 5.6$, i.e., much less acidic than the hydronium ion ($pK_a^{\text{H}_3\text{O}^+} = -1.74$). For the equilibrium shown in (3.8), 0.21 eV of energy is released for transfer of a proton from one phosphoric acid molecule to a benzimidazole site. Compared to water, the benzimidazole is a stronger proton acceptor, promoting the acid dissociation to a higher degree than in water.



Another example is the PFSA membranes, e.g., Nafion[®], which is a strong acid with a pK_a value estimated to be about -16 . When such a strong acid is reacting with phosphoric acid, the acid will function as a Brønsted base, as shown in (3.9).



This should be compared to water, which is a stronger base with $\Delta pK_a^{\text{H}_3\text{O}^+ - \text{RSO}_3\text{H}} \approx 14$. The presence of water in the BIm– H_3PO_4 system has little thermodynamic influence on the acid dissociation equilibrium (3.8) as $pK_a^{\text{BImH}^+} > pK_a^{\text{H}_3\text{O}^+}$. In the PFSA– H_3PO_4 system, however, the presence of water would first of all level off the strength of the sulfonic acid as the acid preferably transfers its proton to water to form H_3O^+ . As a general fact, any acid that is stronger than H_3O^+ would dissociate in water forming H_3O^+ . In other words, no acid stronger than H_3O^+ exists in the aqueous media as it steadily dissociates into H_3O^+ . As $pK_a^{\text{H}_3\text{O}^+} = -1.74 > pK_a^{\text{H}_4\text{PO}_4^+} = -3.0$, the presence of water would sufficiently suppress reaction (3.9). This system will be further discussed in Sect. 3.6.4.

3.3 Hydrogen Bonds

3.3.1 Hydrogen Bonds and Their Correlation with ΔpK_a

The term “hydrogen bond” has been used to describe a weak electrostatic chemical bond formed between a covalently bonded hydrogen atom and a strongly electronegative atom with a lone pair of electrons. The complexity of the phenomenon has been a subject of continuous debates over a century. The debating issues include the nature of physical forces and covalence [21], the range of donors and acceptors [22], crystallographic data of interatomic distances and bond energies [20, 23], spectroscopic measurements by infrared [24] and NMR [25] as well as computational information.

Criteria as evidence have been emphasized and listed for definition and characterization of the hydrogen bond formation [26]. One of the most interesting characteristics is the relation between the hydrogen bonding and proton transfer chemistry, i.e., the correlation observed between the pK_a of the protonated base (BH^+) and that of the free acid (HA) with the energy of the hydrogen bond formed from them [27].

Gilli et al. [27] systematically studied the covalent nature of the strong H-bond and showed

that weak H-bonds are basically electrostatic while stronger H-bonds are mixtures of electrostatic and covalent contributions. The covalent fraction gradually increases as the difference (ΔpK_a) of the acid base acidities or the donor-acceptor proton affinities approaches zero. In the study, pK_a values in water are compiled and used as an appropriate acid-base indicator [27], spanning a range of $-14 \leq pK_a \leq 53$ for proton donors and $-12 \leq pK_a \leq 16$ for proton acceptors, as partly shown in Fig. 3.1.

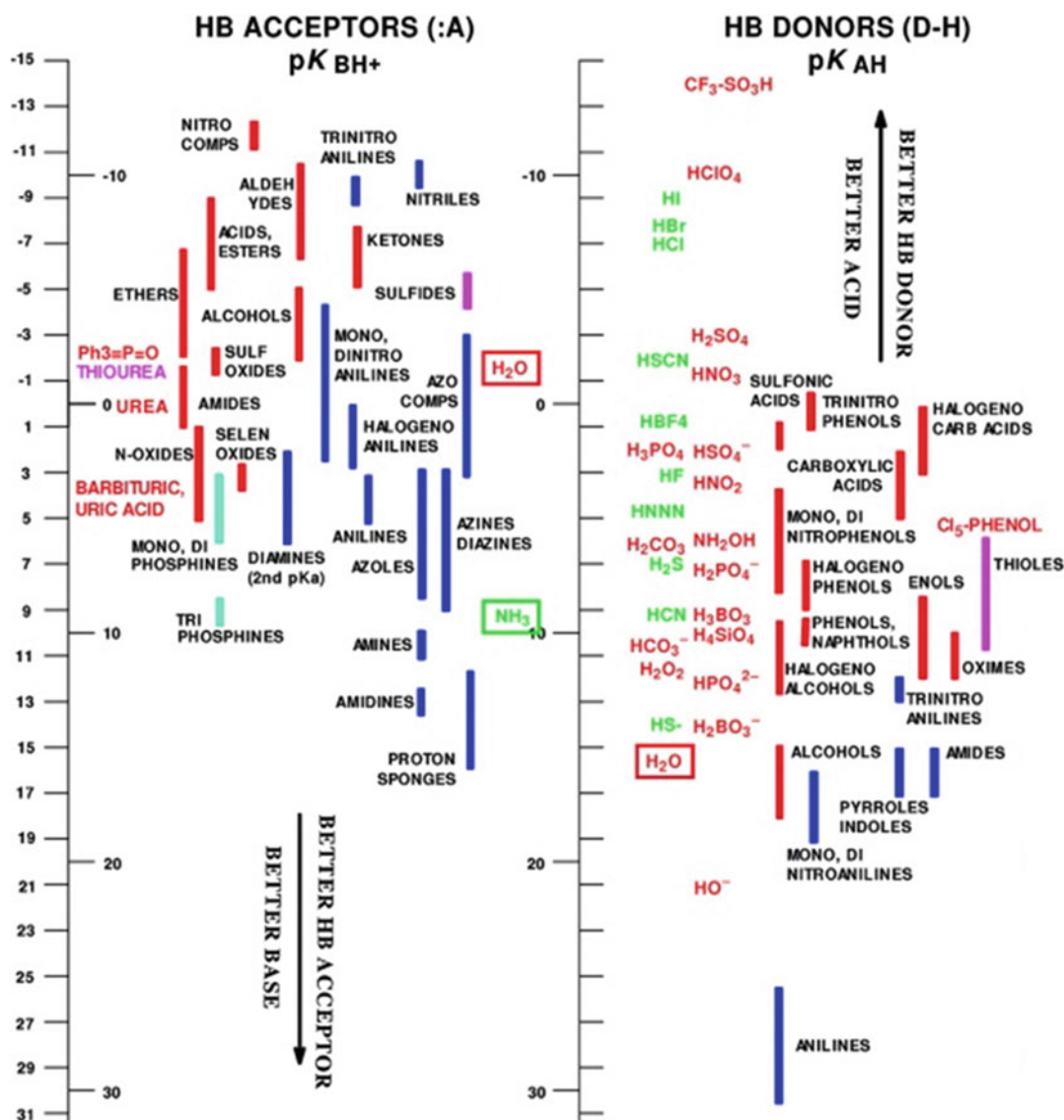


Fig. 3.1 The pK_a chart of important types of hydrogen bond acceptors (left) and donors (right). Reproduced from [27] with permission of the American Chemical Society

The pK_a scale of HB donors (free acids) on the right and the pK_a scale of acceptors (protonated bases BH^+) on the left are placed in such a way that the most common acids and bases are matched in order to achieve strengthened hydrogen bonds.

On the other hand, the authors have estimated the H-bond strengths from the crystallographic databases and gas-phase bond dissociation enthalpies from the thermodynamic NIST Database. Comparison of the compiled ΔpK_a and H-bond strength data verified the hypothesis that the strength of the $A-H \cdots B$ bond increases with decreasing ΔpK_a , i.e. the difference of the acid dissociation constants of the H-bond acceptors and donors. In other words, for acid–base pairs of large negative ΔpK_a values complete proton transfer from the acid to the base occurs, forming ionic bonds. Acid–base pairs of numerically smaller ΔpK_a values allow for partial transfer of proton and formation of hydrogen bonds. The H-bond strength reaches the maximum when the ΔpK_a approaches zero.

The assumption that these strong, short H-bonds occur for acid–base systems with $\Delta pK_a = 0$ is based on the pK_a values in water, a solvent of a high dielectric constant and therefore good ability to stabilize ionic H-bonds. In practice, the pK_a matching can be in a range of 2–3 units for the formation of H-bonds, as to be seen in the following section.

3.3.2 Degree of Proton Transfer of Carboxylic Acid and N-Base Systems

Infrared (IR) spectroscopy has been extensively used for evaluation of the protic ionicity for a large number of acid–base systems in very different ΔpK_a regions, as well summarized by Zundel [28, 29]. As an example, acid–base systems consisting of carboxylic acids and N-bases [29] have been thoroughly investigated in terms of the position of the proton transfer equilibrium in the $OH \cdots N \leftrightarrow O^- \cdots H^+N$ type of hydrogen bonds, as shown in Fig. 3.2.

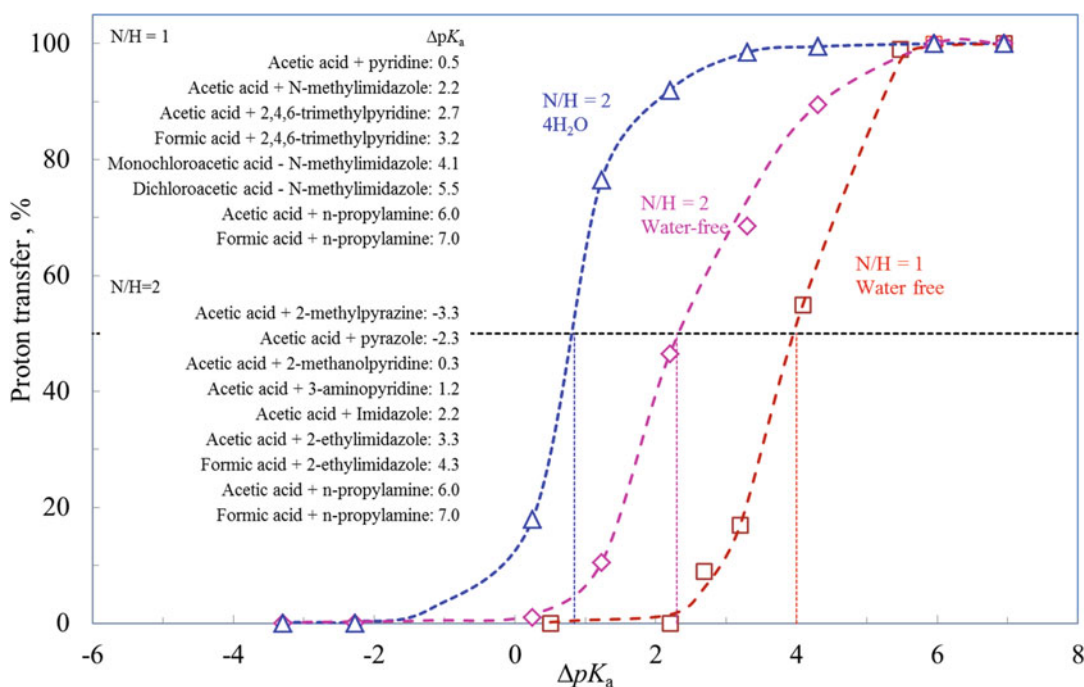


Fig. 3.2 The degree of proton transfer in carboxylic acid and N-base systems as estimated from IR spectra. Data were taken from Zundel et al. [29] for those acid–base

pairs listed in the figure, which are grouped according to the ratio of total number of N sites to the total number of H donor sites

For the group of mixtures where both the numbers of the base or acid functional sites are one ($N/H = 1$), the proton transfer takes place for those with $\Delta pK_a > 2$ and is nearly complete when $\Delta pK_a > 5.5$. The observed $\Delta pK_a^{50\%}$, where 50 % proton transfer occurs, is 4.0. This is the point referred to by the authors where a symmetrical hydrogen bond is assumed to form and that the bond has the greatest polarizability. This might be understood, not as a situation in which a proton is partly transferred and “resting” on the top of the activation energy barrier hill of the transfer process, but in a statistical sense that 50 % of the protons are more or less transferred at any time but each proton may transfer back and forth in a dynamic equilibrium.

It is interesting to note that the 50 % proton transfer in hydrogen bonds does not occur when the pK_a of the acid and the pK_{aH} of the protonated base are equal, i.e., at $\Delta pK_a = 0$, as predicted by Gilli et al. [27]. Apparently, the $\Delta pK_a^{50\%}$ depends on the nature of the proton acceptors as well as on the environment of these bonds. Changes of the molecular structures, for example, in the presence of additional N -sites of the bases, alter the interaction characteristics of the acid–base pairs and consequently the hydrogen bonding equilibrium. For mixtures with N/H ratios of 2, the $\Delta pK_a^{50\%}$ is shifted to 2.3 (see Fig. 3.2), showing the promoted formation of hydrogen bonds by the steadily available basic sites.

Addition of water to these $N/H = 2$ acid–base mixtures also shifts the proton transfer equilibrium. In the presence of four water molecules per acid–base pair, the $\Delta pK_a^{50\%}$ is further reduced from 2.3 to 0.9. In analogy with the effect of the molecular structure, i.e., the fact that increasing the number of N -sites considerably changes the symmetry of the bonds, the presence of water obviously shifts the proton transfer equilibrium in favor of the polar structure of $O \cdots H^+N$ bonds. For dilute aqueous solutions, the behavior may most probably follow the prediction of Gilli et al. [17], i.e., $\Delta pK_a = 0$.

It seems clear that the $\Delta pK_a^{BH^+ - HA}$ value, a thermodynamic measure of the degree of proton

transfer from the acid to the base, is well correlated with the strength as well as the polarizability of the hydrogen bonds formed between the acid and base. The formation and strength of extensive hydrogen bonds is in turn correlated to the proton dynamics, i.e., the breaking and reforming of the hydrogen bonds and therefore allowing for the Grotthuss mechanism of the proton conductivity. The hydrogen bonding may also encourage the cooperative dipole orientation and therefore affect, for example, the dielectric constant, as observed for phosphoric acid [30].

3.4 Ionicity of Protic Liquids and Solids

In case of the hydrogen bond formation, the proton is not stably positioned at either the base B or the conjugated base A^- . In other words, the donor and acceptor cannot always be distinguished. From a chemistry point of view, however, a hydrogen bond can be understood as an incipient proton transfer reaction from a proton donor acid (HA) to a proton acceptor base (B). In this context, the proton transfer and hydrogen bond formation, either in the $A \cdots H - B$ or ionic $A^- \cdots H - B^+$ form, are well correlated with the pK_a values of the acidic and basic components.

For an acid–base mixture, liquid or solid, to be considered as purely ionic, the equilibrium of proton-transfer should be at least 99 %, which means a *complete* transfer of the proton occurs from the donor acid to the acceptor base. Only upon the incomplete transfer of protons from a Brønsted acid to a Brønsted base can hydrogen bonds in the form of networks be built up. The degree of ionic nature of the bonds is named *ionicity*, a measure of how complete the proton transfer occurs. The ionicity can be estimated from the difference of the acidities of the acid and protonated base, ΔpK_a , the driving force shifting the acid–base equilibrium towards the ionic state. A larger ΔpK_a leads to more

complete proton transfer and thus higher ionicity of the acid–base system.

As a qualitative means to investigate the ionic nature of acid–base systems, various techniques have been employed such as one- or two-dimensional nuclear magnetic resonance (NMR) spectroscopy [31], infrared (IR) spectroscopy [32], the Walden plot [33], the ratio of molar conductivities $\Lambda_{\text{imp}}/\Lambda_{\text{NMR}}$ (determined by electrochemical impedance spectroscopy and pulse-field-gradient spin-echo NMR, respectively) [34]. Some of these will be discussed below.

3.4.1 Protic Ionic Liquids

The $\text{p}K_{\text{a}}$ value is a solvent-dependent property. It is not defined in non-solvent systems such as ionic liquids. It is interesting, however, that the $\text{p}K_{\text{a}}$ values of the constituent acid and base, as a measure of proton affinities in aqueous media, have been proposed for use in these nonaqueous protonic systems.

It seems that Ohno and coworkers [35, 36] are the first who reported the protic ionic liquids (PIL) formed by proton transfer from a Brønsted acid to a Brønsted base. The properties of PIL are strongly dependent on the extent of proton transfer from the acid to the base. By definition an ionic liquid is entirely composed of ions, however, 100 % ionization of ionic liquids may not always occur. Angell et al. [37, 38] calculated the Gurney type-free energy level diagram for protic ionic liquids from the $\Delta\text{p}K_{\text{a}}$ values of the respective acids and bases. A good correlation of the $\Delta\text{p}K_{\text{a}}$ was found with the boiling points, vapor pressures, proton conductivity as well as the H_2 -air open circuit voltage of the PIL-based electrolytes.

PILs of larger $\Delta\text{p}K_{\text{a}}$ values, i.e., formed from strong acids and/or bases are classified as “good ionic liquids” [39, 40], which are expected to yield lower equilibrium concentrations of the remaining acid and base molecules. The acid

and/or base components are in general volatile. A correlation of the high $\Delta\text{p}K_{\text{a}}$ with the lower vapor pressure is therefore established [41]. In terms of ionicity, it was proposed that $\Delta\text{p}K_{\text{a}} > 10$ is required to achieve at least 99 % proton transfer in order to form purely ionic salts [37]. Miran et al. [42] prepared a series of PILs with a wide variation of the $\Delta\text{p}K_{\text{a}}$ values of the amines and acids. The used base was 1,8-diazabicyclo-[5,4,0]-undec-7-ene (DBU, $\text{p}K_{\text{aH}} = 13.4$) while the Brønsted acids were of different acidities with $\text{p}K_{\text{a}}$ values ranging from 0.1 to -10 . The authors found that protic ionic liquids with $\Delta\text{p}K_{\text{a}} \geq 15$ exhibited almost complete proton transfer and therefore showed good thermal stability.

Similarly, Angell and coworkers [43] reported that the studied acid–base pairs with the high ionicity are those with a proton transfer gap of about 0.7 eV, corresponding to $\Delta\text{p}K_{\text{a}}$ values of ca. 12. The very high $\Delta\text{p}K_{\text{a}}$ values required to achieve complete proton transfer in protic ionic liquids should be compared with those in aqueous solutions, as discussed above. It seems that the nonaqueous solvation environment of ionic liquids has a very strong effect on the energetics of proton transfer.

3.4.2 Protic Solid Crystals

For solid crystals, it is found that the $\Delta\text{p}K_{\text{a}}$ value defines, to a large extent, the protonation state. Sobczyk [44] studied pentachlorophenolate crystal complexes with a series of ternary amines, showing that the low $\Delta\text{p}K_{\text{a}}$ region ($\Delta\text{p}K_{\text{a}} < 0$) corresponds to the hydrogen-bonded complexes without proton transfer while the high $\Delta\text{p}K_{\text{a}}$ region ($\Delta\text{p}K_{\text{a}} > 4$) corresponds to the ionic pairs. It is reported that for diffraction experiments in the solid state, the $\Delta\text{p}K^{50\%}$, where 50 % proton transfer occurs, is shifted by nearly 1.5 $\text{p}K_{\text{a}}$ units [45]. In another study of crystal structures of a number of compounds formed from acids and bases of varying $\Delta\text{p}K_{\text{a}}$ values, Banerjee et al. [46] showed that

substantial proton transfer took place in the crystalline salt only when $\Delta pK_a > 3$. Below this value, the crystal structure was found to be a kind of co-crystals consisting of salts and solid acid/base molecules. It is in fact a rule of thumb in the co-crystal field [26, 47] that the best interval of the close pK_a matching should be more than three units in order to achieve significant proton transfer in the solid state of an ionic compound.

The effect of the molecular structure on the proton transfer and hydrogen bonding is also observed for solid protic compounds. In a study on the salt form of drug substances, MacFarlane et al. [48] prepared thirteen new protic compounds by reactions between pharmaceutically active compounds of primary amines or tertiary amines with varied pK_a values and organic (gentisic, benzoic, and salicylic) acids. Focusing on the crystal structure, melting point and water solubility, they found that the amine form of bases plays a critical role in the proton transfer and the ionicity of the crystalline salts. With simple primary amines as the basic constituent, $\Delta pK_a > 2$ is sufficient to yield a predominant proton transfer, i.e., ~90 % ionization. With $\Delta pK_a > 4$ the extent of ionization of these salts would be >99 %. When the bases are simple tertiary amines, greater values of $\Delta pK_a > 6$ are required to achieve complete proton transfer.

3.4.3 ^1H NMR Chemical Shift

By means of ^1H NMR spectra, the ^1H chemical shift is reported to change linearly with the proton affinity of a Brønsted base site [49]. Miran et al. [50] used the N–H proton chemical shift to identify strong hydrogen bonds in a series of salts of DBU with a variety of Brønsted acids. They observed chemical shifts at 7.30 ppm for $(\text{CF}_3\text{SO}_2)_2\text{NH}$ ($pK_a = -10.0$), 8.31 ppm for $\text{CF}_3\text{SO}_3\text{H}$ ($pK_a = -7.0$), 9.35 ppm for $\text{CH}_3\text{SO}_3\text{H}$ ($pK_a = -2.0$), and 10.6 ppm for $\text{CF}_3\text{CO}_2\text{H}$ ($pK_a = 0.5$), respectively. The ^1H NMR moves towards the lower field (often

termed downfield, originating from the early days of NMR when the magnetic field was scanned) for the less strong donor acids. This is the result of strong de-shielding of the protons, which is a direct consequence of electron redistribution around the H atom due to the H bond formation.

Using the ^1H NMR chemical shift as a probe towards the chemical environment of a proton in the acid–base complexes, Yan et al. [51] studied equilibria between benzimidazole (BIm) and selected acids of varied acidities. As the authors proposed, a tightly bound proton is shielded and a loosely bound proton is de-shielded by the electron cloud. As a consequence, a mobile proton associated with a carrier molecule usually has a high chemical shift in a range of 10–20 ppm, while an immobile or bound proton has a chemical shift of less than 10 ppm. The chemical shifts of the immobile protons, though not directly reflecting hydrogen bonding of the acid–BIm complexes, reflect the electron redistribution in the benzimidazole ring induced by the complexation acid. As seen from Fig. 3.3, the chemical shift of all protons was found to increase (in particular that of the proton H3 bonded to the C2 position) when the acidity of the acid was increased. When mixed with strong acids such as H_2SO_4 , HCl, and methylsulfonic acid (MSA), the chemical shift of H3 was moved more than 1.0 ppm downfields, compared to the pure BIm. For acids of intermediate strength, the chemical shift of H3 was found to move downfields by 0.11 and 0.71 ppm for phenylphosphonic acid (PPoA) and phosphoric acid, respectively. For the weak acetic acid (HOAc), no apparent chemical shift change of the H3 proton was observed. In other words, for strong acids it could be interpreted as reactions with BIm, forming a salt with complete ionization. For the acids of lower acidity, the proton is less tightly bound to the Brønsted base, which should be a prerequisite for the proton to interchange and conduct via the intermolecular bond breaking and forming process.

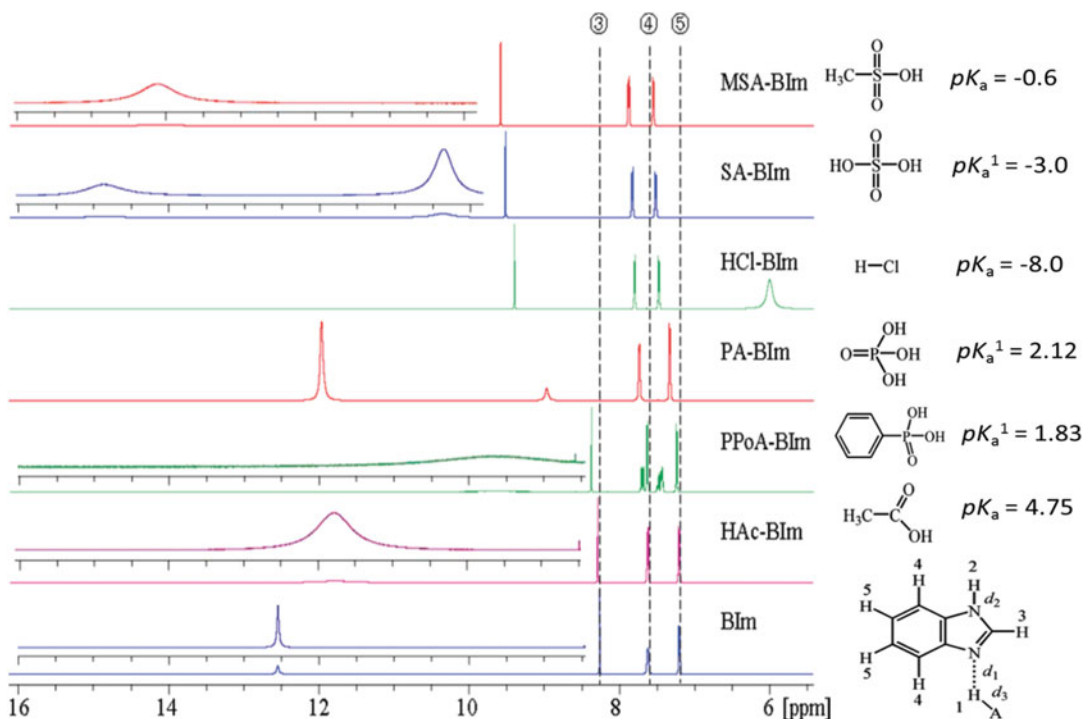


Fig. 3.3 ^1H NMR spectra of the acid-benzimidazole complexes in DMSO-d_6 . The numbers 3, 4, and 5 highlight the shifts for H of the same numbers in

benzimidazole without acid interaction. Reproduced from [51] with permission of the American Chemical Society

3.5 The Walden Rule and Grotthuss Mechanism

For liquid electrolytes, ionic conductivity, self-diffusivity, and viscosity are three key properties. Though originally based on dilute aqueous electrolyte solutions, the Walden rule [52] has been proposed as a tool to provide insight to the proton transfer and ion association. The rule suggests that the molar conductivity of an electrolyte, Λ , is proportional to the fluidity, which can be expressed as the inverse of the shear viscosity η . In other words, the product of the molar conductivity and viscosity of an electrolyte is a constant, as shown in (3.10).

$$\Lambda \cdot \eta = \text{constant} \quad (3.10)$$

An estimate of the constant can be obtained from data for a 0.1 mol L^{-1} aqueous solution of KCl, which is a typical reference of a fully dissociated

salt. The Walden plot is a straight line on a plot of $\log(\Lambda)$ against $\log(1/\eta)$. The deviation of the measured molar conductivity from the ideal line for the KCl reference is an indicator of the ionicity, as any undissociated molecules are mobile but not contributing to the charge conduction. In this case, the conductivity would be lower than the ideal reference line (Fig. 3.4).

Angell et al. [43] investigated protic ionic liquids comprising a few bases and a number of protic acids. The Walden behaviors showed increasing deviations from the ideal KCl line with decreasing $\Delta\text{p}K_a$ values between the components of the respective ionic liquids. In a given series with a common base, the salts with the larger $\Delta\text{p}K_a$ values follow more closely to the Walden rule. For all these ionic liquids, however, the data are close but slightly lower than for the ideal relationship [31]. In protic ionic liquids, in addition to interionic interactions such as coulombic interactions and van der Waals forces,

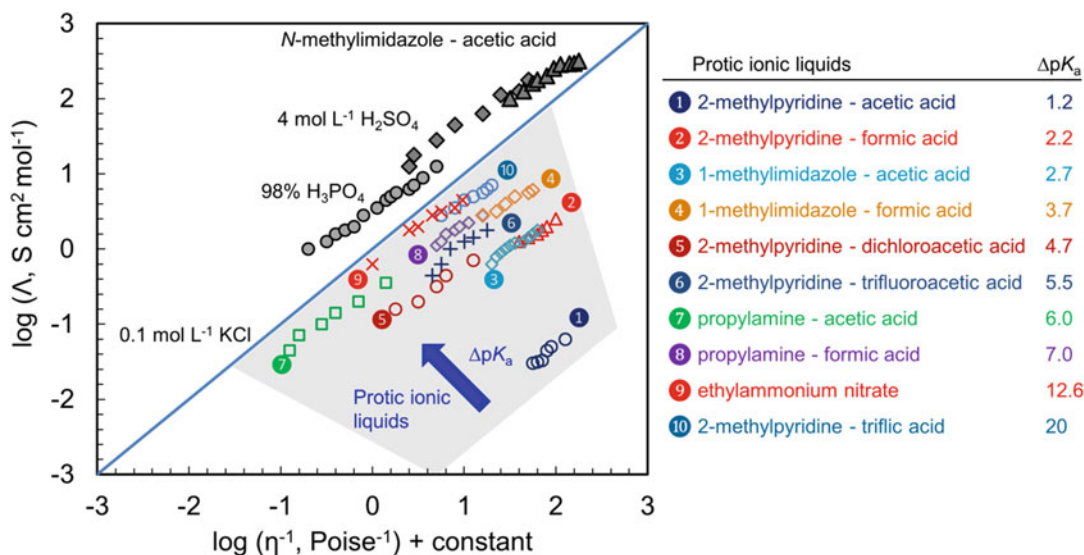


Fig. 3.4 Walden plots for proton conductors. The ideal line is for 0.1 mol L^{-1} KCl. Data for sulfuric acid, phosphoric acid, and the pseudo-ionic liquid of methylimidazole and acetic acid were taken from

Doi et al. [54]. The shaded area is for typical protic ionic liquids taken from Angell et al. [43] with an arrow indicating the direction of increasing ΔpK_a

there may exist strong hydrogen bonds between the protonated cations and anions [48]. As a result, ions, although upon complete proton transfer, are associated as ion pairs and larger clusters with zero net charge. The transport of these paired or clustered charge carriers does not contribute to the molar conductivity of the ionic liquids.

It should be noted that the Grotthuss mechanism via formation and cleavage of hydrogen bonds ideally involves no parasitic transport of the proton solvent. The resultant conductivity is less dependent on the fluidity and therefore is above the ideal Walden relationship. Sulfuric and concentrated phosphoric acids are the typical examples, as seen from Fig. 3.4. For those solutions of fixed concentrations, the conductivity and fluidity are tailored by varying temperatures.

Kanzaki et al. [53] studied ionic liquids consisting of *N*-methylimidazole ($pK_a^{\text{CH}_3\text{ImH}^+} = 7.4$) as the base and a series of acids of varying acidities. It was found that the equimolar mixture of two nonaqueous solvents, *N*-methylimidazole and acetic acid, with $\Delta pK_a = 2.7$, showed little proton transfer from the acid to the base, as

evidenced by the Raman spectra. The liquid mixture was found to primarily consist of electrically neutral molecular species of methylimidazole and acetic acid, forming an extensive hydrogen-bonded network structure [54]. Such a molecular liquid, as authors called, an “ionic liquids with no ions” or a “pseudo-ionic liquid,” showed a significant ionic conductivity of $5.9 \times 10^{-3} \text{ S cm}^{-1}$, in good agreement with the measurements made by MacFarlane et al. [55]. In the Walden plot, the conductivity is above the ideal relationship (Fig. 3.4), apparently via the Grotthuss mechanism.

3.6 Acid–Base Polymer Membranes

3.6.1 Acid-Doped Polybase Membranes

In the absence of free water, pure sulfuric and phosphoric acids undergo self-ionization. Addition of water, as a proton receptor, promotes the dissociation of the acids. Polymers bearing basic sites, such as ether, alcohol, imine, amide, or

imide groups, which react with strong acids, though less efficiently than water, are expected to increase the acid dissociation.

Efforts of early years, as summarized by Lassegues [56], were made to prepare polysalts by dissolving polymers in acid solutions, either aqueous or organic, followed by evaporation of the solvents. The studied polymers include polyethylene oxides (PEO) [57], polyvinyl acetate (PVA) [58]), polyacrylamide (PAAM) [59]), polyvinylpyridine (PVP), and linear or branched polyethyleneimine (L- or B-PEI) [60]. It was found that the conductivity strongly depends on the nature of the two components and on the acid content. A minimum conductivity was generally observed at the acid content corresponding to the maximum degree of protonation where the polymeric base is stoichiometrically neutralized. Excess of the acid seems necessary to achieve high conductivity, suggesting a conduction path in the form of $A^- \cdots H^+ - B$ bonding for the protons. In other words, the proton conduction is supposed to proceed essentially through the hydrogen-bonded anionic chain. The significance of the hydrogen bond dynamics via the anion acid chains seems to be supported by the fact that multiprotic acids (H_2SO_4 and H_3PO_4) showed significantly higher conductivity than that of monoacids (HCl , $HClO_4$). Also the importance of the relative acidities of the acids and polymers was already emphasized; in fact, the systems were classified in terms of pK_a values by Lassegues [56].

For phosphoric acid-doped polybenzimidazole membranes with an intermediate ΔpK_a (3.5), hydrogen bonds are likely formed as shown by infrared spectroscopy [61, 62] and molecular dynamic simulation [63]. The overall proton conductivity of the acid-doped membranes is at least an order of magnitude lower than that of pure phosphoric acid due to the presence of the solid polymer phase. The polymer does not seem to interrupt the extensive hydrogen bond network of the phosphoric acid, though it does decrease the percolation within the liquid-like part of the phosphoric acid domain. As a result, the proton conducting mechanism remains the same, i.e., primarily via the Grotthuss

mechanism. The estimated proton transference number of acid-doped PBI membranes is about 0.96, compared to 0.98 for concentrated phosphoric acid [64]. It is apparent that the rotational motion of phosphoric acid molecules needed for the Grotthuss mechanism is restrained by the PBI-PA interactions, resulting in a lowering of conductivity as protons are less readily transferred between the protonated imidazole (ImH^+) and PA than between phosphoric acid anions or between phosphoric acid and water.

A study on a similar acid-base system, poly(diallyldimethylammonium-dihydrogenphosphate)-phosphoric acid ($PAMA^+ H_2PO_4^- \cdot nH_3PO_4$) [65] showed that the mobility of protonic charge carriers was significantly higher than that given by the self-diffusion coefficient of the phosphate species. Both 1H - and ^{31}P -self-diffusion coefficients decreased with increasing polymer content. However, the ratio of these two coefficients remained the same. As discussed in Sect. 3.2, the presence of water has little effect on the chemistry between the acid and basic polymers, though it promotes the dissociation of excess phosphoric acid, increases the overall concentration of protonic charge carriers, and provides extra hydrogen bonding bridges, all resulting in enhancement of the proton conductivity.

3.6.2 Base-Doped Acidic Polymer Membranes

Kreuer et al. [66] first proposed heterocycles such as imidazole and pyrazole as proton solvents. The unprotonated and protonated nitrogen atoms, instead of water, are expected to act as fluctuating acceptors and donors in proton transfer. Imidazole at the melting point of 90 °C has long been known to possess proton conductivity as high as $10^{-3} \text{ S cm}^{-1}$ [67] via the mechanism of the intermolecular proton transfer [68] and has received much attention in the recent exploration of novel PEM materials [69–72]. Other basic solvents include pyrazole [64, 73], triazole [74, 75], and tetrazoles [76] as shown in Fig. 3.5, where melting points and pK_a values of their protonated forms are also listed.

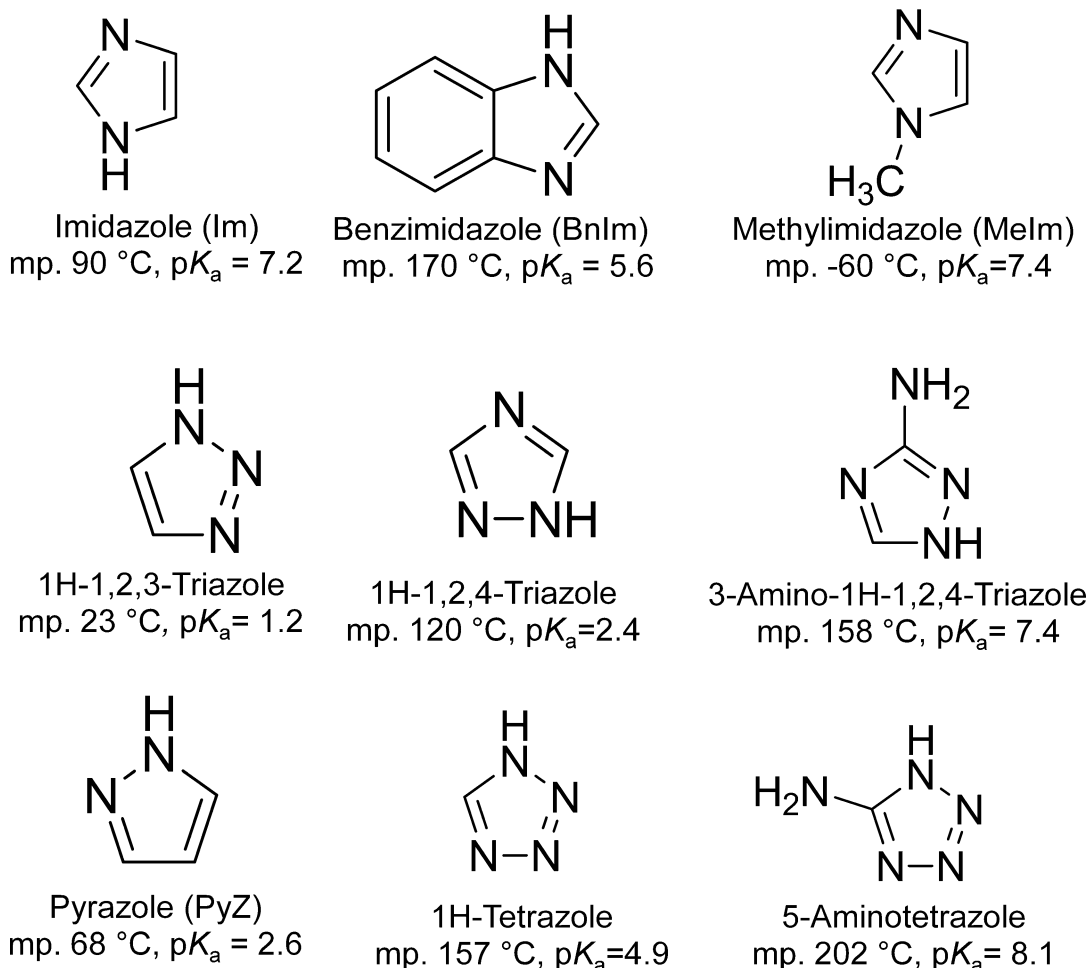


Fig. 3.5 Typically used basic proton solvents and monomers for polyacid membranes

Triazole groups [77] are of particular interest as proton carriers for the development of membranes to be used in fuel cell applications. The basic nitrogen sites act as proton acceptors in combination with acid groups such as sulfonic and phosphonic acid. The rather isometric molecules are advantageous for extended local dynamics and their protonated and unprotonated nitrogen atoms may act as donors and acceptors in proton transfer reactions while the ring itself is nonpolar, causing no strong solvent effects. Acid-doped *N*-heterocyclic-based systems [64, 66] may offer the possibility of suitable proton conductivity over a wide range of

temperature and particularly at elevated temperatures (100–200 °C).

For preparation of acid-base membranes of this type, the used polyacids include polycarboxylic acids, polyphosphonic acid, polysulfonic acid, as well as perfluorinated sulfonic acid membranes. Carboxylic acids and phosphoric acid are weak acids with pK_a ranging from 2 to 5 (see Fig. 3.1), showing a low proton conductivity of 10^{-11} S cm^{-1} level in its crystalline state. When blended with a stronger base than water, e.g., benzimidazole, a high conductivity of 4×10^{-3} S cm^{-1} was reported at 130 °C [78]. Bozkurt et al. [79] prepared polyacrylic

acid membranes containing varied amounts of imidazole. FTIR spectra showed interactions with proton transfer from the carboxylic acid to the free nitrogen site of imidazole, resulting in an increased proton conductivity of up to 10^{-3} S cm^{-1} . In addition, Honma et al. [80] attempted to explore a variety of biopolyacids such as chitin, chitosan, uracil, and alginic acids.

Kreuer et al. [66] doped sulfonated poly(ether ether ketone) (sPEEK) by immersing it into liquid pyrazole and imidazole. A base doping level of 2.3–10, defined as the molar ratio of $[\text{C}_3\text{N}_2\text{H}_4]/[-\text{SO}_3\text{H}]$, could be achieved. The intercalation of imidazole and pyrazole into polymers with Brønsted acid sites is shown to enhance the protonic conductivity. Of the two basic solvents of protons, pyrazole has a lower tendency for the molecular association by hydrogen bonding and therefore a lower proton conductivity, as compared with imidazole. Fu et al. [81, 82] studied acid–base blends based on 2-aminobenzimidazole and sPEEK. They proposed that benzimidazole is protonated by the sulfonic acid, as evidenced by the symmetric stretching of the S–O bonds in FTIR spectra.

Li et al. [83] also prepared blends from sPEEK and a variety of functionalized imidazoles. They evaluated the effect of the $\text{p}K_{\text{a}}$ of the added heterocycles on the unhumidified proton conductivities of the blend membranes over a temperature range from 40 to 150 °C. These membranes showed non-monotonous conductivities with respect to temperature and a clear correlation of the peak temperature conductivity with the $\text{p}K_{\text{a}}$ values of the heterocycles. The authors suggested a theoretical model based on the reaction equilibria between sPEEK sulfonic acid groups and the basicity of the added heterocycles in order to better understand the mechanistic origins of the observed temperature-conductivity profiles.

Another typical kind of sulfonated hydrocarbon polymer, sulfonated polysulfone (sPSU), has also been imbibed with triazole [84, 85]. In a doped membrane of a base doping level of 8.3, the pulsed field magnetic gradient (PFG) NMR spectroscopy showed a self-diffusion coefficient of the triazole 4–5 times lower than that

calculated from the measured conductivity, suggesting that proton transfer between the triazole rings makes the major contribution to the observed ionic conduction. Other sulfonated hydrocarbon polymers used for preparation of blends with heterocycles are poly(styrene sulfonic acid) [86, 87] and poly(2-acrylamido-2-methyl-1-propanesulfonic acid) [88, 89].

N-heterocycles like imidazole as proton solvents were used to replace water in Nafion[®] and found to significantly improve the proton conductivity of these membranes under anhydrous conditions at elevated temperatures. Sun et al. [90] were among the first workers to prepare the water-free Nafion[®] membranes by swelling them in imidazole and imidazolium salt solutions (e.g., trifluoroacetate and trifluoromethane sulfonate). Yang et al. [91] reported that a recast Nafion[®] membrane containing 10 wt % imidazole exhibited a conductivity of as high as 0.1 S cm^{-1} at 160–180 °C. On the other hand, soaking Nafion[®] membranes in either molten imidazole [91] or imidazole solutions in methanol [91, 92] led to much lower conductivities of 10^{-3} S cm^{-1} . 1H-1,2,4-triazole [93, 94], benzimidazole [93], 3-amino-1,2,4-triazole [94], and 5-aminotetrazole [94] have also been explored. These efforts are summarized in Table 3.1.

3.6.3 Polyacid–Polybase Membranes

Kerres et al., among others, developed the acid–base blend membranes from sulfonated polymers and aminated or other basic polymers [98] and concluded that the protonation of the basic groups is incomplete if the base is too weak [99]. Very recently, Frutsaert et al. [70] synthesized novel polymers for the development of high temperature PEMFC membranes comprising a blend of s-PEEK and a fluorinated copolymer bearing imidazole functions as pendant groups. The extensive work on intermediate temperature fuel cell membranes are well reviewed in Chap. 4 of this book including polybenzimidazole as the basic component and sulfonated and phosphonated ionomers of either nonfluorinated or partially fluorinated backbones as the acidic component.

Table 3.1 Base-doped polyacid membranes and their specific conductivities

Acidic polymer	Proton acceptor	Molar ratio (base/acid)	Maximum proton conductivity ($\times 10^3 \text{ S cm}^{-1}$)	Reference
Polyvinyl phosphonic acid (PVPA)	Imidazole	2	5 at 130 °C	[95]
	Benzimidazole	2	1 at 150 °C	[96]
	Pyrazole	~1	8 at 150 °C	[73]
	1-Methylimidazole	~1	7 at 150 °C	
	Triazole	1.5	2.3 at 120 °C	[89]
Poly(ethylene glycol methacrylate phosphate) (PEGMAP)	Benzimidazole	1	3.5 at 160 °C	[97]
	Imidazole	1	2 at 160 °C	
Poly(styrene sulfonic acid) (PSSA)	1H-1,2,4-triazole	1	1.6 at 150 °C	[86]
	Benzimidazole	1.5	0.5 at 150 °C	[87]
Polyacrylic acid	Imidazole	1	1 at 120 °C	[79]
Sulfonated polyetheretherketone (sPEEK)	Imidazole	1/5.5	2.4 at 140 °C	[83]
	Benzimidazole	1/7.7	2 at 140 °C	
	Nitroimidazole	1/7.7	1.2 at 140 °C	
	Dicyanoimidazole	1/7.7	0.7 at 140 °C	
	Polysulfone bearing benzimidazole	?	2 at 120 °C	[81, 82]
Sulfonated polysulfone	1H-1,2,3-triazole	8.3	10 at 110 °C	[84]
	1H-1,2,4-triazole	8	5 at 140 °C	[85]
Poly(2-acrylamido-2-methyl-1-propanesulfonic acid) (PAMPSA)	Imidazole	2	1.5 at 100 °C	[88]
	Triazole	2	0.9 at 140 °C	[89]
Nafion [®]	Water	ca. 22	100 at 80 °C 100 % RH	–
	Imidazole	10 wt%	1 at 100 °C	[90]
			100 at 180 °C	[91]
	Triazole	14.5	23 at 160 °C	[93]
	Benzimidazole	8.5	8.6 at 200 °C	
	Aminotriazole	3.2	1.1 at 180 °C	[94]
	Aminotriazole	2.3	16 at 180 °C	
Phosphoric acid	6	20 at 175 °C	[100]	

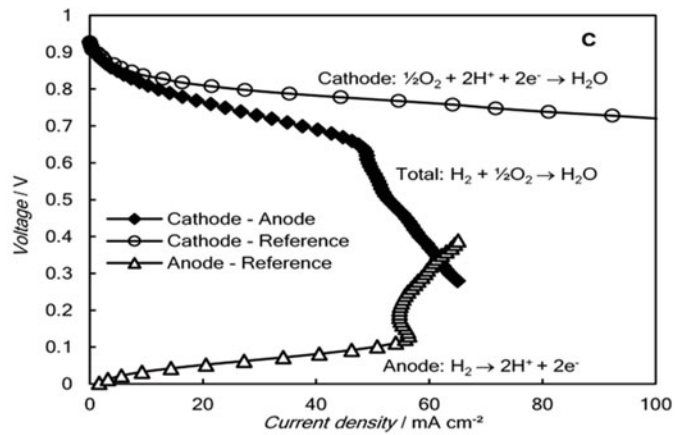
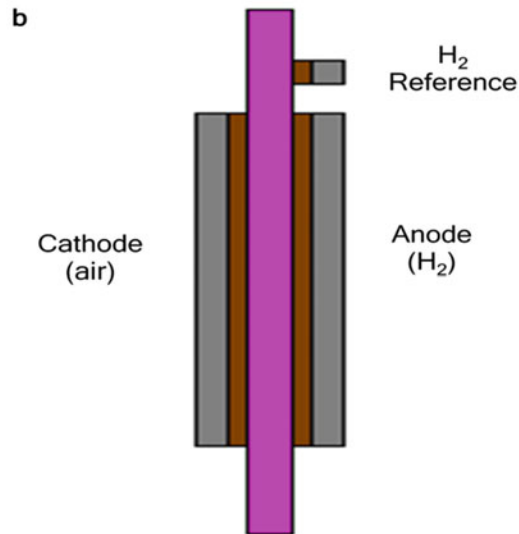
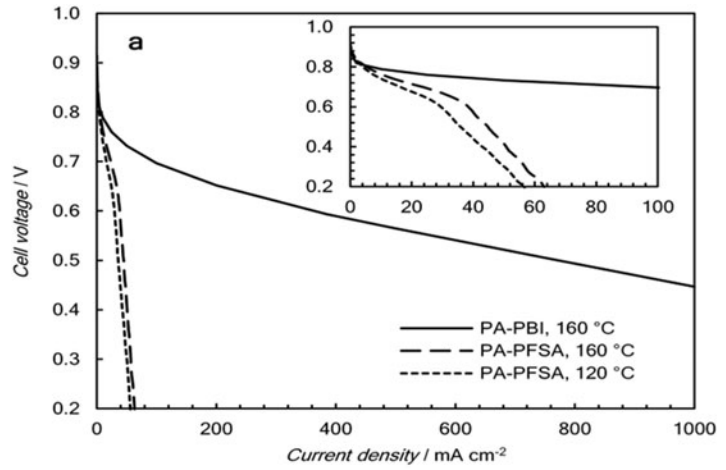
3.6.4 Malfunction of Phosphoric Acid-Doped Perfluorinated Sulfonic Acid Membranes

As already mentioned in previous sections, the sulfonic acid groups in PFSA membranes exhibit remarkably high acidity. In the presence of water, the membrane hydrates to form a continuous hydrated domain in which protons are solvated by water with the immobilized anionic group (R-SO_3^-) as counter-ions [8]. High ionic conductivity of Nafion[®] membranes can also be achieved in solvent environments other than pure water. In 1994, the first attempt was made to

dope PFSA membranes with phosphoric acid instead of water [100]. The acid-doped PFSA membranes have not, after 20 years, been successfully implemented in fuel cells. This is illustrated in Fig. 3.6a where a significant current cannot be supported by the acid-doped PFSA membrane. A recent study [101] showed that the failure of this membrane in fuel cells is due to the anode polarization where an obvious limiting current is observed at a low current density, as seen from Fig. 3.6c. Such a limiting current density in the vicinity of 60 mA cm^{-2} was also observed by operating the electrolytic cell with hydrogen on both sides, i.e., the

Fig. 3.6 (a) I - V curves for fuel cells based on phosphoric acid-doped PFSA (PA-PFSA) and PBI (PA-PBI) membranes operating with non-humidified hydrogen and air. (b) schematic illustration of a hydrogen reference electrode allocated on the anode side. (c) Splitting of the PA-PFSA cell performance into cathodic and anodic potentials with help of a hydrogen reference.

Reproduced from [101] with permission of Wiley



hydrogen oxidation at one electrode and hydrogen evolution on the other. This was explained in such a way that in the absence of water a complete transfer of protons from sulfonic acid to phosphoric acid occurs resulting in the formation of H_4PO_4^+ . The H_4PO_4^+ ions are mobile, detached from the polymer backbone, and contributing to the conductivity through the vehicle mechanism, as discussed by Dippel et al. [15]. The involved parasitic transport of phosphoric acid molecules is assumed to cause the depletion of the acid near the anode, giving rise to the limiting current density.

3.7 Acid–Base Interactions in Inorganic Solid Acids

Solid acids, particularly alkali metal hydrogen sulfates or orthophosphates, e.g., cesium hydrogen sulfates (CsHSO_4 , CHS) [102] or dihydrogen phosphate (CsH_2PO_4 , CDP) [103] are intermediates between salts and acids. At room temperatures solid acids are similar to salts with high water solubility. Most of the solid acid materials exhibit proton conductivities in the 10^{-6} – 10^{-9} S cm^{-1} range at room temperature. A unique property of some alkali metal solid acids is that they undergo an order–disorder solid state phase transition at elevated temperature, as first reported by Komukae et al. [104] for CsHSO_4 . Upon the phase transition, the proton conductivity is increased by 3–4 orders of magnitude [105].

Although no translational motion of complex proton containing species is involved, the local dynamics of the sulfate/phosphate tetrahedron network is essential for the proton conductivity, which is in fact true for other types of Grotthuss conductors. In the superprotonic phase, a dynamically disordered hydrogen bond network is developed [106], providing the capability of conducting protons under anhydrous conditions at elevated operating temperatures [107, 108]. Structural diffusion is the primary mechanism for the anhydrous proton conductivity through a series of rotations of the sulfate or phosphate anions [109–111].

The acid–base chemistry tailors the proton dynamics of the solid acids. Recently, phosphotungstic acid ($\text{H}_3\text{PW}_{12}\text{O}_{40} \cdot n\text{H}_2\text{O}$, PWA) was introduced into CDP, giving a conductivity of 6.6×10^{-4} S cm^{-1} for a composite containing 5 mol% PWA at 170 °C [112]. This temperature is far below the phase transition temperature while the conductivity is significantly higher than the value for either pure CDP or pure WPA under the same conditions. The authors proposed a mechanism working by hydrogen bonding between the two components of the composite. Further acid–base interaction was demonstrated with composites of CDP and organic bases such as guanine and its tautomers [113]. The same phenomenon was observed for the CHS with organic molecules of basic azoles [114]. In both cases, the binary composites showed significantly higher proton conductivities than that of either single component at temperatures below the super transition point. It is most likely that the acid–base interaction establishes a dynamic hydrogen bonding network, enabling efficient proton conduction without demand of an extensive phase disordering at temperatures above the superprotonic transition.

3.8 Conclusive Remarks

Of the two proton conducting mechanisms the Grotthuss mechanism is essential in achieving high anhydrous proton conductivity. The water-independence of the conductivity allows for high temperature operation of electrochemical devices such as fuel cells and electrolyzers under ambient pressure. A prerequisite for the Grotthuss mechanism is the establishment of a dynamic hydrogen bonding network.

Acid–base reaction involving proton transfer from an acid to a base is an effective approach to the development of proton conducting materials. Chemically, the acidity difference ($\Delta\text{p}K_a$) between the conjugate acid of the base and the free acid thermodynamically dictates the degree of proton transfer of the acid–base equilibria and therefore the ionicity, which constitutes the underlying mechanism of proton conduction in

general and of the Grotthuss type in particular. This chapter is an initial effort to compile information of proton conducting acid–base systems including aqueous solutions, ionic liquids, solid crystals, acid-doped basic polymers, base-doped acidic polymers as well as inorganic solid acids. The results emphasize the provisional idea that hydrogen bonds are formed within acid–base systems with a close matching of the acidities of the acid and base components. Of course the dynamics of hydrogen bonds has to be established in order to permit the long-range transport of protons. Further verification of the hypothesis is needed in the future and expected to bring insights of proton conduction and open visions of avenues to new proton conducting materials.

Acknowledgments This work was financially supported by Innovation Fund Denmark (4M Centre 0603-00527B) and Danish Council for Independent Research, Technology and Production Science (no.11-117035/FTP).

References

1. Wikstrom M (1998) Proton translocation by bacteriorhodopsin and heme-copper oxidases. *Curr Opin Struct Biol* 8:480–488
2. Wraight CA, Colín A (2006) Chance and design—proton transfer in water, channels and bioenergetic proteins. *Biochim Biophys Acta* 1757:886–912
3. Kreuer KD (1996) Proton conductivity: materials and applications. *Chem Mater* 8:610–641
4. Marx D (2006) Proton transfer 200 years after von Grotthuss: insights from ab initio simulations. *ChemPhysChem* 7:1848–1870
5. Paddison SJ, Kreuer KD, Maier J (2006) About the choice of the protogenic group in polymer electrolyte membranes: ab initio modelling of sulfonic acid, phosphonic acid, and imidazole functionalized alkanes. *Phys Chem Chem Phys* 8:4530–4542
6. Kreuer KD, Paddison SJ, Spohr E et al (2004) Transport in proton conductors for fuel-cell applications: simulations, elementary reactions, and phenomenology. *Chem Rev* 104:4637–4678
7. Kreuer KD, Rabenau A, Weppner W (1982) Vehicle mechanism, a new model for the interpretation of the conductivity of fast proton conductors. *Angew Chem Int Ed Engl* 21:208–209
8. Steininger H, Schuster M, Kreuer KD et al (2007) Intermediate temperature proton conductors for PEM fuel cells based on phosphonic acid as protogenic group: a progress report. *Phys Chem Chem Phys* 9:1764–1773
9. Stillinger FH (1980) Water revisited. *Science* 209:451–457
10. Eaves JD, Loparo JJ, Fecko CJ et al (2005) Hydrogen bonds in liquid water are broken only fleetingly. *Proc Natl Acad Sci U S A* 102:13019–13022
11. Bakker HJ, Skinner JL (2010) Vibrational spectroscopy as a probe of structure and dynamics in liquid water. *Chem Rev* 110:1498–1517
12. Agmon N (1999) Proton solvation and proton mobility. *Isr J Chem* 39:493–502
13. Munson RA (1964) Self-dissociative equilibria in molten phosphoric acid. *J Phys Chem* 68:3374–3377
14. Vilčiauskas L, Tuckerman ME, Bester G et al (2013) The mechanism of proton conduction in phosphoric acid. *Nat Chem* 4:461–466
15. Dippel T, Kreuer KD, Lassègues JC et al (1993) Proton conductivity in fused phosphoric acid; a $^1\text{H}/^{31}\text{P}$ PFG-NMR and QNS study. *Solid State Ionics* 61:41–46
16. Gilli P, Gilli G (2009) The nature of the hydrogen bond. New York, Oxford
17. Gilli P, Pretto L, Gilli G (2007) $\text{PA}/\text{p}K_a$ equalization and the prediction of the hydrogen-bond strength: a synergism of classical thermodynamics and structural crystallography. *J Mol Struct* 844–845:328–339
18. Kreuer KD (2014) Ion conducting membranes for fuel cells and other electrochemical devices. *Chem Mater* 26:36–380
19. Kreuer K-D (2000) On the complexity of proton conduction phenomena. *Solid State Ionics* 136:149–160
20. Cookson RF (1974) Determination of acidity constants. *Chem Rev* 74:5–28
21. Dykstra CE, Lisy JM (2000) Experimental and theoretical challenges in the chemistry of noncovalent intermolecular interaction and clustering. *J Mol Struct (Theochem)* 500:375–390
22. Desiraju GR, Steiner T (1999) The weak hydrogen bond in structural chemistry and biology. Oxford University Press, Oxford
23. Emsley J (1980) Very strong hydrogen bonding. *Chem Soc Rev* 9:91–124
24. Iogansen AV (1999) Direct proportionality of the hydrogen bonding energy and the intensification of the stretching $\nu(\text{XH})$ vibration in infrared spectra. *Spectrochim Acta* 55A:1585–1612
25. Pecul M, Leszczynski J, Sadlej J (2000) Comprehensive ab initio studies of nuclear magnetic resonance shielding and coupling constants in $\text{XH}\cdots\text{O}$ hydrogen-bonded complexes of simple organic molecules. *J Chem Phys* 112:7930–7938
26. Arunan E, Desiraju GR, Klein RA et al (2011) Defining the hydrogen bond: an account (IUPAC technical report). *Pure Appl Chem* 83:1619–1636
27. Gilli P, Pretto L, Bertolasi V et al (2009) Predicting hydrogen-bond strengths from acid–base molecular properties. The $\text{p}K_a$ slide rule: toward the solution of a long-lasting problem. *Acc Chem Res* 42:33–44

28. Zundel, G (1996) The far infrared vibration of hydrogen bonds with large proton polarizability. *J MOL STRUCT* 381:23–37
29. Lindemann R, Zundel G (1977) Polarizability, proton transfer and symmetry of energy surfaces of carboxylic acid N-base hydrogen bonds—Infrared investigations. *J Chem Soc Faraday Trans 2*(73):788–803
30. Munson RA (1964) Dielectric constant of phosphoric acid. *J Chem Phys* 40:2044–2046
31. Judeinstein P, Iojoiu C, Sanchez JY et al (2008) Proton conducting ionic liquid organization as probed by NMR: self-diffusion coefficients and heteronuclear correlations. *J Phys Chem B* 112:3680–3683
32. Zundel G (2000) Hydrogen bonds with large proton polarizability and proton transfer processes in electrochemistry and biology. In: Prigogine I, Rice SA (eds) *Advances in chemical physics*, vol 111. Wiley, New York, pp 1–217. ISBN 0-471-34990-9
33. MacFarlane DR, Forsyth M, Izgorodina EI et al (2009) On the concept of ionicity in ionic liquids. *Phys Chem Chem Phys* 11:4962–4967
34. Tokuda H, Tsuzuki S, Susan MABH et al (2006) How ionic are room-temperature ionic liquids? An indicator of the physicochemical properties. *J Phys Chem B* 110:19593–19600
35. Hirao M, Sugimoto H, Ohno H (2000) Preparation of novel room-temperature molten salts by neutralization of amines. *J Electrochem Soc* 147:4168–4172
36. Yoshizawa M, Ogihara W, Ohno H (2001) Design of new ionic liquids by neutralization of imidazole derivatives with imide-type acids. *Electrochem Solid-State Lett* 4:E25–E27
37. Belieres J-P, Angell CA (2007) Protic ionic liquids: preparation, characterization, and proton free energy level representation. *J Phys Chem B* 111:4926–4937
38. Bautista-Martinez JA, Tang L, Bellieres J-P et al (2009) Hydrogen redox in protic ionic liquids and a direct measurement of proton thermodynamics. *J Phys Chem C* 113:12586–12593
39. Yoshizawa M, Xu W, Angell CA (2003) Ionic liquids by proton transfer: vapor pressure, conductivity, and the relevance of ΔpK_a from aqueous solutions. *J Am Chem Soc* 125:15411–15419
40. Xu W, Angell CA (2003) Solvent-free electrolytes with aqueous solution—like conductivities. *Science* 302:422–425
41. Luo H, Baker GA, Lee JS et al (2009) Ultrastable superbase-derived protic ionic liquids. *J Phys Chem B* 113:4181–4183
42. Miran MS, Kinoshita H, Yasuda T et al (2012) Physicochemical properties determined by ΔpK_a for protic ionic liquids based on an organic super-strong base with various Brønsted acids. *Phys Chem Chem Phys* 14:5178–5186
43. Angell CA, Ansari Y, Zhao ZF (2012) Ionic liquids: past, present and future. *Faraday Discuss* 154:9–27
44. Sobczyk L (1998) X-ray diffraction, IR, UV and NMR studies on proton transfer equilibrating phenol-N-base systems. *Ber Bunsenges Phys Chem* 102:377–383
45. Huyskens P, Sobczyk L, Majerz I (2002) On a hard/soft hydrogen bond interaction. *J Mol Struct* 615:61–72
46. Banerjee R, Bhatt PM, Ravindra NV et al (2005) Saccharin salts of active pharmaceutical ingredients, their crystal structures, and increased water solubilities. *Cryst Growth Des* 5:2299–2309
47. Stoimenovski J, Izgorodina EI, MacFarlane DR (2010) Ionicity and proton transfer in protic ionic liquids. *Phys Chem Chem Phys* 12:10341–10347
48. Stoimenovski J, Dean PM, Izgorodina EI et al (2012) Protic pharmaceutical ionic liquids and solids: aspects of protonics. *Faraday Discuss* 154:335–352
49. Yi D, Zhang H, Deng Z (2010) ^1H and ^{15}N chemical shifts of adsorbed acetonitrile as measures to probe the Brønsted acid strength of solid acids: a DFT study. *J Mol Catal A Chem* 326:88–93
50. Miran MS, Kinoshita H, Yasuda T et al (2011) Hydrogen bonds in protic ionic liquids and their correlation with physicochemical properties. *Chem Commun* 47:12676–12678
51. Zhang DF, Yan LM (2010) Probing the acid-base equilibrium in acid-benzimidazole complexes by ^1H NMR spectra and density functional theory calculations. *J Phys Chem B* 114:12234–12241
52. Walden P (1906) Organic solutions- and ionisation means III Chapter: internal friction and its connection with conductivity. *Z Phys Chem* 55:207–249
53. Kanzaki R, Doi H, Song X et al (2012) Acid-base property of N-methylimidazolium-based protic ionic liquids depending on anion. *J Phys Chem B* 116:14146–14152
54. Doi H, Song X, Minofar B et al (2013) A new proton conductive liquid with no ions: pseudo-protic ionic liquids. *Chem Eur J* 19:11522–11526
55. MacFarlane DR, Pringle JM, Johansson KM et al (2006) Lewis base ionic liquids. *Chem Commun* 18:1905–1917
56. Lassegues J-C (1992) Mixed inorganic-organic systems: the acid/polymer blends. In: Colombari PH (ed) *Proton conductors: solids, membranes and gels—materials and devices*. Cambridge University Press, New York, p 311
57. Donoso P, Gorecki W, Berthier C et al (1988) NMR, conductivity and neutron scattering investigation of ionic dynamics in the anhydrous polymer protonic conductor $\text{PEO}(\text{H}_3\text{PO}_4)_x$. *Solid State Ionics* 28:969–974
58. Petty-Weeks S, Zupancic JJ, Swedo JR (1988) Proton conducting interpenetration polymer networks. *Solid State Ionics* 31:117–125
59. Stevens JR, Wiczorek W, Raducha D et al (1997) Proton conducting gel H_3PO_4 electrolytes. *Solid State Ionics* 97:347–358
60. Tanaka R, Yamamoto H, Shono A et al (2000) Proton conducting behavior in non-crosslinked and

- crosslinked polyethylenimine with excess phosphoric acid. *Electrochim Acta* 45:1385–1389
61. Glipa X, Bonnet B, Mula B et al (1999) Investigation of the conduction properties of phosphoric and sulfuric acid doped polybenzimidazole. *J Mater Chem* 9:3045–3049
 62. Bouchet R, Siebert E (1999) Proton conduction in acid doped polybenzimidazole. *Solid State Ionics* 118:287–299
 63. Vilčiauskas L, Tuckerman ME, Melchior JP et al (2013) First principles molecular dynamics study of proton dynamics and transport in phosphoric acid/imidazole (2:1) system. *Solid State Ionics* 252:34–39
 64. Li Q, Jensen JO, Savinell RF et al (2009) High temperature proton exchange membranes based on polybenzimidazoles for fuel cells. *Prog Polym Sci* 34:449–477
 65. Bozkurt A, Ise M, Kreuer KD et al (1999) Proton-conducting polymer electrolytes based on phosphoric acid. *Solid State Ionics* 125:225–233
 66. Kreuer KD, Fuchs A, Ise M et al (1998) Imidazole and pyrazole-based proton conducting polymers and liquids. *Electrochim Acta* 43:1281–1288
 67. Kawada A, McGhie AR, Labes MM (1970) Protonic conductivity in imidazole single crystal. *J Chem Phys* 52:3121–3125
 68. Münch W, Kreuer KD, Silvestri W et al (2001) The diffusion mechanism of an excess proton in imidazole molecule chains: first results of an ab initio molecular dynamics study. *Solid State Ionics* 145:437–443
 69. Schuster M, Meyer WH, Wegner G et al (2001) Proton mobility in oligomer-bound proton solvents: Imidazole immobilization via flexible spacers. *Solid State Ionics* 145:85–92
 70. Frutsaert G, Delon L, David G et al (2010) Synthesis and properties of new fluorinated polymers bearing pendant imidazole groups for fuel cell membranes operating over a broad relative humidity range. *J Polym Sci A Polym Chem* 48:223–231
 71. Frutsaert G, David G, Ameduri B et al (2011) Synthesis and characterisation of novel fluorinated polymers bearing pendant imidazole groups and blend membranes: new materials for PEMFC operating at low relative humidity. *J Membr Sci* 367:127–133
 72. Boroglu MS, Celik SU, Bozkurt A et al (2011) The synthesis and characterization of anhydrous proton conducting membranes based on sulfonated poly (vinyl alcohol) and imidazole. *J Membr Sci* 375:157–164
 73. Yamada M, Honma I (2005) Anhydrous proton conducting polymer electrolytes based on poly (vinylphosphonic acid)-heterocycle composite material. *Polymer* 46:2986–2992
 74. Cosgun S, Celik SU, Ozden S et al (2010) Proton conductivity properties of acid doped fluoroalkylated 1,2,3-triazole. *J Fluorine Chem* 131:776–779
 75. Ozden S, Celik SU, Bozkurt A (2010) Synthesis and proton conductivity studies of doped azole functional polymer electrolyte membranes. *Electrochim Acta* 55:8498–8503
 76. Sinirlioglu D, Muftuoglu AE, Bozkurt A (2014) Investigation of proton conductivity of inorganic-organic hybrid membranes based on boronic acid and tetrazole. *J Polym Res* 21:526–538
 77. Subbaraman R, Ghassemi H, Zawodzinski TA Jr (2007) 4,5-Dicyano-1H-[1,2,3]-triazole as a proton transport facilitator for polymer electrolyte membrane fuel cells. *J Am Chem Soc* 129:2238–2239
 78. Karadedeli B, Bozkurt A, Baykal A (2005) Proton conduction in adipic acid/benzimidazole hybrid electrolytes. *Physica B* 364:279–284
 79. Bozkurt A, Meyer WH, Wegner G (2003) PAA/imidazol-based proton conducting polymer electrolytes. *J Power Sources* 123:126–131
 80. Yamada M, Honma I (2004) Alginic acid-imidazole composite material as anhydrous proton conducting membrane. *Polymer* 5:8349–8354
 81. Fu Y, Manthiram A, Guiver MD (2006) Blend membranes based on sulfonated poly(ether ether ketone) and polysulfone bearing benzimidazole side groups for proton exchange membrane fuel cells. *Electrochem Commun* 8:1386–1390
 82. Fu Y, Manthiram A, Guiver MD (2007) Acid-base blend membranes based on 2-amino-benzimidazole and sulfonated poly(ether ether ketone) for direct methanol fuel cells. *Electrochem Commun* 9:905–910
 83. Li W, Norris BC, Snodgrass P et al (2009) Evaluating the role of additive pK(a) on the proton conductivities of blended sulfonated poly(ether ether ketone) membranes. *J Phys Chem* 113:10063–10067
 84. Zhou Z, Li S, Zhang Y et al (2005) Promotion of proton conduction in polymer electrolyte membranes by 1H-1,2,3-triazole. *J Am Chem Soc* 127:10824–10825
 85. Li S, Zhou Z, Zhang Y et al (2005) 1H-1,2,4-triazole: An effective solvent for proton-conducting electrolytes. *Chem Mater* 17:5884–5886
 86. Göktepe F, Bozkurt A, Günday ST (2008) Synthesis and proton conductivity of poly(styrene sulfonic acid)/heterocycle-based membranes. *Polym Int* 57:133–138
 87. Bozkurt A (2005) Anhydrous proton conductive polystyrene sulfonic acid membranes. *Turk J Chem* 29:117–123
 88. Erdemi H, Bozkurt A, Meyer WH (2004) PAMPSA-IM based proton conducting polymer electrolytes. *Synth Met* 143:133–138
 89. Günday ST, Bozkurt A, Meyer WH et al (2006) Effects of different acid functional groups on proton conductivity of polymer-1,2,4-triazole blends. *Polym Sci B Polym Phys* 44:3315–3322
 90. Sun J, Jordan LR, Forsyth M et al (2001) Acid-organic base swollen polymer membranes. *Electrochim Acta* 46:1703–1708
 91. Yang C, Costamagna P, Srinivasan S et al (2001) Approaches and technical challenges to high

- temperature operation of proton exchange membrane fuel cells. *J Power Sources* 103:1–9
92. Fu YZ, Manthiram A (2007) Nafion–imidazole– H_3PO_4 composite membranes for proton exchange membrane fuel cells. *J Electrochem Soc* 154:B8–B12
93. Kim JD, Mori T, Hayashi S et al (2007) Anhydrous proton-conducting properties of Nafion-1,2,4-triazole and Nafion-benzimidazole membranes for polymer electrolyte fuel cells. *J Electrochem Soc* 154:A290–A294
94. Sen U, Celik SU, Ata A et al (2008) Anhydrous proton conducting membranes for PEM fuel cells based on Nafion/azole composites. *Int J Hydrogen Energy* 33:2808–2815
95. Sevil F, Bozkurt A (2004) Proton conducting polymer electrolytes on the basis of poly(vinylphosphonic acid) and imidazole. *J Phys Chem Solids* 65:1659–1662
96. Sevil F, Bozkurt A (2005) Proton conduction in PVPA–benzimidazole hybrid electrolytes. *Turk J Chem* 29:377–383
97. Kufacı M, Bozkurt A, Tülü M (2006) Poly(ethyleneglycol methacrylate phosphate) and heterocycle based proton conducting composite materials. *Solid State Ionics* 177:1003–1007
98. Kerres JA (2001) Development of ionomer membranes for fuel cells. *J Membr Sci* 185:3–27
99. Kerres JA (2005) Blended and cross-linked ionomer membranes for application in membrane fuel cells. *Fuel Cells* 5:230–247
100. Savinell R, Yeager E, Tryk D et al (1994) A polymer electrolyte for operation at temperatures up to 200 °C. *J Electrochem Soc* 141:L46–L48
101. Aili D, Savinell RF, Jensen JO et al (2014) The electrochemical behavior of phosphoric acid doped poly(perfluorosulfonic acid) membranes. *ChemElectroChem* 1:1471–1475
102. Haile SM, Boysen DA, Chisholm CRI et al (2001) Solid acids as fuel cell electrolytes. *Nature* 410:910–913
103. Haile SM, Chisholm CRI, Sasaki K et al (2007) Solid acid proton conductors: from laboratory curiosities to fuel cell electrolytes. *Faraday Discuss* 134:17–39
104. Komukae M, Osaka T, Makita Y et al (1981) Dielectric and thermal studies on new phase-transitions of CsHSO_4 . *J Phys Soc Jpn* 50:3187–3188
105. Baranov AI, Shuvalov LA, Shchagina NM (1982) Superior conductivity and phase-transitions in CsHSO_4 and CsHSO_4 crystals. *JETP Lett* 36:459–462
106. Otomo J, Tamaki T, Nishida S et al (2005) Effect of water vapor on proton conduction of cesium dihydrogen phosphate and application to intermediate temperature fuel cells. *J Appl Electrochem* 35:865–870
107. Traer JW, Goward GR (2007) Solid-state NMR studies of hydrogen bonding networks and proton transport pathways based on anion and cation dynamics. *Magn Reson Chem* 45:S135–S143
108. Uda T, Haile SM (2005) Thin-membrane solid-acid fuel cell. *Electrochem Solid-State Lett* 8:A245–A246
109. Chisholm CR, Jang YH, Haile SM et al (2005) Superprotonic phase transition of CsHSO_4 : a molecular dynamics simulation study. *Phys Rev B Condens Matter Mater Phys* 72:134103
110. Boysen DA, Uda T, Chisholm CRI (2004) High-performance solid acid fuel cells through humidity stabilization. *Science* 303:68–70
111. Mangiatordi GF, Butera V, Russo N et al (2012) Charge transport in poly-imidazole membranes: a fresh appraisal of the Grotthuss mechanism. *Phys Chem Chem Phys* 14:10910–10918
112. Oh S, Insani EK, Nguyen VH et al (2011) Mechanochemically synthesized CsH_2PO_4 – $\text{H}_3\text{PW}_{12}\text{O}_{40}$ composites as proton-conducting electrolytes for fuel cell systems in a dry atmosphere. *Sci Technol Adv Mater* 12:034402
113. Oh S, Kawamura G, Muto H et al (2012) Mechanochemical synthesis of proton conductive composites derived from cesium dihydrogen phosphate and guanine. *Solid State Ionics* 225:223–227
114. Oh S, Kawamura G, Muto H et al (2012) Anhydrous protic conduction of mechanochemically synthesized CsHSO_4 -azole-derived composites. *Electrochim Acta* 75:11–19

Applications of Acid–Base Blend Concepts to Intermediate Temperature Membranes

4

Jochen Kerres

4.1 Introduction

Among the most used materials as proton conductor in membrane fuel cells are sulfonated membranes such as the polymeric perfluorinated sulfonic acids (PFSA) of the Nafion[®] type [1]. Sulfonated membranes have the disadvantage that they require water as “vehicle” for proton transport through the membrane. Therefore, membranes based onto sulfonated polymers can only be used in fuel cells up to temperatures of 100 °C. However, it is desired that fuel cells can be operated at temperatures higher than 100 °C since an increase in temperature leads to the acceleration of electrode kinetics and therefore to an increase in fuel cell efficiency. Phosphoric acid is a proton conductor which has high proton conductivities over a large temperature range of up to more than 200 °C [2], but has the disadvantage being a liquid which makes its utilization as proton-conducting membrane in fuel cells impossible. To exploit the advantages of phosphoric acid for membrane fuel cells, the phosphoric acid molecules have to be immobilized in a solid matrix. Savinell et al. found that basic

engineering polymers such as polybenzimidazoles [3, 4] (PBI) can be doped with phosphoric acid to an acid doping level (ADL) of more than four molecules of phosphoric acid (PA) per polymer repeat unit (PRU) and be used in this form as proton-conducting membrane in fuel cells in the temperature range >100 °C [5], where the phosphoric acid molecules in the membrane matrix build up a hydrogen bridge network which takes over the proton transport [6]. It should be noted that, in case of PBI blends with another acidic component, only the PBI component is taken into account in the ADL calculation and the unit is sometime written as PA/PRU(PBI).

A disadvantage of the H₃PO₄-doped polymer membranes is that they can bleed out a part of the phosphoric acid molecules when the operation temperature of the fuel cells falls below 100 °C and water produced by the fuel cell reaction condenses and dissolves H₃PO₄ [7]. The released H₃PO₄ can cause corrosion damage in the fuel cell system. A further disadvantage of a pure H₃PO₄-doped PBI is chemical degradation of the polymer [8]. As an alternative to polybenzimidazoles, other basic polymers such as pyridine moiety-containing aromatic main-chain polymers can be used. These types of basic polymers are reviewed in Chap. 5 of this book. In the past two decades, several strategies have been implemented to reduce the degradation and to improve the performance of the polymer in

J. Kerres (✉)

Institute of Chemical Process Engineering, University of Stuttgart, Boebling Str. 78, Stuttgart 70199, Germany

Focus Area: Chemical Resource Beneficiation, Faculty of Natural Science, North-West University, Potchefstroom 2520, South Africa

e-mail: jochen.kerres@icvt.uni-stuttgart.de

fuel cell operation. Some of those strategies will shortly be reviewed here.

One possibility for improvement of chemical stability of the polybenzimidazole is the addition of nanoparticles to the polybenzimidazole. For example, OPBI (poly(4,4'-diphenylether-5,5'-bibenzimidazole)) has been blended with amine-modified silica nanoparticles (AMS) [9] or with nanodiamonds [10]. ABPBI (poly(2,5-benzimidazole)) has been modified with sulfonated silica nanoparticles [11]. Poly(2,2'-m-phenylene-5,5'-bibenzimidazole) (PBI Hozol[®])-silica nanocomposites have been synthesized by a sol-gel reaction of tetraethoxysilane in the PBI matrix which was cross-linked to the PBI macromolecules by using (3-glycidoxypropyl)-methyldiethoxysilane [12]. Clay-PBI composites have been prepared by the addition of up to 20 wt % modified laponite clay to PBI solutions, followed by solvent evaporation [13]. It could be ascertained that the introduction of an inorganic phase to the PBI matrix led to mechanical reinforcement and improvement of thermal and chemical ex situ and in situ stabilities of the PBI membrane, and in some cases, as for example for ZrP-modified ($\text{ZrP} = (\text{Zr}(\text{HPO}_4)_2 \cdot n\text{H}_2\text{O})$) and H_3PO_4 -doped PBI membranes, the proton conductivity of the inorganic PBI composite membranes was even higher than that of pure doped PBI [14].

Covalent cross-linking of PBI membranes is another possibility for improvement of their thermal, dimensional, and chemical stability. For example, the PBI can be cross-linked in the imidazole moiety with a low-molecular compound such as bisphenol A-diepoxide [15], divinyl sulfone [16], terephthaldehyde [17], α -dibromop-xylene [18], or dichloromethyl phosphonic acid [19]. Alternatively, the PBI membranes have also been cross-linked with macromolecular cross-linkers based onto halomethylated polymers, where the halomethyl groups alkylate the N-H group of the imidazole moiety. Halomethylated polymers, for example, chloromethylated PSU [20] or bromomethylated polyetherketone [21] have been applied for covalent cross-linking of high-T membranes. Covalently cross-linked high-T membranes are one of the topics of Chap. 9 of this book.

Another strategy for the improvement of the thermal, dimensional, mechanical, and electrochemical stability is the application of acid-base concepts to H_3PO_4 -doped high-T basic polymers. The acid-base blend concept comprises blending of a basic polymer with an acidic polymer, where ionic acid-base cross-links are formed by proton transfer from the acidic group to the basic group (see Fig. 4.1).

The acid-base blend concept has been developed in the author's group about 16 years ago [22, 23] and was initially exploited for the preparation of low-temperature cation-exchange membranes, where the basic polymer was used as macromolecular basic cross-linker for the cation-conducting membranes (CEM) [24–27]. By ionic cross-linking of the cation-exchange polymer, the water uptake of the membrane could be reduced [25, 28], which led to improvement of the mechanical membrane stability. Moreover, it was observed that the ionic cross-linking of the CEM also led to an improvement of thermal stability (as could be proven by thermogravimetry (TGA) of the acid-base low-T CEM [27]) and resistance to radical attack (indicated by reduced weight loss of ionically cross-linked CEM after immersion in H_2O_2 solutions, compared to the pure acidic polymers [29]). By variation of the molar relation between basic and acidic polymers in the blend, the ion conductivity of the CEM could be varied in a broad range [27]. Hasiotis et al. [30] were the first to transform the acid-base blend concept to intermediate-T fuel cell membranes by mixing a molar excess of polybenzimidazole with sulfonated PSU, followed by doping with phosphoric acid and ex situ and in situ characterization of the formed ternary membrane blends. In these blends, the acidic polymer works as the macromolecular cross-linker in the blend membrane, and the phosphoric acid whose content in the membranes can be varied in a broad range (in the cited example the maximum ADL of the blend membranes was 16 [31]), provides H^+ conductivity of the membrane. In Fig. 4.2, the application of the acid-base blend concept to low-T and intermediate-T H^+ -conducting membranes is presented schematically.

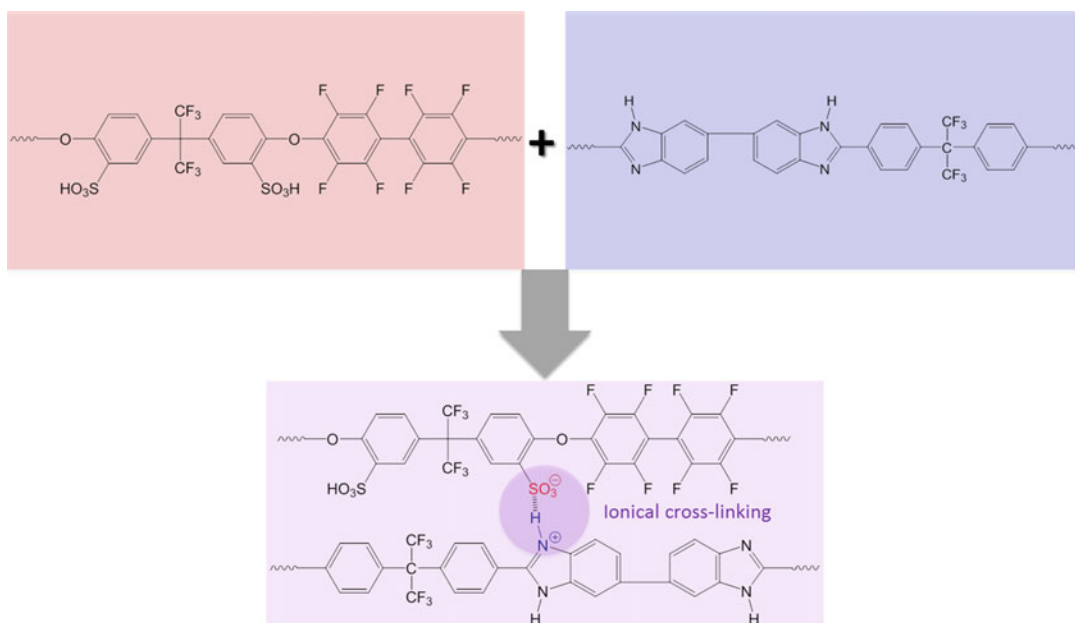
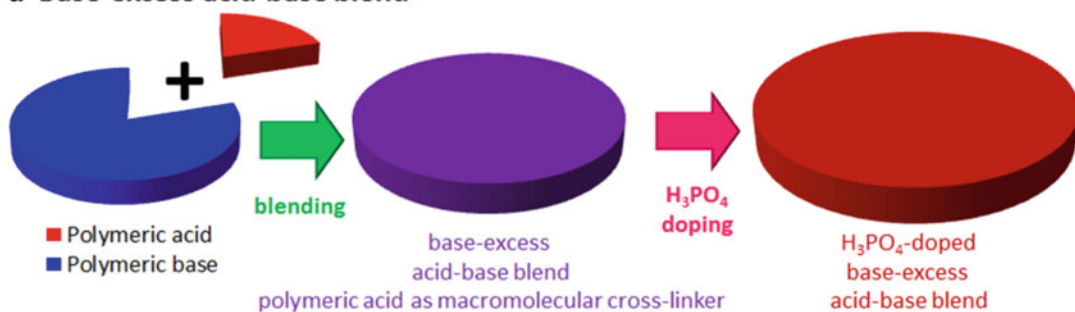


Fig. 4.1 Ionic acid-base cross-linking of an acidic and a basic polymer

a Base-excess acid-base blend



b Acid-excess acid-base blend

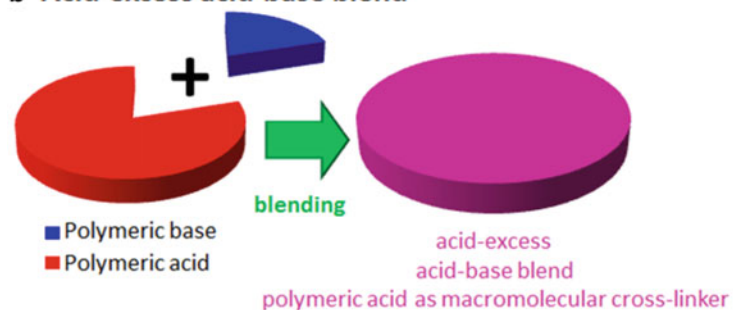


Fig. 4.2 The application of acid-base blend concept to intermediate-T (a) and low-T (b) H^+ -conducting membranes

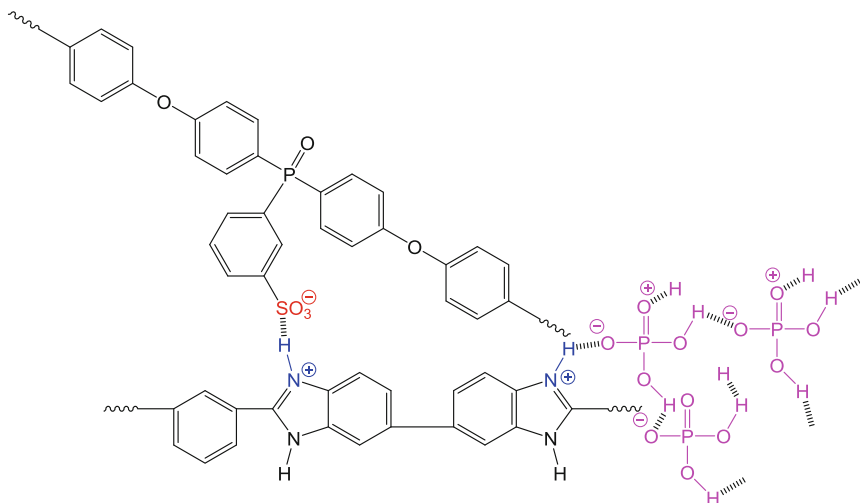


Fig. 4.3 Structure of an H_3PO_4 -doped base-excess blend membrane based on PBI and sulfonated polymers

In Fig. 4.3, the structure of a PA-doped base-excess blend membrane based on PBI and sulfonated polymers is depicted schematically along with the hydrogen bridges between the H_3PO_4 molecules. In ongoing research, the author's group also started synthesis and characterization of H_3PO_4 -doped base-excess acid–base blend membranes for the application in intermediate-T fuel cell systems. The research work done in the application of acid–base blend concepts to intermediate-T electrochemical applications will be reviewed in Sect. 4.2 of this contribution. This chapter will be concluded by a short comparative study covering covalently cross-linked, covalent-ionically cross-linked and ionically cross-linked intermediate-T polybenzimidazole blend membranes (Sect. 4.3).

4.2 State of the Art of the Application of Acid–Base Blend Concepts

The scope of the reviewed R&D work is limited to intermediate-T acid–base blend membranes prepared by mixing polybenzimidazoles and sulfonated or phosphonated acidic polymers. Other membrane types, where the acid–base concept was used to improve their relevant

properties such as proton conductivity, and mechanical and chemical stability, are not discussed in this chapter, but are briefly mentioned below:

- Polybenzimidazoles with pendent acidic groups: sulfopropylated polybenzimidazole [31], sulfonated polybenzimidazole by the grafting of (4-bromomethyl)benzenesulfonate onto PBI [32], phosphonated fully aromatic polyethers containing pyridine building blocks [33], sulfonated aromatic polyethers containing pyridine units [34], sulfonated polybenzimidazoles from sulfonated dicarboxylic acid monomers [35–37].
- Polybenzimidazoles with grafted ionomer side chains: grafting-through and grafting-from polymerization of vinylphosphonic acid onto PBI [38–40].
- Poly(benzimidazole-block-sulfonated arylene ether sulfone)s [41].

In the following, those publications dealing with synthesis and characterization of intermediate-T blend membranes from PBI basic polymers and sulfonated or phosphonated polymers utilized as acidic macromolecular cross-linkers in the blends are discussed. In Fig. 4.4, those polybenzimidazoles along

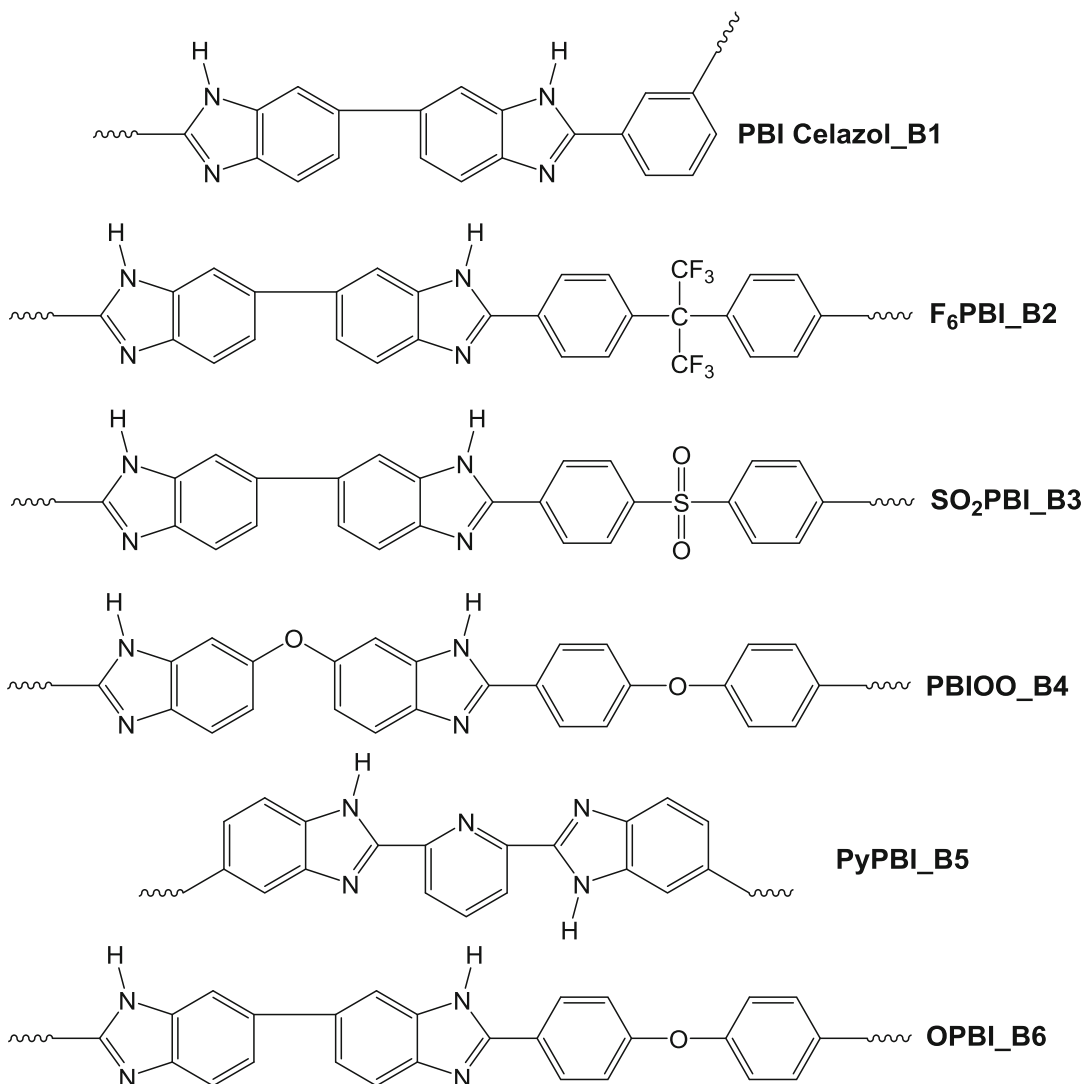


Fig. 4.4 Polybenzimidazoles used as basic blend components in acid–base blends which are reviewed in this chapter

with their abbreviations used as basic blend components in base-excess acid–base blends are depicted. In Fig. 4.5, all acidic polymers which were used as macromolecular ionic cross-linkers in the reviewed publications are listed.

As already mentioned, the acid–base blend concept was applied to intermediate-T fuel cell membranes by Hasiotis et al. [31, 42]. The blend membranes were composed of PBI Celazol[®] (poly(2,2'-*m*-phenylene-5,5'-bibenzimidazole, *m*-PBI, named as **B1**) and polysulfone Udel[®] sulfonated in the bisphenol A section (named

S1 in the following, see Fig. 4.5) [43]. Blend compositions (in wt%) from 100 **B1**/0 **S1** up to 50/50 were investigated. It was noted that the acid doping level decreased with decreasing PBI content which can be traced back to both the ionic cross-links by interactions of **S1** with **B1** and by decreasing **B1** proportion in the blend: for the 50/50 blend, a maximum ADL of 8.5 with respect to the PBI component was reached, while the pure **B1** maximal ADL was 16. The ionic conductivity of the blend membranes was measured in dependence of temperature, acid

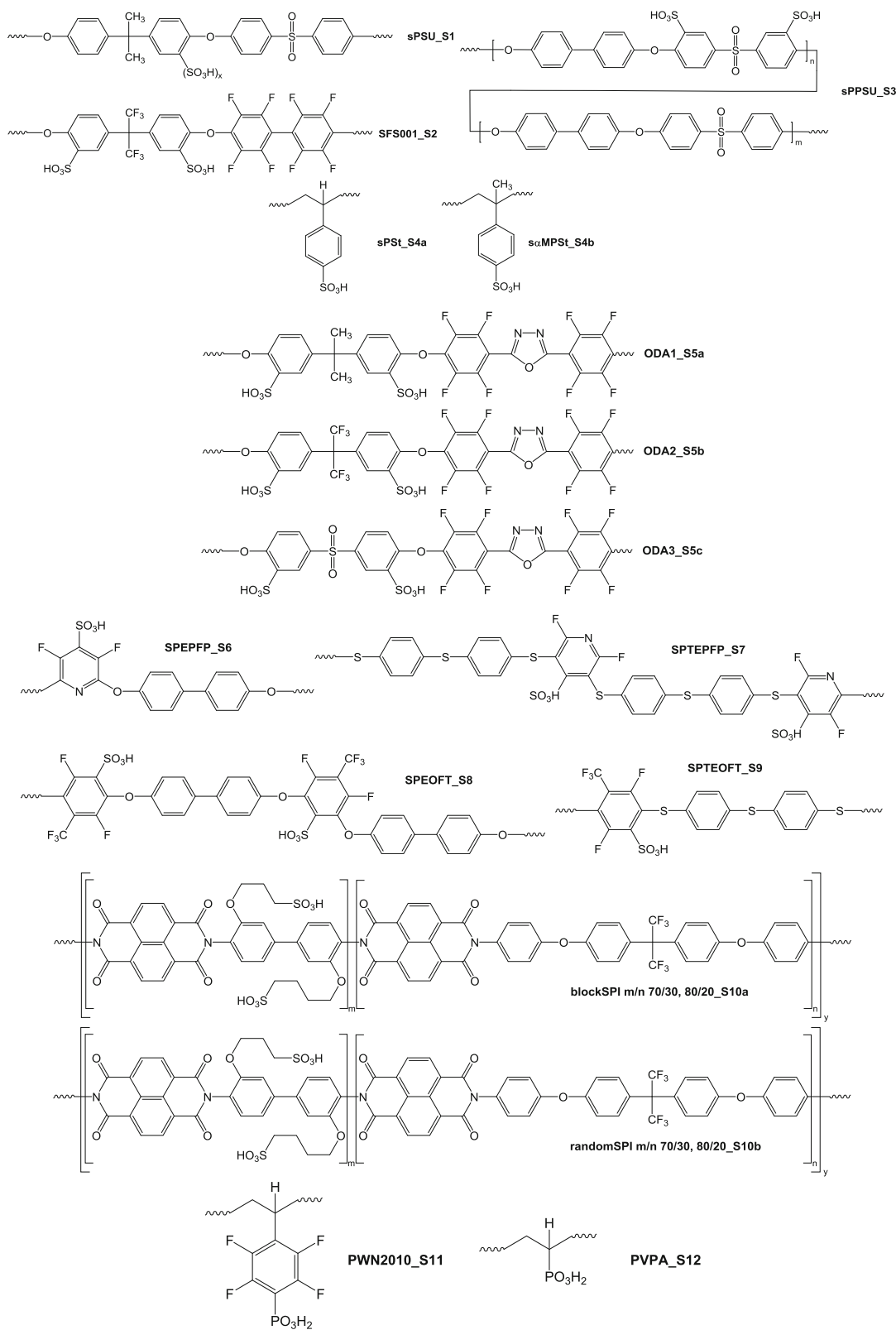


Fig. 4.5 Acidic polymers used as macromolecular ionic cross-linkers in acid–base blend membranes mentioned in this review

doping level, sulfonation degree, relative humidity, and blend composition.

It was found that the doped blend membranes exhibited higher conductivities (in excess of 0.1 S cm^{-1}) than pure **B1** when applying equal doping conditions. The blend membranes showed strongly improved tensile strength, compared to pure **B1** which can be explained by the ionic cross-links within the membrane.

An H_2/O_2 fuel cell test of one of the blend membranes (75 % **B1**, 25 % **S1** with sulfonation degree of 36 %, ADL 4.6) indicated the principal suitability of this membrane type for intermediate-T fuel cells (0.45 mA cm^{-2} at 0.6 V). Since **S1** which is sulfonated in the bisphenol A portion in *ortho* position to the electron-donating ether bridge and in *meta* position to the also electron-donating isopropylidene bridge is therefore prone to splitting-off of the SO_3H groups in acidic environments in the T range around $200 \text{ }^\circ\text{C}$ [44, 45], which is within the operation temperature range of intermediate-T fuel cell systems, it would be advantageous to use such sulfonated polymers as ionic cross-linkers for PBI which show less sensitivity to hydrolytic/acidic (*ipso* reaction) and thermal splitting-off of its SO_3H groups.

Therefore, in a comparative study, different nonfluorinated and partially fluorinated sulfonated aromatic polymers were synthesized and characterized in terms of chemical and thermal stabilities. It was found that SO_3H groups introduced in the electron-deficient sections of the aromatic polymer main chains were much more stable against splitting-off than SO_3H groups pendent to electron-rich sections of the polymer backbones [29]. One of the most stable polymers of this series was a polymer prepared by polycondensation of decafluorobiphenyl and bisphenol (AF), followed by sulfonation with

oleum (60 % SO_3), where the sulfonic acid groups were introduced into the bisphenol AF section of the polymer in *meta* position to the strongly electron-attracting perfluoroisopropylidene bridge. In [46], the synthesis of this polymer (named **S2**, Fig. 4.5) was optimized in terms of molecular weight (up to a stoichiometric imbalance decafluorobiphenyl:bisphenol AF of 0.995:1 non-cross-linked polymers could be obtained with $M_w = 204,500 \text{ Da}$) and sulfonation degree (max. two SO_3H groups per repeat unit were obtained with oleum containing 50 % SO_3). It was noted that even oleum containing 50 % SO_3 did not lead to a degradation of **S2** in terms of molecular weight and sulfonation degree. Therefore, it was concluded that this polymer is a suitable candidate as acidic macromolecular cross-linker for PBI polymers. Consequently, base-excess blend membranes of **S2** have been prepared with **B1** (weight relation **B1/S2** 95/5, 90/10, 80/20, and 70/30). The blend membranes were characterized in terms of solubility by immersion in $60 \text{ }^\circ\text{C}$ hot DMAc, and by treatment with H_2O_2 (5 % H_2O_2 , $60 \text{ }^\circ\text{C}$), and Fenton's Reagent (3 % H_2O_2 , 4 ppm Fe^{2+} , $68 \text{ }^\circ\text{C}$ [47]). The obtained results (only comparison between pure **B1** and 70/30 **B1/S2** is shown) are listed in Table 4.1.

In a further paper, the properties of H_3PO_4 -doped pure **B1** and the 70 **B1**/30 **S2** were determined, including dependence of volume swelling, mechanical properties (stress–strain curves, tensile strength, elongation), and proton conductivity from ADL and temperature [48]. It could be ascertained that the blend membranes showed excellent mechanical strength and low swelling at high ADLs of 10–13 mol H_3PO_4 per PBI repeat unit. The stabilizing effect of the acid–base cross-links can be clearly seen from Table 4.1.

Table 4.1 Results of stability tests in different solutions for pure PBI **B1** and 70/30 **B1/S1** blend membrane

Membrane	60 °C DMAc	60 °C 5 % H_2O_2	Fenton's reaction
	Undissolved (wt%)	Undissolved (wt%) ^a	Undissolved (wt%) ^b
100 % B1	Dissolved after <1 h	20	61
70/30 B1/S2	90	10	84

^aAfter 96 h of immersion

^bAfter 120 h of immersion

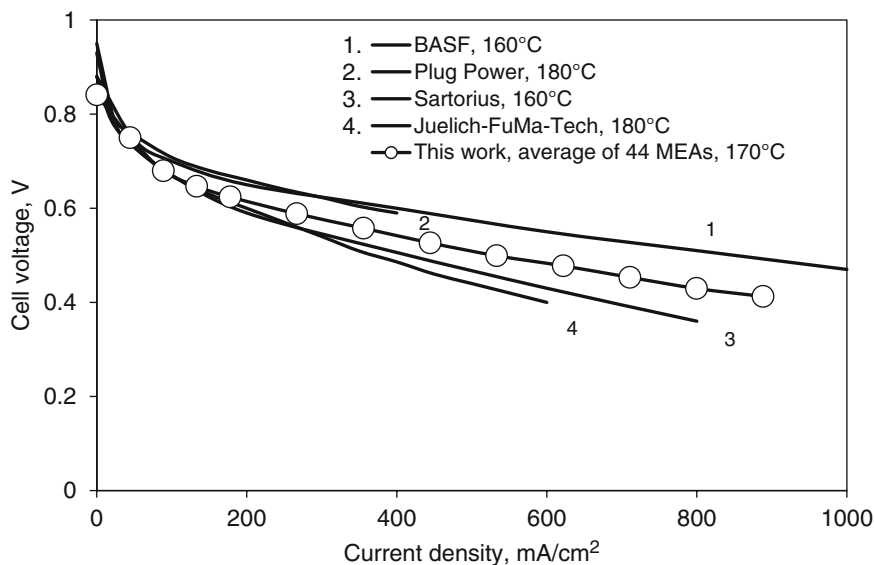


Fig. 4.6 Fuel cell performance of PBI cells (H_2/air), $T = 160\text{--}180\text{ }^\circ\text{C}$ (ambient pressure) [49]. The polarization curve was an average of 44 MEAs using **B1/S1** 70/30 (11 mol H_3PO_4 PBI repeat unit). Electrodes (256 cm^2): 48.6 % Pt/C catalysts, Pt loading of $0.6\text{--}0.7\text{ mg cm}^{-2}$.

Curves 1 by BASF [50] and Curve 2 by PlugPower [51] based on PPA (polyphosphoric acid) membranes, Curve 3 by Sartorius [52] based on PBI membrane cast from DMAc, Curve 4 by Juelich [53] cross-linked AB-PBI (FuMa-Tech). Reproduced with permission of Wiley-VCH

At an ADL of 11, H^+ -conductivities of 0.12 S cm^{-1} ($175\text{ }^\circ\text{C}$, 10 % relative humidity) were measured with the 70/30 blend membranes which showed the following mechanical properties: tensile strength of 6 MPa, elongation of 220 %, modulus of 50 MPa at $150\text{ }^\circ\text{C}$. From this membrane, MEAs with an active area of 256 cm^2 have been prepared, which have been tested in a 2 kW_{el} stack and showed good performance. In Fig. 4.6, the polarization curve of the 70/30 blend is shown at $170\text{ }^\circ\text{C}$ operation temperature along with the polarization curves of other PBI-type membranes.

In a follow-up study, combinations of three different polybenzimidazoles with the partially sulfonated ionomer **S2** were investigated comparatively in terms of their stabilities to identify which **S2**/PBI combinations showed the best stabilities [49]. As polybenzimidazoles, **B1**, **B2**, and **B3** have been used in this study. All blend membranes contained 70 wt% of the polybenzimidazole and 30 wt% of **S2**. The blend membranes have been characterized in terms of oxidative stability by immersion in Fenton's Reagent for up to 120 h and subsequent

determination of weight loss by gravimetry, molecular weight distribution by gel permeation chromatography (GPC) or size exclusion chromatography (SEC), and thermal stability by thermogravimetry. Some of the chemical stability characterization results of the blend membranes and of the pure PBIs are listed in Table 4.2.

From Table 4.2 it can be seen that, in terms of weight loss after FT, both the pure **B2** and the **B2S2** membranes show the best stabilities. The onset of SO_3H group splitting-off temperatures ($T_{\text{onset}}^{\text{SO}_3\text{H}}$) of two of the blend membrane types (**B1S2** and **B2S2**) remains nearly constant which indicates that the structure of **B1** and **B2** is obviously chemically unchanged by Fenton's Test, while the decrease of $T_{\text{onset}}^{\text{SO}_3\text{H}}$ of **B3S2** and the increase of $T_{\text{onset}}^{\text{SO}_3\text{H}}$ of **B3** are inconsistent and need more detailed research. When comparing the values of the $T_{\text{onset}}^{\text{SO}_3\text{H}}$ of the different blend membranes with each other, the following series of $T_{\text{onset}}^{\text{SO}_3\text{H}}$ is detected: $T_{\text{onset}}^{\text{SO}_3\text{H}}$ (**B1**) $>$ $T_{\text{onset}}^{\text{SO}_3\text{H}}$ (**B2**) $>$ $T_{\text{onset}}^{\text{SO}_3\text{H}}$ (**B3**). This finding was explained by decreasing basicity of PBIs in this series,

Table 4.2 Characterization results of the blend membranes (and of pure PBIs, where applicable) before and after Fenton’s Test (FT)

Membrane	Weight loss after 120 h FT	$T_{\text{onset}}^{\text{SO}_3\text{H}}$ (onset temperature of SO_2 signals) ^a	
		Before FT	After 120 h FT
B1	21.2	n.a.	n.a.
B1S2	13.2	434	438
B2	7.7	n.a.	n.a.
B2S2	2.04	417	416
B3	11	438 ^b	466 ^b
B3S2	7.9	403	380

^aThe determination of onset-temperature of SO_3H splitting-off by TGA-FTIR coupling is described in detail in [54]

^b SO_2 signal originates from backbone degradation of SO_2PBI (**B3**)

since the ionic cross-links are stronger when the basicity of the respective PBI is higher. It can be summarized that in terms of chemical stability of PBIs, it is advantageous to choose polybenzimidazoles which consist of electron-deficient aromatic systems, as in the case of **B2** and **B3**. In terms of stability of the acid–base cross-links, one can see clearly that the $T_{\text{onset}}^{\text{SO}_3\text{H}}$ of all blend membranes are markedly above the fuel cell operation temperatures. GPC investigations of the pure PBIs and of their blend membranes before and after FT yielded the result that molecular weight degradation is clearly visible. However, the membranes still keep their mechanical integrity even after 120 h of FT which can be traced back to the ionic cross-links of the membranes which hold together the macromolecular chains of the blend components even after some degradation of the macromolecules has taken place.

Moreover, the blend membranes have been characterized in terms of acid doping, swelling, mechanical properties such as tensile strength, elongation and modulus, and proton conductivities. Two of the membranes were also tested in an H_2 -air fuel cell. It was clearly indicated that volume swelling of the pure PBIs, **S2** and **S3** and their blend membranes at the same doping level was lower than that of **B1** and **B1S2**. This finding was explained by increasing free volume of the **B2** and **B3** membranes, compared to **B1**, due to the introduction of S, O, and F heteroatoms into the PBI, leading to an increase of van der Waals volume: when the membranes are doped with phosphoric acid (PA), the free

volume is occupied by PA molecules before volume swelling takes place. In terms of mechanical properties, it was found that the blends showed clearly better properties due to the ionic cross-links. Since the blend membranes show much higher mechanical stabilities than pure PBIs, they could be doped to much higher degrees (doping level of pure PBIs between 7.1 and 8.3 mol H_3PO_4 (PA) and of **PBI-S2** blends between 10.9 and 13.3 mol PA per PRU(PBI)), which led of course to better proton conductivities of the blend membranes at the same temperature and relative humidity. At a PA doping level of 11, the **B2S2** membranes reached 0.135 S cm^{-1} at 10 % relative humidity (RH), while for the **B3S2** membranes conductivities of 0.145 S cm^{-1} were found under 10 % RH. The three blend membranes were operated in a fuel cell. The obtained polarization curves are shown in Fig. 4.7 [50], indicating good performance which, however, requires further improvement of the electrode design.

From the abovementioned results, it can be concluded that the combination of the partially fluorinated sulfonated ionomer **S2** with the partially fluorinated PBI **B2** is of advantage in terms of chemical stability and compatibility, which can be explained with chemical similarity, since both blend components consist of electron-deficient aromatic ring systems. Good PBI blend membrane stabilities can be achieved by good compatibility between the blend components, electron-deficiency of the aromatic ring systems, or both. To get hints of which is the

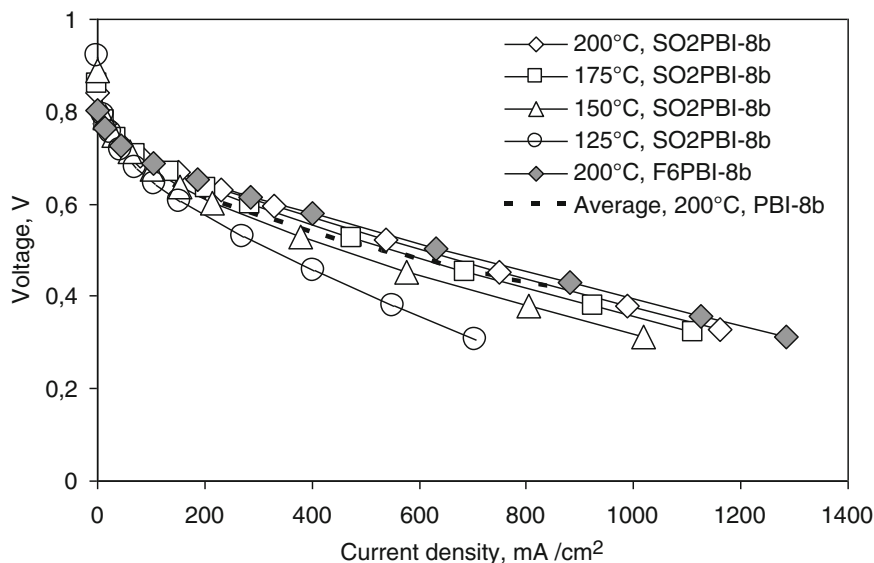


Fig. 4.7 Polarization curves of the **B2S2** (ADL 9.8 PA/PRU), **B3S2** (ADL 8.9 PA/PRU), and **B1S2** (ADL 11 PA/PRU) blend membranes [50]. Electrodes: 0.6 mg Pt cm⁻² from 40 % Pt/C catalyst, binder: pure **B1**. Operation temperatures as indicated in the figure. Reproduced from [50] with permission of Elsevier

Table 4.3 FT and PA doping results of the PBI blend membranes [56]

Membrane	FT mass loss after 48 h (wt%)	FT mass loss after 120 h (wt%)	ADL ^a	PA doping degree ^b	PA swelling (x direction) (%)
B2S2	1.5	2	9.3	120	7
B2S3	4.4	22.5	23.4	300	14
B2 (Table 4.2 [50])	2.5	7.7	n.a.	n.a.	n.a.
B4S2	4	8.9	13.6	224	33
B4S3	1.6	7.6	17	280	20
B4 [56]	8.9	23.9	n.a.	n.a.	n.a.

^aMol PA/PRU(PBI)

^bCalculated according to PA uptake (%) = $100 \times m_{PA}/m_{\text{membrane dry}}$

main factor, a further study was performed, which included the preparation and characterization of different combinations of the electron-deficient partially fluorinated sulfonated ionomer **S2** or the more electron-rich nonfluorinated sulfonated ionomer **S3** (see Fig. 4.5) with the electron-deficient partially fluorinated PBI **B2** or the electron-rich nonfluorinated PBI **PBIOO** (**B4**) [55]. The following blend membranes were prepared, and their properties compared to each other: **B2S2**, **B2S3**, **B4S2**, and **B4S3**. In every case, the blend membranes contained 70 wt% of the PBI and 30 wt% of the sulfonated polymer. As in the aforementioned study, the membranes

were subjected to FT for up to 120 h of Fenton's Reagent treatment time. Moreover, the membranes were PA-doped with 85 % PA for 30 min at 130 °C, and subsequently left in the PA solution for a further 30 min at room temperature. The FT and PA doping results are listed in Table 4.3. From the experimental results presented in Table 4.3, the following conclusions can be made:

- Like in the previous studies, the blend membranes show better FT stabilities than the pure PBIs because of the ionic cross-links.

- There is a clear trend that it is advantageous to combine chemically similar blend components with each other, since the **B2S2** and **B4S3** membranes indicate better FT stability than the electron-rich/electron-deficient blend mixtures.
- The **B4** blend membranes take up more PA under the same conditions than the **B2** blend membranes which can be traced back to the different stiffness and the different hydrophobicity of the PBI chains: the **B4** macromolecules are more flexible and more hydrophilic due to two O bridges in their repeat unit than the **B2** membranes featuring the more bulky and hydrophobic perfluoroisopropylidene unit.

The pure PBIs and PBI blend membranes have been investigated before and after FT in terms of molecular weight degradation using GPC. It was found that the molecular weight distribution (MWD) curves shift to somewhat lower molecular weight, but the MWD decrease was not very pronounced, which confirms the excellent radical stabilities of the blend membranes as already indicated by the weight losses of the membranes through FT. The PA-doped blend membranes were operated in an H₂/air fuel cell. The PA-doped **B4S3** membrane showed one of the best performances found for intermediate-T fuel cell membranes [49, 56, 57] without fuel cell gases pressurization, without humidification and without elaborated MEA preparation techniques, reaching a peak power density of 0.475 W cm⁻² at 180 °C. The polarization curves of **B4S3** and **B2S2**, respectively, in the temperature range 120–180 °C are depicted along with the power density vs. current density curves at 180 °C in Fig. 4.8. Interestingly, the polarization curves of **B2S2** increase up to 130 °C and decrease at higher operation temperatures, while the **B4S3** exposes the expected improvement of polarization curves with temperature. The reason for this opposite behavior might be the observed mechanical properties of the two membranes: while the PA-doped **B4S3** has a

gel-like structure with stronger bound PA, the PA-doped **B2S2** is more rigid due to the stiffer backbone of **B2**, which makes bleeding-out of PA from the **B2S2** membrane matrix easier than from the **B4S3** membrane matrix. The main reason for the markedly better polarization curves of **B4S3**, compared to **B2S2**, is the significantly higher ADL of the **B4S3** membrane (Table 4.3). GPC characterization of the **B2S2** membrane before and after fuel cell revealed that no molecular weight degradation took place during the fuel cell test.

In a further study, it was investigated if sulfonated low-cost ionomers can also be used as acidic cross-linkers for PBI polymers in order to reduce membrane costs. For this purpose, sulfonated polystyrene (**S4a**, Fig. 4.5) and poly(α -methylstyrene sulfonic acid), (**S4b**, Fig. 4.5) have been blended with commercial PBIOO (**B4**, Fuma-Tech) to 70 wt% PBIOO/30 wt% sulfonated polystyrene blend membranes. The membranes were characterized in terms of chemical stability by the immersion in Fenton's Reagent, thermal stability in terms of TGA-FTIR coupling and in terms of proton conductivity after PA doping [58]. Poly(α -methylstyrene sulfonic acid) was chosen for comparison with sulfonated polystyrene since it is known that the main radical attack target of polystyrene is the tertiary C–H bond [59] which is not present in poly(α -methylstyrene), leading to verified better radical stabilities of poly(α -methylstyrene), compared to poly(styrene) [60]. In Table 4.4, the results of thermal and FT stability of the blend membranes **B3/S4a** and **B3/S4b** are listed.

It is clearly seen from the characterization results that (1) the chemical stability of the polystyrene sulfonic acid blends is in the blend much higher than in the pure polymers due to acid–base cross-linking, (2) the radical stability of the blend membranes is higher than that of pure **B4** which is again due to the ionic cross-linking, and (3) the radical stability of the **S4b** blend membrane is much better compared to that of the **S4b** blend membrane. The better radical stability of the **B4S4b** blend can also be seen

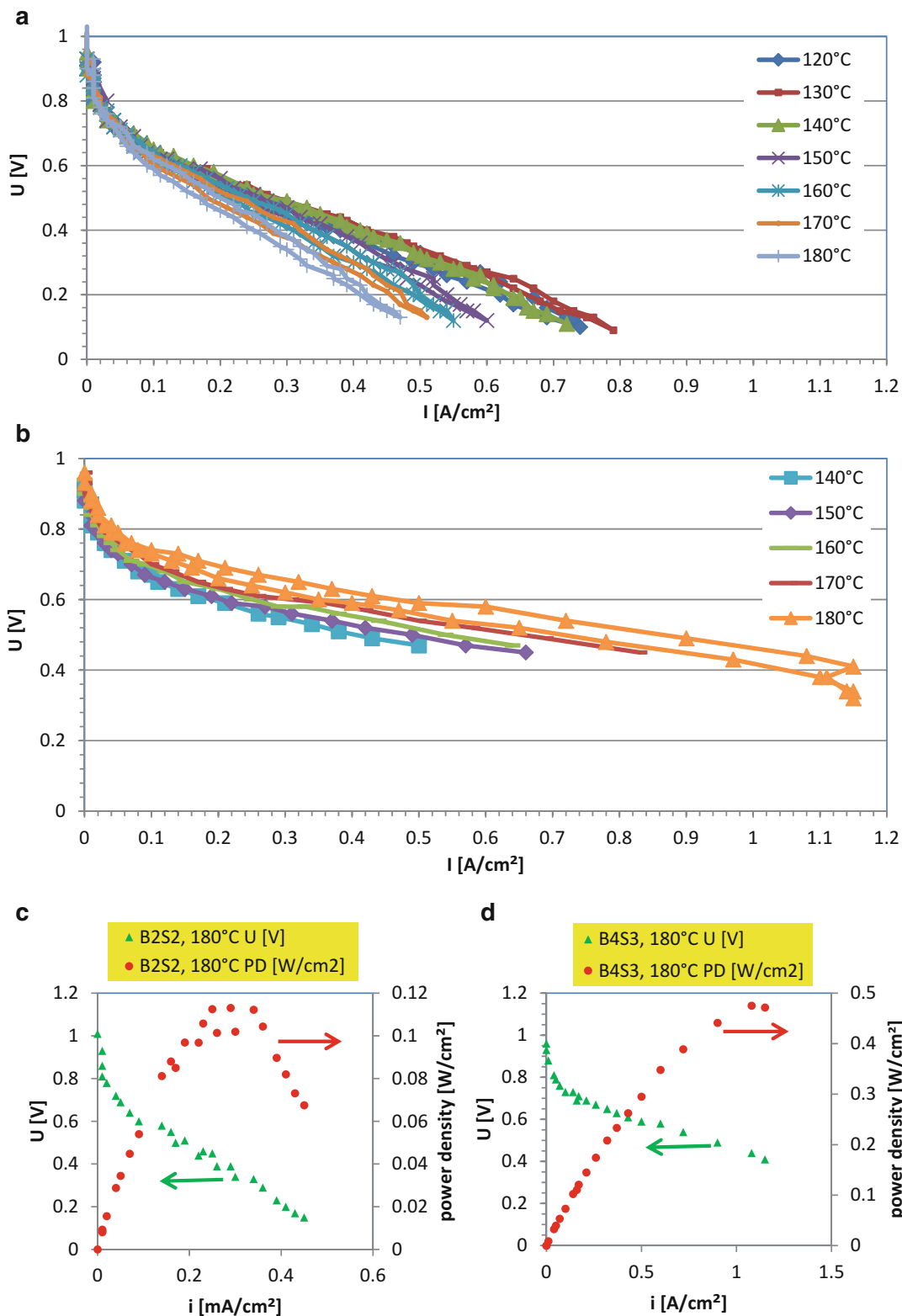


Fig. 4.8 Polarization curves of **B2S2** at temperatures between 120 and 180 °C (a), polarization curves of **B4S3** at temperatures between 120 and 180 °C (b) [56], selected polarization and power density curve of **B2S2** at 180 °C (c), and selected polarization and power density curve of **B4S3** at 180 °C (d). Figures (a) and (b) reproduced from [56] with permission of Elsevier

Table 4.4 Thermal stability (by TGA-FTIR coupling) and radical stability (by immersion of membranes for different times in Fenton’s Reagent and subsequent weight loss and molecular weight loss determination) of **B4/S4a** and **B4/S4b**

Polymer/ membrane	$T_{\text{onset}}^{\text{SO}_3\text{H}}$ (°C)	Weight loss FT (%)
S4a	192	Dissolved after 24 h
S4b	213	Dissolved after 24 h
PBIOO_0 h FT (B4)	n.a.	
PBIOO_24 h FT	n.a.	13.5
PBIOO_120 h FT	n.a.	16
PBIOO_144 h FT	n.a.	16
B4S4a _0 h FT	379	
B4S4a _24 h FT	372	0
B4S4a _120 h FT	372	8
B4S4a _144 h FT	370	10
B4S4b _0 h FT	363	
B4S4b _24 h FT	365	0
B4S4b _120 h FT	356	3
B4S4b _144 h FT	357	3.5

very clearly in SEM micrographs of both membranes: while the surface of the **B4S4b** blend membranes only shows a few 1–4 μm -sized small craters due to the OH radical attack, the surface of the **B4S4a** blend membranes is highly porous, indicating strong radical attack [59]. PA doping experiments of the membranes revealed a faster PA uptake of the **B4S4b** membranes, compared to those of the **B4S4a** membranes, which can most probably be traced back to higher free volume of the **S4b** blends because of their bulky CH_3 groups. Moreover, it was found that the proton conductivities of the **B4S4b** membranes were higher (42 mS cm^{-1}) at the same ADL (18.2) (300 wt%) and temperature (120 °C) than those of the **B4S4a** membranes (30 mS cm^{-1}) which might also be a consequence of higher free volume of the **B4S4b** blends. Summarizing the results of this study, it was shown that low-cost ionomers can also be used as acidic cross-linkers for PBI-type membranes if the radical stability of the low-cost ionomers is sufficiently high due to the absence of oxidation-sensitive chemical bonds.

Since it could be shown that the partially fluorinated sulfonated arylene ionomer **S2** showed excellent oxidation stabilities as blend partner of the partially fluorinated **B2** (Table 4.3 [50, 56]), further partially fluorinated and sulfonated arylene ionomers based on the polycondensation of 2,5-bis(perfluorophenyl)-1,3,4-oxadiazole [61] with the three bisphenols bisphenol A, bisphenol AF, and bisphenol S, followed by sulfonation, have been synthesized [62]. The structure of the three sulfonated poly(perfluorooxadiazole) (sODA) ionomers is shown in Fig. 4.5 (sODA from bisphenol A: **S5a**; sODA from bisphenol AF: **S5b**; sODA from bisphenol S: **S5c**). It was noted that some molecular weight degradation of the sODA polymers takes place during sulfonation which might be due to the harsh reaction conditions of sulfonation since oleum was used as sulfonation agent. The sODA polymers were blended with the fluorinated **B2** and the nonfluorinated **B3** (70 wt% PBI, 30 wt% sODA), and the properties of the blend membranes were determined. Due to the fact that only the blend membranes containing **B2** showed good mechanical stabilities (the **B3**/sODA blends were brittle), the characterization was continued only with the **B2** blend membranes. The blend membranes were characterized in terms of thermal stability (TGA), oxidation stability (weight loss after FT), and conductivity after doping with PA. The characterization results are gathered in Table 4.5.

The characterization results suggested good suitability of this membrane type for intermediate T fuel cells. However, all fuel cell tests of the membranes failed because the membranes showed holes after relatively short fuel cell operation times. This finding can most probably be traced back to the too low-molecular weight of the sODAs after sulfonation (**S5a**: $M_w = 17,000 \text{ Da}$; **S5b**: $M_w = 17,000 \text{ Da}$; **S5c**: $M_w = 18,600 \text{ Da}$) which leads to insufficient mechanical stabilities—the membranes were very soft after PA doping. Therefore, R&D work with these membranes was discontinued.

The search for further chemically highly stable partially fluorinated arylene ionomers as blend partners for polybenzimidazoles was

Table 4.5 Characterization results of **B2**/sODA blend membranes [63]

Membrane	$T_{\text{onset}}^{\text{SO}_3\text{H}}$ (sODA) (°C)	$T_{\text{onset}}^{\text{SO}_3\text{H}}$ (blend membrane) (°C)	Weight loss FT after 96 h (%)	Conductivity ^a (150 °C, 20 % RH) (S cm ⁻¹)
B2S5a	374	431	8.5	35
B2S5b	348	414	7	88
B2S5c	319	452	7	49

^aPA doping degree: 300 wt%, ADL: 23.4

however continued. Due to the fact that high chemical and thermal stabilities and high proton conductivities can be expected from aromatic ionomers with pendent SO₃H groups in an electron-deficient aromatic environment, novel arylene ionomers have been prepared starting from the perfluorinated building blocks octafluorotoluene (OFT) and pentafluoropyridine (PFP). The SO₃H groups were introduced in both monomers following a nucleophilic route initially developed by other research groups [63–66]: first SH groups were introduced into pentafluoropyridine and octafluorotoluene by nucleophilic aromatic substitution with F, followed by oxidation of the SH groups with H₂O₂/HCOOH to SO₃H groups. The formed sulfonic acid monomers (2,3,5,6-tetrafluoro-4-(trifluoromethyl)benzenesulfonic acid (TFTFBSA) and 2,3,5,6-tetrafluoro-pyridine-4-sulfonic acid (TFPSA), respectively), were then polycondensated with 4,4'-diphenol and 4,4'-thiodibenzene-thiol, respectively [67]. The structure of the resulting polymers **S6**, **S7**, **S8**, and **S9** is schematically depicted in Fig. 4.5. Interestingly, the structure of the polymers **S6**, **S8**, and **S9** is angled (revealed by ¹⁹F NMR) which can be traced back to similar nucleophilic displacement reactivities of the different F atoms in the two monomers during polycondensation. The ionomers were then blended with the three PBIs: **B1**, **B2**, and **B3** in different proportions of the blend components. In Table 4.6, some properties of 70 % PBI/ 30 % sulfonated polymer blend membranes from **B1**, **B2**, and **B4** with **S6**, **S7**, **S8**, and **S9** are listed.

It can be clearly seen from Table 4.5 that the two polymers containing the sulfonated pyridine units (**S6** and **S7**) show bad radical stabilities in their blend membranes with **B1** which is

indicated by the strong weight losses after 144 h of FT. Moreover, SEM micrographs of these membranes after FT showed highly porous surfaces, indicating strong membrane degradation by the radical attack [68, 69]—obviously the perfluoropyridine building blocks of **S6** and **S7** are prone to the radical attack degradation despite the electron-deficiency of their aromatic systems.

Therefore, the pyridine-containing sulfonated polymers were not used as acidic cross-linkers for blends with the other PBIs. On the contrary, the blends of **S8** and **S9** with the PBIs expose excellent radical stabilities indicated by very small weight losses after 144 h of FT (Table 4.5). Therefore, only blend membranes from **B1**, **B2**, and **B4** with **S8** and **S9** have been further investigated in terms of suitability for intermediate-T fuel cells [69]. The best fuel cell performance among all tested membranes was reached with a **B2S8** membrane (20 wt% **S8**) comprising a peak power density of 400 mW cm⁻² at 1 A cm⁻² (conditions: $T = 120$ °C, doping degree 400 wt% (ADL: 27.3), GDEs with Pt loading 3 mg Pt cm⁻² which were simply pressed onto the membrane). It can be concluded that the PBI blend membranes containing **S8** and **S9** acidic cross-linkers offer good perspectives for use as membranes in intermediate-T fuel cells due to their excellent radical stabilities.

Apart from the work done under participation of the author of this study reported above, only a few papers have been published dealing with the synthesis and characterization of acid–base blend membranes. One of these publications is an article of Iizuka et al. who described the synthesis of novel sulfonated random or block co-polyimides (blockSPI, **S10a**, randomSPI, **S10b**, Fig. 4.5) [69] and their use as acidic blend components

Table 4.6 Some properties of 70 % PBI/30 % sulfonated polymer blend membranes from **B1**, **B2**, or **B4** with **S6**, **S7**, **S8**, and **S9** [68]

Membrane	M_n (PDI) (sulf. polymers) (Da) (–)	$T_{\text{onset}}^{\text{SO}_3\text{H}}$ (sulf. polymer) ($^{\circ}\text{C}$)	$T_{\text{onset}}^{\text{SO}_3\text{H}}$ (blend membrane) ($^{\circ}\text{C}$)	FT weight decrease after 144 h (%)
B1S6	5900 (1.74)	378	419	39
B1S7	12,500 (2.39)	328	359	27
B1S8	10,100 (2.89)	375	426	8
B1S9	15,000 (1.33)	329	442	9
B2S8	See above	See above	440	4.1
B2S9	See above	See above	425	2.9
B4S8	See above	See above	441	4.5
B4S9	See above	See above	397	1.8

of PBI blend membranes, where the PBI component OPBI (**B6**, Fig. 4.4) was the minor component with only 10 wt% share in the blend [70]. PA doping was performed by immersion of the membranes in 85 % PA for appropriate times. The motivation for preparation of this membrane type was that these membranes should have different proton transport pathways: in the temperature range between 0 and 100 $^{\circ}\text{C}$, the proton conduction should be provided by the SO_3H groups and water, and at <0 and >100 $^{\circ}\text{C}$ via the PA H-bridge network. Indeed, the membranes possessed high proton conductivities between 0 and 100 $^{\circ}\text{C}$ (via the $\text{SO}_3\text{H}/\text{H}_2\text{O}$ pathway, e.g., 0.37 S cm^{-1} at 90 $^{\circ}\text{C}$ and 98 % RH) and higher proton conductivities than Nafion above 100 and below 0 $^{\circ}\text{C}$ (via the PA pathway). It was thereby indicated that the block-type SPI/OPBI blends exhibit higher proton conductivities than the random-type SPI/OPBI blends at same IEC, PA doping degree, T and RH. The higher proton conductivity of block-co-ionomers, compared to random polymers of the same IEC, can be traced back to their nanophase-separated biscontinuous structure comprising proton-conducting channels of high SO_3H group density which facilitates proton conduction [71].

Apart from sulfonated polymers, it could recently be shown that phosphonated polymers can also be used advantageously as macromolecular ionic cross-linkers for PBI blend membranes: poly(tetrafluorostyrene-4-phosphonic acid) (PWN2010, **S11**, Fig. 4.5) was synthesized via nucleophilic aromatic

substitution of poly(pentafluorostyrene) [72]. The phosphonated polymer was then mixed with PBI/OO (**B4**, Fig. 4.4) in a molar relation imidazole/ PO_3H_2 groups = 3/7 [73]. The so-formed blend membranes were characterized in terms of oxidation stability in Fenton's Reagent. It was found that obviously the **B4** blend component had worse chemical stability than the **S11**: while pure **S11** only lost 2 % weight after 96 h of FT (GPC analysis of the pure **S11** revealed only slight molecular weight degradation of low-molecular constituents of the **S11**), both pure **B4** and the **S11B4** membranes showed weight losses of 17 % after 96 h FT. However, it could be seen from SEM inspection of the pure **B4** and **S11B4** membrane surfaces that both membranes maintained their integrity and mechanical stability even after 96 h FT—they only showed some craters with diameters of roughly 10 μm in their surfaces originating from OH radical attack. While pure **S11** showed one of the highest dry proton conductivities measured for phosphonated polymers [74], the **S11B4** blend membranes had to be doped with phosphoric acid (PA) to increase their proton conductivity. A blend membrane doped with 270 wt% PA was operated in an air/ H_2 fuel cell from 80 to 150 $^{\circ}\text{C}$, showing good and increasing performance at an increase of operation temperature (Fig. 4.9).

Ongoing research on the **S11** acid–base ionomer membranes includes the blending of **S11** with **B2** which leads to blend membranes showing excellent oxidation stabilities even after immersion in FT for up to 144 h (see Sect. 4.3).

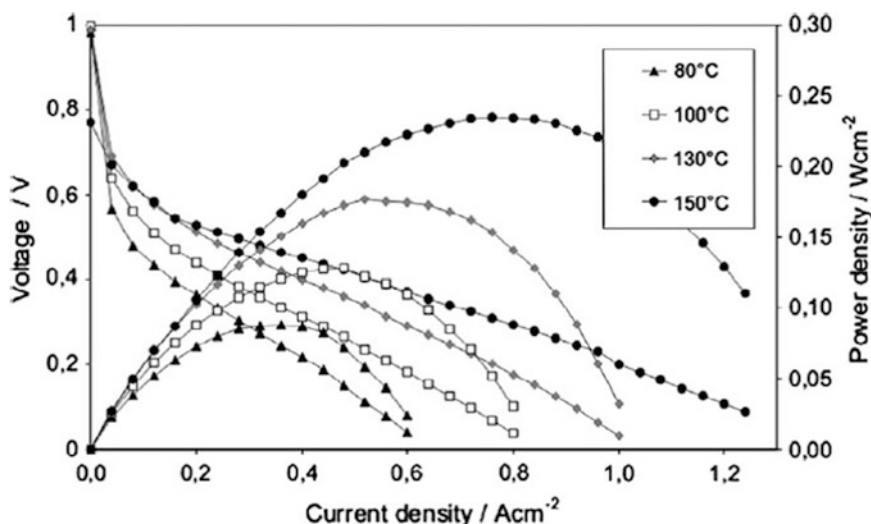


Fig. 4.9 Fuel cell test of an **S11B4** blend membrane, PA doping degree 270 wt% [74]. Reproduced with permission of Elsevier

In [74], completely phosphoric acid-free intermediate-T membranes and MEAs from 1/1 (mole imidazole/mole PO_3H_2) blend membranes of the PBI **B5** (Fig. 4.4) and the phosphonated polymer polyvinyl phosphonic acid (PVPA) **S12** (Fig. 4.5) were presented and compared to PA-doped membranes and MEAs. In the MEAs, a Pt electrocatalyst was deposited onto multiwalled carbon nanotubes (MWNT) which have previously been coated with **B5**. This technique has previously been used for the preparation of electrocatalysts for anion-exchange membrane fuel cells [75]. In the final step, the MWNTs were coated with a layer of **S12**. It turned out that these membranes and MEAs possessed much higher durabilities than membranes and MEAs which have been doped with PA, therefore opening leeway for long-lasting intermediate-T fuel cell membranes without the PA leaching problems which are always present in PA-doped intermediate-T membranes and MEAs [76].

4.3 Short Comparative Study of the Stability and Properties of PBI-Type Membranes

In this section, the properties of PBI-excess acid–base blend membranes will be compared to those of other PBI membrane types to consider

the question of whether one of the investigated membrane types, if any, shows more advantageous properties than the others. The motivation for this short study was the difficulty of comparing the membrane characterization results from different literature sources since the individual characterization methods applied in these references are—in part—varying strongly. The ionically cross-linked PBI blend membranes reviewed in this chapter will be compared to the type of covalently cross-linked PBI blend membranes which has been mentioned in the introduction (blends of PBI with halomethylated polymers whose CH_2Hal groups partially react with the N–H groups of the imidazole moiety of the PBIs [21, 22]). In the third membrane type investigated in this short study, the concepts “ionically cross-linked blend” and “covalently cross-linked blend” have been combined by the preparation of covalent-ionically cross-linked blend membranes via mixing the PBI with both the halomethylated and the cation group-containing polymer.

The following blend components have been varied at the different membranes under investigation: the type of PBI (**B2** and **B4**, Fig. 4.4), the type of acidic macromolecular ionic cross-linker (sulfonated and phosphonated ionomer, **S2** and **S11**, respectively, Fig. 4.5), and the type of macromolecular covalent bromomethylated

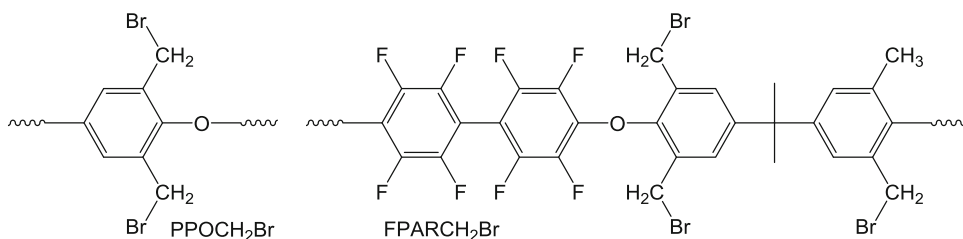


Fig. 4.10 The two investigated bromomethylated polymers

Table 4.7 Investigated blend membrane types

Membrane (No.)	PBI (wt%)	Acidic polymer (wt%)	Polymer-CH ₂ Br (wt%)	Type cross-linking
F ₆ PBI (B2)	B2 : 100	–	–	None
1921C	B4 (PBIOO): 80	–	PPOCH ₂ Br: 20 %	Covalently
1925C	B2 : 80	–	FPARCH ₂ Br: 20 %	Covalently
1927A	B2 : 80	S2 : 20 %	–	Ionically
1938	B2 : 80	–	PPOCH ₂ Br: 20 %	Covalently
1940	B2 : 80	S11 : 20 %	–	Ionically
1943	B2 : 80	S2 : 10 %	FPARCH ₂ Br: 10 %	Covalent-ionically

cross-linker (nonfluorinated PPOCH₂Br and partially fluorinated FPARCH₂Br, respectively, Fig. 4.10).

The preparation (Fig. 4.1) and structure (Fig. 4.3) of an H₃PO₄-doped ionically cross-linked acid–base blend membrane (membranes 1927A and 1940 in Table 4.7) was already depicted schematically in the introduction. Figure 4.11 presents the preparation and the structure of a covalently cross-linked blend membrane (membranes 1921C, 1925C, and 1938), and Fig. 4.12 the preparation and structure of a covalent-ionically cross-linked blend membrane (membrane 1943).

The following properties of the membranes relevant for their potential application in fuel cells have been determined and compared among the different membranes involved in this study, including the benchmark membrane **B2**:

- Thermal stability via TGA
- Cross-linking degree/insolubles fraction by immersion in 90 °C hot DMAc
- Chemical stability via Fenton’s Test (FT)
- Proton conductivity of H₃PO₄-doped membranes

Selected results of membrane characterization will be presented in the subsection below.

4.3.1 Thermal Stability of the Blend Membranes

The thermal stability of all membranes was determined via thermogravimetry under a 65–70 % O₂ atmosphere with a heating rate of 20 K/min [54]. Firstly, it was investigated whether the type of cross-linking influences the thermal stability of the membranes. Therefore, in Fig. 4.13, the TGA traces of the membranes 1925C (covalently cross-linked), 1927A (ionically cross-linked), and 1943 (covalent-ionically cross-linked) are presented together with **B2**.

The TGA traces suggest that the thermal stability of all membranes is similarly excellent up to temperatures of 300 °C which is far above the highest temperature applied in intermediate-T fuel cells (220 °C [77]). Only above 300 °C the influence of the thermally more instable polymer backbones of the other blend components apart from **B2** is apparent.

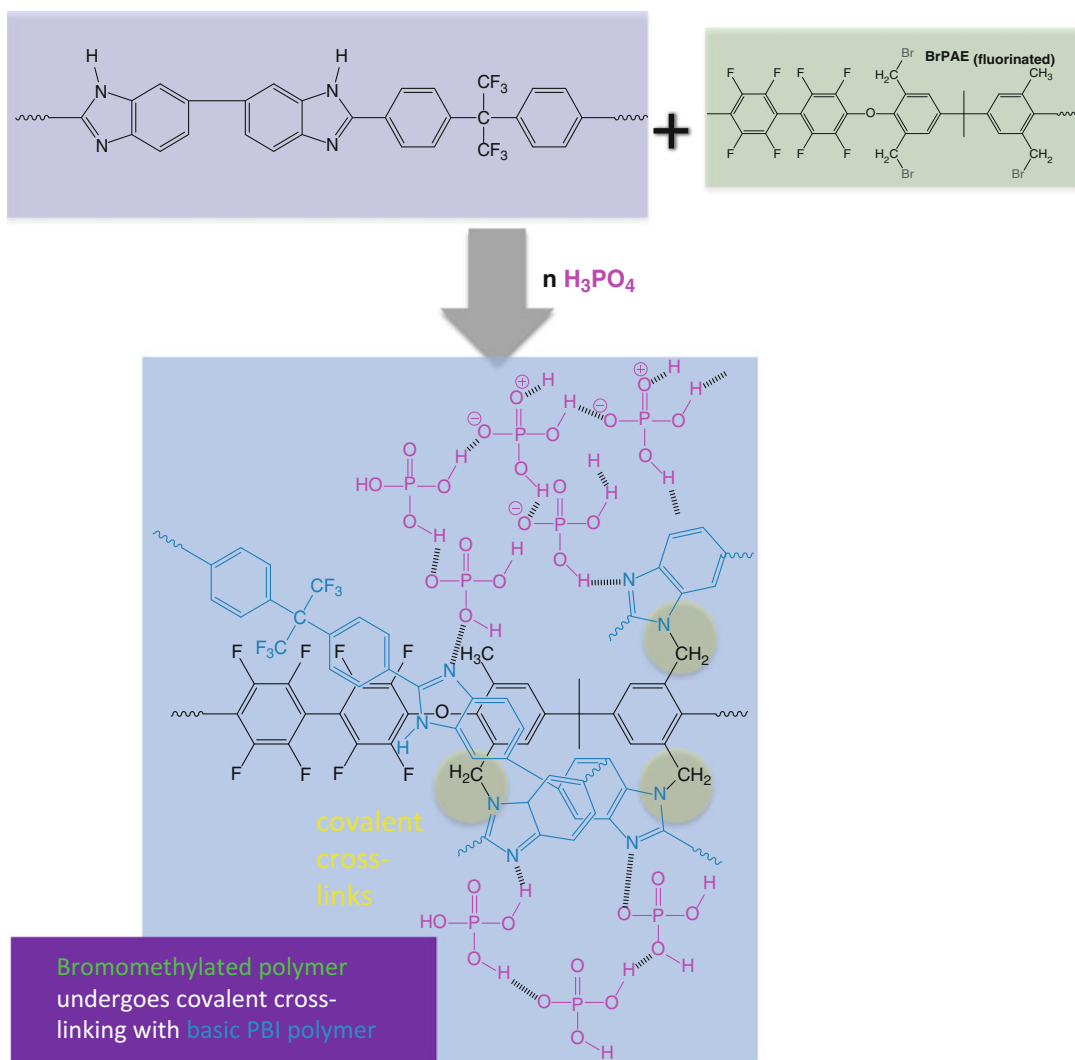


Fig. 4.11 Preparation and structure of covalently cross-linked intermediate-T blend membranes

Secondly, the possible influence of type of cation-exchange group of the acidic cross-linker was inspected. As functional groups for acid–base cross-linking, the strongly acidic sulfonic acid group or the medium-acidic phosphonic acid group are available. As cation-exchange polymers, the highly stable ionomers **S2** [46] and **S11** [73] have been selected. In Fig. 4.14, the TGA traces of the ionically cross-linked membranes 1927A (sulfonated ionic cross-linker **S2**, Fig. 4.5), and 1940 (phosphonated ionic cross-linker

S11, Fig. 4.5) are depicted along with **B2**. Again, all TGAs indicate excellent and similar thermal stabilities of all membranes up to 300 °C. Therefore, it can be concluded that both sulfonated and phosphonated polymers can be selected as acidic cross-linkers for polybenzimidazole membranes.

Furthermore, covalently cross-linked membranes from **B2** and the two different covalent macromolecular cross-linkers PPOCH₂Br and FPARCH₂Br (Fig. 4.10) have been compared to each other and to **B2** in terms of TGA.

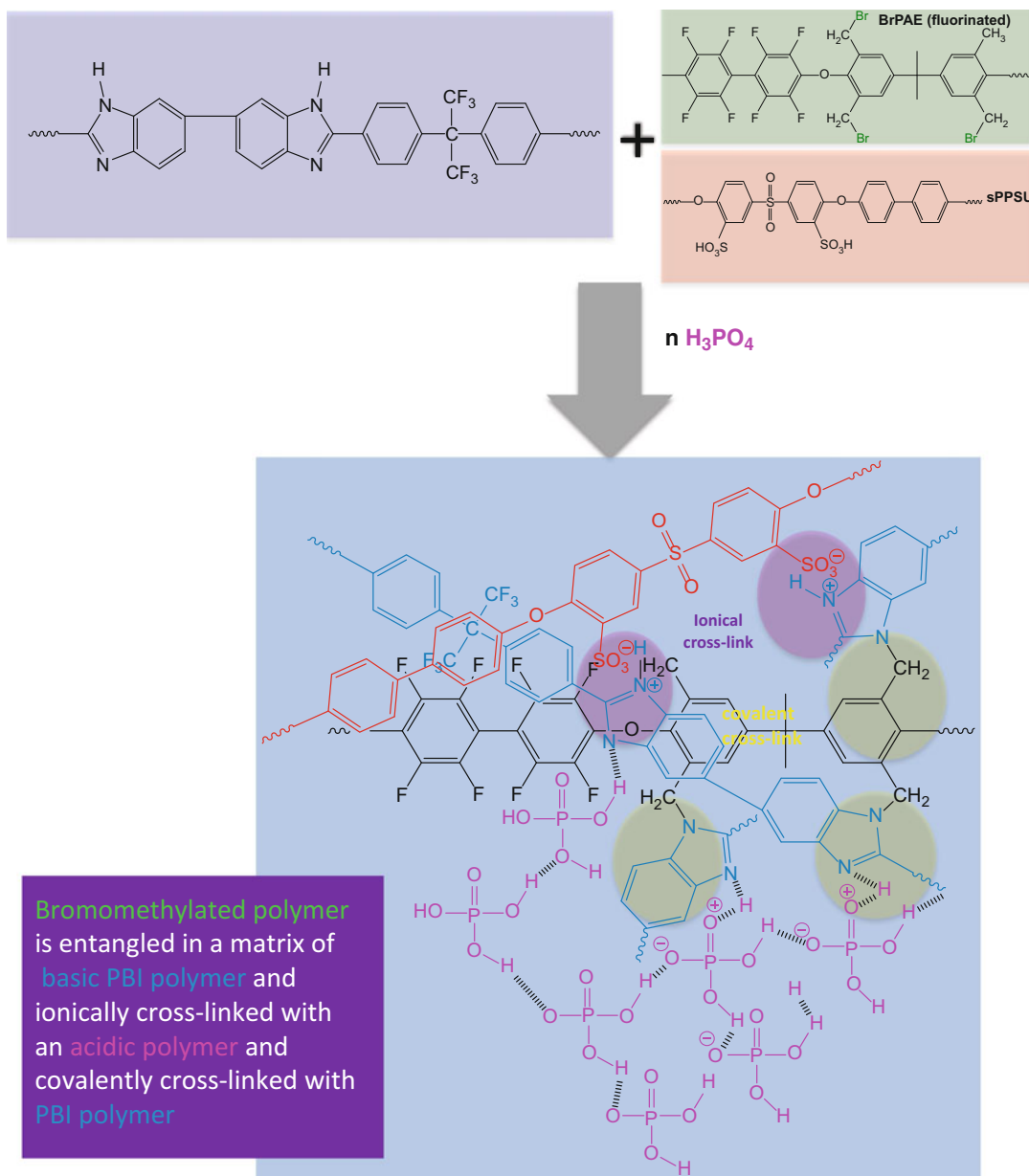


Fig. 4.12 Preparation and structure of covalent-ionically cross-linked intermediate-T blend membranes

Since PPOCH₂Br is a nonfluorinated, electron-rich polymer and FPARCH₂Br a partially fluorinated arylene polymer, one could conclude that the partially fluorinated arylene polymer introduces better thermal stabilities into the blend membrane (Fig. 4.15).

However, contrary to the expectation, both covalently cross-linked blend membranes

possess nearly identical thermal stabilities in the whole TGA range, highlighting the dominant influence of the main blend component **B2** on the thermal membrane properties.

Moreover, a thermal stability comparison has been made between the covalently cross-linked (cross-linker: PPOCH₂Br) membranes 1921C (**B4**-containing) and 1938A (**B2**-containing).

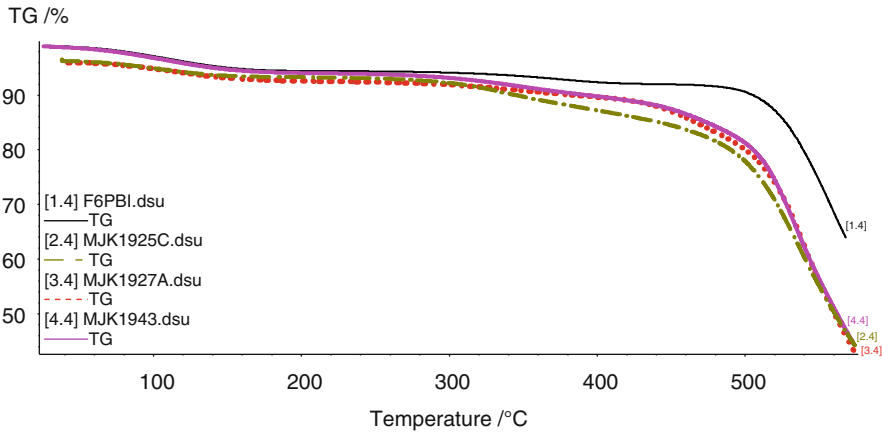


Fig. 4.13 TGA traces of membranes **B2**, 1925C, 1927A, and 1943

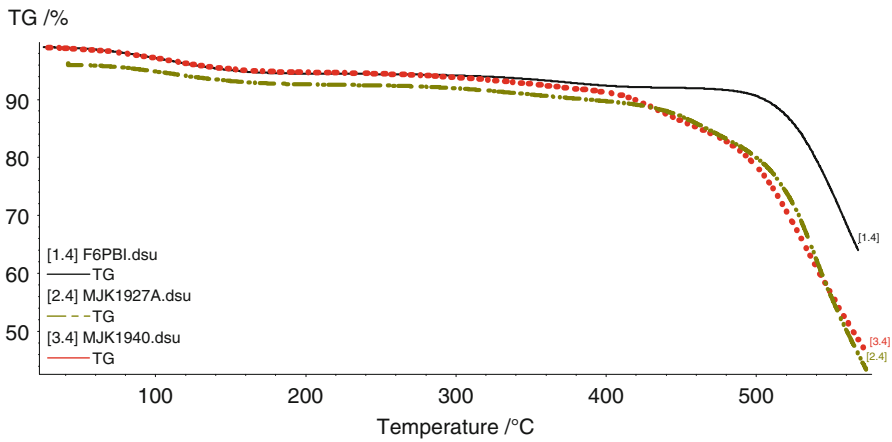


Fig. 4.14 TGA comparison of **B2**, 1927A (sulfonated ionic cross-linker **S2**, Fig. 4.5), and 1940 (phosphonated ionic cross-linker **S11**, Fig. 4.5)

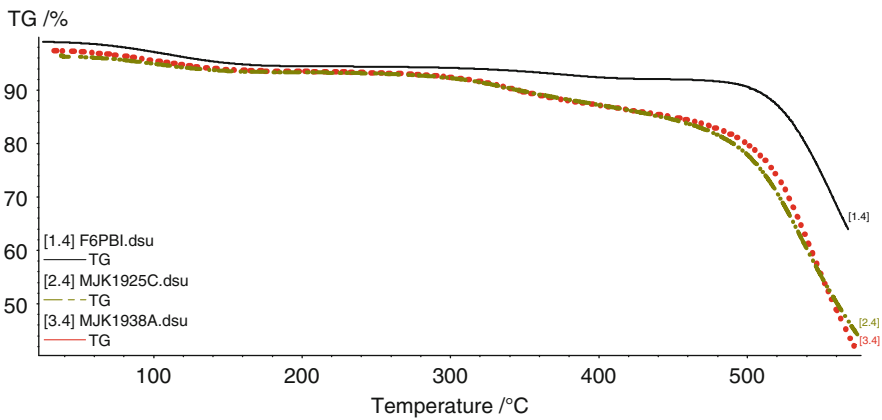


Fig. 4.15 TGA comparison of **B2** with the blend membranes 1938A (PPOCH₂Br as cross-linker) and 1925C (FPARCH₂Br as cross-linker)

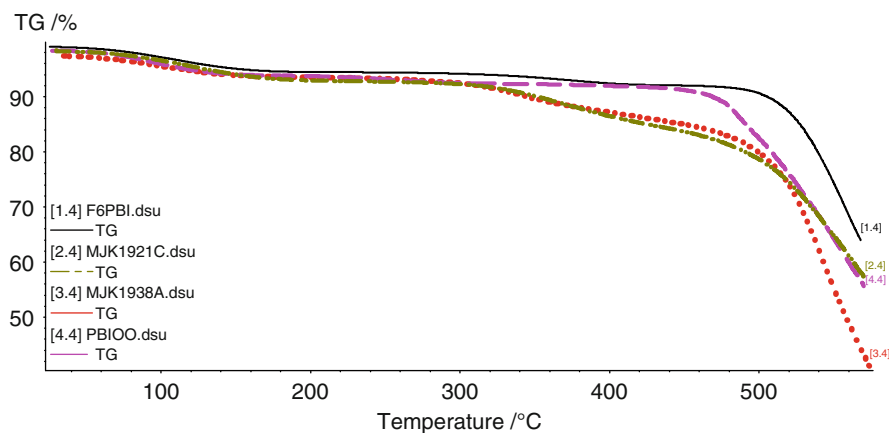


Fig. 4.16 TGA comparison of 1921C (**B4**-containing) and 1938A (**B2**-containing) and pure **B2** and **B4**

The TGA traces of pure **B2** and **B4** have also been included in Fig. 4.16.

From Fig. 4.16 can be read that both covalently cross-linked blend membranes expose nearly similar thermal stabilities, while the thermal stability of pure partially fluorinated **B2** is slightly better than that of the pure fluorine-free **B4** only above 450 °C which is however not relevant for the intended intermediate-T fuel cell application of these membranes. Therefore, covalent cross-linking can be regarded as a good method to improve thermal (and chemical, see below) stabilities of PBI-type membranes.

It can be concluded from the obtained TGA results that all of the investigated PBI blend membranes show, regardless of cross-linking and cross-linker type, comparable thermal stabilities. At higher contents of the non-PBI blend components, the property differences between the different intermediate-T blend membrane types might be more strongly pronounced.

4.3.2 Cross-linking Degree/Insoluble Fraction by Immersion in 90 °C Hot DMAc

The insoluble fraction after the extraction of the membranes in 90 °C hot DMAc is a measure of the extent of cross-linking of the membrane matrix. The extraction results (the extraction

method is described in [78]) are presented in Fig. 4.17. As expected, the pure PBIs completely dissolve in hot DMAc. Interestingly, the ionically cross-linked membranes remain partially undissolved which is an indication for relatively strong acid–base and hydrogen bridge interactions. The phosphonated blend component obviously forms even stronger interactions with the PBI than the sulfonated blend component (insolubles at membrane 1927A = 61.8 %, insolubles at membrane 1940 = 81.7 %) which can most probably be traced back to the two acidic OH groups present per PO_3H_2 group in the phosphonated ionomer **S11** that are available for ionic cross-linking. The three covalently cross-linked membranes (1921C, 1925C, 1938A) and the covalent-ionically cross-linked membrane comprise large insoluble fractions of clearly above 90 %, indicating complete formation of cross-linked network within the membranes. The cross-linked network is an important prerequisite for stability of PBI-type membranes to be applied to PA-doped intermediate-T fuel cells since it was reported that pure PBIs can dissolve during PA doping as it was observed with pure **B4** [59].

The membranes gathered in Table 4.7 were immersed in Fenton's Reagent according to the reviewed literature (e.g., [47]) for 144 h, and after this time the weight loss was determined. The amount of weight loss of membranes is represented in Fig. 4.18.

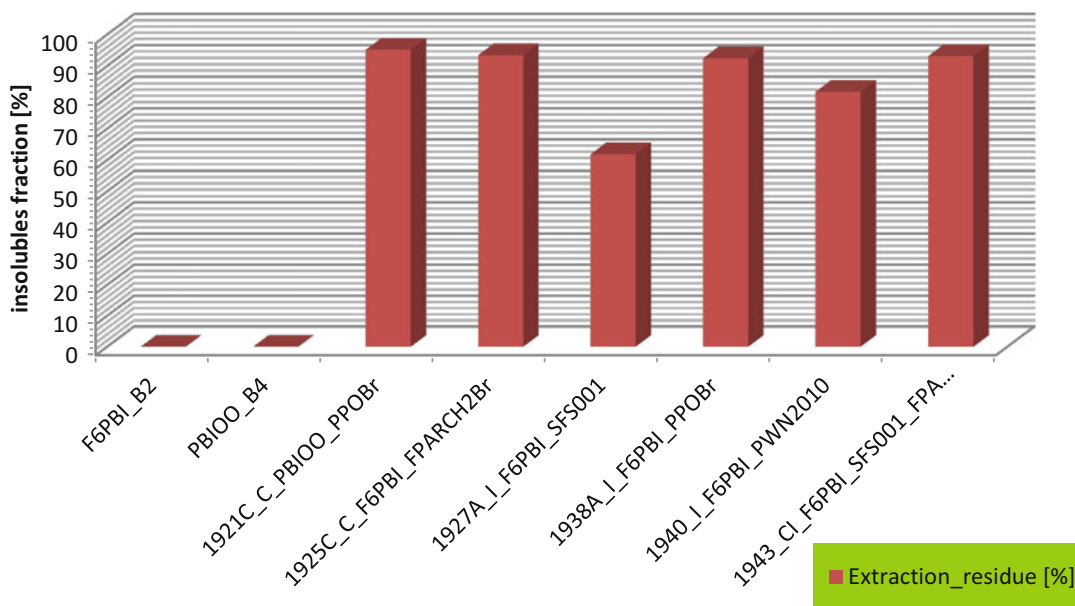


Fig. 4.17 DMAc extraction results of the membranes including the pure membranes F₆PBI (**B2**) and PBIOO (**B4**) (I = ionically cross-linked, C = covalently cross-linked, CI = covalent-ionically cross-linked)

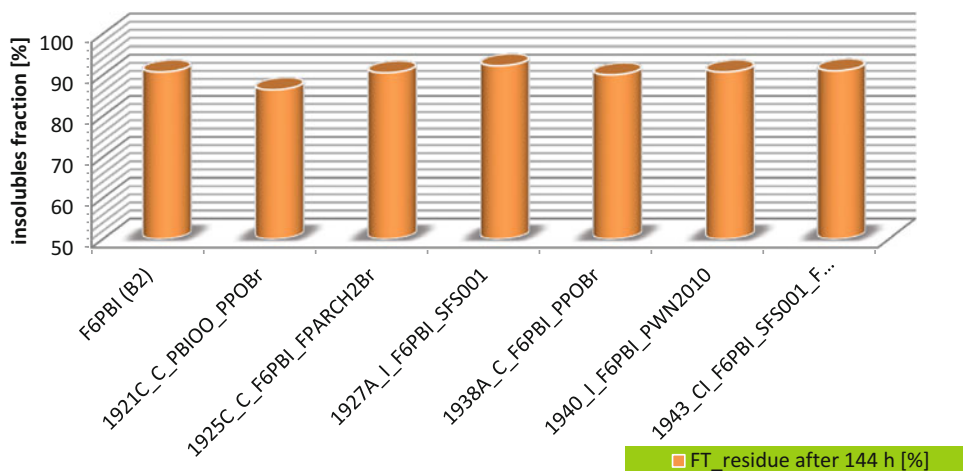


Fig. 4.18 Insoluble residuals of membranes after 144 h of storage in Fenton's Reagent

It can be seen from Fig. 4.18 that all **B2**-containing blend membranes regardless of cross-link type and polymer backbone of the used cross-linkers show very similar weight loss values after the 144 h FT which indicates that **B2** which is known for high oxidative stability as ascertained in the literature reviewed in this chapter (e.g., [49]) determines the excellent oxidative stabilities of those blends. The somewhat

higher weight loss value of the **B4**-containing blend membrane (1921A) reflects the worse chemical stability of this polybenzimidazole, compared to **B2** [56]. It must be mentioned here that all membranes retained their mechanical stability after 144 h of FT.

The membranes subjected to FT were further investigated by SEM to see to what extent the membrane surfaces were corroded by the

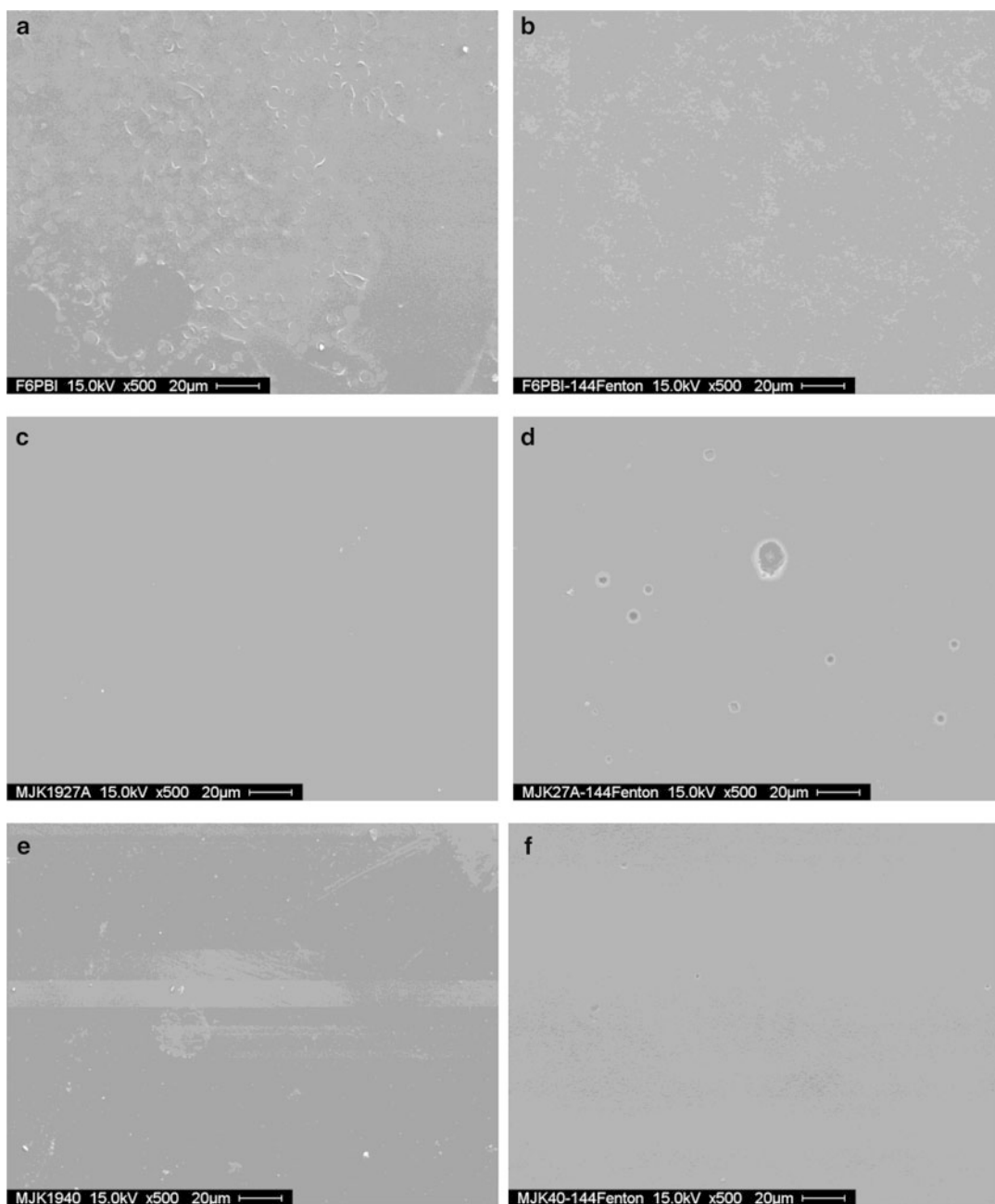


Fig. 4.19 SEM of membranes before and after FT (**a**) **B2** before FT, (**b**) **B2** after FT, (**c**) 1927A before FT, (**d**) 1927A after FT, (**e**) 1940 before FT, (**f**) 1940 after FT, (**g**):

1921C before FT, (**h**) 1921C after FT, (**i**) 1938 before FT, (**j**) 1938 after FT, (**k**) 1925C before FT, (**l**) 1925C after FT. Magnification of all micrographs is $\times 500$

strongly oxidizing Fenton's Solution. In Fig. 4.19, SEM micrographs of the surfaces of the membranes before and after FT are collected.

It is seen from the micrographs that the membrane surfaces exhibit only a few small holes

after FT indicating good stabilities of the membranes in the strongly oxidizing FT environment. Only the surface of the membrane 1921C shows more pronounced defects, indicating and confirming the slightly worse chemical stability

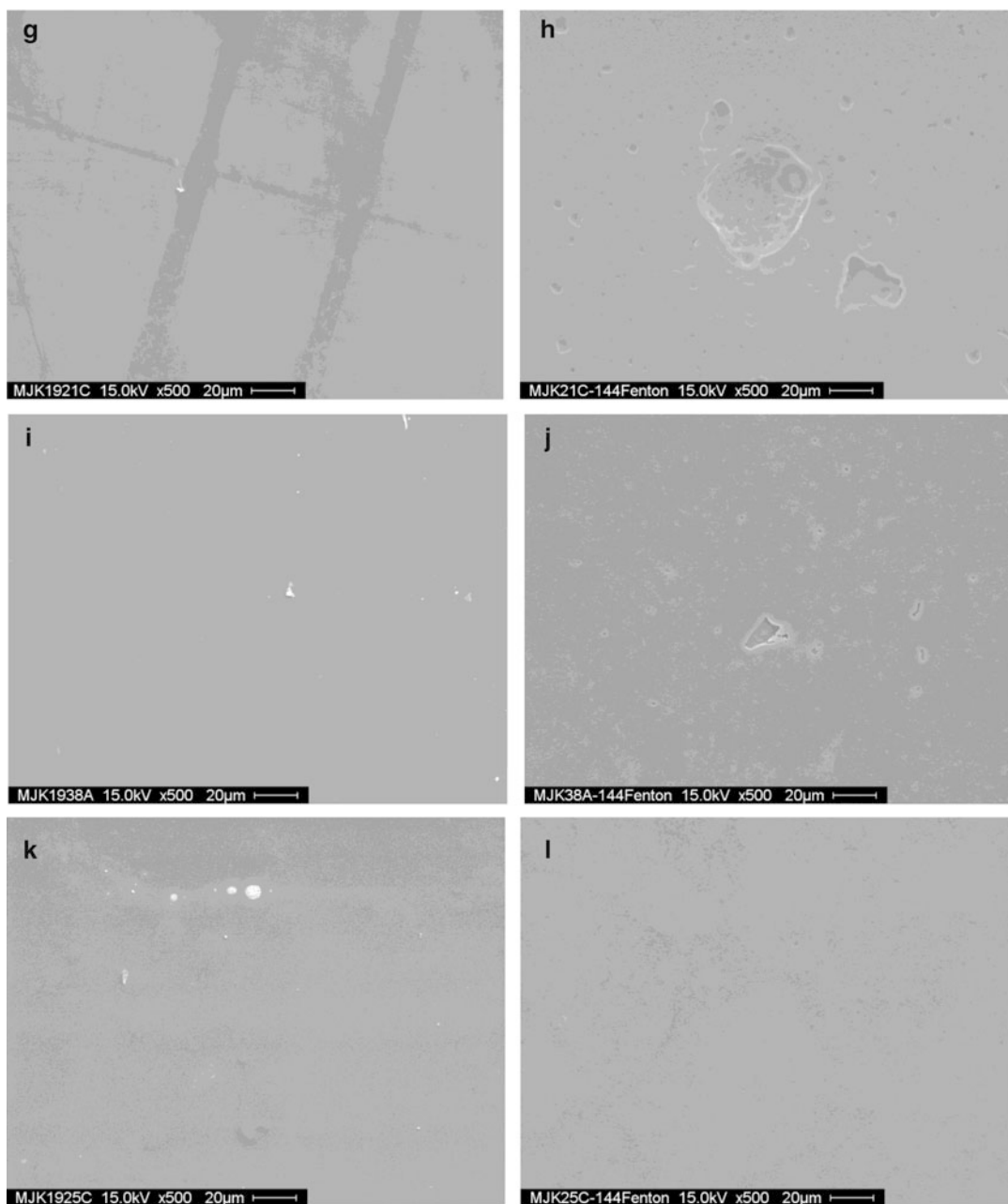


Fig. 4.19 (continued)

of its main blend constituent **B4** as could also be seen from the larger weight loss amount of this membrane after FT (Fig. 4.18), compared to the **B2**-containing membranes. The membranes were also tested via TGA before and after FT to see if the shape of the TGA curve changes through FT which also gives hints for partial chemical

degradation of the membranes. In Fig. 4.20, the TGA traces of 1921C before and after FT are presented, and in Fig. 4.21 those of 1938. In both cases, the covalent cross-linking polymer was PPOCH₂Br, while the 1921C contains **B4** and 1938 **B2** as polybenzimidazole constituent. It can be seen that the TGA traces of 1921C shows a

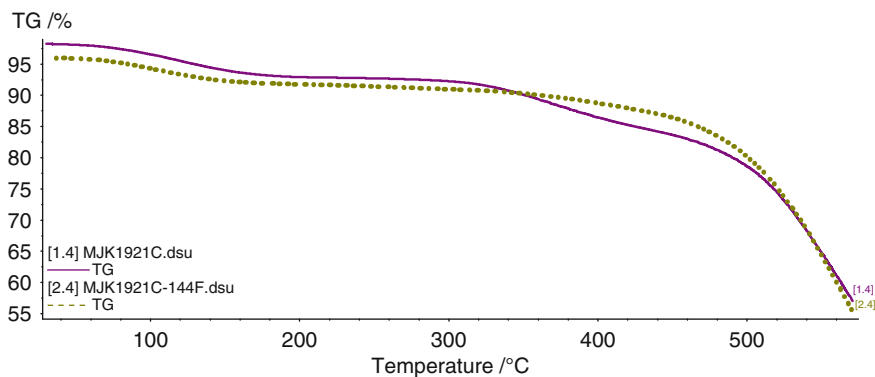


Fig. 4.20 TGA traces of 1921C before and after FT (covalently cross-linked, PPOCH₂Br as cross-linker, **B4** as base)

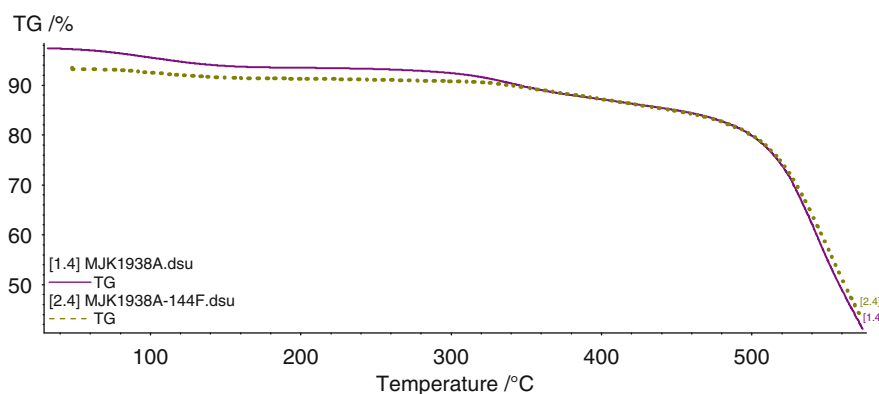


Fig. 4.21 TGA traces of 1938 before and after FT (covalently cross-linked, PPOCH₂Br as cross-linker, **B2** as base)

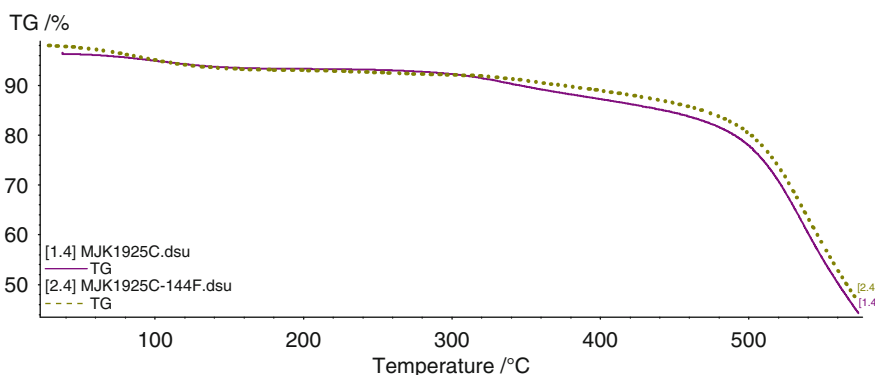


Fig. 4.22 TGA traces of 1925C before and after FT (covalently cross-linked, FPARCH₂Br as cross-linker, **B2** as base)

more distinct change of trace shape before and after FT, compared to 1938, which is an indication of stronger chemical changes in the polymer backbones of the 1921C blend components particularly in the T range >300 °C in which backbone

degradation begins [77]. In Fig. 4.22, the TGA traces of membrane 1925C before and after FT are presented. Both TGA traces of this membrane are nearly identical, reflecting the excellent chemical stability of this membrane. The reason for the

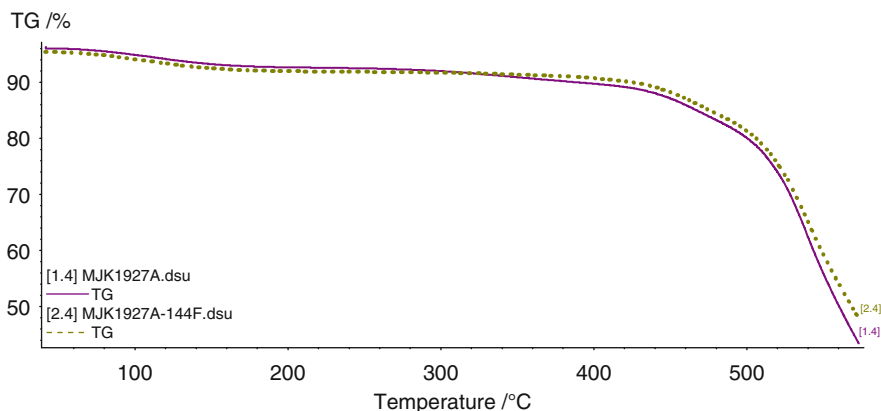


Fig. 4.23 TGA traces of 1927A before and after FT (sulfonated ionic cross-linker **S2**, **B2** as base)

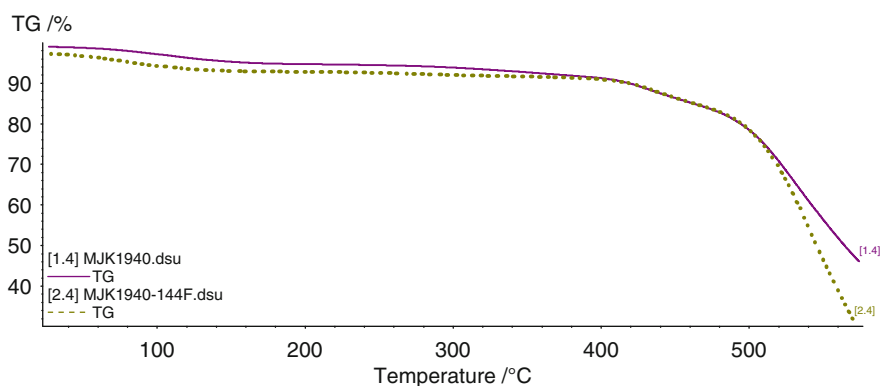


Fig. 4.24 TGA traces of 1940 before and after FT (phosphonated ionic cross-linker **S11**, **B2** as base)

excellent chemical stability of 1925C is most probably that the PPOCH_2Br cross-linker was substituted by the chemically more stable cross-linking polymer FPARCH_2Br in this membrane.

In Fig. 4.23, the TGA traces of the ionically cross-linked membrane 1927A (sulfonated cross-linker) are presented, and in Fig. 4.24 those of 1940 (phosphonated cross-linker), indicating the excellent chemical stabilities of these two blend membranes.

4.3.3 Proton Conductivity of H_3PO_4 -Doped Membranes

Since the proton conductivity is the determinant property of fuel cell membranes, all membranes

of the series were doped with 85 % PA to roughly the same PA doping degree (130 %, ADL = 8.9 in the case of 80 wt% **B2** blends, and ADL = 6.9 in the case of 80 wt% **B4** blends, and ADL = 7.5 in the case of pure **B2**), where possible. Afterwards, the proton conductivity of the membranes was measured under a constant relative humidity of 20 % in a temperature range from 80 to 150 °C. The results of proton conductivity measurements are presented in Fig. 4.25. The proton conductivity measurements were performed with the Membrane Test System (MTS) 740 from Scribner. The method is described in [59].

From Fig. 4.25 no correlation of value of proton conductivity to cross-linking type, F-content or type of cross-linking polymer can be seen: the membrane with the lowest proton

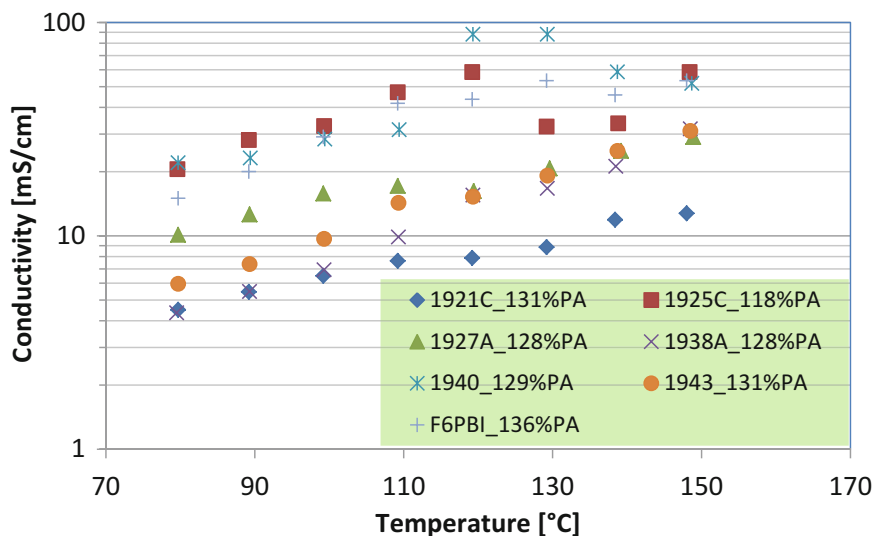


Fig. 4.25 Proton conductivities of the investigated membrane series in dependence of temperature at RH of 20 %

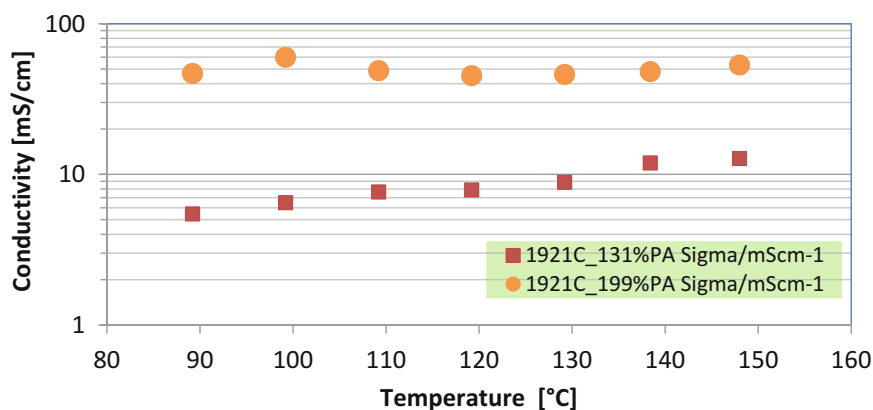


Fig. 4.26 Proton conductivities of the 1921C at 131 and 199 % PA doping degree, respectively, at 20 % RH

conductivities is the covalently cross-linked 1921C containing the nonfluorinated cross-linker PPOCH₂Br, while the 1925C, also a covalently cross-linked blend membrane cross-linked with the partially fluorinated FPARCH₂Br polymer, exposes the highest proton conductivity among the investigated membranes. The reason for this finding might be the fact that the relation between structure and properties of the investigated membranes is very complex due to the difficulty of assessability of the influence of the different blend components and cross-linking type on the membrane properties. To elucidate the complex coherence between proton

conductivity, PA doping, blend composition, and type of cross-linking of the investigated membranes, a detailed study of the dependence of proton conductivities from relation between the blend components, PA doping degree, temperature, and relative humidities is required. One of the advantages of PA-doped intermediate-T fuel cell membranes is that, if a membrane possesses too low proton conductivities at a specific PA doping degree, the PA doping degree simply has to be increased to obtain a higher H⁺ conductivity. This is demonstrated in the membrane 1921C: in Fig. 4.26, the proton conductivities of the 1921C are shown at PA

doping degree of 131 % (ADL = 6.96) and 199 % (ADL = 10.57), respectively.

As indicated in Fig. 4.26, with a PA doping degree increase from 131 to 199 %, an increase of proton conductivities of up to a factor of 9 is observed.

4.4 Conclusions

In this chapter, research work done with intermediate-T fuel cell membranes, in which the acid–base blend concept was applied for membrane preparation, was reviewed. The reviewed studies included membranes, where the different parameters have been varied:

- Type of applied polybenzimidazoles
- Type of used ionic cross-linker, including sulfonated and phosphonated ionomers which were either composed of nonfluorinated or partially fluorinated backbones

A mutual characteristic of all the reviewed acid–base blend membrane types are their improved properties compared to pure PBI:

- The mechanical properties of the base-excess acid–base blend membranes are strongly improved, compared to pure PBI.
- The resistance of the acid–base blend membranes to a strongly oxidizing environment (Fenton’s Reagent) is markedly enhanced, as indicated by smaller weight losses of the acid–base blend membranes, compared to pure PBI, during storage in Fenton’s Reagent.
- The fuel cell performance of the PA-doped base-excess acid–base blend membranes is comparable to that of the best reported pure PA-doped intermediate-T membranes.
- The use of a phosphonated polymer as ionic cross-linker AND proton conductor both in the membrane and the electrodes of intermediate-T MEAs opens perspectives for highly durable intermediate-T fuel cell membranes without PA leaching problems which are always present in PA-doped intermediate-T membranes and MEAs.

When comparing the properties of base-excess blend membranes containing different polybenzimidazoles, it turns out that there is a trend that the use of electron-deficient polybenzimidazoles such as **B2** and **B3** (Fig. 4.4) as basic blend components leads to higher chemical and thermal stabilities of the respective acid–base blend membranes than if more electron-rich PBIs such as **B1** and **B4** are used. However, it must be mentioned here that the molecular weight of the polybenzimidazole also influences the durability of the PBI (blend) membranes: it was observed that after being subjected to FT the membranes lost less weight when their molecular weights were higher [79].

From the reviewed work, it can be concluded that obviously the use of partially fluorinated aromatic cationomers as ionic cross-linkers leads in most cases to better chemical and thermal stabilities of the blend membranes than if nonfluorinated cationomers would be applied as acidic blend components. Among all acidic cross-linkers, the sulfonated and partially fluorinated ionomer **S9** (Fig. 4.5) leads to the best chemical stability of the referring base-excess PBI blend membranes.

From the comparative study covering different ionically, covalently, and covalent-ionically cross-linked PBI blend membrane types, it can be concluded that within the investigated membrane types none of the cross-linking types has principal advantages over the other ones in terms of chemical stability or proton conductivity in PA-doped state.

Future work in the field of PBI blend membranes for use in intermediate-T fuel cells will incorporate:

- Increase of molecular weight of acidic cross-linkers (e.g., of **S9**) to further enhance the chemical, thermal, and mechanical stability of the referring PBI blend membranes
- Investigation of further sulfonated and phosphonated aromatic ionomers as acidic macromolecular cross-linkers (and possibly as proton-conducting blend component) for intermediate-T fuel cell membranes

- Continuation of the R&D work on covalent-ionically cross-linked blend membranes, where the different blend components PBI/acidic polymer/bromomethylated polymer are optimally matched to one another to yield intermediate-T fuel cell membranes with a property profile tailored to the respective membrane application such as fuel cells or electrolysis, respectively
- Electrode and MEA development tailored to the respective intermediate-T membrane(s)

References

1. Grot WG (1994) Perfluorinated ion-exchange polymers and their use in research and industry. *Macromol Symp* 82:161-172
2. Kreuer KD (1996) Proton conductivity: materials and applications. *Chem Mater* 8:610-641
3. Vogel H, Marvel CS (1961) Polybenzimidazoles, new thermally stable polymers. *J Polym Sci* 50:511-539
4. Vogel H, Marvel CS (1963) Polybenzimidazoles 2. *J Polym Sci A* 1:1531-1541
5. Wainright JS, Wang JT, Savinell RF et al (1995) Acid-doped polybenzimidazoles: a new polymer electrolyte. *J Electrochem Soc* 142:L121-L123
6. Kreuer KD, Paddison S, Spohr E et al (2004) Toward a new type of anhydrous organic proton conductor based on immobilized imidazole. *Chem Rev* 104:4637-4678
7. Yu S, Xiao L, Benicewicz BC (2008) Durability studies of PBI-based high temperature PEMFCs. *Fuel Cells* 8:165-174
8. Liao J, Li QF, Rudbeck HC et al (2011) Oxidative degradation of polybenzimidazole membranes as electrolytes for high temperature proton exchange membrane fuel cells. *Fuel Cells* 11:745-755
9. Ghosh S, Maity S, Jana T (2011) Polybenzimidazole/silica nanocomposites: organic-inorganic hybrid membranes for PEM fuel cell. *J Mater Chem* 21:14897-14906
10. Zhang R, Shi ZX, Liu Y et al (2012) Synthesis and characterization of polybenzimidazole-nanodiamond hybrids via in situ polymerization method. *J Appl Polym Sci* 125:3191-3199
11. Mao L, Mishra AK, Kim NH et al (2012) Poly(2,5-benzimidazole)-silica nanocomposite membranes for high temperature proton exchange membrane fuel cell. *J Membr Sci* 411-412:91-98
12. Ossiander T, Heinzl C, Gleich S et al (2014) Influence of the size and shape of silica nanoparticles on the properties and degradation of a PBI-based high temperature polymer electrolyte membrane. *J Membr Sci* 454:12-19
13. Plackett D, Siu A, Li Q et al (2011) High-temperature proton exchange membranes based on polybenzimidazole and clay composites for fuel cells. *J Membr Sci* 383:78-87
14. He R, Li Q, Xiao G et al (2003) Proton conductivity of phosphoric acid doped polybenzimidazole and its composites with inorganic proton conductors. *J Membr Sci* 226:169-184
15. Wang S, Zhang G, Han M et al (2011) Novel epoxy-based cross-linked polybenzimidazole for high temperature proton exchange membrane fuel cells. *Int J Hydrogen Energy* 36:8412-8421
16. Aili D, Li Q, Christensen E et al (2011) Crosslinking of polybenzimidazole membranes by divinylsulfone post-treatment for high-temperature proton exchange membrane fuel cell applications. *Polym Int* 60:1201-1207
17. Xu HJ, Chen KC, Guo XX et al (2007) Synthesis of hyperbranched polybenzimidazoles and their membrane formation. *J Membr Sci* 288:255-260
18. Wang KY, Xiao YC, Chung TS (2006) Chemically modified polybenzimidazole nanofiltration membrane for the separation of electrolytes and cephalixin. *Chem Eng Sci* 61:5807-5817
19. Noyé P, Li QF, Pan C et al (2008) Cross-linked polybenzimidazole membranes for high temperature proton exchange membrane fuel cells with dichloromethyl phosphoric acid as a cross-linker. *Polym Adv Technol* 19:1270-1275
20. Yang J, Li Q, Cleemann LN et al (2013) Crosslinked hexafluoropropylidene polybenzimidazole membranes with chloromethyl polysulfone for fuel cell applications. *Adv Energy Mater* 3:622-630
21. Wang S, Zhao C, Ma W et al (2013) Macromolecular cross-linked polybenzimidazole based on bromomethylated poly(aryl ether ketone) with enhanced stability for high temperature fuel cell applications. *J Power Sources* 243:102-109
22. Cui W, Kerres J (2001) Acid-base polymer blends and their application in membrane processes. US Patent 6,194,474
23. Kerres J, Ullrich A, Häring T (2004) Engineering ionomer blends and engineering ionomer blend membranes. European Patent 1,076,676; US Patent 6,723,757
24. Cui W, Kerres J, Eigenberger G (1998) Development and characterization of ion-exchange polymer blend membranes. *Sep Purif Technol* 14:145-154
25. Kerres J, Ullrich A, Meier F et al (1999) Synthesis and characterization of novel acid-base polymer blends for the application in membrane fuel cells. *Solid State Ionics* 125:243-249
26. Kerres J, Ullrich A, Häring T et al (2000) Preparation, characterization, and fuel cell application of new acid-base blend membranes. *J New Mater Electrochem Syst* 3:229-239

27. Kerres JA (2001) Development of ionomer membranes for fuel cells. *J Membr Sci* 185:3–27
28. Kerres J, Tang CM, Graf C (2004) Improvement of properties of polyetherketone ionomer membranes by blending and cross-linking. *Ind Eng Chem Res* 43:4571–4579
29. Kerres J, Xing D, Schönberger F (2006) Comparative investigation of novel PBI blend ionomer membranes from nonfluorinated and partially fluorinated polyarylene ethers. *J Polym Sci B Polym Phys* 44:2311–2326
30. Hasiotis C, Li Q, Deimede V et al (2001) Development and characterization of acid-doped polybenzimidazole-sulfonated polysulfone blend polymer electrolytes for fuel cells. *J Electrochem Soc* 148: A513–A519
31. Kawahara M, Rikukawa M, Sanui K (2000) Relationship between absorbed water and proton conductivity in sulfopropylated polybenzimidazole. *Polym Adv Technol* 11:544–547
32. Pu H, Liu Q (2004) Methanol permeability and proton conductivity of polybenzimidazole and sulfonated polybenzimidazole. *Polym Int* 53:1512–1516
33. Papadimitriou KD, Andreopoulou AK, Kallitsis JK (2010) Phosphonated fully aromatic polyethers for PEMFCs applications. *J Polym Sci A Polym Chem* 48:2817–2827
34. Kalamaras I, Daletou MK, Gregoriou VG et al (2011) Sulfonated aromatic polyethers containing pyridine units as electrolytes for high temperature fuel cells. *Fuel Cells* 11:921–931
35. Thomas OD, Peckham TJ, Thanganathan U et al (2010) Sulfonated polybenzimidazoles: proton conduction and acid-base crosslinking. *J Polym Chem A Polym Chem* 48:3640–3650
36. Ng F, Peron J, Jones DJ et al (2011) Synthesis of novel proton-conducting highly sulfonated polybenzimidazoles for PEMFC and the effect of the type of bisphenyl bridge on polymer and membrane properties. *J Polym Sci A Polym Chem* 49:2107–2117
37. Angioni S, Villa DC, Dal Barco S et al (2014) Polysulfonation of PBI-based membranes for HTPEMFCs: a possible way to maintain high proton transport at a low H₃PO₄ doping level. *J Mater Chem A* 2:663–671
38. Sukumar PR, Wu W, Markova D et al (2007) Functionalized polybenzimidazoles as membrane materials for fuel cells. *Macromol Chem Phys* 208:2258–2267
39. Gubler L, Kramer D, Belack J et al (2007) Celtec-V, a polybenzimidazole-based membrane for the direct methanol fuel cell. *J Electrochem Soc* 154:B981–B987
40. Sinigersky V, Budurova D, Penchev H et al (2013) Polybenzimidazole-graft-polyvinylphosphonic acid proton-conducting fuel cell membranes. *J Appl Polym Sci* 129:1223–1231
41. Ng F, Bae B, Miyatake K et al (2011) Polybenzimidazole block sulfonated poly(arylene ether sulfone) ionomers. *Chem Commun* 47:8895–8897
42. Hasiotis C, Li Q, Deimede V et al (2001) New polymer electrolytes based on blends of sulfonated polysulfones with polybenzimidazole. *Electrochim Acta* 46:2401–2406
43. Noshay A, Robeson LM (1976) Sulfonated polysulfone. *J Appl Polym Sci* 20:1885–1903
44. Xing D, Kerres J (2006) Improved performance of sulfonated polyarylene ethers for proton exchange membrane fuel cells. *Polym Adv Technol* 17:1–7
45. Takamuku S, Jannasch P (2012) Properties and degradation of hydrocarbon fuel cell membranes: a comparative study of sulfonated poly(arylene ether sulfone)s with different positions of the acid groups. *Polym Chem* 3:1202–1214
46. Kerres J, Schönberger F, Chromik A et al (2008) Partially fluorinated arylene polyethers and their ternary blend membranes with PBI and H₃PO₄: Part I. Synthesis and characterization of polymers and binary blend membranes. *Fuel Cells* 8:175–187
47. Walling C (1975) Fenton's reagent revisited. *Acc Chem Res* 8:125–131
48. Li Q, Jensen JO, Pan C et al (2008) Partially fluorinated arylene polyethers and their ternary blends with PBI and H₃PO₄: Part II. Characterizations and fuel cell tests of the ternary membranes. *Fuel Cells* 8:188–199
49. Li QF, Rudbeck HC, Chromik A et al (2010) Properties, degradation and high temperature fuel cell test of different types of PBI and PBI blend membranes. *J Membr Sci* 347:260–270
50. Henschel C (2006) Membranes and electrodes for fuel cells as PEMEAS merges with E-TEK. *Fuel Cells Bull* 2:12–15
51. Qi ZQ, Buelte S (2006) Effect of open circuit voltage on performance and degradation of high temperature PBI-H₃PO₄ fuel cells. *J Power Sources* 161:1126–1132
52. Reiche A (2006) Sartorius HT-PEMFC membrane electrode assembly. Paper presented at the 2006 fuel cell seminar, November 13–17, 2006, Honolulu, Hawaii. http://www.fuelcellseminar.com/pdf/2006/Wednesday/3B/Reiche_Annette_1010_502&507.pdf
53. Stolten D, Wannek C, Dohle H et al (2007) Strategy, status and outlook for HT-PEFC development for APU application. Paper presented at the 2007 fuel cell seminar, October 15–19, 2007, San Antonio, TX. http://www.fuelcellseminar.com/pdf/2007/Presentations/2A/162%20Stolten_San%20Antonio_2007_final.ppt.pdf
54. Kerres J, Ullrich A, Hein M et al (2004) Cross-linked polyaryl blend membranes for polymer electrolyte fuel cells. *Fuel Cells* 4:105–112
55. Chromik A, Kerres JA (2013) Degradation studies on acid-base blends for both LT and intermediate T fuel cells. *Solid State Ionics* 252:140–151
56. Liu G, Zhang H, Hu J et al (2006) Studies of performance degradation of a high temperature PEMFC based on H₃PO₄-doped PBI. *J Power Sources* 162:547–552
57. Steenberg T, Hjuler HA, Terkelsen C et al (2012) Roll-to-roll coated PBI membranes for high

- temperature PEM fuel cells. *Energy Environ Sci* 5:6076–6080
58. Kerres JA, Katzfuß A, Chromik A et al (2014) *J Appl Polym Sci* 131:39889
59. Hübner G, Roduner E (1999) EPR investigation of HO/radical initiated degradation reactions of sulfonated aromatics as model compounds for fuel cell proton conducting membranes. *J Mater Chem* 9:409–418
60. Assink RA, Arnold C, Hollandsworth RPJ (1991) Preparation of oxidatively stable cation-exchange membranes by the elimination of tertiary hydrogens. *J Membr Sci* 56:143–151
61. Ding J, Day M (2006) Novel highly fluorinated poly(arylene ether-1,3,4-oxadiazole)s, their preparation, and sensory properties to fluoride anion. *Macromolecules* 39:6054–6062
62. Hajdok I, Bona A, Werner HJ et al (2014) Synthesis and characterization of fluorinated and sulfonated poly(arylene ether-1,3,4-oxadiazole) derivatives and their blend membranes. *Eur Polym J* 52:76–87
63. Sartori P, Bauer G (1978) 2,3,5,6-Tetrafluorobenzoldisulfonsäure aus Pentafluorbenzol-sulfonsäure. *J Fluorine Chem* 12:203–210
64. Banks RE, Burgess JE, Cheng WM et al (1965) Heterocyclic polyfluoro-compounds. Part IV. - Nucleophilic substitution in pentafluoropyridine: the preparation and properties of some 4-substituted 2,3,5,6-tetrafluoro-pyridines. *J Chem Soc (resumed)* 1965:575–581
65. Chambers RD, Hutchinson J, Musgrave WKR (1964) Polyfluoroheterocyclic compounds. Part II: Nucleophilic substitution in pentafluoropyridine. *J Chem Soc (resumed)* 1964:3736–3739
66. Alsop DJ, Burdon J, Tatlow JC (1962) Aromatic polyfluoro-compounds. Part XI: Some replacement reactions of octafluorotoluene. *J Chem Soc (resumed)* 1962:1801–1805
67. Seyb C, Kerres J (2013) Novel partially fluorinated sulfonated poly(arylenethioether)s and poly(aryleneether)s prepared from octafluorotoluene and pentafluoropyridine, and their blends with PBI-Celazol. *Eur Polym J* 49:518–531
68. Seyb C (2014) Synthese und Charakterisierung von teilfluorierten sulfonierten poly(arylen)-Ionomeren für den Einsatz in Mitteltemperaturbrennstoffzellen. Dissertation, Universität Stuttgart
69. Nakano T, Nagaoka T, Kawakami H (2005) Preparation of novel sulfonated block copolyimides for proton conductivity membranes. *Polym Adv Technol* 16:753–757
70. Iizuka Y, Tanaka M, Kawakami H (2013) Preparation and proton conductivity of phosphoric acid-doped blend membranes composed of sulfonated block copolyimides and polybenzimidazole. *Polym Int* 62:703–708
71. Einsla ML, Kim YS, Hawley M et al (2008) Toward improved conductivity of sulfonated aromatic proton exchange membranes at low relative humidity. *Chem Mater* 20:5636–5642
72. Atanasov V, Kerres J (2011) Highly phosphonated polypentafluorostyrene. *Macromolecules* 44:6416–6423
73. Atanasov V, Gudat D, Ruffmann B et al (2013) Highly phosphonated polypentafluoro-styrene: characterization and blends with polybenzimidazole. *Eur Polym J* 49:3977–3985
74. Berber MR, Fujigaya T, Sasaki K et al (2011) Remarkably durable high temperature polymer electrolyte fuel cell based on poly(vinylphosphonic acid)-doped polybenzimidazole. *Sci Rep* 3:1–7
75. Matsumoto K, Fujigaya T, Yanagi H et al (2011) Very high performance alkali anion-exchange membrane fuel cells. *Adv Funct Mater* 21:1089–1094
76. Galbiati S, Baricci A, Casalegno A et al (2013) Degradation in phosphoric acid doped polymer fuel cells: a 6000 h parametric investigation. *Int J Hydrogen Energy* 38:6469–6480
77. Papadimitriou KD, Geormezi M, Neophytides SG et al (2013) Covalent cross-linking in phosphoric acid of pyridine based aromatic polyethers bearing side double bonds for use in high temperature polymer electrolyte membrane fuel cells. *J Membr Sci* 433:1–9
78. Kerres J, Zhang W, Häring T (2004) Covalently cross-linked ionomer (blend) membranes for fuel cells. *J New Mater Electrochem Syst* 7:299–309
79. Yang JS, Cleemann LN, Steenberg T et al (2014) High molecular weight polybenzimidazole membranes for high temperature PEMFC. *Fuel Cells* 14:7–15

Joannis K. Kallitsis, Aikaterini K. Andreopoulou,
Maria Daletou, and Stylianos Neophytides

5.1 Introduction

A lot of scientific effort has been devoted to the design and development of the different components (catalysts, membranes) of the polymer electrolyte membrane (PEM) fuel cells (FC) s resulting in a real explosion of field electricity production from hydrogen. This combined with the drastic increase of the natural gas reserves and availability, open new ways of consideration for the decentralized electricity production. One of the main ideas is the use of natural gas for hydrogen production that will be subsequently used as feed for devices that can effectively and with high yield produce energy. In this case the high temperature operation of the PEM FCs can offer a unique solution since even hydrogen containing impurities can be used. The electricity and thermal energy cogeneration is one case where the total energy efficiency can be increased up to 80–90 %. Another option is the operation at temperatures

above 200 °C, so that the high temperature MEA is combined with a methanol reformer, thus enabling the use of liquid fuels like methanol. A further outcome of the high temperature operation is the use of such membranes and membrane electrode assemblies (MEAs) as electrochemical membrane reactors for the hydrogen purification instead of the palladium membranes used up to now. Based on the above considerations, from our perspective it was crucial to substantially increase the operation temperature for HT PEM FCs well above 200 °C. In the following chapter, we describe in detail our efforts and final outcome for the 1000 h stable operation of HT-PEMFCs at temperatures up to 210 °C.

5.2 Synthesis of Linear Aromatic Polyethers Containing Main Chain Pyridine Units

The idea to combine basic polymeric backbones with strong acids resulting in ionic conductive composites has been successfully demonstrated by the Savinell group back in 1995 [1]. This revolutionary approach combined the good mechanical properties of a rigid polymeric backbone with the acid absorption through the interaction with the basic backbone units creating clusters of acid molecules, thus enabling the proton transport. A number of studies were devoted to the understanding of the conduction process [2]. Despite the fact

J.K. Kallitsis (✉) • A.K. Andreopoulou
Department of Chemistry, University of Patras,
Rio-Patras 26504, Greece

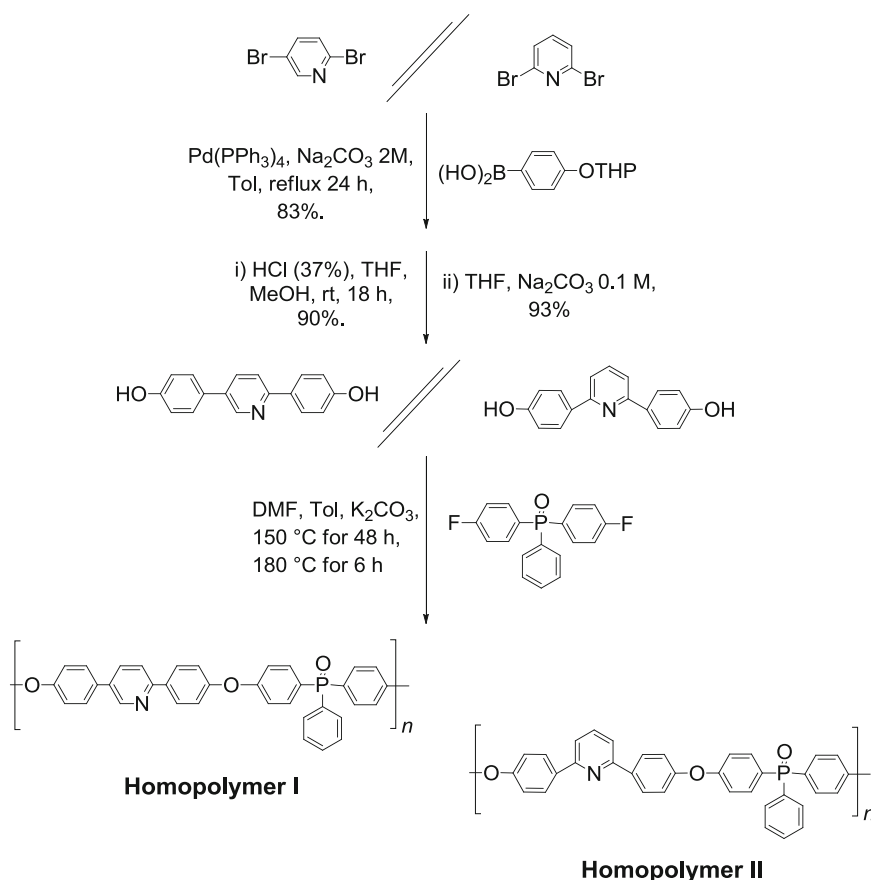
Foundation for Research and Technology Hellas/Institute
of Chemical Engineering Sciences (FORTH/ICE-HT),
Patras 26504, Greece
e-mail: j.kallitsis@upatras.gr

M. Daletou • S. Neophytides
Foundation for Research and Technology Hellas/Institute
of Chemical Engineering Sciences (FORTH/ICE-HT),
Patras 26504, Greece

that this idea was demonstrated for quite a long time, the initial polymer polybenzimidazole (PBI) remained for long time as the only solution. Later on, relative structures like the poly (2,5-benzimidazole) AB-PBI were also used doped with phosphoric acid [3–5] and most recently structures combining the imidazole units with pyridine ones were also developed [6].

The idea to use the pyridine units as basic moieties in a rigid aromatic polymer was firstly demonstrated by our group in 2003 [7]. In this first approach, despite the use of the pyridine main chain units, phenyl phosphinoyl moieties were also included in the polymer structure both to improve solubility and to create more interaction sites with the phosphoric acid doping agent. New monomers were prepared using

palladium-mediated cross coupling of 2,5- or 2,6-dibromopyridine with a properly protected boronic acid [8]. Scheme 5.1 presents the reaction employed for the preparation of the respective diols. 2,5-Dibromopyridine and 2,6-dibromopyridine were reacted via Suzuki coupling with the tetrahydropyranyloxy THP protected hydroxyphenylboronic acid producing the corresponding THP-end protected monomers in gram-scale quantities. The removal of the THP moieties was performed under acidic conditions. High-temperature polymerization of the synthesized diols with phosphinoyl difluoride was employed for various reaction times. **Homopolymers I** and **II** showed solubility in common organic solvents such as CHCl_3 , allowing for their detailed characterization.



Scheme 5.1 Reaction sequences employed for the preparation of 2,5-bis(4-hydroxyphenyl)pyridine and 2,6-bis(4-hydroxyphenyl)pyridine and their polymerization with

bis(4-fluorophenyl)phenylphosphine oxide producing **Homopolymers I** and **II**, respectively. Reproduced from [7] with permission of the American Chemical Society

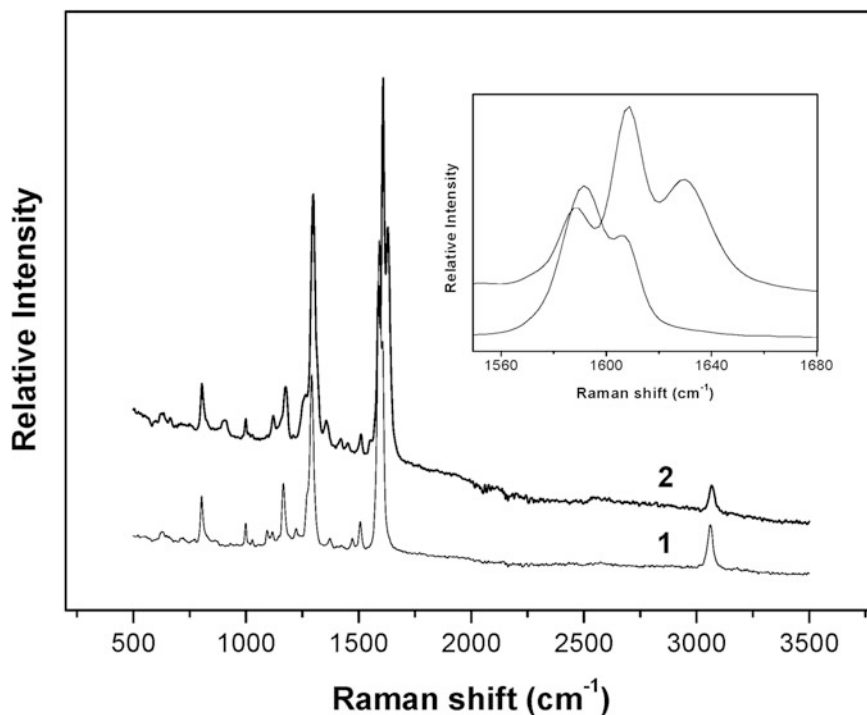


Fig. 5.1 FT-Raman spectra of **Homopolymer I** before (1) and after (2) doping with H_3PO_4 85 %. *Inset*: 1550–1680 cm^{-1} region. Reproduced from [7] with permission of the American Chemical Society

Materials with excellent film-forming properties were obtained. Structural characterization confirmed the expected structure and their physicochemical characterization showed high mechanical and thermal stability. The protonation of the membrane after its exposure to a strong acid could affect its thermal stability, so the thermogravimetric results before and after treatment with H_3PO_4 for 1000 h showed that the membrane is hydrolytically stable. During this study the interaction of the pyridine units with phosphoric acid was demonstrated using Raman by the shift of the peak at 1600 cm^{-1} of the pyridine to 1630 cm^{-1} after protonation, which is attributed to the C=N vibration of the protonated ring (Fig. 5.1). Also the phosphoric acid uptake of these polymers was very high providing the necessary conditions for high ionic conductivity.

However these homopolymers faced two main problems. Limitations in obtaining high molecular weights since insoluble materials were produced when the number average molecular weight (Mn) exceeded 50,000 and extensive

plasticization from phosphoric acid of the low Mn materials. Indeed, a systematic investigation [9] showed that homopolymers containing the 2,5-bis(4-hydroxyphenyl) pyridine, which was the key monomer combining the presence of the pyridine units in the main chain and having the polymerizable phenols in *para* position to avoid sterical hindrance, faced solubility limitations. In order to understand the nature of this insolubility a kinetic study of the polymerization (Fig. 5.2) was performed, which showed that as soon as a critical molecular weight value is reached, the polymer becomes partially soluble and finally insoluble.

In order to overcome this problem two routes were chosen. The first was to incorporate solubilizing side chain substituents along the polymeric main chain. The second was to use small amounts of other comonomers that would enhance solubility. The target of both routes was to achieve higher molecular weights while increasing the solubility of the final homopolymers or copolymers [9–13]. In the same line, extension of the rigid part by

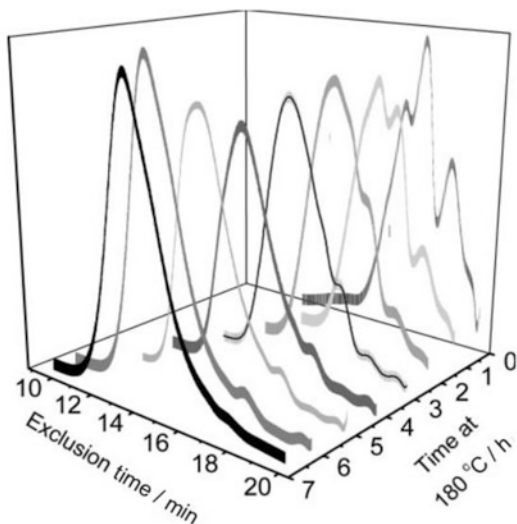
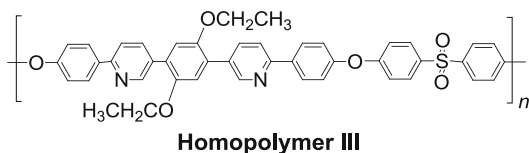


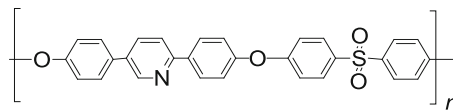
Fig. 5.2 Kinetic study of **Homopolymer's I** polymerization reaction via gel permeation chromatography (GPC). Reproduced from [9] with permission of Wiley-VCH Verlag GmbH & Co. KGaA

introducing two pyridine units per repeating unit combined with the introduction of aliphatic side substituents to improve solubility was also tested, see **Homopolymer III** [9].



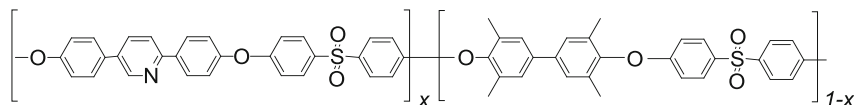
As was expected the homopolymer composed from the 2,5-bis(4-hydroxyphenyl) pyridine and

bisphenylsulfone (**Homopolymer IV**) was completely insoluble in all practical solvents.

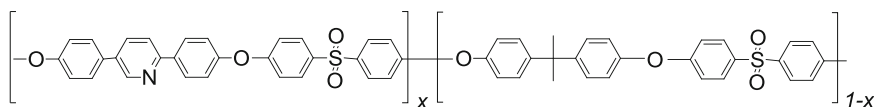


Homopolymer IV

A homopolymer with high basic unit content was desirable in order to create as many interaction sites with the phosphoric acid as possible, which led us to the design of the above-described homopolymers. However the encountered problems of solubility and plasticization softening of the doped membranes forced us to seek alternative structures and thus we designed copolymers that incorporated additional hydrophobic units in order to increase solubility. For that reason, a number of comonomers like the tetramethyl bisphenol [10] and the bisphenol A [13] were explored. These copolymers bearing pyridine units combined with diols having methyl substituents, like tetramethyl bisphenol (**Copolymer I**) and bisphenol A (**Copolymer II**), became a real breakthrough. From the numerous different copolymers synthesized and examined, those that combine the 2,5-bis(4-hydroxyphenyl) pyridine and the 3,3',5,5'-tetramethyl-[1,1'-biphenyl]-4,4'-diol (**Copolymer I**) were easily soluble, even for higher pyridine diol contents, while at the same time preserving their mechanical properties and thermal and oxidative stability.



Copolymer I



Copolymer II

In particular, for the **Copolymer I** with 60 mol% of the 2,5-biphenyl-pyridine diol in the main chain average molecular weights (MW)s up to 70,000 were obtained, while when 70 mol% of the same diol was employed MWs above 60,000 were achieved [10].

Almost all synthesized copolymers were soluble in common organic solvents regardless of their MW and showed excellent film-forming properties and high glass transition temperatures (T_g) up to 290 °C. Especially these high T_g values in all cases fulfill a major prerequisite for high-temperature PEMFC applications. Among the different compositions examined, the copolymer with 60 mol% pyridine units was selected as key copolymer for optimization of its preparation conditions that finally resulted in even higher molecular weights. This easily processable copolymer exhibits excellent film-forming properties, high glass transition temperature up to 280 °C, thermal stability up to 400 °C, and high oxidative stability.

The question of how critical is the oxidative stability of the materials used as membranes in fuel cells has been contradictory for long time. As it is known, PBI and PBI-related materials show a moderate stability in Fenton test conditions [14] while especially the doped PBI membranes lose their integrity within the Fenton test solution even after a few hours [15].

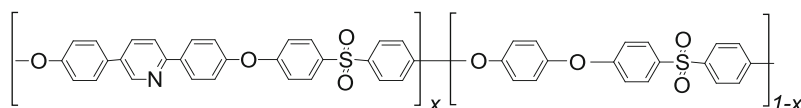
Fenton's test is a frequently used accelerated test for the oxidative stability of polymeric membranes [14]. According to this test, the membranes are exposed to a strong oxidative environment. More specifically, polymeric films are treated with 3 wt% H₂O₂ in the presence of ferrous ions at 80 °C for 72 h. Hydroxyl and hydroperoxyl radicals are created which lead either to chain scission or to ring opening of the benzene rings. In respect to the oxidative stability of the herein studied linear aromatic polyethers, all polymers were treated according to the Fenton's test conditions and remain intact after the treatment. This is proved by comparing the mechanical and thermal properties of the

membranes before and after the treatment [16]. Also, blends of PBI with these aromatic polyethers resist Fenton's test [13], while PBI and its blends with sulfonated aromatic polysulfones did not withstand such a treatment [17]. The resistance to Fenton's test treatment could be due to the hydrophobicity of these aromatic polyethers, thus preventing the penetration of hydroxyl radicals, which can oxidize and disintegrate the polymeric membranes. To exclude this possibility hydrophilic blends of the linear **Copolymer I** [16] with a water-soluble polymer were tested. Depending on the blend composition, the water-soluble polymer was removed during the treatment of these blends with the Fenton's reagent and still the polymeric films maintained their mechanical integrity. The molecular characteristics of the polymers before and after the Fenton's test were determined by means of gel permeation chromatography (GPC) where the molecular weight distribution remained unchanged, thus proving the chemical stability of the polymeric films. Additionally, the spectroscopic characteristics of the treated polymers by means of Fourier transform infrared (FTIR) and nuclear magnetic resonance (NMR) were unaltered. Due to their high pyridine content, these copolymers can be doped with strong acids like the phosphoric acid, at doping levels up to 300 wt% depending on the copolymers' composition. Since conductivity is strongly dependent on doping level and temperature, for these copolymers conductivity values in the range of 10⁻² S cm⁻¹ were obtained at temperatures higher than 130 °C.

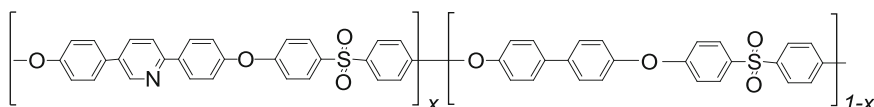
As mentioned before, another approach to improve solubility is the use of different non-substituted monomers that are randomly co-polymerized. Thus, non-substituted aromatic copolyethers containing main chain pyridine units were also synthesized by copolymerization of aromatic diphenols [11] and more particularly 2,5-bis(4-hydroxyphenyl) pyridine and 4,4'-biphenol or hydroquinone, **Copolymer III** and **IV**, respectively. Using the previously

developed methodology it was possible to synthesize such fully aromatic polyethers with high molecular weights, in some cases exceeding 100,000 (M_n value), but still keeping their solubility. Flexible and high quality membrane films were prepared that presented high glass transition temperatures (T_g s) and high decomposition temperatures (T_d s). The oxidative stability of the membranes was examined with Fenton's test and also in this case the membranes remained intact after the treatment. The doping ability and the proton conductivity of the membranes were also studied and the

unsubstituted fully aromatic copolymers were indeed found potential polymeric electrolyte candidates for proton exchange membrane fuel cells. It should be emphasized that for this class of unsubstituted copolyethers the high doping values reached were realized without disturbing the para-aromatic character of the main polymeric backbones. By using the copolymerization approach we incorporated diols of different rigidity in order to disturb the structure regularity and subsequently the extent of the intermolecular interactions that are mainly responsible for insolubility problems [11].



Copolymer III



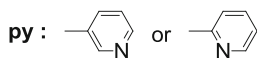
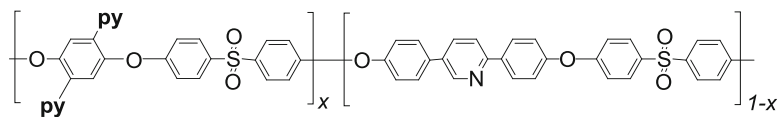
Copolymer IV

Overall, by using different approaches for the combination of the desirable properties a new family of linear aromatic polyethers able to be used as membranes for HT PEMFCs was successfully developed.

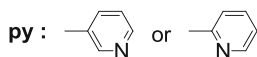
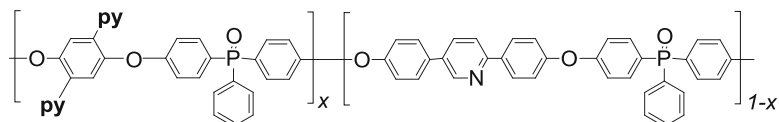
5.3 Side Group Functionalized Linear Aromatic Polyethers Containing Main Chain Pyridine Units

Side functionalities were used both as solubilizing groups and to impart specific functions based on the same polymeric backbone that was examined previously. As a first

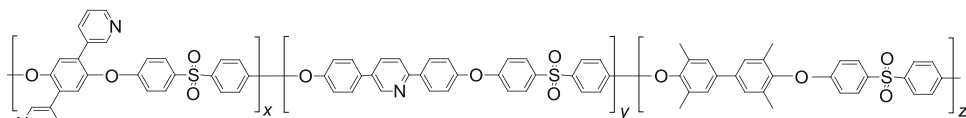
example on this category, side pyridine units were used in homopolymers and copolymers [18]. However limitations in molecular weight were encountered especially in the case of homopolymers and thus copolymers with the 2,5-bis(4-hydroxyphenyl) pyridine diol and the 1,4-dihydroxy-2,5-di(3-or 4-pyridine)benzene diols were synthesized (**Copolymers V–IX**). The doping ability of these copolymers was greatly enhanced as the side pyridine diol content increased, reaching very high phosphoric acid uptakes but at the same time plasticization of the doped membranes was observed making their use in membrane electrode assemblies (MEAs) preparation and testing impossible [18].



Copolymer V or VI



Copolymer VII or VIII

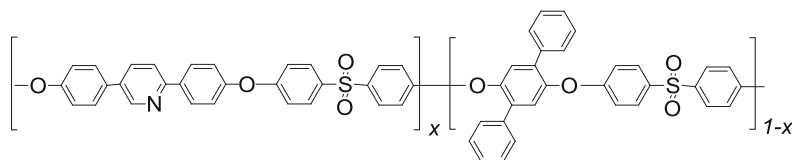
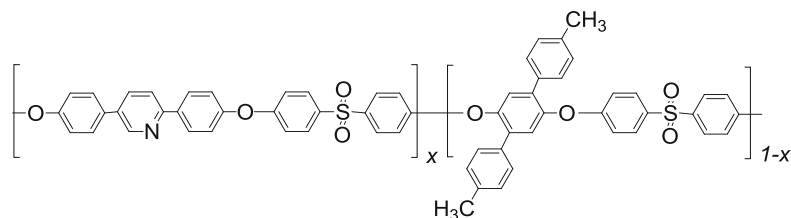


Copolymer IX

Taking into consideration all the positive and negative effects of the introduction of side pyridine units, a new generation of membranes was designed and synthesized incorporating the following monomers, the 2,5-bis(4-hydroxyphenyl)pyridine, a side pyridine diol, and as a third comonomer the tetramethylene bisphenol at selected and optimized ratios that provided the hydrophobic character which was necessary for the stabilization of the highly doped membranes (**Copolymer IX**) [19]. The success of this approach initiated a systematic exploration of the effect of the different functional groups on the membrane properties in terms of phosphoric acid doping ability and their influence on con-

ductivity, doped membrane stability, and possible further reactivity.

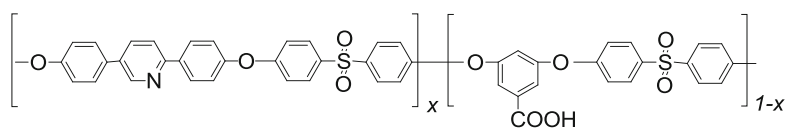
In a subsequent approach bulky but not interacting with the H_3PO_4 substituents were chosen for the preparation of polymer electrolytes keeping the well-established pyridine-based aromatic polyether sulfone backbone [20]. In particular, phenyl and tolyl side moieties were introduced, **Copolymer X** and **XI**, respectively, since their size is expected to increase the free volume among neighboring polymeric chains in the bulk leading to an enhancement of the copolymers' doping ability without the plasticization phenomena of the previously pyridine-substituted copolymers.

**Copolymer X****Copolymer XI**

Both **Copolymers X** and **XI** were soluble in common organic solvents and as a result, they were characterized by means of ^1H NMR and via GPC. Excellent film-forming properties were observed only for the tolyl functionalized copolymers owing to their high MWs rising up to 45,000 (Mn). Membranes of $\sim 100\ \mu\text{m}$ having different pyridine content were examined for their doping in H_3PO_4 85 %. The acquired doping level (DL) increased with the polar pyridine content. This fact points out that with the side tolyl groups it was possible to obtain fully soluble and processable polyether materials of

very high pyridine content and thus increased DL levels without plasticization of the doped membranes. The mechanical properties, T_g s up to $240\ ^\circ\text{C}$, and thermal stability, T_d s up to $450\ ^\circ\text{C}$, of these materials were not altered before and after Fenton's test.

Perhaps an even more interesting class of copolymers studied was that with carboxyl bearing moieties, **Copolymer XII** that was synthesized using an unprotected carboxylic acid containing monomer. High molecular weight copolymers with carboxyl group content up to 50 mol% were synthesized and characterized [20].

**Copolymer XII**

High DLs up to 450 wt% were obtained depending on the pyridine content of the polymers. Moreover, the presence of the carboxylic acid side groups did not decrease the doping ability of these copolymers. On the contrary the presence of the carboxylic acid functionalities led to higher DLs compared to the benchmark **Copolymer I**. High T_g and storage modulus E' values were obtained for most of the **Copolymers XII** but most importantly exposure

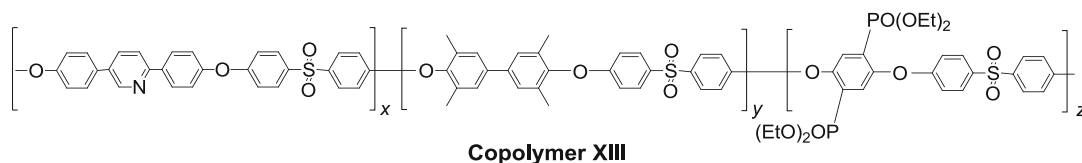
for as long as 3 weeks in Fenton's test oxidizing environment did not deteriorate the membranes even though the carboxylic acid side groups forced the solubility of these copolymers towards more polar solvents like dimethylsulfoxide.

Although these carboxylic acid copolymers are potential candidates for HT-PEMFCs, their most prominent feature was their use for further chemical cross-linking of the carboxylic acid side groups using different cross-linkers creating

stable 1,3,4-oxadiazole linkages as will be described later.

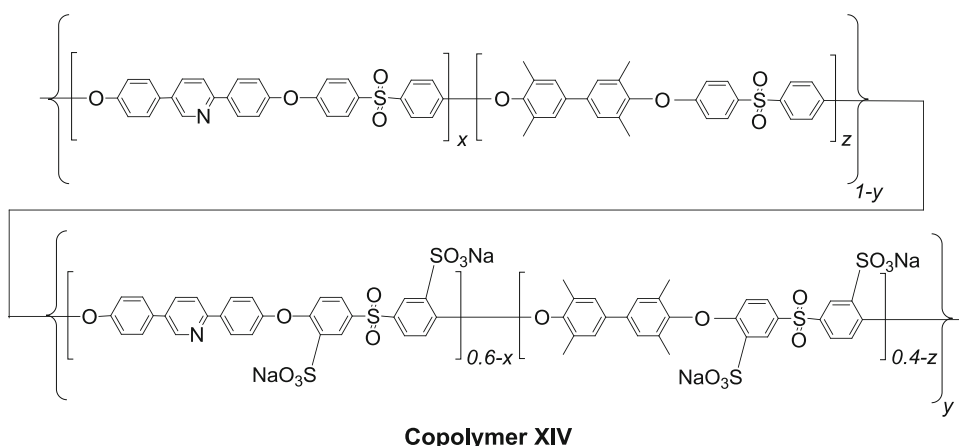
Phosphonate ester or phosphonic acid substituents have been additionally evaluated in an attempt to increase the interacting sites with the phosphoric acid doping agent along the poly-electrolyte macromolecular chains. These were strategically located as side groups in a diol monomer which was prepared by a phosphorus-carbon coupling reaction of tetrahydropyranyloxy diprotected 2,5-dibromo-1,4-dihydroxy benzene with diethylphosphite. Either in the phosphonate ester or in the phosphonic acid form the diol was used in polymerizations with the bis(4-fluorophenyl) sulfone or bis(4-fluorophenyl) phenylphosphin oxide as well as with the 2,5-diphenyl-pyridine diol and the tetramethyl-

biphenyl diol in copolymers and terpolymers, respectively [21]. However, these synthetic efforts resulted in homo and copolymers of high thermal stability but moderate molecular weights. Only the terpolymers (**Copolymer XIII**) could be obtained in higher molecular weights. These phosphonated polyethers were used also for the preparation of blends with the extensively studied **Copolymer I**. For the copolymers and terpolymers it was shown that the combination of the phosphonic acidic groups with the basic pyridine comonomers resulted in polymers with increased thermal stability. Furthermore, it was shown that the incorporation of high percentages of phosphonic acid groups reduces the doping ability of the final blend due to possible interactions of the acidic units with the pyridines.



A series of aromatic polyethersulfones bearing pyridine main chain groups and side sulfonic acid groups were reported (**Copolymer XIV**) [22]. The driving force was to combine the

thermal and chemically stable macromolecular backbones with the phosphoric acid interacting pyridines and the water interacting sulfonic acid moieties.



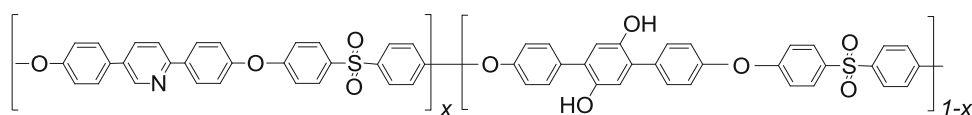
All copolymers with sulfonation degree (SD) = 0–80 % showed excellent film-forming properties and the dynamic mechanical analysis

(DMA) gave T_g values that increased with the sulfonation degree, up to 350 °C in the sodium salt form, which increased even further reaching

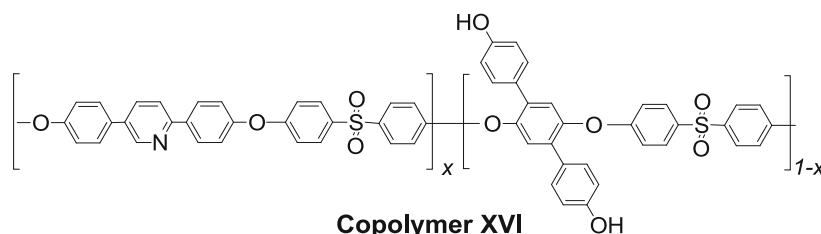
370 °C in the acidic form. The oxidative stability of the copolymers was higher than relevant aromatic sulfones like sulfonated poly(arylene ether sulfone). The water uptake of the sulfonated copolymers was about 30 wt% at 80 °C. On the other hand, the introduction of sulfonate groups onto the main chain decreased the ability of absorbing phosphoric acid due to interactions of the acidic groups with the basic pyridine moieties.

In an additional effort side hydroxyl groups have been incorporated onto the well-established aromatic polyether sulfone backbones bearing

the polar pyridine units in the main chain (**Copolymers XV** and **XVI**). The side chain hydroxyl moieties were further transformed to propargyl moieties. Both cases aimed mainly at preparing chemically cross-linkable linear polymers either through thermal treatment or through etherification with polyfluorine bearing aromatic cross-linkers [23]. Initially dimethoxy diol monomers were designed, which after the high temperature polycondensation with the respective comonomers were deprotected to the hydroxy-based analogs by ether cleavage with boron tribromide.



Copolymer XV



Copolymer XVI

In another attempt double bond side functionalities were introduced onto pyridine-based aromatic poly(ether sulfone)s. The ultimate scope of this approach was the cross-linking of the active double bonds after polymerization and after the preparation of the desired polyelectrolyte membranes in order to mechanically and thermally stabilize the doped membranes, as will be described below in greater detail.

The initial concerns for the viability of the double bonds during the high temperature condensation polymerization were overcome both for allyl (**Copolymers XVII–XX**) [24, 25] and styryl (**Copolymers XXI**) [26] side group containing copolymers. In all these cases special attention was paid to the optimization of the polymerization conditions in order to keep the double bonds intact. Combined FTIR and NMR characterizations were employed and the

copolymers content in double bonds was checked after the different polymerization processes.

In particular, for the allyl containing monomer a high temperature isomerization-rearrangement of the allyl groups of 2,2'-diallyl bisphenol A into propenyl groups was observed during the polymerization reaction. Of course the propenyl moieties retain their reactivity as double bonds, which is the major requirement for their further cross-linking. The observed rearrangement was attributed to the fact that the potassium carbonate acts as a catalyst of isomerisation of allyl groups to propenyl groups. As shown in the below NMR spectra (Fig. 5.3), the double bond protons of the propenyl groups appear at 6.2 and 6.5 ppm. The percentage of the double bonds in the polymeric chain was calculated from the integration ratio of the peak of the aromatic proton neighboring the nitrogen in the pyridine ring and the peaks of the propenyl groups.

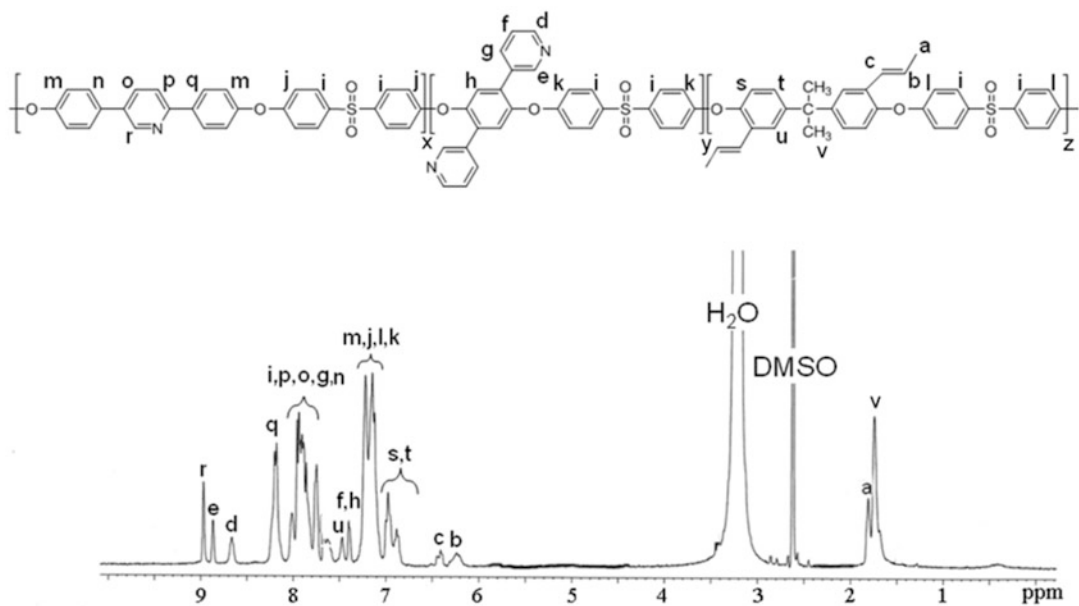
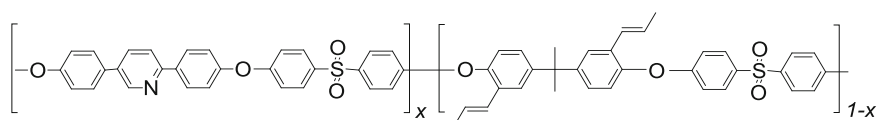
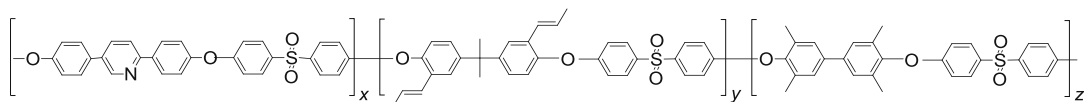


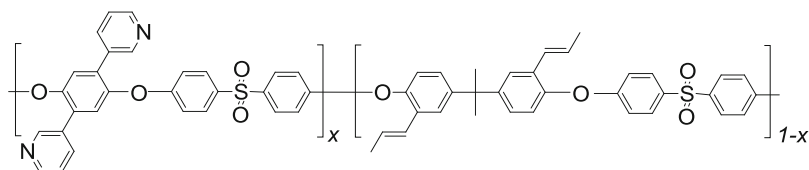
Fig. 5.3 ^1H NMR spectrum of the propenyl functionalized cross-linkable **Copolymer XX**. Reproduced from [25] with permission of Elsevier



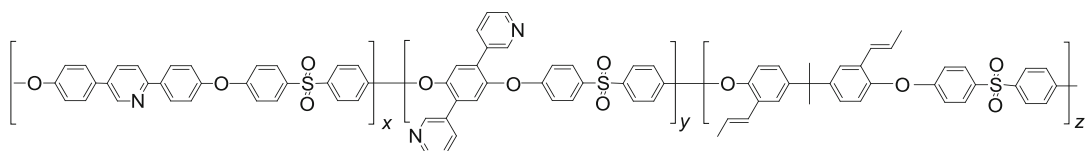
Copolymer XVII



Copolymer XVIII



Copolymer XIX



Copolymer XX

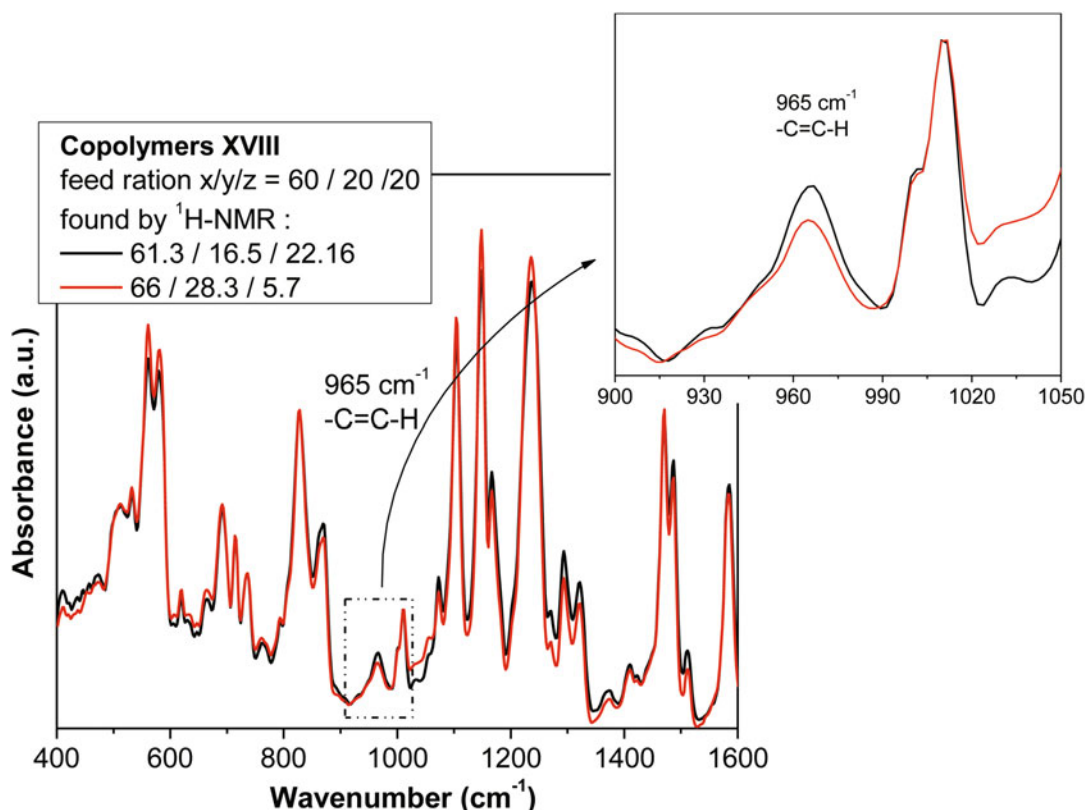


Fig. 5.4 ATIR spectra of **Copolymers XVIII** with identical initial monomers' feed ratio ($x/y/z = 60/20/20$) but with different polymerization

reaction conditions resulting in different calculated ratios of the final materials, *Inset*: enlargement of the area 900–1050 cm^{-1}

As already mentioned great care was devoted to the optimization of the polymerization conditions not only in terms of maintaining the side double bonds after the course of the reaction but also in achieving the desired double bond content. A representative example is shown below where **Copolymers XVIII** with the same monomers feed ratio show different double bond content depending on the preparation conditions. Besides the ^1H NMR characterization of such double bond functionalized materials their FTIR characterization was proven even more valuable for the calculation of the double bond percentage in the final polymeric materials (Fig. 5.4) based on the characteristic and well-resolved peak at

965 cm^{-1} . Since all the resulting polymers were soluble in polar organic solvents, their characterization using GPC took place proving their high molecular weights in all cases.

Fenton test treatment was also performed in these materials in order to evaluate whether the membranes are able to withstand a strong oxidizing environment during the fuel cell operation. The oxidative stability of these copolymers after treatment with the Fenton reagent was examined with dynamic mechanical analysis and thermogravimetric analysis where no significant changes occurred after treatment with hydrogen peroxide neither to the membrane's integrity nor to its mechanical properties

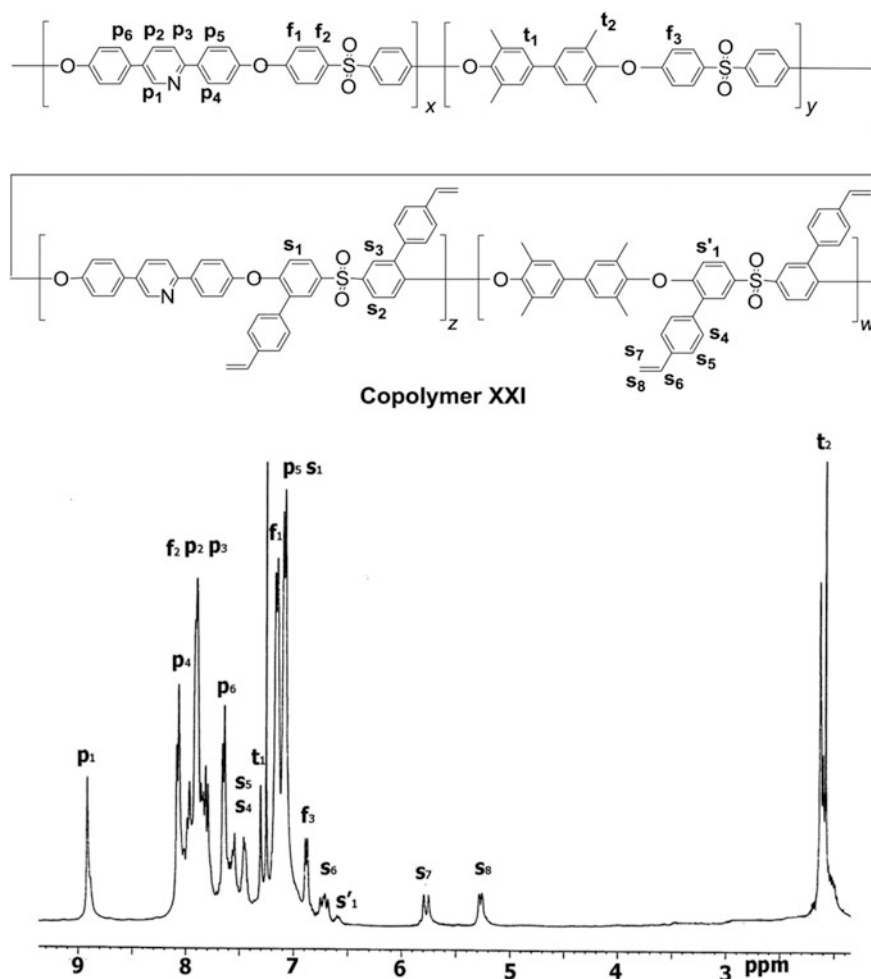


Fig. 5.5 Copolymers XXI with cross-linkable side styrene functionalities and an ^1H NMR spectrum the copolymer with $x + z = 80$, $z + w = 20$, in CDCl_3 with peak assignment. Reproduced from [26] with permission of Elsevier

compared to the polymer before such a treatment. Moreover, the thermal stability of the treated membrane shows a further improvement, probably due to the cross-linking reactions that can happen during the Fenton test treatment.

For the styrene side functionalized **Copolymers XXI** the general structure of the resulted copolymers is given in Fig. 5.5 together with a representative ^1H NMR spectrum at which the protons of the “living” side double bond are observed at 5.3, 5.8, and 6.7 ppm [26]. Copolymers with several percentages of the pyridine diol as well as the difluoride monomer bearing the side

double bond functionalities were obtained. These copolymers were easily soluble in common organic solvents in all compositions synthesized and thus besides their characterization by means of ^1H NMR for the confirmation of the proposed structure and the copolymer composition, their molecular characteristics were evaluated by GPC giving molecular weights between 10,000 and 20,000. The mol percentage of the vinylbenzene groups was close to the theoretically expected as calculated from the ^1H NMR spectra using the integration of the peaks attributed to the protons of the vinyl groups and of the peak of the proton

next to the nitrogen in the pyridine unit. As proven by ^1H NMR, the double bonds remain intact under the polymerization conditions and can be used for further reaction as will be explained in the below section.

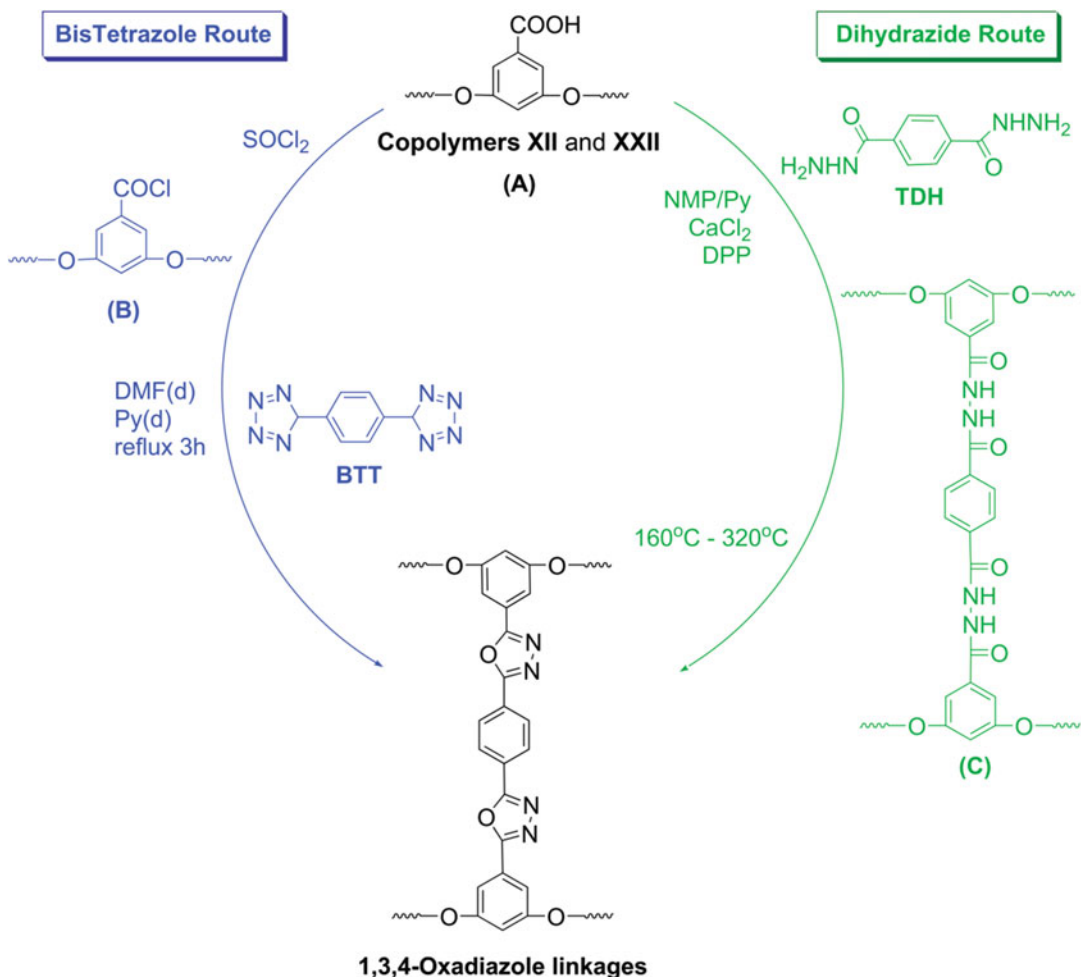
5.4 Cross-Linked Aromatic Polyethers Bearing Pyridine Main Chain Units

A crucial problem of all the polymer electrolytes is the deficient long-term durability of these systems at temperatures as high as 200 °C. The challenge to find materials that show even greater mechanical stability with adequate ionic conductivities was the driving force for extensive research efforts. An effective approach to overcome this problem is the covalent cross-linking. Via the cross-linking route a large, stable network of anchored polymeric chains is achieved, which stabilizes the membrane and improves its mechanical properties. So the possibility to create cross-linked polymers able to be used as membranes at higher operating temperatures was explored by our group. In the course of these efforts to prepare chemically cross-linked high temperature polymer electrolytes, different chemistries having as baseline the chemical and thermal stability of the fragments have been explored. The different side functionalities used for cross-linking of the membranes were side double bonds and side carboxyl groups, as an attempt to create stable cross-linking bonds for even more robust and stable proton conducting polymeric electrolytes that can be used as the core parts of membrane electrode assemblies (MEAs) for HT-PEMFCs.

As a first approach, copolymers and terpolymers combining main chain pyridine units, cross-linkable carboxylic acid side groups, and/or hydrophobic methyl groups were cross-linked [27]. The carboxylic acid groups can lead to thermally and chemically stable bond formation, as, for example, the creation of imidazole or oxadiazole rings. Thus, in our approach we

explored and optimized different methods for cross-linking the carboxyl bearing polymers creating oxadiazole cross-linking groups providing new membranes that were tested in single cells operating at temperatures higher than 200 °C. Initially, **Copolymers XII** of high molecular weights with side carboxylic acid groups, having good film-forming properties and mechanical integrity, were employed as precursors for cross-linking. The formation of 2,5-substituted-1,3,4-oxadiazole bridging linkages was chosen due to their high thermal and chemical stability. Two different routes were used for the covalent cross-linking (Scheme 5.2), the phosphorylation or Higashi process [28, 29] where terephthalic dihydrazide (TDH) was the cross-linking agent and the Huisgen procedure [30, 31] where carboxylic acid chlorides reacted with phenyl bis-tetrazole (BTT). In both methods, the amount of the cross-linking agent was stoichiometric and calculated based on all active carboxylic sites along the polymeric chain.

In the first case, a two-step procedure was followed in order to obtain the final cross-linked oxadiazole containing membranes, where the second step was the cyclodehydration of the intermediate to the final 1,3,4-oxadiazole bridged polymer that was accomplished by heating the membrane under vacuum for several hours at temperatures from 160 °C and up to 320 °C. In the second case, according to the Huisgen method the oxadiazole group was synthesized through the initial nucleophilic substitution of an acylating agent to the nitrogen of the tetrazole moiety. The acylating agent attacks the tetrazole ring resulting in a ring opening at 2,3-position and a recyclization process is followed through the acyl oxygen with simultaneous loss of a neutral nitrogen molecule. A similar procedure was followed in this work for cross-linking the carboxylic acid bearing polymers. Specifically, carboxylic acid groups of the polymeric chains were modified through SOCl_2 to carboxylic acid chlorides. The latter played the role of the acylating agent of the BTT cross-linker, forming the final oxadiazole cross-linked polymer. The



Scheme 5.2 Cross-linking methodologies applied to carboxylic acid bearing aromatic polyethersulfones (**Copolymer XII** and **XXII**) using terephthalic

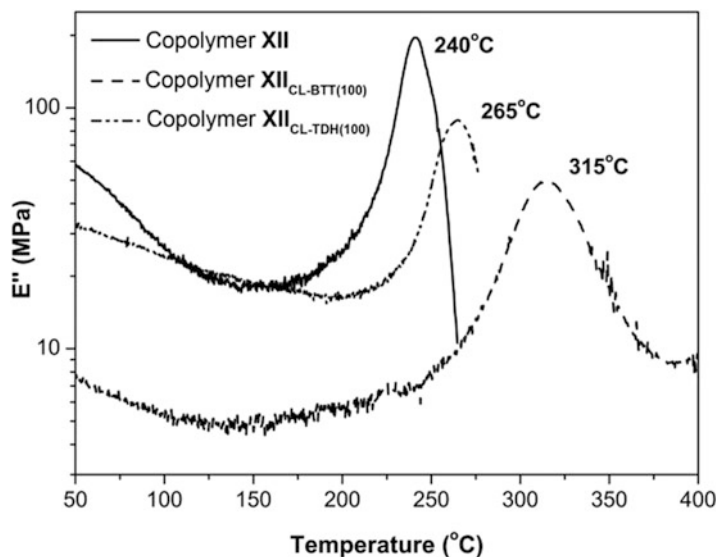
dihydrazide (TDH) or bistetrazole (BTT) as the cross-linking agents. Reproduced from [27] with permission of the Royal Society of Chemistry

two methods are schematically shown in Scheme 5.2 and both methodologies were optimized using as criterion the cross-linked membrane's solubility in organic solvents and also the cross-linked membrane's quality and integrity.

Using the optimized conditions cross-linked membranes with significantly increased glass transition temperatures T_g were obtained for both methodologies as shown in Fig. 5.6. Differences between the two cross-linking methodologies can be observed from the DMA results of the membranes before and after cross-

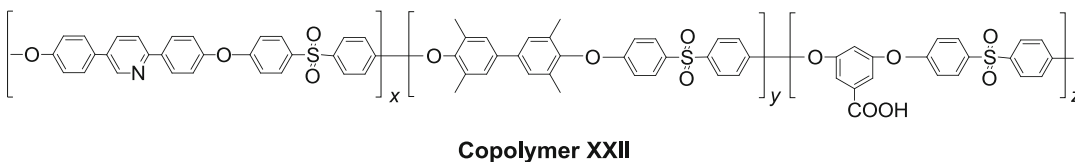
linking. As can be seen in Fig. 5.6, the cross-linked membrane through the dihydrazide route (**Copolymer XII_{CL-TDH}**) has a glass transition temperature increased by 25 °C compared to that of the initial copolymer, whereas the cross-linked membrane through the bistetrazole route (**Copolymer XII_{CL-BTT}**) showed an even higher increase of 75 °C. Based on these results and also on a detailed analysis of the thermal stability and solubility of the cross-linked copolymeric membranes, the superiority of the cross-linking methodology through the bistetrazole (BTT) route was proved. Thus, this particular route

Fig. 5.6 Comparison of the temperature dependence of the loss (E'') modulus for the linear **Copolymer XII** and of the cross-linked copolymers **Copolymer XII_{CL-TDH(100)}** and **Copolymer XII_{CL-BTT(100)}**. Reproduced from [27] with permission of the Royal Society of Chemistry



was chosen and further optimized for the cross-linking of the respective terpolymers that

additionally incorporated the tetramethylbiphenyl diol (**Copolymer XXII**).

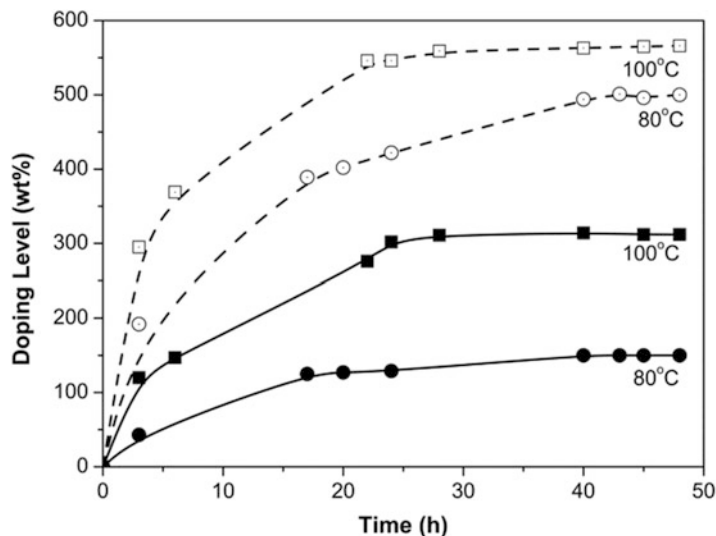


The doping ability of the cross-linked membranes was also evaluated. Figure 5.7 presents an example of the cross-linked terpolymer through the bistetrazole route (**Copolymer XXII_{CL=BTT}**) with 100 % cross-linking degree impregnated in H_3PO_4 85 % at 80 °C and at 100 °C compared to the linear precursor **Copolymer XXII**. In general the cross-linking leads to a more compact chemical structure and as a result the doping ability of cross-linked membranes is expected to decrease. However, there have been some distinct cases at which the doping ability of the cross-linked materials was superior to the initial membranes usually attributed to the introduced functionalities which also interact with the phosphoric acid. Also in herein cross-linking through oxadiazole formation case, the doping ability of the cross-

linked polymers was enhanced compared to their linear analogues since the formed oxadiazole rings can also interact with phosphoric acid contributing, thus, to the overall acid uptake of the final cross-linked membrane [32]. This fact strongly denotes the role of the chemical structure and the resulting morphology on the materials' properties.

The second general approach for the covalent cross-linking was the use of side double bond functionalized copolymers [24]. In this case the synthesis of aromatic polyethers containing polar pyridine units in the main chain and side cross-linkable propenyl groups was the key step. These polymers were subjected to thermal cross-linking with the use of a cross-linker. The effect of the cross-linking on the thermal and mechanical

Fig. 5.7 Time dependence of the doping level of the linear **Copolymer XXII** (filled symbols) and its 100 % cross-linked counterpart **Copolymer XXII_{CL=BTT}** (open symbols) at 100 °C and 80 °C, respectively. Reproduced from [27] with permission of the Royal Society of Chemistry



properties and on the phosphoric acid doping ability of the membranes was studied.

In particular, a detailed study of the cross-linking procedure was performed in order to optimize the cross-linking conditions. During the thermal treatment the bisazide used as cross-linker loses one nitrogen and thus a reactive nitrene is formed. This intermediate product is added to the propenyl groups producing aziridines and amines. The cross-linked structure was confirmed by comparing the FTIR spectra of the pristine and the cross-linked polymers and a characteristic example is given in Fig. 5.8 for the **Copolymer XVII**. The absorption peak at 965 cm^{-1} assigned to the $\text{C}=\text{C}$ double bonds decreased after the cross-linking procedure while a new broad band at 3374 cm^{-1} appeared in the cross-linked polymer which is attributed to the $\text{N}-\text{H}$ stretch vibration of the secondary amines. All the membranes which were successfully cross-linked were almost insoluble in all organic solvents.

The effect of the cross-linking on the mechanical properties of the membranes was examined with DMA measurements. The glass transition temperatures of the cross-linked membranes were increased compared to the virgin polymers, as shown, for example, in Fig. 5.9 where the cross-linked membrane has a T_g value at $290\text{ }^\circ\text{C}$ which is $62\text{ }^\circ\text{C}$ higher compared to the not cross-

linked membrane. Furthermore, the storage modulus after cross-linking is not decreased after $300\text{ }^\circ\text{C}$ but it reaches a plateau and this behavior is characteristic of cross-linked networks. The cross-linked membranes were subjected to treatment with the Fenton's reagent in order to evaluate their oxidative stability. In all cases they preserved their mechanical properties showing thus the high oxidative stability of the cross-linked structures.

The doping ability of the cross-linked membranes in phosphoric acid at $80\text{ }^\circ\text{C}$ in comparison with the doping level of the virgin polymers revealed that these cross-linked membranes showed higher doping levels compared to the neat polymers. That was attributed to the fact that the formation of the aziridines or amines functionalities could also interact with the phosphoric acid resulting in higher doping levels.

The exact chemical structure of the side double bonds is a crucial parameter in respect to their stability but also their reactivity. Thus, the allyl groups used above were thermally transformed to propenyl side group but the latter present lower reactivity to thermal polymerization due to sterical reasons.

An alternative approach was the case of **Copolymers XXI** bearing styrenic side functionalities [26] that would enable the

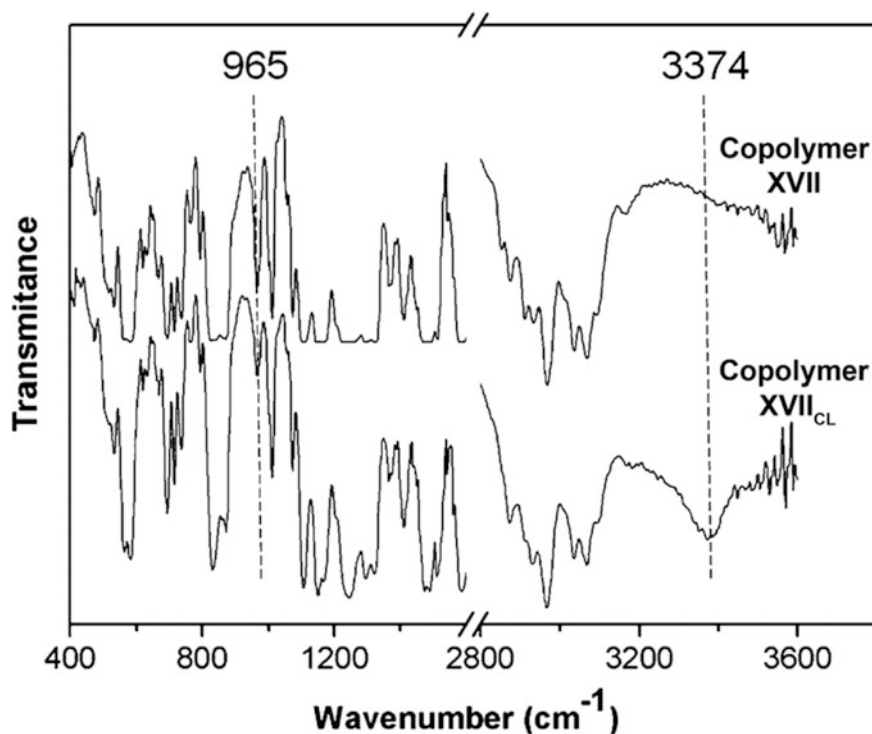
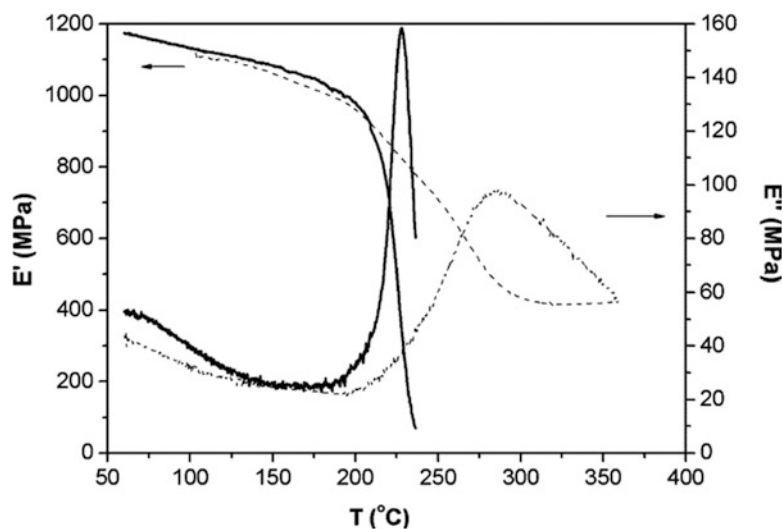


Fig. 5.8 Comparative FT-IR spectra of the pristine linear **Copolymer XVII** and its cross-linked analogue **Copolymer XVII_{CL}**. Reproduced from [24] with permission of the American Chemical Society

Fig. 5.9 Comparative DMA curves of the virgin **Copolymer XVII** (*solid line*) and the cross-linked polymer **Copolymer XVII_{CL}** (*dashed line*). Reproduced from [24] with permission of the American Chemical Society



covalent cross-linking by thermal treatment. In this case, the active vinyl bonds were chosen over propenyl moieties as more drastic to cross-linking by thermal treatment without the need of

a cross-linking agent. **Copolymers XXI** were subjected to post-polymerization cross-linking by thermal treatment of the membranes at 250 °C under inert atmosphere for 12 h towards

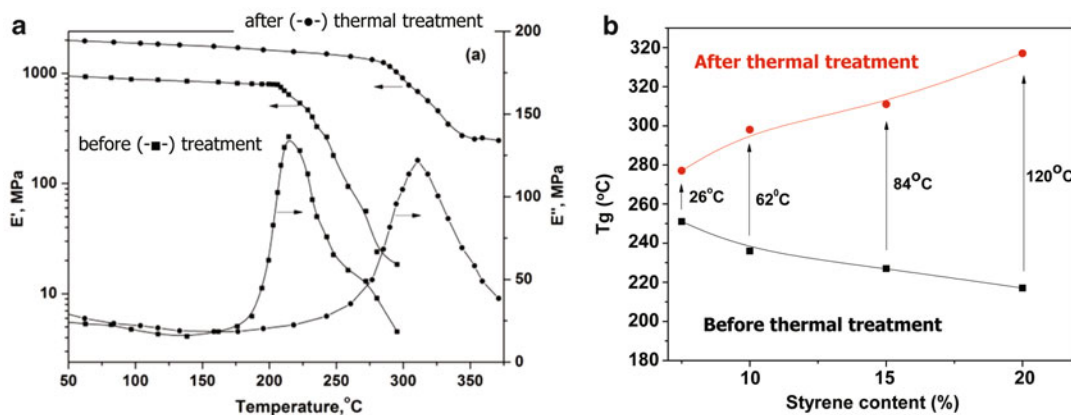


Fig. 5.10 (a) DMA diagrams of **Copolymer XXI** with $x + z = 60$ and $z + w = 15$ before (*filled square*) and after (*filled circle*) thermal treatment; (b) comparison of

the T_g values of the linear **Copolymers XXI** (*black line*) and of their cross-linked counter parts after thermal treatment **Copolymers XXI_{CL}** (*red line*)

the formation of a stable network. The initial **Copolymers XXI** showed T_g between 200 and 250 °C, thus the temperature of 250 °C was selected for the thermal treatment since thermal cross-linking is enhanced at temperatures above the T_g [33, 34]. All initial linear copolymers depicted good solubility in organic solvents, whereas the thermally treated membranes were almost insoluble under the same conditions indicating their successful cross-linking. The effect of the cross-linking on the mechanical properties of the membranes was examined by DMA measurements. As it is shown in Fig. 5.10, the glass transition temperatures of the linear precursors were drastically increased after their thermal treatment. More specifically, increase of the vinyl bond content in the initial copolymer and consequently increase of the cross-linking density after thermal treatment resulted in higher change of the T_g , ΔT_g , leading to superior T_g of the cross-linked polymers reaching values well above 300 °C enabling their use as high temperature polymer electrolytes.

During the above studies of the cross-linking of the side double bonds containing aromatic polyethers it was realized that the membranes' solubility in polar solvents was significantly reduced during the doping of the non-cross-linked linear membranes even those having large contents of side pyridine units. That observation was contradictory to our previous

experience where membranes with high side pyridine contents were extensively plasticized by phosphoric acid which was accompanied by loss of their mechanical properties rendering them unsuitable for MEA preparation [18]. A careful consideration of these two cases helped us to address and achieve our ultimate target. That is the preparation of thermally stable polymer electrolytes, which will be able to retain higher amounts of strong acids without losing their mechanical integrity aiming at their application in fuel cell devices with operating temperatures up to 220 °C [25]. Thus, cross-linkable linear copolymers having side pyridine moieties and side double bonds attached to the polymeric backbone were cross-linked during doping in phosphoric acid (**Copolymers XIX** and **XX**). More specifically the cross-linking was processed by cationic polymerization during the doping procedure in which the phosphoric acid acts as cationic initiator for the opening of the double bonds at high doping temperatures ranging from 80 to 120 °C as it is schematically shown in Scheme 5.3. Strong protonic (Brønsted) acids can initiate cationic polymerizations [35]. The propagation proceeds via the addition of the double bonds to the cation and the cross-linked network is formed.

In order to confirm the successful cross-linking, samples of the membranes were immersed in acid for different times and

Scheme 5.3 Schematic representation of the cross-linking in phosphoric acid through cationic polymerization. Reproduced from [25] with permission of Elsevier

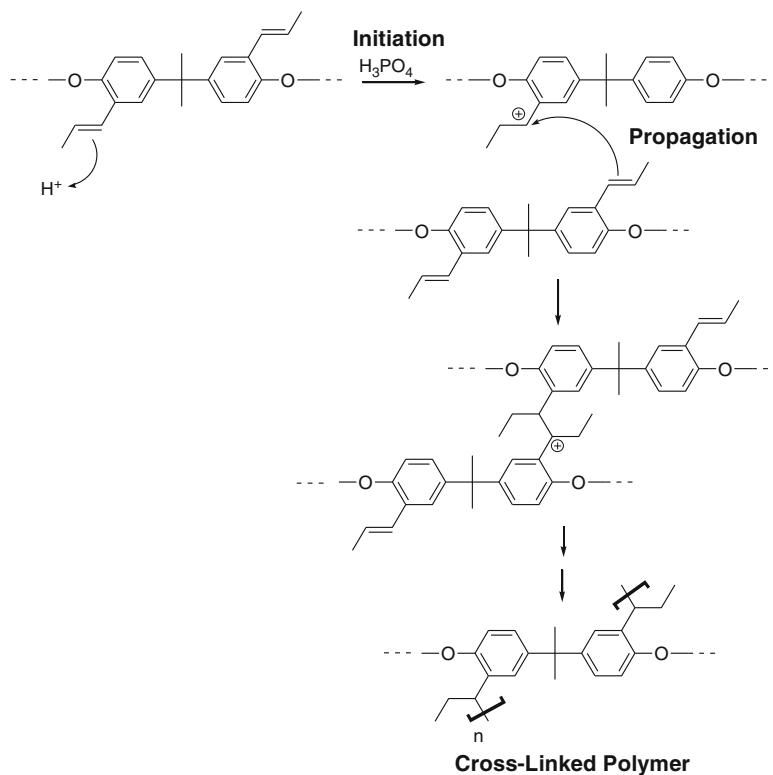
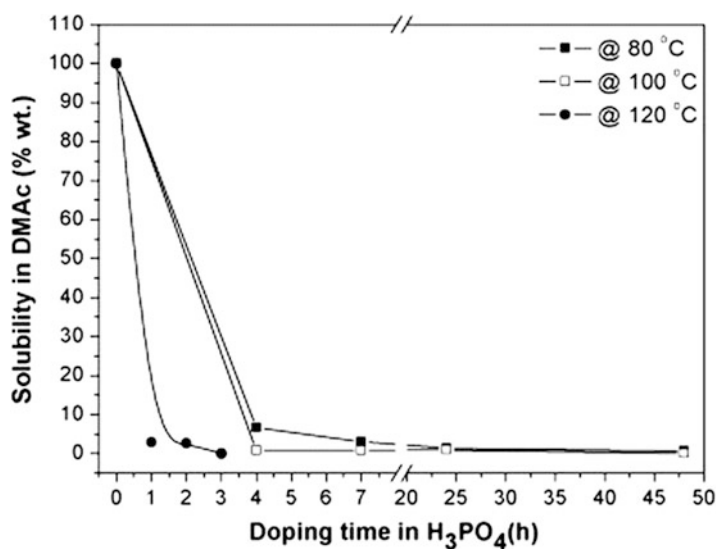


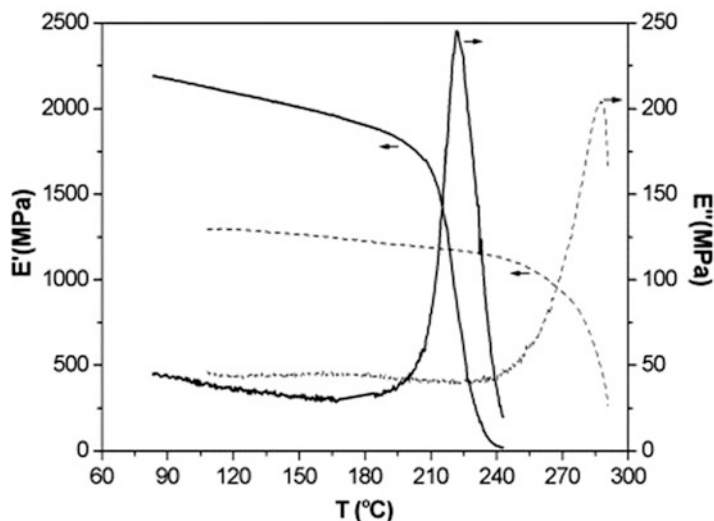
Fig. 5.11 Solubility dependence versus the doping time in phosphoric acid at different temperatures, for the cross-linked **Copolymer XX_{CL}**. Reproduced from [25] with permission of Elsevier



temperatures and their solubility in *N,N*-dimethylacetamide (DMAc) was tested. Figure 5.11 depicts the solubility dependence versus the doping time in phosphoric acid at

different temperatures for the cross-linked **Copolymer XX**. Initially the membranes are completely soluble in DMAc, while the solubility of the acid treated membranes is gradually

Fig. 5.12 Comparative DMA curves of the virgin **Copolymer XX** (black line) and the cross-linked in phosphoric acid **Copolymer XX_{CL}** (dashed line). Reproduced from [25] with permission of Elsevier



reduced as the doping time increases and only few hours are required to obtain almost insoluble materials. Additionally increase of the temperature reduces the time required for the formation of the cross-linked network. The cross-linking reaction was also followed spectroscopically using FTIR where the peak at 965 cm^{-1} which is assigned to the C=C double bonds (as shown in Fig. 5.8) clearly decreases in the case of the acid treated membrane.

The efficient cross-linking was also confirmed by the mechanical properties evaluation of the cross-linked membranes that presented a T_g value of $285\text{ }^\circ\text{C}$, which is about $65\text{ }^\circ\text{C}$ higher compared to the initial terpolymer (Fig. 5.12). Additionally the decomposition temperature of the acid treated cross-linked membranes showed an increase by $125\text{ }^\circ\text{C}$ reaching T_d values above $400\text{ }^\circ\text{C}$, while the pristine terpolymers were thermally stable up to about $280\text{ }^\circ\text{C}$.

All these results prove the successful cross-linking of the double bonds via cationic polymerization. This was the first report of such a cross-linking during the acid doping procedure of polymer electrolyte membranes. The breakthrough of this cross-linking methodology is in its simplicity since the membranes can be prepared by casting, evaluated thoroughly for their quality while still maintaining their

solubility, and in a final step and at any desired time, they can be cross-linked during the doping procedure. Thus, during this new process it is possible to obtain a cross-linked network without adding further steps and additional costs to the overall production sequence. This is of high importance in view of the fact that for the commercialization of fuel cells an important parameter which has to be taken into consideration, along with the least possible cost, is the easiness and reproducibility of the electrolytes' preparation procedure.

5.5 Interaction of Phosphoric Acid and Water with the Polymer Membranes

As mentioned in the previous sections, the electrolyte materials are doped with H_3PO_4 in order to assure high proton conductivity. Acid uptake is a result of the interactions of the polar basic pyridine group with phosphoric acid. The pyridine ring can react and be protonated by H_3PO_4 [7, 36, 37] as illustrated in Fig. 5.13a. These specific interactions were surveyed and demonstrated by means of FT-Raman spectroscopy. Spectra of **Copolymer I**, pristine and after gradual doping with phosphoric acid are depicted

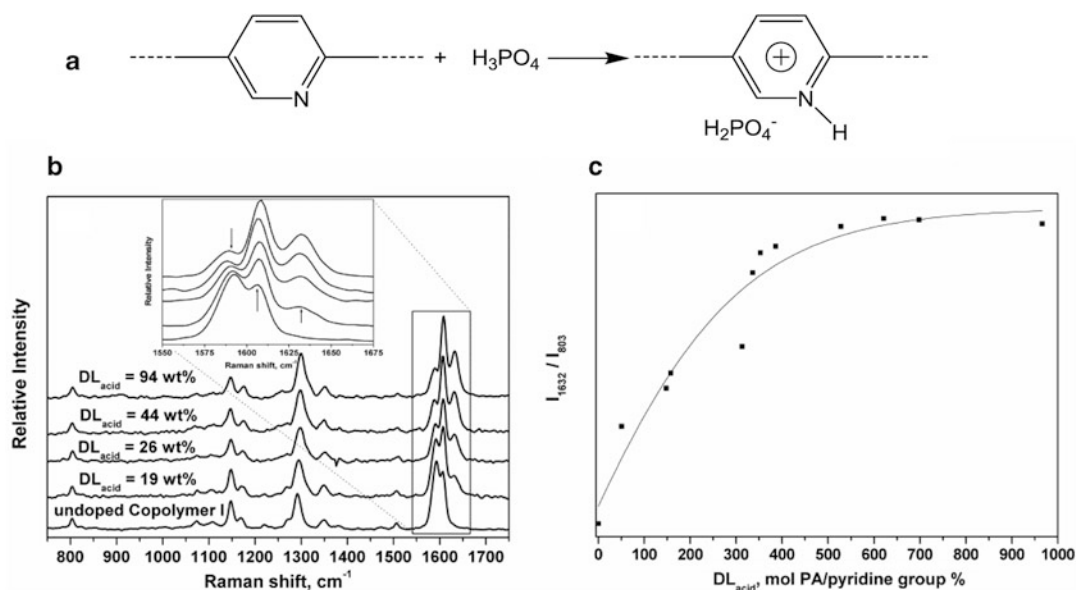


Fig. 5.13 (a) Interaction of phosphoric acid with the pyridine polar group of **Copolymer I**; (b) Raman spectra of **Copolymer I** before and after doping with H_3PO_4 85 wt% at several doping levels; (c) ratio of relative

intensities versus acid doping level expressed in mol H_3PO_4 (PA) per polar group (%) for the peaks 1632 and 803 cm^{-1} for **Copolymer I**/ H_3PO_4 . Reproduced from [37] with permission of the Royal Society of Chemistry

in Fig. 5.13b. Upon doping, the pyridine groups are protonated, as shown by the blue shift from 1593 to 1608 cm^{-1} of the absorption peak of the pyridine group in the Raman spectrum and the appearance of a new peak at 1630 cm^{-1} . This characteristic shift is attributed to the positive charge that is being induced on the N atoms by the phosphoric acid. For the PBI-based materials, a corresponding shift takes place of the symmetric stretch of the imidazole group from 1539 to 1570 cm^{-1} . In the latter case, the Raman shift is larger denoting stronger interaction of the imidazole ring with the acid, which is justified by its stronger basic character compared to pyridine (60 times more basic, the $\text{p}K_{\text{a}}$ of the conjugate acid is about 7, whereas for pyridine it is 5.2 [38]).

The difference in the specific interactions between the two groups is reflected on the doping procedure. The ratio of the peak at 1632 cm^{-1} that appears upon acid doping for **Copolymer I** to the unaffected peak at 803 cm^{-1} was calculated, Fig. 5.13c. The doping levels are expressed in moles of phosphoric acid per polar group.

Complete protonation of all the pyridine units takes place when the ratio reaches its maximum constant value. As can be seen, three molecules of acid per repeat unit, or else five molecules of acid per polar group are needed in order to reach to the full protonation of the pyridine moieties. On the contrary, in the case of PBI each acid molecule entering the matrix protonates one imidazole group [37, 39].

These interactions though of ionic nature could not possibly contribute significantly to the ionic conductivity of the membrane due to the limited network of the H_3PO_4 molecules, as well as the size and the immobilization of the species involved. Thus the acid uptake leading to full protonation is not sufficient to lead to high proton conduction values. Instead they constitute the substrate on which the excess phosphoric acid network will be developed within the matrix. The high proton conductivity is facilitated by this excess amount of acid beyond the primary protonation, which through hydrogen bonding forms a continuous network for the proton conductivity. For a given structure, conductivity

increases with acid uptake since the unbound acid [40] is mainly responsible for the conductivity [39, 41].

The doping behavior of the different polymeric polyether type materials mentioned in the previous sections is reported after immersion in 85 wt% phosphoric acid at various doping temperatures. The acid uptake is not always proportional to the percentage of the polar group in the (co)polymer chain. In fact, it has been proven that the acid doping ability, as well as the ionic conductivity, is strongly influenced by the chemical structure [12, 20, 42]. The monomers used, their ratio, the presence of different side functionalities, and the density of the polar pyridine groups define the final acquired acid doping level and the proton conduction, through differentiations in the chain conformations or the phase separation in the presence of phosphoric acid. Other influencing factors can be the rigidity of the structure and the intermolecular bonds. Moreover, in the case of cross-linked materials, the doping ability and proton conductivity are further strongly influenced not only by the cross-linking density, but also by the chemistry used and the nature of the formed “bridges” between the polymer chains, as will be discussed further in the next section. It should be stated that for each material there is an optimum range of acid uptake combining high conductivity values and good mechanical properties in order to be used in PEMFCs.

A vast literature has been devoted to the study of the proton conduction and the effect of relative humidity on the conductivity of the polymer/phosphoric acid systems [39, 43–48]. The conduction mechanism is substantiated through the proton transfer between a proton donor and a proton acceptor in combination to the ability of the proton carrier (positive ion) to rotate and move so that it will transfer the proton. Proton conductivity increases with relative humidity at a given temperature because the higher water content in the electrolyte lowers the viscosity within the membrane leading to higher mobility and rendering it more conductive [43], while it can play the role of proton carrier itself and provide more pathways (Hydrogen bonds) for protons to

hop. Water molecules can play a significant role in the configurational proton transfer through the H_3PO_4 imbibed polymer electrolytes as they are flexible to move, rotate, and be aligned with H_3PO_4 so that the hopping of H^+ can be facilitated. Moreover, according to calculations of the H–O bond distances, hydrogen bond between water and phosphoric acid has the longest distance (and thus weaker hydrogen bond) allowing a high degree of mobility and rotation, in comparison to hydrogen bonds of other species [39]. In this respect, the equilibrium water content is critical for the improvement of membrane’s proton conductivity. The physicochemical interactions of water vapors with the polymer electrolyte and the promoting effect on the fuel cell performance were also proven [36]. The relative humidity dependence on conductivity is much greater in low temperature water-based systems like Nafion than in acid-based electrolytes [46]. For an acid-doped electrolyte, the conductivity dependence on relative humidity is more pronounced as temperature increases [43]. The conductivity of acid-doped PBI with a doping level of 560 mol% increases from 3.8 to $6.8 \times 10^{-2} \text{ S cm}^{-1}$ at 200 °C with an increase in the relative humidity from 0.15 to 5 % [46, 49]. Moreover, for a PBI/Copolymer II blend with a wet phosphoric acid doping level of 220 wt%, conductivity increases from 2.7 to $8.6 \times 10^{-2} \text{ S cm}^{-1}$ at 170 °C with an increase in the steam partial pressure from 1 to 10 kPa (relative humidity 0.127 and 1.27 %, respectively) [42].

5.5.1 Equilibrium Hydration Levels of Water in the H_3PO_4 Imbibed Membranes

The equilibrium hydration level depends both on temperature and on steam partial pressure. The water generated at the cathode and the extent to which it equilibrates in the membrane may vary between the different polymer electrolytes, their acid doping level, and the preparation method of the electrolyte, e.g., the solvent used for the

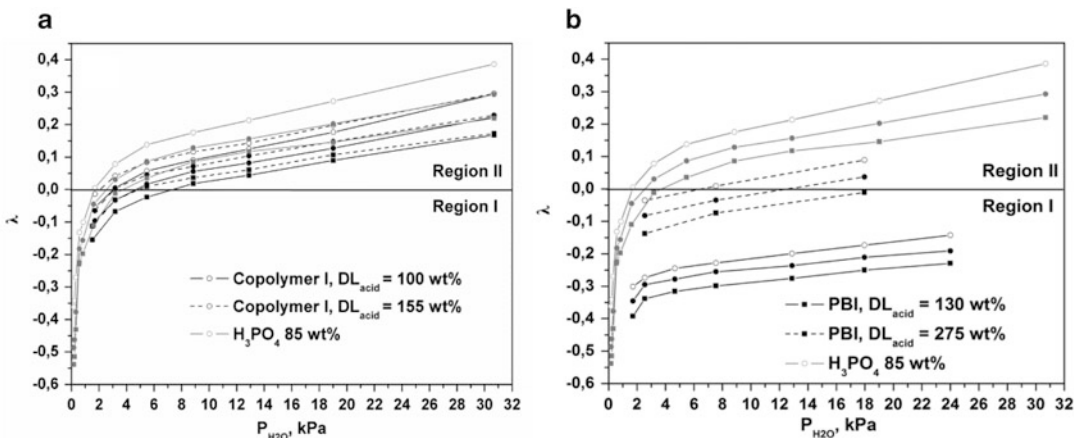


Fig. 5.14 The effect of water vapor partial pressure ($P_{\text{H}_2\text{O}}$) on the hydration level of acid-doped (a) **Copolymer I** and (b) **PBI** at different acid doping levels at 150 °C (open circles), 160 °C (solid circles), and 170 °C (squares).

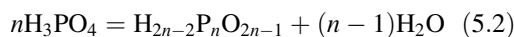
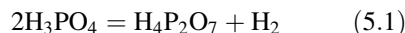
The corresponding results with H_3PO_4 85 wt% (grey lines) are also plotted for comparison. Reproduced from [37] with permission of the Royal Society of Chemistry

casting may determine the free volume expansion and therefore the solubility coefficient of water. The electrolyte affinity to water is of special importance, not only because water can affect the proton conduction, but also due to the possibility of acid dilution (temperature shut-down) or electrolyte redistribution due to volume expansions/contractions (especially during start/stop cycling), which can lead to long-term loss in conductivity or the membrane stability. A series of temperature programmed thermogravimetric (TGA) experiments under controlled humidified atmosphere shed light to the structural effect on water affinity and retention [37]. Two different state-of-the-art high temperature polymer electrolyte structures were used, **Copolymer I** [10] and standard m-PBI, while liquid H_3PO_4 85 wt% was used for comparison.

When temperature increases under dry atmosphere the following sequential processes take place:

- At temperatures below 100 °C, free water is evaporated leaving dry phosphoric acid in the polymer matrix.
- Further increase of the temperature leads to additional water evaporation as a result of the dehydration of H_3PO_4 and the formation of $\text{H}_4\text{P}_2\text{O}_7$ according to reaction (5.1) and in

general the polymerization reaction (5.2) at even higher temperatures. Despite the fact that pyrophosphoric acid is a strong acid, its formation is accompanied by the significant decrease of the fuel cell performance due to the decrease of mobility, as well as the ionic capacity (i.e., two molecules of phosphoric are substituted by one molecule of pyrophosphoric acid).



When the samples are exposed to humidity, water is being adsorbed. In Fig. 5.14, the hydration level of different acid-doped **Copolymer I** and **PBI** systems is depicted varying the temperature and humidity [37]. The hydration level is expressed through the dimensionless parameter, lambda (λ), which corresponds to the number of water molecules associated with one ortho-phosphoric acid molecule and is calculated according to (5.3)–(5.5), where W_{pol} is the weight of the undoped material, MW corresponds to the respective molecular weight of water and of H_3PO_4 , $W_{\text{H}_3\text{PO}_4}$ is the weight of the dry acid imbedded upon doping of the polymers, W is the recorded weight, $W_{\text{H}_2\text{O}}$ is the weight of water

absorbed upon exposure of the sample to humidified gases during the experiment, and W_{ref} is a reference weight where the free water is evaporated from the acid/polymer system.

$$W_{\text{H}_3\text{PO}_4} = W_{\text{ref}} - W_{\text{pol}} \quad (5.3)$$

$$W_{\text{H}_2\text{O}} = W - W_{\text{ref}} \quad (5.4)$$

$$\begin{aligned} \lambda &= \text{mol}_{\text{H}_2\text{O}}/\text{mol}_{\text{H}_3\text{PO}_4} \\ &= (W_{\text{H}_2\text{O}} \times \text{MW}_{\text{H}_3\text{PO}_4}) / (W_{\text{H}_3\text{PO}_4} \times \text{MW}_{\text{H}_2\text{O}}) \end{aligned} \quad (5.5)$$

Two processes take place. Water is absorbed due to the hydrolysis of the pyrophosphoric acid according to the reverse of (5.1), up to the point that $\lambda = 0$, showing that the dimerization of phosphoric acid is a fully reversible process. As expected, the equilibrium constant of phosphoric acid dimerization increases with temperature. Further increase in $P_{\text{H}_2\text{O}}$ resulted in solubility of free water in the H_3PO_4 /polymer system. There is a similar dependence on $P_{\text{H}_2\text{O}}$ for all samples used; sharp increase at low $P_{\text{H}_2\text{O}}$ and thereafter linear variation of λ . An increase of the acid doping level of the polymers results in enhanced ability to absorb water.

The chemical structure strongly influences the thermodynamics of the hydration process of the imbibed acid and therefore the ability of the electrolyte to absorb water molecules from steam. For similar acid contents, doped **Copolymer I** has a higher ability to absorb water than acid-doped PBI. Even at the low initial acid doping levels of 100 wt%, the behavior of acid imbibed **Copolymer I** is closer to that of phosphoric acid, denoting that the interactions of acid with this matrix are not strong or extended enough to disturb the network of the acid and alter its physicochemical properties. By exposing the sample to only 2–3 kPa of water, depending on the doping level at 150 °C all acid is in the orthophosphoric form. On the other hand, acid-doped PBI inhibits the reversion of reaction (5.1) and absorbs less water reflecting a difference on the physicochemical interactions of the acid inside the two matrixes. The stronger basic character of the imidazole group, along with the

formation of the stronger pyrophosphoric acid upon dehydration leads to electrolytes with smaller affinity to water. Equilibrium isotherms at various water content over a range of temperatures from 30 to 180 °C using Celtec[®]-P Series 1000 MEAs also prove this behavior [50]. In the temperature range between 160 and 180 °C, positive values of the hydration level (λ) were only obtained for water partial pressures above 20 kPa. Note that Celtec[®]-P electrolytes are polymer gels containing PBI and phosphoric acid with high phosphoric acid contents of more than 95 wt% or up to 70 phosphoric acid molecules per PBI repeat unit [51].

Similar reports on the affinity of PBI/phosphoric acid systems to water exist. Schechter et al. [52] showed that water is absorbed in the polymer under different water activity and it interacts with phosphorous species changing the concentration of the mobile acid in a similar way to liquid acid, using a series of ¹H and ³¹P liquid probe NMR measurements under carefully controlled humidity. Li et al. [53] examined the relationship between phosphoric acid doping level and water uptake. For pristine PBI membranes and PBI membranes with low acid doping levels (<200 mol%) the water uptake is small. In fact, the water uptake from the vapor phase for PBI with a doping level 170 mol% was found to be lower than that for the pristine PBI, attributed to the fact that the active sites of the imidazole ring are preferably occupied by the acid molecules. A more significant increase was observed for the membranes with high doping acid levels, indicating that this water uptake is associated with the acid doping level. At high acid doping levels, water uptake of m-PBI at room temperature was comparable to or even exceeded that of the commercially available Nafion in the high humidity range.

5.5.1.1 Stability and Volatility of H_3PO_4 in the Imbibed Membranes

The stability and volatility of H_3PO_4 in the polymer matrix was studied by a set of long-term TGA experiments under humidified conditions. Representative examples are presented in

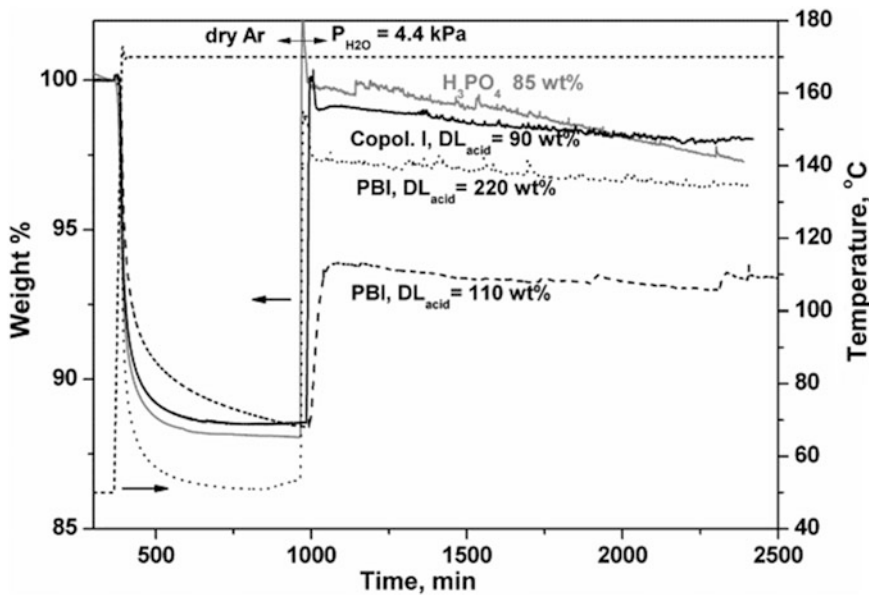


Fig. 5.15 Thermogravimetric analysis of H_3PO_4 and acid-doped **Copolymer I** and PBI under dry and humidified atmosphere, $P_{\text{H}_2\text{O}} = 4.4$ kPa. The dry argon flow rate was $150 \text{ cm}^3/\text{min}$. The contribution of the polymer matrix has been subtracted. The

weight of all samples has been normalized considering that 100 wt% is the initial weight of the dry acid, $100(W_{\text{ref}} - W_{\text{pol}})/W_{\text{ref}} = 100$ wt%. Reproduced from [37] with permission of the Royal Society of Chemistry

Fig. 5.15 for H_3PO_4 and acid-doped **Copolymer I** & PBI. Initially, all samples were equilibrated under dry Ar atmosphere at 50°C . Upon temperature increase to 170°C , the weight decreased due to acid dehydration. Thereafter, a certain water partial pressure was introduced over the samples (4.4 kPa for the examples in Fig. 5.15) and was kept constant for a relatively long period in order to record the stability of the system and evaluate the rate of evaporation of phosphoric acid itself. As also stated earlier, doped **Copolymer I** and liquid phosphoric acid almost recover their initial weight at 50°C , reversing the dehydration reaction (5.1). On the contrary, PBI does not reach W_{ref} even for 220 wt% acid doping level. In [37] the weight loss rate or else the normalized evaporation rate of the H_3PO_4 for several samples and different vapor partial pressures is reported and was concluded that:

1. An increase in evaporation rate is observed upon increasing steam partial pressure and/or acid doping level.
2. The evaporation rate of H_3PO_4 from **Copolymer I** is approximately 60 % higher than the

corresponding rate from the PBI membrane being at the same H_3PO_4 doping level, in accordance to the weaker interaction of the acid with **Copolymer I**, leading to a behavior closer to H_3PO_4 . In any case, the use of a polymer matrix compared to plain phosphoric acid can decrease the evaporation rate even by a factor of 3. The differentiation between the three systems is closely related to modifications in the physico-chemical properties of the H_3PO_4 through its interactions with the polymer matrix.

5.5.2 Steam Permeability Through the Membrane

Using in situ experimental protocols, it has been explicitly proven that the steam permeates through the membrane electrolyte. Given the fact that other gases smaller in the size of their molecules cannot penetrate the electrolyte at comparable high rates as water, the crossover mechanism of steam cannot be interpreted by considering a diffusion process through the void

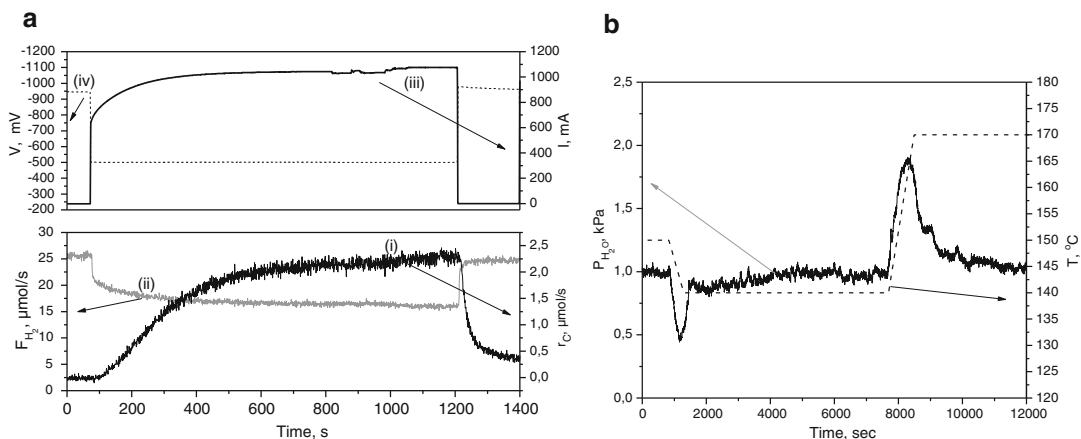


Fig. 5.16 (a) The transient evolution of (i) H_2O and (ii) H_2 flow rates at the anode outlet and (iii) current I upon (iv) voltage application of $V_{\text{cell}} = -0.5$ V. The anode/cathode feed gas composition was dry H_2 30 %–Ar/ O_2 ; (b) H_2O evolution during the stepwise variation of the

reactor's temperature. The feed gas composition to both compartments of the cell is 1 mol% $\text{H}_2\text{O}/\text{He}$ mixture. Electrolyte: PBI/Copolymer II 50/50. Doping level: 200 wt%. Membrane thickness: 70 μm . Reproduced from [36] with permission of Elsevier

volume of the polymer membrane. Taking into consideration that permeability through a membrane is defined by (5.6) [54], it has been proposed that the high permeation rate of water is because of the high solubility of water in phosphoric acid and its chemical interaction with pyrophosphoric acid according to reverse of reaction (5.1) [36].

$$P(\text{permeability}) = S(\text{solubility in electrolyte}) \times D(\text{diffusivity in electrolyte}) \quad (5.6)$$

Though water vapor plays a significant role in conductivity and therefore fuel cell performance, the humidification of H_2 and O_2 is not necessary. The water vapors produced from the electrochemical reaction at the cathode compartment penetrate through the polymer electrolyte to the anode compartment. Upon this back-transport process, the electrolyte is being hydrated with a direct positive effect on the fuel cell performance. This has been shown under real fuel cell operating conditions, Fig. 5.16a [36]. The transient evolution of the anode gases concentration was recorded upon cell potential application of 500 mV. On fuel cell operation, hydrogen is progressively consumed approaching steady state, while the water signal is observed to

increase approaching a constant value. Therefore, the produced water can penetrate and evolve at the anode compartment. In addition, the transient evolution of the water signal is followed by the corresponding increase in hydrogen conversion and cell current, thus indicating the direct effect of water transport through the membrane on the fuel cell performance. Figure 5.16b depicts a temperature variation in situ experiment showing that the acid-doped electrolyte membrane absorbs and retains varying amounts of water at different temperatures. Both compartments were fed with Ar–1% H_2O mixture at 150 $^{\circ}\text{C}$. Upon stepwise decrease or increase of cell's temperature, water is being observed to be absorbed or to be evolved from the membrane, respectively. This shows that varying equilibrium water/MEA conditions are established at different temperatures.

5.6 Application in HT-PEMFCs Operating up to 220 $^{\circ}\text{C}$

The aromatic polyethers bearing pyridine moieties described in the previous sections have been effectively used as polymer electrolytes in fuel cells. Because of the use of several different

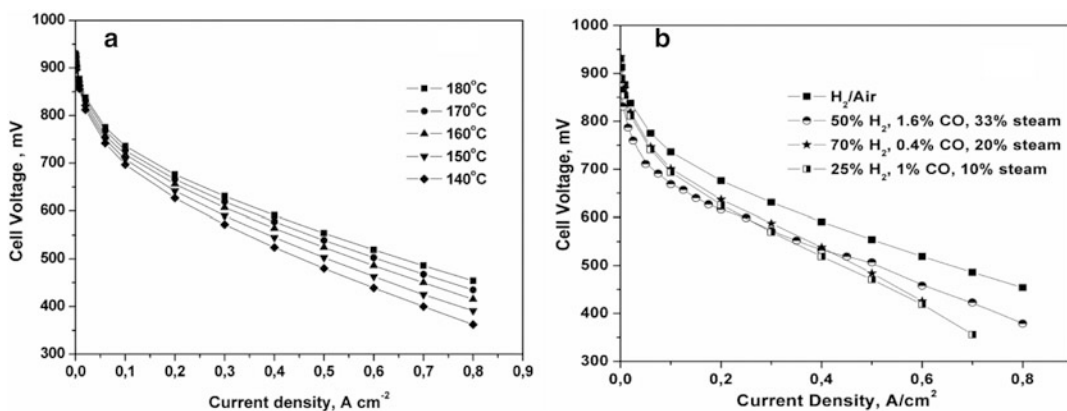


Fig. 5.17 I - V curves of MEA based on Copolymer IX, (a) with H_2 and air feeds (λ_{H_2} : 1.2, λ_{air} : 2.0) and (b) different reformate/air feeds at ambient pressure. Active surface area = 25 cm^2

membranes as electrolytes, it was not feasible to find the optimum conditions for each one, since several parameters regarding the design, construction, and assembling of the membrane electrode assembly (MEA) must be taken into account in order to have optimum performance. It should not be neglected that commercialization of PEMFCs is still restricted by its high cost since noble metals are typically used as electrocatalysts. Reduced cost, resulting from increased catalyst utilization and/or catalyst stability, is highly desirable. The design of electrodes for PEMFCs is a delicate balancing of transport media. Transport of gases and conductance of electrons and protons to the electrochemical interface must be optimized to provide efficient electrochemical reactions [55]. In this respect, for this type of cells, increase of the triple-phase boundaries has been attempted by developing a new type of Pt/carbon nanotubes (Pt/CNTs)-based electrocatalysts, where the carbon substrate, following the pattern of the electrolyte, is chemically functionalized with polar pyridine groups, which are expected to interact with phosphoric acid, secure the uniform distribution of the acid throughout the catalytic layer, and provide a 3D proton ionic link with all deposited Pt particles [56–58]. In the present discussion, focus will be paid on the electrochemical characterization of the polymer

electrolytes discussed. Certainly, in most cases, optimization of the MEA construction and operational parameters will further enhance the performance. The electrochemical characterization will be confined on their fuel cell performance and stability.

5.6.1 Linear Polymeric Membranes

The linear polymeric materials have shown excellent performance and stability operating up to 180 – 200 °C [59]. An example of the cell performance obtained for this category of polymer electrolytes is given in Fig. 5.17, where the polarization curve of a fuel cell operating at 140 – 180 °C using hydrogen and air dry gases with stoichiometric flow rates at anode and cathode is depicted. The durability of these systems is presented in Fig. 5.18, where a long-term fuel cell stability test under steady state operation at 0.22 A cm^{-2} and different feed gases is depicted.

It should be noted here that besides the initial syntheses and studies of the linear copolymers, a lot of effort for the optimization of selected copolymers' preparation in terms of composition control and molecular weight increase together with MEA construction and testing has been devoted by the spin-off company Advent S.A. [60].

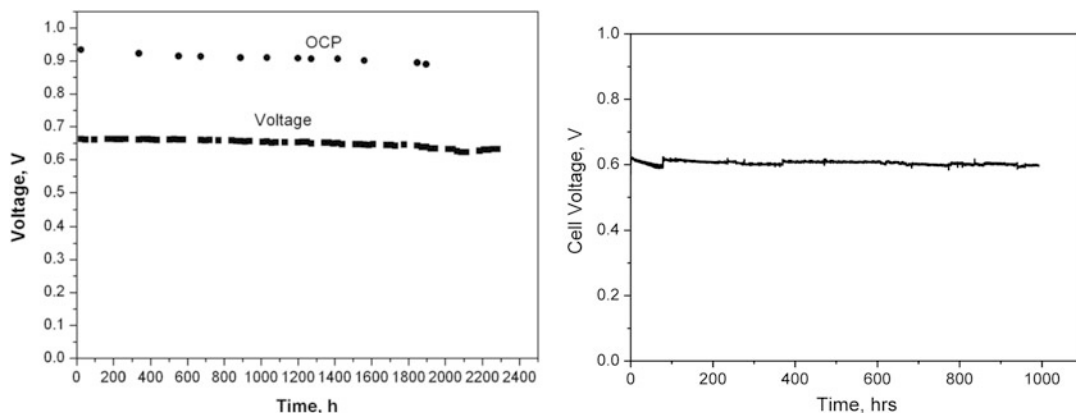


Fig. 5.18 Fuel cell stability test for **Copolymer IX** at 180 °C and ambient pressure. (a) Anode: H₂ ($\lambda = 1.2$), cathode: air ($\lambda = 2$) and (b) anode: 71.3 % H₂ ($\lambda = 1.3$), 2.1 % CO, 26.6 % CO₂, cathode: air ($\lambda = 2.2$)

5.6.2 Cross-Linked Membranes

A critical issue of all the aforementioned linear polymer electrolytes is the deficient long-term durability of these systems at temperatures well above 180 °C. Over 5000 h for vehicles and 40,000 h for stationary applications are the required life times of PEMFCs [61]. At the same time, increasing the fuel cells operation temperature even above 180 °C offers several distinct advantages like increased conductivity of the acid-doped membranes at lower doping levels, increased tolerance of the catalytic layers to contaminants, better heat management and heat utilization and efficient combination with other electrochemical devices, e.g., a methanol or liquid petroleum gas (LPG) reformers. This target requires modifications in the chemical structure of the standard membranes towards the increase of intermolecular interactions. The challenge is to develop materials with increased mechanical stability, but with adequate ionic conductivities. Post-polymerization cross-linking by covalent bonding between the macromolecules has the strongest and more permanent impact on the polymer structure and is thoroughly described in the previous sections of this chapter. In brief, side cross-linkable groups were introduced on the chemical structure like carboxylic acid [27], propenyl [24], or styryl [26] groups. Post-polymerization covalent cross-linking (thermal,

covalent with the use of cross-linkers or covalent in acid [25]) improved the mechanical properties in terms of glass transition temperature. Different chemistries were explored and resulted in materials with differentiations in the properties, as well as their fuel cell performance.

Conductivity of the linear and cross-linked materials with the carboxylic acid functionalities (**Copolymers XII** and **XXII**) was evaluated in situ by means of AC impedance spectroscopy as shown in Fig. 5.19a. For all materials, the conductivity exceeded the value of $8 \times 10^{-2} \text{ S cm}^{-1}$ and in some cases reached $10^{-1} \text{ S cm}^{-1}$ above 180 °C. As expected, temperature increase improved the ionic conductivity. The cross-linked material depicted lower conductivity values compared to its linear counterpart at the same doping levels. In the case of the cross-linked material, this doping level is not the maximum that can be achieved; therefore this drawback can be compensated by increasing the doping level. The non-cross-linked materials showed high performance and good stability at temperatures up to 180 °C [27]. Above that temperature the performance of the corresponding MEAs slowly deteriorated. As explained above, two cross-linking methods were investigated for the cross-linking of **Copolymers XII** and **XXII**, the dihydrazine (TDH) and the bistetrazole (BTT) routes toward the formation of oxadiazole bridging moieties. The cross-linked membranes

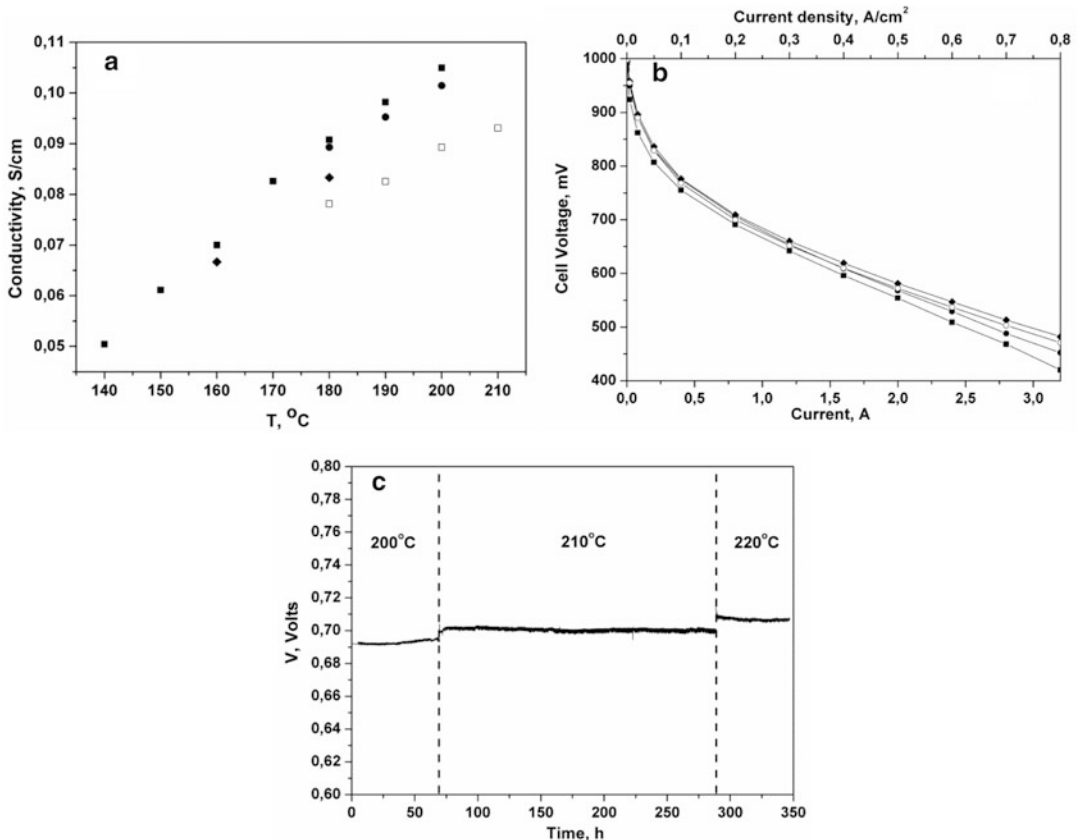


Fig. 5.19 (a) Temperature dependence of ionic conductivity of **Copolymer XXII** ($x = 70$, $z = 10$) with DL = 193 % and thickness 110 μm (filled square) and with DL = 170 % and thickness 160 μm (filled diamond); of **Copolymer XII** ($x = 70$, $z = 20$) with DL = 200 % and thickness 125 μm (filled circle); and of the cross-linked **Copolymer XII_{CL-BTT(100)}** ($x = 70$, $z = 10$) with DL = 210 % and thickness 175 μm (open square). Conductivities measured at 0.2 A cm^{-2} using dry gases with hydrogen and oxygen (stoichiometric ratio of 1.2 and 2, respectively) at ambient pressure. (b)

Current–voltage curves at 200 °C (filled square), 210 °C on the 5th (filled circle) and 15th (open circle) day of operation and 220 °C (filled diamond) and (c) cell potential versus time at 0.2 A cm^{-2} and at several operating temperatures between 200 and 220 °C. For (b) and (c), the MEA was based on the cross-linked **Copolymer XII_{CL-BTT(100)}** ($x = 70$, $z = 10$). Active area: 4 cm^2 . Dry gases with hydrogen and oxygen (stoichiometric ratio of 1.2 and 2, respectively) at ambient pressure. Reproduced from [27] with permission of the Royal Society of Chemistry

through BTT were superior and MEAs were therefore formulated. Initial electrochemical characterization showed very promising results. Figure 5.19b depicts the polarization curves at temperatures up to 220 °C for the MEA based on the cross-linked **Copolymer XXII_{CL-BTT(100)}** using dry gases H_2/O_2 (anode/cathode) with stoichiometric ratio. The fuel cell performance is improved with increasing temperature due to the increased ionic conductivity of the electrolyte and the enhanced reaction kinetics. Potential

values $V = 697$, 703, and 712 mV were obtained at 0.2 A cm^{-2} at ambient pressure and at 200, 210, and 220 °C, respectively. A short stability evaluation test is presented in Fig. 5.19c, showing stable performance with no sign of degradation for at least 350 h at operational temperatures between 200 and 220 °C.

Another example of a chemically cross-linked material is the case of polymers containing cross-linkable propenyl groups cross-linked with the use of a bisazide [24]. Figure 5.20a depicts the

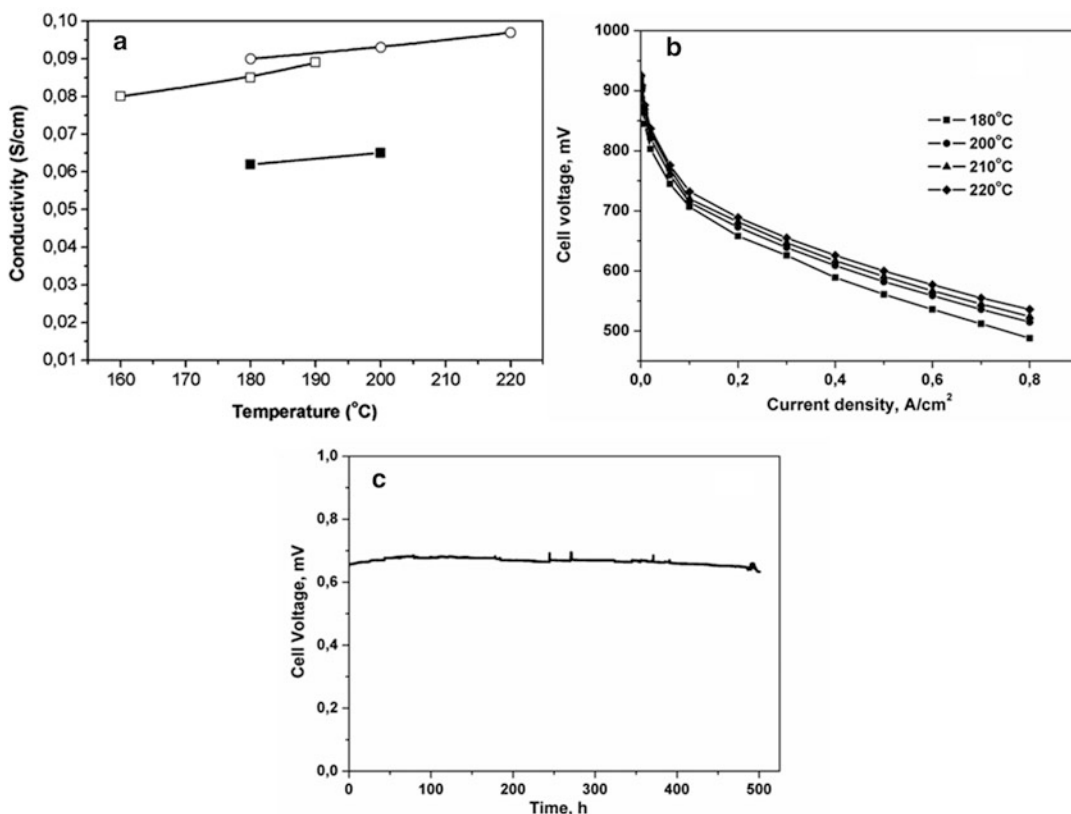


Fig. 5.20 (a) Temperature dependence of ionic conductivity for the **Copolymer XVII** ($x = 75$) with $DL_{acid} = 160$ wt% (filled square) **Copolymer XVII_{CL}** ($x = 75$) with $DL_{acid} = 140$ wt% (open square) and **Copolymer XVII_{CL}** ($x = 70$) with $DL_{acid} = 195$ wt% (open circle). Membrane thicknesses: 140, 120, and 110 μm ,

respectively. Reproduced from [24] with permission of the American Chemical Society; (b) current–voltage curves at temperatures 180–220 °C; (c) long-term stability measurements at 210 °C and 0.2 A cm^{-2} of a cross-linked MEA using the **Copolymer XX_{CL}**, $DL_{acid} = 320$ wt%. Active area 25 cm^2 . Feed: H_2/air 1.2/2.0

temperature dependence of the ionic conductivity for the MEAs which were formed from the cross-linked membranes and the azide-free polymer. It must be noticed that although the cross-linked and non-cross-linked membranes absorbed almost the same quantity of acid, the conductivity of the cross-linked one is slightly higher compared to the neat polymer. This fact is in agreement with previous studies related to the effect of the polymeric structure on the conductivity. In the cross-linked structure, the presence of the aziridines or amines not only increases the materials doping ability, but the conductivity as well. It should be mentioned that although the cross-linking is known to decrease the ionic conductivity, in this case the selected cross-linker

created functional groups which provided more pathways for the proton transfer and subsequently higher conductivity values were noticed. The performance of the MEA comprising the aforementioned covalently cross-linked membrane can be seen in Fig. 5.20b, while as presented in Fig. 5.20c it showed stable operation at 210 °C for 500 h at 0.2 A cm^{-2} with H_2/Air feed. The cell voltage is 660 mV and the corresponding power density is 0.132 W cm^{-2} . Over the course of the experiment the average voltage drop was only 3 $\mu\text{V h}^{-1}$. This provides evidence for their high chemical, thermal, and oxidative stability.

In an attempt to simplify the cross-linking procedure, thermal cross-linking of polymers bearing side styryl double bonds are reported

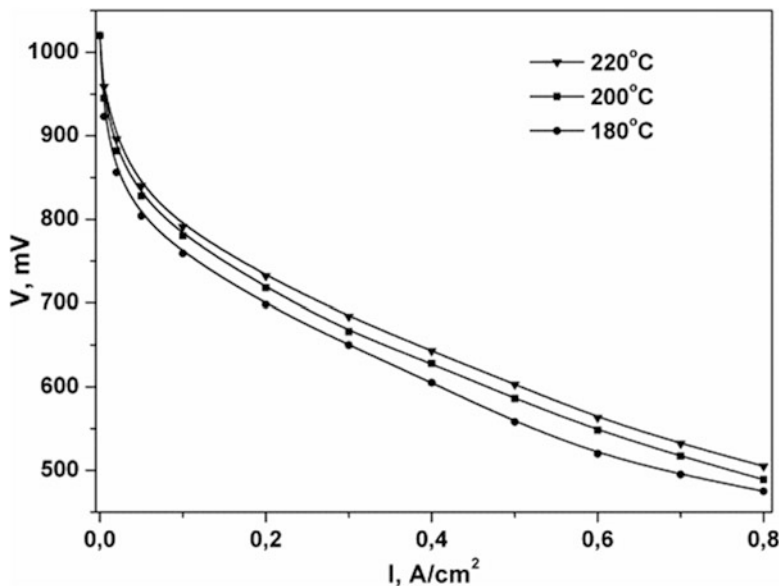


Fig. 5.21 Current–voltage curves for the cross-linked Copolymer XXI_{CL} ($x + z = 60$, $z + w = 15$)-based MEA at several operating temperatures using dry H₂/O₂

gases ($\lambda = 1.2$ and 2 , respectively) at ambient pressure. DL_{acid} = 160 wt%, active area: 4 cm². Reproduced from [26] with permission of Elsevier

[26]. The properties of the virgin materials allowed heating above their glass transition temperature (at 250 °C) where the double bonds become reactive and are able to cross-link without the use of thermal initiators or cross-linking agents. Unfortunately, the doping ability in phosphoric acid was decreased, as is common upon the formation of more compact structures. Despite the moderate phosphoric acid doping levels, in situ conductivity reached values above 5×10^{-2} S cm⁻¹. Preparation of MEAs and preliminary fuel cell tests gave a very promising performance. The polarization curves are shown in Fig. 5.21. Cross-linking allowed measurements up to 220 °C demonstrating the enhanced stability and their feasibility to be used in high temperature PEM fuel cells.

As explained previously, cross-linking during the impregnation of the membranes (bearing propenyl groups) in phosphoric acid remarkably simplifies the whole procedure, while at the same time leads to materials with enhanced ability to absorb and retain high amounts of phosphoric acid without losing their mechanical integrity [25]. As a result of the increased acid uptakes, in situ measurements by means of AC impedance

spectroscopy revealed the high conductivity values obtained, Fig. 5.22a, in most cases in the order of 10⁻¹ S cm⁻¹. The advanced cross-linked membranes were tested in single cells operating at high temperatures up to 220 °C, Fig. 5.22b. A durability measurement at steady state operation at 0.2 A cm⁻² at 210 °C is shown in Fig. 4.22c. The promising performance and stable operation in combination with the simplified technique used for their preparation demonstrate the feasibility of these electrolytes to be used in high temperature PEM fuel cells operating well above 180 °C.

5.7 Conclusions

Taking advantage of the possibilities offered by polymer chemistry for creating novel materials, a new generation of polymeric membranes for HT-PEM fuel cells has been designed and developed. The herein presented aromatic polyether sulfones carrying main chain pyridine units have been proven to be a reliable polymer electrolyte material for the HT-PEM fuel cell technology. These materials exhibit certain

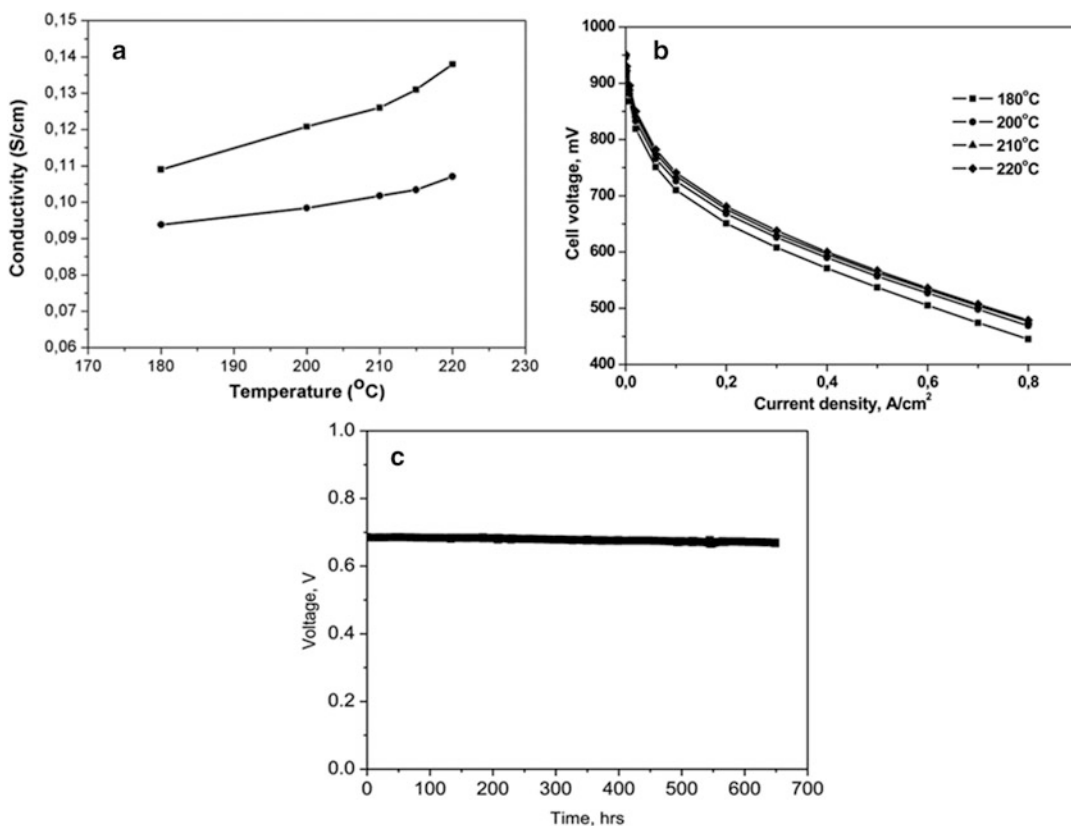


Fig. 5.22 (a) Temperature dependence of ionic conductivity for the cross-linked in acid **Copolymer XX_{CL-acid}** with DL_{acid} = 280 wt% (filled circle) and 350 wt% (filled square). Reproduced from [25] with permission of Elsevier; (b) current–voltage curves of a **Copolymer XX_{CL-acid}**

based MEA with DL_{acid} = 350 wt% at several operating temperatures using dry H₂/O₂ gases ($\lambda = 1.2$ and 2, respectively); (c) long-term stability measurement of **Copolymer XX_{CL-acid}**-based MEA at 210 °C and 0.2 A cm⁻² at ambient pressure. DL_{acid} = 208 wt%, active area: 25 cm²

advantages as compared to PBI polymer electrolytes with regards to their manufacturing properties, their operating conditions, and their performance characteristics. These comprise their very good film-forming properties, thin robust membranes with long lasting mechanical and chemical stability, adequate proton conductivity ($0.8\text{--}1 \times 10^{-1} \text{ S cm}^{-1}$) and operating temperatures ranging between 170 and 210 °C. The latter widens its technological applications so that advanced compact engineering design of fuel cell systems allows either the use of diversity of fuels or the operation of the fuel cell stack

within a wide span of temperatures providing sustainable operation under dynamic load. In particular, the MEA operation at 210 °C allows for the effective integration of a methanol reformer in the HT-PEM fuel cell stack, thus resulting into a compact simple and versatile fuel cell system especially for portable applications.

Acknowledgements Financial support from European Commission and from the Fuel Cell and Hydrogen Joint Undertaking (FCH JU) is greatly acknowledged. The authors are also indebted to Advent SA personnel for their collaboration.

References

1. Li QF, Jensen JO, Savinell RF et al (2009) High temperature proton exchange membranes based on polybenzimidazoles for fuel cells. *Prog Polym Sci* 34:449–477
2. Bouchet R, Siebert E (1999) Proton conduction in acid doped polybenzimidazole. *Solid State Ionics* 118:287–299
3. Kim SK, Kim TH, Ko T et al (2011) Cross-linked poly (2,5-benzimidazole) consisting of wholly aromatic groups for high-temperature PEM fuel cell applications. *J Membr Sci* 373:80–88
4. Asensio JA, Borros S, Gomez-Romero P (2004) Proton-conducting membranes based on poly (2,5-benzimidazole) (ABPBI) and phosphoric acid prepared by direct acid casting. *J Membr Sci* 241:89–93
5. Kim HJ, Cho SY, An SJ et al (2004) Synthesis of poly (2,5-benzimidazole) for use as a fuel-cell membrane. *Macromol Rapid Commun* 25:894–897
6. Yu S, Benicewicz BC (2009) Synthesis and characterization of functionalized polybenzimidazoles for high temperature PEMFC's. *Macromolecules* 42: \$32#8640–8648
7. Gourdoupi N, Andreopoulou AK, Deimede V et al (2003) A novel proton conducting polyelectrolyte composed of an aromatic polyether containing main-chain pyridine units for fuel cells applications. *Chem Mater* 15:5044–5050
8. Andreopoulou AK, Kallitsis JK (2002) From terphenyl-dendronized macromonomers to aromatic-aliphatic polyethers bearing two pendant dendrons per repeating unit. *Macromolecules* 35:5808
9. Gourdoupi N, Papadimitriou K, Neophytides S et al (2008) New high temperature polymer electrolyte membranes. Influence of the chemical structure on their properties. *Fuel Cells* 8:200–208
10. Pefkianakis EK, Deimede V, Daletou MK et al (2005) Novel polymer electrolyte membrane, containing pyridine and tetramethyl biphenyl units, for application in high temperature PEM fuel cells. *Macromol Rapid Commun* 26:1724–1728
11. Geormezi M, Deimede V, Gourdoupi N et al (2008) Novel pyridine-based poly(ether sulfones) and their study in high temperature PEM fuel cells. *Macromolecules* 41:9051–9056
12. Daletou MK, Geormezi M, Pefkianakis EK et al (2010) Fully aromatic copolyethers for high temperature polymer electrolyte membrane fuel cells. *Fuel Cells* 10:35–44
13. Daletou MK, Gourdoupi N, Kallitsis JK (2005) Proton conducting membranes based on PBI/polysulfone copolymer blends. *J Membr Sci* 252:115–122
14. Hubner G, Roduner E (1999) EPR investigation of HO radical initiated degradation reactions of sulfonated aromatics as model compounds for fuel cell proton conducting membranes. *J Mater Chem* 9:409–418
15. Kerres J, Schönberger F, Chromik A et al (2008) Partially fluorinated arylene polyethers and their ternary blend membranes with PBI and H₃PO₄. Part I. Synthesis and characterisation of polymers and binary blend membranes. *Fuel Cells* 8:175–187
16. Kallitsis JK, Geormezi M, Neophytides S (2009) Polymer electrolyte membranes for high temperature fuel cells based on aromatic polyethers bearing pyridine units. *Polym Int* 58:1226–1233
17. Deimede V, Voyiatzis GA, Kallitsis JK et al (2000) Miscibility behavior of polybenzimidazole/sulfonated polysulfone blends for use in fuel cell applications. *Macromolecules* 33:7609–7617
18. Geormezi M, Chochos CL, Gourdoupi N et al (2011) High performance polymer electrolytes based on main and side chain pyridine aromatic polyethers for high and medium temperature PEM fuel cells. *J Power Sources* 196:9382–9390
19. Andreopoulou AK, Daletou MK, Kalamaras I et al (2012) Crosslinked or non-crosslinked aromatic (co)polymers as proton conductors for use in high temperature PEM fuel cells. US Patent Application No. 13367855/02.07.2012
20. Morfopoulou C, Andreopoulou AK, Kallitsis JK (2011) The effect of structural variations on aromatic polyethers for high temperature PEM fuel cells. *J Polym Sci A Polym Chem* 49:4325–4334
21. Papadimitriou KD, Andreopoulou AK, Kallitsis JK (2010) Phosphonated fully aromatic polyethers for PEMFCs applications. *J Polym Sci A Polym Chem* 48:2817–2827
22. Kalamaras I, Daletou MK, Gregoriou VG et al (2011) Sulfonated aromatic polyethers containing pyridine units as electrolytes for high temperature fuel cells. *Fuel Cells* 11:921–931
23. Voegelé A, Deimede VA, Kallitsis JK (2012) Side chain crosslinking of aromatic polyethers for high temperature polymer electrolyte membrane fuel cell applications. *J Polym Sci A Polym Chem* 50:207–216
24. Papadimitriou KD, Paloukis F, Neophytides SG et al (2011) Cross-linking of side chain unsaturated aromatic polyethers for high temperature polymer electrolyte membrane fuel cell applications. *Macromolecules* 44:4942–4951
25. Papadimitriou KD, Geormezi M, Neophytides SG et al (2013) Covalent cross-linking in phosphoric acid of pyridine based aromatic polyethers bearing side double bonds for use in high temperature polymer electrolyte membrane fuel cells. *J Membr Sci* 433:1–9
26. Kalamaras I, Daletou MK, Neophytides SG et al (2012) Thermal crosslinking of aromatic polyethers bearing pyridine groups for use as high temperature polymer electrolytes. *J Membr Sci* 415–416:42–50
27. Morfopoulou CI, Andreopoulou AK, Daletou MK et al (2013) Cross-linked high temperature polymer electrolytes through oxadiazole bond formation and their applications in HT PEM fuel cells. *J Mater Chem A* 1:1613–1622

28. Hsiao SH, Chiou JH (2001) Aromatic poly(1,3,4-oxadiazole)s and poly(amide-1,3,4-oxadiazole)s containing ether sulfone linkages. *J Polym Sci A Polym Chem* 39:2271–2286
29. Higashi F, Ogata SI, Aoki Y (1982) High-molecular-weight poly(*p*-phenyleneterephthalamide) by the direct polycondensation reaction with triphenyl phosphate. *J Polym Sci Polym Chem Ed* 20:2081–2087
30. Huisgen R, Sauer J, Sturm HJ (1958) Acylierung 5-substituierter Tetrazole zu 1.3.4-Ox Diazolen. *Angew Chem* 70:272–273
31. Huisgen R, Sauer J, Sturm HJ et al (1960) Ringöffnungen der Azole, II. Die Bildung von 1.3.4-Ox Diazolen bei der Acylierung 5-substituierter Tetrazole. *Chem Ber* 93:2106–2124
32. Zaidi SMJ, Chen SF, Mikhailenko SD et al (2000) Proton conducting membranes based on polyoxadiazoles. *J New Mater Electrochem Syst* 3:27–32
33. Hibsham C, Cornelius CJ, Marand E (2003) The gas separation effects of annealing polyimide-organosilicate hybrid membranes. *J Membr Sci* 211:25–40
34. Wind JD, Bickel CS, Paul RD et al (2003) Solid-state covalent cross-linking of polyimide membranes for carbon dioxide plasticization reduction. *Macromolecules* 36:1882–1888
35. Matyjaszewski K (ed) (1996) Cationic polymerizations: mechanisms, synthesis, and applications. Marcel Dekker, New York
36. Daletou MK, Kallitsis JK, Voyatzis G et al (2009) The interaction of water vapors with H₃PO₄ imbed electrolyte based on PBI/polysulfone copolymer blends. *J Membr Sci* 326:76–83
37. Daletou MK, Geormezi M, Vogli E et al (2014) The interaction of H₃PO₄ and steam with PBI and TPS polymeric membranes. A TGA and Raman study. *J Mater Chem A* 2:1117–1127
38. Bhatnagar A, Sharma PK, Kumar N (2011) A review on “Imidazoles”: their chemistry and pharmacological potentials. *Int J PharmTech Res* 3:268–282
39. Ma YL, Wainright JS, Litt MH et al (2004) Conductivity of PBI membranes for high-temperature polymer electrolyte fuel cells. *J Electrochem Soc* 151: A8–A16
40. He R, Che Q, Sun B (2008) The acid doping behavior of polybenzimidazole membranes in phosphoric acid for proton exchange membrane fuel cells. *Fiber Polym* 9:679–684
41. Schechter A, Savinell RF (2002) Imidazole and 1-methyl imidazole in phosphoric acid doped polybenzimidazole, electrolyte for fuel cells. *Solid State Ionics* 147:181–187
42. Daletou MK, Kallitsis J, Neophytides S (2011) Materials, proton conductivity and electrocatalysis in high temperature PEM fuel cells. In: Vayenas C (ed) *Interfacial phenomena in electrochemistry*, vol 51, *Modern aspects of electrochemistry*. Springer, New York, pp 301–368
43. Wainright JS, Wang JT, Weng D et al (1995) Acid-doped polybenzimidazoles: a new polymer electrolyte. *J Electrochem Soc* 142:L121–L123
44. Samms SR, Wasmus S, Savinell RF (1996) Thermal stability of proton conducting acid doped polybenzimidazole in simulated fuel cell environments. *J Electrochem Soc* 143:1225–1232
45. Kreuer KD, Paddison SJ, Spohr E et al (2004) Transport in proton conductors for fuel-cell applications: simulations, elementary reactions and phenomenology. *Chem Rev* 104:4637–4678
46. He R, Li Q, Xiao G et al (2003) A study of water adsorption and desorption by a PBI-H₃PO₄ membrane electrode assembly. *J Membr Sci* 226:169–184
47. Lobato J, Cañizares P, Rodrigo M et al (2007) PBI-based polymer electrolyte membranes fuel cells: temperature effects on cell performance and catalyst stability. *Electrochim Acta* 52:3910–3920
48. Galbiati S, Baricci A, Casalegno A et al (2012) Experimental study of water transport in a polybenzimidazole-based high temperature PEMFC. *Int J Hydrogen Energy* 37:2462–2469
49. Li Q, He R, Jensen JO et al (2004) PBI-based polymer membranes for high temperature fuel cells—preparation, characterization and fuel cell demonstration. *Fuel Cells* 4:147–159
50. Gu T, Shimpalee S, Van Zee JW et al (2010) A study of water adsorption and desorption by a PBI-H₃PO₄ membrane electrode assembly. *J Power Sources* 195:8194–8197
51. Schmidt TJ, Baurmeister J (2008) Imidazole and 1-methyl imidazole in phosphoric acid doped polybenzimidazole, electrolyte for fuel cells. *J Power Sources* 176:428–434
52. Schechter A, Savinell RF, Wainright JS et al (2009) ¹H and ³¹P NMR study of phosphoric acid-doped polybenzimidazole under controlled water activity. *J Electrochem Soc* 156:B283–B290
53. Li Q, He R, Berg RW et al (2004) A study of water adsorption and desorption by a PBI-H₃PO₄ membrane electrode assembly. *Solid State Ionics* 168:177–185
54. Li Q, Hjuler HA, Bjerrum NJ (2001) Phosphoric acid doped polybenzimidazole membranes: Physicochemical characterization and fuel cell applications. *J Appl Electrochem* 31:773–779
55. Lister S, McLean G (2004) PEM fuel cell electrodes. *J Power Sources* 130:61–76
56. Daletou MK, Paloukis F, Stefopoulos A (2009) Pt/modified MWNT as electrocatalysts for high temperature Fuel Cells. *ECS Trans* 25:1915–1924
57. Orfanidi A, Daletou MK, Neophytides S (2011) Preparation and characterization of Pt on modified multi-wall carbon nanotubes to be used as electrocatalysts

- for high temperature fuel cell applications. *Appl Catal B Environ* 106:379–389
58. Orfanidi A, Daletou MK, Sygellou L et al (2013) The role of phosphoric acid in the anodic electrocatalytic layer in high temperature PEM fuel cells. *J Appl Electrochem* 43:1101–1116
59. Avgouropoulos G, Papavasiliou J, Daletou MK et al (2009) Reforming methanol to electricity in a high temperature PEM fuel cell. *Appl Catal B Environ* 90:628–632
60. Advanced Energy Technologies S.A.—Advent S.A. <http://www.advent-energy.com/>
61. Schmittinger W, Vahidi A (2008) Imidazole and 1-methyl imidazole in phosphoric acid doped polybenzimidazole, electrolyte for fuel cells. *J Power Sources* 180:1–14

Dirk Henkensmeier and David Aili

6.1 Introduction

The purpose of this chapter is to introduce common methods used for characterization of membranes, especially of polybenzimidazole (PBI) derivative based membranes. Initially we planned also to provide detailed standard procedures for each method, but quickly decided that while some standards need to be maintained, each lab will need adjustments, e.g., where parameters vary based on the used equipment or material. We hope that this text will be a good guidance for newcomers, will raise awareness of the scopes and limitations of the discussed methods, and will help researchers to develop or improve their own standard procedures.

To get reproducible values and data for statistical calculations, multiple samples should be

analyzed wherever possible. The given drying times should be considered as a rule of thumb, which will give reasonably accurate values. The best guideline is to dry until constant weight is reached, because drying processes depend on several factors, including the membrane thickness.

6.2 Molecular Weight of PBI

6.2.1 Definitions

A distinguishing characteristic of polymeric materials is their molecular weight (g mol^{-1}). The number of repeat units in a macromolecular chain is termed the degree of polymerization (DP). For a polymer consisting of repeat units of the relative molecular mass M_{PRU} , the molecular weight is defined as $M = \text{DP} \times M_{\text{PRU}}$. Techniques more commonly used for the determination of molecular weights of polymers include osmometry, light scattering, and ultracentrifugation, although titration (end-group analysis), cryoscopy, and ebulliometry are also used in some applications. As the molecular weight values obtained vary to a large extent with the measuring methods, there are different definitions of the molecular weight. In general, an average molecular weight is expressed by (6.1), where N_i is the number of macromolecules having a molecular weight of M_i .

D. Henkensmeier (✉)
Fuel Cell Research Center, Korea Institute of Science
and Technology, Hwarangro 14gil5, Seongbukgu, Seoul
02792, South Korea
e-mail: henkensmeier@kist.re.kr

D. Aili
Proton Conductors Section, Department of Energy
Conversion and Storage, Technical University of
Denmark, Kemitorvet 207, Kgs., Lyngby 2800, Denmark
e-mail: larda@dtu.dk

$$\bar{M} = \frac{\sum_{i=1}^N N_i M_i^\alpha}{\sum_{i=1}^N N_i M_i^{\alpha-1}} \quad (6.1)$$

For $\alpha = 1$ the number average molecular weight \bar{M}_n is obtained from (6.2).

$$\bar{M}_n = \frac{\sum_{i=1}^N N_i M_i}{\sum_{i=1}^N N_i} \quad (6.2)$$

Methods that depend on end-group analysis or colligative properties (freezing-point depression, boiling-point elevation, osmotic pressure) can be employed to determine \bar{M}_n .

For $\alpha = 1$, the weight average molecular weight \bar{M}_w is thus obtained from (6.3), and usually determined by light scattering or ultracentrifugation.

$$\bar{M}_w = \frac{\sum_{i=1}^N N_i M_i^2}{\sum_{i=1}^N N_i M_i} \quad (6.3)$$

The ratio between the weight average molecular weight and the number average molecular weight is called polydispersity index (PDI), as given by (6.4). For synthetic polymers $\bar{M}_w > \bar{M}_n$, which implies that $\text{PDI} > 1$.

$$\text{PDI} = \frac{\bar{M}_w}{\bar{M}_n} \quad (6.4)$$

6.2.2 Viscosity

The most convenient method for routinely determining molecular weights is to measure the viscosity of a polymer containing solution. This is not an absolute method and it should thus be used in combination with one of the techniques measuring the absolute molecular weight.

The molecular weight of PBI strongly influences the membrane properties and the lifetime of the membrane electrode assembly (MEA), as shown by Yang et al. [1]. Due to the poor solubility of PBI in common solvents such as tetrahydrofuran (THF) or acetonitrile, the most common method to evaluate the molecular weight of PBI is to measure the viscosity dissolved in 96 % sulfuric acid. Care needs to be taken not to heat sulfuric acid-based PBI solutions and not to store them for a long time, to avoid possible side reactions like sulfonation or cross-linking. Also, viscosity depends on temperature, and a strict control of the temperature is necessary. Impurities like dust should be removed by filtration.

To obtain the molecular weight from viscosity measurements, PBI is dissolved in concentrated sulfuric acid to give a solution with a solid content in the range of typically 2–5 g L⁻¹. The viscosity of polymer solutions is usually measured with an Ubbelohde viscometer. To prepare for the measurement, the solution is first sucked through a capillary into a reservoir. During the measurement, the solution is allowed to flow back through the capillary and the flow time of the upper solution level between two marks on the capillary is noted.

The relative viscosity (η_{rel}) and the specific viscosity (η_{sp}) should be determined at different polymer concentrations according to (6.5) and (6.6), respectively, where t and t_0 are the flow time of the polymer solution and pure solvent, respectively.

$$\eta_{\text{rel}} = t/t_0 \quad (6.5)$$

$$\eta_{\text{sp}} = (t - t_0)/t_0 \quad (6.6)$$

The specific viscosities are measured for a series of polymer solutions of varied polymer concentrations, which can easily be done by diluting the initial polymer solution. The obtained specific viscosities are then divided by the respective concentration, to give the reduced viscosity (η_{red}). As can be seen from (6.7), the intrinsic viscosity (η_{IV}) of the polymer solution is

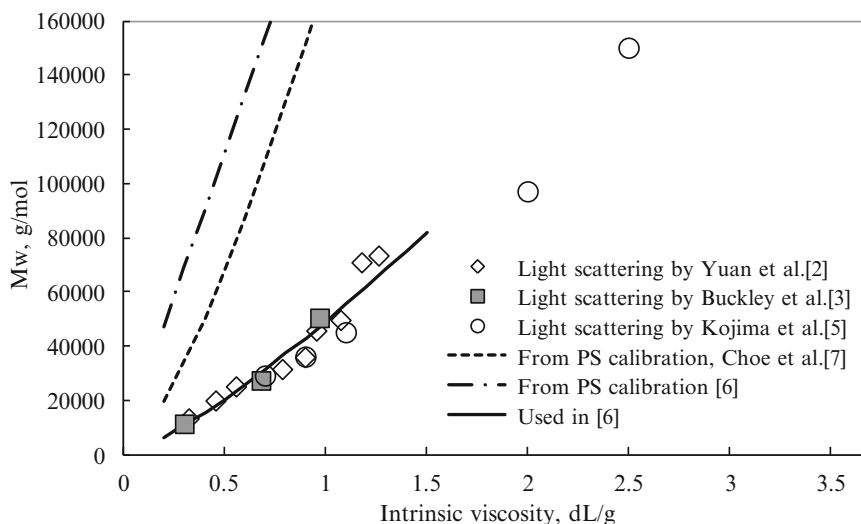


Fig. 6.1 The relation between intrinsic viscosity and polymer molecular weight. Reproduced from [6] with permission of John Wiley and Sons

obtained by plotting the reduced viscosity against the polymer concentration (c) and extrapolating to zero concentration.

$$\eta_{\text{red}}[\text{mL/g}] = \frac{\eta_{\text{sp}}}{c} = \eta_{\text{IV}} + k \cdot \eta_{\text{IV}}^2 \cdot c \quad (6.7)$$

Alternatively the intrinsic viscosity (η_{IV}) can be estimated from a single point measurement by using (6.8), which showed more than 99 % accuracy at relatively low concentrations [2].

$$\eta_{\text{IV}}[\text{dL/g}] = (\eta_{\text{sp}} + 3 \ln(1 + \eta_{\text{sp}}))/4c \quad (6.8)$$

The weight averaged molecular weight (\overline{M}_w) can subsequently be obtained from the Mark–Houwink expression as shown in (6.9), where K and α are the empirical Mark–Houwink constants, depending on the molecular weight range and molecular weight distribution.

$$\eta_{\text{IV}} = K \times \overline{M}_w^\alpha \quad (6.9)$$

Mark–Houwink constants of $K = 1.94 \times 10^{-4}$ dL g $^{-1}$ and $\alpha = 0.791$ can be extracted from light scattering data published by Buckley et al. [3, 4]. Mark–Houwink constants of $K = 4.7 \times 10^{-4}$ dL g $^{-1}$ and $\alpha = 0.93$ were published by

Yuan et al. [2], based on PBI of a molecular weight between 13,200 and 70,800 g mol $^{-1}$ and a PDI of less than 2, obtained by fractionation with DMF at 152 °C. Light scattering and viscosity of PBIs up to the very high molecular weight of 230,000 g mol $^{-1}$ were measured by Kojima et al. [5]. As shown in Fig. 6.1, the three sets of the constants agree to a satisfactory extent within the low intrinsic viscosity range <1.5 dL g $^{-1}$.

Since the determination of the molecular weight strongly depends on the way it is measured, often only the inherent viscosity (η_{inh}) of PBI derivatives is reported. It can be obtained from the relation in (6.10).

$$\eta_{\text{inh}} = \ln(\eta_{\text{rel}})/c \quad (6.10)$$

This can be obtained from a single point measurement, but the used concentration should be specified. The inherent viscosity is especially useful to compare the degree of polymerization of different polymer batches, either as quality control or as a means to find the optimum polymerization conditions. Typical conditions are a temperature of 30 °C, a polymer solution with a solid content of 2 g L $^{-1}$ and a Cannon Ubbelohde viscometer with a 200 μm capillary [8].

6.2.3 Size Exclusion Chromatography

Size exclusion chromatography (SEC), which is also called gel permeation chromatography (GPC), is a method to separate macromolecules with respect to size. As the names already suggest, a polymer solution passes a column filled with a porous gel phase. The pore size in that gel phase varies from, say, 10–100 nm. When a polymer solution passes through the column the individual polymer molecules are separated according to their hydrodynamic radius. The underlying principal is that smaller molecules can enter the pores of the gel phase easier than larger polymer chains, leading to retention of smaller molecules and fast elution of the higher molecular weight macromolecules. At the end of the column, one or two detectors continuously record, e.g., the refractive index (RI) or the ultraviolet (UV) spectrum of the passing solution.

In brief, SEC is a method giving rapid access to the weight distribution (e.g., single or binodal distribution), number and weight average molar mass and thus the PDI. Measurements can be carried out using very small amounts of polymer (e.g., 30 μL injection volume at a concentration of 3 mg mL^{-1}). Figure 6.2 shows the molecular weight distribution for a PBI-based copolymer obtained from SEC measurements.

In order to correlate the elution time with the molecular weight, calibration with polymers of a known, narrow molecular weight distribution is necessary. Most researchers calibrate the column against commercial standards (e.g., polystyrene or poly(methyl methacrylate) (PMMA)), which can be prepared with a narrow molecular weight distribution by living polymerization. Special care should be taken with this calibration. A large deviation is expected because the polarity of, e.g., PS and PBI is so different that different eluents should be used in their SEC measurements. Furthermore, the hydrodynamic radius of the investigated polymer in the chosen solvent system is always different from that of the calibration standard. Another practical issue is that the polymer solutions need to be free from impurities to prevent clogging, and filtration through 0.45 μm PTFE syringe filters may in some cases slightly influence the sample composition.

It should be remarked that the literature work on the SEC analysis has been conducted under very much varied conditions. Table 6.1 gives a few examples. In these works, the system was calibrated against polystyrene or PMMA standards, and the eluents contained lithium salts to prevent PBI agglomeration. The reader should keep this in mind when a comparison of the results is done.

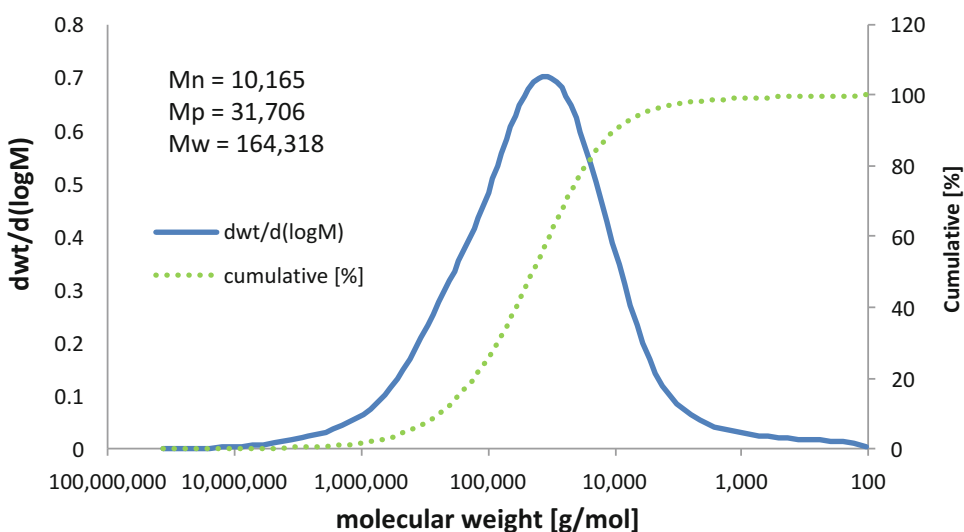


Fig. 6.2 Molecular weight distribution for a PBI-based copolymer obtained from SEC measurements [9]

Table 6.1 Conditions for SEC analysis of PBI derivatives

Polymer	Solvents and other experimental details	Reference
<i>meta</i> -PBI	DMAC + 0.5 wt% LiCl; 40 °C; RI as detector; two columns having a pore size range from 102 to 106 Å; flow rate of 0.2 mL min ⁻¹	[6]
Sulfonated PBI block-copolymer	DMSO/DMF (1/10) mixture; eluent: 0.01 mol L ⁻¹ LiBr DMF solution; UV as detector; column: Shodex KF-805 and Shodex SB-803HQ	[10]
<i>meta</i> -PBI and <i>N</i> -alkylated <i>meta</i> -PBI	0.5 wt% LiBr in NMP; 70 °C; UV and RI as detector; column: GRAM 100 and 1000 Å columns (PSS, Mainz, Germany); flow rate: 0.8 mL min ⁻¹	[11]
<i>meta</i> -PBI and <i>N</i> -alkylated <i>meta</i> -PBI	0.5 wt% LiBr in DMSO; 70 °C; UV and RI as detector; column: 2 PSS GRAL LIN columns; flow rate: 1.0 mL min ⁻¹	[11]
Sulfonated PBI derivative	0.01 mol L ⁻¹ LiBr in DMF; 70 °C; column: mixed 10 μm PS column with a length of 750 mm; flow rate: 1.0 mL min ⁻¹	[12]
PBI copolymer	0.05 mol L ⁻¹ LiBr in NMP; 45 °C; RI as detector; column: 2 TSKgel Alpha-M columns (Tosoh Bioscience); flow rate: 1.0 mL min ⁻¹	[9]

The reader is referred to the original work for further experimental details and complete polymer structures

6.3 Water and Phosphoric Acid Uptake

6.3.1 Water Uptake of Pristine PBI Membranes

PBI derivatives are well known to be highly hydrophilic. The water uptake from the liquid phase can be obtained by submerging a pristine membrane in distilled water. After a certain period of time, typically a few days at room temperature, the membrane is taken out of the water, quickly blotted with a tissue, and weighed immediately. Theoretically it should not matter if the wet or dry weight is obtained first. However, PBI membranes produced by solution casting may still contain some organic solvent, which cannot be removed completely by drying unless very high temperatures are applied, but which may leach out in contact with liquid water. In connection to all the weight measurements of membranes it is thus a general good practice to ensure that the membrane is free from residual organic solvents (e.g., dimethylacetamide, DMAC) and other impurities such as stabilizers (e.g., LiCl).

To determine the water uptake of a pristine membrane from the vapor phase at different humidities and room temperature, a membrane

sample can be suspended above a LiCl aqueous solution in a closed vessel. The relative humidity of the atmosphere above a lithium chloride solution versus the concentration is well defined and known [13]. More than 10 days have been suggested to reach equilibrium.

The water uptake (WU) of a membrane is often reported in percent and defined on the dry polymer basis and calculated by comparing the dry weight (W_{dw}) and the wet weight (W_{ww}) of a membrane according to (6.11)

$$\text{WU} [\%] = 100 \cdot (W_{\text{ww}} - W_{\text{dw}}) / W_{\text{dw}} \quad (6.11)$$

6.3.2 Phosphoric Acid Uptake

When membranes are doped by immersion in an aqueous phosphoric acid (PA) solution the weight gain is due to both acid and water uptake. To distinguish between the contributions to the weight gain from water and acid, the membrane should be dried (e.g., at 110 °C for at least 5 h in vacuo [14]). This process is assumed to remove all the water, and the remaining PA is considered as 100 % PA. According to Majerus et al. [15], further dehydration of phosphoric acid is slowed down by interactions with the polymer chains, and the thermogravimetric analysis (TGA) curve of PA doped ABPBI shows a plateau between

90 and 110 °C. If the weight fraction of the polymer is not known, the membranes need to be de-doped to obtain the polymer content (W_{PBI}). The de-doping can be achieved by immersion of the doped membranes in a large amount of water followed by drying in vacuo at 110 °C [16]. A few hours may be needed under stirring at room temperature or with gentle heating, preferably in dilute alkaline solutions such as aqueous NaOH or NH_4OH [17]. Alternatively the phosphoric acid and water content of PA-doped membranes can be determined by titration with NaOH [16, 18]. In order to determine the acid uptake by titration, PA is first leached out by immersion of the doped membrane in (warm) water [16]. The water is then titrated with aqueous NaOH and the PA doping level can be calculated based on the volume and concentration of spent titrer.

In analogy with the water uptake, the acid uptake (AU) of a membrane is often given in percent on the dry polymer basis as the ratio between the phosphoric acid content (W_{PA}) and the PBI content (W_{PBI}) of the membrane (6.12).

$$\text{AU} [\%] = 100 \cdot W_{\text{PA}}/W_{\text{PBI}} \quad (6.12)$$

Sometimes the amount of acid is also reported as the acid content (AC) on the doped membrane basis according to (6.13).

$$\text{AC} [\%] = 100 \cdot W_{\text{PA}}/(W_{\text{PBI}} + W_{\text{PA}}) \quad (6.13)$$

The term acid doping level (ADL) is widely used and is defined as the number of phosphoric acid molecules per polymer repeat unit and can be calculated according to (6.14), where M_{PBI} is the molar mass of the polymer repeat unit and M_{PA} is the molar mass of PA.

$$\text{ADL} = (W_{\text{PA}}/M_{\text{PA}})/(W_{\text{PBI}}/M_{\text{PBI}}) \quad (6.14)$$

The term ADL allows for a direct comparison of the phosphoric acid content of polymers of the same type. However, since the molar mass of the polymer repeat unit varies with its structure, it does not allow for a direct comparison of the phosphoric acid content for structurally different polymers. It should also be remembered that any incomplete extraction of the acid would lead to underestimation of the ADL.

6.3.3 Dimensional Changes

The water and phosphoric acid uptake cause dimensional changes of the membrane (swelling). The swelling is normally calculated on the dry undoped membrane volume basis according to (6.15), where V_{undoped} and V_{doped} are the volume of the undoped and doped membrane, respectively.

$$\text{Swelling} [\%] = 100 \cdot (V_{\text{doped}} - V_{\text{undoped}})/V_{\text{undoped}} \quad (6.15)$$

The volume of the undoped (usually of the fully dried membrane) and doped membrane can readily be calculated from the dimensional changes of the membrane. The dimensional changes of a membrane can be divided into the length, width, or thickness (for linear swelling), the area (for two dimensional swelling) or volume (for three dimensional swelling). At the first glance, the linear expansion in x , y and z direction should be the same, however, this is not always the case. One reason for anisotropic swelling is that extruded membranes have a machine and a transverse direction, and the polymer chain orientation is preferably in the machine direction. A similar effect may also be observed if an initially isotropic membrane is stretched during processing, e.g., in roll-to-roll processes like drying or cutting. Care must also be taken that swollen, soft membranes are not indented during the thickness measurement. This risk can be reduced by equipping the thickness gauge with an appropriately broad tip or by sandwiching the membrane between sheets of a support material.

6.4 Conductivity

6.4.1 Definitions and Equations

Proton conductivity, the ability of a material to pass an electric current by the movement of protons, is one of the key characteristics of phosphoric acid doped PBI. The opposition of the material to the passage of current is called resistance, which is measured from the voltage loss

(V) across the material upon the current passage. For an object with a uniform cross-section, for example a strip of a film, its resistance (R) is proportional to its resistivity (ρ) and length (L) and inversely proportional to its cross-sectional area (A) by Pouillet's law (6.16).

$$R [\Omega] = \rho \frac{L}{A} = \frac{1}{\sigma} \cdot \frac{L}{A} \quad (6.16)$$

Here σ is the conductivity or the reciprocal of the resistivity, having a unit of $\text{ohm}^{-1} \text{cm}^{-1}$ or more commonly S cm^{-1} . In electrochemical devices, the area-specific resistance (ASR, ohm cm^2) of a flat sheet membrane electrolyte is of engineering importance and can be expressed as the product of the resistance and the surface area, or as the ratio between the thickness and the conductivity. The ASR is directly proportional to the voltage loss (V) of the electrolyte at the current density i (A cm^{-2}), because $V = \text{ASR} \times i$. The expression of the thickness to conductivity ratio indicates that high conductivity (σ) and small electrolyte thickness (L) lead to a low cell resistance.

6.4.2 Conductivity Cells

The accuracy of conductivity measurements can be influenced by several factors including polarization, sample dimensions, contact point resistance, cable/wire resistance or capacitance, and most importantly temperature and humidity (particularly for proton conductivity).

For the conductivity measurement, applying a current through the electronically conducting electrodes to the ionically conducting membrane causes a polarization at the interface due to the concentration changes of active species. Any polarization resistance arising at the electrode surface leads to erroneous results as it is a parasitic component to the resistance. One way to eliminate the polarization effect is to introduce two reference electrodes through which the voltage signals are measured. As there is no current flowing through these reference electrodes, no polarization is developed or included in the measurement. The electrode and membrane geometries for the four-probe method are shown in Fig. 6.3. In analogy to a potentiostat,

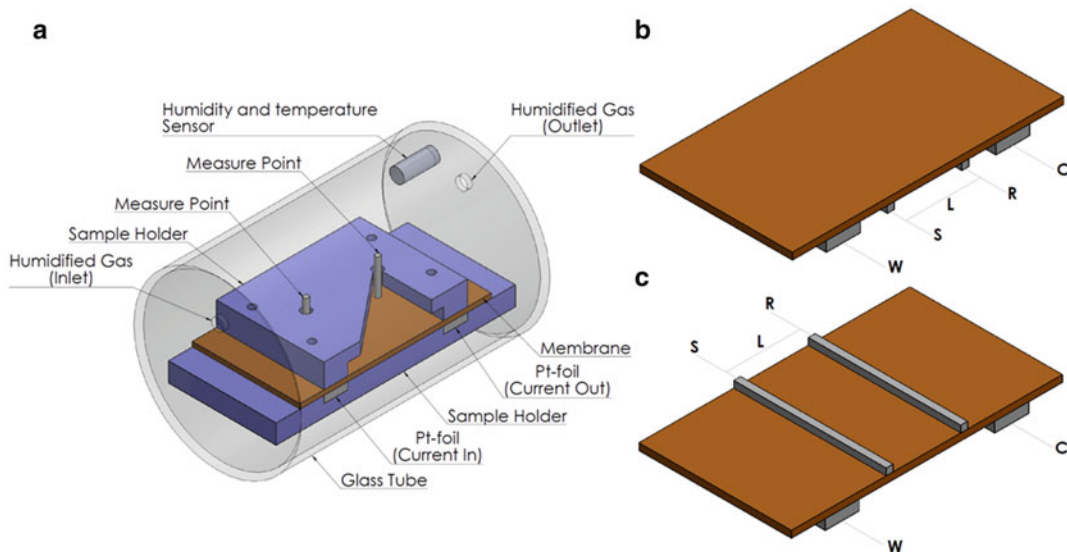


Fig. 6.3 Construction of a four-probe conductivity cell (a) and electrode assembling for in-plane (b) and mixed in-plane and through plane (c) conductivity measurements

the two current supplying electrodes are marked as working (W) and counter (C) while the other two for voltage measurements are marked as reference (R) and sense (S) electrodes. When all four electrodes are located on the same side of the membranes (Fig. 6.3b) the resistance is recorded in the plane of the membrane. When the current supplying electrodes (W and C) and voltage measuring (R and S) electrodes are located on the opposite sides of the membranes (Fig. 6.3c), the resistance is measured in-plane, but reduces the risk of surface effects. For through-plane conductivity measurements, W and R are placed on one side of the membrane and C and S on the other.

A four-probe conductivity cell is schematically represented in Fig. 6.3a. Here, the membrane is fixed between two sample holders. The upper one is made of glass and shows two holes for the potential sensing electrodes (R and S). The distance between the two platinum electrodes is 1 cm. The lower sample holder contains two platinum bands as current supplying electrodes (C and W). The cell is assembled into a glass tube, which has two endplates through which electrical connections and humidified air inlet and outlet are fixed with gas tight seals. The whole cell is kept in an oven for temperature control. Some groups also use platinum tips in a vertical arrangement instead of horizontal wires as potential electrodes [19].

In such measurements, it is assumed that the current is homogeneously distributed throughout the entire membrane cross-section. Any membrane inhomogeneity is problematic.

For PA-doped membranes, a thin liquid film may be formed at high humidities at temperatures around or below 100 °C at atmospheric pressure. In this case the measured conductivity is mainly from the highly conductive surface layer. Mixed in-plane/through-plane assembling minimizes this risk to some extent.

Alternatively the through-plane conductivity is often measured with two-electrode cells. The cell can be similar to a fuel cell where the membrane is sandwiched between two electrodes. The electrodes typically consist of platinum disks or a gas diffusion electrode covering the entire membrane area. The latter allows to measure conductivity under varied atmospheric humidities, but with longer equilibration times than for in-plane cells. For these cells, it is critical to minimize the polarization effect, which can be sufficiently achieved by using a high frequency alternating current, as to be discussed below. A hydrogen flow, as a humidification carrier gas, is recommended on both electrode chambers, because its high electrochemical reversibility further reduces the polarization. Figure 6.4 schematically shows the effect of the uncovered part of the membrane at the edge of the active electrode area. Any mismatching of the electrodes will have a similar effect, i.e., leading to current along the membrane thickness direction.

The contact resistance in the cell is a major source of error for through-plane measurements, and should be registered for each type of material by a series of measurements with membranes of different thickness. A plot of the measured

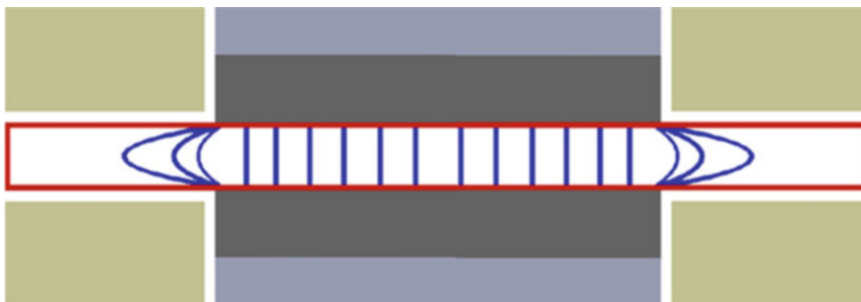


Fig. 6.4 Membrane electrode assembly and current distribution at the membrane edge

resistance against the membrane thickness allows one to obtain the contact resistance (y-axis intercept) and the membrane resistance (slope). Assuming that the resistance between two membrane layers is negligible, also stacks of membrane samples can be used instead of samples with different thickness. Obviously care must be taken to avoid gas bubbles between the layers, which would be insulating and increasing the thickness.

In general for conductivity measurements, two types of alternating current are used, i.e., the square wave current (also called direct current interruption) or electrochemical impedance spectroscopy (EIS). For EIS, the AC frequency is often in a range from 0.1 to 1 MHz down to 1–10 Hz. A more detailed discussion on these techniques is not attempted in this chapter. In theory, the high-frequency intercept with the real impedance axis in a Nyquist plot gives the ohmic resistance. Often, however, also the low frequency intercept gives the resistance, due to other overlaying effects. Alternatively, the ohmic resistance can be measured using a current interruption technique in which a high-frequency symmetric square wave current is supplied to the outer electrodes. The voltage drop between the inner electrodes can be measured using an oscilloscope. The technique can preferably be used in parallel to the AC technique, since it provides information that facilitates the interpretation of the impedance data.

To some extent, conductivity measurements in a through-plane cell depend on the compressive forces on the membranes, and it is recommended to adjust the pressure to a fixed value by using a torque meter. The contact pressure should be enough to guarantee a good contact, but should also be as low as possible. With increasing temperature, dimensions of the membrane samples will change due to thermal expansion, which is expected to have opposite influences on the conductivity of the two types of cells. As little information is available for the membrane thermal expansion, this effect is generally ignored and the conductivity is calculated from the measured resistance using the initial room temperature dimensions. The atmospheric

humidity should be carefully controlled and well specified in measurements of conductivity as well as other properties.

6.4.3 Temperature Dependence and Activation Energy

Conduction of protons is an activated process and the temperature dependence of the conductivity follows the Arrhenius equation as show in (6.17), where E_a is the activation energy for the proton conduction, R the gas constant, T is the absolute temperature, and A is the pre-exponential coefficient.

$$\sigma = A \exp\left(-\frac{E_a}{RT}\right) = \frac{\sigma_0}{T} \exp\left(-\frac{E_a}{RT}\right) \quad (6.17)$$

Physically the proton conductivity is influenced by the concentration of proton carriers and their mobility. In some cases, the temperature dependency may be more complex and cause deviation from the linear relationship obtained by plotting the natural logarithm of the conductivity ($S \text{ cm}^{-1}$) against the inverse absolute temperature [1000 K^{-1}] in an Arrhenius plot. For example, at temperatures above, say 180–200 °C, the resistance of PA-doped membranes increases due to condensation of phosphoric acid to acid anhydrides and ultimately to polyphosphoric acid. From the slope of the linear fit, the activation energy for proton conduction can be obtained. For PA-doped PBI membranes with an ADL above 5, the E_a values are found to be between 20 and 30 kJ mol^{-1} , which is in a typical range for the Grotthuss hopping mechanism. A better linearity is observed by plotting $T\sigma$ versus T^{-1} .

6.5 Solubility and Gel Contents

6.5.1 Solubility

Polymers typically need more time to dissolve than low molecular weight compounds, and often show strong swelling before complete

dissolution. Therefore, polymer powders or particles should be added to the solvent to avoid aggregation, which often slows down dissolution when the solvent is added to polymer powder or pellets. Polymer solubility can also be strongly affected by the degree of crystallinity and the presence of additives or impurities, even water.

Good solvents for PBI are polar aprotic solvents such as *N,N*-dimethylacetamide (DMAc), *N*-methyl-2-pyrrolidone (NMP) or dimethylsulfoxide (DMSO), and strong protic acids like phosphoric acid, sulfuric acid (risking sulfonation reactions), or methanesulfonic acid. In order to dissolve PBI in organic solvents, great care must be taken to remove all phosphoric acid traces from the polymer, since it strongly hinders dissolution in DMAc.

For processing of PBI, it is often dissolved in DMAc. Especially at a high PBI content, e.g., >20 wt%, formation of agglomerates reduces the shelf life of the solution, as indicated by an increase in solution viscosity and resin precipitation. Therefore, a small amount of LiCl (i.e., 1.5 wt%) may be added as stabilizer [20, 21]. Thin films prepared from such solutions can be washed to remove LiCl by immersion in water at 85 °C for 1 h [22]. To speed up the PBI dissolution, increased temperatures are often necessary. In some cases also pressure reactors are used to increase the temperature up to over 260 °C [23]. At these conditions, the water content of the polymer must be reduced by drying at >70 °C in vacuo and the water content of DMAc should be lower than 0.03 %, to avoid hydrolysis of the solvent. It was also reported that the solubility is reduced by the presence of oxygen, and an inert atmosphere (nitrogen or argon) was recommended [23].

6.5.2 Filtration of PBI Solutions

To get defect-free membranes, organic solvent-based polymer solutions should be filtered before casting. For large volumes, a glass filter or membrane filter can be used. For smaller volumes (<50 mL) the losses may be too high, and filtration through a syringe filter (0.45 μm)



Fig. 6.5 Simple apparatus for filtration of small volumes of polymer solution, based on a sealant gun, a syringe, and a syringe filter with threaded connector

with a threaded connector is the preferred method. Due to the high viscosity of polymer solutions, a high pressure needs to be maintained over a long time. There are commercial products for emptying syringes, but a cheap sealant gun from the hardware store works well enough (Fig. 6.5). However, a sufficient gap between the polymer solution and the piston should be maintained as a pressure reservoir and to prevent leakage.

6.5.3 Gel Content

Solubility properties of new polymers are often reported qualitatively, e.g., in terms of insoluble, partially soluble, soluble or very soluble and thus this kind of test is based on personal experience.

A more quantitative measure is the gel content (GC) as defined by (6.18), where W_{initial} and W_{residual} are the initial and residual weight of a polymer membrane sample before and after immersion in a solvent for a certain period of time, respectively.

$$\text{GC} [\%] = 100 \cdot W_{\text{residual}}/W_{\text{initial}} \quad (6.18)$$

A high gel content means that the membrane does not dissolve in the tested solvent. It is especially useful for the characterization of cross-linked membranes. The gel content correlates with the degree of crosslinking and the gel content can be used to compare the effectiveness of different crosslinking methods.

For both gel contents and qualitative solubility tests, membrane samples of similar thickness are immersed in the respective solvent, and kept at a fixed temperature for a fixed period of time, typically a few days. After the test, the membrane sample is dried and weighed to give W_{residual} . If the solution is stirred, care must be taken that the membrane is not hit by the stirrer to prevent mechanical degradation. For this purpose, the membrane samples can be protected by a sieve or wire mesh. In case the membrane disintegrates the solution can be filtered and the dissolved portion can be determined by evaporation of the solvent.

6.6 Mechanical Properties

6.6.1 Tensile Stress and Strain

The most common mechanical testing method for membranes is tensile testing. In these tests membrane specimens with an initial length L_0 , width w_0 and thickness d_0 are mounted between a fixed grip and a moveable grip. The force needed to stretch the material is plotted as a function of elongation to give a stress–strain curve.

When an axial force F is applied, the sample is stretched to the length L . The strain or elongation (ϵ) is defined as the gauge length of the specimen divided by its original length in percentage (100 %) or mm/mm according to (6.19).

$$\epsilon[\text{mm/mm}] = (L - L_0)/L_0 \quad (6.19)$$

Since the cross-sectional area of the sample during stretching can hardly be assessed, practically the initial dimensions are used in the calculation of the stress (engineering stress), as given by (6.20).

$$\sigma_E [\text{MPa}] = F/(w_0 \times d_0) \quad (6.20)$$

The tensile strength of a membrane is the maximum tensile stress that a sample can be subjected to before failure. Since the tensile strength is measured in units of force per unit area, it is basically a pressure and commonly expressed in pascals (Pa).

6.6.2 Tensile Testing

A standard procedure for testing thin films is given by ASTM D 882, which was developed for polymer films thinner than 1 mm. The widely used equipment for measuring mechanical properties is the universal materials strength testing machine. The standard sample geometry is that of 1 in. (2.53 cm) broad and 6 in. (15.24 cm) long rectangular stripes. However, most research groups use smaller sample sizes, e.g., 1 cm broad and 3 cm long, to reduce the amount of material. The crosshead speed is often chosen in the range of 5–10 mm min⁻¹. Some groups also chose slower initial speeds, e.g., 1 mm min⁻¹ until 1 % elongation, to get more reliable data for the Young modulus.

A typical stress–strain curve for a polymer membrane is shown in Fig. 6.6, from which the ultimate tensile strength, tensile strength at break, Young modulus, elongation at break, proportional limit stress and proportional limit strain can be extracted. The area under the curve is proportional to the overall energy needed to break the material.

The Young's modulus or elastic modulus is given by the initial slope of the linear part of the curve. This is the part of the curve, in which the dislocation of the sample is practically reversible, i.e., the elastic deformation region.

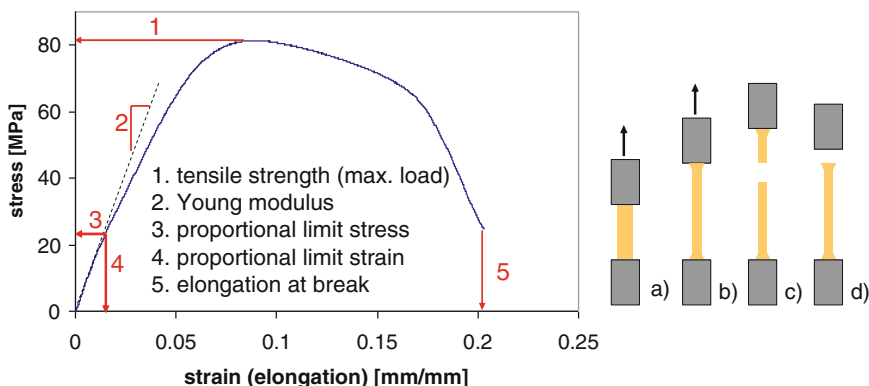


Fig. 6.6 Generic stress–strain curve of a polymer membrane; (a) membrane clamped into the testing machine at the beginning of testing, (b) during the test, (c) successful end of test, (d) failed test

The units for stress and strain should be MPa and mm/mm, respectively. While all mechanical properties give valuable information, the Young modulus correlates with the resistance to be compressed or stretched and may thus be the most important parameter in this connection.

The yield strength is often used, defined as the stress at which material strain changes from elastic deformation to permanent deformation. At this point, the proportional limit stress and strain are defined after which the curve deviates from linearity to exhibit the plastic deformation. In some cases, for example for pristine PBI membranes under dry atmosphere, the tensile strength at yield is the maximum point of the curve. For acid-doped PBI membranes where a significant plasticizing effect is present, the stress values increase further after the yield point [1], reaching the ultimate tensile strength, the peak stress on a stress–strain curve. After a period of necking, the membrane eventually ruptures. The stress on the sample at the time of rupture is called the (engineering) tensile stress at break and the strain the elongation at break.

In addition to the phosphoric acid content, the water uptake or atmospheric humidity, as well as the temperature influence the mechanical properties of membranes. These effects are shown in Fig. 6.7 where *meta*-PBI membranes were tested at 21 and 150 °C under different water activities.

It is noteworthy that most tensile test machines do not provide humidity- and temperature-controlled atmospheres, and most literature data of tensile properties are obtained without specifications of the atmospheric humidities. Therefore, it is recommended to equilibrate the samples in ambient air before the test, and to record the ambient temperature and humidity, so that data can be reproduced and compared.

The standard deviation for tensile tests can be relatively high due to microscopic defects, and the number of tested specimens should be stated. Care must be taken so that the samples are not broken at the grips (Fig. 6.6d), which would lead to irreproducible results. This can be prevented by either the use of rubber-coated grips or, if rubber-coated grips are not available, by protecting the clamped part with tape. Cracks can grow from indentations at the edge of the sample and to prevent premature failure, it is recommended to cut the sample with a sharp blade.

6.6.3 Indentation, Compression, and Creep

In the fuel cell, the membrane is clamped between the electrodes, and is subjected to strong compressive forces. To evaluate the stability of PA-doped PBI membranes, imprint tests and

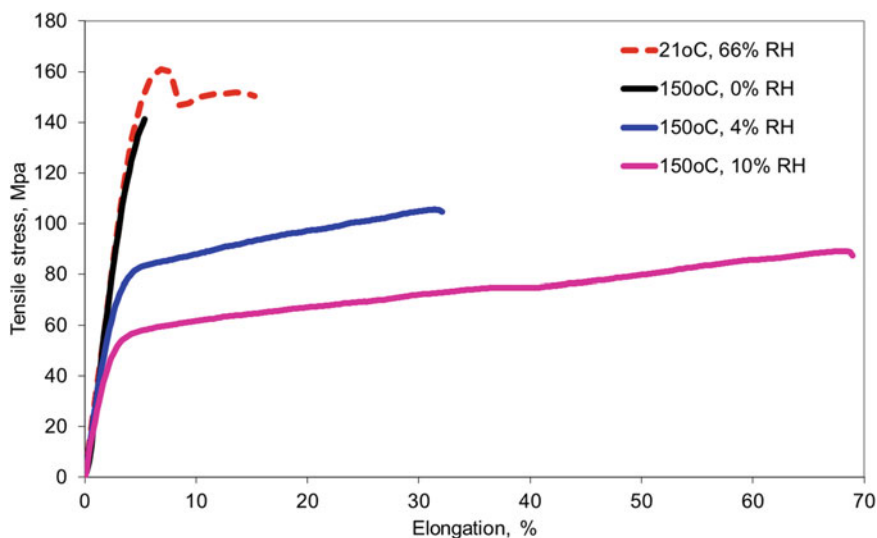


Fig. 6.7 Stress–strain curves of meta-PBI membranes ($M_w = 31,000 \text{ g mol}^{-1}$) obtained at different temperatures and atmospheric humidities

compression creep tests were developed. In static imprint tests [24], a stamp is pressed on a PA-doped membrane at a given temperature (e.g., 200 °C) and under constant load. After the test time, the depth of the imprint is measured and reported as percentage of imprint depth. This test is mainly useful for rapidly comparing the properties of different membrane materials.

In compression creep tests, a flat disk-shaped membrane sample (i.e., 6.3 mm diameter and 0.9–1.2 mm thickness) is positioned between two sample holder plates of a dynamic mechanical analyzer (DMA) [25]. The creep compliance [Pa^{-1}] is obtained by dividing the strain with the applied stress (i.e., 0.1 MPa), and is usually displayed as a plot against the testing time. The creep rate is the slope of the resulting curve. Low compliance and creep rate are characteristics for a material with good creep resistance. Molleto et al. [25] found that the conditioning of the samples is vital for reproducible results, and recommend to store the samples sandwiched between two solid blocks at 180 °C (same as the test temperature) for about 24 h prior to the measurements, to get flat samples in which the PA is well distributed.

6.6.4 Dynamic Mechanical Analysis

Dynamic mechanical analysis (DMA) is also used for measuring the glass transition temperature (T_g) and the storage and loss modulus [26, 27]. The method allows also to measure the change of mechanical properties with the temperature, either in air, or in a liquid medium. This is not easily done in universal testing machines used for tensile strength tests. In general, a small membrane sample is clamped in the machine, and a very small force is repeatedly applied to the sample. If the force (e.g., expansion as in tensile strength tests) is below the proportional limit stress, each cycle should give a reproducible polymer response without degrading the mechanical properties. The measured response of the polymer to an applied stress is strain, the expansion of the sample. When a sinusoidal changing force is applied, the extension of the sample will follow with a small time shift, the phase angle δ . The maximum strain can be used to calculate the storage modulus E' (the elastic response of the system). From E' and δ , the loss modulus E'' can be calculated according to (6.21), which can be understood as the damping,

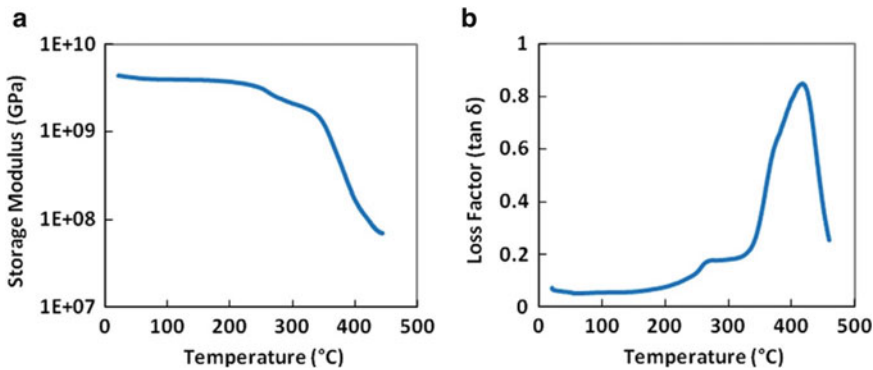


Fig. 6.8 Storage modulus and loss factor of polybenzimidazole as a function of temperature. Reproduced from [28] with permission of Elsevier

which occurs when some of the applied mechanical energy is lost, e.g., by change into internal motion (proportional to E'') or loss to the surroundings.

$$\tan \delta = E''/E' \quad (6.21)$$

When the storage modulus E' is plotted (logarithmically) against the temperature, many materials will show plateau areas (constant modulus) and areas where the modulus changes (see Fig. 6.8a). The latter areas are assigned to phase transitions, e.g., to the T_g . For reproducibility, it is necessary to state how the T_g is obtained from the curve, some workers use the onset of decreasing modulus, some use the point of the most negative slope. The T_g can also be obtained by a plot of $\tan \delta$ against the temperature. This gives a peak, whose maximum can be used to describe the glass transition temperature (Fig. 6.8b). The smaller peak below 300 °C stems from the β relaxation, rotation and oscillation of side groups, while the T_g , the α relaxation, arises from movements of the polymer backbone.

6.7 Permeability, Methanol Crossover, and Electroosmotic Drag

Because of PBI's rigid structure and high degree of hydrogen bonding, PBI membranes have a close chain packing, leading to a density of

1.34 g cm^{-3} and very low gas permeability. When doped with acid, however, the membranes are swollen, resulting in a significant separation of the polymer backbones. This significantly increases the gas permeability and liquid crossover. Different techniques have been developed for the characterization.

6.7.1 Gas Permeabilities

The gas permeability of membranes can be measured by means of a two-chamber cell, as shown in Fig. 6.9. The two chambers have different pressures of up to 10 bar, and are separated by a membrane sample, which is supported by porous carbon or metallic mesh and sealed by, e.g., Viton[®] gaskets [29].

The net gas permeation is from the high pressure cell to the low pressure cell. For highly permeable membranes, it is possible to measure the gas flow volumetrically. This method can also be applied to measure the gas permeability of water-swollen membranes [30]. Alternatively, the variation of pressure with time can be monitored using pressure sensors [9]. This method is particularly suitable for dry membranes, because both cells are usually evacuated before the measurement. The gas diffuses through the membrane, driven by the pressure gradient. The amount of gas passed through the membrane can be calculated from (6.22), where n is the

Fig. 6.9 The cell configuration for gas permeability measurement. Reproduced from [29] with permission of Elsevier

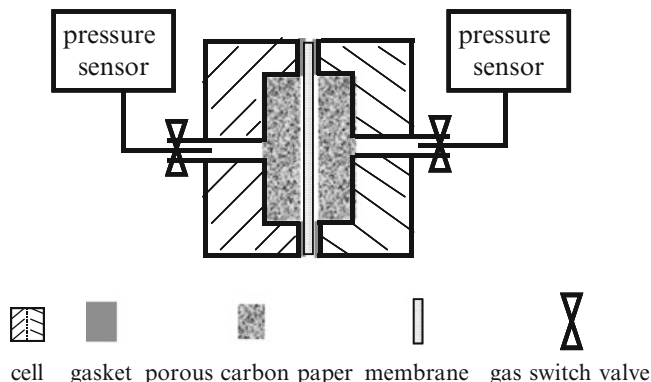


Table 6.2 Gas permeability (10^{-17} mol cm cm $^{-2}$ s $^{-1}$ Pa $^{-1}$) [29]

	H ₂ permeability				O ₂ permeability			
	25 °C	80 °C	120 °C	180 °C	25 °C	80 °C	120 °C	180 °C
Nafion	4.1	15.7	–	–	2.8	3.1	–	–
PBI	–	1.6	3.0	4.3	–	0.05	0.06	0.1
PBI-6 H ₃ PO ₄	–	120	250	380	–	30	70	90

mole number, Δp is the pressure difference, R is the gas constant, T is the absolute temperature, and V is the cell volume.

$$n = \frac{\Delta p \cdot V}{RT} \quad (6.22)$$

The gas permeability coefficient (P) can subsequently be calculated according to (6.23), where t is the time, L is the membrane thickness, A is the membrane area, and Δp is the pressure gradient across the membrane [31]. A common unit for presenting permeability data is the Barrer, 10^{-10} cm³(STP) · cm · cm $^{-2}$ · s $^{-1}$ · cmHg $^{-1}$, STP being standard temperature (0 °C) and pressure (1 atm) [31].

$$P = \frac{n}{t} \cdot \frac{L}{A \cdot \Delta p} \quad (6.23)$$

For both undoped and PA-doped PBI, an increase of the gas permeability with temperature has been observed (Table 6.2) [29]. While pure PBI (as many other hydrocarbon-based polymers) [32] shows about ten times lower hydrogen permeability than Nafion[®], the hydrogen permeability of PA-doped PBI is roughly one order of

magnitude higher than that of Nafion[®]. Furthermore, the hydrogen permeability is usually higher than that of oxygen [29].

In addition, the permeability (P) is the product of the gas diffusion coefficient (D) and the solubility (C) of the gas in the polymer. As the gas solubility in a polymer is in a low range, Henry's law can always be assumed. The Henry's constant, also called the solubility coefficient ($k = Cp^{-1}$), is a constant over the pressure range. Here C is the solubility of the gas in the polymer and p is the pressure. From the measured permeability and Henry's constant, one can calculate the diffusion coefficient of the relevant gases.

6.7.2 Electrochemical Stripping Method for Hydrogen Permeability Measurements

When the cathode of an H₂-air fuel cell is switched from air to nitrogen or argon, the oxygen in the cathode chamber will be depleted and the open circuit voltage (OCV) decreases until a steady state is reached. At this point, the potential

is not zero because the concentration gradient drives hydrogen through the membrane to the cathode by diffusion. A concentration cell is eventually established with pure hydrogen on one side and trace hydrogen in nitrogen or argon on the other. An electromotive force is developed following the Nernst equation (6.24).

$$\text{EMF} = \frac{RT}{nF} \cdot \ln \frac{P_{\text{H}_2}^1}{P_{\text{H}_2}^2} \quad (6.24)$$

Considering $P_{\text{H}_2}^1 = 1 \text{ atm}$ and $P_{\text{H}_2}^2 = 0.001 \text{ atm}$, for example, the above equation gives an EMF of 89 mV at room temperature. In practice the hydrogen electrode is connected to the counter and reference terminals of a potentiostat while the nitrogen electrode is connected to the working electrode (and sensor as well). In a typical linear voltage sweep (LSV) experiment the potential is now increased from, e.g., 0.1 to 0.6 V (see, e.g., Fig. 17.6 in Chap. 17). More positive potentials above 600 mV versus hydrogen reference should be avoided to prevent oxidative side reactions like platinum oxidation. Below the potential of the established concentration cell, a negative current will be measured, and the cell works as a concentration cell. However, if the external potential is high enough to oxidize the trace hydrogen in the nitrogen stream, an oxidation current will be measured. This positive current depends on the hydrogen permeation rate and therefore is a function of the hydrogen partial pressure, the temperature and humidity, and ideally gives a straight line parallel to the x -axis. A positively sloped curve indicates the existence of some shorting (ohmic resistance), as discussed in Chap. 17. In practice, it happens from time to time that only negative currents are measured throughout the whole tested potential range. In this case, the cell or tubings are not perfectly sealed, and the cell still operates as a hydrogen/air fuel cell.

In most cases, a linear fit of the linear, positive part of the LSV curve to 0 V reflects well the hydrogen crossover current. However, the oxidation current under the voltage sweeping contains also contributions of the double layer charging

current, especially at high sweep rates. In principle a background current under the N_2 - N_2 mode should be measured and used for correction of the hydrogen oxidation current. Alternatively, assuming that other contributions are small in comparison to the hydrogen crossover, a constant potential of 0.4 V can be applied and the oxidation current of the permeated hydrogen is recorded as a function of time until a steady-state value is reached [33]. For most purposes, the electrochemically measured hydrogen stripping current density can be converted into the hydrogen permeability in $\text{mol H}_2 \text{ cm}^{-1} \text{ bar}^{-1} \text{ s}^{-1}$ according to (6.25), where i is the hydrogen crossover current density, L is the membrane thickness, Δp is the pressure gradient of hydrogen across the membrane, n is the number of electrons involved in the hydrogen oxidation, and F is the Faraday constant.

$$P_{\text{H}_2} = \frac{i}{nF} \cdot \frac{L}{\Delta p} \quad (6.25)$$

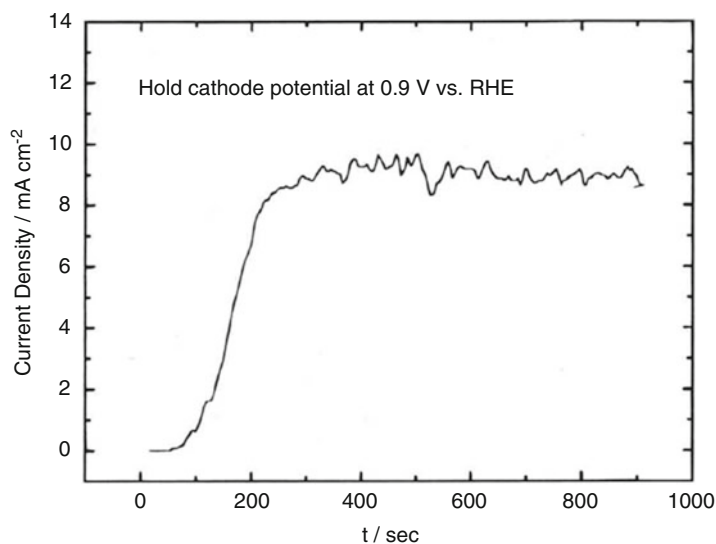
As an example, Cleemann et al. [33] obtained a value around $1.9 \times 10^{-10} \text{ mol cm}^{-1} \text{ s}^{-1} \text{ bar}^{-1}$ at room temperature for a 40 μm -thick PBI membrane doped with 8 mol PA per repeat unit.

6.7.3 Methanol Crossover

Although PA-doped PBI is mainly used for fuel cells fed with hydrogen or hydrogen rich reformat, it has also been evaluated as electrolyte material in direct methanol fuel cells. Several different procedures for determining the methanol crossover have been proposed.

Similar to the hydrogen crossover, the methanol permeability of membranes can be investigated in a fuel cell setup. The fuel cell cathode is connected to a potentiostat as the working electrode and flushed with nitrogen. The fuel cell anode is connected to the potentiostat as the counter electrode. The potential of the cathode is potentiostatically held at a high potential, e.g., 0.9 V or 1.1 V versus a hydrogen reference electrode [34, 35]. Methanol

Fig. 6.10 Methanol oxidation current measured at the cathode versus time during the introduction of a water/methanol mixture to the anode. Cathode potential: 0.9 V versus RHE; Membrane: PBI doped with ADL = 5 and thickness of 0.008 cm; temperature: 150 °C. Reproduced from [34] with permission of The Electrochemical Society



is then introduced into the anode chamber while the current at the cathode is monitored. This high potential is essential to ensure a complete oxidation of the methanol that has permeated through the membrane. The obtained steady-state current is assumed to be the direct measure of the methanol crossover rate. As shown in Fig. 6.10 a time-independent current of ca. 9 mA cm⁻² was obtained after 250 s.

In another method, the CO₂ content of the cathode gas stream is monitored. By keeping a methanol or a water/methanol mixture flow through the anode chamber, methanol steadily permeates through the membrane to the cathode. By holding the cathode potential at OCV to avoid electroosmotic drag of methanol, it is assumed, again, that all permeated methanol is oxidized into CO₂ which is carried out of the cell by the cathode air stream. A mass spectrometer [34] or an infrared sensor [36] have been used to measure the CO₂ content. The methanol crossover rate can be determined by using (6.26), where i_{MeOH} is the methanol crossover rate expressed as a current density, \dot{V}_{air} is the air flow rate under standard conditions ($p_0 = 1$ atm, $T_0 = 273$ K), $X_{\text{O}_2} = 0.209$ is the concentration of oxygen in air, λ is the oxygen flow stoichiometry, X_{CO_2} is the concentration of CO₂ in the cathode exhaust

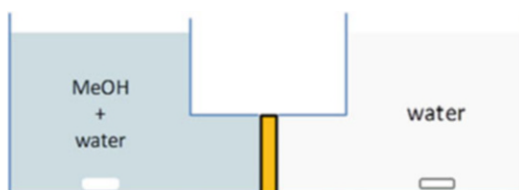


Fig. 6.11 Diffusion cell for measurement of methanol permeability with a membrane clamped between the two compartments and magnetic stir bars

stream, A is the active area of the cell, R the gas constant, and F is the Faraday constant [36].

$$i_{\text{MeOH}} = \dot{V}_{\text{air}} \left(1 - \frac{X_{\text{O}_2}}{\lambda} \right) X_{\text{CO}_2} \frac{p_0}{RT_0} \frac{6F}{A} \quad (6.26)$$

Methanol permeation can also be measured in a diffusion cell. One side of the membrane is in contact with a water-based methanol solution, the other with pure water (Fig. 6.11). The concentration gradient results in diffusion of methanol to the water reservoir, without any interference by electroosmotic drag. The increasing methanol concentration in the water-filled cell is monitored by gas chromatography [37], changes in the refractive index [38] or density [39]. While this method is very useful for sulfonated membranes like Nafion[®], it cannot

be used for PA-doped membranes, because PA would leach out. A detailed description of the measurement and the underlying physical principles can be found in [37].

6.7.4 Electroosmotic Drag of Water

In the fuel cell, protons move through the electrolyte from the anode to the cathode. While over 95 % of the conduction in PA-doped PBI membranes is based on a Grotthus-type conduction mechanism [40], also the vehicular mechanism is observed. Since protons do not exist as naked protons in condensed matter, but rather as solvated protons (e.g., H_3O^+ , H_5O_2^+ or H_4PO_4^+) in PA-doped PBI, these protons move together with their solvation shell, resulting in flow of the proton solvent from the anode to the cathode, the so-called electroosmotic drag. In typical PA-doped PBI, the electroosmotic drag of water molecules is close to 0 [41] but is expected to increase when water-based methanol solutions are used as fuel. For Nafion[®] membranes, the electroosmotic drag coefficient (water molecules per proton) decreases with the current and depends on the membrane hydration. Unfortunately the direction of this dependence is not clear [42, 43].

The electroosmotic drag (EOD) of water molecules in a running fuel cell can be obtained from the balance [36]:

$$\begin{aligned} \text{cathode}_{\text{out}} &= \text{cathode}_{\text{in}} + \text{product water} \\ &+ \text{water from side reactions} \\ &+ \text{EOD} + \text{concentration driven} \\ &\quad \text{water permeation.} \end{aligned}$$

The water which leaves the cell ($\text{cathode}_{\text{out}}$) can be obtained gravimetrically by condensing water from the gas stream in a cooling trap. $\text{Cathode}_{\text{in}}$ can be set to zero (dry gas stream) or be measured in a dummy cell [36]. The produced water can be calculated from the current. Concentration driven diffusion of water can be observed from the anode to the cathode, if humidified anode gas streams are used, but may also be reverted, when the cathode humidity

increases at high currents due to high water production (water-back diffusion). Water can also be formed in side reactions, e.g., when methanol crosses over to the cathode and is directly oxidized to water and CO_2 . This term can be estimated through electrochemically obtained methanol permeation measurements (linear sweep voltammetry) [36].

A simple approach to measure the EOD of a membrane is to run a fuel cell in the hydrogen pumping mode, in which the anode stream is humidified hydrogen or methanol and the cathode stream is dry or only partially humidified hydrogen. In this mode, the fuel is oxidized at the anode, and the resulting protons migrate to the cathode, where they are reduced to hydrogen. This eliminates the contributions of water production, water producing side reactions, and water-back diffusion. All water found in the cathode exhaust gas stream either permeated to the cathode driven by the set humidity gradient (water flux at OCV, a constant value independent of the current), or was transported by EOD (current >0 A) [43]. Instead of condensing water from the gas streams in a fuel cell setup, it is also possible to use closed volume cells separated by a membrane electrode assembly, and to measure the pressure changes of the anode and cathode cell in relation to the electric current [41].

For PA-doped PBI, the contribution of the mobile acid anion species to the conductivity is of great concern from both theoretical and engineering point of view.

6.8 Thermal and Oxidative Stability

6.8.1 Thermal Stability

The thermal stability of polymers can be tested by thermogravimetric analysis (TGA). In this method, a sample of a few milligrams is deposited in a scale pan mounted on a furnace. TGA measurements can be done in isothermal mode by maintaining a certain temperature for a fixed period of time or in temperature cycling mode. Most often the data are obtained with a constant

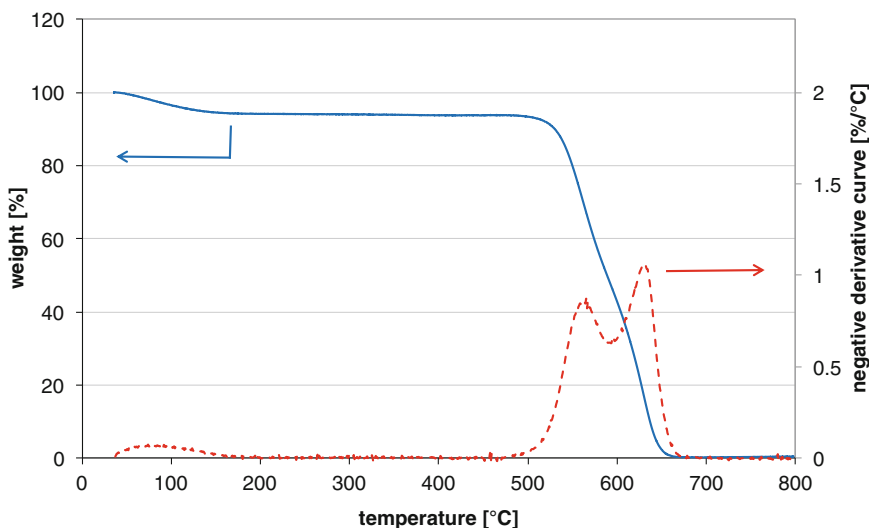


Fig. 6.12 TGA and derivative curve of a membrane made from meta-PBI (Dapozol[®]) recorded in air atmosphere and with a heating rate of $10\text{ }^{\circ}\text{C min}^{-1}$

heating rate. During the measurement, a heated gas stream passes the pan, and the temperature of the gas stream is increased with a constant heating rate. Plotting the weight or the normalized weight against the temperature gives the TGA curve. The first weight loss often stems from water that is not completely removed by drying the sample or is reabsorbed during handling of the dried membrane in ambient atmosphere (Fig. 6.12). To remove traces of high boiling-point solvents like DMAc or NMP, it can be necessary to immerse membranes in water before preparing TGA samples. The dotted line in Fig. 6.12 is the derivative curve, i.e., the slope plotted against the temperature. This representation gives basically the same information, but in some cases, when degradation processes overlap, peak fitting can give access to information hidden in the TGA curve.

While most organic materials are completely oxidized to volatile species in air, inert atmosphere (typically nitrogen or argon) leads to formation of soot, and a significant residual weight. It should be remarked that the TGA curve does not represent a thermodynamic equilibrium, but kinetically controlled degradation processes. Therefore, TGA data is not complete without

mentioning the atmosphere and heating rate. In fact, while *meta*-PBI appears to be stable at temperatures up to $500\text{ }^{\circ}\text{C}$ as shown in Fig. 6.12, a more precise conclusion is that the material is stable at $500\text{ }^{\circ}\text{C}$ within the time scale of the measurement. The long-term thermal stability of a material cannot be deduced from a single TGA curve. For quantitative comparison of materials, a commonly used description of TGA data is to give the temperature at which 3 or 5 % weight loss (ignoring water and solvent evaporation) is observed.

Since TGA curves represent kinetic processes, it is possible to estimate the activation energy of the degradation reaction from TGA data, as shown by Flynn and Wall [44]. For this purpose, it is necessary to measure the TGA curves of a material at different heating rates. From these curves, the temperature at, e.g., 5 % weight loss is extracted and plotted in an Arrhenius plot, i.e., the natural logarithm of the heating rate β against $1000/T(\text{K})$. This representation gives a linear trend with a negative slope, which is proportional to the activation energy E_a of the investigated degradation step. The activation energy can be obtained according to (6.27), where b is a constant and needs to be obtained by iteration.

However, for values of E_a/RT between 29 and 46, b is $0.457 \pm 1\%$ [44–46].

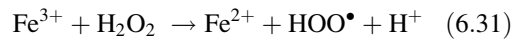
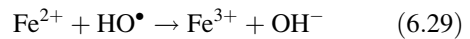
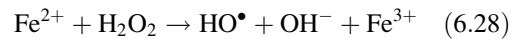
$$E_a = -[d(\log\beta)/d(1/T)] \times (R/b) \quad (6.27)$$

Limitations with this method are the necessity of well-resolved degradation steps without overlapping reactions, first-order kinetics and no dependence of the degradation mechanism on the conversion level. With the help of the estimated activation energy, it is also possible to predict the lifetime of a material at a given temperature, according to Toop [45, 47].

6.8.2 Oxidative Stability by Fenton Test

The gas crossover, as discussed above, leads not only to losses in the efficiency, but is also expected to form active oxygen species such as peroxides, hydroperoxy radicals, and hydroxy radicals. For Nafion[®] based systems it was shown that reactive oxygen species form especially when oxygen crosses over to the anode [48]. These aggressive species attack organic polymers and lead to chemical degradation. In comparison to Nafion[®], PA-doped PBI membranes have a relatively large gas permeability, and thus a large amount of reactive oxygen species may be present in the electrodes and be dragged or diffused to the membrane, where the polymer will be attacked.

To compare different polymers with respect to their chemical stability, the Fenton test is widely applied in fuel cell membrane research. In these tests, membrane samples are immersed in hydrogen peroxide solution containing a small amount of Fe^{2+} , e.g., iron(II)sulfate. In the presence of the metal ion, the decomposition of hydrogen peroxide is accelerated. The ongoing reactions are very complex, and several reactive intermediates are formed. Just as an example and demonstrating the catalytic nature, the following partial reactions of the so-called Haber–Weiss mechanism are highlighted, as shown in (6.28)–(6.31) [49, 50].



Obvious shortcomings of Fenton tests are their strong dependence on not standardized test protocols and the often qualitative nature of the monitored parameter, e.g., time until the membrane breaks or when floccules start to precipitate (see Table 6.3). Even within one paper, several test conditions may be used in parallel. Furthermore, due to the thermal instability of peroxide solutions, the solutions must be refreshed regularly. Sometimes, samples are immediately re-immersed, in other cases, samples are washed

Table 6.3 Selected literature examples for Fenton tests

$[\text{H}_2\text{O}_2]$	$[\text{Fe}^{2+}]$	Conditions	Characterizations	Reference
(a) 30 %	(a) 20 ppm	(a) RT; 0, 8, 16, 24 h	IR, NMR, weight loss and time until floccules could be observed in the solution	[51]
(b) 3 %	(b) 2 ppm	(b) 80 °C; 24 h		
3 wt%	20 ppm	(a) 40 °C; 24 h	Weight loss	[52]
		(b) 160 °C; 24 h		
a) 3 %	a) 4 ppm	Fresh solution: (a) every 24 h, 20 cycles at 70 °C (b) every 18 h, 3 cycles at 85 °C	Weight loss, visual observation, conductivity after PA doping	[53]
b) 30 %	b) 20 ppm			
3 %	4 ppm	68 °C; fresh solution every 20–24 h; 200 h	Weight loss	[1]

with water, dried, and then weighed before re-immersion. Comparison of data from different publications is practically impossible.

In brief, the Fenton test for pristine PBI membranes is informative as an aging tool for qualitative comparison of the chemical stability of different materials. However, the test is apparently an overdoing method. The materials that withstand the test are surely durable in the real fuel cells, but those that cannot survive the test might still be sufficiently durable in fuel cells.

A more critical issue concerns the effect of the phosphoric acid, which as a dopant is always present in the membrane. Most of Fenton studies in literature have been performed in the absence of phosphoric acid. As recently pointed out by Liao et al. [54], the presence of phosphoric acid makes the situation more complicated since it forms complexes with metal ions and thus inhibits the H_2O_2 decomposition. Additionally, the lowered pH of the solution further prevents the decomposition of H_2O_2 . Phosphoric acid present in the Fenton solution will also interact with the N–H groups of PBI, swelling the polymer and thus facilitating the access of the peroxide radicals to the macromolecular chains.

6.9 Humidity Definition and Control

6.9.1 Saturated Water Vapor Pressure, Relative Humidity, and Dew Point

Virtually all physicochemical properties of a polybenzimidazole membrane are strongly dependent on the water content, and it is thus important to investigate the membrane characteristics under humid conditions at elevated temperatures [55]. The membrane is highly hydrophilic and the equilibrium water content within the membrane is developed rather fast. At temperatures below or around $100\text{ }^\circ\text{C}$ there is a risk that water condenses on the membrane at high water partial pressures, i.e., when the temperature falls below the dew point. Condensation of water on the membrane gives a poorly defined two-phase system and leaches out phosphoric acid. As shown in Fig. 6.13, the saturated vapor pressure of water increases dramatically at temperatures above $100\text{ }^\circ\text{C}$, which reduces the risk for condensation.

The relative humidity (RH), which is often used to specify the water content in the atmosphere, is defined as the ratio (in percent) of the

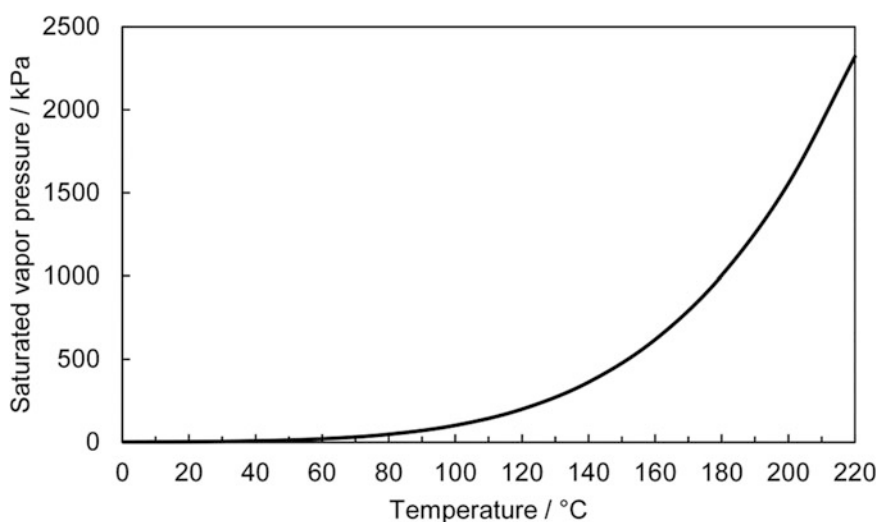


Fig. 6.13 Saturated vapor pressure of water as a function of temperature [56]

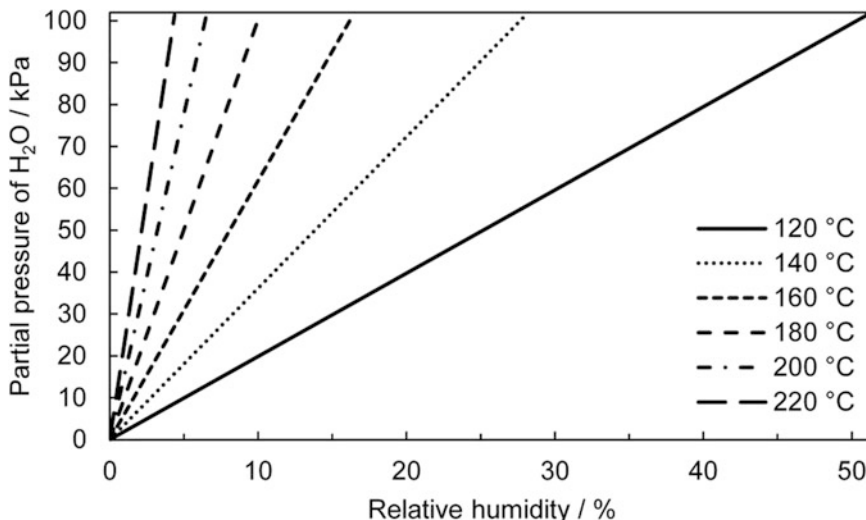


Fig. 6.14 The corresponding partial pressures of water at different relative humidity in the temperature range relevant for high-temperature polymer electrolyte membrane fuel cells

partial pressure of water vapor ($P_{\text{H}_2\text{O}}$) and the saturated vapor pressure of water at that particular temperature (P_{sat}) according to (6.32).

$$\text{RH} = P_{\text{H}_2\text{O}}/P_{\text{sat}} \quad (6.32)$$

At temperatures below 100 °C the relative humidity is a convenient measure to use. At higher temperatures the use of RH can, however, be rather confusing. The relative humidity at different partial pressures of water at temperatures ranging from 120 to 220 °C is given in Fig. 6.14. At atmospheric absolute pressure, the partial pressure of water in kPa roughly equals the water content in mole or volume percent. It can be seen that the relative humidity at a particular partial pressure of water decreases dramatically with increasing temperature. For example, at 120 and 220 °C the pure steam atmosphere ($P_{\text{H}_2\text{O}} = 101 \text{ kPa}$) corresponds to a relative humidity of 51 % and 4.4 %, respectively.

6.9.2 Control of Water Content

One convenient way to control the water content of a gas, particularly in the lower temperature range, is to bubble it through a water bath at a fixed temperature (sparging or dew point

method). Assuming that the gas phase above the surface in the water bath is saturated with water vapor, the partial pressure of water in the gas stream can be calculated [57]. Generally it is of great importance that the temperature of all the tubing is carefully controlled so that condensation of water is avoided, otherwise water condenses at the point where the temperature is lower than the dew point.

Practically the partial pressure of water at temperatures above 100 °C can be controlled by pumping water into an evaporator and converge the steam with a secondary carrier gas [55]. The partial pressure of water in the obtained gas mixture can be adjusted by controlling the pumping rate of liquid water and the flow rate of the carrier gas. Due to the large volume expansion of water the pumping rate has to be delicately controlled at very low values and free from pulses.

In closed systems the partial pressure of water can be controlled using aqueous solutions of LiCl with different concentrations, which have well-defined liquid–vapor equilibria [58, 59].

Acknowledgements The authors acknowledge funding by the Innovation Fund Denmark (4M Centre 0603-00527B and KDFuelCell 3047-00007B), KIST's K-GRL project and the Korea-Denmark green technology cooperative research program.

References

1. Yang JS, Cleemann LN, Steenberg T et al (2014) High molecular weight polybenzimidazole membranes for high temperature PEMFC. *Fuel Cells* 14:7–15
2. Yuan Y, Johnson F, Cabasso I (2009) Polybenzimidazole (PBI) molecular weight and Mark-Houwink equation. *J Appl Polym Sci* 112:3436–3441
3. Buckley A, Stuetz D, Serad GA (1987) Polybenzimidazoles. In: Kroschwitz JI (ed) *Encyclopedia of polymer science and engineering*. Wiley, New York, pp 572–601
4. Savinell RF, Wainright JS, Litt M (1998) High temperature polymer electrolyte fuel cells. In: Gottesfeld S, Fuller TF (eds) *Electrochemical Society Series*. 98(27):81–90
5. Kojima T, Yokota R, Kochi M et al (1980) Dilute solution properties of a polybenzimidazole. *J Polym Sci B* 18:1673–1683
6. Liao JH, Li QF, Rudbeck HC et al (2011) Oxidative degradation of polybenzimidazole membranes as electrolytes for high temperature proton exchange membrane fuel cells. *Fuel Cells* 11:745–755
7. Choe EW, Conciatori AB (1985) Aminoaryl ester reactant, two-stage melt polymerization. US Patent 4,535,144
8. Gullledge AL, Chen X, Benicewicz BC (2014) Investigation of sequence isomer effects in AB-polybenzimidazole polymers. *J Polym Sci A Polym Chem* 52:619–628
9. Han JY, Lee JY, Kim HY et al (2014) Synthesis and characterization of fluorene-based polybenzimidazole copolymer for gas separation. *J Appl Polym Sci* 131:40521
10. Ng F, Bae B, Miyatake K et al (2011) Polybenzimidazole block sulfonated poly(arylene ether sulfone) ionomers. *Chem Commun* 47:8895–8897
11. Dominguez PH, Grygiel K, Weber J (2014) Nanostructured poly(benzimidazole) membranes by N-alkylation. *eXPRESS Polym Lett* 8:30–38
12. Huang W, Qing SB, Yang JT et al (2008) Preparation and characterization of soluble sulfonated polybenzimidazole for proton exchange membrane materials. *Chinese J Polym Sci* 26:121–129
13. Robinson RA (2005) The water activities of lithium chloride solutions up to high concentrations at 25°. *Trans Faraday Soc* 41:756–758
14. Li Q, He R, Berg RW et al (2004) Water uptake and acid doping of polybenzimidazoles as electrolyte membranes for fuel cells. *Solid State Ionics* 168:177–185
15. Majerus A, Conti F, Korte C et al (2012) Thermogravimetric and spectroscopic investigation of the interaction between polybenzimidazole and phosphoric acid. Abstract 1510. Paper presented at Honolulu PRiME 2012, Honolulu, 7–9 October 2012
16. Mader JA, Benicewicz BC (2011) Synthesis and properties of segmented block copolymers of functionalised polybenzimidazoles for high-temperature PEM fuel cells. *Fuel Cells* 11:222–237
17. Lee HJ, Lee DH, Henkensmeier D et al (2012) Synthesis and characterization of H₃PO₄ doped poly(benzimidazole-co-benzoxazole) membranes for high temperature polymer electrolyte fuel cells. *Bull Korean Chem Soc* 33:3279–3284
18. Li X, Chen X, Benicewicz BC (2013) Synthesis and properties of phenylindane-containing polybenzimidazole (PBI) for high-temperature polymer electrolyte membrane fuel cells (PEMFCs). *J Power Sources* 243:796–804
19. Hasiotis C, Li Q, Deimede V et al (2001) Development and characterization of acid-doped polybenzimidazole/sulfonated polysulfone blend polymer electrolytes for fuel cells. *J Electrochem Soc* 148: A513–A519
20. Hanley TR, Helminiak TE, Benner CL (1978) Expansion of aromatic heterocyclic polymers in salt solution. *J Appl Polym Sci* 22:2965–2978
21. Li X, Qian G, Chen X, Benicewicz BC (2013) Synthesis and characterization of a new fluorine-containing polybenzimidazole (PBI) for proton-conducting membranes in fuel cells. *Fuel Cells* 13:832–842
22. Leaflet “Polybenzimidazole (PBI) S26 Solution”, PBI performance products, Inc. http://www.pbiproducts.com/images/uploads/main/Polymers/Solutions_Brochure.pdf
23. Murata M, Nakamura T (1999) Polybenzimidazole compounds in solution and a process for the preparation thereof. US Patent 5,902,876
24. Belack J, Kundler I, Schmidt TJ (2008) Celtec-MEAs: life time, degradation modes and mitigation strategies. Paper presented at Progress MEA 2008, La Grande Motte, 21–24 September 2008
25. Molle MA, Chen X, Ploehn HJ et al (2014) High polymer content 3,5-pyridine-polybenzimidazole copolymer membranes with improved compressive properties. *Fuel Cells* 14:16–25
26. Frequently asked questions: dynamic mechanical analysis (DMA), a beginner’s guide, booklet from Perkin Elmer. http://www.perkinelmer.com/CMSResources/Images/44-74546GDE_IntroductionToDMA.pdf
27. Dynamic mechanical analysis basics: Part 1: How DMA works. Technical note, Perkin Elmer. http://www.perkinelmer.com/CMSResources/Images/44-74304app_thermaldynmechanalybasicspart1.pdf
28. Iqbal HMS, Bhowmik S, Benedictus R (2014) Process optimization of solvent based polybenzimidazole adhesive for aerospace applications. *Int J Adhes Adhes* 48:188–193
29. He R, Li Q, Bach A et al (2006) Physicochemical properties of phosphoric acid doped polybenzimidazole membranes for fuel cells. *J Membr Sci* 277:38–45
30. Sakai T, Takenako H, Wakabayashi N et al (1985) Gas permeation properties of solid polymer

- electrolyte (SPE) membranes. *J Electrochem Soc* 132:1328–1332
31. Baker RW (2004) Membrane technology and applications, 2nd edn. Wiley, Chichester, p 304
 32. Kim BG, Henkensmeier D, Kim HJ et al (2014) Sulfonation of PIM-1—towards highly oxygen permeable binders for fuel cell application. *Macromol Res* 22:92–98
 33. Cleemann LN, Buazar F, Li Q et al (2013) Catalyst degradation in high temperature proton exchange membrane fuel cells based on acid doped polybenzimidazole membranes. *Fuel Cells* 13:822–831
 34. Wang JT, Wasmus S, Savinell RF (1996) Real-time mass spectrometric study of the methanol crossover in a direct methanol fuel cell. *J Electrochem Soc* 143:1233–1238
 35. Mamlouk M, Scott K, Hidayati N (2011) High temperature direct methanol fuel cell based on phosphoric acid PBI membrane. *J Fuel Cell Sci Technol* 8:061009
 36. Gubler L, Kramer D, Belack J et al (2007) Celtec-V. A polybenzimidazole-based membrane for the direct methanol fuel cell. *J Electrochem Soc* 154: B981–B987
 37. Tricoli V (1998) Proton and methanol transport in poly(perfluorosulfonate) membranes containing Cs⁺ and H⁺ cations. *J Electrochem Soc* 145:3798–3801
 38. Woo Y, Oh SY, Kang YS et al (2003) Synthesis and characterization of sulfonated polyimide membranes for direct methanol fuel cell. *J Membr Sci* 220:31–45
 39. Yang CC, Lee YJ, Yang JM (2009) Direct methanol fuel cell (DMFC) based on PVA/MMT composite polymer membranes. *J Power Sources* 188:30–37
 40. Savinell RF (2012) Recent research of the PBI/PA system as a proton conductor in electrochemical systems. Presentation at Carisma 2012, Copenhagen, Denmark. http://www.hotmea.kemi.dtu.dk/~media/Centre/ENRKG_HotMEA/carisma2012/presentations_posters/savinell_carisma_2012.ashx
 41. Weng D, Wainright JS, Landau U et al (1996) Electroosmotic drag coefficient of water and methanol in polymer electrolytes at elevated temperatures. *J Electrochem Soc* 143:1260–1263
 42. Luo Z, Chang Z, Zhang Y et al (2010) Electroosmotic drag coefficient and proton conductivity in Nafion membrane for PEMFC. *Int J Hydrogen Energy* 35:3120–3124
 43. Peng Z, Morin A, Hugué P et al (2011) In-situ measurement of electroosmotic drag coefficient in Nafion membrane for the PEMFC. *J Phys Chem B* 115:12835–12844
 44. Flynn JH, Wall LA (1966) A quick, direct method for the determination of activation energy from thermogravimetric data. *Polym Lett* 4:323–328
 45. TA Instruments Application Brief TA-125. http://www.tainstruments.co.jp/application/pdf/Thermal_Library/Applications_Briefs/TA125.PDF
 46. Yang HE, Chen LJ, He F et al (2012) NM Cable insulation service life time prediction using materials degradation kinetics. Proceedings of the 61st international wire & cable symposium (IWCS), pp 791–798. <http://iwcs.omnibooksonline.com/data/papers/2012/16-5.pdf>
 47. Toop DJ (1971) Theory of life testing and use of thermogravimetric analysis to predict the thermal life of wire enamels. *IEEE Trans Electr Insul* EI-6:2–14
 48. Inaba M, Kinumoto T, Kiriake M et al (2006) Gas crossover and membrane degradation in polymer electrolyte fuel cells. *Electrochim Acta* 51:5746–5753
 49. Gubler L, Koppenol WH (2012) Kinetic simulation of the chemical stabilization mechanism in fuel cell membranes using cerium and manganese redox couples. *J Electrochem Soc* 159:B211–B218
 50. Kinumoto T, Inaba M, Nakayama Y et al (2006) Durability of perfluorinated ionomer membrane against hydrogen peroxide. *J Power Sources* 158:1222–1228
 51. Chang Z, Pu H, Wan D et al (2010) Effects of adjacent groups of benzimidazole on antioxidation of polybenzimidazoles. *Polym Degrad Stab* 95:2648–2653
 52. Qian G, Benicewicz BC (2009) Synthesis and characterization of high molecular weight hexafluoroisopropylidene-containing polybenzimidazole for high-temperature polymer electrolyte membrane fuel cells. *J Polym Sci A Polym Chem* 47:4064–4073
 53. Han M, Zhang G, Liu Z, Wang S et al (2011) Cross-linked polybenzimidazole with enhanced stability for high temperature proton exchange membrane fuel cells. *J Mater Chem* 21:2187–2193
 54. Liao JH, Yang JS, Li QF et al (2013) Oxidative degradation of acid doped polybenzimidazole membranes and fuel cell durability in the presence of ferrous ions. *J Power Sources* 238:516–522
 55. He RH, Li Q, Xiao G et al (2003) Proton conductivity of phosphoric acid doped polybenzimidazole and its composites with inorganic proton conductors. *J Membr Sci* 226:169–184
 56. Wagner W, Pruss A (1993) International equations for the saturation properties of ordinary water substance - revised according to the international temperature scale of 1990. *J Phys Chem Ref Data* 22:783–787
 57. Costamagna P, Srinivasan S (2001) Quantum jumps in the PEMFC science and technology from the 1960s to the year 2000: Part II. Engineering, technology development and application aspects. *J Power Sources* 102:253–269
 58. Gibbard HF, Scatchard G (1973) Liquid-vapor equilibrium of aqueous lithium-chloride, from 25° to 100°C and from 1.0 to 18.5 molal, and related properties. *J Chem Eng Data* 18:293–298
 59. Schechter A, Savinell RF, Wainright JS et al (2009) ¹H and ³¹P NMR study of phosphoric acid-doped polybenzimidazole under controlled water activity. *J Electrochem Soc* 156:B283–B290

Jingshuai Yang, Ronghuan He, and David Aili

7.1 Introduction to Polybenzimidazoles

Polybenzimidazoles (PBIs) refer to a class of linear heterocyclic polymers containing benzimidazole moieties as a part of the repeat unit. In 1961, the PBI polymers in the wholly aromatic form were first synthesized by Vogel and Marvel [1]. Thereafter, various new PBIs have been invented, as reviewed in early references [2, 3]. The aromatic backbone of PBIs provides the polymer with high thermal stability, excellent chemical resistance, stiffness, and toughness. However, only a few PBIs have demonstrated a superior performance and received unimpaired attention for further exploiting in practice. Among the PBI structure derivatives, poly(2,2'-*m*-(phenylene)-5,5'-bibenzimidazole) (*m*PBI) offers a combination of thermal stability and processability. Therefore, it was the first commercialized PBI material and has been available since the middle of the 1980s under the trademark Celazole[®]. The chemical structure of *m*PBI is shown in Fig. 7.1.

J. Yang • R. He (✉)
Department of Chemistry, College of Sciences,
Northeastern University, Shenyang 110819, China
e-mail: herh@mail.neu.edu.cn

D. Aili
Section for Proton Conductors, Department of Energy
Conversion and Storage, Technical University of
Denmark, Kemitorvet 207, DK-2800 Kgs., Lyngby,
Denmark

Due to the excellent thermal stability and flexibility, PBIs have primarily been used as textile fibers for a wide range of high-temperature applications especially in corrosive environments. Synthesis and applications of engineered PBIs from mesoporous networks to nanofibers were recently reviewed [4]. In the form of membranes or films, PBIs have been explored for liquid and gas separation applications at high temperatures and in harsh environments [5–8], due to their durability and relatively low cost.

Recently, one of the most active research areas on PBIs is the development of new base materials as high temperature proton exchange membranes (HT-PEMs) for fuel cells operating from 120 to 200 °C [9–11]. The benzimidazole groups in PBIs ($pK_{\text{aH}} = 5.23$ [12]) give the polymer high affinity to polar protic liquids such as Brønsted acids, which are used as dopants and provide the proton conduction. From proton conducting mechanism point of view, phosphoric and phosphonic acids are preferred because they form dynamic hydrogen bond networks in a complex system of different phosphorous oxoacid species, through which protons can readily transfer by hydrogen bond breaking and forming processes [13]. Other important features of phosphoric or phosphonic acids are their excellent thermal stability and low vapor pressure at elevated temperatures. A breakthrough was achieved when the phosphoric acid doped *m*PBI

membrane was first proposed as HT-PEM for fuel cells in 1995 [14]. Since then phosphoric acid doped PBI membranes have been successfully developed and systematically characterized with high conductivity at low water activities [12, 15, 16], good mechanical strength [17, 18] and excellent thermal stability [19]. Fuel cells and related technologies have been developed with operating features such as suppressed CO poisoning, little humidification of reactant gases, efficient heat utilization, and possible integration with fuel processing units [20–24].

This chapter is devoted to an updated review of the polymers with emphasis on synthesis approaches and modification of the polymer structures for improvements on their properties and processability in applications.

7.2 Procedures for Synthesis of PBIs

7.2.1 Solvent-Free Synthesis

Polymerization of PBI can be carried out in melts or in homogenous solution. In the early 1960s,

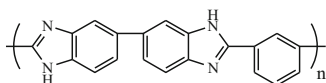


Fig. 7.1 Chemical structure of poly(2,2'-*m*-(phenylene)-5,5'-bibenzimidazole)

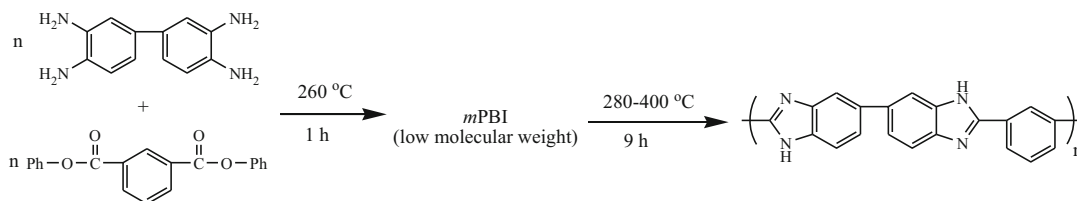


Fig. 7.2 The two-stage melt condensation polymerization of *m*PBI

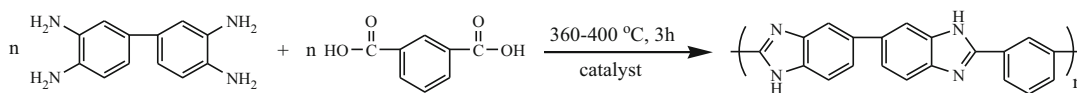


Fig. 7.3 The single-stage melt condensation polymerization of *m*PBI

Vogel and Marvel [1, 25] developed a two-stage polymerization process to obtain PBI from tetraaminobiphenyl (TAB) and diphenyl isophthalate (DPIP), as shown in Fig. 7.2. The first step was carried out in a melt at about 260 °C to produce the low molecular weight polymer in the form of voluminous foams. The low molecular weight pre-polymer was then pulverized and further polymerized by heat-treatment up to 400 °C to increase the molecular weight. The disadvantage of this procedure was the generation of the voluminous foam due to the by-products of polymerization, i.e., phenol and water. The second-stage reaction was needed in order to reach a high polymerization degree, i.e., high molecular weight of PBIs.

By replacing DPIP with isophthalic acid (IPA) in the presence of organo phosphorus and silicon compounds as catalysts, Choe [26, 27] developed a single-stage reaction to synthesize PBI (see Fig. 7.3). This process significantly reduced the foaming phenomenon and meanwhile lowered the raw material cost. In addition, the inherent viscosity (IV) of the prepared PBI could be increased by increasing the catalyst concentration to 1 % [27].

High molecular weight polymers are desirable in order to obtain membranes with adequate mechanical strength, especially at high acid doping levels. However, the IV of *m*PBI prepared by melt condensation must be kept low in order to avoid the polymer being insoluble or infusible due to side reactions. For example, the

commercial *m*PBI (Celazole[®]) exhibited a low to medium molecular weight of 23,000–37,000 g mol⁻¹, corresponding to an IV in the range of 0.55–0.80 dL g⁻¹ [28]. The melt condensation process is still used for the synthesis of PBIs [29], but homogenous solution polymerization has taken over as the most widely used procedure in the literature.

7.2.2 Homogeneous Solution Polymerization

Polymerization of PBIs from monomers of aromatic diamines and dicarboxylic acids in polyphosphoric acid (PPA) is the most commonly used method to prepare this type of polymers, as shown in Fig. 7.4. Here PPA is used as the solvent to form a homogeneous mixture, in which the polycondensation reaction is promoted by the efficient removal of the released water [30]. Taking advantage of a moderate temperature (170–230 °C) and using more stable monomers (TAB stabilized by tetrahydrochloride), this approach is an excellent route for preparing high molecular weight polymers. The main drawback is that the polymer ends up in a very diluted solution in PPA (3–5 wt%), so a small-scale polymerization should be connected with a relatively large amount of the acid. In addition, multiple-step isolation procedures such as neutralization and washing are involved for the acid elimination from the polymer. Nevertheless, this polymerization procedure is widely used to synthesize variously modified polymers due to its convenience on laboratory scale.

Eaton et al. [31] proposed a mixture of methanesulfonic acid (MSA) and phosphorus pentoxide (P₂O₅) as the solvent for the homogeneous synthesis instead of PPA. This MSA-P₂O₅ mixture was afterwards employed to synthesize

PBI by Kim et al. [32] and Jouanneau et al. [33]. Compared to PPA, the mixture of MSA-P₂O₅ is a less viscous liquid and the solvent can subsequently be washed out easily. However, MSA is a toxic acid, compared to PPA which is also widely used in the food industry, and great precaution is thus required during handling. In addition, refluxing sulfolane or diphenyl sulfone were suggested as solvents for PBI synthesis in the early years [34].

For membrane casting purpose, PBIs with high molecular weight are desirable in order to achieve mechanically robust membranes. Generally speaking, the polymerization degree of polymers can be tailored by varying the reaction parameters such as reaction temperature and time, monomer concentrations in PPA and most importantly the stoichiometry of the monomers [18, 35]. It is essential to achieve a linear growth of the macromolecular chain with sufficiently minimized side reactions to attain good solubility in organic solvents. Chain branching and/or cross-linking are among the side reactions of primary concern [2]. Based on Carothers equation, the monomer purity and accurate stoichiometry are crucial to obtain a linear structure polymer with a high molecular weight. In order to get an accurate stoichiometry of monomers, the content of adsorbed water in TAB should be determined, e.g., from the weight loss of the sample treated in vacuum at room temperature as previously reported [36]. Moreover, the initial monomer concentration in the polymerization mixture plays an important role in controlling the molecular weight of the resulting polymers [37, 38]. For example, the increase in IV of the sulfone PBI (SO₂PBI) was only observed when the initial monomer concentration was increased from 1.5 to 3.2 wt% [38]. Thereafter an obvious drop in viscosity was observed, apparently due to the fact that the very viscous solution prevented

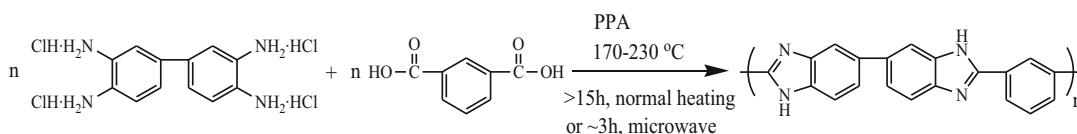


Fig. 7.4 Homogenous solution polymerization of *m*PBI in PPA

the efficient growth of the polymer chain. As previously reported [37–42], the dicarboxylic acid architecture determines the solubility of the monomers and polymers in PPA and influences the molecular weight of the polymers as well. For example, preparation of *m*PBI with typical molecular weights of more than 25,000 g mol⁻¹ was reported using a monomer concentration of around 8 wt% in PPA, which corresponded to a polymer concentration of about 5 wt% in PPA [17, 39, 43]. A lower concentration, typically lower than 2 wt%, was used for synthesis of poly[2,2'-*p*-(phenylene)-5,5'-bibenzimidazole] (*p*PBI) because of its poor solubility in PPA [39–41]. Furthermore, the polymerization temperature should also be optimized aiming at structurally pure polymer with minimized side reactions [39, 44]. Attempts have been made to introduce phosphorus-based catalysts, e.g., triphenyl phosphate in the PPA synthesis [45]. However, it seems that monomer purity, temperature, and removal of oxygen traces in the reactor are more important parameters than adding catalysts for obtaining high molecular weight polymer.

7.3 Microwave-Assisted Synthesis

Synthesis of *m*PBI in homogenous solution is usually conducted over a long period of time, generally more than 20 h. Although performing the polycondensation in molten state can be accomplished within several hours, the operational conditions are complex, including high temperatures of 350–400 °C and requirement for catalysts [27] and isolation under inert atmosphere [2]. In recent years, microwave techniques are employed in chemical synthesis due to its high efficiency and uniform heating [46]. In case of polymer synthesis, microwave irradiation has been adopted mainly for the purpose of acceleration of the polymerizations [47, 48]. Both *m*PBI and poly(2,5-benzimidazole) (ABPBI) have been obtained from homogenous solution polymerization in PPA with microwave assistance [43, 49]. Recently, Quartarone et al. [11] obtained a series of PBIs by using a

microwave-assisted approach. The use of microwave irradiation shortens the reaction time to produce polymers with similar or even higher IVs. In case of ABPBI, for example, the homogenous solution polycondensation needed 5 h to obtain the polymer with IVs of higher than 3 dL g⁻¹. In contrast, only 45 min were required with the microwave-assisted process to achieve a similar polymerization degree [11]. In general, *m*PBI displays slower polymerization kinetics than ABPBI. Nevertheless, *m*PBI with a high IV of 1.16 dL g⁻¹ was produced within 3 h using the microwave-assisted synthesis method, whereas an IV of 0.56 dL g⁻¹ was obtained after 18 h with the conventional heating [43].

7.4 Characterization of PBIs

7.4.1 Viscosity

A simple way to estimate the molecular weight of PBIs is the measurement of intrinsic viscosity (η_{IV}) of the polymer in solution at a fixed temperature (normally 25–30 °C). The intrinsic viscosity is obtained by plotting the specific viscosity (η_{sp}) as a function of the polymer concentration and extrapolating to zero concentration. In order to simplify the measurement process, a single-point method was proposed to calculate the η_{IV} from η_{sp} using (7.1) [35, 50–52], where C is the polymer concentration in a concentrated acid, e.g., 96 wt% sulfuric acid.

$$\eta_{IV} = (\eta_{sp} + 3 \ln(1 + \eta_{sp})) / 4C \quad (7.1)$$

As a protocol test, the η_{sp} of the polymer solution with a concentration of 5 g L⁻¹ in concentrated sulfuric acid at 30 °C was measured using an Ubbelohde viscometer. As Yuan et al. [53] recently reported, the single-point method gave a good estimation of the η_{IV} with more than 99 % accuracy at relatively low concentrations, corresponding to a η_{sp} of less than 0.2. The η_{IV} is in turn related to the weight-averaged molecular weight (M_w) by the Mark–Houwink–Sakurada expression as shown in (7.2), where the Mark–Houwink constants are dependent on

the molecular weight range and molecular weight distribution.

$$\eta_{IV} = KM_W^\alpha \quad (7.2)$$

A set of Mark-Houwink constants of $K = 1.94 \times 10^{-4} \text{ dL g}^{-1}$ and $\alpha = 0.791$ are often used, which were obtained from the light scattering measurements by Buckley et al. [54]. Thereafter, various Mark-Houwink constants were proposed by several groups with similar light scattering measurements using different solvents [53, 55]. It should be noted that the Mark-Houwink constants were obtained from samples of a broad M_W range, which might present certain errors in the calculation. It is also worthwhile to mention that besides concentrated sulfuric acid, other solvents such as formic acid [56] and MSA [57] were used to measure the viscosity of the PBIs. In this case, the viscosity of the polymer obtained in different solvents is incomparable. For the determination of the molecular weight of PBI, a more comprehensive description can be found in Chap. 6.

7.4.2 Structure Identification

Nuclear Magnetic Resonance (NMR) spectroscopy is a powerful technique to identify and determine the structure of a pure organic compound or the repeat unit of a polymer. For polymer materials and composites, infrared (IR) and Raman spectroscopy are commonly used for identification of different functionalities. IR [49, 58–63], Raman [64, 65] and NMR [40, 43, 66, 67] spectroscopy have been carried out on PBIs and their composites to identify and/or confirm the chemical structure of the polymers. As an example of the *m*PBI, the IR spectrum in the region from 2000 to 4000 cm^{-1} is of particular interest since most of the informative N–H stretching modes occur in this range, with typically three distinguishable bands at around 3415, 3145, and 3063 cm^{-1} [49, 58–60]. According to Musto et al. [58], the relatively sharp peak centered at 3415 cm^{-1} is attributed to the stretching vibration of isolated,

nonbonded “free” N–H groups, whereas the broad absorption band located around 3145 cm^{-1} is assigned to stretching vibrations of self-associated, hydrogen-bonded N–H groups. In addition, the absorptions in a region of 1630–1500 cm^{-1} are attributed to the vibration of C=C and C=N [49]. A strong band at 1385 cm^{-1} is probably contributed by the in-plane deformation of benzimidazole rings according to Asensio et al. [68]. As refer to the Raman spectra of *m*PBI, the most significant absorption band is at around 1000 cm^{-1} , which is assigned to the *m*-benzene ring vibration [64, 65].

In addition to the structural information that NMR provides, it can also be used to calculate the ratio of specific functional groups in PBI polymers and copolymers. The chemical shifts of protons change in different NMR solvents, such as deuterated dimethyl sulfoxide (DMSO- d_6) and deuterated sulfuric acid (D_2SO_4). Due to the fast exchange interaction between the solvent of D_2SO_4 and the proton in imine of imidazole rings, the chemical shift of hydrogen in the imidazole rings of the *m*PBI polymer is often indiscernible by ^1H NMR [49]. Therefore, DMSO- d_6 is the most common solvent for recording NMR spectra of PBI. The chemical shift of imidazole protons (–NH–) of *m*PBI is around 13.1–13.2 ppm and the peaks between 7.5 and 9.2 ppm are attributed to aromatic protons [40, 67]. The *m*PBI shows ^1H NMR signals in DMSO- d_6 at 13.2 (2H), 9.1 (1H), 8.3 (2H), 8.0–7.6 (7H) ppm, and the detailed assignments can be found in the reference [43]. Furthermore, NMR is also used to estimate the molar composition of specific blocks in different PBI copolymers [38, 40, 41] or to calculate the grafting degree of grafted PBIs [69–71] according to the ratios of the peak integrals.

7.4.3 Solubility in Organic Solvents

To serve as a proton conducting electrolyte and reactant separator in PEM fuel cells, the PBIs need to be processed into thin membranes. Solution casting is a widely used method to prepare

PBI membranes. For this purpose, the PBI must first be dissolved in a suitable organic solvent. Due to the very rigid macromolecular structure of *m*PBI, a limited number of highly polar aprotic organic solvents are capable of breaking the strong intermolecular hydrogen bonds and solubilize the polymer. The commonly used organic solvents include *N,N*-dimethylacetamide (DMAc), *N,N*-dimethylformamide (DMF), *N*-methyl-2-pyrrolidone (NMP), and dimethylsulfoxide (DMSO). Among these solvents DMAc is the most widely used one for solution casting of *m*PBI membranes. A few weight percents of LiCl is often added to prevent the polymer from phasing out from the solution during storage [72] and to facilitate the polymer dissolution [73].

Besides the organic solvents, *m*PBI also dissolves in strong acids or bases such as PPA, H₂SO₄, and mixtures of aqueous hydroxides and light alcohols [74]. Recently Wang et al. [75] reported that *m*PBI is soluble in 1-butyl-3-methylimidazolium chloride and other hydrophilic ionic liquids, opening the possibility for a more environmentally benign membrane fabrication procedure.

The chemical structure of PBI derivatives significantly influences the polymer solubility in organic solvents. Compared with *m*PBI containing meta-phenylene linkages, both *p*PBI with stiff para-phenylene linkages and ABPBI with single benzimidazole repeat unit are soluble only in MSA among the organic solvents studied [10, 38, 39, 41, 76]. Efforts have also been made to synthesize novel PBI derivatives by modifying the chemical structure in the main chain or grafting side chains in order to improve their solubility and processability. For example, flexible spacers or blocks including ether linkages [37, 41], sulfone groups [38, 77], and hexafluoroisopropylidene bridging groups [78, 79] were introduced into polymer backbones. These moieties reduce the intermolecular forces between the polymer chains and thus improve the polymer solubility in organic solvents.

7.5 Design and Synthesis of PBI Variants

7.5.1 Main-Chain Modifications

In the early years, extensive work was carried out to synthetically modify PBI derivatives using different chemical structures of the monomers, i.e., different tetraamine and dicarboxylic acid derivatives, as comprehensively reviewed by Neuse et al. [2]. Since the *m*PBI membrane was successfully demonstrated as the membrane electrolyte in high temperature PEM fuel cells, much effort has been devoted to the synthesis of various novel PBI derivatives in order to improve the physicochemical properties of the membranes and their durability in fuel cells [9, 10]. This section summarizes the recent synthetic efforts on PBI structure analogues, primarily for applications in the high temperature PEM fuel cells. Table 7.1 lists the chemical structures of PBI variants with modified main chains.

Compared with *m*PBI membranes, *p*PBI membranes containing the para phenylene structure show superior tensile strength and stiffness, and seem to be of more interest in recent years [39, 41, 76]. The synthesis is carried out using terephthalic acid (TPA) instead of IPA. Higher IVs of *p*PBI than those of *m*PBI are achieved, though the solubility of TPA in PPA was lower than that of IPA. As previously reported, *m*PBI showed IV values ranging from 1.3 to 1.5 dL g⁻¹ with monomer concentration in PPA of around 8.5 wt% [35], while the *p*PBI showed IV values of 2.7 dL g⁻¹ with monomer concentration in PPA of around 3.2 wt% [38]. However, the rigid structure of *p*PBI makes it less soluble and thus problematic to cast from solution. Thus efforts have been made to improve solubility of the polymer in organic solvents by introducing flexible spacers or blocks in the structures.

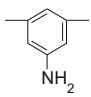
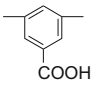
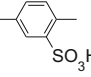
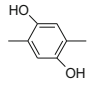
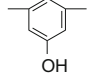
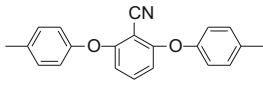
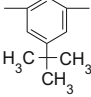
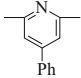
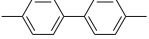
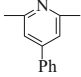
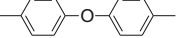
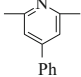
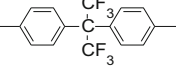
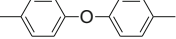
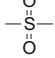
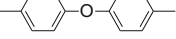
Generally speaking, polymers containing e.g., ether and sulfone linkages exhibit lowered thermooxidative stability but increased solubility and flexibility, which facilitates the further processing, modification (cross-linking and

Table 7.1 Structures of main-chain-modified PBI derivatives for fuel cells

Polymers	R	X	References
<i>m</i> PBI	—		[18, 35, 43, 49]
<i>p</i> PBI	—		[39, 41, 76]
OPBI	—		[37, 41, 80, 81]
SO ₂ PBI	—		[36, 38, 77, 82]
F ₆ PBI	—		[36, 42, 78, 79, 83, 84]
PFCBPBI	—		[85]
F ₁₄ PBI	—	$(\text{CF}_2)_7$	[86]
PyPBI	—		[87–92]
OHPyPBI	—		[93]
BI <i>p</i> PBI	—		[94]
ImPBI	—		[95]
NPTPBI	—		[96]
<i>p</i> -PPBI	—		[97, 98]
PBI-108	—		[99]

(continued)

Table 7.1 (continued)

Polymers	R	X	References
NH ₂ PBI	—		[100, 101]
HPBI	—		[102–104]
sPBI	—		[105–107]
(OH) ₂ PBI	—		[108]
OHPBI	—		[83, 109]
PBI-CN	—		[110]
tert-butyl PBI	—		[5]
Py-PBI-BDA			[111]
Py-PBI-BPDA			[111]
Py-PBI-HFIPA			[111]
PBI-OO	—O—		[112, 113]
PBI-SO ₂			[33]

copolyconcentration) and production of membranes. Typical examples are ether PBI (OPBI) [37, 41, 80, 81], sulfone PBI (SO₂PBI), [36, 38, 77, 82] and hexafluoroisopropylidene containing PBI (F₆PBI) [36, 42, 78, 79, 83, 84], which show good solubilities in organic solvents.

For HT-PEM fuel cell applications the PBI membranes are normally doped with PA to become proton conductors. The proton conductivity increases with increasing acid doping level, which is defined as the number of phosphoric acid molecules per polymer repeat unit. Chemically, the acid uptake is promoted by the basic sites of the benzimidazole which develop adducts with the acid, i.e., between H₂PO₄-H and -N=C- [12, 114]. Therefore PBIs with properly tailored basic functionalities such as pyridine (PyPBI) [87–93], benzimidazole (BIpPBI and PBI-108) [94, 99, 115], imidazole (ImPBI) [95], or other basic groups (NPTPBI and *p*-PPBI) [96–98], were proposed to enhance the basic site density of polymers for an improved acid doping level and corresponding proton conductivity. Taking hydroxyl pyridine containing polybenzimidazole (OHPyPBI) as an example [93], introduction of hydroxylpyridine groups in the polymer resulted in higher acid doping levels in the entire studied range of the doping acid concentration as compared with the reference *m*PBI membrane. Furthermore, the hydroxylpyridine groups facilitated the proton conduction in the acid doped membranes, which was proved by the conductivity results of OHPyPBI and *m*PBI membranes with comparable acid doping levels. Consequently, both the density of NH-groups and their spatial position in the polymer backbone affect the acid doping level and therefore proton conductivity of the doped membranes.

From this point of view, ABPBI ($T_g > 450^\circ\text{C}$ [116]) has a high concentration of basic sites in the structure since it lacks the connecting phenyl rings [10, 117]. ABPBI can be polymerized from a single monomer (3,4-diaminobenzoic acid) (DABA, Fig. 7.5), which is less expensive than diaminobenzidine, commercially available (e.g., used in the pharmaceutical industry) and noncarcinogenic. However, ABPBI only dissolves in MSA due to its rigid structure, which results

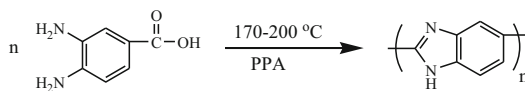


Fig. 7.5 Synthetic route for ABPBI

in membrane fabrication difficulties. More information about ABPBI and its use as high temperature membrane electrolyte in PEM fuel cells can be found in the review by Asensio and Gómez-Romero [118].

In addition, more synthesis on PBI polymers has been made by using a variety of diacids with active groups such as pendant amino [100, 101], carboxyl [102–104], sulfonic acid [105–107], hydroxyl [83, 108, 109], *tert*-butyl [5] or nitrile [110]. These functional groups are expected to be reactive with e.g., cross-linking agents containing epoxy or alkyl halide moieties, which provide polymers potential to be further modified for superior properties of PBI membranes. A comprehensive summary of different PBI main-chain structure derivatives considered for fuel cell applications is given in Table 7.1.

In connection to the polymerization of PBI with alternative tetraamine monomers, Jana et al. [111] recently proposed a novel tetraamine monomer of 2,6-bis(3,4-diaminophenyl)-4-phenylpyridine (Py-TAB) which was polymerized with 4,4'-oxy-bis(benzoic acid). They found that the novel Py-PBIs displayed superior solubility in low boiling solvents, and the corresponding membranes had higher PA doping content with lower swelling than those of conventional PBIs. In addition, PBI-OO polymers were prepared by polycondensation of bisaminobenzidine ether and 4,4'-oxy-bis(benzoic acid) by FuMA-Tech GmbH [112, 113]. PBI-OOs were further used to fabricate sulfonic acid membranes via sulfonation of PBI backbone or blend membranes with Nafion[®], respectively. For this particular polymer, a direct post-sulfonation in concentrated or fuming sulfuric acid was developed through the electrophilic substitution reaction due to the presence of electro donating linkages of ether [112]. The tetraamine monomer containing sulfone linkages was also proposed and used to synthesize sulfonated PBIs [33].

7.5.2 Copolymers with PBI Blocks

Optimization of PBI structures by preparation of PBI copolymers has been explored by using two or more diacids together during the polymerization. An example is the synthesis of random PBI copolymers with *meta*- and *para*-phenylene linkages, i.e., *m*PBI and *p*PBI repeat units, using different amounts of isophthalic and terephthalic acid in the synthesis [40]. The incorporation of increasing amounts of the *p*-isomer in the chain results in higher molecular weights, however, lower thermal stability. The glass transition temperature of *p*-homopolymer, i.e., *p*PBI, is around 361 °C, which is 59 °C lower than that of *m*PBI (420 °C). Other series of pyridine-based PBI random copolymers consisting of *meta*- and *para*-pyridine linkages was synthesized via a similar route by the same group [90].

As discussed above, *p*PBI membranes exhibit excellent chemical and mechanical stability, but poor solubility in organic solvents. Copolymerization of *p*PBI with other PBI polymers having good solubility is an effective approach to obtain PBI copolymers with improved solubility and mechanical stability simultaneously. For example, the incorporation of aryl ether (OPBI) [41] or sulfone (SO₂PBI) [38] linkages into rigid-heterocyclic *p*PBI polymer backbones, provide copolymers combining the excellent membrane properties of *p*PBI with improved solubility.

Kim et al. [119] synthesized copolymers (AB-*p*PBIs) of ABPBI and *p*PBI which circumvented the drawbacks of the individual components through a synergetic effect. Moreover, AB-*p*PBI membranes with a higher DABA mole fraction (70–90 %) could be doped with more acid than either *p*PBI or *m*PBI. The higher acid content was attributed to the increase of the ABPBI content in the copolymer membranes. Yang et al. [43] synthesized copolymers of ABPBI with *m*PBI (AB-*m*PBI), which exhibited, however, similar acid doping levels to *m*PBI membranes. This phenomenon probably originates from the relatively low content of ABPBI units in the copolymers, i.e., up to about 40 mol%.

In addition, Mader and Benicewicz [106, 107] prepared sulfonated *p*PBI-based copolymer membranes using diacid monomers of TPA and the monosodium salt of 2-sulfoterephthalic acid (s-TPA) with TAB in PPA. The rigid *p*PBI repeat units provided the copolymer membranes excellent mechanical strength even bearing excess PA molecules. These membranes exhibited greatly improved properties compared with the post-sulfonated PBI membrane.

The original intention to synthesize PBI copolymers was aimed at fabrication of sulfonated PBI polymers. Using sulfonated monomers in the polycondensation reaction, a number of sulfonated PBI copolymers were developed. Copolycondensation of sulfonated and nonsulfonated aromatic diacids with an aromatic tetraamine has simultaneously been investigated as a better way than post-sulfonation to avoid the side reactions and to control the sulfonation degree. A series of sulfonated PBI copolymers with controlled sulfonation degrees was prepared by solution copolycondensation in PPA [77, 120–122]. The resulting polymers exhibited good solubility in polar organic solvents and good membrane processing behavior. It seems, however, that the conductivity of the sulfonated PBI membranes is highly dependent on the water content of the membrane, just like the poly(perfluorosulfonic acid) membranes. Further doping of these sulfonated PBI membranes is needed to achieve sufficient proton conductivity for practical application as electrolytes at the desired working temperatures of 150–200 °C [106, 107].

Block copolymers combining PBI with other types of macromolecular units have also been developed for superior membrane properties, as shown in Fig. 7.6. Two types of copolymers have been prepared, characterized, and evaluated as fuel cell electrolytes. One is the sulfonated copolymer containing PBI and sulfonated polymer moieties for low temperature PEMs in both PEM fuel cells and direct methanol fuel cells (DMFCs) [123–126]. The other is the random copolymer containing PBI and poly(imine/amide) moieties [127, 128]. For the sulfonated PBI copolymers, benzimidazole monomers

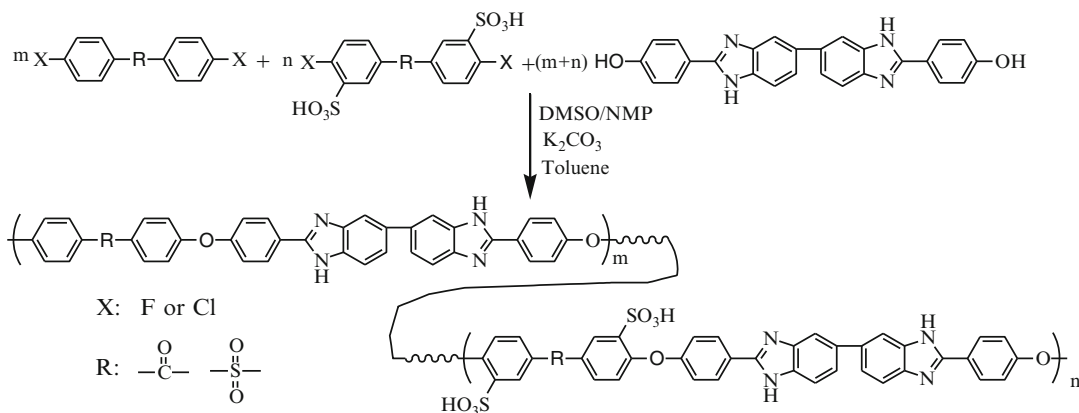


Fig. 7.6 Synthetic route for sulfonic PBI-based copolymers

containing hydroxyphenyl or amino active groups were initially synthesized. The copolymers were then obtained by copolycondensation of benzimidazole monomers with various sulfonated and/or nonsulfonated compounds containing two halogen atoms in the presence of carbonate in a mixture of polar organic solvent and toluene at an elevated temperature.

Wang et al. [123] proposed an alternating copolymer (sPEEK-PBI) by combining the acid (sPEEK) and base (PBI) units in a single polymeric chain. Hong et al. [126] adopted a similar method to synthesize a series of copolymers including PBI and poly(arylene ether sulfone) moieties. This approach resulted in improved mechanical strength and low methanol permeability due to ionic cross-linkable moieties between sulfonic acid and imidazole groups, which, however, reduced the proton conductivity. Miyatake et al. [125] synthesized a novel series of PBI block sulfonated poly(arylene ether sulfone)s via ring-closing condensation. The phase separated morphology could be designed and controlled from the corresponding hydrophilic and hydrophobic oligomers, which led to moderate water uptake and significantly higher proton conductivity compared to the randomly sulfonated PBIs.

As high temperature PEMs, random copolymers containing poly(imide benzimidazole)s (PI-PBIs) and poly(benzimidazole-amide)s were synthesized by Fang et al. [128]

and Ferreiro et al. [127], respectively. As an example, PI-PBI copolymers [127] were synthesized by condensation polymerization of biphenyl-4,4'-diyl-di(oxo)-4,4'-bis(1,8-naphthalenedicarboxylic anhydride), 2-(4-aminophenyl)-5-aminobenzimidazole and 4,4'-diaminodiphenylether in *m*-cresol in the presence of benzoic acid and isoquinoline at 180 °C. The resulting PI-PBIs showed excellent thermal and radical oxidative resistance. The corresponding membranes were to be doped with more PA to achieve high proton conductivities.

7.5.3 Side-Chain Grafting Via N-Substitution

The N-H groups in the benzimidazole rings of PBIs are chemically reactive. Side-chain-grafted PBI can be achieved via a standard S_N2 or Michael addition type reaction between the amine moiety of PBI and the electrophile. In the 1990s, Bower and Sansone et al. [129–131] first developed the approach for preparing *N*-substituted PBIs. The pristine PBI was first reacted with an alkali hydride (NaH or LiH) to produce a PBI poly-anion in DMAc or NMP, which was then reacted with a substituted or unsubstituted alkyl, aryl, or alkenyl methyl halide to produce an *N*-substituted PBI, as shown in Fig. 7.7. The alkali hydride was used to increase the nucleophilicity of the amine.

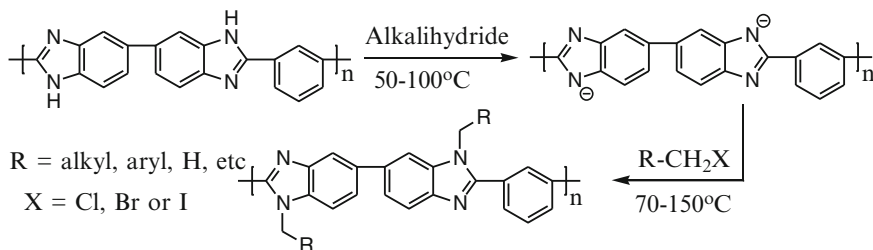


Fig. 7.7 Grafting reactions of *mPBIs*

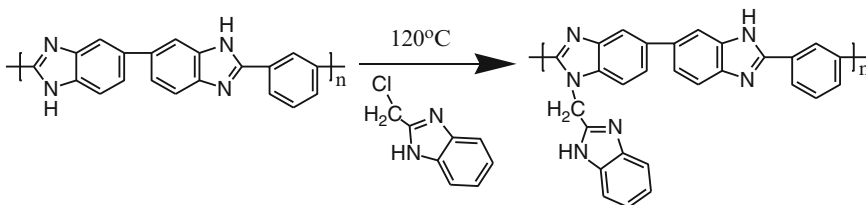


Fig. 7.8 Grafting benzimidazole onto *mPBI*

Substitution of a hydrocarbon group onto the amino nitrogen could bring about significant decreases in softening temperature and thermal stability, as well as enhanced solubility due to the decreased interaction of hydrogen bonding in the *N*-substituted PBI [132]. As reported recently, Klaehn et al. [71] prepared a series of *N*-substituted organosilane *mPBI* derivatives with nearly full substitution and the solubilities of these polymers in common organic solvents were improved significantly.

PBI-based polymer electrolytes with pendant functional groups were proposed by Gieselman and Reynolds [133, 134], by producing *N*-substituted PBI with sulfonates, which could be traced back to Sansone's work [130]. In the following years, more efforts were devoted to prepare sulfonated PBI membranes by reacting PBIs with sodium (4-bromomethyl)benzenesulfonate [135, 136], arylsulfonates, or alkylsulfonates [137]. The introduction of benzylic sulfonic, arylsulfonic, or alkylsulfonic acids was found to create proton conductivity in the presence of water. Using *N*-substitution, the sulfonation degree of the membranes could be accurately controlled [133].

Recently, various grafted *mPBI* membranes were prepared based on *N*-substitution and used

as high temperature PEMs [69, 138–142]. By grafting the alkyl [138, 139] and alkyl sulfonated [141, 142] onto *mPBI* backbones, the obtained membranes were found to exhibit increased PA doping capacity due to the disruption of the rigid structure and the increase of the free volume of the polymers [9]. For instance, a series of benzimidazole moieties grafted *mPBI* membranes with different grafting degrees was prepared by varying the molar ratios of 2-chloromethyl benzimidazole to *mPBI* through a thermal treatment procedure without any base catalyst [69], as shown in Fig. 7.8. The results indicated that the introduced side-chain benzimidazole groups provided additional basic sites for the acid–base interaction, which resulted in a higher acid doping level and improved conductivity of the membranes.

7.6 Summary

Recent progress in the synthesis of PBIs for using as high-temperature membrane electrolyte is updated. The polymer structure design with respect to the optimization of the properties of the polymer membranes and ultimately targeting improved fuel cell performance and durability is

summarized and reviewed. The approaches include:

- Increasing the content of the basic functional groups for promotion of the acid doping.
- Introducing polar groups to enhance the solubility of the polymer in organic solvents.
- Tailoring the polymer structure with high resistance towards free radicals for high stability and durability.
- Balancing the distribution of the hydrophilic and hydrophobic phases in copolymers and optimizing linear, branched or block architectures.

As a result, a wide range of various PBI polymer variants or copolymers with synthetically modified or *N*-substituted structures have been produced, characterized, and evaluated for applications in high-temperature polymer electrolyte membrane fuel cells.

Acknowledgements Funding of this work is acknowledged from the Natural Science Foundation of China (51172039), the Fundamental Research Funds for the Central Universities of China (N130305001), the Scientific Research Fund of Liaoning Provincial Education Department (L2014103) and Innovation Fund Denmark (4M Centre 0603-00527B).

References

1. Vogel T, Marvel CS (1961) Polybenzimidazoles, new thermally stable polymers. *J Polym Sci* 50:511–539
2. Neuse EW (1982) Aromatic polybenzimidazoles—syntheses, properties and applications. *Adv Polym Sci* 47:1–42
3. Chung TS (1997) A critical review of polybenzimidazoles: historical development and future R&D. *J Macromol Sci C* 37:277–301
4. Weber J (2010) Nanostructured poly(benzimidazole): from mesoporous networks to nanofibers. *ChemSusChem* 3:181–187
5. Kumbharkar SC, Karadkar PB, Kharul UK (2006) Enhancement of gas permeation properties of polybenzimidazoles by systematic structure architecture. *J Membr Sci* 286:161–169
6. Wang KY, Chung TS (2006) Fabrication of polybenzimidazole (PBI) nanofiltration hollow fiber membranes for removal of chromate. *J Membr Sci* 281:307–315
7. Yang T, Xiao Y, Chung TS (2011) Poly-/metal-benzimidazole nano-composite membranes for hydrogen purification. *Energy Environ Sci* 4:4171–4180
8. Han YJ, Wang KH, Lai JY et al (2014) Hydrophilic chitosan-modified polybenzimidazole membranes for pervaporation dehydration of isopropanol aqueous solutions. *J Membr Sci* 463:17–23
9. Li Q, Jensen JO, Savinell RF et al (2009) High temperature proton exchange membranes based on polybenzimidazoles for fuel cells. *Prog Polym Sci* 34:449–477
10. Asensio JA, Sánchez EM, Gómez-Romero P (2010) Proton-conducting membranes based on benzimidazole polymers for high-temperature PEM fuel cells. *A chemical quest. Chem Soc Rev* 39:3210–3239
11. Quartarone E, Mustarelli P (2012) Polymer fuel cells based on polybenzimidazole/H₃PO₄. *Energy Environ Sci* 5:6436–6444
12. Ma YL, Wainright JS, Litt MH et al (2004) Conductivity of PBI membranes for high-temperature polymer electrolyte fuel cells. *J Electrochem Soc* 151: A8–A16
13. Vilčiauskas L, Tuckerman M, Bester G et al (2012) The mechanism of proton conduction in phosphoric acid. *Nat Chem* 4:461–466
14. Wainright JS, Wang JT, Weng D et al (1995) Acid-doped polybenzimidazoles—a new polymer electrolyte. *J Electrochem Soc* 142:L121–L123
15. He R, Li Q, Xiao G et al (2003) Proton conductivity of phosphoric acid doped polybenzimidazole and its composites with inorganic proton conductors. *J Membr Sci* 226:169–184
16. Yang JS, He RH (2010) Preparation and characterization of polybenzimidazole membranes prepared by gelation in phosphoric acid. *Polym Adv Technol* 21:874–880
17. He R, Li Q, Bach A et al (2006) Physicochemical properties of phosphoric acid doped polybenzimidazole membranes for fuel cells. *J Membr Sci* 277:38–45
18. Lobato J, Cañizares P, Rodrigo MA et al (2007) Improved polybenzimidazole films for H₃PO₄-doped PBI-based high temperature PEMFC. *J Membr Sci* 306:47–55
19. Samms SR, Wasmus S, Savinell RF (1996) Thermal stability of proton conducting acid doped polybenzimidazole in simulated fuel cell environments. *J Electrochem Soc* 143:1225–1232
20. Li Q, He RH, Gao J et al (2003) The CO poisoning effect in PEMFCs operational at temperatures up to 200 °C. *J Electrochem Soc* 150:A1599–A1605
21. Wang JT, Savinell RF, Wainright JS et al (1996) A H₂/O₂ fuel cell using acid doped polybenzimidazole as polymer electrolyte. *Electrochim Acta* 41:193–197
22. Jensen JO, Li Q, He R et al (2005) 100–200 °C polymer fuel cells for use with NaAlH₄. *J Alloy Compd* 404–406:653–656

23. Jensen JO, Li Q, Pan C et al (2007) High temperature PEMFC and the possible utilization of the excess heat for fuel processing. *Int J Hydrogen Energy* 32:1567–1571
24. Pan C, He R, Li Q et al (2005) Integration of high temperature PEM fuel cells with a methanol reformer. *J Power Sources* 145:392–398
25. Vogel H, Marvel CS (1963) Polybenzimidazoles. II. *J Polym Sci A* 1:1531–1541
26. Choe EW (1982) Single-stage melt polymerization process for the production of high molecular weight polybenzimidazole. US Patent 4,312,976
27. Choe EW (1994) Catalysts for the preparation of polybenzimidazoles. *J Appl Polym Sci* 53:497–506
28. Choe EW, Choe DD (1996) Polybenzimidazoles (overview). In: Salamone JC (ed) *Polymeric materials encyclopedia*, vol 7. CRC, New York, pp 5619–5638
29. Wang S, Zhang G, Han M et al (2011) Novel epoxy-based cross-linked polybenzimidazole for high temperature proton exchange membrane fuel cells. *Int J Hydrogen Energy* 36:8412–8421
30. Iwakura Y, Imai Y, Uno K (1964) Polyphenylenebenzimidazoles. *J Polym Sci A* 2:2605–2615
31. Eaton PE, Carlson GR, Lee JT (1973) Phosphorus pentoxide–methanesulphonic acid. Convenient alternative to polyphosphoric acid. *J Org Chem* 38:4071–4073
32. Kim HJ, Cho SY, An SJ et al (2004) Synthesis of poly(2,5-benzimidazole) for use as a fuel-cell membrane. *Macromol Rapid Commun* 25:894–897
33. Jouanneau J, Mercier R, Gonon L et al (2007) Synthesis of sulphonated polybenzimidazoles from functionalized monomers: preparation of ionic conducting membranes. *Macromolecules* 40:983–990
34. Hedberg FL, Marvel CS (1974) A new single-step process for polybenzimidazole synthesis. *J Polym Sci* 12:1823–1828
35. Yang JS, Cleemann LN, Steenberg T et al (2014) High molecular weight polybenzimidazole membranes for high temperature PEMFC. *Fuel Cells* 14:7–15
36. Li Q, Rudbeck HC, Chromik A et al (2010) Properties, degradation and high temperature fuel cell test of different types of PBI and PBI blend membranes. *J Membr Sci* 347:260–270
37. Sannigrahi A, Ghosh S, Lalnuntluanga J et al (2009) How the monomer concentration of polymerization influences various properties of polybenzimidazole: a case study with poly(4,4'-diphenylether-5,5'-bibenzimidazole). *J Appl Polym Sci* 111:2194–2203
38. Yang J, Li Q, Cleemann LN et al (2012) Synthesis and properties of poly(aryl sulfone benzimidazole) and its copolymers for high temperature membrane electrolytes for fuel cells. *J Mater Chem* 22:11185–11195
39. Kim TH, Lim TW, Lee JC (2007) High-temperature fuel cell membranes based on mechanically stable para-ordered polybenzimidazole prepared by direct casting. *J Power Sources* 172:172–179
40. Sannigrahi A, Arunbabu D, Sankar RM et al (2007) Tuning the molecular properties of polybenzimidazole by copolymerization. *J Phys Chem B* 111:12124–12132
41. Kim TH, Kim SK, Lim TW et al (2008) Synthesis and properties of poly(aryl ether benzimidazole) copolymers for high-temperature fuel cell membranes. *J Membr Sci* 323:362–370
42. Qian GQ, Benicewicz BC (2009) Synthesis and characterization of high molecular weight hexafluoroisopropylidene-containing polybenzimidazole for high-temperature polymer electrolyte membrane fuel cells. *J Polym Sci A* 47:4064–4073
43. Yang J, He R, Che Q et al (2010) A copolymer of poly[2,2'-(*m*-phenylene)-5,5'-bibenzimidazole] and poly(2,5-benzimidazole) for high-temperature proton-conducting membranes. *Polym Int* 59:1695–1700
44. Steenberg T, Højler HA, Terkelsen C et al (2012) Roll-to-roll coated PBI membranes for high temperature PEM fuel cells. *Energy Environ Sci* 5:6076–6080
45. Lobato J, Cañizares P, Rodrigo MA et al (2006) Synthesis and characterisation of poly[2,2-(*m*-phenylene)-5,5-benzimidazole] as polymer electrolyte membrane for high temperature PEMFCs. *J Membr Sci* 280:351–362
46. Nüchter M, Ondruschka B, Bonrath W et al (2004) Microwave assisted synthesis—a critical technology overview. *Green Chem* 6:128–141
47. Singh V, Kumari PL, Tiwariy A et al (2007) Alumina supported synthesis of cassia marginata gum-g-poly(acrylonitrile) under microwave irradiation. *Polym Adv Technol* 18:379–385
48. Hoogenboom R, Schubert US (2007) Microwave-assisted polymer synthesis: recent developments in a rapidly expanding field of research. *Macromol Rapid Commun* 28:368–386
49. He R, Sun B, Yang J et al (2009) Synthesis of poly [2,2'-(*m*-phenylene)-5,5'-bibenzimidazole] and poly (2,5-benzimidazole) by microwave irradiation. *Chem Res Chinese Universities* 25:585–589
50. Kuwahara N (1963) On the polymer-solvent interaction in polymer solutions. *J Polym Sci A* 1:2395–2406
51. Shroff RN (1965) Single-point determination of intrinsic viscosity. *J Appl Polym Sci* 9:1547–1551
52. Liao J, Li Q, Rudbeck HC et al (2011) Oxidative degradation of polybenzimidazole membranes as electrolytes for high temperature proton exchange membrane fuel cells. *Fuel Cells* 11:745–755
53. Yuan YX, Johnson F, Cabasso I (2009) Polybenzimidazole (PBI) molecular weight and Mark-Houwink equation. *J Appl Polym Sci* 112:3436–3441
54. Buckley A, Stuetz D, Serad GA (1987) Polybenzimidazoles. In: Kroschwitz JI (ed) *Encyclopedia of*

- polymer science and engineering. Wiley, New York, pp 572–601
55. Kojima T, Yokota R, Kochi M et al (1980) Dilute solution properties of a polybenzimidazole. *J Polym Sci B* 18:1673–1683
 56. Marvel C S, Ariz T, Vogel HA (1965) Polybenzimidazoles and their preparation. US patent 3,174,947
 57. Dang TD, Wang CS, Click WE (1997) Polybenzobisthiazoles with crosslinking sites for improved fibre axial compressive strength. *Polymer* 38:621–629
 58. Musto P, Karasz FE, Macknight WJ (1989) Hydrogen-bonding in polybenzimidazole polyimide systems—a fourier-transform infrared investigation using low-molecular-weight monofunctional probes. *Polymer* 30:1012–1021
 59. Musto P, Karasz FE, Macknight WJ (1993) Fourier-transform infrared-spectroscopy on the thermooxidative degradation of polybenzimidazole and of a polybenzimidazole polyetherimide blend. *Polymer* 34:2934–2945
 60. Guerra G, Choe S, Williams DJ et al (1988) Fourier-transform infrared-spectroscopy of some miscible polybenzimidazole/polyimide blends. *Macromolecules* 21:231–234
 61. Bouchet R, Siebert E (1999) Proton conduction in acid doped polybenzimidazole. *Solid State Ionics* 118:287–299
 62. Glipa X, Bonnet B, Mula B et al (1999) Investigation of the conduction properties of phosphoric and sulfuric acid doped polybenzimidazole. *J Mater Chem* 9:3045–3049
 63. Kawahara M, Morita J, Rikukawa M et al (2000) Synthesis and proton conductivity of thermally stable polymer electrolyte: poly(benzimidazole) complexes with strong acid molecules. *Electrochim Acta* 45:1395–1398
 64. Voyiatzis GA (2005) Spectroelectrochemical investigation of the ability of PBI-based membranes to be acid doped. Paper presented at symposium on high temperature PEM fuel cells, Rio, Patras, Greece, 13–14 Sept 2005
 65. Li Q, He R, Berg RW et al (2004) Water uptake and acid doping of polybenzimidazoles as electrolyte membranes for fuel cells. *Solid State Ionics* 168:177–185
 66. Hughes CE, Haufe S, Angerstein B et al (2004) Probing structure and dynamics in poly[2,2'-(*m*-phenylene)-5,5'-bibenzimidazole] fuel cells with magic-angle spinning NMR. *J Phys Chem* 108:13626–13631
 67. Kumbharkar SC, Islam MN, Potrekar RA et al (2009) Variation in acid moiety of polybenzimidazoles: investigation of physico-chemical properties towards their applicability as proton exchange and gas separation membrane materials. *Polymer* 50:1403–1413
 68. Asensio JA, Borrós S, Gómez-Romero P (2002) Proton-conducting polymers based on benzimidazoles and sulfonated benzimidazoles. *J Polym Sci A* 40:3703–3710
 69. Yang JS, Aili D, Li QF et al (2013) Benzimidazole grafted polybenzimidazoles for proton exchange membrane fuel cells. *Polym Chem* 4:4768–4775
 70. Hu M, Pearce EM, Kwei TK (1993) Modification of polybenzimidazole: synthesis and thermal stability of poly(N1-methylbenzimidazole) and poly(N1, N3-dimethylbenzimidazolium) salt. *J Polym Sci A* 31:553–561
 71. Klaehn JR, Luther TA, Orme CJ et al (2007) Soluble *N*-substituted organosilane polybenzimidazoles. *Macromolecules* 40:7487–7492
 72. Hanley TR, Helminiak TE, Benner CL (1978) Expansion of aromatic heterocyclic polymers in salt solution. *J Appl Polym Sci* 22:2965–2978
 73. Lin HL, Chen YC, Li CC et al (2008) Preparation of PBI/PTFE composite membranes from PBI in *N*, *N*'-dimethyl acetamide solutions with various concentrations of LiCl. *J Power Sources* 181:228–236
 74. Litt M, Ameri R, Wang Y et al (1999) Polybenzimidazoles/phosphoric acid solid polymer electrolytes: mechanical and electrical properties. In: Nazri GA, Julien C, Rougier A (eds) *MRS Proceedings* 548. Materials Research Society, Warrendale, pp 313–323
 75. Wang B, Tang Y, Wen Z et al (2009) Dissolution and regeneration of polybenzimidazoles using ionic liquids. *Eur Polym J* 45:2962–2965
 76. Xiao L, Zhang H, Scanlon E et al (2005) High-temperature polybenzimidazole fuel cell membranes via a sol-gel process. *Chem Mater* 17:5328–5333
 77. Qing S, Huang W, Yan D (2005) Synthesis and characterization of thermally stable sulfonated polybenzimidazoles. *Eur Polym J* 41:1589–1595
 78. Chuang SW, Hsu SLC (2006) Synthesis and properties of a new fluorine-containing polybenzimidazole for high-temperature fuel-cell applications. *J Polym Sci A* 44:4508–4513
 79. Yang JS, Li QF, Cleemann LN et al (2013) Cross-linked hexafluoropropylidene polybenzimidazole membranes with chloromethyl polysulfone for fuel cell applications. *Adv Energy Mater* 3:622–630
 80. Dai H, Zhang H, Zhong H et al (2010) Properties of polymer electrolyte membranes based on poly(aryl ether benzimidazole) and sulphonated poly(aryl ether benzimidazole) for high temperature PEMFCs. *Fuel Cells* 10:754–761
 81. Li J, Li X, Zhao Y et al (2012) High-temperature proton-exchange-membrane fuel cells using an ether-containing polybenzimidazole membrane as electrolyte. *ChemSusChem* 5:896–900
 82. Yang JS, Aili D, Li QF et al (2013) Covalently cross-linked sulfone polybenzimidazole membranes by poly(vinylbenzyl chloride) for fuel cell applications. *ChemSusChem* 6:275–282
 83. Chuang SW, Hsu SLC, Liu YH (2007) Synthesis and properties of fluorine-containing polybenzimidazole/silica nanocomposite membranes for proton

- exchange membrane fuel cells. *J Membr Sci* 305:353–363
84. Wang JTW, Hsu SLC (2011) Enhanced high-temperature polymer electrolyte membrane for fuel cells based on polybenzimidazole and ionic liquids. *Electrochim Acta* 56:2842–2846
85. Qian GQ, Smith DW, Benicewicz BC (2009) Synthesis and characterization of high molecular weight perfluorocyclobutyl containing polybenzimidazoles (PFCB–PBI) for high temperature polymer electrolyte membrane fuel cells. *Polymer* 50:3911–3916
86. Pu H, Wang L, Pan HY et al (2010) Synthesis and characterization of fluorine-containing polybenzimidazole for proton conducting membranes in fuel cells. *J Polym Sci A* 48:2115–2122
87. Xiao L, Zhang H, Jana T et al (2005) Synthesis and characterization of pyridine-based polybenzimidazoles for high temperature polymer electrolyte membrane fuel cell applications. *Fuel Cells* 5:287–295
88. Carollo A, Quartarone E, Tomasi C et al (2006) Developments of new proton conducting membranes based on different polybenzimidazole structures for fuel cells applications. *J Power Sources* 160:175–180
89. Garbarczyk E, Nowinski JH, Gerbaldi C (2009) Pyridine-based PBI composite membranes for PEMFCs. *Fuel Cells* 9:349–355
90. Sannigrahi A, Ghosh S, Maity S et al (2010) Structurally isomeric monomers directed copolymerization of polybenzimidazoles and their properties. *Polymer* 51:5929–5941
91. Mustarelli P, Quartarone E, Grandi S et al (2012) Increasing the permanent conductivity of PBI membranes for HT-PEMs. *Solid State Ionics* 225:228–231
92. Molle MA, Chen X, Ploehn HJ et al (2014) High polymer content 3,5-pyridine-polybenzimidazole copolymer membranes with improved compressive properties. *Fuel Cells* 14:16–25
93. Yang JS, Xu YX, Zhou L et al (2013) Hydroxyl pyridine containing polybenzimidazole membranes for proton exchange membrane fuel cells. *J Membr Sci* 446:318–325
94. Kim SK, Kim TH, Jung JW et al (2009) Polybenzimidazole containing benzimidazole side groups for high-temperature fuel cell applications. *Polymer* 50:3495–3502
95. Guan Y, Pu H, Jin M et al (2012) Proton conducting membranes based on poly(2,2'-imidazole-5,5'-bibenzimidazole). *Fuel Cells* 12:124–131
96. Potrekar RA, Kulkarni MP, Kulkarni RA et al (2009) Polybenzimidazoles tethered with *N*-phenyl 1,2,4-triazole units as polymer electrolytes for fuel cells. *J Polym Sci A* 47:2289–2303
97. Li X, Liu C, Zhang S et al (2012) Acid doped polybenzimidazoles containing 4-phenyl phthalazinone moieties for high-temperature PEMFC. *J Membr Sci* 423–424:128–135
98. Li X, Liu C, Zhang S et al (2013) Functionalized 4-phenyl phthalazinone-based polybenzimidazoles for high-temperature PEMFC. *J Membr Sci* 442:160–167
99. Angioni S, Villa DC, Barco SD et al (2014) Polysulfonation of PBI-based membranes for HT-PEMFCs: a possible way to maintain high proton transport at a low H₃PO₄ doping level. *J Mater Chem A* 2:663–671
100. Xu N, Guo X, Fang J et al (2009) Synthesis of novel polybenzimidazoles with pendant amino groups and the formation of their crosslinked membranes for medium temperature fuel cell applications. *J Polym Sci A* 47:6992–7002
101. Bhadra S, Kim NH, Lee JH (2010) A new self-cross-linked, net-structured, proton conducting polymer membrane for high temperature proton exchange membrane fuel cells. *J Membr Sci* 349:304–311
102. Xu H, Chen K, Guo X et al (2007) Synthesis of hyperbranched polybenzimidazoles and their membrane formation. *J Membr Sci* 288:255–260
103. Weber J, Kreuer KD, Maier J et al (2008) Proton conductivity enhancement by nanostructural control of poly(benzimidazole)-phosphoric acid adducts. *Adv Mater* 20:2595–2598
104. Bhadra S, Kim NH, Choi JS et al (2010) Hyperbranched poly(benzimidazole-co-benzene) with honeycomb structure as a membrane for high-temperature proton-exchange membrane fuel cells. *J Power Sources* 195:2470–2477
105. Mader JA, Benicewicz BC (2010) Sulfonated polybenzimidazoles for high temperature PEM fuel cells. *Macromolecules* 43:6706–6715
106. Mader JA, Benicewicz BC (2011) Synthesis and properties of random copolymers of functionalised polybenzimidazoles for high temperature fuel cells. *Fuel Cells* 11:212–221
107. Mader JA, Benicewicz BC (2011) Synthesis and properties of segmented block copolymers of functionalised polybenzimidazoles for high-temperature PEM fuel cells. *Fuel Cells* 11:222–237
108. Yu S, Benicewicz BC (2009) Synthesis and properties of functionalized polybenzimidazoles for high-temperature PEMFCs. *Macromolecules* 42:8640–8648
109. Luo H, Pu H, Chang Z et al (2012) Crosslinked polybenzimidazole via a Diels–Alder reaction for proton conducting membranes. *J Mater Chem* 22:20696–20705
110. Guan Y, Pu H, Wan D (2011) Synthesis and properties of poly[2,2'-(4,4'-(2,6-bis(phenoxy)benzotrile))-5,5'-bibenzimidazole] for proton conducting membranes in fuel cells. *Polym Chem* 2:1287–1292
111. Maity S, Jana T (2013) Soluble polybenzimidazoles for PEM: synthesized from efficient, inexpensive, readily accessible alternative tetraamine monomer. *Macromolecules* 46:6814–6823

112. Peron J, Ruiz E, Jones DJ et al (2008) Solution sulfonation of a novel polybenzimidazole. A proton electrolyte for fuel cell application. *J Membr Sci* 314:247–256
113. Hu J, Luo J, Wagner P et al (2009) Anhydrous proton conducting membranes based on electron-deficient nanoparticles/PBI-OO/PFSA composites for high-temperature PEMFC. *Electrochem Commun* 11:2324–2327
114. He R, Li Q, Jensen JO et al (2007) Doping phosphoric acid in polybenzimidazole membranes for high temperature proton exchange membrane fuel cells. *J Polym Sci A* 45:2989–2997
115. Angioni S, Righetti PP, Quartarone E et al (2011) Novel aryloxy-polybenzimidazoles as proton conducting membranes for high temperature PEMFCs. *Int J Hydrogen Energy* 36:7174–7182
116. Nalawade A, Hassan MK, Jarrett WA et al (2011) Broadband dielectric spectroscopy studies of glassy-state relaxations in annealed poly(2,5-benzimidazole). *Polym Int* 61:55–64
117. Asensio JA, Borro S, Gómez-Romero P (2003) Polymer electrolyte fuel cells based on phosphoric acid-impregnated poly(2,5-benzimidazole) membranes. *J Electrochem Soc* 151:A304–A310
118. Asensio JA, Gómez-Romero P (2005) Recent developments on proton conducting poly(2,5-benzimidazole) (ABPBI) membranes for high temperature polymer electrolyte membrane fuel cells. *Fuel Cells* 5:336–343
119. Kim SK, Kim TH, Jung JW et al (2008) Copolymers of poly(2,5-benzimidazole) and poly[2,2'-(*p*-phenylene)-5,5'-bibenzimidazole] for high-temperature fuel cell applications. *Macromol Mater Eng* 293:914–921
120. Qing S, Huang W, Yan D (2005) Synthesis and characterization of thermally stable sulfonated polybenzimidazoles. *Chem J Chinese Universities* 26:2145–2148
121. Qing S, Huang W, Yan D (2005) Synthesis and characterization of thermally stable sulfonated fluorine containing polybenzimidazoles. *Acta Chimica Sinica* 63:667–670
122. Wang G, Xiao G, Yan D (2011) Synthesis and properties of soluble sulfonated polybenzimidazoles derived from asymmetric dicarboxylic acid monomers with sulfonate group as proton exchange membrane. *J Membr Sci* 369:388–396
123. Wang J, Song Y, Zhang C et al (2008) Alternating copolymer of sulfonated poly(ether ether ketone-benzimidazole)s (SPEEK-BI) bearing acid and base moieties. *Macromol Chem Phys* 209:1495–1502
124. Krishnan NN, Prabhuram J, Hong YT et al (2010) Fabrication of MEA with hydrocarbon based membranes using low temperature decal method for DMFC. *Int J Hydrogen Energy* 35:5647–5655
125. Ng F, Bae B, Miyatake K et al (2011) Polybenzimidazole block sulfonated poly(arylene ether sulfone) ionomers. *Chem Commun* 47:8895–8897
126. Ko H, Yu DM, Choi JH et al (2012) Synthesis and characterization of intermolecular ionic cross-linked sulfonated poly(arylene ether sulfone)s for direct methanol fuel cells. *J Membr Sci* 390–391:226–234
127. Ferreira JJ, Campa JDL, Lozano AE et al (2008) Synthesis and evaluation of properties of novel poly(benzimidazole-amide)s. *J Polym Sci A* 46:7566–7577
128. Yuan S, Guo X, Aili D et al (2014) Poly(imide benzimidazole)s for high temperature polymer electrolyte membrane fuel cells. *J Membr Sci* 454:351–358
129. Bower EA, Rafalko JJ (1986) Process for modifying polybenzimidazole polymers with ethylene carbonates. US Patent 4,599,388
130. Sansone MJ, Gupta B, Stackman RW (1989) Sulfoalkylation of polybenzimidazole. US Patent 4,814,399
131. Sansone MJ (1990) *N*-substituted polybenzimidazole polymer. US Patent 4,898,917
132. Cassidy PE (ed) (1980) Thermally stable polymers, synthesis and properties. Marcel Dekker, New York
133. Gieselman MB, Reynolds JR (1992) Water-soluble polybenzimidazole-based polyelectrolytes. *Macromolecules* 25:4832–4834
134. Gieselman MB, Reynolds JR (1993) Aramid and imidazole based polyelectrolytes—physical-properties and ternary phase-behavior with poly(benzobisthiazole) in methanesulphonic-acid. *Macromolecules* 26:5633–5642
135. Glipe X, Haddad ME, Jones DJ et al (1997) Synthesis and characterisation of sulphonated polybenzimidazole: a highly conducting proton exchange polymer. *Solid State Ionics* 97:323–331
136. Roziere J, Jones DJ, Marrony M et al (2001) On the doping of sulphonated polybenzimidazole with strong bases. *Solid State Ionics* 145:61–68
137. Bae JM, Honma I, Murata M et al (2002) Properties of selected sulphonated polymers as proton-conducting electrolytes for polymer electrolyte fuel cells. *Solid State Ionics* 147:189–194
138. Pu H, Liu Q, Liu G (2004) Methanol permeation and proton conductivity of acid-doped poly(*N*-ethylbenzimidazole) and poly(*N*-methylbenzimidazole). *J Membr Sci* 241:169–175
139. Pu H, Liu G (2005) Synthesis and solubility of poly(*N*-methylbenzimidazole) and poly(*N*-ethylbenzimidazole); control of degree of alkylation. *Polym Int* 54:175–179
140. Sukumar PR, Wu W, Markova D et al (2007) Functionalized poly(benzimidazole)s as membrane materials for fuel cells. *Macromol Chem Phys* 208:2258–2267
141. Namazi H, Ahmadi H (2011) Novel proton conducting membranes based on butylsulfonated poly[2,2'-(*m*-pyrazolidene)-5,5'-bibenzimidazole] (BS-PPBI): proton conductivity, acid doping and water uptake properties. *J Membr Sci* 383:280–288
142. Lin HL, Hu CR, Lai SW et al (2012) Polybenzimidazole and butylsulfonate grafted polybenzimidazole blends for proton exchange membrane fuel cells. *J Membr Sci* 389:399–406

Carsten Korte, Fosca Conti, Jürgen Wackerl,
and Werner Lehnert

8.1 Introduction

The performance of a HT-PEMFC depends mainly on the amount of phosphoric acid in the polymer membrane and in the porous catalyst layer as well as on the temperature. Furthermore, it is well known that phosphoric acid dehydrates at low water vapour partial pressure and rehydrates with increasing partial pressure, effects which can be observed in HT-PEMFCs under operating conditions [1, 2]. The composition change of phosphoric acid results in a variation of the ionic conductivity as well as of the viscosity.

In the family of mineral acids, phosphoric acid is the second most important mineral acid in terms of volume and value. It is only exceeded by sulfuric acid. In a large part it is used for the production of fertilisers and industrial phosphates, for metal surface treatment and for the acidulation of beverages. A quite-well overview on the basic properties of phosphoric acid with an emphasis on the technical processing is given by Schrödter et al. [3]. Besides its use in

the chemical industry, phosphoric acid is a widely used electrolyte in phosphoric acid fuel cell (PAFC) and more recently in phosphoric acid-based high-temperature polymer electrolyte membrane fuel cell (HT-PEMFC).

Among the polymer membrane materials, very promising are polybenzimidazole derivatives. Because of the very high softening and decomposition temperatures and the exceptional thermal and chemical stability, polybenzimidazole polymers are commonly used as synthetic fibre to fabricate high-performance protective coats and kits such as for firefighters, welders and astronauts. Upon impregnation with phosphoric acid, membranes based on polybenzimidazole polymers become excellent proton-conducting electrolytes so that they are more recently widely used as proton-conducting membrane in HT-PEMFCs [4].

High working temperatures benefit PEMFC performances because of faster electrode kinetics, higher CO tolerance and the possibility to use the residual heat for energy cogeneration [5, 6]. Among the polybenzimidazole derivatives, the most widely studied are the commercially available poly[2,2'-(*m*-phenylene)-5,5'-bibenzimidazole] with the acronyms *m*-PBI and poly(2,5-benzimidazole), AB-PBI (see Fig. 8.1). The polymers contain a basic imidazole functionality that allows the uptake of the acid protic electrolyte, which is responsible, and required, for the proton

C. Korte • J. Wackerl • W. Lehnert (✉)
Institute for Energy and Climate Research,
Electrochemical Process Engineering (IEK-3),
Forschungszentrum Jülich GmbH,
Jülich D-52428, Germany
e-mail: c.korte@fz-juelich.de; w.lehnert@fz-juelich.de

F. Conti
Department of Chemical Sciences,
University of Padova, Padova I-35131, Italy

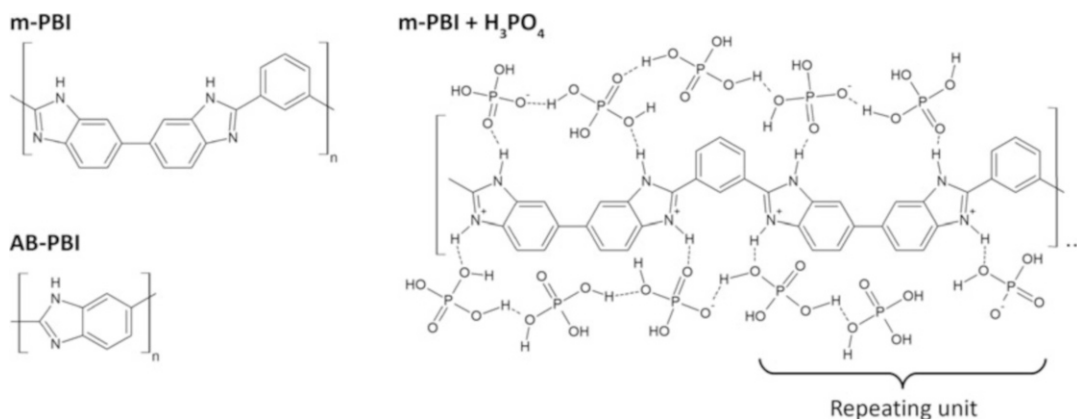


Fig. 8.1 Structure of the repeating units of *m*-PBI and AB-PBI (left). Tentative interactions of phosphoric acid with *m*-PBI (two repeating units are depicted + 5.5 H_3PO_4 molecules per repeating unit). The imidazole

groups are protonated, thus the dihydrogenphosphate anions are subject to strong coulombic interactions. Additional phosphoric acid molecules are interacting only through H bonds (right)

conduction. Polybenzimidazole membranes doped with phosphoric acid maintain their good electrical and mechanical properties without extra humidification up to temperatures as high as 200 °C. An overview can be found in [7–11].

The proton conductivity of phosphoric acid doped polybenzimidazole membranes depends strongly on the doping level and water content. The formation of dynamic hydrogen bonding networks, in which protons can readily transfer by hydrogen bond breaking and forming processes, seems to be a necessary prerequisite for a high proton conductivity. This emphasises the strategic role of the adsorption process of the acidic electrolyte in the membrane.

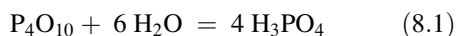
In this chapter we will firstly present a literature survey on vapour pressure, viscosity and conductivity properties of phosphoric acid with an emphasis on the temperature and composition range relevant for fuel cell applications. In a second part we want to elucidate the physico-chemical interactions of a protic electrolyte like phosphoric acid as a doping agent with polybenzimidazole-type polymer membranes. Literature data on *m*-PBI and AB-PBI as well as own measurements on Fumapem AM-55, a commercial PBI derivative, will be considered. On the basis of the observed doping behaviour a model describing the thermodynamics of the adsorption process is presented.

The thermodynamic model is correlated to molecular interactions determined by Raman spectroscopy.

8.2 Basic Chemical Properties of Phosphoric Acid

8.2.1 The Anhydride of Phosphoric Acid

There are three crystalline allotropes of the anhydride of phosphoric acid, phosphorus(V)-oxide. The dimer P_4O_{10} has a hexagonal lattice structure (H-type) and a sublimation point of 359 °C. Also two orthorhombic lattice structures exist (O and O'-type). Due to their polymeric $(\text{P}_2\text{O}_5)_n$ structure they are significantly less volatile, exhibiting melting points of 562 and 580 °C and a boiling point of 605 °C [12]. Orthophosphoric acid is formed by the direct reaction with water as shown in (8.1).

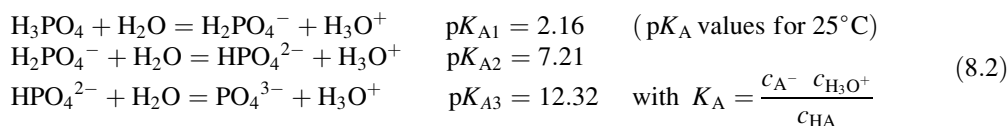


The equilibrium is virtually on the right side. The partial pressure $p_{\text{H}_2\text{O}}$ of water at 20 °C in equilibrium with pure phosphoric acid is only in the order of 10^{-6} mbar.

8.2.2 Acidity and Protolytic Equilibria of Orthophosphoric Acid

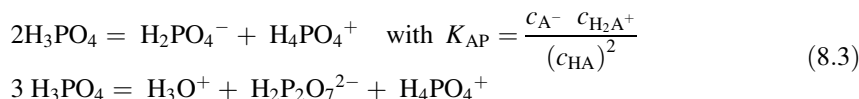
Orthophosphoric acid H_3PO_4 is a medium-strength proton donator, comparable to

hydrogensulfate HSO_4^- , chloroacetic acid $\text{ClCH}_2\text{CO}_2\text{H}$ or oxalic acid $(\text{CO}_2\text{H})_2$. In a dilute aqueous solution only the first proton is considerably dissociated, see (8.2) for the dissociation constants K_A [12–16].

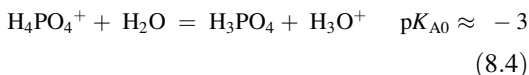


At a composition of 10 wt% H_3PO_4 (7 wt% P_2O_5) a dissociation degree of 16 % is reached. Above 85 wt% H_3PO_4 (61.6 wt% P_2O_5), the ratio

between water and phosphoric acid molecules is less than 1. In such high concentrated acids also autoprotolysis according to (8.3) takes place [17].



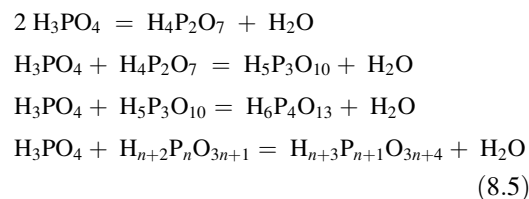
The protonation of H_3PO_4 molecules forms phosphacidium ions H_4PO_4^+ . The phosphacidium ion H_4PO_4^+ is a strong proton donor (see (8.4)).



The concentration of the phosphacidium ions is increasing with decreasing water content. Compared to other simple inorganic and organic acids and bases, orthophosphoric acid as a medium-strong acid has the highest measured autoprotolysis constant K_{AP} , see Table 8.1. At 25 °C for 100 wt% H_3PO_4 a value of about 0.16 is reached [17, 18]. It is about three orders of magnitude higher compared to anhydrous sulfuric acid and about 13 orders of magnitude higher compared to water. More than 50 % of all molecules are dissociated. Due to the high autoprotolysis constant, anhydrous orthophosphoric acid has also the highest conductivity σ_{H^+} compared to the other simple inorganic and organic acids.

8.2.3 Equilibria Between the Polyphosphoric Acid Species

Orthophosphoric acid (H_3PO_4) forms polyphosphoric acids in subsequent condensation equilibria, e.g. see (8.5) for the formation of (pyro-) diphosphoric acid ($\text{H}_4\text{P}_2\text{O}_7$), triphosphoric acids ($\text{H}_5\text{P}_3\text{O}_{10}$) or tetraphosphoric acids ($\text{H}_6\text{P}_4\text{O}_{13}$).



The formal limiting composition is metaphosphoric acid $(\text{HPO}_3)_n$, if only unbranched chains are formed. In addition to $\text{H}[-\text{O}-\text{PO}(\text{OH})-]_n\text{OH}$ chains there are also $[-\text{O}-\text{PO}(\text{OH})-]_n$ rings (see (8.6)).

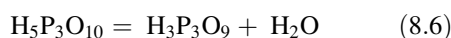


Table 8.1 Acidity pK_A and autoprotolysis constants pK_{AP} of various simple inorganic and organic acids and bases [12, 16, 17, 19]

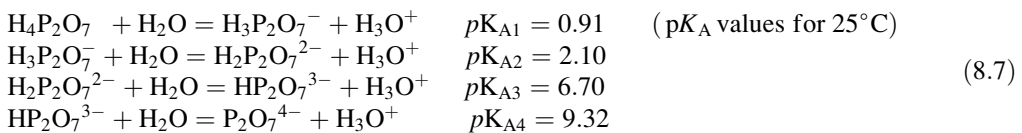
HX	$pK_A(H_2X^+)$	$pK_A(HX)$	pK_{AP}	$\sigma_{H^+}/S\text{ cm}^{-1}$	Boiling point ($^\circ\text{C}$)
NH ₃	9.25	32	29.8	$\sim 10^{-8}$ ($-33\text{ }^\circ\text{C}$)	-33
H ₂ O	0	14	14	5.5×10^{-8} ($25\text{ }^\circ\text{C}$)	100
CH ₃ CO ₂ H	-6.4	4.76	14.5	6×10^{-7} ($25\text{ }^\circ\text{C}$)	118
HF	<i>~ -9</i>	3.2	10.7	7×10^{-8} ($0\text{ }^\circ\text{C}$)	19.5
HCO ₂ H	<i>~ -7</i>	3.77	6.2	6.1×10^{-5} ($25\text{ }^\circ\text{C}$)	101 (decomp.)
H ₃ PO ₄	<i>~ -3</i>	2.16	0.8	4.6×10^{-2} ($25\text{ }^\circ\text{C}$); 0.48 ($150\text{ }^\circ\text{C}$)	>213 (decomp.)
HPO(OH) ₂		1.3		0.2 ($100\text{ }^\circ\text{C}$)	200 (decomp.)
H ₂ SeO ₄		-0.5	~ 2	5.6×10^{-2} ($25\text{ }^\circ\text{C}$)	>260 (decomp.)
CH ₃ SO ₃ H		-1.9		0.41×10^{-2} ($25\text{ }^\circ\text{C}$)	220 (decomp.)
H ₂ SO ₄	<i>~ -8.3</i>	<i>~ -3</i>	3.57	1.0×10^{-2} ($25\text{ }^\circ\text{C}$)	~ 280
HClO ₄	<i>~ -14</i>	<i>~ -10</i>		3.2×10^{-3} ($20\text{ }^\circ\text{C}$)	130
HSO ₃ F		<i>~ -10</i>	7.4	$>1.1 \times 10^{-4}$ ($25\text{ }^\circ\text{C}$)	162.6 ^a
CF ₃ SO ₃ H		<i>~ -13</i>		3.5×10^{-5} ($25\text{ }^\circ\text{C}$)	162

The anhydrous compounds HX in the grey shaded area have conductivities, suitable for technical (fuel cell) applications, i.e. in the range 10^{-1} – 10^{-2} S cm^{-1} . Negative (usually estimated) values of the acidity constant for very strong acids are italicised

^aHSO₃F decomposes in aqueous solutions

The state of the condensation equilibria are functions of temperature T (and pressure p). Thus, in the state of thermodynamic equilibrium, the concentration of each polyphosphoric acid species is essentially only a function of temperature and the initial concentration of P₂O₅.

In contrast to orthophosphoric acid, diphosphoric acid is a strong proton donor. Its dissociation constants K_A are about one order of magnitude larger (see (8.7)).



The number of systematic experimental studies in literature on the state of the condensation equilibria is very small [20–22]. A formal approach using models from polymer science can be found in a key study of Westman and Beatty [23]. In all of these experimental studies concentrated solutions are prepared by mixing phosphoric acid and phosphorous (V)-oxide. The sample solutions were equilibrated at an elevated temperature ($\geq 100\text{ }^\circ\text{C}$) and the subsequent analysis was done at room temperature by using e.g. ion chromatography. This procedure is valid, as the kinetics of all condensation

equilibria is very slow at room temperature and fast enough to establish the thermodynamic equilibrium at the experimental temperature.

The results of the most comprehensive studies of Huthi and Gartagnis [21] and Jameson [22] are in very good agreement compared to each other, as depicted in Fig. 8.2. At equilibration temperatures above $200\text{ }^\circ\text{C}$ a fraction of about 15 wt% pyrophosphoric acid is formed from originally 100 wt% orthophosphoric acid. The result of the study by Higgins and Baldwin [20] is not in agreement and is difficult to compare, because the exact P₂O₅ content of the samples after

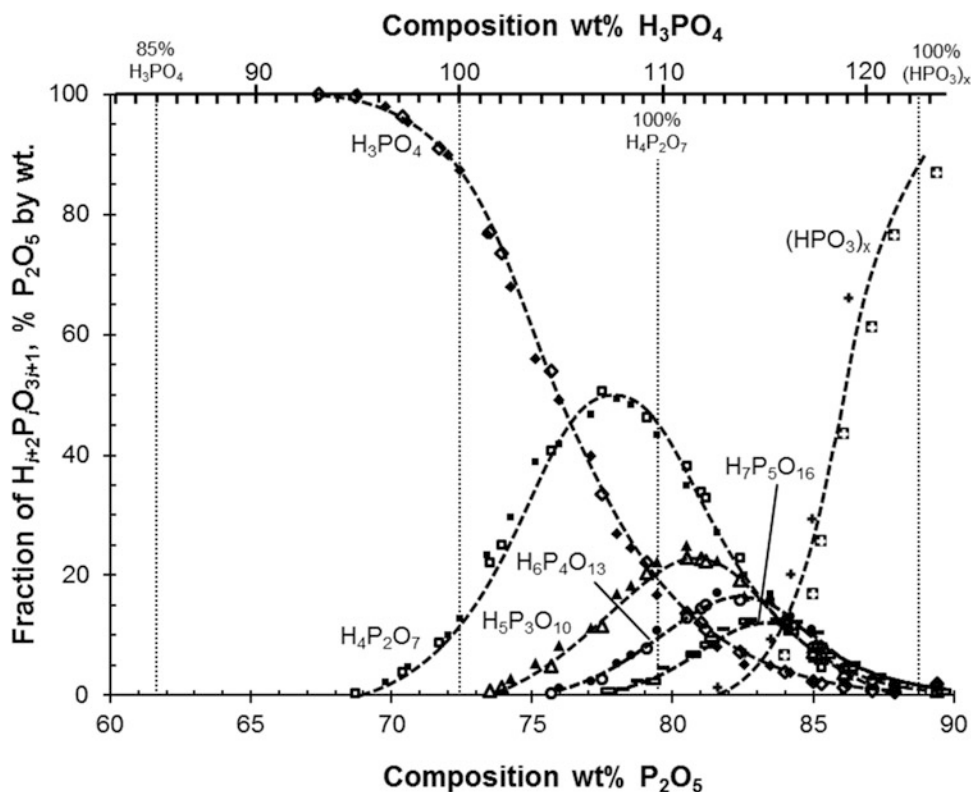


Fig. 8.2 Fractions of the different polyphosphoric acids in the system $\text{H}_2\text{O}-\text{P}_2\text{O}_5$ as a function of P_2O_5 content. Data points taken from Jameson [22] are marked with

solid symbols and data points taken from Huthi and Gartagnis [21] are marked with hollow symbols

equilibration was not indicated. The data found in the literature do not draw a complete picture. The temperature dependence of the polyphosphoric acid equilibria below 200°C is not clear. There is no information on the kinetics of these condensation reactions in the temperature range above room temperature up to 200°C .

8.3 Basic Physical Properties of Phosphoric Acid

8.3.1 Vapour Pressure of Phosphoric Acid Between 25 and 170°C

Data on the water vapour pressure of aqueous phosphoric acid can be found by Fontana [24], Brown and Whitt [25], Kablukov and Zagwodkin [26], McDonald and Boyack [27]

and Schmalz [28]. As depicted in Fig. 8.3, it is possible to evaluate a detailed diagram for the isotherms between 25 and 170°C in a composition range of $0-76.5$ wt% P_2O_5 and a pressure range up to 1013 mbar. The data from the given references fit quite well together without discontinuities. Intermediate compositions and temperatures can be interpolated.

The isotherms in Fig. 8.3 represent contour curves of a $p_{\text{H}_2\text{O},g}-T$ -wt% P_2O_5 plot. The resulting surface represents the boundary between the single-phase field of liquid phosphoric acid and the two-phase field of coexisting liquid phosphoric acid and vapour (bubble point plane). Using the Clausius-Clapeyron relation, the evaporation enthalpy $\Delta_{\text{vap}}H_{\text{H}_2\text{O}}$ of water can be calculated for a fixed composition wt% H_3PO_4 from the $p_{\text{H}_2\text{O},g}-T$ data. For small concentrations below 50 wt% H_3PO_4 $\Delta_{\text{vap}}H_{\text{H}_2\text{O}}$ is almost

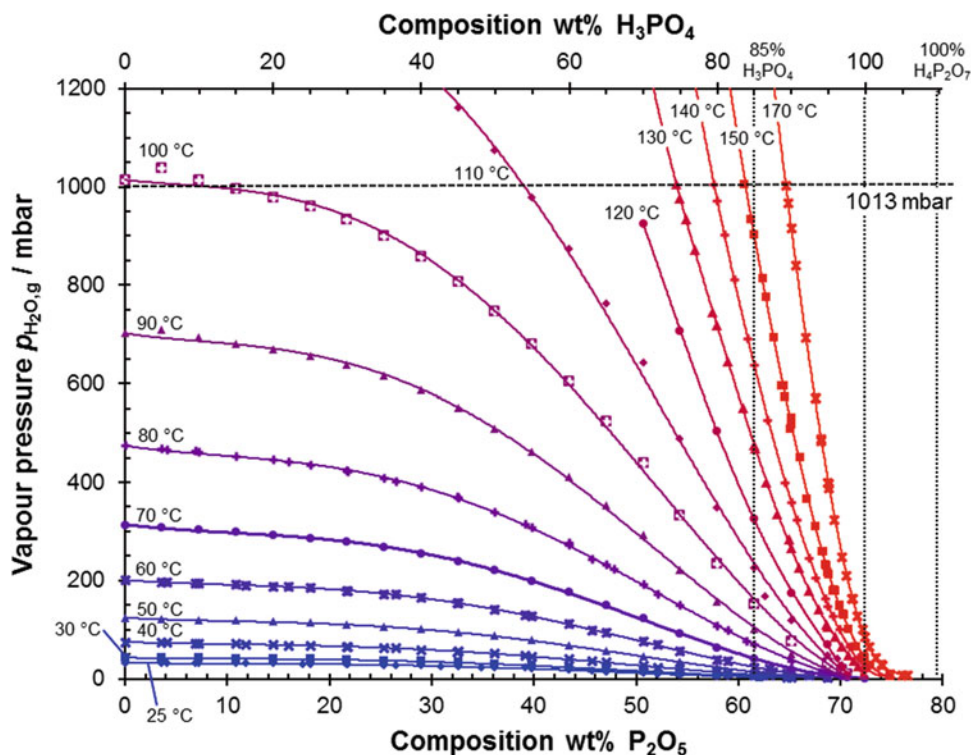


Fig. 8.3 Vapour pressure $p_{\text{H}_2\text{O},g}$ of the system $\text{H}_2\text{O}-\text{P}_2\text{O}_5$ as a function of composition and temperature, evaluated data from [24–28]. Isotherms with (partially)

interpolated compositions. The solid lines are only guides for the eye to connect the data points of the isotherms

constant and amounts to $\sim 43 \text{ kJ mol}^{-1}$. It does not differ significantly from the value found for pure water [16]. At higher concentrations the evaporation enthalpy is strongly increasing. For 100 wt% H_3PO_4 (72.4 wt% P_2O_5) it will reach a value of about 53 kJ mol^{-1} .

Cross sections of the $p_{\text{H}_2\text{O},g}-T$ -wt% P_2O_5 plot in Fig. 8.3 for a fixed vapour pressure of H_2O will result in T -wt% P_2O_5 diagrams, as depicted in Fig. 8.4. In this diagram the missing dew point curves were constructed according to the study of Brown and Whitt [25]. For temperatures below 300 °C the partial pressures of phosphoric acid and P_4O_{10} are negligible. For a distinct water partial pressure the system phosphoric acid–water exits as a single phase only in a field below the corresponding bubble point curve. Above this curve and below the dew point curve liquid aqueous phosphoric acid and vapour coexist. Entering the two-phase field will result

in a preferential evaporation of water until the thermodynamic equilibrium is reached.

8.3.2 Protonic Conductivity in Phosphoric Acid in the Range Between 0 and 170 °C

In aqueous phosphoric acid, electric charge transfer takes place by proton or by anion migration [29, 30]. Proton migration is generally much faster compared to the migration of anions. The transference number of the protonic charge carriers in phosphoric acid is close to one. Using ^1H - and ^{31}P -NMR spectroscopy one finds, that in case of low phosphoric acid concentrations, protons will be transferred by a hopping mechanism mainly between H_3O^+ and H_2O species [29, 31, 32]. In case of high phosphoric acid concentrations, if the fraction of H_2O

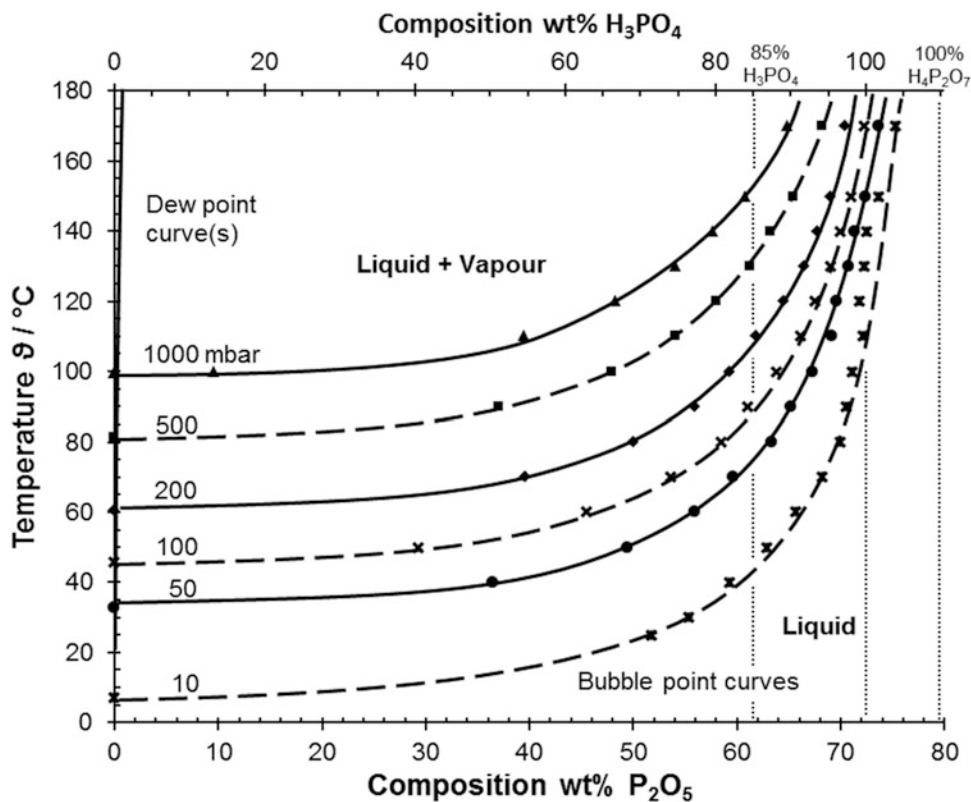


Fig. 8.4 T -wt% P_2O_5 phase diagram of the system H_2O - P_2O_5 constructed from Fig. 8.3 for constant pressures $p_{H_2O,g}$. Bubble point curves for vapour

pressures $p_{H_2O,g}$ from 10 to 1000 mbar. Dew point curve are extrapolated according to the data of Brown and Whitt [25]

molecules is quite low compared to the fraction of H_3PO_4 molecules, an increasing fraction of protons will be transferred directly between $H_4PO_4^+$ and H_3PO_4 molecules. The existence of a hopping mechanism for protons in anhydrous phosphoric acid is also supported by a comparable small activation volume [33].

Data on the protonic conductivity of aqueous phosphoric acid can be found in the works of Smith and Menzies [34], Campbell [35], Kakulin and Fedorchenko [36, 37], Greenwood and Thompson [30], McDonald and Boyack [27], Wydeven [38], Tsurko [39] and Chin and Chang [40]. In Fig. 8.5 the conductivity data are plotted as a function of composition and temperature in the range of 0–86 wt% P_2O_5 and of 0–170 °C.

In the composition range from 0 to 90 wt% P_2O_5 the conductivity of aqueous phosphoric acid varies by three orders of magnitude. At a temperature of 0 °C it reaches a maximum at a

composition of about 45 wt% H_3PO_4 (35 wt% P_2O_5). At a temperature of 100 °C the maximum shifts to a composition of 60 wt% H_3PO_4 (45 wt% P_2O_5). The maximum cannot be detected for temperatures above 100 °C, see Fig. 8.4. The water vapour pressure p_{H_2O} of phosphoric acid with a concentration within the grey shaded area in Fig. 8.5 will exceed 1 bar. For concentrations beyond the maximum, the conductivity is slightly and for concentrations above 100 wt% H_3PO_4 (72 wt% P_2O_5) strongly decreasing.

8.3.3 Dynamic Viscosity of Aqueous Phosphoric Acid in the Range Between 23 and 170 °C

Data for the dynamic viscosity of aqueous phosphoric acid for the same temperature and composition ranges as for the conductivity data can be

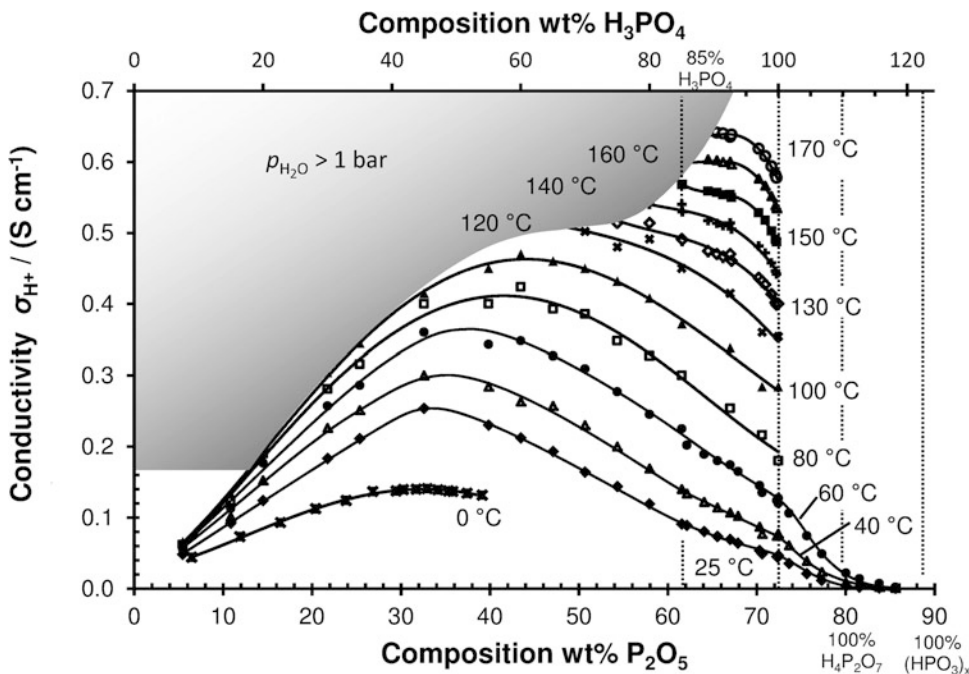


Fig. 8.5 Conductivity of the system $\text{H}_2\text{O}-\text{P}_2\text{O}_5$ as a function of composition and temperature, using evaluated data from [27, 38, 40]. The solid lines connecting the data

points serve only as a guide for the eye. In the shaded area a water vapour pressure $p_{\text{H}_2\text{O}}$ above 1 bar will be reached according to the data from Figs. 8.3 and 8.4

found in the studies of Greenwood and Thomson [30], Chin and Chang [40] and Kondratenko et al. [41, 42]. In Fig. 8.6 the dynamic viscosity η is plotted in a $\ln \eta$ vs. $1/T$ diagram.

The temperature dependence of the dynamic viscosity η of a liquid close to its glass temperature T_g can be described by the Vogel-Tammann-Fulcher (VTF) equation [43–45] or by the ‘Theory of free volume’ introduced by Doolittle [46–48], Cohen and Turnbull [49, 50]. An exponential dependence from the reciprocal temperature $1/T$ is found (see (8.8)).

$$\eta = \eta_0 e^{B_\eta/(T-T_0)} \quad (8.8)$$

Hereby, B_η , η_0 and T_0 are material-dependent parameters. In particular, T_0 is a critical temperature related to the glass transition temperature T_g . In a simple model the dynamic viscosity increases up to infinity, if the temperature of the system approaches the critical temperature T_0 . The parameter B_η is proportional to the activation energy of viscous flow.

The critical temperature T_0 can be determined for H_3PO_4 concentrations between 85 and 103 wt% H_3PO_4 (62–75 wt% P_2O_5) by fitting the data with (8.8). Depending on the concentration, a critical temperature T_0 between 140 and 180 K can be found. The glass transition temperature T_g , calculated from the line broadening in $^1\text{H-NMR}$ spectra is in the range of 200–230 K [51]. This is comparable to the findings from other glassy and high viscous systems, where T_0 is usually about 50 K lower than the glass transition temperature T_g .

8.3.4 Non-Arrhenius Behaviour for the Ionic Transport

Depending on the composition, (aqueous) phosphoric acid is a viscous liquid or a glassy solid. For concentrations above 10 wt% P_2O_5 the (proton) conductivity shows a considerably non-Arrhenius temperature dependence, i.e. the

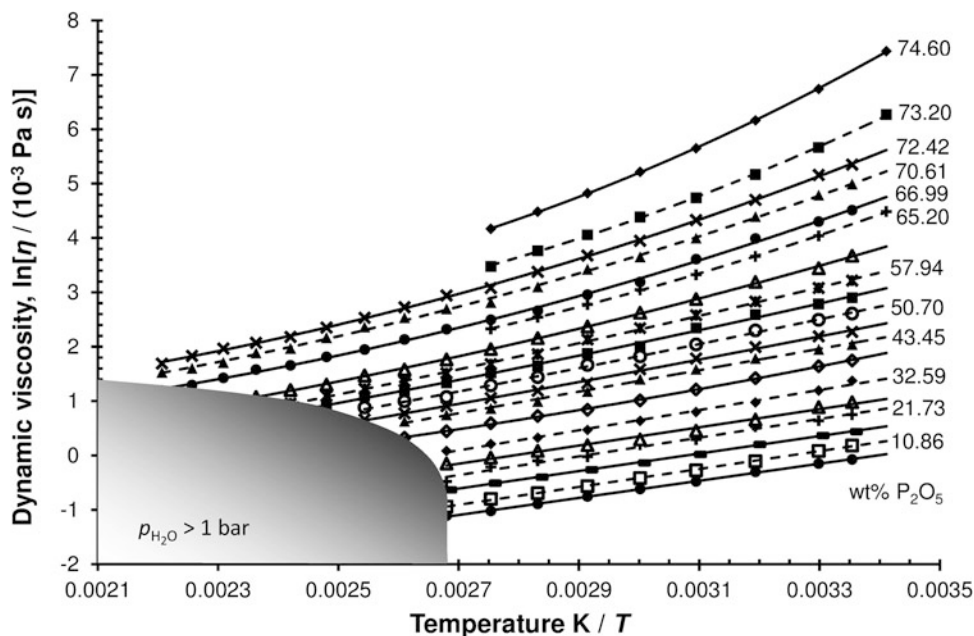


Fig. 8.6 Dynamic viscosity η of the system $\text{H}_2\text{O}-\text{P}_2\text{O}_5$ in a $\ln \eta$ vs. $1/T$ plot as a function of the composition data from [40–42]. In the shaded area a water vapour pressure

$p_{\text{H}_2\text{O}}$ above 1 bar will be reached according to the data from Figs. 8.3 and 8.4

activation energy E_a determined from a $\ln(T\sigma_i)$ vs. $1/T$ plot is temperature dependent (see (8.9)).

$$E_a = -R \left[\frac{\partial \ln(T\sigma_i)}{\partial (1/T)} \right]_{c_i} = RT^2 \left[\frac{\partial \ln(T\sigma_i)}{\partial T} \right]_{c_i} \quad (8.9)$$

Using the conductivity data in Fig. 8.5, the temperature dependence of the activation enthalpy E_a for low H_3PO_4 concentrations is small. In case of a concentration of 7.5 wt% H_3PO_4 (5.43 wt% P_2O_5) E_a has values in the range between 6 and 7.5 kJ mol^{-1} for a temperature between 25 and 100 °C. At these low concentrations the value of E_a is in the same magnitude as other diluted aqueous protic electrolytes. E.g. for pure water and 0.2 mol L^{-1} hydrochloric acid (0.7 wt% HCl), values of 10.9 and 12 kJ mol^{-1} , respectively, can be found in literature [52–55]. The activation energy is increasing with decreasing H_2O content. The temperature dependence is more pronounced at higher H_3PO_4 concentrations. In case of pure phosphoric acid, i.e. a

concentration of 100 wt% H_3PO_4 (72.42 wt% P_2O_5), E_a has values in the range between 28 and 16 kJ mol^{-1} for temperature between 25 and 170 °C. For compositions above 72.42 wt% P_2O_5 (100 wt% H_3PO_4), accompanied by a transition from a viscous liquid to a glassy solid, the activation enthalpy E_a increases even more rapidly. In case of a composition of 85.58 wt% P_2O_5 (88.74 wt% $\text{P}_2\text{O}_5 \triangleq 100$ wt% $(\text{HPO}_3)_x$) it will reach values in the range between 68 and 45 kJ mol^{-1} for temperatures of 25–60 °C.

A non-Arrhenius behaviour can be observed for many ionic conductors in the vicinity of the glass transition temperature T_g , where the dynamic viscosity η is strongly increasing, e.g. in inorganic glasses and polymers. The rate determining step for the molecular, atomic or ionic transport in such highly viscous systems is the formation of a free volume in the vicinity of a mobile particle and the reorientation of molecules, rather than an activated jump over a potential barrier in a free neighbour position itself [49]. This results in a coupling of the ionic transport with viscous rearrangements of

molecules, as described by Doolittle [46–48], Cohen and Turnbull [49, 50]. Just as the dynamic viscosity in (8.8), the conductivity σ_i of a mobile ionic species i has a Vogel-Tammann-Fulcher (VTF) type temperature dependence (see (8.10)).

$$\sigma_i = A e^{B_\sigma/(T-T_0)} \quad (8.10)$$

Hereby, B_σ , A and T_0 are material-dependent parameters. The parameter B_σ is proportional to the activation energy of ionic transport.¹ In a system with a strict coupling between dynamic viscosity and conductivity, as described by the Stokes-Einstein equation, the parameter B_η in (8.8) is equal to the parameter B_σ in (8.10). In a system with a higher probability for the motion of ionic charge carriers than for viscous flow events, as it can be found in case of cooperative proton transport mechanisms, the strict coupling between dynamic viscosity and conductivity does not hold [56–58]. In this case the parameter B_σ in (8.10) will be smaller than B_η in (8.8). Combining (8.8) and (8.10) and considering the concentration dependence of σ_i by introduction of the molar conductivity λ_i , one will yield a ‘fractional’ Walden rule (-product) as shown in (8.11).

$$\eta^\alpha \lambda_i = \text{const.} \quad \text{with} \quad \alpha = \frac{B_\sigma}{B_\eta} \quad (8.11)$$

The exponent α in (8.12) is proportional to the extent of decoupling and can be determined as a slope in a $\lg \lambda_i$ vs. $\lg 1/\eta$ -plot (Walden plot).

In Fig. 8.7a Walden plot of aqueous phosphoric acid is depicted, i.e. $\lg \lambda_{\text{H}^+}$ is plotted vs. $\lg 1/\eta$. Data for the (proton) conductivity and the viscosity for temperatures between 25 and 100 °C and for concentrations between 7.5 and 100 wt% H_3PO_4 (5.43–72.42 wt% P_2O_5) are taken from Figs. 8.5 and 8.6 [38, 40–42]. Data

for the density to calculate the concentration of phosphoric acid are taken from [16].

Within the parameter field of the used data, the molar conductivity λ_{H^+} of aqueous phosphoric acid is only a function of the dynamic viscosity η . The ‘fractional’ Walden rule according to (8.12) holds independently from temperature and composition, but with a varying exponent α . For H_3PO_4 concentrations of 7.5 wt% a value of 0.29 and for 100 wt% H_3PO_4 a value of 0.65 can be measured. The exponent α is increasing with increasing concentration and decreasing temperature—however the slope is always considerably smaller than 1 (45°).

Thus, in aqueous phosphoric acid decoupling phenomena are present over the whole concentration range. The activation energy for proton transport ($\sim B_\sigma$) is always lower than that for viscous flow ($\sim B_\eta$), implying again the presence of cooperative proton transport via hopping mechanisms [59]. With increasing H_3PO_4 concentration the degree of decoupling is decreasing. At low H_3PO_4 concentrations, protons will be transferred mainly between H_3O^+ and H_2O species. With decreasing fraction of H_2O , an increasing fraction of protons will be transferred directly between H_4PO_4^+ and H_3PO_4 molecules. The reorientation processes of the phosphoric acid species, necessary for the proton transfers, are considerably coupled to the increasing viscosity. Vehicle mechanisms for proton transport play no significant role [10]. In a system without decoupling, i.e. with pure vehicle transport and without cooperative transport, ideally an exponent α of 1 is expected. In Fig. 8.7 data for aqueous 0.01 m KCl solution for the same temperature range is added as a reference for non-cooperative ionic transport. An exponent α with a value of 0.85 is found.

Equation (8.12) is strictly valid only in case of complete dissociation. The degree of dissociation depends on the concentration. Concerning the mobile protonic charge carriers in phosphoric acid the degree of dissociation varies between 0.16 (ca. 7 wt% P_2O_5) and about 0.38 (ca. 70 wt% P_2O_5) at a temperature of 25 °C [13–15]. This will shift the data in Fig. 8.7 by a value between -0.4 and -0.8 because of the logarithmic plot.

¹ When considering an Arrhenius-type behaviour of the ionic conductivity σ_i , the temperature-dependent activation energy E_a is given by (8.9). Thus, one obtains with (8.10) for E_a :

$$E_a = RT + R \left(\frac{T}{T - T_0} \right)^2 B_\sigma \quad (8.12)$$

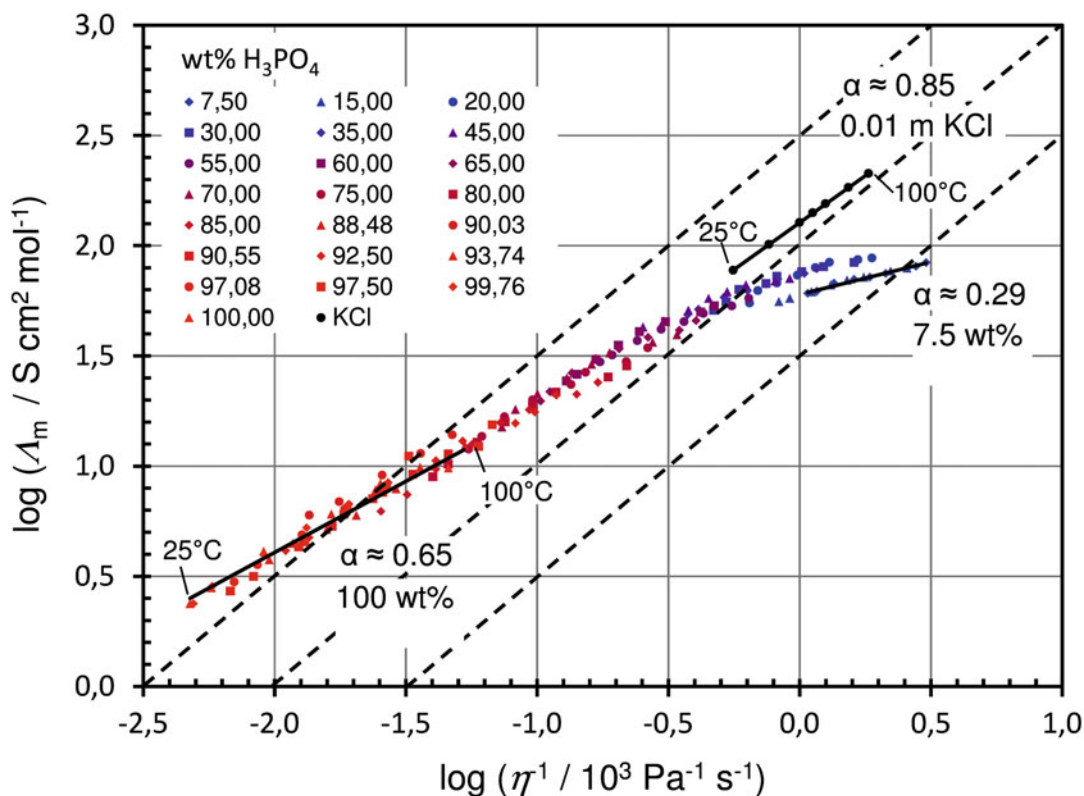


Fig. 8.7 Walden plot ($\lg \lambda_i$ vs. $\lg 1/\eta$) of aqueous phosphoric acid for composition between 7.5 and 100 wt% H_3PO_4 (5.43–72.42 wt% P_2O_5) and temperatures between 25 and 100 °C [16, 38, 40–42]. The molar conductivity is

referred to the concentration of H_3PO_4 molecules. Reference data for aqueous 0.01 mol L^{-1} KCl in the same temperature range is added [16]. The dashed lines have a slope of 1 (45°)

8.4 Interaction of Phosphoric Acid with Polybenzimidazole

In PAFCs the protic electrolyte phosphoric acid is impregnated in a porous separator, e.g. silicon carbide. Thus, considerable amounts of free (highly concentrated) phosphoric acid are present in the cell, which can be a safety issue for certain applications. In case of HT-PEMFCs the protic electrolyte phosphoric acid is adsorbed in a temperature-resistant polybenzimidazole-type (PBI) polymer membrane.

Phosphoric acid, as well as other protic electrolytes with a sufficient acidity, can be adsorbed by PBI-type polymers, because of their basic imidazole structural units. The resulting PBI–protic electrolyte systems exhibit proton conductivities of about one order of

magnitude lower than the free bulk (100 wt%) protic electrolytes.

8.4.1 Adsorption Model for a Protic Electrolyte by an Ionogene Basic Polymer

According to the published literature, two types of molecular interactions can be detected for the uptake of a protic electrolyte as phosphoric acid by a basic polymer [7, 60, 61], see Fig. 8.1 (right).

1. The polymer chain is protonated by the (acidic) protic electrolyte and the corresponding anions are subject to coulomb interactions.
2. Additional molecules of the protic electrolyte can interact with the polymer chain only by the formation of H bonds.

8.4.1.1 Modified BET-Isotherm

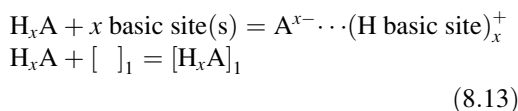
An adsorption process can be described by isotherms, i.e. by the functional relationship between the adsorbed quantities of a species vs. its activity. A direct consequence of the two possible interactions of a protic electrolyte (e.g. phosphoric, sulfuric or perchloric acid) to a polymer chain with basic groups is a ‘multi-layer-like’ adsorption process. Therefore, the use of an adsorption isotherm as described by the BET model (Brunauer-Emmett-Teller) is convenient. The BET model is originally derived for gas adsorption on surfaces [62, 63]. To derive a multilayer-like adsorption model for a basic ionogen polymer in analogy to the original BET model, we attribute the basic groups of the polymer chains, which can be protonated by the protic electrolyte, as adsorption ‘sites.’ In case of PBI-type polymers the basic groups are the imidazole centres.

The extent of the protonation of the polymer chains depends on the difference of the acidity constants ($\text{p}K_{\text{A}} = -\lg K_{\text{A}}$) of the protic electrolyte and of the protonated basic groups of the polymer. Protonated PBI-type polymers are only weak acids (benzimidazolium⁺, $K_{\text{A, HBI}^{\text{m}^+}} = 10^{-5.53}$). In the following the parameter z will denote the number of (first layer) adsorption sites. For a strong monoprotic acid as perchloric acid ($K_{\text{A, HClO}_4} \sim 10^{+10}$) it is necessarily identical to the number of protonable basic sites on the polymer chain, i.e. $z = 1$ for AB-PBI and $z = 2$ for *m*-PBI.

Phosphoric acids as doping electrolyte acts also only as a monoprotic acid. Despite the fact that it is a triprotic acid, actually only one proton can be transferred to a PBI-type polymer. Only the acidity of the first dissociation stage exceeds the acidity of the protonated benzimidazole groups ($K_{\text{A, H}_3\text{PO}_4} = 10^{-2.16}$ and $K_{\text{A, H}_2\text{PO}_4^-} = 10^{-7.21}$). Hence, the second dissociation stage can be safely neglected, resulting again to $z = 1$ for AB-PBI and $z = 2$ for *m*-PBI. This is different in case of the diprotic sulfuric acid. The acidity of the second dissociation stage is also sufficient to protonate PBI-type polymers ($K_{\text{A, H}_2\text{SO}_4} \sim 10^{+3}$

and $K_{\text{A, HSO}_4^-} = 10^{-1.9}$). Thus, the number z of (first layer) adsorption sites is only the half of the number of protonable basic sites, i.e. $z = 1/2$ for AB-PBI and $z = 1$ for *m*-PBI [16].

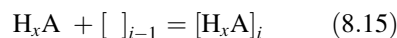
Taking the considerations from above into account, the occupation of a free site $[]_1$ in the first adsorption layer due to protonation of the polymer chain by the protic electrolyte molecule HA can be expressed as a simple reaction.



The electrolyte molecules occupying the first layer in (8.13), i.e. the anionic species A^{x-} , are strongly bound by electrostatic forces to the polymer chain. Denoting the concentration of the protic electrolyte in the doping solution as c_0 , the number of free adsorption sites of the polymer chain as N_0 and the number of sites occupied by one electrolyte molecule as N_1 , i.e. the number of electrolyte molecules occupying the first adsorption layer as anionic species A^{x-} , the occupation of the first adsorption layer can be described by an equilibrium constant K (8.14).

$$K = \frac{N_1}{N_0 c_0} \quad (8.14)$$

The value of the equilibrium constant K in (8.14) depends on the difference of the acidity of the protic electrolyte and the protonated basic groups of the polymer. Additional protic electrolyte molecules will only be bound by H bonds directly to the polymer chain or indirectly to already adsorbed electrolyte molecules. As sketched in Fig. 8.8, this should result in a successive occupation of additional adsorption layers.



The index i in (8.15) denotes the number of molecules which are layer-like adsorbed on a site. Compared to the first layer, the bonding forces of all additional layers are considerably

Basic polymer with *e.g.* 2 adsorption sites per repeating unit
+ protic (acidic) electrolyte

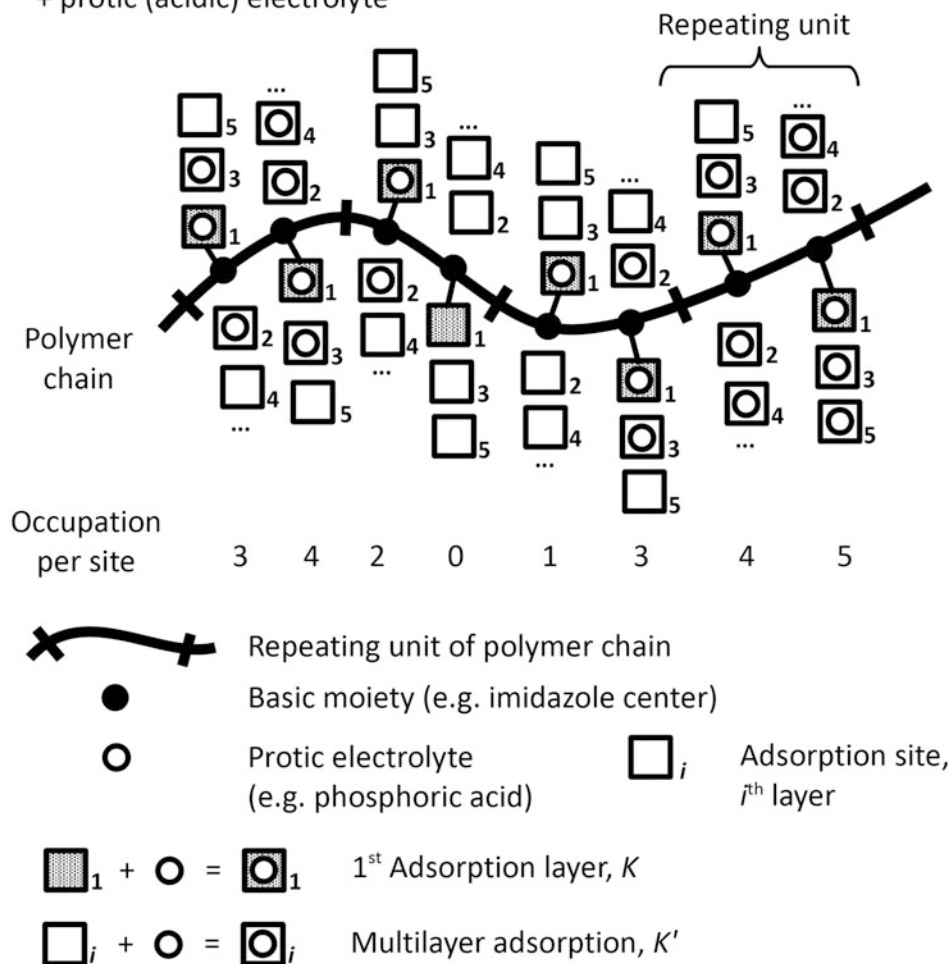


Fig. 8.8 BET-based model for the uptake of a protic electrolyte by a basic polymer (e.g. a monoprotic acid HA and a polymer with two protonable moieties/groups per repeating unit is depicted). The squares represent adsorption sites. The first layer adsorption sites, whose

occupation is accompanied with the protonation of the polymer chain, are represented by *dot-filled squares*. The index number *i* at each square denotes the adsorption layer. The HA molecules and A⁻ anions in the first layer are depicted as *hollow circles*

weaker. Thus, the corresponding equilibrium constant *K'* will be smaller than *K*.

$$K' = \frac{N_i}{N_{i-1} c_0} \quad (8.16)$$

Hereby, N_{i-1} in (8.16) denotes the number of sites with $i - 1$ layers and N_i the number of sites with i layers of electrolyte molecules. Due to the compilation of the mass action laws in (8.14) and (8.16) with concentrations and numbers of occupied sites, the equilibrium constants

K and *K'* will also include the activity coefficients γ_i . In a first approach one can assumed concentration independent equilibrium constants and thus constant activity coefficients. The ratio between the equilibrium constants of (8.14) and (8.16) is introduced as a parameter α .

$$\alpha = \frac{K}{K'} \quad (8.17)$$

Considering (8.14), (8.16) and (8.17), the number of sites N_i with i layers can be generally

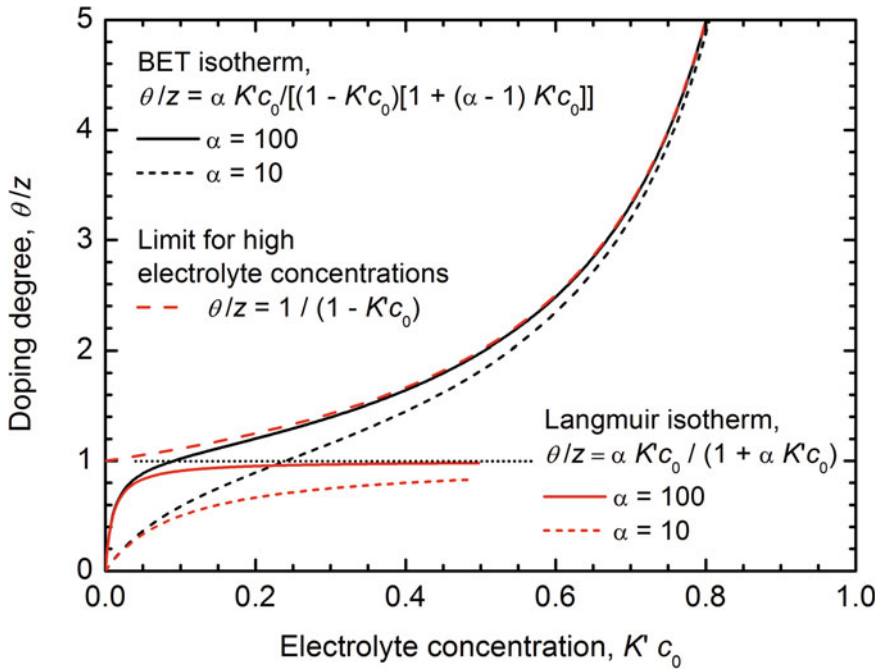


Fig. 8.9 Functional course of the BET isotherms according to (8.22) (black lines), the limiting Langmuir isotherms and the limiting isotherm for high electrolyte

concentrations (red lines) for $\alpha = 10$ and 100. The doping degree and the electrolyte concentration are scaled as dimensionless parameters, θ/z and $K' c_0$

expressed by the equilibrium constants and the number N_0 of unoccupied sites (8.18).

$$N_i = K' N_{i-1} c_0 = \alpha (c_0 K')^i N_0 \quad (8.18)$$

The total number of adsorption sites is equal to the product of the number of repeat units N_{rpu} and the number z of adsorption sites per repeat unit, i.e. to the sum of all N_i sites (8.19).

$$z N_{\text{rpu}} = N_0 + N_1 + N_2 + N_3 + \dots = \sum_{i=0}^{\infty} N_i \quad (8.19)$$

The total number N_{tot} of adsorbed electrolyte molecules can be calculated by multiplying the number of sites N_i with i adsorbed layers with the number of adsorbed layers i (number of electrolyte molecules on the site) and summing up the products for all N_i sites (8.20).

$$N_{\text{tot}} = N_1 + 2N_2 + 3N_3 + \dots = \sum_{i=1}^{\infty} i N_i \quad (8.20)$$

In analogy to the fractional coverage θ of the original BET model, a doping degree $N_{\text{tot}}/N_{\text{rpu}}$ is introduced, which relates the uptake of electrolyte molecules to the number of repeat units of the polymer. By inserting (8.18), (8.19) and (8.20) one obtains.

$$\frac{N_{\text{tot}}}{N_{\text{rpu}}} = \frac{z \sum_{i=1}^{\infty} i N_i}{\sum_{i=0}^{\infty} N_i} = \frac{z \alpha N_0 \sum_{i=1}^{\infty} i (c_0 K')^i}{N_0 + \alpha N_0 \sum_{i=1}^{\infty} (c_0 K')^i} \quad (8.21)$$

Evaluating all infinite sums in (8.21) one obtains a modified BET-isotherm (8.22).

$$\theta = \frac{N_{\text{tot}}}{N_{\text{rpu}}} = \frac{z \alpha K' c_0}{(1 - K' c_0) [1 + (\alpha - 1) K' c_0]} \quad (8.22)$$

The modified BET isotherm can be described by three free parameters z , α and K' . In Fig. 8.9 the functional course of the doping degree θ vs. the

electrolyte concentration c_0 in the doping solution is sketched for $\alpha = 10$ and $\alpha = 100$.

8.4.1.2 Limiting Cases for Low and High Concentrations of the Doping Electrolyte

In relation to the electrolyte concentration c_0 in the doping solution, the following domains can be distinguished in the adsorption isotherms (see Fig. 8.9).

1. At very low electrolyte concentrations c_0 , as long as $K' c_0 \ll 1$, (8.22) can be approximated by a Langmuir isotherm (8.23).

$$\theta|_{K'c_0 \ll 1} = \frac{z\alpha K' c_0}{1 + \alpha K' c_0} = \frac{z K c_0}{1 + K c_0} \quad (8.23)$$

At very low electrolyte concentrations c_0 , essentially only the first adsorption layer will be occupied (protonation of the chain). Thus, the functional course—the steepness² of the increase—is only determined by the first equilibrium constant K .

2. For intermediate to high electrolyte concentrations c_0 , if $\alpha K' c_0 \gg 1$ or $K c_0 \gg 1$, (8.22) can be approximated by (8.24).

$$\theta|_{Kc_0 \gg 1} = \frac{z}{1 - K' c_0} \quad (8.24)$$

The higher the value of α , i.e. $K \gg K'$, the faster the limit of (8.24) will be reached. At intermediate to high electrolyte concentrations c_0 the protonation of the polymer chains is complete, thus the 'first layer' is completely occupied. Additional protic electrolyte molecules will be multilayer-like adsorbed by H bonds. The height of the 'step' at intermediate electrolyte concentrations is determined by

²The derivative of (8.22) with respect to c_0 at $c_0 = 0$ yields (initial slope):

$$\left(\frac{d\theta}{dc_0}\right)_{c_0=0} = zK = z\alpha K' \quad (8.25)$$

z and the onset of the strong increase at high electrolyte concentrations by K' .

Modified BET models are known in literature as GAB adsorption models [64–67] (Guggenheim-Anderson-de Boer). GAB type isotherms are very seldom used. Experimental studies, using this type of isotherm, can be found mainly on (multilayer-) adsorption e.g. of water on synthetic and natural polymers, starch, wood or food [68–72]. To our best knowledge, there are only two studies applying a multilayer adsorption model like GAB or BET on the uptake of phosphoric acid and water in polybenzimidazole [73, 74]. In case of the study on the phosphoric acid uptake by He et al. [74] the approximation according to (8.24) for intermediate to high doping concentration and strong first layer adsorption, is used.

8.4.2 Experimental Studies on the Doping Behaviour of PBI-Type Polymers

Many interesting studies have been published since the introduction of H_3PO_4 doped PBI-type polymers as proton conducting electrolytes for fuel cells. We summarise a number of experimental studies on the doping behaviour of PBI-type polymers with various protic electrolytes. Experimental studies on the H_3PO_4 , H_2SO_4 and HClO_4 uptake of non-cross-linked *m*-PBI [9, 74, 75], the H_3PO_4 uptake of non-cross-linked AB-PBI [7, 61], as well as own investigations on the H_3PO_4 uptake of a cross-linked commercial PBI derivative, Fumapem AM-55 [76, 77], are taken into account. Because of their optimised mechanical properties, such as higher tear-resistance and lower plasticity, cross-linked PBI derivatives are often used for the setup of HT-PEMFC cells [36, 37].

In Fig. 8.1 (left) the chemical structures of *m*-PBI and AB-PBI are depicted. The polymer *m*-PBI has two benzimidazole structural units per repeating unit and thus two protonable sites ($z = 2$). In case of AB-PBI the repeating unit consists of only one benzimidazole structural

unit ($z = 1$). The exact structure of Fumapem AM-55 is confidential and not published yet. It is communicated that the repeating unit includes two benzimidazole structural units. The molecular weight of a repeating unit amounts to $\sim 400 \text{ g mol}^{-1}$. The crosslinking degree is below 10 % (per repeat unit). These specifications are sufficient to compare it with the adsorption behaviour of the other PBI-type polymers. All considered studies were listed in Table 8.2.

8.4.2.1 Adsorption Isotherms

The data on the uptake of protic electrolytes H_xA by *m*-PBI, AB-PBI and Fumapem AM-55 as a function of the concentration of the doping solutions are compiled and carefully analysed from various experimental studies. In Fig. 8.10 the equilibrium uptake of protic electrolytes H_xA is plotted vs. the concentration in the doping solution $c_{0,\text{H}_x\text{A}}$ to obtain the adsorption isotherms. The equilibrium uptake, expressed as (molar) doping degree θ , cannot be generally fitted by a simple Langmuir isotherm as described in (8.23) or a combination of two Langmuir-like adsorption processes, assuming two distinguishable types of adsorption sites with a limited number [60, 74, 75], because of the strong increase of the adsorption isotherms for high doping concentrations $c_{0,\text{H}_x\text{A}}$. This region is not reached in all published experimental studies, because the highest investigated concentration of the protic electrolyte H_xA in the doping solution was below 12–13 mol L^{-1} [7, 61, 75].

Only the modified BET (GAB) model, according to (8.22), is able to describe all adsorption isotherms on the whole concentration range satisfactorily. In Fig. 8.10 the corresponding fit curves are shown as solid lines. The three fit parameters, as the number of (first layer) adsorption sites z , the ratio α between the equilibrium constants and the equilibrium constant K' for multilayer adsorption are reported in Table 8.2.

For *m*-PBI + H_3PO_4 , AB-PBI + H_3PO_4 and *m*-PBI + HClO_4 the obtained values of the fit parameter z correlate well with the known numbers of basic groups per repeating unit. The parameter z is obtained by fitting with an

accuracy of 0.5–5 % (standard error). There is a maximum deviation of about 10 % from the expected value of $z = 2$ for *m*-PBI and from the value of $z = 1$ for AB-PBI.

For Fumapem AM-55 + H_3PO_4 a quite high deviation of about 24 % from the expected value of $z = 2$ and for *m*-PBI + H_2SO_4 even a deviation of 40 % from the expected value $z = 1$ can be observed. In the case of Fumapem AM-55 + H_3PO_4 the (real) error of z is underestimated by the fitting routine, because no data points below a H_3PO_4 concentration of 10 mol L^{-1} are available. This will decrease the accuracy for the determination of the numbers of basic groups. The data points in the study on AB-PBI cover a range down to 3 mol L^{-1} , and in the studies on *m*-PBI down to 0.1 mol L^{-1} . The considerable deviations in case of *m*-PBI + H_2SO_4 may indicate an incomplete transfer of the second proton of the H_2SO_4 molecules, even though its acidity is sufficient for the protonation of the imidazole structure units of the polymer. This might be caused by the assumption of constant activity coefficients in the adsorption model. From the present data this issue cannot be exhaustively cleared, yet.

For all investigated polymers and protic electrolytes the obtained values of the second equilibrium constant K' for multilayer-like adsorption are in the order of $10^{-2} \text{ L mol}^{-1}$. It has a sufficient fitting accuracy of 1–3 % (standard error). Due to the limited number of studies it is difficult to correlate the obtained values clearly to a particular structural property—however, there are distinct trends. The highest values for K' are observed for the H_3PO_4 uptake of non-cross-linked polymers, as AB-PBI with 0.062 L mol^{-1} and non-cross-linked *m*-PBI (two studies) with 0.050 and 0.054 L mol^{-1} . Compared to non-cross-linked polymers, the cross-linked Fumapem AM-55 shows a slightly (about 10–20 %) smaller value of only 0.048 L mol^{-1} . This might be caused by more rigid cross-linked polymer backbones, which hinder the swelling process. The lowest value of only 0.031 L mol^{-1} is observed for the HClO_4 uptake of non-cross-linked *m*-PBI. This might be caused by a weaker H-bond network of the only monoprotic

Table 8.2 Results from fitting the modified BET model according to (8.20) to experimental data from literature

Material	$M_{\text{rpu}}/(\text{g mol}^{-1})$	T/K	Fit parameter			$K'/(l \text{ mol}^{-1})$	Remarks
			Z	α	$K/(l \text{ mol}^{-1})$		
<i>m</i> -PBI + H ₃ PO ₄	308.34	25	2.2 ± 0.1	184 ± 102	9.9 ± 5.6	0.0539 ± 0.0005	Non-cross-linked, Li and He et al. [9, 74]
<i>m</i> -PBI + H ₃ PO ₄	308.34	25	2.08 ± 0.05	522 ± 76	26.0 ± 4.5	0.050 ± 0.001	Non-cross-linked, Sagheddi et al. [75]
<i>m</i> -PBI + HClO ₄	308.34	25	2.00 ± 0.01	1353 ± 66	42 ± 3	0.0312 ± 0.0006	Non-cross-linked, Sagheddi et al. [75]
<i>m</i> -PBI + H ₂ SO ₄	308.34	25	1.40 ± 0.04	1041 ± 249	52 ± 14	0.050 ± 0.001	Non-cross-linked, Sagheddi et al. [75]
AB-PBI + H ₃ PO ₄	116.12	25	1.1 ± 0.1	(55 ± 115)	(3.4 ± 7)	0.062 ± 0.002	Non-cross-linked, Asensio et al. [7, 61]
Fumapem AM-55 + H ₃ PO ₄	~400	110	2.5 ± 0.2	(59 ± 224)	(2.8 ± 11)	0.0478 ± 0.0005	Cross-linked, own data

If a value is given in brackets, the parameter does not converge. The margins of error exceed the absolute value of the parameter [7, 9, 61, 74, 75]

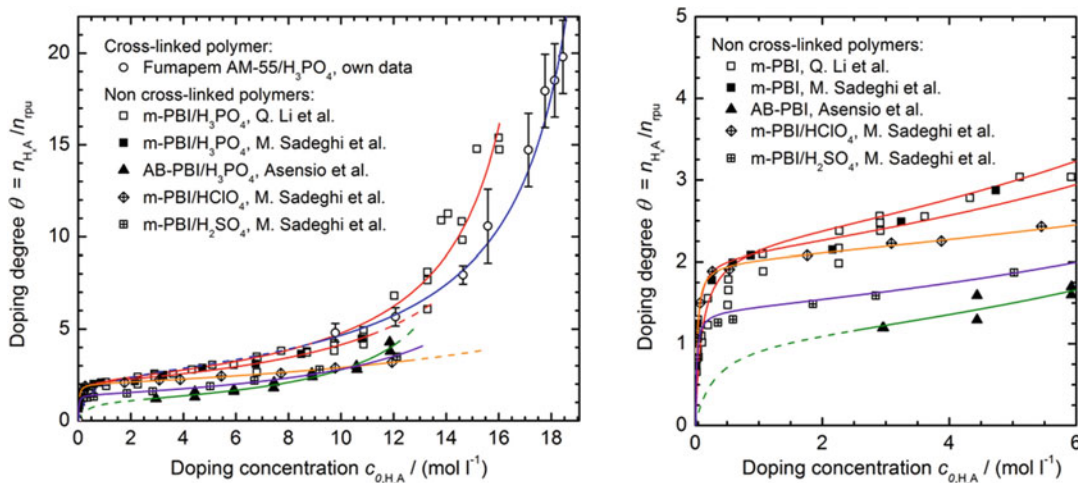


Fig. 8.10 Adsorption isotherms of *m*-PBI (25 °C), AB-PBI (25 °C) and Fumapem AM-55 (110 °C) doped with various protic electrolytes H_xA . The curves are fitted by non-linear regression using (8.22). The

$HClO_4$. For the uptake of the diprotic H_2SO_4 by non-cross-linked *m*-PBI a value of 0.050 L mol^{-1} is obtained, which is in the same range of the value for the H_3PO_4 uptake.

The first equilibrium constant K (first layer adsorption by protonation) can only be determined with a reasonable error for *m*-PBI. The obtained fit values for the H_3PO_4 , $HClO_4$ and H_2SO_4 uptake are in the range between 10 and 52 L mol^{-1} , i.e. the first equilibrium constant K is in the order of 10^1 L mol^{-1} . Thus, in case of H_3PO_4 uptake it is about two and in case of $HClO_4$ and H_2SO_4 uptake about three orders of magnitude higher than the corresponding second equilibrium constant K' .

For the H_3PO_4 uptake of AB-PBI and Fumapem AM-55, no data points for low doping concentrations c_{0,H_3PO_4} are available (see consideration above). Using (8.22), α and thus K does not converge to a distinct value, independently from the other starting values of the fit procedure. As discussed, when introducing the modified BET model, the functional course in this region depends mainly on K . In case of these incomplete data sets, the approximation function in (8.24) for high doping concentrations, using only the parameters z and K' , would also be sufficient for fitting.

numerical results are summarised in Table 8.2. The data for *m*-PBI and AB-PBI are compiled from literature [7, 9, 61, 75]. *Right*: complete concentration range, *left*: detail for low doping concentrations

8.4.2.2 Raman Spectroscopy

IR and Raman spectroscopy are common tools to study organic compounds like. The methods are rapid, non-destructive and with no need for sample preparation [78]. There is a considerable number of experimental studies using IR spectroscopy to characterise PBI-type polymers doped with phosphoric acid [7–9, 60, 61, 74, 79, 80]. The number of Raman studies is still limited, despite the fact that the intensity of vibration modes from polymer skeleton are enhanced compared to N–H and O–H vibration modes, i.e. there are less interferences due to the presence of water.

The Raman signals of pristine *m*-PBI [81] and Fumapem AM-55 and doped with H_3PO_4 at different θ doping degrees are shown on the left side of Figs. 8.11 and 8.12. As more of the protic electrolyte is introduced into the polymer, the Raman bands begin to shift and become diagnostic of the interaction between the basic imidazole group and the phosphoric acid. The vibrations of the polymer backbone become modified due to the protonation, leading to a (partially) delocalised positive charge on the benzimidazole ring and the subsequent formation of H bonds to electrolyte anions and additional bound electrolyte molecules. This will change the

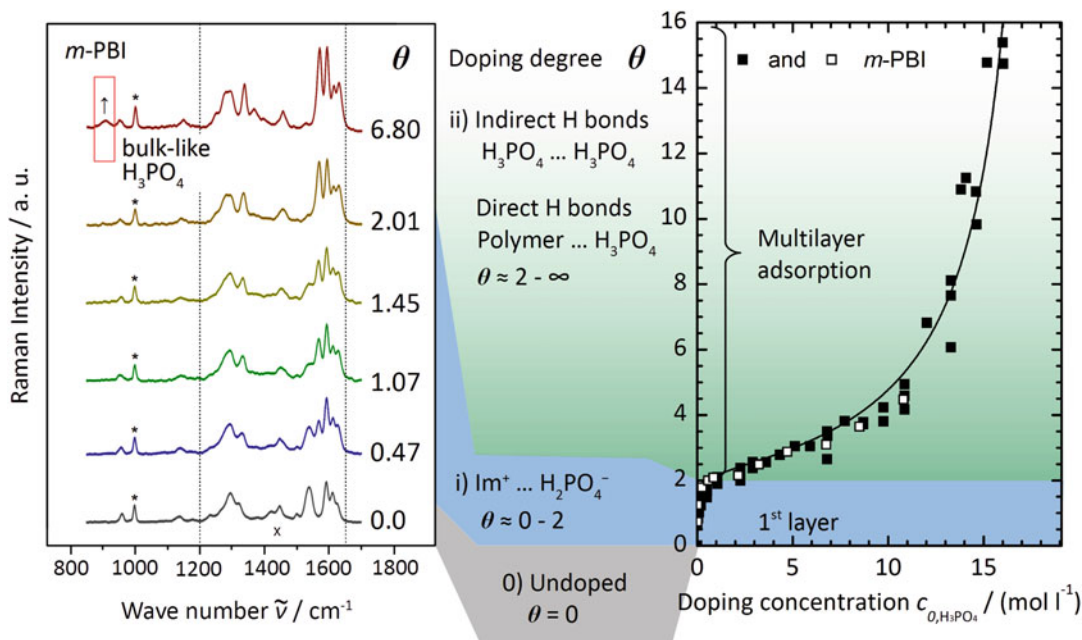


Fig. 8.11 FT-Raman spectra (*left*) of pristine *m*-PBI (*bottom*) and doped with H_3PO_4 at different doping degrees θ (25 °C), taken from Daletou et al. [81]. In the rectangle at $\sim 910 \text{ cm}^{-1}$ the Raman signal of bulk-like H_3PO_4 is marked by an up arrow. Adsorption isotherm (*right*) for H_3PO_4 by *m*-PBI (25 °C, see also Fig. 8.10).

The experimental data points from Li et al. are marked with *solid squares* and from Sadeghi et al. with *hollow squares* [9, 75]. The coloured areas indicate different adsorption stages: (0) undoped (grey, $\theta = 0$), (i) adsorption of first layer (blue, $\theta \leq 2$) and (ii) - multilayer-like adsorption (green, $\theta > 2$)

dipole–dipole interaction. A distortion of the polymer chains can be considered due to the electrolyte uptake, since the membrane swells to more than 100 % of its thickness and more than 50 % of its initial size. The polymer chains are thus farther away from each other.

The Raman spectra of *m*-PBI and Fumapem AM-55 in Figs. 8.11 and 8.12 are both normalised to the peak at 1000 and at 960 cm^{-1} (marked with an *), respectively, which is not sensitive to the doping process [81]. It can be assigned to the trigonal benzene ring deformation. The Raman bands in the spectral region between 1200 and 1650 cm^{-1} , marked with vertical dotted lines and an x, are caused by vibration modes of the polymer chain. In more detail, the three peaks in the range between 1200 and 1350 cm^{-1} and the weaker peaks around 1440 cm^{-1} can be assigned to the $\delta(\text{C-H})$ in-plane vibrations. The peaks of the symmetric $\nu(\text{C}=\text{C})$ and $\nu(\text{C}=\text{N})$ imidazole ring stretching

vibrations can be found in case of *m*-PBI at 1539 and 1570 cm^{-1} . For Fumapem AM-55 these peaks are slightly shifted and located at 1550 and 1576 cm^{-1} . These assignments can be compared with signals from ATR-FTIR spectra and theoretical calculation of normal modes for small molecular models [76, 79].

With increasing doping level θ the intensity of the peaks of the symmetric $\nu(\text{C}=\text{C})$ and $\nu(\text{C}=\text{N})$ imidazole ring stretching vibrations in the region x changes significantly. In case of *m*-PBI, the peak at 1539 cm^{-1} decreases and the peak at 1570 cm^{-1} increases. The same behaviour can be found for Fumapem AM-55 for the peaks at 1550 and 1577 cm^{-1} , respectively. In Fig. 8.13 the peak intensities at 1570 cm^{-1} for *m*-PBI and at 1577 cm^{-1} for Fumapem AM-55 are depicted. When the doping degree θ of the polymer reaches a specific value of about 2 no further (significant) intensity changes occur at these peaks in the diagnostic spectral region x of

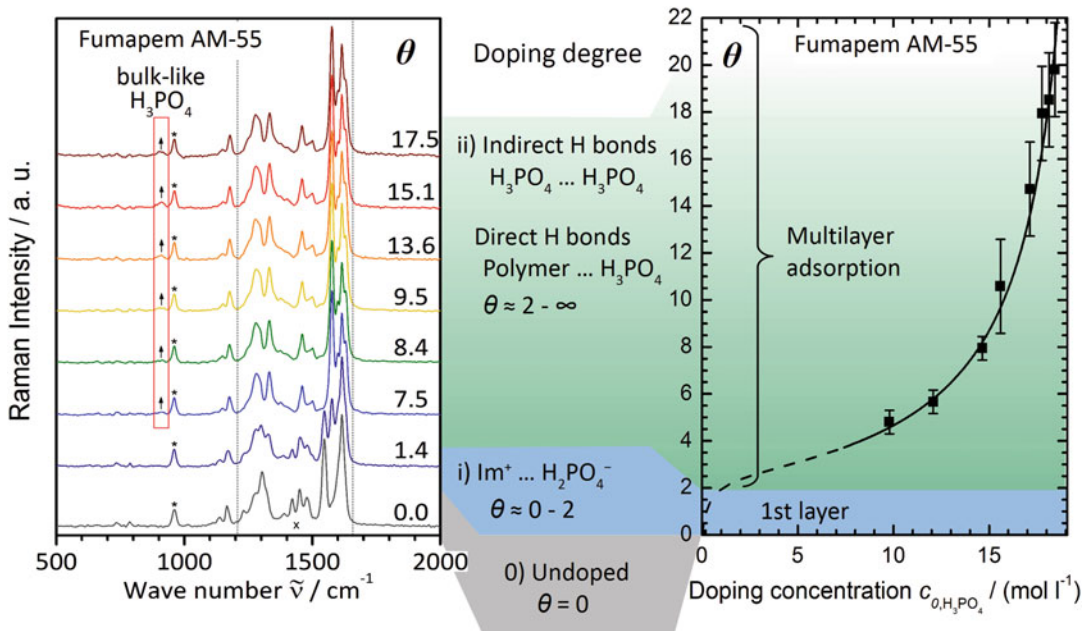


Fig. 8.12 FT-Raman spectra (left) of pristine Fumapem AM-55 (bottom) and doped with H_3PO_4 at different doping degrees θ (25 °C). In the rectangle at $\sim 910 \text{ cm}^{-1}$ the Raman signal of bulk-like H_3PO_4 is marked by an arrow. Adsorption isotherm (right) for H_3PO_4 by

Fumapem AM-55 (110 °C, see also Fig. 8.10). The coloured areas indicate different adsorption stages: undoped (grey, $\theta = 0$), adsorption of first layer (blue, $\theta \leq 2$) and multilayer-like adsorption (green, $\theta > 2$)

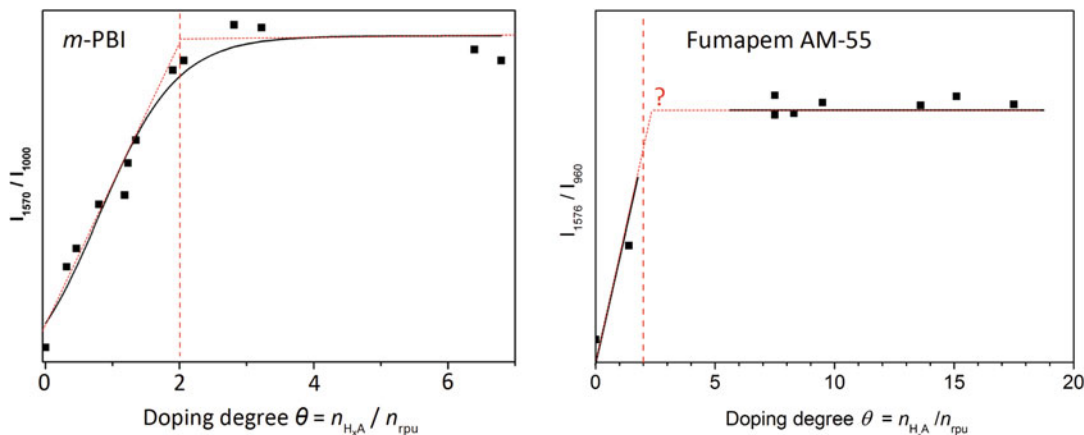


Fig. 8.13 Intensities of the Raman peaks at 1570 cm^{-1} for *m*-PBI (left, Daletou et al. [81]) and at 1577 cm^{-1} for Fumapem AM-55 (right, own measurements) as a function of the H_3PO_4 doping degrees θ . The peak intensities are normalised to the Raman peak at 1000 cm^{-1} (*m*-PBI) and 960 cm^{-1} (Fumapem AM-55). The corresponding

Raman data is shown in Figs. 8.11 and 8.12. The red dashed lines mark the doping degree θ equivalent to full protonation of the polymer chains, i.e. $\theta = z$ in case of a protic electrolyte transferring only one proton per molecule

m-PBI [81] and Fumapem AM-55. In case of Fumapem AM-55, there is a lack of spectroscopic data for doping degrees θ between 1.4 and 7.5, which limits the exact detection of this value.

These findings, detected in the Raman spectra, can be correlated to the characteristic course of the adsorption isotherm of *m*-PBI [9, 75] and Fumapem AM-55, as re-plotted on the right side of Figs. 8.11 and 8.12. Thus, the most remarkably changes in the spectral region x can be observed when the first layer adsorption of H_3PO_4 molecules takes place by protonation of the polymer chains, i.e. in the region of the adsorption isotherm with a doping level θ between 0 and 2 for *m*-PBI and Fumapem AM-55. This is in accordance to the number z of protonable groups per repeating unit. There are no more intensity changes when all imidazole equivalents are protonated. The intensity changes of the symmetric $\nu(\text{C}=\text{C})$ and $\nu(\text{C}=\text{N})$ imidazole ring stretching vibrations are caused by the modification of the bond strengths due to the generation of a (delocalised) positive charges.

The Raman band at about 910 cm^{-1} , marked with an \uparrow , can be attributed to of bulk-like phosphoric acid. An analogous signal is evident in the Raman spectrum of bulk aqueous phosphoric acid [47]. The most intense Raman band of bulk aqueous phosphoric acid is located between 840 and 960 cm^{-1} and is caused by stretching vibrations $\nu(\text{P}(\text{OH})_3)$ of H_3PO_4 molecules and $\nu(\text{P}(\text{OH})_2)$ of H_2PO_4^- ions [15, 82]. The band shifts to higher wavenumbers with increasing H_3PO_4 concentration, due to varying fractions of dissociated and undissociated species. These findings are in accordance to the well-known findings of Asensio et al. [7, 61], He et al. [74] and Li et al. [60] using IR spectroscopy to prove the evidence of the formation of protonated polymer species for AB-PBI and *m*-PBI.

The Raman band at about 910 cm^{-1} can be detected with increasing intensity when increasing the doping level θ , while the position does not shift noticeably. It is well resolved only at high doping levels θ . In case of *m*-PBI, the band can be detected at a doping level θ of 6.80. The critical doping level cannot be determined

exactly due to a lack of Raman data in the range between 2.01 and 6.80 [81]. In case of Fumapem AM-55 the band appears at a critical doping level θ between 8 and 9. According to the GAB model, the appearance of this band can be correlated to a region of the adsorption isotherm with an accelerated uptake of H_3PO_4 molecules due to multilayer-like adsorption and thus to H_3PO_4 molecules with a more bulk-like environment. The presence of free H_3PO_4 at high doping level was also observed by several other authors in phosphoric acid doped PBI membranes using various techniques [9, 60, 83, 84].

On the basis of the above considerations, we suggest that the uptake process of phosphoric acid by PBI-type polymers has two distinguishable 'stages' with the following characteristics:

1. Protonation of the z basic groups of the polymer chain (per repeating unit) for doping degrees θ between 0 and z . This corresponds to first layer adsorption of H_3PO_4 molecules described by the equilibrium constant $K \sim 10^0\text{--}10^1\text{ L mol}^{-1}$ according to a BET-like model (blue region in Figs. 8.11 and 8.12, right).
2. Adsorption of additional H_3PO_4 molecules via direct H bonds to polar groups of the polymer chain and via H bonds with other H_3PO_4 molecules for doping degrees θ above z . This corresponds to multilayer-like adsorption of H_3PO_4 molecules described by the equilibrium constant $K' \sim 10^{-2}\text{ L mol}^{-1}$ (green region in Figs. 8.11 and 8.12, right). According to the functional course of the adsorption isotherm, there is no (significant) difference of the multilayer adsorption equilibrium constant K' for H_3PO_4 molecules directly bound by H bonds to the polymer chain or indirectly bound by H bonds to other H_3PO_4 molecules.

A multi 'stage' adsorption process is also assumed by Leykin et al. [85]. Prior to the increased uptake of the protic electrolyte by 'multilayer-like' adsorption according to the GAB model in stage (2) is the protonation of the polymer chains in stage (1). An analogue

behaviour can be found for the uptake of the proton-conducting ionic liquid (PIL) DemaTfO³ by Nafion[®]⁴ or sulfonated polyimides⁵ (SPI). Nafion[®] and SPI, which are polymers with sulfonic acid groups, absorb only very small amounts of DemaTfO. When pre-treating Nafion[®] or SPI with an organic base as an alkylamine, deprotonating the sulfonic acid groups of the polymer and forming an alkylammonium salt, the uptake of DemaTfO is highly increased [86–88]. Thus, the compatibility with the PIL is strongly enhanced. We suggest that due to the formation of a ‘polymer salt’ with (cationic) charged chains and counter anions a high osmotic pressure between the polymer and the surrounding doping agent is established. This will enable the further uptake of additional (neutral) doping agent molecules.

At the moment the literature data as well as own investigations on Fumapem AM-55 lack detailed information on the different molecular species in the adsorbed phosphoric acid. Future experimental works have to clarify the influence of the H bond formation to the polymer chain on the vibration modes of H₃PO₄ molecules and H₂PO₄[−] ions. Another open question is the correlation of the H₃PO₄ adsorption isotherm and the Raman data to the simultaneous water adsorption as well as to the resulting proton conductivity of the polymer.

8.5 Summary and Conclusions

We have reviewed the fundamental physical and chemical properties of i) bulk phosphoric acid and ii) of PBI-type polymers, doped with phosphoric acid and other protic electrolytes like sulfuric acid and perchloric acid. The knowledge of

the properties is of special importance to understand the behaviour of high-temperature polymer electrolyte fuel cells (HT-PEMFC) under operation, using phosphoric acid doped PBI-type polymers as proton-conducting electrolyte membrane. Bulk phosphoric acid can be found in the attached electrodes as a thin surface film covering the porous structure with the platinum catalyst particles. The phosphoric acid film assures the proton conduction to the electrochemical active regions in the catalyst layer.

8.5.1 Bulk Phosphoric Acid

Anhydrous or highly concentrated phosphoric acid exhibits the highest proton conductivity compared to other simple inorganic and organic electrolytes (acids and bases). The high proton conductivity of anhydrous phosphoric acid is caused by a strong autoprotolysis, which exceeds all measured values for other protic electrolytes. The proton conductivity of the system H₃PO₄–H₂O is strongly composition dependent. Below 100 °C it has a maximum in the composition range between 40 and 60 wt% H₃PO₄. Above 100 °C and at a H₂O partial pressure below 1 bar, i.e. in the region relevant for HT-PEMFC operation, the proton conductivity will always decrease with decreasing H₂O concentration, because compositions only above 60 wt% H₃PO₄ (beyond the maximum) are accessible.

The temperature dependence of the proton conductivity of phosphoric acid, in particular at high concentrations, shows strong non-Arrhenius behaviour (VTF), as it is known for high viscous liquid or glassy solid ion conductors in vicinity to the glass transition temperature. The activation energy for proton transport is always lower than that for viscous flow, i.e. a decoupling of the proton conduction mechanism and viscous flow is present over the whole concentration range. The proton transport in (aqueous) phosphoric acid takes place mainly via a cooperative hopping mechanism. Proton transport via a vehicle mechanism can be neglected.

³ DemaTfO = Diethylmethylammonium trifluoromethanesulfonate.

⁴ NAFION[®] = Sulfonated tetrafluoroethylene based fluoropolymer-copolymer (DuPont).

⁵ E.g. polycondensates from 1,4,5,8-Naphthalene tetracarboxylic dianhydride, 2,2'-Benzidinesulfonic acid and Bis[4-(3-aminophenoxy)-phenyl]sulfone [86, 87].

8.5.2 PBI-Type Polymers and Protic (Acidic) Electrolyte

Phosphoric acid as well as other protic electrolytes with a sufficient acidity can be adsorbed by PBI-type polymers. The resulting PBI-protic electrolyte systems exhibit proton conductivities about one order of magnitude lower than the free bulk (100 wt%) protic electrolytes. The adsorption isotherms of the protic electrolytes by non-cross-linked or cross-linked PBI-type polymers can be satisfactorily described with a modified BET (GAB) model, assuming a 'multilayer-like' adsorption. Only three parameters have to be introduced: The number z of basic groups per repeating unit, the equilibrium constant K for first layer and K' for multilayer-like adsorption. For all in this chapter compiled and analysed studies on PBI-type polymers, doped with phosphoric acid, sulfuric acid or perchloric acid as protic electrolyte, the equilibrium constant K' for multilayer-like adsorption is in the order of $10^{-2} \text{ L mol}^{-1}$. The equilibrium constant K for the first layer adsorption exceeds K' by about three orders of magnitude (10^1 – 10^2 L mol^{-1}). The number z of proton-accepting groups per repeating unit obtained by fitting is in accordance to the chemical structure of the polymers.

The thermodynamic data from the adsorption isotherms can be combined successfully with spectroscopic data from Raman investigations. From the changes of characteristic Raman bands as a function of doping degree θ , two distinguishable 'stages' of protic electrolyte (phosphoric acid) uptake can be identified:

1. Protonation of the z basic groups of the polymer chain. This corresponds to first layer adsorption of electrolyte molecules according to a BET model, described by the equilibrium constant K .
2. Adsorption of additional electrolyte molecules via direct H bonds to polar groups of the polymer chain and via H-bonds to other electrolyte molecules, described by the equilibrium constant K' .

The stage (2) correspond to the multilayer-like adsorption of the protic electrolyte molecules. No significant difference between the equilibrium constant of electrolyte molecules directly bound by H-bonds to the polymer chain or indirectly bound by H-bonds to other electrolyte molecules is evident.

PBI-type polymers are able to uptake vast amounts of a protic electrolyte. In case of non-cross-linked derivatives, the swelling process passes into a complete dissolution. We suggest that due to the protonation of the polymer and the formation of charge chains with counter ions, a high osmotic pressure between the polymer and the surrounding doping agent is established, which will enable its further increased uptake.

These considerations demonstrate the benefit of correlating spectroscopic data on the microscopic interactions between polymer and electrolyte molecules with thermodynamic data and models describing the adsorption isotherm to improve the knowledge on systems consisting of a basic polymer as PBI and protic (acidic) electrolytes.

References

1. Liu F, Mohajeri S, Di Y et al (2014) Influence of the interaction between phosphoric acid and catalyst layers on the properties of HT-PEMFCs. *Fuel Cells* 14:750–757
2. Maier W, Arlt T, Wippermann K et al (2012) Correlation of synchrotron X-ray radiography and electrochemical impedance spectroscopy for the investigation of HT-PEMFCs. *J Electrochem Soc* 159:F398–F404
3. Schrödter K, Bettermann G, Staffel T et al (2000) Phosphoric acid and phosphates. *Ullmann's Encyclopedia of Industrial Chemistry*. Wiley-VCH, Weinheim
4. Wainright JS, Wang J, Weng D et al (1995) Acid-doped polybenzimidazoles: a new polymer electrolyte. *J Electrochem Soc* 142:L121–L123
5. Jones D, Roziere J (2001) Recent advances in the functionalisation of polybenzimidazole and polyetherketone for fuel cell applications. *J Membr Sci* 185:41–58
6. Quartarone E, Mustarelli P (2012) Polymer fuel cells based on polybenzimidazole/ H_3PO_4 . *Energy Environ Sci* 5:6436–6444

7. Asensio JA, Sánchez EM, Gómez-Romero P (2010) Proton-conducting membranes based on benzimidazole polymers for high-temperature PEM fuel cells. A chemical quest. *Chem Soc Rev* 39:3210–3239
8. Chuang S, Hsu SLC (2006) Synthesis and properties of a new fluorine-containing polybenzimidazole for high-temperature fuel-cell applications. *J Polym Sci A* 44:4508–4513
9. Li Q, He R, Berg RW et al (2004) Water uptake and acid doping of polybenzimidazoles as electrolyte membranes for fuel cells. *Solid State Ionics* 168:177–185
10. Vilčiauskas L, Tuckerman ME, Bester G et al (2012) The mechanism of proton conduction in phosphoric acid. *Nat Chem* 4:461–466
11. Wang JT, Savinell RF, Wainright JS et al (1996) A H_2/O_2 fuel cell using acid doped polybenzimidazole as polymer electrolyte. *Electrochim Acta* 41:193–197
12. Holleman AF, Wiberg E, Wiberg N (1995) *Lehrbuch der anorganischen Chemie*. Walter de Gruyter, Berlin
13. Elmore KL, Hatfield JD, Dunn RL et al (1966) Dissociation of phosphoric acid solutions at 25°. *J Phys Chem* 69:3520–3525
14. Rudolph W, Steger WE (1991) Dissociation, structure, and rapid proton exchange of phosphoric acid in dilute aqueous solutions. V. Vibrational spectra of phosphoric acid. *Z Phys Chem* 172:49–59
15. Rudolph WW (2010) Raman- and infrared-spectroscopic investigations of dilute aqueous phosphoric acid solutions. *Dalton Trans* 39:9642–9653
16. Haynes WM (ed) (2012–2013) *CRC Handbook of Chemistry and Physics*, 93rd edn. Taylor & Francis Ltd., Boca Raton
17. Rondini S, Longhi P, Mussini PR et al (1987) Autoprotolysis constants in nonaqueous solvents and aqueous organic solvent mixtures. *Pure Appl Chem* 59:1693–1702
18. Munson RA (1964) Self-dissociative equilibria in molten phosphoric acid. *J Phys Chem* 68:3374–3377
19. Sorensen TS (1964) The pK_a of protonated α , β -unsaturated carboxylic acids. *Can J Chem* 42:724–730
20. Higgins CE, Baldwin WH (1955) Dehydration of orthophosphoric acid. *Anal Chem* 27:1780–1783
21. Huhti AL, Gartaganis PA (1956) The composition of the strong phosphoric acids. *Can J Chem* 34:785–797
22. Jameson RF (1959) The composition of ‘strong’ phosphoric acids. *J Chem Soc* 1:752–759
23. Westman AER, Beatty R (1966) Equations for calculating chain length distributions in polyphosphoric acids and polyphosphate glasses. *J Am Ceram Soc* 49:63–67
24. Fontana BJ (1951) The vapor pressure of water over phosphoric acids. *J Am Chem Soc* 73:3348–3350
25. Brown EH, Whitt CD (1952) Vapor pressure of phosphoric acids. *Ind Eng Chem* 44:615–618
26. Kablukov IA, Zagwosdkin KI (1935) Die Dampfspannung der Phosphorsäurelösungen. *Z Anorg Allg Chemie* 224:315–321
27. McDonald DI, Boyack JR (1969) Density, electrical conductivity, and vapor pressure of concentrated phosphoric acid. *J Chem Eng Data* 14:380–384
28. Schmalz EO (1970) Bestimmung der Dampfdruckkurven von Wasser über Phosphorsäure. *Z Phys Chem (Leipzig)* 245:344–350
29. Dippel T, Kreuer KD, Lassègues JC et al (1993) Proton conductivity in fused phosphoric acid; A $^1H/^31P$ PFG-NMR and QNS study. *Solid State Ionics* 61:41–46
30. Greenwood NN, Thompson A (1959) The mechanism of electrical conduction in fused phosphoric and trideuterophosphoric acids. *J Chem Soc* 1:3485–3492
31. Aihara Y, Sonai A, Hattori M et al (2006) Ion conduction mechanisms and thermal properties of hydrated and anhydrous phosphoric acids studied with 1H , 2H , and ^{31}P NMR. *J Phys Chem B* 110:24999–25006
32. Chung SH, Bajue S, Greenbaum SG (2000) Mass transport of phosphoric acid in water: a 1H and ^{31}P pulsed gradient spin-echo nuclear magnetic resonance study. *J Chem Phys* 112:8515–8521
33. Fontanella JJ, Wintersgill MC, Wainright JS et al (1998) High pressure electrical conductivity studies of acid doped polybenzimidazole. *Electrochim Acta* 43:1289–1294
34. Smith A, Menzies AWC (1909) The electrical conductivity and viscosity of concentrated solutions of orthophosphoric acid. *J Am Chem Soc* 31:1191–1194
35. Campbell AN (1926) The conductivity of phosphoric acid solutions at 0°. *J Chem Soc* 1:3021–3022
36. Kakulin GP, Fedorchenko IG (1962) Electric conductance of concentrated phosphoric acid. *Zh Neorg Khim* 7:2485–2486
37. Fedorchenko IG, Kakulin GP, Kondratenko ZV (1965) Electric conductance of concentrated phosphoric acid at 100–200 °C. *Zh Neorg Khim* 10:1945–1946
38. Wydeven T (1966) Electrical conductivity of concentrated phosphoric acid from 25 °C to 60 °C. *J Chem Eng Data* 11:174–176
39. Tsurko EN, Neueder R, Barthel J et al (1999) Conductivity of phosphoric acid, sodium, potassium, and ammonium phosphates in dilute aqueous solutions from 278.15 K to 308.15 K. *J Solution Chem* 28:973–999
40. Chin DT, Chang HH (1989) On the conductivity of phosphoric acid electrolyte. *J Appl Electrochem* 19:95–99
41. Kondratenko ZV, Fedorchenko IG, Kovalev IA (1967) Mathematical calculation of the density and viscosity of concentrated phosphoric acid solutions. *Zh Prikl Khim* 40:1947–1951
42. Kondratenko ZV, Fedorchenko IG (1959) *Zh Neorg Khim* 4:985

43. Fulcher GS (1925) Analysis of recent measurements of the viscosity of glasses. *J Am Ceram Soc* 8:339–355
44. Tammann G, Hesse W (1926) Die Abhängigkeit der Viskosität von der Temperatur bei unterkühlten Flüssigkeiten. *Z Anorg Allg Chemie* 156:245–257
45. Vogel H (1921) Das Temperaturabhängigkeitsgesetz der Viskosität von Flüssigkeiten. *Phys Z* 22:645–646
46. Doolittle AK (1951) Studies in Newtonian flow. I. The dependence of the viscosity of liquids on temperature. *J Appl Phys* 22:1031
47. Doolittle AK (1951) Studies in Newtonian flow. II. The dependence of the viscosity of liquids on free-space. *J Appl Phys* 22:1471–1475
48. Doolittle AK (1952) Studies in Newtonian flow. III. The dependence of the viscosity of liquids on molecular weight and free space. *J Appl Phys* 23:236–249
49. Turnbull D, Cohen MH (1970) On the free-volume model of the liquid-glass transition. *J Chem Phys* 52:3038–3041
50. Cohen MH, Turnbull D (1959) Molecular transport in liquids and glasses. *J Chem Phys* 31:1164–1169
51. Ellis B (1976) The glass transition temperature of phosphoric acids. *Nature* 263:674–676
52. Duecker HC, Haller W (1962) Determination of the dissociation equilibria of water by a conductance method. *J Phys Chem* 66:225–229
53. Horne RA, Courant RA, Johnson DS (1966) The dependence of ion-, proton-, water and electron transport processes on solvent structure in aqueous electrolyte solutions. *Electrochim Acta* 11:987–996
54. Loewenstein A, Szöke A (1961) The activation energies of proton transfer reactions in water. *J Am Chem Soc* 84:1151–1154
55. Perrault G (1961) Sur la conductibilité protonique dans l'eau pure. *Compt Rend* 252:4145–4147
56. McLin M, Angell CA (1988) Contrasting conductance/viscosity relations in liquid states of vitreous and polymer “solid” electrolytes. *J Phys Chem* 92:2083–2086
57. McLin MG, Angell CA (1991) Ion-pairing effects on viscosity/conductance relations in Raman-characterized polymer electrolytes: LiClO₄ and NaCF₃SO₃ in PPG(4000). *J Phys Chem* 95:9464–9469
58. Xu W, Cooper EI, Angell CA (2003) Ionic liquids: ion mobilities, glass temperatures, and fragilities. *J Phys Chem B* 107:6170–6178
59. Herath MB, Creager SE, Kitaygorodskiy A et al (2010) Perfluoroalkyl, phosphonic and phosphinic acids as proton conductors for anhydrous proton-exchange membranes. *Chem Phys Chem* 11:2871–2878
60. Li Q, Jensen JO, Savinell RF et al (2009) High temperature proton exchange membranes based on polybenzimidazoles for fuel cells. *Prog Polym Sci* 34:449–477
61. Asensio JA, Borro S, Gómez-Romero P (2004) Polymer electrolyte fuel cells based on phosphoric acid-impregnated poly(2,5-benzimidazole) membranes. *J Electrochem Soc* 151:A304–A310
62. Brunauer S, Deming LS, Deming WE et al (1940) On a theory of the van der Waals adsorption of gases. *J Am Chem Soc* 62:1723–1732
63. Brunauer S, Emmett PH, Teller E (1938) Adsorption of gases in multimolecular layers. *J Am Chem Soc* 60:309–319
64. Anderson RB (1946) Modifications of the Brunauer, Emmett and Teller Equation. *J Am Chem Soc* 68:686
65. Anderson RB, Hall KW (1948) Modifications of the Brunauer, Emmett and Teller Equation II. *J Am Chem Soc* 70:1727
66. de Boer JH (1953) The dynamical character of adsorption. Clarendon, Oxford
67. Guggenheim EA (1966) Applications of statistical mechanics. Clarendon, Oxford
68. Bratasz Ł, Kozłowska A, Kozłowski R (2012) Analysis of water adsorption by wood using the Guggenheim-Anderson-de Boer equation. *Eur J Wood Wood Prod* 70:445–451
69. Jonquière A, Fane A (1998) Modified BET models for modeling water vapor sorption in hydrophilic glassy polymers and systems deviating strongly from ideality. *J Appl Polym Sci* 67:1415–1430
70. Karoyo AH, Wilson LD (2013) Tunable macromolecular-based materials for the adsorption of perfluorooctanoic and octanoic acid anions. *J Colloid Interface Sci* 402:196–203
71. Monleón Pradas M, Salmerón Sánchez M, Gallego Ferrer G et al (2004) Thermodynamics and statistical mechanics of multilayer adsorption. *J Chem Phys* 121:8524–8531
72. Timmermann EO (2003) Multilayer sorption parameters: BET or GAB values? *Colloids and Surfaces A* 220:235–260
73. Diaz LA, Abuin GC, Corti HR (2009) Water and phosphoric acid uptake of poly [2,5-benzimidazole] (ABPBI) membranes prepared by low and high temperature casting. *J Power Sources* 188:45–50
74. He R, Che Q, Sun B (2008) The acid doping behavior of polybenzimidazole membranes in phosphoric acid for proton exchange membrane fuel cells. *Fiber Polym* 9:679–684
75. Sadeghi M, Moadel H, Khatti S et al (2010) Dual-mode sorption of inorganic acids in polybenzimidazole (PBI) membrane. *J Macromol Sci B* 49:1128–1135
76. Conti F, Majerus A, Di Noto V et al (2012) Raman study of the polybenzimidazole-phosphoric acid interactions in membranes for fuel cells. *Phys Chem Chem Phys* 14:10022–10026
77. Majerus A, Conti F, Korte C et al (2012) Thermogravimetric and spectroscopic investigation of the interaction between polybenzimidazole and phosphoric acid. *ECS Trans* 50:1155–1165

78. Silverstein RM, Webster FX (2002) Spectroscopic identification of organic compounds. Wiley, New York
79. Giffin GA, Conti F, Lavina S et al (2014) A vibrational spectroscopic and modeling study of poly(2,5-benzimidazole) (ABPBI)—phosphoric acid interactions in high temperature PEMFC membranes. *Int J Hydrogen Energy* 39:2776–2784
80. Glipa X, Bonnet B, Mula B et al (1999) Investigation of the conduction properties of phosphoric and sulfuric acid doped polybenzimidazole. *J Mater Chem* 9:3045–3049
81. Daletou MK, Geormezi M, Vogli E et al (2014) The interaction of H_3PO_4 and steam with PBI and TPS polymeric membranes. A TGA and Raman study. *J Mater Chem A* 2:1117–1127
82. Cherif M, Mgaidi A, Ammar N et al (2000) A new investigation of aqueous orthophosphoric acid speciation using Raman spectroscopy. *J Solution Chem* 29:254–269
83. Nores-Pondal FJ, Buera MP, Corti HR (2010) Thermal properties of phosphoric acid-doped polybenzimidazole membranes in water and methanol-water mixtures. *J Power Sources* 195:6389–6397
84. Ma Y-L, Wainright JS, Litt MH et al (2004) Conductivity of PBI membranes for high-temperature polymer electrolyte fuel cells. *J Electrochem Soc* 151: A8–A16
85. Leykin AY, Askadskii AA, Vasilev VG et al (2010) Dependence of some properties of phosphoric acid doped PBIs on their chemical structure. *J Membr Sci* 347:69–74
86. Lee S-Y, Ogawa A, Kanno M et al (2010) Nonhumidified intermediate temperature fuel cells using protic ionic liquids. *J Am Chem Soc* 132:2183–2195
87. Lee S-Y, Yasuda T, Watanabe M (2010) Fabrication of protic ionic liquid/sulfonated polyimide composite membranes for non-humidified fuel cells. *J Power Sources* 195:5909–5914
88. Di Noto V, Negro E, Sanchez J-Y et al (2010) Structure-relaxation interplay of a new nanostructured membrane based on tetraethylammonium trifluoromethanesulfonate ionic liquid and neutralized Nafion 117 for high-temperature fuel cells. *J Am Chem Soc* 132:2183–2195

David Aili, Jens Oluf Jensen, and Qingfeng Li

9.1 Introduction

Casting by solvent evaporation is a commonly used procedure for fabrication of membranes based on organic polymers. It is probably the most widely used technique for polybenzimidazole membrane preparation for high-temperature polymer electrolyte membrane fuel cells. After casting, doping with phosphoric acid provides proton conductivity to the membrane.

For practical use in fuel cells, the physicochemical characteristics of the polybenzimidazole-based membrane must be balanced since many of the important parameters are linked, either directly or indirectly. For example, high phosphoric acid contents will give high proton conductivity but a membrane with a lower phosphoric acid content (and thus lower conductivity) can give similar area-specific resistance in the fuel cell if it is thinner. A thin membrane with high phosphoric acid content is desired because it gives low area-specific resistance. Such a membrane will be mechanically weak and difficult to process and less durable in an operating cell. Cross-linking, for example, can to some extent allow for thin membranes with good mechanical strength and high phosphoric acid contents. However, a thin

membrane will give higher hydrogen crossover rate resulting in losses due to the lowered open circuit voltage.

This chapter aims at summarizing the research and development of polybenzimidazole membranes that have been prepared by casting from organic solvents and subsequently imbibed with phosphoric acid for application in high-temperature polymer electrolyte membrane fuel cells. The main focus is devoted to membranes based on poly[2,2'-*m*-(phenylene)-5,5'-bibenzimidazole] (*m*PBI) since it is the most thoroughly studied polymer in this connection, but other polybenzimidazole structure derivatives are discussed as well. The name polybenzimidazole, and the commonly used abbreviation PBI, refer to a family of polymers containing benzimidazole moieties in the polymer repeat unit. Sometimes the abbreviation is also used specifically for the *m*PBI structure derivative because it is the most widely used member in this family of materials and was the first commercially available polybenzimidazole. This particular structure derivative is referred to as *m*PBI throughout this contribution, whereas the term polybenzimidazole or PBI is used as a general term for any derivative in this family.

The contribution starts with a discussion about available organic solvents, casting techniques, and workup of the obtained membranes as well as some fundamental physicochemical characteristics of the pristine undoped membranes. Subsequently,

D. Aili (✉) • J.O. Jensen • Q. Li
Department of Energy Conversion and Storage, Proton Conductors Section, Technical University of Denmark, Kemitorvet 207, DK-2800 Kgs., Lyngby, Denmark
e-mail: larda@dtu.dk

the acid doping chemistry is described followed by a discussion about how the acid uptake can be controlled. Structure and morphology on different levels are discussed. It is followed by a description of the parameters that affect the physicochemical properties of the membrane and its functionality (such as proton conductivity, mechanical strength, and gas permeability) are summarized and discussed. Membrane modifications including cross-linking, functionalization, polymer blends, and composites are briefly discussed. The chapter ends with a section devoted to the in situ characteristics of the membranes.

9.2 Membrane Preparation

9.2.1 Solvents

Polybenzimidazoles are normally highly soluble in polyphosphoric acid (PPA) which is commonly used as polycondensation solvent. From this solution, phosphoric acid-doped membranes can be obtained directly by casting the crude mixture as a thin film. A sol–gel transition is subsequently induced by hydrolyzing the PPA (good solvent) to orthophosphoric acid (poor solvent) under an atmosphere with carefully controlled temperature and humidity to control the acid content of the membrane [1]. This approach is further reviewed in Chap. 10.

A more traditional procedure, which involves considerably more process steps, is to isolate the polymer and re-dissolve it in an organic solvent followed by casting by solvent evaporation and finally impregnation with phosphoric acid [2]. A few highly polar aprotic organic solvents can dissolve many of the reported polybenzimidazole derivatives. These include *N,N*-dimethylacetamide (DMAc), *N,N*-dimethylformamide (DMF), *N*-methyl-2-pyrrolidone (NMP), and dimethylsulfoxide (DMSO). Certain ionic liquids, like 1-butyl-3-imidazolium chloride [3], can be used as well. Traditionally, DMAc has been the preferred organic solvent for *m*PBI (Fig. 9.1) since the viscosity of the obtained solution is suitable for dry-spinning of PBI fibers [4].

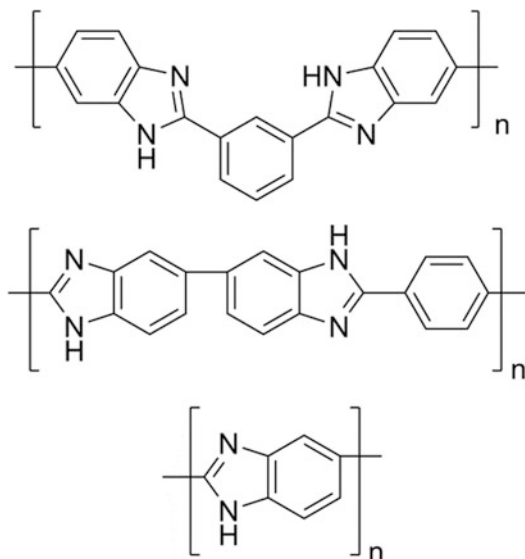


Fig. 9.1 Chemical structure of *m*PBI (top), *p*PBI (middle), and AB-PBI (bottom)

For complete dissolution of the polymer, substantial heating of the mixture is required. Refluxing the *m*PBI in DMAc, which has a boiling point of 165 °C at ambient pressure, at low solid contents for durations of several hours and with vigorous mechanical stirring, is normally needed to completely dissolve the polymer and especially the high molecular weight fraction. The regioisomer poly[2,2'-*p*-(phenylene)-5,5'-bibenzimidazole] (*p*PBI, Fig. 9.1) is, on the other hand, much less soluble in organic solvents than *m*PBI. This is mainly due to its structure which gives a close polymer chain packing (higher density, lower free volume [5]) and a relatively high degree of crystallinity [6]. Attempts to enhance the organosolubility of *p*PBI were carried out by introducing flexible spacers in the main chain of the polymer, but the anticipated increased organosolubility was not observed [7]. Similarly the degree of crystallinity for poly(2,5-benzimidazole) (AB-PBI, Fig. 9.1), which structurally is the most simple polymer of the polybenzimidazole family, is rather high which results in poor organosolubility [8, 9]. Apart from PPA and some other strong acids, methanesulfonic acid (MSA)

seems to be the only solvent that can dissolve AB-PBI for subsequent processing and membrane casting.

Using a set of nuclear magnetic resonance (NMR) techniques, Conti et al. [10] studied the hydrogen bond interactions between DMAc and *m*PBI in detail and provided insights into the dissolution process. Increasing the polymer concentration was shown to induce a conformational change and at high polymer concentrations aggregates were suggested to form due to the intermolecular hydrogen bond interactions [11]. In order to promote the dissolution of the polymer, different amounts of LiCl are sometimes added as stabilizer. It affects the viscosity of the solution and changes the hydrodynamic radius and minima in both viscosity and hydrodynamic radius were observed at a LiCl concentration corresponding to 2.5 LiCl per *m*PBI repeat unit [12]. The LiCl disturbs the intermolecular van der Waals forces and prevents the polymer from phasing out which gives a prolonged shelf-life for the solution [13]. The fundamental physical chemistry of *m*PBI solutions with different concentrations of polymer and LiCl was thoroughly investigated by Shogbon et al. [14]. Based on light scattering studies, the chain conformation was investigated and the molecular parameters were obtained, showing that a conformational transition from a random coil to an extended wormlike chain occurred when the polymer concentration was increased from 0.1 to 20 g L⁻¹ at a given LiCl content.

9.2.2 Membrane Casting from Organic Solvents

Polybenzimidazoles are normally soluble in concentrated sulfuric acid, in which the viscosity usually is determined using a capillary viscometer. For *m*PBI it has been demonstrated that a one-point viscosity measurement at low polymer concentrations can be used to calculate a good approximate value of the intrinsic viscosity [15], which in turn can be used to estimate the weight average molecular weight using the Mark-

Houwink-Sakurada expression. For *m*PBI with inherent viscosities in the 0.6–1.5 dL g⁻¹ range, polymer solutions in DMAc with solid contents ranging from 2–10 wt% are often practical for membrane casting. It corresponds to linear weight average molecular weights of about 30–94 kDa using the correlations between intrinsic viscosity and weight average molecular weight determined by light scattering as reported by Buckley et al. [16] and Yuan et al. [15]. For polymers with molecular weights higher than, say 100 kDa, the processability is strongly constrained due to the high viscosity in solution. It requires very diluted solutions which is unpractical from a technological point of view and also questionable with respect to cost and the environmental impact.

With an average to high molecular weight (e.g., 25–100 kDa), *m*PBI shows excellent film forming properties and membrane casting can be done by slow evaporation of the solvent on a suitable substrate, such as a glass plate, to give films as thin as a few micrometers. This can be done by gradual heating over many hours (or even days) to at least 120 °C [17]. The use of a solvent with a high boiling point facilitates the slow evaporation which is required to obtain a uniform polymer film. To further improve the quality of the polymer film, skin effects can be effectively avoided by maintaining a high partial pressure of the solvent above the surface. Practically this can be done by covering the tray partially. For applications in fuel cells, and especially with respect to the long-term durability, it is likely of great importance that the membrane is very even in thickness. An uneven membrane will give a membrane-electrode assembly (MEA) that is slightly warped with a poorly defined membrane-electrode interface. It will ultimately result in variations of the current distribution and in turn develop into hotspots that could damage the membrane [18]. As a step towards mass production a roll-to-roll process for *m*PBI membrane casting from DMAc was recently reported [19]. Using both knife coating and slot-die coating the process could give 250 mm-wide uniform membranes with a thickness of 40 μm at a speed of 12 m h⁻¹.

9.2.3 Workup

After casting, the membrane should be peeled off from the supporting substrate. Soaking in, e.g., water effectively reduces the adhesion to the substrate which facilitates the delamination. Further treatment with hot water is required to completely remove the solvent residuals and the eventual stabilizer [20]. The strong interaction between the polymer and the solvent makes it difficult to remove the solvent residuals completely during casting, and membranes cast at 120–150 °C from DMAc can contain as much as 10–20 wt% solvent residuals. Even though a *m*PBI membrane appears completely dry, it can contain as much as 50 wt% DMAc [19]. Treatment with hot water effectively washes out the solvent residuals and *m*PBI membranes show water uptakes of about 20 wt% which corresponds to about 3 water molecules per polymer repeat unit [21, 22]. The water uptake is accompanied by volume swelling in the range 20–25 vol% [23]. The strong water affinity implies that further heat treatment, preferably under vacuum, at temperatures well above 100 °C is required to evaporate the tightly bound water and to obtain a membrane with very low water content. Some fundamental physical parameters for a set of polybenzimidazole derivative membranes prepared by solution casting from DMAc are summarized in Table 9.1.

9.2.4 Doping

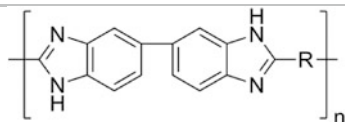
The PBI derivatives possess both proton acceptor and proton donor sites. They are thus chemically amphoteric with pK_a and pK_{aH} values typically of around 13 and 5, respectively [24, 25]. However, the polybenzimidazoles are more basic than water, and thus commonly referred to as basic polymers. They show high affinity towards polar compounds such as liquid acids and bases, which are used as dopants to provide ion conductivity to the membrane. Depending on the chemical nature and the concentration of the dopant it results in partial or full protonation or

deprotonation to give polymeric salts shown in Fig. 9.2.

Many different acids and bases have been considered and evaluated as dopants in connection with electrochemical energy conversion devices, including H_2SO_4 [26–31], H_3PO_4 [20, 21, 26–38], $HClO_4$ [26], HBr [27], HCl [29], HNO_3 [26], $LiOH$ [39], $NaOH$ [39, 40], KOH [39, 41, 42], CH_3SO_3H , and $CH_3CH_2SO_3H$ [29]. When doped in acids with concentrations higher than 11 mol L^{-1} the relative proton conductivity of *m*PBI decreases in the order of $H_2SO_4 > H_3PO_4 > HClO_4 > HNO_3 > HCl$ [26]. The conductivity of H_2SO_4 doped *m*PBI is in a practically interesting range and it can be used as electrolyte material for electrolytic hydrogen and sulfuric acid production [43]. However, a drawback is that H_2SO_4 has a significant vapor pressure.

As shown in Fig. 9.2, each *m*PBI repeat unit has two basic sites and the maximum degree of protonation is thus 2. For phosphoric acid-doped membranes, the ionic interactions have been confirmed and studied with infrared [21, 27], Raman [21] and nuclear magnetic resonance spectroscopy (NMR) [34]. The equilibrium constant for the protonation of *m*PBI by H_3PO_4 at 25 °C was calculated based on the dissociation constants of the membrane constituents to 1.17×10^3 by Ma et al. [33]. Furthermore, He et al. [36] studied the doping chemistry of *m*PBI using the Scatchard method. Two different acid dissociation constants were reported (5.4×10^{-4} and 3.6×10^{-4}), which indicates that two different types of interactions with the polymer are present. Each repeat unit of the polymer has also two acidic protons, which can be subtracted with a strong base such as an alkali hydride, alkoxide, or hydroxide. It forms a polymer that is highly reactive with negative charges delocalized on the polymer backbone that can be employed for further *N*-functionalization [44–46]. Equilibrated with aqueous KOH , this material shows high ion conductivity well above $10^{-2} \text{ S cm}^{-1}$ at room temperature and has been demonstrated with encouraging results as electrolyte in alkaline fuel cells [39] as well as for alkaline water electrolysis [41, 42].

Table 9.1 Density (ρ) at 35 °C, d-spacing (d_{sp}) from wide angle X-ray diffraction, fractional free volume (v), and water uptake at 35 °C (H_2O per polymer repeat unit in parenthesis) for membranes based on polymers obtained by polycondensation of 3,3'-diaminobenzidine with different dicarboxylic acids



R	$\rho/g\text{ cm}^{-3}$	$d_{sp}/\text{\AA}$	$v/\%$	Water uptake/wt%	H_3PO_4 uptake/wt%
	1.331	4.05	31.0	20.4 (3.5)	493 (15.1)
	1.351	3.70	29.8	21.3 (3.6)	332 (10.4)
	1.193	4.69 4.04	33.9	12.3 (2.5)	526 (20)
	1.371	5.37 4.05	36.1	5.9 (1.8)	167 (9)
	1.553	3.70	31.0	12.2 (2.6)	351 (13.9)
	1.717	3.63	32.3	8.5 (2.2)	430 (20.1)
	1.340	3.96	32.3	71.6 (3.0)	579 (18.3)

The phosphoric acid uptakes (H_3PO_4 per polymer repeat unit in parenthesis) were recorded gravimetrically after equilibrating the membranes in 16.2 mol L⁻¹ H_3PO_4 (the bromine containing polymers were equilibrated in 14.3 mol L⁻¹ H_3PO_4). All membranes were prepared by solution casting from DMAc. All data are from reference [5]

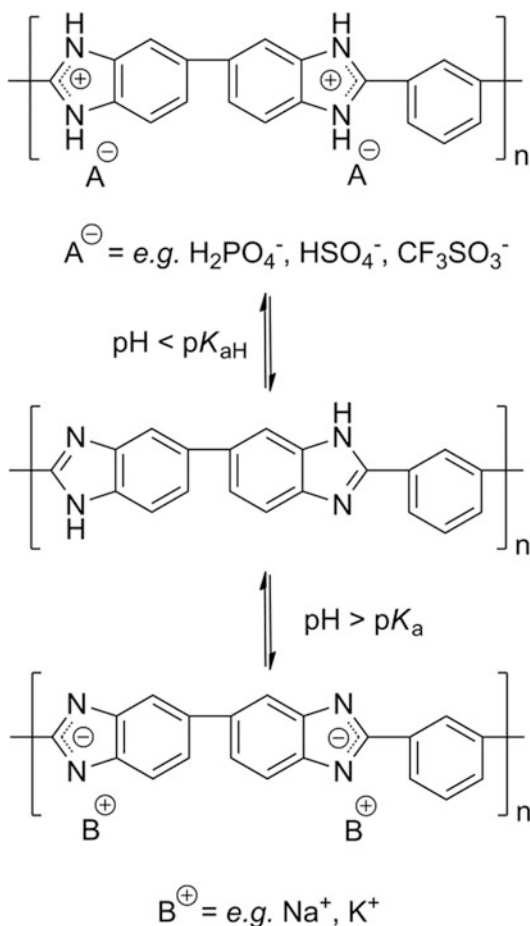


Fig. 9.2 Schematic illustration showing the amphoteric nature of *mPBI* and its salt formation

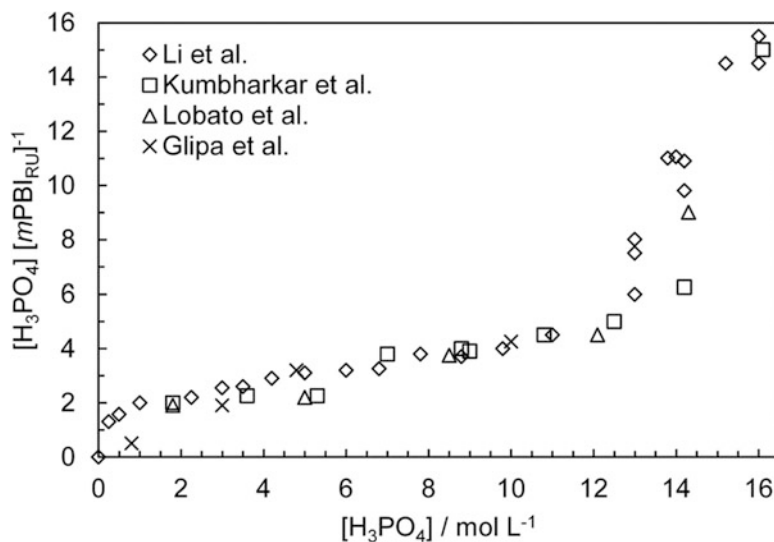
Phosphoric acid is of special interest as dopant for fuel cell applications in the 120–200 °C range due to its excellent thermal stability, low vapor pressure, and high proton conductivity at very low water contents [47, 48]. It completely dissolves in the *mPBI* matrix to form a material that, at high acid contents, more resembles a gel than a solid [49]. Among the different acid-doped polymer membranes this is also by far the most thoroughly studied system. The phosphoric acid doping chemistry of polybenzimidazoles is, however, rather complex. Phosphoric acid can form a variety of ionic species and depending on the temperature and water content the

composition of the phosphoric acid changes due to the shifting condensation/hydrolysis equilibrium [50]. The presence of a basic polymer and the varying water contents strongly affect this process [21, 51], as discussed in more detail in Chap. 8.

Virtually all the physicochemical properties including, e.g., proton conductivity, gas permeability, and mechanical strength of membranes based on *PBI* derivatives are highly dependent on the phosphoric acid contents [35, 52]. It is thus of great importance to be able to control the acid doping level (ADL), which is often defined as the number of phosphoric acid molecules per polymer repeat unit. The ADL is primarily controlled by adjusting the temperature and concentration of the bulk phosphoric acid solution. Submerging membranes of *mPBI* in aqueous solutions of H_3PO_4 with concentrations of 2.9, 5.9, and 9.8 mol L^{-1} at room temperature gives ADLs of 2.3, 3.0, and 4.0, respectively, when the equilibrium is reached after about 50 h [21]. At phosphoric acid concentrations higher than about 12 mol L^{-1} , the ADL increases dramatically with increasing acid concentration in the bulk solution. By increasing the H_3PO_4 concentration of the bulk solution to 14.8 mol L^{-1} (85 wt%) the equilibrium ADL at room temperature for *mPBI* is typically 10–11 when the molecular weight of the polymer is high (e.g., above 54 kDa) and 12–14 when the molecular weight is lower [17]. The H_3PO_4 adsorption isotherm at 25 °C for membranes of *mPBI* with arbitrary molecular weight is shown in Fig. 9.3, compiling adsorption data from four independent research groups.

The phosphoric acid uptake causes swelling of the membrane in all dimensions. The volume swelling data in the literature are rather scattered, which may be explained by the practical difficulty in accurately determining the dimensions of the very soft phosphoric acid-doped membrane. Generally, for a *mPBI* membrane that has been doped in 85 wt% H_3PO_4 to give an ADL of 10–11 the volume swelling is in the range 150–250 vol.% on the dry undoped membrane basis [23].

Fig. 9.3 H_3PO_4 adsorption isotherm for *m*PBI membranes at 25 °C. The data are compiled from the work by Kumbharkar et al. [5], Li et al. [21], Lobato et al. [53], and Glipta et al. [28] for membranes based on *m*PBI with arbitrary molecular weight



9.3 Structure and Morphology

9.3.1 Structural Features on a Larger Scale

On the scale ranging from a few nanometers up to about a tenth of a micrometer, pristine polybenzimidazole membranes prepared by solution casting from organic solvents show no pronounced structural features. However, defects and inhomogeneities originating from skin formation due to fast solvent evaporation may be observed. Different approaches have been considered for altering the morphology of polybenzimidazoles on this length scale. For example, the morphology of polybenzimidazole precipitates can to a certain extent be controlled by reaction-induced phase separation during synthesis, by carrying out the polycondensation in a poor solvent for the resulting polymer [54]. Depending on the reaction conditions the polymer precipitates showed well-defined particle size and shape. Porous *m*PBI have been prepared by casting the membranes together with a porogen that was dissolved and washed out after membrane casting (e.g., alkyl phthalates) [55]. Cross-linking of the polymer has been demonstrated to further stabilize the structure of such membranes [56]. Another technique for fabricating nanoporous membranes is track etching using intensive irradiation. It has

been demonstrated to give membranes with interface-cross-linked structures and with end pore diameters in the range of 15–50 nm and overall porosities of about 10 % [57]. The porous membranes show enhanced phosphoric acid uptakes which facilitates the proton transport.

9.3.2 Nanomorphology

On the nanometer to sub-nanometer scale, *m*PBI membranes are known to be amorphous in nature. The *d*-spacing as obtained from the peak maximum in the wide angle X-ray diffractograms (Table 9.1), is considerably lower than for, e.g., polysulfone. It is likely due to the extensive hydrogen bonding network which brings the polymer chains closer together [5]. Conciatori et al. [58] developed a process for increasing the degree of crystallinity of polybenzimidazoles, based on annealing at temperatures up to 350 °C together with certain aromatic additives. As discussed in Sect. 9.2.1, the amorphous nature of *m*PBI may be the main reason for its relatively good solubility in polar aprotic solvents [6]. Numerous reports show that the degree of crystallinity of polybenzimidazoles is highly dependent on the linear structure of the polymer [5–7, 59]. The morphology is also strongly affected by the presence of pendant groups, and

polybenzimidazoles with various side chains have been demonstrated to increase the chain separation resulting in larger free volume [5, 59, 60].

After phosphoric acid doping, crystalline regions develop in *m*PBI membranes as shown by Sannigrahi et al. [61] and Kumbharkar et al. [5]. Heat treatment at 120–150 °C increases the degree of crystallinity even further [49], resulting in a dramatic increase of the elastic modulus of the membrane [62]. At a given ADL, *m*PBI membranes prepared by direct casting from PPA [49] or a mixture of phosphoric acid and trifluoroacetic acid [63] exhibit higher proton conductivity than membranes prepared by solution casting from organic solvents. This is likely due to morphological effects. Membranes prepared by direct casting from PPA have also been shown to be less anisotropic than membranes prepared by solution casting from organic solvents, showing a well-defined interconnected fibrillar network structure [61]. The density of *m*PBI prepared by solution casting from DMAc was reported to increase from 1.33 to about 2.0 g cm⁻³ when the ADL was increased from 0 to 6 [5]. Further increasing the ADL did not significantly change the density of the membrane and it was speculated to be correlated with the transition of the membrane from a glassy to a rubbery state [5], i.e., a reduction of the glass transition temperature of the membrane.

9.4 Stability and Mechanical Strength

9.4.1 Chemical and Thermal Stability

Polybenzimidazole derivatives are well recognized for their remarkable thermal stability. Quantitative information about thermal stability

under different atmospheres can be readily obtained using thermogravimetric analysis (TGA), preferably in combination with online infrared- or mass spectroscopy of the purge gas. When heated under helium from room temperature to 900 °C, with a rate of 15 °C min⁻¹, 80 wt % of the original polymer weight was still remaining with ammonia and hydrogen cyanide as the predominating decomposition products [64]. Under air atmosphere undoped *m*PBI membranes show an onset temperature of major decomposition of around 500 °C (heating rate 10–15 °C min⁻¹) originating from oxidative pyrolysis [64, 65]. Phosphoric acid-doped *m*PBI membranes containing small amounts of platinum appeared to be stable up to at least 600 °C in air (heating rate 20 °C min⁻¹) [66].

Aili et al. [62] treated a set of neat *m*PBI membranes isothermally for 16 h at temperatures ranging from 200 to 500 °C under air or argon atmosphere. The membrane treated at 350 °C under air was darkened and the infrared spectrum showed features indicating severe thermo-oxidative degradation. Under protective argon atmosphere the membrane was apparently unaffected after 16 h at 400 °C. After the heat treatment the membrane was completely insoluble in DMAc, indicating that the membrane had irreversibly cured to form a nonspecific cross-linked network, as also discussed by Gillham [67]. In the early stage of development it was recognized that *m*PBI behaves as a redox polymer system (Fig. 9.4) and the presence of radicals has been experimentally verified repeatedly [64], which may be involved in this process.

Hydrogen peroxide and other reactive oxygen species, e.g., hydroxyl and perhydroxyl radicals are expected to be formed at the electrodes during fuel cell operation and are suspected to be

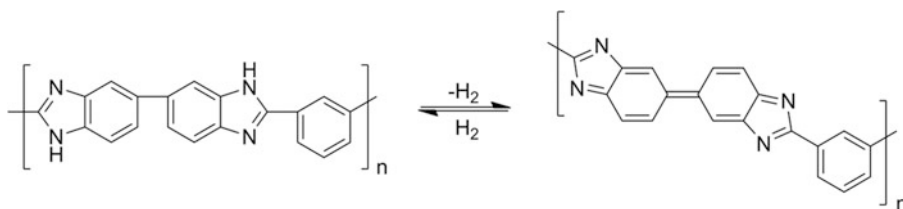


Fig. 9.4 Proposed redox system for *m*PBI [64]

involved in the principal degradation modes of the membranes in polymer electrolyte membrane fuel cells. The relative chemical stability of different materials is often evaluated by treating the membranes in aqueous solutions of hydrogen peroxide containing catalytic amounts of Fe^{2+} to enhance the radical formation rate (Fenton test), typically at 68 °C. For *m*PBI with weight average molecular weights of 24.7 and 54.5 kDa the remaining mass was 65 and 92 wt%, respectively, after 100 h in the Fenton solution [68].

The presence of phosphoric acid makes the chemistry in the Fenton test far more complex [69]. Firstly, the presence of phosphoric acid was shown to suppress the formation of radicals due to the lowered pH. Secondly, it was suggested that the presence of phosphoric acid further suppressed the degradation rate, possibly due to the formation of iron phosphates or by the ionization of the polymer. It was concluded that the presence of ferrous ion in the membrane-electrode interface had a negative impact on the fuel cell durability. However, this effect was mainly connected to the deterioration of the catalyst activity [69].

9.4.2 Mechanical Strength

In the dry undoped state, the intermolecular van der Waals forces between the $-\text{N}=\text{}$ and $-\text{NH}-$ in the benzimidazole moieties give the membrane good mechanical strength. Although *m*PBI is less crystalline than *p*PBI [6], the extensive hydrogen bonding gives a relatively close polymer chain packing (density around 1.33 g cm^{-3}) [5, 55]. At room temperature and ambient relative humidity, pristine *m*PBI membranes prepared by solution casting from DMAc typically show high elastic modulus of around 3–4 GPa, moderate engineering tensile strength of 100–160 MPa and low elongation at break of 5–10 % [52, 70]. The storage modulus of *m*PBI (3.15 GPa) remains almost unchanged up to about 250 °C and falls dramatically at temperatures above 340 °C [71]. Most of the mechanical parameters are naturally strongly dependent on the linear molecular weight of the polymer, especially in the low molecular weight

regime since the dependence on molecular weight levels off at the higher end.

As electrolytes for high-temperature PEM fuel cells, high phosphoric acid contents are desired since the proton conductivity of the membrane increases with increasing acid content, which will be discussed in more detail in Sect. 9.5.1. Due to the extensive swelling of the membrane as a result of the phosphoric acid uptake, the intermolecular hydrogen bonding is weakened. Phosphoric acid is thus, like water, a strong plasticizer and the ADL has to be balanced so that the membrane remains sufficiently strong for processing and MEA fabrication. The mechanical properties of the membrane may also be of importance for the long-term durability of the cell because of the stresses induced by the expansion/contraction during dynamic operation with temperature and humidity fluctuations.

In the early years, fractionation of the polymer batch was carried out in order to concentrate the high molecular weight fraction of *m*PBI for the subsequent membrane casting [72]. It seemed to be necessary to obtain mechanically robust membranes after doping with phosphoric acid. The engineering tensile strength and elongation at break for a set of membranes with ADLs around 11 prepared from *m*PBI with inherent viscosities ranging from 0.63 to 1.51 dL g^{-1} are shown in Fig. 9.5 [17, 70]. The inherent viscosity range corresponds to a molecular weight range 30–94 kDa using the Mark-Houwink constants reported by Buckley et al. [16]. The engineering tensile strength at break increased from 4 to 28 MPa when the inherent viscosity increased from 0.63 to 0.98 dL g^{-1} . At the same time the elongation at break increased from 39 to 149 %. At 130 °C the engineering tensile strength was considerably lower and was determined to 4 and 7 MPa at inherent viscosities of 0.98 and 1.51 dL g^{-1} , respectively.

At a given inherent viscosity of the polymer from which the membrane is made, the mechanical properties deteriorate dramatically with increasing ADL. For example, the elastic modulus was found to decrease from about 4 GPa for pristine *m*PBI with an inherent viscosity of 0.73 dL g^{-1} to 176 and 38 MPa at ADLs of 6.4

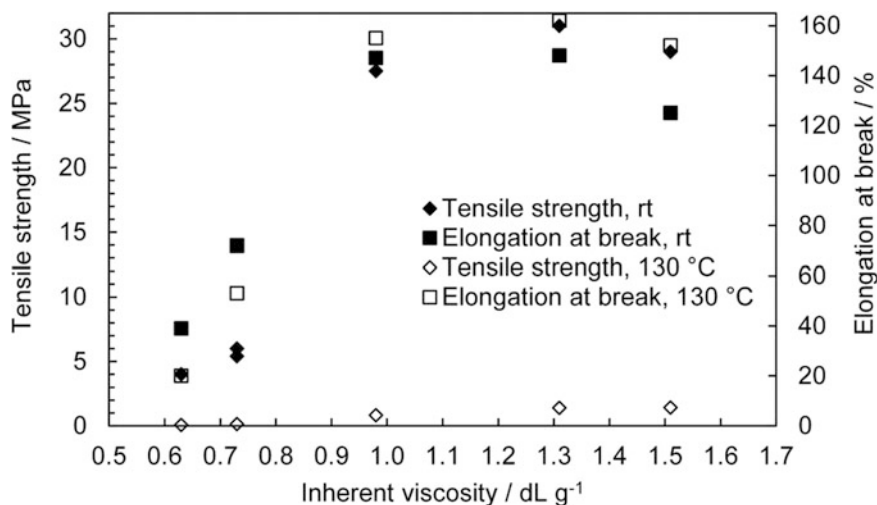


Fig. 9.5 Engineering tensile strength at break and elongation at break at room temperature (rt) and 130 °C for *m*PBI membranes with ADLs around 11 at different inherent viscosities of the polymer. The data is from Yang et al. [17, 70]

and 11.5, respectively [70]. For a membrane based on *m*PBI with inherent viscosity of about 0.6 dL g⁻¹, the engineering tensile stress at break at 125 °C was 110, 80, and 10 MPa at ADLs of 2, 3, and 6, respectively [35]. At ADLs below 2, the cohesion between the polymer chains is reduced but it is compensated for by the hydrogen bonding between the phosphoric acid and nitrogen moieties in the benzimidazole groups [63]. As a result, no significant change of the elastic modulus or engineering tensile strength is observed.

9.5 Electrochemical and Transport Properties

9.5.1 Conductivity

The electronic conductivity of pristine polybenzimidazole is very low and practically it behaves as an insulator [73]. The first published studies on the proton conductivity of polybenzimidazoles were conducted in the early 1970s, although under poorly defined experimental conditions. In the pristine form the conductivity of poly(2,5-trimethylene benzimidazole) was recorded to 10⁻¹² S cm⁻¹, using silver paste electrodes on a pressed tablet of the polymer [74]. Under

hydrogen atmosphere and using electrodes made of platinum black the conductivity of pristine *m*PBI was reported to be as high as in the 10⁻⁴ S cm⁻¹ range [75] at unspecified temperature. Numerous reports on the proton conductivity of phosphoric acid-doped polybenzimidazole membranes have been published during the last 20 years following the pioneering work by Wainright et al. [2], who recorded the proton conductivity of *m*PBI with an ADL of about 5 at 130–190 °C to 0.005–0.02 S cm⁻¹ under relatively dry conditions. It was found to be considerably higher during active humidification.

Figure 9.6 summarizes conductivity data from several research groups for phosphoric acid-doped *m*PBI membranes with different acid contents prepared by casting from DMAc, recorded at 120 °C without humidification. The data are scattered due to small variations in experimental conditions and experimental uncertainties in the reported acid contents. The conductivity for 99 wt% phosphoric acid is shown as a dotted line for comparison and it can be seen that the conductivity of the doped membranes is considerably lower than that of the pure acid. Consequently a large excess of the acid is required to reach sufficient proton conductivity for practical use in fuel cells [76]. However, as can be seen in Fig. 9.6, it is evident that the

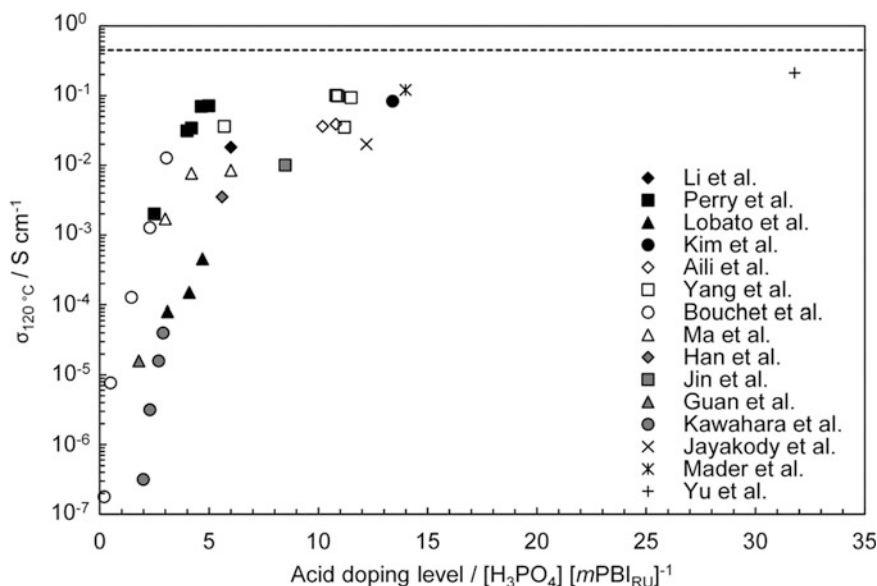


Fig. 9.6 Conductivity data for phosphoric acid-doped *m*PBI prepared by casting from DMAc. The data were recorded at 120 °C without humidification and are compiled from the work by Li et al. [77], Perry et al. [49], Lobato et al. [53], Kim et al. [78], Aili et al. [23, 62], Yang et al. [17, 70], Bouchet and Siebert [27], Ma et al. [33], Han et al. [79], Jin et al. [80], Guan

et al. [81], Kawahara et al. [29], and Jayakody et al. [82]. Conductivity data at 120 °C for 99 wt% phosphoric acid (dotted line) [83] and for phosphoric acid-doped membranes-based *m*PBI (ADL 14) and *p*PBI (ADL 32) prepared by direct casting from PPA from Mader et al. [84] and Yu et al. [85] are shown for comparison

conductivity increases dramatically by 5–6 orders of magnitude when the ADL is increased from about 1 to 4–6. By further increasing the ADL to around 10 the conductivity increases to around 0.05 S cm^{-1} , which is still one order of magnitude lower than that of pure phosphoric acid.

As a rule of thumb, proton conductivity well above $10^{-2} \text{ S cm}^{-1}$ is needed to approach an in situ area-specific resistance of $0.1 \text{ } \Omega \text{ cm}^2$ with practical membrane thicknesses of 40–100 μm . In phosphoric acid-doped polybenzimidazole membranes the proton transport is mainly mediated by the phosphoric acid molecules that are dissolved in the polymer matrix. In phosphoric acid, water molecules effectively participate in the conductivity mechanism due to its unique proton acceptor/donor characteristics and a maximum in proton conductivity is observed at a certain level of water content [86]. Phosphoric acid-doped PBI membranes are highly hygroscopic and the equilibrium water content at a certain temperature and ADL in a humid

atmosphere is established rather fast [87]. The proton conductivity of the membrane generally increases with increasing partial pressure of water vapor in the atmosphere above the membrane, as demonstrated in the pioneering work by Wainright et al. [2] (Fig. 9.7). Without humidification the orthophosphoric acid condenses to pyrophosphoric acid or higher oligomers at temperatures around 160–170 °C, which can be seen as a decrease of the membrane conductivity due to the lower conductivity of the condensed phosphorous oxyacid species [62, 83].

At room temperature the conductivity of phosphoric acid-doped *m*PBI was found to decrease with increasing pressure, which is also observed for pure phosphoric acid due to the increase in viscosity [32]. Based on the calculations of the activation volumes it was however concluded that the phosphoric acid-doped membrane behaves strikingly different than aqueous phosphoric acid but similar to

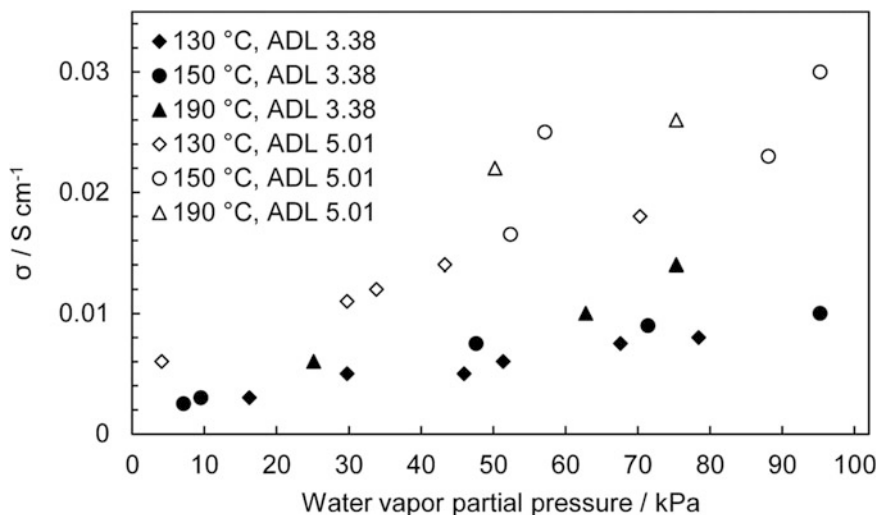


Fig. 9.7 Proton conductivity at different temperatures and partial pressures of water vapor for *m*PBI membranes with phosphoric acid doping levels of 3.38 and 5.01. Data compiled from Wainright et al. [2]

conventional polymer electrolytes. The predominating underlying elementary process for the proton transport in phosphoric acid-doped polybenzimidazole membranes is, like for neat aqueous phosphoric acid, the Grotthuss mechanism also commonly referred to as structure diffusion. The Grotthuss mechanism of proton conduction also seems supported by nuclear magnetic resonance spectroscopy measurements, showing that the self-diffusion coefficient for ^{31}P is about two orders of magnitude lower than that of ^1H [82] and that the activation energy for ^1H diffusion is consistent with what can be expected for a structure diffusion mechanism [38]. Though the proton migration from a protonated imide site to a neighboring one assisted by the dihydrogen phosphate anion has been suggested to contribute [27, 30], the predominating proton transport in *m*PBI membranes doped with excess phosphoric acid seems to be mediated along either the $\text{H}_2\text{PO}_4^- \text{-H}^+ \text{-H}_2\text{PO}_4^-$ chain or the $\text{H}_2\text{PO}_4^- \text{-H}^+ \text{-H}_2\text{O}$ chain depending on the water content of the membrane. The rate of proton transfer between different species present was determined as H_3PO_4 and H_2PO_4^- to $\text{H}_2\text{O} > \text{H}_3\text{PO}_4$ to $\text{H}_2\text{PO}_4^- > \text{N-H}^+$ to H_2PO_4^- and N-H^+ to $\text{H}_2\text{O} > \text{N-H}^+$ to N-H [33].

9.5.2 Electro-Osmotic Drag

The electro-osmotic drag coefficient refers to the number of water molecules parasitically transported together with each proton in the absence of a concentration gradient [88]. For poly(perfluorosulfonic acid) membranes with water-mediated proton transport mechanisms it has been reported to about 2.5–3.0 H_2O per H^+ [89, 90]. Ideally, the Grotthuss mechanism of proton conduction would not give rise to any net transport of the proton solvent and the electro-osmotic drag coefficient would thus be zero [91]. For phosphoric acid-doped *m*PBI, on one hand, the electro-osmotic drag coefficient of water has been found to be close to zero supporting the structure diffusion mechanism [92]. Phosphoric acid-doped poly(perfluorosulfonic acid), on the other hand, was suggested as electrolyte for high-temperature PEM fuel cells 20 years ago [93]. The rapid failure of this membrane type in fuel cells was recently suggested to be linked to the electro-osmotic drag of phosphoric acid from the anode towards the cathode, causing severe phosphoric acid imbalance [94].

Low electro-osmotic drag for methanol has been identified as one of the prerequisites for

obtaining direct methanol fuel cells with enhanced fuel utilization and with less adverse effects of the mixed cathode potential [95]. For *m*PBI membranes doped with phosphoric acid the electro-osmotic drag coefficient for methanol has been found to be close to zero [92]. It was thus initially considered as electrolyte material for direct methanol fuel cells [2], which is a concept that has been extensively studied throughout the years [96, 97]. Alternative methods based on methanol sorption/permeation [2] and mass spectrometric analysis of the cathode exhaust gas [98] further confirmed the low electro-osmotic drag for methanol.

9.5.3 Solubility, Diffusivity, and Permeability of Gases

In addition to the electro-osmotic transport of certain species, the permeation of, e.g., hydrogen and oxygen can play an important role for the cell performance. The gas permeability of hydrogen is usually higher than for oxygen because of the smaller molecular size. For undoped *m*PBI the permeability of hydrogen and oxygen at standard temperature and pressure has been determined to 1.9×10^{-13} and $4.5 \times 10^{-15} \text{ mol cm}^{-1} \text{ s}^{-1} \text{ bar}^{-1}$, respectively, which gives a selectivity coefficient α of 42 [5, 59]. The hydrogen permeability was found to increase dramatically with increasing temperature and was determined to 1.2×10^{-12} and $2.8 \times 10^{-12} \text{ mol cm}^{-1} \text{ s}^{-1} \text{ bar}^{-1}$ at 150 and 200 °C, respectively [99]. For the membrane with an ADL of 6 the permeability in this temperature regime is in the range of 2–3 orders of magnitude higher than the pristine *m*PBI membrane [35]. For the phosphoric acid-doped membrane with a high ADL of 15, the permeability of hydrogen and oxygen at standard temperature and pressure was reported to 3.9×10^{-13} and $9.5 \times 10^{-14} \text{ mol cm}^{-1} \text{ s}^{-1} \text{ bar}^{-1}$, respectively, which gives a selectivity coefficient α of 4.1, i.e., one order of magnitude lower than for the pristine *m*PBI membrane [5].

For the undoped *m*PBI membrane the solubility coefficients, defined as the ratio between the

gas concentration in the membrane and the applied pressure, was found to be 1.6×10^{-5} and $1.9 \times 10^{-5} \text{ mol cm}^{-3} \text{ bar}^{-1}$ for hydrogen and oxygen, respectively [59]. Using an electrochemical technique, the solubility coefficient of oxygen in *m*PBI with an ADL of 6 was found to be $6.8 \times 10^{-8} \text{ mol cm}^{-3} \text{ bar}^{-1}$ at 150 °C and at an oxygen partial pressure of about 50 kPa [100]. In the same work, the diffusion coefficient of oxygen was determined to $3.2 \times 10^{-6} \text{ cm}^2 \text{ s}^{-1}$, which is consistent with the diffusion of oxygen in phosphoric acid under similar conditions [100].

9.6 Structure Modifications, Polymer Blends, and Composite Systems

9.6.1 Composite Systems

One way to tailor the properties of polybenzimidazole membranes in terms of, e.g., phosphoric acid doping, water and acid retention, dimensional stability, and mechanical properties is to incorporate additional components in the polymer matrix. Composite materials containing hygroscopic inorganic materials such as titanium dioxide [101], silica [102, 103] or clays [104, 105] show encouraging results. Alternatively, a wide range of different additives with intrinsic acid functionality have been considered. Most of them are inorganic solid acids such as zirconium phosphate ($\text{Zr}(\text{HPO}_4)_2 \cdot n\text{H}_2\text{O}$, ZrP) [86], caesium substituted heteropolyacids [106–108], phosphotungstic acid ($\text{H}_3\text{PW}_{12}\text{O}_{40} \cdot n\text{H}_2\text{O}$, PWA) [86, 109, 110], silicotungstic acid ($\text{H}_4\text{SiW}_{12}\text{O}_{40} \cdot n\text{H}_2\text{O}$, SiWA) [86, 110–112], titanium oxysulfate (TiOSO_4) [113], boron phosphate (BPO_4) [114], sulfonated graphite oxide [115], sulfonated silica [116] or sulfonated oligosilsequioxane (S-POSS) [23]. The inorganic solid acids contribute to the total ion exchange capacity of the membrane and can thus enhance the proton conductivity at a given phosphoric acid content. Similarly, composite material with secondary components for pure mechanical reinforcement such as porous poly(tetrafluoroethylene) (PTFE) allows for higher

ADLs and thinner membranes which gives reduced area-specific resistance with maintained mechanical strength [12, 117–119]. However, it imposes challenges with respect to interfacial adhesion and surface treatment of the PTFE seems necessary to avoid delamination.

Virtually all physicochemical characteristics of composite electrolyte systems strongly depend on the dispersion of the secondary component in the polymer matrix. A true nanocomposite of *m*PBI visually appears transparent and clear at low contents of the secondary component. It can give a material with enhanced mechanical strength due to the lowered polymer chain mobility [104]. The most common way to produce polybenzimidazole-based composite materials for high-temperature PEM fuel cell is to dissolve or disperse the secondary component in the membrane casting solution. Practically, this method is easy to operate and the control of the ratio between the components is straightforward. However, the secondary components are liable to aggregate during membrane casting which results in materials that are not true nanocomposites [120]. The dispersion can, however, often be improved by chemical modification of the inorganic component to improve the compatibility and thus prevent the aggregation during membrane casting [104].

9.6.2 Polymer Modifications and Blends

Cross-linking has been demonstrated to effectively reduce the dramatic softening of the membrane with increasing phosphoric acid content. As demonstrated by Li et al. [77] it allows for enhanced ADLs and thus higher proton conductivity. The weight loss rate in the Fenton test was also shown to be considerably reduced, and approached the low weight loss rate of Nafion[®]. The cross-linked membranes were considerably stiffer than their linear counterparts as indicated by increased elastic modulus and reduced elongation at break. The cross-linked membranes were prepared by mixing α,α' -dibromo-*p*-xylene (DBpX) in the polymer solution and the cross-

linking was initiated by thermal treatment [77]. A large number of reports on different cross-linking concepts have been published during the last few years. Generally, the suggested cross-linking agents are bifunctional electrophiles that are mixed into the membrane casting solution, e.g., dichloromethyl phosphinic acid (DCPA) [121], chloromethyl polysulfone (CMPSU) [70], poly(vinylbenzyl chloride) (PVBC) [122], or 4,4'-diglycidyl (3,3',5,5'-tetramethylbiphenyl) epoxy resin (TMBP) [79]. Alternatively, cross-linked *m*PBI can be prepared by treating the membrane with divinyl sulfone (DVS) in a subsequent step [65]. Thermal treatment at temperatures close to the decomposition temperature of *m*PBI is known to result in nonspecific cross-linking of the polymer [67], which may be ascribed to radical reactions as discussed in Sect. 9.4.1. Elevated temperatures and high phosphoric acid concentrations in the bulk solutions are normally required for cross-linked membranes to reach sufficient ADLs for practical use in fuel cells, since the volume swelling is strongly restricted depending on the degree of cross-linking and type of cross-linking agent used. The conditions for the hot-pressing of the membrane-electrode assemblies (MEAs) with respect to temperature, time, and pressure must also be optimized for the particular membrane type. Cross-linking of the polymer will significantly change the viscoelastic properties of the membranes. The high elastic modulus and the very limited flow (low or no plastic deformation) of such a membrane makes it more challenging to get good interfacial contact between the membrane and the gas diffusion electrodes.

Grafting of pendant groups on the polymer backbone significantly changes the physicochemical properties on the membrane level. Grafting of *m*PBI is most often carried out by *N*-substitution in solution [60]. However, it can also be achieved by mixing a monofunctional electrophile into the membrane casting solution, followed by casting and subsequent thermal treatment to initiate the *N*-functionalization. This has been carried out by adding 2-chloromethyl benzimidazole to the membrane

casting solution, giving *m*PBI with pendant benzimidazole moieties after casting at 120 °C [123]. This gave a material with a higher concentration of basic sites and thus better phosphoric acid doping characteristics.

Polybenzimidazole-based blends with an acid polymer as secondary component give cross-linked membranes in which the cross-linking is ionic [124]. Membranes of this type are generally prepared by co-dissolving the two polymers in, e.g., DMAc followed by membrane casting by solvent evaporation. Before mixing with the polybenzimidazole, the acidic polymer must be converted into the neutral salt form (e.g., Na⁺, K⁺ or NH₄⁺). This is carried out to avoid the immediate proton transfer from the acidic polymer to the polybenzimidazole, which results in instant precipitation of a polymeric salt from which a membrane cannot be cast. Using different polybenzimidazole structure derivatives as the basic constituent, a number of different sulfonated polymers such as sulfonated poly(arylene ether sulfone)s [22, 52, 125–130], sulfonated poly(arylene ether ketone)s [125, 126, 131, 132] sulfonated polyphosphazene [133], or poly(perfluorosulfonic acid) [134–137] have been used for the preparation of blend membranes. If the concentration of acidic groups in the secondary polymer is high, the secondary polymer can be considered as a dopant. For example, poly(vinyl phosphonic acid) has been effectively immobilized in polybenzimidazole to give an electrolyte with good conductivity under humid conditions (0.1 S cm⁻¹ at 80 °C) without further acid doping [138, 139].

9.7 Aspects on Fuel Cell Performance and Durability

One of the biggest challenges in connection to high-temperature PEM fuel cell technology is to improve the longevity. The reasons for the decay of the performance for PEM fuel cells in general are many and not fully understood [140]. The degradation modes can be connected to different cell components depending on the operating conditions. For example, loss of active surface

area of the platinum electrocatalysts is responsible for a part of the performance decay [141, 142]. It is known to be more pronounced during operation at or close to idling mode [143]. Fuel cell idling at 150 °C was on the contrary found to gradually increase the open circuit voltage of the cell. This could eventually be due to the drying out or crystallization of the membrane resulting in a more dense membrane with lower hydrogen permeability [144]. During operation at high current loads (low voltage) the membrane degradation appears to be the predominant mode, as confirmed by the large dependence on membrane thickness [62].

Phosphoric acid loss during operation will inevitably increase the area-specific resistance in the cell. It is thus important to avoid condensation of liquid water inside the cell when the cell is shut-down or operated at temperatures close to the dew point of water. For a membrane prepared by direct casting from PPA, the phosphoric acid loss during continuous operation at 200 mA cm⁻² at 80–160 °C was determined to be less than 10 ng cm⁻² h⁻¹, corresponding to 2.6 % of the total amount of acid in the membrane after 40,000 h [145]. By increasing the temperature to 190 °C, the phosphoric acid loss rate was increased by more than an order of magnitude. However, this only accounted for the acid that had completely left the cell housing and thus not for the acid that had redistributed or leached out from the membrane and had been trapped in, e.g., the catalyst layers, gas diffusion layers, flow fields, or cell housing. This is supported by the findings by Oono et al. [146] who based on *post mortem* analysis of the used membrane-electrode assembly found that the acid loss was considerably higher and that the amount of acid collected at the cell outlet was negligible in this connection.

Galibati et al. [147] observed gradually increased hydrogen crossover and short circuit current during continuous operation at 400 mA cm⁻² for 6000 h at 180 °C, which is an indication of membrane-related degradation. *Post mortem* analysis of membrane-electrode assemblies that had been operated at constant load of 200 mA cm⁻² at 150 °C, revealed considerable membrane thinning starting after about

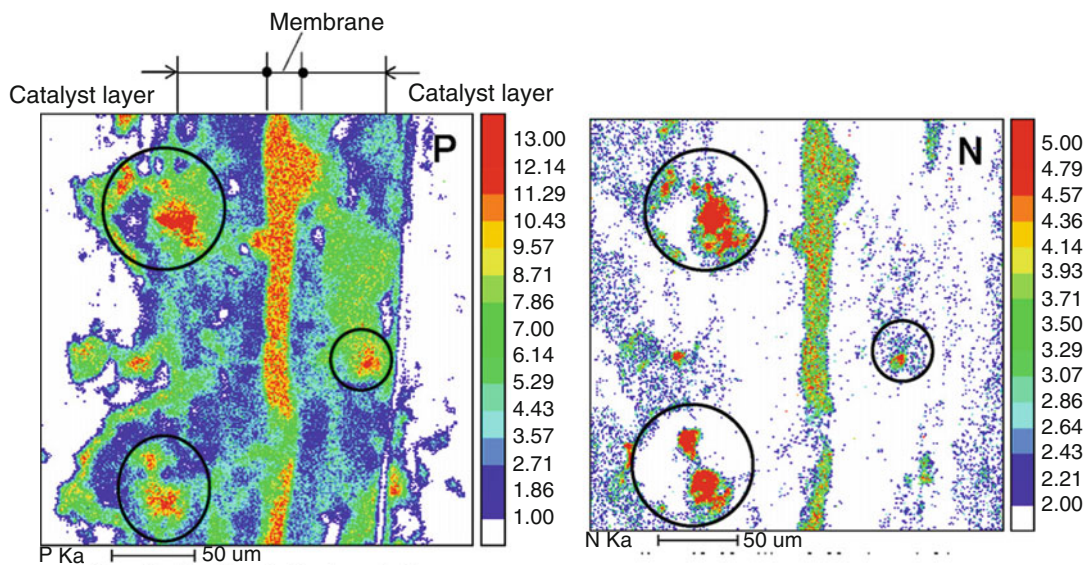


Fig. 9.8 Cross-sectional electron probe micro-analysis elemental mapping for phosphorous (*left*) and nitrogen (*right*) of a membrane-electrode assembly

14,000 h of operation accompanied by a reduced cell voltage [148]. Fragments of the polymer membrane material were found deep in the catalyst/gas diffusion layers indicating severe degradation of the polymer, as shown in the cross-sectional electron probe microanalysis (EPMA) images in Fig. 9.8.

Logically, when the polymer has degraded to a certain molecular weight it will dissolve in the doping acid. It can thus start to flow into the catalyst layers, which could explain the sudden thinning of the membrane. Oono et al. [148] suggested that cross-linking could potentially be the key to the degradation mitigation. After a 17,500 h durability test at 200 mA cm^{-2} at $150 \text{ }^\circ\text{C}$, Oono et al. [149] demonstrated that the fuel cell based on cross-linked AB-PBI showed considerable lower rate of performance loss than the fuel cell based on *m*PBI. The *post mortem* analysis of the membrane-electrode assemblies revealed considerable membrane thinning and acid migration of the fuel cell based on linear *m*PBI after 17,500 h, whereas the thickness of the membrane based on cross-linked AB-PBI remained almost unchanged. This is further supported by the dramatically

improved long-term durability at high current loads observed for a fuel cell based on a cross-linked *m*PBI membrane prepared by thermal treatment [62, 150].

Acknowledgements This work was financially supported by ForskEL program (DuRaPEM III no.2013-1-12064 and SmartMEA no.2014-1-12218) and Innovation Fund Denmark (4M Centre 0603-00527B).

References

1. Xiao LX, Zhang HF, Scanlon E et al (2005) High-temperature polybenzimidazole fuel cell membranes via a sol-gel process. *Chem Mater* 17:5328–5333
2. Wainright JS, Wang JT, Weng D et al (1995) Acid-doped polybenzimidazoles—a new polymer electrolyte. *J Electrochem Soc* 142:L121–L123
3. Wang B, Tang Y, Wen Z et al (2009) Dissolution and regeneration of polybenzimidazoles using ionic liquids. *Eur Polym J* 45:2962–2965
4. Chung TS (1997) A critical review of polybenzimidazoles: historical development and future R&D. *J Macromol Sci Rev Macromol Chem Phys C* 37:277–301
5. Kumbharkar SC, Islam MN, Potrekar RA et al (2009) Variation in acid moiety of polybenzimidazoles: investigation of physico-chemical properties towards their applicability as proton

- exchange and gas separation membrane materials. *Polymer* 50:1403–1413
6. Vogel H, Marvel CS (1961) Polybenzimidazoles, new thermally stable polymers. *J Polym Sci* 50:511–539
 7. Scariah KJ, Krishnamurthy VN, Rao KVC et al (1987) Synthesis and properties of new polybenzimidazoles and N-phenyl polybenzimidazoles with flexible spacers on the polymer backbone. *J Polym Sci Part A: Polym Chem* 25:2675–2687
 8. Asensio JA, Borro S, Gomez-Romero P (2004) Polymer electrolyte fuel cells based on phosphoric acid-impregnated poly(2,5-benzimidazole) membranes. *J Electrochem Soc* 151:A304–A310
 9. Asensio JA, Borros S, Gomez-Romero P (2004) Proton-conducting membranes based on poly(2,5-benzimidazole) (ABPBI) and phosphoric acid prepared by direct acid casting. *J Membr Sci* 241:89–93
 10. Conti F, Willbold S, Mammi S et al (2013) Carbon NMR investigation of the polybenzimidazole-dimethylacetamide interactions in membranes for fuel cells. *New J Chem* 37:152–156
 11. Sannigrahi A, Arunbabu D, Sankar RM et al (2007) Aggregation behavior of polybenzimidazole in aprotic polar solvent. *Macromolecules* 40:2844–2851
 12. Lin HL, Chen YC, Li CC et al (2008) Preparation of PBI/PTFE composite membranes from PBI in N, N'-dimethyl acetamide solutions with various concentrations of LiCl. *J Power Sources* 181:228–236
 13. Hanley TR, Helminiak TE, Benner CL (1978) Expansion of aromatic heterocyclic polymers in salt solution. *J Appl Polym Sci* 22:2965–2978
 14. Shogbon CB, Brousseau JL, Zhang HF et al (2006) Determination of the molecular parameters and studies of the chain conformation of polybenzimidazole in DMAc/LiCl. *Macromolecules* 39:9409–9418
 15. Yuan Y, Johnson F, Cabasso I (2009) Polybenzimidazole (PBI) molecular weight and Mark-Houwink equation. *J Appl Polym Sci* 112:3436–3441
 16. Buckley A, Stuetz D, Serad GA (1987) Polybenzimidazoles. In: Kroschwitz JI (ed) *Encyclopedia of polymer science and engineering*. Wiley, New York, pp 572–601
 17. Yang JS, Cleemann LN, Steenberg T et al (2014) High molecular weight polybenzimidazole membranes for high temperature PEMFC. *Fuel Cells* 14:7–15
 18. Úbeda D, Pinar FJ, Orozco DC et al (2012) Life study of a PBI-PEM fuel cell by current distribution measurement. *J Appl Electrochem* 42:711–718
 19. Steenberg T, Hjuler HA, Terkelsen C et al (2012) Roll-to-roll coated PBI membranes for high temperature PEM fuel cells. *Energy Environ Sci* 5:6076–6080
 20. Li Q, Hjuler HA, Bjerrum NJ (2001) Phosphoric acid doped polybenzimidazole membranes: physicochemical characterization and fuel cell applications. *J Appl Electrochem* 31:773–779
 21. Li Q, He RH, Berg RW et al (2004) Water uptake and acid doping of polybenzimidazoles as electrolyte membranes for fuel cells. *Solid State Ionics* 168:177–185
 22. Kerres J, Schönberger F, Chromik A et al (2008) Partially fluorinated arylene polyethers and their ternary blend membranes with PBI and H₃PO₄. Part I. Synthesis and characterisation of polymers and binary blend membranes. *Fuel Cells* 8:175–187
 23. Aili D, Allward T, Alfaro SM et al (2014) Polybenzimidazole and sulfonated polyhedral oligosilsesquioxane composite membranes for high temperature polymer electrolyte membrane fuel cells. *Electrochim Acta* 140:182–190
 24. Walba H, Isensee RW (1961) Acidity constants of some arylimidazoles and their cations. *J Org Chem* 26:2789–2791
 25. Leykin AY, Askadskii AA, Vasilev VG et al (2010) Dependence of some properties of phosphoric acid doped PBIs on their chemical structure. *J Membr Sci* 347:69–74
 26. Xing BZ, Savadogo O (1999) The effect of acid doping on the conductivity of polybenzimidazole (PBI). *J New Mater Electrochem Sys* 2:95–101
 27. Bouchet R, Siebert E (1999) Proton conduction in acid doped polybenzimidazole. *Solid State Ionics* 118:287–299
 28. Glipe X, Bonnet B, Mula B et al (1999) Investigation of the conduction properties of phosphoric and sulfuric acid doped polybenzimidazole. *J Mater Chem* 9:3045–3049
 29. Kawahara M, Morita J, Rikukawa M et al (2000) Synthesis and proton conductivity of thermally stable polymer electrolyte: poly(benzimidazole) complexes with strong acid molecules. *Electrochim Acta* 45:1395–1398
 30. Bouchet R, Miller S, Duclot M et al (2001) A thermodynamic approach to proton conductivity in acid-doped polybenzimidazole. *Solid State Ionics* 145:69–78
 31. Pu HT, Meyer WH, Wegner G (2002) Proton transport in polybenzimidazole blended with H₃PO₄ or H₂SO₄. *J Polymer Science Part B: Polym Phys* 40:663–669
 32. Fontanella JJ, Wintersgill MC, Wainright JS et al (1998) High pressure electrical conductivity studies of acid doped polybenzimidazole. *Electrochim Acta* 43:1289–1294
 33. Ma YL, Wainright JS, Litt MH et al (2004) Conductivity of PBI membranes for high-temperature polymer electrolyte fuel cells. *J Electrochem Soc* 151: A8–A16
 34. Hughes CE, Haufe S, Angerstein B et al (2004) Probing structure and dynamics in poly[2,2'-(*m*-phenylene)-5,5'-bibenzimidazole] fuel cells with

- magic-angle spinning NMR. *J Phys Chem B* 108:13626–13631
35. He RH, Li Q, Bach A et al (2006) Physicochemical properties of phosphoric acid doped polybenzimidazole membranes for fuel cells. *J Membr Sci* 277:38–45
 36. He RH, Li Q, Jensen JO et al (2007) Doping phosphoric acid in polybenzimidazole membranes for high temperature proton exchange membrane fuel cells. *J Polym Sci Part A: Polym Chem* 45:2989–2997
 37. Schechter A, Savinell RF, Wainright JS et al (2009) ^1H and ^{31}P NMR study of phosphoric acid-doped polybenzimidazole under controlled water activity. *J Electrochem Soc* 156:B283–B290
 38. Suarez S, Kodiweera N, Stallworth P et al (2012) Multinuclear NMR study of the effect of acid concentration on ion transport in phosphoric acid doped poly(benzimidazole) membranes. *J Phys Chem B* 116:12545–12551
 39. Xing B, Savadogo O (2000) Hydrogen/oxygen polymer electrolyte membrane fuel cells (PEMFCs) based on alkaline-doped polybenzimidazole (PBI). *Electrochem Commun* 2:697–702
 40. Luo H, Vaivars G, Agboola B et al (2012) Anion exchange membrane based on alkali doped poly(2,5-benzimidazole) for fuel cell. *Solid State Ionics* 208:52–55
 41. Aili D, Hansen MK, Renzaho RF et al (2013) Heterogeneous anion conducting membranes based on linear and crosslinked KOH doped polybenzimidazole for alkaline water electrolysis. *J Membr Sci* 447:424–432
 42. Jensen JO, Aili D, Hansen MK et al (2014) A stability study of alkali doped PBI membranes for alkaline electrolyzer cells. *ECS Trans* 64:1175–1184
 43. Jayakumar JV, Gullede A, Staser JA et al (2012) Polybenzimidazole membranes for hydrogen and sulfuric acid production in the hybrid sulfur electrolyzer. *ECS Electrochem Lett* 1:F44–F48
 44. Sansone MJ (1987) Crosslinking of polybenzimidazole polymer with divinyl sulfone. US Patent 4,666,996
 45. Thomas OD, Soo K, Peckham TJ et al (2012) A stable hydroxide-conducting polymer. *J Am Chem Soc* 134:10753–10756
 46. Henkensmeier D, Kim HJ, Lee HJ et al (2011) Polybenzimidazolium-based solid electrolytes. *Macromol Mater Eng* 296:899–908
 47. Li Q, Jensen JO, Savinell RF et al (2009) High temperature proton exchange membranes based on polybenzimidazoles for fuel cells. *Prog Polym Sci* 34:449–477
 48. Vilčiauskas L, Tuckerman ME, Bester G et al (2012) The mechanism of proton conduction in phosphoric acid. *Nat Chem* 4:461–466
 49. Perry AK, More LK, Andrew Payzant E et al (2014) A comparative study of phosphoric acid-doped *m*-PBI membranes. *J Polym Sci Part B: Polym Phys* 52:26–35
 50. Munson RA (1964) Self-dissociative equilibria in molten phosphoric acid. *J Phys Chem* 68:3374–3377
 51. Daletou MK, Geormezi M, Vogli E et al (2014) The interaction of H_3PO_4 and steam with PBI and TPS polymeric membranes. A TGA and Raman study. *J Mater Chem A* 2:1117–1127
 52. Li Q, Jensen JO, Pan C et al (2008) Partially fluorinated aarylene polyethers and their ternary blends with PBI and H_3PO_4 . Part II. Characterisation and fuel cell tests of the ternary membranes. *Fuel Cells* 8:188–199
 53. Lobato J, Cañizares P, Rodrigo MA et al (2006) Synthesis and characterisation of poly[2,2-(*m*-phenylene)-5,5-benzimidazole] as polymer electrolyte membrane for high temperature PEMFCs. *J Membr Sci* 280:351–362
 54. Kohama S-I, Gong J, Kimura K et al (2008) Morphology control of poly(2,2'-phenylene-5,5'-bibenzimidazole) by reaction-induced crystallization during polymerization. *Polymer* 49:1783–1791
 55. Mecerreyes D, Grande H, Miguel O et al (2004) Porous polybenzimidazole membranes doped with phosphoric acid: Highly proton-conducting solid electrolytes. *Chem Mater* 16:604–607
 56. Shen C-H, Jheng L-C, Hsu SL-C et al (2011) Phosphoric acid-doped cross-linked porous polybenzimidazole membranes for proton exchange membrane fuel cells. *J Mater Chem* 21:15660–15665
 57. Eguizábal A, Sgroi M, Pullini D et al (2014) Nanoporous PBI membranes by track etching for high temperature PEMs. *J Membr Sci* 454:243–252
 58. Conciatory AB, Chenevey EC, Noether HD et al (1970) Process for crystallizing polybenzimidazoles. US Patent 3,495,931
 59. Kumbharkar SC, Karadkar PB, Kharul UK (2006) Enhancement of gas permeation properties of polybenzimidazoles by systematic structure architecture. *J Membr Sci* 286:161–169
 60. Kumbharkar SC, Kharul UK (2009) *N*-substitution of polybenzimidazoles: synthesis and evaluation of physical properties. *Eur Polym J* 45:3363–3371
 61. Sannigrahi A, Arunbabu D, Jana T (2006) Thermoreversible gelation of polybenzimidazole in phosphoric acid. *Macromol Rapid Commun* 27:1962–1967
 62. Aili D, Cleemann LN, Li Q et al (2012) Thermal curing of PBI membranes for high temperature PEM fuel cells. *J Mater Chem* 22:5444–5453
 63. Litt M, Ameri R, Wang Y et al (1999) Polybenzimidazoles/phosphoric acid solid polymer electrolytes: Mechanical and electrical properties. In: Nazri GA, Julien C, Rougier A (eds) *MRS Proceedings* 548. Materials Research Society, Warrendale, pp 313–323
 64. Belohlav LR (1974) Polybenzimidazole. *Angew Makromol Chem* 40:465–483
 65. Aili D, Li Q, Christensen E et al (2011) Crosslinking of polybenzimidazole membranes by divinylsulfone post-treatment for high-temperature proton exchange membrane fuel cell applications. *Polym Int* 60:1201–1207

66. Samms SR, Wasmus S, Savinell RF (1996) Thermal stability of proton conducting acid doped polybenzimidazole in simulated fuel cell environments. *J Electrochem Soc* 143:1225–1232
67. Gillham JK (1963) Polymer Structure: cross-linking of a polybenzimidazole. *Science* 139:494–495
68. Liao JH, Li QF, Rudbeck HC et al (2011) Oxidative degradation of polybenzimidazole membranes as electrolytes for high temperature proton exchange membrane fuel cells. *Fuel Cells* 11:745–755
69. Liao J, Yang J, Li Q et al (2013) Oxidative degradation of acid doped polybenzimidazole membranes and fuel cell durability in the presence of ferrous ions. *J Power Sources* 238:516–522
70. Yang J, Li Q, Cleemann LN et al (2013) Cross-linked hexafluoropropylidene polybenzimidazole membranes with chloromethyl polysulfone for fuel cell applications. *Adv Energy Mater* 3:622–630
71. Iqbal HMS, Bhowmik S, Benedictus R (2014) Process optimization of solvent based polybenzimidazole adhesive for aerospace applications. *Int J Adhes Adhes* 48:188–193
72. Wainright JS, Litt MH, Savinell RF (2003) High temperature membranes. In: Vielstich W, Lamm A, Gasteiger HA (eds) *Handbook of fuel cells*. Wiley, New York, pp 436–446
73. Pohl HA, Chartoff RP (1964) Carriers and unpaired spins in some organic semiconductors. *J Polym Sci Part A: Polym Chem* 2:2787
74. Aharoni SM, Litt MH (1974) Synthesis and some properties of poly-(2,5-trimethylene benzimidazole) and poly-(2,5-trimethylene benzimidazole hydrochloride). *J Polym Sci Part A* 12:639–650
75. Hoel D, Grunwald E (1977) High protonic conduction of polybenzimidazole films. *J Phys Chem* 81:2135–2136
76. Vilčiauskas L, Tuckerman ME, Melchior JP et al (2013) First principles molecular dynamics study of proton dynamics and transport in phosphoric acid/imidazole (2:1) system. *Solid State Ionics* 252:34–39
77. Li Q, Pan C, Jensen JO et al (2007) Cross-linked polybenzimidazole membranes for fuel cells. *Chem Mater* 19:350–352
78. Kim SK, Choi SW, Jeon WS et al (2012) Cross-linked benzoxazine-benzimidazole copolymer electrolyte membranes for fuel cells at elevated temperature. *Macromolecules* 45:1438–1446
79. Han M, Zhang G, Liu Z et al (2011) Cross-linked polybenzimidazole with enhanced stability for high temperature proton exchange membrane fuel cells. *J Mater Chem* 21:2187–2193
80. Jin YC, Nishida M, Kanematsu W et al (2011) An H₃PO₄-doped polybenzimidazole/Sn_{0.95}Al_{0.05}P₂O₇ composite membrane for high-temperature proton exchange membrane fuel cells. *J Power Sources* 196:6042–6047
81. Guan YS, Pu HT, Jin M et al (2011) Preparation and characterisation of proton exchange membranes based on crosslinked polybenzimidazole and phosphoric acid. *Fuel Cells* 10:973–982
82. Jayakody JRP, Chung SH, Durantino L et al (2007) NMR studies of mass transport in high-acid-content fuel cell membranes based on phosphoric acid and polybenzimidazole. *J Electrochem Soc* 154: B242–B246
83. Schechter A, Savinell RF (2002) Imidazole and 1-methyl imidazole in phosphoric acid doped polybenzimidazole, electrolyte for fuel cells. *Solid State Ionics* 147:181–187
84. Mader J, Xiao L, Schmidt TJ et al (2008) Polybenzimidazole/acid complexes as high-temperature membranes. In: Scherer G (ed) *Advances in polymer science—fuel cells II*. Springer, Berlin, pp 63–124
85. Yu S, Zhang H, Xiao L et al (2009) Synthesis of poly(2,2'-(1,4-phenylene) 5,5'-bibenzimidazole) (*para*-PBI) and phosphoric acid doped membrane for fuel cells. *Fuel Cells* 9:318–324
86. He RH, Li Q, Xiao G et al (2003) Proton conductivity of phosphoric acid doped polybenzimidazole and its composites with inorganic proton conductors. *J Membr Sci* 226:169–184
87. Gu T, Shimpalee S, Van Zee JW et al (2010) A study of water adsorption and desorption by a PBI-H₃PO₄ membrane electrode assembly. *J Power Sources* 195:8194–8197
88. Pivovar BS (2006) An overview of electro-osmosis in fuel cell polymer electrolytes. *Polymer* 47:4194–4202
89. Zawodzinski TA, Derouin C, Radzinski S et al (1993) Water-uptake by and transport through Nafion[®] 117 membranes. *J Electrochem Soc* 140:1041–1047
90. Xie G, Okada T (1995) Water transport behaviour in Nafion 117 membranes. *J Electrochem Soc* 142:3057–3062
91. Pivovar BS, Smyrl WH, Cussler EL (2005) Electro-osmosis in Nafion 117, polystyrene sulfonic acid, and polybenzimidazole. *J Electrochem Soc* 152:A53–A60
92. Weng D, Wainright JS, Landau U et al (1996) Electro-osmotic drag coefficient of water and methanol in polymer electrolytes at elevated temperatures. *J Electrochem Soc* 143:1260–1263
93. Savinell R, Yeager E, Tryk D et al (1994) A polymer electrolyte for operation at temperatures up to 200 °C. *J Electrochem Soc* 141:L46–L48
94. Aili D, Savinell RF, Jensen JO et al (2014) The electrochemical behavior of phosphoric-acid-doped poly(perfluorosulfonic acid) membranes. *ChemElectroChem* 1:1471–1475
95. Pivovar BS, Wang YX, Cussler EL (1999) Pervaporation membranes in direct methanol fuel cells. *J Membr Sci* 154:155–162
96. Lobato J, Cañizares P, Rodrigo MA et al (2008) Performance of a vapor-fed polybenzimidazole (PBI)-based direct methanol fuel cell. *Energy Fuels* 22:3335–3345
97. Araya S, Andreasen SJ, Nielsen HV et al (2012) Investigating the effects of methanol-water vapor

- mixture on a PBI-based high temperature PEM fuel cell. *Int J Hydrogen Energy* 37:18231–18242
98. Wang JT, Wasmus S, Savinell RF (1996) Real-time mass spectrometric study of the methanol crossover in a direct methanol fuel cell. *J Electrochem Soc* 143:1233–1239
 99. Pesiri DR, Jorgensen B, Dye RC (2003) Thermal optimization of polybenzimidazole meniscus membranes for the separation of hydrogen, methane and carbon dioxide. *J Membr Sci* 218:11–18
 100. Liu Z, Wainright JS, Litt MH et al (2006) Study of the oxygen reduction reaction (ORR) at Pt interfaced with phosphoric acid doped polybenzimidazole at elevated temperature and low relative humidity. *Electrochim Acta* 51:3914–3923
 101. Lobato J, Cañizares P, Rodrigo MA et al (2011) A novel titanium PBI-based composite membrane for high temperature PEMFCs. *J Membr Sci* 369:105–111
 102. Kurdakova V, Quartarone E, Mustarelli P et al (2010) PBI-based composite membranes for polymer fuel cells. *J Power Sources* 195:7765–7769
 103. Ghosh S, Maity S, Jana T (2011) Polybenzimidazole/silica nanocomposites: organic-inorganic hybrid membranes for PEM fuel cell. *J Mater Chem* 21:14897–14906
 104. Plackett D, Siu A, Li Q et al (2011) High-temperature proton exchange membranes based on polybenzimidazole and clay composites for fuel cells. *J Membr Sci* 383:78–87
 105. Ghosh S, Sannigrahi A, Maity S et al (2011) Role of clays structures on the polybenzimidazole nanocomposites: potential membranes for the use in polymer electrolyte membrane fuel cell. *J Phys Chem C* 115:11474–11483
 106. Li M-Q, Shao Z-G, Scott K (2008) A high conductivity $\text{Cs}_{2.5}\text{H}_{0.5}\text{PMo}_{12}\text{O}_{40}$ /polybenzimidazole (PBI)/ H_3PO_4 composite membrane for proton-exchange membrane fuel cells operating at high temperature. *J Power Sources* 183:69–75
 107. Oh S-Y, Yoshida T, Kawamura G et al (2010) Inorganic-organic composite electrolytes consisting of polybenzimidazole and Cs-substituted heteropoly acids and their application for medium temperature fuel cells. *J Mater Chem* 20:6359–6366
 108. Xu C, Wu X, Wang X et al (2011) Composite membranes of polybenzimidazole and caesium-salts-of-heteropolyacids for intermediate temperature fuel cells. *J Mater Chem* 21:6014–6019
 109. Staiti P, Minutoli M, Hocevar S (2000) Membranes based on phosphotungstic acid and polybenzimidazole for fuel cell application. *J Power Sources* 90:231–235
 110. Verma A, Scott K (2010) Development of high-temperature PEMFC based on heteropolyacids and polybenzimidazole. *J Solid State Electrochem* 14:213–219
 111. Staiti P, Minutoli M (2001) Influence of composition and acid treatment on proton conduction of composite polybenzimidazole membranes. *J Power Sources* 94:9–13
 112. Staiti P (2001) Proton conductive membranes based on silicotungstic acid/silica and polybenzimidazole. *Mater Lett* 47:241–246
 113. Lobato J, Cañizares P, Rodrigo MA et al (2011) Promising TiOSO_4 composite polybenzimidazole-based membranes for high temperature PEMFCs. *ChemSusChem* 4:1489–1497
 114. Di SQ, Yan LM, Han SY et al (2012) Enhancing the high-temperature proton conductivity of phosphoric acid doped poly(2,5-benzimidazole) by preblending boron phosphate nanoparticles to the raw materials. *J Power Sources* 211:161–168
 115. Xu C, Cao Y, Kumar R et al (2011) A polybenzimidazole/sulfonated graphite oxide composite membrane for high temperature polymer electrolyte membrane fuel cells. *J Mater Chem* 21:11359–11364
 116. Suryani, Liu YL (2009) Preparation and properties of nanocomposite membranes of polybenzimidazole/sulfonated silica nanoparticles for proton exchange membranes. *J Membr Sci* 332:121–128
 117. Lin HL, Yu TL, Chang WK et al (2007) Preparation of a low proton resistance PBI/PTFE composite membrane. *J Power Sources* 164:481–487
 118. Li M, Scott K (2010) A polymer electrolyte membrane for high temperature fuel cells to fit vehicle applications. *Electrochim Acta* 55:2123–2128
 119. Park J, Wang L, Advani SG et al (2014) Mechanical stability of H_3PO_4 -doped PBI/hydrophilic-pretreated PTFE membranes for high temperature PEMFCs. *Electrochim Acta* 120:30–38
 120. Cong H, Radosz M, Towler BF et al (2007) Polymer-inorganic nanocomposite membranes for gas separation. *Sep Purif Technol* 55:281–291
 121. Noyé P, Li Q, Pan C et al (2008) Cross-linked polybenzimidazole membranes for high temperature proton exchange membrane fuel cells with dichloromethyl phosphinic acid as a cross-linker. *Polym Adv Technol* 19:1270–1275
 122. Yang J, Aili D, Li Q et al (2013) Covalently cross-linked sulfone polybenzimidazole membranes with poly(vinylbenzyl chloride) for fuel cell applications. *ChemSusChem* 6:275–282
 123. Yang J, Aili D, Li Q et al (2013) Benzimidazole grafted polybenzimidazoles for proton exchange membrane fuel cells. *Polym Chem* 4:4768–4775
 124. Kerres JA (2005) Blended and cross-linked ionomer membranes for application in membrane fuel cells. *Fuel Cells* 5:230–247
 125. Kerres J, Ullrich A, Meier F et al (1999) Synthesis and characterization of novel acid-base polymer blends for application in membrane fuel cells. *Solid State Ionics* 125:243–249
 126. Kerres J, Ullrich A, Häring T et al (2000) Preparation, characterization and fuel cell application of new acid-base blend membranes. *J New Mater Electrochem Sys* 3:229–239
 127. Deimede V, Voyiatzis GA, Kallitsis JK et al (2000) Miscibility behavior of polybenzimidazole/sulfonated polysulfone blends for use in fuel cell applications. *Macromolecules* 33:7609–7617

128. Hasiotis C, Li Q, Deimede V et al (2001) Development and characterization of acid-doped polybenzimidazole/sulfonated polysulfone blend polymer electrolytes for fuel cells. *J Electrochem Soc* 148: A513–A519
129. Li Q, Rudbeck HC, Chromik A et al (2010) Properties, degradation and high temperature fuel cell test of different types of PBI and PBI blend membranes. *J Membr Sci* 347:260–270
130. Katzfuß A, Krajcinovic K, Chromik A et al (2011) Partially fluorinated sulfonated poly(arylene sulfone)s blended with polybenzimidazole. *J Polym Sci Part A: Polym Chem* 49:1919–1927
131. Zaidi SMJ (2005) Preparation and characterization of composite membranes using blends of SPEEK/PBI with boron phosphate. *Electrochim Acta* 50:4771–4777
132. Zhang H, Li X, Zhao C et al (2008) Composite membranes based on highly sulfonated PEEK and PBI: Morphology characteristics and performance. *J Membr Sci* 308:66–74
133. Wycisk R, Lee JK, Pintauro PN (2005) Sulfonated polyphosphazene-polybenzimidazole membranes for DMFCs. *J Electrochem Soc* 152:A892–A898
134. Ainla A, Brandell D (2007) Nafion®-polybenzimidazole (PBI) composite membranes for DMFC applications. *Solid State Ionics* 178:581–585
135. Wycisk R, Chisholm J, Lee J et al (2006) Direct methanol fuel cell membranes from Nafion-polybenzimidazole blends. *J Power Sources* 163:9–17
136. Zhai YF, Zhang HM, Zhang Y et al (2007) A novel H₃PO₄/Nafion-PBI composite membrane for enhanced durability of high temperature PEM fuel cells. *J Power Sources* 169:259–264
137. Aili D, Hansen MK, Pan C et al (2011) Phosphoric acid doped membranes based on Nafion®, PBI and their blends—membrane preparation, characterization and steam electrolysis testing. *Int J Hydrogen Energy* 36:6985–6993
138. Gubler L, Kramer D, Belack J et al (2007) Celtec-V—a polybenzimidazole-based membrane for the direct methanol fuel cell. *J Electrochem Soc* 154:B981–B987
139. Berber MR, Fujigaya T, Sasaki K et al (2013) Remarkably durable high temperature polymer electrolyte fuel cell based on poly(vinylphosphonic acid)-doped polybenzimidazole. *Sci Rep* 3:1–7
140. Borup R, Meyers J, Pivovar B et al (2007) Scientific aspects of polymer electrolyte fuel cell durability and degradation. *Chem Rev* 107:3904–3951
141. Hu J, Zhang H, Zhai Y et al (2006) 500 h continuous aging life test on PBI/H₃PO₄ high-temperature PEMFC. *Int J Hydrogen Energy* 31:1855–1862
142. Zhai YF, Zhang HM, Liu G et al (2007) Degradation study on MEA in H₃PO₄/PBI high-temperature PEMFC life test. *J Electrochem Soc* 154:B72–B76
143. Qi Z, Buelte S (2006) Effect of open circuit voltage on performance and degradation of high temperature PBI-H₃PO₄ fuel cells. *J Power Sources* 161:1126–1132
144. Aili D, Li Q (2011) Unpublished results
145. Yu S, Xiao L, Benicewicz BC (2008) Durability studies of PBI-based high temperature PEMFCs. *Fuel Cells* 8:165–174
146. Oono Y, Sounai A, Hori M (2009) Influence of the phosphoric acid-doping level in a polybenzimidazole membrane on the cell performance of high-temperature proton exchange membrane fuel cells. *J Power Sources* 189:943–949
147. Galbiati S, Baricci A, Casalegno A et al (2013) Degradation in phosphoric acid doped polymer fuel cells: a 6000 h parametric investigation. *Int J Hydrogen Energy* 38:6469–6480
148. Oono Y, Sounai A, Hori M (2012) Long-term cell degradation mechanism in high-temperature proton exchange membrane fuel cells. *J Power Sources* 210:366–373
149. Oono Y, Sounai A, Hori M (2013) Prolongation of lifetime of high temperature proton exchange membrane fuel cells. *J Power Sources* 241:87–93
150. Ossiander T, Perchthaler M, Heinzl C et al (2014) Influence of thermal post-curing on the degradation of a cross-linked polybenzimidazole-based membrane for high temperature polymer electrolyte membrane fuel cells. *J Power Sources* 267:323–328

Kayley Fishel, Guoqing Qian, and Brian C. Benicewicz

10.1 Introduction

Polyphosphoric acid (PPA) has long been used as a polymerization solvent. Its ability to be used at high temperatures and lack of side reactions and tar formation in the presence of organics has proven useful in polymer syntheses that require high temperatures for condensations, ring closure and aromaticity formation [1]. Thermally stable polymers, such as polybenzothiazoles, polyquinazolines, and polybenzimidazoles (PBIs), have all been successfully synthesized in PPA [2, 3]. PBI polymer and fibers have typically been produced through melt/solid polycondensation processes and spun from solutions of DMAc at concentrations over 20 wt% polymer as reported by Celanese and Conciatori et al. [2, 4]. Although the solubility of PBI in PPA would not allow for this high wt % of polymer to be dissolved for fiber production, PBI has sufficient solubility in PPA in order to produce films. For this reason, PPA is used as the polymerization solvent in both the conventional method of film formation and in the PPA process. The methods through which PBI membranes are processed have been found to greatly affect the properties and morphology of the membrane.

K. Fishel • G. Qian • B.C. Benicewicz (✉)
Department of Chemistry and Biochemistry, University
of South Carolina, 541 Main Street, Horizon 1 Room 232,
Columbia, SC 29208, USA
e-mail: benice@sc.edu

Differences in acid loading, conductivity, mechanical properties, inherent viscosity and fuel cell performance have been shown to vary depending on the method through which the PBI was synthesized and processed. Two methods of processing have been shown to produce greater conductivity than the conventional imbibing method. Recent reviews by Savinell, Bjerrum, Li, Benicewicz, and Schmidt discuss PBI membranes for fuel cells prepared by many different methods [5–7]. In this review, we will focus on the preparation, properties and fuel cell performance of acid-doped membranes made by a unique sol–gel method termed the PPA process.

10.2 The Sol–Gel Process

In 2005, Benicewicz et al. (in cooperation with BASF Fuel Cell GmbH) reported a new method for producing PBI films imbibed with phosphoric acid [8]. This process, termed the PPA process, represents a sol–gel process that utilizes PPA as both the polymerization medium and the casting solvent for PBI polymers. In the PPA Process, dicarboxylic acids and tetramines such as 3,3',4,4'-tetraaminobiphenyl (TAB) (or AB type monomers) are polymerized in PPA between 195 and 220 °C to produce high molecular weight PBI polymers. After polymerization, the PPA solution containing PBI is directly cast onto

glass plates or other suitable substrates. Since both PBI and PPA are hygroscopic, moisture from the surrounding environment readily hydrolyzes the PPA to phosphoric acid (PA). A sol-to-gel transition can occur which is attributed to the change in the nature of the solvent, i.e., many PBIs show higher solubility in PPA and poorer solubility in phosphoric acid. This process encompasses many favorable attributes. For example, high molecular weight polymer (typically determined through inherent viscosity measurements) can be readily produced using the PPA process. Since the process does not use organic solvents for the polymerization or casting steps, the PPA process eliminates the cost of such solvents, worker exposure, and solvent recovery and disposal costs. Also, separate unit operations for imbibing are not needed as the solvent is transformed into the dopant as part of the process. Mechanical properties of PBI membranes produced through the PPA process also demonstrate greater mechanical properties with greater acid loadings and higher conductivities than membranes formed through other methods [8].

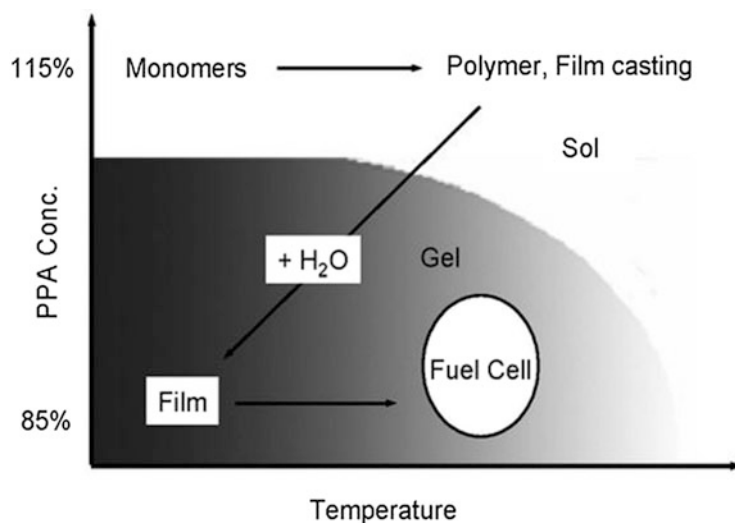
Figure 10.1 provides a summary of the multiple chemical and physical transformations that occur in the PPA Process. Preliminary simulations by Padmanabhan and Kumar of the phase behavior and formation of a physical

gel from semiflexible polymer chains provide some insights into the process [9, 10]. Increases in chain stiffness of semiflexible polymer chains will increase chain association in solution and are likely to play a role in the formation of reversible gels with liquid crystalline-like order. Molecular dynamics simulations have also indicated that chain stiffness, depth and rate of the temperature change, and the additional quench provided by the solvent quality (via PPA hydrolysis) result in the transformation of a homogeneous solution into a trapped, three-dimensional network of nematic-like bundles forming a percolated gel as shown in Fig. 10.2. Many of the predictions from these simulations are consistent with the observations made over the past 10–15 years.

10.3 Direct Acid Casting

Researchers at Case Western Reserve University reported a method for casting PBI films directly from acid solutions [11]. This direct acid casting method was performed by initially dissolving PBI in trifluoroacetic acid (TFA). Phosphoric acid was then added to create a single-phase solution which was filtered and cast onto untreated glass plates. The film was heated at 140 °C for 15 min in air. Finally, the film was

Fig. 10.1 The sol–gel state diagram. Reproduced from [8] with permission of the American Chemical Society



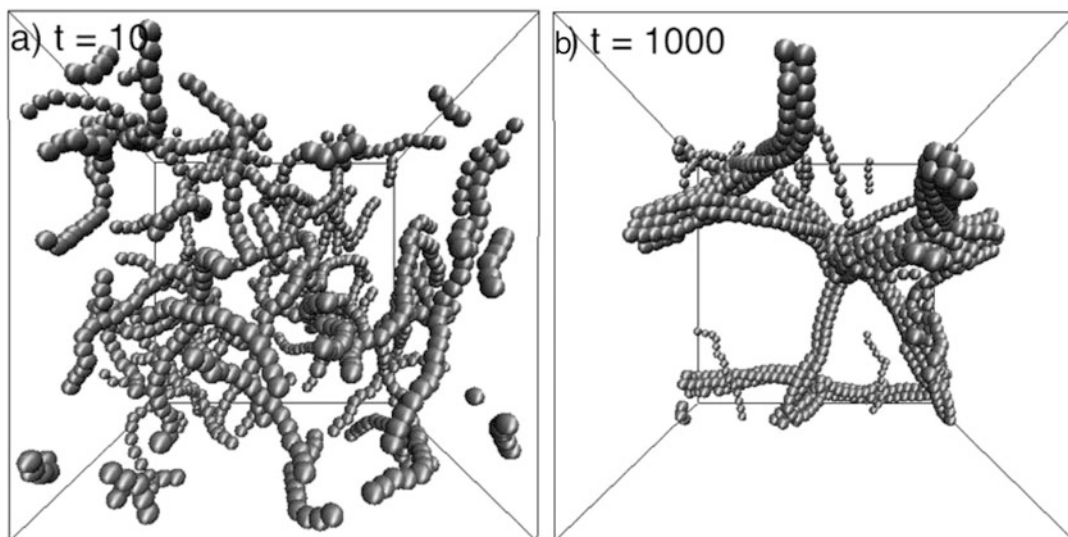


Fig. 10.2 Simulation of (a) isotropic homogeneous solution of polymer chains and (b) dynamically arrested network of nematic-like bundles

after thermally quenching the system. Reproduced from [10] with permission of AIP Publishing LLC

removed from the glass plate and heated in a vacuum oven overnight to produce a dry film. Just as PBI prepared through the PPA process exhibits different properties than PBI prepared through the conventional imbibing method, PBI films produced from direct acid casting also display unique properties. It was commonly observed that PBI films prepared through conventional imbibing are tougher and stronger than those prepared by direct acid casting [12]. It was reported that PBI of high inherent viscosity must be used for films cast from TFA to produce films of reasonable strength [12].

10.4 Conductivities and Acid Content

Since the processing method greatly affects the properties of the PBI films, differences in phosphoric acid content and conductivities vary among the PPA process, direct casting, and traditional casting from DMAc even with identical PBI chemistry. When meta-PBI was cast from DMAc and doped in PA baths, conductivities ranged from 0.01 to 0.05 S cm⁻¹ [11, 13]. Savinell et al. [11] found that by casting from

trifluoroacetic acid rather than DMAc, conductivities for meta-PBI membranes could reach as high as 0.083 S cm⁻¹. This is a significant increase from the traditional casting/imbibing method and demonstrates the influence the processing method has on the membrane properties, such as conductivity. Conductivities for meta-PBI can be significantly increased when membranes are prepared through the PPA process. Perry et al. [13] reported conductivities for meta-PBI membranes made via the PPA process of 0.13 S cm⁻¹. This is nearly a threefold improvement from films cast from DMAc and almost double the conductivity of films cast from trifluoroacetic acid. The PPA process produces membranes that contain more acid than those prepared from conventional imbibing. Acid loadings of 14–26 mol PA per moles polymer repeat unit (PRU) were reported for meta-PBI membranes prepared through the PPA process and 6–10 mol PA per PRU when prepared by conventional DMAc casting and PA imbibing [13]. Additionally, the membranes prepared by the conventionally imbibed technique and PPA process exhibited fundamentally different responses of ionic conductivity on acid doping level.

10.5 Variations in PBI Chemistry

The properties of the polymer gel film are not only affected by processing and morphology, but also by the chemistry of the PBI polymers. The chemistry of the polymer affects acid doping levels, conductivities, mechanical properties, and the polymer solids content. Many PBI chemistries can be synthesized through the PPA process by varying the chemistry of the monomers and the combination of monomers used. The ability to prepare and process many different PBI chemistries using the PPA process is a great advantage because it is less restricted by polymer solubility issues. The properties of these PBI membranes have been thoroughly studied to evaluate structure–property relationships and ultimately to enhance their properties for use in high-temperature PEM fuel cells.

10.5.1 Para-PBI (p-PBI)

Poly(2,2'-(p-phenylene)5,5'-bibenzimidazole) (para-PBI) exhibits excellent performance when used as a membrane in fuel cells.[5] Para-PBI is prepared through the PPA process using equimolar amounts of terephthalic acid and

3,3',4,4'-tetraaminobiphenyl in PPA under a nitrogen atmosphere. Unlike Vogel and Marvel's early attempts of preparing p-PBI through a melt process which resulted in low molecular weight polymer ($IV=1.0 \text{ dL g}^{-1}$), high molecular weight para-PBI ($IVs > 3.0 \text{ dL g}^{-1}$) can be prepared through the PPA process [14, 15]. High molecular weight polymer was achieved after approximately 24 h when polymerized between 195 and 220 °C. This is a significantly more time efficient method than previous work reported by the US Air Force Materials Lab that reported high molecular weight para-PBI could take up to 5 weeks to produce [16]. Extensive studies of para-PBI produced through the PPA process have been conducted. Yu et al. [15] systematically explored the effect of monomer concentration on polymer IV. It was reported that high IVs ($\sim 3.0 \text{ dL g}^{-1}$) could be obtained up to approximately 4.5 wt% monomer charges (Fig. 10.3) that could be easily cast into high-quality PA-doped membranes. Monomer charges greater than 4.5 wt% resulted in high solution viscosities, insufficient stirring and early loss of polymer solubility resulting in low IVs and unprocessable solutions. Membranes produced from the lower concentrations exhibited higher levels of acid doping than membranes prepared through direct casting [15]. Since high molecular weight para-PBI is insoluble in organic solvents, it cannot be dissolved and directly cast from organic

Fig. 10.3 Effect of monomer concentration on inherent viscosity for para-PBI. Reproduced from [15] with permission of John Wiley and Sons

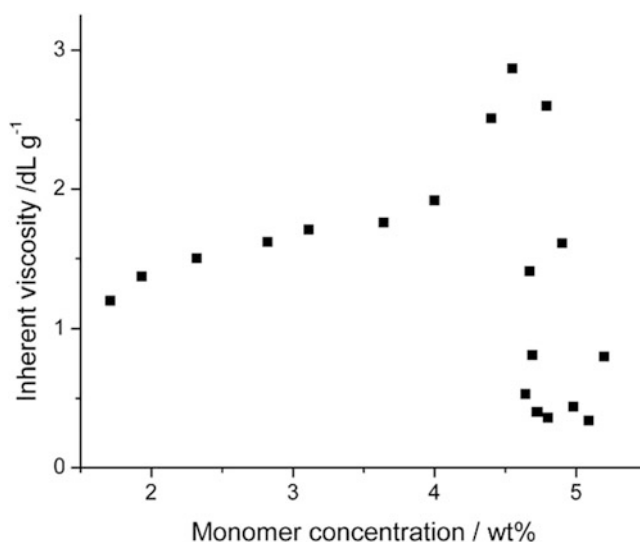
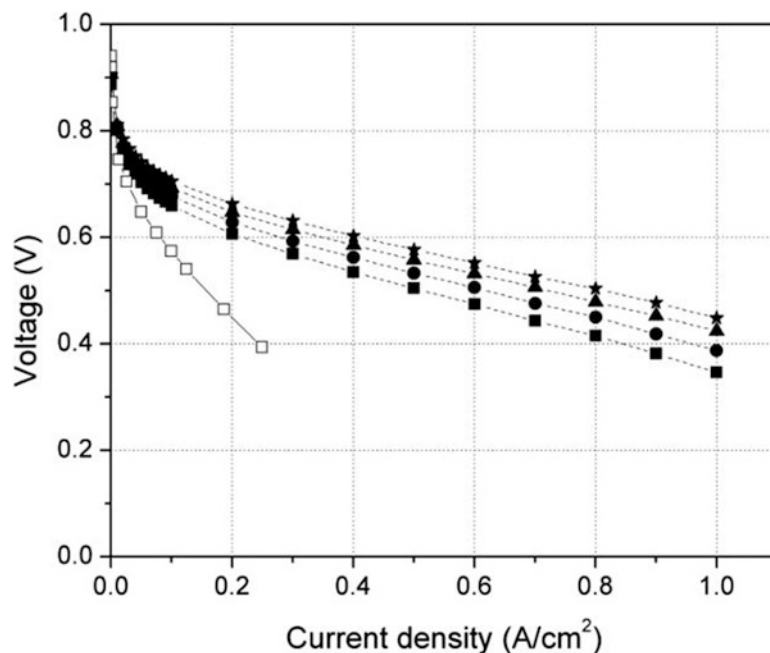


Fig. 10.4 Polarization curves of para-PBI membrane-based fuel cells with hydrogen ($\lambda = 1.2$)/air ($\lambda = 2.00$) at various temperatures at 1 atm. Squares: 120 °C, circles: 140 °C, triangles: 160 °C, stars: 180 °C. Open squares are data from Wang et al. *Electrochim. Acta* 1996, 41, 193. Reproduced from [15] with permission from John Wiley and Sons



solvents. Para-PBI membranes prepared by the PPA process contain approximately 30–40 mol of PA/PRU, which are much higher acid doping levels than observed in typical membranes prepared by conventional imbibing (≤ 13 –14 PA/PRU) [15]. The anhydrous conductivity for para-PBI produced from the PPA process is greater than 0.2 S cm^{-1} at 160 °C. When fuel cell performance was evaluated on these membranes at a constant current density of 0.2 A cm^{-2} with hydrogen and air, the voltage was 0.606 V at 120 °C and 0.663 V at 180 °C [15].

Figure 10.4 shows the polarization curves of para-PBI at 120, 140, 160, and 180 °C. Meta-PBI membrane prepared by conventional imbibing is included for comparison. It should be noted that the fuel cell was operated without humidification [15]. At high temperatures para-PBI can also be operated in a fuel cell using gas mixtures other than hydrogen and air. Fuel cells run on reformat gases consisting of varying amounts of hydrogen, carbon monoxide, and carbon dioxide operated reliably even with high concentrations of carbon monoxide, with only slight decreases in voltage. Figure 10.5 shows the polarization curves for para-PBI membrane run on various gas mixtures. Additional testing also demonstrated long-term

durability ($>1400 \text{ h}$) and very low acid loss rates. Yu et al. [17] reported phosphoric acid loss rates of $3.0 \text{ ng cm}^{-2} \text{ h}^{-1}$ from the cathode and $1.9 \text{ ng cm}^{-2} \text{ h}^{-1}$ from the anode. These results indicate that PA loss from the MEAs is not likely a failure mode under normal operating conditions.

10.5.2 Sulfonated-PBI

A sulfonated version of para-PBI has been produced using the PPA process by reacting equimolar amounts of 3,3',4,4'-tetraaminobiphenyl and 2-sulfoterephthalic acid in PPA (Fig. 10.6).

Mader et al. [18] originally investigated this chemistry to see if the addition of a stronger acid group would improve conductivity and therefore the overall fuel cell performance. Inherent viscosity was tested with various monomer charges and it was found that the highest IV, 1.71 dL g^{-1} , was obtained at a monomer charge of 3.61 wt%. Monomer concentrations ranged from 2.48 to 7.39 wt% and IVs ranged from 1.03 to 1.71 dL g^{-1} . The membrane mechanical properties were found to increase with increasing polymer solids concentration. Tensile stress at

Fig. 10.5 Polarization curves of para-PBI membrane-based fuel cells with various gas mixtures at 180 °C under ambient pressure. (Squares: hydrogen/air), (triangles: H₂ 70 %, CO 1 %, CO₂ balance/air) and (circles: (H₂ 35.8 %, CO 0.2 %, CO₂ 11.9 %, N₂ balance/air). Reproduced from [15] with permission John Wiley and Sons

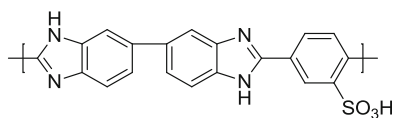
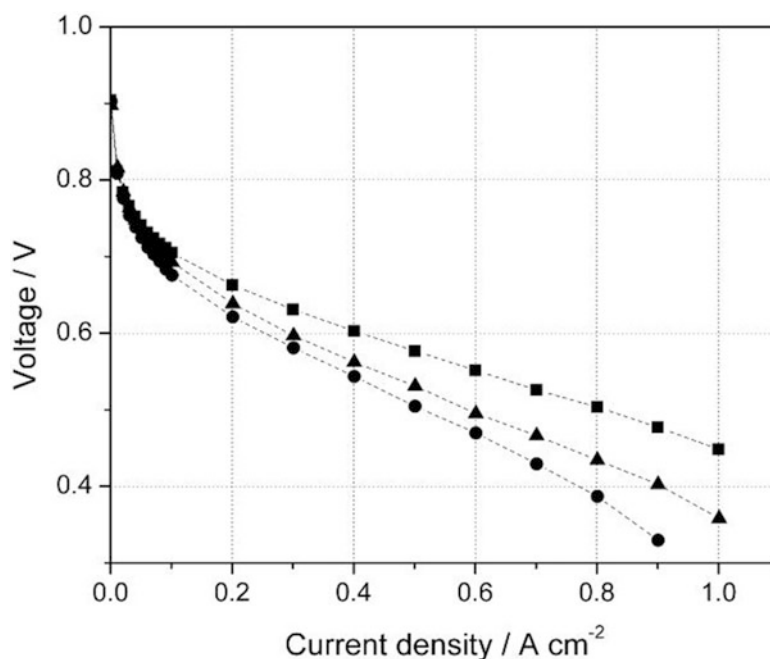


Fig. 10.6 Chemical structure of sulfonated-PBI repeat unit

break reached a maximum of 2.25 MPa and a modulus of 15.1 MPa. The pristine sulfonated-PBI membrane demonstrated high phosphoric acid loadings, 28–53 mol PA/PRU, though an increase in conductivity was not seen when samples contained more than 39 mol PA/PRU (maximum conductivity was approximately 0.32 S cm⁻¹). Fuel cell testing was performed on membranes with the highest IVs (Fig. 10.7). The highest performance was seen in the membrane with the highest level of acid loading, 0.679 V at 160 °C and 0.2 A cm⁻². The lowest performance, 0.617 V, was seen with the membrane that had the lowest level of acid loading. These results indicate a correlation between fuel cell performance and acid loading but not fuel cell performance and conductivity directly. Since PBI is known to be both thermally and chemically stable, further studies were performed on

sulfonated-PBI doped with sulfuric acid. This was performed by first synthesizing sulfonated-PBI in PPA, casting films and hydrolyzing the PPA to PA, and exchanging the PA under different conditions in concentrated sulfuric acid baths. Conductivities were tested for nearly 500 min from room temperature (~20 °C) to 100 °C and reached 0.54 S cm⁻¹ but decreased with time at 100 °C. Acid loadings ranged from approximately 25–50 mol of sulfuric acid/PRU (Table 10.1). These acid loadings were found to be similar to the phosphoric acid loadings in sulfonated-PBI prepared through the PPA process. A comparison of conductivities at various temperatures and over time for these films doped in different sulfuric acid baths can be seen in Fig. 10.8.

10.5.3 AB-PBI and Isomeric AB-PBI (*i*-PBI)

The simplest PBI chemistry is AB-PBI with a repeat unit consisting solely of one 2,5-benzimidazole ring. AB-PBI is synthesized using 3,4-diaminobenzoic acid as the only

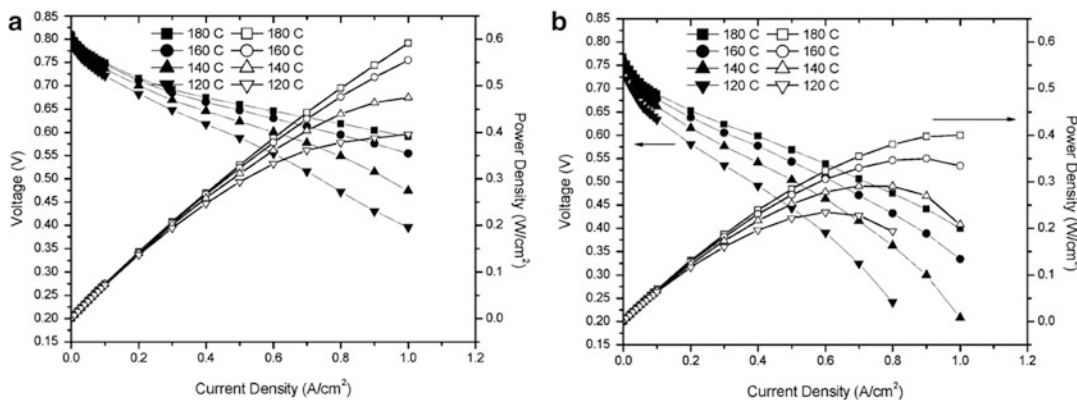


Fig. 10.7 Fuel cell performance of PA-doped sulfonated-PBI (3.13 wt% polymer, IV = 1.67 dL/g, and 28.41 mol PA/PBI): polarization curves (filled symbols) and power

density curves (open symbols) with (a) hydrogen and oxygen and (b) hydrogen and air. Reproduced from [18] with permission of the American Chemical Society

Table 10.1 Acid content, sulfuric and phosphoric acid, in sulfonated polybenzimidazoles. Reproduced from [18] with permission of the American Chemical Society

Film	Polymer contents (g)	Acid loading (mol acid/PRU)
PA-doped s-PBI	0.0413	39.84
30 wt% SA room temp bath	0.0516	25.47
30 wt% SA heated bath	0.0553	30.36
50 wt% SA room temp bath	0.0583	50.49
50 wt% SA heated bath	0.0587	31.48

monomer since it contains both the o-diamine and the carboxylic acid functionality. Because there are no additional phenyl rings or other aromatic rings in the repeat unit as there are in other PBI chemistries, the solubility of AB-PBI in phosphoric acid is greater than most other types of PBIs. In past work, AB-PBI was polymerized through the PPA process and was found to be too soluble in PA to produce a gel membrane that could maintain gel stability at high temperatures, even at high IVs (~ 10 dL g⁻¹) [19]. This is due to the greater acid loading of the AB-PBI membranes produced from the PPA process (22–35 mol PA/PRU) versus the conventionally imbibed membranes (2–10 mol PA/PRU) [6]. In 2011, Gullidge et al. [20] reported a method of

synthesizing a new isomeric version of AB-PBI, also consisting solely of 2,5-benzimidazole repeat units, however, these repeat units were no longer in a strictly head-to-tail arrangement like AB-PBI, but rather contained head-to-head, head-to-tail, and tail-to-tail arrangements. This polymerization was done through the use of a novel monomer, 2,2'-bisbenzimidazole-5,5'-dicarboxylic acid to create an isomeric AB-PBI (*i*-AB-PBI) shown in Fig. 10.9.

This change in sequence introduced new types of bonds. Benzimidazole–benzimidazole and phenyl–phenyl linkages were now part of the backbone along with the benzimidazole–phenyl linkages. Unlike conventional AB-PBI, *i*-AB-PBI was not as soluble in PA, allowing for the formation of gel membranes via the PPA process containing large amounts of PA that maintained gel stability at elevated temperatures (130–180 °C). Polymerizations in PPA up to ~ 6 wt% yielded IVs > 3.0 dL g⁻¹ [20]. Isomeric AB-PBI membranes had conductivities of ~ 0.2 S cm⁻¹ at 180 °C which is approximately a tenfold increase in conductivity over AB-PBI prepared by the conventional imbibing method (0.02 S cm⁻¹) [20, 21]. Figure 10.10 shows the conductivity of *i*-AB-PBI at various temperatures. The higher conductivity was largely due to the greater stability of *i*-AB PBI at higher temperatures with

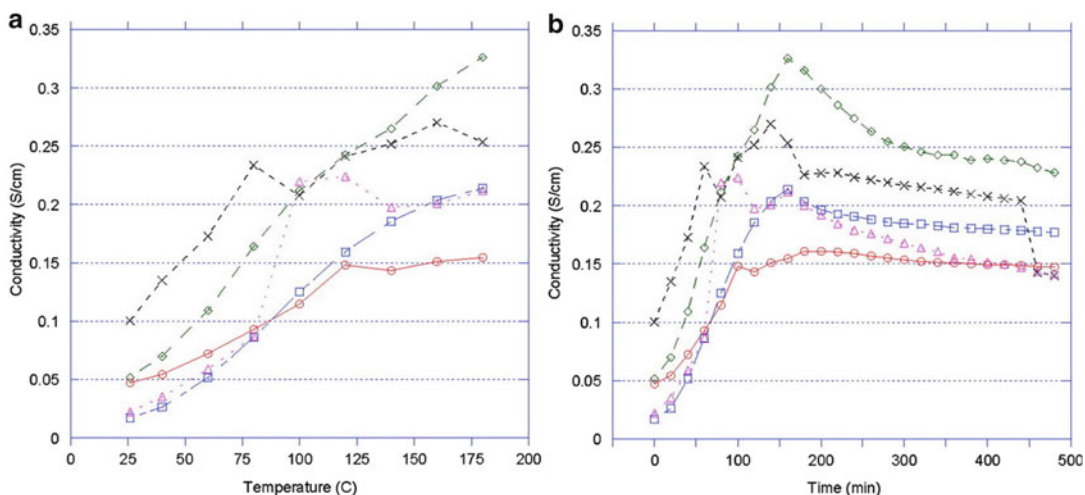


Fig. 10.8 Conductivity as a function of temperature and time (a) short-term testing, (b) long-term testing. Red circles: 30 wt% sulfuric acid bath at room temperature, blue squares: 20 wt% heated sulfuric acid bath, green

diamonds: 50 wt% sulfuric acid bath at room temperature, black crosses: 50 wt% heated sulfuric acid bath. Reproduced from [18] with permission of the American Chemical Society

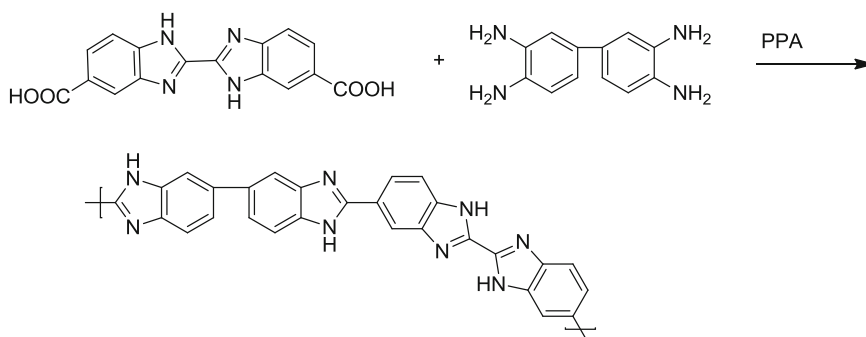


Fig. 10.9 Synthetic scheme for *i*-AB-PBI. Reproduced from [20] with permission of John Wiley and Sons

increased acid doping levels, apparently derived from the sequence isomerism. The high conductivity of these membranes indicated they would be excellent candidates for use in HT-PEM fuel cells. Isomeric AB-PBI membranes displayed much improved fuel cell performance, ~ 0.65 V when run at 180 °C and 0.2 A cm^{-2} , compared to AB-PBI prepared through conventional imbibing [20]. The fuel cell performance comparison of these two chemistries can be seen in Fig. 10.11. The fuel cell using *i*-AB PBI as the membrane was able to operate for over 3500 h with little decrease in performance further demonstrating the gel stability of this sequence isomer.

10.5.4 Pyridine-Based PBIs

Due to the large affect chemistry has on the properties of PBI membranes, Xiao et al. [22] investigated the properties of PBI membranes that contained a pyridine moiety in the repeat unit rather than a phenyl moiety. Four different PBI homopolymers were synthesized that contained pyridine moieties in the repeat unit. These homopolymers were synthesized by reacting TAB with a pyridine diacid, (3,5-, 2,4-, 2,5-, and 2,6-pyridine dicarboxylic acid). Figure 10.12 shows the repeat unit of each of the four pyridine PBIs. 2,5-Pyridine PBI differs from the other three chemistries in that it is the

Fig. 10.10 Conductivity of i-AB PBI (black squares) and AB-PBI (red circles): data from Asensio, J. et al. Fuel Cells 2005, 3, 336–343). Reproduced from [20] with permission of John Wiley and Sons

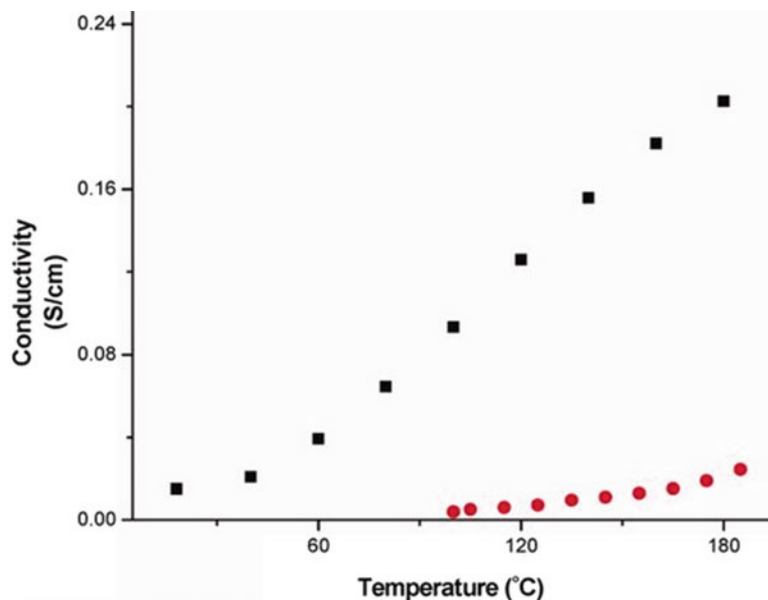
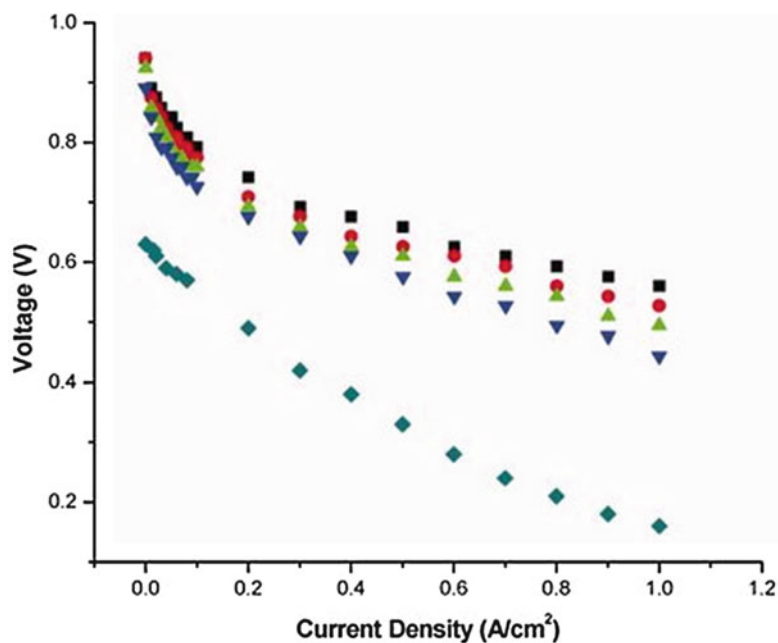


Fig. 10.11 Polarization curves for i-AB-PBI membranes with hydrogen/oxygen at 1.2:2.0 stoichiometric flows, respectively. (Squares: 180 °C, circles: 160 °C, triangles: 140 °C, inverted triangles: 120 °C, diamonds: reference data for AB-PBI at 130 °C) (Asensio, J. et al. Fuel Cells 2005, 3, 336–343). Reproduced from [20] with permission of John Wiley and Sons



only pyridine PBI in this series that has para-orientation within the backbone. Due to its more rigid nature than the other three pyridine PBI chemistries, it reportedly became more viscous during polymerization than the others after equivalent polymerization times.

All pyridine PBI chemistries achieved IVs $\geq 1.0 \text{ dL g}^{-1}$, indicating high molecular weight polymer was obtained from all four homopolymers. Specific IVs are listed in Table 10.2. Mechanically strong membranes of 2,5-pyridine PBI were obtained through the PPA

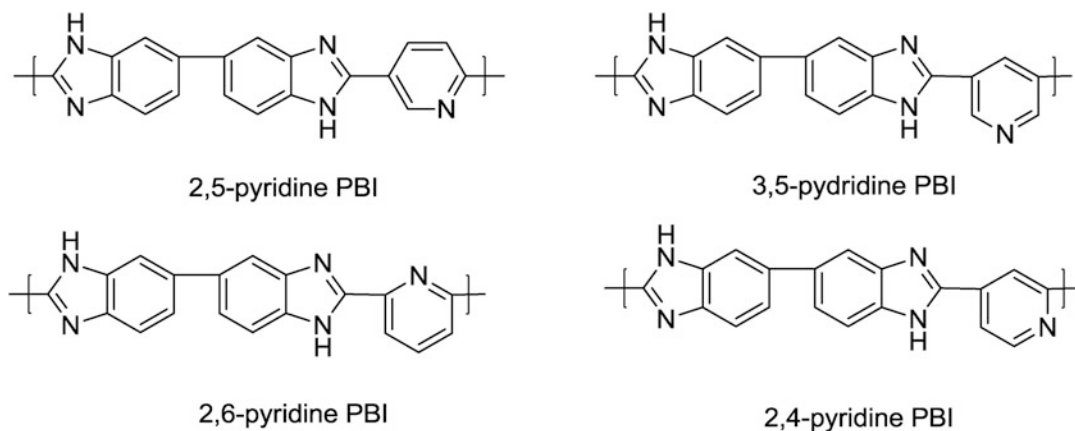


Fig. 10.12 Chemical structure of repeat units for pyridine-based polybenzimidazoles

Table 10.2 Pyridine PBIs and polymerization data where represents final monomer concentration

Polymer	Monomer purity	$\eta_{inh}/$ $dL\ g^{-1}$	Polymerization concentration (%)
2,5-PPBI	As received	0.5	4–18
	Recrystallized	2.5–3.1	
3,5-PPBI	As received	0.6	4–20
	Recrystallized	1.3–1.9	
2,4-PPBI	As received	0.3	~7
	Recrystallized	1.0	
2,6-PPBI	As received	0.2	~7
	Recrystallized	1.3	

Reproduced from [22] with permission of John Wiley and Sons

process when cast from a 4.5 wt% polymer solution [22]. Acid doping levels were found to be 15–25 mol PA/PRU which is much higher than acid loadings in PBI membranes made via the conventional imbibing method. In comparison, 3,5-pyridine PBI membranes exhibited significantly different properties than 2,5-pyridine PBI membranes. Although, 3,5-pyridine PBI attained an IV of $1.8\ dL\ g^{-1}$, mechanically stable membranes could not be produced via the PPA process. After casting and hydrolysis, the solution remained a viscous solution rather undergoing gelation and film formation. The polymerization studies examined a wide range of monomer charges (5–20 wt%), but the high solubility of 3,5-pyridine PBI prevented film

formation at all polymer loadings [22]. 2,4-pyridine PBI membranes were found to be mechanically weak, therefore, further characterization of membrane properties was not performed. Mechanically stable membranes of 2,6-pyridine PBI were produced through the PPA process and acid doping levels of the membranes were found to be between 8 and 10 mol PA/PRU with polymer contents between 15 and 20 wt%. Conductivities of both 2,5-pyridine PBI and 2,6-pyridine PBI were tested under anhydrous conditions from 20 to 210 °C (Fig. 10.13) and 2,5-pyridine PBI ($\sim 0.2\ S\ cm^{-1}$) was found to have almost twice the conductivity of 2,6-pyridine PBI ($\sim 0.1\ S\ cm^{-1}$) from 160 to 210 °C [22]. The higher conductivity of the 2,5-pyridine PBI membranes was attributed to the significantly higher acid loading than the 2,6-pyridine PBI membranes and to its para-orientation. These results contribute to our general understanding that demonstrate significant effects of polymer design such as chain stiffness, functional group incorporation, and orientation on the properties of PBI membranes.

10.5.5 Meta-PBI

Meta-PBI, poly(2,2'-(m-phenylene)5,5'-bibenzimidazole), has gained great attention since

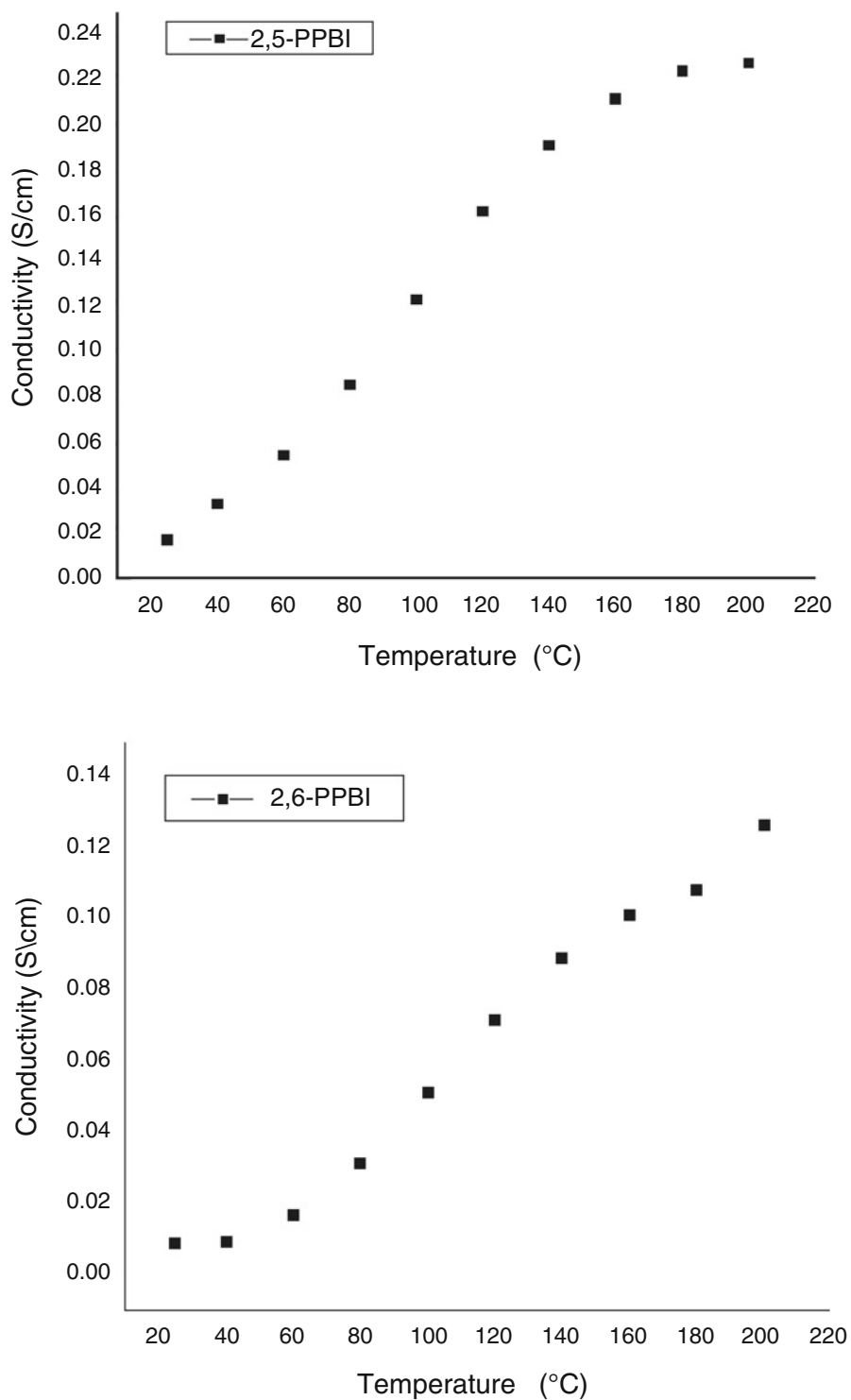
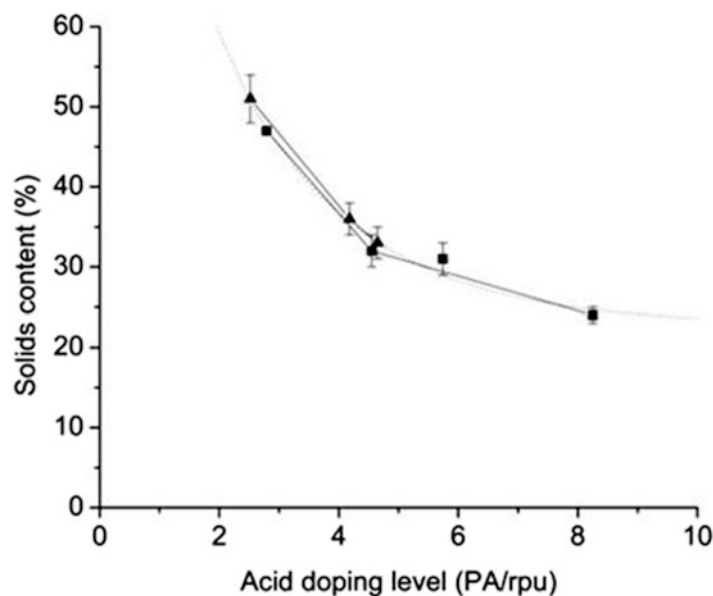


Fig. 10.13 Conductivities of phosphoric acid doped pyridine polybenzimidazoles. Reproduced from [22] with permission of John Wiley and Sons

Fig. 10.14 Relationship of solids content and acid doping levels of heat-treated phosphoric acid imbibed meta-PBI prepared by *squares*: sol-gel process, *triangles*: conventional imbibing. Reproduced from [13] with permission of John Wiley and Sons



Wainright et al. [23] showed that meta-PBI films doped with phosphoric acid can be used in fuel cells operating at 100–200 °C. Since meta-PBI can be prepared by both the conventional imbibing method and the PPA processes, many studies have been performed on comparing meta-PBI membranes prepared by both processes. Meta-PBI prepared by the PPA process produces membranes with higher levels of acid doping, i.e., 14–26 mol PA/PRU versus 6–10 mol PA/PRU by conventional imbibing [5, 6]. Due to the higher acid doping levels in membranes prepared by the PPA process, it is no surprise that these membranes displayed higher conductivities than those prepared by conventional imbibing, i.e., 0.13 S cm⁻¹ at 160 °C and 0.04–0.05 S cm⁻¹ at 150 °C, respectively [5, 6]. Perry et al. [13] recently conducted carefully controlled comparisons of membranes produced by each process. Membranes with similar solid contents were prepared by each method and treated using acid baths and heat treatments to assess acid uptake. Figure 10.14 shows that membranes prepared by the sol-gel process were able to take up more acid while still retaining mechanical integrity. Additionally, at similar acid doping levels, membranes prepared by the PPA process consistently demonstrated higher

conductivities than membranes prepared by conventional imbibing (Fig. 10.15). Interestingly, the fundamental dependence of ionic conductivity and acid doping level was different for the membranes made by the two processes, pointing to potentially important contributions of the membrane morphology on proton mobilities.

10.5.6 Dihydroxy-PBI

Previous literature [24] on rigid-rod polymers containing nitrogen heterocycles reported strong hydrogen bonds with polymers containing hydroxyl groups. Yu et al. [25] investigated dihydroxy-PBI (2OH-PBI) prepared from 2,5-dihydroxyterephthalic acid and TAB. The chemical structure, membrane properties, and fuel cell performance were all evaluated. During polymerization, solutions were reportedly viscous for monomer charges of ~3 wt% which is lower than many other PBIs. It was also observed that 2OH-PBI powders would not fully dissolve in sulfuric acid for IV testing [25]. Small molecule studies were conducted which indicated that the high solution viscosity and insolubility in sulfuric acid resulted from intermolecular

Fig. 10.15 Ionic conductivities for heat-treated PA-doped meta-PBI at various acid doping levels (averages) conventionally imbibed membranes (*open triangles: 3, open square: 4, open circle: 5*) and sol-gel membranes (*filled triangle: 3, filled square: 5, filled circle: 6, filled sideways triangle: 8*) moles PA/mol of polymer repeat units. Reproduced from [13] with permission of John Wiley and Sons

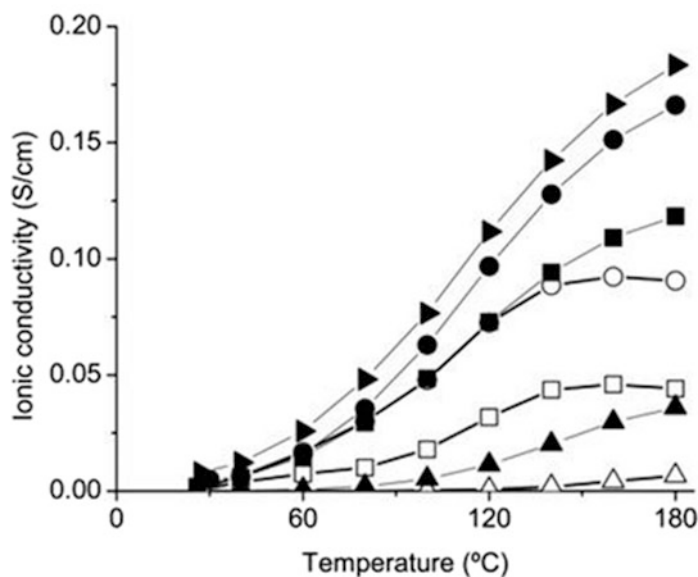
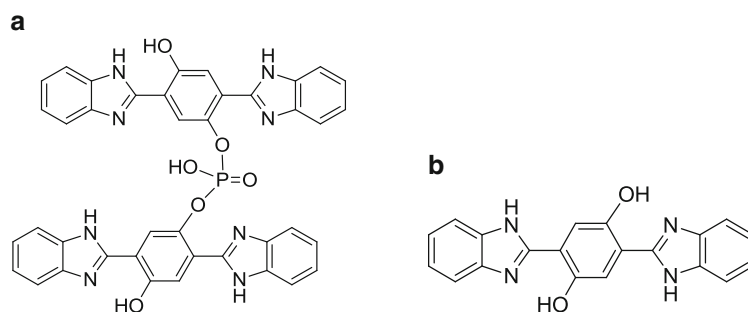


Fig. 10.16 (a) Phosphate bridge in small molecule 2OH-PBI study. (b) Model compound 2,5-bis(2-benzimidazolyl)hydroquinone. Reproduced from [25] with permission of the American Chemical Society



phosphate bridges as shown in Fig. 10.16a [26]. The model compound, 2,5-bis(2-benzimidazolyl)hydroquinone (Fig. 10.16b), was heated in PPA for 13 h and FTIR was used to confirm the formation of phosphate bridges.

Acid doping levels of the 2OH-PBI membranes were determined to be ~ 28 mol PA/PRU and the proton conductivity reached 0.43 S cm^{-1} at $180 \text{ }^\circ\text{C}$ which is even higher than that of para-PBI (0.35 S cm^{-1}) [25]. The 2OH-PBI membranes exhibited higher conductivities than para-PBI at all temperatures (Fig. 10.17) and also higher conductivities when the PA doping levels were adjusted to identical levels. Suarez et al. [27] conducted more detailed NMR experiments on 2OH-PBI membranes that showed lower proton diffusion

for the 2OH-PBI membranes, indicating that enhanced proton transport could be due to a Grotthuss or structural diffusion mechanism, with likely participation of the phosphate groups. Due to the high conductivity found in 2OH-PBI membranes, fuel cell testing was performed. Fuel cell testing using hydrogen ($\lambda = 1.2$)/air ($\lambda = 2.0$) at $160 \text{ }^\circ\text{C}$ produced a voltage of 0.642 V at 0.2 A cm^{-2} which was found to be very close to that of para-PBI when operated under the same conditions ($\sim 0.64 \text{ V}$), showing that while a good conductivity is important for fuel cell performance, other factors can effect cell performance [25]. When testing on Pt alloy cathode catalysts, the 2OH-PBI membranes showed improved performance, exhibiting 0.69 V at 0.2 A cm^{-2} .

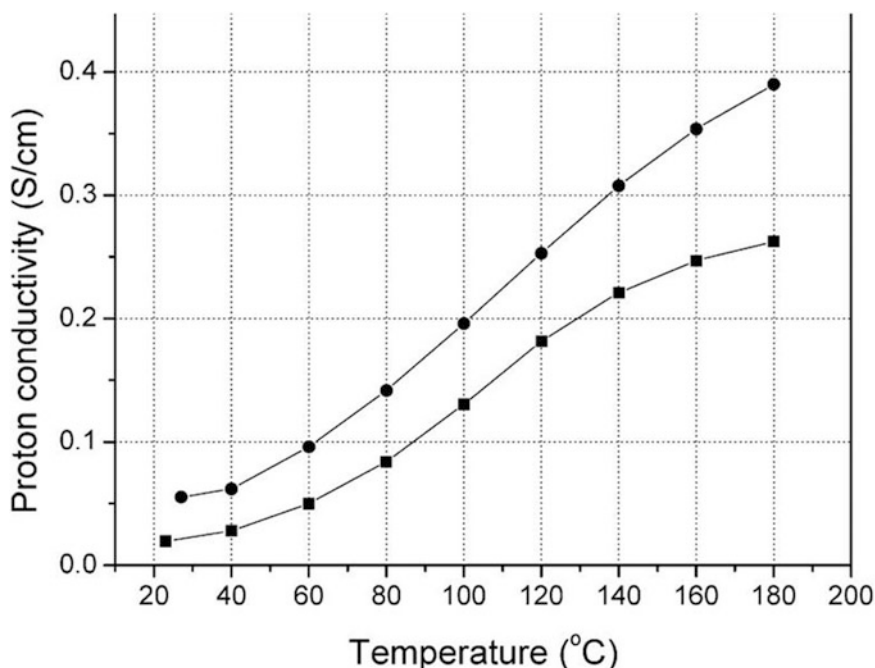


Fig. 10.17 Proton conductivities of phosphoric acid doped 2OH-PBI (circles) and para-PBI (squares) membranes. Reproduced from [25] with permission of the American Chemical Society

10.6 Copolymers Through the PPA Process

In the previous section, various homopolymer analogs of PBI prepared through the PPA process were reviewed to show the effects of chemical structure on membrane properties. The properties of various PBI derivatives are summarized in Table 10.3. Since it is commonly observed that copolymers can have characteristics of both their homopolymers, it is interesting to study the effects of copolymerization on PBI membrane properties. Countless random copolymers can be made through the PPA process by varying the combinations of diacids or tetramines. A few that have been previously studied through the PPA process are reported below.

10.6.1 Sulfonated Para-PBI

A random copolymer series of sulfonated and para-PBI was synthesized by Mader et al. [28]

by varying the ratios of 2-sulfoterephthalic acid and terephthalic acid for polymerization. Sulfo/para-PBI ratios of 75/25, 50/50, and 25/75 were compared to the homopolymers of sulfonated-PBI and para-PBI. Polymer IVs decreased with increasing sulfonated content of the copolymers. Conductivities of the random copolymers 75/25, 50/50, and 25/75 sulfonated-to-para all demonstrated high conductivities at 180 °C, 0.157 S cm⁻¹, 0.148 S cm⁻¹, and 0.291 S cm⁻¹, respectively [28]. The increase in conductivity with greater para-character was attributed to the greater acid loadings. Fuel cell performance was evaluated for all three variations and showed better performance with increasing amounts of para-character, however, all of the copolymers had lower fuel cell performance than the para homopolymer [28].

10.6.2 Segmented Block AB-Para-PBI

As previously mentioned, AB-PBI forms unstable gels when prepared by the PPA process due

Table 10.3 Properties of various chemistries of PBI prepared through the PPA process

PBI chemistry	Structure of polymer repeat unit	Monomer charges (wt %)		Inherent viscosity ranges (dL g ⁻¹)	Approximate membrane acid loading (mols PA/mol PRU)	Conductivity (S cm ⁻¹) at 180 °C	Ref.
		Tested via PPA process					
Meta-PBI		2-12		0.8-2.3	14-26	0.13	6
Para-PBI		1-5		0.3-2.9	30-40	0.25	15
Sulfonated-PBI		2.48-7.4		1.03-1.71	28-53	0.33	18
AB-PBI		N/A		≤10.0	22-35	N/A	19
<i>i</i> -AB-PBI		2.9-8.2		1.0-3.1	24-37	0.2	20

(continued)

Table 10.3 (continued)

PBI chemistry	Structure of polymer repeat unit	Monomer charges (wt %) Tested via PPA process	Inherent viscosity ranges (dL g ⁻¹)	Approximate membrane acid loading (mols PA/mol PRU)	Conductivity (S cm ⁻¹) at 180 °C		Ref.
2,5-pyridine PBI		4–18 ^a	0.8–3.1	15–25	0.22		22
3,5-pyridine PBI		4–20 ^a	0.6–3.1	N/A	N/A		22
2,6-pyridine PBI		~7 ^a	0.2–1.3	8–10	0.1		22
2,4-pyridine PBI		~7 ^a	0.3–1.00	N/A	N/A		22

N/A = film was too unstable to test

^aPolymer concentration

to its higher solubility than many other PBIs and the high PA content of the membranes produced by the PPA process. One way to stabilize membranes is copolymerization using another polymer system that exhibits lower solubility in PA. Yu et al. [19] attempted to improve the PA stability of AB-PBI membranes by preparing segmented block (sb) copolymers with para-PBI. This was done by setting up two separate pre-polymerizations, one for each homopolymer, and then combining them for the final polymerization step. Various mole ratios of para-PBI to AB-PBI were evaluated, i.e., 90/10, 75/25, 50/50, 25/75, and 10/90. Proton conductivities of all copolymers showed a similar proton conductivity to that of para-PBI ($\sim 0.25 \text{ S cm}^{-1}$) at 160°C with the exception of the 10/90 ratio (0.15 S cm^{-1}) [19]. This was attributed to its lower acid doping level ($\sim 17 \text{ mol PA/mol 2-benzimidazoles}$) than the other copolymer membranes ($\sim 19\text{--}24 \text{ mol PA/mol 2-benzimidazoles}$) [19]. Since the AB-PBI membrane is not stable when prepared through the PPA process, it cannot be used as a baseline for comparison, however, all of the copolymer membrane conductivities demonstrated greater acid doping levels and conductivities ~ 20 times higher than AB-PBI membranes prepared by the conventional imbibing method [19]. Polymers containing 90/10, 75/25, 50/50, and 25/75 para-to-AB compositions were evaluated in fuel cells. The 10/90 membrane was not durable at high temperatures and therefore not used in fuel cell testing. The 90/10, 75/25, and 50/50 membranes showed similar fuel cell performances while the 25/75 membrane showed lower fuel cell performance. This could be due to the lower conductivity and the lower gel stability at high temperatures from the higher AB content in the copolymer [19].

10.6.3 Dihydroxy Para-PBI

Along with the homopolymers of 2OH-PBI, Yu et al. [25] synthesized a copolymer series of 2OH-PBI with para-PBI. Compositions of 75/25, 50/50, and 25/75 2OH-to-para were all

made at $\sim 3 \text{ wt\%}$ monomer charges and compared to the respective homopolymers. Acid doping levels of the three copolymers were found to be approximately equivalent ($\sim 21\text{--}23 \text{ mol PA/PRU}$) and all were found to have similar conductivities at 160°C ($0.27\text{--}0.33 \text{ S cm}^{-1}$) [25]. No particular trend was detected in the room temperature mechanical properties, however, all compositions of the 2OH-para-PBI copolymer membranes showed they were sufficiently stable for MEA fabrication and fuel cell testing.

10.7 Membrane Electrode Assemblies and Fuel Cell Testing

Membrane electrode assemblies (MEA) were fabricated by hot-pressing a piece of PPA-processed PBI membrane between the two Pt/C electrodes, typically using 1 mg Pt cm^{-2} on each electrode. The electrodes for fuel cells based on PPA-processed PBI membranes are usually PTFE-bound electrodes. In the PTFE-bound electrode, the Pt/C catalyst particles are bound by a hydrophobic PTFE network, which is commonly cast onto the gas diffusion layer. The PTFE network provides the channel for gas transportation and water removal; the electrons are conducted through the carbon black network while proton transport is dependent on the phosphoric acid in the catalyst layer. The MEAs are assembled into a single-cell fuel cell testing hardware using graphite gas flow plates with serpentine gas channels. Stainless steel end plates with attached heaters were used to clamp the graphite flow plates. The fuel cell performance evaluations were usually performed at high temperatures (120°C up to 200°C), and gases were supplied to both electrodes without external humidification and under ambient pressure. These PPA-processed PBI membranes showed excellent high-temperature performance in fuel cells. The polarization curves of p-PBI membranes at various temperatures are shown in Fig. 10.4 with the comparison to conventionally imbibed membranes [15]. These membranes also showed exceptionally high tolerance to typical

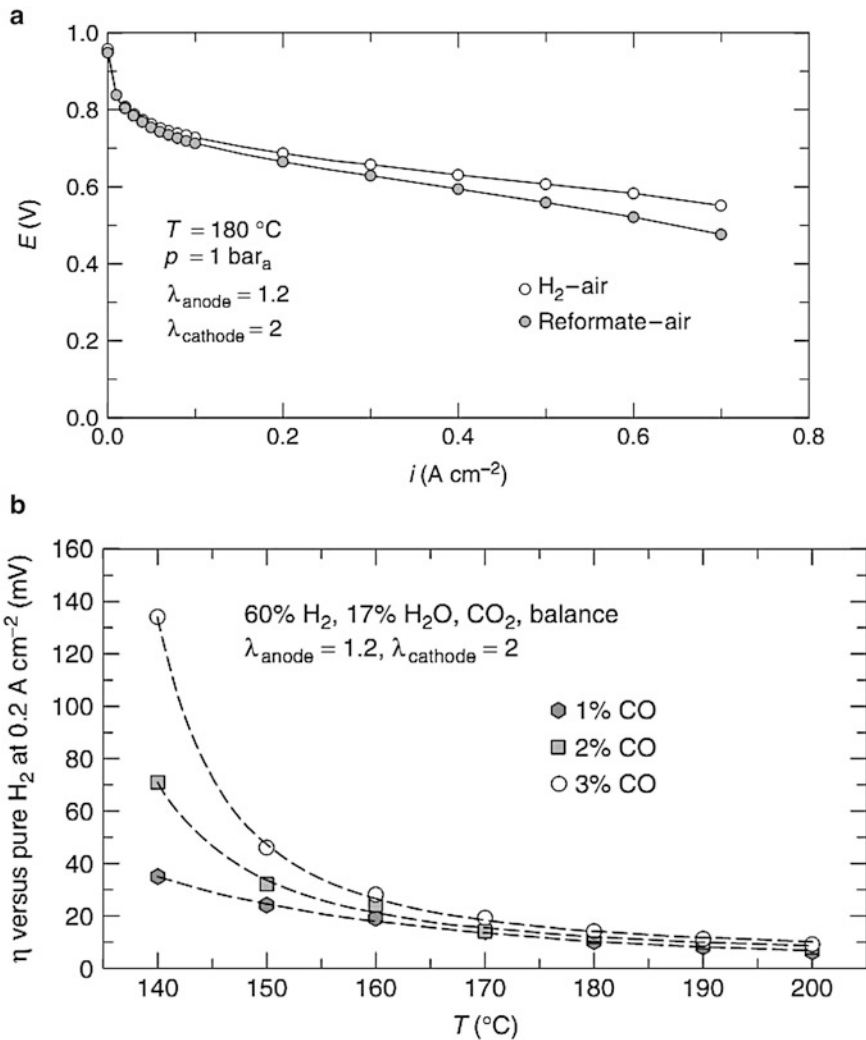


Fig. 10.18 Celtec-P1000 MEA performance and degradation (single-cell data, 50 cm^2 , 1.7 mg cm^{-2} total Pt loading). (a) H_2 -air and reformat-air polarization curves at $180\text{ }^\circ\text{C}$, 1 bar_a , stoichiometry 1.2/2, reformat composition 70 % H_2 , 2 % CO, balance CO_2 (nonhumidified gases). (b) anode overpotential versus pure hydrogen

operation as a function of temperature and CO partial pressure. Base reformat contains 60 % H_2 , 17 % H_2O , balance CO_2 and the CO concentration as shown in the figure. Anode stoichiometry 1.2, 1 bar_a (anode Pt loading is 1 mg cm^{-2}). Reproduced from [31] with permission of The Electrochemical Society

reformat impurities such as carbon monoxide (CO) and hydrogen sulfide (H_2S) in fuel cell performance tests. Schmidt et al. [29] reported the CO tolerance and fuel cell performances of Celtec-P 1000 (p-PBI membrane prepared by the PPA process) with up to 3 % CO in the fuel stream feed. These studies examined the anode overpotentials resulting from different CO containing steam reformates (reformat composition was 60 % H_2 , 17 % H_2O , 1–3 % CO,

balance CO_2) versus the same reformat without CO contamination at various operational temperatures. At a typical operational temperature range of 170 – $180\text{ }^\circ\text{C}$, only very small overpotential changes were observed when the CO partial pressure was changed. This can be seen in Fig. 10.18. Qian et al. [30] also reported that the fuel cell performance at $180\text{ }^\circ\text{C}$ was mainly related to the hydrogen gas content, and was less dependent on the CO content in the feed

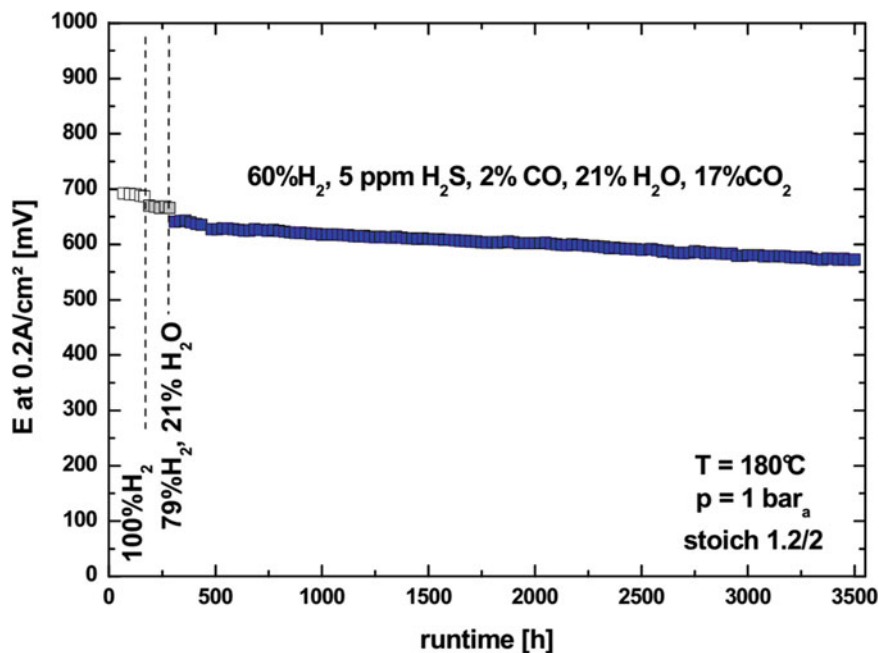


Fig. 10.19 Durability of a Celtec[®]-P Series 1000 MEA at 180 °C, 1 bar using realistic reformat as denoted. Reproduced from [31] with permission of The Electrochemical Society

gases. The hydrogen dilution effect was the main factor affecting fuel cell performance, and CO poisoning showed smaller effects on fuel cell performance compared to hydrogen dilution at 160 or 180 °C. As the operational temperature of the fuel cell decreased, the sensitivity to the presence of CO dramatically increased. CO poisoning became the dominant factor for fuel cell performance decreases at 140 °C. At 120 °C, the fuel cell voltage quickly dropped to 0 V when the feed gases changed from pure hydrogen to reformat with CO content at 2000 ppm or higher. However, this decrease in fuel cell performance was reversible and the fuel cell performance immediately recovered when the feed gas was changed back to pure hydrogen.

The exceptionally high hydrogen sulfide tolerance of PPA-processed membranes was also demonstrated. Celtec-P 1000 testing at 180 °C using humidified reformat with 2 % CO and 5 ppm H₂S showed an average voltage drop of approximately 17 μV h⁻¹ during a 3500 h test, demonstrating high tolerance to sulfur impurities and no additional anode degradation compared to

pure reactants at 180 °C [31]. This durability can be seen in Fig. 10.19. Qian et al. [30] reported the nearly full recovery of fuel cell performance after 24 h operation with 25 ppm H₂S in the anode gas at the temperature range of 120–180 °C.

The long-term durability of PPA-processed membranes is an important and commercially relevant issue. The constant current operation at 0.2 A cm⁻², 160 °C using dry hydrogen and air is shown in Fig. 10.20 [29]. The performance degradation rate under these conditions was -6 μV h⁻¹ over more than a 2-year period. The low fuel cell performance degradation rates were also observed in a cell operated with constant current at 0.4 A cm⁻². Aili et al. [32] reported that the long-term durability of conventionally imbibed PBI membranes is highly dependent on the current loads. The fuel cell performance degradation rates were 6 μV h⁻¹ and 308 μV h⁻¹ at current densities of 0.2 and 0.6 A cm⁻², respectively. The PPA-processed PBI membranes demonstrated a much lower performance degradation rate at high current operation, 18 μV h⁻¹ at 0.6 A cm⁻². Yu et al. [17] reported the

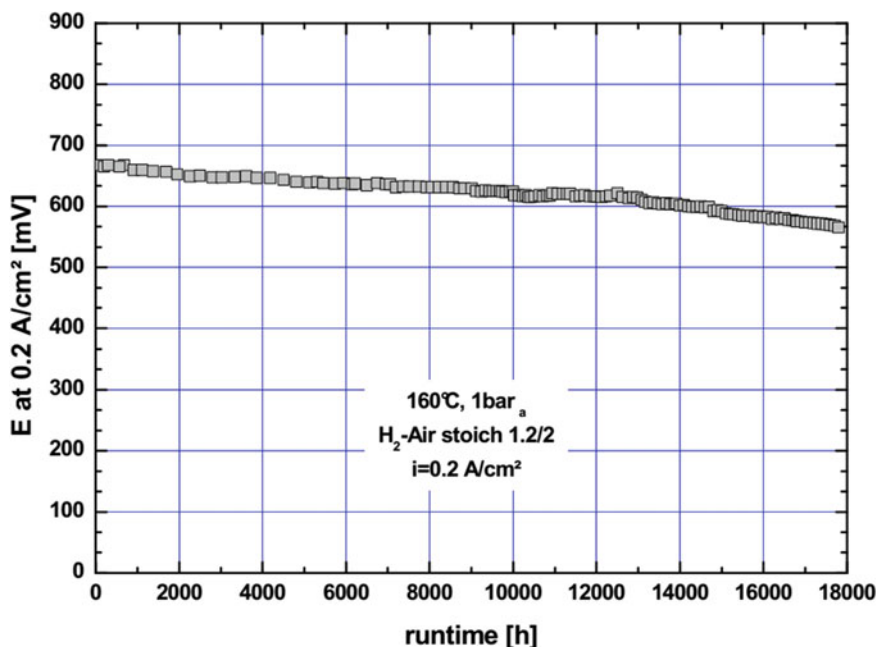


Fig. 10.20 Durability of a Celtec-P-1000 MEA at 160 °C, 1 bara using pure hydrogen and air with stoichiometries of 1.2 and 2, respectively. Reproduced from [31] with permission of The Electrochemical Society

phosphoric acid evaporative loss through the gas exhaust was extremely low. Qian et al. [33] analyzed the phosphoric acid loss from the MEA at the different stages of cell assembly, initial heat-up, and cell operation. The phosphoric acid evaporative loss was not the main pathway of phosphoric acid loss from the MEAs, and a significant amount of phosphoric acid was found in the micropores of the graphite flow plates, which illustrates that the stability of the materials employed as bipolar plates is a key property for long-term operation and durability of PPA-processed membranes in high-temperature PEM fuel cell applications [33, 34].

10.8 Conclusions

The PPA process is a simple, straightforward method for directly preparing high molecular weight polymers and PA-doped PBI membranes with relatively few process steps. There are many

advantages of the process that are commercially attractive and early work has shown that the process can be scaled up to reliably produce high-quality membranes. The PPA process also allows for the investigation of different monomers and polymers, which has formed the basis for understanding structure–property relationships. Modeling and simulation studies have provided interesting insights and promise to provide an even more thorough understanding of the process and structure. Many PBI chemistries have shown high performance in operating fuel cells and can be reliably operated for extended periods of time. More detailed studies have shown that the evaporative PA loss from the membranes is typically low, with the data suggesting that extrapolated lifetimes should be many years and other degradation modes may eventually be the limiting factors. Continued development of membranes produced by this process is still being pursued with a focus on addressing the issues of longer term durability and possible failure modes, new devices, and improved manufacturability.

Acknowledgment The authors would like to thank BASF, DOE, and NSF for support in many aspects of the work conducted at Rensselaer Polytechnic Institute and the University of South Carolina.

References

1. Popp F, McEwen W (1959) Polyphosphoric acid as a reagent in organic chemistry. *Chem Rev* 58:321–401
2. Yang H (1989) Aromatic high-strength fibers. Wiley, New York
3. Cassidy P (1980) Thermally stable polymers. Marcel Dekker, New York
4. Conciatori A, Buckley A, Stuetz D (1985) Polybenzimidazole fibers. High technology fibers part A, Handbook of fiber science and technology. Marcel Dekker, New York
5. Molle M, Schmidt T, Benicewicz B (2012) Polybenzimidazole fuel cell technology: theory, performance, and applications. Encyclopedia of sustainability, science and technology. Springer, New York, pp 391–431
6. Mader J, Xiao L, Schmidt T et al (2008) Polybenzimidazole/acid complexes as high-temperature membranes. In: Scherer G (ed) Fuel cells II, vol 216, Advances in polymer science. Springer, Berlin, pp 63–124
7. Li Q, Jensen JO, Savinell R et al (2009) High temperature proton exchange membranes based on polybenzimidazoles for fuel cells. *Prog Polym Sci* 34:449–477
8. Xiao L, Zhang H, Scanlon E et al (2005) High-temperature polybenzimidazole fuel cell membranes via a sol-gel process. *Chem Mater* 17:5328–5333
9. Padmanabhan V, Kumar S, Yethiraj A (2008) Phase behavior of semiflexible polymer chains. *J Chem Phys* 128: 124908(1–4)
10. Padmanabhan V, Kumar S (2011) Gelation in semiflexible polymers. *J Chem Phys* 134: 174902(1–7)
11. Savinell R, Litt M (2000) Proton conducting polymer electrolyte prepared by direct acid casting. US Patent 6,099,988
12. Ma Y, Wainright J, Litt M et al (2004) Conductivity of PBI membranes for high-temperature polymer electrolyte fuel cells. *J Electrochem Soc* 151: A8–A16
13. Perry K, More K, Payzant A et al (2014) A comparative study of phosphoric acid-doped m-PBI membranes. *J Polym Sci Part B* 52:26–35
14. Vogel H, Marvel C (1961) Polybenzimidazoles, new thermally stable polymers. *J Polym Sci* 50:511–539
15. Yu S, Zhang H, Xiao L et al (2009) Synthesis of poly (2,2'-(1,4-phenylene) 5,5'-bibenzimidazole) (para-PBI) and phosphoric acid doped membrane for fuel cells. *Fuel Cells* 9:318–324
16. Delano C, Doyle R, Milligan R (1974) High strength thermally stable polymeric fibers. United States Air Force Materials Laboratory Technical Report AFML-TR-74-22
17. Yu S, Xiao L, Benicewicz B (2008) Durability studies of PBI-based high temperature PEMFCs. *Fuel Cells* 8:165–174
18. Mader J, Benicewicz B (2010) Sulfonated polybenzimidazoles for high temperature PEM fuel cells. *Macromolecules* 43:6706–6715
19. Yu S (2006) Novel polybenzimidazole derivatives for high temperature PEM fuel cells. Ph.D. thesis, Rensselaer Polytechnic Institute
20. Gulledge A, Gu B, Benicewicz B (2012) A new sequence isomer of AB-polybenzimidazole for high-temperature PEM fuel cells. *J Polym Sci Part A* 50:306–313
21. Asensio J, Gómez-Romero P (2005) Recent developments on proton conducting poly (2,5-benzimidazole) (AB-PBI) membranes for high temperature polymer electrolyte membrane fuel cells. *Fuel Cells* 5:336–343
22. Xiao L, Zhang H, Jana T et al (2005) Synthesis and characterization of pyridine-based polybenzimidazoles for high temperature polymer electrolyte membrane fuel cell applications. *Fuel Cells* 5:287–295
23. Wainright J, Wang J, Weng D et al (1995) Acid-doped polybenzimidazoles: a new polymer electrolyte. *J Electrochem Soc* 142:L121–L123
24. Tan L, Arnold F, Dang T et al (1994) Pseudo-ladder rigid-rod polymers: dihydroxy pendant benzothiazole aromatic heterocyclic polymer and copolymers. *Polymer* 35:3091–3101
25. Yu S, Benicewicz B (2009) Synthesis and properties of functionalized polybenzimidazoles for high-temperature PEMFCs. *Macromolecules* 42:8640–8648
26. Kosolapoff G (1950) Organophosphorous compounds. Wiley, New York
27. Suarez S, Kodiweera N, Stallworth P et al (2012) Multinuclear NMR study of the effect of acid concentration on ion transport in phosphoric acid doped poly (benzimidazole) membranes. *J Phys Chem B* 116:12545–12551
28. Mader J (2010) Novel sulfonated polybenzimidazole derivatives for high temperature fuel cell applications. Ph.D. thesis, Rensselaer Polytechnic Institute
29. Schmidt T (2006) Durability and degradation in high-temperature polymer electrolyte fuel cells. *ECS Trans* 1:19–31
30. Qian G, Benicewicz B (2011) Fuel impurity effects on high temperature PBI based fuel cell membranes. *ECS Trans* 41:1441–1448

31. Schmidt T, Baurmeister J (2006) Durability and reliability in high-temperature reformed hydrogen PEFCs. *ECS Trans* 3:861–869
32. Aili D, Cleemann L, Li Q et al (2012) Thermal curing of PBI membranes for high temperature PEM fuel cells. *J Mater Chem* 22:5444–5453
33. Qian G, Benicewicz B (2008) Phosphoric acid movement in phosphoric acid doped polydibenzimidazole membrane-electrode assemblies. *Prepr Symp—Am Chem Soc, Div Fuel Chem* 53:540–542
34. Hartnig C, Schmidt T (2011) On a new degradation mode for high-temperature polymer electrolyte fuel cells: how bipolar plate degradation affects cell performance. *Electrochim Acta* 56:4237–4242

Simone Angioni, Davide Carlo Villa, Piercarlo Mustarelli, and Eliana Quartarone

11.1 The Leaching of Free Phosphoric Acid and Membrane Permanent Proton Conductivity

Nowadays the worldwide fuel cell programs point towards a widespread commercialization of such devices for a huge spectrum of applications, from the transport to the stationary and auxiliary power units (APUs). Among them, PEMFCs seem to have some promising potentiality [1]. In this field, the US Department of Energy has defined three specific technical challenges: (a) materials cost, (b) cell durability and (c) balance of plant, which may be tackled by means of the development of new and more performing materials. The current PEMFC technology deals with two types of systems, low-temperature (LT) and high temperature (HT) ones, which differ for operating temperatures, type of electrolytes and electrocatalyst loadings [1, 2]. HT-polymer fuel cells exhibit several advantages in terms of higher tolerance to poisons (e.g. CO) and absence of water management [3, 4]. From this point of view, acid-doped polybenzimidazoles (PBI) membranes are likely the best candidate as

electrolyte for HT-PEMFCs due to a number of positive aspects including excellent thermal stability, low gas permeability and good proton transport above 150 °C even at low humidification conditions [5–7].

Basically, PBI-based membranes show high proton conductivities when properly doped with strong acids such as H₃PO₄ (PA) [5, 8]. PBI is, in fact, a basic polymer, which chemically dissociates the PA with an equilibrium constant has been calculated to be 1.17×10^3 [9].

H⁺ ions can migrate through the polymer backbone and phosphate anions by means of hydrogen bonds. The most investigated polymer is poly [(2,2'-(*m*-phenylene)-5,5'-(bibenzimidazole))], as shown in Scheme 11.1 and referred to as PBI_4N in the present chapter, as it contains four basic nitrogen atoms.

By immersing a PBI membrane in aqueous solutions of phosphoric acid, the system may absorb a specific amount of dopant, which is defined by the acid doping level, ADL, as the ratio between the number of PA molecules n_{PA} per polymer repeat unit (PRU) according to (11.1).

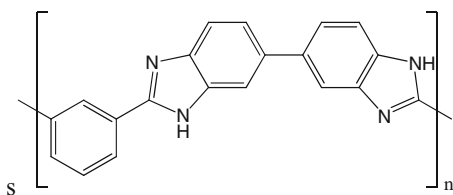
$$ADL = n_{PA}/PRU \quad (11.1)$$

Typically, an ADL of about 6 is obtained by immersing a thin PBI membrane in a 75 wt% acid solution [5, 8]. Several spectroscopic and thermogravimetric studies suggested that the maximum degree of protonation in case of

S. Angioni • D.C. Villa • P. Mustarelli
E. Quartarone (✉)
Department of Chemistry and INSTM, University
of Pavia, Via Taramelli 16, Pavia 27100, Italy
e-mail: eliana.quartarone@unipv.it

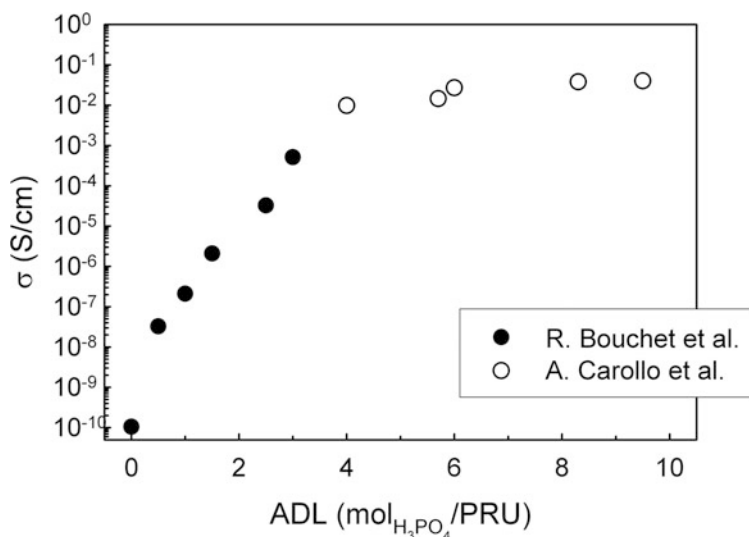
PBI_4N system is reached for $ADL = 2$, which corresponds to the number of basic sites in the unit structure [10, 11]. This means that two acid molecules are bonded to the backbone and the excess of PA is distributed in the free form inside the membrane.

Indeed, the proton conductivity of PA-doped PBIs is strictly related to the acid doping level. Generally speaking, conductivity values exceeding 0.1 S cm^{-1} are easily obtained above $150 \text{ }^\circ\text{C}$ at high ADLs (at least >6). Contrary to Nafion[®] membranes, where conduction occurs via the vehicular mechanism assisted by water molecules [12], in case of the PA-PBI membrane the proton transport does not need humidification and it is governed mainly by the Grotthuss mechanism through two pathways, which depend on the amount of doping acid in the membrane [9, 13]. Figure 11.1 shows, as an example, the conductivity behaviour vs. the acid doping level



Scheme 11.1 Chemical structure of poly[(2,2'-(*m*-phenylene)-5,5'-(bibenzimidazole))] (PBI_4N)

Fig. 11.1 Membrane proton conductivity at $80 \text{ }^\circ\text{C}$ and $50 \text{ } \%$ RH vs. the acid doping level before acid leaching. *Filled circles*: Data compiled from [10] (*solid circles*) and [16] (*open circles*). Reproduced from [14] with permission of Elsevier



at $80 \text{ }^\circ\text{C}$ and $50 \text{ } \%$ RH for PA-PBI_4N-based membranes. At low ADLs (up to 2), as a consequence of the polymer protonation, the conduction occurs via the H^+ hopping between the N–H site and the phosphate anions. In this region, the acid is bonded to the polymer and the conductivity is low. By increasing the acid amount, the conductivity also increases. At high doping level ($ADL > 4$), due to the presence of free acid in the membrane, the proton migration takes place along the acid and anion ($\text{H}_2\text{PO}_4^- \cdots \text{H} \cdots \text{H}_2\text{PO}_4^-$) or acid and water ($\text{H}_2\text{PO}_4^- \cdots \text{H} \cdots \text{H}_2\text{O}$) chains, depending on the water uptake. In this case, the systems behave like concentrated H_3PO_4 solutions [10, 14].

In spite of the interesting benefits shown by PBI-based membranes in terms of proton transport, some important questions are still open and further improvements are desirable. As already stressed and shown by the figure, the conductivity is significant only at high doping levels and in particular in the presence of free acid. Unfortunately, too large acid amounts lead to issues severely limiting the cell durability due to the leaching out of PA, which causes dramatic drops in conductivity and membrane degradation.

In recent years, our research group tried to achieve a proper compromise between H_3PO_4 doping level and membrane stability. Our strategy

pointed towards the enhancement of the remaining proton conductivity of the PBI-based membranes after a forced leaching process in order to control and limit the drops of functional performances [15]. In the following, this remaining conductivity is sometime termed as permanent conductivity. To this aim, we proceeded through three main approaches, all of them exploiting the rich chemistry of the benzimidazole group: (a) to increase the basicity of the polymer and consequently the acid retention capacity by structural modulation of the polymer chain, introducing additional nitrogen-based units [15–18], (b) to enhance the membrane proton transport at low doping levels by properly anchoring further active units for the proton migration, namely PBI sulfonation [19–22], (c) to use of inorganic fillers, nanometric and/or mesoporous, with proper functionalization [23–28].

The permanent proton conductivity of the PA-PBI-based membranes was investigated on membranes subjected to accelerated leaching in order to completely remove the fraction of the free acid. Such tests were carried out by means of washing steps of the doped membranes in water–methanol mixtures at 80 °C for several days. Quantitative determinations of H_3PO_4 released in the water baths were carried out by inductively coupled plasma (ICP) analyses and/or proper titration procedures.

This chapter will describe in detail the results in terms of leaching control and improvement of the membrane stability, which were recently obtained in our lab, by following the approaches (a) and (c) indicated above.

11.2 Novel Benzimidazole Monomers with Additional Basic Heterocycles

Polybenzimidazoles are heterocyclic, thermo-plastic and basic polymers characterized by at least one aromatic unit, which confers high mechanical and thermal stability ($T_g > 400$ °C). As already introduced, the most investigated basic unit of this class of polymers is poly [2,2'-(*m*-phenylene)-5,5'-bibenzimidazole]

(*m*PBI or PBI_4N as referred to in this chapter, Scheme 11.1). This macromolecule was synthesized for the first time in 1961 by Vogel and Marvel [29]. Basically, the synthetic procedure is based on the thermal poly-condensation in the temperature range 180–200 °C of an amino-group, namely diaminobenzidine and carboxylic units, e.g. isophthalic acid, using polyphosphoric acid (PPA) as the polymerization agent.

The PBI syntheses are quite simple to perform, and polymers with high polymerization degrees may be achieved. As already deeply discussed in another chapter, the weight average molecular weight of the PBI-based polymers is commonly obtained by means of intrinsic viscosity measurements, performed on polymer solutions in sulfuric acid, through the Mark-Houwink-Sakurada equation (11.2), where M_w is the average molecular weight of the polymer and K' and a are the Mark-Houwink phenomenological constants, whose values for PBI are equal to 1.94×10^{-4} and 0.791, respectively [17 and reference herein cited].

$$\eta_{IV} = K'(M_w)^a \quad (11.2)$$

The M_w is related to the polymerization degree, DP, by the expression $DP = M_w/M_{PRU}$, where M_{PRU} is the molar mass of the PRU. For a rough estimate of the molecular weight for other polymers of the PBI family, it is assumed that the K and α values are the same. In order to avoid insoluble residues, polymers with the intrinsic viscosity ranging between 0.5 and 1 dL g⁻¹ are usually synthesized, which corresponds to an average M_w of 23,000–40,000 g mol⁻¹. However, for use as electrolyte for polymer fuel cells, PBIs with higher molecular weights are preferred in order to obtain membranes with good free-standing properties and satisfying mechanical performances.

In addition to the standard poly-condensation in PPA, other synthesis methods were proposed in literature, e.g. by using novel preparation media containing methane-sulfonic acid and P₂O₅ [5, 6, 8]. Recently, in our laboratory, we synthesized a series of PBIs via a

microwave-assisted organic synthesis (MAOS) approach [21, 22]. MAOS is an innovative strategy to produce, in shorter times, polymers with similar or even higher inherent viscosity, and with larger yields with respect of the standard thermal methods. In the case of 2,5-polybenzimidazole (ABPBI), for instance, the thermal poly-condensation gives polymers with intrinsic viscosities higher than 3 dL g^{-1} after 5 h of reaction. In contrast, similar polymerization degrees can be obtained in only 45 min by MAOS. Even better results were reached for PBI_4N, which display a slower polymerization kinetics than ABPBI. In this case, MAOS produces polymers with longer chains ($\eta_{IV} = 0.68 \text{ dL g}^{-1}$) in 2 h than those ones obtained after 5 h of thermal polymerization ($\eta_{IV} = 0.42 \text{ dL g}^{-1}$).

Benzimidazole-based molecules show a good reactivity and a consequent wide chemistry. This is a striking advantage from a chemical point of view. In fact, by changing the chemical nature of the starting monomers, it is relatively easy to modify the polymer backbone in order to modulate its physico-chemical properties, including thermo-oxidative stability, mechanical performances, methanol permeability, polymer solubility and film processing. To this aim, several new systems were recently proposed including functional groups based on ketone, ether, sulfone and fluoroalkyl units [5–8]. PBIs were also cross-linked in order to improve the final mechanical strength of the acid-doped membranes. Several types of cross-linking processes have been tested including covalent, ionic and mixed ionic-covalent. However, if the membrane toughness increases, the polymer solubility in the casting conventional solvents decreases as well [6].

By taking into account such a chemical richness, in the recent years, we synthesized polybenzimidazoles with a properly tailored basicity, simply by playing with the number of the nitrogen atoms in the monomer and their distribution along the polymer backbone. Our basic aim was to reduce the acid leaching, to favour the proton transport and, finally, to enhance the permanent conductivity by increasing the acid–base interactions between the

polymer and the doping acid [14–18]. Table 11.1 reports a series of new polymers developed in our lab and tested as proton exchange membranes for polymer fuel cells.

In this series, the number of nitrogen atoms and their interspacing along the polymer backbone were modulated by using different monomers, including pyridine-, bi-pyridine, and pyrazole units. First of all, both the chemical nature of the monomer and its basicity remarkably affect the polymerization yields and the polymer average molecular weight. Table 11.1 shows the intrinsic viscosity and the polymerization degree of the polymers. Similar reaction times and temperature were chosen for all the investigated polymers. From the analysis of the data reported in the Table, some important points may be stressed. First, the obtained intrinsic viscosities exceed 0.5 dL g^{-1} and these high values allow to prepare films with satisfying hardness and processability. In addition, the increase of the monomer molecular weight reduces the poly-condensation kinetics. Finally, the enhanced basicity provided by the presence of extra N-atoms in the PBI backbone (see, for example, PBI_5N) determines an increase of the *DP* value for equal condensation times, probably because of the improved monomer solubility in PPA [15–18].

All these aspects will also influence the phosphoric acid uptake and leaching, as well as proton transport. As previously stressed, one of the major drawbacks of PBI membranes is related to the leaching of the free phosphoric acid during the fuel cell operation. Table 11.2 reports the H_3PO_4 doping level of the PBI-based membranes before and after the leaching test, performed as described in the previous section [17]. In case of the as-doped films, the presence of additional basic *N*-units in the standard PBI (PBI_4N) backbone remarkably enhances the acid uptake. Each system, in fact, shows as-doped ADLs, $\text{ADL}_{a.d.}$, higher than that determined for PBI_4N. In particular, the highest acid affinity is provided by the PBI_5N_2,6 membrane, where an $\text{ADL}_{a.d.}$ value of 9.5 was reached. During the elution test in water/methanol, the free acid is released out of the electrolyte. Again, the acid retention

Table 11.1 Chemical structure and polymerization results for some novel PBI-based polymers

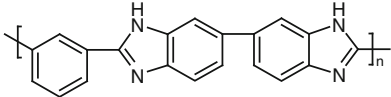
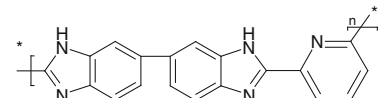
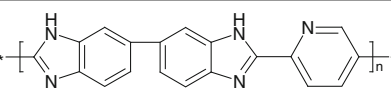
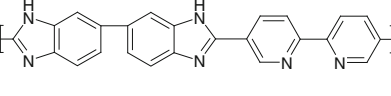
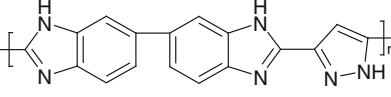
Polymer	η_{iv} (dL g ⁻¹)	M_{PRU}	DP	M_w	Casting
PBI_4N 	0.7	308	98	30,352	Free standing
PBI_5N_2,6 	1.7	309	300	92,840	Free standing
PBI_5N_2,5 	0.5	309	64	19,864	Free standing
PBI_6N_bipy 	1.0	386	123	47,574	Free standing
PBI_6N_pyra 	n.a.	298	n.a.	n.a.	Free standing

Table 11.2 Doping levels of the investigated membranes before and after the forced acid leaching tests

Polymer	$ADL_{a.d.}$	ADL_r	$E_{a, a.d.}$ (eV)	$E_{a, r}$ (eV)
PBI_4N	4.0	2.0	0.27	0.30
PBI_5N_2,6	9.5	4.5	0.25	0.29
PBI_5N_2,5	6.0	2.2	0.31	0.42
PBI_6N-bipy	5.7	2.6	0.31	0.33
PBI_6N_pyra	8.0	3.0	0.38	0.45

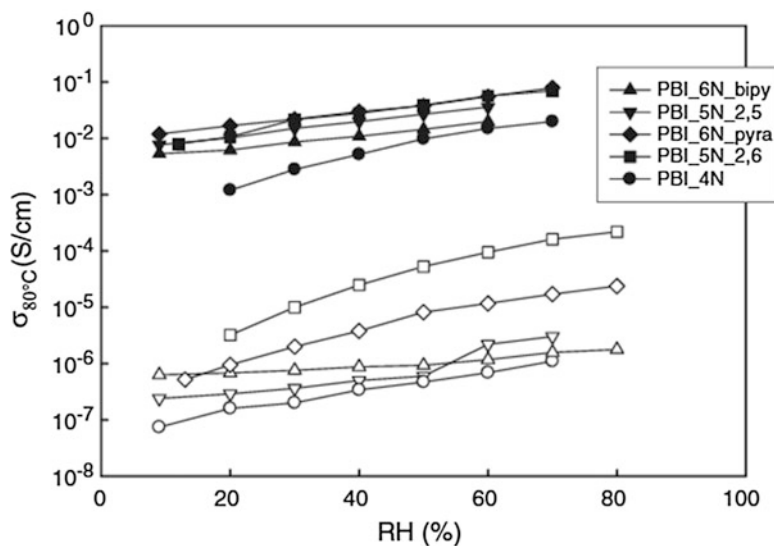
The $E_{a,s}$ are the corresponding activation energies calculated from the conductivity measurements [17]

capability depends on the chemical structure of the pristine polymer. In case of the films based on PBI with pyridine and bi-pyridine units in *para*-configuration (PBI_5N_2,5 and PBI_6N_bipy), as well as in the case of the PBI_4N sample, two molecules of H₃PO₄ per PRU remain in the membrane. This residual acid doping level value, ADL_r , corresponds to the maximum protonation degree of the standard polybenzimidazole, which is commonly reported in literature [5]. In contrast, promising results are obtained in the case of PBI_5N_2,6 and PBI_6N_pyra, where the residual doping levels are 4.5 and 3.0, respectively.

As expected, the loss of the free PA causes dramatic drops of conductivity, which is an issue for the long-term fuel cell performances. Figure 11.2 reports the behaviour of the proton conductivity vs. the relative humidity at 80 °C for the polymers reported in Table 11.2, both as prepared (filled symbols), and after the acid leaching (open symbols).

Concerning the as-doped membranes, the addition of nitrogen atoms with respect to the commercial PBI_4N leads to an increase of the conductivity at 80 °C by a factor of up to 10. In addition, the conductivity is less dependent on

Fig. 11.2 Proton conductivity at 80 °C vs. relative humidity (RH) for the polymer reported in Table 11.2, both as doped (*filled symbols*) and after the leaching tests (*open symbols*). The lines are only guides for the eye. Reproduced from [14] with permission of Elsevier



the relative humidity, and values in excess of $10^{-2} \text{ S cm}^{-1}$ can be obtained even at low humidity conditions (RH = 8–10 %). In terms of proton transport, the membranes based on PBI with five nitrogen atoms and the PBI_6N_pyra do offer the best performances.

As a consequence of the forced leaching, the loss of phosphoric acid leads to a conductivity drop of several orders-of-magnitude, depending both on the starting monomer and the relative humidity. For example, the conductivity of PBI_4N at 50 % RH decreases by about four orders-of-magnitude, from $9.8 \times 10^{-3} \text{ S cm}^{-1}$ to $4.7 \times 10^{-7} \text{ S cm}^{-1}$. In contrast, better results in terms of permanent conductivity after leaching are observed for the PBI_5N_2,6-based membrane that reaches $5.3 \times 10^{-5} \text{ S cm}^{-1}$ at 50 % RH and 80 °C, which is almost one order-of-magnitude better than the value measured for the PBI_6N_pyra sample. At the same time, the PBI_5N_2,5 membrane behaves much worse than the other ones. While one could expect that the residual doping would display a simple correlation between the number of nitrogen atoms in the PRUs, which can interact with the PA molecules and the protonation degree, our results clearly show that the situation is not so trivial. As a matter of fact, the acid retention capability as well as the permanent conductivity

is a complex function of important factors such as, for instance, the interspacing of N–N and P–P distance of the acid molecules along the polymer backbone.

From the point of view of the absolute values, on the other hand, it is noteworthy to consider that PBI_5N_2,6 displays a permanent conductivity two orders-of-magnitude higher than that of PBI_4N, which is indeed an impressive result. Figure 11.3 shows the conductivity values at 20 and 50 % RH vs. the acid doping level for both the as prepared and the washed membranes. The samples can be identified by referring to the ADL values listed in Table 11.2. A stepwise increase of the conductivity is observed in the region ADL = 4–5. However, it should be pointed out that PBI_4N as prepared has an ADL of 4 while PBI_5N_2,6 has an ADL of 9.5. This means that the free acid is much more effective than the bonded ones in determining the actual conductivity levels of the membranes.

Additional information on the transport mechanisms can be obtained by considering the activation energies for the conductivity. The values of the as prepared membranes fall in the range 0.25–0.38 eV (see Table 11.2). Following the PA loss, the activation energy values increase by ~10 % to ~40 % depending on the membrane, however the final values still belong to the range

Fig. 11.3 Conductivity at 80 °C vs. the doping level, ADL, for the washed membranes, reported in Table 11.2, at 20 % RH (*open squares*) and 50 % RH (*open circles*). The open symbols are referred, in particular, to the as-doped PBI_4N membranes. The lines are guides for the eye. Reproduced from [14] with permission from Elsevier

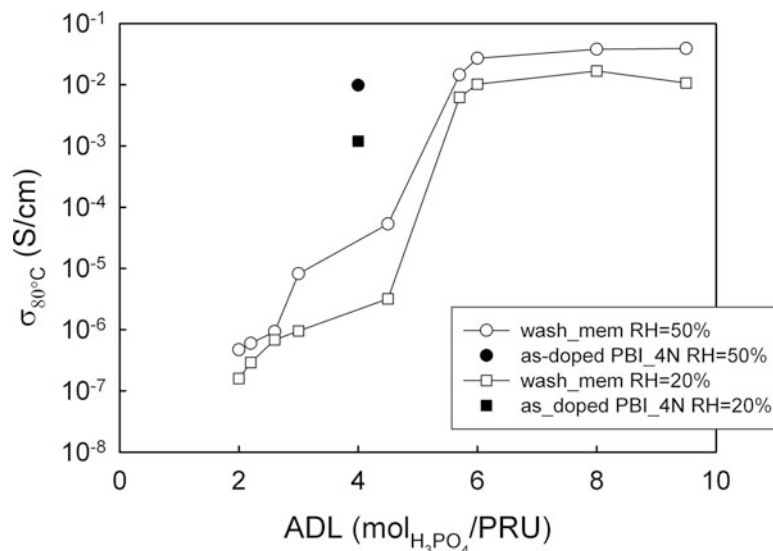
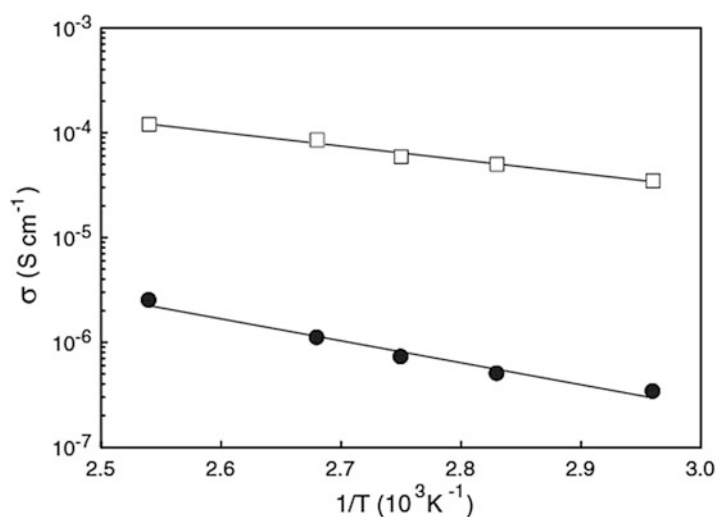


Fig. 11.4 Arrhenius plots of the proton conductivity for PBI_4N (*filled*) and PBI_5N_2,6 (*open*) after the leaching test at 50 % RH. The lines are linear regression fits. Reproduced from [14] with permission of Elsevier



0.29–0.45 eV, which likely means that the transport mechanism is substantially left unchanged by the primary hopping mechanism [14].

Figure 11.4 compares the Arrhenius behaviours of PBI_4N and PBI_5N_2,6 after the PA leaching. The difference of two orders-of-magnitude found at 80 °C is maintained all over the explored temperature range, and values in excess of 10⁻⁴ S cm⁻¹ are obtained at 50 % RH and 120 °C.

The more controlled leaching observed in the case of membranes based on PBI_5N_2,6 has

been further confirmed by means of functional tests on MEAs prepared by using commercially available GDEs (HT-Elak ETEK) with a Pt loading of 0.5 mg cm⁻². Figure 11.5 shows a typical polarization curve (a) and a durability test at 0.2 A cm⁻² (b) obtained for PBI_5N_2,6 at 150 °C in the absence of humidification. An OCV of 0.9 V and a peak of power density of 310 mW cm⁻² were measured respectively, the latter depending on the air stoichiometry and cell backpressure, as recently reported [19]. Proper durability tests showed an electrochemical

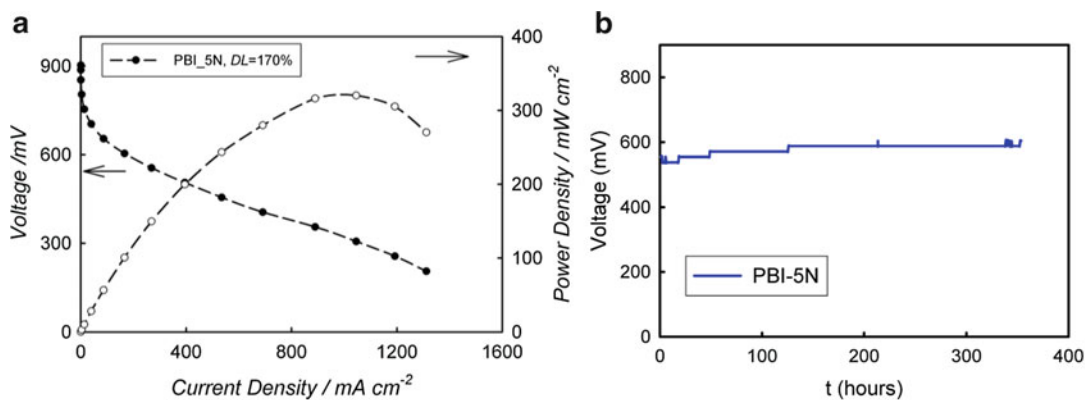


Fig. 11.5 *I/V* curves at 150 °C and low humidification for MEA based on PBI_5N_2,6 (ADL = 6) (a), and the performance of the same cell at 0.2 A cm⁻² vs. the testing time (b)

performance of about 0.6 V during a testing period of about 400 h without any detectable cell degradation or loss of doping acid.

Relevant PA leaching values may be, in contrast, found in literature, in particular at high temperature and electric load, which were explained by an evaporation mechanism in the steam containing atmosphere [30].

Our studies show how it is possible to control the leaching of free phosphoric in PBI-based systems by tailoring up appropriate benzimidazoles, whose monomer basicity and dimension, as well as active site (N–N and P–P) interspacing, are properly modulated. More generally, the chemical strategy of the design of new materials by means of the introduction of suitable functionalities seems to offer promising opportunities leading to more performing cells, in terms of long-term durability.

11.3 Silica with Basic Functionalities as Active Fillers for Stable PBI Composite Membranes

Inorganic fillers may be added to polymer electrolytes in order to improve their functional properties, including mechanical resistance, chemical durability and ion conductivity

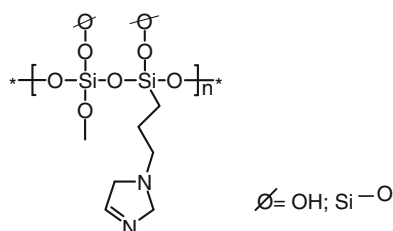
[31]. From the point of view of the conductivity, the fillers can be classified as “passive”, i.e. inert towards the ions motion or “active” when containing chemical moieties, which may be involved in the transport mechanisms. In case of PBI, the most interesting applications of fillers are indeed expected to improve: (a) the ionic conductivity by increasing the amount of the doping acid in the PBI membrane and (b) the long-term durability by reducing the acid leaching. Several materials were checked to this aim, including micrometric TiO₂ [32], BPO₄ [33], titano-silicates [34] and variously shaped silicas [14, 24–26].

Due to the large availability of precursors, silica-based organic–inorganic fillers functionalized with acidic or basic moieties can be easily obtained by sol–gel methods. Both of these possibilities have been recently explored [24]. There we showed that silica with basic moieties (imidazole groups) works much better than that modified with acidic ones. Therefore, in the following we will focus on this filler, which will be compared with other silica-based products, e.g. SBA-15, and HiSil™ (Degussa). SBA-15 is a mesoporous silica with pore diameter of 6 nm, and surface area of 1100 m² g⁻¹. The SBA-15 particle diameters are in the micrometer range. HiSil™ is a nanoscale silica with primary

particles of about 20 nm, and a surface area of about $240 \text{ m}^2 \text{ g}^{-1}$.

The silica-based filler containing the imidazole unit (referred to as $\text{SiO}_2\text{-Im}$ in the following, see Scheme 11.2) was synthesized by means of a standard basic hydrolysis/condensation process, starting from tetraethoxysilane (TEOS) and N-(3-triethoxysilylpropyl)-4,5-dihydroimidazole in molar ratio 2:1 [27].

Figure 11.6 shows the proton conductivity behaviour of the samples as prepared and after the washing procedure. In the case of the as-prepared membranes, the conductivity is nearly independent on the filler amount. In the case of the washed membranes, in contrast, the addition of the filler determines dramatic increases of the conductivity of more than a



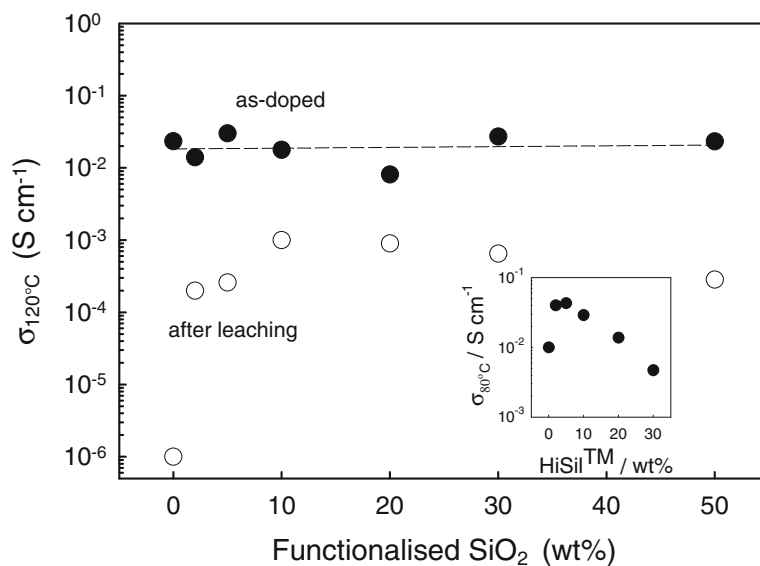
Scheme 11.2 Sol-gel silica filler functionalized with imidazole groups

factor of 1000 with respect to the pure membrane. Moreover, an increase of more than 100 times is already obtained with 2 wt% of filler, which means it is very efficient in promoting the acid retention. As a matter of fact, the amount of retained acid increases from ~ 18 to ~ 37 wt% [27].

It should also be stressed that the conductivity is only weakly dependent on the $\text{SiO}_2\text{-Im}$ filler, for both concerns the as-prepared membranes and the washed ones. This is due to the active nature of this filler, which participates to the proton transport mechanism by means of the imidazole units. The inset of Fig. 11.6 shows the typical behaviour of a nanoscale passive filler (HiSil™): here there is an initial increase of the conductivity due to acid-base interactions and/or to the formation of space-charge layers, which is followed by a strong decrease due to dilution effects [31].

Figure 11.7 shows the conductivity values at 50 % RH and 120°C for PBI_4N (#1), PBI_5N (#5) and for several composite and nanocomposite membranes (see Caption). All the composite membranes contain 5 wt% of filler, but for code 2 which contains 10 wt% of $\text{SiO}_2\text{-Im}$ filler. We observe that there are no great differences among all the as-prepared

Fig. 11.6 Conductivity behaviour of composite PBI_4N membranes containing $\text{SiO}_2\text{-Im}$ filler, both as prepared and after washing. The inset shows the behaviour of composite membranes of the same polymer with a commercial nanoscale silica (HiSil™). Reproduced from [27] with permission of Wiley



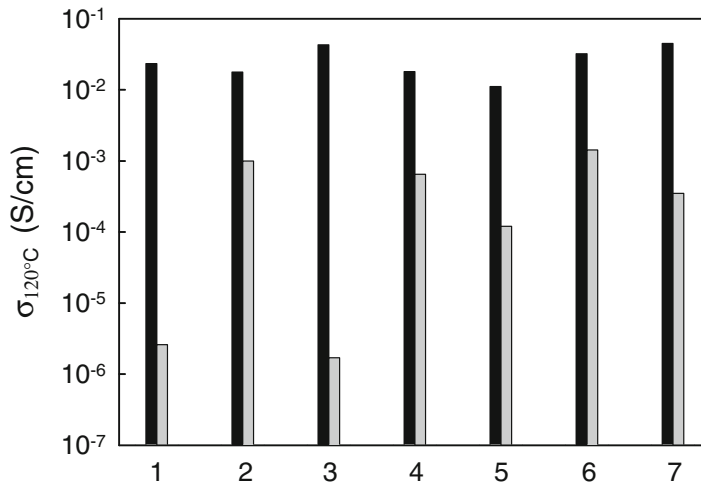


Fig. 11.7 Conductivity values at 120 °C and 50 % RH for several composite membranes, both as prepared (*black*) and after acid leaching (*grey*). 1: PBI_4N; 2: PBI_4N + 10 wt% SiO₂_Im; 3: PBI_4N + 5 wt% HiSil™; 4: PBI_4N + 5 wt% SBA-15; 5: PBI_5N; 6:

PBI_5N + 5 wt% SiO₂_Im; 7: PBI_5N + 5 wt% SBA-15. The RH value is estimated by thermodynamic considerations, on the basis of both saturator and conductivity cell temperatures (as done by our Bekktech test stand). Reproduced from [14] with permission of Elsevier

membranes (at best a factor of 6), the best results being offered by PBI_4N + 5 wt% HiSil™ and PBI_5N + 5 wt% SBA-15. Therefore, we can infer that both the matrix and the filler play a minor role as far as the proton conductivity is concerned, when enough free acid is present in the membrane. Of course, a lower acid content will increase the mechanical properties and hence the durability of the membrane, and this should be taken into account in designing proper electrolytes.

By comparing the washed membranes, we see that HiSil™ gives a very bad result, whereas the best performances are observed for SiO₂_Im and, to a less extent, by SBA-15. At the same time, there are no great differences between the SiO₂_Im composite membranes based on PBI_4N and PBI_5N polymers. We can conclude that the proton conductivity of the composite membranes after acid leaching is determined by the properties of the filler rather than the nature of the polymer. In fact, improvements of the conductivity by up to three orders-of-magnitude are observed in the composite membrane containing SiO₂_Im active filler. It is noteworthy mentioning that the dimension of the filler

particles does not seem to be a critical issue, contrary to what commonly observed in the case of the electrolytes for lithium batteries [31]. In contrast, in case of PA-doped PBI membranes a too low dimension of the particles can be detrimental for the cell durability, at least in case of silica-based fillers. At the same time, the presence of mesoporous structures (e.g. those present in SBA-15) does offer good pathways for H⁺ migration, likely assisted by PA and/or water molecules. We also stress again that our results are obtained by employing a simple washing procedure, which is only an approximation of the complex processes taking place in a real fuel cell operating above 100 °C. We cannot rule out that further PA loss could take place during actual operating conditions, which however would contribute additional effect on top of the observation discussed in the present chapter.

11.4 Conclusions

Phosphoric acid leaching during operation is a problem, which can affect the long-term durability of PBI-based cells and stacks. While other

solutions to the problem such as fuel cell design and stack management are under active development, we explore the polymer chemistry and membrane composite to reduce the acid leaching.

Two approaches to improve acid retention are presented and evaluated by the specially designed acid leaching method. The remaining conductivity after the acid leaching is called “permanent conductivity”. The first approach is to synthesize PBI variants by monomer/chain modification and other second is to prepare (nano)composite systems with basic moieties. Although both of these strategies can lead to improved membranes and the presence of proper fillers can assure higher conductivity levels, we conclude that the former way is preferred. In fact, whereas a direct comparison of fuel cell performances of MEAs assembled following the two strategies is difficult because of a number of involved experimental parameters (doping level, polymer batches, etc.), we have a quite strong evidence that PBI_5N is unsurpassed in giving good fuel cell performances and long-term stability.

References

1. DOE Fuel Cells Technical Plan, Hydrogen and Fuel Cells Programs (2012) www.eere.energy.gov/hydrogenandfuelcells/mypp/pdfs/fuel_cells.pdf
2. Zhang L, Chae S-R, Hendren Z et al (2012) Recent advances in proton exchange membranes for fuel cells application. *Chem Eng J* 204–206:87–97
3. Chandan A, Hattenberger M, El-Kharouf A et al (2013) High temperature (HT) polymer electrolyte membrane fuel cells (PEMFC)—a review. *J Power Sources* 231:264–278
4. Bose S, Kuila T, Ngyyen TXH et al (2011) Polymer membranes for high temperature proton exchange membrane fuel cells: recent advances and challenges. *Prog Polym Sci* 36:813–843
5. Li Q, Jensen JO, Savinell RF et al (2009) High temperature proton exchange membranes based on polybenzimidazoles for fuel cells. *Prog Polym Sci* 34:449–477
6. Subianto S (2014) Recent advances in polybenzimidazole/phosphoric acid membranes for high temperature fuel cells. *Polym Int* 63:1134–1144
7. Zhang H, Shen PK (2012) Recent development of polymer electrolyte membranes for fuel cells. *Chem Rev* 112:2780–2832
8. Asensio JA, Sanchez EM, Gomez-Romero P (2010) Proton-conducting membranes based on polybenzimidazole polymers for high-temperature PEM fuel cells. A chemical quest. *Chem Soc Rev* 39:3210–3239
9. Ma YL, Wainright JS, Litt MH, Savinell RF (2004) Conductivity of PBI membranes for high-temperature polymer electrolyte fuel cells. *J Electrochem Soc* 151: A8–A16
10. Bouchet R, Siebert E (1999) Proton conduction in acid doped polybenzimidazole. *Solid State Ion* 118:287–299
11. Li QF, He RH, Berg RW et al (2004) Water uptake and acid doping of polybenzimidazoles as electrolyte membranes for fuel cells. *Solid State Ion* 168:177–185
12. Kreuer KD (1996) Proton conductivity: materials and applications. *Chem Mater* 8:610–641
13. Kreuer KD (2014) Ion conducting membranes for fuel cells and other electrochemical devices. *Chem Mater* 26:361–380
14. Mustarelli P, Quartarone E, Grandi S et al (2012) Increasing the permanent conductivity of PBI membranes for HT-PEMs. *Solid State Ion* 225:228–231
15. Quartarone E, Mustarelli P (2012) Polymer fuel cells based on polybenzimidazole/H₃PO₄. *Energy Environ Sci* 5:6436–6444
16. Carollo A, Quartarone E, Tomasi C et al (2006) Developments of new proton conducting membranes based on different polybenzimidazole structures for fuel cells applications. *J Power Sources* 160:175–180
17. Quartarone E, Carollo A, Mustarelli P et al (2006) New polybenzimidazole-based membranes for fuel cells. *Mater Res Soc Symp Proc* 972:125
18. Mustarelli P, Quartarone E, Magistris A (2009) Membranes: polybenzimidazoles. In: Garche J, Dyer C, Moseley P, Ogumi Z, Rand D, Scrosati B (eds) *Encyclopedia of electrochemical power sources*, vol 2. Elsevier, Amsterdam, pp 734–740
19. Angioni S, Righetti PP, Quartarone E (2011) Novel aryloxy-polybenzimidazoles as proton conducting membranes for high temperature PEMFCs. *Int J Hydrogen Energy* 36:7174–7182
20. Villa DC, Angioni S, Quartarone E et al (2013) New sulfonated PBIs for PEMFC application. *Fuel Cells* 13:98–103
21. Angioni S, Villa DC, Dal Barco S et al (2013) Polysulfonation of BI-based membranes for HT-PEMFCs: a possible way to maintain high proton transport at a low H₃PO₄ doping level. *J Mater Chem A* 2:663–671

22. Villa DC, Angioni S, Dal Barco S et al (2014) Polysulfonated fluoro-oxyPBI membranes for PEMFCs: an efficient strategy to achieve good fuel cell performances with low H₃PO₄ doping levels. *Adv Energy Mater* 4:1031949
23. Kurdakova V, Quartarone E, Mustarelli P et al (2010) PBI-based composite membranes for polymer fuel cells. *J Power Sources* 195:7765–7769
24. Grandi S, Mustarelli P, Carollo A et al (2010) New fillers for PBI-based composite electrolytes in polymer fuel cells. *Composite Interfaces* 17:649–662
25. Quartarone E, Magistris A, Mustarelli P et al (2009) Pyridine-based PBI composite membranes for PEMFCs. *Fuel Cells* 9:349–355
26. Quartarone E, Mustarelli P, Carollo A et al (2009) PBI composite and nanocomposite membranes for PEMFCs: the role of the filler. *Fuel Cells* 9:231–236
27. Mustarelli P, Quartarone E, Grandi S et al (2008) Polybenzimidazole-based membranes as a real alternative to Nafion for fuel cells operating at low temperature. *Adv Mater* 20:1339–1343
28. Mustarelli P, Carollo A, Grandi S et al (2007) Composite proton-conducting membranes for PEMFCs. *Fuel Cells* 7:441–446
29. Vogel T, Marvel CS (1961) Polybenzimidazoles: new thermally stable polymers. *J Polym Sci* 50:511–539
30. Zhai Y, Zhang G, Liu JH et al (2007) Degradation study on MEA in H₃PO₄/PBI high-temperature PEMFC life test. *J Electrochem Soc* 154:B72–B76
31. Quartarone E, Mustarelli P (2011) Electrolytes for solid-state lithium rechargeable batteries: recent advances and perspectives. *Chem Soc Rev* 40:2525–2540
32. Pinar JF, Cañizares P, Rodrigo MA et al (2012) Titanium composite PBI-based membranes for high temperature polymer electrolyte membrane fuel cells. Effect on titanium dioxide amount. *RSC Adv* 2:1547–1556
33. Javaid Zaidi SM (2005) Preparation and characterization of composite membranes using blends of SPEEK/PBI with boron phosphate. *Electrochim Acta* 50:4771–4777
34. Eguizábal A, Lemus J, Urbiztondo M et al (2011) Novel hybrid membranes based on polybenzimidazole and ETS-10 titanosilicate type material for high temperature proton exchange membrane fuel cells: a comprehensive study on dense and porous systems. *J Power Sources* 196:8994–9007

T. Leon Yu

12.1 Reinforced Nafion Membranes

The membrane electrode assembly (MEA) for polymer electrolyte membrane fuel cells (PEMFCs) consists of a polymer electrolyte membrane (PEM) sandwiched between two porous electrodes, anode and cathode. Reactant gases H_2 and O_2 (or air) are fed from the back of the anode and cathode, respectively, and brought into contact with the catalyst layers located at the interface between the electrode and the PEM. One of the important factors that determine the performance of a PEMFC is the efficiency of proton transfer across the PEM from the anode to the cathode. The combination of the membrane thickness (L) and ionic conductivity (σ) of the PEM, which is the resistance per unit area (L/σ) across the membrane thickness direction, rather than σ alone, determines the proton transfer efficiency, and thus fuel cell performance. A PEM with a lower L and higher σ has a lower L/σ and higher proton transport efficiency. However, a thin PEM may have weak mechanical strength and exhibit high gas crossover in the PEM, thereby lowering the open circuit voltage (OCV) and fuel cell performance. Thus obtaining

a PEM with low thickness, high mechanical strength, and at the same time low gas crossover are important parameters for obtaining a high performance PEMFC.

Perfluorosulfonated ionomer/poly(tetrafluoro ethylene) (e.g., Nafion/PTFE) composite membranes, fabricated using a high mechanical strength porous PTFE thin film as reinforcement, have demonstrated high mechanical strength and high proton conductivity. Such composites exhibit low fuel gas crossover and high performance when tested in PEMFCs [1–5]. In these thin composite PEMs, the porous supporting film provides the membrane with mechanical strength, and the Nafion ionomer provides the membrane with proton conducting paths. After the report of the Nafion/PTFE composite membrane, several articles regarding the properties, modifications, and applications of these composite membranes to PEMFCs and direct methanol fuel cells (DMFCs) have been reported [6–20]. To prepare Nafion/PTFE composite membranes, the porous PTFE thin film with a thickness of ~ 10 – $20\ \mu\text{m}$ (Fig. 12.1a) was impregnated with a 5 wt% Nafion dispersion (DuPont Co., 1100 EW Nafion diluted in a solvent mixture containing water, propanol, methanol, and unspecified ethers) mixed with Triton surfactant, which helps in the dispersion of Nafion polymer chains in solutions [9]. Before impregnation, the porous PTFE membrane was

T.L. Yu
Department of Chemical Engineering and Materials
Science, Fuel Cell Center, Yuan Ze University, Chung-Li,
Taoyuan 32003, Taiwan
e-mail: cetlyu@saturn.yzu.edu.tw

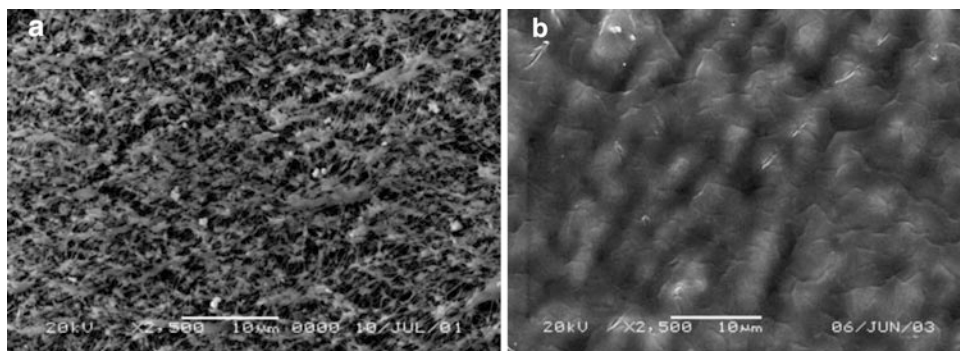


Fig. 12.1 SEM micrographs of (a) porous poly(tetrafluoro ethylene) (PTFE) thin film; (b) Nafion/PTFE. Reproduced from [7] with permission of Elsevier Science Ltd.

Table 12.1 Membrane thickness (L), conductivity (σ), and resistance (L/σ) of Nafion and Nafion/PTFE composite membranes

Membrane	L (μm)	σ (10^{-2} S cm^{-1})	L/σ ($\Omega \text{ cm}^2$)	Ref.
Nafion/PTFE	20	0.052 (25 °C, 100 % RH)	3.84	[5]
Nafion/PTFE	5	0.028 (25 °C, 100 % RH)	1.78	[5]
Nafion-117	200	0.14 (25 °C, 100 % RH)	14.3	[5]
Nafion-112	60	0.10 (25 °C, 100 % RH)	6.0	[5]
Nafion/PTFE	14	6.2 (60 °C, 100 % RH)	0.023	[13]
Nafion-211	25	9.1 (60 °C, 100 % RH)	0.028	[13]

boiled in acetone at 55 °C. These pre-treated PTFE thin films were then impregnated with Nafion solution. The impregnated membranes were then dried and annealed at ~120–130 °C and then swollen in distilled water. The swollen membranes were put into isopropanol to dissolve out Triton and then the membranes were washed with distilled water (Fig. 12.1b). The thickness of the obtained Nafion/PTFE composite membrane was around 20–25 μm . Due to the fact that PTFE and Nafion backbone have the same chemical structure, the Nafion backbone was compatible with the PTFE support and the composite membranes exhibited good interface bonding between Nafion and PTFE. No delamination between the Nafion ionomer and PTFE support occurred when applied to PEMFCs and DMFCs.

The main advantage of Nafion/PTFE composite membranes is their low fuel gas crossover and high mechanical strength despite the low thickness L , and thus a low L/σ as summarized in Table 12.1. Nafion/PTFE composite membranes can thus be made considerably thinner (<25 μm) than the commercially available Nafion-117,

Nafion-115, Nafion-112, and Nafion-212 which have thickness of 175 μm , 125 μm , 50 μm , and 50 μm , respectively. These thinner composite PEMs contain significantly less amounts of the expensive Nafion resin than the thicker neat Nafion membranes. Thus, another advantage of Nafion/PTFE composite PEMs is the fact that they are inexpensive. Besides porous PTFE films, porous films such as polyethylene (PE) [21, 22] and electro-spun polymer nanofiber films such as those of poly(vinylidene fluoride) (PVdF) [23, 24], poly(vinylidene fluoride-co-hexafluoropropylene) (PVdF-co-HFP) [25], and poly(vinyl alcohol) (PVA) [26–31] have also been used as supporting films for impregnating Nafion ionomer solutions to prepare Nafion/fiber composite PEMs for PEMFC and DMFC applications.

The main problem with DMFCs is the high methanol crossover of the conventional PEMs, which results in a lower OCV and poor fuel utilization. To reduce the methanol crossover in the PEMs, most researchers, instead of using thinner membranes such as Nafion-115,

Table 12.2 Tensile stress of Nafion and Nafion/PTFE composite membranes

Membrane	Thickness L (μm)	Tensile strength (MPa)	Ref.
Nafion/PTFE	20	34.4 (Dry)	[5]
Nafion/PTFE	20	32.5 (Wet)	[5]
Nafion-117	180	29.8 (Dry)	[5]
Nafion-117	180	13.9 (Wet)	[5]
Nafion/PTFE	14	34.1	[13]
Nafion-211	25	21.3	[13]

Nafion-112, and Nafion-212, use the thicker membrane Nafion-117 in DMFCs. The use of crosslinked PVA electrospun nano-fiber film supported Nafion composite membranes (Nafion/PVA-fiber, thickness $\sim 50 \mu\text{m}$) in DMFCs has been reported to exhibit a much better DMFC performance than Nafion-117 and Nafion/PVA blended PEMs [26–31]. Several researchers blended the Nafion PEMs with low methanol compatible PVA to reduce the methanol crossover in the PEMs [32–35]. However, these modified Nafion membranes had thicknesses greater than $175 \mu\text{m}$, which were similar to (or higher than) that of the neat Nafion-117 membrane. Although there was a decrease in the methanol crossover from these Nafion/PVA blended membranes, the proton transfer resistance of these membranes increased, resulting in a lower DMFC performance. The advantage of applying the thin Nafion/PVA-fiber PEMs to the DMFCs is that the methanol crossover can be reduced without increasing the area specific resistance (i.e., L/σ) because of low membrane thickness. Table 12.1 summarizes the thickness, proton conductivity, and L/σ of the fiber reinforced Nafion composite membranes obtained from literature reports. The mechanical properties of the composite membranes reported in literature are also listed in Table 12.2.

12.2 Reinforcement of Polybenzimidazole with Porous Poly(Tetrafluoro Ethylene)

12.2.1 Introduction

As discussed in Sect. 12.1, the polymer membrane reinforced with a high mechanical strength

porous thin film support was preceded by impregnating the porous thin film support with a dilute polymer solution and then evaporating the solvent, which is similar to the process for preparing polymer solution cast membranes. Thus, the properties of the polymer solution are important factors for controlling the properties of fiber reinforced polymer composite membranes and also the solution cast membranes. Before discussing the preparations and properties of polybenzimidazole/poly(tetrafluoro ethylene) (PBI/PTFE) composite membranes, we first discuss the properties of PBI in dilute solution, preparations and characterizations of PBI/PTFE composite membranes, and the application of these composite membranes in high temperature PEMFCs (HT-PEMFCs) operating in the temperature range (about $\sim 120\text{--}200 \text{ }^\circ\text{C}$).

12.2.2 PBI Solution Properties

PBI is insoluble in most solvents due to the strong interpolymer hydrogen bonding between the imidazole moieties (Fig. 12.2) [36]. Several researchers have prepared PBI membranes by casting from *N,N*-dimethylacetamide (DMAc) and formic acid (FA) solutions mixed with lithium chloride (LiCl) or lithium bromide (LiBr) as stabilizer [37–46]. Solution viscosities, polymer particle size distributions, and interpolymer interactions are important parameters that determine the properties of solution cast PBI and solution impregnated PBI/PTFE composite membranes. In the following sections, viscosities, polymer particle size distributions, and interpolymer hydrogen bonding interactions of dilute PBI solutions are discussed.

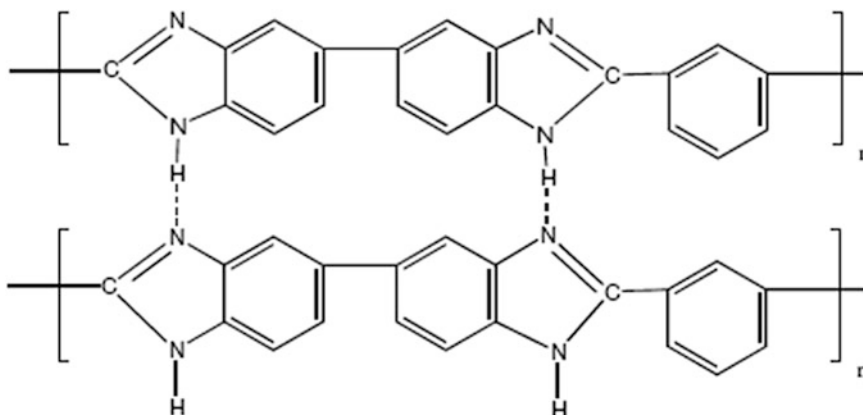


Fig. 12.2 Hydrogen bonds between $-N-H \cdots N=C-$ groups. Reproduced from [36] with permission of Elsevier Science Ltd.

12.2.2.1 Viscosity of Dilute PBI Solutions

The viscosity of the dilute solutions of PBI in FA and DMAc containing LiBr or LiCl has been studied by Kojima et al. [44, 45], Shogbon et al. [46], and Lin et al. [36]. The variations of solution viscosity as a function of PBI concentration under a fixed salt stabilizer (i.e., LiBr or LiCl) concentration and as a function of stabilizer concentration under a fixed PBI concentration have been reported. The solution viscosity strongly depends on the molar ratio of the salt and PBI repeat unit (i.e., $[LiBr]/[BI]$ or $[LiCl]/[BI]$, where $[BI]$ is the concentration of the PBI repeat unit).

Kojima et al. [44, 45] studied the effects of salt concentration and temperature on dilute solution viscosities of PBI in DMAc and FA solutions. The reduced viscosities η_{sp}/c of PBI/FA solutions without salt are plotted against PBI concentration (Fig. 12.3, curve (a)). The η_{sp}/c data exhibited an increasing trend with decreasing PBI concentration. However, this trend was decreased by the addition of 0.0045 N LiBr in the solutions (Fig. 12.3, curve (b)), corresponding to a $[LiBr]/[BI]$ ratio of 1.737×10^4 – 5.79×10^3 at PBI concentration ranging from 0.1 to 0.3×10^{-3} g mL $^{-1}$) [45]. These results suggest the polyelectrolyte behavior of PBI in dilute FA solutions, which is caused by the bonding of H^+ and $HCOO^-$ ions dissociated from FA ($HCOOH$) on the PBI imidazole $N=C-$ and $H-N-C$ groups, respectively [47, 48].

The temperature effect on the solution viscosity of PBI in DMAc was also studied by Kojima et al. using intrinsic viscosity $[\eta]$ measurement. The $[\eta]$ data of dilute PBI in DMAc solutions without mixing with salt showed a decrease of $[\eta]$ with increasing temperature (Fig. 12.4), suggesting that the agglomerates of PBI present in the low temperature range dissociated with increasing temperature [43]. This PBI aggregation behavior in solutions can be attributed to the interpolymer hydrogen bonding [36].

Shogbon et al. [46] conducted viscosity measurements of dilute PBI in DMAc/LiCl solutions ($[PBI] \leq 1.8$ mg mL $^{-1}$). Figure 12.5 shows the plot of the reduced viscosity η_{sp}/c of PBI in DMAc solutions containing 4 wt% LiCl ($[LiCl] = 0.884$ N or $[LiCl] = 37.5$ mg mL $^{-1}$) as a function of PBI concentration. In these solutions, the concentration of LiCl was significantly higher than that of PBI, and all inter-PBI polymer hydrogen bonds (Fig. 12.2) were dissociated by the interaction of Li^+Cl^- with the PBI imidazole group via $Li^+ \cdots N=C-$ and $Cl^- \cdots H-N-C$. Thus the PBI chains exhibited single polymer chain behavior in solutions. As shown in Fig. 12.5, a sharp decrease was observed in η_{sp}/c when the PBI concentration was increased from 0.3 mg mL $^{-1}$ (i.e., $[PBI] = 0.032$ wt%, $[LiCl]/[BI] = 908$ by mol ratio) to 0.7 mg mL $^{-1}$ ($[PBI] = 0.075$ wt%, $[LiCl]/[BI] = 389$ by mol ratio). When the PBI concentration was increased from 0.7 to 0.85 mg mL $^{-1}$

Fig. 12.3 Plots of reduced viscosity η_{sp}/c of PBI/FA solutions versus PBI concentration. (a) without LiBr; (b) with 0.0045 N LiBr. Reproduced from [45] with permission of John Wiley & Sons, Inc.

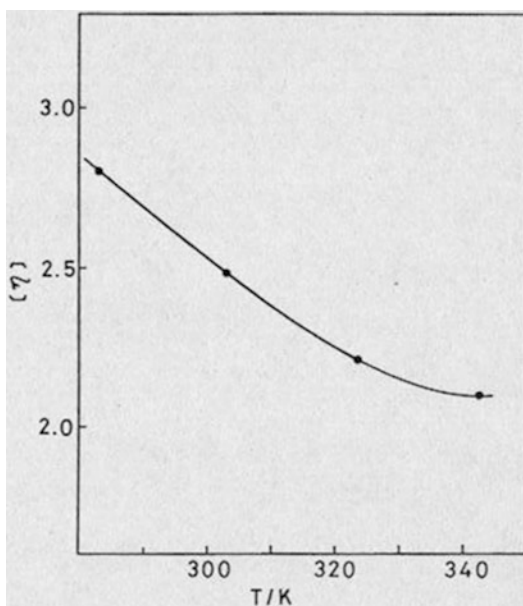
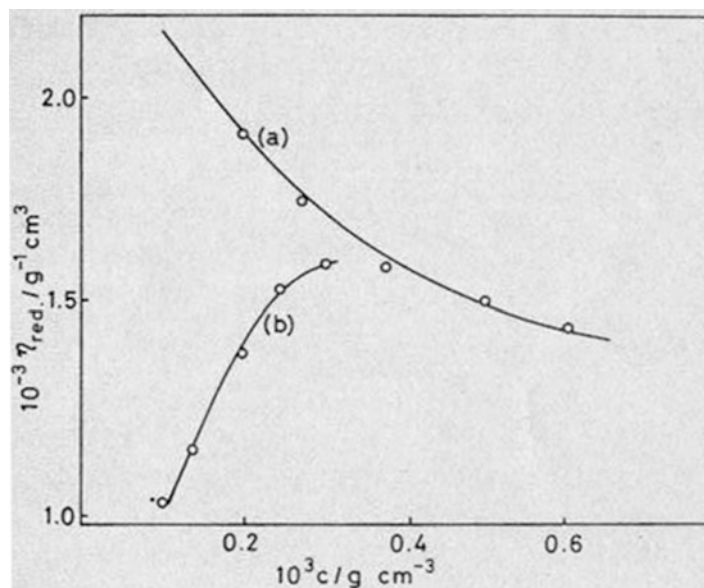


Fig. 12.4 Temperature dependence of the intrinsic viscosity of PBI in DMAc solutions. The PBI molecular weight determined by static light scattering was 1.5×10^5 g mol⁻¹. Reproduced from [44] with permission of John Wiley & Sons, Inc.

([PBI] = 0.098 wt%, [LiCl]/[BI] = 320 by mol ratio) the viscosity slightly increased and then it slightly decreased with increasing PBI concentration to 1.8 mg mL⁻¹ ([PBI] = 0.192 wt%,

[LiCl]/[BI] = 151 mol ratio). These results are consistent with the variation of the radius of gyration R_g of PBI in DMAc solutions containing 4.0 wt% of LiCl (Fig. 12.7), as will be discussed in Sect. 12.2.2.2. The polymer chains exhibited a coil-like structure at low concentrations ([PBI] < 0.4 mg mL⁻¹), and the polymer chain collapsed as the PBI concentration was increased from 0.4 to 0.7 mg mL⁻¹. The conformation of the polymer chain was changed from a coil-like to worm-like chain when the PBI concentration was increased above 0.7 mg mL⁻¹ [46].

Lin et al. [36] determined the dynamic shear viscosity η' of 2.0 mg mL⁻¹ PBI/DMAc solutions mixed with various LiCl concentrations at a shear frequency of 1.07 rad s⁻¹ using a capillary VE viscoelastic analyzer (Vilastic Co., Inc., Austin, TX). The data of η' are plotted as a function of LiCl concentration (Fig. 12.6). There was a drastic decrease in η' when the initial feed molar ratio of [LiCl]/[BI] was increased from 3.63 to 8.00. However, when the initial feed molar ratio of [LiCl]/[BI] was increased from 8.00 to 14.51, η' slowly increased. The data indicated that the lowest η' was observed when the initial feed molar ratio of [LiCl]/[BI] of PBI/DMAc/LiCl solutions was around 7–8 (i.e., [LiCl]/[PBI] = 0.96–1.1 by wt.), where the

Fig. 12.5 Reduced viscosity η_{sp}/c of PBI/DMAc solutions containing 4 wt% LiCl as a function of PBI ($[\eta] = 1.59 \text{ dL g}^{-1}$) concentration. Reproduced from [46] with permission of the American Chemical Society

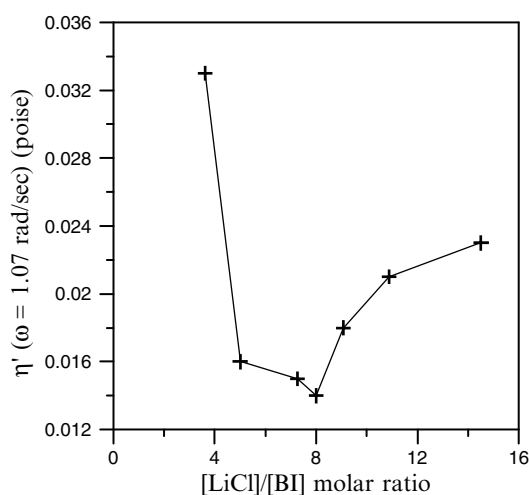
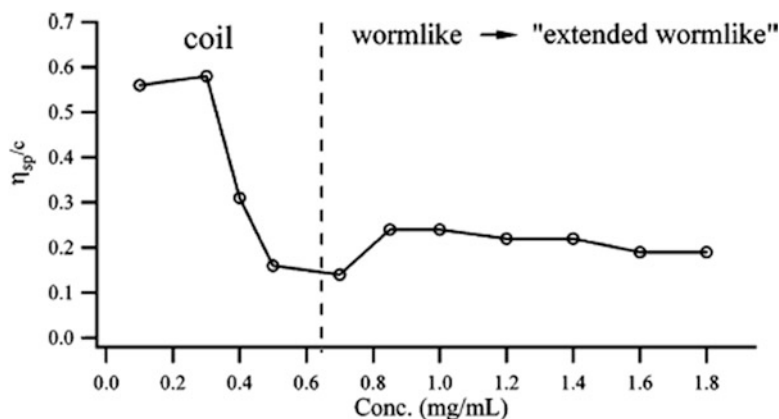


Fig. 12.6 Plot of dynamic shear viscosity η' at 1.07 rad s^{-1} of 2.0 mg mL^{-1} PBI/DMAc/LiCl solutions versus initial fed molar ratio of $[\text{LiCl}]/[\text{BI}]$. Reproduced from [36] with permission of Elsevier Science Ltd.

number of LiCl molecules bonded on PBI was around ~ 2.5 per BI repeat unit, as shown in Fig. 12.11. The variation of solution viscosity against LiCl concentration will be discussed in Sect. 12.2.2.3, based on the interaction of LiCl with PBI and PBI interpolymer hydrogen bonds in dilute solutions.

12.2.2.2 PBI Particle Size Distributions in Dilute Solutions

Shogbon et al. [46] also conducted static light scattering (SLS) to determine the radius of gyration R_g of PBI in dilute DMAc solutions with PBI concentrations ranging from 0.2 mg mL^{-1} ($[\text{LiCl}]/[\text{BI}] = 2724$ by mol ratio) to 20 mg mL^{-1} ($[\text{LiCl}]/[\text{BI}] = 13.6$ by mol ratio) and a fixed LiCl concentration of 4 wt%. Similar to their reduced viscosity data (Fig. 12.5), the R_g data of PBI/DMAc solutions (Fig. 12.7) indicated

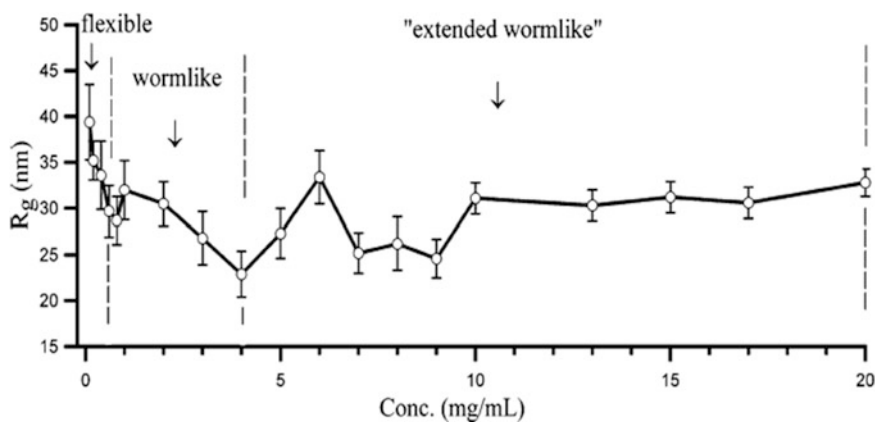


Fig. 12.7 R_g of PBI as a function of PBI ($[\eta] = 1.59 \text{ dL g}^{-1}$) concentration in DMAc solutions containing 4 wt% LiCl. Reproduced from [46] with permission of the American Chemical Society

that the structure of the polymer chain collapsed with increasing PBI concentration from 0.1 to 0.4 mg mL⁻¹ followed by fluctuations in particle size ([PBI] = 4–10 mg mL⁻¹). Similar to the η_{sp}/c of PBI/DMAc solutions, Shogbon et al. [46] attributed the polymer chain collapse to the polymer conformation transition from coil-like to an “extended worm-like” chain with increasing PBI concentration. Similar polymer chain size and shape changes were also observed for PBI/DMAc/LiCl solutions at a fixed PBI concentration of 0.3 mg mL⁻¹ as a function of increasing LiCl concentration (Fig. 12.8) [46]. At low salt concentrations ([LiCl] < 2 wt %), a worm-like chain conformation was observed. However, with increasing LiCl concentration from 0.1 to 2.0 wt%, the structure of the polymer chain collapsed followed by a fluctuation in polymer R_g ([LiCl] = 2.0–7.0 wt%).

Lin et al. [36] reported the hydrodynamic radii (R_h) of 2.0 mg mL⁻¹ PBI/DMAc solutions mixed with various LiCl by dynamic light scattering (DLS) at a scattering angle of 90°, respectively. Similar to the η' (Fig. 12.6), R_h dramatically decreased when the initial feed molar ratio of [LiCl]/[BI] increased from 3.63 to 8.00 (Fig. 12.9). However, when the initial feed molar ratio of [LiCl]/[BI] was increased from 8.00 to 14.51, R_h slowly increased. These data indicated that R_h was lowest when the initial feed

molar ratio of [LiCl]/[BI] of PBI/DMAc/LiCl solutions is around 7–8 (i.e., [LiCl]/[PBI] = 0.96–1.1 by wt.), where the number of LiCl ion pairs interacting with PBI is around 2.5 per PBI repeat unit (Fig. 12.11). Both η' and R_h showed a minimum at a molar ratio [LiCl]/[BI] of 7–8, which will be discussed in the next section.

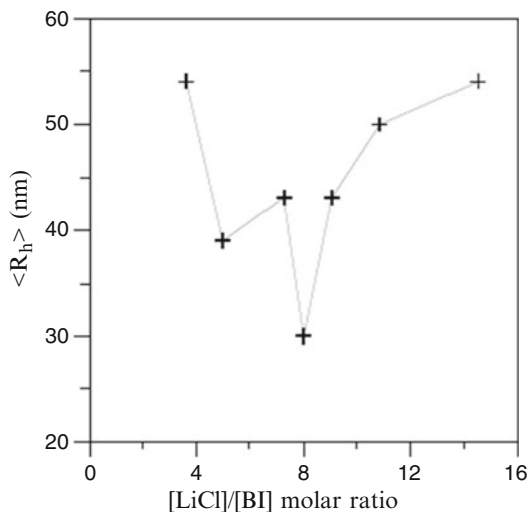


Fig. 12.9 Plot of DLS R_h of PBI against initial feed molar ratio of [LiCl]/[BI] of PBI/DMAc/LiCl solutions. DLS scattering angle of 90°. Reproduced from [36] with permission of Elsevier Science Ltd.

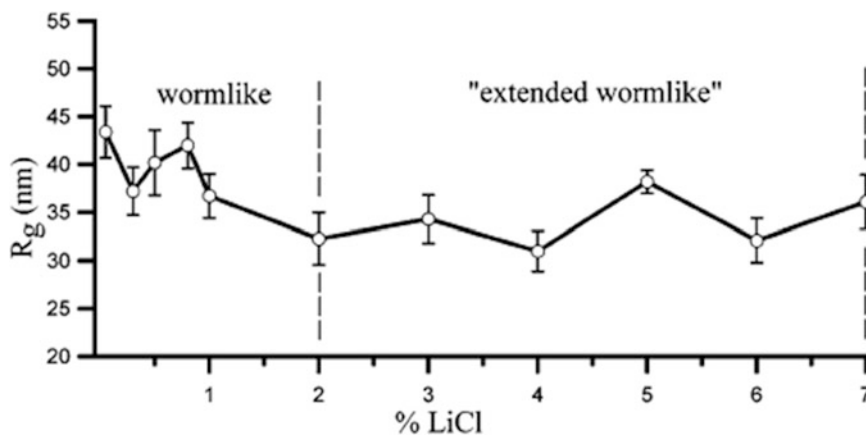


Fig. 12.8 Radius of gyration R_g of PBI ($[\eta] = 1.59 \text{ dL g}^{-1}$) in DMAc solutions containing 0.3 mg mL⁻¹ PBI as a function of LiCl. Reproduced from [46] with permission of the American Chemical Society

12.2.2.3 Interpolymer Interactions for PBI in Dilute Solutions

Lin et al. [36] used Fourier transform infrared spectroscopy (FTIR) and dialysis in conjunction with conductivity measurements to study the influence of the LiCl stabilizer on the morphology of PBI in DMAc solutions ($[PBI] = 2.0 \text{ mg mL}^{-1}$ and $[LiCl]/[BI] = 3.63\text{--}14.51 \text{ M}$ ratio or $[LiCl]/[PBI] = 0.5\text{--}2.0$ by weight ratio). It was demonstrated that interpolymer hydrogen bonding was developed via the $-N-H \cdots N=C-$ interaction for PBI in DMAc solutions (Fig. 12.10). On the basis of the dialysis measurements, it was shown that the $-N-H \cdots N=C-$ hydrogen bonds were disrupted

by the presence of LiCl in the solutions via the $Li^+ \cdots N=C-$ and $Cl^- \cdots H-N<$ interactions. The IR spectra of PBI/DMAc/LiCl solutions were obtained using the DMAc spectrum as the background, and the absorbance of DMAc was subtracted from the spectra of PBI/DMAc/LiCl solutions using the $-C=O$ absorption of DMAc at 1700 cm^{-1} as the reference (Fig. 12.10). With increasing $[LiCl]/[BI]$ molar ratio, the IR spectra showed a decrease of the N–H stretching peak intensity and a shift from 3402 cm^{-1} to a higher wave number 3482 cm^{-1} with peak narrowing and a slight shift of the C–H stretching peak from 2926 to 2932 cm^{-1} and an increase of the peak intensity at 2926 cm^{-1} , which became visible.

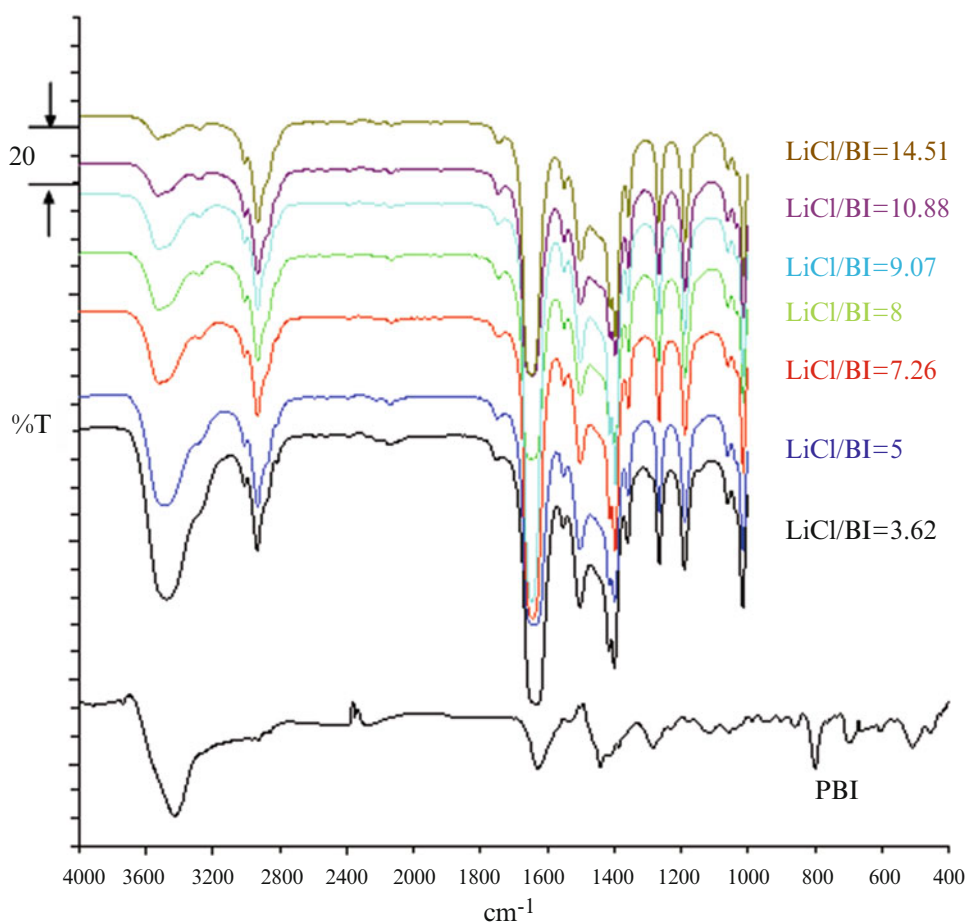


Fig. 12.10 FTIR spectra of PBI/LiCl/DMAc solutions and solid PBI. The initial fed molar ratio of $[LiCl]/[BI]$ of each solution is indicated in each spectrum. $[LiCl]/$

$[BI]$ molar ratio increases from second *bottom* to *top*. The *bottom* spectrum is solid PBI. Reproduced from [36] with permission of Elsevier Science Ltd.

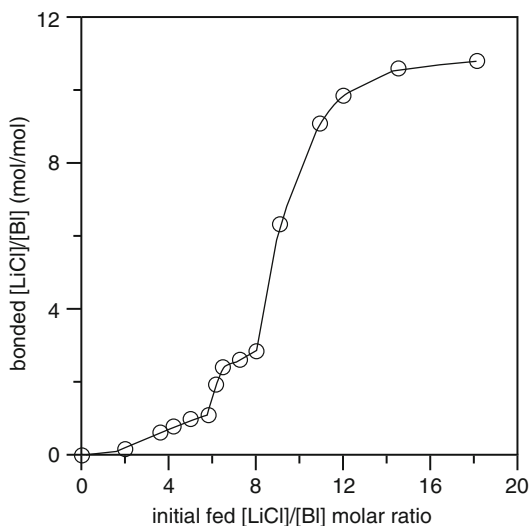


Fig. 12.11 LiCl bonded per BI repeat unit versus initial [LiCl]/[BI] feed molar ratio of PBI/DMAc/LiCl solutions. Reproduced from [36] with permission of Elsevier Science Ltd.

Furthermore, a slight shift of C=C/C=N stretching peak at 1614–1646 cm^{-1} suggested the presence of hydrogen bonds between $-\text{NH}$ and $-\text{N}=\text{C}-$ groups (Fig. 12.2). The hydrogen bonds dissociated as LiCl was mixed into PBI/DMAc solutions due to the interactions of LiCl with imidazole functional group via the $\text{Li}^+ \cdots \text{N}=\text{C}-$ and $\text{Cl}^- \cdots \text{H}-\text{N}-$ associations.

The number of LiCl ion pairs bonded on each PBI repeat unit in the 2 mg mL^{-1} PBI/DMAc solutions consisting of various LiCl concentrations was investigated by dialysis in combination with conductivity measurements [36]. Figure 12.11 shows the variation of Li^+Cl^- bonded on PBI per benzyl imidazole (BI) repeat unit versus the initial [LiCl]/[BI] feed molar ratio. There are three regions in this plot: (1) In the region of $0 < [\text{LiCl}]/[\text{BI}] < 8.0$, the number of LiCl bonded on PBI slowly increased with increasing initial feed molar ratio of [LiCl]/[BI]; (2) in the region of $8.0 < [\text{LiCl}]/[\text{BI}] < 12$, the number of LiCl bonded on PBI dramatically increased with increasing [LiCl]/[BI] feed molar ratio; and (3) in the region of $[\text{LiCl}]/[\text{BI}] > 12$, the number of LiCl bonded on PBI reached an asymptote. An inflection point of around 7.0–8.0 was observed

at the initial [LiCl]/[BI] feed molar ratio (i.e., $[\text{LiCl}]/[\text{PBI}] = 0.96\text{--}1.04$ by wt. ratio), where the number of LiCl bonded on PBI per BI repeat unit was around 2.5, which is close to the number of “2 $-\text{NH}$ groups” and “2 $-\text{N}=\text{C}-$ groups” which are present in the chemical structure of a BI repeat unit, as shown in Fig. 12.2. The slow increase of LiCl interaction on PBI in the region $0 < [\text{LiCl}]/[\text{BI}] < 8.0$ in Fig. 12.11 can be attributed to the strong hydrogen bonding between $-\text{N}-\text{H}$ and $-\text{N}=\text{C}-$ groups, which causes difficulty for LiCl to interact with either the $-\text{NH}$ groups or the $-\text{N}=\text{C}-$ groups. In the region $8.0 < [\text{LiCl}]/[\text{BI}] < 12$ in Fig. 12.11, where the hydrogen bonds between the $-\text{N}-\text{H}$ and $-\text{N}=\text{C}-$ groups are almost completely dissociated, the LiCl is loosely bound to the BI units. The number of LiCl bonded on PBI dramatically increased with increasing [LiCl]/[BI] feed molar ratio in PBI/DMAc solutions. In the region $[\text{LiCl}]/[\text{BI}] > 12$, the association of the second LiCl on BI was attributed to the interactions of $\text{Cl}^- \cdots \text{LiN}-\text{BI}$ and $\text{Li}^+ \cdots \text{Cl}^+\text{HN}-\text{BI}$, and of Li^+ on $\text{BI}-\text{NLi}^+\text{Cl}^-$, resulting in hydrophobic behavior and agglomeration of PBI in solutions (Figs. 12.6 and 12.9).

12.2.3 Preparation and Characterizations of PBI/Porous PTFE Composite Membranes

Similar to the preparation of Nafion/PTFE composite membranes, PBI/PTFE composite membranes were prepared by impregnation of the porous PTFE support film with a PBI solution followed by solvent evaporation. Because of the poor compatibility of PTFE with PBI, before impregnating the PTFE film support with the PBI solution, pretreatment was conducted to activate PTFE for obtaining a good bonding interface between PTFE and PBI. Two methods for pretreating PTFE film have been reported: chemical activation [49] and coupling agent pretreatment [50–53]. In chemical activation [49], the porous PTFE film was surface-activated by immersing the porous PTFE film in

$\text{H}_2\text{SO}_4/\text{H}_2\text{O}_2$ mixture solution at $80\text{ }^\circ\text{C}$ for 1 h and then rinsing with water. Subsequently, it was immersed in a solution containing one part of 1.0 mol L^{-1} aqueous NaOH, one part of a 30 wt% H_2O_2 aqueous solution, and five parts of deionized water at $70\text{ }^\circ\text{C}$ for 30 min, followed by immersion in 50 mL DMAc at $50\text{ }^\circ\text{C}$ for 30 min. Hereafter, the PTFE film pre-treated by chemical activation will be referred to as PTFE-ca.

In the coupling agent method, Nafion was used as the coupling agent [50–53]. The porous PTFE thin film was immersed in a 0.7 wt% Nafion/DMAc solution to form a thin film of Nafion on the surface of a PTFE fiber. The chemical structure of Nafion consists of a perfluorocarbon main chain, which is compatible with the PTFE supporting thin film, and ethersulfonic acid side chains, which have $-\text{SO}_3\text{H}$ groups for interaction with the imidazole groups of PBI via Lewis acid–base interaction. Figure 12.12 shows the role of Nafion acting as an interface coupling agent for PBI and PTFE. Hereafter, the PTFE film pre-treated by the Nafion coupling agent method will be referred to as PTFE-nc.

Li et al. [49] used chemical activation to pretreat and activate the porous PTFE thin film

support. The activated porous PTFE-ca thin film (thickness $\sim 30\text{ }\mu\text{m}$) was immersed in a 1 mg mL^{-1} PBI in DMAc solution for 30 min at $50\text{ }^\circ\text{C}$ and then dried at $100\text{ }^\circ\text{C}$. The final thickness of the PBI/PTFE-ca composite membrane was about $30\text{ }\mu\text{m}$, which was similar to that of the original PTFE thin film support. Figure 12.13a, b shows scanning electron microscopy (SEM) micrographs of the surfaces of porous PTFE thin film and PBI/PTFE-ca composite membrane, respectively [49]. The SEM micrograph of PBI/PTFE-ca composite membrane showed a rough surface (Fig. 12.13b). Since the thickness of the PBI/PTFE-ca composite membrane was similar to that of the PTFE film support, small amounts of microvoids may be present in the composite membrane. This might be the reason for observing a slightly lower OCV in its HT-PEMFC single cell test as discussed in the next section.

Lin et al. [50–53] used Nafion coupling agent to treat porous PTFE thin film support before impregnating PTFE film with PBI solution. They immersed the pretreated porous PTFE-nc thin film (thickness $16\text{ }\mu\text{m}$) in a PBI/LiCl/DMAc (4.5/4.5/100 by wt.) solution and then heated at $80\text{ }^\circ\text{C}$ for 30 min and then $120\text{ }^\circ\text{C}$ under vacuum

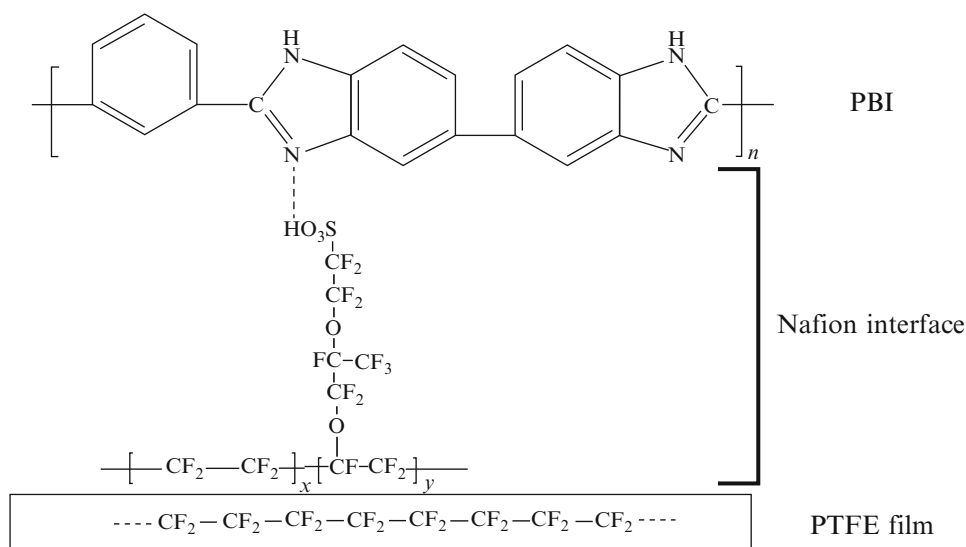
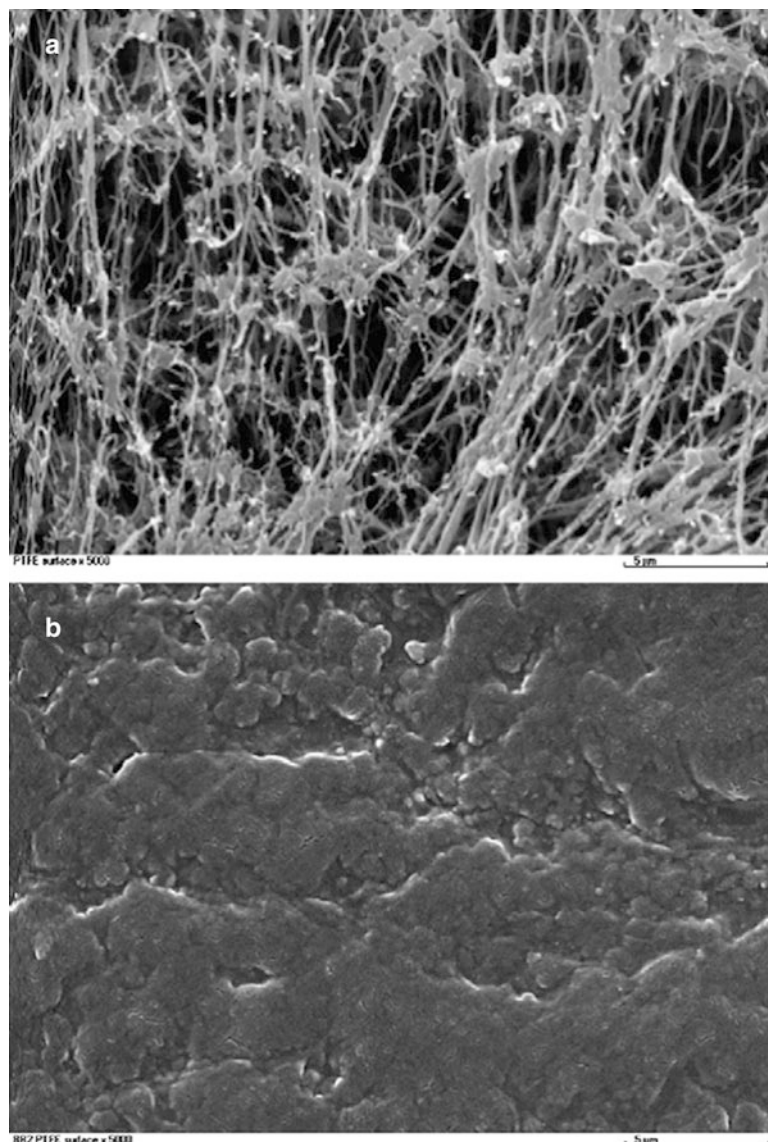


Fig. 12.12 Nafion acting as a coupling agent between PTFE and PBI. The main chain of Nafion is compatible with PTFE and the side chains $-\text{SO}_3\text{H}$ groups of Nafion

interacts with PBI imidazole groups via Lewis acid–base interaction. Reproduced from [53] with permission of Springer

Fig. 12.13 SEM of the surface of PBI/PTFE-ca composite membrane without acid doping and porous PTFE membrane. ((a) top) Surface of PTFE and ((b) bottom) surface of PBI/PTFE-ca. Scale bar 5 μm . The membrane thickness was $\sim 30 \mu\text{m}$. Reproduced from [49] with permission of Elsevier Science Ltd.



for 1 h. The membrane was subsequently immersed in distilled water to remove LiCl to obtain the PBI/PTFE-nc composite membrane. LiCl was mixed into the solution to avoid PBI aggregation in DMAc solutions and to reduce solution viscosity. The [LiCl]/[PBI] weight ratio of the solution was 1/1, which is close to the [LiCl]/[BI] molar ratio of 8/1, i.e., the [LiCl]/[BI] feed molar ratio for the lowest solution viscosity (Fig. 12.6) and smallest PBI particle size (Fig. 12.9) in solution. Lin et al. [36] demonstrated that the PBI/PTFE-nc composite

membrane fabricated using 4.5 wt% PBI in DMAc solution with the concentration of LiCl same as that of PBI (i.e., [LiCl] = 4.5 wt%) has a smooth membrane surface morphology and a higher proton conductivity than those fabricated using 4.5 wt% PBI/DMAc solutions but with different LiCl concentration. A PBI/PTFE-nc membrane with a larger thickness can be obtained by repeated impregnation of the porous PTFE-nc film with a PBI/DMAc solution and solvent evaporation or spray-coating a dilute 1 wt% PBI/DMAc solution onto the surface of

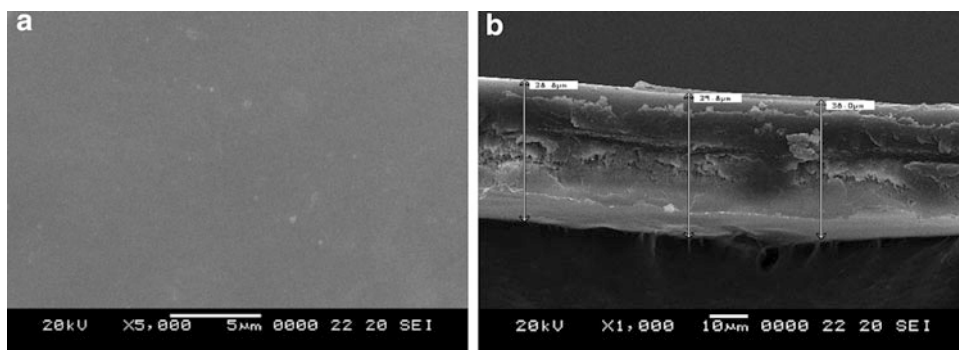


Fig. 12.14 SEM micrographs of PBI/PTFE-nc composite membranes. (a) Plane surface of PBI/PTFE-nc ($\times 5000$; scale bar $5\ \mu\text{m}$), which fabricated using PTFE support pretreated with Nafion coupling agent; (b) cross

section of the same PBI/PTFE-nc membrane ($\times 1000$; scale bar $10\ \mu\text{m}$). The membrane thickness was $38 \pm 2\ \mu\text{m}$. Reproduced from [53] with permission of Springer

Table 12.3 Membrane thickness (L), phosphoric acid dop level (PA_{dop}), proton conductivities (σ), and area specific resistances (L/σ) of PBI/fiber reinforced composite membranes

Membrane	L (μm)	PA_{dop} (wt. %)	$\sigma_{160\ ^\circ\text{C}}$ (S cm^{-1})	$\sigma_{180\ ^\circ\text{C}}$ (S cm^{-1})	RH (%)	L/σ at $160\ ^\circ\text{C}$ ($\Omega\ \text{cm}^2$)	Ref.
PBI/PTFE-ca ^a	30	175	0.10	0.12	8.5	0.030	[49]
PBI	30	175	0.083	0.094	8.5	0.036	[49]
PBI/PTFE-nc ^b	38 ± 2	145	0.014		0.0	0.27	[53]
PBI	80 ± 2	201	0.022		0.0	0.36	[53]
PBI/PBI-PBz-nf	75	420	0.17		0.0	0.044	[68]
PBI	70	398	0.08		0.0	0.088	[68]
QNPSU/PTFE-ca ^a	40	400	0.22	0.33	<0.5	0.018	[69]
PES-PVP/PTFE ^c	40 ± 5	580	0.24	0.27	0.0	0.017	[71]

Thickness of porous PTFE film support: (a) $30\ \mu\text{m}$; (b) $16 \pm 3\ \mu\text{m}$; (c) $13 \pm 5\ \mu\text{m}$

the PBI/PTFE-nc membrane to reach the required thickness. The final thickness of the composite obtained in this way was $38\ \mu\text{m}$. Figure 12.14a, b shows SEM micrographs of the plane surface and cross section, respectively, of the composite membrane [53]. These micrographs demonstrated that all the pores of the porous PTFE were filled with PBI. From the cross-sectional scanning electron micrographs of the PBI/PTFE-nc composite membrane (Fig. 12.14b), it was also found that with the Nafion coupling agent, PBI was well bonded on the fiber of the porous PTFE film.

Before being assembled with gas diffusion electrodes (GDEs), the composite membranes were doped with a phosphoric acid aqueous solution to provide proton conductivity. The membrane thickness (L), phosphoric acid doping level (PA_{dop}), proton conductivity (σ), and the area

specific resistance $r = L/\sigma$ of acid-doped membranes are summarized in Table 12.3. The L , PA_{dop} , σ , and $r = L/\sigma$ data of the neat-PBI membrane obtained by different research groups are also listed in Table 12.3 for comparison. The PA_{dop} data shown in Table 12.3 were estimated using $\text{PA}_{\text{dop}} = [(W_1 - W_0)/W_0]$, where W_0 is the weight of the dry membrane, W_1 the weight of the membrane containing doped phosphoric acid. These data show that the pure PBI membrane had higher conductivity than PBI/PTFE-nc. However, because of the smaller thickness of the PBI/PTFE-nc composite membrane, the PBI/PTFE-nc composite membrane has a lower area specific resistance r than the neat-PBI membrane. The mechanical properties of the PBI/fiber reinforced composite and neat-PBI membranes obtained from literature are also summarized in Table 12.4.

Table 12.4 Mechanical properties at room temperature for PBI/fiber reinforced composite membranes without doping with H₃PO₄

Membrane	<i>L</i> (μm)	Tensile strength (MPa)	Strain at break (%)	Ref.
PBI/PTFE-ca	30	34.7	11.4	[49]
PBI/PBI-PBz-nf	75	115 ± 3	8.8 ± 1.8	[68]
PBI	70	85 ± 6	6.4 ± 1.1	[68]
PES-PVP/PTFE	40 ± 5	39.9	3.9	[71]

12.2.4 Applications of PBI/Porous PTFE Composite Membranes

12.2.4.1 MEA Preparations

The phosphoric acid-doped neat-PBI and PBI/PTFE PEMs were used to prepare MEAs, and high-temperature fuel cell tests were conducted using the prepared MEAs. Most of the GDEs were fabricated by coating a Pt-C/PBI/DMAc ([PBI]/[PBI + Pt-C] = ~5–10 wt %) catalyst solution on a carbon paper and drying it at 120–150 °C under vacuum to evaporate DMAc. The GDE was then doped with 85 wt% phosphoric acid. The phosphoric acid-doped PEM was sandwiched in between the two phosphoric acid-doped GDEs and then pressed to obtain the MEA. The detailed procedures of GDE fabrication and MEA preparation can be obtained in literature [49, 53–60].

12.2.4.2 Single Cell Performance of PBI/PTFE/H₃PO₄ Based MEAs

PBI/PTFE/H₃PO₄ based MEAs, similar to neat-PBI/H₃PO₄ based MEAs, are suitable for high temperature (i.e., 120–200 °C) operation with nonhumidified fuel gases. Li et al. [49] used the same PBI/PTFE-ca composite membranes as listed in Tables 12.3 and 12.4 to perform high temperature single cell tests. Figure 12.15 shows the polarization curves of a PBI/PTFE-ca/H₃PO₄ based MEA obtained at 150 and 170 °C with nonhumidified H₂/O₂ and H₂/air at ambient pressure and at an over-pressure of 1 bar. The fuel cell exhibited good performance at 1 bar over-pressure and the cell performance increased with increasing operating temperature, gas pressure, and oxygen partial pressure. However, the OCVs were rather low, attributed to the fuel gas

crossover by the presence of a small degree of porosity in the composite membrane [49].

Lin et al. [53] used the same PBI/PTFE-nc composite membranes listed in Table 12.3 to perform high temperature single cell tests. Figure 12.16 shows the polarization curves of the single cell tests of neat-PBI (membrane thickness 80 μm) and PBI/PTFE-nc (membrane thickness 38 μm) based MEAs. The OCVs of the neat-PBI and PBI/PTFE-nc based MEAs were around 0.92 V and 0.93 V, respectively, indicating low gas permeation of these two membranes. The PBI/PTFE-nc MEA had a slightly better fuel cell performance than neat PBI MEA due to the lower *L*/ σ of PBI/PTFE-nc membrane as compared to the neat PBI membrane (see Table 12.3).

12.2.4.3 Durability of PBI/PTFE/H₃PO₄ Based MEAs

The durability of the PBI/PTFE-ca/H₃PO₄ and PBI/PTFE-nc/H₃PO₄ based MEAs were investigated by Li and Scott [49] and Lin et al. [53], respectively. Figure 12.17 shows the variation of a single cell voltage during the 50 h intermittent operation at 150 °C under a constant current density $i = 700 \text{ mA cm}^{-2}$ with non-humidified H₂/air without back pressure for a PBI/PTFE-ca/H₃PO₄ based MEA, in which the PBI/PTFE-ca composite membrane was the same as that listed in Tables 12.3 and 12.4. The cell was intermittently operated for periods of 10 h day⁻¹. The results showed a slight decay in the cell voltage after 10 h of operation. The composite membrane showed potential stability during high-temperature fuel cell operation.

Figure 12.18 shows the variation of the OCV and cell voltage as a function of the testing time for the PBI/PTFE-nc/H₃PO₄ based single cell

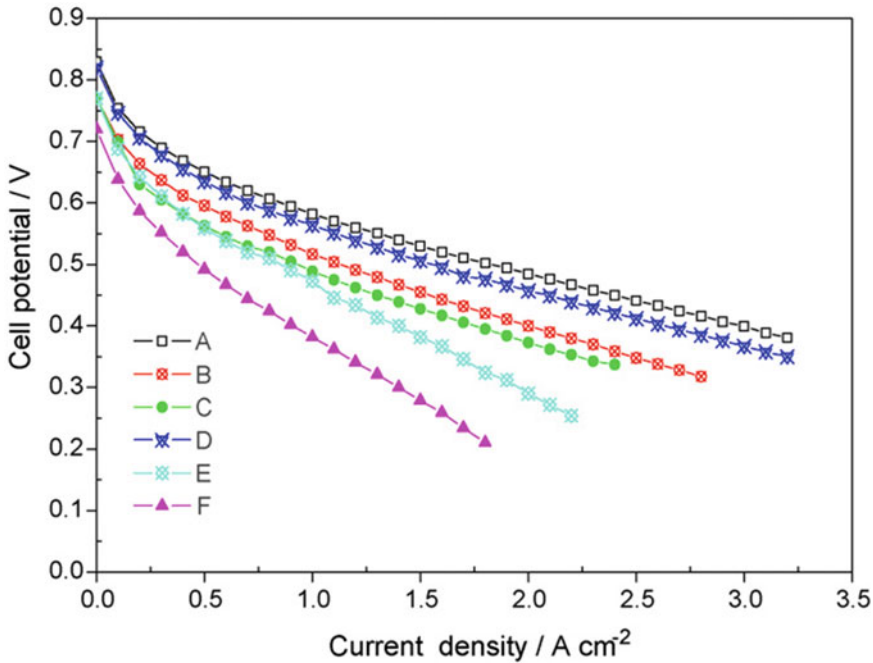


Fig. 12.15 PEMFC polarization curves of a PBI/PTFE-ca/ H_3PO_4 based MEA, in which the PBI/PTFE-ca was the same as that listed in Tables 12.3 and 12.4. Pt loading: cathode 0.81 mg cm^{-2} ; anode 0.81 mg cm^{-2} ; nonhumidified fuel gases. (a) 170°C , 1 bar over-pressure,

H_2 , O_2 ; (b) 170°C , atmospheric pressure, H_2 , O_2 ; (c) 150°C , atmospheric pressure, H_2 , O_2 . (d) 150°C , 1 bar over-pressure, H_2 , O_2 ; (e) 150°C , 1 bar over-pressure, H_2 , air; (f) 150°C , atmospheric pressure, H_2 , air. Reproduced from [49] with permission of Elsevier Science Ltd.

Fig. 12.16 Single cell test i - V curves at 160°C with nonhumidified H_2/O_2 gases for neat-PBI/ H_3PO_4 and PBI/PTFE-nc/ H_3PO_4 based MEAs, in which the PBI/PTFE-nc was the same as that listed in Table 12.3. Pt loading: cathode 1.0 mg cm^{-2} ; anode 1.0 mg cm^{-2} . Membranes of MEAs: (circle) PBI/PTFE-nc (thickness $\sim 38 \mu\text{m}$ before doping with H_3PO_4 , $\text{PA}_{\text{dop}} = 145 \text{ wt\%}$); (triangle) PBI (thickness $\sim 80 \mu\text{m}$ before doping with H_3PO_4 , $\text{PA}_{\text{dop}} = 201 \text{ wt\%}$). Reproduced from [53] with permission of Springer

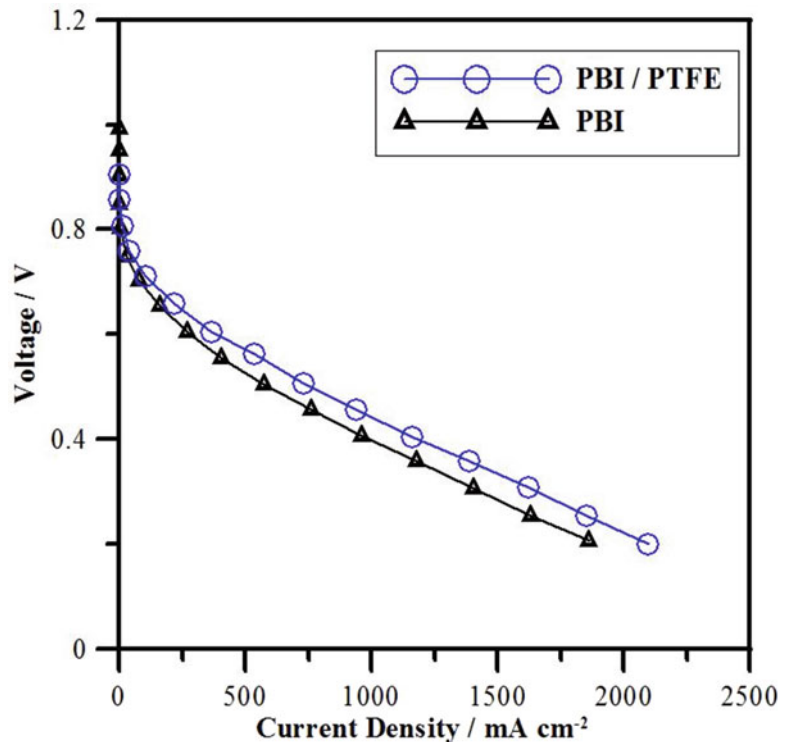


Fig. 12.17 PBI/PTFE-ca/ H_3PO_4 based MEA 50 h single cell life test operated at 150°C under a constant current density of 700 mA cm^{-2} . The cell was operated intermittently for periods of 10 h day^{-1} . Thickness of membrane: $30\text{ }\mu\text{m}$. Pt loading: cathode 0.81 mg cm^{-2} , anode 0.81 mg cm^{-2} . Nonhumidified H_2/air gases. Reproduced from [49] with permission of Elsevier Science Ltd.

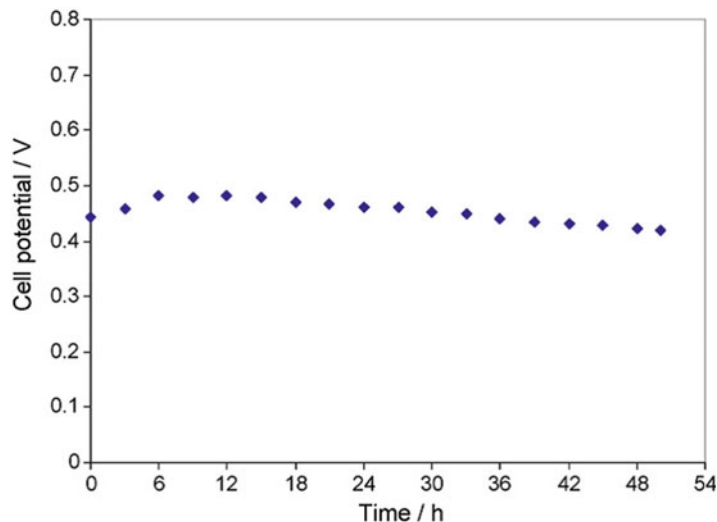
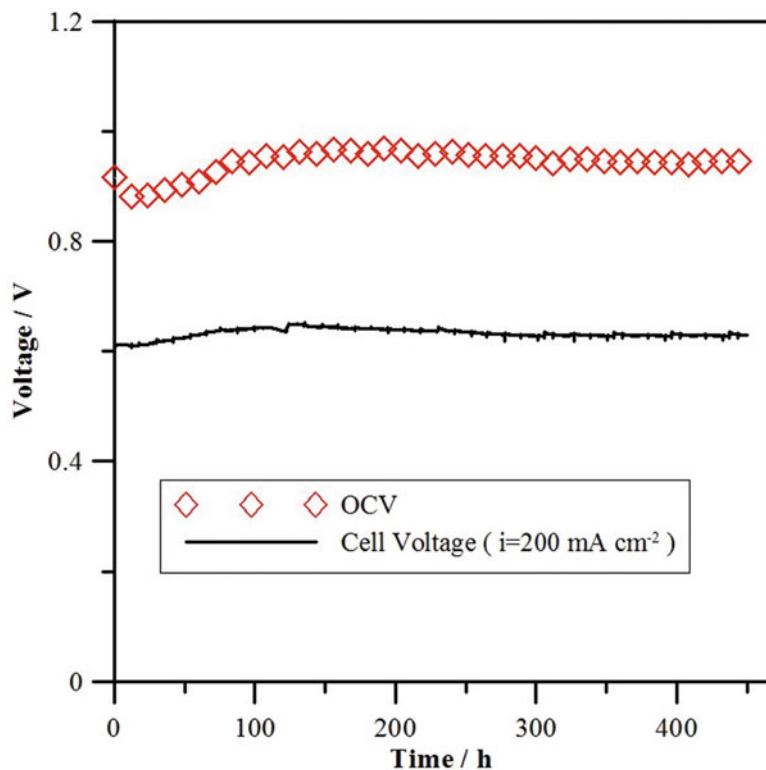


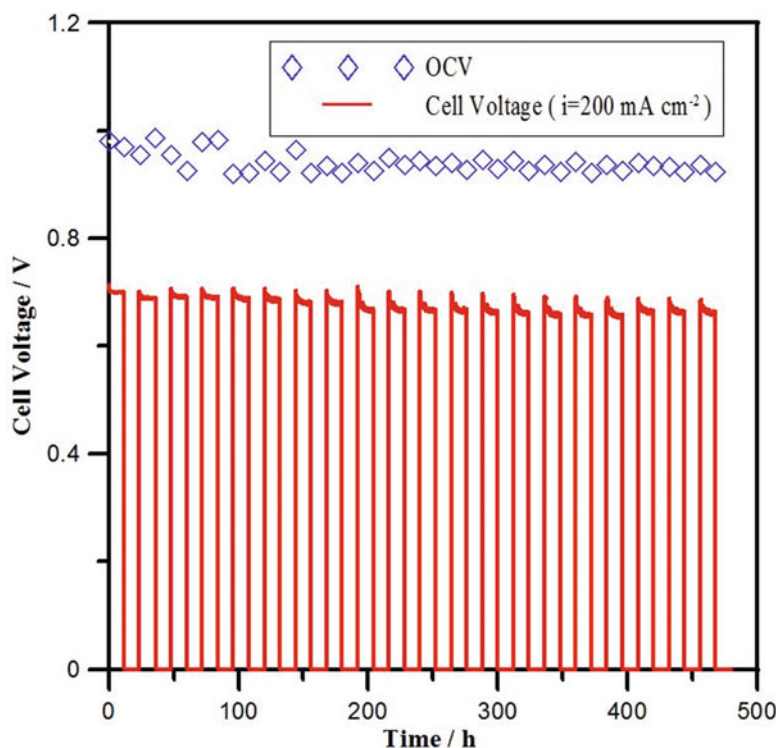
Fig. 12.18 The variation of unit cell voltage and open circuit voltage (OCV) versus testing time of the PBI/PTFE MEA during a 450 h continuous life test under a constant current of $i = 200\text{ mA cm}^{-2}$ and at ambient pressure. (diamond) OCV; (solid line) cell voltage. The temperature was 160°C and the nonhumidified H_2/O_2 flow rates were 200 mL min^{-1} . Reproduced from [53] with permission of Springer



operated at 160°C with a constant current load $i = 200\text{ mA cm}^{-2}$ for 450 h [53]. The PBI/PTFE-nc composite membrane used in this life test was the same membrane as that listed in Table 12.3. The cell voltage increased from

0.64 to 0.67 V during the first 96 h of the test, which is similar to that observed for the neat-PBI/ H_3PO_4 based PEMFC and is the so-called activation region [61–66]. The improvement in the fuel cell performance in the “activation

Fig. 12.19 PBI/PTFE-nc/ H_3PO_4 based PEMFC start/stop cycling test. For each cycle of the test, the cell was operated at 160°C with a constant $i = 200 \text{ mA cm}^{-2}$ for 12 h, and then switched off and cooled to room temperature and kept at an $i = 0.0 \text{ mA cm}^{-2}$ for 12 h. Reproduced from [53] with permission of Springer



region” was attributed to the better contact of the membrane with the catalyst layers due to the pressure of the end plates at high temperature and the rearrangement and optimization of the catalyst layer microstructure for the electrochemical reaction [61, 67]. The cell voltage did not significantly change in the time period of 96–140 h. However, it fell from 0.67 to 0.65 V in the time period of 140–450 h. The cross-sectional morphology of PBI/PTFE-nc/ H_3PO_4 based MEA before and after the 450 h continuous life test was investigated by SEM and energy dispersive spectroscopy (EDS) analyses, which showed good lamination between the PBI/PTFE-nc membrane and anode and cathode catalyst layers and well distribution of Pt catalyst and phosphoric acid in the MEA after 450 h operation at 160°C [53]. Lin et al. [53] conducted single cell start/stop cycling tests for PBI/PTFE-nc/ H_3PO_4 based MEA to investigate its stability. For each cycle of the test, the cell was operated at 160°C with a constant $i = 200 \text{ mA cm}^{-2}$ for 12 h, and then switched off and cooled to room temperature at $i = 0.0 \text{ mA cm}^{-2}$ for 12 h. Figure 12.19 shows the variations of the cell voltage

and OCV against the testing time. Similar to the results of 450 h continuous life test, the start/stop cycling test also exhibited an almost constant cell voltage during the operation of the first 6 start/stop cycles. After the first 6 start/stop cycles, the cell voltage was slightly decreased with a decay rate of $1.08 \times 10^{-4} \text{ V h}^{-1}$ (from 144 to 456 h) or $2.5 \times 10^{-3} \text{ V}$ per cycle from the 6th cycle to the 20th cycle. All these results demonstrated potential stability of the composite membrane for high-temperature fuel cells.

12.3 Other Reinforced Polymer Composite Membranes

12.3.1 Crosslinked Polybenzimidazole-Polybenzoxazine Electrospun Nano-fibers

Similar to the preparation of Nafion/nano-fiber composite PEMs using electro-spun PVdF [23, 24], PVdF-co-HFP [25], and PVA nano-fiber films [26–31] as supporting films for impregnating Nafion ionomer solutions, the

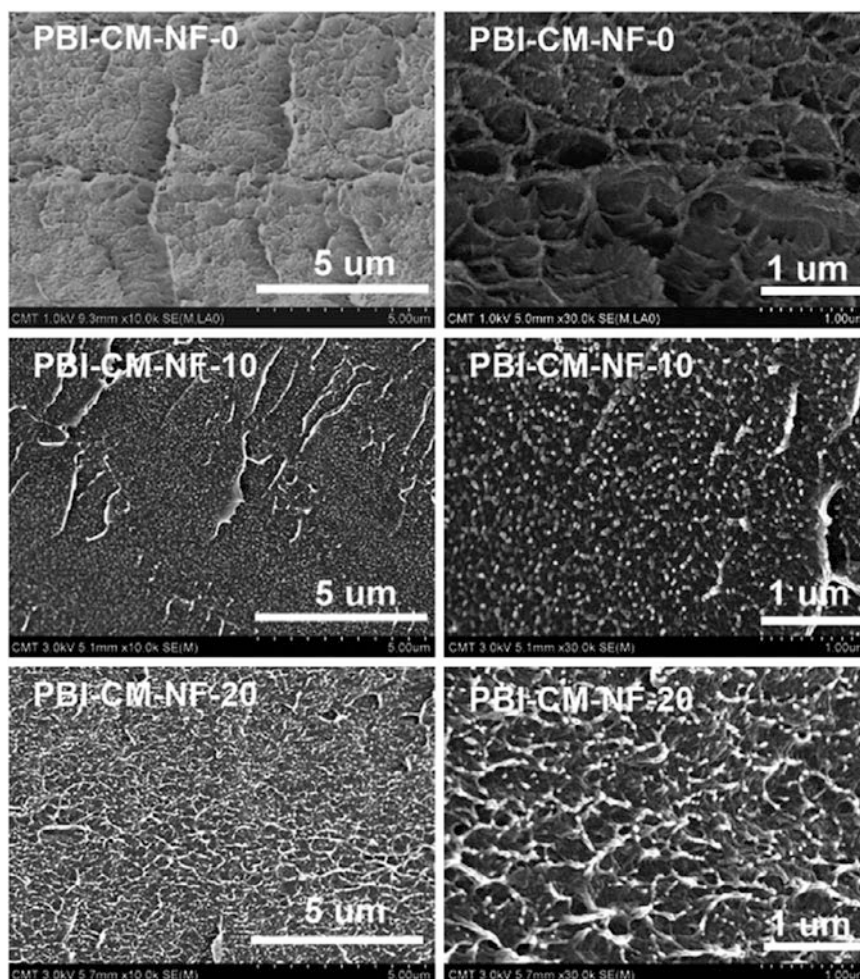


Fig. 12.20 SEM micrographs of PBI/PBI-PBz-f composite membranes. Each membrane consisted of 75 wt% PBI and 25 wt% PBI-PBz-f fiber film with different amounts of the PBz crosslinking agent. (top) PBI-CM-NF-0, the PBI-PBz-f fiber of PBI/PBI-PBz-f composite membrane contained 0 wt% of PBz; (middle) PBI-CM-

NF-10, the PBI-PBz-f fiber of PBI/PBI-PBz-f composite membrane contained 10 wt% of PBz; (bottom) PBI-CM-NF-20, the PBI-PBz-f fiber of PBI/PBI-PBz-f composite membrane contained 20 wt% of PBz. Reproduced from [68] with permission of the Royal Society of Chemistry

crosslinked polybenzimidazole-polybenzoxazine (PBI-PBz) electrospun nano-fiber (PBI-PBz-f) was also prepared by Li and Liu [68] for impregnation with PBI/DMAc solution to prepare PBI-PBz fiber reinforced PBI (PBI/PBI-PBz-f) composite membranes for high temperature PEMFCs. Since the PBI nano-fiber is soluble in DMAc, the crosslinked PBI-PBz nano-fiber film was prepared by blending PBz (which is a crosslinking agent of PBI) into a PBI/DMAc solution to perform electrospinning, and then

the electrospun fiber film was crosslinked by heat treatment at 140–200 °C to obtain a crosslinked PBI-PBz-f film. The crosslinked PBI-PBz-f nano-fiber film, which was insoluble, was then impregnated with PBI/DMAc solution, followed by solvent evaporation to obtain PBI/PBI-PBz-f composite membranes.

Figure 12.20 shows SEM micrographs of the PBI/PBI-PBz-f composite membranes, in which each membrane contained 75 wt% of PBI and with 25 wt% of the PBI-PBz-f fiber film for

Table 12.5 Single cell PEMFC performance current density i (at 0.6 V and at 0.4 V) of MEAs prepared from various membranes

Membrane	Pt loading (mg cm^{-2})	i at 0.6 V (mA cm^{-2})	i at 0.4 V (mA cm^{-2})	Temperature ($^{\circ}\text{C}$)	Fuel	Back pressure	Ref.
PBI/PBI-PBz-nf	0.48	396	1450	150	H_2/O_2	None	[68]
QNPSU/PTFE	0.58	394	1460	175	H_2/O_2	2 atm	[69]
PES-PVP/PTFE	0.50	314	1620	180	H_2/O_2	None	[71]
PBI/PTFE	0.81	600	3000	170	H_2/O_2	1 bar	[49]
PBI/PTFE	1.0	395	1180	160	H_2/O_2	None	[53]

reinforcement. These micrographs showed that the composite membrane fabricated using the PBI-PBz electrospun fiber film containing 10 wt % of PBz crosslinker had a smooth surface (Fig. 12.20, middle row micrographs). The SEM micrographs (Fig. 12.20, top row micrographs) of the PBI/PBI-f composite membrane, which was fabricated using a neat-PBI electrospun fiber without containing PBz crosslinker, revealed voids present in the membrane, due to the dissolution of the non-crosslinked electrospun PBI fiber during the impregnation. On the other hand, the SEM micrographs (Fig. 12.20, bottom row micrographs) showed a rough surface of the PBI/PBI-PBz-f composite membrane, which was fabricated using PBI-PBz electrospun fiber containing 20 wt% PBz crosslinker. The highly crosslinked PBI-PBz fiber was visible on the surface of the PBI/PBI-PBz-f composite membrane (Fig. 12.20, bottom row micrographs).

The PBI/PBI-PBz-f (thickness $\sim 75 \mu\text{m}$) composite membrane containing 20 wt% of the PBI-PBz electrospun nano-fiber, of which 10 wt % was the PBz crosslinker, was doped with a phosphoric acid aqueous solution followed by MEA preparation to perform high-temperature fuel cell tests. The phosphoric acid doping level and proton conductivity, membrane mechanical properties, and fuel cell performance of this PBI/PBI-PBz-f composite are listed in Tables 12.3, 12.4, and 12.5, respectively. The data for neat PBI are given for comparison. The PBI/PBI-PBz-f composite membrane showed higher PA_{dop} and σ , higher mechanical strength and strain at break, and better fuel cell performance than the neat-PBI membrane. Compared to the hydrophobic porous PTFE film, the

PBI-PBz crosslinked nano-fiber film, which is composed of imidazole functional groups, has advantages of more coordinating sites for interaction with H_3PO_4 . Thus the PBI/PBI-PBz-f composite membrane had higher PA_{dop} and σ than the PBI/PTFE composite membrane. Li and Liu [68] used a PBI/PBI-PBz-f composite membrane (thickness $75 \mu\text{m}$), which was thicker than a neat-PBI membrane (thickness $70 \mu\text{m}$) for high temperature PEMFC test. We expect that the PEMFC performance can be further increased by using a thinner PBI/PBI-PBz-f composite membrane for MEA preparation. Unfortunately, Li and Liu did not report durability test data. Further, more investigation of the durability of the PBI/PBI-PBz-f composite membrane for high temperature PEMFC applications would be of great interest for this composite membrane.

12.3.2 Other Polyelectrolytes Reinforced with Porous PTFE Film Support

The conventional phosphoric acid fuel cell (PAFC), which is operated at high temperatures ranging $150\text{--}220 \text{ }^{\circ}\text{C}$, has suffered limitations connected to the poor immobilization in matrices. The problem of immobilization of H_3PO_4 was solved by doping it into PBI, in which H_3PO_4 is physically absorbed. Recent reports have shown that quaternized polysulfone (QNPSU) [69, 70] and poly(ether sulfone)/poly(vinyl pyrrolidone) (PES/PVP) blend [71] membranes are also suitable for doping H_3PO_4 and HT-PEMFC applications. The reinforcement of these polymers using porous PTFE film support has also been reported in literature [69, 71].

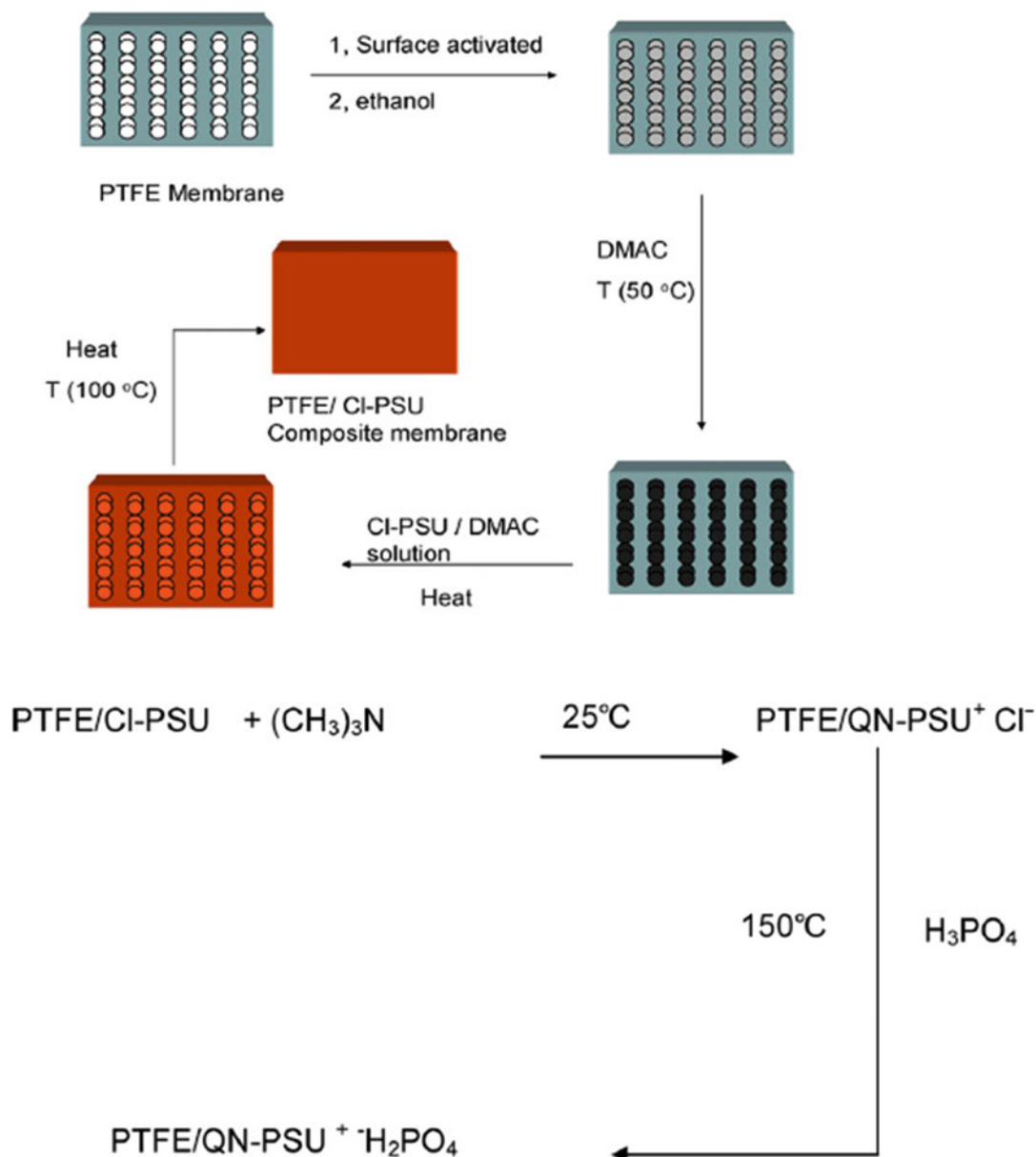


Fig. 12.21 Preparation procedure scheme for QNPSU/PTFE composite membrane. Reproduced from [69] with permission of Elsevier Science Ltd.

The porous PTFE reinforced QNPSU (QNPSU/PTFE) composite membrane was prepared by surface activation of porous PTFE (thickness 30 μm) as described in Sect. 12.2.3 [69]. The activated PTFE-ca was used for preparing the QNPSU/PTFE-ca composite membrane following the scheme as shown in Fig. 12.21.

The activated PTFE-ca was immersed in a solution (1 mg mL^{-1}) of chloromethylated PSU (Cl-PSU) in DMAc at 50 °C for 30 min and then dried at 100 °C. The Cl-PSU/PTFE-ca membrane was then immersed in $\text{N}(\text{CH}_3)_3$ solution at 25 °C for 7 days to form the QNPSU/PTFE-ca composite membrane (thickness $\sim 40 \mu\text{m}$)

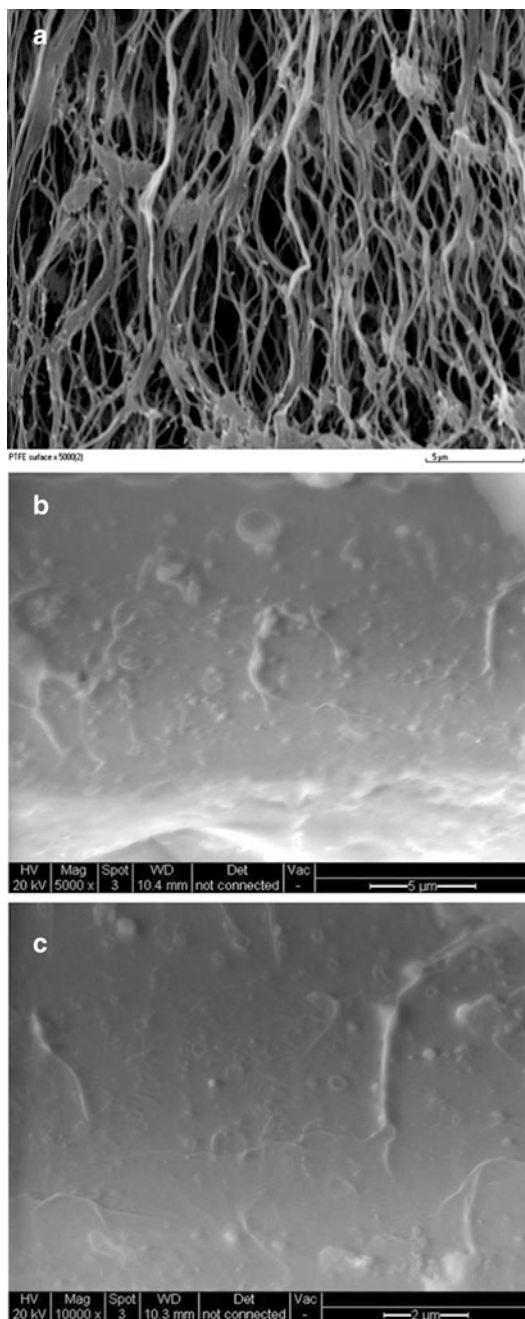


Fig. 12.22 SEM micrograph of Cl-PSU/PTFE composite membrane. (a) plane surface of porous PTFE membrane; (b) and (c) the cross section of Cl-PSU/PTFE composite membrane. Reproduced from [69] with permission of Elsevier Science Ltd.

[69]. The SEM micrograph of the cross section of the Cl-PSU/PTFE showed a dense structure in which the Cl-PSU was uniformly distributed

(Fig. 12.22). The membrane was immersed in phosphoric acid at 150 °C and to give a H_3PO_4 doping level of 400 wt%. The PA_{dop} and conductivities of the membrane at temperatures of 120, 140, and 160 °C with a relative humidity less than 0.5 % were recorded as summarized in Table 12.3. The fuel cell performance at 175 °C under 2 atm back pressure with nonhumidified H_2/O_2 fuel gases is listed in Table 12.5.

Polyvinylpyrrolidone (PVP), which contains a *N*-heterocycle, is also suitable for H_3PO_4 doping. However, the high hydrophilicity and brittleness limit its applications. The blending of PVP with PSU and reinforcement with hydrophobic and high mechanical strength porous PTFE can solve these problems. The porous PTFE reinforced PES/PVP blend membrane was prepared by impregnating the porous PTFE thin film (thickness $\sim 13 \pm 5 \mu m$) with PES/PVP (1/4 by weight ratio) dissolved in *N,N*-dimethylformamide (DMF) (5 wt% and 5 wt% Triton surfactant). Before impregnation, the PTFE film was soaked with ethanol for 30 min at room temperature. The final thickness of the PES-PVP/PTFE composite membrane was $\sim 40 \pm 5 \mu m$. The membrane was immersed in 85 wt% phosphoric acid at room temperature for 24 h. The PA_{dop} and conductivities of the membrane at 160 and 180 °C and relative humidity less than 0.5 % are also summarized in Table 12.3. The fuel cell performance at 180 °C and ambient pressure with nonhumidified H_2/O_2 fuel gases is also listed in Table 12.5.

12.4 Summary

Compared with Nafion/porous PTFE and Nafion/electrospun nano-fiber composite membranes, there are few reports of PBI/porous PTFE and PBI/electrospun nano-fiber composite membrane for high temperature PEMFC application. The PBI/porous PTFE composite membrane was shown to exhibit excellent mechanical strength and good durability, which allowed researchers to reduce the membrane thickness and thus reduce the area specific resistance and ultimately improve fuel cell performance. After the report of PBI/porous PTFE composite membrane, two

main groups of polyelectrolyte/fiber reinforced composite membranes were reported. One was the PBI reinforced with the phosphoric acid compatible nano-fiber film (i.e., crosslinked PBI-PBz electrospun nano-fiber film), which was proton conductive and had higher conductivity than the hydrophobic porous PTFE film. The second was using the high mechanical strength porous PTFE film to reinforce highly conductive polyelectrolytes with inherently low mechanical strength (i.e., QNPSU/PTFE and PES-PVP/PTFE composite membranes). The durability of these composite membranes has not been reported. However, the two concepts, i.e., PBI reinforced with the phosphoric acid compatible nano-fiber film and highly conductive polyelectrolyte reinforced with a high mechanical strength nano-fiber film, are interesting topics for a future research work.

References

1. Ukihashi H, Asawa T, Gunjima T (1980) Cation exchange membrane of fluorinated polymer containing polytetrafluoroethylene fibrils for electrolysis and preparation thereof. US Patent 4,218,542
2. Penner RM, Martin CR (1985) Ion-transporting composite membranes. I. Nafion-impregnated Gore-Tex membranes. *J Electrochem Soc* 132:514–515
3. Liu C, Martin CR (1990) Ion-transporting composite membranes. II. Ion transport mechanism in Nafion-impregnated Gore-Tex membranes. *J Electrochem Soc* 137:510–517
4. Bahar B, Hobson AR, Kolde JA (1996) Ultra-thin film integral composite membrane. US Patent 5,547,551
5. Kolde JA, Bahar B, Wilson MS et al (1995) Advanced composite polymer electrolyte fuel cell membranes. Proceedings of the first international symposium on proton conducting membrane fuel cells I. *Electrochem Soc Proc* 95–23:193–201
6. Liu F, Yi B, Xing D et al (2003) Nafion/PTFE composite membranes for fuel cell applications. *J Membr Sci* 212:213–223
7. Lin HL, Yu TL, Shen KS et al (2004) Effect of Triton-X on the preparation of Nafion/PTFE composite membranes. *J Membr Sci* 237:1–7
8. Yu TL, Lin HL, Shen KS et al (2004) Nafion/PTFE composite membranes for fuel cell applications. *J Polym Res* 11:217–224
9. Lin HL, Yu TL, Huang LN (2005) Nafion/PTFE composite membranes for direct methanol fuel cell applications. *J Power Sources* 150:11–19
10. Huang LN, Chen LC, Yu TL et al (2006) Nafion/PTFE/silicate composite membranes for direct methanol fuel cells. *J Power Sources* 161:1096–1105
11. Wang L, Xing DM, Liu YH et al (2006) Pt/SiO₂ catalyst as an addition to Nafion/PTFE self-humidifying composite membrane. *J Power Sources* 161:61–67
12. Zhang Y, Zhang H, Zhu X et al (2007) Fabrication and characterization of a PTFE-reinforced integral composite membrane for self-humidified PEMFC. *J Power Sources* 165:786–792
13. Tang H, Pan M, Jiang SP et al (2007) Fabrication and characterization of PFSI/ePTFE composite proton exchange membranes of polymer electrolyte fuel cells. *Electrochim Acta* 52:5304–5311
14. Lin HL, Chang TJ (2008) Preparation of Nafion/PTFE/Zr(HPO₄)₂ composite membranes by direct impregnation. *J Membr Sci* 325:880–886
15. Chen LC, Yu TL, Lin HL et al (2008) Nafion/PTFE and zirconium phosphate modified Nafion/PTFE composite membranes for direct methanol fuel cells. *J Membr Sci* 307:10–20
16. Lin HL, Yeh SH, Yu TL et al (2009) Silicate and zirconium phosphate modified Nafion/PTFE composite membranes for high temperature PEMFC. *J Polym Res* 16:519–527
17. Jung GB, Weng FB, Su A et al (2008) Nafion/PTFE/silicate membranes for high-temperature proton exchange membrane fuel cells. *Int J Hydrogen Energy* 33:2413–2417
18. Jao TC, Ke ST, Chi PH et al (2010) Degradation on a PTFE/Nafion membrane electrode assembly with accelerating degradation technique. *Int J Hydrogen Energy* 35:6941–6949
19. Yang L, Li H, Ai F et al (2013) A new method to prepare high performance fluorinated sulfonic acid ionomer/porous expanded polytetrafluoroethylene composite membranes based on perfluorinated sulfonyl fluoride polymer solution. *J Power Sources* 243:392–396
20. Xing D, He G, Hou Z et al (2013) Properties and morphology of Nafion/polytetrafluoroethylene composite membrane fabricated by a solution-spray process. *Int J Hydrogen Energy* 38:8400–8408
21. Hakan Yildirim M, Stamatialis D, Wessling M (2008) Dimensionally stable Nafion-polyethylene composite membranes for direct methanol fuel cell applications. *J Membr Sci* 321:364–372
22. Cho MS, Son HD, Nam JD et al (2006) Proton conducting membrane using multi-layer acid-base complex formation on porous PE film. *J Membr Sci* 284:155–160
23. Choi SW, Fu YZ, Ahn YR et al (2008) Nafion-impregnated electrospun polyvinylidene fluoride composite membrane for direct methanol fuel cells. *J Power Sources* 180:167–171
24. Jang WG, Hou J, Byun HS (2011) Preparation and characterization of PVdF nanofiber ion exchange membrane for the PEMFC application. *Desalination Water Treat* 34:315–320

25. Wei X, Yates MZ (2010) Control of Nafion/poly(vinylidene fluoride-co-hexafluoropropylene) composite membrane microstructure to improve performance in direct methanol fuel cells. *J Electrochem Soc* 157:B522–B528
26. Lin HL, Wang SH, Chiu CK et al (2010) Preparation of Nafion/poly(vinyl alcohol) electro-spun fiber composite membranes for direct methanol fuel cells. *J Membr Sci* 365:14–122
27. Molla S, Compan V, Lafuente SL (2011) On the methanol permeability through pristine nafion and PVA membranes measured by different techniques. A comparison of methodologies. *Fuel Cells* 11:897–906
28. Molla S, Compan V, Gimenez E et al (2011) Novel ultrathin composite membranes of Nafion/PVA for PEMFCs. *Int J Hydrogen Energy* 36:11025–11033
29. Molla S, Compan V (2011) Polyvinyl alcohol nanofiber reinforced nafion membranes for fuel cell applications. *J Membr Sci* 372:191–200
30. Molla S, Compan V (2011) Performance of composite Nafion/PVA membranes for direct methanol fuel cells. *J Power Sources* 196:2699–2708
31. Lin HL, Wang SH (2014) Nafion/poly(vinyl alcohol) nano-fiber composite and Nafion/poly(vinylalcohol) blend membranes for direct methanol fuel cells. *J Membr Sci* 452:253–262
32. Shao ZG, Wang X, Hsing IM (2002) Composite Nafion/poly(vinyl alcohol) membranes for direct methanol fuel cell. *J Membr Sci* 210:147–153
33. Xu W, Liu C, Xue X et al (2004) New proton exchange membranes based on poly(vinyl alcohol) for DMFCs. *Solid State Ion* 171:121–127
34. DeLuca NW, Elabd YA (2006) Nafion/poly(vinyl alcohol) blends: effect of composition and annealing temperature on transport properties. *J Membr Sci* 282:217–224
35. DeLuca NW, Elabd YA (2006) Direct methanol fuel cell performance of Nafion/poly(vinyl alcohol) blend membranes. *J Power Sources* 163:386–391
36. Lin HL, Chen YC, Li CC et al (2008) Preparation of PBI/PTFE composite membranes from PBI in N,N'-dimethyl acetamide solutions with various concentrations of LiCl. *J Power Sources* 181:228–236
37. Ma YL, Wainright JS, Litt M et al (2004) Conductivity of PBI membranes for high-temperature polymer electrolyte fuel cells. *J Electrochem Soc* 151:A8–A16
38. Li Q, Hjuler HA, Bjerrum NJ (2001) Phosphoric acid doped polybenzimidazole membranes: physiochemical characterization and fuel cell applications. *J Appl Electrochem* 31:773–779
39. Conciatori AB, Smart CL (1970) Production of shaped PBI articles. US Patent 3,502,606
40. Samms SR, Wasmus S, Savinell RF (1996) Thermal stability of proton conducting acid doped polybenzimidazole in simulated fuel cell environments. *J Electrochem Soc* 143:1225–1232
41. Li Q, He R, Jensen JO et al (2004) PBI-based polymer membranes for high temperature fuel cells—preparation, characterization and fuel cell demonstration. *Fuel Cells* 4:147–159
42. Lobato J, Cañizares P, Rodrigo MA et al (2006) Synthesis and characterization of poly[2,2-(m-phenylene)-5,5-benzimidazole] as polymer electrolyte membrane for high temperature PEMFCs. *J Membr Sci* 280:351–362
43. Kim TH, Lim TW, Lee JC (2007) High-temperature fuel cell membranes based on mechanically stable para-ordered polybenzimidazole prepared by direct casting. *J Power Sources* 172:172–179
44. Kojima T, Yokota R, Kochi M et al (1980) Dilute solution properties of a polybenzimidazole. *J Polym Sci Part B* 18:1673–1684
45. Kojima T (1980) Studies of molecular aggregation of a polybenzimidazole in solution by fluorescence spectroscopy. *J Polym Sci Part B* 18:1685–1695
46. Shogbon CB, Brousseau JL, Zhang H et al (2006) Determination of the molecular parameters and studies of the chain conformation of polybenzimidazole in DMAc/LiCl. *Macromolecules* 29:9409–9418
47. Hara M (1993) Polyelectrolyte in nonaqueous solution. In: Hara M (ed) *Polyelectrolytes—science and technology*. Marcel Dekker, New York (Chap. 4)
48. Dautzenberg H, Jaeger W, Kotz J et al (1994) *Polyelectrolytes—formation, characterization and application*. Hanser, Munich (Chap. 5)
49. Li M, Scott K (2010) A polymer electrolyte membrane for high temperature fuel cells to fit vehicle applications. *Electrochim Acta* 55:2123–2128
50. Lin HL, Yu TL, Chang WK et al (2007) Preparation of a low proton resistance PBI/PTFE composite membrane. *J Power Sources* 164:481–487
51. Lin HL, Hsieh YS, Chiu CW et al (2009) Durability and stability test of proton exchange membrane fuel cells prepared from PBI/PTFE composite membrane. *J Power Sources* 193:170–174
52. Yu TL, Lin HL (2009) Preparation of PBI/H₃PO₄-PTFE composite membranes for high temperature fuel cells. *Open Fuels Ener Sci J* 2:129–135
53. Lin HL, Huang JR, Chen YT et al (2012) Polybenzimidazole/poly(tetrafluoro ethylene) composite membranes for high temperature proton exchange membrane fuel cells. *J Polym Res* 19:9875–9878
54. Su H, Pasupathi S, Bladergoen B et al (2013) Optimization of gas diffusion electrodes for polybenzimidazole-based high temperature proton exchange membrane fuel cell: evaluation of polymer binders in catalyst layer. *Int J Hydrogen Energy* 38:11370–11378
55. Mazur P, Soukup J, Paidar M et al (2011) Gas diffusion electrodes for high temperature PEM-type fuel cells: role of a polymer binder and method of the catalyst layer deposition. *J Appl Electrochem* 41:1013–1019

56. Lobato J, Cañizares P, Rodrigo MA et al (2010) Study of the influence of the amount of PBI- H_3PO_4 in the catalyst layer of a high temperature PEMFC. *Int J Hydrogen Energy* 35:2513–2530
57. Mamlouk M, Scott K (2010) The effect of electrode parameters on performance of a phosphoric acid-doped PBI membrane fuel cell. *Int J Hydrogen Energy* 35:784–793
58. Matar S, Higer A, Liu H (2010) The effects of excess phosphoric acid in a polybenzimidazole-based high temperature proton exchange membrane fuel cell. *J Power Sources* 195:12–15
59. Su PH, Lin HL, Lin YP et al (2013) High temperature membrane electrode assembly catalyst layer preparation using various molecular weight polybenzimidazole binders. *Int J Hydrogen Energy* 38:13742–13753
60. Su PH, Cheng J, Li JF et al (2014) High temperature polybenzimidazole membrane electrode assemblies using pyridine-polybenzimidazole as catalyst layer binder. *J Power Sources* 260:131–139
61. Hu J, Zhang H, Zhai Y et al (2006) 500 h continuous aging life test on PBI/ H_3PO_4 high-temperature PEMFC. *Int J Hydrogen Energy* 31:1855–1862
62. Xiao L, Zhang H, Scanlon E et al (2005) High-temperature polybenzimidazole fuel cell membranes via a sol-gel process. *Chem Mater* 17:5328–5333
63. Liu G, Zhang H, Hu J et al (2006) Studies of performance degradation of a high temperature PEMFC based on H_3PO_4 -doped PBI. *J Power Sources* 162:547–552
64. Zhai Y, Zhang H, Liu G et al (2007) Degradation study on MEA in H_3PO_4 /PBI high-temperature PEMFC life test. *J Electrochem Soc* 154:B72–B76
65. Schmidt T, Baurmeister J (2008) Properties of high-temperature PEMFC Celtec-P 1000 MEAs in start/stop operation mode. *J Power Sources* 176:428–434
66. Li Q, Jensen JO, Savinell RF et al (2009) High temperature proton exchange membranes based on polybenzimidazoles for fuel cells. *Prog Polym Sci* 34:449–477
67. Boaventura M, Mendes A (2010) Activation procedures characterization of MEA based on phosphoric acid doped PBI membranes. *Int J Hydrogen Energy* 35:11649–11660
68. Li HY, Liu YL (2013) Polyelectrolyte composite membranes of polybenzimidazole and crosslinked polybenzimidazole-polybenzoxazine electrospun nanofibers for proton exchange membrane fuel cells. *J Mat Chem A* 1:1171–1178
69. Li M, Scott K (2011) A polytetrafluoroethylene/quaternized polysulfone membrane for high temperature polymer electrolyte membrane fuel cells. *J Power Sources* 196:1894–1898
70. Li M, Scott K, Wu X (2009) A poly($R_1R_2R_3-N^+$)/ H_3PO_4 composite membrane for phosphoric acid polymer electrolyte membrane fuel cells. *J Power Sources* 194:811–814
71. Lu S, Xiu R, Xu X et al (2014) Polytetrafluoroethylene (PTFE) reinforced poly(ether sulfone)-poly(vinyl pyrrolidone) composite membrane for high temperature fuel cells. *J Membr Sci* 464:1–7

José J. Linares, Liliane C. Battirola, and Justo Lobato

13.1 Introduction

Over the last century, many investigations were devoted to the development of various components of polymer electrolyte membrane fuel cell (PEMFC): gas diffusion layer, bipolar plates, microporous layer, catalyst, and membranes. The research activities have been focused their interest towards the development of polymer electrolyte membranes, as they are considered the heart of the PEMFCs. Significant advances in the field of low temperature PEMFC (LT-PEMFC), also known as Nafion-based PEMFC, have been recently reached [1]. However, as stated in this book, there are many disadvantages of using this system, which can be overcome working with high temperature PEMFC, HT-PEMFC (HT: high temperature, 100–200 °C). Obviously, these high temperatures require new type of materials and one

of them is the *ortho*-phosphoric acid-doped polybenzimidazole (PBI) membranes [2].

The aims of the research efforts have been focused in the development of novel membrane materials in order to increase the performance and durability, and to reduce the overall cost of fuel cells [3]. Table 13.1 summarizes the main features that the membranes must address in future for an 80 kW PEMFC system running with direct hydrogen [4]. The membrane must act as a barrier to gas transport and as a mechanical separator between anode and cathode; it must act as an ionic conductor and an electronic insulator; it must be made using materials and processes that are inexpensive; and it must last for thousands of hours in a corrosive environment containing oxygen, peroxides, and Pt-based catalysts. Although the DOE (United State Department of Energy) target temperature is 120 °C, many researchers are working at higher temperatures in order to increase the CO tolerance of the electrocatalysts [5]. Moreover, HT-PEMFCs that utilize a PBI membrane, which operates at temperatures between 150 and 200 °C, are an ideal option for a micro-CHP (combined heat and power) system. This is due to the faster kinetics of the electrochemical reactions, the easier water managements, the simplification of the cooling system, the recovery of useful heat, and the opportunity of usage of lower quality reformed [6].

J.J. Linares
Instituto de Química, Universidade de Brasília,
Campus Universitário Darcy Ribeiro CP 4478, Brasília,
DF 70910-900, Brazil

L.C. Battirola
Instituto de Química, Universidade de Campinas, Campus
Universitário CP 6154, Campinas, SP 13083-970, Brazil

J. Lobato (✉)
Chemical Engineering Department, Universidad de
Castilla-La Mancha, Av. Camilo José Cela 12,
Ciudad Real 13071, Spain
e-mail: justo.lobato@uclm.es

Table 13.1 The U.S. Department of Energy (DOE) membrane targets for an 80 kW_e (net) integrated transportation fuel cell power system operating on direct hydrogen

Characteristic	Units	2011 ^a	2017 (Targets)	2020 (Targets)
Maximum hydrogen crossover ^b	mA cm ⁻²	<1.8	2	2
Maximum oxygen crossover ^b	mA cm ⁻²	1	2	2
Area specific proton resistance:	Ω cm ⁻²			
At 120 °C and water partial pressures from 40–80 kPa		0.023 (40 kPa)	0.02	0.02
		0.012 (80 kPa)		
At 80 °C and water partial pressures from 25–45 kPa		0.017 (25 kPa)	0.02	0.02
		0.006 (44 kPa)		
At -20 °C		0.1	0.2	0.2
Operating temperature	°C	<120	≤120	≤120
Cost ^c	\$ m ⁻²	–	20	20
Durability ^d :	Cycles with <10 scem crossover hours			
Mechanical		>20,000	>20,000	>20,000
Chemical		>2300	>500	>500

^aStatus represents PFSA membrane

^bTested in MEA at 1 atm O₂ or H₂ at nominal stack operating temperature, humidified gases at 0.5 V DC

^cCosts projected to high-volume production (500,000 stacks per year)

^dBased on U.S. DRIVE Fuel Cell Tech Team Cell Component Accelerated Stress Test as described in [7]

Generally, the proton exchange membranes are comprised of the polymer backbone, the side chains and any filler or support materials that have been added, and a proton carrier, which is either water or an ionic carrier, such as phosphoric acid (PA) or an ionic liquid (IL), such as H-3-methylimidazolium bis(trifluoromethanesulfonyl)imide [8]. Independently of the considered proton carriers, there are similar considerations to bear in mind: (a) the membrane material must absorb an optimum amount of the proton carrier; too much weakens the membrane, too little results in inadequate proton conductivity; (b) the membrane material must retain the maximum amount of the proton carrier under the operating conditions over a long period of time (5000 h for transport use, 40,000 h for stationary use). The loss of the conducting medium results in the reduction of conductivity, degradation of the membrane, damage of the electrodes, and blockage of flow field plate (FFP) channels [9].

Composite polymer membranes have been already proved as an effective technique for the strengthening of higher temperature and lower humidity fuel cell applications. The improvements that have been made are related with

the water adsorption and retention, acid uptake and phosphoric acid retention, proton conductivity, thermo and mechanical properties, fuel cell performance and durability issues.

This chapter is devoted to PBI composite membranes involving a polymer matrix, in this case, the PBI, and another compound in the form of filler (solid oxides, solid acids, heteropolyacids and derived heteropolysalts, pyrophosphates, ionic liquids and even carbonaceous materials). A synergic effect between the two elements always appears crucial in order to improve the membrane characteristics. As in the case of Nafion[®] membranes, the motivations for fabricating composite PBI-based membranes fall into the following classification:

- Adding a hygroscopic moiety to increase water and phosphoric acid retention and, consequently, the proton conductivity.
- Adding a carbon-based material for the modification of the polymer to improve the mechanical resistance and the proton conductivity.
- Adding ionic liquids, materials that by themselves could provide ion conductivity with a high chemical and thermal stability, with no degradation compared to H₃PO₄.

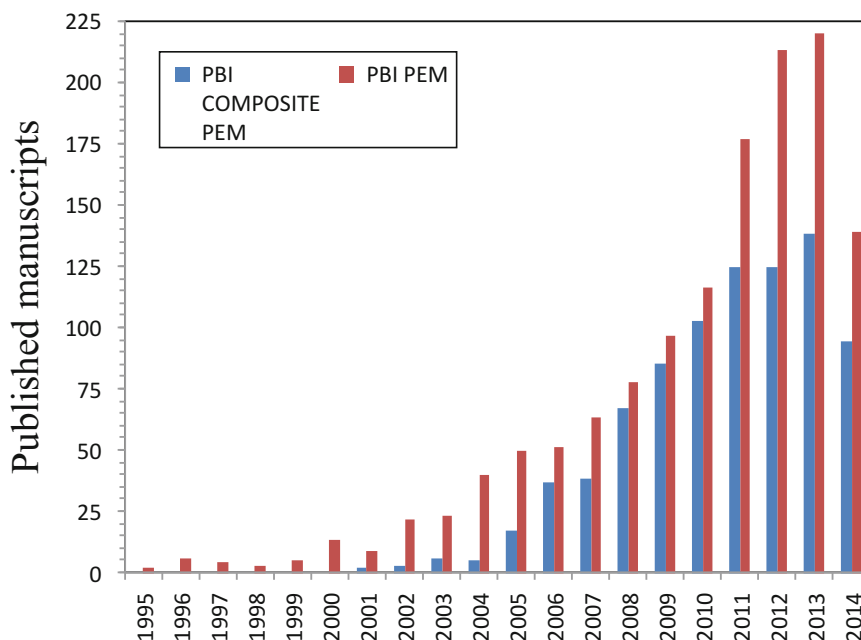


Fig. 13.1 Published items of the topic PBI membranes and composite PBI membranes indexed within Scopus (June, 2014)

Most of the reviews on composite membranes have been focused on Nafion[®] membrane. These composites have the aim of making Nafion[®]-like membranes suitable for operating at medium temperature, around 130 °C and under low relative humidity conditions [10–14]. Nevertheless, most of the fillers used for Nafion[®]-like membranes have also been used for PBI-based materials. Figure 13.1 collects the number of articles published on this topic in recent years. A monotonous increase can be observed, clearly indicating that PBI-based materials can be still considered a hot topic, despite the PBI membranes were proposed as electrolyte for the first time in 1995 [15].

13.2 PBI-Based Composite Membranes with Hygroscopic Oxides

13.2.1 Introduction

Promising results were achieved by the incorporation of hygroscopic inorganic materials. Two of them were the most

extensively studied, as far the authors know, silica and titanium dioxide, but other fillers were also used, e.g., ZrO₂ [16, 17] and different clays [18–20]. Moreover, the use of SiO₂ +PBI-based composite membranes was not only restricted their use only for fuel cell applications but also for gas separations [21, 22].

13.2.2 Preparation of PBI Composite Membranes with Hygroscopic Oxides

Although it is said that the silica is added to the PBI structure, the reality is that, in most of the cases, the silica is modified or functionalized in order to improve their characteristics of the PBI composite membrane. The incorporation of inorganic nanofillers in the polymer matrix is often carried out by in situ sol–gel creation of the particles during membrane casting [12, 13]. This method avoids silica nanoparticles agglomeration and therefore enables higher inorganic contents [14].

Mustarelli et al. [23] functionalized silica with imidazole by means of a standard basic hydrolysis/condensation process, starting from tetraethoxysilane (TEOS) and *N*-(3-triethoxysilylpropyl)-4,5-dihydroimidazole. Then the active silica was added to a PBI solution and finally, by a well-known casting method the PBI composite membranes can be prepared. A similar procedure was followed to prepared PBI–silica nanocomposite membranes, via sol–gel process from an organosoluble, fluorine containing copolymer with a silica precursor, TEOS, and a bonding agent to reinforced interfacial interaction between PBI chains and silica nanoparticles [19, 24]. More recently, the research group headed by Mustarelli prepared poly(2,2,-(2,6-pyridine)-5,5,-bibenzimidazole) (PBI-5N) composite membranes containing PBI functionalized silica particles or mesoporous silica MCM-41 [25]. Silica nanoparticles (diameter 10–20 nm) and sulfonated silica nanoparticles prepared in the lab according to a method reported elsewhere [26] were added to a PBI solution in *N,N*-dimethylacetamide to get nanocomposite PBI membranes with different fillers contents from 5 to 20 wt% [27]. A similar procedure was used for TiO₂-based composite PBI membranes prepared by the group of Lobato et al. [28–31]. On the other hand, modified TiO₂ and SiO₂ nanoparticles were added to a poly[2,2-5,5-(*m*-pyrazolidene)-bibenzimidazole] (PPBI) solution and by a casting method the composite PBI-based membrane was obtained [32]. The modification of both SiO₂ and TiO₂ nanoparticles was achieved by radical polymerization of some vinyl monomers such as sulfonated polyvinylbenzene (PSV) or polyvinylimidazole (PVI) on the surface of the nanoparticles to which vinylic groups were bonded covalently.

13.2.3 Physicochemical Characterization

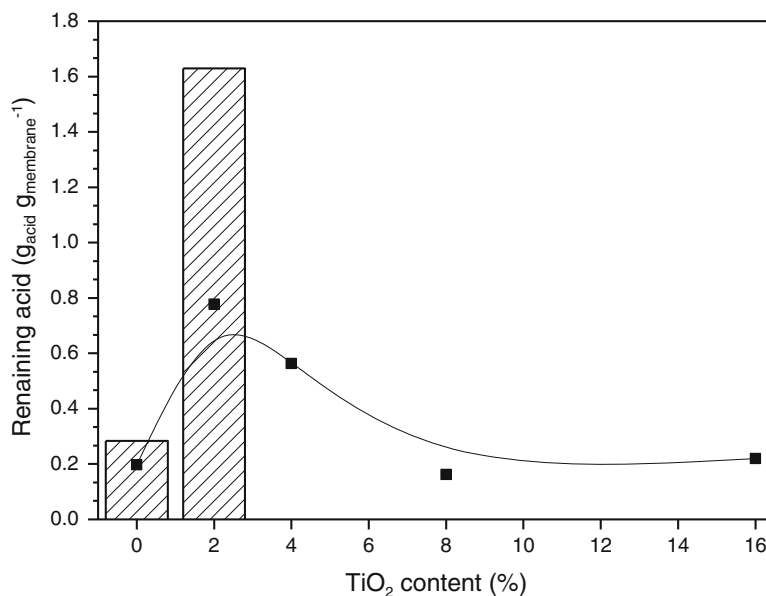
An improvement in the thermal stability of the new composite PBI-based membranes was found when either TiO₂ or SiO₂ was added. For example, the glass transition temperatures

(T_g) were shifted to higher temperatures (450–455 °C) when sulfonated silica nanoparticles were added to the PBI polymer. The T_g increase implied that the presence of those sulfonated silica nanoparticles restricted the mobility of the PBI chains. The ionic linkages between the fillers and the polymeric matrix brought a cross-linking effect to the nanocomposite sulfonated silica PBI membrane. The positive effect on the thermal stability of the –SO₃H/–NH ionic linkages was demonstrated with the lower T_g (423 °C) showed by the silica nanoparticles (non-sulfonated) PBI membranes [27]. In the case of composite PBI membranes with silica nanoparticles formed from different contents of TEOS and cross-linked to the PBI matrix with (3-glycidylxypropyl)-trimethoxysilane (GPTMS), an increase in the thermal resistance was not observed. Nevertheless, all the prepared samples were stable up to 300 °C, high enough for operating in a fuel cell system [24]. On the other hand, the degradation of both polyvinylimidazole nanosilica and titania occurred at 185 °C, limiting the operation at temperatures higher than 150 °C. However, the sulfonated PSV modified with TiO₂- and SiO₂-modified nanoparticles were adequate to operate in the whole range of the HT-PEMFC.

Water and PA uptakes are very important for the PBI-based membranes. From the study of the both silica and titania modified with PSV and PVI composite PPBI membranes, it was clear that the addition of silica-based nanoparticles was more appropriate than the TiO₂-based nanoparticles in order to increase the water uptake. In the case of the PA uptake, the influence of the filler content was not clear. In Ref. [32], it was shown that the amino groups of the PPBI chains were blocked by the sulfonic acid groups of the PSV and thus limited the PA uptake for those samples.

Even more important than obtaining a very high doping level is to get a very good acid retention capability, as acid leaching is one of the main degradation factors of the phosphoric acid-doped PBI membranes [33]. Thus, Mustarelli et al. performed acid leaching tests by washing the as-doped membranes in hot water (80 °C) up to complete removal of the

Fig. 13.2 Phosphoric acid retained by the composite membranes containing TiO_2 after leaching test. Lines: membranes immersed into 75 wt% H_3PO_4 bath concentration. Columns: membranes immersed into 85 wt% H_3PO_4 bath concentration.



free acid [23]. The filler (imidazole functionalized silica) had two effects: it first increased the retention capability and allowed the composite membranes to retain larger quantity of PA (up to three times more). Similar results were found by Pinar and coworkers from their titania-based composite PBI membranes [31]. In this case, 2–4 wt% was enough to retain higher amounts of acid than the pristine PBI membrane. Larger amounts of filler did not contribute to any further advantage. The formed agglomerates for the composite membranes with filler concentrations higher than 2 wt% harmed the acid retention. Figure 13.2 shows this behavior for the cases when the PBI membrane was doped in PA of two different concentrations, 75 and 85 wt%. The same trends were obtained by the same research group when titanium oxysulfate (TiOSO_4) was added instead of TiO_2 to the PBI [29].

Finally, another important characteristic usually evaluated in the composite membranes is the mechanical stability. Thus, an improvement of the mechanical strength (evaluated at 125 °C) with the content of TiO_2 and for the case of TiOSO_4 was observed in doped PA PBI-based composite membranes. Formation of nanocomposites with silica nanoparticles results in an increase of the

tensile strengths and a decrease in the elongations at break for the PBI-based membranes. However, the introduction of the silica nanoparticles increased the brittleness of the PBI-based membranes [27]. On the other hand, higher amounts of TEOS in the PBI composite membranes did not contribute to enhance the mechanical properties but all the silica-based composite PBI membranes showed higher mechanical strength than the pristine one [24, 34]. The elastic deformation of those composite membranes was improved compared to pristine ones. The slight differences in ultimate strain of the samples with different TEOS content were attributed to the different morphologies of the silica-based fillers [24].

13.2.4 Proton Conductivity

Proton conductivity is the main parameter that must be improved from the point of view of the PBI-based membranes. Non-modified and modified silica and titania particles with PSV and PVI were used as fillers for a PPBI to form a composite PBI-based membrane, and the proton conductivity under high humidity degree (100 % relative humidity and at 205 kPa) and dry

conditions was studied. Under high humid conditions, the presence of non-modified particles did not favor the proton conduction which was similar to the observed trend by other silica-based composite membranes [19, 35]. This reduction was attributed to silica-induced changes in the tortuous paths and in the distribution of hydrophilic/hydrophobic domains. Nevertheless, when the modified silica and titania particles were added, an improvement of proton conductivity was achieved [32]. Similar behavior was obtained by the sulfonated silica nanoparticle-based PBI composite membranes [27]. Under harsh conditions, dry environment, a clear advantage of using modified fillers was observed. The PVI-based composite PPBI membranes performed better than PSV-based composite PPBI membranes, and the silica-based nanoparticles outperformed the corresponding composites with titania. Three different concerns must be born in mind in order to explain the proton conductivity of the composite PBI-based membranes: the water uptake, the PA doping level, and the number of proton conductive functional groups such as sulfonic groups [32].

An interesting study of the proton conductivity of composite PBI-based membranes with functionalized SiO_2 was carried out by Mustarelli et al. [23]. The conductivity at 120 °C and 50 % relative humidity was measured for the as-prepared doped PBI-based membranes and after a leaching test without and with different wt. % functionalized SiO_2 . Before the leaching test the conductivity did not rely on the amount of filler and similar values were obtained. This was expected, since at doping levels higher than four PA molecules per PBI repeat unit, the conductivity is similar to that of the free PA acid [36]. After the leaching test, the addition of the filler preserves the proton conductivity. The addition of only 2 wt% of filler led to more than 100 times higher conductivity after the leaching test compared to the pristine PBI-based membrane. The addition of fillers to polymer electrolytes generally gives well-defined conductivity maxima for filler contents in the range 5–10 wt%, followed by a decrease owing to a dilution effect [37].

The conductivity achieved with the composite PBI membrane with 2 wt% of TiO_2 after doping in 85 wt% PA was around 0.1 S cm^{-1} at temperatures from 125 to 175 °C. The high doping level reached for this composite PBI membrane, due to the hygroscopic character of the titania, which also led to a high water and acid retention capability [28], explained the high proton conductivity values.

13.2.5 Fuel Cell Results

Table 13.2 summarizes the fuel cell performances of different composite PBI membranes with silica- or titania-based fillers. A direct comparison between the outputs is not recommended due to the different membrane-electrode-assembly preparation procedure, cell size, etc.

Two interesting essays related with the durability, which is nowadays one of the challenges to be overcome by PEMFC technology, were reported for composite PBI-based membranes. This latter material was able to operate for longer periods with smaller performance drop compared to pristine PBI membranes. Ossiander et al. [24] reported a stable performance over 1300 h for a fuel cell with a PBI composite membrane which incorporated fibrous silica particles (40 % TEOS content) and cross-linking them to the polymer. Moreover, the composite PBI membrane showed better performance and durability than the standard PBI membrane under the same operation conditions [24]. In the same way, an assessment of the life time of a short stack (3 MEAs of 50 cm^2 each) with a composite PBI membrane with 2 wt% of TiO_2 was carried at 0.2 A cm^{-2} and 150 °C. Different shut-downs, polarization curves, and dynamic load tests were carried out. Figure 13.3 shows the stack voltage changes during the life test of the stack with the PBI with 2 wt% of TiO_2 . As can be observed, over 1700 h of study, a very high stability was maintained despite the shut-down stages. During this study, the acid leached was measured and found to be lower than that of a stack running with a standard PBI membrane [38].

Table 13.2 Important parameters defining the fuel cell performance of the different composite PBI membranes with silica or titania

Reference	Sample ^a	Temperature and fuel conditions	Peak power and OCV
[25]	H ₃ PO ₄ /PBI-5N	150 °C; H ₂ /air. Dry conditions. Constant flow: 0.07 L min ⁻¹ for H ₂ and 0.30 L min ⁻¹ for air	40 mW cm ⁻² at 0.6 V
	H ₃ PO ₄ /PBI-5N with 25 wt% SiO ₂ -IM		83 mW cm ⁻² at 0.75 V
	H ₃ PO ₄ /PBI-5N with 5 wt% MCM-41		70 mW cm ⁻² at 0.75 V
[29]	PBI · 11 mol H ₃ PO ₄	150 °C; H ₂ /O ₂ . Dry conditions. Constant flow: 0.134 L min ⁻¹ for H ₂ and 0.076 L min ⁻¹ for O ₂	610 mW cm ⁻² at 0.84 V
	2wt% TiSO ₄ -PBI · 10 mol H ₃ PO ₄		450 mW cm ⁻² at 0.84 V
[30]	PBI · 11 mol H ₃ PO ₄	150 °C; H ₂ /O ₂ . Dry conditions. Constant flow: 0.134 L min ⁻¹ for H ₂ and 0.076 L min ⁻¹ for O ₂	610 mW cm ⁻² at 0.84 V
	sPBI · 15 mol H ₃ PO ₄		615 mW cm ⁻² at 0.84 V
	PBI-TiO ₂ · 15 mol H ₃ PO ₄		800 mW cm ⁻² at 0.84 V
	PBI · 11 mol H ₃ PO ₄	175 °C; H ₂ /O ₂ . Dry conditions. Constant flow: 0.134 L min ⁻¹ for H ₂ and 0.076 L min ⁻¹ for O ₂	660 mWcm ⁻² at 0.83 V
	sPBI · 15 mol H ₃ PO ₄		860 mW cm ⁻² at 0.83 V
	PBI-TiO ₂ · 15 mol H ₃ PO ₄		1000 m Wcm ⁻² at 0.83 V
[24]	PBI-40 % TEOS	160 °C. H ₂ /Air. Active area 50 cm ²	33 mW cm ⁻² at 0.89 V
	PBI-80 % TEOS		32 mW cm ⁻² at 0.90 V
	PBI-120 % TEOS		30 mW cm ⁻² at 0.90 V

^aDenoted as found in the reference; \cong means data from interpolation of Figures

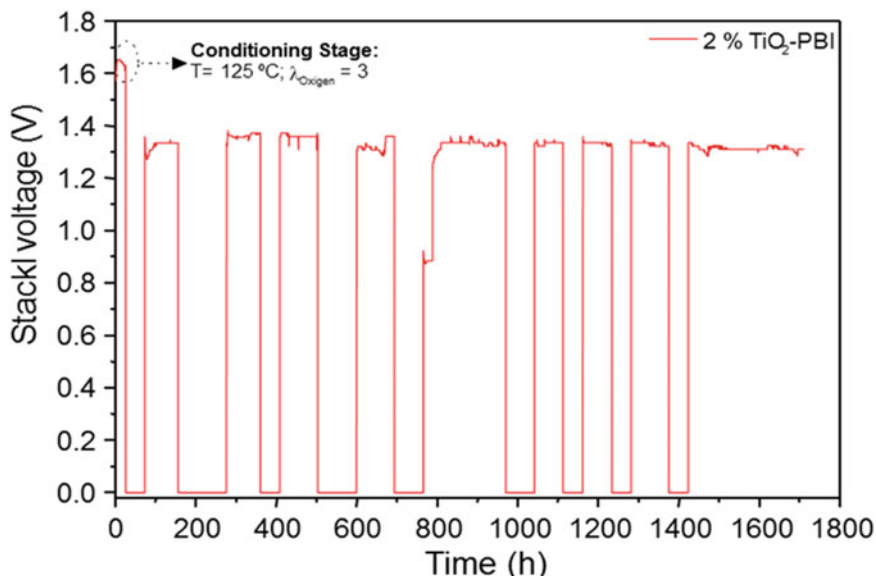


Fig. 13.3 Stack voltage degradation during life tests including length of shut-down stages and conditioning stages of a stack of 3 MEAs with composite PBI

membranes with 2 wt% of TiO₂. Current density = 0.2 A cm⁻²; $\lambda(\text{H}_2) = 2$, $\lambda(\text{air}) = 3$; $T = 150$ °C; $P = 1$ atm

13.3 PBI-Based Composite Membranes with Solid Acids and Salts

13.3.1 Introduction

Other type of inorganic modifications used for PBI membranes was the formation of composites with solid acids such as heteropolyacids or derived salts and pyrophosphates. The strategy of these inorganic materials was to increase the conductivity of the membrane at lower acid contents, keeping or even improving other properties such as the mechanical and chemical stability [39].

- Heteropolyacids (HPA): These solid acids possess high conductivity and strong acidity and are generally surrounded by a large number of water molecules, making them especially suitable for operation under anhydrous conditions. The most well known are phosphomolybdic acid ($\text{H}_3\text{PMo}_{12}\text{O}_{40}$, PMA) [40], phosphotungstic acid ($\text{H}_3\text{PW}_{12}\text{O}_{40}$, PWA) [41–43], and silicotungstic acid ($\text{H}_3\text{SiW}_{12}\text{O}_{40}$, SWA) [42–46]. Furthermore, that high water affinity gives them the special ability of increasing the CO tolerance, due to the supply of the necessary oxygenated species when dry $\text{H}_2 + \text{CO}$ stream are used [47].
- Cesium acid heteropolysalts (CsHPA): One interesting modification of the HPA is the partial substitution with Cs, especially in the case of 2.5 atoms, where the surface acidity achieves its maximum [39, 48, 49]. The water solubility of the salt is reduced and the surface area increased, maximizing the interaction with the polymer matrix. The use of a phosphorous-based salt of this type maximizes the membrane conductivity, whereas the silica-based salt reinforces the mechanical properties. Very interesting results are also obtained when W was replaced by Mo [49].
- Zirconium and boron phosphate: Interesting results have been obtained by using this approach in order to prepare PBI composite

membranes [42, 50–52], especially in the case of the phosphate ($\text{Zr}(\text{HPO}_4)_2 \cdot n\text{H}_2\text{O}$, ZrP) and boron phosphate (BPO_4 , BP).

- Pyrophosphates (PP): These materials present high conductivity at temperatures above $150\text{ }^\circ\text{C}$ under anhydrous conditions, which is a key property for application in high temperature PEMFC. Promising results have been presented in the literature for the preparation of PBI with pyrophosphates, showing benefits in terms of conductivity and single cell performance [53, 54].

13.3.2 Preparation of the Inorganic Component

The first works on heteropolyacids were carried out by Prof. Staiti et al. [41, 44, 45]. The strategy they followed was to form first the silica support on which the heteropolyacids were adsorbed. They prepared an alcoholic solution of TEOS (tetraethyl orthosilicate) onto which the corresponding SWA or PWA were added. Next, the solution was neutralized in order to facilitate the subsequent mixture with the PBI dispersion. The procedure was repeated by Lee et al. [46]. Finally, He et al. [42] and Verma and Scott [43] used the commercial SWA and PWA accompanied with a neutralization in 1 mol L^{-1} NaOH.

In the case of the alternative use of the Zr- and B-based solid acids, He et al. [42] prepared the ZrP by the reaction of zirconyl chloride with *ortho*-phosphoric. Qian et al. [51] followed a similar procedure to that described by He et al. A stringent washing procedure was necessary in order to ensure the removal of Cl^- ions. In the case of the zirconium tricarboxybutylphosphonate (ZrTCP), 2-phosphonobutane-1,2,4-tricarboxylic acid (Yamazaki et al. 2004) was used instead in order to obtain the final salt. Finally, Di et al. [52] acquired commercially the boron phosphate that subsequently mixed with, in this case, ABPBI polymer support.

The CSHPA was prepared through a condensation reaction by mixing cesium carbonate with the heteropolyacid in water. By controlling the ratio of carbonate to the acid, it was possible to prepare salts with different stoichiometries [48, 49]. One alternative was proposed by Oh et al. [55], who suggested the possibility of preparing the corresponding salt by a mechanochemical method, usually by ball milling followed by thermal treatment.

Finally, in the case of the PBI + PP membranes, Wu et al. [54] prepared the pyrophosphate by mixing SnO_2 and Sb_2O_3 in orthophosphoric acid at $300\text{ }^\circ\text{C}$, and a subsequent calcination at $650\text{ }^\circ\text{C}$ for 2 h to produce $\text{Sb}_{0.2}\text{Sn}_{0.8}\text{P}_2\text{O}_7$ (SSPP). Jin et al. [53] prepared the composite membrane consisting of the PBI polymer and a mixture of the precursors SnO_2 and $\text{Al}(\text{OH})_3$. They subsequently cast the membrane and doped it with phosphoric acid, with a final calcination stage in 10 % H_2/Ar in the temperature, obtaining the desired $\text{Sn}_{0.95}\text{Al}_{0.05}\text{P}_2\text{O}_7$ (SAPP).

13.3.3 Physicochemical Characterization

When PBI was combined with heteropolyacids, one indication of a good dispersion of the inorganic material in the polymer matrix was the general absence of any crystalline peak in the

composite membrane associated to the solid acid. In general, the classical wide amorphous halo was observed in the region of 2θ $15\text{--}40^\circ$ [40, 41, 43–46]. In the case of the Zr-based salts, Yamazaki et al. (2004) reported a similar behavior to that of the heteropolyacids. Finally, in the case of the CsHPA [49] and SAPP [53], the composite membrane still showed the crystalline structure of the salt even after doping with phosphoric acid.

Scanning electron microscopy images of the composite membranes revealed some surface and bulk heterogeneities, especially at large contents of the inorganic material (see Fig. 13.4a). In the case of the CsHPA, a more homogeneous distribution could be obtained, which had a positive effect on the proton conduction. In the case of the PBI + SSPP, an even distribution was achieved over the membrane as displayed in Fig. 13.4b, c.

Infrared spectra of the PBI + inorganic component showed the appearance of peaks associated to the PBI membrane and the inorganic materials, confirming the successful production of the composite membranes. In some cases, especially for the CsHPA composites, small alterations were observed in the spectra, indicative of a close interaction between the PBI and the inorganic salt, as confirmed by UV–Vis spectra and ^{31}P nuclear magnetic resonance (NMR) spectroscopy [48]. A similar behavior was found in the PBI + $\text{Sb}_{0.2}\text{Sn}_{0.8}\text{P}_2\text{O}_7$

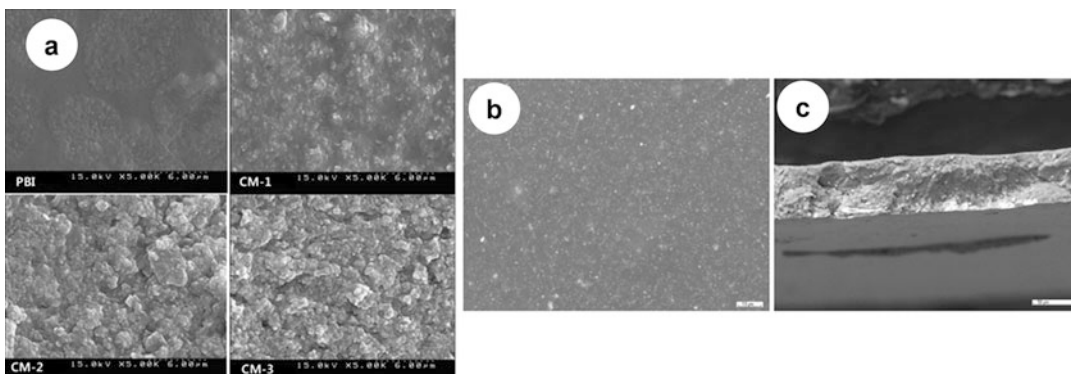


Fig. 13.4 (a) SEM images of the PBI + SWA: PBI: pristine PBI; CM-1: 65 % PBI + 35 % inorganic; CM-2: 50 % PBI + 50 % inorganic; CM-3: 35 % PBI + 65 % inorganic

([46]; open access journal); (b) surface and (c) cross-section image of a PBI + SSPP composite membrane. Reproduced from [54] with permission of John Wiley and Sons

composite with the disappearance of bands associated to PO_3 vibrations in the hybrid membrane [54].

The thermal stability of all the composite materials was rather satisfactory. Regardless of the inorganic material used, the composite presented thermal stability quite similar to that of the pristine PBI [40, 46, 48, 55] with a thermal stability guaranteed up to 500°C in air atmosphere.

In terms of the mechanical properties, the addition of the HPA maintained the good mechanical resistance of the PBI membrane except for excessive addition of the inorganic component (above 70 %) [44]. On the contrary, in the case of the PBI + CsHPA, the experimental data showed a weakening of the mechanical properties for the PBI composite membranes [49, 55]. However, an interesting feature shown by Oh et al. [55] was that H_3PO_4 -doped composite membranes were more mechanically resistant than pure ones. In general, the use of silicon led to more stable membranes in comparison to phosphorous in the HPA structure [56]. In the case of PBI + PP composite, doping levels higher than 4.3 attempted against the mechanical integrity of the membrane at temperatures above 120°C , suggesting the use of moderate doping levels in order to preserve the mechanical stability of the composite membrane [54].

All the hybrid membranes needed to be doped with acid doping in order to achieve satisfactory conductivity values (see Sect. 13.3.4). Therefore, the membranes were immersed in phosphoric acid baths of different concentrations for different periods of time. For all the hybrid membranes, high H_3PO_4 doping levels could be achieved [46, 54, 55]. However, in the case of the PBI + PP, Wu et al. [54] observed that large immersion times are detrimental for the membrane stability due to the polymer dissolution. The more adequate doping conditions were established (5 days in 85 % H_3PO_4 at room temperature). On the contrary, Jin et al. [53] observed a decrease in the doping level in the presence of the pyrophosphate, ascribed exclusively to the presence of the inorganic material.

Direct fuel permeability data were scarce in the literature for these inorganic/PBI hybrid

materials. As far as the authors know, an equivalent H_2 crossover current of 12 mA cm^{-2} at 120°C was reported for a PBI/40 % SWA [43], which indeed was higher than that reported by Neyerlin et al. [57] ($4\text{--}5\text{ mA cm}^{-2}$) at 160°C . Di et al. [52] showed that the addition of boron phosphate to the ABPBI polymer matrix reduced the vapor methanol permeability compared to pure PBI to half.

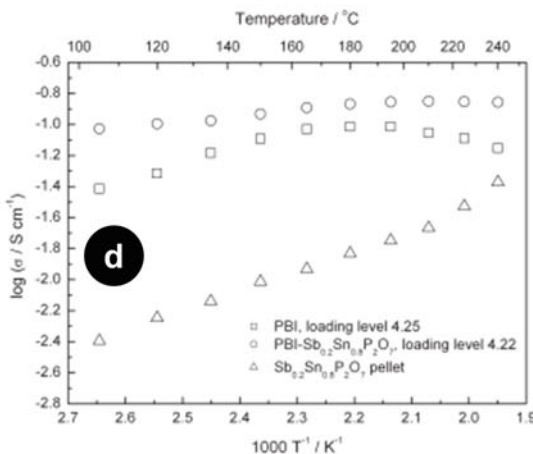
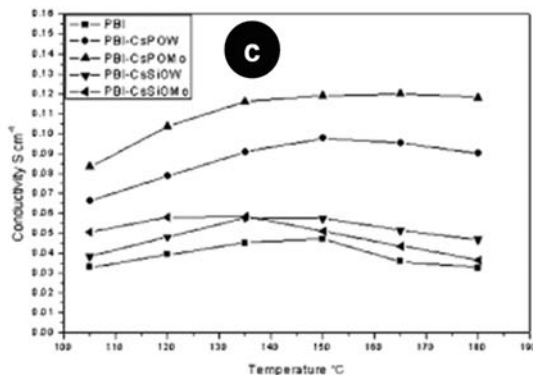
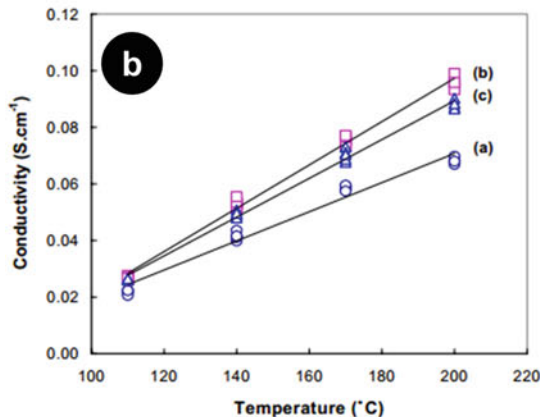
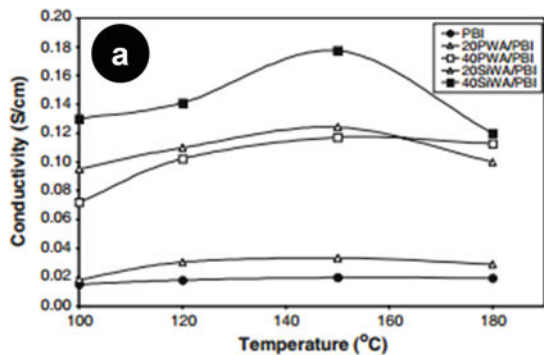
13.3.4 Proton Conductivity

The first tentative of preparing composite membranes of PBI + HPA were unsuccessful in terms of achieving high proton conductivity without PA doping [41, 44, 45, 56]. This proved the necessity of doping the composite membranes with H_3PO_4 in order to increase the proton conductivity. Verma and Scott [43] and Lee et al. [46] observed an enhancement in the proton conductivity of the doped composite membranes compared to the pristine-doped membrane (see Fig. 13.5a).

When ZrP, ZrTPC, and BP were used, there was an increase in the membrane conductivity compared to the doped pure PBI membranes [42, 50–52]. He et al. [42] reported an optimum percentage of ZrP in the membrane of 15 % and explained the increase in the conductivity in terms of the presence of proton conductor surface groups in the ZrP (Fig. 13.5b). Furthermore, PBI and PBI + ZrP membranes presented similar proton conduction activation energies, indicative of an analogous proton transport mechanism. Di et al. [52] reported a drop in the PBI + BP activation energy, attributed to a more facile proton transportation in the composite material.

The composite material formed by PBI + CsHPA also led to an enhancement of the proton conductivity. Xu et al. [49] carried out an extensive study testing different CsHPA, with CsPOM, CsPOW, CsSiOM, and CsSiOW (Fig. 13.5c). They observed that for all the cases, the membrane conductivity exceeded that of PBI. Indeed, a value of 0.12 S cm^{-1} could be achieved at 150°C under a relative humidity $<1\%$ for a PBI + 30 % CsPOM.

Fig. 13.5 Membrane conductivity of different composite material: (a) PBI with HPA, where the number designs the HPA percentage, and P and Si denote phosphorous or silicon in the structure (doping level of 5) Reproduced from [43] with permission from Springer; (b) PBI + ZrP (curve a: pure PBI, curve b: PBI + 15 % ZrP, curve c: PBI + 20 % ZrP, doping level of 5.5). Published from [42] with permission of Springer; (c) PBI with different Cs-based heteropolysalts (doping level 4.5, relative humidity <1 %). Reproduced from [49] with permission from the Royal Society of Chemistry; and (d) PBI + SSPP composite membranes. Reproduced from [54] with permission of John Wiley and Sons



Finally, the composite H_3PO_4 -doped PBI + PP membranes [53, 54] presented larger proton conductivity values than that of pure acid-doped PBI (Fig. 13.5d shows the values for [54]). Wu et al. [54] pointed out a possible synergic effect of the two components in the hybrid membrane, leading to a significant decrease of the activation energy for the proton transportation.

13.3.5 Fuel Cell Results

Verma and Scott [43] showed some polarization curves at different temperatures for the *ortho*-phosphoric acid-doped pure PBI and composite membranes at different temperatures. They reported that at low temperature (120 °C) the hybrid membranes, especially the PBI + 40 % SWA, achieved the best performance. Nevertheless, at 150 and 180 °C, there was a large drop in the performance of the hybrid materials below that of PBI. They explained this in terms of the fuel crossover in the thin (30 μm) composite membrane. In the case of the PBI + CsHPA and PBI + PP, the cell performance could be significantly enhanced at high temperatures. In the case of the cesium hydrogen heteropolysalts, Xu et al. attributed the enhancement to the higher proton conductivity of the hybrid materials and to the stronger acid and water retention properties. A similar explanation was given in the case of the PBI + PP hybrid membrane, which also had a positive impact in the protons transportation within the electrode structure. Table 13.3 summarizes some performance parameters obtained with these materials.

13.4 PBIs Modified with Ionic Liquids

13.4.1 Introduction

High conductivity is one of the major limitations to solve in high temperature polymer electrolyte fuel cell, once anhydrous conditions are required. Considerable progress has been made including doped PBI membranes with phosphoric acid (H_3PO_4). However, at high temperatures, the condensation of phosphoric acid takes place and the thermo-chemical stability of PBI decreases. As an alternative to phosphoric acid, it has been proposed the use of ionic liquids (IL) as conductive fillers to replace water, phosphoric acid, or even inorganic nanoparticles for improving both conductivity and thermo-chemical stability in high temperatures fuel cells (HTFC) [58, 59].

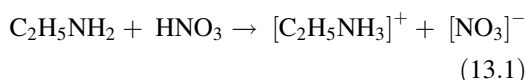
Ionic liquids are salts with melting points below 100 °C. Ionic liquids which are liquids at/or below room temperature are commonly can be called room temperature ionic liquid (RTIL). The IL comprise a class of very interesting compounds and have shown useful in application in many research areas, for instance in organic synthesis and catalysis. The wide application range of the ionic liquids is connected to their excellent advantages, such as high ionic conductivity, high thermal conductivity and heat capacity, high polarity, low melting point ($T_m < 100$ °C), high thermal stability, low vapor pressure due to strong ion-ion interaction, low toxicity and easily recycling, and high flame resistance or low flame retardancy. In addition,

Table 13.3 Important parameters defining the cell performance of the different hybrid materials

Reference	IM ^a	PBI: IM	Temperature/°C	P ² for H ₂ -O ₂	P ³ for H ₂ -O ₂
[49]	CsPOM	70:30	150	0.43	0.63
	CsPOW				0.59
	CsSiOM				0.48
	CsSiOW				0.51
[54]	SSPP	4:1	175	0.45	0.67
[53]	SAPP	60:40	200	0.369	0.437

^aIM inorganic material; P² is the maximum power density of the acid-doped PBI membrane, whereas P³ is the corresponding maximum of the hybrid material

IL are highly versatile in terms of designing many different materials with tailored properties because of the availability of a large number of organic cations and inorganic/organic anions which can be combined. The ionic liquids are salts consisting only of cations not protonated, and anions are known as aprotic. In contrast, IL are formed by proton transfer from an acid to a base, i.e., a type of Brønsted acid–base ionic liquids, and are called as protic. A typical example of a protic IL is given by the protonation of ethylamine as shown in (13.1) [59–62].



IL have been extensively studied due to the different characteristics of these materials. The wide spectrum in properties opens up numerous opportunities for modifying the properties of cations and anions independently, yielding a wide field of application of these materials. Nevertheless, a limited number of studies have focused on the application of IL in fuel cells. In particular, PBIs doped with IL working as polymer electrolyte in fuel cells are a research area that is still under development. Thus, this section will display a general overview, not totally comprehensive, but with coverage of specific and significant results obtained in this area.

13.4.2 Membrane Preparation

In general, different routes for preparation of polymer electrolyte membrane based on IL have been used and classified into three categories: (I) *doping of polymers with IL* by (a) the immersion of an already formed polymer membrane into a IL solution and (b) by mixing both IL and polymer solution for a certain period of time followed by evaporation of solvent, membranes prepared by this route have been also labeled as polymer gel-type; (II) *in situ polymerization or cross-linking of monomers in IL* by the reactions between IL and polymeric monomers to form IL/polymer membranes;

these two approaches involve the design of polymer electrolytes composed of conventional polymer matrix and IL; and (III) *synthesis of polymeric ionic liquids (PIL)* by designing functional polymers presenting some of the characteristics of IL. An overview of each route is schematized in Fig. 13.6 [63]. PBI/IL membranes have been usually prepared by doping of polymers with IL. Phosphoric acid can also be used in the PBI/IL composite to improve the ion conduction.

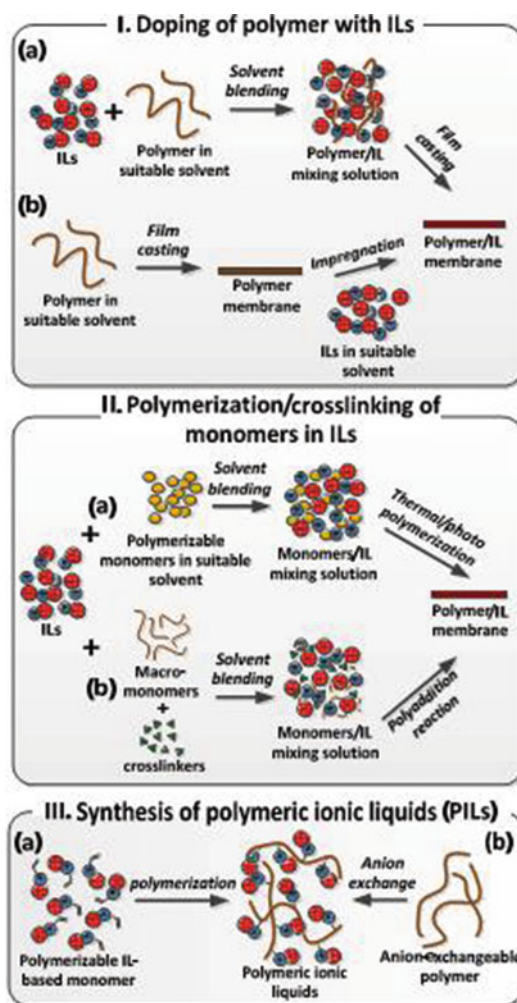


Fig. 13.6 Schematic representation showing preparation of IL-based polymer electrolytes. Reproduced from [63] with permission of the Royal Society of Chemistry

13.4.3 Physicochemical Characterization

Different techniques of characterization can be used to give important information concerning the physicochemical properties as well as the morphology of the conductive PBI/IL membranes.

Investigation by vibrational spectroscopy in the infrared region (FTIR) is straightforward to observe changes in both band positions and band intensities as a consequence of chemical interactions between PBI groups and IL functional groups. As an example, Liu et al. [64] studied an IL-doped PBI proton conducting membrane for an anhydrous H_2/Cl_2 fuel cell, observing the characteristics band of the polymeric matrix and the IL present in the membrane structure. Furthermore, it was possible to corroborate the existence of interactions between the IL and PBI by some changes in the base PBI spectrum.

In general, the thermal stability of PBI/IL composite was improved when compared to H_3PO_4 /PBI, which started to degrade at around 160–180 °C due to the dehydration of phosphoric acid. The higher thermal stability of IL made the composites stable, in general, up to 200 °C. The improvement in thermal stability obtained by PBI/IL composites could reach over 350 °C, fulfilling the requirement for polymer electrolytes working at higher temperatures. However, the mechanical properties of PBI matrix, such as tensile modulus, tensile strength as well as elongation at break, changed after introduction of IL. Particularly, ionic liquids may act as a

plasticizer, decreasing the modulus and strength by making the polymer backbone more flexible [65].

NMR spectroscopy was used to identify carbons and hydrogen from the PBI backbone. However, in PBI samples doped with H_3PO_4 and IL, NMR was able to also provide information concerning the dynamic of the mobile species within the membrane structure. Moreover, NMR could also provide evidences of ions interaction, more specifically between PBI groups, H_3PO_4 and IL [66, 67].

Scanning electron microscopy proved to be a very useful instrument for the assessment of membrane morphology, especially to study the effect of impregnation of the IL in the PBI support. van de Ven et al. [59] showed pronounced changes in PBI morphology after IL addition by SEM investigation (Fig. 13.7), such as in the membrane roughness and porosity.

An important aspect in PBI/IL composite membranes is the IL lixiviation rate. When the IL were not effectively immobilized, a progressive release of the IL components during a long period of fuel cell operation took place, thus resulting in the decline of fuel cell performance [63]. In order to overcome this drawback, the sulfonation of polymer matrices led to a better dispersion of ionic domains and the retention of IL, along with a reduction of the proton conductivity loss, as shown by Ye et al. [68]. Polymerization techniques by introducing IL molecules in the polymer matrix were an actual alternative to overcome this drawback in polymer/IL composites.

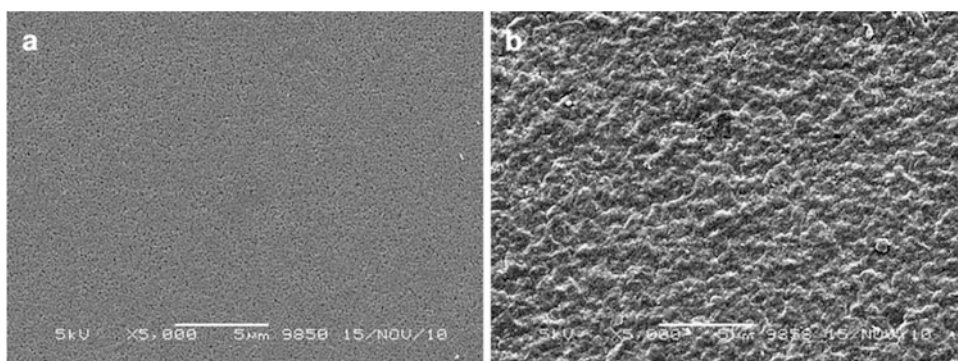


Fig. 13.7 Cross section of (a) bare PBI and (b) PBI/IL composite. Reproduced from [59] with permission of Elsevier

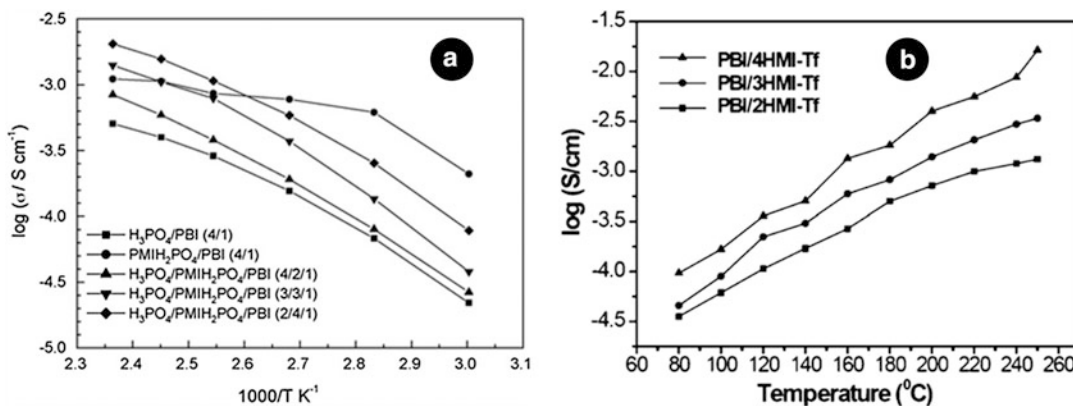


Fig. 13.8 (a) Temperature-dependent ionic conductivity of $\text{H}_3\text{PO}_4/\text{PBI}$, $\text{PMIH}_2\text{PO}_4/\text{PBI}$ and $\text{H}_3\text{PO}_4/\text{PMIH}_2\text{PO}_4/\text{PBI}$ membranes under anhydrous condition. Reproduced from [66] with permission

Finally, the PBI/IL membranes presented a lower methanol permeability compared to Nafion[®] 117, as measured with a two-compartment glass cell. Additionally, depending on the amount of IL employed, the methanol permeability varied. The increase of methanol crossover with the IL loading in PBI/HMI-Tf composite membrane could be explained by the increase of PBI's free volume after HMI-Tf doping, because of the HMI-Tf could decrease the intermolecular interaction forces. Nevertheless, the permeability of PBI/HMI-Tf composite membranes was still below the Nafion[®] 117 membrane [65].

13.4.4 Proton Conductivity

As already explained, IL exhibit numerous advantages as candidates for electrolyte in high temperature PEMFC. The introduction of IL into acid-doped PBI membranes significantly increases the ionic conductivity in the polymeric electrolyte and the mechanism of conduction seems to be the same as that of $\text{H}_3\text{PO}_4/\text{PBI}$. Protons are conducted by both hopping and vehicular mechanism, but hopping is the main mechanism of conduction. Vehicular mechanism is dependent of IL content due to the availability of free ions [64]. Ye et al. [66] found that the

of Elsevier; (b) Ionic conductivity of PBI/HMI-Tf composite membranes at different temperatures. Reproduced from [65] with permission of Elsevier

higher the IL content, the larger the ion conductivity (Fig. 13.8a). A similar result was found by Wang and Hsu [65] (Fig. 13.8b). The authors stated that the IL acts as a plasticizer, promoting the mobility of the PBI chain, and concomitantly the ion transport. In both works, the *Grotthuss mechanism* (proton hopping) was determined to be the predominant conduction mechanism.

13.4.5 Fuel Cell Results

Up to now, there are few results related to fuel cell performance by using PBI/IL composites, in spite of the potential of these materials in such devices. Van de Ven et al. [59] showed some fuel cell results in which they observed an enhancement in the performance with the increase in the temperature in the range of 30–150 $^{\circ}\text{C}$ compared to conventional Nafion[®] membrane (Fig. 13.9). However, the open circuit voltage (OCV) was low compared to the standard Nafion[®]-membrane. Furthermore, the cell performance was somehow insufficient for real fuel cell application, evidencing that further research are necessary in order to enhance the properties of this composite membrane materials. Greaves and Drummond [60] recently showed that the nature of IL allows the use of protic acid–base combinations, including nonstoichiometric ones,

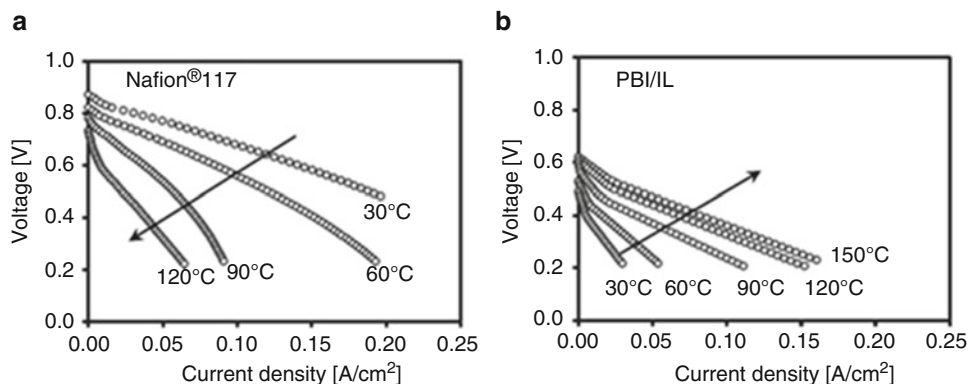


Fig. 13.9 $\text{H}_2\text{-O}_2$ polarization curves as a function of the operating temperature without humidification for: (a) Nafion[®] 117 and (b) PBI/IL membranes.

The *arrows* indicate the direction of increasing temperature. Reproduced from [59] with permission of Elsevier

in order to obtain materials with high ionic conductivity and stable at elevated temperatures.

13.5 PBI-Based Composite Membrane with Carbon-Based Materials

13.5.1 Carbon Nanotube Composites

Carbon nanotubes (CNTs) have been added to a polymeric matrix to improve their mechanical and other properties [69]. The use of CNTs in PEM must be carried out with caution because the well-known high electrical conductivity may cause short circuiting in proton exchange membrane fuel cells. The $\pi\text{-}\pi$ interaction between PBI and the side walls of CNT makes these two different materials compatible. Despite CNT-PBI composite membranes have shown enhancement in mechanical strength, the proton conductivity resulted in some cases compromised [70, 71]. Hence, different authors functionalized the CNTs in order to increase both the proton conductivity and the mechanical properties for hydrogen fed PBI-based HT-PEMFC [72, 73]. In this context, phosphonated multi-walled CNTs MWCNT were added to a PBI membrane (pCNT-PBI) in different concentrations (0.05–2.5 wt%, higher values were not used to avoid agglomeration and possible short circuit) and the composites

were subsequently doped in phosphoric acid. Similar doping level was achieved for all samples, pristine and composite-based PBI membranes [74]. The pCNT-PBI membranes showed higher proton conductivity than the pristine PBI and CNT-PBI membrane (the CNTs were not phosphonated). The authors explained this result by the network formed by the phosphonic groups in the CNT which facilitated proton conduction. This assumption was confirmed by SAXS measurements [74]. Furthermore, a drop in the activation energy from 40 to 25 kJ mol^{-1} was observed for the case of the pCNT-PBI composite membrane with 1 wt% which is indicative of a synergistic role played by the phosphonate MWCNTs. With respect to the fuel cell performance, the highest peak power density was reached for the PBI composite membrane with 1 wt% of phosphonated MWCNT (780 mW cm^{-2}) by feeding H_2 and O_2 and at 140 °C. This data implied an improvement of 30 % with respect to the value reached by the pristine PBI membrane under the same operation conditions. An interesting discussion on the fuel cell performance through impedance and cyclic voltammetry measurements was given by the authors [74].

A more complicated or sophisticated system was prepared by Suryani et al. [73]. Nafion- and PBI-functionalized MWCNT were synthesized and used as fillers in the preparation of MWCNT-PBI composite membranes. The

proton conductivities of the PBI-MWCNT-Nafion membranes were higher than that of the PBI membrane, but lower than the values of the PBI-MWCNT-PBI composite PBI membranes. After phosphoric acid doping, sulfonated PBI membranes showed higher proton conductivity compared to the non-sulfonated PBI membrane [28, 75, 76]. Acidic groups, such as sulfonic acid, could act as proton donors and acceptors. Hence, the protonated and non-protonated amine groups of PBI and the sulfonic acid group of Nafion might act as proton donors and acceptors for proton conduction. This could explain the better proton conductivity of the Nafion-based PBI composite PBI membrane with respect to the pristine PBI, despite the lower doping level reached. The fuel cell tests revealed that the modification of PBI with 0.2 wt% of MWCNT-PBI and MWCNT-Nafion resulted in 13 and 32 % enhanced single cell performance, respectively. The enhanced performance of the composite PBI membrane with the CNT modified with Nafion was attributed to the use of Nafion as ionomer in the electrodes instead of PBI [73].

Very recently, Wu et al. reported the preparation of PBI composite membranes containing small amounts (lower than 1 %) of functionalized multi-walled CNTs (MWCNTs). The membranes were doped with potassium hydroxide and applied in an alkaline direct methanol fuel cell [77]. The main advantages obtained by the incorporation of the CNT fillers were the reduction of the methanol permeability, a higher thermal stability, and the improvement of the ionic conductivity. The maximum power density (104.7 mW cm^{-2}) was achieved for the composite PBI membrane with the lowest CNT content, 0.05 %, running at $90 \text{ }^\circ\text{C}$ and with 2 M methanol in 6 M KOH. This peak power density was more than three times higher than for a KOH-doped pristine PBI [78]. Nonetheless, the amount of Pt catalyst on each electrode was very high, around 5 mg Pt cm^{-2} , which could be the actual reason for the better performance achieved by the composite PBI-based alkaline direct methanol fuel cell (DMFC).

13.5.2 Graphite Oxide Composites

Graphite oxide (GO) have been also added to PBI-based membranes [79, 80]. GO consists of carbon, oxygen, and hydrogen in variable ratios. GO itself is an electronic insulator with a very low electronic conductivity [81, 82]. However, the presence of different acidic functional groups, like carboxylic acid and epoxy oxygen, provides pathways for the hopping of protons [83, 84]. Xu et al. [80] prepared GO-PBI and sulfonated graphite oxide (SGO-PBI) (2 wt% of filler) composite membranes. The in-plane conductivity of the composite membrane was higher than that of the pristine PBI membranes, measured under the same operational conditions with very low PA doping levels in all cases (1.9 PA per PBI repeat unit). The proton transport activation energy (E_a) was 16.1, 11.4, and 9.3 kJ mol^{-1} for the PBI, GO-PBI, and SGO-PBI membranes, respectively. The lower activation energy of the composite PBI membrane was attributed to the synergetic effect of the carbon fillers with the PBI matrix. The fuel cell tests displayed OCVs for both H_2/air and H_2/oxygen higher than 0.9 V, which indicated that all membranes possessed a low fuel permeability. With atmospheric air, the peak power density at $175 \text{ }^\circ\text{C}$ was 0.144, 0.31, and 0.43 W cm^{-2} for the PBI, GO-PBI, and SGO-PBI membranes, respectively. One interesting finding was the very low doping level used or reached by their GO-based PBI composite membranes. As a reference, a PBI membrane with a high doping level ($11 \text{ mol L}^{-1} \text{ H}_3\text{PO}_4$) achieved a maximum power density with air of 0.34 W cm^{-2} [49].

Xue et al. [79] very recently prepared a modified PBI membrane by 3,3'-diaminobenzidine and 5-tert-butyl-isophthalic acid (BuIPBI) with GO-based materials as fillers. The surface of GO was treated with tert-butyl-isocyanate to improve the dispersion of the modified GO (iGO) in both water and organic media. The amount of fillers was varied from 1 to 15 wt%. The phosphoric acid doping level of BuIPBI, GO-BuIPBI, and iGO-BuIPBI membrane decreased with increasing

amount of the carbon-based filler. The authors attributed this behavior to the lower alkalinity of the BuIPBI with respect to the PBI. Moreover, the carbon fillers could occupy the interspaces of the polymer chains, thus preventing the PA molecules from penetrating the membranes. Nevertheless, the doping level was much higher than in the previous case of the GO-PBI-based membranes prepared by Xu et al. [80].

Proton conductivities of the carbon-based PBI composite membranes were measured at different temperatures. In all cases, higher values compared to pristine PBI-based membranes were obtained. The presence of GO in the polymer matrix was reported to interconnect the proton transfer channels, favoring the proton hopping through the membrane [85]. However, the degradation of acidic functional groups like carboxylic acid and epoxy oxygen groups in the GO sheets led to a decrease of the proton conductivity at temperatures above 160 °C [79].

13.6 Summary

Composites PBI and hygroscopic oxides, solid acids (and their derived salts), or pyrophosphates can be easily prepared and lead to final materials with enhanced mechanical and thermal resistances, in addition to, in general, larger phosphoric acid uptakes. The proton conductivity of the H₃PO₄-doped composite membranes is enhanced when the PBI: inorganic material ratio is optimized compared to sole H₃PO₄-doped PBI membranes, which directly impacts on the fuel cell performance. PBI/IL composite is also a promissory candidate to improve fuel cell performance due to their properties. However, high ion conductivity is only achieved when using the appropriate IL. In addition, IL retention is also a problem that must be overcome in this system. All these drawbacks encourage the scientific community to continue studying PBI/IL as polymer electrolyte membrane in fuel cell devices working at elevated temperature. Interesting results and more promising results have been shown by the PBI composite membranes with carbon-

based materials, where it has been demonstrated that these materials reached better performances in fuel cell. Nevertheless, from the author point of view, more performance fuel cell results and, overall, long-term studies are left and required to demonstrate the feasibility of these novel materials in this technology.

Acknowledgments José J. Linares thanks Conselho Nacional de Desenvolvimento Científico e Tecnológico (CNPq) for the financial support through the project (Universal Call 474381/2013-7). Liliane Battirola also thanks CNPq and Coordenação de Aperfeiçoamento de Pessoal de Nível Superior (CAPES) for the financial support. Finally, Justo Lobato wishes to thank the European Commission as this work was supported by the Seventh Framework Programme of the CISTEM project (FCH-JU Grant Agreement Number 325262).

References

1. Millington B, Du S, Pollet BG (2011) The effect of materials on proton exchange membrane fuel cell electrode performance. *J Power Sources* 196:9013–9017
2. Wieser C (2004) Novel polymer electrolyte membranes for automotive applications—requirements and benefits. *Fuel Cells* 4:245–250
3. Bose S, Kuila T, Nguyen TXH et al (2011) Polymer membranes for high temperature proton exchange membrane fuel cell: Recent advances and challenges. *Prog Polym Sci* 36:813–843
4. Cassidy H, Greg JK, Jacob SS et al (2012) U.S. DOE progress towards developing low-cost, high performance, durable polymer electrolyte membranes for fuel cell applications. *Membranes* 2:855–878
5. Yang C, Costamagna P, Srinivasan S et al (2001) Approaches and technical challenges to high temperature operation of proton exchange membrane fuel cells. *J Power Sources* 103:1–9
6. Arsalis A, Nielsen MP, Kær SK (2012) Modeling and optimization of a 1 kWe HT-PEMFC-based micro-CHP residential system. *Int J Hydrogen Energy* 37:2470–2481
7. (EERE) DOoEEaRE. Fuel Cell Technologies Office Multi-Year Research, Development and Demonstration (MYRD&D) Plan, Section 3.4 “Fuel Cells”
8. Eguizábal A, Lemus J, Roda V et al (2012) Nanostructured electrolyte membranes based on zeotypes, protic ionic liquids and porous PBI membranes: preparation, characterization and MEA testing. *Int J Hydrogen Energy* 37:7221–7234
9. Chandan A, Hattenberger M, El-kharouf A et al (2013) High temperature (HT) polymer electrolyte membrane fuel cells (PEMFC)—a review. *J Power Sources* 231:264–278

10. Dupuis A-C (2011) Proton exchange membranes for fuel cells operated at medium temperatures: materials and experimental techniques. *Prog Mater Sci* 56:289–327
11. Savadogo O (2004) Emerging membranes for electrochemical systems: part II. High temperature composite membranes for polymer electrolyte fuel cell (PEFC) applications. *J Power Sources* 127:135–161
12. Herring AM (2006) Inorganic-polymer composite membranes for proton exchange membrane fuel cells. *Polym Rev* 46:245–296
13. Alberti G, Casciola M (2003) Composite membranes for medium-temperature PEM fuel cells. *Ann Rev Mater Res* 33:129–154
14. Jones DJ, Rozière J (2008) Advances in the development of inorganic-organic membranes for fuel cell applications. In: Scherer GG (ed) *Advances in polymer science* 215. Springer, Berlin, pp 219–264
15. Wainright JS, Wang JT, Weng D et al (1995) Acid-doped polybenzimidazoles: a new polymer electrolyte. *J Electrochem Soc* 142:L121–L123
16. Di Noto V, Rivetti J, Bertasi F et al (2014) Nanocomposite membranes based on PBI and ZrO₂ for HT-PEMFCs. Meeting Abstracts MA2014-01:1017–1017
17. Lysova AA, Ponomarev II, Yaroslavtsev AB (2011) Composite materials based on polybenzimidazole and inorganic oxides. *Solid State Ion* 188:132–134
18. Plackett D, Siu A, Li Q et al (2011) High-temperature proton exchange membranes based on polybenzimidazole and clay composites for fuel cells. *J Membr Sci* 383:78–87
19. Chuang S-W, Hsu SL-C, Hsu C-L (2007) Synthesis and properties of fluorine-containing polybenzimidazole/montmorillonite nanocomposite membranes for direct methanol fuel cell applications. *J Power Sources* 168:172–177
20. Hsu SL-C, Chang K-C (2002) Synthesis and properties of polybenzoxazole-clay nanocomposites. *Polymer* 43:4097–4101
21. Choi S, Coronas J, Lai Z et al (2008) Fabrication and gas separation properties of polybenzimidazole (PBI)/nanoporous silicates hybrid membranes. *J Membr Sci* 316:145–152
22. Sadeghi M, Semsarzadeh MA, Moadel H (2009) Enhancement of the gas separation properties of polybenzimidazole (PBI) membrane by incorporation of silica nano particles. *J Membr Sci* 331:21–30
23. Mustarelli P, Quartarone E, Grandi S et al (2008) Polybenzimidazole-based membranes as a real alternative to Nafion for fuel cells operating at low temperature. *Adv Mater* 20:1339–1343
24. Ossiander T, Heinzl C, Gleich S et al (2014) Influence of the size and shape of silica nanoparticles on the properties and degradation of a PBI-based high temperature polymer electrolyte membrane. *J Membr Sci* 454:12–19
25. Kurdakova V, Quartarone E, Mustarelli P et al (2010) PBI-based composite membranes for polymer fuel cells. *J Power Sources* 195:7765–7769
26. Liu YL, Hsu CY, Su YH et al (2005) Chitosan-silica complex membranes from sulfonic acid functionalized silica nanoparticles for pervaporation dehydration of ethanol-water solutions. *Biomacromolecules* 6:368–373
27. Suryani, Liu Y-L (2009) Preparation and properties of nanocomposite membranes of polybenzimidazole/sulfonated silica nanoparticles for proton exchange membranes. *J Membr Sci* 332:121–128
28. Lobato J, Cañizares P, Rodrigo MA et al (2011) A novel titanium PBI-based composite membrane for high temperature PEMFCs. *J Membr Sci* 369:105–111
29. Lobato J, Cañizares P, Rodrigo MA et al (2011) Promising TiOSO₄ composite polybenzimidazole-based membranes for high temperature PEMFCs. *ChemSusChem* 4:1489–1497
30. Lobato J, Cañizares P, Rodrigo MA et al (2011) Enhancement of the fuel cell performance of a high temperature proton exchange membrane fuel cell running with titanium composite polybenzimidazole-based membranes. *J Power Sources* 196:8265–8271
31. Pinar FJ, Cañizares P, Rodrigo MA et al (2012) Titanium composite PBI-based membranes for high temperature polymer electrolyte membrane fuel cells. Effect on titanium dioxide amount. *RSC Adv* 2:1547–1556
32. Namazi H, Ahmadi H (2011) Improving the proton conductivity and water uptake of polybenzimidazole-based proton exchange nanocomposite membranes with TiO₂ and SiO₂ nanoparticles chemically modified surfaces. *J Power Sources* 196:2573–2583
33. Borup R, Meyers J, Pivovar B et al (2007) Scientific aspects of polymer electrolyte fuel cell durability and degradation. *Chem Rev* 107:3904–3951
34. Wang S, Zhao C, Ma W et al (2013) Silane-cross-linked polybenzimidazole with improved conductivity for high temperature proton exchange membrane fuel cells. *J Mater Chem A* 1:621–629
35. Li C, Sun G, Ren S et al (2006) Casting Nafion-sulfonated organosilica nano-composite membranes used in direct methanol fuel cells. *J Membr Sci* 272:50–57
36. Carollo A, Quartarone E, Tomasi C et al (2006) Developments of new proton conducting membranes based on different polybenzimidazole structures for fuel cells applications. *J Power Sources* 160:175–180
37. Quartarone E, Mustarelli P, Magistris A (1998) PEO-based composite polymer electrolytes. *Solid State Ion* 110:1–14
38. Pinar FJ, Cañizares P, Rodrigo MA et al (2015) Long-term testing of a high-temperature proton exchange membrane fuel cell short stack operated with improved polybenzimidazole-based composite membranes. *J Power Sources* 274:177–185
39. Scott K, Xu C, Wu X (2014) Intermediate temperature proton-conducting membrane electrolytes for fuel cells. *WIREs Energy Environ* 3:24–41
40. Gómez-Romero P, Asensio JA, Borrós S (2005) Hybrid proton-conducting membranes for polymer

- electrolyte fuel cells: phosphomolybdic acid doped poly(2,5-benzimidazole)—(ABPBI- $\text{H}_3\text{PMo}_{12}\text{O}_{40}$). *Electrochim Acta* 50:4715–4720
41. Staiti P, Minutoli M, Hocevar S (2000) Membranes based on phosphotungstic acid and polybenzimidazole for fuel cell application. *J Power Sources* 90:231–235
 42. He R, Li Q, Xiao G et al (2003) Proton conductivity of phosphoric acid doped polybenzimidazole and its composites with inorganic proton conductors. *J Membr Sci* 226:169–184
 43. Verma A, Scott K (2010) Development of higher temperature PEMFC based on heteropolyacids and polybenzimidazole. *J Solid State Electrochem* 14:213–219
 44. Staiti P (2001) Proton conductive membranes based on silicotungstic acid/silica and polybenzimidazole. *Mater Lett* 47:241–246
 45. Staiti P (2001) Proton conductive membranes constituted of silicotungstic acid anchored to silica-polybenzimidazole matrices. *J New Mater Electrochem Sys* 4:181–186
 46. Lee JW, Khan SB, Akhtar K et al (2012) Fabrication of composite membrane based on silicotungstic heteropolyacid doped polybenzimidazole for high temperature PEMFC. *Int J Electrochem Sci* 7:6276–6288
 47. Gatto I, Saccà A, Carbone A et al (2007) CO-tolerant electrodes developed with phosphomolybdic acid for polymer electrolyte fuel cell (PEFCs) application. *J Power Sources* 171:540–545
 48. Li MQ, Shao ZG, Scott K (2008) A high conductivity $\text{Cs}_{2.5}\text{H}_{0.5}\text{PMo}_{12}\text{O}_{40}$ /polybenzimidazole (PBI)/ H_3PO_4 composite membrane for proton-exchange membrane fuel cells operating at high temperature. *J Power Sources* 183:69–75
 49. Xu C, Wu X, Wang X et al (2011) Composite membranes of polybenzimidazole and caesium-salts-of-heteropolyacids for intermediate temperature fuel cells. *J Mater Chem* 21:6014–6019
 50. Yamazaki Y, Jang MY, Taniyama T (2004) Proton conductivity of zirconium tricarboxybutylphosphonate/PBI nanocomposite membrane. *Sci Technol Adv Mater* 5:455
 51. Qian W, Shang Y, Fang M et al (2012) Sulfonated polybenzimidazole/zirconium phosphate composite membranes for high temperature applications. *Int J Hydrogen Energy* 37:12919–12924
 52. Di S, Yan L, Han S et al (2012) Enhancing the high-temperature proton conductivity of phosphoric acid doped poly(2,5-benzimidazole) by preblending boron phosphate nanoparticles to the raw materials. *J Power Sources* 211:161–168
 53. Jin YC, Nishida M, Kanematsu W et al (2011) An H_3PO_4 -doped polybenzimidazole/ $\text{Sn}_{0.95}\text{Al}_{0.05}\text{P}_2\text{O}_7$ composite membrane for high-temperature proton exchange membrane fuel cells. *J Power Sources* 196:6042–6047
 54. Wu X, Mamlouk M, Scott K (2011) A PBI- $\text{Sb}_{0.2}\text{Sn}_{0.8}\text{P}_2\text{O}_7$ - H_3PO_4 composite membrane for intermediate temperature fuel cells. *Fuel Cells* 11:620–625
 55. Oh SY, Yoshida T, Kawamura G et al (2010) Inorganic-organic composite electrolytes consisting of polybenzimidazole and Cs-substituted heteropoly acids and their application for medium temperature fuel cells. *J Mater Chem* 20:6359–6366
 56. Staiti P, Minutoli M (2001) Influence of composition and acid treatment on proton conduction of composite polybenzimidazole membranes. *J Power Sources* 94:9–13
 57. Neyerlin KC, Singh A, Chu D (2008) Kinetic characterization of a Pt–Ni/C catalyst with a phosphoric acid doped PBI membrane in a proton exchange membrane fuel cell. *J Power Sources* 176:112–117
 58. Chuang SW, Hsu SLC (2006) Synthesis and properties of a new fluorine-containing polybenzimidazole for high-temperature fuel-cell applications. *J Polym Sci Part A* 44:4508–4513
 59. van de Ven E, Chairuna A, Merle G et al (2013) Ionic liquid doped polybenzimidazole membranes for high temperature proton exchange membrane fuel cell applications. *J Power Sources* 222:202–209
 60. Greaves TL, Drummond CJ (2008) Protic ionic liquids: properties and applications. *Chem Rev* 108:206–237
 61. Freemantle M (2010) An introduction to ionic liquids. Royal Society of chemistry, Cambridge
 62. Singh MP, Singh RK, Chandra S (2014) Ionic liquids confined in porous matrices: physicochemical properties and applications. *Prog Mater Sci* 64:73–120
 63. Ye Y-S, Rick J, Hwang B-J (2013) Ionic liquid polymer electrolytes. *J Mater Chem A* 1:2719–2743
 64. Liu S, Zhou L, Wang P et al (2014) Ionic-liquid-based proton conducting membranes for anhydrous H_2/Cl_2 fuel-cell applications. *ACS Appl Mater Interfaces* 6:3195–3200
 65. Wang JT-W, Hsu SL-C (2011) Enhanced high-temperature polymer electrolyte membrane for fuel cells based on polybenzimidazole and ionic liquids. *Electrochim Acta* 56:2842–2846
 66. Ye H, Huang J, Xu J et al (2008) New membranes based on ionic liquids for PEM fuel cells at elevated temperatures. *J Power Sources* 178:651–660
 67. Erdemi H, Akbey Ü, Meyer WH (2010) Conductivity behavior and solid state NMR investigation of imidazolium-based polymeric ionic liquids. *Solid State Ion* 181:1586–1595
 68. Ye YS, Cheng MY, Tseng JY et al (2011) New proton conducting membranes with high retention of protic ionic liquids. *J Mater Chem* 21:2723–2732
 69. Coleman JN, Khan U, Blau WJ et al (2006) Small but strong: a review of the mechanical properties of carbon nanotube–polymer composites. *Carbon* 44:1624–1652
 70. Li N, Zhang F, Wang J et al (2009) Dispersions of carbon nanotubes in sulfonated poly[bis(benzimidazobenzisoquinolinones)] and their proton-conducting composite membranes. *Polymer* 50:3600–3608

71. Lu Y, Chen J, Cui H et al (2008) Doping of carbon fiber into polybenzimidazole matrix and mechanical properties of structural carbon fiber-doped polybenzimidazole composites. *Composites Sci Technol* 68:3278–3284
72. Kannan R, Parthasarathy M, Maraveedu SU et al (2009) Domain size manipulation of perfluorinated polymer electrolytes by sulfonic acid-functionalized MWCNTs to enhance fuel cell performance. *Langmuir* 25:8299–8305
73. Suryani, Chang C-M, Liu Y-L et al (2011) Polybenzimidazole membranes modified with polyelectrolyte-functionalized multiwalled carbon nanotubes for proton exchange membrane fuel cells. *J Mater Chem* 21:7480–7486
74. Kannan R, Kagalwala HN, Chaudhari HD et al (2011) Improved performance of phosphonated carbon nanotube-polybenzimidazole composite membranes in proton exchange membrane fuel cells. *J Mater Chem* 21:7223–7231
75. Asensio JA, Borrós S, Gómez-Romero P (2002) Proton-conducting polymers based on benzimidazoles and sulfonated benzimidazoles. *J Polym Sci Part A* 40:3703–3710
76. Glipa X, El Haddad M, Jones DJ et al (1997) Synthesis and characterisation of sulfonated polybenzimidazole: a highly conducting proton exchange polymer. *Solid State Ion* 97:323–331
77. Wu J-F, Lo C-F, Li L-Y et al (2014) Thermally stable polybenzimidazole/carbon nano-tube composites for alkaline direct methanol fuel cell applications. *J Power Sources* 246:39–48
78. Hou H, Sun G, He R et al (2008) Alkali doped polybenzimidazole membrane for alkaline direct methanol fuel cell. *Int J Hydrogen Energy* 33:7172–7176
79. Xue C, Zou J, Sun Z et al (2014) Graphite oxide/functionalized graphene oxide and polybenzimidazole composite membranes for high temperature proton exchange membrane fuel cells. *Int J Hydrogen Energy* 39:7931–7939
80. Xu C, Cao Y, Kumar R et al (2011) A polybenzimidazole/sulfonated graphite oxide composite membrane for high temperature polymer electrolyte membrane fuel cells. *J Mater Chem* 21:11359–11364
81. Eda G, Chhowalla M (2010) Chemically derived graphene oxide: towards large-area thin-film electronics and optoelectronics. *Adv Mater* 22:2392–2415
82. Jung I, Dikin D, Park S et al (2008) Effect of water vapor on electrical properties of individual reduced graphene oxide sheets. *J Phys Chem C* 112:20264–20268
83. Cai D, Song M, Xu C (2008) Highly conductive carbon-nanotube/graphite-oxide hybrid films. *Adv Mater* 20:1706–1709
84. Chen D, Tang L, Li J (2010) Graphene-based materials in electrochemistry. *Chem Soc Rev* 39:3157–3180
85. Tseng C-Y, Ye Y-S, Cheng M-Y et al (2011) Sulfonated polyimide proton exchange membranes with graphene oxide show improved proton conductivity, methanol crossover impedance, and mechanical properties. *Adv Energy Mater* 1:1220–1224

Tom Engl, Lorenz Gubler, and Thomas J. Schmidt

14.1 Introduction

The catalyst is a crucial component in all fuel cell types, since without catalysts both the anode and cathode reaction are not proceeding with high enough rates. More precisely, the catalyst, which is noble metal based in low temperature fuel cells, needs to be highly active towards the hydrogen oxidation reaction (HOR) and the oxygen reduction reaction (ORR), respectively. Whereas the HOR is a lesser issue in acidic electrolyte due to its simple reaction mechanism and the high exchange current density [1, 2], the ORR is a complex multi-electron transfer reaction with various intermediates and is therefore rather slow [3, 4]. An ORR reaction pathway proposed by Wroblowa and Razumney [5] in 1976 is illustrated in Fig. 14.1.

The sluggish reaction rate is associated with large fuel cell cathode overpotential of a few hundred millivolts. It is therefore necessary to improve the ORR kinetics in order to reduce the corresponding fuel cell efficiency losses.

Moreover, catalysts require chemical and electrochemical, thermal and mechanical robustness during their entire lifetime. After decades of intensive research, the most commonly used catalysts in HT-PEMFC are still based on platinum and platinum alloys [6]. Even though the activity was improved over time the platinum raw material cost kept pace and increased from around 20 \$ g⁻¹ in 1960 (inflation adjusted) to approximately 50 \$ g⁻¹ in 2014 [7]. The dilemma between good performance due to higher catalyst loadings and reasonable cost per kilowatt power is therefore still unresolved and needs to be carefully considered for each fuel cell system individually.

Catalysts in HT-PEMFC usually consist of high surface area carbon (graphitized or non-graphitized) supported Pt nanoparticles which are combined with a binder in order to form the catalyst layer (CL) within a membrane electrode assembly (MEA). The catalyst's high surface area is the basis for an extended three phase boundary, which is required to maximize the catalyst surface in contact with the electrolyte to achieve high catalyst utilization. Moreover, carbon is a suitable electron conductor due to its low ohmic resistance. The catalyst layer is held together by a high temperature stable polymer binder, e.g., PTFE. The binder is vital for establishing a good mechanical CL-membrane interface (Fig. 14.2). Unlike in LT-PEMFC, where a proton exchange ionomer is used as

T. Engl • L. Gubler
Electrochemistry Laboratory, Paul Scherrer Institut,
Villigen PSI 5232, Switzerland

T.J. Schmidt (✉)
Electrochemistry Laboratory, Paul Scherrer Institut,
Villigen PSI 5232, Switzerland

Laboratory of Physical Chemistry, ETH Zürich,
Zürich 8093, Switzerland
e-mail: thomasjustus.schmidt@psi.ch

binder, the binder in HT-PEMFC does not provide a proton conduction pathway between the catalyst and the membrane. Phosphoric acid (PA) within the CL is therefore enabling proton transport to and from the catalyst. However, too much PA (known as electrode flooding) impedes gas accessibility and leads to performance losses and performance deterioration.

In general, there are two methods to introduce the PA to the CL. The first one relies on a highly PA-doped membrane. The PA is transferred between membrane and catalyst layer upon MEA preparation and/or cell assembly, respectively. The second method involves depositing (spraying, painting, etc.) PA directly onto the CL. The PA content in the membrane is one of the decisive factors for the selection of one of the two preparation methods. Overall, the CL needs to provide electron and proton transport pathways, gas accessibility, high catalytic activity towards HOR and ORR, a high electrochemically active surface area (ECSA) and has to withstand the harsh HT-PEMFC environment (acidity close to pH = 0, temperature up to 180 °C, and electrochemical potentials up to 1.5 V).

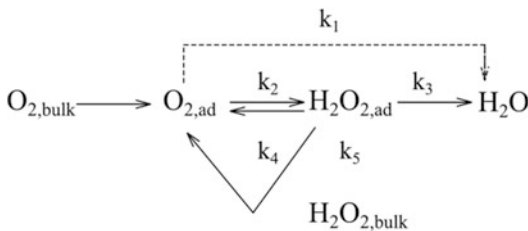
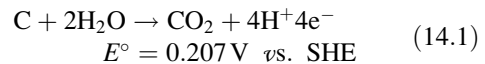


Fig. 14.1 Simplified ORR reaction mechanism [5]

Those challenging conditions lead to some well-known CL degradation effects, which are summarized in Table 14.1 [8]. They are triggered individually by certain fuel cell operation modes and cause ECSA and performance losses. One of the prominent degradation mechanisms is known as the “start/stop”—or “reverse-current decay” mechanism [9, 10]. During start-up or shut-down of a PEMFC (LT as well as HT), a fuel/air gas front can propagate through the anode (fuel electrode) compartment (Fig. 14.3a). This transient gas front causes high potentials (up to 1.5 V [8, 11]) on the cathode side (air electrode). Although carbon is already beyond its thermodynamic stability (14.1) on the air electrode under steady state conditions, its sluggish corrosion rate at potentials below 0.9 V does not lead to too high corrosion rates. The high potential peaks during start/stop operation, in contrast, are very much relevant and lead to rapid and irreversible carbon corrosion (Fig. 14.3b).



As aforementioned, high surface area carbon is used as support in the CL, for the noble metal catalyst nanoparticles. Therefore, if the carbon is gradually oxidized, the ECSA decreases and the fuel cell power concomitantly declines. The decrease of the ECSA can mainly be attributed to coalescence (Ostwald ripening), detachment, and dissolution of Pt particles, respectively.

It is essential to precisely measure and quantify the damage caused by the listed degradation modes in order to evaluate new materials or operation strategies regarding their mitigation

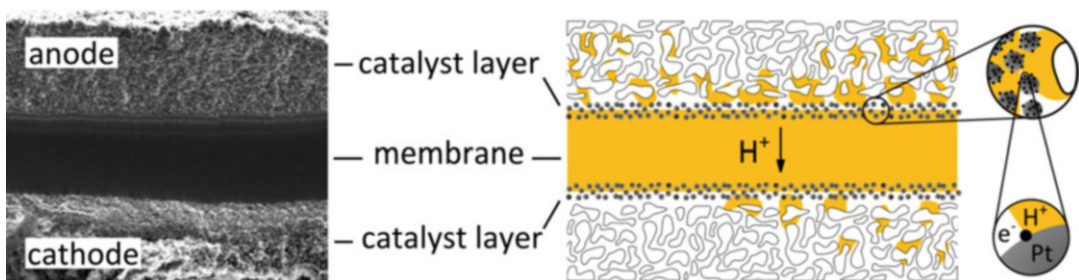


Fig. 14.2 Cross-section image of an HT-PEMFC MEA (captured via secondary electron detection, *left*) and sketch (*right*)

Table 14.1 Relevant catalyst layer degradation modes

Cause	Mechanism	Parameters	Effect
Catalyst particle growth	Migration, Ostwald ripening, dissolution/recrystallization	T, E	ECSA and performance loss
Catalyst dissolution	Electrochemical dissolution	T, E	
PA evaporation/oversupply within the CL	Evaporation/flooding	T, p	
Carbon corrosion	Chemical and electrochemical oxidation	T, E, p	

T temperature, E electrochemical potential, p pressure

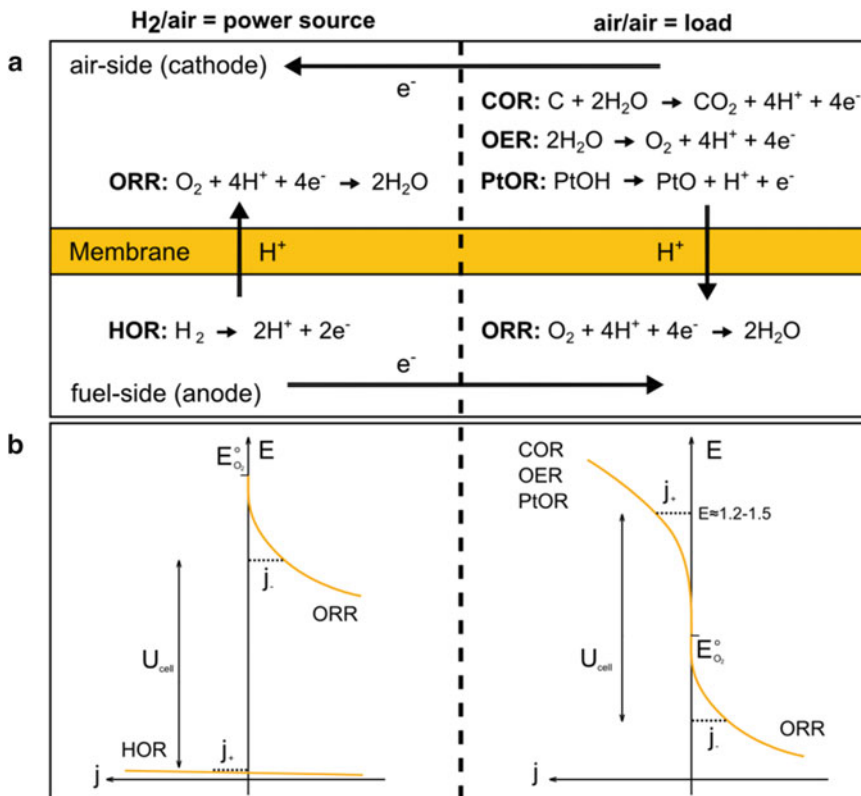


Fig. 14.3 Start/stop degradation mechanism including the main reaction pathways (a) and schematic polarization curves (b) within the different characteristic fuel

cell regions caused by the gas front passing through the fuel compartment. Reproduced from [9, 12] with permission of the Electrochemical Society

capability. Whereas the difference in fuel cell performance can be measured in straightforward manner via polarization curves, determining the ECSA of the electrode is more challenging in an HT-PEMFC environment.

This chapter therefore mainly addresses two questions: how can one precisely and reliably measure the ECSA in HT-PEMFC and how can carbon corrosion be mitigated on an operation and material-based level?

14.2 Catalyst and Catalyst Layer Characterization

The change in ECSA is a key descriptor for identifying and characterizing the degradation within the electrode and the catalyst layer since it can be used to estimate the kinetic performance of an electrode. Cyclic voltammetry (CV) is a common and established method for ECSA

determination of an electrode. Nevertheless, measuring the ECSA is not as straightforward as recording a polarization curve, especially in HT-PEMFCs. Hydrogen underpotential deposition (H_{upd}) and/or CO oxidation is used for ECSA measurements in LT-PEMFCs [13]. Unfortunately, for HT-PEMFCs those techniques are not directly applicable. Due to the presence of highly concentrated phosphoric acid, specific adsorption of hydrogen phosphate ($H_2PO_4^-$) even close to the hydrogen equilibrium potential H_{UPD} is largely suppressed.

In addition, at elevated temperatures, specifically above 100 °C, high faradaic hydrogen evolution reaction (HER) currents are superimposing the pseudocapacitive H_{upd} currents. Those reasons render H_{upd} charge determination rather unreliable and unsuitable for HT-PEMFC ECSA measurements. The second method to be considered is based on the electrooxidation of one monolayer of adsorbed CO on the electrode surface (“CO stripping”). It is only partially affected by the aforementioned issues due to the very high tendency of CO to adsorb on available catalytically active platinum sites compared to hydrogen (protons). In addition, the HER is not interfering with the CO oxidation because they occur at different potentials. Nevertheless, CO stripping also needs to overcome some

drawbacks in order to be applied to HT-PEMFC. Side reactions (e.g., surface oxidation, anion adsorption, PA decomposition [14]), which are not related to the CO oxidation, do influence the ECSA determination at elevated temperatures. Additionally, CO adsorption is strongly temperature dependent, see, e.g., the CO adsorption isotherms in [15–18]. Without consideration of the CO adsorption isotherm, CO stripping measurements at elevated temperature would therefore yield a too small ECSA. In order to compensate this behavior, a calibration curve needs to be established to measure the ECSA based on the oxidation of one monolayer of CO ($ECSA_{\text{mono}}$) at any given temperature.

There are two different strategies reported to overcome the influence of side reactions and temperature effects in HT-PEMFCs during in situ CO stripping at elevated temperatures (for details, see [19]). The first one is based on the so-called reference CV. The reference CV simulates the actual CO stripping CV process. All parameters are kept identical compared to the CO stripping, but no CO adsorption is allowed to happen (N_2 is used instead). Afterwards, the recorded reference CV is subtracted from the CO stripping CV, thus the effect of all side reactions is taken care of (cf. Fig. 14.4a, $ECSA_{\text{CV vs. ref. CV}}$).

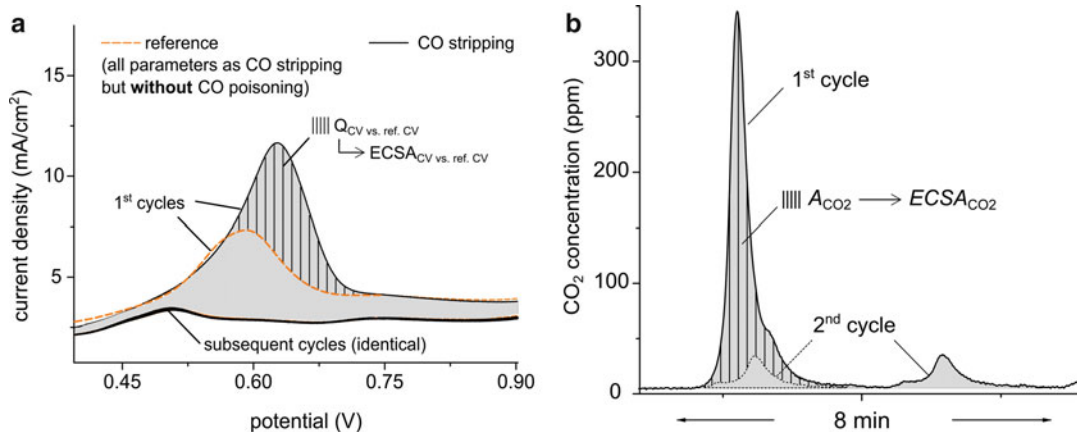


Fig. 14.4 (a) Reference and CO stripping CV close-ups. The *hatched area* indicates the charge for the $ECSA_{\text{CV vs. ref. CV}}$ calculation. (b) Real-time CO_2 concentration in the examined electrode’s exhaust during the first

two CO stripping potential cycles. The *peak area* of the second potential cycle is subtracted from the area of the first one. The resulting *hatched area* is used for the $ECSA_{CO_2}$ calculations

The second strategy is based on the detection of CO_2 , which is present in the exhaust gas of the working electrode during CO stripping, in real time. In Fig. 14.4b, the CO_2 signal of the first two CO stripping potential cycles are shown. The CO_2 signal is correlated to the ECSA but only the peak during the first cycle can mainly be attributed to the CO oxidation process whereas the peak appearing during the second cycle originates from the oxidation of various carbonaceous species at the working electrode during the potential sweeps. Therefore, the peak area of the second cycle needs to be subtracted from the peak area of the first cycle to determine the amount of CO_2 originating from the CO oxidation process only. Consequently, the $\text{ECSA}_{\text{CO}_2}$ can now be calculated via A_{CO_2} (Fig. 14.4b) without the influence of any side reactions.

Both methods provide very reliable and comparable results, which can be fitted by a Langmuir adsorption isostere [19]. The CO_2 method has the advantage that no reference CV needs to be recorded. Nevertheless, in practice not every laboratory is equipped with the required CO_2 detector and the method using the reference CV may be more generally applicable.

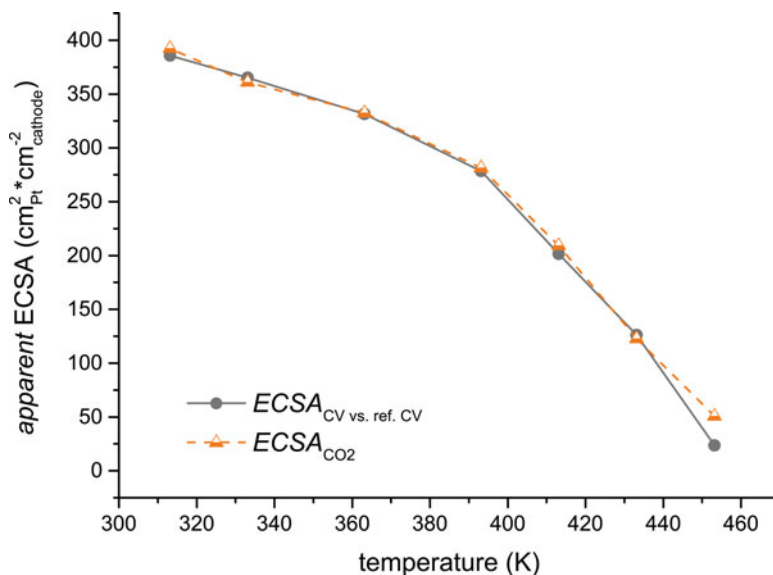
As depicted in Fig. 14.5, CO adsorption on Pt is a temperature-dependent process. Therefore,

even if one now can precisely measure the amount of oxidized CO, this value does not yet represent the absolute ECSA based on one monolayer of adsorbed CO on platinum ($\text{ECSA}_{\text{mono}}$). For the estimation of $\text{ECSA}_{\text{mono}}$ at target operating conditions, it is necessary to establish a temperature calibration curve. In Fig. 14.5, the apparent ECSA trend from 40 to 180 °C is shown. The ECSA approaches a maximum value at 40 °C. At this temperature, a 1:1 adsorption of CO on the Pt surface can be assumed and an empirical calibration equation can be deduced ((14.2), based on $\text{ECSA}_{\text{CV vs. ref. CV}}$) for one specific catalyst layer configuration.

$$\begin{aligned} \text{ECSA}_{\text{mono}} &= \text{ECSA}_{\text{CV vs. ref. CV}} \\ &\times (1.01 - 5.32 \times 10^{-7} \times \vartheta^{2.77})^{-1} \pm 3\% \end{aligned} \quad (14.2)$$

It is then possible to determine $\text{ECSA}_{\text{mono}}$ from the measured $\text{ECSA}_{\text{CV vs. ref. CV}}$ at any given temperature between 40 and 180 °C. Besides the traditional method to measure the ECSA globally for the entire electrode, it is furthermore possible to create spatially resolved ECSA mappings, which are specifically important if local catalyst layer degradation effects are of interest. Those mappings yield an in-plane

Fig. 14.5 Measured apparent ECSA trend at different temperatures determined via the two introduced methods. The gray line is used to establish a calibration curve



distribution of the ECSA across the electrode. This diagnostic method provides the opportunity to describe condition and performance of the fuel cell very precisely. One can trace ECSA changes as function of material or operational changes accurately and in situ.

The example shown in Fig. 14.6 uses a 10 by 10 array of gold-plated shunt resistors positioned between a thin graphitic flow field and the current collector [20] to measure the oxidation/reduction currents during ECSA measurements. Following the CV vs. ref. CV routine mentioned earlier, it is possible to deduce the ECSA based on a monolayer of adsorbed CO on Pt for 100 segments (Fig. 14.6). In recent studies, this spatially resolved measurement technique was successfully used to investigate the heterogeneous ECSA change across the air electrode before and after 100 simulated fuel cell start-ups and shut-downs [21].

14.3 Mitigating Carbon Corrosion During Start-Up and Shut-Down

Start-/stop-induced carbon oxidation mitigation strategies can be divided into two categories. One is focused on developing new materials, such as carbon-free electrodes [22–24] or selective hydrogen oxidation catalysts [4, 25, 26]. The second category consists of cell or system operating strategies. Different approaches such as flow rate adjustments [27, 28], cell potential control [9], or nitrogen purging [9, 29] have been proposed. A vast number of patents have been published in both categories.

Two patents from Reiser et al. and Balliet et al. [30, 31] are based on air and fuel purge with high flow rate at the fuel cell electrode compartments. An increased gas flow rate is taking advantage of the sluggish reaction kinetics of

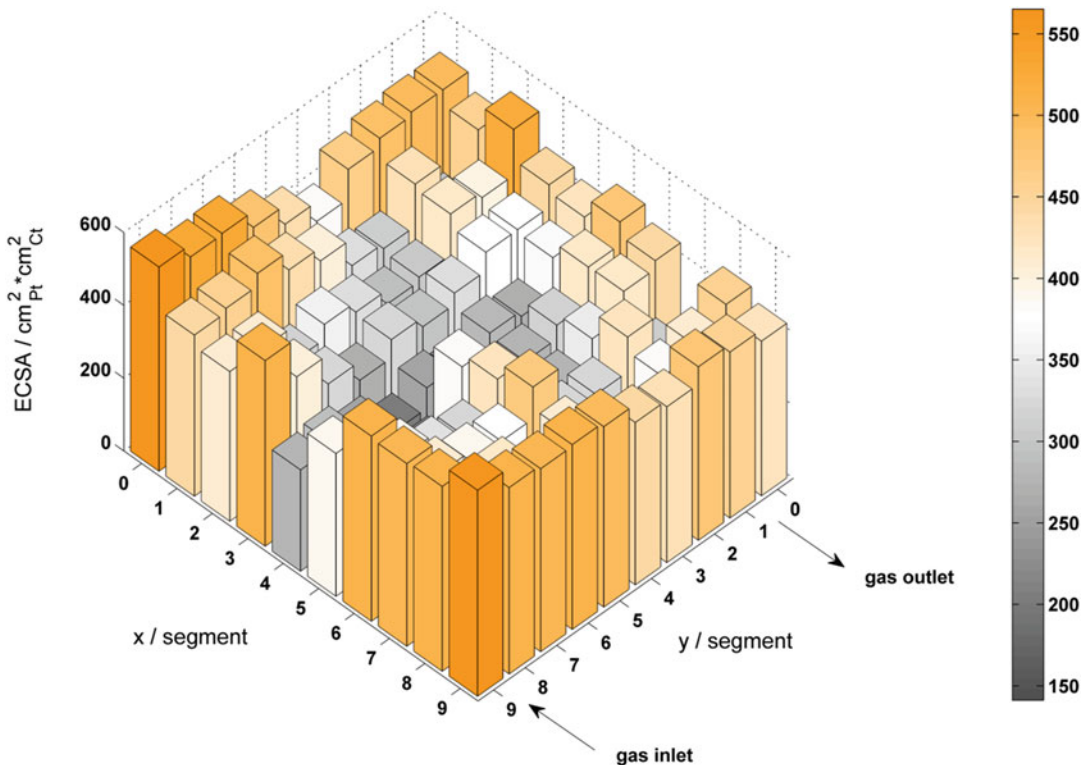


Fig. 14.6 Calculated individual ECSA values per CL segment deduced from spatially resolved CO stripping CVs at 160 °C

the ORR and COR. By reducing the time for the gas front to propagate through the cell, the duration of the adverse reverse-current situation is shortened, and thus the time for carbon oxidation reduced. The purging can be combined with reduced fuel cell temperature during start-up or shut-down [32]. In another setup, the fuel gas is recirculated in the anodic compartment until H_2 is oxidized to H_2O [33] or the oxygen partial pressure on the air side is reduced to negligible values [34]. Using auxiliary loads or shunt resistors to reduce the maximum cathodic potential is another widely claimed approach for reducing the amount of oxidized carbon during start-up and shut-down [32, 33, 35, 36]. The total amount of corroded carbon is directly correlated to the maximum air electrode potential. Therefore, if the potential on the air side is not allowed to exceed a certain threshold, the corrosion can be reduced effectively. The electrical energy produced during the process in the auxiliary load can furthermore be stored in, for example, a battery or capacitor [37].

A prior-art example for modifying the composition of the CL and, in particular, the catalyst

itself has also been patented. Bett et al. have proposed the incorporation of a catalyst at the cathode that favors the oxygen evolution reaction (OER) instead of the COR [38]. Therefore, water is split preferentially over carbon corrosion in order to provide electrons during the reverse-current situation. Furthermore, on the fuel side a selective HOR catalyst, i.e., poor ORR catalyst, can be included [38]. If there is no electron demand on the fuel side during start/stop, the air electrode is not forced to provide any and the internal currents remain low. Besides the purging approach, all of the aforementioned examples are more or less complex in terms of manufacturing and system control or require additional system or cell hardware. The following example for mitigating carbon corrosion in the catalyst layer is taking advantage of the properties of CO, which in general are negatively connotated in the fuel cell community due to its poisoning effect in the fuel gas stream.

An increased CO partial pressure on the fuel electrode (anode) during start/stop results in a reduced amount of oxidized carbon on the air electrode (cathode). Compared to pure H_2 without

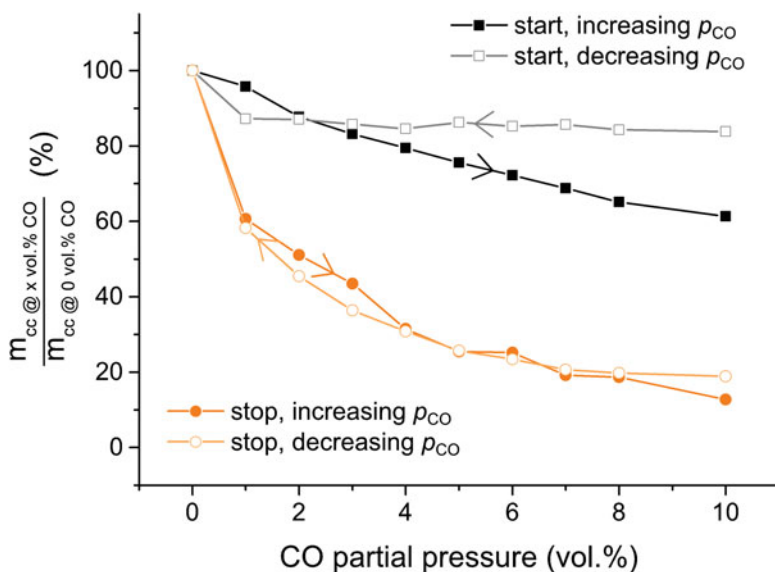


Fig. 14.7 Change of corroded carbon on the air electrode corresponding to a given CO partial pressure on the fuel electrode. The *solid symbols* represent the measurements with increasing p_{CO} whereas the *open*

symbols indicate the measurements with decreasing p_{CO} . Measuring conditions: 180 °C, fuel electrode with varying supply gas composition at 40 L_nh⁻¹, cathode with O₂ at 40 L_nh⁻¹

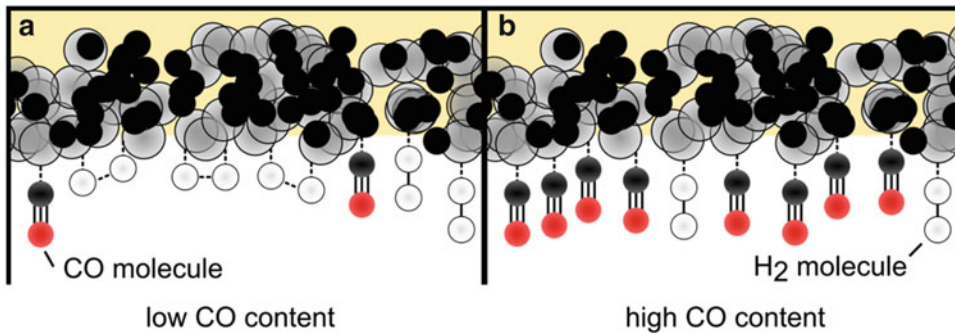


Fig. 14.8 Sketches of the anode catalyst surface with low and high CO partial pressures in the reformate gas resulting in low (a) and high (b) CO equilibrium coverages on the fuel electrode catalyst surface

CO, a partial pressure of 10 vol.% CO in a reformate gas (typical CO volume fraction directly at the reformer exhaust [39]) reduces the amount of corroded carbon up to 40 % for start and around 80 % for stop events (Fig. 14.7 [40]). Therefore, it is not only possible but desirable to use CO-containing fuel gas to improve the overall lifetime of the fuel cell. Conceptually, this positive effect of the presence of CO on the corrosion during start/stop processes might be even more pronounced in LT-PEMFC due to very fast CO adsorption kinetics on Pt and significantly higher CO saturation coverages [15–19].

The sketch in Fig. 14.8 provides a conclusive explanation why less carbon is oxidized on the air electrode during start-up and shut-down of the cell with an increasing CO partial pressure in the fuel gas. The driving force for oxidizing carbon on the air electrode in the passive section of the fuel cell (=load) is the HOR in the active section of the fuel cell (=source, see [9, 10] and Fig. 14.3) on the fuel electrode. The amount of oxidized hydrogen is directly correlated to the amount of oxidized carbon. Prior to its oxidation, hydrogen needs to adsorb on the fuel electrode's free active sites. If CO is introduced to the electrode alongside hydrogen, there adsorption of CO and H₂ is competitive, with CO having the higher adsorption energies [41] leading quickly to a CO-covered Pt surface reducing the number of sites for the HOR. This trend (diminishing hydrogen adsorption and oxidation sites) increases with an increasing CO partial pressure (Fig. 14.8a vs. Fig. 14.8b). Due to the reduced

overall hydrogen oxidation rates in the presence of a CO-covered surface less carbon is oxidized at the air electrode. This is in agreement with the observed increasing anode overpotential during fuel cell operation with CO-containing hydrogen as shown in [18]. Increasing the CO coverage on the fuel electrode catalyst surface causes therefore a similar effect than reducing the Pt loading on the same electrode, as was discussed previously in [42].

The proposed model can additionally explain why the CO mitigation effect is more pronounced for shut-downs compared to start-ups. If the cell is in operation, there is a stationary CO adsorption equilibrium covering the electrode surface. The fraction of covered surface area is mainly determined by the operation temperature (in this case 180 °C) and CO partial pressure. The adsorption equilibrium is furthermore homogeneously established across the whole electrode. If the cell is now stopped (Fig. 14.9a) and O₂ is introduced into the fuel electrode, the possibility of oxidizing hydrogen or reducing oxygen is strongly suppressed due to the high CO coverage at the fuel electrode. Subsequently, because the HOR current is directly correlated to the amount of oxidized carbon on the air electrode, less carbon is getting corroded compared to a CO-free shut-down. Additionally, during the introduction of oxygen onto a CO-covered Pt surface, an air-bleed effect may be observed, i.e., the chemical oxidation of CO by O₂ reduces the number of electrochemical oxygen reduction turnovers due to surface-near

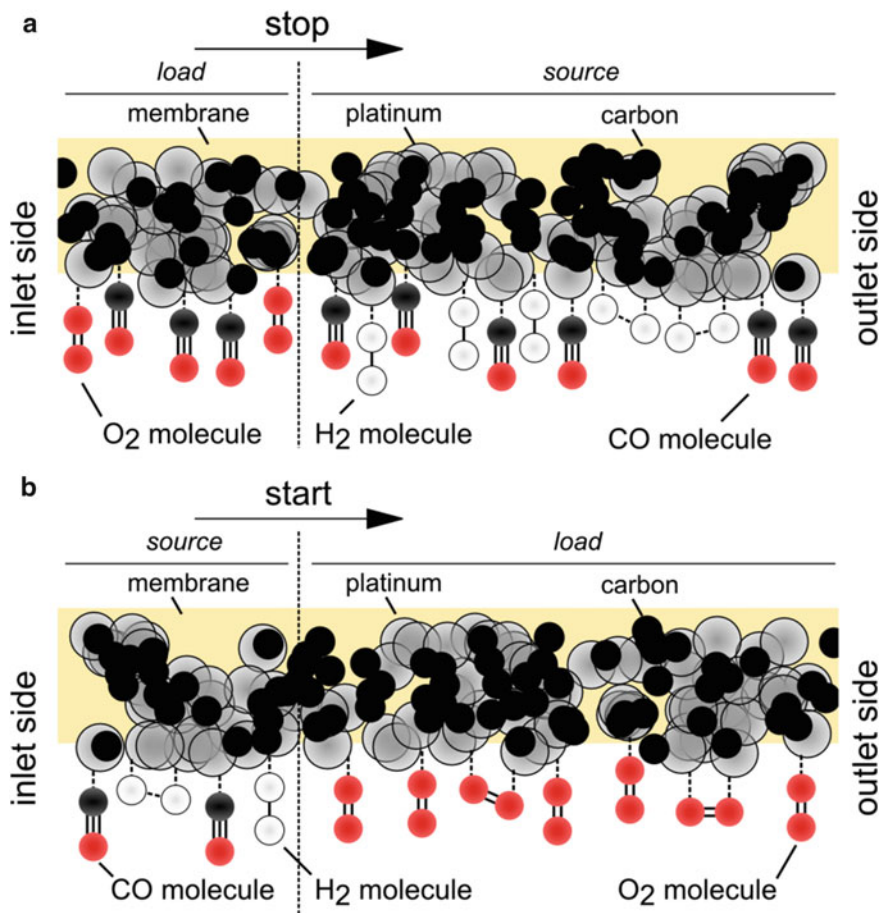


Fig. 14.9 Sketch of the fuel electrode processes during a start (a) and stop (b) transient with CO in the reformat gas

reduction of the O_2 partial pressure. A contrary behavior can be observed if the cell is started. Only air/ O_2 is present in the fuel electrode and no or only a negligible number of surface sites are covered by CO. When H_2/CO is now introduced to the fuel electrode, CO needs to compete with the very fast hydrogen oxidation kinetics for adsorption on the catalyst surface. Therefore, only a limited number of active sites will be covered by CO (Fig. 14.9b), and the overall hydrogen oxidation/carbon corrosion current is significantly higher compared to the shut-down process when there is almost CO saturation coverage especially at high CO partial pressures.

Another differentiating factor favoring shut-downs over start-ups regarding their CO supported carbon corrosion mitigation performance

is that during start-up only the fuel side of the propagating gas front (=source) is affected by the presence of CO. The oxygen side (=load) is free of CO. During a shut-down, in contrast, both sides of the gas front (source and load) are benefiting from a CO-covered electrode surface leading to smaller corrosion currents during shut-down.

In order to gain more detailed information on the effect of CO regarding carbon corrosion the CO partial pressure was correlated with the gas flow rate and the cell temperature during start/stop. Figure 14.10 highlights a very clear correlation between those parameters for start-ups (introduction of H_2 to the air-filled fuel electrode). Low flow rates and CO partial pressures in combination with high temperatures lead to

start-up

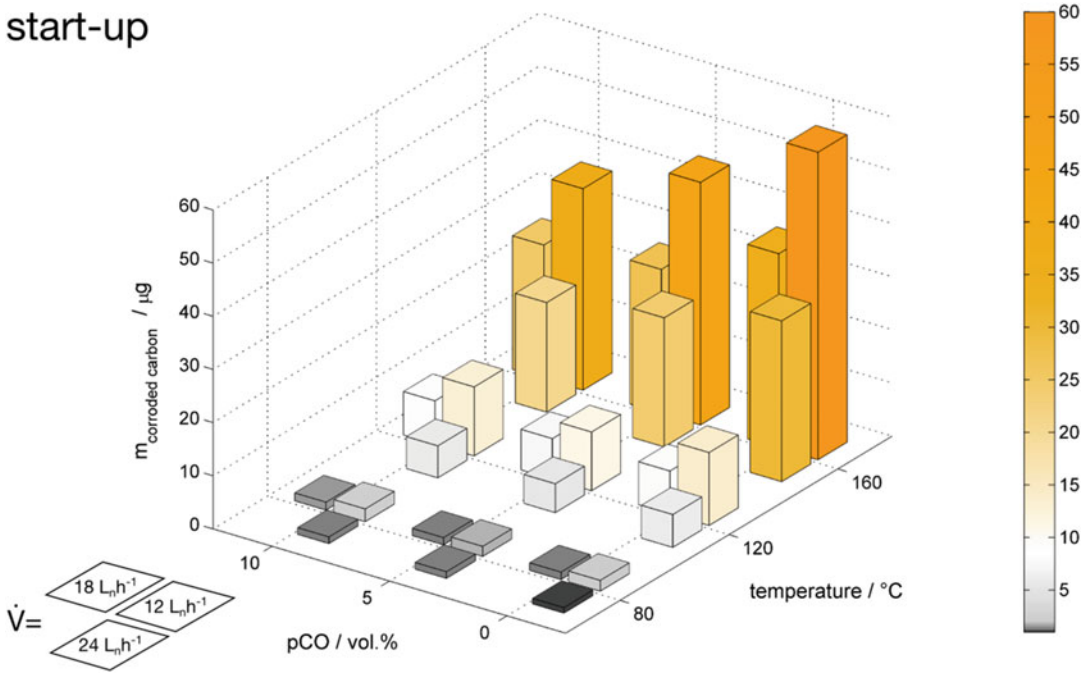


Fig. 14.10 Amount of corroded carbon m during start-up as a function of temperature ϑ , flow rate \dot{V} , and CO partial pressure p_{CO}

the highest amount of corroded carbon. The positive effect of CO is more pronounced at lower flow rates because CO has more time to adsorb on the platinum surface even though the CO dose during the start-up is smaller at low flow rates compared to higher ones. This behavior is in support of the aforementioned mitigation mechanism. At temperatures below 160 $^{\circ}\text{C}$, the flow rate is the most relevant parameter for mitigating carbon corrosion. Furthermore, it is rather obvious that at 80 $^{\circ}\text{C}$ the amount of corroded carbon is almost negligible compared to 160 $^{\circ}\text{C}$.

During shut-down, the findings are quite similar yet the effect of CO is more pronounced (Fig. 14.11) compared to start-ups due to the increased residence time of CO in the electrode compartment. At 120 $^{\circ}\text{C}$, only 5 vol.% of CO in the fuel gas can almost completely suppress carbon oxidation during shut-down, which is quite remarkable. The effect of temperature itself is again comparable between shut-down and start-up whereas the flow rate is more crucial at shut-downs especially at 160 $^{\circ}\text{C}$ and in the absence of CO.

Those findings can potentially be implemented fairly easily in reformat operated HT- or even LT-PEMFC systems by bypassing the steam reformer during start-up or shut-down. The adsorbed CO will not decrease the fuel cell performance during operation because it is oxidized quickly after switching back to regular gas conditions (low CO partial pressure).

14.4 Carbon Support and Alloy Catalysts

Besides the already-mentioned system-based strategies for mitigating carbon oxidation, there is obviously also the possibility to improve the CL composite (Pt/carbon, binder, PA) regarding start-/stop-induced degradation. It was shown that Pt alloys in HT-PEMFC exhibit reduced electrode overpotentials subsequent to simulated start/stop cycling compared to pure Pt. It was furthermore found that changing the catalyst carbon support to stabilized (graphitized) carbon (SC) also positively affects fuel cell durability.

shut-down

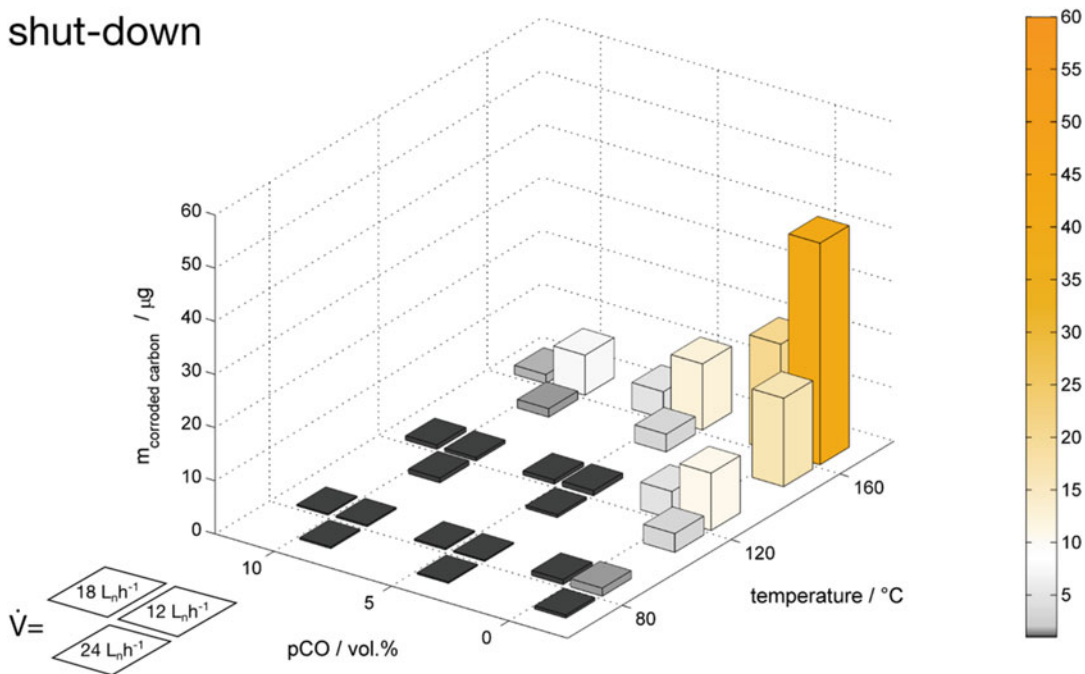


Fig. 14.11 Amount of corroded carbon m during shut-down as a function of temperature ϑ , flow rate \dot{V} , and CO partial pressure p_{CO}

The effect of both modifications is illustrated in Fig. 14.12. Polarization curves were recorded and the change in IR-corrected voltage at two different current densities and three different catalyst types (Pt/Vulcan XC 72, Pt-Alloy/Vulcan XC72 and Pt-Alloy/SC) is correlated with the number of simulated start/stop cycles. The voltage drop for all three samples increases with increasing cycle number at both current densities. Nevertheless, the Pt alloy is more stable at 0.3 A cm^{-2} compared to the pure Pt where mostly the changes in catalyst kinetics are dominating. It is furthermore noticeable that at the lower current density the SC is boosting the mitigation effect. At 0.7 A cm^{-2} where additionally mass transport effects come into play, the positive alloy effect cannot be observed whereas the SC effect is still very much pronounced.

Further insight is gained if the performance loss upon start/stop cycling is correlated with the accumulated total carbon loss at 0.1 and 0.7 A cm^{-2} (Fig. 14.13a, b). At lower current densities, where kinetic ORR losses ($\Delta\eta_{\text{ORR}}$) are dominant, it seems that the relationship between

activation overpotential and the accumulated carbon loss follows a different trend for the different catalysts. After 150 cycles, the Pt/Vulcan and the Pt-Alloy/Vulcan catalyst lost both around 30 % of their initial carbon support, but the overpotential for the pure Pt/Vulcan is twice as high as that of the Pt-Alloy/Vulcan (Fig. 14.13a). In contrast, at the higher current density (Fig. 14.13b), at which mass transport losses ($\Delta\eta_{\text{mtx}}$) dominate, the Vulcan-based catalysts exhibit almost an identical correlation between total carbon loss and overpotential. After 150 cycles, they have lost both around 30 % carbon and an increase of the mass transport overpotential is observed ($\Delta\eta_{\text{mtx}} = 60 \text{ mV}$). The catalyst based on stabilized carbon is following a different trend. Its overpotential saturates at 20 mV even though the total carbon loss is increasing from 5 % after 50 cycles up to 20 % after 150 cycles. Stabilizing the platinum support is therefore, in this case, beneficial at higher current densities regarding start/stop degradation mitigation.

The effect of simulated start/stop cycling can not only be measured electrochemically as shown before but also visualized by SEM imaging. In

Fig. 14.14, one can see two SEM cross-section images of the Pt-Alloy/SC MEA at beginning of life (BOL) and after 150 start/stop cycles (EOL). Clearly, there is a redistribution of platinum on the cathode CL subsequent to the cycling. A 5–7 μm thick enriched platinum layer appears between the CL and the membrane interface, while the CL

platinum content is reduced. The formation of a platinum band due to start/stop cycling is also well known for LT-PEMFC [44]. The origin of the band is generally explained by (1) catalyst agglomeration triggered by carbon corrosion; (2) electrochemical Ostwald-ripening; and (3) coalescence of particles via nanocrystallite

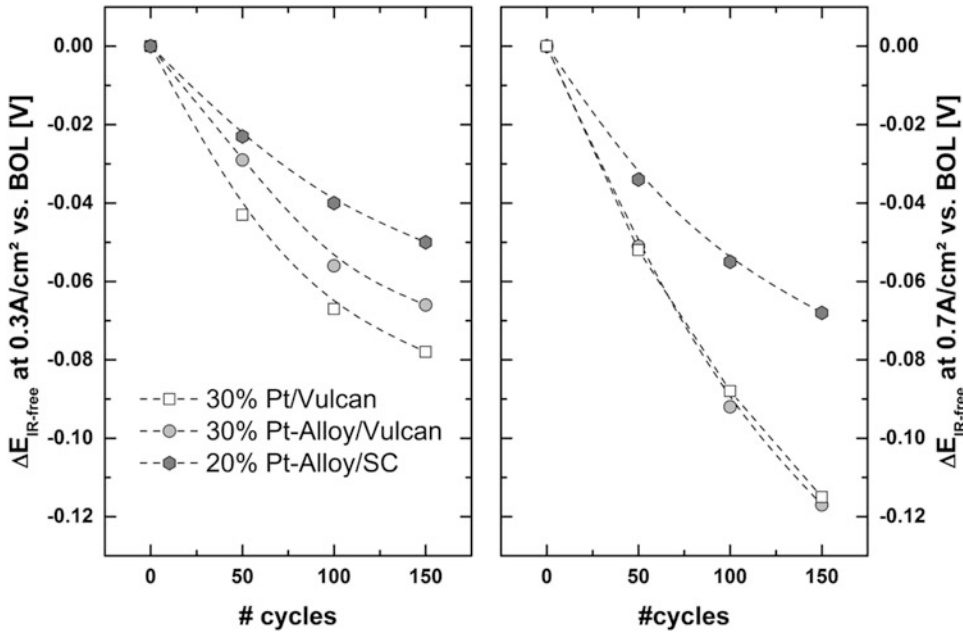


Fig. 14.12 Relative performance decrease vs. beginning of life as a function of simulated start/stop cycles at 0.3 and 0.7 A cm⁻² extracted from *I*-*E* curves for cathodes

with 30 % Pt/Vulcan, 30 % Pt-alloy/Vulcan, and 20 % Pt-alloy/SC. Reproduced from [43] with permission of Elsevier

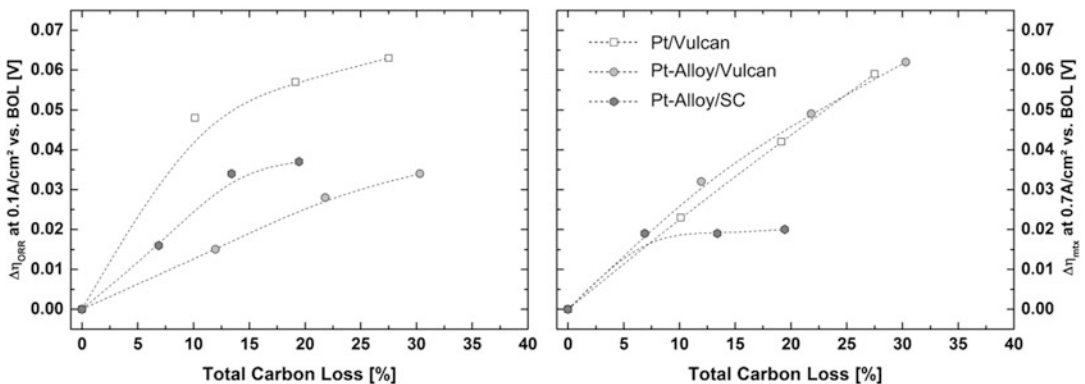


Fig. 14.13 Overpotential changes vs. BOL as a function of the loss of the carbon inventory from the catalyst support (a, b) deduced from the online CO₂

emission rate during simulated start/stop at 0.1 and 0.7 A cm⁻². Reproduced from [43] with permission of Elsevier

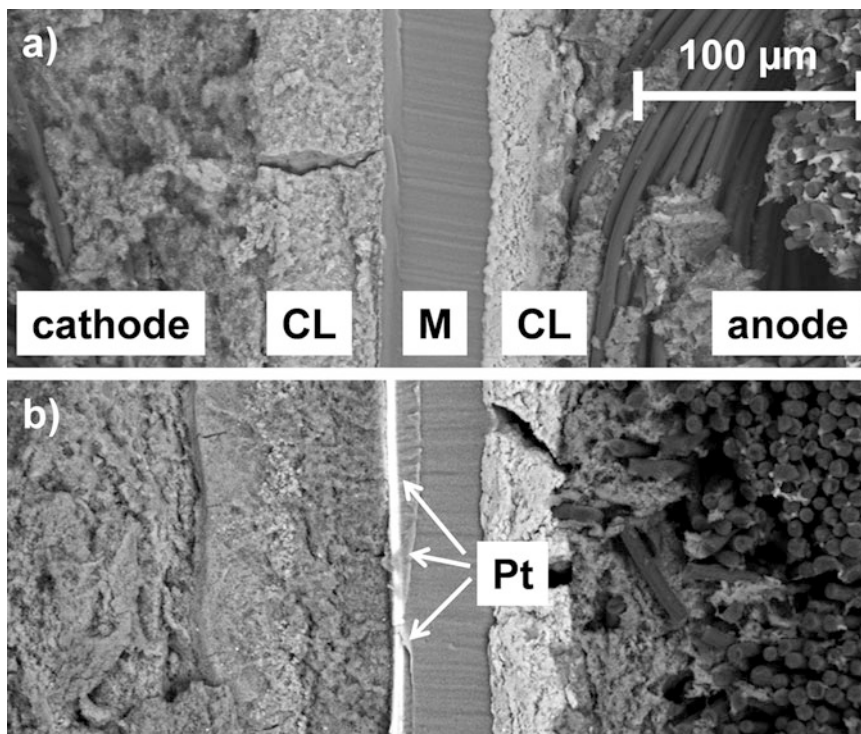


Fig. 14.14 SEM cross-section (backscattering mode) MEA images (Pt-Alloy/SC) at BOL (a) and EOL (b). Reproduced from [43] with permission of Elsevier

migration on the support [43, 45, 46]. The platinum band still exhibits good catalytic activity but its electrochemically active surface is reduced compared to the initial CL.

14.5 Conclusion and Outlook

The harsh environment in HT-PEMFCs is extremely demanding for all materials. It is therefore a very complex task to develop robust catalysts without compromising their activity. Activity and durability are equally important and should be considered when new materials are developed.

In terms of durability, there are several approaches for improving the catalyst and catalyst layer on a material level.

The corrosion resistance of the carbon catalyst support can be improved by graphitization, as highlighted in the text. Nevertheless, a catalyst with graphitized carbon support can exhibit a

lower ECSA [47], which has negative consequences for the cell performance. It is also possible to replace carbon as support by metal oxides. They provide a promising durability but, among other things, still need to be improved especially regarding their specific surface area and electrical conductivity [48–51]. Metal oxides are gaining increasing attention due to increased research efforts in water electrolyzers [52], which may result in a fruitful synergy. In the research and development of HT-PEMFC CLs, approaches similar to those demonstrated in LT-PEMFC could also be adopted, such as avoiding a catalyst support by using platinum black, Pt-based aerogels [53], nanostructured thin films [54, 55], or sputtered electrodes [56]. An example for the two latter is given in Fig. 14.15. Pt alloy sputter-coated whiskers are grown on a microstructured catalyst transfer substrate. The catalyst exhibits a 5–10 times higher specific activity for oxygen reduction compared

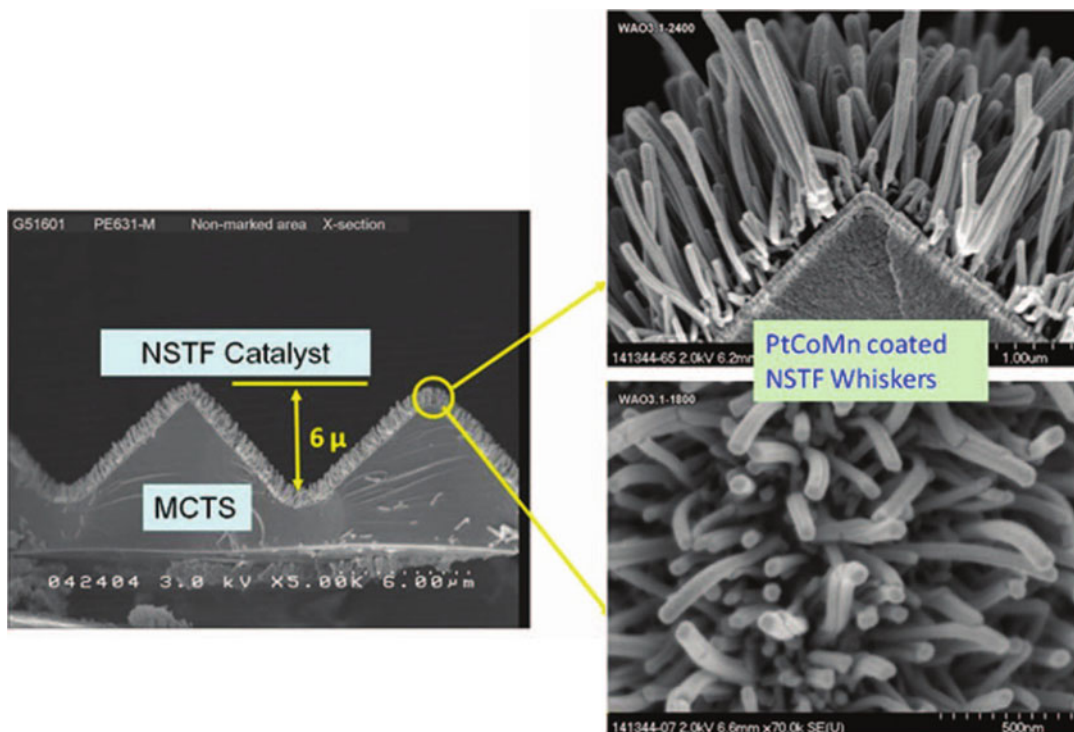


Fig. 14.15 SEM views of the catalyst coated whiskers on a microstructured substrate after sputter coating with a PtCoMn alloy. Reproduced from [54] with permission of the Electrochemical Society

to 2–3 nm diameter particles compensating for the reduced absolute electrode surface area [54].

Anode catalysts which are highly selective for hydrogen oxidation over oxygen reduction would also increase the HT-PEMFC lifetime. A unique and clever idea fulfilling these criteria was published by Genorio et al. [25]. Calix[4]arene molecules cover the surface of the Pt catalyst. Their truncated conical shape blocks the access for large oxygen molecules to the surface but not for small hydrogen molecules. The catalytic activity for HOR is therefore only slightly reduced, but for ORR greatly inhibited. The stability of these modified catalysts in an HT PEMFC environment, however, remains to be demonstrated. Tailor-made catalysts would also be helpful on the cathode electrode, similar to the anode. Catalysts selective for oxygen evolution over carbon oxidation during start/stop events would decrease the amount of corroded carbon support [49, 57].

In terms of improving the catalyst activity, the main research focus is on Pt alloys and non-carbon support catalysts, which show promising results especially towards the ORR.

As final conclusion, the two questions asked in the beginning of this chapter can now be answered. Firstly, there are two techniques which can be used for precise and reliable ECSA determination. This is highly useful for the HT-PEMFC community in order to create comparable data in catalyst and catalyst layer research. Secondly, there are indeed several effective approaches to successfully reduce start-/stop-induced carbon corrosion (e.g., CO-enriched fuel gas, graphitization). If all enhancements on the materials side are combined with the system-based fuel cell degradation mitigation strategies mentioned earlier, HT-PEMFCs are on a good path to reach the 40,000 h operation time target.

Acknowledgement The authors want to acknowledge BASF SE for financial assistance. We want to thank K.E. Waltar and J. Käse for assistance in setting up the locally resolved measurements and for performing some experiments.

Appendix: MEA Specifications and Abbreviations

For all experiments reported in this chapter, BASF Celtec[®]-based MEAs were used. These MEAs exhibit a thickness of approximately 820 μm including a membrane thickness of around 50–75 μm . They furthermore consist of a highly H_3PO_4 -doped PBI membrane, electrodes with a symmetrical platinum loading of $1 \text{ mg}_{\text{Pt}}\text{cm}^{-2}$ with an active area of 45.15 cm^2 and a carbon paper (Sects. 14.2 and 14.3) or carbon cloth (Sect. 14.4) gas diffusion layer. Furthermore, if it was not specifically noted otherwise, only dry gases were used for start/stop simulation and investigation.

Abbreviation	Meaning
BOL	Beginning of life
CL	Catalyst layer
CV	Cyclic voltammetry
ECSA	Electrochemically active surface area
$\text{ECSA}_{\text{CO}_2}$	Electrochemically active surface area measured by CO_2 detection
$\text{ECSA}_{\text{CV vs. ref. CV}}$	Electrochemically active surface area measured by a reference cyclic voltammogram
$\text{ECSA}_{\text{mono}}$	Electrochemically active surface area based on the oxidation of one complete monolayer of CO
EOL	End of life
HER	Hydrogen evolution reaction
HOR	Hydrogen oxidation reactions
HT/LT-PEMFC	High temperature/low temperature polymer electrolyte fuel cell
H_{upd}	Hydrogen underpotential deposition
MEA	Membrane electrode assembly
ORR	Oxygen reduction reaction
PA	Phosphoric acid
$\Delta\eta_{\text{mtx}}$	Mass transport losses
$\Delta\eta_{\text{ORR}}$	Kinetic oxygen reduction reaction losses

References

1. Neyerlin KC, Gu W, Jorne J et al (2007) Study of the exchange current density for the hydrogen oxidation and evolution reactions. *J Electrochem Soc* 154: B631–B635
2. Sheng W, Gasteiger HA, Shao-Horn Y (2010) Hydrogen oxidation and evolution reaction kinetics on platinum: acid vs alkaline electrolytes. *J Electrochem Soc* 157:B1529–B1536
3. Marković NM, Schmidt TJ, Stamenković V (2001) Oxygen reduction reaction on Pt and Pt bimetallic surfaces: a selective review. *Fuel Cells* 1:105–116
4. Rabis A, Rodriguez P, Schmidt TJ (2012) Electrocatalysis for polymer electrolyte fuel cells: recent achievements and future challenges. *ACS Catal* 2:864–890
5. Wroblowa HS, Razumney G (1976) Electroreduction of oxygen. *J Electroanal Chem Interfacial Electrochem* 69:195–201
6. Schmidt TJ, Neophytides G (2014) High-temperature polymer electrolyte fuel cells. In: Kreysa G, Ota K, Savinell RF (eds) *Encyclopedia of applied electrochemistry*. Springer, New York, pp 996–1004
7. Kitco Metals Inc. (2014) Historical platinum prices. http://www.kitco.com/scripts/hist_charts/yearly_graphs.plx. Accessed 14 May 2014
8. Schmidt TJ (2009) High-temperature polymer electrolyte fuel cells: durability insights. In: Inaba M, Schmidt TJ, Büchi FN (eds) *Polymer electrolyte fuel cell durability*. Springer, New York, pp 199–221
9. Reiser CA, Bregoli L, Patterson TW et al (2005) A reverse-current decay mechanism for fuel cells. *Electrochem Solid-State Lett* 8:A273–A276
10. Gu W, Carter RN, Yu PT (2007) Start/stop and local H_2 starvation mechanisms of carbon corrosion: model vs. experiment. *ECS Trans* 11:963–973
11. Tang H, Qi Z, Ramani M (2006) PEM fuel cell cathode carbon corrosion due to the formation of air/fuel boundary at the anode. *J Power Sources* 158:1306–1312
12. Linse N (2012) Start/stop phenomena in polymer electrolyte fuel cells. Dissertation, ETH Zürich, no. 20132
13. Vidaković T, Christov M, Sundmacher K (2007) The use of CO stripping for in situ fuel cell catalyst characterization. *Electrochim Acta* 52:5606–5613
14. Doh WH, Gregoratti L, Amati M et al (2013) Scanning photoelectron microscopy study of the Pt/phosphoric-acid-imbibed membrane interface under polarization. *ChemElectroChem* 1:180–186
15. Engel T, Ertl G (1979) Elementary steps in the catalytic oxidation of carbon monoxide on platinum metals. *Adv Catal* 28:1–78
16. Kunimatsu K, Sato T, Uchida H (2008) Adsorption/oxidation of CO on highly dispersed Pt catalyst studied by combined electrochemical and ATR-FTIRAS methods: oxidation of CO adsorbed on carbon-supported Pt catalyst and unsupported Pt black. *Langmuir* 24:3590–3601

17. Dhar HP, Christner LG, Kush AK (1987) Nature of CO adsorption during H₂ oxidation in relation to modeling for CO poisoning of a fuel cell anode. *J Electrochem Soc* 134:3021–3026
18. Schmidt TJ, Baurmeister J (2008) Development status of high-temperature PBI-based membrane electrode assemblies. *ECS Trans* 16:263–270
19. Engl T, Waltar KE, Gubler L et al (2014) Second cycle is dead: advanced electrode diagnostics for high-temperature polymer electrolyte fuel cells. *J Electrochem Soc* 161:F500–F505
20. Kraume R (2013) S++ Simulation Services. S++ Simul Serv. <http://www.splusplus.com/>
21. Engl T, Gubler L, Schmidt TJ (2015) Think Different! Carbon Corrosion Mitigation Strategy in High Temperature PEFC: A Rapid Aging Study. *J Electrochem Soc* 162:F291–F297
22. Rabis A, Fabbri E, Foelske A et al (2013) Durable oxide-based catalysts for application as cathode materials in polymer electrolyte fuel cells (PEMFCs). *ECS Trans* 50:9–17
23. Huang S-Y, Ganesan P, Popov BN (2012) Electrocatalytic activity and stability of titania-supported platinum–palladium electrocatalysts for polymer electrolyte membrane fuel cell. *ACS Catal* 2:825–831
24. d'Arbigny J, Taillades G, Rozière J (2011) High surface area tungsten carbide with novel architecture and high electrochemical stability. *ECS Trans* 41:1207–1213
25. Genorio B, Strmcnik D, Subbaraman R et al (2010) Selective catalysts for the hydrogen oxidation and oxygen reduction reactions by patterning of platinum with calix[4]arene molecules. *Nat Mater* 9:998–1003
26. Genorio B, Subbaraman R, Strmcnik D et al (2011) Tailoring the selectivity and stability of chemically modified platinum nanocatalysts to design highly durable anodes for PEM fuel cells. *Angew Chem Int Ed Engl* 50:5468–5472
27. Perry ML, Patterson T, Reiser CA (2006) Systems strategies to mitigate carbon corrosion in fuel cells. *ECS Trans* 3:783–795
28. Linse N, Scherer GG, Wokaun A et al (2012) Quantitative analysis of carbon corrosion during fuel cell start-up and shut-down by anode purging. *J Power Sources* 219:240–248
29. Meyers JP, Darling RM (2006) Model of carbon corrosion in PEM fuel cells. *J Electrochem Soc* 153: A1432–A1442
30. Reiser CA, Yang JD, Sawyer RD (2002) Procedure for shutting down a fuel cell system using air purge. US Patent 2002/0076583 A1
31. Balliet RJ, Reiser CA, Patterson TW et al (2004) Start up system and method for a fuel cell power plant using a cathode electrode fuel purge. US Patent 2004/0126628 A1
32. Yu PT (2006) Procedures for shutting down fuel cell system by using air purge at low cell temperature. US Patent 2006/0040150
33. Van Dine LL, Steinbugler MM, Reiser CA et al (2002) Procedure for shutting down a fuel cell system having an anode exhaust recycle loop. US Patent 2002/0098393 A1
34. Schmidt TJ (2008) Method for operating a fuel cell. EP 08007168.1
35. Balliet RJ, Reiser CA (2004) System and method for shutting down a fuel cell power plant. US Patent 2004/0001980 A1
36. Bekkedahl TA, Breault RD (2004) Reducing fuel cell cathode potential during startup and shutdown. US Patent 2004/0081866 A1
37. Fredette SJ (2005) Storage of fuel cell energy during startup and shutdown. WO 2005/031905 A1
38. Bett JAS, Breault RD, Cipollini N et al (2004) Fuel cell having a corrosion resistant and protected cathode catalyst layer. US Patent 2004/0126644 A1
39. Ghenciu AF (2002) Review of fuel processing catalysts for hydrogen production in PEM fuel cell systems. *Curr Opin Solid State Mater Sci* 6:389–399
40. Engl T, Käse J, Gubler L et al (2014) On the positive effect of CO during start/stop in high-temperature polymer electrolyte fuel cells. *ECS Electrochem Lett* 3:F47–F49
41. Marković NM, Schmidt TJ, Grgur BN et al (1999) Effect of temperature on surface processes at the Pt (111)-liquid interface: hydrogen adsorption, oxide formation, and CO oxidation. *J Phys Chem B* 103:8568–8577
42. Gu W, Yu PT, Carter RN et al (2010) Modeling of membrane-electrode-assembly degradation in proton-exchange-membrane fuel cells—local H₂ starvation and start–stop induced carbon-support corrosion. In: Pasaogullari U, Wang C-Y (eds) *Modeling and diagnostics of polymer electrolyte fuel cells*. Springer, New York, pp 45–87
43. Hartnig C, Schmidt TJ (2011) Simulated start–stop as a rapid aging tool for polymer electrolyte fuel cell electrodes. *J Power Sources* 196:5564–5572
44. Sasaki K, Shao M, Adzic R (2009) Dissolution and stabilization of platinum in oxygen cathodes. In: Inaba M, Schmidt TJ, Büchi FN (eds) *Polymer electrolyte fuel cell durability*. Springer, New York, pp 7–27
45. Ferreira PJ, la O' GJ, Shao-Horn Y et al (2005) Instability of Pt/C electrocatalysts in proton exchange membrane fuel cells. *J Electrochem Soc* 152:A2256
46. Ross PN Jr (1987) Deactivation and poisoning of fuel cell catalysts. In: Bell AT, Petersen EE (eds) *Catalyst deactivation*. Marcel Dekker Inc., New York, pp 167–187
47. Cleemann LN, Buazar F, Li Q et al (2013) Catalyst degradation in high temperature proton exchange membrane fuel cells based on acid doped polybenzimidazole membranes. *Fuel Cells* 13:800–831
48. Antolini E, Gonzalez ER (2009) Ceramic materials as supports for low-temperature fuel cell catalysts. *Solid State Ion* 180:746–763

49. Binninger T, Fabbri E, Koetz R (2013) Iridium-titanium oxide as support for Pt catalyst in PEMFC cathodes. *ECS Trans* 58:1835–1841
50. Fabbri E, Pătru A, Rabis A et al (2014) Advanced cathode materials for polymer electrolyte fuel cells based on Pt/ metal oxides: from model electrodes to catalyst systems. *Chimia (Aarau)* 68:217–220
51. Rabis A, Kramer D, Fabbri E et al (2014) Catalyzed SnO₂ thin films: theoretical and experimental insights into fabrication and electrocatalytic properties. *J Phys Chem C* 118:11292–11302
52. Fabbri E, Haberer A, Waltar K et al (2014) Developments and perspectives of oxide-based catalysts for the oxygen evolution reaction. *Catal Sci Technol* 4 (11):3800–3821. doi:[10.1039/C4CY00669K](https://doi.org/10.1039/C4CY00669K)
53. Liu W, Rodriguez P, Borchardt L et al (2013) Bimetallic aerogels: high-performance electrocatalysts for the oxygen reduction reaction. *Angew Chem Int Ed Engl* 52:9849–9852
54. Debe MK (2013) Tutorial on the fundamental characteristics and practical properties of nanostructured thin film (NSTF) catalysts. *J Electrochem Soc* 160:F522–F534
55. Debe MK (2012) Electrocatalyst approaches and challenges for automotive fuel cells. *Nature* 486:43–51
56. Schwanitz B, Rabis A, Horisberger M et al (2012) Sputtered cathodes for polymer electrolyte fuel cells: insights into potentials, challenges and limitations. *Chimia (Aarau)* 66:110–119
57. Suntivich J, May KJ, Gasteiger HA (2011) A perovskite oxide optimized for oxygen evolution catalysis from molecular orbital principles. *Science* 334:1383–1385

Marina Welsch and Markus Perchthaler

Abbreviations

CCM	Catalyst coated membrane
DEFC	Direct ethanol fuel cell
DMFC	Direct methanol fuel cell
GDE	Gas diffusion electrode
GDL	Gas diffusion layer
HT-PEM	High temperature polymer electrolyte fuel cell
MCFC	Molten carbonate fuel cell
MEA	Membrane electrode assembly
LT-PEM	Low temperature polymer electrolyte fuel cell
PAFC	Phosphoric acid fuel cell
PBI	Polybenzimidazole
PFSA	Perfluorosulfonic acid
PTFE	Polytetrafluoroethylene
SOFC	Solid oxide fuel cell

15.1 Introduction

In this chapter, the electrode construction of a high temperature (HT) polymer electrolyte membrane (PEM) electrode assembly (MEA) will be explained. The different functionalities of the electrode layers like the gas diffusion layer (GDL), the micro porous layer (MPL), and the

catalyst support material will be enlightened in the following chapter. The last one is one of the most interesting of them. The main responsibility of this layer is to support the catalyst. In this layer, the electrochemical reactions, the interaction between the catalyst and the electrolyte and the proton and electron separation takes place.

The requirements, the positive and negative aspects of actual used support materials and the mechanism of their degradation are content of the first part of this chapter. Further alternatives will get introduced and compared with the widely used catalyst support material. The second part of this chapter deals with electrode fabrication methods and the influences of them to the MEA properties.

15.2 Electrode Construction

The requirement and the importance of the catalyst support material in an MEA become evident when the position and the function of the support layer are explained. For this, a schematic layout of a typical high temperature MEA is shown in Fig. 15.1.

The typical MEA construction has in its original form a symmetric layout. The core unit consists of the membrane. For HT-PEM MEAs, usually polybenzimidazole in several polymeric modifications like sulfonation, blending of the polymer with other polymers or additives to

M. Welsch • M. Perchthaler (✉)
Elcomax GmbH, Bayerwaldstr. 3, Munich 81737,
Germany
e-mail: Markus.Perchthaler@elcomax.com

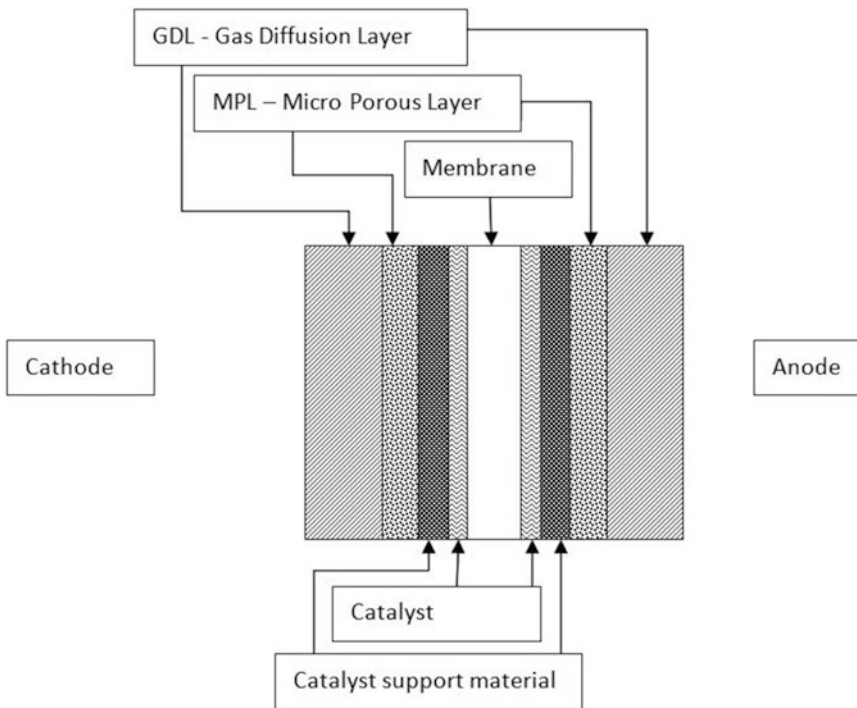


Fig. 15.1 Schematic representation of a widely used MEA construction [7]

enhance the proton conductivity and chemical and mechanical stability is used. To reach the needed high proton conductivity the membrane is usually get doped with acids. A typical proton conductor for HTPEM membrane is phosphoric acid [1].

Adjacent to the membrane two electrodes are placed [2]. The reason is to create direct contact between the membrane and the electrode. The electrode is constructed as the catalyst layer covering the MPL and the GDL. The catalyst layer is consisting of the catalyst and its support material [3]. The contact area between the catalyst layer and the membrane which is doped with phosphoric acid creates the three phase boundary, where the catalytic active reactions take place. On the anode, the oxidation of hydrogen to protons and electrons takes place. The protons are migrating through the membrane to the cathode, where the reduction of oxygen and protons to water takes place [4, 5].

One of the most important preconditions for the redox reaction of the reactants is the

formation of a three phase boundary. The catalyst initiates the reaction if it has contact with the electrolyte, in the case of HT-PEM usually phosphoric acid, and the feed gases of the fuel cell. The acid is getting brought into the catalyst layer during the MEA manufacturing. But the feed gases have to be transported to the catalyst layer during the operation. Reactants are typically hydrogen or reformed hydrocarbons and an oxygen containing gas like air or even pure oxygen. The electron transport between MEAs active area to the outer circuit is one of the core function of the MPL and the GDL. Further they have to ensure the migration of reactants and the product water to the reactive MEA areas and back out of the cell [6].

In the following passages, the function and the design of the GDL and MPL will be explained.

The GDL is usually a flexible carbon paper with wide pores which gives the MEA its flexibility and certain insensitivity against mechanical abrasion of the catalyst layer from the membrane. GDL materials are often

hydrophilic and can get soaked with phosphoric acid. This leads to inhomogeneous gas diffusion and acid loss in MEA, both causes voltage losses. To antagonize these degradation mechanisms, it is state of the art to cover the GDL with a MPL made out of carbon black and hydrophobic agents. Positive side effect is the creation of smaller pore sizes in electrode causing a more homogeneous gas diffusion and an improved contact area to the catalyst support giving improved electrical conductivity [3, 7, 8].

In some latest MEA designs, a combination between the MPL and the catalyst support material are used.

15.2.1 Catalyst Support Material

As described above, the electrodes are consisting of a catalyst covered support material which is usually coated on an MPL. This layer is forming a barrier for phosphoric acid to migrate from the membrane and the catalyst reaction zone to the outer carbon layer named GDL. The function and the construction of the catalyst support material is the main content of this chapter.

15.2.1.1 Requirements to Catalyst Support Materials

The catalyst support has two different functions within an MEA. First, it has to support the catalyst. Furthermore, this material has to transport electrons. This means that the catalyst support is a connector between the noble metal catalyst and the electrode components, which are in protonic conductive contact with the membrane and electronic conductive contact with the external circuit.

Due to the mediating role of the catalyst support between electrolyte and other electrode components, some unique requirements are set to the catalyst support material which often competes. Main goals for the development of the catalyst support is the minimization of transfer losses and degradation rates and maximizing the platinum dispersion and stability in the electrode. Table 15.1 gives an overview of the desired properties.

Basically, it has to be stated that all electrode components have to have good electrical conductivity. To ensure a good electron transport through multiple layers, a nearly lossless path from three phase boundary zone to the bipolar plates has to be created. The bonding between the

Table 15.1 Overview of desired properties for catalyst support materials

<p>Minimize transfer losses</p> <ul style="list-style-type: none"> • good bonding of support material to MPL or GDL • good bonding between carrier surface and catalyst • good interaction between catalyst and support material • good electrical conductivity • good proton conductivity
<p>Minimize degradation</p> <ul style="list-style-type: none"> • high stability against acidic electrolytes like phosphoric acid and sulfuric acid • high stability during electrochemical reactions • high oxidation stability • high agglomeration stability
<p>Maximize platinum utilization</p> <ul style="list-style-type: none"> • high surface area • high porosity

individual electrode layers has to be optimized. For the catalyst support, this means that an optimized bonding to the catalyst itself and to MPL or GDL material has to be ensured. Moreover, a good interaction and adhesion between catalyst and its support material is crucial. To minimize degradation and performance losses during the MEA operation, a material has to be chosen with high stability against acidic electrolytes, high electrochemical potentials, and oxidative operation conditions.

One additional function of catalyst support material is to enhance the platinum utilization in the electrode. This leads to an enlarged three phase reaction zone in the MEA and higher electrochemical active catalyst areas at the same catalyst loading of the electrode. For this reason, support materials with adequate surface area and porosity have to be chosen. Antolini [9] shows the benefits of using meso porous structured carriers with pore sizes between 2 and 50 nm. Here, free pore volume is available for the electrolyte which enables an additional rise of three phase boundary zone and an increased interaction between catalyst and electrolyte [5, 6, 9–15].

15.2.1.2 Benefits and Problems of Actual Catalyst Support Material

Actually, two different kinds of catalyst support materials are in wide use for fuel cells. On the one hand, you can find ceramic-based electrodes

for SOFCs and MCFCs. While they show high temperature resistance and low degradation in constant operation they are very brittle and have difficulties, when the operation conditions are changed often. On the other hand, you can find carbon-based materials like carbon black like materials. Due to the lower stability at higher temperatures compared to ceramic materials, they often find application in fuel cells with moderate operating temperatures like PAFC, DMFC, DEFC, HT-PEM and LT-PEM. The most important benefits of carbon-based catalyst support are their high mechanical flexibility, the low price, and that a wide variety of materials with different properties are available. These important properties are surface area, graphitization degree, porosity, temperature resistance, and impurities. This means that the choice of material is crucial and is defining, if the MEA is working or not. Furthermore, carbon-based materials are easy in handling during manufacturing of HT-PEM MEAs.

Usual disadvantages of carbon-based materials are the low stability against chemical and thermal degradation, as listed in Table 15.2. This leads to agglomeration of platinum resulting in low catalytically active surface areas. Another negative aspect is the change of hydrophobicity of the catalyst support during operation. This results in the use of additives to the carbon catalyst support to get a uniform hydrophobic layer

Table 15.2 Benefits and disadvantages of carbon black-based support materials

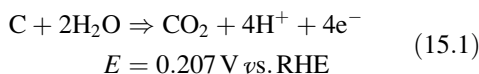
<p>Advantages of carbon black based support materials</p> <ul style="list-style-type: none"> •Mechanical Flexible •Widely used and cheap material •Non complex production handling
<p>Disadvantages of carbon black based support materials</p> <ul style="list-style-type: none"> •Very prone to oxidation •Agglomeration in preparation of inks and during processing of inks •Adding of additives is necessary to meet requirement of adhesion on GDL and hydrophobicity

which is in good contact with GDL and catalyst over the lifetime of fuel cell [9, 12, 16].

15.3 Mechanism of Degradation

15.3.1 Carbon Corrosion

In the introduction, it is mentioned that the use of carbon-based catalyst support materials leads to major degradation mechanisms, which are occurring during fuel cell operation. The most common known and well-understood phenomenon is carbon corrosion. According to (15.1), carbon gets oxidized with water to CO₂ [17].



This generation of CO₂ is believed to occur via surface oxide species, which are formed as intermediates [18]. These surface oxides are formed simultaneously during the CO₂ evolution as initial corrosion on high surface area carbon blacks.

The kinetics of this reaction are in the focus of research groups worldwide. The studies of Kinoshita in PAFC-based Systems showed that the carbon corrosion of the most commonly used Vulcan XC-72 catalyst support material starts at potentials higher than 0.8 V and temperatures higher than 65° C. When the carbon material is at room temperature, the oxidation starts at potentials higher than 1.0 V. So the corrosion of

carbon is a function of temperature, potential, and even water partial pressure [19].

Especially for HT-PEM MEAs, the higher operation temperature of 160 °C and the harsh oxidizing H₃PO₄ electrolyte inducts a very pronounced corrosion of carbon materials. This carbon corrosion phenomenon leads to the formation of surface oxides. The surface oxides are causing a decrease in hydrophobicity of the electrode material. In the case of PAFC or HT-PEM MEAs, which are based on liquid electrolytes, this decrease of electrode hydrophobicity causes an increase in electrolyte loss and in mass transport limitation due to flooding of the electrodes.

Moreover, carbon support corrosion also results in thinning of the electrodes. The solid carbon material is oxidized to CO₂ and a very thin layer is remaining in the MEA. This very thin layer is consisting of only small amounts of carbon, but a very high platinum and binder concentration can be observed (Fig. 15.2).

15.3.2 Electrolyte Loss

For fuel cells, which are working with a liquid electrolyte, the loss of this electrolyte under different operation conditions has to be minimized.

Under optimum operation conditions, the loss of electrolyte can be neglected. According to T.J. Schmidt, the loss of H₃PO₄ of a Celtec MEA due to acid evaporation at an operation temperature of 180 °C is around 2 μg m⁻² s⁻¹

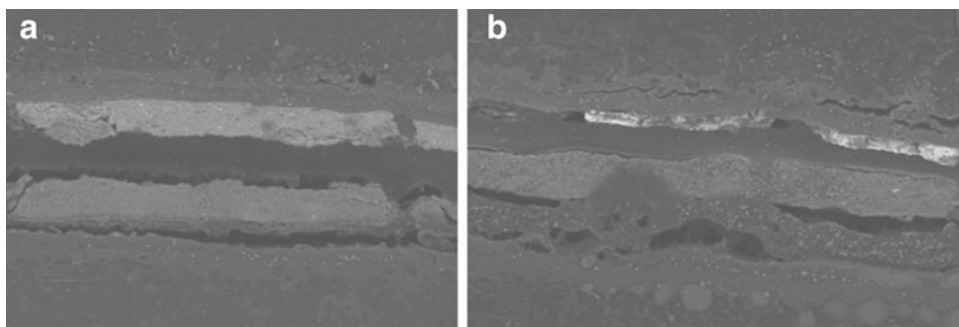


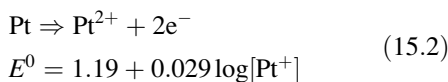
Fig. 15.2 HT-PEM MEA before (a) and after (b) exposition to high cathode potentials. The cathode layer in the upper part shows significant thinning

and only a slight increase in the ohmic cell resistance by $\pm 15 \text{ m}\Omega \text{ cm}^{-2}$ was observed in 8800 h test. Only at higher temperatures up to $200 \text{ }^\circ\text{C}$, the acid evaporation rate increases significantly up to $4 \mu\text{g m}^{-2} \text{ s}^{-1}$ [20].

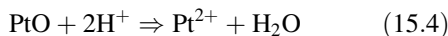
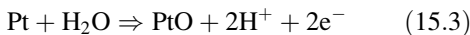
This degradation phenomenon becomes more pronounced for real life systems, which are working with reformed fuels and having their own start–stop and operation logics. The reformed hydrocarbon fuels, which are mostly converted in hydrogen-rich gases via steam reforming processes, contain water vapor in a certain extent, which leads to an uptake of water in the phosphoric acid of the MEA. Moreover, the design of the flowfield channels, the compression set and the use of counter or co-flow configuration are influencing the phosphoric acid redistribution inside the MEA and so lead to a non-uniform current density distribution [21].

15.3.3 Platinum Agglomeration

Due to the thermodynamic properties of platinum, which can be seen in the potential-pH diagram, the dissolution of Pt can follow two different reaction paths under fuel cell conditions, which is either the direct dissolution of the metal:



Or the intermediate formation of a Pt-Oxide film with reduction afterwards:



The dissolved platinum species, which are very mobile in the liquid electrolyte of a HT-PEM FC, tend to agglomerate on other metallic platinum particles via an electrochemical Ostwald ripening process [20]. When the fuel cell is cycled under different potentials, e.g., at start–stop conditions or under fast load changes, the

platinum dissolution is higher compared to potentiostatic conditions [18], but the reasons for this are not yet completely understood.

Moreover, a higher operating temperature leads to a thermodynamic faster agglomeration of the small platinum nanoparticles.

15.3.4 Conclusion

HT-PEM MEAs are suffering from different degradation mechanisms, where cathode carbon corrosion and membrane thinning are the lifetime limiting factors under real system operation. Acid evaporation out of the MEA into the offgas and the bipolar plates can be neglected and have little influence on the constant degradation.

15.4 Manufacturing of Inks, Electrodes and MEAs

Following the above description of the typical electrode construction, the actual used catalyst support materials and the electrode degradation mechanisms, the following section focuses on the fabrication of electrodes and MEAs.

First it will be explained what an electrode ink is, what requirements are set on it and how it defines the properties of the electrode. This is followed by typical ways to manufacture gas diffusion electrodes for fuel cells. Afterwards the dependence between the electrode and MEA fabrication will be discussed. Due to the distinct affinity between HT-PEM, LT-PEM, and PAFC electrodes, the most here invented techniques are usable for fabrication of GDEs for all three fuel cell types.

15.4.1 Electrode Inks

The most effective way to cover GDL with MPL and the catalyst carrier is to disperse the chosen ingredients in solvents and form the so-called ink or slurry. The ink can then be brought up on the

GDL or another carrier by use of the later described manufacturing techniques.

Main advantage of using inks to coat GDL is the easy and fast manufacturing with common coating machineries. This lowers investment for equipment immensely. In addition, the incorporation of fluid additives like Nafion solution or PTFE dispersion is more effective than the mixing of granulates.

Depending on the electrode preparation procedure, inks for the different electrode manufacturing techniques have to fulfill different requirements. They are discussed in the next section.

15.4.1.1 Ink Requirements and Composition

Fernández et al. showed that there are a series of parameters affecting the structure and properties of gas diffusion electrodes [22]. They are not only dependent on the formula of the ink; they are also dependent on the characteristics of the used dispersant to create the slurry. Usually, developers of inks have the aim to create improved slurries which are manufacturable on the existing production equipment. This normally sets the requirements on viscosity, particle size, and solid content of inks.

After dispersing catalyst loaded particles or catalyst carrier in solvents, sedimentation of particles is normal. This lead to short lifetime of inks or complex equipment to keep the particles dispersed. Alternative stabilization agents can be added to the dispersion to avoid phase separation. According to the added stabilizer, foam blocker, thickener or additional solvent may be necessary to adjust the slurry to the machinery requirements.

Passalacqua et al. [23] showed that the use of additional additives can improve the performance and adhesion of catalyst supports on their carrier. For LT-PEM, for example, the addition of Nafion dispersions is usual to enhance the compatibility between the electrode and membrane. Further, it's in wide use to add agents like PTFE and PVDF to improve the adhesion of the carrier to the GDL of HT- and LT-PEMFCs [24]. Both lead to better performance. Other development groups show the

possibilities to improve the degradation of electrodes by adding additives to the electrode [25].

Final slurries should show below listed properties:

- Stable dispersion to get uniform layers during the coating
- No particle agglomeration
- Homogeneous distribution of electrode binder and other additives
- Adjusted content of volatile solvents to manufacturing process
- Adjusted content of solids to manufacturing process (i.e., carbon and binder)
- Ink components have to be stable at for electrode drying steps set conditions, i.e., temperature, pressure, medium, time, etc.

Other properties should be chosen adjusted to the used production technique and the demands of the concrete MEA design. Even small variations in doping level or membrane components can change the necessary items of electrode dramatically.

15.4.1.2 Ink Preparation

Equally to the requirements and properties to the ink, the methods of ink preparation have to be adjusted to the chosen MEA system and formula. If no experience or results are available, it is wise to start with the following preparation way.

- Step 1: Dilution of binder suspension
The binder material, most common PTFE-based aqueous dispersions are used, is mixed with a defined amount of deionized water or another solvent and dispersed with a dispersing tool to get a homogeneous binder distribution.
- Step 2: Addition of carbon or platinum loaded carbon materials
During the dispersion of the binder material, carbon or platinum loaded carbon materials are added and homogeneously distributed.
- Step 3: Opening of agglomerates
The ink is mixed vigorously until the carbon agglomerates are dispersed. Therefore, propeller stirrer or dissolver disks can be used.

- Step 4: Adding of additives
Here, the adding of additives takes place. After this, extra stirring should be proceeded to improve the distribution of the chemicals in the ink.

15.4.1.3 Characterization of Inks

Inks are commonly characterized via rheological techniques. From rheological studies, the viscosity η , the shear stress τ , and the shear rate dv/dy are determined. Due to the internal friction of the molecules in dispersion, the substance flows with an internal resistance against forces. The force necessary for this can be measured as changes in shape of the dispersed particles. The graphical representation of rheological testing is shown in the flow curves. The shear stress and shear rate are plotted in Fig. 15.3.

For the production of fuel cell electrodes via a doctor blade process, a Newtonian behavior of carbon-based inks is very desirable. This means, that the viscosity is not changing, no matter what shear stress is applied on the ink or slurry, what is leading to the fact, that the ink or slurry can be pumped from a storage vessel to the doctor blade with low changes in viscosity. The low change of viscosity leads to a very constant flow of ink to the doctor blade.

15.4.2 Manufacturing of Gas Diffusion Electrodes

Due to the high analogy in the properties electrodes must have for LT-PEM, HT-PEM, and PAFC the possible preparation methods for GDEs for all three fuel cell types are the same. They differ just in the demanded final properties of the electrode and with this in the properties of the ink and the final settings at the manufacturing of the electrode.

The preparation methods of gas diffusion electrodes, short GDE, have strong influence on the properties of the electrode. Within the manufacturing process, for example, the formation of electron conducting pathways through the electrode, the formation of pores to get a high gas distribution, and the effective connection of the electrolyte with proton and product water transport channels can get controlled. All this parameters are very important to get a good three phase boundary zone inside the catalyst layer and with this a working MEA [3].

A detailed list of important electrode properties which are dependent to the manufacturing of the GDE can be seen in Table 15.3.

Various different preparation procedures are available for the manufacturing of gas diffusion

Fig. 15.3 Flow curve of systems with characteristic different behaviors (a) Newtonian behavior, (b) shear thinning behavior, (c) shear thickening behavior, (d) pseudo-plastic behavior

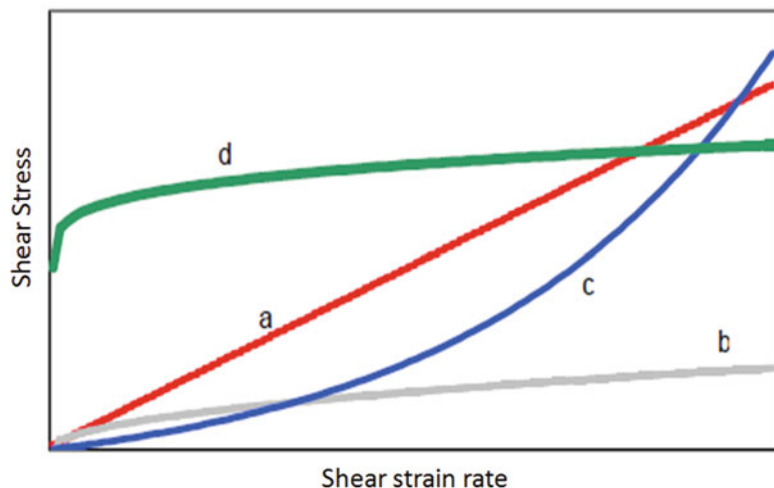


Table 15.3 List of manufacturing techniques, possible post-treatments of electrodes and during this influenced electrode properties

<p>Parameters which are depending on the manufacturing way of electrode</p> <ul style="list-style-type: none"> • catalyst distribution • pore size • particle size • electrolyte distribution • formation of hydrophobic and hydrophilic pores • electrode quality • material and manufacturing costs • adhesion of electrode on the carrier and on the membrane • amount of remained solvents, salts and other ink-ingredients
<p>Electrode manufacturing procedures</p> <ul style="list-style-type: none"> • screen printing • decal process • doctor blade process • electrodeposition process • electrode spraying • electrode painting • electrode rolling
<p>Possible post treatments of electrodes</p> <ul style="list-style-type: none"> • calandering • sintering • multiple layering • washing

electrodes, which can be divided into painting, spraying, rolling, screen printing, and doctor blade processes. The choice of the manufacturing way, and with this of the manufacturing equipment for LT- and HT-PEM electrodes, depends on just two parameters. The first is the viscosity and the rheology of the used ink.

And the second are the settings on the manufacturing process of the MEA. A good support at selection of the fitting manufacturing process can get given by mechanical engineering specialists. They are specialized on conception of coating equipment due to the specialized requirement of their customer. The most interesting and wide used manufacturing processes of electrodes are screen printing, the decal process, the doctor blade process, and the electro

deposition of the electrode why just these four will get discussed in the following passages. While at doctor blade and electro deposition processes, a GDL is getting combined with the carrier material and the catalyst, by use of screen printing and decal processing the use of a GDL is not necessary to get an MEA. At the last to production techniques, the so-called catalyst coated membranes, short CCM, get produced. Here, the manufacturer can add the GDL if wanted after the electrode manufacturing to the CCM. At production of CCMs, high stability of the electrode against abrasion is needed as result of absence of against mechanical stress protecting GDL on MEA, so no damages of electrode occur during manufacturing or using the CCM in fuel cell.

15.4.2.1 Screen Printing

The screen printing process is the most used process to manufacture gas diffusion electrodes for HT- and LT-PEM. This process works in a very efficient way. Here the membrane of a fuel cell, for HT-PEM it's usually a polybenzimidazole and for LT-PEM a Nafion-based membrane, is fixed in its undoped form in a holder. After that a catalyst slurry, what is an electrode ink mixed with catalyst, is getting sprayed on the membrane and afterwards dried. The slurry is usually consisting of binder materials like poly(1,1,2,2-tetrafluoroethylene) and newest more often poly-1,1-difluoroethene, catalyst-loaded support material what is most likely carbon, for example, and dispersing agents like water and alcohols.

Most beneficial on this manufacturing process is the very effective way of slurry deposition. Furthermore with this production way, no assembling and hot pressing of electrode and membrane is needed what reduces the production costs immensely compared to the other electrode manufacturing processes. Additionally, a high production speed with low loadings under 0.5 mg slurry per cm² membrane and very homogeneous slurry distribution are possible.

The biggest disadvantages of this technique are the high needs on the quality of the slurry and the design of the doping procedure of the MEA.

To guarantee a reliable production, the sedimentation and separation of the slurry has to get excluded. These effects can lead to plug of the printing tip and to higher material viscosities what leads to loss of production and unstable material qualities. Furthermore, the handling of substrates with high viscosities and non-Newtonian flowing behavior is challenging with spraying manufacturing techniques.

Due to the use of one of the most expensive MEA components as electrode carrier, the membrane, high costs can get created in case of

production or quality problems. Then, not just the catalyst containing slurry has to get reproduced but also the membrane.

A further disadvantage of screen printed electrodes is the resulting doping procedure of the electrode and membrane. The electrodes have to get soaked in case of LT-PEM with water and in case of HT-PEM with phosphoric acid to dope the MEA with electrolyte. Therefore, the flooding of electrode with electrolyte impacts the gas permeation to the three phase boundary negatively. Furthermore tricks have to get used to push the solvent into the mostly hydrophobic electrode. Because of the additional swelling of the membrane during the doping process cracks can occur on the electrode that can lead to sensitive loss in MEA performance. The most important advantages and disadvantages of screen printing of electrodes are shown in Table 15.4.

15.4.2.2 Doctor Blade Process

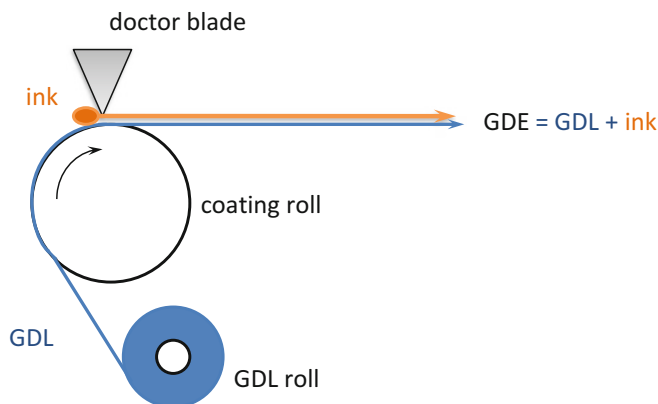
The doctor blade process consists on the applying of the catalyst slurry on a wet-proofed GDL. One possible way to design the doctor blade process is shown in Fig. 15.4.

Therefore, GDL has to be wrapped over the so-called coating or transport roll. This roll is usually rotating in the same direction as the GDL roll. With this motion the GDL is getting unrolled from the supply roll and transported over the coating roll. Over the coating roll, the doctor blade can get positioned. The distance between the doctor blade and the GDL defines the so-called wet film thickness. This parameter is always smaller than the width between the knife and GDL and depends on the speed of the coating. In first approximation for slow coatings, the wet film thickness can be set equal to distance between doctor blade and GDL. By multiplication of the wet layer thickness with the solid content of the slurry, the rough GDE thickness can get received.

$$\text{GDE thickness} \approx \text{solid content of ink} \times \text{distance between GDL and doctor blade}$$

Table 15.4 Benefits and disadvantages of screen printing for electrode manufacturing

Advantages
<ul style="list-style-type: none"> • more effective use of platinum through low loadings on membrane • no additional assembling or hot pressing of electrode and membrane needed • high production speed possible • high layer homogeneity • minimized waste through access lengths of membrane and electrode can get realized
Disadvantages
<ul style="list-style-type: none"> • slurry must be designed as Newtonian fluid with low viscosities • slurry must be rheological stable • slurry must be stable against sedimentation and separation • membrane have to get screen printed on both sides • in case of production waste high additional costs due to membrane as carrier • complex doping procedure • flooding of electrodes with electrolyte during doping • membrane swelling during doping can lead to cracks in electrode • high stability of dried electrode on membrane against abrasion needed

Fig. 15.4 Production scheme of a doctor blade process [26]

By using of a not-wet-proofed GDL at this manufacturing way, the ink can saturate the GDL. In this case, the catalyst carrier will block the gas diffusion channels of the GDL so the benefits of this special layer will get rescinded. Further depending on the used ingredients, the leaking ink or slurry can lead to damages on the coating machinery, incrustations on the coating

roll, and consequently to differences in the wet film thickness.

Usually, just the ink viscosity and particle size are limiting parameters at doctor blade processes. At not absorbing materials, liquids with viscosities between 100 and 50,000 mPa s can get applied with ink loadings from 10 up to 1250 g m⁻² GDL. By coating of porous materials

via doctor blade like in electrode production, the viscosity of the ink has to be adjusted to the absorptivity of the GDL [26].

Because the ink or slurry can be stored in a stirred reservoir straight before its application on GDL no specific requirements have to receive attention at ink sedimentation and separation characteristics. Instead of this, the particle size of ink components is critical. All particles of the ink and their possible agglomerates have to be smaller than the distance between the GDL and the doctor blade.

If the ink particles and agglomerates are bigger or have nearly the same size like the recess between the doctor blade and GDL, a not-controlled GDE thickness can get be produced. Resulting in the formation of stripes on

the GDE what is the first index for a not homogeneous surface and thickness of the electrode. The created imperfection in the GDE surface can lead to inhomogeneous gas distribution in the MEA, hot spots, and shortcuts. All this failures can cause lower cell performance and higher degradation of MEA. Table 15.5 gives an overview about the benefits and disadvantages of this and following manufacturing processes compared to screen printing.

15.4.2.3 Decal Process

As described above, the decal process is very similar to the screen printing of electrodes. During this production way, the catalyst ink can get applied via spraying, doctor blading, or other deposition techniques on an inert and

Table 15.5 Summarizing comparison of electrode fabrication techniques

Property ^a	Screen printing	Decal process	Doctor blade	Electro deposition
Effective use of platinum	0	–	–	+
Requirements on the ink/slurry	Newtonian fluid, rheological stable, no sedimentation and separation	Low	Low	None
Layer homogeneity	+	+	–	0
Minimized waste	–	+	–	–
Production speed	+	+	+	–
Manufacturing costs	0	+	+	–
GDL needed	No	No	Yes	No
Membrane has to get screen printed on both sides	–	+	+	+
In case of production waste high additional costs due to membrane as carrier	–	+	+	+
High stability of dried electrode on membrane against abrasion is needed	–	+	+	+
No additional assembling or hot pressing of electrode and membrane needed	+	–	–	–

^a+: positive effect, –: negative effect, 0: no effect

compared with the membrane very cheap carrier foil like PTFE, PET, or others. Like at screen printing the liquids of the slurry have to be evaporated in one or more heat treatment steps to form a functionally electrode. Very beneficial at this manufacturing way is that damaged or qualitative not fitting electrode areas can get removed before their lamination with the membrane what lowers MEA production costs significantly.

After drying of the ink, a catalyst coated membrane can get manufactured here also. Different to the screen printing here for HT-PEM and PAFC membrane can get doped before the lamination process. Changes of water concentration in phosphoric acid during hot pressing can get equalized through using of lower concentrated acids for membrane doping if the used fuel cell is sensitive to this parameter. For creating a CCM the membrane can get sandwiched in the on a foil carried electrode and laminated with them under pressure and heat. During the pressing and the following storing of CCM, the carrier foil protects the electrode against abrasion or damaging by handling. Obviously, the isolating carrier foil have to get removed before using the catalyst coated membrane for further manufacturing steps like doping, assembling with GDL, or use in fuel cell directly.

15.4.2.4 Electro Deposition Process

In comparison with the before described electrode manufacturing processes, the electro deposition process is unique. While the other procedures works with inks made of carbon and other ingredients, this process is specialized on the deposition of platinum or other catalysts, for LT-PEM also iridium, palladium, and others are in wide use. That means that before electro deposition can be performed, a ready electrode has to be present already. It is typical to use the above-described doctor blade and decal manufacturing processes to create the electrode. Is a subsequent electro deposition of the electrode planned, so in the former steps inks without

catalyst have to be used to form the porous electrode structure. After the drying of the catalyst support layer, dissolved catalyst with precursor has to be topically applied on the catalyst support layer. After that a galvanostatic or potentiostatic deposition of the catalyst takes place. For that the electrode must be included as working electrode in a three electrode set up. The other two electrodes are one reference electrode and one counter electrode. Now the working electrode, which is the catalyst with precursor-loaded catalyst support layer, is pulsed in potentiostatic or galvanostatic mode to get a reduction of the precursor from the catalyst on the catalyst support layer. For the reduction of the precursor in the easiest way, hydrogen is used to create a reductive production atmosphere. In this step, platinum disconnects from the precursor what forms in best way a gas that can be transported from the reaction zone by an exhaust. The reactive platinum particles can now bound on the carbon of the catalyst carrier. Obviously, the duration and the intensity of the potentiostatic or galvanostatic pulses are very important to get small catalyst particles with a good distribution.

By this process, platinum particles are only deposited on the surface of the electrode what will build a three-phase boundary with the membrane. In the layers next to the GDL, in which no catalytic reaction takes place, no catalyst is located. By optimal set parameters just a few atomic layer thick catalyst deposition can be created what is not possible with the alternative. Accordingly, very high catalyst efficiency can get reached.

While in first moment the method seems to be perfect to bring fuel cells closer to commercial use, operator of this method have to deal with negative aspects too. One of them is the long value chain to create a catalyst containing electrode that can consume the savings at the catalyst purchase side. Further users have to handle the enhanced need for safety issues depending on the precursor toxic by-products of the electrode fabrication.

15.4.3 MEA Production Techniques

The manufacturing of a CCM has already been explained. As can be seen in this example, the manufacturing technique of electrode influences the manufacturing of MEA extremely. Based on the electrode manufacturing processes, the most important MEA production techniques can get categorized in three, which are described below. As at the manufacturing of the electrode, the techniques described here can find application for LT-PEM too. Differences in manufacturing of MEAs for PAFC are mostly based on the properties of the used ceramic electrolyte matrix. The characteristics in use of brittle materials don't have to be looked at for manufacturing polymer electrolyte fuel cells.

1. GDE process:

This process is usually performed for manufacturing of single MEAs discontinuous. Via the GDE process, the pre-manufactured catalyst-loaded gas diffusion electrode loaded with catalyst is pressed together with a polymer electrolyte membrane to form an MEA. The doping procedure can take place on the membrane or the electrode. This process is widely used due to the fact that the polymeric membrane is not stressed as much as in the other manufacturing techniques. Less beneficial, here the production and assembling costs have to be mentioned. Every component has to get manufactured, cut, and assembled separately. But this lead to excellent possibilities to exclude material with low quality early.

2. CCM process:

This manufacturing process can be used for coating of whole MEA rolls. This fits continuous production in best way. Via the CCM process, the catalyst ink is applied directly via a spray or doctor blade process on the polymeric membrane. Due to the swelling and shrinking behavior of the membrane when in contact with liquids, this process causes high mechanical stress during the application of the catalyst ink on the membrane. In special

Nafion membranes are stressed by production due to water containing solvents in inks. Polybenzimidazole-based membranes usually which have a significant smaller water uptake show less affection to the swelling stress through aqueous components. Either the membrane is usually fixed or pre-swollen to avoid cracks on the surface of the CCM structure and to reduce the mechanical stress. Further with this procedure, the formation of very thin active layers near the membrane are possible, which can then result in very high catalyst efficiencies of the MEA. Also the use of expensive GDL is not necessary to create an MEA by this way.

3. Decal process:

The decal process is a mixture of the CCM and the GDE process. Within this process, the catalyst ink for the manufacturing of a GDE is applied on an inert material (mostly PTFE-based sheets are used) and after drying and sintering of the layer, the formed active layer is pressed together with the membrane. Now, the PTFE sheet can get removed. So a CCM is obtained without applying mechanical stress on the membrane due to coating with ink. Unfortunately, the swelling problem due to doping in case of HTPEMFC remains.

15.4.4 Special Requirements for PBI based MEA productions

The most commonly used membrane material for HT-PEM MEAs (PBI based) has to be soaked or doped with phosphoric acid to get sufficient proton conductivity. This doped or soaked membrane shows a lowering of the mechanical strength, due to the fact that the uptake of phosphoric acid leads to swelling of the PBI.

So high mechanical stress of phosphoric acid-soaked PBI-membrane must not be applied during the production or the phases of high mechanical stress on the membrane only have to be done without phosphoric acid doping. If so, the formation of electrical shortcuts due to squeezing, due

to uneven pressure, or uneven GDE surfaces is very likely. When looking at the above-described manufacturing techniques, the decal process applies the lowest mechanical stress on the membrane. Moreover, the undoped membrane can be used during the formation of a CCM, which leads to a very stable process.

References

1. Li Q, Jensen JO, Savinell RF et al (2009) High temperature proton exchange membranes based on polybenzimidazoles for fuel cells. *Prog Polym Sci* 34:449–477
2. Scherer GG, Gürsel SA (eds) (2008) *Fuel cells*. I. Springer, Berlin
3. Zhang J (2008) *PEM fuel cell electrocatalysts and catalyst layers: fundamentals and applications*. Springer, London
4. Hamann CH, Vielstich W (eds) (2004) *Elektrochemie*, 3. völlig überarb. und erw. Aufl., 3. Nachdr. Wiley-VCH, Weinheim
5. Kurzweil P (2003) *Brennstoffzellentechnik: Grundlagen, Komponenten, Systeme, Anwendungen; mit 178 Tabellen*, 1. Aufl. Vieweg, Wiesbaden
6. Larminie J, Dicks A (eds) (2003) *Fuel cell systems explained*, 2nd edn. Wiley, Chichester
7. Williams MW, Begg E, Bonville L et al (2004) Characterization of gas diffusion layers for PEMFC. *J Electrochem Soc* 151:A1173–A1180
8. U.S. Department of Energy (2014), *Fuel Cell Handbook* 7th edn
9. Antolini E (2009) Carbon supports for low-temperature fuel cell catalysts. *Appl Catal B: Environ* 88:1–24
10. Jha N, Reddy LM, Shaijumon AMM et al (2008) Pt–Ru/multi-walled carbon nanotubes as electrocatalysts for direct methanol fuel cell. *Int J Hydrogen Energy* 33:427–433
11. Lin Y, Cui X, Yen C et al (2005) Platinum/carbon nanotube nanocomposite synthesized in supercritical fluid as electrocatalysts for low-temperature fuel cells. *J Phys Chem B* 109:14410–14415
12. Halder A, Sharma S, Hegde MS et al (2009) Controlled attachment of ultrafine platinum nanoparticles on functionalized carbon nanotubes with high electrocatalytic activity for methanol oxidation. *J Phys Chem C* 113:1466–1473
13. Kua J, Goddard WA (1999) Oxidation of methanol on 2nd and 3rd row group VIII transition metals (Pt, Ir, Os, Pd, Rh, and Ru): application to direct methanol fuel cells. *J Am Chem Soc* 121:10928–10941
14. Chen J, Wang M, Liu B et al (2006) Platinum catalysts prepared with functional carbon nanotube defects and its improved catalytic performance for methanol oxidation. *J Phys Chem B* 110:11775–11779
15. Mench MM (2008) *Fuel Cell Engines* [Elektronische Ressource]. Wiley, Hoboken
16. Kordesch K, Simader G (eds) (1996) *Fuel cells and their applications*. VCH, Weinheim
17. Yu P, Gu W, Zhang J et al (2009) In: Büchi F, Inaba M, Schmidt T (eds) *Polymer electrolyte fuel cell durability*. Springer, New York, pp 29–53
18. Kinoshita K (1988) *Carbon: electrochemical and physicochemical properties*. Wiley, New York
19. Antonucci PL, Romeo F, Minutoli M et al (1988) Electrochemical corrosion behavior of carbon black in phosphoric acid. *Carbon* 26:197–203
20. Schmidt T (2009) High-temperature polymer electrolyte fuel cells: durability insights. In: Büchi F, Inaba M, Schmidt T (eds) *Polymer electrolyte fuel cell durability*. Springer, New York, pp 199–221
21. Lüke L (2013) *Analyse des Betriebsverhaltens von Hochtemperatur-Polymer-elektrolyt-Brennstoffzellen*. Forschungszentrum, Jülich
22. Fernández R, Ferreira-Aparicio P, Daza L (2005) Selected papers presented at the first congress of fuel cells in Spain (CONAPPICE 2004), first congress of fuel cells in Spain, vol 151, pp 18–24
23. Passalacqua E, Lufrano F, Squadrito G et al (2001) Nafion content in the catalyst layer of polymer electrolyte fuel cells: effects on structure and performance. *Electrochim Acta* 46:799–805
24. Holst-Olesen K, Nesselberger M, Perchthaler M et al (2014) Activity inhibition and its mitigation in high temperature proton exchange membrane fuel cells: the role of phosphoric acid, ammonium trifluoromethanesulfonate, and polyvinylidene difluoride. *J Power Sources* 272:1072–1077
25. Perchthaler M, Osslander T, Juhart V et al (2013) Tungsten materials as durable catalyst supports for fuel cell electrodes. *J Power Sources* 243:472–480
26. Coatema. http://www.coatema.de/ger/lab_solutions/auftragssysteme/knife_system.php. Accessed 8 Jan 2015

Jung Ock Park and Suk-Gi Hong

16.1 Cost and Durability Targets for HT-PEMFC MEAs

16.1.1 Cost Target

The high temperature polymer electrolyte membrane fuel cell (HT-PEMFC) is mostly developed targeting the applications in residential combined heat and power (CHP) and auxiliary power unit (APU) because of their high heat quality and tolerance to wide choices of fuels. The CHP systems can tap into the existing market for the residential boiler heating system which uses the pipeline natural gas and generate electricity and hot water for the individual households. Thus, the CHP systems need to be able to operate with reformat gas which contains high content of carbon monoxide (CO) which poisons the platinum anode catalyst [1, 2]. The high operation temperature of HT-PEMFC which is between 150 and 180 °C provides tolerance to higher content of CO compared to the low temperature (LT) PEMFC systems, and the design of reformer for HT-PEMFC can be simplified [3]. Thus, the high heat quality and the compact system design that results from the simpler reformer and removal of humidifier give advantages to the HT-PEMFC systems in CHP applications. Because of its

tolerance to impurities in the fuel, the HT-PEMFC can also be suitable for APU applications which utilize fuel such as liquid petroleum gas (LPG) and natural gas.

To commercialize the fuel cell systems in the CHP and APU applications, the systems need to meet the cost target of \$1000 kW⁻¹ by the year 2020 [4, 5]. The cost of the systems is determined by the costs of manufacturing and the components which include the components necessary to convert gas fuel into electricity (fuel cell stack, fuel processing system, inverter and balance of plants), heat exchangers, and control system. The targeted cost was based on the production volume of 50,000 units per year [4, 5]. The HT-PEMFC systems have been commercialized in APU and CHP applications which have the electrical output between 0.3 and 5 kW [6–8]; however, the cost of the commercialized HT-PEMFC systems remains high, and further improvements in components and manufacturing process need to be made. The most widely commercialized fuel cell system in the CHP market is the LT-PEMFC system that was released in Japan as “Ene-Farm” residential fuel cell cogeneration system in 2009 [9]. The price of the 0.75 kW LT-PEMFC CHP systems has been reduced from \$30,000 in 2011 to \$22,600 in 2012 with estimate annual sales of 12,000 units in 2012 [9, 10]. The increase in the production volume has the possibility of further reducing the system cost by lowering the manufacturing cost

J.O. Park (✉) • S.-G. Hong
Samsung Advanced Institute of Technology, Samsung
Electronics, Co. Ltd., Seoul, South Korea
e-mail: jungock.park@samsung.com

Table 16.1 Cost comparison of LT-PEMFC and HT-PEMFC systems (cost values taken from [12])

Annual production volume (units)	LT-PEMFC (1 kW)		HT-PEMFC (1 kW)	
	System cost (\$)	Stack cost (\$)	System cost (\$)	Stack cost (\$)
100	10,106	1200	10,130	1420
50,000	6032	400	6101	700
		Membrane: 27 % ^a catalyst: 21 % ^a		Membrane: 11 % ^b catalyst: 45 % ^b

MEA specification: LT-PEMFC (0.4 mg_{Pt}/cm², 0.676 V/cell, 408 mW/cm²) and HT-PEMFC (1.0 mg_{Pt}/cm², 0.6 V/cell, 240 mW/cm²)

^aValues taken from [13]

^bValues calculated assuming that PBI membrane costs 50 % of Nafion membrane, and Pt loading of HT-PEMFC electrode is 2.5 times higher than that of LT-PEMFC electrode (costs of MEA fabrication, GDL, bipolar plates and gaskets are the same for LT-PEMFC and HT-PEMFC stacks)

of the components. The increase of annual production rate from 10,000 units to 50,000 units is reported to decrease the cost of a CHP system from \$20,200 per unit to \$7500 per unit [11]. However, in order to meet the target cost of \$1000 kW⁻¹, the material cost of each component needs to be further reduced.

The material cost of membrane electrode assemblies (MEAs) is mainly determined by the catalyst, membrane, and gas diffusion layer (GDL). As shown in Table 16.1, the membrane is the most expensive component in a stack for LT-PEMFC, and it makes up 27 % of the stack cost [13]. However, the cost of membranes becomes less critical for the MEAs for HT-PEMFC because of the low material cost of H₃PO₄-doped polybenzimidazole (PBI) membranes. The material cost of the H₃PO₄-doped PBI membranes is estimated to be less than 5 €/m² at 100 g/m² of area specific weight and is lower than the perfluorinated Nafion which is estimated to be 5–10 €/m² at 100 g/m² [14]. Thus, the cost of PBI-based membrane can be estimated to be about 50 % of the cost of the Nafion membrane. On the other hand, the cost of catalyst becomes critical in determining the stack cost of HT-PEMFC because higher Pt loading is required to generate comparable electrical output. Because of the high cost of catalysts, the stack for HT-PEMFCs is more expensive than that of LT-PEMFC [12, 13]. However, the cost of HT-PEMFC becomes competitive at the system level because of its simpler system design as shown

in Table 16.1. At the annual production of 100 units of the 1 kW system, the HT-PEMFC system is estimated to cost \$10,130 which is close to the cost of the LT-PEMFC system which is estimated to be \$10,106 [12]. For the calculation of LT-PEMFC system cost, the cell voltage and power output values of 0.676 V/cell and 408 mW/cm² were assumed to be generated from the MEA that contained Pt loading of 0.4 mg/cm². For HT-PEMFC, the cell voltage and power output from the MEA that contained 1.0 mg/cm² Pt loading were assumed to be 0.6 V/cell and 240 mW/cm². By increasing the annual production volume of HT-PEMFC systems from 100 units to 50,000 units, the system cost decreased from \$10,130 to \$6101 [12]. Even with the large annual production volume, the cost of both LT-PEMFC and HT-PEMFC systems are six times higher than the target cost of \$1000 kW⁻¹. As shown in Table 16.1, the cost of catalysts is by far the largest portion of the HT-PEMFC stack cost based on the assumption that the Pt loading of HT-PEMFC electrode is 2.5 times higher than that of LT-PEMFC electrode. Thus, in order to contribute to the cost competitiveness of the HT-PEMFC system at the stack level, it might be necessary to take account the Pt recycling into the cost calculation of the HT-PEMFC system. Because the cost of stacks is only 11 % of the HT-PEMFC system cost at high production volume, it is critical that cost reduction efforts be made at every level of the system to reduce the cost of the system further.

16.1.2 Durability Target

The required durability target of HT-PEMFC systems differs for APU and CHP applications. For the APU application, the systems need to satisfy the durability target of 20,000 h with the degradation rate of 1 %/1000 h by 2015 [4]. The APU systems need to operate in the mode of daily cycles to stand-by condition and weekly cycles to off condition [4]. For the micro-CHP in the power range of 1–10 kW, the lifetime of 60,000 h is targeted by 2020 [5]. The targeted degradation rate of 0.3 %/1000 h is to be reached with startup/shutdown cycles that are expected to occur less than once a month and total of less than 100 on–off cycles [15]. The most widely commercialized fuel cell system in CHP application market is the LT-PEMFC system which entered the market as “Ene-Farm” cogeneration home fuel cell system. The Ene-Farm system which generates 0.75 kW power output with LT-PEMFC has the reported lifetime of 60,000 h [16]. Compared to the LT-PEMFC systems, the HT-PEMFC systems contain fewer components and are less sensitive to the impurities in the fuel [17]. Thus, the HT-PEMFC has the prospective for achieving higher durability in the system level if the durability of stack can be established. At the stack level, establishing the durability target is more challenging for HT-PEMFC than LT-PEMFC because of its high operating temperature and the presence of phosphoric acid in the MEA.

16.2 Developments in HT-PEMFC MEA

16.2.1 Components of HT-PEMFC MEA

Because of the phosphoric acid-filled catalyst layer, the HT-PEMFC encounters the same limitations as the phosphoric acid fuel cell (PAFC) in developing high performance MEAs. The sluggish oxygen reduction reaction (ORR) kinetics which are caused by the low O₂ solubility in phosphoric acid and the strong adsorption

of phosphoric acid anions on Pt are the barriers that need to be overcome when designing highly efficient MEAs for HT-PEMFC [18–22]. In the following section, the recent studies that contributed to the understanding and improvements of the performance of HT-PEMFC MEAs are discussed.

16.2.1.1 Catalyst

To reduce the large ORR overpotential in the cathode of HT-PEMFC MEAs, the choice of catalyst becomes critical. Because of the slow ORR in the presence of phosphoric acid, the typical Tafel slopes of 90–100 mV/dec for HT-PEMFC are measured [18, 23, 24], and the values are higher than the value reported for the LT-PEMFC which is 60 mV/dec [25, 26]. The large ORR overpotential of HT-PEMFC also results in the low ORR exchange current density value of 2.2×10^{-9} A/cm² which is two orders of magnitude lower than the exchange current density for ORR in the LT-PEMFC which is reported to be 2.8×10^{-7} A/cm² [18, 27]. To overcome the effect of anion adsorption in phosphoric acid, the Pt transition metal alloys were used as cathode catalysts for PAFC [28, 29]. The specific activity values at 0.9 V were compared for Pt–Cr, Pt–V, Pt–Ti, and Pt–Al alloys, and it was concluded that the Pt–Cr alloy which exhibited the smallest nearest-neighbor distance showed the highest ORR activity in 100 % H₃PO₄ solution at 200 °C. Although the mechanism that the ORR rate is affected by the composition of Pt alloys is not fully understood, some of the factors that are suggested in the literature include surface roughening due to the dissolution of the alloy metal, electronic effects, and oxygen interaction difference on the alloyed catalyst [28, 30–33]. Further developments on the Pt alloy catalysts have been made to enhance the ORR kinetics in cathode of PEMFC, and several studies reported that the Pt–Co and Pt–Ni alloys showed the highest activity toward ORR [31–33]. Mamlouk and Scott [34] studied four different Pt alloys of Pt–Ni, Pt–Co, Pt–Ru, and Pt–Fe as HT-PEMFC cathode catalysts in a phosphoric acid-doped PBI membrane fuel cell. The cell performances of all alloys except Pt–Ru were better than that of Pt

alone in a lower current density region. In particular, Pt–Co and Pt–Ni showed the cell voltage that was 25 mV higher than the voltage measured with Pt catalyst in the current density region lower than 0.1 A/cm^2 , and the peak power density of 0.25 W/cm^2 was measured with $0.2 \text{ mg}_{\text{Pt}}/\text{cm}^2$ of Pt–Co alloy catalyst. The 25 mV increase in the cell voltage corresponds to twofold increase in ORR activity which is in agreement with the activity increases reported by other studies [30, 31]. The crystallographic structure effect on the ORR activity and durability of Pt–Co alloys in PAFC operating conditions was studied [29]. The specific ORR activity of the ordered Pt alloy which was obtained by heat treating the “as-received” alloy was 1.35 times higher than that of the disordered alloy. However, the Co dissolution rate was found to be higher for the ordered alloy after 50 h of exposure to 0.8 V in 105 % H_3PO_4 solution at 205 °C. The ordered Pt–Co alloy showed higher specific ORR activity; however, the disordered Pt alloy was preferred over the ordered alloy when designing an HT-PEMFC MEA with higher durability [29].

High utilization of the Pt catalysts is achieved by dispersing the Pt nanoparticles of 2–5 nm on the support material that has high surface area, high electrical conductivity, and chemical and electrochemical stability. The carbon materials of Vulcan carbon and Ketjen blacks are most widely used as the support material. The surface area is 200–300 m^2/g for Vulcan carbon black and 700–1600 m^2/g for Ketjen black. The surface area of carbon support materials is a critical parameter that affects the size of Pt particles, and it is reported that the size of Pt particles that were supported on Vulcan (Pt/Vulcan) with the surface area of 254 m^2/g was 2.0 nm, while the Pt particles supported on Ketjen black (Pt/KB) with the surface area of 1270 m^2/g had the size of 1.1 nm [35]. The smaller particle size of Pt supported on Ketjen black resulted in the Pt surface area that is 1.8 times higher than the surface area of Pt supported on Vulcan assuming that the Pt particles are present as spheres on carbon. Because of the high Pt surface area, the electrodes prepared with Pt/KB catalyst exhibited higher cell performance than the

electrodes prepared with Pt/Vulcan catalyst [35]. However, the Pt/Vulcan catalyst is known to exhibit far greater resistance to oxidation in fuel cell operating conditions, and Vulcan carbon black may be a better option as the catalyst support for HT-PEMFC [36].

The Pt content of carbon-supported catalysts is also an important parameter because Pt particle size and the electrode thickness are affected by the Pt content of the catalyst. The catalyst with lower Pt metal contents results in thicker catalyst layers which causes the increase in mass transport and electrical resistances. On the contrary, the higher Pt metal loading catalyst produces thinner catalyst layers. Three different catalysts that had Pt contents which ranged from 20 to 50 % were evaluated in HT-PEMFC [37]. The thickness values of the catalyst layers were measured to range from 15.3 to 5.6 μm [37]. The thin catalyst layer with the thickness of 5.6 μm which contained catalysts with 50 % Pt gave the best performance, and the improvement in cell performance was attributed to the vicinity of catalyst to the membrane. Achieving the best cell performance from the thin catalyst layer is expected; however, additional considerations need to be taken in designing durable HT-PEMFC MEAs. For the catalyst layer to contain a sufficient amount of acid without being flooded and act as a buffer layer that can suppress acid leaching from membrane to bipolar plate, optimum thickness of catalyst layer needs to be designed.

16.2.1.2 Binder

Unlike LT-PEMFC electrodes where the binder in the catalyst layer acts as ionomer, the binder in the catalyst layer of HT-PEMFC electrodes does not act as ionomer and is often added to serve other functions in the catalyst layer. The binders that are used in the catalyst layer of HT-PEMFC can be divided into the acid-absorbing and hydrophobic binder as shown in Fig. 16.1. The acid-absorbing binders such as PBI and AB-PBI are often used to control and retain the distribution of phosphoric acid in the catalyst layer [37]. As shown in Fig. 16.1a, the catalyst particles form agglomerates with the binder,

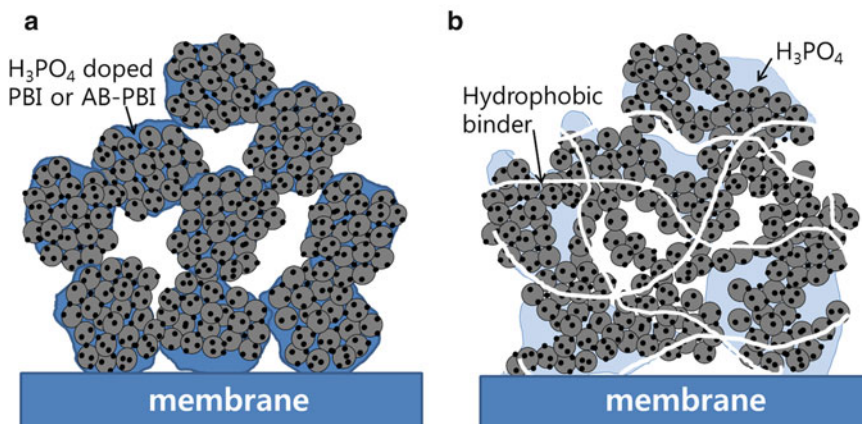


Fig. 16.1 Schematic diagram of the binder presence in the catalyst layer of HT-PEMFC MEAs with the carbon-supported catalyst and H₃PO₄-doped membrane. (a) The

acid-absorbing PBI or AB-PBI binder in the catalyst layer and (b) the hydrophobic PTFE or PVDF binder in the catalyst layer

Table 16.2 Binders used in HT-PEMFC MEAs and the cell performances

Binder material	Cell performance V at 0.2 A/cm ²	Pt loading (mg _{Pt} /cm ²)	Operating condition	Reference
PBI	0.56	0.5	125 °C, air/H ₂	[23]
ABPBI	0.61	0.75	160 °C, O ₂ /H ₂	[42]
PVDF	0.70	0.5	160 °C, air/H ₂	[39]
PTFE	0.60	1.0	160 °C, air/H ₂	[38]
Teflon AF	0.67	1.0	160 °C, air/H ₂	[43]

and the phosphoric acid which is absorbed into the binder can be uniformly distributed within the catalyst layer. The O₂ can diffuse through the secondary pores that are not occupied by the binder material. Like the catalyst layer in PAFC, polytetrafluoroethylene (PTFE) is often used in the catalyst layer of HT-PEMFC as a hydrophobic binder [38, 39]. The hydrophobic binders are used to form a network of path for gas phase O₂ diffusion within the catalyst layer. Other than PTFE, polyvinylidene fluoride (PVDF) is also used as a hydrophobic binder in the catalyst layer of HT-PEMFC [40, 41]. Table 16.2 compares the cell voltage values measured from the MEAs that used different kinds of binder materials in the catalyst layer.

By using the acid-absorbing binder materials, the distribution of acid in the catalyst layer, acid retention ability of the catalyst layer, and the interfacial resistance between the catalyst layer and membrane can be improved. The most

logical choice for the binder material to accomplish the purpose is PBI or AB-PBI which is the same material as the membrane [23, 37, 42]. Lobato et al. [23] optimized the PBI content in the catalyst layer and obtained the highest cell performance of 0.56 V at 0.2 A/cm² when the carbon to PBI weight ratio in the catalyst layer was 20. The lowest ohmic resistance and the highest electrochemical surface area (ECSA) of Pt were obtained by using the optimum PBI content, and it was concluded that the structure of the catalyst layer which could provide sufficient electronic and proton conductivity as well as the mass transport of O₂ in the gas phase was realized. Su et al. [44] investigated the effect of the molecular weight (MW) of the PBI binder on the cell performance and concluded that the cell with lower MW PBI exhibited higher ECSA of Pt catalysts and lower charge transfer resistance, thus resulting in the higher cell performance. The improvement in the cell performance was

attributed to the enhanced dispersion of the low MW PBI in the catalyst layer. Another form of PBI, poly (2,5-benzimidazole) (AB-PBI), was also used as binder to improve the cell performance of HT-PEMFC [42]. The optimum amount of AB-PBI binder was well mixed with a sonicator when catalyst coating slurry was prepared, and the performance of the electrodes that contained different AB-PBI contents in the catalyst layer were compared [42]. The optimum amount of AB-PBI binder in catalyst layer was found to be 15 wt%, and the cell voltage of 0.61 V at 0.2 A/cm² was measured with O₂ oxidant at 150 °C [42]. Instead of dispersing uniformly in the catalyst layer, when the AB-PBI binder was added by forming a layer of AB-PBI on the catalyst layer, Wannek et al. [38] observed that the introduction of even 2 wt% of the AB-PBI binder led to the significant decrease in cell performance. The low cell performance was ascribed to low gas permeability of the AB-PBI electrode. By introducing the AB-PBI binder on the coated catalyst layer, it was possible that the AB-PBI binder occupied the secondary pores in the catalyst layer and blocked the path for the O₂ diffusion [38]. Thus, it is important that the PBI or AB-PBI binder is dispersed uniformly, and the content and dispersion of the binder need to be controlled so that the secondary pores are free of the binder. In addition to the increased ECSA and the reduced ohmic resistance [23], it was observed that the Tafel slope in the activation region of the *I*-*V* curve measured from a cell operated at 150 °C decreased from 100 to 87 mV/dec when PBI was used as the binder [45]. The reduction of the Tafel slope indicated that addition of the PBI binder to the catalyst layer may have caused a change in the ORR mechanism. However, a couple of negative effects were brought up when the PBI binder was used in HT-PEMFC MEAs. The Pt utilization was observed to decrease by 5 % when the binder material in the catalyst layer changed from PTFE to PBI, and the possible Pt poisoning or blockage effect by PBI was suggested [45]. During long-term operation of the MEAs, the electrode with PBI binder was found to be more susceptible to flooding

[45]. The acid-absorbing binder materials such as PBI and AB-PBI can enhance the cell performance of HT-PEMFC by providing uniform distribution of phosphoric acid in catalyst layer, but retaining the path for O₂ diffusion in the catalyst layer may be challenging because of the swelling and morphology change of PBI that occur during the long-term cell operation.

For the facile diffusion of O₂ reactants within the catalyst layer, the hydrophobic binders which include PVDF and PTFE are often used [38, 39, 41, 45]. As shown in Fig. 16.1b, the hydrophobic binder forms a network of path for the O₂ diffusion in catalyst layer and increases the O₂ concentration near the catalyst sites. The properties of the electrodes prepared with PTFE, PVDF, PBI, and Nafion binders were compared by measuring their pore distributions, cell performance, and electrochemical characteristics [39]. The electrodes with PTFE and PVDF binders showed the higher ECSA and higher volume of macropores (5–100 μm) than those with PBI and Nafion binders, and the electrodes with the hydrophobic binders performed better in both low and high current density regions. The cell performance measured at 160 °C with H₂ and air gas feeds showed that the highest cell performance of 0.7 V at 0.2 A/cm² was achieved with the electrode prepared using the PVDF binder. It was suggested that the electrode with the PVDF binder performed better than the one with the PTFE binder because more uniform distribution of the binder could be achieved with the PVDF binder. Although PTFE is more difficult to get uniform distribution within the catalyst layer, its higher thermal stability which has the crystalline melting point of 327 °C compared to PVDF which has the crystalline melting point of 170 °C [46] makes it the most widely used hydrophobic binder in PEMFC electrodes. For the catalyst layer in PAFC electrodes, the PTFE content in the catalyst layer was optimized to obtain the desired microstructure of catalyst layers [47]. The PTFE content of 30 % gave the highest Pt utilization and the highest cell performance. The utilized Pt particles were in the primary pores which were mostly occupied by phosphoric acid, and the PTFE binder was found to be

mostly located in the secondary pore where the path for the O_2 diffusion occurred. When using the hydrophobic binders in the catalyst layer of HT-PEMFC, it is important to achieve a uniform dispersion of the binder in the secondary pores and occupy the primary pores with phosphoric acid so that the gas path and Pt utilization are optimized.

16.2.1.3 Phosphoric Acid

The phosphoric acid content in the MEA of HT-PEMFC is also reported to affect the cell performance [20, 48]. The cell performances of the MEAs which contained varying amounts of phosphoric acid in PBI membranes were compared [48]. The acid doping levels in the PBI membrane were between 18 and 25 mg/cm^2 , and the ohmic and charge transfer resistance values were greatly dependent on the initial acid content of the membrane. After 450 h of cell operation at 0.2 A/cm^2 , the acid contents of the membranes were between 13 and 14 mg/cm^2 regardless of the initial acid content of the membrane. It was suggested that the phosphoric acid moved to the catalyst layer during cell operation until a critical acid content of 13 and 14 mg/cm^2 remained in the membrane. It was found that the MEA with the phosphoric acid content of 23 mg/cm^2 in the membrane which would provide 10 mg/cm^2 of phosphoric acid to the catalyst layer gave the best cell performance [48]. Wanek et al. [20] also investigated the redistribution of phosphoric acid in MEAs during cell operation. The MEAs that contained different initial contents of phosphoric acid in the cathode, anode, and membrane were evaluated. The total acid contents in the MEAs were between 24 and 40 mg/cm^2 . The acid content in the cathode, anode, and membrane after 100 h of operation at 0.2 A/cm^2 did not depend on the initial acid distribution in the MEA. For all MEAs, the membrane contained 15–16 mg/cm^2 of acid, and the electrodes contained 3–5 mg/cm^2 of acid which resulted in the total acid amount of 21–25 mg/cm^2 in the MEA [20]. The acid content in the membrane after 100 h of cell operation depended on the polymer content (AB-PBI) of the membrane, and the acid content was 4.1

times of the polymer content. It was concluded that the excess phosphoric acid in the MEA was squeezed out during compression of the cell, and the acid content in the MEA was maintained between 21 and 25 mg/cm^2 [20]. The amount of phosphoric acid that remained in the membrane depended on its polymer content, and it is likely that the thickness of the catalyst layer influenced the amount of acid remaining in the electrode. Although the MEA was able to tolerate the excess amount of phosphoric acid to a certain level, increasing the phosphoric acid content in MEA can cause flooding which leads to the failure of cell operation [41].

The magnitudes of the ohmic, proton transport, charge transfer, and mass transport resistance values were found to depend on the distribution of phosphoric acid and Pt loading of the MEA [49]. The resistance values and the cell performances were investigated by varying the total amount of phosphoric acid in the MEAs with different anode and cathode catalyst loadings [49]. The lowest charge transfer resistance value was measured from the MEA with the highest cathode Pt loading and highest acid content, and the lowest proton transport resistance was measured from the MEA with the highest acid content and lowest anode Pt loading. The highest cell voltage at 0.2 A/cm^2 was measured from the MEA with the lowest charge transfer resistance which was the MEA that contained the highest acid content of 20 mg/cm^2 and highest cathode Pt loading of 1.0 mg/cm^2 [49]. For the typical HT-PEMFC MEAs which have the pre-doped membrane thickness of 40 μm and the catalyst layer thickness of 30–50 μm , the acid content of 20–25 mg/cm^2 was found to provide a sufficient saturation level of phosphoric acid content and resulted in the best cell performance.

16.2.2 Durability of HT-PEMFC MEAs

To penetrate successfully into the fuel cell market, HT-PEMFC systems need to prove durability and reliability in real operation conditions. For the HT-PEMFC systems to reach their

durability targets, the durability of MEAs needs to be proved in various operation modes. The reported voltage decay rates during continuous operation range from 5 to 25 $\mu\text{V}/\text{h}$ [24, 50–52]. The voltage decay rate during start/stop operation mode was measured to be 11 $\mu\text{V}/\text{h}$, and it was twice of the decay rate of 5 $\mu\text{V}/\text{h}$ which was measured during the continuous operation [24]. Many studies have been conducted to investigate the cause of the voltage loss and improve the durability of HT-PEMFC MEAs. The voltage decay of HT-PEMFC MEA is mainly resulted from the polymer membrane degradation, catalyst degradation, and phosphoric acid loss. The degradation of polymer membrane is reported to result from the attack by H_2O_2 and $-\text{OH}$ and/or $-\text{OOH}$ radicals [53], and the membrane degradation is detrimental to cell operation and sometimes leads to sudden death of the cell. The catalyst degradation and acid loss are shown in the form of the ECSA reduction and increases in proton transport and ohmic resistance in MEAs. It is reported that the gradual decrease of voltage up to 14,000 h of cell operation is caused by the decrease of the active surface area of catalysts, and migration of phosphoric acid from the membrane and depletion of acid from the catalyst layer were found to occur after 15,000 h of cell operation [54]. Suzuki et al. [55] also reported that the cell voltage decay occurred due to the decreased electrochemical active surface area caused by the agglomeration of Pt electrocatalyst particles as well as the phosphoric acid loss by evaporation. In this section, the effects of the catalyst degradation and acid loss on the voltage decay during the operation of HT-PEMFC are discussed.

16.2.2.1 Catalyst Degradation

Catalyst degradation is known to be one of the main causes for the voltage loss during the operation of HT-PEMFC [55–61]. During the cell operation of PEMFC, the growth in the size of Pt nanoparticles which led to the decrease in the active surface area and cell performance was observed [62]. The catalyst degradation is found to be affected by the cell voltage [60, 61], operation temperature [56, 57, 59, 60], presence of

anion species [63], and alloying element [56]. The Pt particle growth was proposed to occur by Ostwald's ripening mechanism which suggested that the dissolved Pt ions from nanoparticle catalysts deposited on other Pt particles, leading to the increase in particle sizes [64, 65]. Honji et al. [66] investigated the agglomeration of carbon-supported Pt particles in phosphoric acid solution and reported that the Pt agglomeration was accelerated in the presence of phosphoric acid. The Pt particles with the initial size of 5 nm were found to agglomerate at a faster rate initially, and the size grew to 10 nm after 25 h. The growth rate of the Pt particles slowed down and continued to grow to 12 nm after 110 h. The operation temperature of fuel cell is also reported to have detrimental effect on the stability of catalyst [55, 56]. It is reported that after only a short exposure to the temperature of 130 °C, significant changes in ECSA of the Pt catalyst occurred [56]. Suzuki et al. [55] found that the binding energy between the Pt catalyst and carbon support became gradually smaller as the temperature increased, and the Pt-carbon binding energy values of -49.51 , -48.87 , and -46.24 kcal/mol were obtained at 150 °C, 170 °C, and 190 °C, respectively. By using the 3D Kinetic Monte Carlo (KMC) method, the diameters of Pt particles were estimated to grow from the fresh Pt particles of 3.8 nm to the particles with diameter of 4.4, 5.5, and 6.2 nm after aging 1000 h at 150 °C, 170 °C, and 190 °C, respectively. From the literature, it is obvious that the Pt agglomeration in the MEA of HT-PEMFC can be severe and cause high voltage decay during cell operation. Oono et al. [54] observed that the average size of Pt particles grew from 4.6 to 7.9 nm after 17,800 h of cell operation at 0.2 A/cm^2 at 150 °C, and the voltage decay rate of 4 $\mu\text{V}/\text{h}$ was measured. Wannek et al. [51] evaluated the durability of HT-PEMFC MEAs for 1000 h at different operating conditions and obtained the degradation rate of 20 and 120 $\mu\text{V}/\text{h}$ from the cells that operated in constant current density and start–stop operation modes. The Pt particles grew from 2.7 to 6.5 nm after 1000 h of continuous operation at a constant current density. The

Pt agglomeration was reported to occur at a faster rate in the initial stage [66], and the actual measurements of the Pt size change showed that the size of Pt particles doubled after only 1000 h of cell operation [51]. Because the reported voltage decay rates and the Pt agglomeration measurements of HT-PEMFCs are obtained from the cells operated under 20,000 h, the possibility of achieving the voltage decay rate target of $-0.3 \%/1000$ h after 60,000 h cell operation can only be estimated. The contribution of Pt agglomeration on the long-term durability of HT-PEMFC MEA is estimated and discussed in Sect. 16.3.2.

The HT-PEMFC also provides the conditions that accelerate the oxidation of carbon support which occurs when the cell is exposed to high potentials at high operating temperature. The oxidation becomes more severe for the carbons with higher Pt loading at the elevated temperatures [67–69]. The oxidation of carbon was analyzed by measuring the weight loss of carbon-supported Pt particles at the elevated temperatures [69]. Over 50 % weight loss of carbon was measured for the carbon-supported catalysts that contained more than 30 % Pt when the particles were exposed to dry air between the temperature of 150 and 195 °C [69]. For the catalyst that contained 20 % Pt showed carbon loss that was less than 1/3 of the carbon loss measured from the catalyst with 30 % Pt content. The oxidation of carbon also showed great dependence on temperature. For the carbon-supported catalyst that contained 30 % Pt, the carbon loss was less than 5 % after 400 h exposure in dry air condition at 125 °C, and the weight loss increased to 15 and 60 % when the temperature increased to 150 and 173 °C [69]. Thus, the carbon oxidation at the operation temperature of HT-PEMFC can be many folds higher than that observed in LT-PEMFC. The carbon oxidization accelerates the reduction of ECSA by causing the detachment of the Pt particles from the carbon support. In addition, the carbon oxidation during operation of HT-PEMFC can cause thinning of the catalyst layer. Oono et al. [54] operated HT-PEMFC MEA at 150 °C and 0.2 A/cm² for 17,800 h and reported that the

thickness of the catalyst layers reduced from 30 to 20 μm, suggesting that a large amount of carbon support was oxidized. The start–stop operation mode which exposes the cathode to the potential higher than 1 V is also known to accelerate carbon oxidation. Schmidt and Baurmeister [24] showed that carbon oxidation caused flooding in electrodes and increased the voltage decay rate during the start–stop operation mode. It was demonstrated that the carbon oxidation could be suppressed by improving the intrinsic stability of carbon supports, and the durability of the MEA was shown to improve significantly during start–stop operation mode by using the oxidation-resistant carbon support. Because flooding can cause fast and sudden decrease in the cell voltage of MEAs, mitigation of carbon oxidation in the operation conditions of HT-PEMFC can have great impact on the durability of the MEAs.

16.2.2.2 Phosphoric Acid Loss

The loss of phosphoric acid occurs during cell operation by diffusion, capillary transport through electrode, MEA compression, evaporation, and leaching [53]. The estimated evaporation rate of phosphoric acid in a commercialized HT-PEMFC MEA, Celtec-P1000, was measured to be 0.6 μg/m² s at 150 °C [70]. The acid evaporation rate increased with temperature, and the rates of 1 and 2 μg/m² s at 160 and 180 °C were measured. It was estimated that a Celtec-P1000 MEA could operate for 100,000 h if the acid is lost only by evaporation [70]. Other studies which measured acid contents from the anode and cathode gas outlets reported even lower acid loss rates of 0.02 [50] and 0.26 μg/m² s [51] during continuous operation at 160 °C. Such low acid loss rates should not cause significant voltage losses during cell operation; however, the investigations into the long-term operation of HT-PEMFC often concluded that the acid loss contributed to the voltage decay [54, 71].

The long-term operation of an HT-PEMFC MEA that operated for 17,800 h at 150 °C showed an increase in the voltage decay rate after 14,000 h of cell operation. The increase in

the voltage decay rate was attributed to the loss of the active surface area which was caused by the depletion of phosphoric acid in the catalyst layer. According to the reported acid evaporation rate of $0.6 \mu\text{g}/\text{m}^2 \text{ s}$ at 150°C [70], the amount of lost acid can be estimated to be $3 \text{ mg}/\text{cm}^2$ after 14,000 h. The MEA had the initial phosphoric acid content of $20 \text{ mg}/\text{cm}^2$, and it is unlikely that only 15 % loss of phosphoric acid can cause the depletion of acid in the catalyst layer. Kim et al. [71] reported the voltage decay rate of a 6 cell HT-PEMFC stack that operated for 4000 h. It was observed that the average voltage decay rate of the 6 cell stack changed from 15.6 to $52.7 \mu\text{V}/\text{h}$ after 2000 h of operation, and the increase in the voltage decay rate was attributed to the increase in proton transport resistance in the catalyst layer. The loss of phosphoric acid was found to be significant enough to influence the cell performance after only 2000 h of operation. The reported works that showed the lack of phosphoric acid in the MEAs after operating for less than 15,000 h of HT-PEMFC indicate that the rate of phosphoric acid loss from MEAs could be higher than the reported evaporation rates.

In addition to the evaporation which mainly depends on the operation temperature, the loss of phosphoric acid is reported to be influenced by other operating conditions. Yu et al. [50] measured the rates of phosphoric acid loss at different temperatures during continuous operation and reported that the acid loss increased with operating temperature, and the acid loss rate from cathode was significantly higher than the acid loss rate from the anode. The higher acid content in the cathode gas outlet indicates that the evaporation is not the only route that the phosphoric acid is lost from the MEA. The phosphoric acid loss is reported to be affected by the operating current density because the hydration state of phosphoric acid is changed by the amount of water generated at different operation current densities [72]. The variations in concentration of phosphoric acid at different current densities affected the distribution of phosphoric acid in the MEA and the acid loss rate [72]. The volume expansion and contraction of phosphoric acid in the MEA can be also caused by the

change in vapor pressure of water in the cell that occur during dynamic operations of load, thermal and shutdown-startup cycling, and the volume change of phosphoric acid is reported to redistribute the acid within the MEA and accelerate the acid loss [53]. When voltage cycling was applied, the measured acid loss rates were $20.4 \text{ ng}/\text{cm}^2 \text{ h}$ from cathode and $0.78 \text{ ng}/\text{cm}^2 \text{ h}$ from anode [50]. The acid loss rate during voltage cycling was four times higher than that measured from the continuous operation. The acid loss during the voltage cycling can be caused by volume change of the acid which leads to acid leaching.

The voltage decay analysis of the MEA which showed the depletion of acid indicates that the acid loss rate from the MEA may be greater than the acid loss measured from the anode and cathode gas outlets during operation. In addition to the acid which exits the cell in the gas outlets, the bipolar plates were shown to take in phosphoric acid during cell operation. The amount of acid absorbed in different bipolar plates after cell operation at 180°C was compared, and it was found that the rate of acid loss greatly depended on the property of bipolar plates [73]. Compared to the gold plated bipolar plate which shows no detectable amount of acid uptake, the composite bipolar plates contained over 10 % of the initial amount of acid in the MEA after 1600 h of operation. The uptake of acid by the bipolar plates contributed to the loss of cell performance by increasing ohmic resistance and reducing active sites in the MEA [73]. The acid that is transferred out of an MEA by diffusion, compression of MEA, and leaching may stay in liquid form in the cell and can be absorbed in the bipolar plates. Such loss of acid is not detected in the gas outlet and is difficult to quantify during cell operation. Thus, the acid loss during cell operation is most likely not negligible, and efforts need to be made to maintain acid within the MEA during cell operation.

Other than the membrane degradation which leads to an MEA failure, the main causes of the voltage decay of HT-PEMFC MEAs in the literature are catalyst degradation and acid loss. Figure 16.2 shows a schematic diagram that

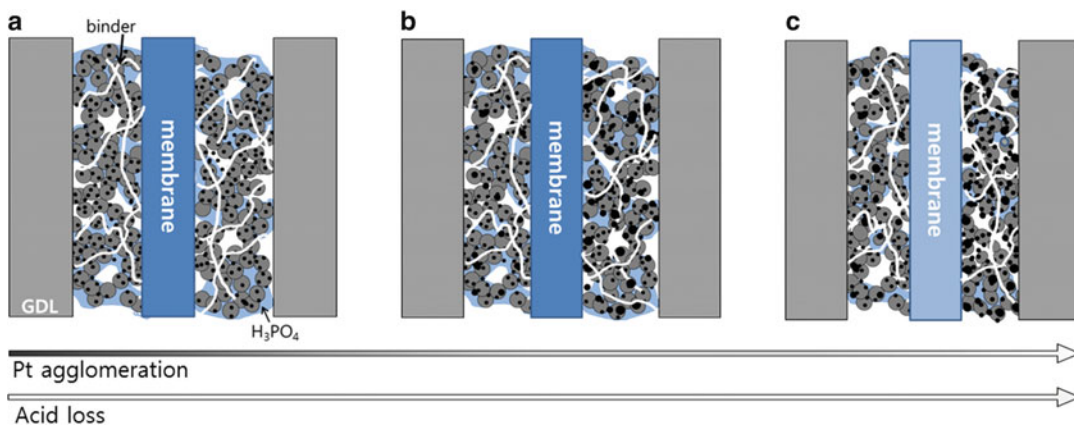


Fig. 16.2 Diagrams representing the changes within an HT-PEMFC MEA during cell operation. The Pt agglomeration occurs at a higher rate initially and slower rate in latter stage. The acid loss occurs at a

constant rate. (a) Initial stage; (b) after significant Pt agglomeration occurred; and (c) in the latter stage where the membrane and catalyst layer lack phosphoric acid content

summarizes the changes that an MEA undergoes during operation of HT-PEMFC. In the initial stage, the MEA contains sufficient amount of acid in the catalyst layer and membrane, and the catalyst layer has high active surface area as shown in Fig. 16.2a. As the cell operation continues, the Pt agglomeration and acid loss occur. The Pt agglomeration occurs at a faster rate in the initial stage, and the Pt particles become larger as shown in Fig. 16.2b. The acid loss occurs at a constant rate during cell operation, and the membrane and catalyst layer lack phosphoric acid in the latter stage of cell operation as shown in Fig. 16.2c. The oxidation of carbon support which occurs during cell operation causes reduction in the thickness of catalyst layer as can be seen by comparing the thickness of catalyst layers in Fig. 16.2a, c. The magnitude of the voltage decay rate depends on the rates of Pt agglomeration and acid loss. The carbon oxidation can cause collapse of the structure of catalyst layer which may lead to flooding of MEAs.

electrical power output from 250 W to 5 kW were introduced to markets in the APU and CHP applications [6, 7, 74]. To contribute to achieving the cost and durability targets and to give competitive edge to the HT-PEMFC systems in the fuel cell market, the performance of HT-PEMFC MEAs needs to be further improved. In the following section, the possibilities of reducing Pt loading and improving durability of HT-PEMFC MEA are discussed.

16.3.1 Improvement of Cell Voltage

The reported cell voltage values of HT-PEMFC MEAs are between 0.65 and 0.7 V at 0.2 A/cm² [24, 41, 45], and the values are considerably lower than those measured from the LT-PEMFC whose cell voltage values are over 0.75 V at 0.2 A/cm² [75]. Despite the low cell voltage, the HT-PEMFC may be more suitable for the systems that use the fuel containing high content of CO because the HT-PEMFC system can operate with H₂ gas that contains CO content as high as 5 % [76]. However, it is essential to increase cell voltage and reduce Pt loading of the MEAs for HT-PEMFC to gain cost competitiveness in the fuel cell market. The largest cause of the voltage loss for the HT-PEMFC

16.3 Design of Optimum MEA Structure

The performance of HT-PEMFC MEAs has been considerably improved in the past decade, and the HT-PEMFC systems that can generate

MEAs is the ORR overpotential, and the catalyst composition and structure of the catalyst layer can be designed to reduce the ORR overpotential and the amount of Pt in the catalyst layer.

16.3.1.1 Catalyst

Several approaches can be taken to reduce the overpotential caused by the low ORR in the cathode of HT-PEMFC MEAs. The most effective and widely used method is the use of Pt alloy catalysts. The ORR rates on Pt and Pt alloy catalysts were compared by measuring the magnitude of Tafel slopes of ORR in different concentrations of H_3PO_4 solution [77]. It was reported that the increase of H_3PO_4 concentration from 10 to 85 wt% increased the Tafel slope from 110 to 134 mV/dec when ORR was measured with rotating disk electrode at room temperature. The Tafel slope was found to decrease when Pt was alloyed with 35 at.% of Cr, and the Tafel slope of ORR on Pt–Cr alloy catalyst was measured to be 101 mV/dec in 10 wt % H_3PO_4 and 118 mV/dec in 85 wt% H_3PO_4 solutions indicating decrease in the ORR overpotential [77]. In the single cell measurement, the Pt alloys such as Pt–Co and Pt–Ni showed the cell voltage values that were 25–50 mV higher than the Pt catalyst in the low current density region where the voltage is activation controlled [34]. In the MEAs for HT-PEMFC, it is necessary to use the Pt alloy catalysts such as Pt–Co and Pt–Ni to increase ORR kinetics in the cathode.

Among the methods of preparing the Pt alloy catalysts, the core–shell structured Pt alloys offer the possibilities of reducing the Pt loading in MEAs because of its high activity and the unique Pt-free core structure. The core–shell catalyst where the core is the alloy element and the shell is the catalyst material has been investigated for fuel cell application [78–81]. The Au–Ni core and Pt shell catalyst dispersed on carbon supports showed high Pt mass activity for ORR at 0.8 V vs. Ag/AgCl, and the 20-fold higher ORR activity of Pt/Au–Ni core–shell catalyst than the Pt catalyst was attributed to the decrease of PtOH formation on the Pt/Au–Ni core–shell catalyst [78]. In other works, the Co core and Pt shell

catalyst with an average particle size of 3–5 nm was found to show an ORR mass activity 1.5 times higher than that of Pt catalysts [81]. Moreover, the core–shell configuration was found to protect the dissolution of the Co alloy material and give more stable performance and ECSA changes after 130 h of cell operation [81]. By using the core–shell structured catalyst in the HT-PEMFC MEAs, in addition to achieving an increase in the ORR activity by selecting the optimum core alloy element, the amount of Pt used in the catalyst can also be reduced because the core of the catalyst is filled with the less costly alloy element.

16.3.1.2 Catalyst Layer

Although the catalyst activity is the most important factor in improving cell performance of HT-PEMFC, the catalyst layer structure can also be optimized to increase the concentration of O_2 in phosphoric acid near the catalyst sites. To establish a diffusion path for O_2 in gas phase, two possible approaches can be taken. One is the dispersion of the hydrophobic binder such as PTFE within the catalyst layer. For the MEAs that contain the high content of phosphoric acid, it would be best to use the PTFE binder in the catalyst layer. The other way is to control the pore size within the catalyst layer so that the pores that are filled with phosphoric acid and pores that provide path for O_2 diffusion in the gas phase can be separated according to the pore size. The primary pores between catalyst particles are known to be filled with phosphoric acid, while the larger secondary pores between the agglomerates of catalyst particles provide O_2 diffusion path [47]. If the O_2 diffusion path within the catalyst layer can be established and maintained without the use of the hydrophobic binder which increases the ohmic resistance in MEAs [45], the cell performance of HT-PEMFC can be improved.

The catalyst particles are found to exist as agglomerates in the catalyst layer of PEMFC electrodes, and the simulation of cell performance is often conducted by using the agglomerate model shown in Fig. 16.3 [83–86]. The agglomerate with the radius of r_{agg} is filled with

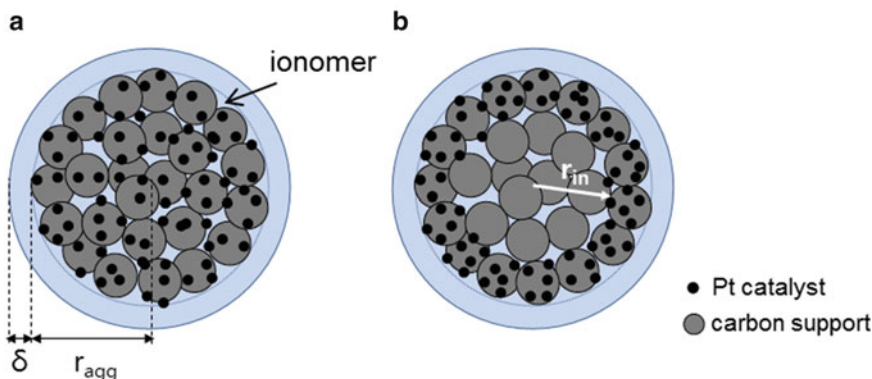


Fig. 16.3 (a) Schematic representation of the spherical catalyst agglomerate model. (b) Modified agglomerate model with distribution of discrete Pt particles. Reproduced from [82] with permission of The Electrochemical Society

ionomer, and the agglomerate is covered with a thin film of ionomer with the thickness of δ . The O_2 diffuses to the agglomerates in gas phase through the secondary pores which exist between agglomerates. Once the O_2 reaches the agglomerates, the O_2 dissolves into the ionomer. When the diffusion of dissolved O_2 into the agglomerates was considered, the simulation of cell performance indicated that the cell performance deteriorated as the size of agglomerates increased [83, 84]. The increase in the size of agglomerates caused greater diffusion length for O_2 before reaching the catalyst sites, eventually resulting in the increase of activation overpotential. For both cases where Nafion and phosphoric acid were assumed to fill the agglomerates, it was found that the cell performance showed small decrease when the agglomerate size increased from 10 to 100 nm. The magnitude of cell performance decrease with the increase of agglomerate size became greater once the agglomerate size was larger than 100 nm [83, 84]. However, the cell performance dependence on the agglomerate size showed different trends when the tortuosity of the secondary pores was included in the simulation. The change in the agglomerate size contributed to the cell performance in two ways. The increase of agglomerate size resulted in the longer diffusion length for the dissolved O_2 within the agglomerate and contributed to increasing the activation overpotential. However, the subsequent larger

secondary pores between agglomerates led to higher diffusion coefficient of O_2 in the gas phase. When the size of the agglomerate was too small, the cell performance was found to deteriorate because the tortuosity of pores was large [85, 86]. The cell voltage at high current densities showed an increase when the agglomerate size increased from 50 to 100 nm [85]. At low current density, the cell performance did not show significant change when the agglomerate size increased from 50 to 200 nm. From the results, it can be concluded that the optimum size of agglomerates was between 100 and 200 nm. The presence of optimum agglomerate size was observed in another reported work where the agglomerate size of 500 nm gave the lowest activation overpotential [86]. The ionomer coating surrounding the agglomerates contributed to adding diffusion resistance of dissolved O_2 within the agglomerates, thus elimination of the ionomer film was most beneficial to the cell performance [86].

The agglomerate model assumes that the Pt particles are evenly distributed inside the agglomerates. To optimize the structure of the agglomerate, a modified agglomerate model was developed to account for the variations in Pt particle distribution in the agglomerates [82]. The diffusion effects of O_2 in the agglomerates that were filled with ionomer were incorporated, and the impact of variations in Pt distribution in the agglomerates on the cell

voltage in the diffusion limited current density region was investigated [82]. By concentrating Pt particles in the outer periphery of the agglomerates, the Pt utilization was found to improve, and it was possible to reduce the Pt loading from 207 uniformly distributed Pt particles to 104 Pt particles. By placing the Pt particles in the outer periphery that was within 10 % of the radius of the agglomerate, it was possible to result in less overpotential in the diffusion limited current density region than the agglomerates in which the Pt particles were uniformly distributed [82]. The modified catalyst agglomerate design which results in the same activation overpotential with significantly less Pt particles can contribute to reducing the amount of Pt used in the HT-PEMFC MEA.

In summary, the core-shell catalyst can be used in the catalyst layer to reduce the Pt loading without sacrificing the cell performance of HT-PEMFC MEAs. To maximize the O₂ concentration at the catalyst particles, the modified catalyst agglomerates, as shown in Fig. 16.3, where the catalyst particles are placed in the outer part of agglomerate sphere can be adapted. The reported works indicate that the agglomerate size of 200–500 nm optimizes the diffusion of O₂ in the gas phase and dissolved phase [85, 86].

16.3.2 Improvement of MEA Durability

The systems of LT-PEMFC and PAFC are reported to have operation time of 60,000 and

80,000 h, respectively [16, 87]. The operation temperature of HT-PEMFC falls between those of LT-PEMFC and PAFC systems, and it can be expected that the HT-PEMFC system operates over 60,000 h because the components such as catalyst and GDL used in HT-PEMFC MEAs have similar properties as those used in PAFC and LT-PEMFC MEAs. Many attempts have been made to improve the durability of HT-PEMFC at the MEA level, and the analysis of the voltage decay can provide more definite directions to the future activities. In the following section, the factors that contribute to the voltage loss and the approaches that can be taken to further improvement of the durability of HT-PEMFC MEAs are discussed.

16.3.2.1 Analysis of Voltage Decay

Pt Agglomeration

The high operation temperature and the presence of phosphoric acid in HT-PEMFC MEAs are reported to accelerate the catalyst degradation [48, 55, 58, 60]. The reported values of the fraction of remaining active surface area (SA/SA₀) after cell operation are summarized in Table 16.3. The table indicates that the most influential factor in loss of the surface area is the operation temperature. The 3D KMC simulation results indicated that the fraction of the remaining Pt surface area after 15,500 h at 150 °C was 0.79, and the value decreased to 0.60 when the operation temperature increased to 190 °C despite the considerably shorter cell operation time of

Table 16.3 Fraction of the Pt surface area remaining (SA/SA₀) after cell operation (KMC: 3D Kinetic Monte Carlo method)

Operation time (h)	SA/SA ₀	Catalyst (Pt wt%)	Operation temperature (°C)	Fuel cell type	Reference
15,500	0.79 (KMC simulation)	46.8	150	HT-PEMFC	[55]
1250	0.60 (KMC simulation)	46.8	190	HT-PEMFC	[55]
17,800	0.58 (estimated from Pt size change)	50	150	HT-PEMFC	[54]
9000	0.28 (ECSA measurement)	15	175	PAFC	[58]
43,000	0.12 (ECSA measurement)	15	175	PAFC	[58]

1250 h [55]. After the actual cell operation, the change in the Pt surface area showed similar trend at different temperatures. The fraction of surface area remaining after the operation time of 17,800 h at 150 °C was 0.58 [54], and the fraction decreased to 0.28 after operating 9000 h at 175 °C [58]. The highest rate of the surface area loss is reported to occur at the initial 1000 h of cell operation [55]. After the initial stage of Pt agglomeration, gradual agglomeration of Pt particles was found to occur [54].

The mechanism of migration and coalescence of Pt particles is suggested to account for the change of the Pt surface area on carbon supports, and the surface area (SA) of Pt particles at the aging time of t can be described by (16.1) [88], where SA_0 and SA are the Pt surface area per unit volume before and after time t .

$$\frac{1}{SA^{n-1}} = \frac{1}{SA_0^{n-1}} + kt \quad (16.1)$$

It was reported that the change in Pt surface area can be derived from (16.1) using the values of constants, k and n , and the values of constants k and n depend on the mechanism of Pt surface area change. The Pt migration-coalescence mechanism was considered to take place in two steps [89]. The first step is the particle migration process in which the mobility of the particle is relatively great at high temperatures. The following step is the coalescence of the particles. Ruckenstein and Pulvermacher [89] suggested that the surface area loss was dominated by the coalescence step when n was smaller than 3, and particle migration was the rate-determining step when n was greater than 3. After monitoring the change of the Pt surface area from 0 to 57,000 h of PAFC operation, the n value of 3.2 was obtained [58]. If the rate-determining steps of the surface area change during cell operation for PAFC and HT-PEMFC are assumed to be the same, the n value of 3.2 can be used to calculate the k value for an HT-PEMFC electrode by using the SA/SA_0 value of 0.58 that was reported by Oono et al. [54] after operating an HT-PEMFC at 150 °C for 17,800 h. The k value of 1.28×10^{-4} can be obtained, and the SA/SA_0

values as a function of aging time for the HT-PEMFC electrode can be estimated using (16.1). By using the calculated SA/SA_0 values at different aging time of t , the voltage loss (ΔV) caused by the change in Pt surface area can be calculated using (16.2), where B is the Tafel slope.

$$\Delta V = B \log \left(\frac{SA}{SA_0} \right) \quad (16.2)$$

By using the reported Tafel slope of 100 mV/dec [40], the voltage loss caused by the change in Pt surface area in an HT-PEMFC that operates at 150 °C can be calculated. Figure 16.4a shows the SA/SA_0 values and the resulting voltage loss values which can be expected from an HT-PEMFC that operates at 150 °C for 60,000 h.

Figure 16.4a shows that the SA/SA_0 decreases rapidly to the value of 0.61 in the initial 15,000 h; however, the rate of decrease slows down gradually resulting in the SA/SA_0 value of 0.36 at 60,000 h. Because of the flattening in the change of SA/SA_0 values over time, the change in ΔV values also shows the similar behavior. The magnitude of ΔV values changes somewhat linearly with time until 15,000 h, resulting in the loss of 21 mV. However, the change in ΔV flattens out giving 43 mV voltage loss at 60,000 h. Figure 16.4a indicates that the voltage loss caused by the loss of Pt surface area is significant in the initial stage of cell operation; however, the effect of the Pt surface area loss becomes less significant as operation time increases. Even after 60,000 h of cell operation and over 64 % of the Pt area loss, the cell voltage loss of 43 mV is less than 7 % loss of typical HT-PEMFC cell voltage value of 0.65 V. In order to improve the voltage decay rate of HT-PEMFCs during the target lifetime of 60,000 h, it is necessary to reduce Pt agglomeration; however, Fig. 16.4a suggests that the loss of the Pt surface area is not likely to cause a large cell voltage decrease which leads to MEA failures.

Acid Loss

The loss of phosphoric acid during cell operation of HT-PEMFC can occur by ways of evaporation

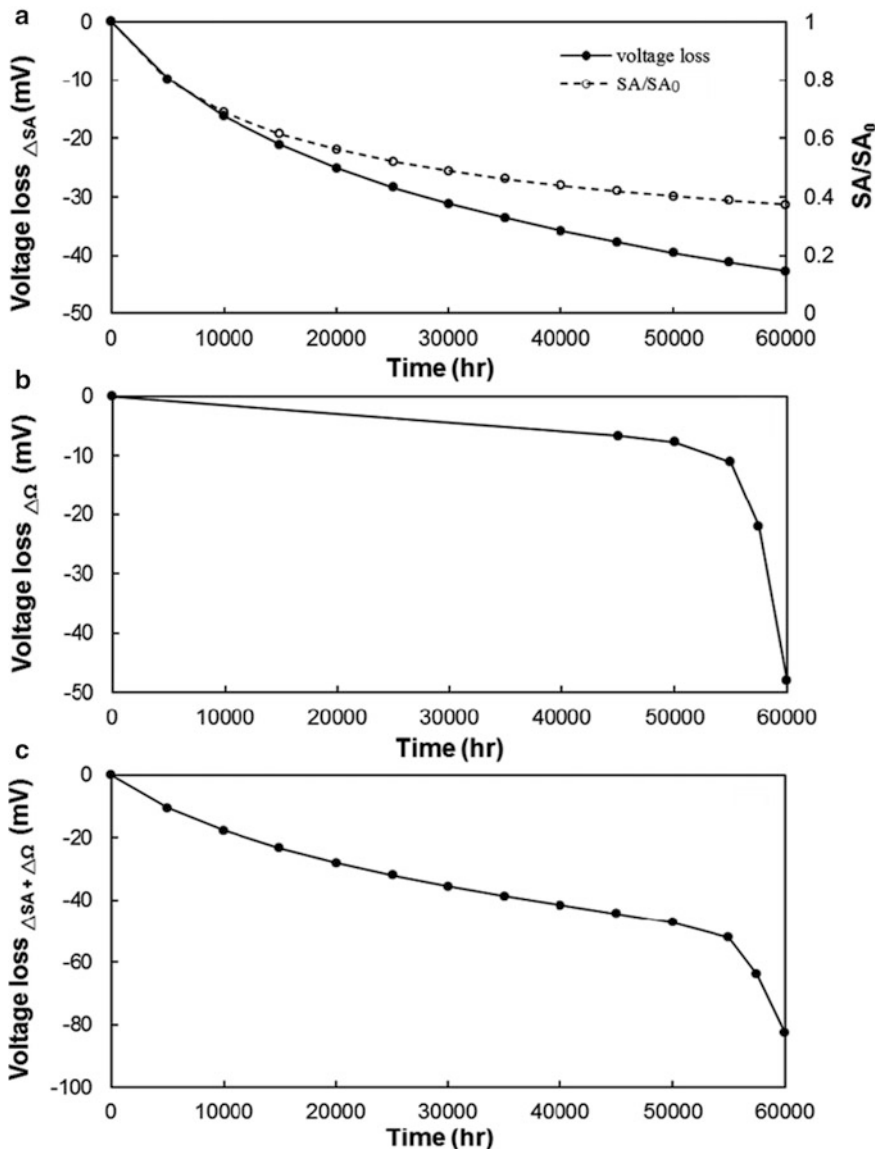


Fig. 16.4 Simulated voltage loss of HT-PEMFC over time, 150 °C, H₂/air. (a) Voltage loss caused by Pt surface area (SA) loss, SA change over time was calculated using the experimental ECSA measurement values from [48] and (16.1). (b) Voltage loss caused by the increase in ohmic resistance of MEA which is resulted from acid loss

from membrane (proton conductivity dependence on acid content of membrane from [90]), membrane is assumed to have 20 mg/cm² of phosphoric acid (PA) and 27 PA/PRU initially and lose 3 mg/cm² of PA every 10,000 h (membrane thickness: 50 μm). (c) Sum of voltage losses caused by the changes in SA and ohmic resistance

and leaching. The evaporation rate of phosphoric acid depends on temperature, and the rates at the initial stage of HT-PEMFC MEA Celtec[®] operation vary from 0.6 μg/m² s at 150 °C to 2 μg/m² s at 180 °C [70]. Using the reported value of the

evaporation rate, it can be estimated that 2.16 mg/cm² of phosphoric acid is lost every 10,000 h of cell operation at 150 °C. The acid loss from the MEA can cause increase in ohmic resistance of the membrane. It is reported that the

ionic conductivity of sol-gel m-PBI membranes depends on the acid doping level which is measured in terms of moles of phosphoric acid per polymer repeating unit (PA/PRU) [90]. When the acid content was greater than 6 PA/PRU, the dependence of ionic conductivity of membranes on the acid content was relatively small. The conductivity decreased from 0.17 to 0.15 S/cm when the acid content decreased from 8 PA/PRU to 6 PA/PRU. However, when the acid content was lowered to 3 PA/PRU, the conductivity decreased to 0.03 S/cm. The voltage loss caused by the change in membrane conductivity can be calculated by (16.3), where σ is the conductivity of the membrane, δ is the thickness of membrane and A is the current density of the cell.

$$\Delta V = \frac{1}{\sigma} \delta A \quad (16.3)$$

The voltage loss caused by increase in the ohmic resistance of the membrane is calculated by using the data from [90] which shows the proton conductivity dependence on acid content of the membrane. For the calculation, the membrane with the thickness of 50 μm is assumed to have 20 mg/cm^2 and 27 PA/PRU initially, and the acid loss rate of 3 mg/cm^2 every 10,000 h is assumed. Figure 16.4b shows the trend of voltage loss caused by the decrease in membrane conductivity over 60,000 h of operation. Figure 16.4b indicates that the voltage loss caused by acid loss is relatively small in the initial stage of cell operation, but when the acid content reaches the critical content where the conductivity of the membrane changes rapidly with the acid content, the cell voltage shows a sharp decrease. The total voltage loss shown in Fig. 16.4c confirms that the loss of SA determines the initial voltage loss and the acid loss effect remains insignificant until the acid content reaches the critical level. The similar voltage loss behavior is observed experimentally, and the gradual voltage loss during initial 14,000 h of cell operation was found to be caused by Pt agglomeration, and the rapid voltage loss which occurred after 14,000 h was proposed to be the result of lack of acid in the catalyst layer [48]. When there is sufficient phosphoric acid in the membrane to replenish the acid content in the

catalyst layer, the MEA operates with no visible effect of the acid loss. Once the acid in the membrane was not able to provide sufficient acid into the catalyst layer, the loss of the active area and increase of proton transport resistance in the catalyst layer caused additional decrease in the cell voltage [71]. If the acid loss of HT-PEMFC occurs only via evaporation, the acid loss rate is not significant, and the initial acid content of 20 mg/cm^2 is sufficient for 50,000 h of cell operation at 150 °C. However, if the initial acid content is not sufficient or the acid loss is to occur by other mechanisms such as leaching to the bipolar plates, the lack of acid in the membrane as well as catalyst layer can lead to drastic decrease in cell voltage and the eventual MEA failure.

16.3.2.2 Approaches to Improving MEA Durability

The lifetime of HT-PEMFC MEAs can be improved by using durable catalysts and suppressing the acid loss from MEAs. To reduce the rate of the Pt area loss during cell operation, the Pt catalyst particles need to be stabilized onto carbon supports. The attempts to improve the stability of Pt particles on support materials include enhancing Pt-support interaction by using metal oxide supports or Pt-metal oxide-carbon triple junction points [91, 92]. For HT-PEMFC MEAs, the choice of carbon support materials is especially important because of its highly oxidative operation conditions [93]. The oxidation of the support material leads to the detachment of Pt catalysts and the changes in the functional groups on its surfaces which lead to a more hydrophilic catalyst layer [94]. The loss of carbon support can also cause reduction in the pore volume. The decrease of pore volume, thinning of catalyst layer, and the increase of hydrophilicity in the catalyst layer can accelerate acid leaching and also cause flooding. Thus, protecting catalyst support materials from oxidation is important not only for mitigating the loss of the Pt surface area but also for maintaining gas permeability and retaining phosphoric acid in the electrode.

In the electrodes for PAFC, the Vulcan XC-72 carbon black is most widely used catalyst support material [95]. The oxidation of Vulcan carbon black in the presence of phosphoric acid at 191 °C showed that the disordered central part of carbon particles was oxidized while the outer crystalline part remained intact [96]. Among the attempts to improve the oxidation resistance of Vulcan carbon black, the most widely used method is the heat treatment which increases the level of graphitization on the carbon surface [97]. The heat treatment of Vulcan carbon black at the temperature of 2200 °C which reduced the surface area of Vulcan from 240 to 80 m²/g improved oxidation resistance more than twofold [98, 99]. Other highly graphitic carbon materials such as CNT [100] and graphene [101] have been used as support materials because of their high surface area and electrical conductivity. When selecting the carbon support material, the oxidation resistance is the critical property for carbon supports to enhance the durability of HT-PEMFC MEAs; however, the surface area, shape, and size of support material should also be considered to achieve the desired dispersion of Pt particles as well as the pore structure within the catalyst layer.

The suppression of acid loss can be a more challenging problem for improving the durability of HT-PEMFC MEA. The acid loss is caused by evaporation, compression pressure of stack, diffusion from MEA to flow field, and volume change caused by hydration of acid which can occur when exposed to highly humid environment. The retention of acid within the catalyst layer can be improved by adding materials that can either absorb acid [40] or form

solid proton conducting medium with phosphoric acid [102]. However, to maintain the uniform distribution of phosphoric acid in the catalyst layer during cell operation and shut-down periods, it would be beneficial to have a solid form of phosphoric acid in the membrane and catalyst layer. The poly(vinylphosphonic acid) (PVPA) is a polymeric acid which is reported to form hydrogen networks with neighboring phosphonic acid groups and provide proton pathways. The PVPA showed the proton conductivity of 1 mS/cm at 150 °C [103], and it binds to PBI via multipoint acid-base reactions and can be used both in the membrane and catalyst layer [104]. It was found that the hydrogen bonding network of PVPA was sufficient to carry proton through the catalyst layer and membrane via Grotthuss mechanism, and both activity and durability of the MEA were found to enhance [104]. Unlike the phosphoric acid-doped MEAs, the PVPA-doped MEAs did not show visible leaching out from the membrane and showed significant improvements of durability after the accelerated durability test [104]. To assure a more robust design of HT-PEMFC MEAs that can endure the operating conditions which include the exposure to the high humidity, high stack compression pressure, high temperature, and high current density, it may be necessary to replace the liquid form of acid with a solid form of proton conductors such as PVPA.

To reduce the cost and improve the durability of HT-PEMFC MEAs, the schematic of catalyst layer shown in Fig. 16.5 is proposed. To reduce the amount of Pt used in the catalyst layer, the catalyst agglomerate configuration in which the Pt particles are placed in the outer periphery of the

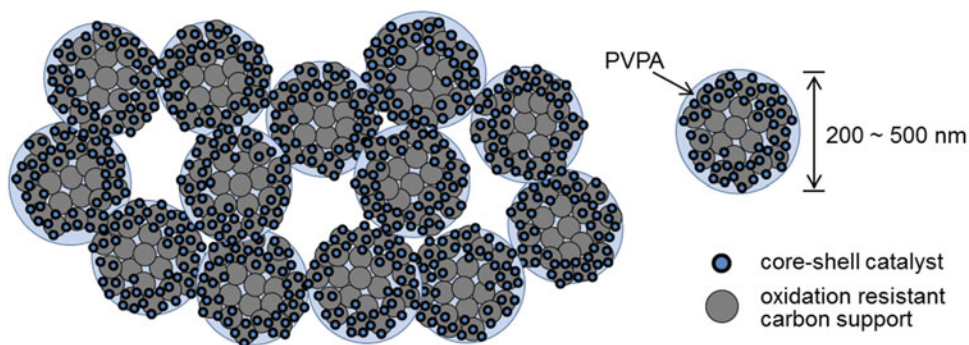


Fig. 16.5 Schematic representation of a durable low cost HT-PEMFC catalyst layer

agglomerate is proposed. By controlling the size of the agglomerate to 200–500 nm, sufficiently large secondary pores can be formed so that the diffusion of O₂ in the gas phase can occur without significant increase in the diffusion resistance of the dissolved O₂ in the agglomerates. The amount of Pt used in the catalyst can be further reduced by using the core–shell catalyst. To improve durability of HT-PEMFC MEAs, PVPA can be used to minimize the acid leaching that can occur during cell operation. To maintain the O₂ availability to the Pt particles, it is critical that the structure of the catalyst layer is maintained during the cell operation. Thus, the use of oxidation resistant carbon support materials is essential.

16.4 Conclusions

The recent investigations into the performance of HT-PEMFC MEAs showed that use of Pt alloys such as Pt–Co and Pt–Ni, enhancement of binder distribution in the catalyst layer and optimization of the phosphoric acid content in MEAs can increase the cell voltage. The voltage decay rates during cell operation depended mainly on the catalyst degradation and acid loss that caused reduction of the ECSA and increase in proton transport and ohmic resistance in MEAs. The cells that operated between 10,000 and 20,000 h demonstrated a voltage decay rate close to 5 μV/h. The analysis of the cell voltage decay revealed that the Pt agglomeration rate determined the initial voltage decay rate but its effects became smaller as the operation time increased. The initial acid content and the acid loss rate were found to determine the voltage decay rate in the latter stage of operation, assuming that the MEA operated without the occurrence of flooding. In order to reduce the cost and improve the durability of HT-PEMFC MEAs, a structure of catalyst layer was proposed.

References

- Kim J-D, Park Y-I, Kobayashi K et al (2001) Effect of CO gas and anode-metal loading on H₂ oxidation in proton exchange membrane fuel cell. *J Power Sources* 103:127–133
- Baschuk JJ, Li X (2001) Carbon monoxide poisoning of proton exchange membrane fuel cells. *Int J Energy Res* 25:695–713
- Das SK, Reis A, Berry KJ (2009) Experimental evaluation of CO poisoning on the performance of a high temperature proton exchange membrane fuel cell. *J Power Sources* 193:691–698
- Spendelow J, Donna H, Papageorgopoulos D (2010) Revised APU targets. U.S. Department of Energy. www.hydrogen.energy.gov
- Spendelow J, Marcinkoski J, Papageorgopoulos D (2012) Micro CHP fuel cell system targets. U.S. Department of Energy. www.hydrogen.energy.gov
- Truma (2012) Truma launches VeGA fuel cell for caravans and motorhomes. *Fuel Cell Today*. <http://www.fuelcelltoday.com/news-archive/2012/august/truma-launches-vega-fuel-cell-for-caravans-and-motorhomes>
- Elcore (2013) Elcore to install 135 micro-CHP fuel cells in Europe under enefield project. *Fuel Cell Today*. <http://www.fuelcelltoday.com/news-archive/2013/august/elcore-to-install-135-micro-chp-fuelcells-in-europe-under-ene-field-project>
- ClearEdge Power (2011) ClearEdge Power expands portfolio of continuous onsite power systems. *Fuel Cells Works*. <http://fuelcellworks.com/news/2011/11/29/clearedge-power-expands-portfolio-of-continuous-onsite-power-systems>
- Boyer M (2013) Panasonic's new Ene-Farm is the world's most efficient home fuel cell. *Inhabitat*. <http://inhabitat.com/panasonic-launches-more-efficient-ene-farm-home-fuel-cell/>
- Fuel Cells Works (2011) Tokyo gas and Panasonic to launch new improved "Ene-Farm" home fuel cell with world-highest generation efficiency at more affordable price. *Fuel Cell Works*. <http://fuelcellworks.com/news/2011/02/09/tokyo-gas-and-panasonic-to-launch-new-improved-%E2%80%9Cene-farm%E2%80%9D-home-fuel-cell-with-world-highest-generation-efficiency-at-more-affordable-price/>
- Staffell I, Green R (2012) The cost of domestic fuel cell micro-CHP systems. Imperial College, London
- James BD, Spisak AB, Colella WG (2012) Manufacturing cost analysis of stationary fuel cell systems. Strategic Analysis Inc., Arlington
- Milburn SM, Adamson K-A (2012) The fuel cell stack supply chain. Pike Research LLC, Boulder
- Gebert M, Höhle B, Stolten D (2004) Benchmark cost analysis of main PEFC-ionomer membrane solutions. *J Fuel Cell Sci Technol* 1:56–60
- Bruijn F (2011) PEMFC lifetime and durability. Nedstack, Arnhem
- Tokyo Gas Co., Ltd., Panasonic Corporation (2013) Launch of new 'Ene-Farm' home fuel cell product. Panasonic. <http://panasonic.co.jp/corp/news/official.data/data.dir/2013/01/en130117-5/en130117-5.html>
- Jannelli E, Minutillo M, Perna A (2013) Analyzing microcogeneration systems based on LT-PEMFC and HT-PEMFC by energy balances. *Appl Energy* 108:82–91

18. Liu Z, Wainright JS, Litt MH et al (2006) Study of the oxygen reduction reaction (ORR) at Pt interfaced with phosphoric acid doped polybenzimidazole at elevated temperature and low relative humidity. *Electrochim Acta* 51:3914–3923
19. Li Q, Hjuler HA, Bjerrum NJ (2001) Phosphoric acid doped polybenzimidazole membranes: physicochemical characterization and fuel cell applications. *J Appl Electrochem* 31:773–779
20. Wannek C, Konradi I, Mergel J et al (2009) Redistribution of phosphoric acid in membrane electrode assemblies for high-temperature polymer electrolyte fuel cells. *Int J Hydrogen Energy* 34:9479–9485
21. Takahashi I, Kocha SS (2010) Examination of the activity and durability of PEMFC catalysts in liquid electrolytes. *J Power Sources* 195:6312–6322
22. Neyerlin KC, Singh A, Chu D (2008) Kinetic characterization of a Pt-Ni/C catalyst with a phosphoric acid doped PBI membrane in a proton exchange membrane fuel cell. *J Power Sources* 176:112–117
23. Lobato J, Cañizares P, Rodrigo MA et al (2010) Study of the influence of the amount of PBI-H₃PO₄ in the catalytic layer of a high temperature PEMFC. *Int J Hydrogen Energy* 35:1347–1355
24. Schmidt TJ, Baurmeister J (2008) Properties of high-temperature PEFC Celtec[®]-P 1000 MEAs in start/stop operation mode. *J Power Sources* 176:428–434
25. Zhang X, Shi P (2006) Nafion effect on dual-bonded structure cathode of PEMFC. *Electrochem Commun* 8:1615–1620
26. Lee SJ, Mukerjee S, McBreen J et al (1998) Effects of Nafion impregnation on performances of PEMFC electrodes. *Electrochim Acta* 43:3693–3701
27. Parthasarathy A, Srinivasan S, Appleby AJ et al (1992) Temperature dependence of the electrode kinetics of oxygen reduction at the platinum/Nafion[®] interface—a microelectrode investigation. *J Electrochem Soc* 139:2530–2537
28. Jalan V, Taylor EJ (1983) Importance of interatomic spacing in catalytic reduction of oxygen in phosphoric acid. *J Electrochem Soc* 130:2299–2302
29. Watanabe M, Tsurumi K, Mizukami T et al (1994) Activity and stability of ordered and disordered Co-Pt alloys for phosphoric acid fuel cells. *J Electrochem Soc* 141:2659–2668
30. Ralph TR, Hogarth MP (2002) Catalysis for low temperature fuel cells. *Platin Met Rev* 46:3–14
31. Mukerjee S, Srinivasan S (1993) Enhanced electrocatalysis of oxygen reduction on platinum alloys in proton exchange membrane fuel cells. *J Electroanal Chem* 357:201–224
32. Stamenkovic V, Mun BS, Mayrhofer KJJ et al (2006) Changing the activity of electrocatalysts for oxygen reduction by tuning the surface electronic structure. *Angew Chem Int Ed* 45:2897–2901
33. Stamenkovic VR, Mun BS, Arenz M et al (2007) Trends in electrocatalysis on extended and nanoscale Pt-bimetallic alloy surfaces. *Nat Mater* 6:241–247
34. Mamlouk M, Scott K (2011) An investigation of Pt alloy oxygen reduction catalysts in phosphoric acid doped PBI fuel cells. *J Power Sources* 196:1084–1089
35. Uchida M, Fukuoka Y, Sugawara Y et al (1996) Effects of microstructure of carbon support in the catalyst layer on the performance of polymer-electrolyte fuel cells. *J Electrochem Soc* 143:2245–2252
36. Zhao X, Hayashi A, Noda Z et al (2013) Evaluation of change in nanostructure through the heat treatment of carbon materials and their durability for the start/stop operation of polymer electrolyte fuel cells. *Electrochim Acta* 97:33–41
37. Seland F, Berning T, Børresen B et al (2006) Improving the performance of high-temperature PEM fuel cells based on PBI electrolyte. *J Power Sources* 160:27–36
38. Wannek C, Lehnert W, Mergel J (2009) Membrane electrode assemblies for high-temperature polymer electrolyte fuel cells based on poly (2,5-benzimidazole) membranes with phosphoric acid impregnation via the catalyst layers. *J Power Sources* 192:258–266
39. Su H, Pasupathi S, Bladergroen B et al (2013) Optimization of gas diffusion electrode for polybenzimidazole-based high temperature proton exchange membrane fuel cell: evaluation of polymer binders in catalyst layer. *Int J Hydrogen Energy* 38:11370–11378
40. Park JO, Hong S-G, Kim T et al (2006) Role of binders in high temperature PEMFC electrode. *ECS Trans* 3:447–451
41. Kwon K, Kim TY, Yoo DY et al (2009) Maximization of high-temperature proton exchange membrane fuel cell performance with the optimum distribution of phosphoric acid. *J Power Sources* 188:463–467
42. Jung G-B, Tseng C-C, Yeh C-C et al (2012) Membrane electrode assemblies doped with H₃PO₄ for high temperature proton exchange membrane fuel cells. *Int J Hydrogen Energy* 37:13645–13651
43. Elmanovich IV, Kondratenko MS, Kolomytkin DO et al (2013) Active layer materials coated with Teflon AF nano-films deposited from solutions in supercritical CO₂ for fuel cell applications. *Int J Hydrogen Energy* 38:10592–10601
44. Su P-H, Lin H-L, Lin Y-P et al (2013) Influence of catalyst layer polybenzimidazole molecular weight on the polybenzimidazole-based proton exchange membrane fuel cell performance. *Int J Hydrogen Energy* 38:13742–13753
45. Park JO, Kwon K, Cho MD et al (2011) Role of binders in high temperature PEMFC electrode. *J Electrochem Soc* 158:B675–B681
46. Beyler CL, Hirschler MM (1995) Thermal decomposition of polymers. In: *SFPE handbook of fire protection engineering*. National Fire Protection Association, Quincy

47. Watanabe M, Tomikawa M, Motoo S (1985) Experimental analysis of the reaction layer structure in a gas diffusion electrode. *J Electroanal Chem Interfacial Electrochem* 195:81–93
48. Oono Y, Sounai A, Hori M (2009) Influence of the phosphoric acid-doping level in a polybenzimidazole membrane on the cell performance of high-temperature proton exchange membrane fuel cells. *J Power Sources* 189:943–949
49. Liu F, Mohajeri S, Di Y et al (2014) Influence of the interaction between phosphoric acid and catalyst layers on the properties of HT-PEFCs. *Fuel Cells* 14:750–757
50. Yu S, Xiao L, Benicewicz BC (2008) Durability studies of PBI-based high temperature PEMFCs. *Fuel Cells* 8:165–174
51. Wannek C, Kohnen B, Oetjen HF et al (2008) Durability of ABPBI-based MEAs for high temperature PEMFCs at different operating conditions. *Fuel Cells* 8:87–95
52. Staudt R, Intwala KF (2006) Development of polybenzimidazole-based high temperature membrane and electrode assemblies for stationary applications. DOE Hydrogen Program. FY 2006 annual progress report
53. Li Q, Jensen JO, Savinell RF et al (2009) High temperature proton exchange membranes based on polybenzimidazoles for fuel cells. *Prog Polym Sci* 34:449–477
54. Oono Y, Sounai A, Hori M (2012) Long-term cell degradation mechanism in high-temperature proton exchange membrane fuel cells. *J Power Sources* 210:366–373
55. Suzuki A, Oono Y, Williams MC et al (2012) Evaluation for sintering of electrocatalysts and its effect on voltage drops in high-temperature proton exchange membrane fuel cells (HT-PEMFC). *Int J Hydrogen Energy* 37:18272–18289
56. Aricò AS, Stassi A, Modica E et al (2008) Performance and degradation of high temperature polymer electrolyte fuel cell catalysts. *J Power Sources* 178:525–536
57. Bi W, Fuller TF (2008) Temperature effects on PEM fuel cells Pt/C catalyst degradation. *J Electrochem Soc* 155:B215–B221
58. Aindow TT, Haug AT, Jayne D (2011) Platinum catalyst degradation in phosphoric acid fuel cells for stationary applications. *J Power Sources* 196:4506–4514
59. Cai M, Ruthkosky MS, Merzougui B et al (2006) Investigation of thermal and electrochemical degradation of fuel cell catalysts. *J Power Sources* 160:977–986
60. Yoda T, Uchida H, Watanabe M (2007) Effects of operating potential and temperature on degradation of electrocatalyst layer for PEFCs. *Electrochim Acta* 52:5997–6005
61. Zhang S, Yuan X-Z, Hin JNC et al (2009) A review of platinum-based catalyst layer degradation in proton exchange membrane fuel cells. *J Power Sources* 194:588–600
62. Wilson MS, Garzon FH, Sickafus KE et al (1993) Surface area loss of supported platinum in polymer electrolyte fuel cells. *J Electrochem Soc* 140:2872–2877
63. Matsuoka K, Sakamoto S, Nakato K et al (2008) Degradation of polymer electrolyte fuel cells under the existence of anion species. *J Power Sources* 179:560–565
64. Ferreira PJ, la O' GJ, Shao-Horn Y et al (2005) Instability of Pt/C electrocatalysts in proton exchange membrane fuel cells: a mechanistic investigation. *J Electrochem Soc* 152:A2256–A2271
65. Shao-Horn Y, Sheng WC, Chen S et al (2007) Instability of supported platinum nanoparticles in low-temperature fuel cells. *Top Catal* 46:285–305
66. Honji A, Mori T, Tamura K et al (1988) Agglomeration of platinum particles supported on carbon in phosphoric acid. *J Electrochem Soc* 135:355–359
67. Maass S, Finsterwalder F, Frank G et al (2008) Carbon support oxidation in PEM fuel cell cathodes. *J Power Sources* 176:444–451
68. Shao Y, Yin G, Wang Z et al (2007) Proton exchange membrane fuel cell from low temperature to high temperature: material challenges. *J Power Sources* 167:235–242
69. Stevens DA, Dahn JR (2005) Thermal degradation of the support in carbon-supported platinum electrocatalysts for PEM fuel cells. *Carbon* 43:179–188
70. Seel DC, Benicewicz BC, Xiao L et al (2010) High-temperature polybenzimidazole-based membranes. *Handbook of fuel cells*
71. Kim J-R, Yi JS, Song T-W (2012) Investigation of degradation mechanisms of a high-temperature polymer-electrolyte-membrane fuel cell stack by electrochemical impedance spectroscopy. *J Power Sources* 220:54–64
72. Galbiati S, Baricci A, Casalegno A et al (2013) Degradation in phosphoric acid doped polymer fuel cells: a 6000 h parametric investigation. *Int J Hydrogen Energy* 38:6469–6480
73. Hartnig C, Schmidt TJ (2011) On a new degradation mode for high-temperature polymer electrolyte fuel cells: how bipolar plate degradation affects cell performance. *Electrochim Acta* 56:4237–4242
74. Wang U (2011) ClearEdge designs fuel cells to replace power from the grid. *Forbes*. <http://www.forbes.com/sites/uciliawang/2011/11/29/clearedge-designs-fuel-cells-to-replace-power-from-the-grid/>
75. Gasteiger HA, Kocha SS, Sompalli B et al (2005) Activity benchmarks and requirements for Pt, Pt-alloy, and non-Pt oxygen reduction catalysts for PEMFCs. *Appl Catal B: Environ* 56:9–35
76. Bandlamudi G (2011) Systematic characterization of HT PEMFCs containing PBI/H₃PO₄ systems. Logos Verlag Berlin GmbH, Berlin

77. Glass JT, Cahen GL Jr, Stoner GE (1989) The effect of phosphoric acid concentration on electrocatalysis. *J Electrochem Soc* 136:656–660
78. Zhang J, Lima FHB, Shao MH et al (2005) Platinum monolayer on nonnoble metal-noble metal core-shell nanoparticle electrocatalysts for O₂ reduction. *J Phys Chem B* 109:22701–22704
79. Zhang Y, Ma C, Zhu Y et al (2013) Hollow core supported Pt monolayer catalysts for oxygen reduction. *Catal Today* 202:50–54
80. Koh J-H, Abbaraju R, Parthasarathy P et al (2014) Design and synthesis of degradation-resistant core-shell catalysts for proton exchange membrane fuel cells. *J Power Sources* 261:271–277
81. Lin R, Cao C, Zhao T et al (2013) Synthesis and application of core-shell Co@Pt/C electrocatalysts for proton exchange membrane fuel cells. *J Power Sources* 223:190–198
82. Cetinbas FC, Advani SG, Prasad AK (2013) A modified agglomerate model with discrete catalyst particles for the PEM fuel cell catalyst layer. *J Electrochem Soc* 160:F750–F756
83. Siegel NP, Ellis MW, Nelson DJ et al (2003) Single domain PEMFC model based on agglomerate catalyst geometry. *J Power Sources* 115:81–89
84. Choudhury SR, Deshmukh MB, Rengaswamy R (2002) A two-dimensional steady-state model for phosphoric acid fuel cells (PAFC). *J Power Sources* 112:137–152
85. Kamarajugadda S, Mazumder S (2008) Numerical investigation of the effect of cathode catalyst layer structure and composition on polymer electrolyte membrane fuel cell performance. *J Power Sources* 183:629–642
86. Khajeh-Hosseini-Dalasm N, Ahadian S, Fushinobu K et al (2011) Prediction and analysis of the cathode catalyst layer performance of proton exchange membrane fuel cells using artificial neural network and statistical methods. *J Power Sources* 196:3750–3756
87. Fukumura T (2008) Current status of development of PAFC system in Fuji Electric group. 2008 FC Seminar
88. Bett JA, Kinoshita K, Stonehart P (1974) Crystallite growth of platinum dispersed on graphitized carbon black. *J Catal* 35:307–316
89. Ruckenstein E, Pulvermacher B (1973) Growth kinetics and the size distributions of supported metal crystallites. *J Catal* 29:224–245
90. Perry KA, More KL, Payzant EA et al (2014) A comparative study of phosphoric acid-doped m-PBI membranes. *J Polym Sci, Part B: Polym Phys* 52:26–35
91. Kwak JH, Hu J, Mei D et al (2009) Coordinatively unsaturated Al³⁺ centers as binding sites for active catalyst phases of platinum on γ -Al₂O₃. *Science* 325:1670–1673
92. Kou R, Shao Y, Mei D et al (2011) Stabilization of electrocatalytic metal nanoparticles at metal-metal oxide-graphene triple junction points. *J Am Chem Soc* 133:2541–2547
93. Passalacqua E, Antonucci PL, Vivaldi M et al (1992) The influence of Pt on the electrooxidation behaviour of carbon in phosphoric acid. *Electrochim Acta* 37:2725–2730
94. Kangasniemi KH, Condit DA, Jarvi TD (2004) Characterization of Vulcan electrochemically oxidized under simulated PEM fuel cell conditions. *J Electrochem Soc* 151:E125–E132
95. Choudhury SR (2007) Phosphoric acid fuel cell technology. In: Basu S (ed) *Recent trends in fuel cell science and technology*. Springer, New York
96. Gruver GA (1978) The corrosion of carbon black in phosphoric acid. *J Electrochem Soc* 125:1719–1720
97. Bezerra CWB, Zhang L, Liu H et al (2007) A review of heat-treatment effects on activity and stability of PEM fuel cell catalysts for oxygen reduction reaction. *J Power Sources* 173:891–908
98. Kocha SS (2012) Electrochemical degradation: electrocatalyst and support durability. In: Kumbur EC, Veziroglu TN, Mench MM (eds) *Polymer electrolyte fuel cell degradation*. Academic, New York
99. Stonehart P (1984) Carbon substrates for phosphoric acid fuel cell cathodes. *Carbon* 22:423–431
100. Liao S, Holmes K-A, Tsapralis H et al (2006) High performance PtRuIr catalysts supported on carbon nanotubes for the anodic oxidation of methanol. *J Am Chem Soc* 128:3504–3505
101. Choi SM, Seo MH, Kim HJ et al (2011) Synthesis of surface-functionalized graphene nanosheets with high Pt-loadings and their applications to methanol electrooxidation. *Carbon* 49:904–909
102. Oh H-S, Cho Y, Lee WH et al (2013) Modification of electrodes using Al₂O₃ to reduce phosphoric acid loss and increase the performance of high-temperature proton exchange membrane fuel cells. *J Mater Chem A* 1:2578–2581
103. Lee YJ, Bingöl B, Murakhtina T et al (2007) High-resolution solid-state NMR studies of poly(vinyl phosphonic acid) proton-conducting polymer: molecular structure and proton dynamics. *J Phys Chem B* 111:9711–9721
104. Berber MR, Fujigaya T, Sasaki K et al (2013) Remarkably durable high temperature polymer electrolyte fuel cell based on poly(vinylphosphonic acid)-doped polybenzimidazole. *Sci Rep* 3:1764

F. Javier Pinar, Maren Rastedt, Nadine Pilinski,
and Peter Wagner

17.1 General Introduction to Characterization Techniques

“Characterization” of fuel cells covers an extremely wide range of measuring systems and applied techniques and methods. Therefore, we need to specify our understanding of characterization in the sense of this chapter.

On one hand, the term characterization is related to pure and basis material questions by investigating physical and chemical parameters like viscosity of inks [1] needed to coat catalysts on membranes or gas diffusion layers (GDLs). Or it can be related to electrochemical data of fuel cells (FC) components like the determination of the ion conductivity of membranes [2–5]. It is obvious to the reader that a really large variety of different characterization methods exist in order to determine several physical, chemical, and electrochemical parameters of fuel cell components.

This is only one side of the medal. The other side is the wide field of characterization of FCs in operation, either under laboratory conditions or even in real-life applications [6–11]. Research here is dominated by the question: What are the efficiency and the durability of the fuel cell under

defined operational conditions? To achieve these data, several standardized electrochemical characterization techniques are utilized. By taking into account the results from such measurements, fuel cell groups worldwide are involved in the identification of the various underlying degradation processes that shorten the lifetime of fuel cells [6–10, 12–17]. Only by thorough investigation and evaluation of data measures can be taken by researchers and industry to improve the efficiency and long-term durability of fuel cell components and systems to achieve the goals given by funding agencies [18, 19].

This book chapter will therefore only focus on details from the electrochemical characterization of single fuel cells in test benches, exemplarily on high temperature polymer electrolyte membrane electrode assemblies (HT-PEM MEAs). In addition, we will provide a deeper look into the effect of mechanical compression on MEAs and its influence on performance [17, 20, 21]. Here, new characterization techniques will be utilized like imaging technology like micro-computed tomography (μ -CT) in hyphenation with electrochemical methods. The combination of completely different characterization methods provides a much deeper insight into degradation effects by allowing the visualization of mechanical defects within MEAs [21–23].

We will neglect all the intensive and of course also absolutely required research on short and full stacks or systems which is covered in Chap. 21.

F.J. Pinar • M. Rastedt • N. Pilinski • P. Wagner (✉)
NEXT ENERGY-EWE Research Centre for Energy
Technology at the University of Oldenburg, Carl-von-
Ossietzky-Str. 15, Oldenburg 26129, Germany
e-mail: peter.wagner@next-energy.de

Another big issue and main driving force are the difficulty to compare data obtained from several working groups around the world. The wide variety of test benches, instruments, methods, and especially test conditions require in our opinion some kind of standardization or at least agreement on test protocols in order to allow any comparison of data between laboratories.

Within the two European projects, DEMMEA (Grant Agreement Number 245156, Duration: 01.01.2010–31.12.2012) and CISTEM (Grant Agreement Number 325262, Duration: 01.06.2013–31.05.2016) the participants have agreed on standardized experimental conditions for several tests like fuel cell investigation under constant load conditions or accelerated stress tests (AST) with load cycling between open circuit voltage (OCV) and a load of 0.3 A/cm^2 .

17.2 Standard Electrochemical Techniques for HT-PEM Fuel Cell Characterization

This chapter section summarizes the most widely used electrochemical techniques for HT-PEM MEA characterization. As it has been already mentioned in Sect. 17.1, the focus of the chapter is not a description on fundamentals of each one of the electrochemical techniques used. Besides, several references can be found in literature describing in detail the fundamentals of the electrochemical techniques [24–26]. Although a description of each one of the techniques is given, the main focus of this section is to show what kind of detailed information the reader can subtract from each electrochemical technique for a correct diagnosis of the HT-PEMFC behavior. Thus, the combination of the electrochemical characterization techniques can help to identify the different mechanisms and processes that take place in the fuel cell and lead to its degradation.

Owing to the difficulty of comparing data from different working groups and the need to follow standardized test protocols, this section also shows the test procedures and methodology routines for each of the electrochemical techniques presented. The routines have been

adapted for operating single HT-PEMFCs, and they have been already verified in two European Projects with the agreement of all the participants.

17.2.1 Polarization Curve

The polarization curve, also known as I-V curve, is one of the most important features of a fuel cell because it provides information about the performance. The polarization curve shows the relationship of fuel cell voltage and the applied current density. Therefore, if the fuel cell is fed with reactant gases and the electrical circuit is closed with a resistor (fuel cell connected to a load), the fuel cell voltage is reduced. Thus, the voltage reduction is a function of the generated current density. The voltage reduction or potential losses are caused by different factors as electrochemical reaction kinetics, electrical and ionic resistances or reactants transport limitations to the catalytic active sites among others. In this way, the polarization curve depends on several factors such as electrolyte membrane, GDL, micro-porous layer (MPL), catalyst layer (CL), bipolar plates (BPPs) flow field design, operating temperature, pressure, and reactant flow rates. Figure 17.1 shows a typical polarization curve from an HT-PEMFC based on phosphoric acid-doped polybenzimidazole (PBI) electrolyte polymer.

In Fig. 17.1, three different regions are clearly seen as the current density increases. When no current density is drawn, the OCV is below 1 V but the theoretical voltage of a PEMFC at standard conditions is 1.23 V [27]. From Nernst equation, the theoretical potential is a function of pressure and temperature conditions of the fuel cell [28]. Thus, increase of the operation temperature of the fuel cell from 25 to 160 °C (typical operation temperature in HT-PEMFC [17, 29]) reduces the theoretical voltage of the fuel cell down to ~1.11 V. Nevertheless, a difference between the theoretical voltage ($T = 160 \text{ }^\circ\text{C}$; 1 atm) and the actual fuel cell voltage (0.95 V) is observed. The irreversible voltage loss is due to parasitic reactions. These reactions are caused by hydrogen crossover and electronic conduction through the

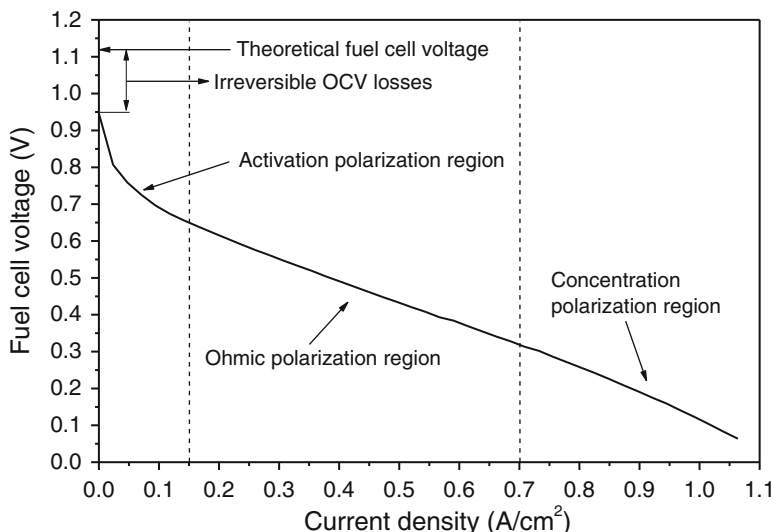


Fig. 17.1 Polarization curve for a fuel cell utilizing synthetic reformat/air ($\lambda_{\text{Ref}}/\lambda_{\text{Air}} = 1.5/2$) after a 1000 h ageing test at constant load. MEA type: Dapozol[®]-G55.

Synthetic reformat composition: 78 % H₂, 22 % CO₂. $T = 160$ °C, $p = 1$ atm, fivefold serpentine flow fields, contact pressure = 0.75 MPa

polymer membrane, oxide formation or platinum corrosion on the cathode side, reduction of the oxygen partial pressure as the fuel cell is operating with air, and variation of the water vapor pressure. Therefore, the reaction processes result in a mixed potential on the cathode side [30].

The activation polarization region is observed at low current densities. In this region, the voltage losses are associated with the activation energy barrier that must be overcome in the cathode and anode electrodes. The current density dependency on parameters related to overcoming the activation energy barrier is expressed in the Butler–Volmer equation [31]. Thus, activation losses are function of electrode properties, temperature, and pressure conditions. The performance of an HT-PEMFC is represented by (17.1).

$$E = E_0 - (a + b \cdot \ln j) - R \cdot j + b \cdot \ln \left(1 - \frac{j}{j_{\text{lim}}} \right) \quad (17.1)$$

The parameters of (17.1) stand for E , the fuel cell voltage at a current density (j). E_0 is the reversible potential or OCV, and it also includes the contribution of the mixed potential of the

oxygen electrode and the hydrogen crossover rate. a is a parameter that is function of the exchange current density, and b is a parameter commonly named Tafel slope which is related to the kinetic overvoltage. R is the ohmic resistance, and j_{lim} is the limiting current density, related to the diffusion overvoltage. At low current densities, the reactants are abundant and ohmic losses are negligible. Thus, (17.1) can be simplified into (17.2) that describes the polarization curve in this region. The Tafel slope (b) is a parameter inversely related to the cathode charge transfer coefficient. In such a way, the Tafel slope is a function of the cathode kinetics.

$$E = E'_0 - b \cdot \ln j \quad \text{where} \quad E'_0 = E_0 - a \quad (17.2)$$

For an intermediate current density range, fuel cell voltage losses are according to the Ohm's law. Thus, a linear relation can be observed between the fuel cell voltage and the current density in this region. Therefore, the voltage losses are caused by the limited polymer membrane proton conductivity and by the electronic resistance generated in electrodes, wires, and connections to the fuel cell [32, 33]. However, the electronic resistance is much smaller than the resistance to proton conduction through the

electrolyte membrane and hence, improving the proton conductivity of the electrolyte membrane may reduce the ohmic losses. Equation (17.1) can be simplified into (17.3) as ohmic losses dominate the intermediate current region.

$$E = E_0 - R \cdot j \quad (17.3)$$

Usually, the first step for analyzing the polarization curve is its correction for ohmic losses (IR-correction). As a consequence, the IR-corrections remove the ohmic losses from the cell, which can be used to better isolate kinetic losses [34]. Thus, the catalyst behavior in the fuel cell can be studied using IR-corrected polarization curves. Electrochemical impedance spectroscopy (EIS) or current interrupt method can be used to determine experimentally the ohmic drop of the fuel cell. Thus, the polarization curve IR-correction is typically done by using (17.3) [34]. From EIS, R is assumed to be R_{Ohm} which is the resistance from electronic and proton conduction (see EIS technique section). The EIS must therefore be performed within a current density range, where Ohm's law is valid. On one hand, the polarization curve can be IR-corrected using one value of R but the ohmic drop is also function of current density and its reduction from low to high current density generation due to the

production of water that enhances the proton conductivity of the electrolyte. On the other hand, the polarization curve can be IR-corrected using a correlation of ohmic drop with the current density so the IR-corrections are improved. This correlation can be acquired performing the EIS measurements at different intermediate current densities. Figure 17.2 shows the relation between R_{Ohm} and current density and the IR-corrected polarization curve from Fig. 17.1.

In Fig. 17.2a, it can be seen that the R_{Ohm} relation with current density is not linear. At 0.03 A/cm^2 , the R_{Ohm} is influenced by activation polarization as it has already shown previously and Ohm's law is not obeyed. The IR-corrected polarization curve in Fig. 17.2b has been done using Fig. 17.2a data from 0.2 to 0.4 A/cm^2 (open circles).

For the high current density range, mass transport of reactants and products becomes a limiting factor. So the oxidant and fuel concentration is significantly reduced at high current densities, and they cause fuel cell voltage losses. The mass transport mechanisms within the fuel cell include convection, diffusion, and/or convection. Simplification of (17.1) for simple concentration polarization is shown in (17.4). Thus, j_{lim} can be also defined as current density, where the

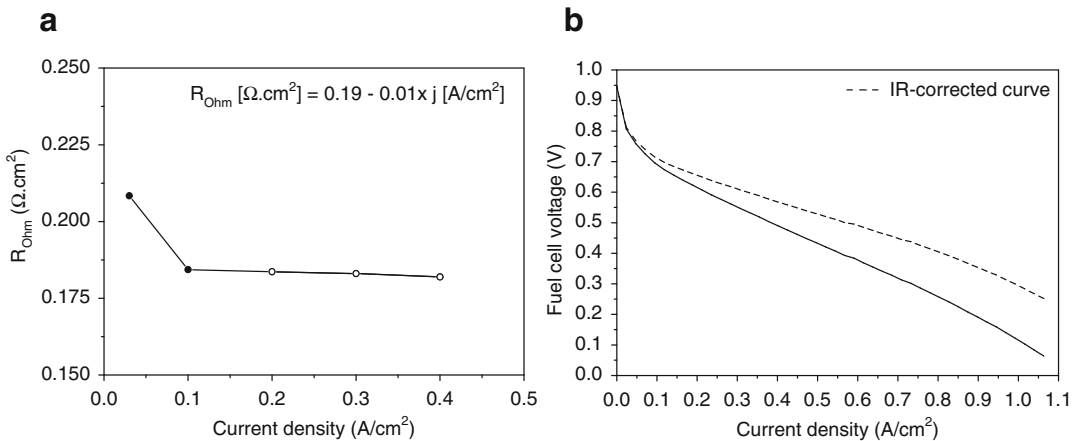


Fig. 17.2 (a) Ohmic resistance as function of current density from EIS and equation of linear relation between ohmic resistance and current density from 0.2 to 0.4 A/cm^2 (open circles). (b) Polarization curve and IR-corrected polarization curve for the fuel cell under

synthetic reformat/air ($\lambda_{\text{Ref}}/\lambda_{\text{Air}} = 1.5/2$) after 1000 h ageing test. MEA type: Dapozol[®]-G55. Synthetic reformat composition: 78 % H_2 , 22 % CO_2 . $T = 160 \text{ }^\circ\text{C}$, $p = 1 \text{ atm}$, fivefold serpentine flow fields, contact pressure = 0.75 MPa

concentration of reactants in the catalyst active sites is zero [35]. Moreover, concentration polarization is influenced by structure of the electrodes, fuel cell temperature, pressure, and flow rates of the reactants.

$$E = E_0 + b \cdot \ln\left(1 - \frac{j}{j_{\text{lim}}}\right) \quad (17.4)$$

Nevertheless, quantification of losses on the basis of a polarization curve is difficult because contributions from the different underlying processes overlap. Consequently, other electrochemical methods are needed to be carried out for an exhaustive fuel cell behavior diagnostic.

17.2.2 Electrochemical Impedance Spectroscopy

EIS has been established as one of the most popular analytical tools in materials research. The technique is being widely used to a large number of important areas of materials research and analysis. Thus, EIS is applicable to, e.g., studies of electrochemical kinetics and determination of electronic or ionic conduction

mechanisms. Impedance is based on an electrical measurement that can be automated and remotely controlled [36–38]. Moreover, EIS is a noninvasive technique that can be used for online analysis and diagnosis of the fuel cell [39]. Therefore, monitoring the rate of degradation is possible without interfering in the fuel cell operation and predictive maintenance of the fuel cell components can be accomplished. In Chap. 21, the EIS technique is widely discussed for its application to HT-PEMFC, although a brief description of interpretation and diagnosis of the results must be given in this section.

A common representation of EIS spectra are Nyquist plots [25, 36, 38]. The plots represent the imaginary and real parts of the impedance as function of voltage or current AC signal frequency. Figure 17.3 shows typical Nyquist plots recorded for two kinds of HT-PEMFC at 0.2 A/cm².

In Fig. 17.3, three regions are distinguished in the spectra for high, medium, and low frequency ranges. At the high frequency range, both Nyquist plots show an interception of the impedance spectra with the real axis. The high frequency interception represents the sum of the resistance to conduction of protons and electrons

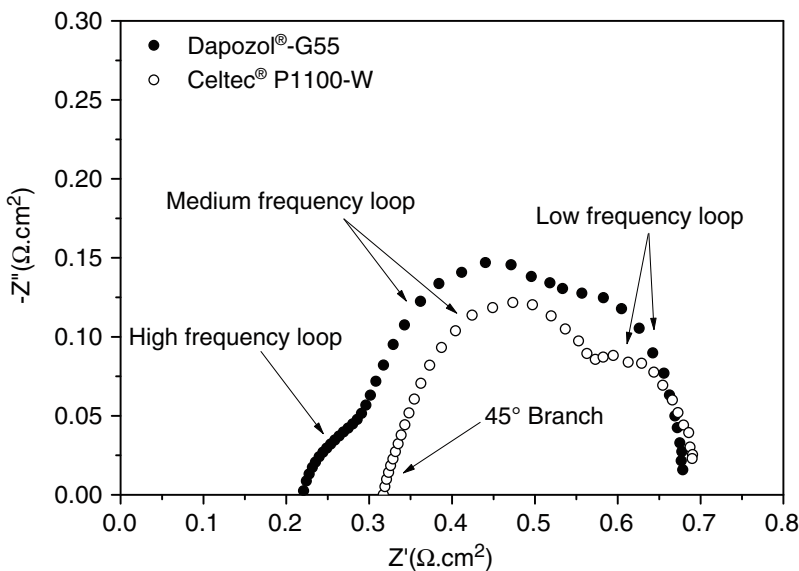


Fig. 17.3 Nyquist plot for HT-PEMFC operating with MEAs from different suppliers at 0.2 A/cm². H₂/Air ($\lambda_{\text{H}_2}/\lambda_{\text{Air}} = 1.2/2$). $T = 160$ °C, $p = 1$ atm, fivefold serpentine flow fields, contact pressure = 0.75 MPa

[25]. Moreover, this interception is used to count the resistance between wires and contact interfaces as BBP/GDL and GDL/CL [17, 40, 41]. Thus, contact resistances are usually neglected when fixed compression forces are applied. After the real axis interception, it can be seen a high frequency loop for the Dapozol[®]-G55 MEA or a 45° branch for the Celtec[®] P1100W MEA. This high frequency loop is recognized as potential independent [42], and its meaning is still an open question due to lack of confidence. Usually, in literature the high frequency loop is attributed to the anode charge transfer resistance which is related to hydrogen oxidation reaction (HOR) activation losses [41, 43]. The 45° branch observed for the Celtec[®] P1100W MEA is an incomplete semicircle which resembles Warburg impedance. Generally, this 45° branch is attributed to limited proton transport in the catalyst layer [21, 44, 45]. Thus, the different observations in the high frequency domain between the two kinds of HT-PEM MEAs must be their anode electrode composition as sort of GDL, catalyst loading, or amount of electrolyte in the catalyst layer.

At the medium frequency range, the loop is associated to the cathode charge transfer related to oxygen reduction reaction (ORR) activation losses [46]. This medium frequency loop is

much bigger than high frequency loop as ORR is the limiting reaction in the fuel cell when hydrogen is used as fuel. The low frequency range loop is characteristic of gas diffusion limitations in the GDL [47]. However, Andreassen et al. [46] describes this loop as oscillations in reactant concentrations along the gas channels. The low frequency loop can be vanished by using pure H₂ and O₂ to the fuel cell instead of diluted H₂ from reformat containing CO₂, CO, and/or H₂O in the anode side or air in the cathode side. Moreover, a reduction in the low frequency loop due to oxidant partial pressure increase also implies reduction of the medium frequency loop as sufficient reactant gases are available for the ORR [48]. Boillot et al. [48] studied the effect of gas dilution on LT-PEMFCs performance. They concluded that by diluting H₂ stream the high frequency loop must increase but the low frequency loop appeared to result just from the diffusion of O₂.

EIS spectra from two Dapozol[®]-G55 MEAs are shown in Fig. 17.4. The measurements have been performed with pure H₂ and diluted H₂ from a synthetic reformat. Unfortunately, the H₂ stoichiometry is different between both MEAs (MEA 1: $\lambda_{H_2} = 1.2$; MEA 2: $\lambda_{Ref} = 1.5$) so conclusions regarding the increase of the high frequency loop for the fuel cell operated with the

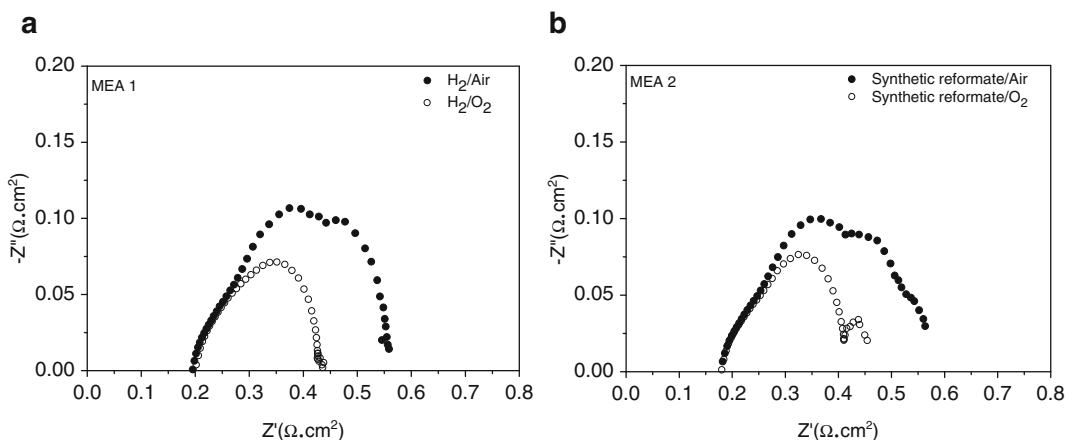


Fig. 17.4 EIS spectra at 0.3 A/cm² for (a) HT-PEMFC under H₂/air ($\lambda_{H_2}/\lambda_{Air} = 1.2/2$) and H₂/O₂ ($\lambda_{H_2}/\lambda_{O_2} = 1.2/9.5$). (b) HT-PEMFC under Synthetic reformat/air ($\lambda_{Ref}/\lambda_{Air} = 1.5/2$) and Synthetic reformat/O₂

($\lambda_{Ref}/\lambda_{O_2} = 1.5/9.5$), synthetic reformat: 78.1 % H₂ and 21.9 % CO₂. MEA type: Dapozol[®]-G55. $T = 160$ °C, $p = 1$ atm, fivefold serpentine flow fields, contact pressure = 0.75 MPa

synthetic reformat cannot be drawn. Nevertheless, this fuel cell has developed a new loop in the low frequency domain when it has been operated under synthetic reformat and air conditions [49] (Fig. 17.4b). Thus, one of the two loops at the low frequency domain is vanished when the fuel cell is operated under synthetic reformat and O_2 . Therefore, the remaining loop at the low frequency domain must be due to mass transfer limitations on the anode that have been created by the H_2 dilution with CO_2 . In case of the fuel cell operated with the synthetic reformat and air, further investigations must be carried out to understand which one of the two low frequency loops belong to fuel or oxidant diffusion limitations. A variation of the anode stoichiometry could provide hints to identify the H_2 limitation loop.

As it can be seen, EIS may be used to analyze the voltage losses observed in polarization curves as EIS has the ability to distinguish between influences from different processes that usually overlap. Therefore, the use of both methods can improve understanding of the different processes that take place within the fuel cell. Figure 17.5 shows EIS spectra recorded at different current densities and a polarization curve highlighting the points, where the EIS spectra have been recorded. Thus, EIS spectra are usually recorded

in the range between low and intermediate current densities.

The relationship between EIS spectra and polarization curves is the polarization resistance of the cell (R_{Pol}) measured at a certain fuel cell voltage [43]. On the one hand, R_{Pol} corresponds to the slope of the polarization curve at that fuel cell voltage. On the other hand, the AC impedance at frequencies near 0 Hz where only ohmic parts attract attention is R_{Pol} as well. Thus, R_{Pol} can be obtained by extrapolation from the EIS spectra at the lowest recorded frequency or even summing up the individual resistance contributions, which can be obtained by fitting the EIS spectra with an equivalent circuit [42]. The use of equivalent circuits for fitting EIS spectra is discussed in Chap. 20. From Fig. 17.5a, R_{Pol} becomes smaller when the current density increases from low to intermediate current densities. Moreover, the higher the current density, the smaller the R_{Pol} decrease is when approaching the intermediate current density range. In Fig. 17.5b, the slope of the polarization curve is reduced from low to intermediate current densities. Thus, the slope of the polarization curve is $0.73 \Omega \text{ cm}^2$ at 0.1 A/cm^2 and $0.52 \Omega \text{ cm}^2$ at 0.3 A/cm^2 . Similar values can be extracted from the EIS spectra in Fig. 17.5a for those current densities (0.80 and $0.49 \Omega \text{ cm}^2$ for

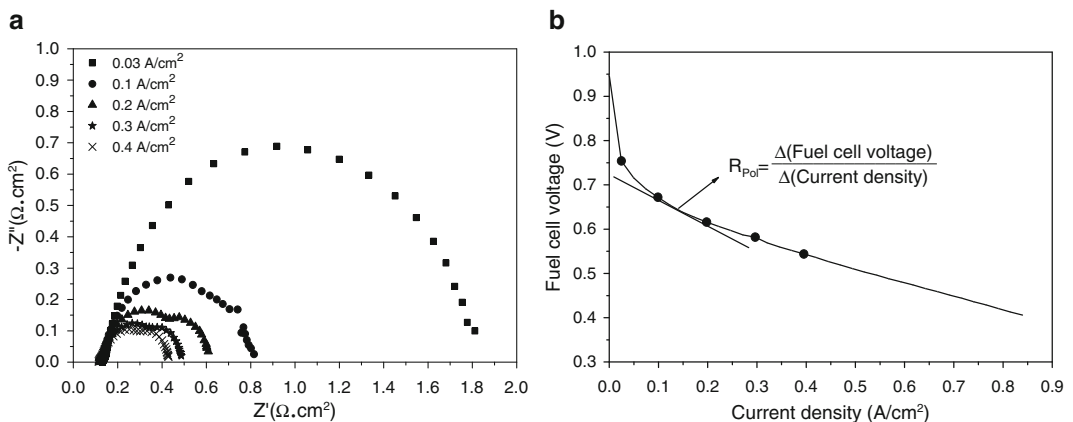


Fig. 17.5 (a) Nyquist plot at different current densities. (b) Polarization curve, where EIS recorded from (a) have been highlighted (black dots) and correlation between fuel cell impedance and polarization curve.

MEA type: Celtec[®] P1100W, H_2 /Air ($\lambda_{H_2}/\lambda_{Air} = 1.2/2$). $T = 160 \text{ }^\circ\text{C}$, $p = 1 \text{ atm}$, grid flow fields, contact pressure = 0.5 MPa

0.1 and 0.3 A/cm², respectively). At low current densities, a huge semicircle can be observed in Fig. 17.5a that corresponds to charge transfer limitations as the measurement has been performed in the activation region, so reaction kinetics dominate the fuel cell behavior. By increasing the current density, the main semicircle is reduced and it seems to be more or less constant at the highest current density. Therefore, charge transfer is enhanced. Moreover, a new semicircle appears at 0.2 A/cm². So, mass transport limitations are detected in the Nyquist plot at intermediate current densities but these mass transfer limitations cannot be detected in the polarization curve from Fig. 17.5b.

17.2.3 Linear Sweep Voltammetry

Linear sweep voltammetry (LSV) formally named as linear potential sweep chronoamperometry is a method, where the potential is linearly varied with time. In the experiment, it is customary to record the current as a function of potential, which is equivalent to recording current vs. time [24]. In PEMFCs, this technique is used to determine the hydrogen crossover through the membrane from anode to cathode and also the internal short-circuit between the electrodes. The importance to determine these two parameters lies in terms of efficiency, performance, and durability of the fuel cell. Thus, the hydrogen that permeates through the membrane is consumed with oxygen at cathode with the generation of heat and water but without generating the useful work, leading to fuel inefficiency [50]. In such a way, direct conduction of electrons through the membrane between the electrodes also diminishes fuel cell efficiency as the electrical work is not captured in the external electrical circuit [51]. Moreover, the hydrogen crossover has also a relationship to OCV in the fuel cell. As mentioned before in the section where polarization curves were described, the OCV is the result of different processes, including hydrogen crossover, that takes place from anode to the cathode side. Thus, a decrease in OCV could be a sign of hydrogen crossover increase.

Sweeping the potential of the fuel cell cathode by means of a linear scan to potentials at which the hydrogen gas present at the cathode is oxidized under mass transfer limiting conditions, both hydrogen crossover and internal short-circuit can be estimated. The LSV must be carried out using hydrogen on the anode and inert gas, i.e., nitrogen, on the cathode. However, the electrochemical technique requires the use of a potentiostat as power supply. Thus, the cathode electrode can be scanned with a small sweep potential rate from the rest potential to anodic potentials less than 1 V. Usually, sweep rates between 1 and 4 mV/s are found in literature [17, 22, 29, 51–53]. Moreover, polarization to anodic potentials lower than 1 V must be done to avoid irreversible electrode damage owing to carbon corrosion and catalyst oxidation. Therefore, potential ranges from the rest potential to 0.6 V are also found in literature [17, 22, 29, 50, 52, 53]. Figure 17.6a shows a typical LSV carried out for an HT-PEMFC at 160 °C.

From Fig. 17.6a, the current density rapidly attains a linear increasing value with increasing electrode potential from the rest potential. The current density dependency to the increase of potential indicates that the fuel cell has an internal resistance due to shorting. Thus, the internal short-circuit resistance can be estimated from the inverse of the potential vs. current density slope within the range, where linear relation between current density and potential is observed (88 Ω cm²). At potentials around 0.45 V is observed a change in the slope potential vs. current density due to the effect of double-layer capacitance [24]. On the one hand, unmediated estimation of the hydrogen crossover can be done when a limiting current density is reached but so far the fuel cell develops internal short-circuit, LSV must be internal short-circuit corrected for hydrogen crossover estimation as Fig. 17.6b shows. Thus, the current density is now limited for the LSV with the short-circuit correction between the range, where current density is linearly dependent with potential. Therefore, the fuel cell exhibits a limiting current density of 2.35 mA/cm² at 0.3 V. Applying Faraday's law (17.5) [51], the hydrogen crossover flux ($\dot{\eta}_{\text{H}_2 \text{ Crossover}}$) through the membrane can be

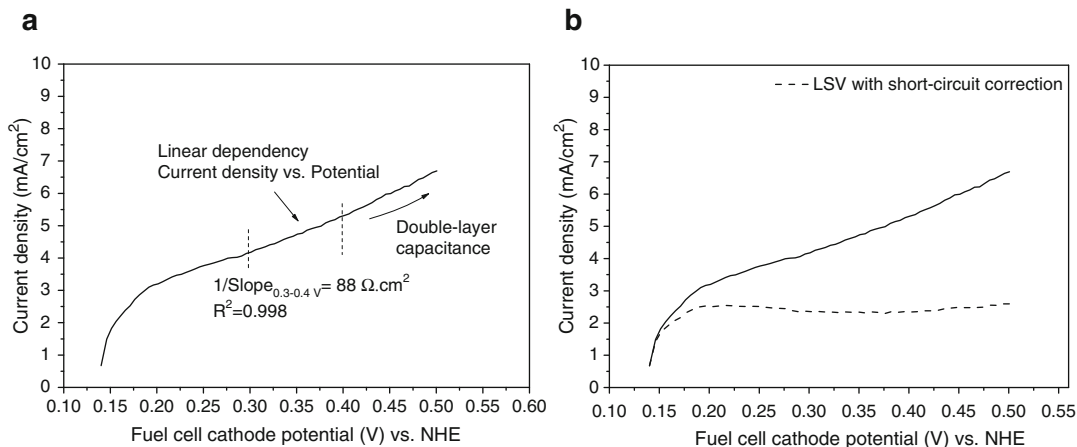


Fig. 17.6 (a) Linear sweep voltammogram and (b) linear sweep voltammogram with internal short-circuit correction. MEA type: Celtec®-P1100W. Flow rates: H₂

= N₂ = 0.3 NL/min, 2 mV/s. $T = 160 \text{ }^\circ\text{C}$, $p = 1 \text{ atm}$, fivefold serpentine flow fields, contact pressure = 1.5 MPa

calculated from the limiting current density ($j_{\text{H}_2 \text{ Cross}}$).

$$\dot{n}_{\text{H}_2 \text{ Crossover}} = \frac{j_{\text{H}_2 \text{ Cross}} \times A}{n \times F} \quad (17.5)$$

A is the fuel cell active area, n is the number of electrons taking part in the reaction ($2 e^-$ per H₂ molecule), and F is Faraday's constant (96,485 C/mol). The hydrogen permeation flux from the LSV shown in Fig. 17.6 is $2.46 \times 10^{-7} \text{ mol/s}$. Galbiati et al. [29] reported hydrogen crossover and internal short-circuit resistance in a 6000 h long-term test of an HT-PEMFC. The hydrogen crossover values reported are between 0.5 and 13.9 mA/cm² and the short-circuit resistance reported values are between 2150 and 431 $\Omega \text{ cm}^2$, from the beginning until the end of the test. Parrondo et al. [54] in their investigations about different supporting materials for platinum catalyst also reported hydrogen crossover values below 3 mA/cm² and no evidence of short-circuit formation in HT-PEM MEAs.

17.2.4 Cyclic Voltammetry

Cyclic voltammetry (CV) is also a method, where potential is varied linearly with time as

LSV but the potential scan is reversed once potential limits are reached. Thus, CV is a reversal technique and is the potential scan equivalent of double potential step chronoamperometry [24]. CV is commonly used to diagnose the electrochemical activity of the catalyst spread on top of the electrodes. Typically, the catalyst for HT-PEMFC consists of platinum (Pt) carbon supported and a binder material such as phosphoric acid-doped PBI or other ionomers [55–58]. The binder serves to facilitate proton conduction between electrolyte membrane and the Pt active sites, whereas the carbon support enhances Pt dispersion through the catalyst layer and the electronic conductivity. Therefore, the electrochemical activity of the electrode catalyst layer strongly depends on the contact between catalyst active sites, reactants, and proton/electron-conducting materials.

The electrochemical activity of fuel cell electrodes may be investigated by ex situ and in situ CV experiments. Ex situ method is a relatively fast method for electrocatalysts screening but in situ method allows the electrocatalysts investigation in the fuel cell which provides a more realistic approach of the catalyst activity. In the in situ method, CV of the fuel cell can be performed in one electrode at a time, by making the other a pseudo-hydrogen reference electrode. Thus, the working electrode is the cathode as it is

of most interest owing to the sluggish kinetics of the ORR [26].

The electrochemical active surface area (EASA) may be determined using hydrogen stripping and/or CO-stripping [59]. For CO-stripping, the working electrode is saturated with CO. Then, the potential is cycled between the open circuit potential to ~ 1.0 V with a scan rate between 10 and -20 mV/s [26, 59–61]. Subsequently, the working electrode is purged with an inert gas, i.e., nitrogen or argon, to remove all the traces of CO in the gas phase. A second potential cycle then is performed and used for baseline subtraction. The CO oxidation peak is integrated to calculate the EASA. Nevertheless, hydrogen stripping is more broadly used than CO-stripping. CO is dangerous in ppm levels and experiments using this molecule should be conducted within a fume hood with adequate exhaust airflow [26]. An example of hydrogen stripping CV is shown in Fig. 17.7. In this case, potential is also cycled between open circuit potential to ~ 1.0 V but scan rates between 10 and 100 mV/s has been found in literature [17, 20, 57, 59, 62].

In Fig. 17.7, the two peaks identified between 0.05 and 0.4 V represent the hydrogen adsorption and desorption peaks on the platinum catalyst surface [62]. The double layer region appears between 0.4 and 0.8 V, the interface of the electrode and electrolyte is charge and discharge performing as a capacitor. The Pt is oxidized to PtO and reduced to Pt between 0.8 and 1 V region.

EASA can be calculated from both the hydrogen adsorption or desorption peaks. Nevertheless, in this case EASA calculation is made from the hydrogen desorption peak. From Fig. 17.7, the dotted area in the CV represents the hydrogen desorption peak and the dashed line is the capacitive charging current which is offset from the zero current. Thus, the EASA of the cathode electrode is estimated based on the relationship between the hydrogen adsorption area of the electrode ($A_{\text{Pt-H}_2}$) and the hydrogen adsorption charge on a smooth Pt electrode (2.1 C/m^2 Pt) [62]. The EASA is calculated using (17.6),

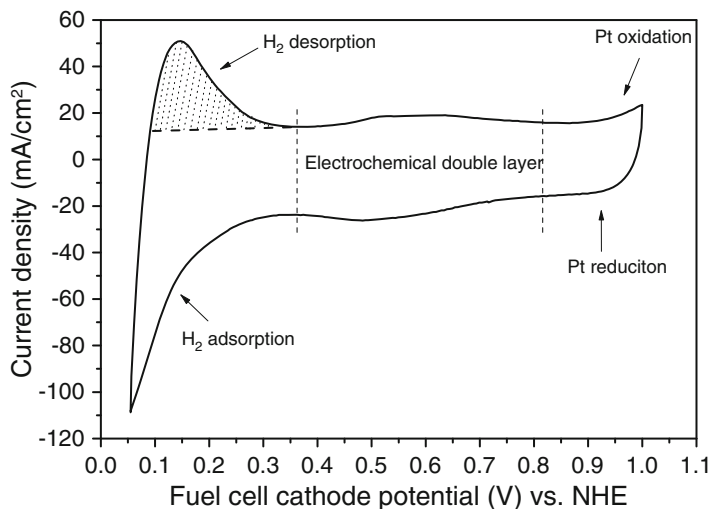
v is the CV scan rate, and L_c is the Pt loading in the catalyst.

$$\text{EASA} \left(\frac{\text{m}^2 \text{ Pt}}{\text{g Pt}} \right) = \frac{A_{\text{Pt-H}_2} \left(\frac{\text{A}}{\sqrt{\text{V/s cm}^2} \right)}{2.1 \frac{\text{C}}{\text{m}^2 \text{ Pt}} \times v \left(\frac{\text{V}}{\text{s}} \right)} \times \frac{1}{L_c \left(\frac{\text{g Pt}}{\text{cm}^2} \right)} \quad (17.6)$$

Thus, the EASA from the voltammogram shown in Fig. 17.7 is $\sim 19 \text{ m}^2 \text{ Pt/g Pt}$, but catalyst loading of cathode cannot be revealed due to proprietary data. Lobato et al. [63] has shown an EASA for commercial HT-PEMFC electrocatalysts between 40 and $55 \text{ m}^2 \text{ Pt/g Pt}$ although scan rate, gas flow rates, and measuring temperature are different to those used to carry out the CV in Fig. 17.7. So comparison of results cannot be done. EASA data between 7 and $20 \text{ m}^2 \text{ Pt/g Pt}$ for an HT-PEM MEA have been shown by Galbiati et al. [29]. In this case, the data may be more comparable with the one presented here but different parameters have been selected to perform the CV. For example, inert gas flow rates have a high impact on accurate determination of the EASA as reported Schneider et al. [64].

Furthermore, estimation of the EASA in phosphoric acid-doped PBI-based HT-PEMFC is less rigorous than for Nafion[®]-based LT-PEMFC. Ferrier et al. [65] carried out ex situ investigations of Pt carbon-supported electrocatalysts in hot and concentrated phosphoric acid. They realized that impurities present in phosphoric acid can poison the Pt surface. Further in situ investigations in HT-PEMFCs [29, 59] show that small peaks during CV are the results of phosphoric acid species adsorption on the Pt surface and subsequent oxidation followed by polarization. These peaks generate distortion in the shape of the measured voltammogram. Thus, as far as the phosphoric acid anions blockage the Pt active sites, the greater the distortion in the voltammogram is [29]. In this manner, the estimated EASA is approximated for HT-PEMFC but it stands for indication of the catalyst activity. Recent investigations have shown new CV methods developed to determine a more reliable EASA in order to overcome the problem of side reactions in HT-PEMFC. The methods are based

Fig. 17.7 Cyclic voltammogram. MEA type: Dapozol[®]-G55. Flow rates: $H_2 = N_2 = 0.1$ NL/min, 100 mV/s. $T = 160$ °C, $p = 1$ atm, grid flow fields, contact pressure = 0.75 MPa



on CO-stripping and measurements of the CO_2 content of the working electrode's exhaust gas in real time [66].

17.2.5 MEA Characterization Test Procedure

In relation to the need of standardized test protocols for HT-PEM MEA characterization to make the results comparable between different research groups, the test procedure and methodology used and agreed by the participants of DEMMEA and CISTEM projects granted by the Fuel Cell and Hydrogen Joint Undertaking (FCH-JU) is going to be shown in this section. Nevertheless, Table 17.1 summarizes the main parameters used in each one of the characterization techniques at the end of this section.

Previous before starting the characterization of an HT-PEMFC, the fuel cell must pass a break-in procedure proposed by the MEA manufacturer or the one that is common practice at the testing organization. Once the break-in procedure has finished, stable conditions have been reached in the HT-PEMFC at fixed operation conditions. For HT-PEMFC, the length of the break-in procedure is an object of study nowadays. Several research groups set a galvanostatic

break-in procedure between 50 and 100 h of duration [67–70].

17.2.5.1 Polarization Curve Test Procedure

The methodology suggested to perform polarization curves starts with a conditioning stage during 10 min at 0.2 A/cm² that ensures stable temperature, pressure, and reactants flow rates conditions. Then, the current is increased in steps of 0.5 A while keeping the fuel cell voltage higher than 0.4 V. Thus, the maximum current density of the fuel cell will correspond with the maximum current reachable at 0.4 V. The duration of each current step is 30 s. This step time is considered enough to reach stable voltage in the fuel cell. Thus, the data acquisition is done before the current is stepped up. Once the maximum current density is reached, 0.5 A steps are used to reduce the current density until reach OCV conditions. At these conditions, the current density raises again up to the maximum current density at same steps conditions and finally, the current is reduced until it reaches the starting point. Figure 17.8 shows schematically this methodology routine and polarization curves of three different HT-PEM MEAs performed at the same operation conditions.

As it can be seen in Fig. 17.8b, the three MEAs behave similarly under the method to

Table 17.1 Summary of main parameters used in HT-PEM MEA characterization techniques

MEA characterization technique	Main parameters
Polarization curve	<ul style="list-style-type: none"> – 10 min conditioning time at 0.2 A/cm² – Current step: 0.5 A – Step time: 30 s – Minimum voltage: 0.4 V
Electrochemical impedance spectroscopy	<ul style="list-style-type: none"> – Potentiostatic mode – AC signal amplitude: 10 mV – Frequency range: 100 kHz–100 mHz – 8 min pre-polarization time at measuring cell voltage – Set of EIS measurements at cell voltages for current densities: 0.03, 0.1, 0.2, 0.3, and 0.4 A/cm²
Linear sweep voltammetry	<ul style="list-style-type: none"> – Anode hydrogen flow rate: 0.3 NL/min – Cathode nitrogen flow rate: 0.3 NL/min – Working electrode: cathode – Potential sweep rate: 2 mV/s – Potential range: rest potential to 0.5 V
Cyclic voltammetry	<ul style="list-style-type: none"> – Anode hydrogen flow rate: 0.1 NL/min – Cathode nitrogen flow rate: 0.1 NL/min – Working electrode: cathode – Potential sweep rate: 100 mV/s – Potential range: 0.05–1.0 V – 7 cycles

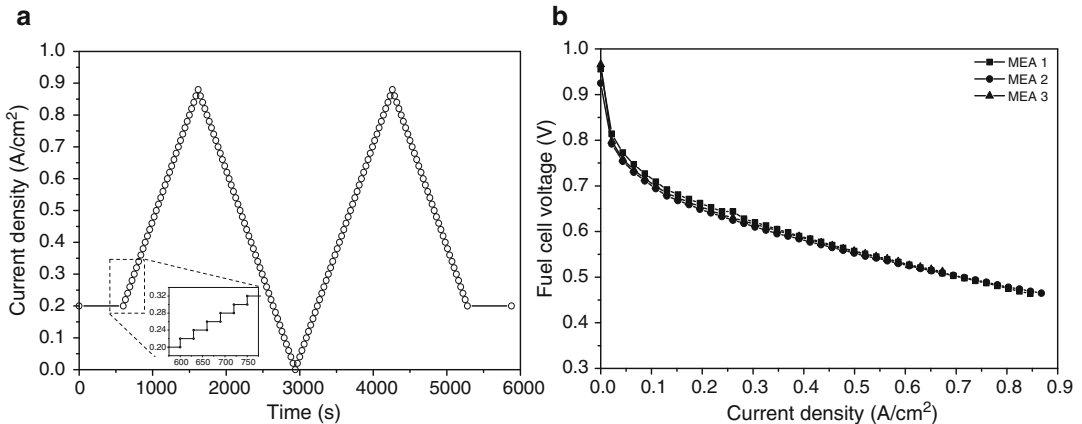


Fig. 17.8 (a) Schematic representation how current density changes over time during the performance of a polarization curve. (b) Reproducibility of 3 Dapozol[®]-G55

MEAs at same operation conditions. H₂/Air ($\lambda_{\text{H}_2}/\lambda_{\text{Air}} = 1.2/2$), $T = 160$ °C, $p = 1$ atm, grid flow fields, contact pressure = 1 MPa

perform polarization curves explained above. Thus, the differences between MEAs are due to the manufacturing process.

17.2.5.2 Electrochemical Impedance Spectroscopy Test Procedure

An EIS spectrum must be measured under steady-state conditions; otherwise, fluctuations

of fuel cell voltage, temperature, or reactants flow rates can result in a non-accurate EIS spectrum of the system. To achieve steady-state conditions, the fuel cell system must be polarized at the desired conditions during a certain period of time. For example, Wagner [43] pre-polarized the fuel cell during 15 min at the measuring potential, Yuan et al. [71] operated the cell at

constant current for at least 1 h, Kondratenko et al. [72] assumed steady-state conditions after 15 min at constant load and Lobato et al. [63] pre-conditioned the fuel cell for 10 min at constant voltage. In other way, Andreassen et al. [46] assessed EIS spectra after achieving a root-mean-square deviation less than 5 % between spectra. As it can be observed, authors use either potentiostatic or galvanostatic modes for assessing the EIS spectra. In general, the use of these different EIS modes should not give discernible differences between the results, although each mode has its advantages and disadvantages [25]. Nevertheless, the amplitude applied for the AC perturbation signal plays an important role in obtaining the best results. Typically, AC amplitude signal is between 0.5 and 6 % of the DC signal for either potentiostatic [63, 73–75] or galvanostatic [71, 72, 76, 77] modes. Thus, minimal changes are within the cell as small perturbances are used. Another one important parameter is the frequency range used to measure the EIS spectrum. A broad frequency range between 100 kHz and 1 mHz, recording 10 points per decade are generally used in PEMFC [13, 17, 25, 29, 76]. Thus, this frequency range allows performing Nyquist plots close to complete a second X-axis interception without consuming long measuring time.

Having reached this point, the test procedure routine developed to perform a set of EIS spectra is as follows. Potentiostatic mode is preferred as impedance data at imposed voltages are more representative of electrode performance [25]. AC perturbation amplitude signal of 10 mV is also preferred as constant amplitude signal allows linearity assumption to hold for all the measurements [77, 78]. The impedance spectra would be measured by sweeping frequencies over the range from 100 kHz to 100 mHz. Before proceeding with the EIS spectrum record at a certain cell voltage, fuel cell may be pre-polarized for a minimum period of 8 min at the cell voltage of interest. Thus, fuel cell voltage will correspond with a current density of 0.03, 0.1, 0.2, 0.3, or 0.4 A/cm². Examples of EIS spectra recorded under the EIS test procedure

here introduced can be found in Figs. 17.3, 17.4, and 17.5a.

Nevertheless, EIS spectra can even be performed at lower cell voltages, although the cell voltage is unstable at high current densities so the accuracy of the AC impedance could impair the measurement, especially for low frequency measurements [25]. Indeed, if test aim would be the investigation of fuel pollutants, the galvanostatic mode would be used. For example, CO poisoning the anode complicates the evaluation of EIS measurements as cell voltage changes with time. Andreassen et al. [46] figured out that the EIS measurements which showed significant deviation were those conducted under the influence of CO.

17.2.5.3 Linear Sweep Voltammetry Test Procedure

LSV should be performed after characterization of the fuel cell with polarization curves and EIS technique. Thereby, the fuel cell is firstly characterized at normal operation conditions in terms of reactant flow rates and then, cathode reactant gas can be switched from oxygen or air to the inert gas. The gas flow rates used to record the LSV are 0.3 NL/min of hydrogen and nitrogen for anode and cathode, respectively. Thus, the cathode is the working electrode and the anode is counter and reference electrode. Before starting the LSV measurement, the rest potential must reach a pseudo-steady-state value. After that, the LSV must start from the rest potential until 0.5 V, sweeping the potential with a rate of 2 mV/s. LSV from Fig. 17.6 has been recorded following the mention test procedure.

17.2.5.4 Cyclic Voltammetry Test Procedure

CV should be performed after characterization of the fuel cell with polarization curves and EIS technique as well as LSV reported above. The CV test procedure agreed for the EU Projects mentioned previously is as follows. The gas flow rates are 0.1 NL/min of hydrogen and nitrogen for anode and cathode, respectively. Similarly to LSV test procedure, the cathode is the

working electrode and the anode is counter and reference electrode. The cathode potential is sweep between 0.05 and 1.0 V with a scan rate of 100 mV/s. Then, one cycle is completed when potential comes back to 0.05 V. The test procedure is finished after completing seven cycles. Thus, a steady voltammogram must be reached before completing the latest cycle.

17.3 Micro-Computed Tomography Technique for *Post-mortem* Analysis

The combination of in situ electrochemically measurements and ex situ optical analysis facilitates a holistic overview of the processes within a fuel cell during operation [17]. Usual microscopy techniques, both optical and using electrons or ions, provide only two-dimensional information of the specimen investigated. They allow extensive investigations of surface areas [79]. By using ultrathin cross-section samples, also two-dimensional imaging of buried layers and interfaces is possible. A great drawback of the latter method is the time-consuming sample preparation. The ultrathin slices of membrane-electrode-assemblies have to be cut by Focused Ion Beam Methodology in a meticulous precise process and are analyzed by transmission electron microscopy. Only a very limited area of the

fuel cell can be investigated in one measurement and the sample preparation is far from being nondestructive. Thus, detected defects can likewise be caused by this kind of preparation rather than being a result of the fuel cell treatment during operation.

An advanced and more sophisticated *post-mortem* method for the examination of degradation effects within HT-PEM fuel cells is high resolution X-ray tomography. This ex situ technique enables the nondestructive characterization of hidden interfaces in HT-PEM MEAs [79]. In computed tomography numerous radiographs are merged into a three-dimensional image volume/model [80]. Each of the individual radiographs represents a shadow image of the sample due to the X-ray illumination. The brightness of each pixel in a radiograph is determined by the amount of X-ray intensity recorded by the detector. It contains the integrated absorption of the sample along the given direction, which is given by the material and geometrical properties. To obtain a three-dimensional image volume, the sample is rotated in small steps in a range of 180° to 360° and at each angle step a radiograph is recorded. The multitude of X-ray photographs can be computer assisted combined into a volume model (reconstruction) [81, 82].

The significant sample area should be placed close to the X-ray source in order to yield the best resolution (see Fig. 17.9). The method, which is

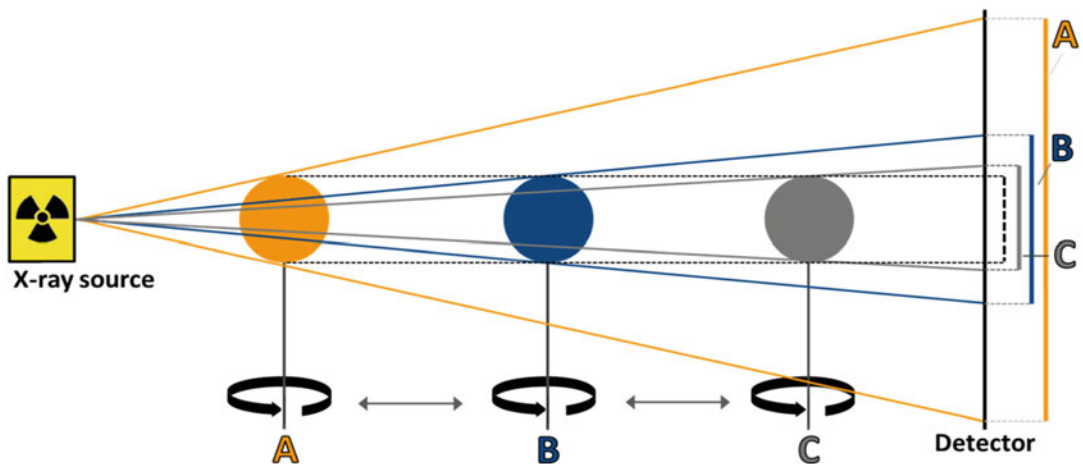


Fig. 17.9 Schematic set-up of μ -CT with an objects in three different positions [80, 81]

used for the reconstruction, is called back-projection. This technique should be explained on the basis of an object with only one significant absorption point. In every single X-ray image, a decrease of intensity of the shadow of absorption can be observed. Because the position of the shadow of the absorption point of the object on the single radiograph is known, all possible positions of the absorption point can be marked as line on the area of reconstruction. With every rotation step, this procedure is repeated and new information (possible position lines) is added. The higher the number of radiographs at different angles/rotation steps, the more precise is the localization of the absorption point in the area of reconstruction (see Fig. 17.10) [80–82].

In Fig. 17.11, the process of reconstruction is summarized. In the first step, the radiographs, which are obtained in the way as it is described above, are combined digitally. This combination allows the creation of two-dimensional volume slices. These slices will be assembled to construct the three-dimensional model of the scanned sample [80, 82].

In Fig. 17.12, an example of a three-dimensional tomographic image volume is presented. This is a model of a Celtec® P2100 MEA, which has been analyzed *post-mortem* by μ -CT investigations. It shows the GDL material that has been significantly deformed by the compression forces of the serpentine flow field, the imprint of the flow fields (channel and land area) is clearly visible, also showing the irreversible effect of compression on the GDL under the land area.

17.4 The Role of Membrane-Electrode-Assembly Contact Pressure

MEA compression is a key parameter for degradations of materials due to its impact on MEA properties as few research groups have also reported [17, 20, 22, 28, 83–88]. Table 17.2 summarizes some of the observed failures due to MEA compression and their possible causes.

On the one hand, high compressive forces may improve the contact between different

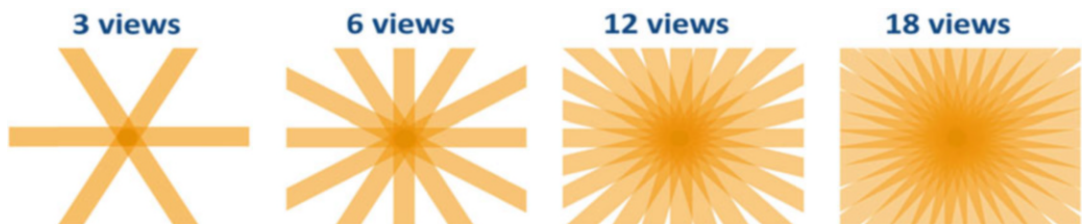


Fig. 17.10 Reconstruction of one single point with increasing number of rotation steps [80, 81]

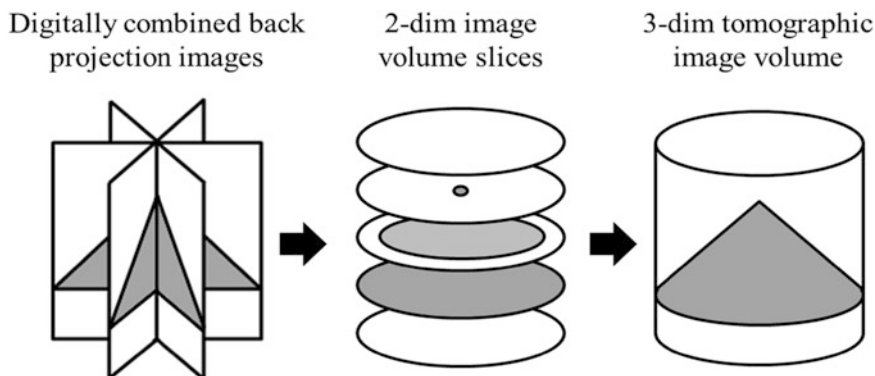


Fig. 17.11 Process to gain a three-dimensional image volume [80]

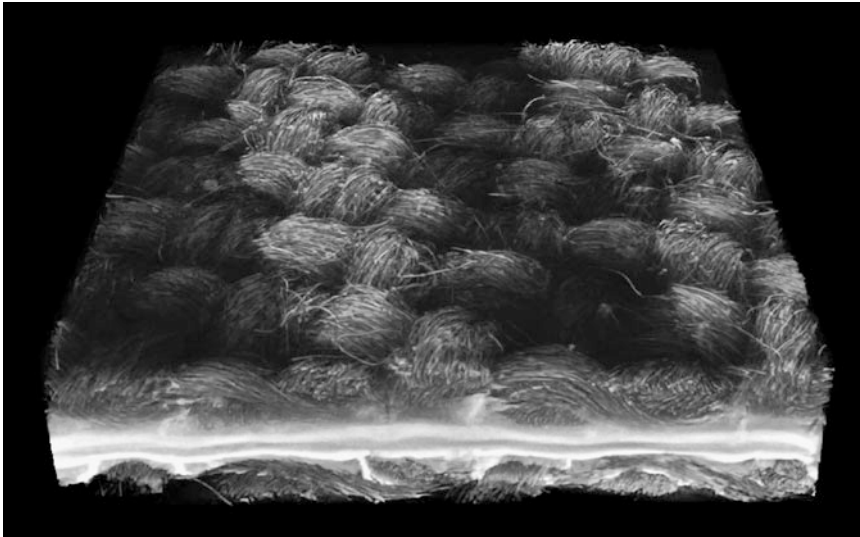


Fig. 17.12 Three-dimensional image volume of Celtec® P2100 MEA

Table 17.2 Failures and possible causes due to HT-PEM MEA compression

Observed failure	Possible causes
Loss of electronic conductivity	Poor contact between MEA components
	Poor contact between electrodes and bipolar plates
	Membrane crossed by electrode fibers
Loss of proton conductivity	Electrolyte squeeze from membrane to electrodes
Loss of catalytic activity	Catalyst layer fracture
Reactants crossover	Membrane rupture
Loss of gases mass transport	Porous structure fracture

layers of the MEA and between MEA electrodes and the BPPs and hence, ohmic resistance may be reduced. A compression change may also affect the distribution of the electrolyte in the catalyst layers which may lead to an enhanced three-phase reaction boundary or electrode flooding. The applied compression should also influence the thickness of the individual layers because these are not stiff. Besides, high compression forces could lead to a membrane thickness reduction so the ionic conductivity resistance could be decreased because the pathway length for the protons will be shorter. In this way, fuel cell performance and efficiency should be improved. On the other hand, a thinner membrane will also shorten the pathway length for reactants crossover and for electrons. A GDL thickness reduction should have an effect on the

GDL porosity and, therefore, the access for the reactant gases might be changed.

In real operation, the fuel cell is built up with the MEA and BPPs. Then, they are compressed with a fixed pressure using bolts and nuts. The selected pressure must warranty sealing against gas leakages and ensuring enough contact between the MEA and BPPs for electronic conduction. Nevertheless, if contact pressure is too high, the MEA can be damaged right from the beginning of its life and lead to poor fuel cell efficiencies. Once the fuel cell is built up, the fuel cell must reach the working temperature before starting with its operation. As mentioned previously, an HT-PEMFC operates normally at around 160 °C, so heating up the fuel cell from room until operation temperature will expand the whole fixture and press the MEA against the

BPPs. So the initially fixed compression will be also increased. During long-term operation, degradation of MEA materials occurs that leads to MEA thickness reduction and MEA contact pressure will be also reduced over time. Other factors that can cause MEA contact pressure change and even fluctuations are fuel cell operations under different load regimes. Thus, the amount of fuel, oxidant, and product water under different load regimes may create expansion or contraction of the MEA itself. There may be more environmental or operation factors that can alter the MEA compression force and cause mechanical stress or even fatigue. Consequently, MEA compression control has great importance to extend its life.

There are few researches in the literature investigating the effect of MEA compression forces and most of the investigations have been performed for LT-PEMFC. Lee et al. [86] have investigated changes in the performance of an LT-PEMFC as function of the compression pressure resulting from torque on the bolts that clamp the fuel cell with three types of GDL. Compression force optimum was observed in terms of the changes in the porosity and the electrical contact resistance. Thus, fuel cell performance was shortened when high bolt torque was applied. Ge et al. [87] have also investigated the effect of GDL compression on LT-PEMFC performance using carbon cloth and carbon paper as GDL material. Their experimental results have shown that the amount of compression lead to a significant effect on fuel cell performance for both carbon cloth and carbon paper, and the effect is greater when carbon paper GDL has been used. Moreover, the effect of GDL compression is also greater in the high current density region. Chang et al. [89] have studied the effect of clamping pressure on the performance of an LT-PEMFC but also measuring electro-physical properties of a carbon paper GDL such as porosity, gas permeability, electrical resistance, and thickness. Results have shown that at clamping pressures less than 5 bar, increasing the clamping pressure reduces the interfacial resistance between the BPPs and GDL that enhances the performance of the fuel cell. In contrast, at

clamping pressures higher than 10 bar, increasing the clamping pressure also narrows down the diffusion path for mass transfer from gas channels to the catalyst layers. Furthermore, GDL porosity develops an exponential pattern as the clamping pressure is increased, indicating that the carbon paper shows a mild thickness change but severe shrinkage in the pore volume under high clamping pressure range. Nitta et al. [83, 84] have investigated the effect of compression forces in the GDL. It was found that the GDL is compressed very little under the channel area, whereas GDL under the land area is compressed to gasket thickness. It was also observed that the compression of GDL reduces gas permeability and contact resistance, but improves bulk conductivity. Hence, the compression of GDL may lead into significant local variation of mass and charge transport properties of the GDL. Besides, the contact resistance between the GDL and CL were found to be more than one order of magnitude larger than contact resistance between the GDL and BPP, and even comparable to the ionic resistance of the membrane. Mathias et al. [90] reviewed diffusion media materials and their characterization methods. Among other GDL behaviors, they showed the compressive and flexural behaviors of carbon paper and carbon cloth in a compression cycle test. They observed that the carbon cloth is more compressible than the carbon paper but also that both the GDL materials do not recover to their initial thickness when the load was removed, exhibiting a residual strain. Moreover, it was shown that carbon paper exhibits better elasticity than the carbon cloth and the last but not the least, carbon cloths tend to intrude into channels and cause reactant flow field pressure drop resulting in higher compressor power requirements.

Figure 17.13 shows the MEA thickness changes as function of contact pressure and flow field geometry for two HT-PEM MEA suppliers [17, 20, 22]. It must be pointed out that Celtec[®] P2100 MEAs are made of woven carbon cloth GDL material and Dapozol[®]-G55 MEAs are made of non-woven carbon cloth GDL material. Both Celtec[®] P2100 MEAs show that thickness loss is logarithmically depending on

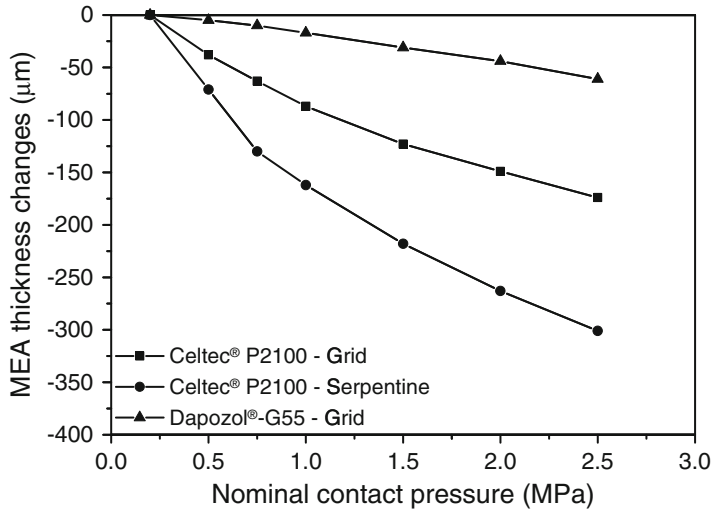


Fig. 17.13 MEA thickness changes as function of contact pressure for MEAs of different suppliers and measured with grid and fivefold serpentine flow fields.

H_2/Air ($\lambda_{H_2}/\lambda_{Air} = 1.2/2$), $T = 160$ °C, $p = 1$ atm. Reproduced from [17] with permission of Springer

contact pressure. Thickness changes are much smaller for the MEA using grid flow fields than the MEA using serpentine flow fields. In Fig. 17.13 is observed the flat ending of a logarithm function for the MEA with grid flow fields and the steep beginning of the curve is completely missing. Therefore, it could be stated that the MEA with grid flow fields is much more compressed from the beginning so the following compression increase just produce a smaller thickness change. Thus, it may be assumed that the MEA with grid flow fields can strongly deform itself into the channels before the compression force sensor measures the initial contact pressure of 0.2 MPa. MEA thickness loss in the Dapozol®-G55 MEA is much less when compared with the Celtec® P2100 MEAs. The non-woven carbon cloth is less compressible than woven one so Dapozol®-G55 MEA is less compressible. Furthermore, Dapozol®-G55 MEA thickness reduction has linear dependency with contact pressure increase that suggests that the MEA does not deform itself into the channels as non-woven cloth is stiffer than the woven one. μ -CT imaging for Dapozol®-G55 and Celtec® P2100 MEA compressed with a grid flow field replica from [17, 22] are shown in Fig. 17.15 to support the MEA deformation into the flow

field channels assumption. The compression tool, which has been utilized to imitate the contact pressure cycling/increasing in μ -CT investigations, and the flow field replica are presented in Fig. 17.14. With help of the spring, the flow field replica applies a defined nominal contact pressure (up to 2.5 MPa) to the MEA sample [17].

It is clearly observed in Fig. 17.15 that almost no bulging into the channel occurs for the Dapozol®-G55 MEA neither for 0.2 nor for 2.5 MPa, for the highest contact pressure the thickness slightly increases about 20 μ m. In contrast, the Celtec® P2100 MEA shows a dilatation into the channel. Moreover, the compressibility of the Celtec® P2100 MEA under the land area is also much higher than the one from the Dapozol®-G55 MEA. On the one hand, the MEA made of the stiffest GDL (non-woven carbon cloth) shows neither micro-cracks in the CL nor GDL material intrusion into the membrane nor other damages. On the other hand, the MEA made of woven carbon cloth presents mechanical stress, due to compression, which causes some failures such as micro-cracks in the CL and GDL fiber intrusion into the membrane. The observed failures affect the overall efficiency of the fuel cell by increasing the hydrogen crossover and

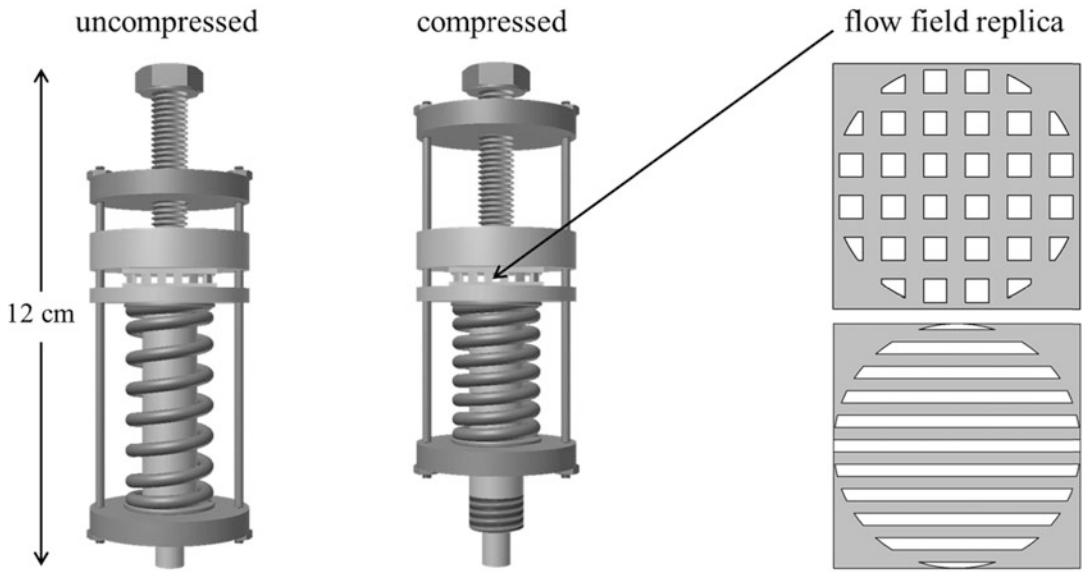


Fig. 17.14 Drawing of the compression tool and the flow field replica for μ -CT investigations—Reproduced from [17, 91] with permission of Springer

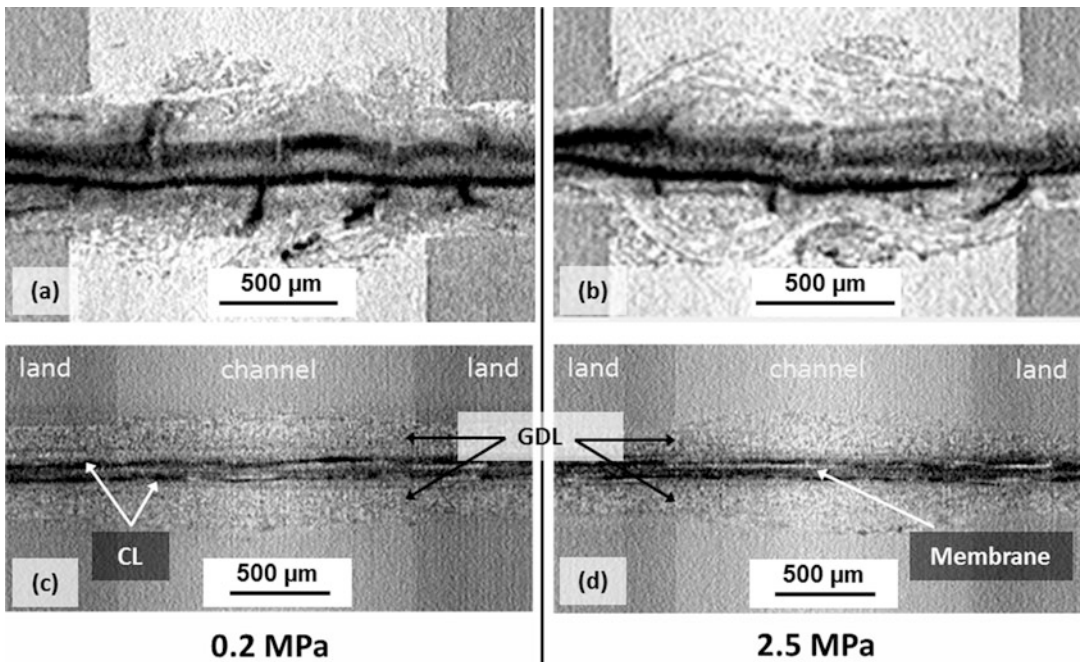


Fig. 17.15 μ -CT images for comparison of a Celtec[®] P2100 MEA (a, b) and Dapozol[®]-G55 MEA (c, d) in the compression tool (channel and land area of the grid flow field) showing the effect of bulging into the channel area as well as the breaking of the catalytic layer. Contact pressure: 0.2 MPa (left), 2.5 MPa (right). Reproduced from [17, 22] with permission of Springer and the Electrochemical Society

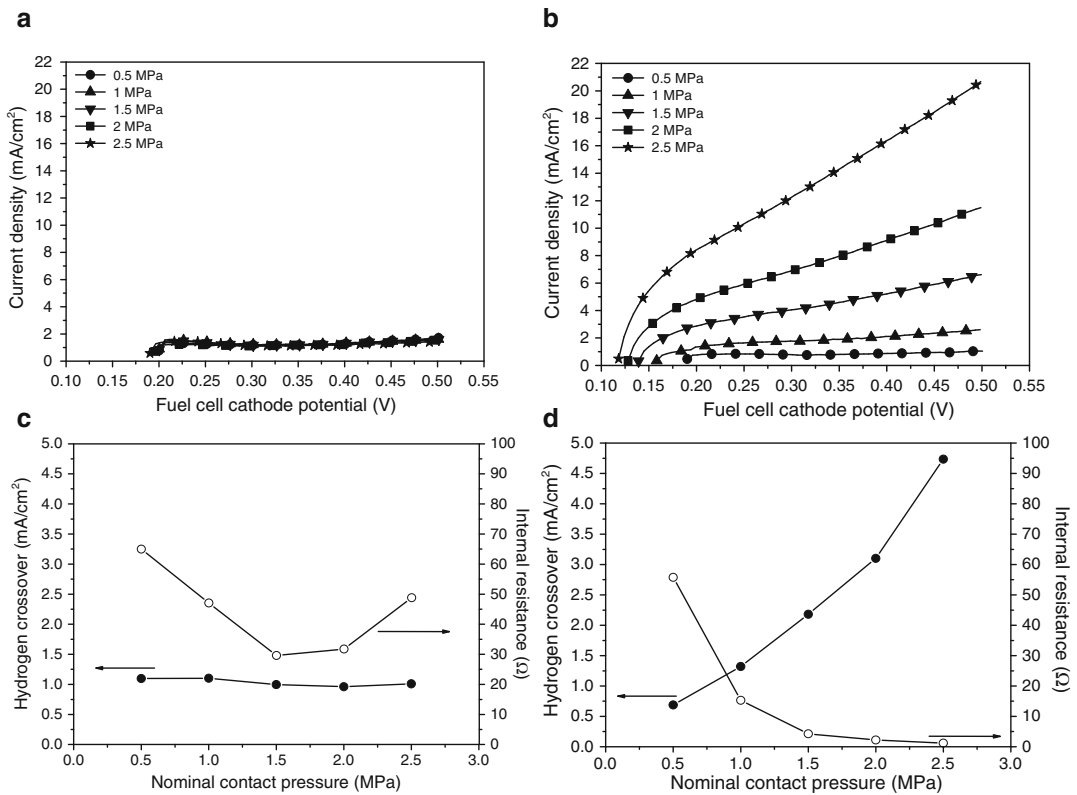


Fig. 17.16 Linear sweep voltammograms as function of contact pressure of (a) Dapozol[®]-G55 MEA and (b) Celtec[®]-P2100 MEA. Limiting hydrogen crossover current (filled circle) and internal resistance (open circle) as function of contact pressure of (c) Dapozol[®]-G55 MEA

and (d) Celtec[®]-P2100 MEA. Flow rates: $H_2 = N_2 = 0.3$ NL/min, 2 mV/s. $T = 160$ °C, $p = 1$ atm, grid flow fields. Reproduced from [22] with permission of the Electrochemical Society

short-circuit formation between the two electrodes. As an example, Fig. 17.16 shows LSV of Celtec[®] P2100 and Dapozol[®]-G55 MEAs as a function of contact pressure increase. Hydrogen crossover and internal resistance of the MEAs calculated from the LSV have been also included and plotted as function of contact pressure increase. As it can be seen, the Dapozol[®]-G55 MEA shows quite stable hydrogen crossover current and there is no indication that short-circuit formation takes place in the whole range of contact pressure studied. In case of the Celtec[®] P2100 MEA, the hydrogen crossover current increases, whereas the internal resistance decreases with raising contact pressure. Thus, fiber intrusion into the membrane on the strength of the compression may be the reason for this behavior because the GDL fiber intrusion causes

firstly electrical short-circuit and secondly micro-holes that abets hydrogen gas crossover from anode to cathode [22].

Figure 17.17 presents selected points of polarization curves as function of contact pressure for MEAs from three HT-PEM MEA suppliers operating with H_2 and air. From Fig. 17.17a, b, the fuel cells behavior of Celtec[®] P2100 MEAs exhibit a strong voltage drop at OCV and low current densities with increasing contact pressure. This is caused by an increase in hydrogen crossover and electrical short-circuit as shown in Fig. 17.16b, d. From Fig. 17.17c can be deduced that the Dapozol[®]-G55 MEA fuel cell performance is nearly immune against contact pressure increase. The OCV is nearly constant in the whole range of contact pressure as hydrogen crossover has also been (Fig. 17.16c). At higher

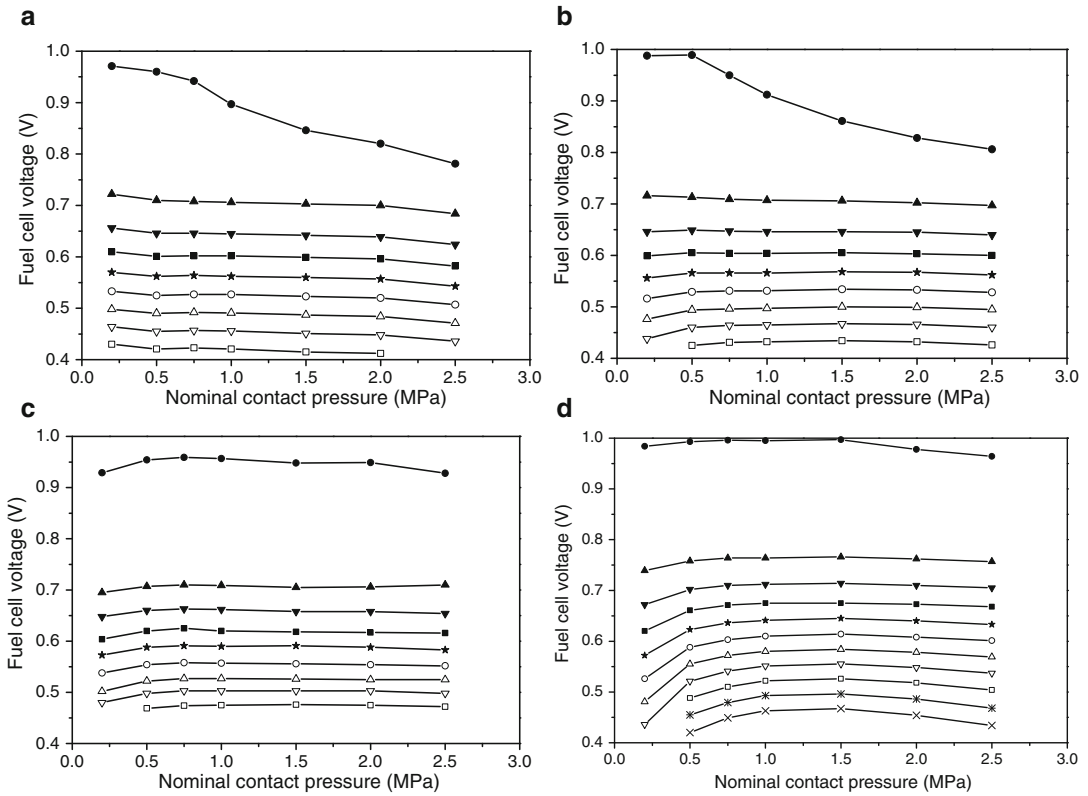


Fig. 17.17 Selected points of polarization curves as function of contact pressure for MEAs from different suppliers and measured with different flow field types. (a) Celtec®-P2100 MEA with grid flow fields, (b) Celtec®-P2100 MEA with fivefold serpentine flow fields and (c) Dapozol®-G55 MEA with grid flow fields ($\lambda_{H_2}/\lambda_{Air} = 1.2/2$). (d) FuMA-Tech MEA with fivefold

serpentine flow fields ($\lambda_{H_2}/\lambda_{Air} = 1.4/2$). H_2/Air , $T = 160\text{ }^\circ\text{C}$, $p = 1\text{ atm}$, j in A/cm^2 : 0 (filled circle), 0.1 (filled triangle), 0.2 (filled inverted triangle), 0.3 (filled square), 0.4 (filled star), 0.5 (open circle), 0.6 (open triangle), 0.7 (open inverted triangle), 0.8 (open square), 0.9 (asterisk), 1 (cross)

current densities, the fuel cell voltage slightly increases from 0.2 to 1 MPa. Mainly, the fuel cell voltage improvement is due to BPP/GDL and GDL/CL electrical contact improvement [17]. FuMA-Tech MEA (Fig. 17.17d) shows quite stable OCV until 1.5 MPa. Higher contact pressure decrease OCV and voltage at higher current densities that means hydrogen crossover current and short-circuit formation as observed in previous publications [17]. In the contact pressure range from 0.2 to 1 MPa, voltage at high current densities of the FuMA-Tech MEA are highly enhanced but the contact pressure increase from 0.2 to 0.5 MPa is the one that shows the highest voltage improvement. Thus, the FuMA-Tech MEA needs a certain compression level to

develop an optimum performance. On the one hand, the first compression step brings all catalyst sites in contact with the electrolyte and on the other hand, the contact resistance between BPP/GDL and GDL/CL strongly decreases from 0.2 to 1 MPa [17]. Therefore, the three kind of MEAs that belong to the same kind of HT-PEMFC technology behave differently due to the MEAs are made of different GDL materials, CL materials, catalyst loadings, and/or have different amounts of phosphoric acid.

As previously said, the fuel cell can operate at different operation modes during its lifetime, so contact pressure can also be varied and stress the MEA. Therefore, other interesting point is if the fuel cell properties are reversible during contact

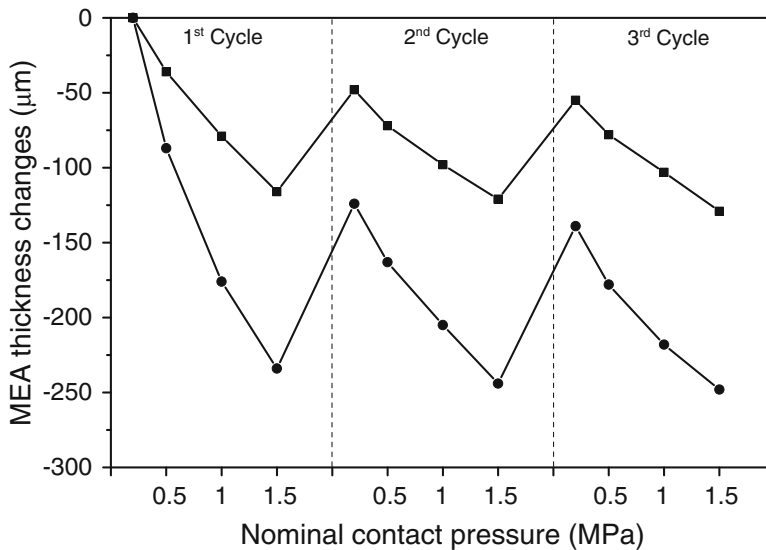


Fig. 17.18 MEA thickness changes as function of contact pressure cycling. H₂/Air ($\lambda = 1.2/2$), grid flow fields, $T = 160^\circ\text{C}$, $p = 1\text{ atm}$. Celtec®-P1100W MEA: (filled

circle), Dapozol®-G55 MEA: (filled square). Reproduced from [21] with permission of Wiley

pressure cycling. In the next paragraphs, investigations of HT-PEM MEAs under contact pressure cycling in a contact pressure range between 0.2 and 1.5 MPa are shown. Figure 17.18 shows MEA thickness changes for Dapozol®-G55 and Celtec® P1100W MEAs as function of contact pressure cycling.

In Fig. 17.18, the MEAs reduce their thicknesses in the whole range of contact pressure during the first cycle and the following reduction of the contact pressure leads to an increase of the MEAs thickness. Nevertheless, the MEAs do not recover back to their initial thickness. In the second cycle, the MEAs thickness is not recovered again to the same value, but their behavior is similar to the previously observed. The GDL loses most of its elasticity in the first cycles and approaches a constant value over time [90]. MEA thickness change consists of a reversible and an irreversible part [17, 21]. Thus, the loss of elasticity in the MEA is owing to the irreversible destruction of GDL pores. Electrolyte reallocation in CL and GDL and/or even membrane/polymer creeping due to compression forces are other phenomena that can

influence the MEA behavior under contact pressure cycling [92].

The ohmic resistance (R_{Ohm}) as function of contact pressure cycling is shown in Fig. 17.19 for Dapozol®-G55 and Celtec® P1100W MEAs. The values have been extracted from the Nyquist plots at 0.3 A/cm^2 shown in [21]. As previously defined, ohmic or high frequency resistances are used to differentiate the resistance of conduction of protons and electrons and resistances of wires and MEA contact interfaces as BBP/GDL and GDL/CL. If one assumes a constant or nearly constant contribution from proton conductivity resistance through the membrane as the membrane thickness is nearly constant in comparison with GDL thickness changes with increasing the contact pressure [17] and resistance related to fuel cell wires and connections is constant [40, 41], the observed changes in the ohmic resistance will be mainly due to variation of contact between BPP/GDL and GDL/CL interfaces. R_{Ohm} decreases in the first cycle of contact pressure as shown in Fig. 17.19 for both the MEAs so contact between BPP/GDL and GDL/CL interfaces has been enhanced. This

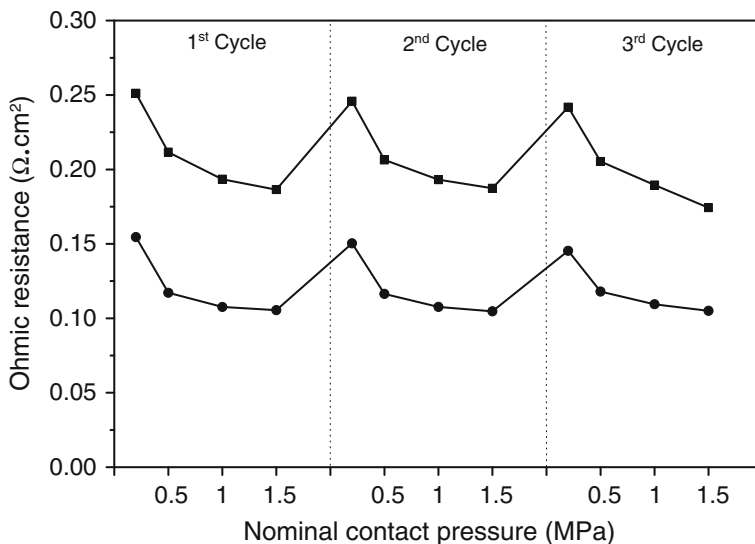


Fig. 17.19 Ohmic resistance for (*filled circle*) Celtec®-P1100W and (*filled square*) Dapozol®-G55 MEAs as function of contact pressure cycling from Nyquist plots

at 0.3 A/cm². H₂/Air ($\lambda = 1.2/2$), grid flow fields, $T = 160$ °C, $p = 1$ atm. Reproduced from [21] with permission of Wiley

contact improvement must also lead to an overall fuel cell performance enhancement as shown in Fig. 17.17. When contact pressure has been reduced to 0.2 MPa in the second and third cycles, the MEAs suffer a reversible increase on the ohmic resistance. Diedrichs et al. [17, 20] concluded for their investigations with Celtec®-P2100 MEAs that R_{Ohm} is more influenced by the GDL/CL contact resistance in the whole cycling experiments when grid flow fields are used, whereas the BPP/GDL contact resistance may contribute no longer to the total R_{Ohm} after the first application of 0.5 MPa, where MEAs deformation is more intense. Therefore, the irreversible R_{Ohm} improvement after the first contact pressure reduction must be attributed to the BPP/GDL contact resistance. However, Fig. 17.19 does not show a large irreversibility in R_{Ohm} when contact pressure has been turned back to 0.2 MPa after completion of each one of the cycles as Diedrichs et al. showed in their investigations. Therefore, Celtec® P1100W MEA and DPS Dapozol®-G55 MEA are still flexible enough after being exposed to 1.5 MPa during the three cycles. Thus, it can be seen that the use of different GDL materials or even the use of similar GDL materials with different

properties will provide a different behavior regarding irreversibility and reversibility of MEA properties under contact pressure cycling stress.

Hydrogen crossover current as well as internal resistance of two types of HT-PEM MEAs calculated from LSV as function of contact pressure cycling are shown in Fig. 17.20 [21]. During the first cycle, both MEAs have developed similar response as the one shown in Fig. 17.16 when contact pressure increase was studied. In case of the Celtec®-P1100W MEA, the short-circuit is formed at the end of the first cycle. Hydrogen crossover current starts its increase from 0.5 until 1.5 MPa. The reason for these observations may be fiber intrusion into the membrane as compression force has been increased. It was observed in previous publications [22] that GDL fibers penetration causes firstly electrical short-circuit formation and then pin holes which lead to hydrogen gas crossover increase. Internal resistance is partially recovered as well as hydrogen crossover when contact pressure has been reduced for starting the second cycle. After reaching the contact pressure of 1 MPa as second time, both the hydrogen crossover and internal resistance show similar values than the ones at 1.5 MPa in the first

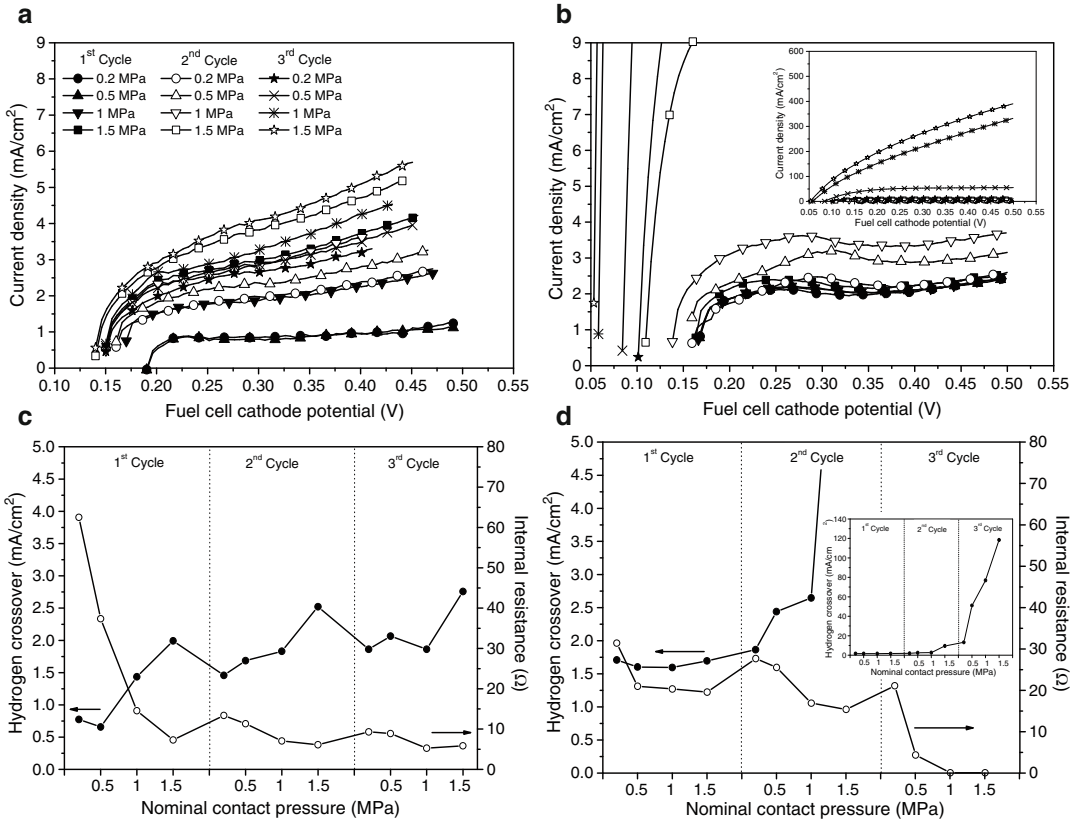


Fig. 17.20 Linear sweep voltammetry as function of contact pressure cycling (a, b). Hydrogen crossover current (filled circle) and internal resistance (open circle) calculated from linear sweep voltammetry as function of contact pressure cycling (c, d). Celtec®-P1100W MEA:

(a, c) and Dapozol®-G55 MEA: (b, d); grid flow fields, H₂ = N₂ = 0.3 NL/min, T = 160 °C, p = 1 atm. Symbol code in (a) is also applicable in (b). Reproduced from [21] with permission of Wiley

cycle. Thus, increase contact pressure from 1 to 1.5 MPa in second cycle causes slightly further short-circuit formation but larger hydrogen crossover. In the third cycle, hydrogen crossover current and internal resistance are partially recovered again after contact pressure reduction to 0.2 MPa, and they reach similar values that the ones get in the second cycle at 1 MPa. Then, hydrogen crossover seems nearly constant for further contact pressures but it starts tilting again when contact pressure is finally increased up to 1.5 MPa. Therefore, further MEA damages are facilitated from cycle to cycle at the highest contact pressure. However, Dapozol®-G55 MEA behavior during contact pressure cycling is not as stable as reported for contact pressure increase. When the contact pressure is further increased than 0.2 MPa

in the second cycle, the hydrogen crossover current starts tilting and internal resistance is reduced to lower values than the lowest one reached in the first cycle. So the membrane may be damaged as a consequence of contact pressure cycling. Again, fibers from the GDL may intrude into the membrane and may create pin holes as well as for the Celtec®-P1100W MEA. It could be said that Dapozol®-G55 MEA is more sensitive to contact pressure changes once damages have already arisen [21]. Nevertheless, the contact pressure range studied is quite wide in comparison with the expected contact pressures changes that could happen into the fuel cell during operation. Besides, it has been demonstrated that exceeding a certain contact pressure may damage the whole MEA independent from the supplier.

In the following section, results from the μ -CT analyses will be presented. With the help of a compression tool (a sample holder with adjustable compression force up to 1.5 MPa and a grid flow field replica [17, 91]) the contact pressure cycling of the test station procedure could be imitated *ex situ* during the μ -CT investigations. For the imitation, the same MEA type (Dapozol[®]-G55 MEA) like for *in situ* electrochemical analysis was used. In Fig. 17.21, radiographs of the MEA for each contact pressure and all three cycles are shown. The used operational parameter for the here-

presented μ -CT investigation is listed in Table 17.3. In the first cycle, no deformations or mechanical changes can be observed. At higher contact pressure forces in the second cycle, first defects are visible. Irreversible cracks in the catalyst layer (CL) and pin holes can be found. The amount of defects and failures is increasing during the third cycle. A typical kind of defect, cracking of the CL, is marked with white circles in Fig. 17.21. These observations by μ -CT investigation match pretty well with the results from the electrochemical *in situ* analysis. The hydrogen

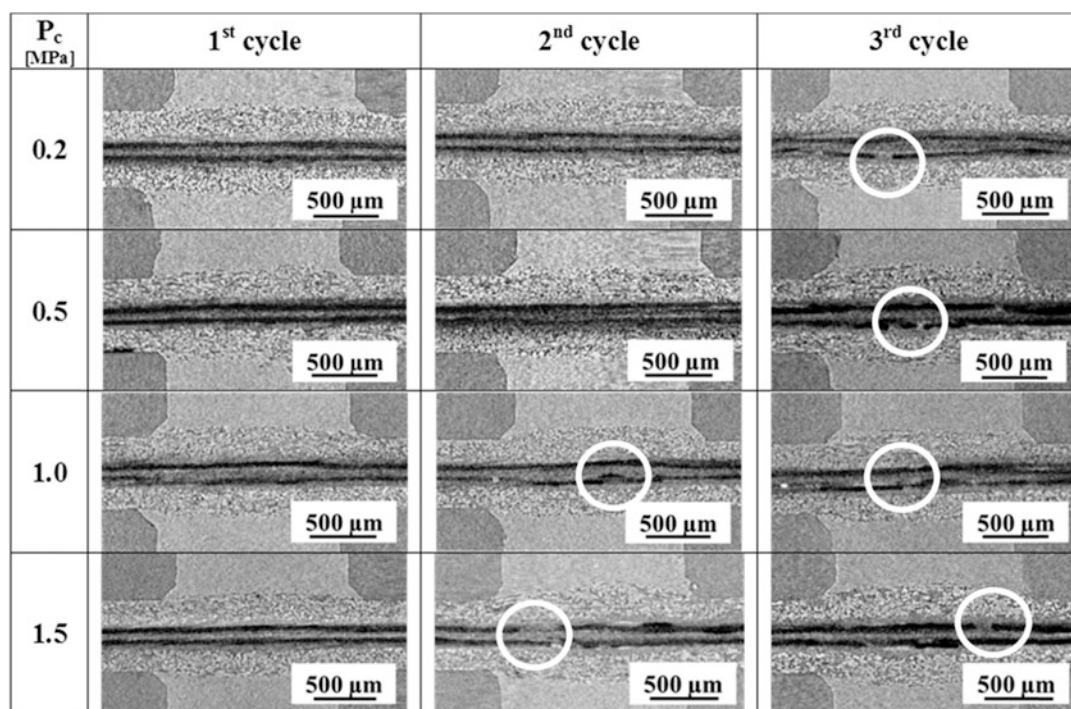


Fig. 17.21 Reconstructed μ -CT images within the grid flow field (GFF) replica of complete contact pressure cycling; the dark grey parts at the edges are the land area of the GFF [23]

Table 17.3 μ -CT operational parameters for measurement of MEA sample [21, 23]

Parameter	Value (within compression tool)	Value (without compression tool)
Acceleration voltage (kV)	78–82	78–82
Sample size \varnothing (mm)	8	8
Rotation step ($^{\circ}$)	0.15	0.1
Averaging	4	4
Optical resolution (μm)	~ 3	~ 2.5
Duration (h)	~ 2.75	~ 3
Filter	No filter	No filter

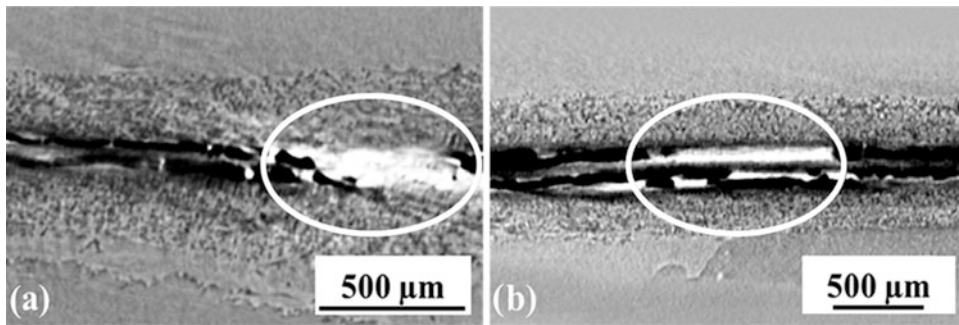


Fig. 17.22 Reconstructed μ -CT images of *post-mortem* analyses of MEAs under (a) in situ cell conditions and contact pressure cycling and (b) ex situ standard conditions and contact pressure cycling [21, 23]

crossover starts to increase at the end of the second contact pressure cycle (see Fig. 17.20d), at this point the first mechanical defects can be observed in the MEA and especially in the catalyst layer [21, 23].

For a better comparison, *post-mortem* μ -CT analysis of both MEAs, in situ (characterization in the fuel cell test station) and ex situ (imitation of contact pressure cycling procedure under ambient conditions), have been performed. The results are presented in Fig. 17.22.

While comparing the in situ and ex situ *post-mortem* investigations, it is evident that the contact pressure cycling has an enormous impact on the mechanical conditions of the MEAs and the defects seem to be only slightly increased by fuel cell operation conditions. In both cases, extensive defects like 400 μ m wide cracks through all layers of the MEA could be detected (see Fig. 17.22) [21, 23].

It has been shown that the results from the electrochemically investigation during the fuel cell procedure and the *post-mortem* and also ex situ μ -CT analysis coincide and the combination of both investigation allow a comprehensive characterization of the processes within an HT-PEM MEA.

17.5 Long-Term Testing in HT-PEM Single Fuel Cells

Other important key parameter and surely one of the most important ones for reaching a

commercial product is the fuel cell lifetime. Fuel cell requirements vary significantly on the kind of application that the fuel cell is designed for. For example, from 3000 to 5000 h (~240,000 km) of operation are expected for car application, up to 20,000 h of operation for bus applications and from 40,000 to 90,000 h of operation for stationary applications [93, 94]. Moreover, the fuel cell must deliver enough power to allow its application during the whole life cycle, even at the end of its life. Thus, end-of-life (EoL) as well as beginning-of-life (BoL) of the fuel cell must be defined. BoL may be defined as the first performance of the fuel cell directly after break-in procedure. Therefore, BoL reference would be the voltage of the fuel cell at a typical working load. Usually, EoL is considered to be reached when the performance or voltage at a working load has decreased more than 10 % from the BoL [94, 95].

In real life, testing fuel cells for such a lengthy period of time is very costly and even impractical (90,000 h > 10 years). Besides, learning of key issues as well as implementing mitigation strategies is too slow, if such a long life tests must be completed. Nevertheless, the need to understand degradation mechanisms to improve lifetime cycle of a fuel cell has arrayed the fuel cell research activities to develop long-term testing methods. On one side, several thousand hours of operation is not feasible. On the contrary, 1000 h seems to be not enough for identification of degradation mechanisms that are responsible of fuel cell performance depletion [10, 49, 96–100]. Thus, to understand what is going on

Table 17.4 Overall degradation rates of PBI-based HT-PEM fuel cells

Fuel cell long-term test results	Operation conditions	Reference
>5000 h; degradation rate: <5 $\mu\text{V/h}$	H_2/O_2 ; 150 °C; 1 atm	[101]
>18,000 h; degradation rate: 6 $\mu\text{V/h}$	H_2/Air , 160 °C, 1 atm; $j = 0.2 \text{ A/cm}^2$	[102]
>3000 h; degradation rate: 20 $\mu\text{V/h}$	$\text{H}_2/\text{Reformate}$, 180 °C, 1 atm; $j = 0.2 \text{ A/cm}^2$; Reformate: 60 % H_2 , 2 % CO , 5 ppm H_2S , 21 % H_2O , and CO_2	[6, 7]
6000 h; degradation rate: 4–19 $\mu\text{V/h}$	H_2/Air , 160–180 °C, 1 atm; $j = 0.2\text{--}0.4 \text{ A/cm}^2$	[29]
>17,000 h; 10 % voltage loss (EoL)	H_2/Air , 150 °C, 1 atm; $j = 0.2 \text{ A/cm}^2$	[8]
>14,000 h; degradation rate: 6.3 $\mu\text{V/h}$	H_2/Air , 120 °C, 1 atm; $j = 0.2 \text{ A/cm}^2$	[9]

in the fuel cell, testing the system over half a year is required (>5000 h). Long-term test investigations over 1000 h of time lapse for HT-PEM MEAs are currently found in literature and some of them are summarized in Table 17.4.

As it can be seen in Table 17.4, the operation of the fuel cell at constant current density conditions is quite common although most of the studies are carried out at different temperatures, loads, reactant gases, and period of time between them. The constant load operation conditions are favored because they are most easily applied. Another reason is that the test is useful since data interpretation is simpler, and it also provides a baseline for more complicated tests [93]. Moreover, the test operation conditions must be under the normal ones of the fuel cell application providing the most relevant PEM lifetime data. Li et al. [101] showed a set of durability test results of PBI cells operating with hydrogen and oxygen under continuous operation at ambient pressure. At 150 °C, a lifetime of 5000 h was achieved at a constant cell voltage of 0.5 V. At temperatures above 180 °C, the lifetime was limited, and polymer-oxidative degradation was mainly the reason for the failure. Schmidt [102] presented the durability and degradation of a Celtec[®]-P Series 1000 MEA over 18,000 h of operation at 0.2 A/cm² with an overall degradation rate of only 6 $\mu\text{V/h}$. It was concluded that the main part of the degradation was due to increased mass transport over potential and by reduced oxygen reduction kinetics. Moreover, Schmidt et al. [6, 7] investigated the effect of a realistic reformat in a PBI-based fuel cell over 3000 h. Stable cell voltage was recorded with an overall degradation rate of approximately 20 $\mu\text{V/h}$, which was identical to degradation

rates when the MEA was operated with pure hydrogen at the same load conditions. Galbiati et al. [29] reported a 6000 h test with a Celtec[®]-P 2100. The study investigated operation at 160 and 180 °C, operation at current densities of 0.2 and 0.4 A/cm², and double air flow rate (from $\lambda_{\text{Air}} 2$ to 4) over time. They observed that temperature increase accelerates the degradation of the MEA, but the operation at 0.4 A/cm² reduces voltages degradation. Nevertheless, they observed loss of catalyst active area, slight decrease on proton conductivity and a major effect on degradation was played by hydrogen crossover and short-circuit current. Oono et al. [8] tested five identical cells at 150 °C and a current density of 0.2 A/cm² for a period up to 17,860 h. Each of the cells was then analyzed using transmission electron microscopy and electron probe microanalysis. The results indicated that the cell voltage declined very gradually until 14,000 h and was caused by platinum particles growth as well as carbon support corrosion. The remaining operating hours, the cell voltage showed a more rapid decrease that correlated well with decreases in the membrane thickness due to its dissolution together with its migration with the phosphoric acid into the catalyst layer. Yu et al. [9] showed a PBI-based fuel cell operated under steady-state conditions for greater than 14,000 h. The voltage degradation rate was 6.3 $\mu\text{V/h}$.

Figure 17.23 presents an example of load profile characteristics of a CHP system for a stationary application. As it can be observed, the electrical power generation of the fuel cell is constant most of the day but few hours per day there is no real thermal demand from the house and the CHP system is shutdown automatically

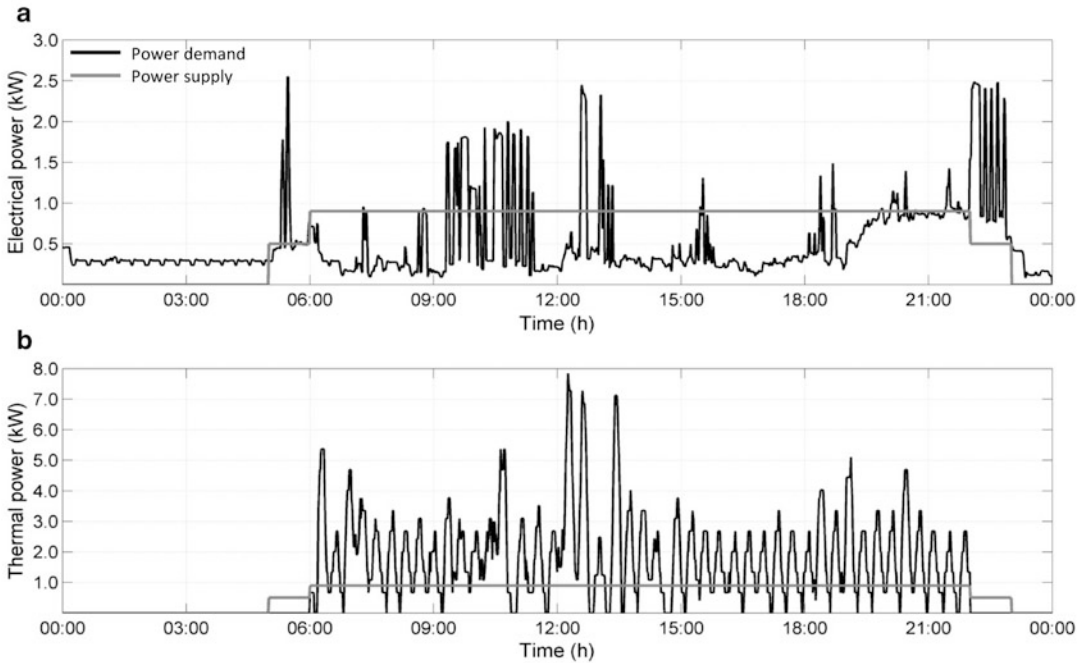


Fig. 17.23 Daily profile characteristic of a single family house 1 kW μ -CHP system. (a) Electrical power demand (black) and electrical power supplied by the fuel cell (grey). (b) Thermal power demand (black) and thermal

power supplied by the fuel cell (grey). Four people, house size: 120 m², area: Oldenburg, Germany, working day between summer and winter time based on the standard VDI-4655

to safe fuel. This CHP operation strategy is of common use as it provides good system efficiencies without wasting resources in small size applications. Furthermore, for these small power demand applications, single family house-holds, e.g., an intermediate step of the nominal electrical/thermal power generation should be needed to keep the house on a certain temperature or even heat it up during cold periods of time. In summer time, the thermal demand is limited to tap water and the CHP system strategy could even consider a shutdown of the system during most of the day. Thus, the fuel cell can experience constant load and dynamic load operation modes with varying load demand applications. Besides, thermal cycling like freezing/thawing and cold startup must take into consideration. Therefore, the development of tests that can approach to real operation will provide a more realistic overview and a more fully determination of degradation,

durability, and feasibility of the fuel cell components.

Long-term tests for investigating LT-PEMFC durability and degradation have been thoroughly developed [93]. Usually, these tests can be easily adapted to HT-PEMFC owing to the similarity of both fuel cell technologies. Nevertheless, a fuel cell is a complex system comprising various components for which the degradation mechanisms, component interactions, and effects of operating conditions need to be fully understood. Thus, one kind of test is not enough to face these tricky issues but combination between constant load, dynamic, and thermal tests can be the solution. AST are also used to enhance failure mechanisms in the MEA, reduce valuable operation time, and increase sample throughput. An AST method should not only activate the degradation mechanism of a specific component, but it should also minimize the confounding effects from other components.

Currently, several research institutions are each trying to establish PEM fuel cell durability testing protocols with the intent to provide a standard set of test conditions and operating procedures for evaluating new cell component materials [95, 103]. There are few studies in the literature available for HT-PEMFC. Mocotéguy et al. [10] reported a single cell and a 500 W HT-PEMFC stack under accelerated typical annual μ -CHP profile. The single cell was unaffected by 500 h of current cycling while shutdown/startup cycles induced some voltage loss. The stack performance decreased its electrical efficiency from 30 to 28 %. The stack performance decrease was associated to four initial shutdown/startup cycles that weakly impacted its performance, indicating that the used shutdown/startup protocol was more convenient for a field application. Conversely, after additional shutdown/startup cycles, degradation rate was increased by shutdown/startup cycling and some specific cells (mostly associated with lower initial OCV) exhibited significantly higher degradation rates. Yu et al. [9] presented different long-term durability testing for PBI-based HT-PEMFC. The investigations were conducted performing test protocols designed to simulate fuel cell operational situations which may be found in real applications. The test protocols consisted of steady-state and dynamic operation. The steady-state operation has been already discussed above but the dynamic operation tests were featured with load cycling, thermal cycling, and shutdown/startup cycling. From the dynamic durability tests, a consistent dependency of the phosphoric acid loss rates on key operating conditions was observed. The combination of high temperatures and high load conditions (high water generation at the cathode) led to a proposed steam distillation mechanism for phosphoric acid removal from the MEA.

Figure 17.24 shows AST results of a Dapozol[®]-G55 MEA operated with synthetic reformat and air enriched to 30 % oxygen from [49]. The fuel cell was continuously operated for 4 min at OCV and 16 min with a load of 0.3 A/cm². The load cycling was interrupted once a week for IV, EIS, CV, and

LSV measurements, and reactant gases were switched to air and pure oxygen during MEA characterization. MEA displacement sensor also monitored the MEA thickness changes continuously. Thus, more than 800 h of testing corresponding to more than 2400 load cycles have been achieved before finishing the experiment.

It can be immediately perceived that fuel cell voltage at 0.3 A/cm² decreases as function of time with a much steeper rate than OCV. In addition, OCV reaches an almost steady-state after 13 days of operation, whereas the voltage at 0.3 A/cm² keeps on decreasing until the end of the test period. In the investigations, it was concluded that cathode reaction kinetics were improved after fuel cell operation with oxygen enrichment. After 7 days of operation with the AST, catalyst degradation over time hindered the fuel cell improvement observed after oxidant concentration change from 30 % O₂ to air. Nevertheless, loss of ohmic resistance was also observed, and it could be connected with membrane thinning. On the one hand, it has been reported in literature that OCV without electric loading operation mode enhances membrane electrolyte degradation mechanisms [103, 104]. Peroxide radicals from incomplete reduction of oxygen at the cathode can lead to chemical decomposition of the membrane. Load cycling is another membrane stressor. The frequent wetting and drying during load cycles can create mechanical stress on the membrane. On the other hand, OCV operation also enhances carbon support corrosion that leads to Pt particles growth and GDL wettability. In addition, Pt dissolvability also increases after potential cycling to high cathode potentials or OCV.

If the AST would have been conducted at even higher current densities than 0.3 A/cm², other degradations mechanisms would have led to components failure over time. At high loads, the water production is increased and some surface of the catalyst layer could suffer fuel starvation so oxidation of carbon support would be caused by these mechanisms as well. Moreover, high water production may also more strongly leach phosphoric acid from membrane and

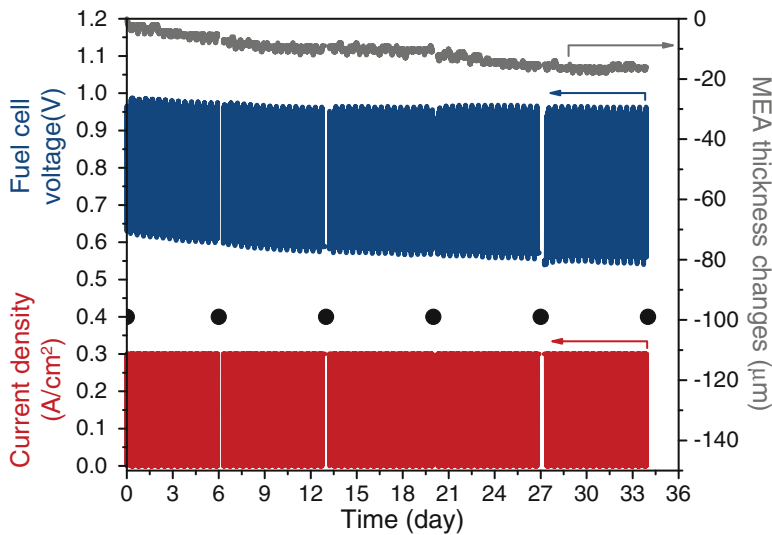


Fig. 17.24 AST of a fuel cell operated with synthetic reformat/30 % O₂ ($\lambda_{\text{Ref}}/\lambda_{30\% \text{O}_2} = 1.5/2.85$). Load cycling was interrupted for electrochemical characterization on day 0, 6, 13, 20, 27, and 34 (black

circles). Synthetic reformat: 78.1 % H₂ + 21.9 % CO₂, $T = 160$ °C, $p = 1$ atm, fivefold serpentine flow fields, Contact pressure = 0.75 MPa. Reproduced from [49] with permission of Springer

catalyst interfaces leading to an irreversible loss of proton conductivity.

Startup/shutdown cycling may also develop another mode of carbon corrosion from non-uniform distribution of fuel to the anode and the crossover of reactant gas through the membrane, resulting in tragic reduction in EASA and fuel cell performance [9, 94, 103, 105, 106]. Therefore, different operation methods can turn into different component degradation mechanisms during in situ investigations. Thus, investigation of single components of the fuel cell cannot be easily carried out in the fuel cell. In addition, agreement in one basis of long-term test protocols for identifying component failures is needed to understand in deeper detail degradation mechanisms, develop mitigation strategies, and have results comparable between different research groups.

17.6 Conclusive Remarks

The most used in situ electrochemical techniques for HT-PEMFCs have been discussed as well the main information that can be drawn from each

one. Moreover, the combination of the information subtracted from the different electrochemical and *post-mortem* imaging techniques may facilitate to achieve a right diagnosis of the fuel cell behavior. Nevertheless, the electrochemical techniques that have been broadly developed for LT-PEMFC must be further developed to adapt them for HT-PEMFC, such as cyclic voltammetry in order to measure a more quantitative EASA of the catalyst. In addition, further analytical instrument improvement will also enhance this approach.

Standardized test protocols and routines must be also further developed to make data subtracted from the fuel cell more reliable and comparable. Specific long-term test protocols should be also developed to investigate durability of individual fuel cell components and interactions among themselves. Besides, each fuel cell application may require its own adapted testing protocols.

From the MEA compression, investigations can be concluded that non-woven and woven carbon cloth GDL materials used to make the MEAs have a different impact on the performance of the fuel cell under different contact pressures. Thus, an intermediate nominal

contact pressure around 0.75 MPa seems to be a contact pressure that supplies enough contact between MEA layers without damaging them. In addition, irreversible loss of MEA performance has been observed after the pressure cycling test. Irreversible destruction of GDL pores as well as increase of hydrogen crossover and short-circuit may be the main factors that abet performance loss.

Acknowledgements The authors thank the European Commission for supporting this work by the FCH-JU through the project CISTEM (01.06.2013–30.06.2016, Grant Agreement Number 325262) and the project DEMMEA (01.01.2010–31.12.2012, Grant Agreement Number 245156). Marco Zobel and Benedict Hartmann valuable help from CHP group at NEXT ENERGY are widely appreciated.

References

1. Seland F, Berning T, Borresen B et al (2006) Improving the performance of high-temperature PEM fuel cells based on PBI electrolyte. *J Power Sources* 160:27–36
2. Aleksandrova E, Hiesgen R, Eberhard D et al (2007) Proton conductivity study of a fuel cell membrane with nanoscale resolution. *ChemPhysChem* 8:519–522
3. Jensen JO, Li Q, Pan C et al (2009) Degradation of high temperature PEM fuel cells. Paper presented at the HyFC Academy School on Fuel Cells and Hydrogen, Vancouver, Canada
4. Lehnert W, Maier W, Wanek C et al (2012) Mobility and distribution of phosphoric acid in high-temperature polymer electrolyte fuel cells. Paper presented at the 3rd CARISMA international conference, Copenhagen, Denmark
5. Chandan A, Hattenberger M, El-kharouf A et al (2013) High temperature (HT) polymer electrolyte membrane fuel cells (PEMFC)—a review. *J Power Sources* 231:264–278
6. Schmidt TJ, Baurmeister J (2006) Durability and reliability in high-temperature reformed hydrogen PEFCs. *ECS Trans* 3:861–869
7. Mader J, Xiao L, Schmidt TJ et al (2008) Polybenzimidazole/acid complexes as high-temperature membranes. *Adv Polym Sci* 216:63–124
8. Oono Y, Sounai A, Hori M (2012) Long-term cell degradation mechanism in high-temperature proton exchange membrane fuel cells. *J Power Sources* 210:366–373
9. Yu S, Xiao L, Benicewicz BC (2008) Durability studies of PBI-based high temperature PEMFCs. *Fuel Cells* 8:165–174
10. Mocotéguy P, Ludwig B, Scholta J et al (2010) Long-term testing in dynamic mode of HT-PEMFC H₃PO₄/PBI Celtec-P based membrane electrode assemblies for micro-CHP applications. *Fuel Cells* 10:1–13
11. Gou B, Na WK, Diong B (2009) Fuel cells: modeling, control, and applications. Power electronics and applications series. CRC, Boca Raton
12. Yang JS, Cleemann LN, Steenberg T et al (2014) High molecular weight polybenzimidazole membranes for high temperature PEMFC. *Fuel Cells* 14:7–15
13. Lobato J, Cañizares P, Rodrigo MA et al (2011) Enhancement of the fuel cell performance of a high temperature proton exchange membrane fuel cell running with titanium composite polybenzimidazole-based membranes. *J Power Sources* 196:8265–8271
14. Aili D, Cleemann LN, Li Q et al (2012) Thermal curing of PBI membranes for high temperature PEM fuel cells. *J Mater Chem* 22:5444–5453
15. Debe MK (2012) Electrocatalyst approaches and challenges for automotive fuel cells. *Nature* 486:43–51
16. Cleemann LN, Buazar F, Li Q et al (2013) Catalyst degradation in high temperature proton exchange membrane fuel cells based on acid doped polybenzimidazole membranes. *Fuel Cells* 13:822–831
17. Diedrichs A, Rastedt M, Pinar JF et al (2013) Effect of compression on the performance of a HT-PEM fuel cell. *J Appl Electrochem* 43:1079–1099
18. Fuel cells and hydrogen joint undertaking (2011) Multi-annual implementation plan 2008–2013
19. Department of Energy (2012) Technical plan—fuel cells
20. Diedrichs A, Wagner P (2012) Performance analysis of a high-temperature polymer electrolyte membrane fuel cell under mechanical compression control. *ECS Trans* 50:1137–1153
21. Pinar FJ, Rastedt M, Pilinski N et al (2014) Effect of compression cycling on polybenzimidazole-based high-temperature polymer electrolyte membrane fuel cells. *Fuel Cells* 15(1):140–149
22. Rastedt M, Pinar FJ, Bruns N et al (2013) Micro-computed tomography imaging of HT-PEM fuel cells under contact pressure control. *ECS Trans* 58:443–452
23. Rastedt M, Pinar FJ, Wagner P (2014) Impact of contact pressure cycling on non-woven GDLs of HT-PEM fuel cells. *ECS Trans* 64:509–514
24. Bard AJ, Faulkner LR (2001) Electrochemical methods: fundamentals and applications, 2nd edn. Wiley, New York
25. Yuan X-Z, Song C, Wang H et al (2010) Electrochemical impedance spectroscopy in PEM fuel cells: fundamentals and applications, 1st edn. Springer, London
26. Srinivasan S (2006) Fuel cells—from fundamentals to applications. Springer, New York

27. Carrette L, Friedrich KA, Stimming U (2001) Fuel cells—fundamentals and applications. *Fuel Cells* 1:5–39
28. Zhang J, Zhang H, Wu J et al (2013) PEM fuel cell testing and diagnosis. Elsevier, New York, pp 225–241
29. Galbiati S, Baricci A, Casalegno A et al (2013) Degradation in phosphoric acid doped polymer fuel cells: a 6000 h parametric investigation. *Int J Hydrogen Energy* 38:6469–6480
30. Trasatti S (2003) Reaction mechanism and rate determining steps. In: Vielstich W, Gasteiger HA, Lamm A (eds) *Handbook of fuel cells—fundamentals, technology and application*, vol 2. Wiley, Chichester, pp 79–87
31. Sammes N (2006) Fuel cell technology. *Engineering materials and processes*. Springer, London
32. Williams MC (2004) Fuel cell handbook. US Department of Energy, Morgantown
33. Seyfang BC (2009) Simplification and investigation of polymer electrolyte fuel cells using micro-patterned glassy carbon flow fields. PhD, Swiss Federal Institute of Technology Zürich (ETHZ), Zürich
34. Naughton MS, Moradia AA, Kenis PJA (2012) Quantitative analysis of single-electrode plots to understand in-situ behavior of individual electrodes. *J Electrochem Soc* 159:B761–B769
35. Cooper KR, Ramani V, Fenton JM et al (2005) Experimental methods and data analyses for polymer electrolyte fuel cells. Scriber Associates, Southern Pines
36. Orazem ME, Tribollet B (2008) *Electrochemical impedance spectroscopy*, The electrochemical society series. Wiley, Hoboken
37. Orazem ME (2013) Application of impedance spectroscopy to characterize polymer-electrolyte-membrane (PEM) fuel cells. *ECS Trans* 50:247–260
38. Lvovich VF (2012) *Impedance spectroscopy: applications to electrochemical and dielectric phenomena*. Wiley, New Jersey
39. <https://dcode.eifer.uni-karlsruhe.de/D-CODE-Project>
40. Chen C-Y, Lai W-H (2010) Effects of temperature and humidity on the cell performance and resistance of a phosphoric acid doped polybenzimidazole fuel cell. *J Power Sources* 195:7152–7159
41. Andreasen SJ, Jespersen JL, Schaltz E et al (2009) Characterisation and modelling of a high temperature PEM fuel cell stack using electrochemical impedance spectroscopy. *Fuel Cells* 4:463–473
42. Yuan X, Wang H, Sun JC et al (2007) AC impedance technique in PEM fuel cell diagnosis—a review. *Int J Hydrogen Energy* 32:4365–4380
43. Wagner N (2002) Characterization of membrane electrode assemblies in polymer electrolyte fuel cells using a.c. impedance spectroscopy. *J Appl Electrochem* 32:859–863
44. Paganin VA, Oliveira CLF, Ticianelli EA et al (1998) Modelistic interpretation of the impedance response of a polymer electrolyte fuel cell. *Electrochim Acta* 43:3761–3766
45. Springer TE, Zawodzinski TA, Wilson MS et al (1996) Characterization of polymer electrolyte fuel cells using AC impedance spectroscopy. *J Electrochem Soc* 143:587–598
46. Andreasen SJ, Vang JR, Kær SK (2011) High temperature PEM fuel cell performance characterisation with CO and CO₂ using electrochemical impedance spectroscopy. *Int J Hydrogen Energy* 36:9815–9830
47. Zhang J, Tang Y, Song C et al (2007) Polybenzimidazole-membrane-based PEM fuel cell in the temperature range of 120–200 °C. *J Power Sources* 172:163–171
48. Boillot M, Bonnet C, Jatroudakis N et al (2006) Effect of gas dilution on PEM fuel cell performance and impedance response. *Fuel Cells* 6:31–37
49. Pinar Pérez FJ, Pilinski N, Rastedt M et al (2015) Performance of a high-temperature PEM fuel cell operated with oxygen enriched cathode air and hydrogen from synthetic reformat. *Int J Hydrogen Energy* 40(15):5432–5438
50. Kocha SS, Yang JD, Yi JS (2006) Characterization of gas crossover and its implications in PEM fuel cells. *AIChE J* 52:1916–1925
51. Cooper KR (2008) In situ PEMFC fuel crossover & electrical short circuit measurement. *Fuel Cell Magazine* August/September, pp 34–35
52. Zhang J, Xie Z, Zhang J et al (2006) High temperature PEM fuel cells. *J Power Sources* 160:872–891
53. Vengatesan S, Fowler MW, Yuan X-Z et al (2011) Diagnosis of MEA degradation under accelerated relative humidity cycling. *J Power Sources* 196:5045–5052
54. Parrondo J, Mijangos F, Rambabu B (2010) Platinum/tin oxide/carbon cathode catalyst for high temperature PEM fuel cell. *J Power Sources* 195:3977–3983
55. Li QF, Rudbeck HC, Chromik A et al (2010) Properties, degradation and high temperature fuel cell test of different types of PBI and PBI blend membranes. *J Membr Sci* 347:260–270
56. Bai Z, Bello M, Chang H et al (2009) *Polymer membranes for fuel cells*. Springer, New York
57. Lobato J, Cañizares P, Rodrigo MA et al (2010) Study of the influence of the amount of polybenzimidazole-H₃PO₄ in the catalytic layer of a high temperature proton exchange membrane fuel cell. *Int J Hydrogen Energy* 35:1347–1355
58. Su H, Jao T-C, Pasupathi S et al (2014) A novel dual catalyst layer structured gas diffusion electrode for enhanced performance of high temperature proton exchange membrane fuel cell. *J Power Sources* 246:63–67
59. Orfanidi A, Daletou MK, Sygellou L et al (2013) The role of phosphoric acid in the anodic electrocatalytic layer in high temperature PEM fuel cells. *J Appl Electrochem* 43:1101–1116

60. Lindström RW, Kortsdottir K, Wesselmark M et al (2010) Active area determination of porous Pt electrodes used in polymer electrolyte fuel cells: temperature and humidity effects. *J Electrochem Soc* 157:B1795–B1801
61. Vidakovic T, Christov M, Sundmacher K (2007) The use of CO stripping for in situ fuel cell catalyst characterization. *Electrochim Acta* 52:5606–5613
62. Wu J, Yuan XZ, Wang H et al (2008) Diagnostic tools in PEM fuel cell research: part I. Electrochemical techniques. *Int J Hydrogen Energy* 33:1735–1746
63. Lobato J, Cañizares P, Rodrigo MA et al (2010) Study of the catalytic layer in polybenzimidazole-based high temperature PEMFC: effect of platinum content on the carbon support. *Fuel Cells* 10:312–319
64. Schneider IA, Kramer D, Wokaun A et al (2007) Effect of inert gas flow on hydrogen underpotential deposition measurements in polymer electrolyte fuel cells. *Electrochem Commun* 9:1607–1612
65. Ferrier D, Kinoshita K, McHardy J et al (1975) Hydrogen adsorption on platinum in hot concentrated phosphoric acid. *J Electroanal Chem Interfacial Electrochem* 61:233–237
66. Engl T, Waltar KE, Gubler L et al (2014) Second cycle is dead: advanced electrode diagnostics for high-temperature polymer electrolyte fuel cells. *J Electrochem Soc* 161:F500–F505
67. Jespersen JL, Kær SK (2007) Break-in and Performance Issues on a Single Cell PBI-based PEM Fuel Cell. Interantional workshop on degradation issues of fuel cells Crete, Greece:Poster
68. Tingeloeff T, Ihonen JK (2009) A rapid break-in procedure for PBI fuel cells. *Int J Hydrogen Energy* 34:6452–6456
69. Maier W, Arlt T, Wippermann K et al (2012) Correlation of synchrotron X-ray radiography and electrochemical impedance spectroscopy for the investigation of HT-PEFCs. *J Electrochem Soc* 159:F398–F404
70. Andreasen SJ, Kær SK (2012) Analysis of high temperature polymer electrolyte membrane fuel cell impedance during break-in. *Fuel Cells 2012 Science and Technology:Oral Publication*
71. Yuan X, Sun JC, Blanco M et al (2006) AC impedance diagnosis of a 500 W PEM fuel cell stack. Part I: stack impedance. *J Power Sources* 161:920–928
72. Kondratenko MS, Gallyamov MO, Khokhlov AR (2012) Performance of high temperature fuel cells with different types of PBI membranes as analysed by impedance spectroscopy. *Int J Hydrogen Energy* 37:2596–2602
73. Kwon K, Park JO, Yoo DY et al (2009) Phosphoric acid distribution in the membrane electrode assembly of high temperature proton exchange membrane fuel cells. *Electrochim Acta* 54:6570–6575
74. Parrondo J, Rao CV, Ghattly SL et al (2011) Electrochemical performance measurements of PBI-based high-temperature PEMFCs. *Int J Electrochem* 2011:1–8
75. Boaventura M, Mendes A (2010) Activation procedures characterization of MEA based on phosphoric acid doped PBI membranes. *Int J Hydrogen Energy* 35:11649–11660
76. Jalani NH, Ramani M, Ohlsson K et al (2006) Performance analysis and impedance spectral signatures of high temperature PBI-phosphoric acid gel membrane fuel cells. *J Power Sources* 160:1096–1103
77. Araya SS, Andreasen SJ, Kær SK (2012) Experimental characterization of the poisoning effects of methanol-based reformate impurities on a PBI-based high temperature PEM fuel cell. *Energies* 5:4251–4267
78. Andreasen SJ, Mosbæk R, Vang JR et al (2010) EIS characterization of the poisoning effects of CO and CO₂ on a PBI based HT-PEM fuel cell. In: *ASME 2010 eighth international fuel cell science, engineering and technology conference*, New York, p 10
79. Jhong H-RM, Brushett FR, Yin L et al (2012) Combining structural and electrochemical analysis of electrodes using micro-computed tomography and a microfluidic fuel cell. *J Electrochem Soc* 159: B292–B298
80. James JP (2012) Micro-computed tomography reconstruction and analysis of the porous transport layer in polymer electrolyte membrane fuel cells. Master, Queen's University, Kingston
81. Runte M (2012) Untersuchung des Einflusses verschiedener Anpressdrücke auf Hochtemperatur Polymerelektrolytmembranbrennstoffzellen mittels μ -Computertomographie. Bachelor, Fachhochschule Münster, NEXT ENERGY EWE-Forschungszentrum für Energietechnologie e.V., Münster, Oldenburg
82. SkyScan NV (2005) Desktop X-ray microtomograph. SkyScan Instruction Manual Aartselaar, Belgium
83. Nitta I, Hottinen T, Himanen O et al (2007) Inhomogeneous compression of PEMFC gas diffusion layer: part I. Experimental. *J Power Sources* 171:26–36
84. Nitta I, Himanen O, Mikkola M (2008) Contact resistance between gas diffusion layer and catalyst layer of PEM fuel cell. *Electrochem Commun* 10:47–51
85. Nitta I (2008) Inhomogeneous compression of PEMFC gas diffusion layers. Dissertation, University of Technology, Helsinki
86. Lee W, Ho C-H, Van Zee JW et al (1999) The effects of compression and gas diffusion layers on the performance of a PEM fuel cell. *J Power Sources* 84:45–51
87. Ge J, Higier A, Liu H (2006) Effect of gas diffusion layer compression on PEM fuel cell performance. *J Power Sources* 159:922–927
88. Kleemann J, Finsterwalder F, Tillmetz W (2009) Characterisation of mechanical behaviour and coupled electrical properties of polymer electrolyte membrane fuel cell gas diffusion layers. *J Power Sources* 190:92–102
89. Chang WR, Hwang JJ, Weng FB et al (2007) Effect of clamping pressure on the performance of a PEM fuel cell. *J Power Sources* 166:149–154
90. Mathias MF, Roth J, Fleming J et al (2003) Diffusion media materials and characterisation. In:

- Vielstich W, Gasteiger HA, Lamm A (eds) Handbook of fuel cells—fundamentals, technology and application, vol 3. Wiley, New York, pp 517–537
91. Karwey M (2012) Untersuchung der mechanischen Belastung von Brennstoffzellenmembranen in Testzellen durch auftretenden Anpressdruck. Bachelor, Fachhochschule Südwestfalen and Next Energy, Oldenburg
 92. Molleo M, Qian G, Chen X et al (2013) Mechanical property improvements in PBI membranes. In: 4th European PEFC and H₂ forum 2013, Luzerne, Switzerland 2nd to 5th of July 2013
 93. Wilkinson DP, St-Pierre J (2003) Durability. In: Vielstich W, Gasteiger HA, Lamm A (eds) Handbook of fuel cells—fundamentals, technology and applications, vol 3. Wiley, New York, pp 611–626
 94. Borup R, Meyers J, Pivovarov B et al (2007) Scientific aspects of polymer electrolyte fuel cell durability and degradation. *Chem Rev* 107:3904–3951
 95. Wu J, Yuan XZ, Martin JJ et al (2008) A review of PEM fuel cell durability: degradation mechanisms and mitigation strategies. *J Power Sources* 184:104–119
 96. Hu J, Zhang H, Zhai Y et al (2006) Performance degradation studies on PBI/H₃PO₄ high temperature PEMFC and one-dimensional numerical analysis. *Electrochim Acta* 52:394–401
 97. Liu G, Zhang H, Hu J et al (2006) Studies of performance degradation of a high temperature PEMFC based on H₃PO₄-doped PBI. *J Power Sources* 162:547–552
 98. Zhang H, Zhai Y, Liu G et al (2007) Degradation study on MEA in H₃PO₃/PBI high-temperature PEMFC life test. *J Electrochem Soc* 154:B72–B76
 99. Oono Y, Sounai A, Hori M (2009) Influence of the phosphoric acid-doping level in a polybenzimidazole membrane on the cell performance of high-temperature proton exchange membrane fuel cells. *J Power Sources* 189:943–949
 100. Wannek C, Kohnen B, Oetjen HF et al (2008) Durability of ABPBI-based MEAs for high temperature PEMFCs at different operating conditions. *Fuel Cells* 8:87–95
 101. Li Q, Jensen JO, Savinell RF et al (2009) High temperature proton exchange membranes based on polybenzimidazoles for fuel cells. *Prog Polym Sci* 34:449–477
 102. Schmidt TJ (2006) Durability and degradation in high-temperature polymer electrolyte fuel cells. *ECS Trans* 1:19–31
 103. Zhang S, Yuan X, Wang H et al (2009) A review of accelerated stress tests of MEA durability in PEM fuel cells. *Int J Hydrogen Energy* 34:388–404
 104. Aarhaug A (2011) Assessment of PEMFC durability by effluent analysis. PhD, Norwegian University of Science and Technology, Trondheim
 105. Spornjak D, Fairweather J, Mukundan R et al (2012) Influence of the microporous layer on carbon corrosion in the catalyst layer of a polymer electrolyte membrane fuel cell. *J Power Sources* 214:386–398
 106. Tang H, Qi Z, Ramani M et al (2006) PEM fuel cell cathode carbon corrosion due to the formation of air/fuel boundary at the anode. *J Power Sources* 158:1306–1312

Christian Siegel, Sebastian Lang, Ed Fontes,
and Peter Beckhaus

18.1 Introduction

Fuel cells are considered as a candidate to power a variety of electrical applications. In the last decade, the fuel cell industry made significant progress in terms of product development and cost reduction. Fuel cell systems were established in a number of markets where they are now recognized as a better technology option than conventional internal combustion engine generators. As reported by [1], in 2012 the shipments of fuel cell systems continued to grow, almost doubling versus 2011 and reaching a total of 45,700 units. The year 2013 again showed a growth for the industry with shipments approaching 67,000 units. From the various types of fuel cells, the polymer electrolyte membrane (PEM) fuel cell is the dominant one in terms of

units shipped. This technology is well suited for applications from the watt scale to the megawatt scale including microcombined heat and power (mCHP) units for residential use, power units for larger buildings, and automotive applications.

To continuously increase the number of shipping units, improvement of all components and general cost reductions are necessary to make this technology more attractive and cost competitive with current energy conversion devices. Open questions related to the layout of key components still persist. There is a lack of information available on the internal behavior of a working fuel cell since it is complicated to directly measure internal quantities distributions. This fact has prompted researchers to develop various invasive and noninvasive measuring techniques and fuel cell models. The purpose of modeling and simulation is usually to get an intuitive understanding for a fuel cell, which can be obtained by solving the model equations for many different conditions and for different formulated hypotheses. When such an understanding has been reached, fuel cell models can be used for design optimization, to continuously improve the layout of all components, to adapt operating schemes as controlled start-up and shut-down procedures, and for designing control systems for fuel cells. The main benefit of modeling and simulations is the shorter development time made possible by the reduction of the number of time demanding trials and prototypes.

C. Siegel (✉)

Siegel Schleimer Ingénieurs-conseils SARL, 150-159,
rue Waassertrap, Belvaux L-4408, Luxembourg
e-mail: christian.siegel@siegelschleimer.lu

S. Lang

Technische Universität Darmstadt, Fachgebiet
Thermische Verfahrenstechnik, Otto-Berndt-Straße 2,
Darmstadt 64287, Germany

E. Fontes

COMSOL AB, Tegnérgatan 23, Stockholm SE-111 40,
Sweden

P. Beckhaus

ZBT GmbH - Zentrum für BrennstoffzellenTechnik,
Carl-Benz-Straße 201, Duisburg 47057, Germany

Various fuel cell modeling and simulation reviews can be found in literature and elucidate the modeling approaches, strategies, computational single-, and multi-domains, governing equations, boundary conditions, initial conditions, simplifications, and commonly used assumptions [2–18]. This work reviews the current status of phosphoric acid fuel cell (PAFC) and HT-PEM fuel cell modeling and simulation.

18.2 State-of-the-Art Technologies

18.2.1 Phosphoric Acid Fuel Cell

Anahara [19, 20], Shibata and Watanabe [21], Nymoer [22], Hojo et al. [23], Vanhanen et al. [24], Whitaker [25], Kasahara et al. [26], Spiegel and Preston [27], and Sammes et al. [28] highlighted the PAFC fundamentals and reported experiences of PAFC field trials all over the world. Doosan [29] (formerly ClearEdge Power) sells a system in the 400 kWel range (formerly UTC Power—United Technologies Corporation). Fuji Electric [30] and N2telligence [31] continue to develop the technology and offer a 100 kWel system which is able to supply electrical power, heat, and cooling using absorber/adsorber systems. Moreover, the system can be used for preventive fire protection through oxygen reduction using the low oxygen exhaust of the fuel cell. It is expected that several dozen units are installed in Japan and Germany operating with an electrical efficiency of 42 % (up to 48 % when operating on hydrogen as anode gas) and a thermal efficiency up to 50 %. The design lifetime of such a system is 15 years with one stack replacement after 60,000 h and an availability of ≥ 95 % of the runtime.

18.2.2 HT-PEM Fuel Cells

Polybenzimidazole (PBI) doped with phosphoric acid has been proposed as a proton conducting membrane being able to operate at 120–170 °C [32–34]. Extensive research and development efforts continuously improve the performance,

durability, and long-term stability of the PBI/H₃PO₄ membrane electrode assembly (MEA), sealings, and bipolar-plate material. Today, single fuel cells and systems are commercially available [35–37]. According to [1], HT-PEM fuel cell related automotive activities are reported by the manufacturer Serenergy, Denmark [38], who develops a version of the QBEAK lightweight city car. HT-PEM fuel cell mCHP units are available from Elcore, Germany [39]. More details about the status of the technology as well as cost targets are reviewed in [40–45].

18.3 Literature Review

18.3.1 PAFC Modeling and Simulation

18.3.1.1 PAFC System Level

Sugano et al. [46] reported the analysis of the dynamic behavior of a PAFC stack cooling systems. Miki and Shimizu [47] reported the results of the dynamic characteristics of a fuzzy control based stack cooling system. An analytical, exergetic, and thermoeconomic analysis of a 200 kWel PAFC power plant was presented by Kwak et al. [48]. In [49], a novel optimization tool was developed that realistically described and optimized the performance of a PAFC system. Zhang et al. [50] presented an analytical model to optimize several parameters using a thermodynamic-electrochemical analysis. In [51], a dynamic model was developed to simulate a PAFC system and associated components.

18.3.1.2 PAFC Cell and Stack Level

In [52], a schematic structure for the catalyst layer was presented. The authors introduced two kinds of pores, namely primary pores (<0.1 mm) and secondary pores (>0.1 mm). It was found that the electrolyte within the catalyst layer mainly resides in the primary pores. The secondary pores are mainly for gas transport, and a very thin electrolyte film exists and covers the secondary pore surface. Yang et al. [53] and Yang [54] presented a porous gas diffusion electrode model considering the microstructure

characteristics of the catalyst layer. In [55], a PAFC cooling system was evaluated and mathematical relations for the overall heat transfer coefficient as a function of the stack clamping pressure and Reynolds number developed. Yoshioka et al. [56, 57] developed a mathematical model for the evaporation and condensation of phosphoric acid. This model was able to predict the evaporation and condensation rates of phosphoric acid under various operating conditions. In [58], a model which simulates both direct current (DC) and alternate current (AC) responses of the cathode side with various oxidant compositions was developed and applied to the in situ analysis of the laboratory cell. The catalyst layer was modeled as a slab agglomerate which is a mixture of electrolyte, catalyst particle dispersed carbon powder, and polytetrafluoroethylene (PTFE) powder. Maggio [59] published a model to describe the behavior of the cathode side of a PAFC. The equations take the activation and diffusional problems into account and an agglomerate cathode layer structure was used. Choudhury et al. [60] presented a two-dimensional, steady-state PAFC model to study and understand the relationship between the performance of the fuel cell and various design options. It was considered that the carbon particles containing catalyst formed small agglomerates that are completely flooded with phosphoric acid. The interagglomerate space is only partially filled with electrolyte due to the presence of PTFE. Oxygen and hydrogen can diffuse through the interagglomerate space and can reach the agglomerate surface. In [61], a dynamic two-dimensional model for simulating the cathode side of a PAFC was developed. The model was solved to study the impact of various parameters such as the Tafel slope and diffusivity on the step response of the fuel cell. The effect of partial pressure variation in bulk gas at the cathode side was also analyzed. In [62], a mathematical model was developed and used to predict the performance of direct propane phosphoric acid (PPAFC) fuel cells. Choudhury and Rengaswamy [63] presented a study to characterize and diagnose the cathode side of a PAFC by electrochemical impedance spectroscopy (EIS)

technique and by a mathematical model approach. For diagnostics, the EIS data was proposed to be analyzed using a dynamic distributed parameter model. The flooded spherical agglomerate characterization was employed for the experimental characterization. Zervas et al. [64] published a three-dimensional PAFC model to investigate the effects of process parameters on the performance. The model accounted for the local distribution of the concentration of reactant and product gases in the anode and cathode flow regions and the electrical potential distribution on the surface of the cathode electrode. In [65], the numerical analyses included the behavior of evaporation and condensation of phosphoric acid. The behavior of gas flow and heat transfer was conducted for the developed cell model. Hirata et al. [66] investigated the phosphoric acid reduction by the evaporative and condensational dissipation on the effect of liquid phase migration by numerical analysis. The cell model consisted of a porous electrode substrate and matrix with conditions that correspond to experimental investigations. In [67], different experimental and analytical techniques were employed to generate rule sets for identification of the phosphoric acid drying and dilution phenomena.

18.3.2 HT-PEM Fuel Cell Modeling and Simulation

18.3.2.1 HT-PEM Fuel Cell System Level

Korsgaard et al. [68] developed a simple semi-empirical model to describe and support their experimental data. A control-oriented, one-dimensional model was developed in [69], addressing the transient responses of a HT-PEM fuel cell. Andreasen and Kær [70] developed a dynamic model to simulate the temperature behavior of a fuel cell stack. Korsgaard et al. [71, 72] presented a complete model of a system consisting of the fuel cell stack, steam-reforming reactor, burner, heat reservoir, and other auxiliary equipment. The model setup allowed the evaluation of static system integration and dynamical control strategies. Arsalis et al. [73] presented another thermodynamic,

kinetic, and geometric model of a mCHP. In [74], a performance analysis on the basis of a simulation model and experimental data of a 1 kWel mCHP system was presented. The system was composed of a steam reforming unit that can be operated with natural gas. The performance was predicted by means of a zero-dimensional semi-empirical model. In [75], a mCHP system has been modeled and simulated. The modeling aimed to fit the hydrogen production to the demand of the fuel cell to provide 1 kWel, maintaining a carbon monoxide (CO) concentration always lower than 30,000 ppm. Another fuel cell system model was presented in [76]. Conventional operational strategies, such as heat-led and electricity-led, were applied to the simulated system to investigate their performance characteristics. Authayanun et al. [77] presented an interesting study comparing LT-PEM and HT-PEM fuel cell systems with a glycerol reforming process for stationary applications. The system models included all important subsystems. Jannelli et al. [78] analyzed LT-PEM and HT-PEM fuel cell mCHP systems by evaluating the energy balances. In [79], a mathematical model was developed to investigate the theoretical performance of HT-PEM fuel cells fueled by reformat gas. A similar approach was used in [80].

18.3.2.2 HT-PEM Fuel Cell and Stack Level

Cheddie and Munroe [81–85] published one-, two-, and three-dimensional models accounting for different operating conditions, membrane and catalyst layer properties, layout optimization, gas diffusion, and gas solubility into the aqueous phase. Steady-state and dynamic three-dimensional HT-PEM fuel cell models were presented by Peng and Lee [86, 87]. The authors demonstrated that thermal management strongly affects the performance, and discussed key optimization parameters for performance improvements. Wang et al. [88] investigated the transient evolution of the CO poisoning effect using a one-dimensional model. Scott et al. [89] proposed a one-dimensional model to simulate the effects of catalyst loading and the Pt/C-ratio

on the performance. Various HT-PEM fuel cell models were presented in [90–92], addressing the fluid-(gas)-, solid-phase temperature, fluid-flow distribution, and the PBI/H₃PO₄ sol-gel membrane conductivity. Localized fluid-structural interactions (LFSI) were discussed in [93]. Ubong et al. [94] developed a single-channel three-dimensional model in which the catalyst layer was assumed to be infinitely thin and the electrochemical reactions were described using an agglomerate approach. A complete three-dimensional model was developed and solved in [95], highlighting catalyst layer kinetics. Segmented current density measurements of a HT-PEM fuel cell were presented in [96, 97] and compared to simulations. In [98], a model for predicting the dynamic temperature of a HT-PEM fuel cell stack was presented. The model was developed to test different thermal control strategies before implementing them in a system. Scholta et al. [99] investigated different design concepts for external cooling using modeling techniques and measurements. The experiments proved the feasibility of the external cooling design and showed that the temperature gradients within the active area are below 15 K under typical operating conditions. In [100], a zero-dimensional isothermal model equation was developed and expressed as a semi-empirical relationship for cell potential as a function of current density. Shamardina et al. [101] presented a simple and quickly solvable steady-state, isothermal, pseudo two-dimensional model that accounted for crossover effects. An analytical HT-PEM fuel cell model, published by Kulikovskiy et al. [102], included important basic kinetic and transport parameters. A two-dimensional isothermal model was published by Sousa et al. [103], who treated the catalyst layer as spherical catalyst agglomerates with porous interagglomerate spaces. The model was used to study the influence of the catalyst layer properties on the performance. A work that deals with the CO poisoning and its dynamics was presented in [104]. Sousa et al. [105] presented a non-isothermal model and investigated the influence of different modeling geometries on the performance and found that

the along-the-channel model did not represent the general performance trend. A theoretical-practical study was published in [106], presenting the influence of the flow-field geometry. Sousa et al. [107] presented a dynamic two-dimensional non-isothermal model to simulate the transient response of a HT-PEM fuel cell. Lobato et al. [108] highlighted the application of various artificial neural networks to predict the fuel cells results on the basis of several properties that define a gas diffusion layer (GDL). Jiao et al. [109, 110] presented a three-dimensional model and investigated the effects of operating temperature, phosphoric acid doping level, inlet relative humidity, stoichiometry ratios of the feed gases, operating pressure, and the carbon monoxide poisoning on the HT-PEM fuel cell performance. In [111], a HT-PEM fuel cell was modeled and the predicted values were compared to measurements for typical operating conditions. The simulated current density distribution and the fluid-(gas)-, and the solid-phase temperature distributions were also analyzed. The Arrhenius approach was found to be valid within a defined temperature range and over-predicts the membrane conductivity at a higher solid-phase temperature. Moreover, the influence of the fluid-(gas)-phase temperature on the solid-phase temperature was investigated. Two three-dimensional models (an agglomerate model and pseudohomogeneous model) were presented in [112], focusing on different approaches for modeling HT-PEM fuel cells. A one-dimensional model for analyzing the influence of CO, carbon dioxide, and methane, which would be present in a reformat gas, considered in terms of the effect at the anode polarization and kinetics behavior was discussed in [113]. Kurz [114] presented a method for modeling and simulation of a HT-PEM fuel cell using a coupled two-, and three-dimensional approach. Siegel et al. [115] presented segmented solid-phase temperature measurements for three types of flow-fields. Computational fluid dynamics calculations supported the observed distributions using a three-dimensional model. A one-dimensional model was used in [116] to study the morphological properties of

HT-PEM fuel cell components for effective membrane hydration. Falcucci et al. [117] analyzed different gas flow channel designs using a three-dimensional model addressing pressure losses, gas distribution over the electrode area, and residence time with focus on channel hydraulic diameter, active surface ratio, and gas path. Kvesić et al. [118] and Kvesić [119] published a three-dimensional model of a five cell short stack. Simulation results were compared to segmented measurements of temperature and current density and showed a good agreement. Lüke et al. [120] presented a performance analysis of a HT-PEM fuel cell stack, addressing temperature and current density measurements acquired while using pure hydrogen and synthetic reformat as the anode gas. A three-dimensional model was used for validation purposes. The authors found that oxygen depletion was the primary cause of the uneven current density distribution. Moreover, it was shown that homogenization can be achieved without a reduction of the stack voltage if the stack is operated with reformat when switching from co-flow to counter-flow configuration. Chippar and Ju [121] presented a three-dimensional non-isothermal model of a HT-PEM fuel cell to investigate various key thermal aspects. Park and Min [122] presented a non-isothermal dynamic model of a HT-PEM fuel cell. In the model, dynamic conservation equations and electrochemical reaction were solved within a simplified quasi-three-dimensional geometry. Reddy and Jayanti [123] investigated the viability of different heat removal strategies. Calculations, partly done using computational fluid dynamics simulations showed that a combination of excess stoichiometric factor and forced draft appeared to provide the optimal strategy for the thermal management. The authors also included the heat removal by natural convection and radiation. In [124], studies about the influence of the flow field (straight, serpentine, pin-in, interdigitated) on the performance of a HT-PEM fuel cell using a three-dimensional model were presented. All transport phenomena were taken into account except the species crossover through the membrane. The cathode catalyst layer was

treated as spherical catalyst agglomerates with porous interagglomerate spaces, filled with a mixture of electrolyte and PTFE. It was shown that the dimension and position of the inlet and outlet manifolds had a significant influence on the species distribution and overall performance. In [125], a parametric study of the external coolant system of a HT-PEM fuel cell was published, focusing on the temperature variations within the stack, the number of coolant plates, and the coolant flow. In [126], the effect of CO poisoning with various types of flow-fields was numerically studied. Chippar and Ju [127] published a gas crossover model for a HT-PEM fuel cell. The model considered the dissolution of reactants into electrolyte phase in the catalyst layers and subsequent crossover of reactant gases through the membrane. Furthermore, the model accounted for mixed potentials on the anode side and cathode side. In [128], the effect of GDL compression on the performance was investigated. Simulations were conducted under various displacement clamping conditions to analyze cell deformation characteristics. Furthermore, a computational fluid dynamics model was applied to the deformed cell geometries to study the transport and electrochemical processes during operation. Supra et al. [129] analyzed the temperature distribution in a liquid-cooled HT-PEM fuel cell stack and compared the theoretical results to experimental results. In [130], the bipolar-plates and gas diffusion electrodes were optimized with a two-dimensional geometry. Salomov et al. [131] developed a deterministic model for a woven GDL and a stochastic model for the catalyst layer based on clusterization of carbon particles. They verified that both of the developed models accurately recover the experimental values of the permeability, without any special ad hoc tuning. Moreover, they investigated the effect of catalyst particle distributions inside the catalyst layer on the degree of clusterization and on the microscopic fluid flow, which is relevant for the modeling of degradation. The three-dimensional pore-scale simulations of the fluid flow for the direct numerical calculation of the permeability were performed by the lattice Boltzmann method

(LBM). In [132], a study of water transport in a HT-PEM fuel cell stack was reported. Internal water transport profiles across the membrane and in along-the-channel direction were presented and discussed. Chippar et al. [133] numerically investigated the effects of gas crossover due to membrane pinholes on the performance. The simulation results clearly showed that the presence of pinholes in the membrane significantly disrupts the species, current density, and temperature distributions. In [134], the inlet relative humidity dependence on the performance of a HT-PEM fuel cell was studied by numerical simulations. The water diffusion coefficient in the membrane was considered as an adjustable parameter to fit the experimental water transport data. Oh et al. [135] numerically examined the thermal stress distributions in a HT-PEM fuel cell. A fluid–structure interaction (FSI) method was adopted to simulate the expansion and compression that arises in various components of the MEA during the assembly processes, as well as during operations. In [136], the authors investigated the thermal and water balance as well as the electro-kinetics during the warm-up process of a HT-PEM fuel cell from room temperature up to the desired temperature of 180 °C. A simple analytical dynamic model was derived addressing the boiling phase changing phenomenon in the cathode catalyst layer and cathode GDL. In [137], a generic model was developed, capable of estimating the contact resistance as a function contact pressure at the interface of graphite bipolar-plate and carbon fiber based GDL at different temperatures. Kazdal et al. [138] used a two-dimensional model to simulate the local concentration of phosphoric acid. The model included the vapor–liquid equilibrium of $\text{H}_3\text{PO}_4\text{-H}_2\text{O}$ and evaporation kinetics and set the basis for calculating the locally varying conductivity and other physical properties. By describing the volume expansion behavior of phosphoric acid, it was possible to predict the catalyst particle deactivation due to the electrolyte swelling. Yin et al. [139] presented a three-dimensional non-isothermal of a sulfonated polybenzimidazole (SPBI) membrane and compared the numerical results to published

experimental data. In [140], a one-dimensional model was used to analyze the performance degradation. Oh et al. [141] used a three-dimensional model to study adsorption and desorption processes of CO and hydrogen on the anode platinum (Pt) catalysts.

18.4 Mathematical Modeling of Fuel Cells

18.4.1 Introduction

In chemical reaction engineering, fuel cells are considered as continuous electrochemical reactors that convert chemical energy to electrical energy. Oxidation takes place at the anode and reduction takes place at the cathode, in contrast to thermochemical catalytic reactors where oxidation and reduction takes place at the same active site in a catalyst. The separation of oxidation and reduction to the different electrodes allows for the conversion from chemical to electrical energy. The electrical energy is recovered by conducting the electrons between the anode and cathode through an external circuit where a load is connected. In thermochemical reactors, an exothermic reaction would instead give heat as output. The possibility of separating the oxidation and reduction reactions also introduces the ability to change the free energy of the reactants and products at the electrode interface. This allows for an external control of the activation energy for the reactions by changing the electric potential of the electrodes; see Fig. 18.1 for the example of the reversible electrode reaction [142].

The ability to change the activation energy of the electrodes also introduces the main difference between the modeling of fuel cells and the modeling of thermochemical reactions. In modeling of fuel cells, and in electrochemical cells in general, the electric potential in the electrodes and in the electrolyte has to be introduced as dependent variables. To avoid the sharp gradients across the charged double layer at the electrode–electrolyte interface two different dependent variables are used, one for the electrolyte potential and one for the electrode

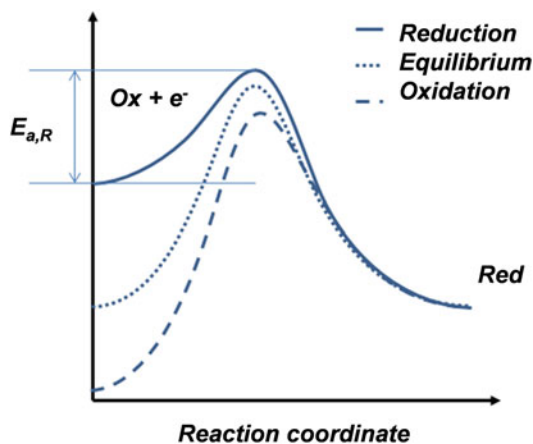


Fig. 18.1 Activation energy for a one-electron transfer reaction as a function of the reaction coordinate. The activation energy contains a contribution from the potential difference across the charged double layer at the electrode–electrolyte interface

potential on each side of the double layer. A discontinuity in potential is introduced instead across this thin charged double layer [142].

18.4.2 Model Equations and Their Origin

The basis for the model equations in fuel cell modeling originate from different laws of conservation, which for detailed models can be combined with constitutive relations, equations for describing reaction kinetics, thermodynamic data, and material properties [13, 143]. In detailed models, the model variables, referred to as dependent variables, are described along space and time variables, so-called independent variables. The conservation equations and the constitutive relations result in equations that describe a change in the modeled quantities, i.e., differential equations. If there is more than one independent variable, for example, time, and one space variable, the derivatives are taken along one independent variable at a time. These are called partial derivatives, and the equations are therefore referred to as partial differential equations (PDEs). In less detailed models, averaging is done along the space variables and the

equations of change are then described along the time axis only. This is often the case for system modeling where the fuel cell model is described as a coupled system of ordinary differential equations (ODEs) with time being the only independent variable. For steady-state models, the time derivatives vanish and the coupled system of ODEs becomes an algebraic system of equations. Below follows a short introduction to the model equations for a microscopic level of detail (not at a molecular level) including space and time dependency. As mentioned, the model equations can be simplified and averaged to obtain simpler models described by ODEs or algebraic equations for system modeling.

18.4.3 Fundamental Fuel Cell Modeling Equations

18.4.3.1 Material Balance

Fuel cell electrodes are porous gas diffusion electrodes, which are usually described in modeling using homogenization [144]. This means that the pore electrolyte and the electrode material share the same geometrical domain and the electric potential in the electronic and ionic conductors are present in the same geometrical domain. Also the concentration variables for the species in the gas phase, the species dissolved in the electrolyte, and the constituents of the electrolyte may be present in the same geometrical domain defined by the gas diffusion electrodes. The electrochemical reactions that occur at the interface between the pore electrolyte and the electrode are introduced as sources or sinks in the material and current balances. To calculate the chemical composition in the electrolyte and in the gas phase in every point in space in a geometrical domain, material balances for each of the species in the solution as well as a conservation of mass for the whole have to be defined. The conservation of mass for the whole solution may eliminate one of the species material balances, which for a dilute solution usually is the solvent's material balance. The constitutive relations in the electrolyte may be the

Nernst–Planck equations that describe the flux of chemical species through diffusion, migration, and convection, see the equations below. The material balance includes the accumulation or depletion term, the difference between the flux in and out in an infinitesimally small volume element (second term), and the production or consumption terms for species in reactions (third term):

$$\frac{\partial c_i}{\partial t} + \nabla \cdot \mathbf{N}_i - R_i = 0 \quad (18.1)$$

The Nernst–Planck equation describes the flux for each species:

$$\mathbf{N}_i = -D_i \nabla c_i - z_i m_i c_i \nabla \phi_i + c_i \mathbf{u} \quad (18.2)$$

The first term represents the flux by diffusion, the second term the flux by migration of ions in the electric field, while the third term represents convective flux. Combining the material balance and the Nernst–Planck equation yields the model equation for each species material balance:

$$\frac{\partial c_i}{\partial t} + \nabla \cdot (-D_i \nabla c_i - z_i m_i c_i \nabla \phi_i + c_i \mathbf{u}) - R_i = 0 \quad (18.3)$$

In the gas phase the Maxwell–Stefan equations can be used to describe the interaction between all species in the gaseous mixture [143]. Out of the various diffusion models (mixture average, Maxwell–Stefan, Fick's law), the computationally expensive Maxwell–Stefan formulation employs the most detailed diffusion model but it requires that the multicomponent Maxwell–Stefan diffusivities of all component pairs are known [145].

18.4.3.2 Charge and Current Balance

The electrochemical reactions and the migration of ions introduce the electric potential as a dependent variable. The electric potential is usually treated with two independent variables and a discontinuity is introduced to avoid the sharp gradients in the charged double layer between the electronic and ionic conductor. Charge and current balances give the equations for the

electric potential. In the electrolyte, the charge balance is usually the electroneutrality condition (a simplification of Poisson's equation) which together with the material balances for the ions and Faraday's law results in a balance of current:

$$\sum_i z_i c_i = 0 \quad (18.4)$$

The only part of the electrolyte where there is substantial deviation from electroneutrality is in the charged double layer. However, this problem is avoided by introducing the abovementioned discontinuity in the electric potential. For electrolytes with constant composition, a conservation of current and Ohm's law form the model equations. This equation can be derived from Faraday's law and the electroneutrality condition. Faraday's law gives the current density vector as a function of the transport of ions:

$$\mathbf{j} = F \sum_i z_i \mathbf{N}_i \quad (18.5)$$

In combination with the Nernst–Planck equation the following equation is obtained:

$$\begin{aligned} \mathbf{j} = F \sum_i (-z_i D_i \nabla c_i - z_i^2 m_i c_i \nabla \phi_l) \\ + \mathbf{u} F \sum_i (z_i c_i) \end{aligned} \quad (18.6)$$

In a perfectly mixed and electroneutral electrolyte, the diffusion term vanishes since there are no concentration gradients and the convective term, last term on the right-hand side, vanishes due to the electroneutrality condition:

$$\mathbf{j} = -F \sum_i (z_i^2 m_i c_i) \nabla \phi_l \quad (18.7)$$

Finally, the model equation for the balance of current for a perfectly mixed and electroneutral electrolyte becomes:

$$\nabla \cdot (-\sigma_l \nabla \phi_l) + F \sum_k n_k R_k = 0 \quad (18.8)$$

An analogous equation also describes the conservation and conduction of current in the electrodes electronic conducting material:

$$\nabla \cdot (-\sigma_s \nabla \phi_s) - F \sum_k n_k R_k = 0 \quad (18.9)$$

The solution of these equations gives the potential distribution in the electrodes and in the electrolyte. The reaction terms couple the electrolyte and electrode potentials through the reaction kinetics, which are described by Arrhenius expressions for both forward and backward reactions at one electrode surface for a one-electron charge transfer reaction. These terms become a Butler–Volmer expression by introducing the contribution of the electric potential difference at the electrode surface to the activation energy. This results in the following expression for the local charge transfer current density in the electrode [142]:

$$i_{ct} = i_0 \left(\frac{c_{\text{Red}}}{c_{\text{Red,eq}}} e^{\left(\frac{(1-\beta)F((\phi_s - \phi_l) - \Delta\phi_{\text{eq}})}{RT} \right)} - \frac{c_{\text{Ox}}}{c_{\text{Ox,eq}}} e^{\left(\frac{\beta F((\phi_s - \phi_l) - \Delta\phi_{\text{eq}})}{RT} \right)} \right) \quad (18.10)$$

The charge transfer current density is related to the reaction term through Faraday's law:

$$R_k = \frac{S_a}{n_k F} i_{ct,k} \quad (18.11)$$

The overpotential is defined as follows:

$$\eta = \phi_s - \phi_l - \Delta\phi_{\text{eq}} \quad (18.12)$$

In the active parts of a gas diffusion electrode, the pore electrolyte is contained in the small pores between the catalyst particles and the carbon support particles. The larger pores are then filled with gas. Gas has to diffuse through a thin film of electrolyte and in the small pores that contain the pore electrolyte. This introduces an additional mass transfer resistance that can be described with an agglomerate model. Such a model is described with a diffusion-reaction equation for the gaseous species dissolved in the pore electrolyte with the charge transfer reactions as source or sink. The solution to this reaction diffusion model is used to calculate new reaction terms that replace the reaction terms in the balance of charge, material, mass, and energy. These models can often be solved analytically for steady-state if the reactions are of

first or second order with respect to the participating species. This means that an analytical expression is obtained that replaces the reaction terms in the mathematical model, at least for steady-state models [146].

18.4.3.3 Momentum Balance

The flow in the gas channels and in the porous gas diffusion electrodes is described by the equations for the conservation of momentum and conservation of mass in the gas phase. The solution of these equations results in the velocity and pressure fields in the cell. The Navier–Stokes equations are mostly used for the gas channels while Darcy’s law may be used for the gas flow in the GDL, the microporous layer (MPL), and the catalyst layer [147]. Darcy’s law describes the flow where the pressure gradient is the major driving force and where it is mostly influenced by the frictional resistance within the pores [145]. Alternatively, the Brinkman equations can be used to compute the fluid velocity and pressure field in porous media. It extends the Darcy law to describe the momentum transport by viscous shear, similar to the Navier–Stokes equations. The velocity and pressure fields are continuous across the interface of the channels and the porous domains. In the presence of a liquid phase in the pore electrolyte, two-phase flow models may be used to account for the interaction between the gas phase and the liquid phase in the pores. When calculating the fluid flow through the inlet and outlet feeders of a large fuel cell stack, the Reynolds-averaged Navier–Stokes (RANS), k - ω , or k - ϵ turbulence model equations should be used due to the presence of turbulence.

Note that an electrochemical reaction consumes gaseous species that disappear from the gas phase and form species dissolved in the liquid electrolyte. For example, hydrogen oxidation forms hydrogen ions, where the net reaction is then a consumption of hydrogen in the anode gas in the gas pores. This means that the electrochemical reactions are mass sinks or sources in the mass balances for the gaseous mixture in the pores. In the case of hydrogen oxidation, the

continuity equation at steady-state for the gas mixture in combination with Faraday’s law is

$$-\nabla \cdot (\rho \mathbf{u}) = \frac{S_a M_{H_2}}{2F} i_{ct} \quad (18.13)$$

When using Darcy’s law, the equation above is rewritten in the following form:

$$\mathbf{u} = -\frac{k_p}{\mu} \nabla p \quad (18.14)$$

$$-\nabla \cdot \left(\rho \left(-\frac{k_p}{\mu} \nabla p \right) \right) = \frac{S_a M_{H_2}}{2F} i_{ct} \quad (18.15)$$

18.4.3.4 Energy Balance

The temperature distribution in the fuel cell is described by the equations for the conservation of energy, which results in the heat transfer equations with heat production from the electrochemical reactions and other sources and sinks (ohmic and protonic heating, irreversible reaction heat, and reaction entropy, and heat transfer between the phases) [145]. The heat transfer equations are defined for porous and free media, and in solids. The flux may take into account heat transfer by conduction, advection, and radiation. Alternatively, and depending on the size of the cell and experimental setup, heat transfer can be described using two different temperature fields in two coupled thermal balances, where sources and sinks in the respective thermal balance represent transfer of heat between the two phases. This is done in the presence of large temperature difference between the gas temperature (fluid-(gas)-phase temperature) and the cell operating temperature (solid-phase temperature).

18.4.4 Dedicated PAFC and HT-PEM Fuel Cell Modeling Equations

18.4.4.1 PAFC Electrolyte and PBI/H₃PO₄ Membrane Conductivity

Conductivity data of phosphoric acid is available in various publications [148–152] and in the literature cited therein. It depends on local concentration, temperature, and viscosity and is often described with nonlinear curves that are fitted to

correlate with the literature data. The variety of empirical correlations presented in Table 18.1 indicates that the interactions of free, amorphous, and bonded phosphoric acid are strongly dependent on the membrane system, casting methods,

acid concentrations, and doping levels. For highly doped membranes with predominant free acid the conductivity can be modeled by Archie's law considering the bulk phase conductivity [153]. The proton conduction in the PBI/H₃PO₄

Table 18.1 Selection of modeling equations for the PAFC and PBI/H₃PO₄ membrane conductivity

Equations	Reference	Note
$\sigma_{\text{H}_3\text{PO}_4/\text{SiC}} = 0.72796 - 6.5068 e^{(-0.07)C_{\text{H}_3\text{PO}_4}}$	[60]	PAFC model. Phosphoric acid concentration is in percent orthophosphoric acid equivalent
$\sigma_{\text{H}_3\text{PO}_4/\text{SiC}} = \frac{702.7x^{1.5} - 1734.2x^2 + 1446.5x^{2.5} - 350.7x^3}{100\mu} e^{[-0.010163 + 0.011634x + 0.08313x^2]T}$	[50]	PAFC model. 298–473 K. $0.0147 < x < 1.0$. x is the mole fraction of phosphoric acid in the electrolyte
$\sigma_m = \frac{100}{T} e^{(8.0219 - \frac{2605.6}{T} - \frac{70.1X}{T})}$ $\epsilon_{\text{PBI}/(X-2)\text{H}_3\text{PO}_4} = \left(\frac{4.81}{X-2} + 1\right)^{-1}$	[84]	Doping level $X = 6.2$. Amorphous phase phosphoric acid volume fraction used to correct various parameters
$\sigma_m = \frac{\sigma_0}{T} e\left(-\frac{E_a}{RT}\right)$ $E_a = 2273.3RH + 11,608$ $\ln(\sigma_0) = 0.7710RH + 10.219$	[107]	Doping level $X = 5.6$
$\sigma_m = \frac{B}{T} e\left(-\frac{E_a}{RT}\right)$ $E_a = (174.86RH + 698.47)R$ $B = e^{(0.5677RH + 8.6535)}$	[103]	Doping level $X = 8$
$\sigma_m = \frac{\sigma_0(k_i, X)}{T_s} e\left(-\frac{E_a(k_i, X)}{RT_s}\right)$ $\sigma_0(k_i, X) = \left(\frac{z^2 F^2}{R}\right) \alpha v_0 d^2 c e^{\frac{S+S_f}{R}}$ $E_a(k_i, X) = k_1 \ln(X) + k_2$ $\sigma_0(k_i, X) = k_3 \ln(X) + k_4$	[111]	Celtec [®] -P 1000 MEA. Solid-phase temperature used. Activation energy and pre-exponential factor varies with doping level
$\sigma_{\text{H}_3\text{PO}_4} = 1.01365 - 1.21548 \times 10^{-2}W - (1.5447 \times 10^{-7} - 6.42463 \times 10^{-5}W)T$	[113]	$84\% \leq W \leq 94\%$ (phosphoric acid concentration in wt%)
$\sigma_{\text{H}_3\text{PO}_4} = -3.45285 + 7.77294 \times 10^{-2}W - 4.50762 \times 10^{-4}W^2 - (6.24637 \times 10^{-2} - 1.387186 \times 10^{-3}W + 7.18336 \times 10^{-6}W^2)T$	[113]	$95\% \leq W \leq 99\%$ (phosphoric acid concentration in wt%)
$\sigma_m T = Ae^{\left(\frac{-B}{R(T-T_0)}\right)}$ $A = e^{[(0.0002RH^3) + (-0.0132RH^2) + (0.2257RH) + 9.6082]}$ $B = (0.62RH^3) + (-39.7RH^2) + (527RH) + 26,300$	[113]	Function A and B fitted on the relative humidity at given doping level $X = 5.6$
$\sigma_m = \frac{AB}{T} e\left(-\frac{E_a}{RT}\right)$ $E_a = -619.6X + 21,750$ $A = 168X^3 - 6324X^2 + 65,750 + 8460$	[110]	Parameter B same as in [134]
$\sigma T = Ae^{\left(-\frac{B}{T}\right)}$ $A = e^{(11.4 - 1.5RH)}$ $B = 33,200 - 16,000RH$	[130]	Doping level $X = 6$

(continued)

Table 18.1 (continued)

Equations	Reference	Note
$\sigma_m = \frac{AB}{T} e^{\left(\frac{-E_a}{RT}\right)}$ $B = \begin{cases} 1 + (0.01704T - 4.767)RH & (373.15 \text{ K} \leq T \leq 413.15 \text{ K}) \\ 1 + (0.1432T - 56.89)RH & (413.15 \text{ K} \leq T \leq 453.15 \text{ K}) \\ 1 + (0.7T - 309.2)RH & (453.15 \text{ K} \leq T \leq 473.15 \text{ K}) \end{cases}$	[134]	Celtec [®] -P 1000 MEA. A = 3.0 × 10 ⁶ S K/m. Activation energy is 20.0 kJ/mol
$\sigma_m = 0.42\sigma_{\text{PBI}/(X-2)\text{H}_3\text{PO}_4}(T, \omega_{\text{H}_3\text{PO}_4})\epsilon_{\text{PBI}/(X-2)\text{H}_3\text{PO}_4}^{2.1}$ $\epsilon_{\text{PBI}/(X-2)\text{H}_3\text{PO}_4} = \frac{(X - 1.25)V_{m,\text{H}_3\text{PO}_4}}{X V_{m,\text{H}_3\text{PO}_4} + V_{m,\text{H}_3\text{PO}_4}}$ $\sigma_{rl} = \sigma_{\text{PBI}/(X-2)\text{H}_3\text{PO}_4}(T, \omega_{\text{H}_3\text{PO}_4})\epsilon_{\text{PBI}/(X-2)\text{H}_3\text{PO}_4}^{1.5}$	[138]	Celtec [®] -P 1000 MEA
$\sigma_m = \sigma_0 e^{\left(\frac{E_a}{R}\left(-\frac{1}{T} + \frac{1}{443.15}\right)\right)}$	[139]	SPBI membrane doping level 13 and 9.1
$\sigma = \frac{AB}{T} e^{\left(\frac{-b_{\text{act}}}{RT}\right)}$ $b_{\text{act}} = -916.6X + 21,750$ $A = 1618X^3 - 6324X^2 + 65,750 + 8460$ $B = 1 + (0.1432T - 56.89)RH^{\text{eff}}$	[140]	

Table 18.2 Selection of modeling equations for the phosphoric acid concentration and water partial pressure

Equations	Reference	Note
$c_{\text{H}_3\text{PO}_4} = \frac{1}{0.008623 + 0.004187 p_{\text{H}_2\text{O}}^{0.5}}$	[60]	PAFC model. Water pressure in atm
$X_{\text{H}_3\text{PO}_4} = \frac{\ln(p_{\text{H}_2\text{O}}) + \frac{2765.1}{T} - 22.002}{-3121.9 + 2.5929}$	[107]	Doping level X = 5.6. Phosphoric acid concentration (mole fraction) coupled to water partial pressure
$\log(p_{\text{H}_2\text{O}}) = -AT^{-1} + B$ $A = 4.761 \times 10^{-5} (c_{\text{H}_3\text{PO}_4})^4 - 1.135 \times 10^{-2} (c_{\text{H}_3\text{PO}_4})^3 + 0.969 (c_{\text{H}_3\text{PO}_4})^2 - 33.253 c_{\text{H}_3\text{PO}_4} + 639.232$ $B = 2.793 \times 10^{-7} (c_{\text{H}_3\text{PO}_4})^4 - 6.744 \times 10^{-5} (c_{\text{H}_3\text{PO}_4})^3 + 5.714 \times 10^{-3} (c_{\text{H}_3\text{PO}_4})^2 - 0.21 c_{\text{H}_3\text{PO}_4} + 7.594$	[113]	Partial pressure is in (mmHg) and T in °C. Phosphoric acid concentration in mol%

membrane or in the electrolyte phase of the catalyst layer was proposed to obey an Arrhenius law [154, 155]. The activation energy depends on multiple factors such as the polymer backbone structure or the membrane doping level. It sharply decreases with low doping levels whereas no significant change in the activation energy is observed at higher doping levels. The pre-exponential factor may be independent of the operating temperature and decreases with higher doping levels.

18.4.4.2 Phosphoric Acid Concentration and Water Partial Pressure

An important modeling aspect in PAFC and HT-PEM fuel cells is the coupling of phosphoric acid concentration, local water partial pressure, and temperature (Table 18.2) [148–152]. A common modeling assumption is that the concentration of phosphoric acid inside the agglomerate remains constant and that outside the agglomerate the local equilibrium concentration is instantaneously adjusted.

18.4.4.3 Oxygen and Hydrogen Diffusivity and Solubility in Phosphoric Acid

As reported in literature the diffusivity and solubility of oxygen and hydrogen in phosphoric acid depends on the temperature and concentration [148–152]. Furthermore, it was suggested that the diffusivity and solubility exhibit exponential reciprocal temperature dependence. Various polynomial functions were used to correlate these properties with experimental data (Table 18.3).

18.4.4.4 Water Transport and Gas Crossover in HT-PEM Fuel Cells

Only minor valuable data on water transport in a PBI/H₃PO₄ membrane is currently available. It may be described using Fick's first law or Darcy's law. The mass sources represent the evaporation and condensation of water. The kinetics of the phase change can be calculated with the Hertz–Knudsen equation. The driving force is the chemical potential difference, expressed by the difference of the vapor pressure according to the liquid phase composition and the partial pressure of water in the gas phase. When assuming local interfacial equilibrium between the gas and the membrane phase of water, the calculations may be performed using a fictitious water diffusivity. The total effective diffusivity within the catalyst layer may account for water transport through the gas and membrane phase.

During experimental investigations, the observed open circuit voltage is lower than the estimated value from the thermodynamics due to the effect of gas crossover and other phenomena (e.g., carbon corrosion, platinum oxidation, Pt-OH). Nevertheless, gas crossover through the PBI/H₃PO₄ membrane is mostly neglected in HT-PEM modeling and simulation. It is supposed that in various types of membranes this crossover causes a mixed potential at both catalyst layers. An assumption may be that the crossed hydrogen is uniformly and completely oxidized in the cathode catalyst layer (represented as hydrogen crossover current

density). The oxygen crossover leads to hydrogen oxygen combustion in the anode catalyst layer due to small potential difference between the solid and electrolyte phases at the anode. The influence of the gas crossover on the source terms of the governing equations must be accounted for. Based on the gas crossover current density a crossover overvoltage can be defined (Table 18.4).

18.4.4.5 Electrochemistry

The majority of the published PAFC and HT-PEM fuel cell models use a Nernst type equation to calculate the open circuit potential. Alternatively, empirical expressions may be used to express the cell voltage for a given operating temperature (Table 18.5).

For HT-PEM fuel cells, Reimer [18] presented an interesting discussion on the various Butler–Volmer and Tafel type equations and the commonly used fundamental parameters that appear within these equations. It must be noted that one has to pay attention when using effective, average, or intrinsic parameters which are often only valid for a specific experimental setup or experimental conditions. In various publications, the Butler–Volmer equation is modified to account for spherical agglomerates of catalyst particles with interagglomerate spaces and for a thin film of amorphous phase phosphoric acid and/or a H₃PO₄–H₂O mixture covering the agglomerates. An effectiveness factor (Thiele modulus) accounts for the geometry of the agglomerate and the diffusion resistance of reactant molecules inside the agglomerate.

18.4.4.6 Carbon Monoxide Coverage and Degradation Modeling

Only a few modeling and simulation works studied the CO coverage in HT-PEM fuel cells. This coverage may be described with the bridge model of CO adsorption on platinum. Alternatively, the CO coverage on platinum can be described as a function of the temperature and hydrogen concentration.

As for the modeling and simulation of phosphoric acid loss over time, only minor studies are currently available. Based on experimental

Table 18.3 Selection of modeling equations for the oxygen and hydrogen diffusivity and solubility in phosphoric acid

Equations	Reference	Note
<i>Oxygen and hydrogen diffusivity</i>		
$\ln(10^9 D_{O_2}^{H_3PO_4}) = (-192.55m_{H_3PO_4}^2 + 323.55m_{H_3PO_4} - 125.61) + \frac{(62,010m_{H_3PO_4}^2 - 105,503m_{H_3PO_4} + 40929)}{T}$ $D_{O_2}^{PBI/H_3PO_4} = D_{O_2}^{H_3PO_4} \epsilon_{PBI/(X-2)H_3PO_4}^{1.8}$	[84]	Diffusion coefficient in m ² /s. Phosphoric acid concentration in mass fraction
$D_{H_2}^{H_3PO_4} = e^{(A/T - 1 + B)}$ $A = -9.21 \times 10^5 \omega_{H_3PO_4}^3 + 2.47 \times 10^6 \omega_{H_3PO_4}^2 - 2.21 \times 10^6 \omega_{H_3PO_4} + 6.54 \times 10^5$ $B = 1.66 \times 10^3 \omega_{H_3PO_4}^3 - 4.46 \times 10^3 \omega_{H_3PO_4}^2 - 4.01 \times 10^3 \omega_{H_3PO_4} + 1.21 \times 10^3$	[107]	Diffusion coefficient in m ² /s. Phosphoric acid concentration in mass fractions
$D_{O_2}^{H_3PO_4} = Ae\left(\frac{-E_a}{RT}\right)$ $A = 0.0000025 e^{(1.76593W)}$ $E_a = -0.011607142857W^2 + 1.9642142857W - 75.376$	[113]	Phosphoric acid concentration in wt%. Activation energy in kcal/mol
$D_{H_2}^{H_3PO_4} = 2D_{O_2}^{H_3PO_4}$	Various publications	Same behavior assumed as in water systems
<i>Oxygen and hydrogen solubility</i>		
$\ln(10H_{O_2}^{H_3PO_4}) = (257.13m_{H_3PO_4}^2 - 431.08m_{H_3PO_4} + 178.45) + \frac{(-93,500m_{H_3PO_4}^2 + 156,646m_{H_3PO_4} - 64,288)}{T}$ $H_{O_2}^{PBI/H_3PO_4} = (\epsilon_{H_2}^{H_3PO_4})^{1.945} \left(H_{O_2}^{H_3PO_4} + 5.79 \left(1 - (\epsilon_{H_2}^{H_3PO_4})^{1.8} \right) \right)$	[84]	Solubility in mol/m ³ /atm. Phosphoric acid concentration in mass fraction
$H_{O_2} = e\left(\left(-1.27 \times 10^4 \omega_{H_3PO_4} + 1.23 \times 10^4\right) \frac{1}{T} + (35.2\omega_{H_3PO_4} - 46.6)\right)$	[103]	Phosphoric acid concentration in mass fractions. Equation valid only until 96 wt% phosphoric acid
$c_{O_2}^{H_3PO_4} = Ae\left(\frac{-\Delta H_{O_2}}{RT}\right)$ $A = (0.00044(100 - W)^5 - 0.01678(100 - W)^4 + 0.2476(100 - W)^3 - 1.7144(100 - W)^2 + 5.8157(100 - W) - 7.6626)^{-1}$ $\Delta H_{O_2} = -0.003125W^3 + 0.8371429W^2 - 74.95179W + 2,244.786$	[113]	Phosphoric acid concentration in wt%. Oxygen concentration in mol/cm ³
$H_{H_2}^{H_3PO_4} = 4H_{O_2}^{H_3PO_4}$	Various publications	Same behavior assumed as in water systems
$c_i = \frac{p_i H_i}{P_i}$ $c_i = \frac{H_i}{H_i}$	Various publications	Different units used (e.g., mol/m ³ /Pa or Pa m ³ /mol)

Table 18.4 Selection of modeling equations water transport and gas crossover

Equations	Reference	Note
<i>Water transport</i>		
$k = \frac{\dot{Q}}{\left(\frac{\Delta p_{in} - \Delta p_{out}}{\ln\left(\frac{\Delta p_{in}}{p_{out}}\right)} \right) P_{\overline{m}} \frac{k\delta_m}{0.95}}$	[132]	Celtec [®] -P 1000. Membrane water permeability coefficient 2.4×10^{-13} mol/s/cm/Pa at 160 °C
$J_D = D_{H_2O}^{mem} \nabla c_{H_2O}$ $D^{eff} = \varepsilon^{\tau} D_{H_2O}^g + \varepsilon^{\tau}_{mem} D_{H_2O}^{mem}$	[134]	Celtec [®] -P 1000. Fictitious water diffusivity of 1×10^{-7} m ² /s used. Effective water diffusivity in catalyst layer accounts for transport in the gas and membrane phase
$P_{H_2O} = \frac{r_c L}{\Delta \Delta p_{H_2O}}$	[156]	PBI/PPy(50)coPSF 50/50 MEA. Permeability coefficient 1.1×10^{-14} mol cm/cm ² /s/Pa at 150 °C
$K_w = 3.2 \times 10^{-9} e^{\left(-\frac{3172}{T} - 4.7(6-X)\right)}$	[130]	Permeability of water vapor
<i>Gas crossover (e.g., hydrogen crossover) and related</i>		
$N_i^{cross} = -\psi_i \nabla p_i$	[101]	PBI-O-PhT membrane. Molar flux of gas through the membrane (mol/cm ² /s). Hydrogen permeation 3.1×10^{-16} mol cm/cm ² /s/Pa. Oxygen permeation 7.8×10^{-17} mol cm/cm ² /s/Pa
$\eta_{crossover} = \frac{-RT}{aF} \ln \left[\frac{j_{crossover}}{2 i_{0,c}} + \sqrt{1 + \left(\frac{j_{crossover}}{2 i_{0,c}} \right)^2} \right]$	[113]	Doping level 5.6. Voltage loss in V
$I_{H_2}^{crossover} = 2FD_{H_2}^{PBI} e^{1.8} \frac{C_{H_2}^{PBI} _{a,r,l}}{\delta_{mem}}$ $j_c = -a i_{0,c}^{ref} \left(\frac{c_{O_2}}{c_{O_2,ref}} \right)^{\frac{3}{4}} e^{\left(-\frac{a_c F \eta}{RT}\right)} + \frac{I_{H_2}^{crossover}}{\delta_{rl}}$	[133, 134]	Celtec [®] -P 1000 MEA and MEA with doping level (X = 5.6). Various source terms in conservation equations corrected

Table 18.5 Selection of modeling equations for electrochemistry

Equations	Reference	Note
<i>Nernst type equation</i>		
$E_{rev} = E_{rev}^0 + \frac{RT}{nF} \ln \left[\frac{a_{H_2} a_{O_2}^{0.5}}{a_{H_2O}} \right]$	[64]	PAFC model
$E_{rev} = -\left(\frac{\Delta H}{nF} - \frac{T\Delta S}{nF}\right) + \frac{RT}{nF} \ln \left[\frac{(RT)^{1.5} c_{H_2} c_{O_2}^{0.5}}{a_{H_2O}} \right]$	[107]	Concentrations (solubility) expressed in Nernst equation using Henry's law
$E_{rev} = 1.259266 - 0.2466 \times 10^{-3} T$	[157]	Celtec [®] -P 1000 MEA. Calculated voltage of 1.155 V at 150 °C/1.152 V at 160 °C
$E_{rev} = 1.1669 - 0.24 \times 10^{-3} (T - 373.15 \text{ K})$	[121]	Derived equation based on value for 100 °C
$E_{rev} = 1.185 - 2.3 \times 10^{-4} (T_{op} - 298.15 \text{ K}) + \frac{RT_{op}}{2F}$ $\times \left(\ln p_{H_2}^{in} + \frac{1}{2} \ln p_{O_2}^{in} \right)$	[139]	SPBI membrane
<i>Butler-Volmer type equations and exchange current density</i>		
$j = i_0 \left[e^{\left(-\frac{a_{O_2} F \eta}{RT}\right)} - e^{\left(\frac{a_{O_2} F \eta}{RT}\right)} \right]$	Various publications	Similar expressions without or with correction factors may be used
$\log(i_0^{PBI}) = \log(i_0^{H_3PO_4}) - 4.16 (1 - \varepsilon_{PBI/(X-2)H_3PO_4})$ $\log(i_0^{H_3PO_4}) = 3.509 - 2193 T^{-1}$	[84]	Corrected equation for the exchange current density due to platinum catalyst in contact with PBI/H ₃ PO ₄
$i_0 = i_0^{ref} a_{Pt}^{eff} \left(\frac{c_i}{c_i^{ref}} \right)^{\gamma} e^{\left(-\frac{E_0}{RT}\right)} \left(1 - \frac{T}{T_{ref}} \right)$	Various publications	Similar expressions may be used
$\alpha = A + BT$	[113]	Dependent on temperature, catalyst treatment, and impurity content in the phosphoric acid

phosphoric loss rate data, a simple equation can be used. Alternatively, the evaporation and condensation rates of phosphoric acid can be derived by an activation process based on the vapor–liquid equilibrium of a two components system. Experimental data should also be used, to account for the change in platinum particles radius with time (Table 18.6).

18.4.4.7 Thermo-Mechanical Modeling

Thermo-mechanical modeling and simulation should account for the compression of the porous media and the membrane in terms of thickness reduction, deflection into the gas channel (LFSI), and local variations of the material parameters (e.g., reduced porous media porosity and permeability). Another topic is the description of the

Table 18.6 Selection of modeling equations for CO coverage and degradation modeling

Equations	Reference	Note
<i>CO coverage</i>		
$\Theta = -0.893\eta^2 + 1.714\eta$	[84]	General blockage factor varies with phosphoric acid concentration, temperature, and electrode overpotential and reduces the effective surface area per unit volume
$\Theta_{CO}(T) = 19.9e^{(-7.69 \times 10^{-3}T)} + 0.085 \ln \frac{c_{CO}}{c_{H_2}}$ $i_0^{CO} = i_0^{H_2}(1 - \Theta_{CO})^2$	[119]	CO coverage varies with temperature
$\Theta_{CO}(T) = A(T) \ln \frac{[CO]}{[H_2]} + B(T) \ln(i) \ln \frac{[CO]}{[H_2]} + C(T)$	[77]	CO coverage varies with temperature
$k_{fh}(\Theta_{CO}) = k_{fh}^0 e^{\left(\frac{-\delta(\Delta E_{H_2})}{RT} \left(1 - e^{\frac{-p}{1-\Theta_{CO}}} \right) \right)}$ $\Theta_{H_2} = \frac{A_2 + A_3}{\frac{A_1 + A_2 + A_3}{B_1} (B_1 + B_2 + B_3) - A_1}$ $\Theta_{CO} = \frac{A_1(1 - \Theta_{H_2})}{A_1 + A_2 + A_3}$ $A_1 = k_{fc} c_{CO} RT$ $A_2 = b_{fc} k_{fc}$ $A_3 = i_{0,CO} e^{\left(\frac{a_{CO} F \eta_a}{RT} \right)}$ $B_1 = k_{fh} c_{H_2} RT$ $B_2 = b_{fh} k_{fh}$ $B_3 = i_{0,a} \left(e^{\left(\frac{a_a F \eta_a}{RT} \right)} - e^{\left(\frac{-a_a F \eta_a}{RT} \right)} \right)$	[141]	Celtec®-P 1000 MEA. Kinetic parameters for CO poisoning model given
$\Theta_H = \gamma_H \left(\frac{k_H^{ads} c_{H_2} (1 - \Theta_H^p - \Theta_{CO})^2 - b_H^{ads} k_H^{ads} (\Theta_H^p)^2}{2k_H^{eox} \sinh \left(\frac{2\alpha_a F}{RT} \eta_{act} \right)} \right) + (1 - \gamma_H) \Theta_H^p$ $\Theta_{CO} = \gamma_{CO} \left(\frac{k_{CO}^{ads} c_{CO} (1 - \Theta_H - \Theta_{CO}^p)^2}{b_{CO}^{ads} k_{CO}^{ads}} \right)^{0.5} + (1 - \gamma_{CO}) \Theta_{CO}^p$	[110]	Coverage fraction updated at every iteration. Kinetic parameters for CO poisoning model given
<i>Degradation modeling</i>		
$J_D = \tilde{c} e^{\left(\frac{-\tilde{\Delta G}^*}{RT} \right)}$	[65, 66]	Evaporation and condensation rates of phosphoric acid derived by an activation process based on the vapor–liquid equilibrium of a two components system (Knudsen relationship)

(continued)

Table 18.6 (continued)

Equations	Reference	Note
$L_{\text{H}_3\text{PO}_4} = L_{\text{H}_3\text{PO}_4}^0 - r_{\text{H}_3\text{PO}_4} t$ $r_{\text{Pt}} = 5.66 \times 10^{-22} t^2 + 1.99 \times 10^{-15} t + 1.39 \times 10^{-9}$	[107]	At $t = 0$ s, the phosphoric acid loading was 1.28 mg/cm ² . The loss rate was 7.1×10^{-6} mg/cm ² /s. Platinum particles radius variation with time taken from literature (TEM analyses)
$X = X_0 - 0.0020267t$ $y_{\text{O}_2} = 2.06923 \times 10^{-5} t$	[140]	Dropping of the doping level over time with $X_0 = 30$. Decrease amount of oxygen concentration in the reaction site

contact resistances between the bipolar-plate and the GDL and the evaluation of deformation of the asperity under applied load and temperature. As for the description of the electrical and thermal contact resistances, a fractal asperity based contact resistance model can be used. Solid mechanics analysis is of importance when modeling large HT-PEM fuel cell stacks (material stress–strain analysis).

18.5 Electrolyte Modeling

18.5.1 Physicochemical Properties of Phosphoric Acid

Physicochemical properties and experimental data of phosphoric acid can be found in textbooks and various publications [148–152] and in the literature cited therein. The available works cover, e.g., evaporation and condensation considerations, acidity and proteolytic equilibria, composition specifications and condensation equilibria, vapor pressure of water as a function of composition and temperature, proton conductivity as a function of composition and temperatures, dynamic viscosity, and phase equilibria. The available data builds the foundation for modeling and simulation of a H₃PO₄-H₂O system (and PBI/H₃PO₄-H₂O) which is important to further improve the quality and reliability of HT-PEM fuel cell models. The combination of electrolyte modeling

along with computational fluid dynamics modeling is the key to further develop HT-PEM fuel cell models. Various modeling approaches have been proposed to describe electrolyte solutions, as reviewed by Zemaitis et al. [150], Pitzer [158], Rafal et al. [159], Loehe and Donohue [160], and Anderko et al. [161]. As discussed, polybenzimidazole is an intrinsically nonconducting polymer that needs to be doped by an electrolyte to become an ion conductor which is then suitable for fuel cell operation [162]. Phosphoric acid performs remarkably well as proton conductor and is therefore used in combination with polybenzimidazole for the application in HT-PEM fuel cells [163–166]. The doping phosphoric acid is not covalently bonded to the polybenzimidazole polymer backbone and even though there are hydrogen bonds present, at least a part of the phosphoric acid is considered to be free/amorphous phosphoric acid that is located in the cavities of the membrane. This is especially the case for membranes with high doping levels achieved by the sol–gel method [167]. Furthermore phosphoric acid has a pretty low fugacity at least for concentrations below 100 wt%. Consequently the electrolyte can be maintained within the system and is not instantly lost by evaporation. The evaporation rate of phosphoric acid is strongly dependent on the phosphoric acid concentration in the highly concentrated range which makes it very complex for general statements [168]. This issue and the fact that not only the

Table 18.7 Phosphoric acid concentration dependent physical properties and their importance to fuel cell performance (practical and theoretical)

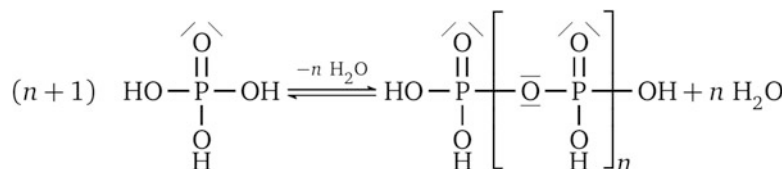
Physical property	Concentration dependency (%/10 wt% in the range of ~90 wt%) (high > 5; medium 5–1; low < 1)	Importance to HT-PEM fuel cell performance (practical and theoretical) (high/medium/low)	Reference
Conductivity	High	High	[163]
Density	High	Medium	[169]
Exchange current density of oxygen reduction reaction	High	High	[170]
Diffusion coefficient of oxygen	High	High	[171, 172]
Vapor pressure of phosphoric acid	High	Low (short-term) high (long-term)	[168, 173]
Water pressure above phosphoric acid	High	Medium	[168, 173]
Heat of vaporization (water)	High	Low	[148, 173]
Viscosity	High	Low	[163, 174]
Oxygen solubility	High	High	[175]
Hydrogen solubility	High	Low	[176]
Diffusion coefficient of hydrogen	Medium	Low	[176]
Heat capacity	High	Low	[177]
Thermal conductivity	Medium	Low	[178]
Corrosivity	High	Low	[179, 180]
Electrochemically active surface area	Medium	High	[181]

vapor pressure of the acidic species, but also many other physical properties strongly depend on phosphoric acid concentration, illustrate the necessity of a profound description of the phase equilibrium of phosphoric acid within a HT-PEM fuel cell to be able to predict the local phosphoric acid concentration. Table 18.7 gives an overview of physical properties important to fuel cell performance and their level of concentration dependency.

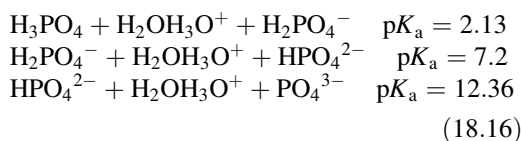
It can be seen that several important physical properties are highly concentration dependent. Properties affecting electrochemistry are impacted the most, but also mass and heat transfer is influenced by a change of acid concentration. A holistic modeling approach should include these effects with the ability to cover for a broad range of operational parameters, e.g., different humidification levels of reaction gases or the simulation of dynamic load patterns. To be in the position to calculate phosphoric acid

concentrations within the fuel cell, one has to describe the transmembrane species transport and the phase change, respectively [138, 182]. Knowledge of the vapor–liquid equilibrium is essential and therefore, an experimental data base is needed. Various publications concerning vapor pressure data over phosphoric acid solutions of different concentrations can be found in [148–152] and in the literature cited therein. Usually the vapor composition is assumed to solely consist of water vapor. Hence, these experimental data reflect vapor pressure curves for phosphoric acid solutions of different concentrations [152, 166, 183–188]. Neglecting acidic species in the vapor phase below concentrations of 100 wt% is justifiable, as experimental data of Brown and Whitt [173] and Lang et al. [168] have shown. Above concentrations of 100 wt% the acid content in the gas phase increases and reaches over 1000 ppm for a liquid phase concentration of

Fig. 18.2 Reaction scheme of the polycondensation of orthophosphoric acid to polyphosphoric acid



105 wt%. Calculating the vapor–liquid equilibrium in the H₃PO₄–H₂O system is quite complex and requires different modeling approaches for different concentration ranges. The difficulty lies in the fact that phosphoric acid forms numerous species as a function of the concentration of the solution. First of all phosphoric acid is a weak triprotic acid. This means for all dissociation stages the phosphoric acid dissociates to only a moderate extent, hence the percent dissociation does not reach 100 % and we get ionic species besides molecular phosphoric acid species (H₃PO₄) in the liquid phase [189–193]. During neutralization, all three dissociation stages are sequentially reached at the respective pK_a values:



As indicated by the pK_a value, only the first dissociation stage is of concern when it comes to HT-PEM fuel cell application. Besides the dissociation equilibria, the chemical reaction equilibrium of the polycondensation reaction of orthophosphoric acid to polyphosphoric acid is of vital importance. By changing the concentration of the solution, the chemical equilibrium composition shifts as well. The polycondensation reaction, shown by Fig. 18.2, is a dehydration reaction, hence the equilibrium state shifts towards a composition containing more polymeric species when water is removed and the solution gets more concentrated.

The polymerization starts in the concentration range above 90 wt% with the formation of dimeric species (pyrophosphoric acid) and forms longer oligomers with further acid concentration [194–196]. For a concentration of 120 wt %, with respect to the apparent orthophosphoric acid content, the solution contains less than 2 wt

% ortho species and more than 50 wt% of polymeric species with a chain length of 10 repeating units or more. The chain structure formed during polymerization can be linear, as indicated by Fig. 18.2, but also cyclic (metaphosphoric acid) and branched configurations occur with up to a few thousand repeating units. This reversible condensation reaction takes place within hours at room temperature and lasts only a few minutes at typical operating temperatures of a HT-PEM fuel cell [197–199]. In general dimeric, trimeric, oligomeric, and polymeric species of phosphoric acid can also dissociate, resulting in a multicomponent system of ionic and uncharged species. Therefore, choosing the concentration range has a tremendous influence on the modeling due to the species that have to be considered. Hence, knowledge of the liquid phase compositions at chemical equilibrium, within the concentration range of interest, is essential for the calculation of the vapor–liquid equilibrium.

18.5.2 Modeling of the Vapor–Liquid Equilibrium

For calculation of the equilibrium compositions of the liquid phase either the equilibrium constants of the dissociation and polycondensation reactions have to be known or they can be computed by methods which use the approach of minimizing Gibbs free energy [200–202]. In addition, ab initio modeling techniques such as density functional theory (DFT) in combination with reactive molecular dynamic (MD) simulations could be used. Once the liquid phase system is modeled, there are in principle two options to describe the vapor–liquid equilibrium. Either equations of state (EOS) or excess Gibbs free energy models (g^E-models) may be used to describe the thermodynamics of the liquid

phase. In both cases the gas phase can either be modeled as ideal up to moderate pressures (<5 bar) or by an equation of state for higher pressures.

For calculation of the vapor–liquid equilibrium composition, the activity coefficients of each species in the liquid phase are necessary. They can directly be computed from g^E -models or from EOS with an intermediate step involving the fugacity coefficients as follows:

$$\gamma_i = \frac{\phi_i(T, p, x_i)}{\phi_{0,i}(T, p, x_i = 1)} \quad (18.17)$$

In the above equation, the denominator symbolizes the ideal reference state of the pure component. Hence the activity coefficient is covering for the non-ideality of the mixture. Complementing Raoult's law by the activity coefficients yields the corresponding vapor phase composition for the non-ideal mixture at equilibrium:

$$P y_i = p_{v,p,i} x_i \gamma_i \quad (18.18)$$

From a historic perspective, all models describing the vapor–liquid equilibrium of electrolytic systems evolved from nonelectrolyte models. Regardless of the general approach mentioned before, the theoretical fundamentals to describe the Coulomb interactions of ions in electrolytes were built on the work of Debye and Hückel [203] and accordingly Waisman and Lebowitz [204]. With this theoretical basis the classic non-electrolyte models, which only covered the short-term interactions of molecules next to each other, could be complemented with the long-term ionic interactions present in an electrolyte solution. The most common g^E -models listed, according to the timeline of their development, are the Margules, Van Laar, Wilson, the NRTL (Non-random Two Liquid), UNIQUAC (Universal Quasi Chemical), and UNIFAC (Universal Quasichemical Functional Group Activity Coefficients) models. A detailed overview can be found in the textbook of Prausnitz et al. [205]. Publications concerning the modeling of the vapor–liquid equilibrium in the H_3PO_4 - H_2O system are briefly introduced below.

Wang et al. introduced an UNIQUAC-model extended by a Pitzer–Debye–Hückel expression for the long-term electrolytic interactions [206]. Without taking polymeric species into account, they could model the vapor pressure curves up to a concentration of 100 wt%. They regressed the necessary binary interaction parameters from experimental data of Kablukov and Zagwodkin [185] and MacDonald and Boyack [166]. Messnaoui and Bounahmidi [207] used an elec-NRTL-model with inclusion of the anionic dimer species. Along with vapor pressures, they computed osmotic coefficients and pH values in the concentration range of up to 77 wt% with fairly good accordance to experimental data. Jiang et al. [188] also took a modeling approach that included the dimeric anion of phosphoric acid for concentrations of up to 70 wt% using the original equations developed by Pitzer and Silvester [208]. They were the first to model the vapor–liquid equilibrium in the H_3PO_4 - H_2O system, being valid up to a concentration of 45 wt%. Cherif et al. [209, 210] as well as Rumpf and Maurer [211] intensively studied the modeling approach of Pitzer et al. for phosphoric acid. Regarding the concentration range, their models were not substantially improved as they also only described the system below 50 wt%. All models mentioned above are g^E -models with a semi-empirical character. The regression of interaction parameters from experimental data was needed. Extrapolation of the modeled range to investigate regions of higher concentration holds a high risk of uncertainties and is not feasible without further validation. For HT-PEM fuel cells, the concentration range greater than 100 wt% up to approximately 110 wt% is of particular interest (Fig. 18.3), and therefore, advanced modeling approaches that include polymeric phosphoric acid species are needed.

Figure 18.3 shows an exemplary simulation of the phosphoric acid concentration (molecular H_3PO_4) at the cathode side catalyst–membrane interface for various load currents. The phosphoric acid distribution depends on, e.g., the water pressure and temperature and undergoes concentration changes when changing the load current. In this case, it varies between 95.9 % (5 A) and

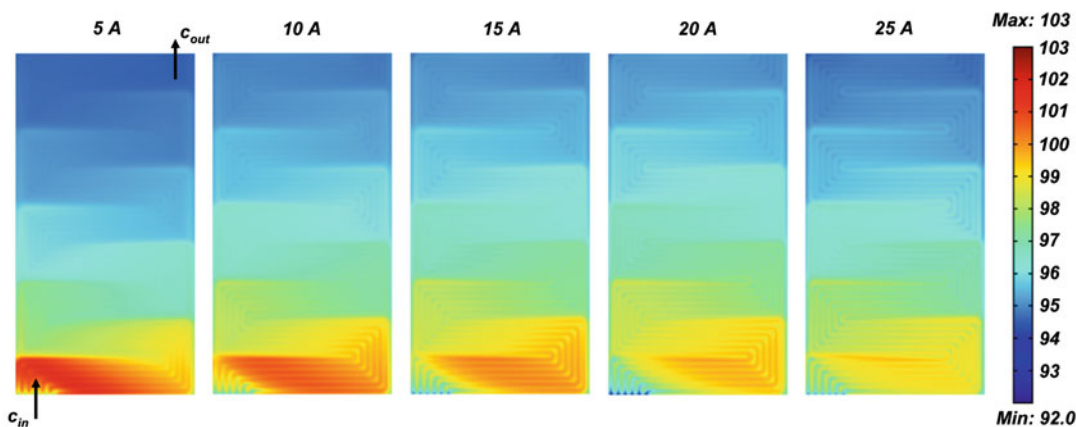


Fig. 18.3 Phosphoric acid concentration (wt%) at the cathode side catalyst–membrane interface at 160 °C and various load currents (50 cm² MEA, H₂/Air operation, no backpressure)

96.9 % (25 A) with the highest values near the inlet and the lowest values near the outlet. The mean concentration values may increase to >100 % at the cathode side if transmembrane water transport is accounted for.

Experimental data including the acidic species in the vapor phase within the above concentration range are scarce. Only very few publications of VLE data in that range are available [168, 173]. In contrast, numerous vapor pressure curves are accessible in literature. Chemical equilibrium data for the polycondensation and dissociation reaction in that range (>100 wt%) are so far not published [148]. However, a starting point to describe the vapor–liquid equilibrium at those high concentrations is given by an EOS which is based on the fundamentals of the perturbation theory of Barker [212, 213]. Built on this theory, Sadowski et al. [214] have developed the PC-SAFT (Perturbed Chain Statistical Associated Fluid Theory) equation of state. The PC-SAFT EOS and its derivatives offer the ability to be fully predictive in combination with quantum mechanically based estimated parameters [215] and can therefore be used for systems without or with very little experimental data. Nevertheless, a model validation should be undertaken. Cameretti et al. [216] adopted the PC-SAFT EOS for electrolyte systems (ePC-SAFT), but the quality for weak electrolytes as phosphoric

acid was poor. Held et al. [217] introduced an advanced version of the ePC-SAFT EOS with much better accuracy for weak electrolytes. One big advantage of the PC-SAFT EOS is that they can also be used to model polymer solutions, which is exactly the case for highly concentrated phosphoric acid. A modification, which was developed to combine electrolytic and polymeric properties of liquid solutions, was published under the acronym pePC-SAFT [218]. So far, there are no publications regarding the application of this model for the polyphosphoric acid system, but it seems to be a very promising approach as it is capable of describing charged polymer species.

18.5.3 Non-equilibrium Effects at the Interphase

The liquid product water that is formed on the cathode side dilutes the electrolyte and diffuses in part through the membrane as shown by Fig. 18.4. The water diffusion results from a concentration gradient of the phosphoric acid caused by the phase change of water at the interphase in the catalytic layers and the water production at the cathode. In general, the mathematical description of the net-mass flux could be accomplished by an interphase mass transfer theory. The two-film theory [219],

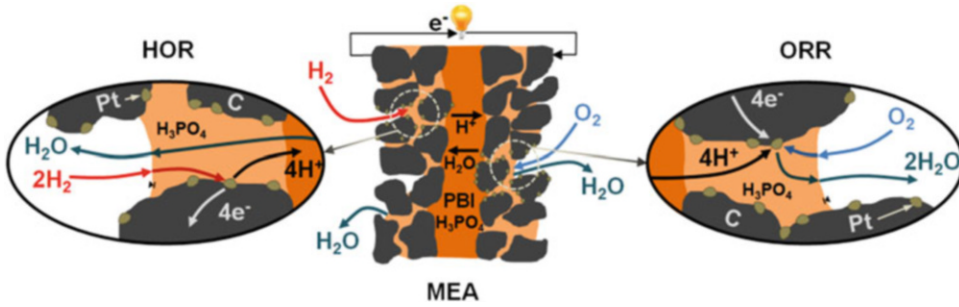


Fig. 18.4 Phosphoric acid dilution, transmembrane transport, and water evaporation in a HT-PEM fuel cell

film-penetration model [220], and penetration model [221, 222] cannot be used in this case because of the assumption of ideally mixed turbulent bulk phases. The flow regime in the catalytic layers is strictly laminar and at best a creeping flow at the vicinity of the interphase.

From the kinetic theory of gases, an expression for the net-mass flux at the interphase can be derived based on the works of Hertz [223] and Knudsen [224]. From a statistical consideration under the assumption of a Maxwell–Boltzmann distribution for the velocity of the gas molecules, the maximum condensation mass flux can be calculated. The evaporation mass flux has to equal the condensation mass flux at equilibrium. The resulting Hertz–Knudsen equation for calculating the area specific net-mass flux is given below:

$$\dot{m}_{\text{net}} = \sqrt{\frac{M_i}{2\pi R}} \left(\kappa_e \frac{p_{v,p,i}}{\sqrt{T_l}} - \kappa_c \frac{p_i}{\sqrt{T_g}} \right) \quad (18.19)$$

The gas phase temperature and the liquid phase temperature are also defined, which equal each other in the case of vapor–liquid equilibrium. The evaporation coefficient was introduced by Hertz to account for evaporating molecules colliding with molecules in the gas phase and getting reflected back into the liquid phase. Therefore, it is also a measure of the percent of the theoretical maximum evaporation rate reached. The condensation coefficient is analogously defined as the ratio of molecules actually condensing to molecules hitting the surface [225]. The phase change coefficients are similar

to kinetic parameters, which can be adopted in order to describe experimental data. Numerous publications are investigating these coefficients experimentally or by means of molecular dynamics [226–228]. Marek and Straub [229] have prepared a detailed review on phase change coefficients for water. The evaporation coefficient ranges here from 1×10^{-3} to 1 and seems to be in general smaller than the condensation coefficient, which ranges from 1×10^{-2} to 1. The deviations are explained by several possible effects biasing the measurements such as contamination with surface-active components. Neglecting the temperature jump condition at the interphase and using the extension proposed by Schrage [230] and Nabavian and Bromley [231], an implementation-friendly equation is derived:

$$\dot{m}_{\text{net}} = \frac{2}{2 - \kappa_c} \sqrt{\frac{M_i}{2\pi R T_{ip}}} (\kappa_e p_{v,p,i} - \kappa_c p_i) \quad (18.20)$$

Mass and heat flux during evaporation are strongly coupled by the heat of vaporization of water from phosphoric acid. Kablukov and Zagwodskina [185] and Brown and Whitt [173] published data for the heat of vaporization for acid concentrations up to 100 wt%. Very little is known about the vapor–liquid interphase area within the catalytic layer, which is needed for the calculation of the evaporation mass flux. The interphase area within the porous medium depends on the acid holdup and the wetting behavior of the catalyst surface which both also

depend on the acid concentration. The effect on vapor pressure caused by the curvature of the interfacial surface in the pores can be neglected in a first step for pore radii bigger than 10 nm as the deviation (Kelvin equation) to a clean surface is less than 10 %. A detailed investigation of those relations is strongly desirable as there are no publications dealing with the occurrence of the vapor–liquid interphase within the catalyst layers of HT-PEM fuel cells.

18.5.4 Coupling of the Vapor–Liquid Equilibrium to Electrochemistry and Mass Transport Properties

The vapor–liquid equilibrium and transmembrane species transport determine the local acid concentration within a HT-PEM fuel cell. As the acid density strongly depends on its concentration, there is always a volume change when it comes to a concentration shift, which provokes a redistribution of the acid in the cavities of the catalyst layer. Such concentration changes can occur during load changes, temperature variation or during start-up time of the fuel cell or an upstream reformer system. Besides the effect on many physical properties by their concentration dependency, the swelling and shrinking of acid and the accompanied electrolyte redistribution within the MEA shows a distinct impact on fuel cell performance [132, 182, 232–234]. Hence, electrochemistry is influenced by the vapor–liquid equilibrium via direct and indirect effects. Exchange current density is directly affected by a concentration shift, while at the same time the volume change leads to an acid redistribution altering the electrochemically active surface area (ECSA) [232, 235]. The influence on mass transfer can also be classified in that manner. A concentration shift directly alters gas solubilities and diffusion coefficients in the liquid electrolyte. An indirect effect by the volume change of the acid can be expected via the acid volume fraction in the catalyst layers, which modifies the permeability and the effective gas diffusion in the porous medium as well as the thickness of the electrolyte film covering the platinum

catalyst. The modeling of all these effects depends on the scale of the overall simulation model. Describing the two-phase behavior within the catalytic layers on a microscopic scale capturing the interphase position is feasible with numerical methods (Eulerian) such as the volume of fluid (VOF) or level set (LS) method [236, 237]. The effort of locally discretizing the interphase in the porous structures is quite large and needs a lot of computational power to be solved, especially when it comes to the simulations of single cells or even stacks with respectively high numbers of degrees of freedom. An overview of models used for pore-scale modeling in the context of two-phase flow in PEM fuel cells is given by Mukherjee et al. [238]. Those models were developed for LT-PEM fuel cells but an adaption to HT-PEM fuel cells seems viable. The models differ in the way of representing the porous structures, which is either directly done or indirectly by depicting idealized pore networks, which is advantageous concerning the computational effort and the generation of the microstructured domains. On a macroscopic scale more abstract models are needed to couple the vapor–liquid equilibrium and two-phase behavior to simulations on the continuum scale. At least some transport properties can be modeled by the effective medium (EM) theory such as, e.g., the well-known Bruggeman model [239, 240]. Direct concentration dependencies of physical properties can be implemented by correlation equations. Experimental data on gas solubilities of hydrogen and oxygen in phosphoric acid at elevated temperatures and high concentrations are scarce. The effects on the exchange current density were shown by Kunz and Gruver [170]. In general, literature data on the exchange current density in phosphoric acid seems to be extremely scattered, varying over four orders of magnitude and needs further investigations [170, 241–245].

Figure 18.5 summarizes important transport parameters, the transfer coefficient (various concentrations and various doping levels), and the exchange current density for HT-PEM fuel cell modeling taken from various literature cited herein.

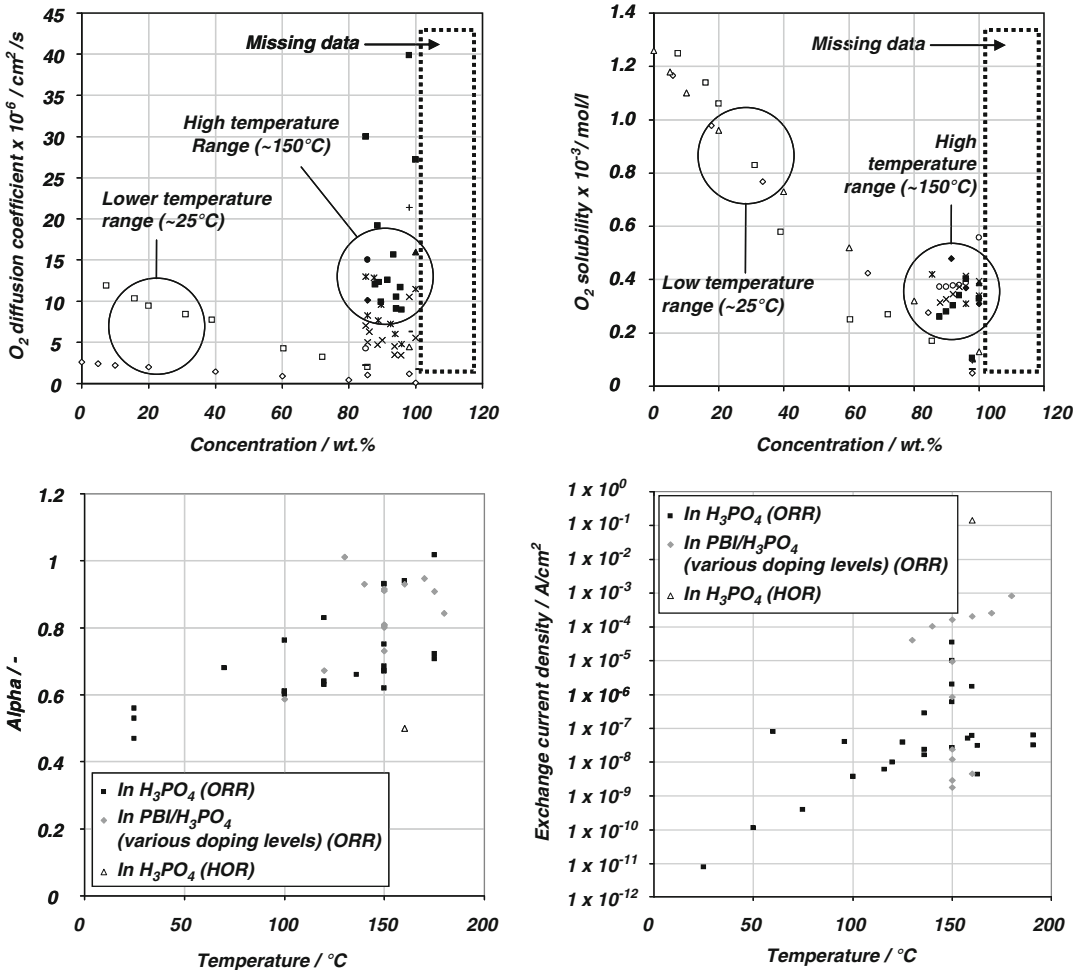


Fig. 18.5 Important modeling parameters, the transfer coefficient (various concentrations and various doping levels), and the exchange current density (a selection of values taken from the literature cited herein)

18.6 Numerical Aspects

18.6.1 Overview

The fact that the model equations and the variables in the model equations depend on each other, usually in highly nonlinear relations, is a challenge when solving the equations in fuel cell simulations. In most cases, analytical solutions are not possible to derive and numerical methods have to be used to solve the equations. The variables for the chemical composition of the gas phase and the electrolyte are coupled

through the electrode kinetics, where composition dependence may be described. Fluid flow is directly coupled with composition through the mass balances. The electric potential in the electrodes and in the pore electrolyte is also coupled through the electrode kinetics. The transport equations in the electrolyte couple the composition and the electric potential in the electrolyte. Temperature influences all transport and reacting properties in the cell. These variables couplings are a minimum in high-fidelity models. Also couplings described by the Onsager relations may be introduced [143].

The model equations described above can be solved using numerical methods. However, these equations have to be well posed and accurately describe the conservation laws and constitutive relations. If the fuel cell model equations are well posed, they usually have a unique and stable solution, although this may be very difficult to prove in theory.

The model equations can be discretized and solved using numerical methods such as finite element, finite difference, or finite volume methods. These three methods are based on dividing geometrical domains in the model into volume elements of finite size, i.e., going from a continuous problem to a discrete problem. The time variable is often discretized using finite difference, also in the cases where finite elements or finite volumes are used for the space variables. This discretization generates a new set of equations and a new (numerical) model. The error introduced when going from the mathematical model to the numerical model is called the truncation error.

If the numerical model is consistent and stable, then the solution to the numerical model equations should approach the solution to the mathematical model equations as the element size approaches zero. This means that convergence is obtained in the numerical solution. Due to the complexity of the fuel cell models described above, it is very difficult to analytically prove uniqueness, consistency, stability, and convergence. It is also difficult to make error estimates, even if the solution to the numerical equations does converge.

A high fidelity model of a fuel cell may include many dependent variables such as concentration, temperature, velocity, potential, pressure, and other fields described in the model. For this reason, a segregation of the solution procedure is required by solving a smaller set of equations fully coupled and then iterating over all possible smaller sets in one nonlinear iteration. To obtain faster convergence, variables such as the potential in the electrodes and in the electrolyte should then be solved in the same set, due to their tight coupling and presence in the

exponent in the reaction kinetics expressions. The equations for the material balances can usually be solved one at a time in the segregated scheme. The flow equations can be solved fully coupled or segregated but then using a so-called projection method.

18.6.2 Examples of Practical Implications

When modeling fuel cells and gas diffusion electrodes, simplifications are almost always inevitable. These have to be handled with care, since they may easily introduce physical inconsistencies that lead to ill-posed problems or inaccuracy in the mathematical model. If the Tafel equations are used as a simplification to the Butler–Volmer equations, then it has to be established that all part of the electrodes are far from equilibrium. If not, then substantial errors may be introduced by such simplifications (Fig. 18.6). The concentration overpotential has to be accurately introduced in the model, since starved part of the electrodes may have small activation overpotentials and therefore be close to equilibrium for the local gas and electrolyte composition. The use of the Tafel equations in combination with a poor description of the concentration overpotential is a common source of inaccuracy in fuel cell modeling. This may also lead to convergence problems, since the model may not follow the conservation laws and therefore become ill-posed.

Once the numerical model equations are solved, the convergence of the solution can be studied. This can be achieved by solving the problem for different element sizes and also for different element orders. One possible method for developing high fidelity models of the reaction kinetics and mass transport effects in the gas diffusion electrodes, and in the electrolyte, is to start with one-dimensional models. These model equations are relatively quick to solve and it is also possible to run the simulation for many different element sizes, which may give a hint of the accuracy and convergence that may be

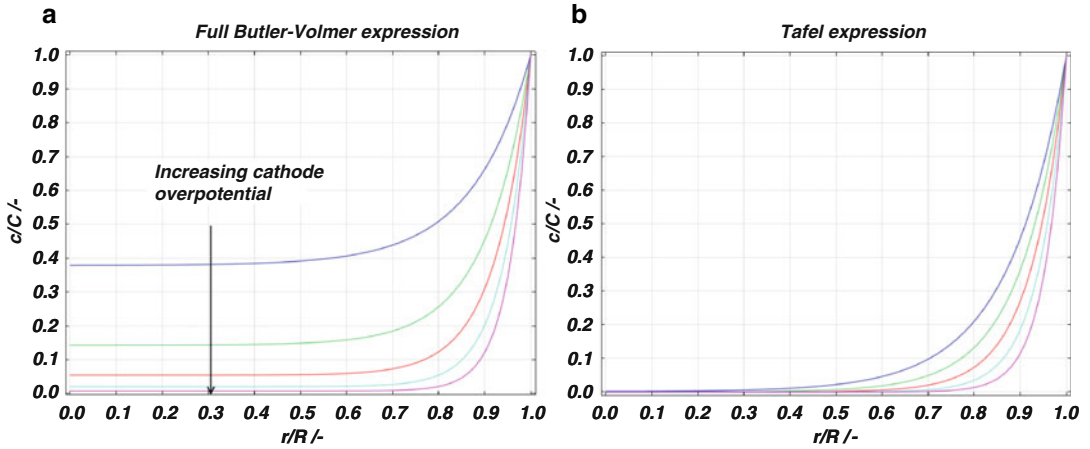
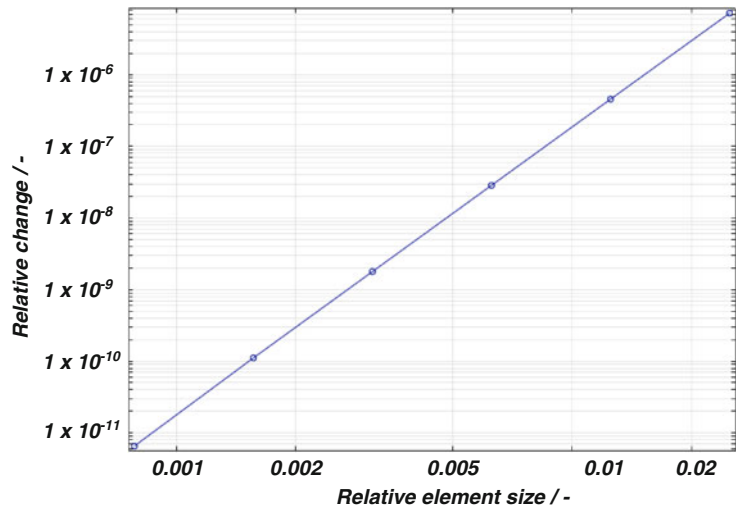


Fig. 18.6 Dimensionless concentration profiles of oxygen in an agglomerate for different overpotentials with full Butler–Volmer expression accounting for concentration overpotential (a) and Tafel expression (b). The reaction rate close to the middle of the agglomerates in (a) is

almost 0 due to the concentration overpotential even when the oxygen concentration is not 0 while in (b) the concentration becomes 0 for all overpotentials (infinite concentration overpotential in theory)

Fig. 18.7 Relative change in average local current density in an agglomerate as a function of the relative element size



expected from the results in a two-dimensional or three-dimensional model. As shown in Fig. 18.7, plotting a relevant quantity, such as the change in current density as a function of the logarithm of the element size, also gives an estimate of the order of convergence of the numerical solution with respect to the element size.

Due to the large number of dependent variables and the discretization that requires

millions of elements, high-fidelity three-dimensional models are almost always under-resolved, at least in some regions in the modeled domain. If sharp gradients are present in these under-resolved areas, then instabilities may be created, which may propagate to the whole domain. In order to better resolve these gradients, local mesh refinement may be applied to these regions. Adaptive mesh refinement and boundary layer

meshing are meshing functionality available in most commercial numerical packages. In addition, different methods for streamline or artificial diffusion and shock capturing may be applied to the cost of reduced accuracy. The reduced accuracy may be a decent trade-off if the alternative is no numerical solution at all.

When convergence has been established using different element sizes and checking that the results make sense, then the sensitivity to input data in the numerical model may also be investigated. Advanced simulation software usually includes functionality for sensitivity analysis. Checking the sensitivity to different input data is the first step towards optimizing a design. Parameters that have a large impact on the operation and on the performance of the cell may be investigated further and may be used for optimization of a design. More on computational strategies for solving fuel cell models and super-computer calculation capacity are found in [13, 246].

18.7 Input Parameters and Experimental Data for Model Validation

A common source of error in fuel cell modeling is poor use of input data which must be relevant for the studied condition. For example, the exchange current density for the charge transfer reaction have to be valid for the reference concentrations and reference electrode potential used for the calculation of the concentration overpotential, since this will determine the convergence to the correct equilibrium currents. If possible, values for transport properties must also follow the same reference state to avoid unnecessary sources of inconsistency.

Depending on the situation, a simple comparison of the simulated data with the experimentally measured current–voltage data may be not enough. Profound internal information of a working HT-PEM fuel cell is indispensable when it comes to full model validation and interpretation

of the simulated quantity distributions. On one hand an adequate hardware must be used to perform experimental investigations, on the other hand it is important to define corresponding subdomain and boundary conditions. For example, the definition of the model operating temperature is not as easy as it seems since a simple constant temperature boundary condition may sometimes not be appropriate. Single HT-PEM fuel cells and small stacks must be heated up to the desired operating temperature using heating elements, which will also be used to keep that temperature constant. The tempering of large HT-PEM fuel cell stacks is mostly done with thermo oil. In any case, the cells and stacks should be thermally insulated which again increases the complexity of a detailed model setup. Generally spoken, the more complex the model geometry is, the more difficult it is to apply the correct boundary conditions on all boundaries. Table 18.8 summarizes several model validation quantities.

Figure 18.8 shows a typical comparison between simulated and measured solid-phase temperature and current density values within the cathode side catalyst layer. The experimental setup for segmented measurements was presented in detail in [96, 97, 115]. A straight parallel flow-field was used (channel-to-land ratio 1 mm/1 mm). A 50 cm² MEA (Celtec[®]-P 1000) was used and the cell was operated as 160 °C (solid-phase-set-temperature controlled with four temperature sensors PT-100 placed at four different locations). Both distributions are very similar but the observed gradients are much more pronounced in the measurements. The solid-phase temperature distribution follows the current density distribution and the fluid-flow (mal)distribution defined by the straight flow-field. The highest solid-phase temperature values are seen in the region of the highest current density values. The current density distribution is mainly defined by the oxygen availability overlapped by the fluid-flow distribution. Especially in the region of the middlemost gas channel, a notable difference between the simulated and measured values is observed.

Table 18.8 Several model validation quantities

Measurement	HT-PEM fuel cell model	Note
Dimensions and geometrical aspects of the cell	Part of the model setup	Mostly easy to get. Geometrical MEA data can be extracted from SEM/TEM images
Current and voltage	May be defined as boundary condition	Can directly be measured
Gas composition, relative humidity, and gas flow rate	Defined as boundary conditions and gas composition	Correct density and viscosity of gas mixture must be used
Pressure loss over flow-field	Defined as boundary condition at the outlet	Correct density and viscosity of gas mixture must be used
Gas velocity (e.g., particle image velocimetry (PIV))	Defined as boundary condition at the inlet	Experimental data difficult to get
Gas temperature	Defined as boundary condition	Difficult to measure at the flow-field inlet (radiation should not be neglected)
Operating temperature	Defined as boundary condition (solid-phase)	Correct placement of the temperature sensors is important
Solid-phase temperature distribution	Simulated distribution available (e.g., CFD model)	Available through segmented measurements
Current density distribution	Simulated distribution available (e.g., CFD model)	Available through segmented measurements
Heat transfer (e.g., free or forced convection)	Defined as boundary condition	Correct heat transfer coefficients must be used (analytically calculated)
Material data	Defined as model constants, parameters, and functions	Difficult to get for commercially available products
Phosphoric acid behavior	Electrolyte modeling	Available via in-situ diagnostics (e.g., Raman spectroscopy)
Membrane and catalyst layer composition	Defined as model constants, parameters, and functions	Difficult to get for commercially available products. Experimental investigations needed
Membrane resistance	Part of the model setup (conductivity)	Available via EIS measurements
Material parameters	Part of the model setup	Use in-plane and through-plane material parameters (e.g., electrical and thermal conductivity)
So-called tuning parameters	e.g., (reference) exchange current density, transfer coefficient, active surface area	Literature values can only be used if the experimental conditions agree with the simulated operating conditions. Values should be used in a reasonable range only. The transfer coefficient strongly influences the simulation results (can reliably be estimated at very low current densities)

18.8 Conclusions

The first works on PAFC modeling and simulation came up many years ago whereas HT-PEM fuel cell modeling and simulation is relatively new. During the last years, the level of detail

gradually increased in the model setups, directly influencing the reliability of the reported results. Today, profound experimental data is available in literature, but additional investigations must be performed to verify the scope and reliability of the important modeling parameters such as the so-called tuning parameters out of which the

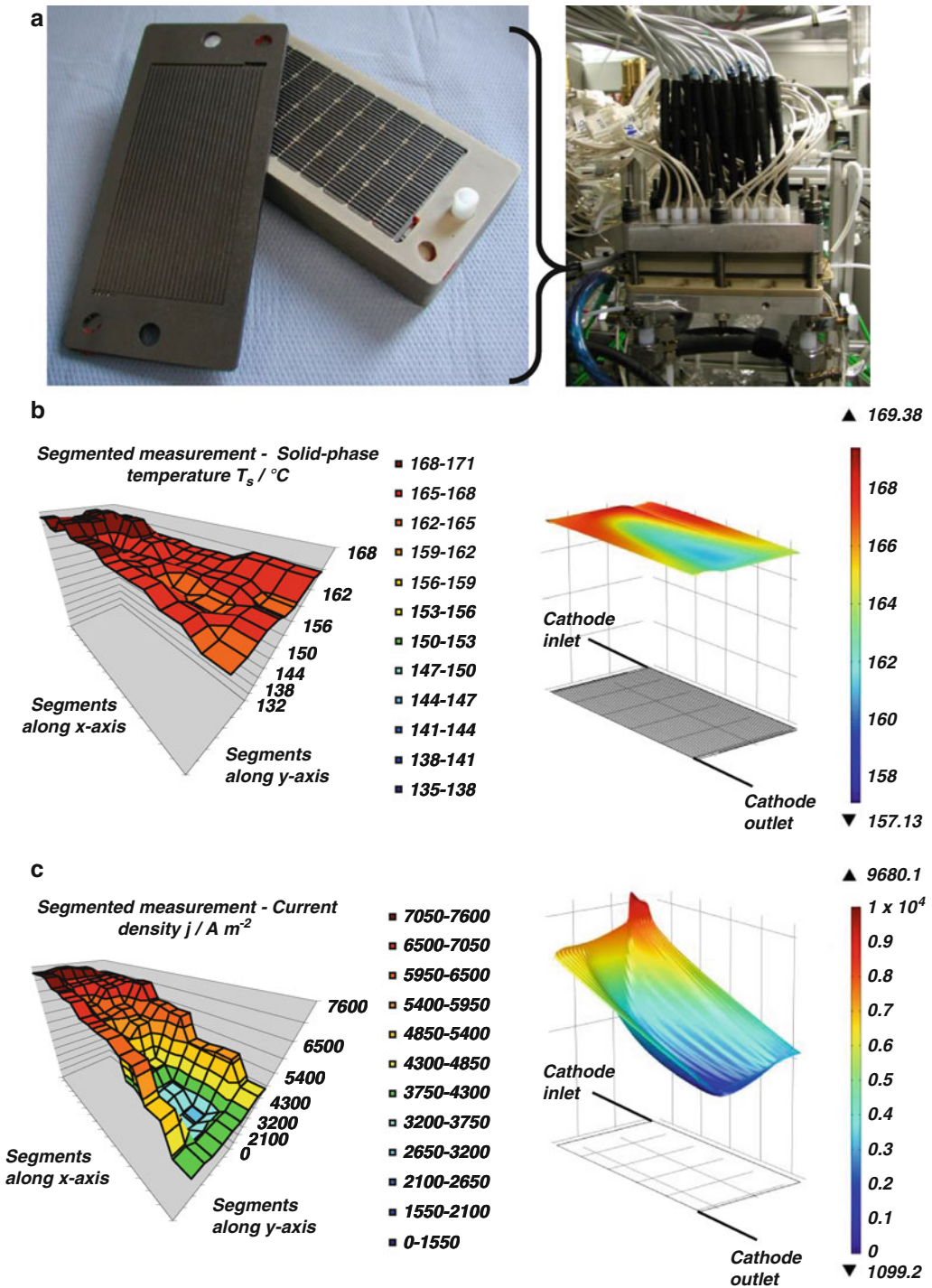


Fig. 18.8 Comparison between simulated and measured values at 24 A load current, $\lambda_a = 1.3$, $\lambda_c = 1.6$, $U = 0.36$ V. The segmented cathode side measurement plate and complete segmented HT-PEM fuel cell (thermal insulation removed) (a). Simulated and measured solid-phase temperature (b) and current density (c)

transfer coefficient has the most important influence on the simulation results. As can be seen from Tables 18.1, 18.2, 18.3, 18.4, 18.5, and 18.6, higher order polynomials are mostly used to fit experimental data relevant to HT-PEM fuel cell modeling. In fact, the fundamental studies on hot, concentrated phosphoric acid, published some 50–60 years ago, are currently experiencing a real renaissance. To recapitulate, there are many electrolyte models able to describe the $\text{H}_3\text{PO}_4\text{-H}_2\text{O}$ system. However, none of those models were adapted to the concentration range greater than 100 wt% which is of interest for HT-PEM fuel cell application. Regression of interaction parameters in that range might be difficult as experimental data with the entire representation of all species in the liquid and gas phase is scarce. Therefore, further experimental investigations are desirable. When it comes to coupling of the vapor–liquid equilibrium and electrolyte model with an overall fuel cell CFD model, one has to consider the modeling scale and which information is really desired. For example, the activity coefficients that are needed to describe the vapor–liquid equilibrium can be calculated from a dedicated electrolyte model. Moreover, these coefficients serve to adequately describe the multicomponent diffusion in the liquid phase via the Maxwell–Stefan approach. The exact description of the swelling and shrinking of electrolyte, its redistribution, and the loss of active surface area coupled to a validated agglomerate model approach would be of great interest. To simulate charge transfer (Nernst–Planck) in detail, the exact species distribution in the liquid phase might be of interest, or to investigate acid evaporation, the exact species distribution in the vapor phase is of interest. For the calculation of the local apparent acid concentration a model with only two pseudo components may be sufficient. On the lower modeling scale, molecular dynamics simulations could be used to calculate, e.g., various diffusion coefficients, solubilities, or the ionic transference numbers to support HT-PEM fuel cell modeling and simulation approaches. Finally, it must be noted that the current HT-PEM fuel cell models are rather qualitatively than quantitatively able to

describe the operational behavior. Much work remains until predictive HT-PEM fuel cell models becomes reality.

References

1. Carter D, Wing J (2013) Fuel cell today—the fuel cell industry review 2013. Wonderberry UK Ltd, London
2. Costamagna P, Srinivasan S (2001) Quantum jumps in the PEMFC science and technology from the 1960s to the year 2000: part I. Fundamental scientific aspects. *J Power Sources* 102:242–252
3. Costamagna P, Srinivasan S (2001) Quantum jumps in the PEMFC science and technology from the 1960s to the year 2000: part II. Engineering, technology development and application aspects. *J Power Sources* 102:253–269
4. Weber AZ, Newman J (2004) Modeling transport in polymer-electrolyte fuel cells. *Chem Rev* 104:4679–4726
5. Wang CY (2004) Fundamental models for fuel cell engineering. *Chem Rev* 104:4727–4766
6. Haraldsson K, Wipke K (2004) Evaluating PEM fuel cell system models. *J Power Sources* 126:88–97
7. Yao KZ, Karan K, McAuley KB et al (2004) A review of mathematical models for hydrogen and direct methanol polymer electrolyte membrane fuel cells. *Fuel Cells* 4:3–29
8. Bıyıkoğlu A (2005) Review of proton exchange membrane fuel cell models. *Int J Hydrogen Energy* 30:1181–1212
9. Faghri A, Guo Z (2005) Challenges and opportunities of thermal management issues related to fuel cell technology and modeling. *Int J Heat Mass Transfer* 48:3891–3920
10. Cheddıe D, Munroe N (2005) Review and comparison of approaches to proton exchange membrane fuel cell modeling. *J Power Sources* 147:72–84
11. Tao WQ, Min CH, Liu XL et al (2006) Parameter sensitivity examination and discussion of PEM fuel cell simulation model validation: part I. Current status of modeling research and model development. *J Power Sources* 160:359–373
12. Djilali N (2007) Computational modelling of polymer electrolyte membrane (PEM) fuel cells: challenges and opportunities. *Energy* 32:269–280
13. Siegel C (2008) Review of computational heat and mass transfer modeling in polymer-electrolyte-membrane (PEM) fuel cells. *Energy* 33:1331–1352
14. Kulikovskiy AA (2010) Analytical modelling of fuel cells, 1st edn. Elsevier, Amsterdam
15. Mench MM (2010) Advanced modeling in fuel cell systems: a review of modeling approaches. In: Stolten D (ed) *Hydrogen and fuel cells—fundamentals, technologies and application*. Wiley-VCH, Weinheim, pp 89–118

16. Wannek C (2010) High-temperature PEM fuel cells: electrolytes, cells, and stacks. In: Stolten D (ed) *Hydrogen and fuel cells—fundamentals, technologies and applications*. Wiley-VCH, Weinheim, pp 17–40
17. Kulikovskiy A (2012) Messages from analytical modeling of fuel cells. In: Stolten D, Emonts B (eds) *Fuel cell science and engineering—materials, processes, systems and technology*. Wiley-VCH, Weinheim, pp 647–668
18. Reimer U (2012) High-temperature polymer electrolyte fuel-cell modeling. In: Stolten D, Emonts B (eds) *Fuel cell science and engineering—materials, processes, systems and technology*. Wiley-VCH, Weinheim, pp 819–838
19. Anahara R (1990) Fuji electric phosphoric acid fuel cell activities. *J Power Sources* 29:109–117
20. Anahara R (1992) A perspective on PAFC commercialization by Fuji Electric. *J Power Sources* 37:119–131
21. Shibata K, Watanabe K (1994) Philosophies and experiences of PAFC field trials. *J Power Sources* 49:77–102
22. Nymoen H (1994) PAFC demonstration plants in Europe: first results. *J Power Sources* 49:63–76
23. Hojo N, Okuda M, Nakamura M (1996) Phosphoric acid fuel cells in Japan. *J Power Sources* 61:73–77
24. Vanhanen JP, Kauranen PS, Lund PD (1997) Operation experiences of a phosphoric acid fuel cell in a solar hydrogen energy system. *Int J Hydrogen Energy* 22:707–713
25. Whitaker R (1998) Investment in volume building: the ‘virtuous cycle’ in PAFC. *J Power Sources* 71:71–74
26. Kasahara K, Morioka M, Yoshida H et al (2000) PAFC operating performance verified by Japanese gas utilities. *J Power Sources* 86:298–301
27. Spiegel RJ, Preston JL (2003) Technical assessment of fuel cell operation on anaerobic digester gas at the Yonkers, NY, wastewater treatment plant. *Waste Manag* 23:709–717
28. Sammes N, Bove R, Stahl K (2004) Phosphoric acid fuel cells: fundamentals and applications. *Curr Opin Solid State Mater Sci* 8:372–378
29. <http://www.doosan.com/>. Accessed Aug 2014
30. <http://www.fujielectric.com/>. Accessed June 2014
31. <http://www.n2telligence.com/>. Accessed June 2014
32. Wainright JS, Wang JT, Weng D et al (1995) Acid-doped polybenzimidazoles: a new polymer electrolyte. *J Electrochem Soc* 142:L121–L123
33. Samms SR, Wasmus S, Savinell RF (1996) Thermal stability of proton conducting acid doped polybenzimidazole in simulated fuel cell environments. *J Electrochem Soc* 143:1225–1232
34. Wang JT, Savinell RF, Wainright JS et al (1996) A H₂/O₂ fuel cell using acid doped polybenzimidazole as a polymer electrolyte. *Electrochim Acta* 41:193–197
35. <http://www.fumatech.com>. Accessed June 2014
36. <http://www.adventech.gr/>. Accessed June 2014
37. <http://daposy.com/>. Accessed June 2014
38. <http://serenergy.com/>. Accessed June 2014
39. <http://www.elcore.com/>. Accessed June 2014
40. Li Q, He R, Jensen JO et al (2004) PBI-based polymer membranes for high temperature fuel cells—preparation, characterization and fuel cell operation. *Fuel Cells* 4:147–159
41. Zhang J, Xie Z, Zhang J et al (2006) High temperature PEM fuel cells. *J Power Sources* 160:872–891
42. Li QF, Rudbeck HC, Chromik A et al (2010) Properties, degradation and high temperature fuel cell test of different types of PBI and PBI blend membranes. *J Membr Sci* 347:260–270
43. Aili D, Hansen MK, Pan C et al (2011) Phosphoric acid doped membranes based on Nafion[®], PBI and their blends—membrane preparation, characterization and steam electrolysis testing. *Int J Hydrogen Energy* 36:6985–6993
44. Bose S, Kuila T, Nguyen TXH et al (2011) Polymer membranes for high temperature proton exchange membrane fuel cell: recent advances and challenges. *Prog Polym Sci* 36:813–836
45. Chandan A, Hattenberger M, El-kharouf A et al (2013) High temperature (HT) polymer electrolyte membrane fuel cells (PEMFC)—a review. *J Power Sources* 231:264–278
46. Sugano N, Ishiwata T, Kawai S et al (1994) Investigation on dynamic characteristics of fuel cell stack cooling system. *Trans Jpn Soc Mech Eng* 60:1597–1601
47. Miki H, Shimizu A (1998) Dynamic characteristics of phosphoric-acid fuel-cell stack cooling system. *Appl Energy* 61:41–56
48. Kwak HY, Lee HS, Jung JY et al (2004) Exergetic and thermoeconomic analysis of a 200-kW phosphoric acid fuel cell plant. *Fuel* 83:2087–2094
49. Zervas PL, Tatis A, Sarimveis H et al (2008) Development of a novel computational tool for optimizing the operation of fuel cells systems: application for phosphoric acid fuel cells. *J Power Sources* 185:345–355
50. Zhang H, Lin G, Chen J (2012) Multi-objective optimization analysis and load matching of a phosphoric acid fuel cell system. *Int J Hydrogen Energy* 37:3438–3446
51. Tanni MA, Arifujjaman M, Iqbal T (2013) Dynamic modeling of a phosphoric acid fuel cell (PAFC) and its power conditioning system. *J Clean Energy Technol* 1:178–183
52. Iczkowski RP, Cutlip MB (1980) Voltage losses in fuel cell cathodes. *J Electrochem Soc* 127:1433–1440
53. Yang SC, Cutlip MB, Stonehart P (1990) Simulation and optimization of porous gas-diffusion electrodes used in hydrogen/oxygen phosphoric acid fuel cells. *Electrochim Acta* 35:869–878

54. Yang SC (2000) Modeling and simulation of steady-state polarization and impedance response of phosphoric acid fuel-cell cathodes with catalyst-layer microstructure consideration. *J Electrochem Soc* 147:71–77
55. Abdul-Aziz A, Alkasab KA (1994) Performance of serpentine passages in the cooling system of a phosphoric fuel cell stack. *Exp Therm Fluid Sci* 8:101–111
56. Yoshioka S, Mitsuda K, Horiuchi H et al (1997) Mechanism of vaporization of phosphoric acid in a PAFC. *Denki Kagaku* 65:314–319
57. Yoshioka S, Mitsuda K, Horiuchi H et al (1998) Condensation of vaporized phosphoric acid in a PAFC cathode. *Denki Kagaku* 66:41–47
58. Yamashita K, Taniguchi T (1998) Agglomerate model for DC and AC response of phosphoric acid fuel cell cathode. *J Electrochem Soc* 145:45–49
59. Maggio G (1999) Modelling of phosphoric acid fuel cell cathode behaviour. *J Appl Electrochem* 29:171–176
60. Choudhury SR, Deshmukh MB, Rengaswamy R (2002) A two-dimensional steady-state model for phosphoric acid fuel cells (PAFC). *J Power Sources* 112:137–152
61. Choudhury SR, Choudhury SR, Rangarajan J et al (2005) Step response analysis of phosphoric acid fuel cell (PAFC) cathode through a transient model. *J Power Sources* 140:274–279
62. Psofogiannakis G, Bourgault Y, Conway BE et al (2006) Mathematical model for a direct propane phosphoric acid fuel cell. *J Appl Electrochem* 36:115–130
63. Choudhury SR, Rengaswamy R (2006) Characterization and fault diagnosis of PAFC cathode by EIS technique and a novel mathematical model approach. *J Power Sources* 161:971–986
64. Zervas PL, Koukou MK, Markatos NC (2006) Predicting the effects of process parameters on the performance of phosphoric acid fuel cells using a 3-D numerical approach. *Energy Convers Manag* 47:2883–2899
65. Hirata H, Aoki T, Nakajima K (2011) Numerical study on the evaporative and condensational dissipation of phosphoric acid in PAFC. *J Power Sources* 196:8004–8011
66. Hirata H, Aoki T, Nakajima K (2012) Liquid phase migration effects on the evaporative and condensational dissipation of phosphoric acid in phosphoric acid fuel cell. *J Power Sources* 199:110–116
67. Paul T, Seal M, Banerjee D et al (2014) Analysis of drying and dilution in phosphoric acid fuel cell (PAFC) using galvanometric study and electrochemical impedance spectroscopy. *J Fuel Cell Sci Technol* 11:041001-1–041001-7
68. Korsgaard AR, Refshauge R, Nielsen MP et al (2006) Experimental characterization and modeling of commercial polybenzimidazole-based MEA performance. *J Power Sources* 162:239–245
69. Zenith F, Seland F, Kongstein OE et al (2006) Control-oriented modelling and experimental study of the transient response of a high-temperature polymer fuel cell. *J Power Sources* 162:215–227
70. Andreassen SJ, Kær SK (2008) Modelling and evaluation of heating strategies for high temperature polymer electrolyte membrane fuel cell stacks. *Int J Hydrogen Energy* 33:4655–4664
71. Korsgaard AR, Nielsen MP, Kær SK (2008) Part one: a novel model of HT-based micro-combined heat and power fuel cell system. *Int J Hydrogen Energy* 33:1909–1920
72. Korsgaard AR, Nielsen MP, Kær SK (2008) Part two: control of a novel HT-based micro combined heat and power fuel cell system. *Int J Hydrogen Energy* 33:1921–1931
73. Arsalis A, Nielsen MP, Kær SK (2011) Modeling and parametric study of a 1 kW_e HT-PEMFC-based residential micro-CHP system. *Int J Hydrogen Energy* 36:5010–5020
74. Zuliani N, Taccani R (2012) Microcogeneration system based on HTPEM fuel cell fueled with natural gas: performance analysis. *Appl Energy* 97:802–808
75. Romero-Pascual E, Soler J (2013) Modelling of an HT-based micro-combined heat and power fuel cell system with methanol. *Int J Hydrogen Energy* 39:4053–4059
76. Arsalis A, Nielsen MP, Kær SK (2013) Application of an improved operational strategy on a PBI fuel cell-based residential system for Danish single-family households. *Appl Therm Eng* 50:704–713
77. Authayanun S, Mamlouk M, Scott K et al (2013) Comparison of high-temperature and low-temperature polymer electrolyte membrane fuel cell systems with glycerol reforming process for stationary applications. *Appl Energy* 109:192–201
78. Jannelli E, Minutillo M, Perna A (2013) Analyzing microcogeneration systems based on LT-PEMFC and HT-PEMFC by energy balances. *Appl Energy* 108:82–91
79. Authayanun S, Saebea D, Patcharavorachot Y, Arpornwichanop A (2014) Effect of different fuel options on performance of high-temperature PEMFC (proton exchange membrane fuel cell) systems. *Energy* 68:989–997
80. Park J, Min K (2014) Dynamic modeling of a high-temperature proton exchange membrane fuel cell with a fuel processor. *Int J Hydrogen Energy* 39:10683–10696
81. Cheddie D, Munroe N (2006) Parametric model of an intermediate temperature PEMFC. *J Power Sources* 156:414–423
82. Cheddie D, Munroe N (2006) Three dimensional modeling of high temperature PEM fuel cells. *J Power Sources* 160:215–223
83. Cheddie D, Munroe N (2006) Mathematical model of a PEMFC using a PBI membrane. *Energy Convers Manag* 47:1490–1504

84. Cheddie D, Munroe N (2007) A two-phase model of an intermediate temperature PEMFC. *Int J Hydrogen Energy* 32:832–841
85. Cheddie DF, Munroe NDH (2008) Semi-analytical proton exchange membrane fuel cell modeling. *J Power Sources* 183:164–173
86. Peng J, Lee SJ (2006) Numerical simulation of proton exchange membrane fuel cells at high operating temperature. *J Power Sources* 162:1182–1191
87. Peng J, Lee SJ (2008) Transient response of high temperature PEM fuel cell. *J Power Sources* 179:220–231
88. Wang CP, Chu HS, Yan YY et al (2007) Transient evolution of carbon monoxide poisoning effect of PBI membrane fuel cells. *J Power Sources* 170:235–241
89. Scott K, Pilditch S, Mamlouk M (2007) Modelling and experimental validation of a high temperature polymer electrolyte fuel cell. *J Appl Electrochem* 37:1245–1259
90. Siegel C, Bandlamudi G, Heinzl A (2007) Numerical simulation of a high-temperature PEM (HT) fuel cell. In: *Proceedings of the European COMSOL conference, Grenoble*
91. Siegel C, Bandlamudi G, Heinzl A (2008) Modeling polybenzimidazole/phosphoric acid membrane behaviour in a HTPEM fuel cell. In: *Proceedings of the European COMSOL conference, Hannover*
92. Siegel C, Bandlamudi G, van der Schoot N et al (2009) Large scale 3D flow distribution analysis in HTPEM fuel cells. In: *Proceedings of the European COMSOL conference, Milan*
93. Siegel C, Bandlamudi G, Heinzl A (2008) Evaluating the effects of stack compression on the physical characteristics of HT PEMFCs with CFD modelling software. In: *Proceedings of the fuel cell science and technology conference, Copenhagen*
94. Ubong EU, Shi Z, Wang X (2008) A-3D-modeling and experimental validation of a high temperature PBI based PEMFC. *ECS Trans* 16:79–90
95. Schaar B (2008) Simulation einer Hochtemperatur-PEM-Brennstoffzelle. Dissertation, AutoUni - Schriftreihe, Logos Verlag, Berlin
96. Siegel C, Bandlamudi G, Beckhaus P et al (2009) Segmented current and temperature measurement in a HTPEM fuel cell. In: *Proceedings of the 6th symposium on fuel cell modelling and experimental validation, Bad Herrenalb/Karlsruhe*
97. Siegel C, Bandlamudi G, Heinzl A (2011) Locally resolved measurements in a segmented HTPEM fuel cell with straight flow-fields. *Fuel Cells* 11:489–500
98. Andreasen SJ, Kær SK (2009) Dynamic model of the high temperature proton exchange membrane fuel cell stack temperature. *J Fuel Cell Sci Technol* 6:041006-1–041006-8
99. Scholta J, Messerschmidt M, Jörissen L et al (2009) Externally cooled high temperature polymer electrolyte membrane fuel cell stack. *J Power Sources* 190:83–85
100. Scott K, Mamlouk M (2009) A cell voltage equation for an intermediate temperature proton exchange membrane fuel cell. *Int J Hydrogen Energy* 34:9195–9202
101. Shamardina O, Chertovich A, Kulikovskiy AA et al (2010) A simple model of a high temperature PEM fuel cell. *Int J Hydrogen Energy* 35:9954–9962
102. Kulikovskiy AA, Oetjen HF, Wanek C (2010) A simple and accurate method for high-temperature PEM fuel cell characterisation. *Fuel Cells* 10:363–368
103. Sousa T, Mamlouk M, Scott K (2010) An isothermal model of a laboratory intermediate temperature fuel cell using PBI doped phosphoric acid membranes. *Chem Eng Sci* 65:2513–2530
104. Bergmann A, Gerteisen D, Kurz T (2010) Modelling of CO poisoning and its dynamics in HTPEM fuel cells. *Fuel Cells* 10:278–287
105. Sousa T, Mamlouk M, Scott K (2010) A non-isothermal model of a laboratory intermediate temperature fuel cell using PBI doped phosphoric acid membranes. *Fuel Cells* 10:993–1012
106. Lobato J, Cãnzizares P, Rodrigo MA et al (2010) Three-dimensional model of a 50 cm² high temperature PEM fuel cell. Study of the flow channel geometry influence. *Int J Hydrogen Energy* 35:5510–5520
107. Sousa T, Mamlouk M, Scott K (2010) A dynamic non-isothermal model of a laboratory intermediate temperature fuel cell using PBI doped phosphoric acid membranes. *Int J Hydrogen Energy* 35:12065–12080
108. Lobato J, Cãnzizares P, Rodrigo MA et al (2010) Direct and inverse neural networks modelling applied to study the influence of the gas diffusion layer properties on PBI-based PEM fuel cells. *Int J Hydrogen Energy* 35:7889–7897
109. Jiao K, Li X (2010) A three-dimensional non-isothermal model of high temperature proton exchange membrane fuel cells with phosphoric acid doped polybenzimidazole membranes. *Fuel Cells* 10:351–362
110. Jiao K, Alaefour IE, Li X (2011) Three-dimensional non-isothermal modeling of carbon monoxide poisoning in high temperature proton exchange membrane fuel cells with phosphoric acid doped polybenzimidazole membranes. *Fuel* 90:568–582
111. Siegel C, Bandlamudi G, Heinzl A (2011) Systematic characterization of a PBI/H₃PO₄ sol-gel membrane—modeling and simulation. *J Power Sources* 196:2735–2749
112. Doubek G, Robalinho E, Cunha EF et al (2011) Application of CFD techniques in the modelling and simulation of PBI PEMFC. *Fuel Cells* 11:764–774
113. Mamlouk M, Sousa T, Scott K (2011) A high temperature polymer electrolyte membrane fuel cell

- model for reformat gas. *Int J Electrochem*, Article ID 520473:1–18
114. Kurz T (2011) Entwicklung und Charakterisierung eines portable Hochtemperatur-PEM-Brennstoffzellensystems. Dissertation, Fraunhofer Verlag, Stuttgart
 115. Siegel C, Bandlamudi G, Heinzel A (2011) Solid-phase temperature measurements in a HTPEM fuel cell. *Int J Hydrogen Energy* 36:12977–12990
 116. Olapade PO, Meyers JP, Borup RL et al (2011) Parametric study of the morphological proprieties of HT-PEMFC components for effective membrane hydration. *J Electrochem Soc* 158:B639–B649
 117. Falucci G, Jannelli E, Minutillo M et al (2012) Fluid dynamic investigation of channel design in high temperature PEM fuel cells. *J Fuel Cell Sci Technol* 9:021014-1–021014-10
 118. Kvesić M, Reimer U, Froning D et al (2012) 3D modeling of a 200 cm² HT-PEFC short stack. *Int J Hydrogen Energy* 37:2430–2450
 119. Kvesić M (2012) Modellierung und Simulation von Hochtemperatur-Polymerelektrolyt-Brennstoffzellen. Dissertation, Forschungszentrum Jülich GmbH, Zentralbibliothek Verlag, Jülich
 120. Lüke L, Janßen H, Kvesić M et al (2012) Performance analysis of HT-PEFC stacks. *Int J Hydrogen Energy* 37:9171–9181
 121. Chippar P, Ju H (2012) Three-dimensional non-isothermal modeling of a phosphoric acid-doped polybenzimidazole (PBI) membrane fuel cell. *Solid State Ion* 225:30–39
 122. Park J, Min K (2012) A quasi-three-dimensional non-isothermal dynamic model of a high-temperature proton exchange membrane fuel cell. *J Power Sources* 216:152–161
 123. Reddy EH, Jayanti S (2012) Thermal management strategies for a 1 kWe stack of a high temperature proton exchange membrane fuel cell. *Appl Therm Eng* 48:465–475
 124. Sousa T, Mamlouk M, Scott K et al (2012) Three dimensional model of a high temperature PEMFC. Study of the flow field effect on performance. *Fuel Cells* 12:566–576
 125. Reddy EH, Monder DS, Jayanti S (2013) Parametric study of an external coolant system for a high temperature polymer electrolyte membrane fuel cell. *Appl Therm Eng* 58:155–164
 126. Jiao K, Zhou Y, Du Q et al (2013) Numerical simulations of carbon monoxide poisoning in high temperature proton exchange membrane fuel cells with various flow channel designs. *Appl Energy* 104:21–41
 127. Chippar P, Ju H (2013) Numerical modeling and investigation of gas crossover effects in high temperature proton exchange membrane (PEM) fuel cells. *Int J Hydrogen Energy* 38:7704–7714
 128. Chippar P, Oh K, Kim D et al (2013) Coupled mechanical stress and multi-dimensional CFD analysis for high temperature proton exchange membrane fuel cells (HT-PEMFCs). *Int J Hydrogen Energy* 38:7715–7724
 129. Supra J, Janßen H, Lehnert W et al (2013) Temperature distribution in a liquid cooled HT-PEFC stack. *Int J Hydrogen Energy* 38:1943–1951
 130. Grigoriev SA, Kalinnikov AA, Kuleshov NV et al (2013) Numerical optimization of bipolar plates and gas diffusion electrodes for PBI-based PEM fuel cells. *Int J Hydrogen Energy* 38:8557–8567
 131. Salomov RU, Chiavazzo E, Asinari P (2014) Pore-scale modeling of fluid flow through gas diffusion and catalyst layers for high temperature proton exchange membrane (HT-PEM) fuel cells. *Comput Math Appl* 67:393–411
 132. Bezmalinović D, Strahl S, Roda V et al (2014) Water transport study in a high temperature proton exchange membrane fuel cell stack. Water transport study in a high temperature proton exchange membrane fuel cell stack. *Int J Hydrogen Energy* 39:10627–10640
 133. Chippar P, Oh K, Kim WG et al (2014) Numerical analysis of effects of gas crossover through membrane pinholes in high-temperature proton exchange membrane fuel cells. *Int J Hydrogen Energy* 39:2863–2871
 134. Chippar P, Kang K, Lim YD et al (2014) Effects of inlet relative humidity (RH) on the performance of a high temperature-proton exchange membrane fuel cell (HT-PEMFC). *Int J Hydrogen Energy* 39:2767–2775
 135. Oh K, Chippar P, Ju H (2014) Numerical study of thermal stresses in high temperature proton exchange membrane fuel cell (HT-PEMFC). *Int J Hydrogen Energy* 39:2785–2794
 136. Abdul Rasheed RK, Ehteshami SMM, Chan SH (2014) Analytical modelling of boiling phase change phenomenon in high-temperature proton exchange membrane fuel cells during warm-up process. *Int J Hydrogen Energy* 39:2246–2260
 137. Singdeo D, Dey T, Ghosh PC (2014) Contact resistance between bipolar plate and gas diffusion layer in high temperature polymer electrolyte fuel cells. *Int J Hydrogen Energy* 39:987–995
 138. Kazdal TJ, Lang S, Kühl F et al (2014) Modelling of the vapour-liquid equilibrium of water and the in situ concentration of H₃PO₄ in a high temperature proton exchange membrane fuel cell. *J Power Sources* 249:446–456
 139. Yin Y, Wang J, Yang X et al (2014) Modeling of high temperature proton exchange membrane fuel cells with novel sulfonated polybenzimidazole membranes. *Int J Hydrogen Energy* 39:13671–13680

140. Kim M, Kang T, Kim J et al (2014) One-dimensional modeling and analysis for performance degradation of high temperature proton exchange membrane fuel cell using PA doped PBI membrane. *Solid State Ion* 262:319–323
141. Oh K, Jeong G, Cho E et al (2014) A CO poisoning model for high-temperature proton exchange membrane fuel cells comprising phosphoric acid-doped polybenzimidazole membranes. *Int J Hydrogen Energy* 39(36):21915–21926. <http://dx.doi.org/10.1016/j.ijhydene.2014.06.101>
142. Bockris O'MJ, Reddy AKN (1970) *Modern electrochemistry*. Plenum, New York
143. Bird RB, Stewart WE, Lightfoot EN (2007) *Transport phenomena*, revised 2nd edn. Wiley, New York
144. Newman JS (1990) *Electrochemical systems*, 2nd edn. Prentice Hall, Englewood Cliffs
145. COMSOL Multiphysics 5.0 (2014) *Batteries & fuel cells module—user manual*
146. Björnbom P (1987) Modelling of a double-layered PTFE-bonded oxygen electrode. *Electrochim Acta* 32:115–119
147. COMSOL Multiphysics 5.0 (2014) *CFD module manual—user manual*
148. Korte C (2012) Phosphoric acid, an electrolyte for fuel cells—temperature and composition dependence of vapour pressure and proton conductivity. In: Stolten D, Emonts B (eds) *Fuel cell science and engineering—materials, processes, systems and technology*. Wiley-VCH, Weinheim, pp 335–359
149. Schrödter K, Bettermann G, Staffel T, Wahl F, Klein T, Hofmann T (2008) Phosphoric acid and phosphates. In: *Ullmann's encyclopedia of industrial chemistry*. Wiley-VCH, Weinheim, pp 1–48
150. Zemaitis JF Jr, Clark DM, Rafal M et al (1986) *Handbook of aqueous electrolyte thermodynamics: theory & application*. Wiley, New York
151. Platonov VA (2000) Properties of polyphosphoric acid. *Fibre Chem* 32:325–329
152. Othmer K (2007) *Kirk-Othmer encyclopedia of chemical technology*, 5th edn. Wiley, Hoboken
153. Archie GE (1941) Electrical resistivity log as an aid in determining some reservoir characteristics. *Soc Petrol Eng J* 146:54–62
154. Bouchet R, Siebert E (1999) Proton conduction in acid doped polybenzimidazole. *Solid State Ion* 118:287–299
155. Ma YL, Wainright JS, Litt MH et al (2004) Conductivity of PBI membranes for high-temperature polymer electrolyte fuel cells. *J Electrochem Soc* 151: A8–A16
156. Daletou MK, Kallitsis JK, Voyiatzis G et al (2009) The interaction of water vapors with H₃PO₄ imbibed electrolyte based on PBI/polysulfone copolymer blends. *J Membr Sci* 326:76–83
157. Bandlamudi G (2011) *Systematic characterization of HT PEMFCs containing PBI/H₃PO₄ systems*. Dissertation, Logos Verlag, Berlin
158. Pitzer KS (ed) (1991) *Activity coefficients in electrolyte solutions*, 2nd edn. CRC, Boca Raton
159. Rafal M, Berthold JW, Scrivner NC et al (1994) *Models for electrolyte solutions*. In: Sandler SI (ed) *Models for thermodynamic and phase equilibria calculations*. Marcel Dekker, New York, pp 601–669
160. Loehe JR, Donohue MD (1997) Recent advances in modeling thermodynamic properties of aqueous strong electrolyte systems. *AIChE J* 43:180–195
161. Anderko A, Wang P, Rafal M (2002) *Electrolyte solutions: from thermodynamic and transport property models to the simulation of industrial processes*. *Fluid Phase Equilib* 194–197:123–142
162. Pohl HA, Chartoff RP (1964) Carriers and unpaired spins in some organic semiconductors. *J Polym Sci Part A* 2:2787–2806
163. Chin D, Chang H (1989) On the conductivity of phosphoric acid electrolyte. *J Appl Electrochem* 19:95–99
164. Mason CM, Culvern JB (1949) Electrical conductivity of orthophosphoric acid and of sodium and potassium dihydrogen phosphates at 25°C. *J Am Chem Soc* 71:2387–2393
165. Greenwood NN, Thompson A (1959) The mechanism of electrical conduction in fused phosphoric and trideuterophosphoric acids. *J Chem Soc* 3485–3492
166. MacDonald DI, Boyack JR (1969) Density, electrical conductivity, and vapor pressure of concentrated phosphoric acid. *J Chem Eng Data* 14:380–384
167. Xiao L, Zhang H, Scanlon E et al (2005) High-temperature polybenzimidazole fuel cell membranes via a sol-gel process. *Chem Mater* 17:5328–5333
168. Lang S, Kazdal TJ, Kühl F et al (2014) Diffusion coefficients and VLE data of aqueous phosphoric acid. *J Chem Thermodyn* 68:75–81
169. Christensen JH, Reed RB (1955) Design and analysis data—density of aqueous solutions of phosphoric acid measurements at 25°C. *Ind Eng Chem* 47:1277–1280
170. Kunz H, Gruver G (1978) The effect of electrolyte concentration on the catalytic activity of platinum for electrochemical oxygen reduction in phosphoric acid. *Electrochim Acta* 23:219–222
171. Klinedinst K, Bett J, Macdonald J, Stonehart P (1974) Oxygen solubility and diffusivity in hot concentrated H₃PO₄. *J Electroanal Chem Interfacial Electrochem* 57:281–289
172. Scharifker BR, Zelenay P, Bockris O (1987) The kinetics of oxygen reduction in molten phosphoric acid at high temperatures. *J Electrochem Soc* 134:2714–2725
173. Brown EH, Whitt CD (1952) Vapor pressure of phosphoric acids. *Ind Eng Chem* 44:615–618
174. Wartenberg V (1937) *The thermochemistry of the chemical substances*. Russel Bichowsky RR, Rossini DF. Book Department Reinhold Publishing Corporation, New York. *Z Elektrochem Angew Phys Chem* 43:72

175. Gubbins KE, Walker RD (1965) The solubility and diffusivity of oxygen in electrolytic solutions. *J Electrochem Soc* 112:469–471
176. Yatskovskii F (1969) Solubility and diffusion of hydrogen in solution of potassium hydroxide and phosphoric acid. *Russ J Phys Chem* 43:575–776
177. Wakefield ZT, Luff BB, Reed RB (1972) Heat capacity and enthalpy of phosphoric acid. *J Chem Eng Data* 17:420–423
178. Turnbull AG (1965) Thermal conductivity of phosphoric acid. *J Chem Eng Data* 10:118–119
179. Walters HV (1983) Corrosion of a borosilicate glass by orthophosphoric acid. *J Am Ceram Soc* 66:572–574
180. Kreysa G, Schütze M (eds) (2008) Corrosion handbook—corrosive agents and their interaction with materials. Wiley-VCH, Weinheim
181. Li Q, Gang X, Hjuler HA et al (1994) Limiting current of oxygen reduction on gas-diffusion electrodes for phosphoric acid fuel cells. *J Electrochem Soc* 141:3114–3119
182. Galbiati S, Baricci A, Casalegno A et al (2012) Experimental study of water transport in a polybenzimidazole-based high temperature PEMFC. *Int J Hydrogen Energy* 37:2462–2469
183. Hirschberg HG (1999) Handbuch Verfahrenstechnik und Anlagenbau. Chemie, Technik und Wirtschaftlichkeit. Springer, Berlin
184. Schmalz EO (1969) Bestimmung der Dampfdruckkurven von Wasser über Phosphorsäuren. *Z Phys Chem Leipzig* 245:344–350
185. Kablukov IA, Zagwosdkin KI (1935) Die Dampfspannungen der Phosphorsäurelösungen. *Z Anorg Allg Chem* 224:315–321
186. Fontana BJ (1951) The vapor pressure of water over phosphoric acids. *J Am Chem Soc* 73:3348–3350
187. Elmore KL, Mason CM, Christensen JH (1946) Activity of orthophosphoric acid in aqueous solution at 25°C from vapor pressure measurements. *J Am Chem Soc* 68:2528–2532
188. Jiang C (1996) Thermodynamics of aqueous phosphoric acid solution at 25°C. *Chem Eng Sci* 51:689–693
189. Elmore KL, Hatfield JD, Dunn RL et al (1965) Dissociation of phosphoric acid solutions at 25°C. *J Phys Chem* 69:3520–3525
190. Mesmer RE, Baes CF (1974) Phosphoric acid dissociation equilibria in aqueous solutions to 300°C. *J Solution Chem* 3:307–322
191. Preston CM, Adams WA (1979) A laser Raman spectroscopic study of aqueous orthophosphate salts. *J Phys Chem* 83:814–821
192. Cherif M, Mgaidi A, Ammar N et al (2000) A new investigation of aqueous orthophosphoric acid speciation using raman spectroscopy. *J Solution Chem* 29:255–269
193. Marshall WL, Begun GM (1989) Raman spectroscopy of aqueous phosphate solutions at temperatures up to 450°C. Two liquid phases, supercritical fluids, and pyro- to ortho-phosphate conversions. *J Chem Soc, Faraday Trans* 2(85):1963–1978
194. Higgins CE, Baldwin WH (1955) Dehydration of orthophosphoric acid. *Anal Chem* 27:1780–1783
195. Jameson RF (1959) The composition of the strong phosphoric acids. *J Chem Soc*: 752–759
196. Huhti AL, Gartaganis PA (1956) The composition of the strong phosphoric acids. *Can J Chem* 34:785–797
197. Nelson AK (1964) Hydrolysis rates of solutions of pyrophosphoric acid. *J Chem Eng Data* 9:357
198. Bunton CA, Chaimovich H (1965) The acid-catalyzed hydrolysis of pyrophosphoric acid. *Inorg Chem* 4:1763–1766
199. Nuri B (2011) Das Dampf-flüssig-Gleichgewicht Phosphorsäure-Wasser bei Anwesenheit von Polybenzimidazol. Diplomarbeit, Technische Universität Darmstadt
200. Squires RG, Reklaitis GV (eds) (1980) Computer applications to chemical engineering. Computation of phase and chemical equilibrium: a review. ACS symposium series. American Chemical Society, Washington, DC, pp 115–134
201. Smith WR (1980) The computation of chemical equilibria in complex systems. *Ind Eng Chem Fund* 19:1–10
202. Greiner H (1988) Computing complex chemical equilibria by generalized linear programming. *Math Comput Model* 10:529–550
203. Debye P, Hückel E (1923) Zur Theorie der Elektrolyte. I. Gefrierpunktniedrigung und verwandte Erscheinungen. The theory of electrolytes. I. Lowering of freezing point and related phenomena. *Physik Z* 24:185–206
204. Waisman E, Lebowitz JL (1970) Exact solution of an integral equation for the structure of a primitive model of electrolytes. *J Chem Phys* 52:4307–4309
205. Poling BE, Prausnitz JM, O'Connell JP (2001) The properties of gases and liquids, 5th edn. McGraw-Hill, New York
206. Wang P, Springer RD, Anderko A et al (2004) Modeling phase equilibria and speciation in mixed-solvent electrolyte systems. *Fluid Phase Equilib* 222–223:11–17
207. Messnaoui B, Bounahmidi T (2005) Modeling of excess properties and vapour-liquid equilibrium of the system $H_3PO_4-H_2O$. *Fluid Phase Equilib* 237:77–85
208. Pitzer K, Silvester L (1976) Thermodynamics of electrolytes. VI. Weak electrolytes including H_3PO_4 . *J Solution Chem* 5:269–278
209. Cherif M, Mgaidi A, Ammar MN et al (2000) Modelling of the equilibrium properties of the

- system H₃PO₄-H₂O: Representation of VLE and liquid phase composition. *Fluid Phase Equilib* 175:197–212
210. Cherif M, Mgaidi A, Ammar MN et al (2002) Representation of VLE and liquid phase composition with an electrolyte model: application to H₃PO₄-H₂O and H₂SO₄-H₂O. *Fluid Phase Equilib* 194–197:729–738
211. Rumpf B, Maurer G (1994) Solubility of ammonia in aqueous solutions of phosphoric acid: model development and application. *J Solution Chem* 23:37–51
212. Barker JA (1967) Perturbation theory and equation of state for fluids: the square-well potential. *J Chem Phys* 47:2856–2861
213. Barker JA (1967) Perturbation theory and equation of state for fluids. II. A successful theory of liquids. *J Chem Phys* 47:4714–4721
214. Gross J, Sadowski G (2001) Perturbed-chain SAFT: an equation of state based on a perturbation theory for chain molecules. *Ind Eng Chem Res* 40:1244–1260
215. van Nhu N, Singh M, Leonhard K (2008) Quantum mechanically based estimation of perturbed-chain polar statistical associating fluid theory parameters for analyzing their physical significance and predicting properties. *J Phys Chem B* 112:5693–5701
216. Cameretti LF, Sadowski G, Mollerup JM (2005) Modeling of aqueous electrolyte solutions with perturbed-chain statistical associated fluid theory. *Ind Eng Chem Res* 44:3355–3362
217. Held C, Reschke T, Mohammad S, Luza A, Sadowski G (2014) ePC-SAFT revised. *Chem Eng Res Des*. <http://dx.doi.org/10.1016/j.cherd.2014.05.017>
218. Naeem S, Sadowski G (2010) pePC-SAFT: modeling of polyelectrolyte systems. *Fluid Phase Equilib* 299:84–93
219. Lewis WK, Whitman WG (1924) Principles of gas absorption. *Ind Eng Chem* 16:1215–1220
220. Toor HL, Marchello JM (1958) Film-penetration model for mass and heat transfer. *AIChE J* 4:97–101
221. Higbie R (1935) The rate of absorption of a pure gas into still liquid during short periods of exposure. *Trans Am Inst Chem Eng* 35:36–60
222. Danckwerts PV (1951) Significance of liquid-film coefficients in gas absorption. *Ind Eng Chem* 43:1460–1467
223. Hertz H (1882) Ueber die Verdunstung der Flüssigkeiten, insbesondere des Quecksilbers, im luftleeren Raume. *Ann Phys* 253:177–193
224. Knudsen M (1915) Die maximale Verdampfungsgeschwindigkeit des Quecksilbers. *Ann Phys* 352:697–708
225. Prüger W (1940) Die Verdampfungsgeschwindigkeit der Flüssigkeiten. *Z Phys* 115:202–244
226. Eames IW, Marr NJ, Sabir H (1997) The evaporation coefficient of water: a review. *Int J Heat Mass Transfer* 40:2963–2973
227. Matsumoto M (1998) Molecular dynamics of fluid phase change. *Fluid Phase Equilib* 144:307–314
228. Meland R, Frezzotti A, Ytrehus T et al (2004) Non-equilibrium molecular-dynamics simulation of net evaporation and net condensation, and evaluation of the gas-kinetic boundary condition at the interphase. *Phys Fluids* 16:223–243
229. Marek R, Straub J (2001) Analysis of the evaporation coefficient and the condensation coefficient of water. *Int J Heat Mass Transfer* 44:39–53
230. Schrage RW (1953) A theoretical study of interphase mass transfer. Columbia University Press, New York
231. Nabavian K, Bromley LA (1963) Condensation coefficient of water. *Chem Eng Sci* 18:651–660
232. Kwon K, Park JO, Yoo DY et al (2009) Phosphoric acid distribution in the membrane electrode assembly of high temperature proton exchange membrane fuel cells. *Electrochim Acta* 54:6570–6575
233. Chen C, Lai W (2010) Effects of temperature and humidity on the cell performance and resistance of a phosphoric acid doped polybenzimidazole fuel cell. *J Power Sources* 195:7152–7159
234. Matar S, Higier A, Liu H (2010) The effects of excess phosphoric acid in a polybenzimidazole-based high temperature proton exchange membrane fuel cell. *J Power Sources* 195:181–184
235. Kaserer S, Caldwell KM, Ramaker DE, Roth C (2013) Analyzing the influence of H₃PO₄ as catalyst poison in high temperature PEM fuel cells using in-operando X-ray absorption spectroscopy. *J Phys Chem C* 117:6210–6217
236. Sui Y, Ding H, Spelt PD (2014) Numerical simulations of flows with moving contact lines. *Annu Rev Fluid Mech* 46:97–119
237. Lee MS, Aute V, Riaz A, Radermacher R (2012) A review on direct two-phase. Phase change flow simulation methods and their applications. In: International refrigeration and air conditioning conference, Purdue University Purdue e-Pubs, Paper 1289. <http://docs.lib.purdue.edu/iracc/1289>
238. Mukherjee PP, Kang Q, Wang C (2011) Pore-scale modeling of two-phase transport in polymer electrolyte fuel cells—progress and perspective. *Energy Environ Sci* 4:346–369
239. Garnett JCM (1904) Colours in metal glasses and in metallic films. *Philos Trans R Soc A* 203:385–420
240. Das PK, Li X, Liu Z (2010) Effective transport coefficients in PEM fuel cell catalyst and gas diffusion layers: beyond Bruggeman approximation. *Appl Energy* 87:2785–2796
241. Huang JC (1979) Oxygen reduction on platinum in 85% orthophosphoric acid. *J Electrochem Soc* 126:786–792
242. Kunz HR, Gruver G (1975) The catalytic activity of platinum supported on carbon for electrochemical oxygen reduction in phosphoric acid. *J Electrochem Soc* 122:1279–1287

243. Neyerlin K, Singh A, Chu D (2008) Kinetic characterization of a Pt-Ni/C catalyst with a phosphoric acid doped PBI membrane in a proton exchange membrane fuel cell. *J Power Sources* 176:112–117
244. Liu Z, Wainright JS, Litt MH, Savinell RF (2006) Study of the oxygen reduction reaction (ORR) at Pt interfaced with phosphoric acid doped polybenzimidazole at elevated temperature and low relative humidity. *Electrochim Acta* 51:3914–3923
245. Li Q, Gang X, Hjuler HA, Bjerrum NJ (1995) Oxygen reduction on gas-diffusion electrodes for phosphoric acid fuel cells by a potential decay method. *J Electrochem Soc* 142:3250–3256
246. Peters R, Scharf F (2012) Computational fluid dynamic simulation using supercomputer calculation capacity. In: Stolten D, Emonts B (eds) *Fuel cell science and engineering—materials, processes, systems and technology*. Wiley-VCH, Weinheim, pp 703–732

Isabel Kundler and Thorsten Hickmann

Abbreviations

BBP4	Phenolic resin bipolar plate (Brand name of Eisenhuth)
CNT	Carbon nanotubes
CR	Chloroprene rubber
EPDM	Ethylene propylene diene monomer
F	Fluor
FKM	Fluor caoutchouc material
H ₃ PO ₄	Phosphoric acid
HNBR	Hydrogenated nitrile butadiene rubber
LCP	Liquid crystal polymer
LSR	Liquid silicon rubber
MFI	Mold flow index
MFR	Mold flow rate
NBR	Nitrile butadiene acrylonitrile rubber
NR	Natural rubber
PPS	Polyphenylene sulfide
PSU	Polysulfone
PVDF	Polyvinylidene fluoride
SBR	Styrene butadiene rubber
TGA	Thermogravimetric analysis
VMQ	Varmaq = Silicone-based solid raw material

19.1 Introduction

Fuel cells are basically galvanic cells converting chemical energy directly into electrical energy. Depending on the specific technology, this reaction may take place at elevated temperatures, thus technical requirements for materials and components of the stack become more and more challenging. The fuel cell technology has reached a considerable degree of technical maturity by now. However, market introduction still suffers from the challenge of supplying a high performing and reliable product on one hand and acceptable cost on the other hand. Besides the membrane electrode assembly (MEA), which is considered as the heart of a fuel cell, the bipolar plate is one of the key components of a fuel cell stack. Sizes and dimensions, weight, thermal and electrical properties of the stack are to a great extent determined by the bipolar plate technology.

In general, there are two different types of bipolar plate technologies: one based on metal and the other based on graphite as a conductive component. The latter can be pure (expanded) graphite or a graphite composite material containing a polymer binder. Metal plates offer excellent electrical and thermal conductivities and they can be machined to very small thicknesses. Additionally, they do not tend to form cracks or break even at small thicknesses and their nonporous structure offers good gas

I. Kundler • T. Hickmann (✉)
Eisenhuth GmbH & Co. KG, Friedrich-Ebert-Straße 203,
Osterode am Harz 37520, Germany
e-mail: t.hickmann@eisenhuth.de

tightness. However, metal plates are inherently prone to corrosion under the aggressive oxidizing conditions in a fuel cell. Even high grade stainless steel does not resist the contact to both oxygen and electrochemical potential on the cathode side. Considerable effort has been devoted to the development of protective coatings for steel plates, both precious metal coatings and, preferentially, cost-effective coatings and surface treatments. However, for high temperature polymer electrolyte (HT-PEM) fuel cell applications the corrosion problem of metal plates appears to be unsolved by now and graphite-based materials are the preferred material according to current state-of-the-art.

The thermal and chemical conditions for materials applied in fuel cells are challenging, in particular in HT-PEM fuel cells. This fuel cell type operates at around 160 °C and in most cases in the presence of phosphoric acid in the electrolyte. As mentioned above, graphite composite-based bipolar plates with polymer binders are a superior material regarding their stability under corrosive conditions of acid contact and the presence of oxygen, electrochemical potential, and high temperature. However, composites require thicker plates than metal plates, resulting in more weight and volume of the stack. The MEA is always considered to be the dominating part of the stack in terms of cost and performance; however the bipolar plates have been underestimated both regarding their technical requirements and their contribution to the cost.

Graphite composite-based bipolar plates are manufactured using highly filled compounds [1]. They contain fillers like graphite or other electrically conductive carbons and binder polymers with appropriate heat deflection temperature. The key challenge is the competing interaction between electrical conductivity, provided by the carbon component, and mechanical stability as well as gas tightness, provided by the binder polymer. Both compounding and molding processes, which can be injection molding, compression molding, or others, are very sensitive to process parameters and need to be carefully controlled. The target is to manufacture bipolar plates in large volumes and with high quality, using

standard methods for plastic processing such as injection molding. Only by using price attractive materials and the consequent focus on process automation when having higher volume, the bipolar plate can contribute significantly to a better market acceptance of fuel cells.

Besides the bipolar plate, the gasket material is an important component of the fuel cell stack and tends to be heavily underestimated. It plays a key role in the mechanical properties of the stack, compensated tolerances and partially determines the mechanical compression of the MEA. Inappropriately selected gasket materials may cause failure of the MEA or fracture of the bipolar plates. Despite the fact that the gasket has only to seal the stack, it is a highly challenging issue due to the tolerances of the other components which have to be managed. And last but not the least, the gasket has to be cost attractive.

Technically, the bipolar plate of the HT-PEM fuel cell stack has to accomplish the following functions [2, 3]:

- To conduct electrical current
- To conduct heat and distribute coolant in the cooling flow field
- To separate gases of adjacent cells
- To supply reactant gases homogeneously distributed in the flow field
- To transport product water (steam) out of the cell in the flow field
- To provide mechanical stability of the stack

The main functions of the gaskets in a HT-PEM fuel cell stack are

- To seal and prevent leakage of anode and cathode area
- To seal and prevent leakage of cooling plates
- Compensate tolerances and dimensional changes during temperature cycling
- Provide defined gap for the MEA or defined contact pressure between plate and gas diffusion layer (GDL) surface over a long time

Based on these basic functions of each component the technical requirements for plates and gaskets are described in the next section.

19.2 Technical Requirements of Bipolar Plates and Gaskets

Based on the technical functions described above, the US Department of Energy (DoE) suggested development targets for fuel cell components as shown in Table 19.1 for bipolar plates. These data are apparently based on communication with and input from conventional low temperature PEM fuel cell developers. Some of the data are directly transferred to the HT-PEM fuel cell technology. This has also been discussed by DoE [4] and Liao et al. [5]. However, depending on the specific application in HT-PEM fuel cells, priorities of the target values may significantly differ.

Additionally, the chemical resistance of the bipolar plate can be characterized by measuring the corrosion current under a potential typical for fuel cell operation and using 85 % phosphoric acid as an electrolyte. The relevance, detailed parameters, and development targets of this corrosion test are still subject to technical discussions and depend on the anticipated application of the plate. The accepted corrosion current under reference conditions is lower for long

term co-generation of heat and power (CHP) applications than that for auxiliary power unit (APU) systems. The main functional requirements for the gaskets in the HT-PEM fuel cell technology are summarized in Table 19.2.

Additionally, the gasket material has to be resistant to the selected coolant under operating conditions. Since some rubber composites contain carbon fillers to improve their mechanical properties, unintended electrical conductivity of the material needs not be ruled out. It has to be noted that the values mentioned above are for orientation and refer to standard elastomer materials available on the market.

Based on these technical requirements, appropriate structural materials for both bipolar plates and gaskets have to be selected. In particular, the plate is exposed to challenging conditions since it faces high temperature, acid and oxygen contact, combined with an electrochemical potential. The plate has to provide mechanical integrity, gas tightness, and high conductivity over several thousand hours of operation, thus development and manufacturing of these materials is a challenging undertaking.

Table 19.1 Target specifications for bipolar plates in HT-PEM fuel cell applications

Technical property	Target value
Density	$<2 \text{ g cm}^{-3}$
Electrical conductivity	$>100 \text{ S cm}^{-1}$
Thermal conductivity	$>10 \text{ W mK}^{-1}$
Flexural strength	$>50 \text{ MPa}$
Shore hardness	>40
Temperature resistance	$180 \text{ }^\circ\text{C}$ (thermo-mechanical test)
Phosphoric acid uptake	Low (specific target values depend on application and MEA technology)

Table 19.2 Proposed benchmarks for gaskets in HT-PEM fuel cell applications

Property	Target value
Density	$<2 \text{ g cm}^{-3}$
Shore hardness	$<70 \text{ Shore A}$, lower limit depends on application
Compression set	$<18 \%$
Temperature resistance	$180 \text{ }^\circ\text{C}$
Chemical stability	Resistant against 75–95 % H_3PO_4 at $180 \text{ }^\circ\text{C}$

19.3 General Concepts of Bipolar Plate Manufacturing

19.3.1 Compounding

As mentioned above, composite bipolar plates consist of a binder polymer which is highly filled with a conductive carbon component. Typical compositions are >80 % conductive filler and <20 % binder polymer. Compounding, processing, and manufacturing are substantially different from conventional polymers due to the high content of filler material in the compound [6]. The function of the carbon filler is to provide electrical and thermal conductivity. Therefore, a 3-dimensional percolating carbon structure is required. Usually, the main carbon component of the plate is synthetic graphite. Due to its crystalline layer structure the graphite platelets are inherently anisotropic in their physical properties. Electronic conductivity is provided by the mobility of electrons within the graphite layers of each platelet and not in transverse direction. Thus, for the bipolar plate the manufacturing process has to promote the formation of different orientations of the platelets to obtain isotropic physical properties of the macroscopic plate material. In the following, material aspects of bipolar plates are discussed in more detail.

19.3.2 Binder Polymers

In general, two different concepts of polymer binders can be applied in bipolar plates. First, the binder material can be polymerized or cross-linked in situ in the composite during molding of the plate (*resin method*). Second, a thermoplastic polymer material can be used in the compounding process (*thermoplastic method*).

In case of the *resin method* the graphite is carefully mixed with a prepolymer resin (e.g., phenolic resin) and a cross-linker and then compression molded to the final dimensions of the plate. During the molding process the cross-linking reaction is initiated thermally forming a

3-dimensional duomer network which is insoluble in any solvent under any conditions. The whole process needs to be carefully controlled in order to achieve the correct features of the flow field and to meet the tolerance requirements. The advantage of this method is a lower effort of compounding because of the rather low viscosity of the resin prepolymer. The disadvantage is that the polymerization and cross-linking process on the absorbing graphite process are rather difficult to control and may result in a broad distribution of chain segment lengths and inhomogeneous structures within the duomer network.

Eisenhuth's bipolar plates called BPP4 are developed for HT-PEM fuel cells and based on the phenolic resin technology. These plates are consistent and well performing for high temperature PEM fuel cells operating approximately 3000 h, e.g., in auxiliary power unit (APU) applications. However, for long term applications, such as combined heat and power generation (μ CHP) with anticipated 20,000 h of operation, other materials may be preferred.

In case of the thermoplastic method a thermoplastic binder with a defined degree of polymerization is compounded with the graphite material. The chemical structure of the polymer remains unchanged during compounding or molding process. The polymer has to be selected with sufficient chemical and thermal stability (e.g., data from [7]). Several material candidates are available on the market in high quality and well-defined configurations. The disadvantage of the thermoplastic method for HT-PEM plates is the high effort in the compounding process which needs high temperature and strong mechanical forces. The same applies for the molding process, which requires a high amount of energy (heat and mechanical pressure). Both compression molding and injection molding are applicable for thermoplastic-based compounds. The main advantage of this method is a well-defined, reproducible composite material consistent in its chemical composition from lot to lot.

In both methods, after removal from the mold certain posttreatment procedures may be necessary, for example, to remove the skin of the mold release agent from the surface of the plate.

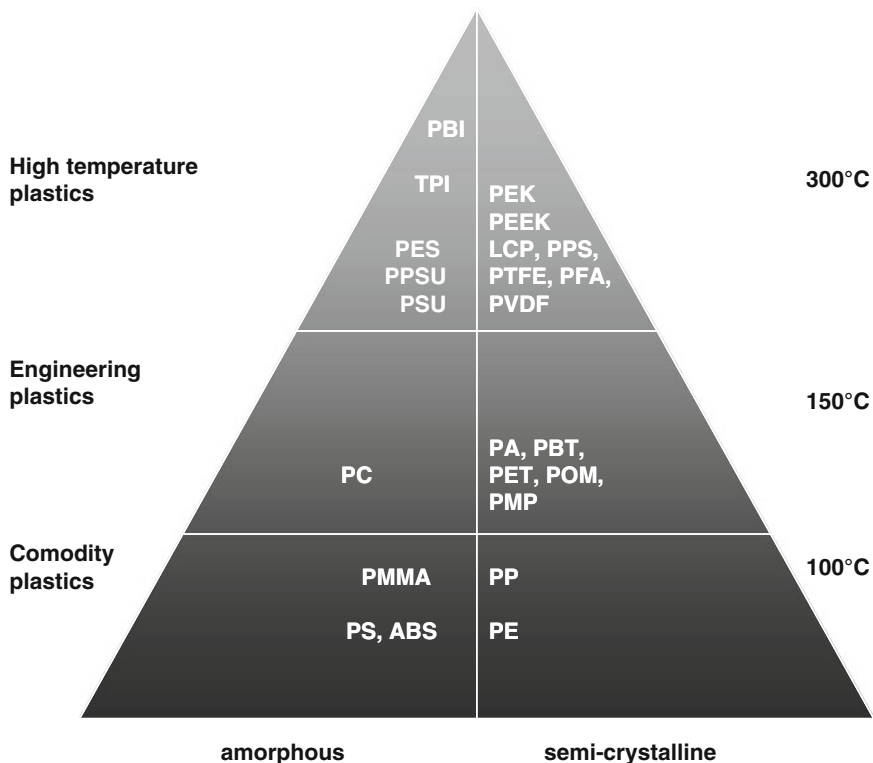


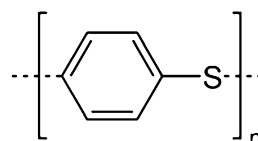
Fig. 19.1 The plastics pyramid according to thermal literature data of common polymers: preferred materials for HT-PEM applications are in the upper right region (*TPI* thermoplastic polyimide, *PES* polyether sulfone, *P(P)SU* poly(phenylene)sulfone, *PE(E)K* polyether(ether) ketone, *LCP* liquid crystal polymer, e.g., Vectra, *PPS* polyphenylene sulfide, *PTFE* polytetrafluoroethylene,

e.g., Teflon[®], *PFA* thermoplastic fluoro-copolymer, *PVDF* polyvinylidene fluoride, *PC* polycarbonate, *PA* polyamide, *PBT* polybutylene terephthalate, *PET* polyethylene terephthalate, *POM* polyoxymethylene, *PMP* polymethylpentene, *PMMA* acrylic glass, e.g., Plexiglas[®], *PS* polystyrene, *ABS* acrylonitrile butadiene styrene copolymers, *PP* polypropylene, *PE* polyethylene)

Typical thermoplastic polymers as binders in HT-PEM bipolar plates are polyphenylensulfide (PPS), polyetheretherketone (PEEK), and derivatives of polyphenylsulfone (PSU). Looking at the plastics pyramid (Fig. 19.1), all of these polymers are in the upper right region of high temperature stability and semi-crystallinity. These polymers safely resist the acid and oxygen contact and provide heat deflection temperature far above the operating point of a high temperature PEM fuel cell.

Within the last years, considerable effort has been devoted to the development of innovative bipolar plate solutions at Eisenhuth. A broad variety of potential binder polymers have been tested. A major finding of the research activities is that semi-crystalline binders appear to be

Fig. 19.2 Structure formula of poly (p-phenylene) sulfide (PPS)



superior compared to amorphous polymers in terms of processability and mechanical properties of the plate material. Finally, the poly(p-phenylene sulfide) (PPS)-based material turned out to be the most well-suited polymer binder for HT-PEM fuel cell plates, so this chapter shall focus on PPS-based plates.

PPS is a chemically and thermally highly stable material, consisting of aromatic rings linked with sulfur atoms (Fig. 19.2). It shows a glass transition temperature at 90 °C and a melting

point at approximately 285 °C. The maximum long term service temperature (DIN53476) is 218 °C, thus significantly higher than the normal operating temperature of a HT-PEM fuel cell. PPS is an engineering thermoplastic polymer which can be molded, extruded, or machined to high tolerances.

Eisenhuth has developed and manufactured PPS-based composite plates and evaluated them both in situ and ex situ. In general, with PPS plates the same conductivity as known from the state-of-the-art and resin-based BPP4 material has been achieved ($>100 \text{ S cm}^{-1}$, meeting the targets of DoE). The detailed test data are to be discussed below.

19.3.3 Graphite Materials and Fillers

Carbon, most commonly graphite-based, provides at least 80 wt % and even more in volume percent of the bipolar plate material. While synthetic graphite materials are the basis of bipolar plates, several carbon additives can be employed in order to boost conductivity properties of the composite material. Examples for such additives are highly conductive carbon nanotubes (CNT) or high surface area carbon blacks. Carbon blacks can be formed by thermal decomposition of hydrocarbons in the gas phase [8] and a broad variety of different materials with different surface area, hydrophobicity, and conductivity are available. It has to be considered that high surface area carbons are more prone to undesired corrosion effects than graphite-based materials, thus their positive conductivity effect has to be balanced against long term stability requirements. This proposes to use conductivity boosters rather for auxiliary power unit (APU) and uninterrupted power supply (UPS) applications and employ stable graphite materials for long term CHP usage.

Another important aspect of carbon materials is purity. Since most fuel cell membranes and catalysts are highly sensitive to contamination with Fe-ions and other metal residuals, the raw materials for bipolar plates have to be carefully characterized with respect to their Fe content.

The carbon or graphite type also mainly determines the properties of the bipolar plate like porosity, phosphoric acid uptake, and hydrophobicity, both regarding the surface and the bulk. For the HT-PEM fuel cell technology, preferred configurations are hydrophobic structures with low phosphoric acid uptake.

One of the key properties of the bipolar plate is electronic conductivity. This is generated by a 3-dimensional percolating network of conductive graphite or carbon particles. The graphite/binder system is always inhomogeneous and can be considered as a two-phase system of conductive carbon paths and a polymer matrix for mechanical integrity. Figure 19.3 shows the scanning electron microscopic (SEM) images of a bipolar plate compound, where the crystalline and amorphous regions in the graphite are visible. The mesoscopic binder polymer distribution cannot be characterized with REM because of similar average electron densities of carbon and the polymers. The mesoscopic structure of the material highly depends not only on the chemical composition, but also on processing, such as compounding and molding parameters. The overall process from the raw material to the molded plate has to be carefully controlled to ensure consistency and reproducibility of the bipolar plates from lot to lot.

19.4 Characterization Data of HT-PEM Bipolar Plate Materials

19.4.1 General Remarks

Certainly, the final success criterion for any bipolar plate is the in situ performance and stability under real fuel cell operating conditions. However, fuel cells are highly complex systems with numerous sources of inconsistency. Thus, ex situ bipolar plate characterization is required for material development and quality control. Several test methods are well established for bipolar plates and a few selected shall be presented here with an example for test results.

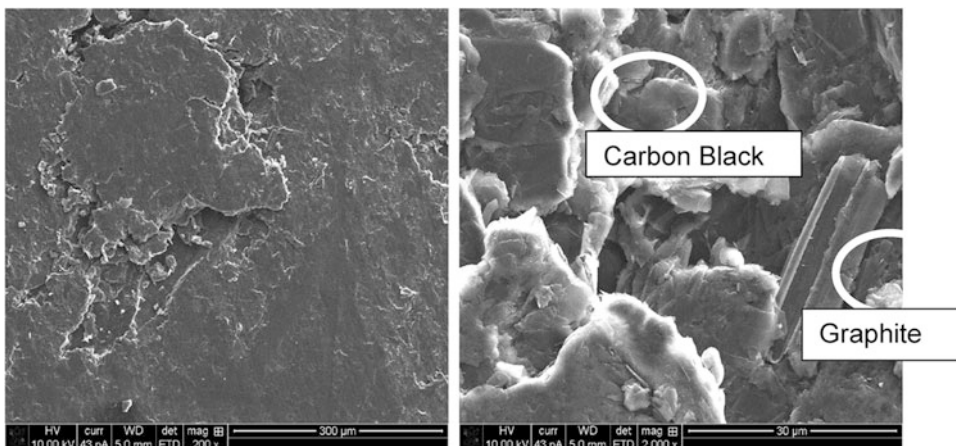


Fig. 19.3 Scanning electron microscopy (SEM) of a bipolar plate compound

19.4.2 Thermogravimetric Analysis

During fuel cell operation HT-PEM bipolar plates are exposed to high temperatures up to about 180 °C and sometimes even higher. Consequently, all raw materials used for plate manufacturing have to be resistant to approximately 200 °C, assuming 20 °C as a safety distance for a prolonged period.

Figure 19.4a shows examples for thermogravimetric analysis (TGA) analysis for state-of-the-art HT-PEM plates of type “BPP4” and low temperature LT-PEM materials as a reference. Recently developed HT-PEM materials with high temperature resistant thermoplastic binder polymers (PPS and PSU Ultrason[®]) are shown in Fig. 19.4b.

As expected, the LT-PEM material clearly failed at temperatures below 200 °C showing a significant decrease in weight due to chemical degradation of the binder polymer. The TGA of phenolic resin-based BPP4 material shows a slight decrease in weight when approaching the 200 °C benchmark and then continuously degrades between 200 and 400 °C. This can be explained by a broad distribution of chain segment lengths of the duromer network and residual oligomers from the resin because the polymer structure has been generated on the graphite surface without any purification steps after polymerization or cross-linking.

In contrast, the two bipolar plate samples containing thermoplastic binders (here PPS and PSU Ultrason[®] from BASF) show a constant weight up to >400 °C, followed by a well-defined weight drop at >500 °C, far beyond the relevant temperature range for PEM fuel cells. The results clearly show the benefits of thermoplastic high temperature resistant binders compared to in situ polymerized resin-based materials: the more defined structure of thermoplastics enables better reproducibility of the composites and excellent thermal stability over the full temperature range of HT-PEM operation. Under real fuel cell conditions, e.g., operating at 170 °C, BPP4 was successfully tested for systems with approximately 3000 h of operation. However, for long term CHP applications, e.g., with a target 20,000 h, the bipolar plate material needs to be improved. In this case, the PPS-based bipolar plate, currently under development by Eisenhuth and research partners, is a candidate providing improved thermal and mechanical stability.

Not only the binder polymer, but also the carbon fillers have to be characterized with respect to their thermal stability. In the next TGA example, several PPS-bonded bipolar plate samples with different contents of highly conductive carbon nanotubes (0–4 % CNT) are investigated by TGA. As shown in Fig. 19.5, the peak of thermal decomposition at approximately

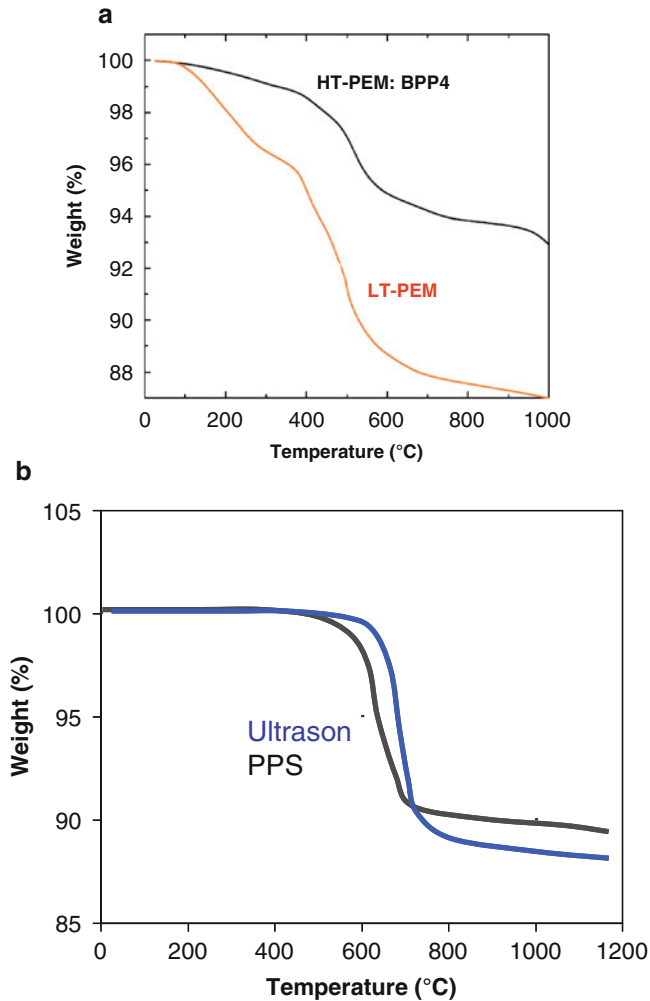


Fig. 19.4 Thermogravimetric analysis of state-of-the-art HT-PEM material BPP4 compared to LT-PEM bipolar plate (a) and the advanced HT-PEM bipolar plates based

on high temperature polymer binders of Ultrason and PPS (b), heating rate 10 K min^{-1} , inert atmosphere [9]

$550 \text{ }^\circ\text{C}$ is equal for all samples. However, in the region between 200 and $300 \text{ }^\circ\text{C}$ a small weight loss was detected, which seems to be related to the CNT concentration. Despite this reaction takes place at temperatures higher than the HT-PEM fuel cell, it has to be considered as a potentially significant degradation mode for long term operations, e.g., in CHP applications. Further experiments with conductivity boosters will be performed in the near future in order to evaluate the critical limits for these additives. These results are preliminary and further experiments are necessary for conclusions about critical

parameters and relevant degradation mechanisms from carbon additives.

19.4.3 Electrical Conductivity Measurements (In-Plane)

Clearly, electrical conductivity both in-plane and through-plane is one of the most important properties of the bipolar plate. Despite most fuel cell (component) laboratories have access to electrical conductivity testing equipment, by now there is no standardized test method for

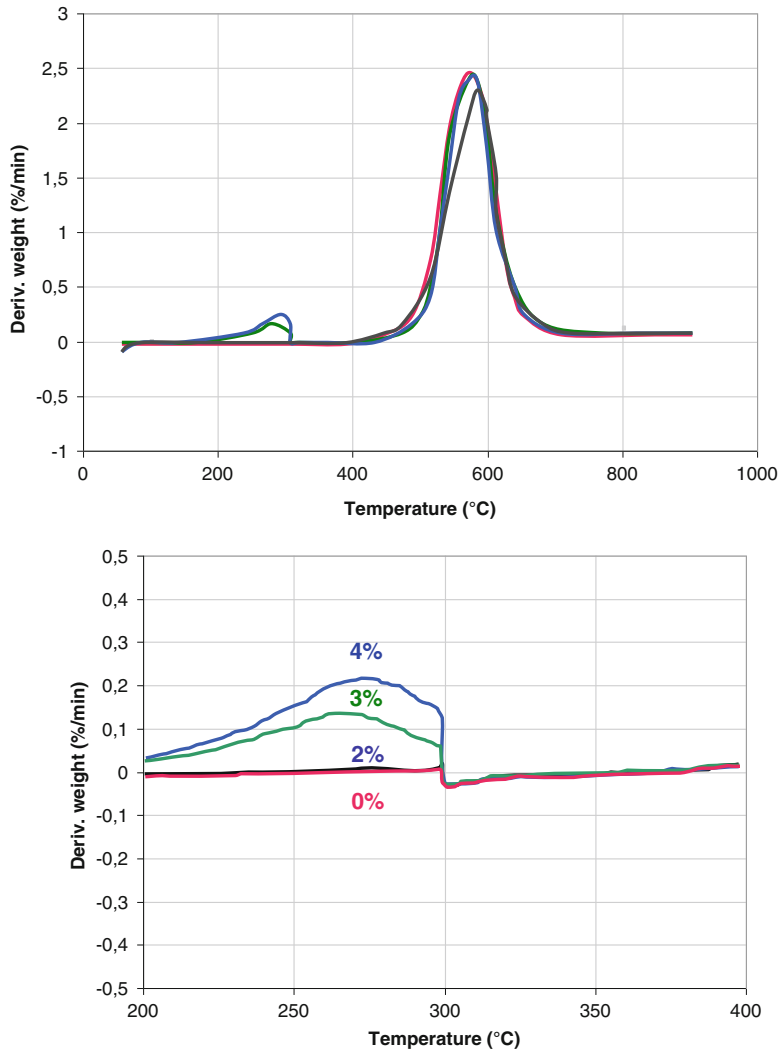


Fig. 19.5 Thermogravimetric analysis of PPS-based HT-PEM plates doped with 0–4 % carbon nanotubes CNT

bipolar plates, and comparing results from different sources can show significant differences even if the same samples are tested. One of the main reasons may be surface effects and pre-treatment of the sample. As shown in Fig. 19.6, Eisenhuth has implemented an own testing system for this application, which is suited for in-plane conductivity testing.

The in-plane conductivity device allows for a conductivity mapping over the whole sample area of $200 \times 300 \text{ mm}^2$. Therefore, it can characterize the material with respect to the degree of homogeneity. Conductivity mapping

is an important tool both for quality control and for material and process development. For graphite composite plates it is well known that compounding and molding are highly sensitive to process details and may generate inhomogeneous structures of surface and bulk of the material. Certainly, the development target is a homogeneous distribution of conductivity with only minimal deviations between different points on the sample. In BPP4 plates the compounding and manufacturing process are mature and well controlled, and the conductivity mapping shows an even distribution with values of



Fig. 19.6 Testing device for in-plane electrical conductivity measurement at Eisenhuth

approximately 100 S cm^{-1} ($0.01 \text{ } \Omega \text{ cm}$). In case of the newly developed PPS materials the manufacturing process is under development and some material samples still show a significant relief structure in the conductivity mapping. Two examples of the mapping for PPS-based plates are shown in Fig. 19.7.

In the case of the (a) sample the data propose the molding process as a source of inconsistency because the same pattern—higher resistivity on the lower and right edge—was found in several samples. One explanation for these results is that graphite platelets are oriented parallel to the surface when filling the mold and therefore less contribute to conductivity than in the case of a fully isotropic material.

19.4.4 Electrical Conductivity Measurements (Through-Plane)

Theoretically, in an isotropic material in-plane and through-plane conductivities are supposed to be equal. However, in many bipolar plate materials the through-plane values tend to be

lower than their in-plane counterparts. One explanation for this effect is that during the molding process graphite platelets are oriented preferentially parallel to the sample's surface, thus transporting the electrons faster within the in-plane direction than the through-plane. In Fig. 19.8 examples for through-plane results are presented, with the key messages that (a) the through-plane conductivity tends to be systematically lower than in-plane (approximately 0.02 instead of $0.01 \text{ } \Omega \text{ cm}$ in-plane) and (b) in mature materials, such as resin-based BPP4, the values covers smaller range due to better control of the process. In development materials, such as PPS of different configurations and fluoropolymer-bonded PVDF types, the range is broader and small changes of process parameters still cause significant deviations in conductivity. In the course of process and product development for each new material this will be improved.

19.4.5 Phosphoric Acid Uptake of Bipolar Plates

HT-PEM fuel cells operate with phosphoric acid doped polymer membrane as electrolyte. The acid is physically adsorbed to the membrane. The phosphoric acid distribution within the fuel cell components, such as membrane, catalyst layers, microporous layer, gas diffusion layers, and bipolar plates, is known to be a critical parameter for performance and life time of this type of fuel cells [10]. There are no defined specifications about phosphoric acid uptake of the bipolar plate because its impact on the fuel cell performance strongly depends on several parameters and always has to be considered in a context of the overall fuel cell design.

In general, the phosphoric acid electrolyte is required to conduct protons in the membrane and a certain limited amount of the doping acid is needed to provide ionic conductivity in the catalyst layers. In the GDL (microporous layer and bulk) as well as in the bipolar plate, phosphoric acid is not required and even highly undesired because it compromises the gas transport properties in the GDL and may catalyze

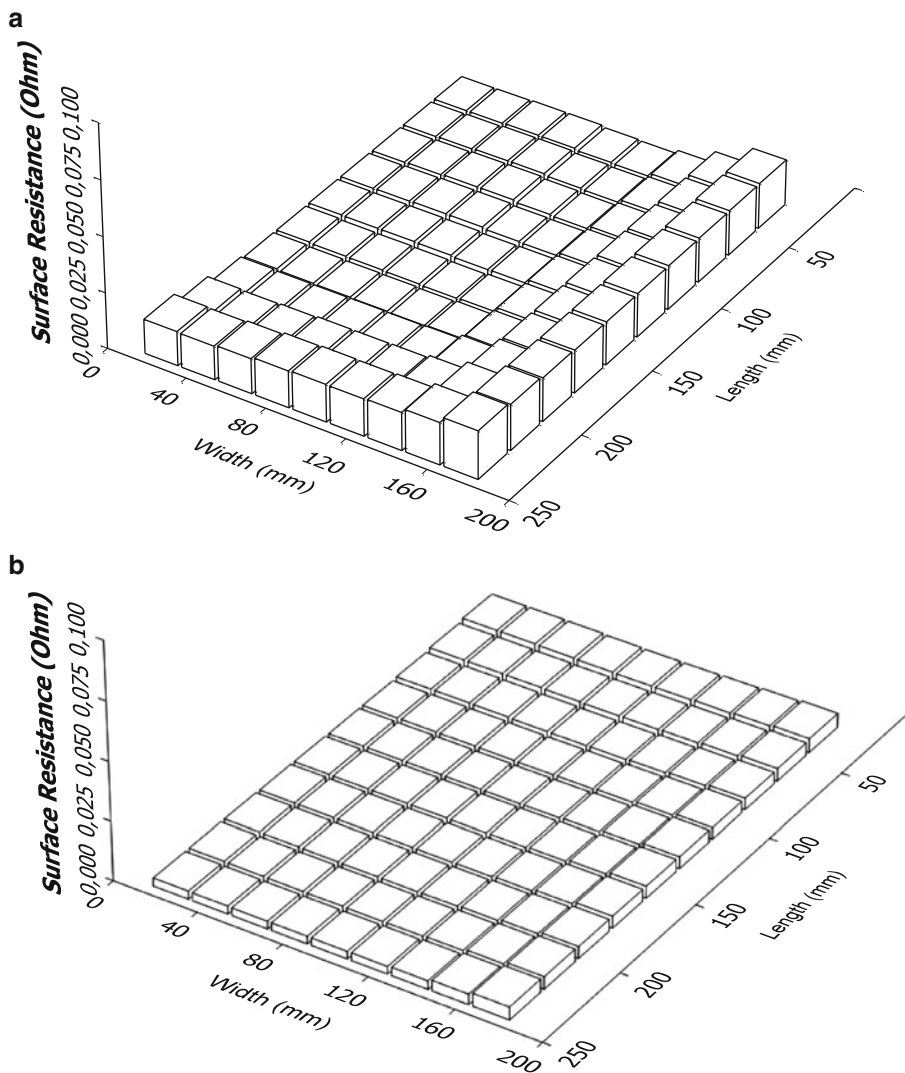


Fig. 19.7 Surface resistance mapping (in Ohm, relative test method the characterize homogeneity) of two high temperature PEM bipolar plates. (a) The material shows a higher resistance at the edges with 80 % of data points

between 0.01 and 0.02 Ω (b) The material displays a lower resistance and improved homogeneity, all data points $<0.01 \Omega$ with only minor deviations

undesired oxidation processes in the bipolar plates material. Any phosphoric acid uptake of the bipolar plate can have the following effects:

- The bipolar plate may compete with the membrane and catalyst layer regarding the acid retention. Then degradation of the cell performance occurs because of insufficient ionic conductivity in one of these components,

although the plate itself does not become damaged by the acid.

- Acid contact accelerates carbon corrosion in all carbon components of the cathode. However, the high surface area and Pt-loaded carbons in the catalyst layer are significantly more prone to this degradation mechanism than the graphite of the bipolar plate. Nevertheless, this is considered and the plates will

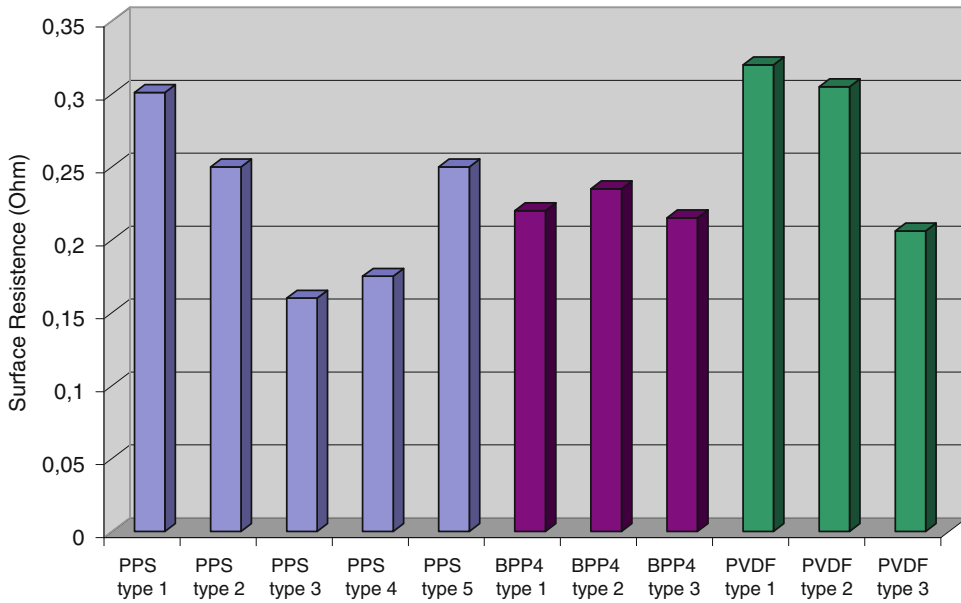


Fig. 19.8 Through-plane surface resistance (relative test method) results of HT-PEM bipolar plates with different configurations where BPP4 is mature material while PPS and PVDF are development materials. The data show

higher homogeneity of the mature BPP4 material compared to the new configurations with PPS and PVDF (Status as of 2014)

be further improved with respect to their corrosion stability—within the frame given by thermodynamics.

- A certain acid concentration in the bipolar plates causes a vapor pressure of phosphoric acid in the gas stream and may prevent against acid evaporation in the catalyst layers and membrane. In this case, the acid content in the plate may have a positive effect on long term stability in certain applications.

All these arguments are only for a brief overview, show the complexity of the system and cannot at all be considered as a complete set of information or even as a recommendation for certain membrane, MEA or bipolar plate configurations.

Eisenhuth has characterized different bipolar plates with respect to their acid uptake. In general, a low acid uptake, corresponding to a high hydrophobicity, is desired in order to keep the acid management in the overall cell under

control. The acid uptake is mainly determined by the carbon component (graphite), which constitutes >80% of the volume of the material. However, also the binder may influence the porosity in particular on the surface of the plate. Detailed studies about structure–property relationships regarding acid uptake with different materials are in progress at Eisenhuth. Preliminary results are shown in Fig. 19.9. Here, different bipolar plates have been tested in an HT-PEM rainbow stack for more than 3000 h. After disassembling, the plates were characterized by titration and the phosphoric acid uptake in a unit of gram per cm² plate (or MEA respectively) was calculated. While the two samples PPS and PVDF, both containing the same synthetic graphite and a different binder polymer, show very similar values and, in general, a low acid uptake, the plates containing other carbon materials strongly absorbed phosphoric acid. This material was manufactured using another carbon type, yielding a completely

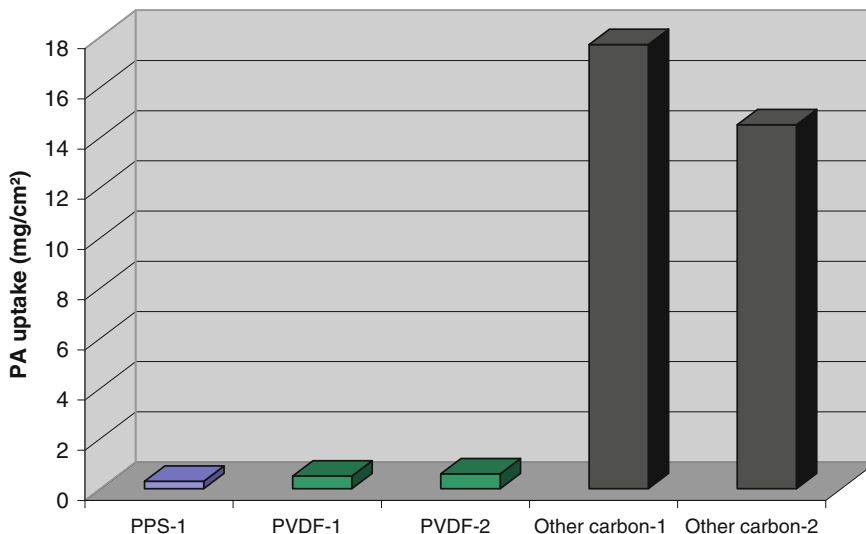


Fig. 19.9 Phosphoric acid uptake in different bipolar plates after >3000 h HT-PEM fuel cell stack operation. The samples based on PPS and PVDF contained the same type of synthetic graphite, whereas the sample called

other carbon contained another type of carbon. It shows the strong contribution of the carbon, and only minor contribution of the binder polymer (test data kindly provided by NEXT ENERGY, Oldenburg, Germany)

different behavior with respect to hydrophobicity and porosity.

contributes to life time and reliability of fuel cells. The key functions of the gaskets are:

19.5 Gaskets

The fuel cell developers have for many years invested tremendous efforts in improvement and technological readiness of the core components, such as membranes, electrodes, GDLs, the overall MEA configuration, and also the bipolar plates. The significance of gasket materials has been underestimated until the last years. Despite the gasket does not directly contribute to the electrochemical processes, inappropriate gaskets can cause leakage or coolant contamination of the MEA. Additionally, in particular for phosphoric acid containing fuel cells, gasket thinning can cause MEA over-compression, resulting in over-compression of the membrane causing gas crossover through the membrane. On the other hand, too thick gaskets can cause MEA under-compression, resulting in a high contact resistance between GDL and plate. These examples clearly indicate that gasket properties and stability significantly

- To seal the cell
- To catch up tolerances (from membrane, GDL, plate, and gasket)
- To provide appropriate compression of the MEA over a long time

In case of the HT-PEM fuel cell technology the compression of the MEA or the membrane respectively is known to be a critical parameter for performance and stability. The gasket thickness has to be appropriately selected, also considering potential creep of the materials. Hard gaskets support well-defined gaps, however may be compromised in their sealing properties, do not compensate tolerances very well, and may cause mechanical distortion on the bipolar plates, which in turn can cause cracks or beak after a long time. On the other hand, with soft gaskets it is more difficult to control the compression ratio, but they are superior with respect to tolerances and mechanical stabilization of the stack. Beside the mechanical properties, thermal and chemical stability as well as compatibility with a

Table 19.3 Gasket material overview with physical properties

Description/intern. term	NR	SBR	EPDM	CR	NBR	HNBR	Si/VMQ	FKM
Hardness shore A ^a	35–95	40–95	25–85	30–90	20–95	40–90	25–85	50–90
Tear strength N mm ⁻²	30	25	20	29	25	25	8	20
Elongation at break %	800	450	450	450	500	500	300	400
Temperature min./max.	−0.63	−0.5	−0.5	−0.32	−0.29	−0.2	−0.35	−0.09
Steam resistance	0	++	++	++	+	++	++	++
Oil resistance	−	−	−	+	++	++	+	++
Acid resistance	+	+	++	+	0	+	−	++

^aHardness measured with a shore durometer according to standard ASTM D2240, an established standard test method for polymers and rubbers

nonaqueous coolant are crucial material criteria of the gaskets. In general, like the other HT-PEM fuel cell components the gaskets have to resist temperatures up to 200 °C, concentrated phosphoric acid contact and oxygen contact. Fluoroelastomers (FKM) are most likely the material of choice for HT-PEM fuel cell applications, and for certain applications the ethylene propylene diene monomer (EPDM) rubber may be a cost efficient alternative. The arguments clearly show that gaskets are a highly customized component for each stack manufacturers. For an overview, some typical gasket properties for a broad variety of materials are listed in Table 19.3.

In order to supply consistent gaskets with appropriate tolerances the viscoelastic properties of the gasket prepolymers are an important parameter. A low viscosity is beneficial for processing. For plastic materials usually the mold flow rate (MFR) or mold flow index (MFI) are specified by the supplier, supporting the manufacturer for plastic parts with information relevant for processing properties. However, these data are standard data and not always compatible with the molding conditions or equipment

at the part manufacturer. In addition, for rubber materials or their prepolymers these data are not available in most cases. Therefore, Eisenhuth developed a phenomenological test method to characterize polymer materials with respect to processability, as schematically represented in Fig. 19.10. In this test, a polymer is pressed into a helix-shaped mold with a defined pressure under process-relevant temperatures. The viscous polymer flows into the helix mold and finally stops, when the applied pressure is equal to the “back-pressure” of the mold. The length of the helix can be correlated to the low viscosity or good processability. This mold can also be used to find the processing windows of materials as far as the viscosity is concerned.

Figure 19.11 presents a typical result of the helix test. As mentioned above, the length of the extended helix is a measure of the processability. This test has been performed with a variety of potential gasket materials to achieve a data baseline. The values are listed in Table 19.4. The results show that the processability depends on the type (silicon > fluoro-elastomer FKM) and also on specific material configuration (FKM “low viscosity” > regular FKM).

Fig. 19.10 Helix mold for elastomer processability characterization (by Eisenhuth)

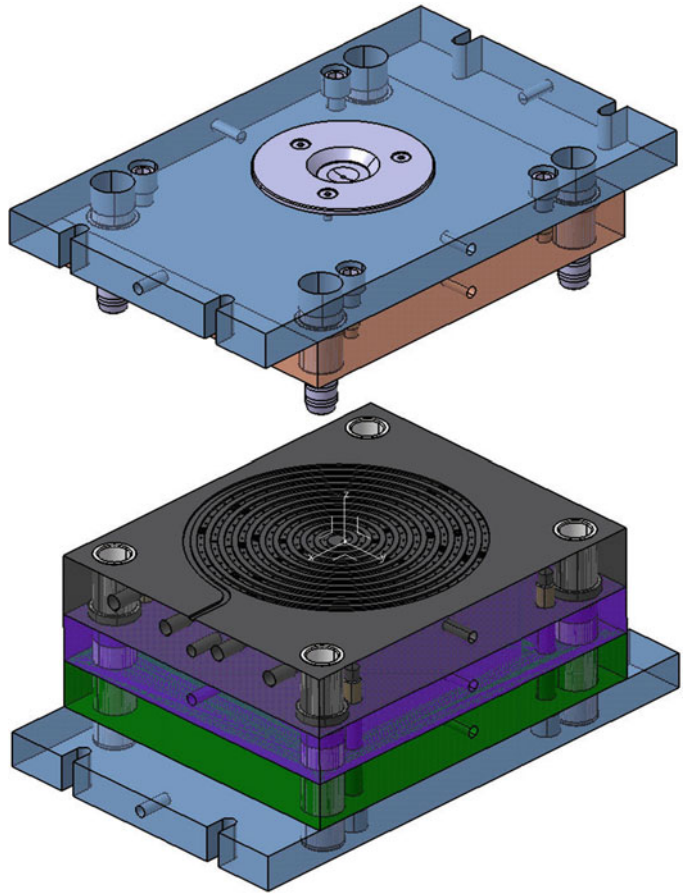


Fig. 19.11 Elastomer sample after vulcanization in the helix test

Table 19.4 Results of the helix test for potential HT-PEM gasket materials (in the Eisenhuth mould)

Material	Length (cm)
EPDM 60 shore A	37.9
EPDM 40 shore A	41.0
EPDM 50 shore A	47.0
FKM 60 shore A—low viscosity	109
FKM 65 shore A	59.5
FKM 47 shore A	14.5
Silicon, 30 shore A	123.4
Silicon, 45 shore A	104.4
Silicon, 60 shore A	124.5

Acknowledgements The authors acknowledge fruitful collaboration with, extensive test work by, and the positive relationship with TU Clausthal, Next Energy Research Institute of University of Oldenburg, ZBT (Research Center of Fuel Cell Technology) in Duisburg. Thanks are also extended to the colleagues from Elcore and Truma for their input and inspiration. Public funding is gratefully acknowledged from BMWi/Projekttraeger Juelich in the project “Rationalisierung” (#0327849), “HT-Dicht” (03ET2050A) and from the European Commission in the project CISTEM (325262).

References

1. Apelt S, Hickmann T, Marek A et al (2006) Wie leitfähige compounds wirken. *Kunststoffe* 12:86–90
2. Larminie J, Dicks A (2000) Fuel cell systems explained. Wiley, New York
3. Kakati BK, Verma A (2011) Carbon polymer composite bipolar plate for PEM fuel cell. Lap Lambert, Saarbrücken
4. U.S. Department of Energy; Hydrogen and fuel cells program, Guiding documents, DoE Hydrogen and Fuel Cells Plan. http://www.hydrogen.energy.gov/guiding_documents.html
5. Liao SH, Hung CH, Ma CCM et al (2008) Preparation and properties of carbon nanotube reinforced vinyl ester nanocomposite bipolar plates for polymer electrolyte membrane fuel cells. *J Power Sources* 176:175–182
6. Hickmann T (2008) Kunststoffe in der PEM Brennstoffzelle—plastic applications in PEM fuel cells. *VDI Ber* 2035:81–83
7. Bonnet M (2013) *Kunststofftechnik*. Springer, Hamburg
8. Pierson HO (1993) *Handbook of carbon, graphite diamond and fullerenes*. Noyes, Park Ridge
9. Stübler N, Hickmann T, Ziegmann G (2013) Effect of methanol absorption on properties of polymer composite bipolar plates. *J Power Sources* 229:223–228
10. Hartnig C, Schmidt TJ (2011) *Electrochim Acta* 56:4237–4242

Holger Janßen, Jen Supra, and Werner Lehnert

20.1 Introduction

Stationary and mobile applications are attractive applications for high temperature polymer electrolyte membrane fuel cells (HT-PEMFC). Examples for stationary applications are electricity and heat generation for households or uninterruptible power supply (UPS) systems. In the case of mobile applications the on board power supply with auxiliary power units (APUs) and backup power for the recreation area are most promising. In comparison to the low temperature PEMFC (operated at 60–80 °C) the operating temperature of a HT-PEMFC, which is between 120 and 200 °C, allows a more effective co-generation of power and heat. The higher temperature also leads to an improved tolerance to fuel impurities and a simpler system design [1]. Therefore applications where hydrogen is generated with reformer systems are ideally suited for a HT-PEMFC due to the increased CO tolerance [1, 2]. The majority of these demands have electric power requirements between some hundred Watt and the low kW range.

H. Janßen (✉) • J. Supra
Forschungszentrum Jülich GmbH, Jülich, Germany
e-mail: h.janssen@fz-juelich.de

W. Lehnert
Institute of Energy and Climate Research,
Electrochemical Process Engineering (IEK-3),
Forschungszentrum Jülich GmbH, Jülich, Germany

In order to meet the power demands for those applications HT-PEM single cells must be stacked. In comparison to single cells with usually small active MEA areas less than 100 cm² a HT-PEMFC stack challenges further tasks, for example, the gas distribution inside each cell of the stack. Another major topic where single cell behavior cannot be used to predict stack behavior is the heat management. Even for applications in the power range of several 100 W up to the kW range stack cooling is a major design criterion for the stack development. HT-PEMFC stacks perform advantageously when they are used in reformat operation. However, this greatly affects the heat management of the stack. In order to develop a suitable heat management system and with this an appropriate stack design, knowledge of the thermal behavior is required.

20.2 Basic Stack Concepts

The difference between HT-PEM single cells and stacks is usually the increasing cell number with more than one cell and the size of the active MEA area. These are the main parameters for a power related sizing of the stack. In a first step we consider a single cell to evaluate the influence of the active cell area on the electric power. As a basis for the calculations the experimentally determined standardized polarization curve for reformat operation, shown in Fig. 20.1, was

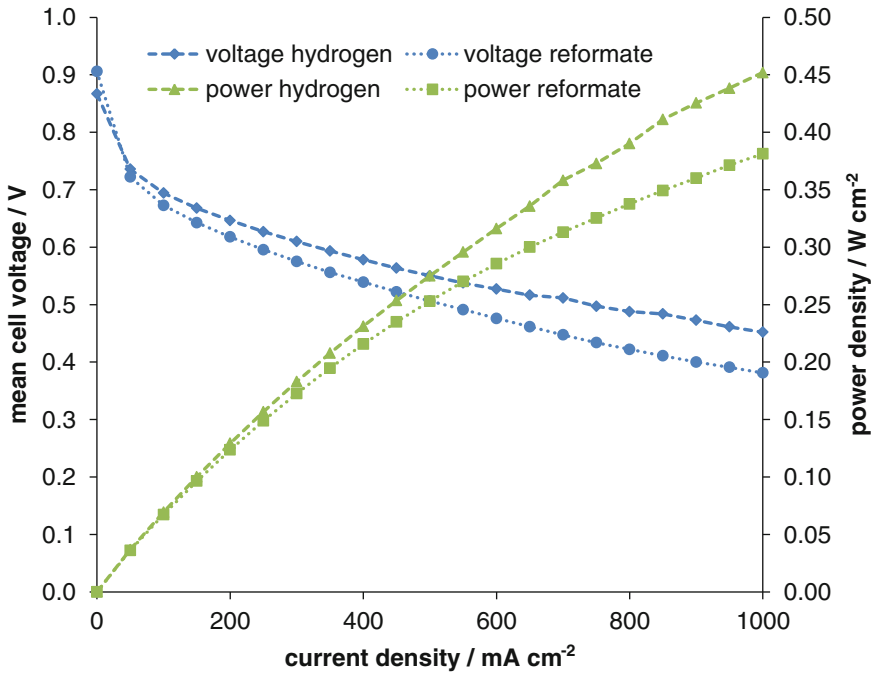


Fig. 20.1 Mean cell voltage and power density for a HT-PEMFC stack operated with hydrogen/air and synthetic reformat/air. Operating conditions according to Table 20.1, MEA used: BASF Celtec® P-1000 [3]

Table 20.1 Reference conditions

Parameter	Value
Number of cells	10
Active cell area	200 cm ²
Anode stoichiometry λ_{an}	2
Cathode stoichiometry λ_{ca}	2
Gas inlet temperature	160 °C
Liquid coolant inlet temperature	160 °C
Reformat composition	42 vol% H ₂ , 1 vol% CO, and 57 vol% N ₂

used. The results for different current densities at the reference conditions (except number of cells and active cell area), given in Table 20.1, are shown in Fig. 20.2.

From Fig. 20.2 it can be seen that there is a linear increase of the produced electric power with increasing active cell area under the assumption that scaling up of the active area does not influence the cell behavior. For a current density of 450 mA cm⁻² at reformat operation the produced electric power increases from 2.35 W at 10 cm² active cell area to 235 W at 1000 cm². For the designated applications in the power range of some hundred watts or even

higher an active cell area of more than 1000 cm² is necessary. A setup with only one single cell is extremely challenging because of the very high demands on the gas distribution, active heat dissipation and manufacturing accuracy due to sealing requirements and MEA compression. Additionally the low voltage of a single cell setup in the range of 0.5–0.6 V is not useful for most applications. A step-up converter has to be introduced. For these reasons it is advisable to reduce the active cell area and use more cells. Cell areas between 100 and 350 cm² are ideally suited to fulfill the requirements for the targeted power range between some hundred Watt and

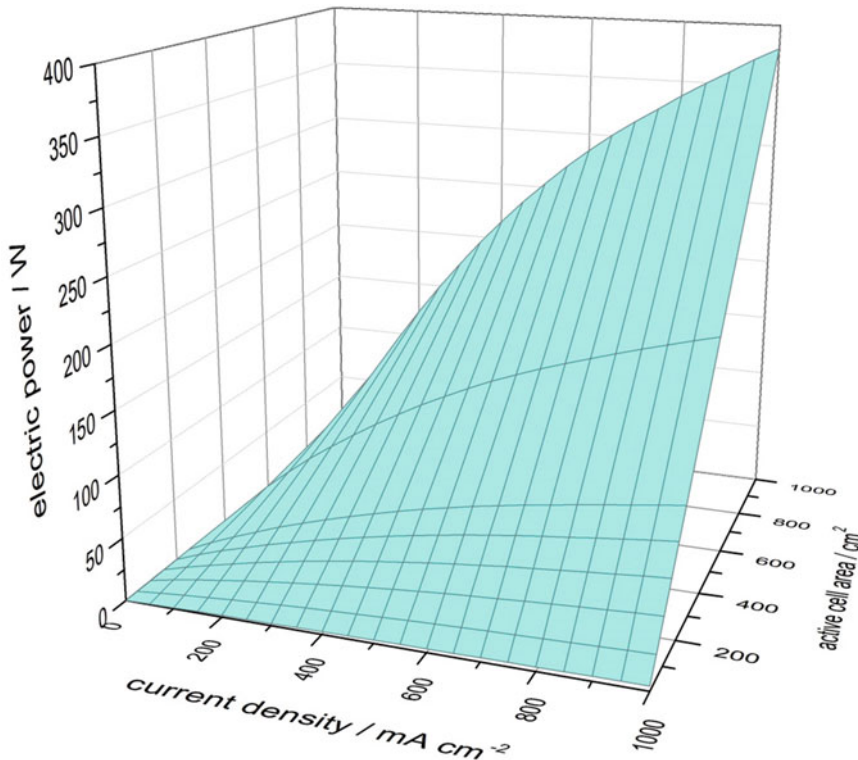


Fig. 20.2 Influence of the active cell area on the produced electric power for a single cell at reformat operation

some kilo Watt. For this reason, the following considerations will be carried out on HT-PEMFC stack concepts having a cell area of 200 cm². The influence of the cell number on the produced electric power for such a stack is shown in Fig. 20.3. Here it is assumed that each cell performs on the same level.

Corresponding to the curve shape in Fig. 20.2 the generated electric power increases linearly with increasing number of cells. For a common current density of 450 mA cm⁻² the produced electric power rises from 47 W for 1 cell up to 4700 W for 100 cells.

It can be concluded for a reformat stack operation that active cell areas between 100 and 350 cm² and cell numbers between 10 and 100 are technically feasible and suitable for the most envisaged applications which was also demonstrated by different groups [4, 5]. The scalability of fuel cell stacks in terms of active cell area and number of cells and also the modularity of a fuel cell system give the stack and systems designer some degrees of freedom.

Possible application oriented target parameters for the stack development are, e.g., space restrictions or nominal voltages. Especially a high voltage transfer ratio from stack to systems voltage possibly affects the systems efficiency negatively due to the increased losses of the converter.

For the development of HT-PEMFC stacks it is essential to determine detailed knowledge about the thermal behavior. Calculations and experimental investigations are key aspects of the following sections.

20.3 Energy Balance for a HT-PEMFC Stack

For a first approach the energy balance equation has to be solved for a simplified stack model. The stack is assumed to be ideally insulated and the stack is in a steady state operation. The energy balance control volume is given in Fig. 20.4.

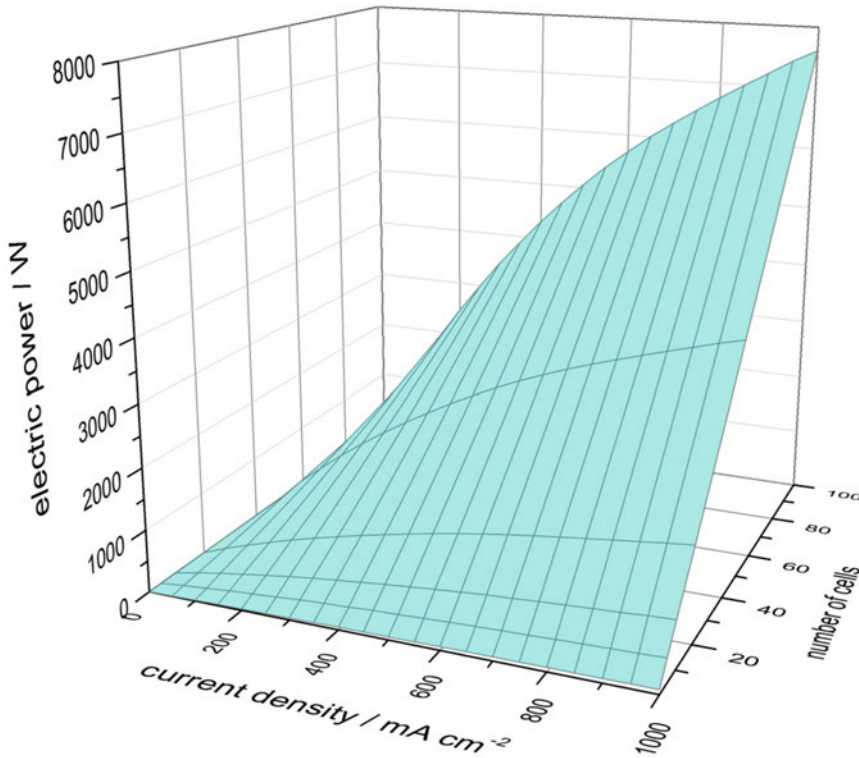


Fig. 20.3 Influence of the number of cells on the produced electric power for a HT-PEMFC stack with 200 cm² active cell area at reformate operation

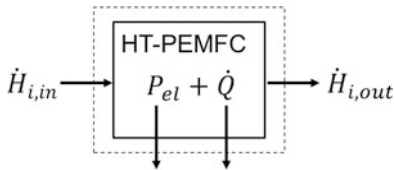


Fig. 20.4 Energy balance control volume

With this simplified model the percentage of heat to be removed (\dot{Q}) by the stack cooling system can be identified by solving 20.1, where $\dot{H}_{i, in}$ is the enthalpy of component i at the inlet of the control volume, $\dot{H}_{i, out}$ is the enthalpy of component i at the outlet, \dot{Q} is the heat to be removed by the cooling medium, and P_{el} is the produced electrical power output of the stack.

$$\sum \dot{H}_{i, in} = P_{el} + \sum \dot{H}_{i, out} + \dot{Q} \quad (20.1)$$

The electrical power output depends on the operating conditions and the gases used for

stack operation. Due to the lower cell efficiency in reformate operation compared to hydrogen operation at the same stack power a distinction between pure hydrogen operation and the operation with different reformate compositions has to be made [6]. In the following, dry reformate gas based on a diesel reforming process is taken into account. This reformate contains 42 vol% H₂, 1 vol% CO, and other gases (mostly CO₂) which are replaced here by N₂ (57 vol%) because of their inert behavior in HT-PEMFC operation [7, 8]. All anode side gases with the exception of hydrogen are considered as inert gases in the energy balance. With this assumption 20.1 can be specified for hydrogen/air operation (20.2) and reformate/air operation (20.3).

$$\begin{aligned} \dot{Q} = & -P_{el} + \dot{H}_{air, in} + \dot{H}_{H_2, in} - \dot{H}_{air, out} \\ & - \dot{H}_{H_2, out} - \dot{H}_{H_2O, out} \end{aligned} \quad (20.2)$$

Table 20.2 Enthalpy and mass flow equations

Incoming enthalpy flows	Outgoing enthalpy flows
$\dot{H}_{\text{air, in}} = \dot{m}_{\text{air, in}} \cdot c_{p, \text{air}} \cdot \vartheta_{\text{in}}$	$\dot{H}_{\text{air, out}} = (\dot{m}_{\text{O}_2, \text{out}} \cdot c_{p, \text{O}_2} + \dot{m}_{\text{N}_2, \text{out}} \cdot c_{p, \text{N}_2}) \cdot \vartheta_{\text{out}}$
$\dot{H}_{\text{H}_2, \text{in}} = \dot{m}_{\text{H}_2, \text{in}} \cdot (c_{p, \text{H}_2} \cdot \vartheta_{\text{in}} + h_{\text{HHV}}^0)$	$\dot{H}_{\text{H}_2, \text{out}} = \dot{m}_{\text{H}_2, \text{out}} \cdot (c_{p, \text{H}_2} \cdot \vartheta_{\text{out}} + h_{\text{HHV}}^0)$
$\dot{H}_{\text{ig, in}} = \dot{m}_{\text{ig, in}} \cdot c_{p, \text{ig}} \cdot \vartheta_{\text{in}}$	$\dot{H}_{\text{ig, out}} = \dot{m}_{\text{ig, out}} \cdot c_{p, \text{out}} \cdot \vartheta_{\text{out}}$
	$\dot{H}_{\text{H}_2\text{O, gen}} = \dot{m}_{\text{H}_2\text{O, gen}} \cdot (c_{p, \text{H}_2\text{O, gen}} \cdot \vartheta_{\text{out}} + h_{\text{fg}}^0)$
Incoming mass flows	Outgoing mass flows
$\dot{m}_{\text{air, in}} = \frac{\lambda_{\text{O}_2}}{\chi_{\text{O}_2}} \cdot \frac{M_{\text{air}}}{4F} \cdot I \cdot n_{\text{cell}}$	$\dot{m}_{\text{O}_2, \text{out}} = (\lambda_{\text{O}_2} - 1) \cdot \frac{M_{\text{O}_2}}{4F} \cdot I \cdot n_{\text{cell}}$
	$\dot{m}_{\text{N}_2, \text{out}} = \frac{(1 - \chi_{\text{O}_2})}{\chi_{\text{O}_2}} \cdot \frac{M_{\text{N}_2}}{4F} \cdot I \cdot n_{\text{cell}}$
$\dot{m}_{\text{H}_2, \text{in}} = \lambda_{\text{H}_2} \cdot \frac{M_{\text{H}_2}}{2F} \cdot I \cdot n_{\text{cell}}$	$\dot{m}_{\text{H}_2, \text{out}} = (\lambda_{\text{H}_2} - 1) \cdot \frac{M_{\text{H}_2}}{2F} \cdot I \cdot n_{\text{cell}}$
$\dot{m}_{\text{ig, in}} = \frac{1 - \chi_{\text{H}_2}}{\chi_{\text{H}_2}} \cdot \frac{M_{\text{ig}}}{2F} \cdot I \cdot n_{\text{cell}}$	$\dot{m}_{\text{ig, out}} = \dot{m}_{\text{ig, in}} = \frac{1 - \chi_{\text{H}_2}}{\chi_{\text{H}_2}} \cdot \frac{M_{\text{ig}}}{2F} \cdot I \cdot n_{\text{cell}}$
	$\dot{m}_{\text{H}_2\text{O, gen}} = \frac{M_{\text{H}_2\text{O}}}{2F} \cdot I \cdot n_{\text{cell}}$

\dot{H}_i : Enthalpy flow of component i , W

\dot{m}_i : Mass flow of component i , kg s^{-1}

$c_{p,i}$: Specific heat capacity of component i , $\text{J kg}^{-1} \text{K}^{-1}$

ϑ : Temperature difference to the reference temperature (0°C), K

h_{HHV}^0 : Higher heating value of hydrogen at reference temperature, J kg^{-1}

h_{fg}^0 : Enthalpy of condensation for water at reference temperature, J kg^{-1}

λ_i : Stoichiometric factor for component i , –

χ_i : Mass fraction of component i , –

M_i : Molar mass of component i , kg mole^{-1}

I : Electric current, A

$F = 96,485 \text{ A s mol}^{-1}$: Faraday constant

n_{cell} : Number of cells, –

$$\begin{aligned} \dot{Q} = & -P_{\text{el}} + \dot{H}_{\text{air, in}} + \dot{H}_{\text{H}_2, \text{in}} + \dot{H}_{\text{ig, in}} \\ & - \dot{H}_{\text{air, out}} - \dot{H}_{\text{H}_2, \text{out}} - \dot{H}_{\text{H}_2\text{O, out}} \\ & - \dot{H}_{\text{ig, out}} \end{aligned} \quad (20.3)$$

The required enthalpy for the calculation can be determined using the equations shown in Table 20.2, for tabulated values (e.g., [9]) and the mass flow rates calculated from Faraday's law. The reference temperature for the energy balance is set to 0°C .

To determine the heat flux to be dissipated, the value for the generated electric power is still missing. One possible way is to determine the electric power experimentally. For a HT-PEMFC stack operation with hydrogen/air, respectively, reformat/air at reference conditions defined in Table 20.1 the measured values are shown in Fig. 20.1.

From Fig. 20.1 it can be seen that for all current densities the voltage efficiency for pure hydrogen operation is higher than for the

synthetic reformat operation due to the lower hydrogen concentration and the CO content in the reformat. The difference in the average power density in the whole current density range shown in Fig. 20.2 is about 10 %. Using these experimentally determined values for P_{el} , the energy balance equation for pure hydrogen/air and reformat/air operation can be solved. The results are shown in Fig. 20.5.

It can be seen that a waste heat flow of 0.86 W cm^{-2} at 1000 mA cm^{-2} in reformat operation has to be removed from the stack. For an ideally insulated HT-PEMFC stack this heat flux must be dissipated exclusively by the thermal management system to maintain a steady operating temperature. Due to the higher amount of heat to be dissipated at a given current density (in average 6 %) in comparison to the pure hydrogen operation the reformat operation is the design reference for the thermal management system and with this as well for the stack concept.

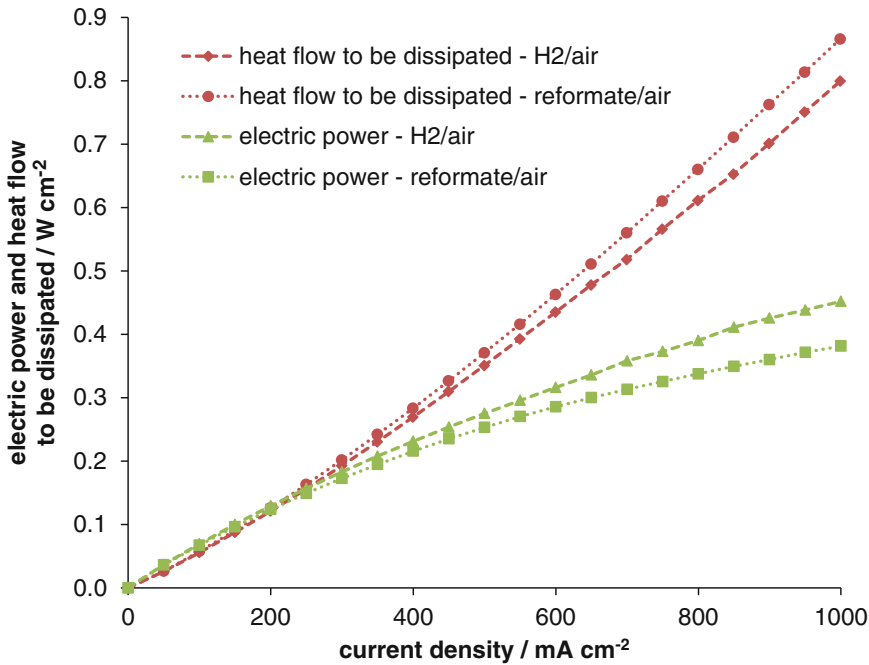


Fig. 20.5 Results of the energy balance on the basis of the experimentally determined electric power (green curves). Calculated heat flow (red curves) for hydrogen/air and reformat/air operation

20.4 Thermal Management of a HT-PEMFC Stack

The thermal management has a high impact on the HT-PEMFC stack concept when changing from single cells to stacks. Therefore this sub-chapter focuses on basic thermal management concepts for HT-PEMFC stacks. First, principal methods of heat removal from the heat generating MEA are explained, focusing on the possible heat transfer media. Both directly affect the stack concept. The thermal management system needs to provide cooling during operation and heat up on temperatures above 100 °C at the start-up process when the stack will be operated with hydrogen or to a temperature of 160 °C when reformat gas will be used. During operation local temperatures below 100 °C lead to condensation of product water. Phosphoric acid will be lost by leaching and the protonic conductivity will be reduced. When operated with reformat the higher temperature is necessary due to the poisoning effect of CO at low temperatures.

For a HT-PEMFC stack the generated heat must be taken out of the stack according to the energy balance (see Sect. 20.3). Figure 20.6 shows different methods to transport, transfer, and remove the heat.

Basically a distinction between internal and external cooling is made. For internal cooling the heat generated in the MEAs will be carried out of the stack by means of a liquid or gaseous heat transfer medium flowing through the fuel cell stack. A special case for internal cooling is the adaption of the air flow rate on the cathode side to a value which is sufficient for the heat removal. The heat transport between the MEAs and the internal flow structures of the heat transfer medium takes place due to heat conduction through the solid stack materials driven by the temperature difference. For the external cooling the heat transport takes place by means of heat conduction via the stack materials to the surface of the stack, where the heat transfer takes place. This can happen either by means of forced convection to a heat transfer fluid flowing at the outside or by means of free convection and radiation to the surrounding environment. The

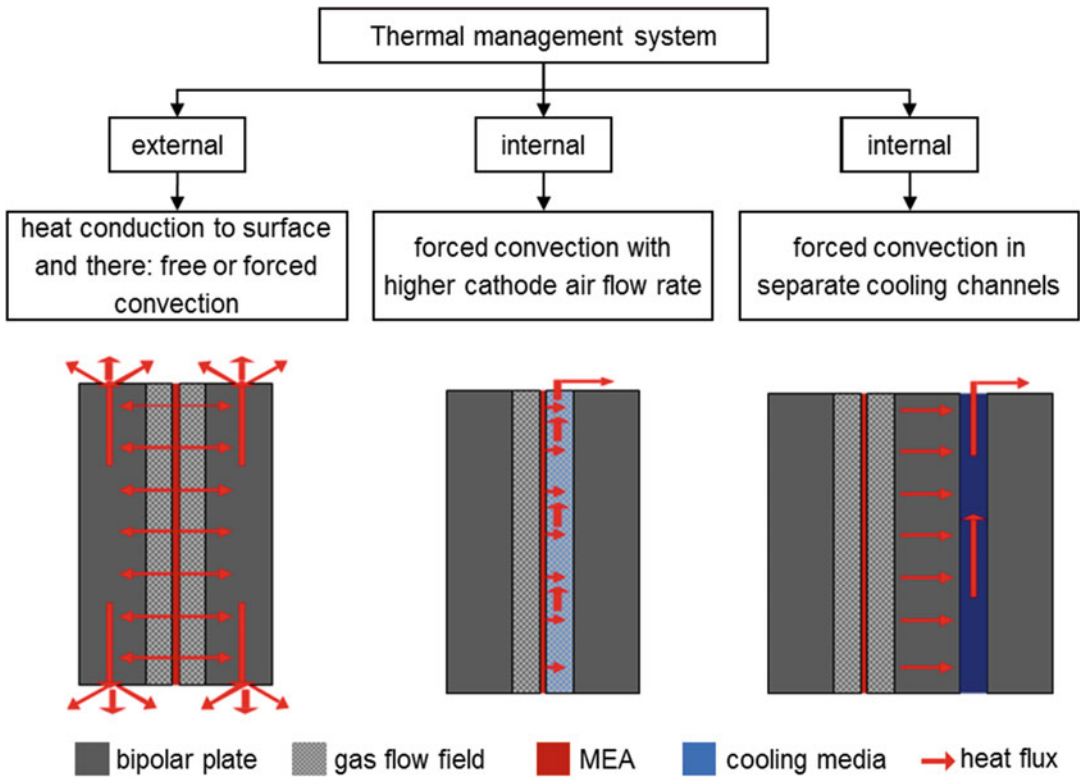


Fig. 20.6 Different methods for heat removal from HT-PEMFC stacks

heat discharge by natural convection and radiation at the surface of the fuel cell stack is equivalent to a purely passive cooling.

These three basic thermal management concepts influence the stack design in various ways. In the following, some possible designs and their influence on the operating behavior of the stack are considered. For all considerations stacks with an active area of 200 cm² are used as previously defined.

20.4.1 Passive Cooling of HT-PEMFC Stacks

In this section stack concepts with an external thermal management will be discussed. If the heat transfer at the surface of the stack takes place only by radiation and free convection no additional power consumption for the cooling is necessary. In addition, it requires no further

components for the heat conduction if the already used stack materials have proper heat conductivity. The amount of heat to be dissipated strongly depends on the surface area and the temperature difference between the HT-PEMFC stack surface and the surrounding which is mostly ambient air. Due to the fixed operating temperature of around 160 °C, the more or less constant ambient temperature and under the assumption of sufficient thermal conductivity of the stack material only the stack surface can be modified to have an influence on the heat dissipation. This directly leads to changes in the HT-PEMFC stack design. Therefore the influence of the surface area on the dissipated heat must be calculated in order to determine whether this thermal management concept provides sufficient heat dissipation or not. Exemplary this is done in the following for a stack with an active cell area of 200 cm². The stack design is inspired by the stack described in Table 20.4 except that the internal cooling

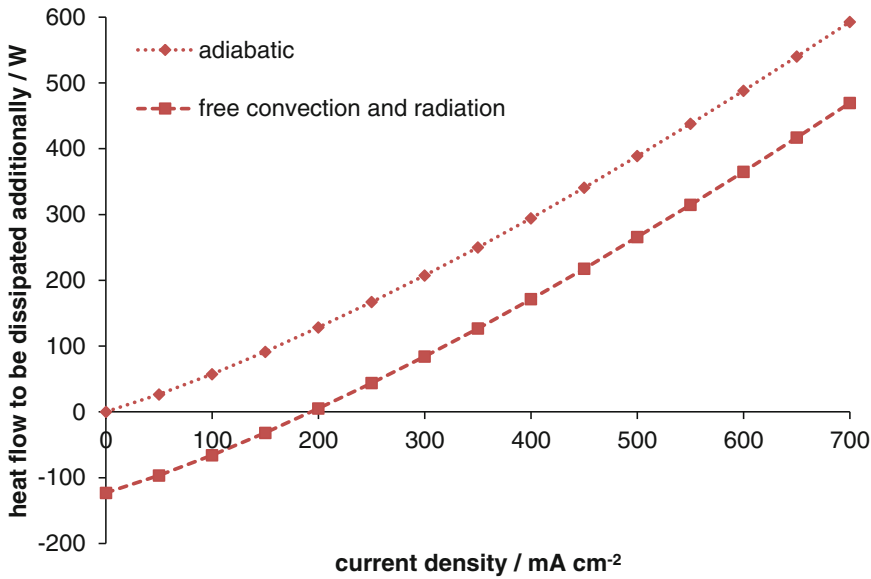


Fig. 20.7 Energy balance based calculation of the heat flow to be dissipated by an additional cooling system, five cells, $A_{\text{act}} = 200 \text{ cm}^2$, $t_{\text{stack}} = 160 \text{ }^\circ\text{C}$, $t_{\text{amb}} = 20 \text{ }^\circ\text{C}$

structures are omitted. Considering that the heat dissipation takes place at the surface only by free convection and radiation the energy balance equation has been solved for an exemplary stack with five cells and an active cell area of 200 cm^2 . For the calculations the stack temperature and with this the surface temperature is fixed at $160 \text{ }^\circ\text{C}$ and the ambient temperature is fixed to $20 \text{ }^\circ\text{C}$. The results are shown in Fig. 20.7 and compared with a thermal ideally insulated stack (adiabatic boundary conditions).

In comparison to the adiabatic stack, of course less heat needs to be removed additionally for the not insulated stack. However, as Fig. 20.7 shows only one operating point at a current density of 200 mA cm^{-2} exists, where no additional cooling besides the passive surface cooling is necessary. At this operating point a steady stack operation would be possible at the chosen temperature of $160 \text{ }^\circ\text{C}$. For a stack operation at higher current densities additional cooling is necessary, or the temperature will increase. For lower current densities a heating must be provided even at steady-state operation. In order to accomplish increased heat dissipation, the surface area can be increased by additional parts (like, e.g., fins). Another possibility to enlarge the stack surface

for the heat transfer is to change the aspect ratio of the MEA, respectively, bipolar plate edges at a constant active cell area. Calculations show that the effect of the ratio change is small. If the ratio of the active cell area is changed from 141×141 to $50 \times 400 \text{ mm}^2$ only 4 % more heat will be dissipated over the enlarged surface [10]. Another disadvantage of this cooling system is the dependence on the number of cells. For most applications an increased number of cells are required. With this, the influence of the surface cooling decreases.

Figure 20.8 shows that the influence of surface cooling decreases with increasing number of cells. The current density where steady-state stack operation at $160 \text{ }^\circ\text{C}$ is possible decreases with increasing number of cells. The reason is the decreasing influence of the end plates surface and the associated lower surface to active cell area ratio with high cell numbers. As a result of the increasing heat production with increasing number of cells, small changes in the current density have a high impact on the heat to be dissipated additionally by active cooling due to the increasing slope of the curve. The current density range where an active heat supply is necessary is reduced from 200 mA cm^{-2} down to 25 mA cm^{-2}

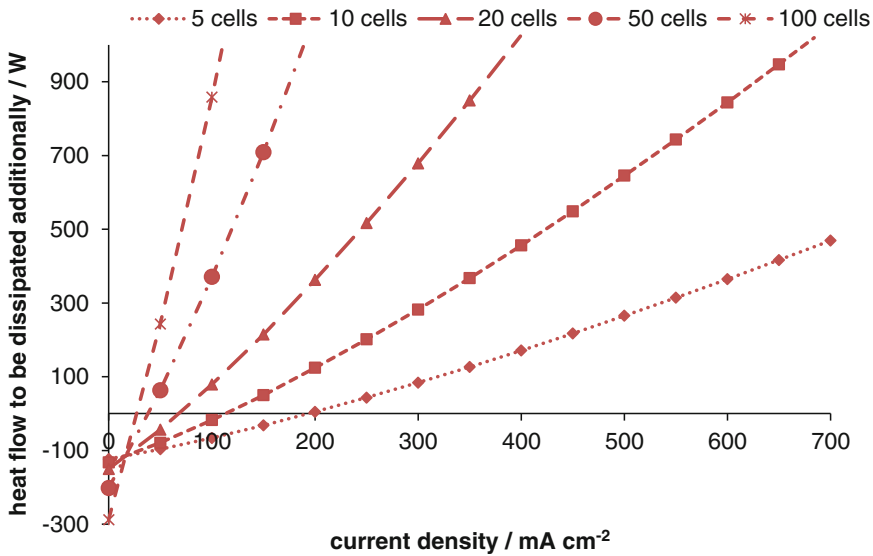


Fig. 20.8 Influence of the number of cells on the heat flow to be dissipated, $A_{\text{act}} = 200 \text{ cm}^2$, $t_{\text{Stack}} = 160 \text{ }^\circ\text{C}$, $t_{\text{amb}} = 20 \text{ }^\circ\text{C}$

by increasing the number of cells from 5 to 100. This also means that a purely passive cooled stack with 100 cells can only be operated at the fixed boundary conditions setting the current density to a value of 25 mA cm^{-2} . At this operating point the generated electric power is only 360 W (18 mW cm^{-2}). Thus, a high number of cells reduce the impact of the external surface cooling on the total cooling effort.

It can be concluded that a stack concept with pure passive cooling is not advisable because the stack temperature varies strongly with the stack power and as a result the specified temperature range may be exceeded. Dependent on the stack power (full load, partial load) during normal operation additional cooling or heating is required. Therefore an active thermal management system is mandatory.

20.4.2 Active Cooling of HT-PEMFC Stacks

One possibility for an internal thermal management concept is the cooling with increased and adapted cathode air flow rate. This influences the HT-PEMFC stack design only slightly. Only the

cathode flow field structure needs to be adjusted to the higher air flow rate to restrict the parasitic power consumption by the fan or compressor. Previously, some HT-PEMFC stacks have been studied and developed according to this concept. For all stack concepts the power range is limited to a maximum of around 1 kW_{el} and the maximum active cell area is restricted to 50 cm^2 [11–15]. Moreover, experiences from the low temperature PEMFC show that this type of stack cooling with a power generation of more than 5 kW_{el} is insufficient or not advantageous [16, 17]. Nevertheless, for the here examined stack concept with an active area of 200 cm^2 and exemplary ten cells, the prerequisites for a potential cathode air cooling will be calculated. Further boundary conditions are reformate operation, a cathode air inlet temperature of $25 \text{ }^\circ\text{C}$ and an outlet temperature of $160 \text{ }^\circ\text{C}$. The heat to be dissipated is calculated using the energy balance equation. The required cathode air flow for steady state stack operation is shown in Table 20.3.

As Table 20.3 shows, the necessary cathode stoichiometry is between 11 and 18 for a temperature difference of 135 K between incoming and exiting air. Using a meander type flow field with

Table 20.3 Required cathode air flow rates for appropriate cooling

Current density/ mA cm^{-2}	Heat flow to be dissipated/W	Required cathode air flow rate/ $\text{m}^3 \text{h}^{-1}$	Stoichiometry
50	53	1.4	11
100	115	2.8	12
150	182	4.6	13
200	257	6.7	14
250	334	8.5	14
300	415	10.6	15
350	500	13.1	15
400	589	15.3	16
450	681	17.7	16
500	778	20.2	17
550	876	22.7	17
600	976	25.5	17
650	1080	28.0	18
700	1185	30.9	18

Table 20.4 Parameters of the HT-PEMFC stack concept with internal cooling

Stack component	Specification
MEA type	BASF Celtec® P-1000 [3]
Active cell area	200 cm^2 (110 mm × 182 mm), reference, cf. Table 20.1
Number of cells	10, reference, cf. Table 20.1
Gaseous cooling fluid	Ambient air
Liquid cooling fluid	FRAGOLTHERM® S-15-A, polyglycol based [20]
Cooling flow field	45 straight rectangular channels (1.5 mm × 2 mm)
Bipolar plate material	Composite of graphite and phenolic resin, Eisenhuth BBP 4 [21]
Anode side flow field	10 parallel meanders; channel width/depth: 1 mm/1 mm, land width: 1 mm
Cathode side flow field	Same design as anode side flow field
End plates	Aluminum
Thermal insulation	>20 mm silicon foam

parameters given in Table 20.4 results in a high cathode side pressure drop at elevated air stoichiometry. A Computational Fluid Dynamics (CFD) simulation of the structure showed a pressure drop of 149.8 Pa at a comparatively low air stoichiometry of 2 [18]. Increasing the stoichiometry to values feasible for the heat removal leads to parasitic power consumptions of more than 10 % of the produced electric power even if the flow field structure would be changed from meander type to straight channels [10]. Another drawback is the heat integration in the system or application using air as the heat transfer medium. Compared to liquid cooling media the specific heat capacity and the heat transfer coefficient are significantly lower. Therefore this concept is

suitable to fulfill the thermal management of stacks in the kW range. Nevertheless, the simple stack construction and the low space and weight requirements provide an attractive way of cooling for applications with low power consumption.

Another possibility for an active thermal management concept is to use cooling channels which are separated from the anode and cathode side gas channels.

Due to separate cooling flow fields which prevent a mixture of the cooling media and reactant gases and also a contact with the MEA, different possible cooling media can be used. Generally the cooling medium should not be electrically conductive, absorb and release heat

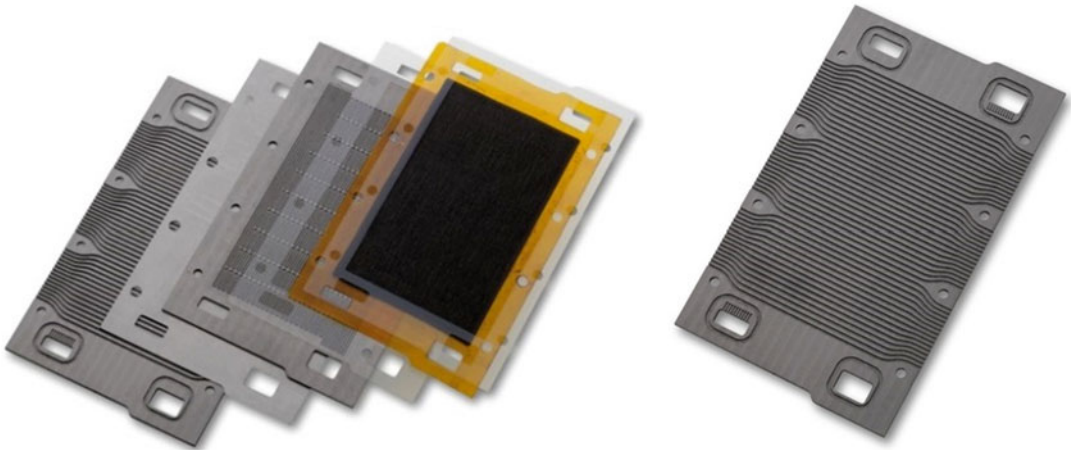


Fig. 20.9 Repeating unit of the basic stack setup (*left*); coolant flow field on the rear of the cathode side bipolar plate half-shell (*right*)

in the temperature range of the HT-PEMFC, have a low viscosity to restrict the pressure drop in the cooling circuit, and should not be harmful to the environment. In general, three different cooling media classes can be defined:

- Fluids which are gaseous in the whole temperature operating range of the HT-PEMFC. Here air is the preferred medium.
- Fluids which stay liquid in the whole temperature operating range. Here a broad range of different products exist. The majority is based on mineral oil or polyglycol. Necessarily the evaporation temperature is above 200 °C. For the further discussion these products are collectively referred to oil.
- Fluids with phase changes during cooling and heat-up. Here water is the best known representative.

For the internal thermal management concept with forced convection in separate cooling channels, the bipolar plates are split into two half-shells. The cooling channels can either be integrated into the bipolar plate material on the back side of one of the half-shells or within separate cooling cells. Both methods allow the usage of different heat transfer media.

In the following we will experimentally analyze and compare stack concepts on the basis of

active cooling with air and oil. To eliminate influences coming from different test setups, cell sizes, and stacks the investigations were performed using the same basic stack components. Figure 20.9 shows the elements of the repeating unit. It consists of two bipolar plate half-shells connected with an electrically conductive flat gasket from expanded graphite (Sigraflex[®]) and a MEA with two non-conductive flat gaskets from perfluoroalkoxy polymer (PFA).

The bipolar plates comprise flow field structures with a total area of 200 cm². As for the MEA the dimensions are 110 mm × 182 mm. The gas flow fields on the anode and on the cathode side are equal due to similar flow rates of air and reformat (diesel based) at stack operation. The flow field structures consist of ten parallel meanders. On the back of the cathode side bipolar plate half-shell, straight channels for the heat transfer media flow are integrated. Sealing is achieved if the stack is clamped using tie rods.

From these basic components stacks were assembled as shown in Fig. 20.10. The supply and removal of the liquid heat transfer media and the distribution on every cell is provided by externally mounted manifolds. The heat transfer fluids flow from the top downwards through the straight channel structure on the back of the cathode side half-shell.

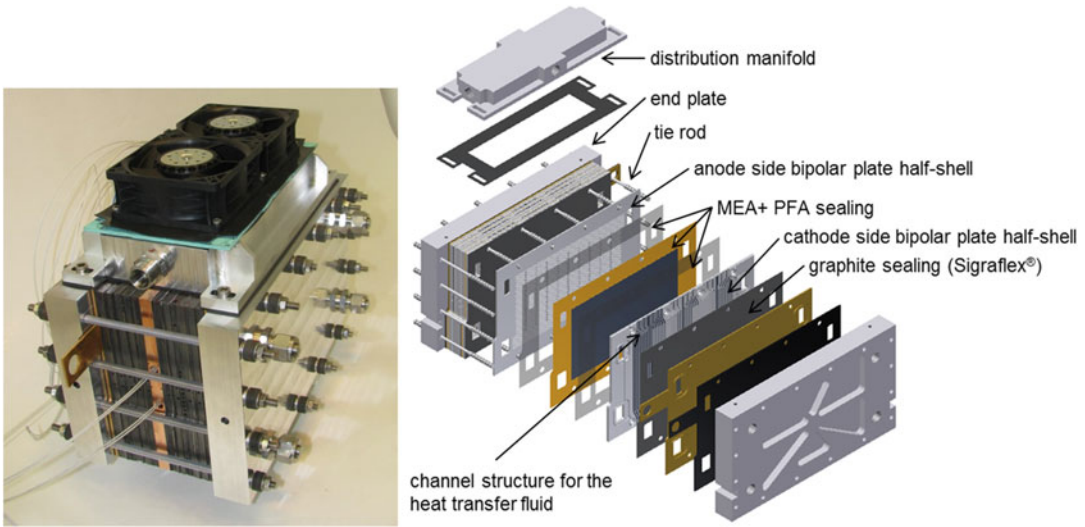


Fig. 20.10 Basic HT-PEMFC stack concepts with internal air cooling (*left*) and internal liquid cooling (*right*) [19]

Table 20.5 Experimental boundary conditions

Stack component	Design
Anode gas	Synthetic reformat, composition: reference, cf. Table 20.1
Cathode gas	Air
Stoichiometry	$\lambda_{an/ca} = 2/2$, reference, cf. Table 20.1
Gas inlet temperature	160 °C, reference, cf. Table 20.1
Inlet temperature cooling air	Ambient temperature, 20–25 °C
Inlet temperature liquid coolant	160 °C, reference, cf. Table 20.1
Cooling air mass flow	2.2 kg min ⁻¹ in total
Liquid coolant mass flow	4 kg min ⁻¹ in total

For the stack setup with air cooling (Fig. 20.10, left) two axial blowers are mounted on top of the distributor manifold. Heat-up of the stack is achieved by heating cartridges integrated in the center plate of the stack. In the case of the stack setup with liquid cooling (Fig. 20.10, right) two external manifolds (top and bottom (not shown in Fig. 20.10) of the stack) are necessary to realize a closed oil loop. Heat-up and cooling of the oil is done by heat exchangers integrated into the test station. In Table 20.4 the specifications of the stack setups are summarized.

The shown stack concept is used to determine the temperature distribution across the active cell area. Further experimental boundary conditions are listed in Table 20.5.

For the air cooled stack setup the results of the temperature distribution measurements are given in Fig. 20.11. The thermocouples were positioned in the horizontal center of the cell. Five sensors were distributed vertically comprising the limits of the active cell area. Due to the influence of the external distributor manifold and the heat transfer in the upper bipolar plate region (sealing area) the minimum local temperature exceeds 120 °C at every position within the active cell area, although the cooling air enters the stack at ambient temperature. Towards the center of the cell the temperature rises linearly. Due to the missing insulation at the cooling air outlet at the bottom of the stack the temperature decreases slightly between the last two sensors. The maximum

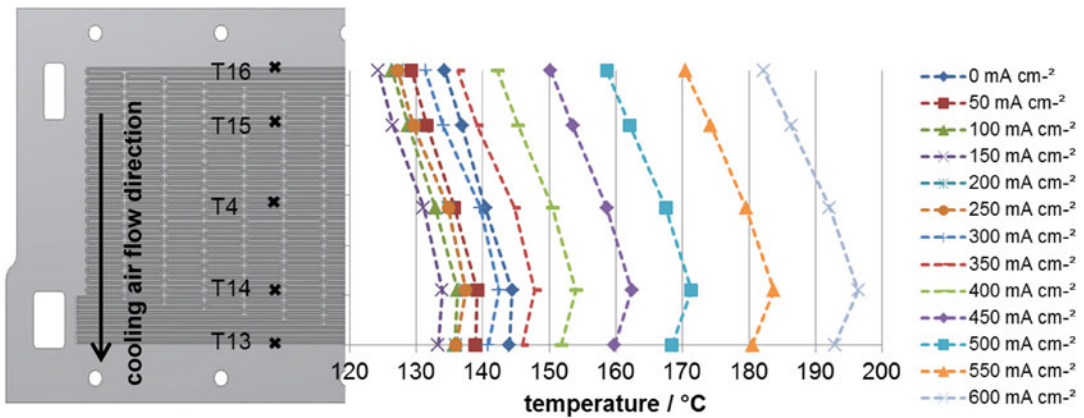


Fig. 20.11 Vertical temperature distribution across the active cell area for an air cooled stack where every cell is cooled

temperature gradient of 14.2 K was measured at a current density of 600 mA cm^{-2} . $180 \text{ }^\circ\text{C}$ as a limiting temperature was exceeded locally at a current density of 550 mA cm^{-2} .

One possibility to decrease the temperature gradients and the maximum local temperature is to increase and control the cooling air mass flow. As a drawback of this procedure the power consumption of the coolant blowers increases dramatically. For current densities of more than 800 mA cm^{-2} the blower consumed more than 14 % of the stack power [10].

In the next section we will present the test results with a liquid cooled stack setup. As another parameter the number of cooling cells in relation to the electrochemical cells (MEAs) was varied. The difference between the cooling of every cell and the cooling of every third cell are the omitted cooling structures, which leads to a stack size reduction. For the experiments the total mass flow of the coolant was set to a constant value of 4 kg min^{-1} at both configurations.

Regarding the temperature distribution between the single cells in a stack, cooling of each cell is advantageous but stack concepts where only every second or third cell is in contact with a cooling cell can also be found. For the chosen active cell area of 200 cm^2 a cooling of every third cell is possible [22]. However, this increases both the temperature gradient across the active cell area, as well as from cell to cell.

In order to demonstrate the differences between a cooling of each cell and a cooling of every third cell, two stacks based on the same concept (Fig. 20.10, right) have been build up to demonstrate experimentally the difference in the temperature profiles. The stack structure and the temperature measurement position for both stack concepts are shown in Fig. 20.12.

From Fig. 20.12 it can be seen that the temperature measuring positions are the same as for the tests with cooling air. Additionally the detailed sequence of the single components in the two setups is given. The results of the experimentally determined temperature distribution are shown in Fig. 20.13 for a stack where every cell is cooled and in Fig. 20.14 for a concept where every third cell is cooled.

Figures 20.13 and 20.14 indicate a rise in the average stack temperature level with rising current density due to the higher amount of heat to be dissipated in combination with the fixed cooling inlet conditions. Although the total volume flow rate of the cooling medium for both experiments is comparable the average temperature of the every-third-cell-cooled stack is 4 % higher. The reason is the increased distance between two cooling cells and the higher amount of heat to be dissipated by each cooling cell and thus the necessary temperature difference for the heat transfer.

For both cooling concepts it can be seen that the temperature first rises in flow direction with a

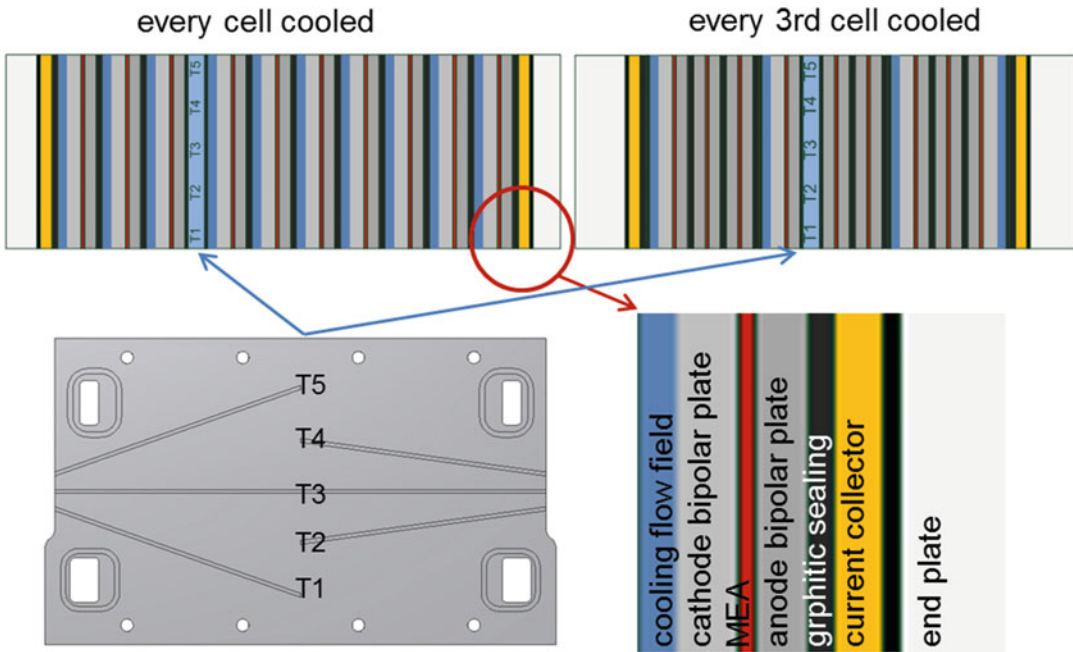


Fig. 20.12 Stack structure and temperature measurement positions

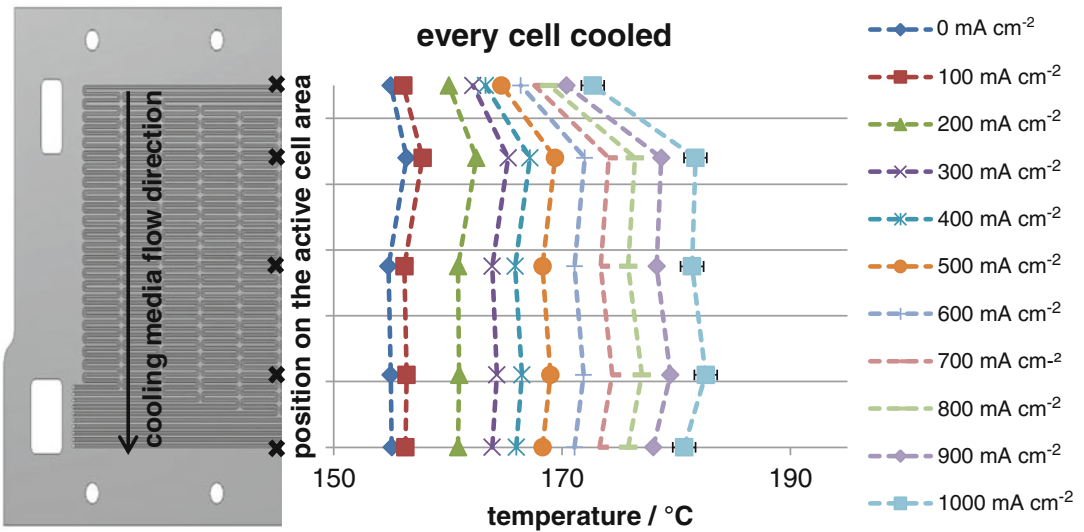


Fig. 20.13 Vertical temperature distribution across the active cell area for a stack where every cell is cooled

peak in the center of the stack and then falls slightly or remains at the same temperature level for higher current densities. The reason for this behavior is the temperature rise in the coolant due to the heat dissipation which is superimposed during the further progress of the heat dissipation

by the non-ideal thermal insulation. In comparison to the every-cell-cooled concept the temperature difference for the every-third-cell cooled stack rises due to the higher amount of heat to be dissipated by each cooling cell. In average (over the whole operating range) the temperature

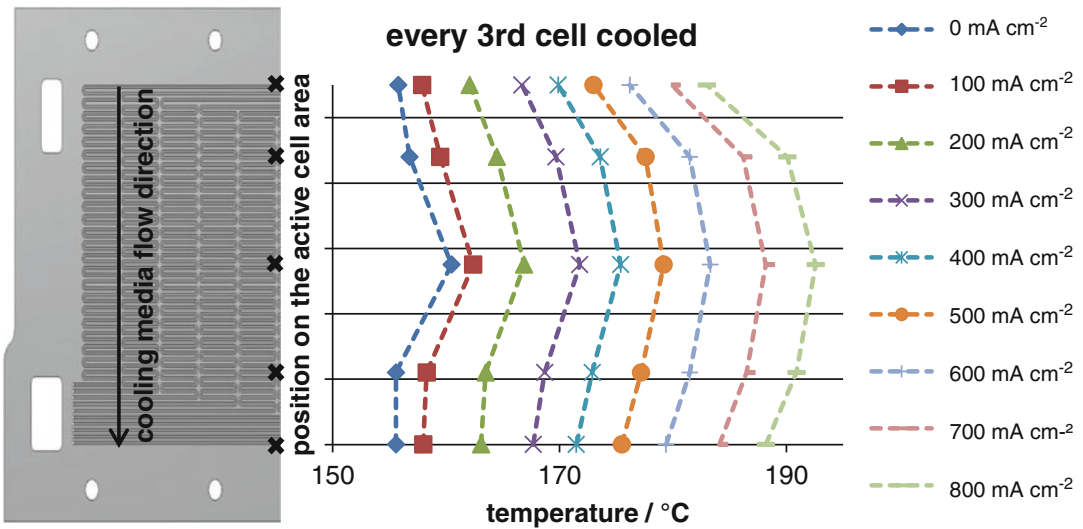


Fig. 20.14 Vertical temperature distribution across the active cell area for a stack where every third cell is cooled

difference is 35 % higher than for the stack where every cell is cooled. Nevertheless, the maximum temperature difference across the active cell area of less than 10 K occurring at the highest current density is relatively small for both stack concepts. The temperature difference from cell to cell for a stack where every third cell is cooled was published in [22]. It is clear that the maximum temperature was measured in the center cell between two cooling cells. For the allowed operation range, where the maximum local temperature does not exceed 180 °C, the maximum temperature difference is also in the range of 10 K. In general it can be stated that there is a clear relation between cell operation temperature and cell degradation rate. In [8] this was investigated systematically. So one can assume that the highest degradation rate will occur in the middle of the center cell at high current densities. The temperature difference as well as the maximum temperature can be limited by optimizing the cooling system in terms of coolant flow rate and coolant inlet temperature.

It can be concluded that both variants of cooling via forced convection in separate channels are well suited as an active thermal management concept for HT-PEMFC stacks. In the whole operating range the produced heat can be removed by means of this active cooling

concept. Also heating up from ambient to operation temperature of the stack (>120 °C to avoid local condensation) is possible. On the systems level stack heating-up and cooling can be integrated into the thermal management of the reformer subsystem [23]. A start-up burner and an integrated cooling loop serve as main components of the thermal part of the system. As a consequence of this internal cooling concept the stack design has to provide for additional cooling structures which need to be integrated into the bipolar plate. This leads to further areas which need to be sealed and to an increase in the gravimetric and volumetric power density.

20.5 Alternative Cooling Concepts and Conclusions

Besides active cooling with air or with liquids like oil, stacks can also be cooled with water. The effects of water cooling are estimated by the authors only theoretically. The reason is the pressurization of the water cooling circuit, which is necessary not only for the conventional water cooling but also for the phase change concept. At ambient pressure of 1 bar the internal water cooling would cause a stack temperature of round about 100 °C due to the evaporation at

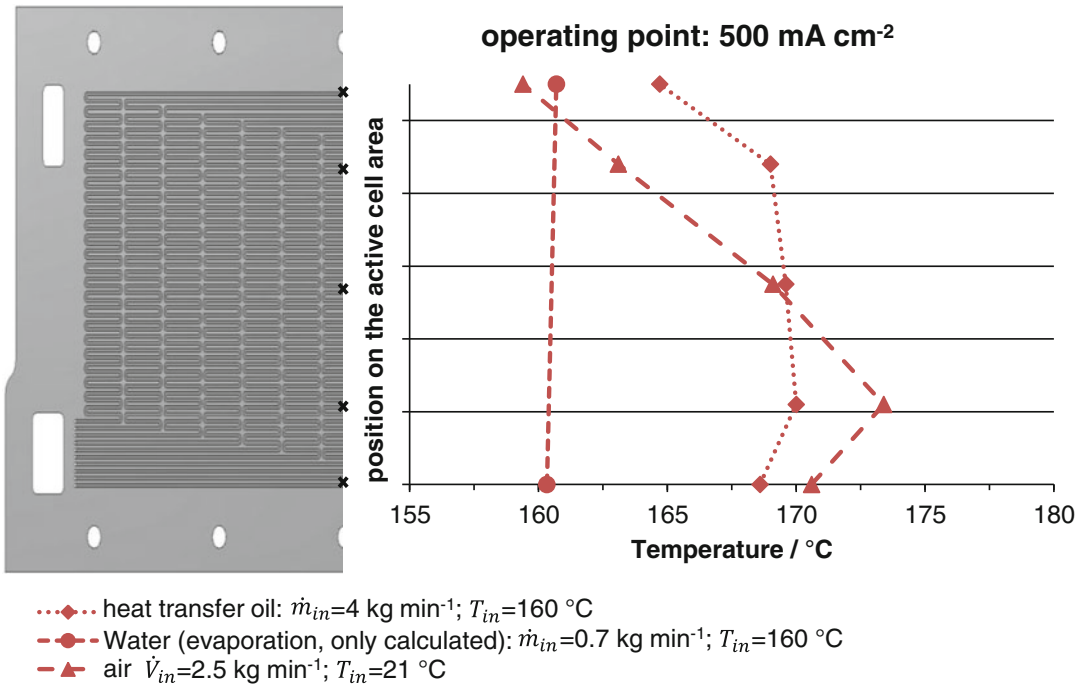


Fig. 20.15 Comparison of the temperature distribution across the active cell area for three different cooling media at reformate operation

this temperature. Therefore a pressure of more than 5 bars is necessary to reach adequate operating temperatures. Due to this reason an experimental investigation of the temperature distribution for a water cooled stack was not performed with the described setup. Instead of this, calculations based on the energy balance equation were performed. The results of these calculations and the experimental investigations with thermo oil and air cooling are presented in Fig. 20.15 for a typical operating point at a current density of 500 mA cm^{-2} . From Fig. 20.15 it can be seen that all cooling concepts sufficiently cool the stack at this operating point. The lowest temperature gradient with 0.4 K across the active cell area can be achieved by water evaporation. The reason is the isothermal energy dissipation during the phase change. In comparison to water oil has a larger temperature gradient with 5.3 K across the active cell area. The largest temperature gradient of 14 K at this operating point was measured with air. The reason is the low specific heat capacity ($1019 \text{ J kg}^{-1} \text{ K}^{-1}$ at 160 °C) and

the low heat transfer coefficient ($<100 \text{ W cm}^{-2} \text{ K}$). Therefore a large volume flow or a high temperature gradient is required. The increase of the volume flow is limited by the heat transfer. This leads to the comparatively high temperature gradient.

Overall it can be concluded that oil, air, or water are suitable to cool HT-PEMFC stacks. Passive air cooling of a stack is not advisable because of the limited power range in an appropriate stack temperature range.

Active air cooling of stacks in the kW range is possible but a high energy demand for the external air blower limits the area of application. Another drawback of air cooling is that heating-up of the stack to the desired temperature typically requires an extra heating system. This can be implemented either by the introduction of an electric heating plate into the stack or by an additional electric air heater and heat exchanger.

Oil cooling has the advantages of effective heat removal at small temperature gradients, easy heat-up, robust behavior with a simplified

control of the heating system and good thermal integration into the entire system (fuel cell system and/or adjacent systems). Due to the high creeping capability of thermo oil the sealing of the cooling compartments inside the stack is a challenge. A leakage of oil with access to the gas compartment will cause MEA poisoning.

Cooling water has the highest potential due to the latent heat transfer but pressurization in the cooling loop is essential. Therefore heat transfer oil based cooling concepts are most practical.

Acknowledgments The described research work has been partly supported by the German Federal Ministry of Economics and Technology under Grant No. 20Y0803H. We thank the lab staff, namely Jens Bohner, Birgit Schumacher, Matthias Prawitz, and Irina Kühn for their useful support in design of experiments and stack operation.

References

- Zhang J, Xie Z, Tang Y et al (2006) High temperature PEM fuel cells. *J Power Sources* 160:872–891
- Lee SJ, Mukerjee S, Ticianelli EA et al (1999) Electrocatalysis of CO tolerance in hydrogen oxidation reaction in PEM fuel cells. *Electrochim Acta* 44:3283–3293
- BASF (2012) Celtec[®] P1000 MEA. http://www.fuel-cell.basf.com/ca/internet/Fuel_Cell/en_GB/content/Microsite/Fuel_Cell/Products/Celtec-P_1000. Accessed 02 Aug 2012
- Janßen H, Supra J, Lüke L et al (2013) Development of HT-PEFC stacks in the kW range. *Int J Hydrog Energy* 38:4705–4713
- Serenergy (2014) S 165L—Liquid cooled HT PEM stack. <http://serenergy.com/products/stacks/liquid-cooled-s165-l/>. Accessed 21 Jul 2014
- Lüke L, Janßen H, Kvesić M et al (2012) Performance analysis of HT-PEFC stacks. *Int J Hydrog Energy* 37:9171–9181
- Pasel J, Meißner J, Porš Z et al (2007) Autothermal reforming of commercial Jet A-1 on a 5 kW_e scale. *Int J Hydrog Energy* 32:4847–4858
- Lüke L (2013) Analyse des Betriebsverhaltens von Hochtemperatur-Polymer-elektrolyt-Brennstoffzellen, Schriften des Forschungszentrums Jülich, Reihe Energie & Umwelt/Energy & Environment Band/Volume 192. Dissertation, RWTH Aachen University. ISBN 978-3-89336-909-6
- Verein Deutscher Ingenieure (Hrsg.) (2006) VDI-Wärmeatlas. 10. bearbeitete und erweiterte Auflage. Springer, Berlin
- Supra J (2014) Kühlkonzepte für Hochtemperatur-Polymer-elektrolyt-Brennstoffzellen-Stacks, Schriften des Forschungszentrums Jülich, Reihe Energie & Umwelt/Energy & Environment Band/Volume 209. Dissertation, RWTH Aachen University. ISBN 978-3-89336-946-1
- Jensen H-C B, Kær SK (2011) Boundary model-based reference control of blower cooled high temperature polymer electrolyte membrane fuel cells. *Int J Hydrog Energy* 36:5030–5037
- Kurz T, Keller J (2011) Heat management in a portable high temperature PEM fuel cell module with open cathode. *Fuel Cells* 11:518–525
- Andreasen SJ, Ashworth L, Menjón Remón IN et al (2008) Directly connected series coupled HTPEM fuel cell stacks to a Li-ion battery DC bus for a fuel cell electrical vehicle. *Int J Hydrog Energy* 33:7137–7145
- Andreasen SJ, Kær SK (2008) Modelling and evaluation of heating strategies for high temperature polymer electrolyte membrane fuel cell stacks. *Int J Hydrog Energy* 33:4655–4664
- Andreasen SJ, Kær SK (2007) 400 W high temperature PEM fuel cell stack test. *ECS Trans* 5:197–207
- Asghari S, Akhgar H, Imani BF (2011) Design of thermal management subsystem for a 5kW polymer electrolyte membrane fuel cell system. *J Power Sources* 196:3141–3148
- Squadrito G, Giacoppo G, Barbera O et al (2010) Design and development of a 7kW polymer electrolyte membrane fuel cell stack for UPS application. *Int J Hydrog Energy* 35:9983–9989
- Kvesić M (2012) Modellierung und Simulation von Hochtemperatur-Polymer-elektrolyt-Brennstoffzellen, Schriften des Forschungszentrums Jülich, Reihe Energie & Umwelt/Energy & Environment Band/Volume 158. Dissertation, RWTH Aachen University. ISBN 978-3-89336-835-8
- Bendzulla A (2010) Von der Komponente zum Stack: Entwicklung und Auslegung von HT-PEFC-Stacks der 5 kW-Klasse, Schriften des Forschungszentrums Jülich, Reihe Energie & Umwelt/Energy & Environment Band/Volume 69. Dissertation, RWTH Aachen University. ISBN 978-3-89336-634-7
- Fragol (2014) FRAGOL THERM[®] S-15-A. <http://www.fragol.de/produkte/waermetraegerfluessigkeiten/produktuebersicht/fragolthermR-s-15-a.html>. Accessed 6 June 2014
- Eisenhuth (2013) SIGRACET bipolar plates BBP 4. <http://www.eisenhuth.de/pages/frameset.html>. Accessed 5 June 2013
- Supra J, Janßen H, Lehnert W et al (2013) Temperature distribution in a liquid-cooled HT-PEFC stack. *Int J Hydrog Energy* 38:1943–1951
- Samsun RC, Pasel J, Janßen H et al (2014) Design and test of a 5kW_e high-temperature polymer electrolyte fuel cell system operated with diesel and kerosene. *Appl Energy* 114:238–249

Søren Juhl Andreasen, Søren Knudsen Kær,
Kristian Kjær Justesen, and Simon Lennart Sahlin

21.1 Introduction

Design of high temperature PEM (HTPEM) fuel cell systems requires special consideration of the elevated temperatures, and proper heat integration. Due to the increased tolerance to impurities, such as CO, in the anode hydrogen fuel flow these systems have a high degree of flexibility when it comes to choice of fuel.

The shift towards higher temperatures is not without challenges, the materials (membranes, catalysts, stack and system components) are further stressed while also less mature, system start-up time is longer and performance is lower than Nafion-based systems. However, HTPEM fuel cell systems have the potential of obtaining comparable efficiencies with other fuel cell technologies and in some cases provide more advantageous solutions due to the ease of cooling, reduced requirements for fuel quality and the possibility of using more readily available fuels that require smaller investments in

infrastructure [1–4]. The introduction of fuel reformers also introduce additional complexity to a fuel cell system, and require in turn proper control strategies in order to obtain reliable and efficient system performance. This chapter presents some of the challenges and strategies involved with HTPEM fuel cell system design, some of the considerations to make, and examples of different relevant control strategies and their potentials for use in real operating systems.

21.2 Methanol Reformer Systems

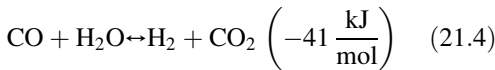
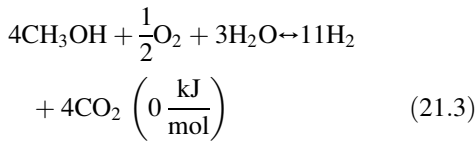
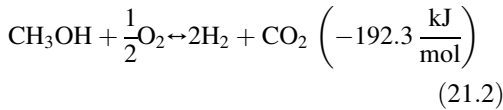
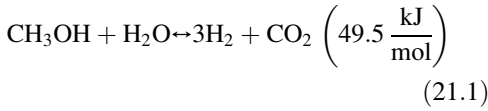
Using a liquid fuel, such as methanol, for fuelling a fuel cell system reduces or even eliminates some of the challenges involved with pure hydrogen-based fuel cells, such as the handling of non-conventional fuels, the distribution and availability, investments in infrastructure, and the low volumetric energy density, compared with liquid fuels even at high pressure (70 MPa). Methanol is the simplest alcohol, commonly used in the industry and therefore widely available. Although methanol mainly is produced from fossil natural gas, other, renewable onsite production methods are possible [5–9]. The temperatures of methanol steam reforming are low (220–300 °C) compared to the reforming of other commonly used fuels, such as natural gas or diesel (>700 °C). Low cost catalysts such as

S.J. Andreasen (✉)
Department of Energy Technology, Aalborg University,
Pontoppidanstræde 101, Aalborg East, Denmark

Serenergy A/S, Research and Development, Lyngvej 8,
Denmark
e-mail: sja@et.aau.dk; sja@serenergy.com

S.K. Kær • K.K. Justesen • S.L. Sahlin
Department of Energy Technology, Aalborg University,
Pontoppidanstræde 101, Aalborg East, Denmark

CuZn-based catalysts can be used, and different operating methods are possible. The most common reformer reactions can be seen in (21.1)–(21.4).



The most common efficient reforming method is the steam reforming reaction shown in (21.1), which is an endothermic reaction requiring addition of heat to the process. The other reactions ((21.2) and (21.3)) use an additional oxygen supply to the process, which in turn partially combusts some of the developed gasses. In the autothermal reforming reaction, (21.3), the heat generated by fuel oxidation is balanced to match the heat requirement for reforming. The resulting gasses of the steam reforming reaction are H_2 , CO_2 , H_2O , and CO and unconverted methanol fuel. It is of high importance to minimize the different pollutants in the hydrogen rich gas that enters the fuel cell stack, especially when it comes to CO and unconverted methanol, which will affect both the immediate stack performance and also lifetime [10–14]. Furthermore, the water-gas shift reaction (21.4) is an important process that typically occurs in parallel to the steam reforming reaction, converting part of the produced H_2 and CO_2 into CO and water forming a small amount of impurity in the fuel stream [15–18].

For methanol reformer systems to achieve optimal efficiencies proper heat integration is needed, i.e., all practically usable waste heat should be utilized. Different major heat consumers exist in HTPEM fuel cell systems,

such as fuel-water mixture evaporation and superheating as well as reformer reaction heat requirements. The main heat sources considered in the following shown cases are the fuel cell stack cathode exhaust and the unused anode exhaust gasses. Different system configurations are possible for transferring heat from and to these sources; the following examples will present a system topology using air and combusted gasses as the main heat carrier for transferring heat in the system. Mainly heat from the fuel cell stack is used to facilitate the evaporation of the methanol/water mixture entering the reformer. An alternative system is presented that uses a heat transfer oil as medium for transferring heat in the system using two different cooling circuit topologies.

21.3 Air Cooled Systems

Previous work has presented the use of air and as the heat transfer medium in HTPEM fuel cell stacks, this can be either as stacks with separate cooling channels or as cathode air cooled stacks, where cathode air at very high stoichiometry is used for controlling the temperature of a fuel cell stack [19]. This often yields very simple systems because fewer Balance-of-Plant components are needed and stack design often is simpler [20]. Careful flow field design is required in order to ensure low pressure drops in manifolds and cathode air flow fields. Both are required in order to use low power consuming air supplies, such as blowers and fans, and still ensure minimal parasitic losses in the system. Obtaining a uniform cell temperature is another challenge, ensuring a low temperature difference, not only within the individual MEAs from outlet to inlet, but also within the fuel cell stack. In the case where a methanol reformer system is introduced, the waste heat from the fuel cell cathode can effectively be used as process heat for evaporating the methanol/water mixture used in the reformer system. Figure 21.1 shows a schematic of a reformed methanol HTPEM fuel cell system using air-based cooling and heat transfer.

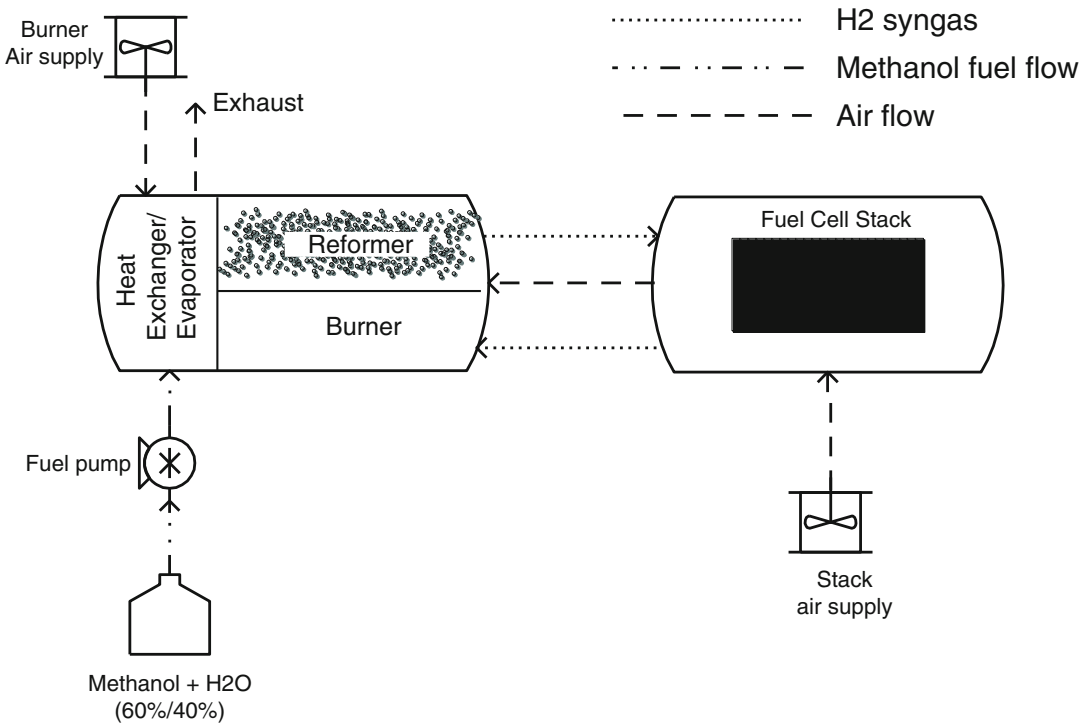


Fig. 21.1 Reformer system using air and flue gasses for heat transfer

The heat required by the methanol reforming process, which normally takes place at temperatures higher than the 160–180 °C of the fuel cell stack, can be supplied from the combustion of excess hydrogen exiting the fuel cell stack anode. An excess amount of hydrogen is normally supplied to the fuel cell stack, i.e., the fuel cell stack is running at a stoichiometry of $\lambda_{(H_2)} = 1.1\text{--}1.4$ in order to avoid dilution effects and ensure proper performance, because of the presence of residual gasses such as CO₂, CO, H₂O, and unconverted CH₃OH. This anode waste gas is catalytically combusted in a burner, and the heat is used to keep the reformer active at the desired operating temperatures (280–300 °C). Air is supplied to the anode waste gas, and provides the oxidant for the combustion process. The burner air flow is adjusted to control the resulting flue gas temperature, which is sent across a network of heat exchangers that preheat incoming gasses and supplies the catalyst bed with heat. Several authors have examined reformers using different types of system

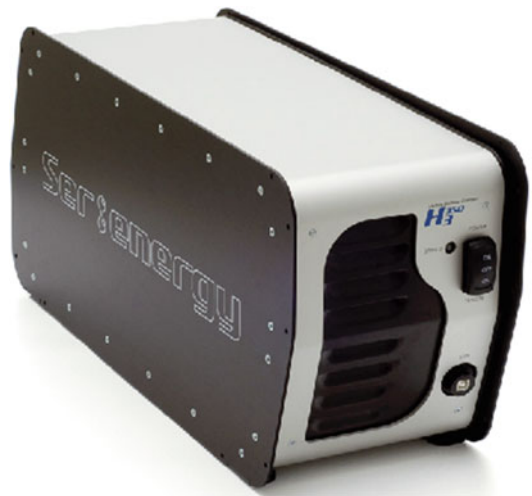


Fig. 21.2 Commercial HTPeM reformed methanol fuel cell system (Serenergy H3-350) [25]

integration approaches [21–24]. An example of a commercial HTPeM fuel cell system as the one exemplified above is the Serenergy H3-350, which uses a similar operating principle as

shown in Fig. 21.1. The system can be seen in Fig. 21.2, and is usable as an off grid battery charger, as it has a DC/DC controlled power output able to charge, for example, a battery pack.

The system includes the integrated fuel cell stack and methanol reformer system, DC/DC converter and Balance-of-Plant components and a small fuel buffer tank. The system requires connection to a battery pack and a fuel tank dimensioned to the desired run-time of the system. Generally start-up is one of the main challenges with high temperature PEM systems and reformers also add additional components that require heating. System components such as stacks and reformers can often be heated by electrical heating elements because of the low mass and fast temperature transients, but in order to increase the system round trip efficiency, decrease initial required battery capacity, and reduce required battery pack load in the initial stage of system start-up, it is also possible to use the available methanol fuel for system preheating, as discussed later in “Methanol combustion heating.”

21.4 Liquid Cooled Systems

When increasing power levels, losses are also increased, and in order to keep system size

compact, efficiency high and ease connections to utilize waste heat, liquid-based heat transfer is often advantageous. Several authors have examined such cooling strategies for high temperature PEM fuel cell stacks [26–31]. Using a liquid cooling media of course requires additional cooling channels in the fuel cell stack assembly, and in many cases a high degree of engineering in order to properly chose gaskets and materials that are able to handle the high temperatures and offer stability over the entire lifetime of the fuel cell system. Furthermore, additional system components are needed in order to exchange heat between different temperature levels, and properly cool the different components; different heat exchangers and coolers are in this case needed. With circulating liquids, flows can be increased efficiently compared to increasing the flow from air compressors and fans that have larger energy consumption. Hence, more uniform temperature profiles can be expected on both reformer and fuel cell stack compared to systems using air cooling. Amongst others, Dudfield et al. [31] present an example of a reformer system using a thermal oil.

An example of a prototype reformer design for a liquid thermal oil system is presented in Fig. 21.3. In this case the reformer is designed as a cylindrical reactor with internal pipes containing catalyst material resembling a shell-and-tube heat exchanger. The methanol fuel

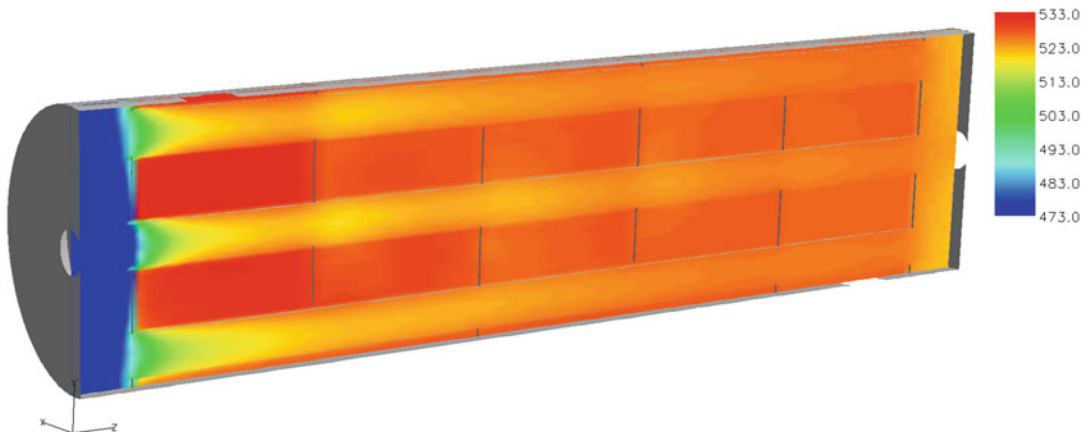


Fig. 21.3 Oil heated methanol reformer for 5 kW HTPEM fuel cell system. Temperature in the reactor center plane. Oil inlet temperature: 533 K. Methanol water mixture inlet temperature: 473 K

mixture flows in the tubes and thermal oil on the shell side provides heat for the reforming reactions. Figure 21.3 shows a cross section of the reactor temperature distribution in the center plane based on a detailed computational fluid dynamics analysis. The left cold part of the reformer is the fuel inlet manifold, not surrounded by the thermal oil, therefore at a lower temperature than the reformer itself. Simulations such as this are important tools in identifying possible shortcomings of reformer designs and identification of possible features that could benefit system design and control. Reformer reactor designs and operation conditions can be studied in detailed before the reactor is manufactured leading to significantly faster product development.

One desired feature to introduce to system control could be the possibility of changing output gas composition by shaping the temperature

profile of the reactor. The output gas composition is highly dependent on temperature and proper knowledge of reformer behavior could enable more intelligent control of the entire system to possibly decrease CO concentration in different system operating states or during transients, and hereby optimize performance and lifetime of the systems.

There are several system heat integration topologies using thermal oils such as Duratherm [32], Paratherm [33], and similar as heat transfer fluid. Two examples will be shown here, a parallel and serial topology. First, an example of a parallel system configuration is shown in Fig. 21.4.

The parallel system configuration shows two thermal oil subsystems, a low temperature (160–180 °C) and a high temperature (300 °C) subsystem. The low temperature subsystem includes the fuel cell stack, the evaporator for

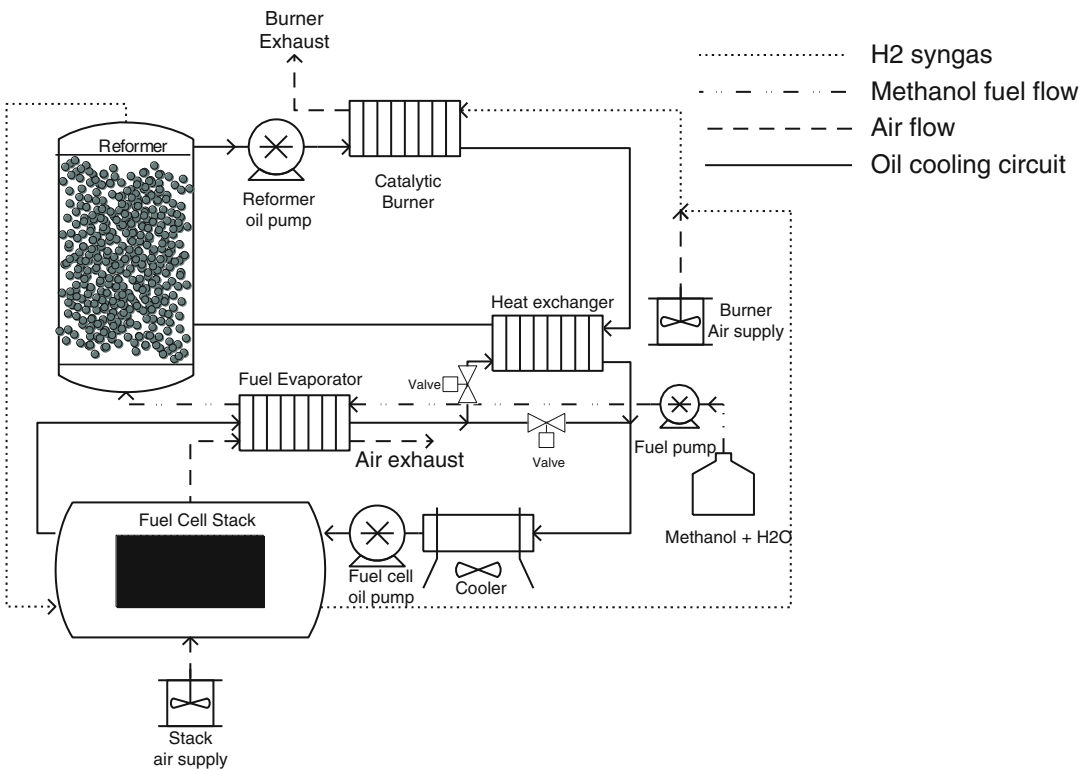


Fig. 21.4 Parallel thermal network example, liquid heat transfer using thermal oil. Two thermal subsystems, one with high temperatures (280–300 °C) including the

reformer and one with low temperatures including the fuel cell stack (160–180 °C)

the fuel water mixture, and a convective cooler with a fan. In the presented case, the evaporator receives heat from the cathode exhaust and the fuel burner. The high temperature subsystem includes the methanol reformer, a heat exchanger for extracting excess heat from the fuel burner, which runs of the unused fuel exiting the fuel cell stack anode. In start-up mode, the fuel burner runs of the methanol/water mixture assisted by a few electrical heaters for the initial start of the burner in case of low temperatures. The heat generated is transferred to the two subsystems, and preheats the fuel cell stack and the reformer before the systems are ready to deliver power. With individual pumps in each oil circuit, efficiency can be maximized by adjusting pump flow according to the particular state that the system is in or adjusting it according to the load on the system. One of the challenges when using reformer systems is during reductions in the load on the fuel cell stack. In such cases, fuel delivery must closely follow the reduction in power delivery from the fuel cell stack; otherwise the burner can experience a sudden temperature increase due to the increase in residual

hydrogen in the anode exhaust leading to a sudden increase in the heating value of the gas entering the burner. Such sudden changes could result in failure of the burner and possible meltdown due to extreme temperatures. For this reason a cooler is mounted to enable the possibility of reducing too high inlet temperatures during thermal transients, and for safe shut down of the system. Because the burner is the main source of heat, this is also the active part when starting up the system. The most efficient way of heating the system would be to combust fuel during start-up. As the oil in the high temperature circuit heats, the low temperature oil circuit can be bypassed through a heat exchanger for preheating the fuel cell stack. Start-up time of fuel cell stacks is a continuous focus point of high temperature fuel cell systems [34–38].

In order to simplify system design a serial thermal connection can be designed using a single pump, and an oil subsystem with several temperature levels. An example of such a system design is presented in Fig. 21.5.

The oil flow exiting the fuel burner represents the highest temperature, cooling the oil slightly

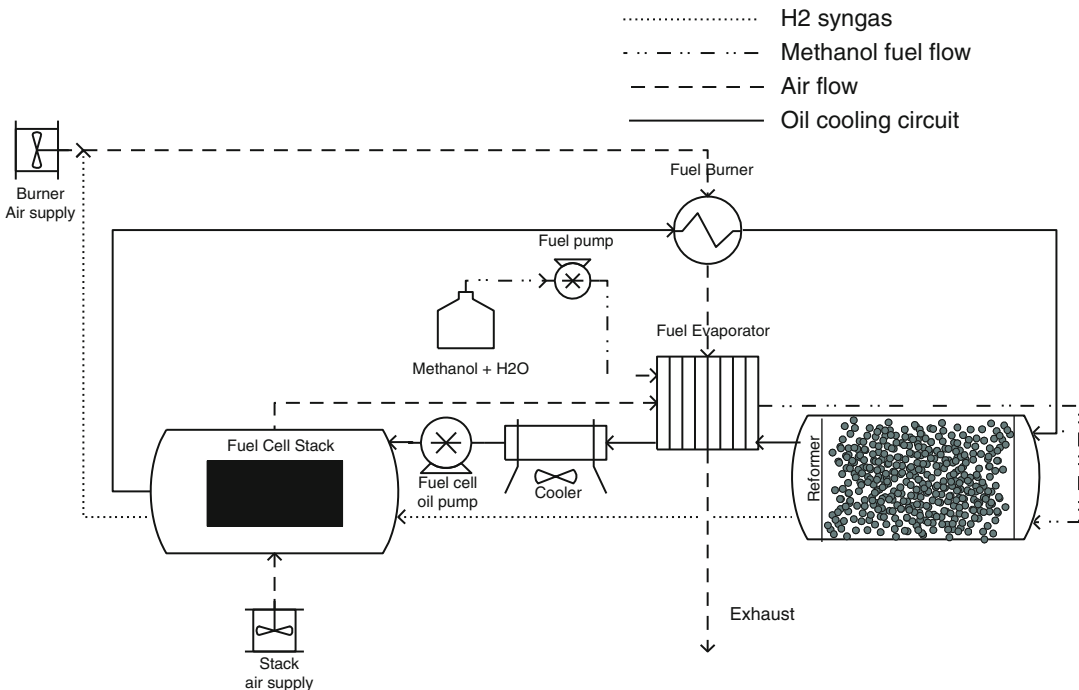


Fig. 21.5 Serial thermal network example, liquid heat transfer using thermal oil

as it transfers heat to the reformer. The main cooling under normal operation is in the fuel evaporator, where the oil needs to be cooled to around stack temperature. In case of temperature transients and critically high temperatures a cooler can be inserted enabling more control of the oil temperature. During start-up the fuel burner will initially be heated by a small amount of electrical energy, once switching to the combustion of the methanol fuel mixture, the components in the system will gradually heat. Thermal management of such a system is complex, and many of the components are able to affect the oil temperature. The components that can be directly controlled are the fuel burner, where air supply can be used to control temperature, the cooler, where an air fan can adjust the heat removal, and the fuel pump, which can change temperature profiles throughout the system.

Other thermal topologies within each of the proposed cases are also possible, and in case of further use for heat, heat exchangers can easily be added. Other more exotic cooling strategies are examined [39–41], but the objectives still remain, good temperature distribution, low parasitic losses, and good heat transfer.

21.5 Hydrogen vs. Reformer Systems

Pure hydrogen-based, and reformer-based systems have each their advantages and disadvantages. Hydrogen systems offer high electrical stack efficiencies, due to the absence of impurities and diluents, show the simplest system design, with low components count, and low parasitic losses. They have the possibility of dead-end operation because build-up of excess water is not an issue as it sometimes is in Nafion-based systems. The reformer-based systems on the other hand have the possibility of a higher degree of fuel flexibility, but at the cost of higher system complexity, introducing more components, and increasing the importance of predicting gas composition and stack performance. Dependence on CO concentration and

the dilution effect of CO₂ can induce significant changes in performance. Figure 21.6 shows a series of polarization curves of a single cell BASF PBI MEA, where various concentrations of CO and CO₂ in hydrogen is examined. Performance clearly diminishes with increasing CO concentrations, and the dilution effects of CO₂ are also visible.

The plot shows the immediate effects of CO over a few hours of operation, other than affecting this immediate performance, CO also has effects of the degradation of the MEA particularly at high concentrations. Modifications to the MEAs can often improve the performance of the increased degradation when running with impurities and higher temperatures [42]. Besides the immediate effects of CO poisoning visible on the polarization curve, the AC impedance is also affected. Figure 21.7 shows the impedance of single cell performance under different syngas compositions.

This effectively means that variations in gas composition affect not only the steady-state performance of the fuel cell, but also the transient electrical characteristics. Upon closer analysis it is clear that CO primarily changes the low frequency behavior of the fuel cell, resulting in a more sluggish electrical behavior at high CO concentrations. In order to compensate for the decreased voltage performance of the fuel cells when running with CO in the anode, the stack temperature can be elevated, which effectively increases the rate of CO kinetics and regains parts of the lost performance however at the expense of increased degradation by other mechanisms. Figure 21.8 shows polarization curves based on the semi-empirical model of Korsgaard et al. [43], comparing the performance between operation at 160 and 180 °C at different CO concentrations.

In order to show the significant influence, CO concentrations up to 50,000 ppm are shown. Increasing temperatures by 20 °C significantly improves the performance of the fuel cell.

Not only CO and CO₂ cause performance changes when using reformer systems, the exact influence from the presence of increased water content and possible membrane hydration is not

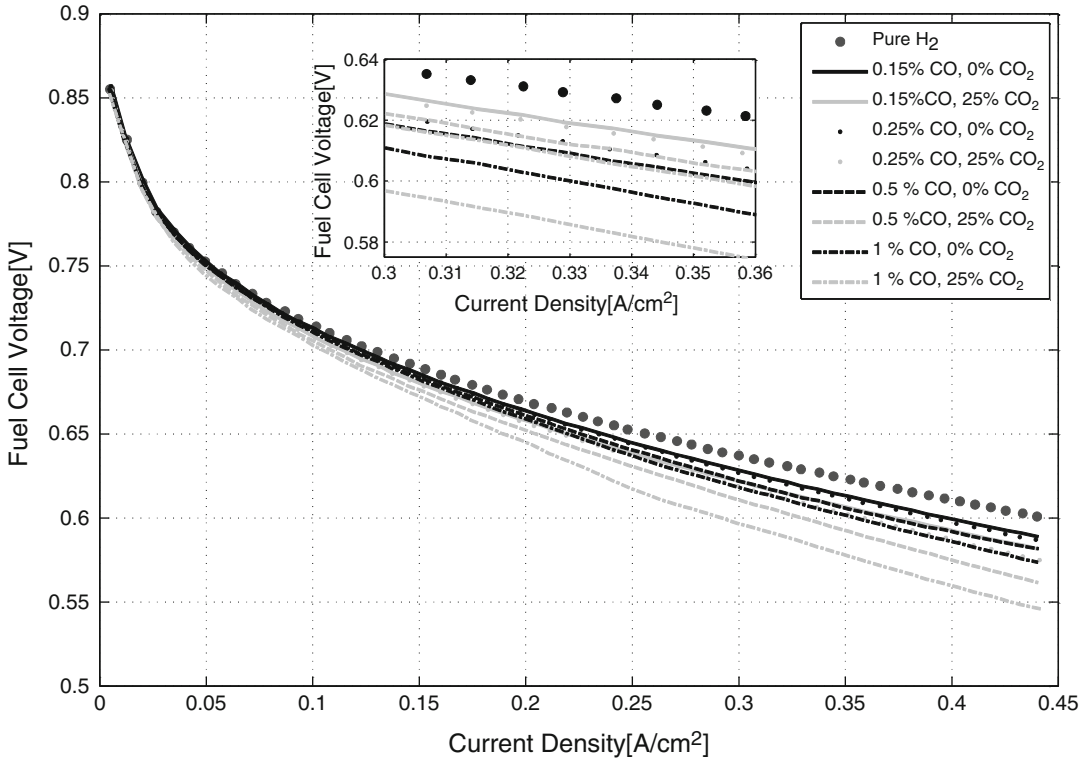


Fig. 21.6 Polarization curve on a 45 cm² single cell at 160 °C with different gas concentrations. Reproduced from [13] with permission Elsevier

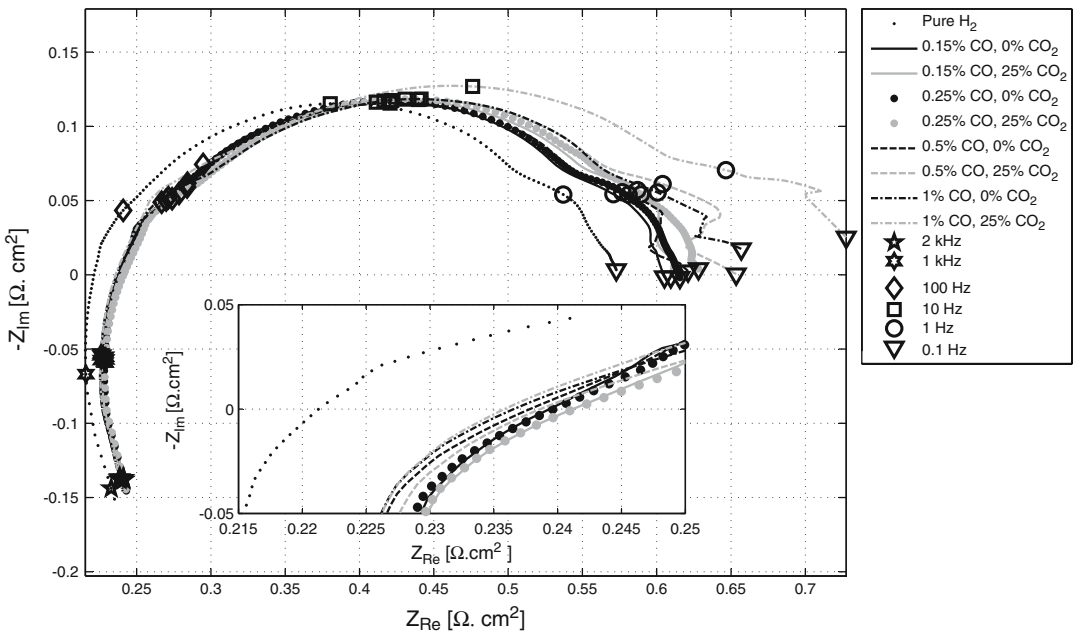


Fig. 21.7 Impedance plot of single cell performance on different syngas concentrations at 160 °C. Reproduced from [13] with permission of Elsevier

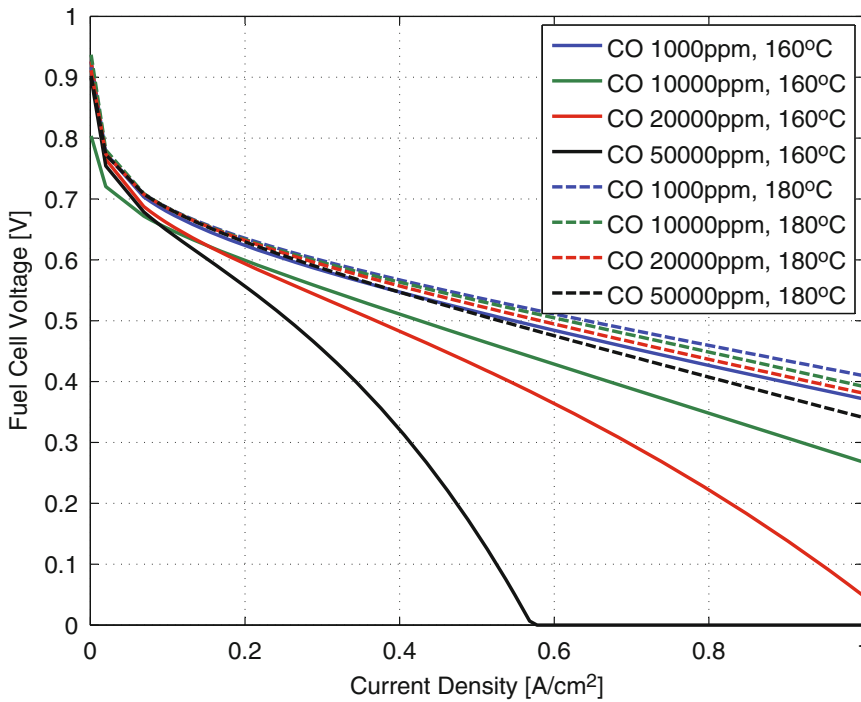


Fig. 21.8 Polarization curve of BASF HTPEM Celtec MEA at different temperatures and different CO concentrations [44]

fully understood. Several authors have examined the topic in recent studies [45–49]. Furthermore the effect of accumulated water in a system can affect the start-up time due to the additional requirement of water evaporation before start-up temperatures can be achieved.

Systems using HTPEM fuel cells and methanol reformers offer a solution where the electrical efficiency often is smaller than that of pure hydrogen-based HTPEM fuel cell systems, but there are still possibilities of improving many different aspects of these technologies, to increase performance, and the potentials could be to improve the total system efficiency beyond that of the pure hydrogen-based HTPEM systems. A large amount of heat is needed to evaporate the water/fuel mixture, which is often running at steam-to-carbon ratios of down to 1.5. Further increases in system efficiency could be achieved by lowering the amount of water and hereby the needed for additional energy for evaporation. Figure 21.9 explores the potential by comparing an ideal reformer system where

reforming temperature corresponds to the stack temperature, the steam-to-carbon ratio is 1, and no CO is present in the produced hydrogen. In such a case the waste heat is not only usable to evaporate the water/fuel mixture, but could potentially also be used as heat input to the reformer.

Such low temperature methods and catalysts are examined and show promising results [50–54]. Further details analyzing Balance-of-Plant power consumption of such system is needed as well as a thorough understanding of the feasibility from an engineering point of view is needed in order to evaluate the true potential of such a solution however it still indicates the potential of such systems.

21.6 Control of HTPEM FC Systems

In order to fully utilize the benefits of fuel cell systems and the power they deliver, and ensure stable reliable operation, proper control during

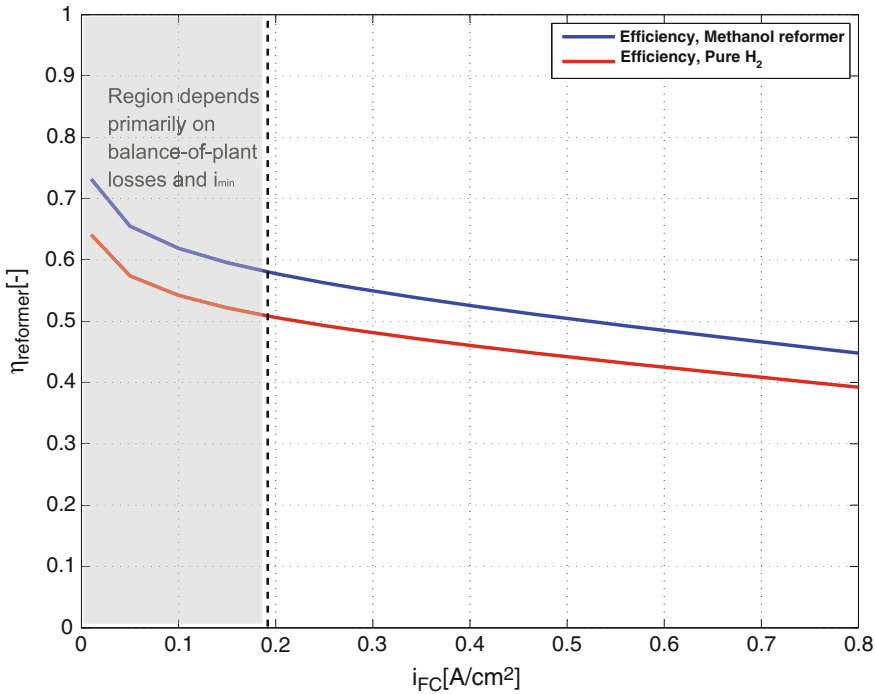


Fig. 21.9 System efficiency of fuel cell stack reforming at stack temperature and running on pure hydrogen, respectively [44]

the different operating regimes and lifetime of the fuel cell systems is critical. Fuel cell systems are highly nonlinear and complex and therefore often a challenging control task, especially if adaptability to changing ambient conditions and varying load profiles are of importance. The different operating regimes of fuel cell systems include:

- System start-up
- Power delivery
- System shutdown

In each of such operating regimes control plays an important part for ensuring long lifetime, safe operation, and optimized performance. In the following sections each of these regimes will be addressed, and examples of critical issues to address will be brought forth.

21.6.1 System Start-Up State

High Temperature PEM fuel cells use the proton conducting capabilities of phosphoric acid in order to conduct protons, as opposed to water-based PEM FCs, this allows operation above 100 °C with the increased boiling point of phosphoric acid. Although the increased temperatures offer faster kinetics and a much higher tolerance to pollutants, there is still a risk of acid leaching due to various mechanisms, one of which could occur during start-up of these systems if, for example, liquid water is produced. For this reason it is often important to preheat HTPEM FCs before drawing current [34, 36, 55]. This is in any case needed because fuel cells perform poorly at low temperatures. Figure 21.10 shows a comparison of the performance of a 45 cm² BASF Celtec-P MEA on pure hydrogen at different temperatures.

In the shown example a difference in voltage of 100 mV at the same current but different

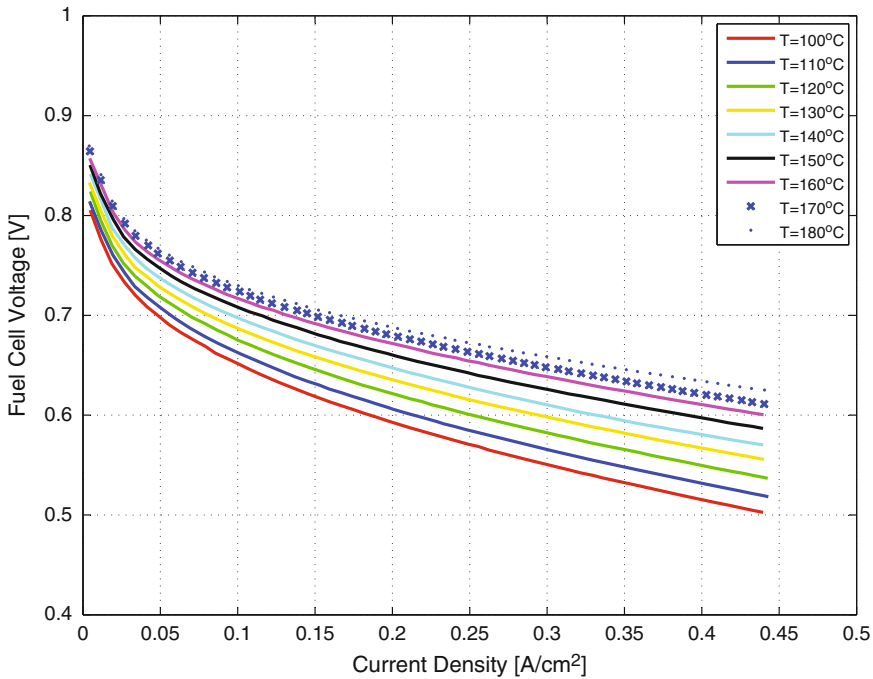


Fig. 21.10 Polarization curve using pure hydrogen at different temperatures [56]

temperatures can be observed, which is one of the reasons why reaching the correct temperatures before drawing high currents is important. Little knowledge of low temperature operations impact on lifetime exists. Although tendencies indicate that lower temperatures in the range of 140–150 °C increases lifetime, no one has examined how temperature below that will affect lifetime. Low temperature operating capabilities differ between MEA types and is an area only a few authors have explored.

21.6.1.1 Electrical Heating

Preheating of fuel cell stacks can be done in many ways, often the challenge is not only ensuring a certain temperature above 100 °C before drawing a current, but optimizing start-up speed and avoiding potentially harmful temperature overshoots while heating is also important. Figure 21.11 shows, for a particular system, how electrical input power affects fuel cell stack heating time.

Of course the challenge is not only achieving fast enough heating time, but just as much ensuring efficient heat. The use of direct electrical heating is often not a good idea, when also accounting for the additional power production need for recovering this used electricity and ensuring the availability of it in a system upon shutdown, such that the next start-up of the system is also possible.

21.6.1.2 Methanol Combustion Heating

The power required for preheating is also of significant importance. The energy used to heat a system should always be taken into account when calculating the efficiency and energy use of a fuel cell system. This means that the use of electrical heating often leads to a poor round-trip efficiency because the fuel cell system needs to produce the energy spent during preheating before a net power production is achieved. Furthermore electrical systems must take into account the extra electrical energy storage needed for enabling start-up which is both costly,

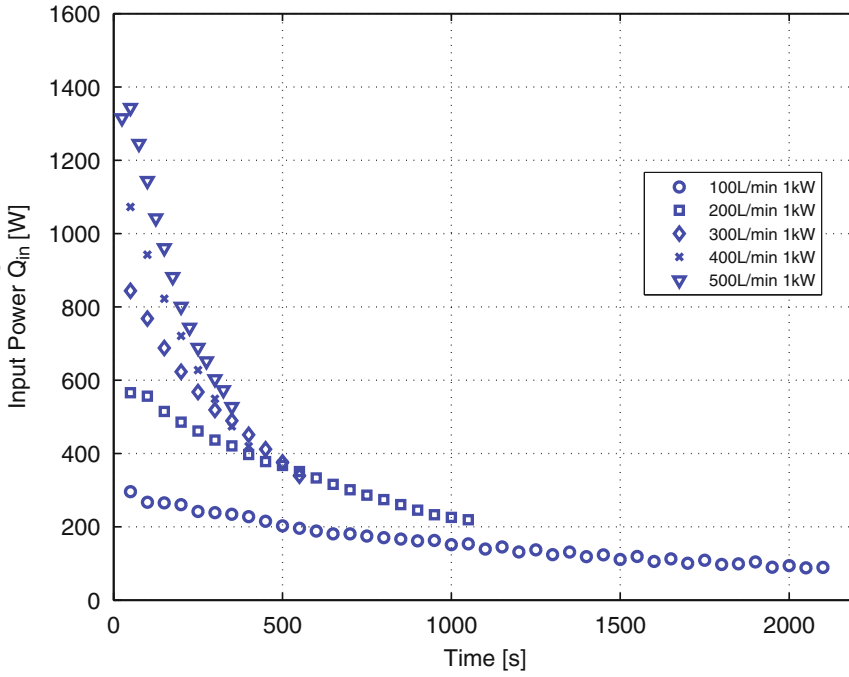


Fig. 21.11 Input power as a function of heating time at different cathode air flows at electrically preheated 1 kW cathode air cooled fuel cell stack. Reproduced from [34] with permission of Elsevier

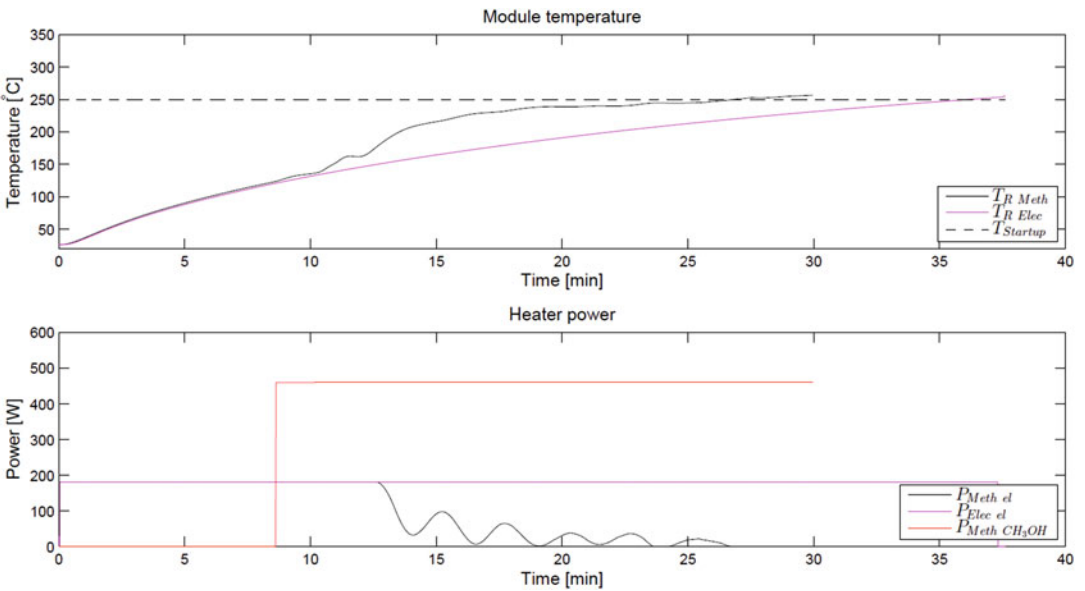


Fig. 21.12 Temperature development during heating of methanol reformer for H3-350 HTPEM FC system with and without methanol combustion

and often puts a significant additional load on a battery system during start-up because it not only needs to handle power consumption of the given application, but also the power requirements for starting up the fuel cell system. Figure 21.12 shows an example of the temperature development of a methanol reformer with an integrated burner for more efficient system start-up. In the shown example, T_{R_Meth} in the top plot is the temperature development in the reformer when a methanol/water mixture, with a steam-to-carbon ratio of 1.5, is added during start-up and T_{R_Elec} is the temperature development when pure electrical heating is used. The bottom plot shows the power added to the burner during the experiments. P_{Meth_el} is the electric power added during the experiment and $P_{Meth_CH_3OH}$ is the power added to the burner in the form of methanol during the same experiment. P_{Elec_el} is the electrical heating power during the pure electric experiment. Fuel with this steam-to-carbon ratio is used because it is available in the system already, eliminating the need for an extra tank.

From the figure it can be seen that the reformer reaches an operating point of 250 °C 10 min faster and at the cost of less electrical energy using methanol in the burner. The total energy consumption of a start-up is, however, larger during a methanol start-up due to the heating and evaporation of the water in the fuel and the heating of the burner's process air flow. But as the reduction in electric energy consumption means that the module achieves positive energy production more rapidly and increases the roundtrip efficiency, it is still considered a good idea.

The shown start-up example did not include an optimization or exploration of optimizing the start-up time. But several parameters can be adjusted to affect the dynamic characteristics of the initial preheating process of the reformer in question: fuel flow, air-to-fuel ratio, oxidant supply control, and steam-to-carbon ratio.

Start-up of an entire fuel cell reformer system could also be divided into different phases in order to decrease start-up time, by, for example,

starting to deliver a small amount of fuel cell stack power at 80 °C. This will often decrease heating time because the power production and losses, which are occurring on the MEAs themselves, are often more efficient than indirect heating by external heating elements, liquid heat transfer, or similar.

21.6.2 Power Delivery State

Upon proper system heating, and introduction of anode and cathode species, the fuel cell voltage will start rising to open circuit potential, and power can be drawn from the system. OCV operation of HTPEM fuel cells involves high potentials and as carbon corrosion is severely increased at high temperatures a certain amount of load is therefore recommendable to avoid these increased losses. One strategy is to use an external dump load, and waste the electrical energy, but a better option is to dissipate the energy in the systems electric heaters to keep the system heated. One of the challenges of operating at low power for systems like this is the required heat to keep the system at full operating temperature. Another solution could be to use part of the fuel cell power to supply power for the balance of plant, keeping system components powered. In any case both would be required in order to avoid prolonged exposure to the high potentials of OCV operation or possibly the need to shut down due to the system not being able to sustain the temperatures required for operation. Typically the regimes of operation can be defined, as the example shown in Fig. 21.13.

At low currents the fuel cell stack is typically very efficient, but at too high efficiencies stack temperature can drop and lower performance and eventually require system shutdown. In the same region of operation, there will be a point at which the fuel cell system components, the Balance-of-Plant, are using more power than the system is actually producing, at some point it would be a better solution to shut down the system and wait

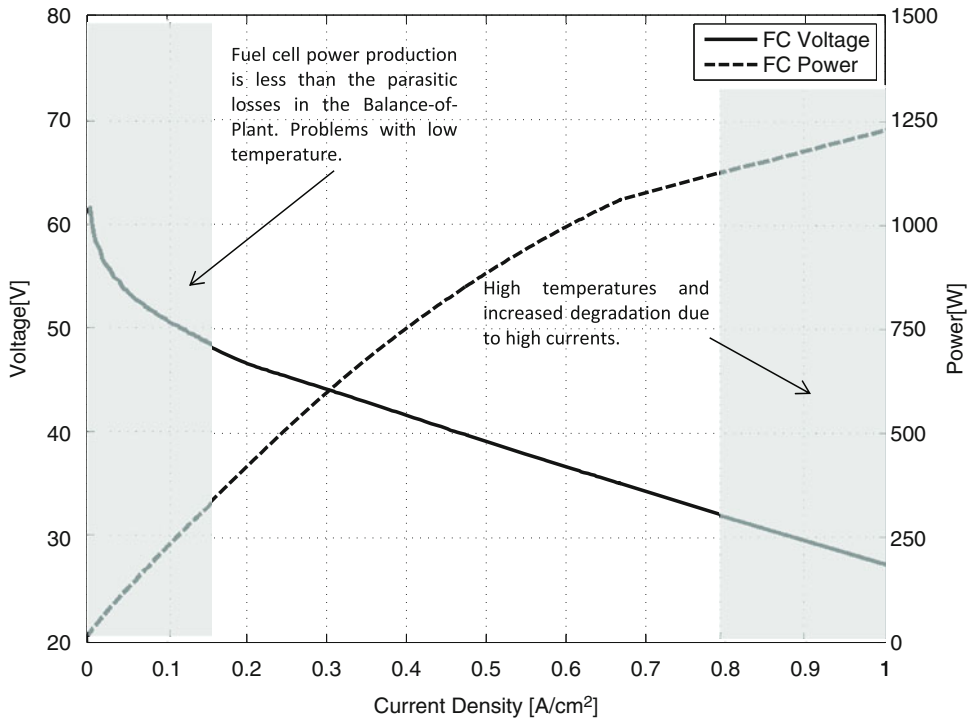


Fig. 21.13 Illustration on polarization and power curve of the problematic regions of operation from a system point of view

for a situation to enable it where more power is needed. Alternatively, and depending on the application the system could be put into a standby mode ensuring that it is always ready to deliver power when needed. In the other extreme, there is a certain limit as to how high currents are advisable to draw from the system. The subsystem cooling the fuel cell stack needs to be able to handle the high losses at these operating points, and in a similar way, for reformer systems, the required heat needs to be added to the reforming reaction in order to keep the correct reformer temperature. The fuel evaporator could also lose some of its heating abilities at very high flow, moving some of the superheating of the evaporated fuel into the reformer, requiring even more heat. The reformer catalyst volume will also at particularly high loads have problems converting the fuel, and the amount of unconverted fuel in the anode inlet of the stack.

21.6.2.1 Output Power Control

Proper control of the output current and power of the systems are one of the key areas in ensuring long and reliable lifetime. A DC/DC converter on the fuel cell output is a critical component when it comes to limiting the output current of the fuel cell stack, hereby protecting it from some of the mentioned undesired operating conditions. Figure 21.14 shows a typical configuration of a hybrid electrical system, where the fuel cell is charging the battery pack on-the-fly. As long as the available fuel cell power covers more than the average power consumption drawn from the battery pack, the system will see significant increase in run-time at a fairly low cost per kWh because of the low investment cost in additional fuel tank versus adding more batteries.

Using the fuel cell DC/DC converter it is possible to introduce current limits avoiding too low or too high currents, but more importantly, when working with reformer systems, limits to

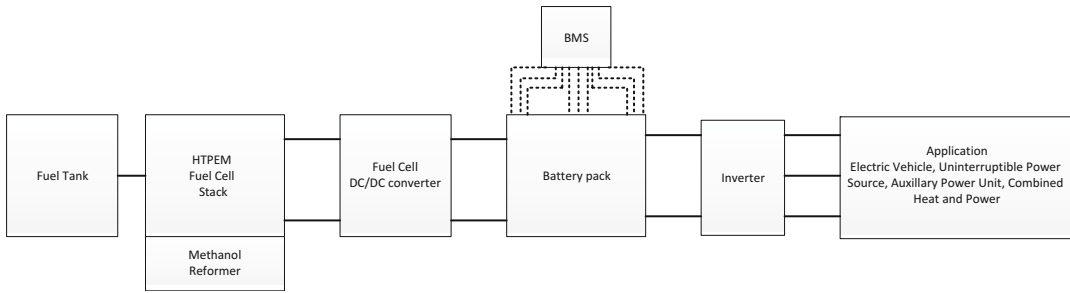


Fig. 21.14 Example of fuel cell reformer system hybrid electric power system

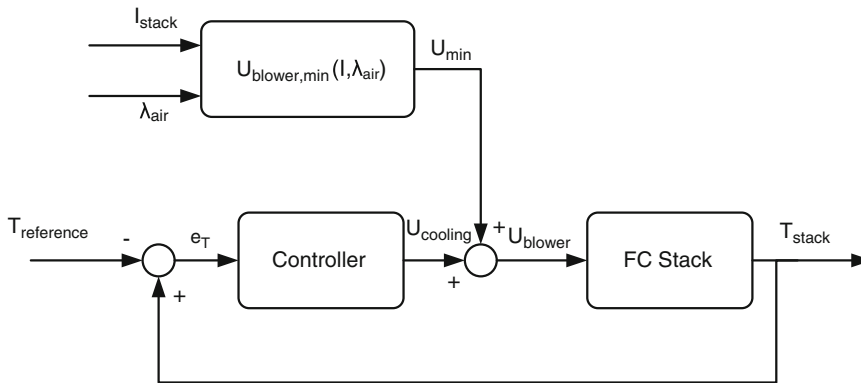


Fig. 21.15 Control structure for control of cathode air cooled HTPEM fuel cell stack. Reproduced from [57] with permission of Elsevier

how fast load transitions can be made, i.e., current ramp limitations. Hard restrictions on the current through the DC/DC converter will diminish the load following capabilities of the fuel cell system, but on the other hand, this can in turn lead to more stable system operation, ensuring that the system receives the right amount of fuel, avoiding critical starvation and high burner temperatures. In the case of the fuel cell system acting as a battery charger, the DC/DC converter simply has a preprogrammed charging curve, depending on the particular type of battery, and chemistry. This ensures safe operation by starting the charging at, for example, a certain threshold voltage or state-of-charge, and stopping the system again upon going through a full charge cycle.

21.6.2.2 System Temperature Control

The type of temperature control used in a fuel cell system depends on the type of fuel cell in the system. If the fuel cell is cathode air cooled, the blower which also supplies the cathode process air flow is used to cool the fuel cell stack. In such a control structure, it is important to include a blower model which can predict a minimum blower set point to ensure that a certain minimum stoichiometry is respected at all times. Figure 21.15 shows a diagram of such a control system.

The controller in such a system can be any kind of controller, e.g., a PI, PID, PID with a feed forward term, or any advanced control structure.

When performing temperature control it is important to have good and reliable temperature measurements. It is also important to be aware that temperature gradients might exist in the fuel cell, meaning that the temperature locally might

be higher or lower than the measured temperature, which could damage the fuel cell. This problem can be solved by using a temperature set point, which has a certain safety margin to critically high or low values. An alternative is to implement a thermal model of the fuel cell in the controller, in order to choose an appropriate temperature set point, for a given set of operating conditions. If several temperature measurements exists, the control variable for the controller can be chosen to be either an average of these, the highest or the most representative.

21.6.2.3 Control of Methanol Reformer Temperature

In a highly integrated system like the one in Fig. 21.5 it is important to have a stable and efficient temperature control, both in stationary and dynamic operation. The most difficult temperature to control is that of the reformer. This is because the heating power for the reformer is not

supplied directly, but through the burner, which is supplied with varying amounts of exhaust gas from the fuel cell anode.

One way of remedying this issue is to exploit the fact that thermal mass of the burner is much smaller than that of the reformer and use a cascade control structure. Figure 21.16 shows a diagram of such a control structure from [58]. Here the inner, faster, control loop controls the burner temperature by varying the air supply to the burner. The outer, slower, control loop controls the reformer temperature by changing the set point for the burner temperature.

The structure used for the two controllers can be any of those available in literature, such as PI, PID, PID with a feed forward term, or any advanced control structure. Another, simpler, control structure is to omit the inner burner temperature controller and use the outer controller to control the reformer temperature by varying the burner air supply.

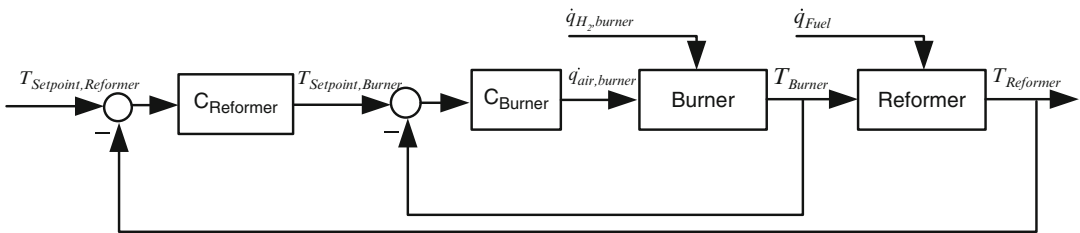


Fig. 21.16 Cascade control structure of reformer temperature. Reproduced from [58] with permission of Elsevier

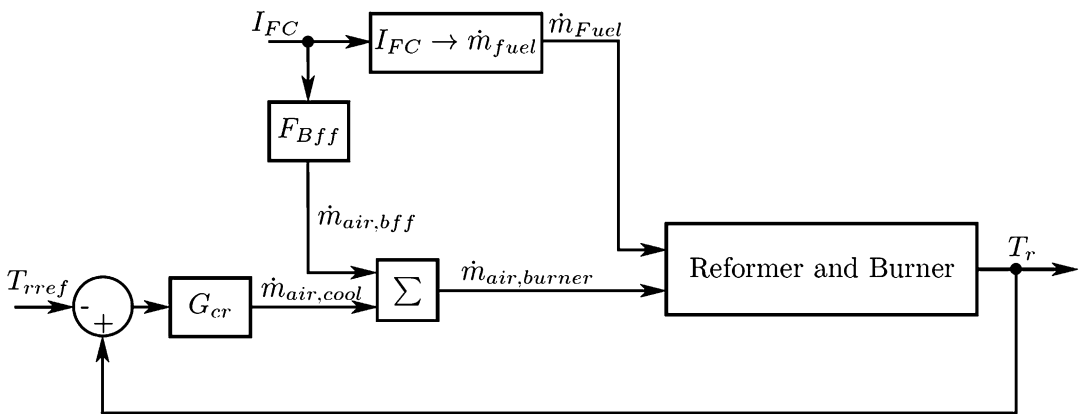


Fig. 21.17 Feed forward structure for a reformer temperature controller

As with the fuel cell temperature, the controller output which is necessary at a high output power is very different than that which is necessary at a low output power. It therefore makes sense to use a feed forward model necessary controller output in the controller for the reformer temperature. As the amount of fuel coming into the reformer and the burner relates to the current of the fuel cell, it makes sense to use the fuel cell current as the input to the feed forward model. Figure 21.17 shows a block diagram of a feed forward control structure, where the fuel cell current is passed into a feed forward model, F_{Dff} , which calculates an estimated necessary cooling mass flow. This mass flow is then summed with a correction from a controller to give the burner air mass flow.

The feed forward model can be made more advanced by adding other measurable inputs, such as the ambient air temperature and humidity, which affects the cooling power of the supplied air.

21.6.3 System Shutdown

As mentioned earlier in this chapter, HTPEM fuel cells are subject to severe carbon corrosion during open circuit operation. Therefore a shutdown strategy is necessary to avoid this during system shutdown.

One such strategy, which is used often, is to shut off the fuel supply for the fuel cell and draw a current from the cell until all the residual fuel in the cell is used. The current is typically drawn by a bleeder resistor, which can be connected to the terminals of the fuel cell stack. The fuel cell can then be cooled down to a temperature where carbon corrosion is not an issue.

When integrating a HTPEM fuel cell into a complex system, like a methanol reformer it can be advantageous or even necessary to implement more advanced control algorithms or models in the control systems. The next chapter describes some of the possible issues and a possible solution to them.

21.7 Advanced Control Strategies Using ANFIS Modelling

Control of different system states is manageable to a certain extent, as long as sensors can be placed to monitor the states in question, such as pressure, temperature, and humidity. Many internal states in fuel cell systems are, however, often not measured due to the available sensors being impractical either due to very high costs, or volumetric, weight or data acquisition constraints. If monitoring or measurements of such non-accessible states are required, either a modelling-based approach or an ex situ experimental characterization is the only possibility of predicting these states, and in turn controlling them. In high temperature PEM fuel cell systems using a reformer, some of the critical system states are CO concentration of the anode gas and the hydrogen mass flow into the fuel cell stack anode. The reason for calling them critical is that they both have a direct impact on stack lifetime and performance. Due to the complex dynamics of the fuel delivery system of a methanol reformer system, such as the ones shown in Figs. 21.1, 21.4, and 21.5, it is not trivial knowing how fast load changes can be allowed. The challenge is threefold; firstly, it is important to know exactly how long time passes before fuel is available in the anode when the fuel pump flow is increased. If the load on the fuel cell stack is changed too quickly, the fuel cell stack will experience anode starvation and the accelerated degradation related to this. Secondly, if the load is decreased too quickly, high amounts of hydrogen will be entering the fuel burner, which could lead to extreme temperatures and possible burner meltdown. Lastly, the varying reformer output composition, which is a function of space velocity, temperature, and fuel concentration, also makes the exact prediction of hydrogen content, and therefore anode stoichiometry, complex and this has a direct influence on the system efficiency, because excess fuel simply will be combusted in the burner. One approach to address these challenges is using Adaptive

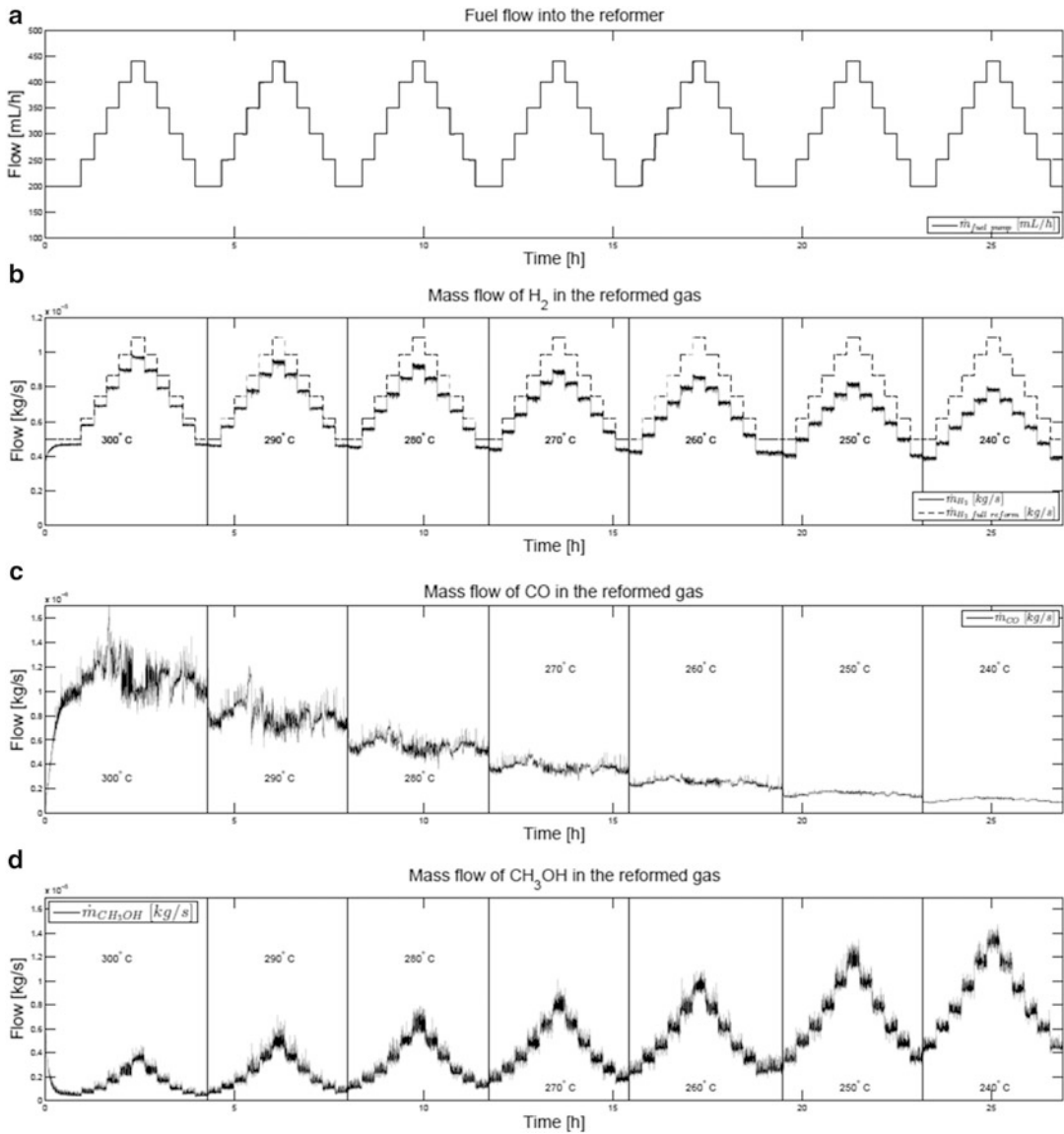


Fig. 21.18 Output reformer mass flows, fuel flow and reformer temperature from ex situ characterization tests on methanol reformer. Reproduced from [60] with permission of Elsevier

Neuro-Fuzzy Inference System models first described in [59] and used in [60, 61]. This approach has proven to be a powerful means of using detailed experimental characterization knowledge online for system control. The methodology has been tested on a Serenergy H3-350 methanol reformer HTPEM fuel cell system, and includes characterizing the steam reformer ex

situ in a dedicated setup [60], yielding a full performance map testing it in all relevant operating points. An example is shown in Fig. 21.18, where changes in concentrations are seen while going through different steps in pump flow and reformer temperature.

The shown measurement indicated the CO concentration increasing with increasing

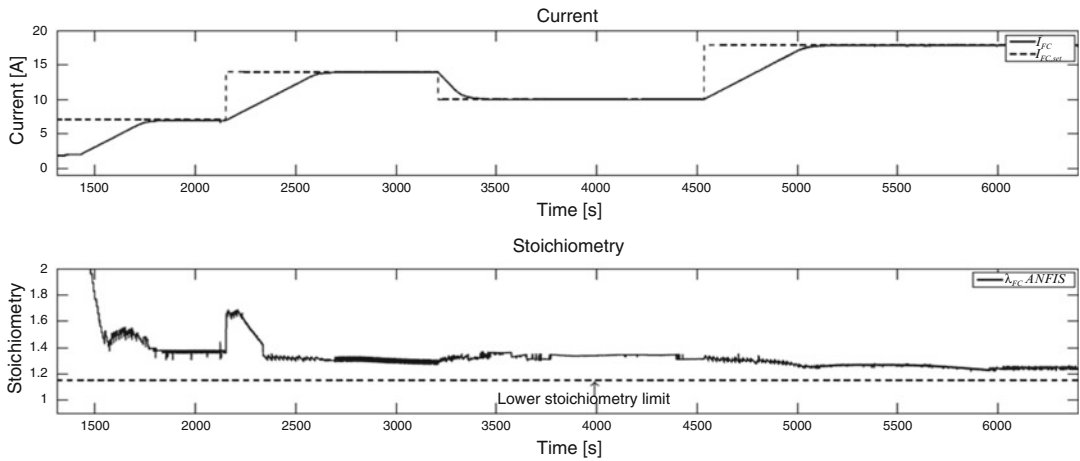


Fig. 21.19 Figure shows the predicted stoichiometry of implemented ANFIS model during load variations. Reproduced from [60] with permission of Elsevier

temperature, and the opposite occurring for residual methanol concentration. Based on such experimental data, an ANFIS model can be trained to behave as the experimental data. The model combines fuzzy logic with neural network theory to create a series of mathematical equations to predict the steady-state behavior of the reformer output composition depending on temperature and fuel flow [60].

The implementation of the model yields a possibility of monitoring the stoichiometry of the anode, as shown in Fig. 21.19 where the stoichiometry during a series of changes in fuel cell current is seen.

In the shown figure, it is clear that the stoichiometry is changing during the different operating points: This happens because the fuel flow is calculated based on the desired fuel cell current using a linear relation and assuming a full reforming of the fuel. This calculation is usually done by calculating the necessary hydrogen production according to (21.5), where $\dot{m}_{\text{H}_2, \text{FC}}$ is the needed hydrogen flow, λ is the wanted stoichiometry, N_{cell} is the number of cells in the fuel cell, and F is Faradays constant.

$$\dot{n}_{\text{H}_2} \left[\frac{\text{mol}}{\text{s}} \right] = \frac{\lambda \cdot N_{\text{cell}}}{2 \cdot F \left[\frac{\text{C}}{\text{mol}} \right]} \cdot i_{\text{FC}} \left[\frac{\text{C}}{\text{s}} \right] \quad (21.5)$$

From the steam reforming reaction it is known

that 1 mol of methanol yields 3 mol of hydrogen. The necessary methanol flow into the module then calculated according to (21.6).

$$\dot{n}_{\text{CH}_3\text{OH}} \left[\frac{\text{mol}}{\text{s}} \right] = \frac{\lambda \cdot N_{\text{cell}}}{6 \cdot F \left[\frac{\text{C}}{\text{mol}} \right]} \cdot i_{\text{FC}} \left[\frac{\text{C}}{\text{s}} \right] \quad (21.6)$$

Using a model-based approach with, for example, an ANFIS model that predicts the hydrogen production under a given set of conditions and the stoichiometry can then be controlled more precisely.

Another way of using such advanced models is to examine the dynamics of the system and including it in the control structure. Often reformer systems, and fuel cell systems in general, are used in hybrid electric systems, because they are good candidates as range extenders, providing cheap energy compared to expanding battery capacity, because increasing tank size on a reformer system is much more cost effective compared to adding additional batteries. By detailed analysis of optimizing the balance between battery and fuel cell power it is possible to find optimized solutions, to specific applications. One of the disadvantages of increasing system complexity by adding reformers is the added thermal dynamics of increased masses, pipe volumes, etc. adding to the dynamic behavior of the system, thus

affecting the fuel cells load following capabilities. One typical method for handling such delays, and ensuring safe system operation, is to put a rate limiter on the current set point for the fuel cell stack. This requires a DC/DC converter able to control the output power from the fuel cell stack, which in many cases is available. A current ramp limitation would typically allow the stack to change load point in a matter of, for example, 30 s instead of instantaneously, but in order to reintroduce load following capabilities detailed knowledge is needed on the dynamics of the system.

21.8 HTPEM Fuel Cell System Diagnostics

The commercial success of not only HTPEM fuel cells, but fuel cell systems in general depends on their performance, reliability, durability, and competitiveness compared to other power generation devices. A large part of this can be improved by advanced state-of-health monitoring and the ability of diagnosing problems before they occur. With the implementation of such features, the systems can be protected from additional destructive operation due to failures in, for example, the fuel cell stack, in system components and in sensors. If a failing fuel cell stack or other system components can be replaced during already planned maintenance

visits, operating costs could be reduced and system on-time increased by avoiding system breakdown, damage of other system components and un-planned service visits. Figure 21.20 shows some of the primary components of a HTPEM fuel cell system, and the usual monitored states. Of the many methods existing, a lot of focus has been on diagnostic issues and state-of-health of the fuel cell stack as one of the more critical components of the system.

Several diagnostic methods exist that are able to monitor the performance of, for example, the fuel cell stack, and possibly conduct an in situ diagnostic method able to characterize and isolate the particular error, and implement a proper mitigation strategy for compensating for the problem, or safely shut down the system. Some of the more common practice diagnostic methods for analyzing stack behavior are

- U, I characterization, open circuit voltage, polarization curves
- Performance degradation over time
- Electrochemical Impedance Spectroscopy (EIS)
- Chronoamperometry, current interruption (CI)
- Total harmonic distortion analysis (THDA)

Measuring the voltage and current of a fuel cell is one of the most used characterization tools for benchmarking the performance of a fuel cell.

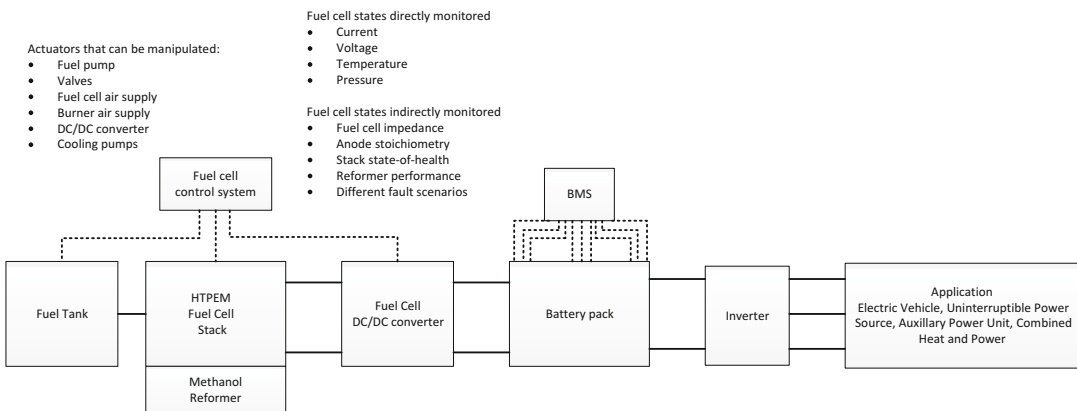


Fig. 21.20 Typical configuration of an electric hybrid system using a HTPEM fuel cell

Polarization curves further detail such measurements by including the current dependence on the voltage performance of the fuel cell by examining the voltage at different steady-state currents, different temperatures, etc. Figure 21.10 shows a set of polarization curves made on a 45 cm² BASF MEA. The fuel cell dependence on temperature is visible, showing increasing performance with increasing temperatures.

On running systems, polarization curves can be constructed by making a controlled slowly ramped current ensuring the system is in a pseudo-steady state. This is only possible in systems where fuel cell stacks output power is conditioned using a DC/DC converter or other power electronic component, and where the system shortly is allowed to conduct such a diagnostic routine. In hybrid electric system this is often easy because the fuel cell power is used to charge a battery pack and the output power can briefly be manipulated. In applications where the fuel cell power is dominating and the power directly needed a better approach is to look at the voltage

as a function of current for a short amount of time where a partial polarization curve often can be evaluated.

In order to capture the dynamic nature, and electrical characteristics of a fuel cell, methods like chronoamperometry or current interruption techniques are an option. The method is able to separate the contributions of ohmic and non-ohmic processes and capture the dynamic voltage response during a few steps in the current. A generic plot of the expected voltage and corresponding current step signal is shown in Fig. 21.21.

The dynamic electrical response of the fuel cell could include information on temperature, gas quality, degradation state, etc. and the method can be implemented using simple resistors and switches. Using steps to characterize and diagnose certain anomalous behavior is a common system identification tool and can also be applied to other aspects of examining HTPEM fuel cell system behavior. Figure 21.22 shows an example in a HTPEM fuel cell system, measuring on a HTPEM short stack, where a step is induced in the anode fuel stoichiometry, the response on the fuel cell voltage can be registered and depending on the stack state-of-health or the status and quality of the anode fuel supply system, it could be possible to determine certain errors in a system or adjust various system parameters to mitigate the potential problems. In a similar way many other fuel cell system components can also be manipulated and be part of a larger system diagnostic procedure in order to identify or isolate certain system faults.

Electrochemical impedance spectroscopy (EIS) has been used extensively to characterize HTPEM fuel cells [13], and also stacks [62, 63], in order to increase the understanding of the different mechanisms occurring within the fuel cell and have a means for quantifying the changes occurring. Often the results of EIS are evaluated in the frequency domain, analyzing Nyquist plots and bode diagrams, looking at the changes occurring over the entire range of frequencies. Equivalent electrical circuits are often used to fit models representing the electrical behavior of the fuel cell using different

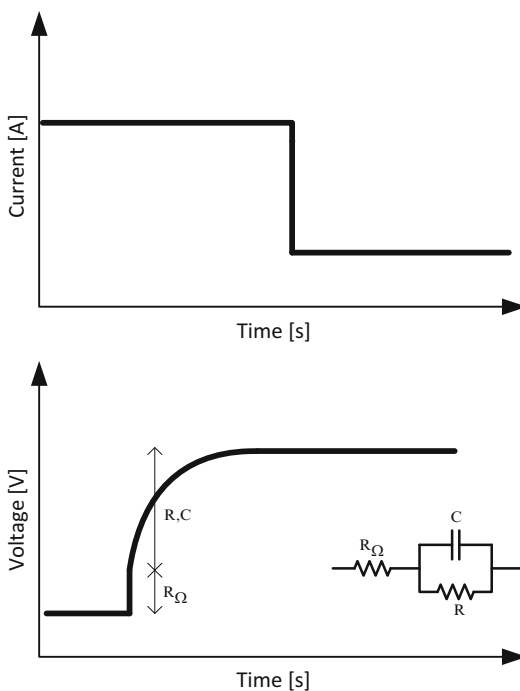


Fig. 21.21 Fuel cell voltage response during current step

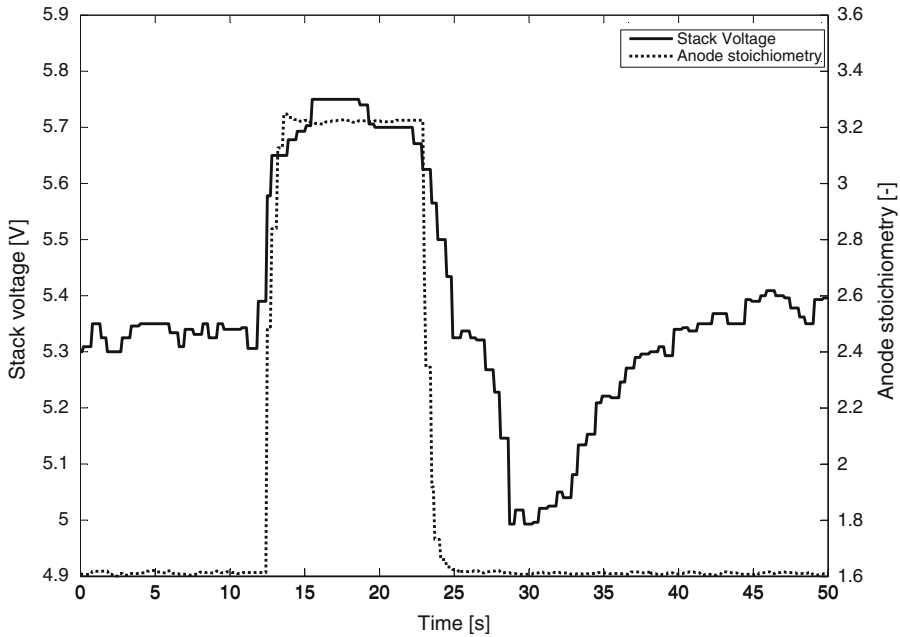
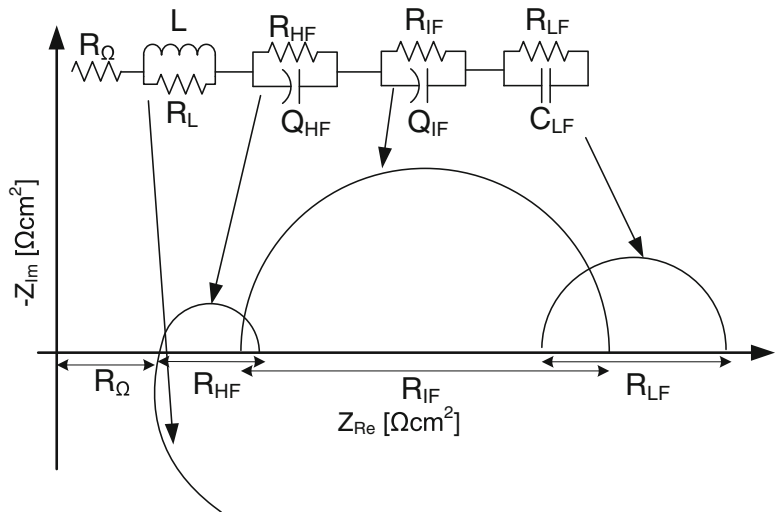


Fig. 21.22 HTPEM short stack voltage response to a step in the anode stoichiometry

Fig. 21.23 Example of impedance spectrum for the shown equivalent electrical circuit. Reproduced from [13] with permission of Elsevier



networks of resistors, capacitors, inductors, and more exotic elements such as constant phase, Warburg elements and similar (An example can be found in Fig. 21.23).

Examples exist of, for example, using EIS as a monitoring tool for the activation of HTPEM fuel cells [64–66]. Using a single frequency also

provides a good tool for quantify stability and the difference between the use of, for example, different types of bipolar plate material. In this case, two phenolic resins, a surface treated graphite material and a gold plated stainless steel plate. In this case only the 1 kHz frequency was monitored and proved as a good tool for

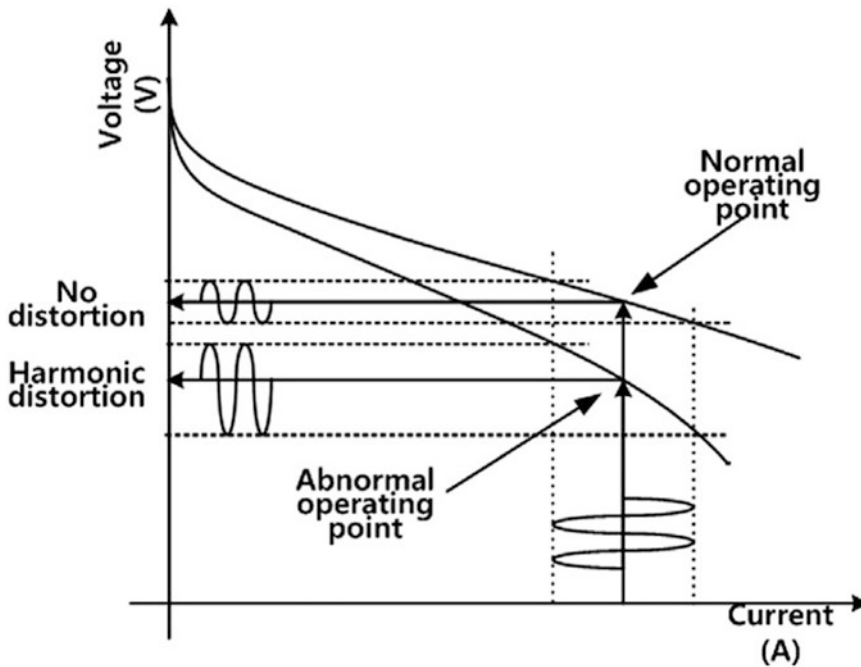


Fig. 21.24 Example of current and voltage behavior on polarization curve in different situations. Reproduced from [67] with permission of Elsevier

characterizing the differences in the performance of the plate material. Although EIS is a somewhat more complicated measurement technique, the use of it online in systems could be an interesting tool that in some cases possibly could quantify the propagation of certain fault scenarios or be part of isolating a particular error occurring.

Total harmonic distortion is another diagnostic tool usable in situ, the general method includes superimposing a load current with a harmonic content and afterwards analyzing the total harmonic distortion of the fuel cell voltage. Used in HTPEM fuel cell diagnostics, it is possible to, for example, identify anode and cathode starvation that is distinguishable using total harmonic distortion analysis (THDA) (Example of method is visualized in Fig. 21.24) [67].

Fuel starvation in HTPEM fuel cells is a critical stressor which should be avoided at any cost due to the increased carbon corrosion of the cells under such conditions.

21.9 Applying Diagnostic Procedures

Many diagnostic methods exist, involving either manipulating the current or voltage delivered from the stack, introducing specialized power electronics circuits, either added to the system or preferably as an added feature to the already existing DC/DC converter, conditioning the power delivered by the fuel cell stack [68]. From a cost point of view, adding features to existing components is a more viable method than introducing new and expensive components.

Usually the different diagnostic tools such as current interruption, total harmonic distortion, and impedance spectroscopy or other tools requiring signal analysis can require high speed sampling that is often not available in the cost optimized types of electronics that are used on commercial system for controlling and monitoring the fuel cell systems. A good understanding of the failure patterns of the critical components and their causality is needed in order to

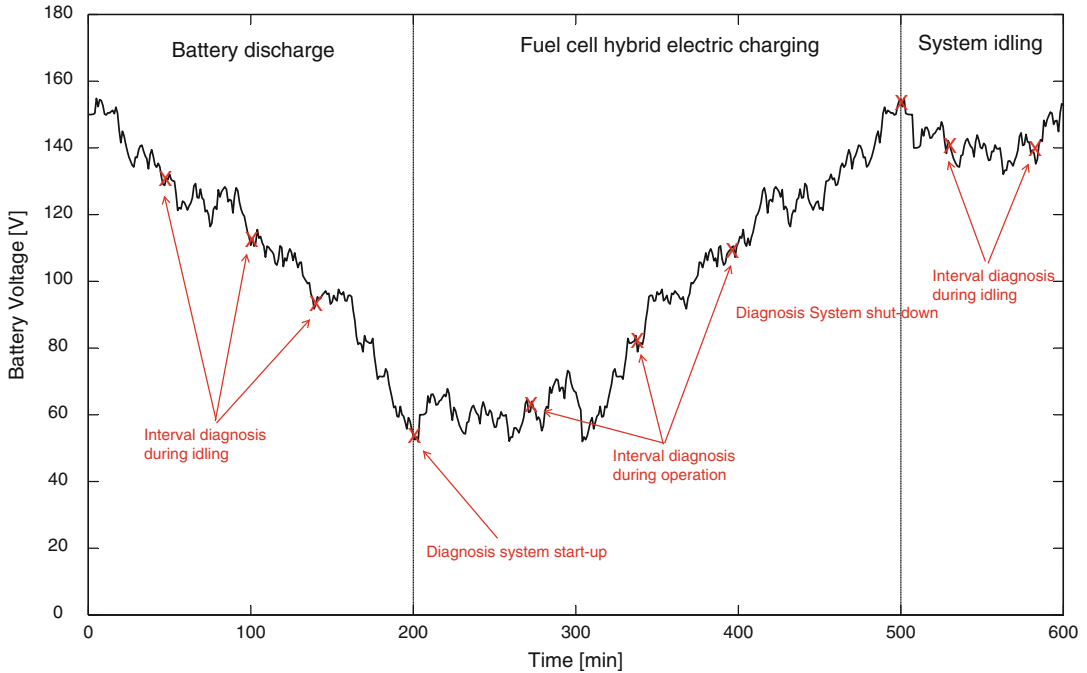


Fig. 21.25 Examples of planned and continuous activation of diagnostic strategies during various fuel cell states

implement tools able to monitor various fault, states-of-health and remaining useful lifetime of the system. In the more developed Nafion-based systems, examples exist of promising diagnostic methods that are able to predict possible problems related to flooding or drying of a stack. Impedance spectroscopy can be used to analyze the hydration status of idling fuel cell stacks in order to predict whether or not re-humidification is needed before start-up [69]. Similar techniques could possibly be used in HTPEM fuel cell system to analyze phosphoric acid quality, membrane conductivity, to update state-of-health and lifetime algorithms.

Several diagnostic methods exist, their relevance often depends on the particular diagnostic results that are desired, and this in turn depends on the specific application. Mainly *in situ* or *in operando* methodologies, such as CI, THDA, and EIS, are relevant for systems that are operating, and besides fault detection, state-of-health monitoring it is desired to also possibly use these techniques to continuously update parameter-based models used for predicting various internal states and updating controller parameters,

everything being executed while system is running. Offline, *ex situ* techniques can give valuable information about the operation history of a fuel cell but are usually more suited for characterizing, performance characterization, different physical quantities, and mechanisms or for quality assessment and lifetime analysis.

The particular timing of when a certain diagnosis in a fuel cell system is conducted can vary from system to system, some techniques require steady-state operation, and others can operate on being fed with historical data of the system performance. Looking at HTPEM fuel cell systems with fuel reformers, they have some interesting possibilities, as mentioned before, when working in electric hybrid systems where a battery pack is being charged by the fuel cell system. In such cases it is possible to implement several different diagnostic strategies because it is often possible to separate the fuel cell power delivery from the hybrid electric system power delivery. An example is shown in Fig. 21.25 of some of the different strategies and situations where a diagnostic procedure could be executed.

The figure shows the battery voltage in a hybrid electric fuel cell system, where, for example, a fuel cell acts as a run-time extender, and providing energy from a given fuel. In the case, three different operating modes are visualized.

- *Battery discharge mode:* The battery is running in discharge mode with the fuel cell system either off or idling. In such cases a fuel cell diagnostic system could perform various performance tests or failure diagnostics, the advantage being that the fuel cell stack, and components are available for manipulation and not necessarily required to support energy production in the system. Performance tests of blowers, valves, and pumps could be performed depending on which sensors are present. The reaction of various levels, flows, pressures, concentrations, temperatures, etc. on given cycling procedures of these actuators. A reference set of normal response of the different sensors can usually be identified, and in case of differences to these reference responses, either system errors can be activated rendering the system unusable until service has been performed or the various control parameters, set points, and state-of-health algorithms can be adjusted to ensure optimum system performance. Usually the fuel cell stack will not be able to deliver power because of the absence of fuel, but small diagnostic circuits could still analyze the conditions of the fuel cell stack as mentioned before.
- *Fuel cell start-up:* Just before, during, or after fuel cell start-up a diagnostic routine could be initiated to update control parameters, system monitoring models, lifetime algorithms or simply compare system behavior to a reference case of the expected normal behavior or the response from a recent start-up. This could be done using electric stimulation of the fuel cell stack in some of the earlier mentioned methods, or by analyzing heating behavior of the system start-up response.
- *Fuel cell charging:* In fuel cell charging mode the fuel cell is actively providing power, either at a fixed operating current, voltage or

power or using a load following algorithm adapting to user interaction with the application in question or the power drawn from the battery pack. In the different situations various diagnostic approaches are possible. In the case where, for example, the current is constant, both EIS and current step procedures could be used that could provide information on cell performance, degradation as described above. Diagnostics can be more challenging when the power is changing dynamically, EIS is difficult to apply in such cases because the DC component of the voltage and current is dynamically changing and could move into highly nonlinear operating areas of the polarization curve. Furthermore with changing current and voltage, temperatures also change proving it difficult to get proper steady-state measurements. Diagnostics during such operating mode need special considerations and careful signal analysis due to complex nonlinear behavior.

- *Fuel cell system shutdown:* Before shutting the system down, diagnostic tools could be used to extract information of the performance of the fuel cell system at the moment of shutdown, later comparison of that performance could yield important information regarding the state of the system prior to or after start-up.
- *Fuel cell system idling:* After system shutdown a period of idling or complete power down can be experienced. Depending on the application in question different approaches are relevant. In systems that undergo long periods before start-up is required, and where, for example, “critical power” is delivered, it becomes relevant to periodically check the responsiveness of the system either by planned start-ups or by using a diagnostic approach able to check the state-of-health of the system and possibly detect potential malfunctions or possible service requirements.

Diagnostic tools become more and more relevant as HTPEM fuel cell systems are

commercialized. They can be usable in fault detection, optimization of system operation, efficiency, and reliability. Different regimes of fuel cell system diagnosis exist, some are related to short term time constant and need to be able to identify and isolate issues within seconds, others use minutes and hours of performance data to predict possible problematic behavior in the long term. Mitigation strategies can also have impact on different times scales, some problems require immediate action and failure handling, other perhaps initiate follow up procedures during next maintenance check others adapt the system controls to the changing behavior over time, to ensure robust behavior over the entire lifetime of the systems.

HTPEM fuel cells are still at an early stage when it comes to the development and implementation of diagnostic methods for monitoring the fuel cell system state-of-health, the identification of potential faults leading to failure or diminished lifetime, and the mitigation of different strategies to avoid severe problems, adapt system control to changing performance, or simply acknowledge the need for maintenance.

References

- Ouzounidou M, Ipsakis D, Voutetakis S et al (2009) A combined methanol autothermal steam reforming and PEM fuel cell pilot plant unit: experimental and simulation studies. *Energy* 34:1733–1743
- Olah GA, Goepfert A (2009) *Prakash, beyond oil and gas: the methanol economy*, 2nd edn. Wiley, Weinheim
- Iulianellia A, Ribeirinha P, Mendes A et al (2014) Methanol steam reforming for hydrogen generation via conventional and membrane reactors: a review. *Renew Sustain Energy Rev* 29:355–368
- Ogden JM, Steinbugler MM, Kreutz TG (2009) A comparison of hydrogen, methanol and gasoline as fuels for fuel cell vehicles: implications for vehicle design and infrastructure development. *J Power Sources* 79:143–168
- Bromberg L, Cheng WK (2010) Methanol as an alternative transportation fuel in the U.S.: options for sustainable and/or energy-secure transportation. Final report presented at Massachusetts Institute of Technology, Cambridge.
- Cifre PG, Badr O (2007) Renewable hydrogen utilisation for the production of methanol. *Energy Convers Manage* 48:519–527
- Sayah AK, Sayah AK (2011) Wind-hydrogen utilization for methanol production: an economy assessment in Iran. *Renew Sustain Energy Rev* 15:3570–3574
- Mignard D, Sahibzada M, Duthie JM et al (2003) Methanol synthesis from flue-gas CO₂ and renewable electricity: a feasibility study. *Int J Hydrog Energy* 28:455–464
- Olah GA, Goepfert A, Prakash GS (2009) Chemical recycling of carbon dioxide to methanol and dimethyl ether: from greenhouse gas to renewable, environmentally carbon neutral fuels and synthetic hydrocarbons. *J Org Chem* 74:487–498
- Araya SS, Andreasen SJ, Nielsen HV et al (2012) Investigating the effects of methanol-water vapor mixture on a PBI-based high temperature PEM fuel cell. *Int J Hydrog Energy* 37:18231–18242
- Chen C-Y, Lai W-H, Chen Y-K et al (2014) Characteristic studies of a PBI/H₃PO₄ high temperature membrane PEMFC under simulated reformat gases. *Int J Hydrog Energy* 39(25):13757–13762
- Wang C-P, Chu H-S, Yan Y-Y et al (2007) Transient evolution of carbon monoxide poisoning effect of PBI membrane fuel cells. *J Power Sources* 170:235–241
- Andreasen SJ, Vang JR, Kær SK (2011) High temperature PEM fuel cell performance characterisation with CO and CO₂ using electrochemical impedance spectroscopy. *Int J Hydrog Energy* 36:9815–9830
- Authayanun S, Saebea D, Patcharavorachot Y et al (2014) Effect of different fuel options on performance of high-temperature PEMFC (proton exchange membrane fuel cell) systems. *Energy* 68:989–997
- Nieto-Márquez A, Sánchez D, Miranda-Dahdal A et al (2013) Autothermal reforming and water-gas shift double bed reactor for H₂ production from ethanol. *Chem Eng Process* 74:14–18
- Choi Y, Stenger HG (2003) Water gas shift reaction kinetics and reactor modeling for fuel cell grade hydrogen. *J Power Sources* 124:432–439
- Ilinich O, Ruettinger W, Liu X et al (2007) Cu–Al₂O₃–CuAl₂O₄ water-gas shift catalyst for hydrogen production in fuel cell applications: mechanism of deactivation under start-stop operating conditions. *J Catal* 247:112–118
- Chen W-H, Hsieh T-C, Jiang T-L (2008) An experimental study on carbon monoxide conversion and hydrogen generation from water gas shift reaction. *Energy Convers Manage* 49:2801–2808
- Reddy EH, Jayanti S (2012) Thermal management strategies for a 1 kWe stack of a high temperature proton exchange membrane fuel cell. *Appl Therm Eng* 48:465–475
- Andreasen SJ, Kær SK (2007) 400W high temperature PEM fuel cell stack test. *Electrochem Soc Trans* 5:197–207

21. Kolb G, Keller S, Tiemann D et al (2012) Design and operation of a compact microchannel 5 kW_{el}, net methanol steam reformer with novel Pt/In₂O₃ catalyst for fuel cell applications. *Chem Eng J* 207–208:388–402
22. Pan L, Wang S (2005) Modeling of a compact plate-fin reformer for methanol steam reforming in fuel cell systems. *Chem Eng J* 108:51–58
23. Lindström B, Pettersson LJ (2003) Development of a methanol fuelled reformer for fuel cell applications. *J Power Sources* 118:71–78
24. Schuessler M, Portscher M, Limbeck U (2003) Monolithic integrated fuel processor for the conversion of liquid methanol. *Cata Today* 79–80:511–520
25. Serenergy H3-350 Datasheet (2014). http://serenergy.com/wp-content/uploads/2013/04/H3-350-datasheet_v2.0-0313.pdf. Accessed 2014
26. Supra J, Janßen H, Lehnert W et al (2013) Temperature distribution in a liquid-cooled HT-PEFC stack. *Int J Hydrog Energy* 38:1943–1951
27. Reddy EH, Monder DS, Jayanti S (2013) Parametric study of an external coolant system for a high temperature polymer electrolyte membrane fuel cell. *Appl Therm Eng* 58:155–164
28. Weiss-Ungethüm J, Bürger I, Schmidt N et al (2014) Experimental investigation of a liquid cooled high temperature proton exchange membrane (HT-PEM) fuel cell coupled to a sodium alanate tank. *Int J Hydrog Energy* 39:5931–5941
29. Scholta J, Messerschmidt M, Jörissen L et al (2009) Externally cooled high temperature polymer electrolyte membrane fuel cell stack. *J Power Sources* 190:83–85
30. Scholta J, Zhang W, Jörissen L et al (2008) Conceptual design for an externally cooled HT-PEMFC stack. *Electrochem Soc Trans* 12:113–118
31. Dudfield CD, Chen R, Adcock PL (2001) A carbon monoxide PROX reactor for PEM fuel cell automotive application. *Int J Hydrog Energy* 26:763–775
32. Duratherm Heat Transfer Fluids. <http://www.heat-transfer-fluid.com/>. Accessed 8 June 2014
33. Paratherm Heat Transfer Fluids. <http://www.paratherm.com/>. Accessed 8 June 2014
34. Andreasen SJ, Kær SK (2008) Modelling and evaluation of heating strategies for high temperature polymer electrolyte membrane fuel cell stacks. *Int J Hydrog Energy* 33:4655–4664
35. Wiethage C, Samsun R, Peters R et al (2013) Start-up of HT-PEFC systems operating with diesel and kerosene for APU applications. *Fuel Cells* 14:266–276
36. Rasheed RKA, Ehteshami SMM, Chan SH (2014) Analytical modelling of boiling phase change phenomenon in high-temperature proton exchange membrane fuel cells during warm-up process. *Int J Hydrog Energy* 39:2246–2260
37. Samsun RC, Pasel J, Janßen H et al (2014) Design and test of a 5 kW_e high-temperature polymer electrolyte fuel cell system operated with diesel and kerosene. *Appl Energy* 114:238–249
38. Maximini M, Engelhardt P, Brenner M et al (2014) Fast start-up of a diesel fuel processor for PEM fuel cells. *Int J Hydrog Energy* 39(31):18154–18163
39. Song T-W, Choi K-H, Kim J-R et al (2011) Pumpless thermal management of water-cooled high-temperature proton exchange membrane fuel cells. *J Power Sources* 196:4671–4679
40. Supra J, Janßen H, Lehnert W et al (2013) Design and experimental investigation of a heat pipe supported external cooling system for HT-PEFC stacks. *J Fuel Cell Sci Technol* 10(5):051002(1–7)
41. Peters R, Düsterwald HG, Höhle B (2000) Investigation of a methanol reformer concept considering the particular impact of dynamics and long-term stability for use in a fuel-cell powered passenger car. *J Power Sources* 86:507–514
42. Schmidt TJ, Baurmeister J (2008) Properties of high-temperature PEFC Celtec®-P 1000 MEAs in start/stop operation mode. *J Power Sources* 176:428–434
43. Korsgaard AR, Refshauge R, Nielsen MP et al (2006) Experimental characterization and modeling of commercial PBI-based MEA performance. *J Power Sources* 162:239–245
44. Andreasen SJ (2009) Design and control of high temperature PEM fuel cell system. Ph.D. Dissertation, Aalborg
45. Maier W, Arlt T, Wippermann K et al (2011) Investigation of HT-PEFCs by means of synchrotron X-ray radiography and electrochemical impedance spectroscopy. *Electrochem Soc Trans* 41:1413–1422
46. Gu T, Shimpalee S, Van Zee JW et al (2010) A study of water adsorption and desorption by a PBI-H₃PO₄ membrane electrode assembly. *J Power Sources* 195:8194–8197
47. Galbiati S, Baricci A, Casalegno A et al (2012) Experimental study of water transport in a polybenzimidazole-based high temperature PEMFC. *Int J Hydrog Energy* 37:2462–2469
48. Li Q, He R, Berg RW et al (2004) Water uptake and acid doping of polybenzimidazoles as electrolyte membranes for fuel cells. *Solid State Ion* 168:177–185
49. Bezmalinović D, Strahl S, Roda V et al (2014) Water transport study in a high temperature proton exchange membrane fuel cell stack. *Int J Hydrog Energy* 39:10627–10640
50. Nielsen M, Alberico E, Baumann W et al (2013) Low-temperature aqueous-phase methanol dehydrogenation to hydrogen and carbon dioxide. *Nature* 495:85–89
51. Yu KMK, Tong W, West A et al (2012) Non-syngas direct steam reforming of methanol to hydrogen and carbon dioxide at low temperature. *Nat Commun* 3:1230
52. Segal SR, Anderson KB, Carrado KA et al (2002) Low temperature steam reforming of methanol over layered double hydroxide-derived catalysts. *Appl Catal A* 231:215–226

53. Ma Y, Guan G, Shi C et al (2014) Low-temperature steam reforming of methanol to produce hydrogen over various metal-doped molybdenum carbide catalysts. *Int J Hydrog Energy* 39:258–266
54. Wang C, Boucher M, Yang M et al (2014) ZnO-modified zirconia as gold catalyst support for the low-temperature methanol steam reforming reaction. *Appl Catal B* 154–155:142–152
55. Singdeo D, Dey T, Ghosh PC (2011) Modelling of start-up time for high temperature polymer electrolyte fuel cells. *Energy* 36:6081–6089
56. Andreasen SJ, Vang JR, Kær SK (2010) Experimental analysis of the effects of CO and CO₂ on high temperature PEM fuel cell performance using electrochemical impedance spectroscopy. Poster session presented at 2nd CARISMA International Conference on Progress in MEA Materials for High Medium and High Temperature Polymer Electrolyte Fuel Cells, France
57. Andreasen SJ, Ashworth L, Menjón Remón IN et al (2008) Directly connected series coupled HTPEM fuel cell stacks to a Li-ion battery DC bus for a fuel cell electrical vehicle. *Int J Hydrog Energy* 33:7137–7145
58. Andreasen SJ, Kær SK, Sahlin SL (2013) Control and experimental characterization of a methanol reformer for a 350 W high temperature polymer electrolyte membrane fuel cell system. *Int J Hydrog Energy* 38:1676–1684
59. Jyh-Shing RJ (1993) ANFIS: adaptive-network-based fuzzy inference system. *IEEE Trans Syst Man Cybern* 23:665–685
60. Justesen KK, Andreasen SJ, Shaker HR et al (2013) Gas composition modeling in a reformed methanol fuel cell system using adaptive neuro-fuzzy inference systems. *Int J Hydrog Energy* 38:10577–10584
61. Justesen KK, Andreasen SJ, Shaker HR (2014) Dynamic modeling of a reformed methanol fuel cell system using empirical data and adaptive neuro-fuzzy inference system models. *J Fuel Cell Sci Technol* 11:021004
62. Zhu Y, Zhu WH, Tatarchuk BJ (2014) Performance comparison between high temperature and traditional proton exchange membrane fuel cell stacks using electrochemical impedance spectroscopy. *J Power Sources* 256:250–257
63. Andreasen SJ, Jespersen JL, Schaltz E et al (2009) Characterisation and modelling of a high temperature PEM fuel cell stack using electrochemical impedance spectroscopy. *Fuel Cells* 9:463–473
64. Vang JR, Andreasen SJ, Araya SS et al (2014) Comparative study of the break in process of post doped and sol-gel high temperature proton exchange membrane fuel cells. *Int J Hydrog Energy* 39:14959–14968
65. Galbiati S, Baricci A, Casalegno A et al (2012) On the activation of polybenzimidazole-based membrane electrode assemblies doped with phosphoric acid. *Int J Hydrog Energy* 37:14475–14481
66. Boaventura M, Mendes A (2010) Activation procedures characterization of MEA based on phosphoric acid doped PBI membranes. *Int J Hydrog Energy* 35:11649–11660
67. Thomas S, Lee SC, Sahu AK et al (2014) Online health monitoring of a fuel cell using total harmonic distortion analysis. *Int J Hydrog Energy* 39:4558–4565
68. Narjiss A, Depernet D, Candusso D (2008) Online diagnosis of PEM fuel cell. Proceedings Power Electronics and Motion Control Conference EPE-PEMC, pp 734–739
69. Bidoggia B, Kær SK (2013) Estimation of membrane hydration status for standby proton exchange membrane fuel cell systems by complex impedance measurement: constant temperature stack characterization. *Int J Hydrog Energy* 38:4054–4066
70. Andreasen SJ, Kær SK (2009) Dynamic model of the high temperature proton exchange membrane fuel cell stack temperature. *J Fuel Cell Sci Technol* 6:041006 (1–8)
71. Boaventura M, Sander H, Friedrich KA et al (2011) The influence of CO on the current density distribution of high temperature polymer electrolyte membrane fuel cells. *Electrochim Acta* 56:9467–9475
72. Suzuki A, Oono Y, Williams MC et al (2012) Evaluation for sintering of electrocatalysts and its effect on voltage drops in high-temperature proton exchange membrane fuel cells (HT-PEMFC). *Int J Hydrog Energy* 37:18272–18289
73. Qi Z, Buelte S (2006) Effect of open circuit voltage on performance and degradation of high temperature PBI–H₃PO₄ fuel cells. *J Power Sources* 161:1126–1132
74. Ye D, Gauthier E, Benziger JB et al (2014) Bulk and contact resistances of gas diffusion layers in proton exchange membrane fuel cells. *J Power Sources* 256:449–456
75. Lobato J, Cañizares P, Rodrigo MA et al (2007) PBI-based polymer electrolyte membranes fuel cells: temperature effects on cell performance and catalyst stability. *Electrochim Acta* 52:3910–3920
76. Zhai Y, Zhang H, Xing D et al (2007) The stability of Pt/C catalyst in H₃PO₄/PBI PEMFC during high temperature life test. *J Power Sources* 164:126–133

Mark Tonny Dalsgaard Jakobsen, Jens Oluf Jensen,
Lars Nilausen Cleemann, and Qingfeng Li

22.1 Introduction

A fuel cell experiences a gradual decline in power output from the beginning of life (BOL) and during operation. Performance loss within a defined extent is often acceptable depending on the overall power output and the application envisioned. As degradation continues, a point is eventually reached where the required power cannot be supplied any longer. This is a common definition of the end of life (EOL) of the power unit. During the lifetime of a fuel cell, failure of different characteristics may occur. The degradation can be either permanent or simply a performance decay that can be restored. The performance loss can be a catastrophic failure leading to an entire system interruption or a gradual decrease in power output.

From a materials science point of view, PEMFC components are exposed to a very aggressive environment where strong oxidizing and reducing agents are present together with water, acids, and radicals while subjected to elevated electrochemical potentials and temperatures. As a result, the durability of PEMFCs is recognized as the most critical issue

to be addressed before widespread commercialization of the technology can become a reality [1–5]. Fundamental aspects of the durability and degradation of this type of fuel cell have been reviewed by Borup et al. [6], whereas Wu et al. [7] has presented a comprehensive overview of degradation mechanisms and associated mitigation strategies. As an approach to evaluate the PEMFC durability, several accelerated stress tests (ATS) have been developed as reviewed by Zhang et al. [8].

Briefly speaking, durability issues of a PEMFC include dissolution and sintering of catalyst nanoparticles, corrosion of catalyst supports, and membrane thinning. The lifetime is significantly influenced by the applied operating parameters, e.g., temperature, pressure, level of fuel impurities, cell voltage/load magnitude, and the cycling of these parameters. Higher operational temperatures, being the major subject of this book, evidently entails greater material durability challenges since aggravation of carbon corrosion, platinum dissolution, and polymer oxidation is apparent [9, 10]. Furthermore, the presence of phosphoric acid and its maintenance within the HT-PEMFC add new issues that are not present in the LT-PEMFC, which is frequently chosen for benchmarking purposes.

Technical targets have been established for commercializing PEMFCs as electrical power sources for vehicles as well as for stationary and portable power applications. These targets

M.T.D. Jakobsen • J.O. Jensen (✉) • L.N. Cleemann
Q. Li
Department of Energy Conversion and Storage,
Technical University of Denmark, Kemitorvet 207,
DK-2800 Lyngby, Denmark
e-mail: jojen@dtu.dk

Table 22.1 DOE durability targets for PEMFCs for automotive and stationary systems, power units, stacks, and components, updated 2014 [11]

Characteristics	Units	Status 2011	Targets	
			2015	2020
Automotive 80 kW _e systems on direct H ₂ : durability with cycling (10 % degradation)	h	2500	–	5000
CHP systems on natural gas 1–10 kW _e : degradation with cycling	%/1000 h	<2	0.5	0.3
Durability with cycling (20 % degradation)	h	12,000	40,000	60,000
100 kW _e –3 MW _e : Durability (10 % degradation)	h	40,000–80,000	50,000	80,000
Portable power system (2–250 W _e): durability (20 % degradation)	h	1500	5000	–
Mean time between failures	h	500	5000	–
APU on ultra-low sulfur diesel (1–10 kW _e): degradation with cycling	%/1000 h	2.6	1.3	1.0
Durability (20 % degradation)	h	3000	15,000	20,000
Electrode for transportation applications: Catalyst stability (mass activity loss after 30,000 cycles between 0.6–1.0 V)	%	48	–	<40
Support stability (mass activity loss after 400 h at 1.2 V)	%	<10	–	<10
Membrane electrode assemblies (MEAs): durability with cycling (10 % degradation)	h	–	–	5000

are developed for LT-PEMFCs, but are, due to their formulation, partly relevant for HT-PEMFCs. The durability items of these targets from the US Department of Energy (DOE, Office of Energy Efficiency & Renewable Energy, updated November 2014) are collected in Table 22.1 [11] where the status of 2011 and targets for 2015 and/or 2020 are listed. No similar specific targets are defined for HT-PEMFCs.

The durability of automotive fuel cell systems operating with direct hydrogen is often measured in terms of service life until 10 % performance degradation. Compared to present automotive engines, the durability should be at least 5000 h (equivalent to 200,000 driven kilometers) including daily drive cycling. However, cells for stationary applications will likely require more than 40,000 h of reliable operation, including effects of transient operation, start-up, and shutdown. A routine lifetime greater than 40,000 h has been demonstrated with a variety of fuel cell types operating on natural gas, e.g., with phosphoric acid fuel cell systems. For portable power units in a range from a few watts to a few hundred watts the durability target is usually defined as the time until the unit rate power degrades by 20 %, though other levels of power degradation may be acceptable depending on the application.

During durability evaluations, testing should obviously be performed using an operating cycle that is realistic for the target application including transient mode, start-up/shutdown, and standby degradation. In addition, the mean time between failures (MTBF) should be specified to include system component failures that render the system inoperable without maintenance. Both the durability and the MTBF are targeted at 5000 h for portable power systems by 2015.

This chapter is devoted to a review of material issues for HT-PEMFC components and is built on relevant evaluation of data from literature on membrane oxidation, acid loss, platinum dissolution, and carbon corrosion. Finally, the state-of-the-art durability of PBI-based fuel cells is summarized. For certain applications, like in mobile auxiliary power units exposed to severe vibrations and road dust or to maritime saline mists, the picture becomes more complicated and knowledge today is rather limited.

22.2 Polymer Membrane Degradation

Membrane degradation is one of the main modes for PEMFC performance decay and eventual failure. Such degradation can take place via

chemical processes which are accelerated by higher temperature. It can also result from mechanical impact or as a combination of the two stressors. HT-PEMFCs are mostly based on non-fluorinated hydrocarbon polymers and this might lead to expectations of poorer chemical resistance than that of the conventional perfluorinated sulfonic acid (PFSA)-based membranes. On the other hand, certain aromatic polymers like polybenzimidazole (PBI) are chosen due to their high chemical and thermal stability, so it is not given that degradation is prohibitively fast. Polymer degradation can result in thinning, pinhole formation, and strength reduction leading to increased gas crossover and eventually collapse. An early indication of increased gas crossover is a depression in the open circuit voltage of the cell. Transfer and loss of acid are also important issues associable with degradation of the HT-PEM electrolyte. However, a separate section has been designated to discussion of the doping acid.

22.2.1 Mechanical Failure

PBI membranes are mechanically rigid and strong due to the hydrogen bonding between imidazole rings. The undoped PBI membrane has a small elongation at break of around 1–3 % and an intermediate tensile strength of about 60–70 MPa at room temperature. When saturated with water, the elongation and tensile strength increase to about 7–10 % and 100–160 MPa, respectively [12]. Doping with phosphoric acid makes the membrane very soft, particularly at elevated temperatures and high humidity. During fuel cell operation, the humidity, and therefore the membrane swelling and shrinking, varies with the current load, i.e., the rate of water formation. Maier et al. [13] reported a membrane swelling for a HT-PEMFC of approximately 20 % due to a change in current from 0 to 0.140 A/cm².

22.2.2 Thermal Degradation of PBI

An early study by Gaudiana and Conley [14] showed that the weakest part of the PBI in an oxidative atmosphere is the aromatic rings bearing the nitrogen atoms. The rupture of the bulk polymer backbone happens through the carbon in the imidazole ring linked with the phenylene group towards the amine nitrogen (–NH–) [15]. An FTIR study on the thermo-oxidative degradation of PBI in air at 350 °C by Musto et al. [16] revealed two new adsorption peaks, indicating the stretching vibrations of products or intermediates of the polymer oxidative degradation. They concluded that the oxidative attack resulted in the cleavage of imidazole rings, eventually leading to formation of aromatic nitrile groups. To simulate the conditions in a HT-PEMFC, PBI samples were loaded with platinum black catalyst, doped with phosphoric acid and heated under atmospheres of either nitrogen with 5 % hydrogen or air in a thermogravimetric analyzer (TGA) equipped with a mass spectrometer [15]. In all cases a weight loss below 400 °C was found to be mainly due to loss of water while the polymer itself is thermally stable, as summarized in Table 22.2.

22.2.3 Oxidative Degradation

Oxidative degradation of the membrane is believed to occur due to attack from peroxide radicals, e.g., ·OH and ·OOH. Peroxide formation is suggested in connection with oxygen diffusion through the electrolyte towards the anode followed by incomplete reduction. Subsequent reaction of the peroxide with transition metal ions, e.g., Fe²⁺ leads to formation of the detrimental peroxide radicals. In practice, a trace amount of transition metals may be present as impurities in the MEA, originating from corrosion of metallic components such as bipolar plates, end plates, and tubing [6].

As an accelerated aging test of the resistance towards radical oxidation, the so-called Fenton

Table 22.2 Summary of temperatures for the generation of different PBI decomposition products when heated in nitrogen with 5 % hydrogen or air [15]

Product	Nitrogen with 5 % hydrogen (°C)			Air (°C)		
	PBI	PBI-H ₃ PO ₄	PBI-H ₃ PO ₄ -Pt	PBI	PBI-H ₃ PO ₄	PBI-H ₃ PO ₄ -Pt
Water	100–250	100–400, >600	>200	125–275	100–200	>150
				550–750	200–300	
					>650	
Benzene	625–725	–	625–725	–	–	–
Acetonitrile	625–750	–	–	–	–	–
Hydrogen cyanide	625–850	–	–	600–750	–	–
Ammonia	>775	–	–	–	–	–
Methane	625–700	–	–	–	–	–
Carbon dioxide	100–300	>600	>650	550–750	>650	>650
	450–500					
Isocyanic acid	–	–	–	600–750	–	–
Nitric oxide	–	–	–	600–750	–	675–725
Cyanogen	–	–	–	600–750	–	–

test is frequently conducted for the ex situ evaluation of polymer membranes. The test is carried out by immersing a membrane into a Fenton agent containing both hydrogen peroxide and Fe²⁺ ions. Depending on the time of exposure and the molecular weight of the PBI, a significant weight loss in the range of 10–38 % has been reported after the typical Fenton test in 3 % H₂O₂ containing 4 ppm Fe²⁺ at 68 °C [17–19]. Size exclusive chromatography (SEC) analyses on the PBI membranes before and after the Fenton test showed a shift in the molecular weight distribution (MWD) curves, i.e., a decrease in the polymer molecular weight [20]. A monomodal distribution in the PBI MWD curves suggested an endpoint scission degradation mechanism of the macromolecular polymer structure, being in good agreement with the weight loss dependence on the polymer molecular weight. The reaction mechanism of a midpoint scission of the polymer chain has also been proposed [21] with the final hydrolysis step leading to formation of both terminal amine and carboxylic acid groups. The latter group is susceptible to further oxidation and thus leads to polymer weight loss. With progressive chain scission, the endpoint unzipping mechanism becomes accelerated due to formation of new terminal end groups. Ultimately, endpoint scission leads to direct weight loss as opposed to midpoint scission which reduces the molecular weight.

It should be mentioned that the relevance of the Fenton test to predict lifetime of a fuel cell has been frequently debated. It is a common view that it is a very tough test and that fast degradation cannot be interpreted as a disqualification of the membrane material for fuel cell use. However, it is an easy tool for comparative accelerated testing of polymer materials and improved resistance to the Fenton test is an indication of improved oxidative stability.

22.2.4 Effect of Phosphoric Acid

The conductivity of PBI membranes is provided by phosphoric acid doping. The presence of phosphoric acid may have several effects on durability and degradation. Phosphoric acid is a complexing agent for metal ions and precipitation of iron phosphates may occur due to its very low solubility (with a solubility product of $1.3 \times 10^{-22} \text{ mol}^2 \text{ l}^2$), resulting in reduced activity of the ferrous ions and hence inhibition of the H₂O₂ decomposition. Another effect of phosphoric acid on the peroxide stability is the decreased pH value of the environment, further stabilizing the hydrogen peroxide as confirmed by the SEC test [22]. On the other hand, phosphoric acid is involved in the acid–base interactions with the N–H groups of PBI [23], leading to swelling and separation of the polymer

backbone and therefore allowing for easier access of hydroxyl radicals to the carbon atom of the imidazole ring that is linked to the benzenoid ring. However, the acid–base interaction between the phosphoric acid molecules and nitrogen atoms of the imidazole rings, in itself, might impede the attack of radicals. The overall effect is likely a much lower degradation rate of the polymer in a HT-PEMFC environment than under Fenton test conditions. As a consequence,

translation of the Fenton test results in the absence of phosphoric acid should be done with great care.

22.2.5 Radical Oxidation Degradation of PBI and Its Variants

Table 22.3 summarizes the literature data of Fenton test results for *m*PBI, its structurally

Table 22.3 Polybenzimidazole degradation during the Fenton test translated into the rate of the polymer weight loss (in percent)

Conditions	Weight loss after <i>x</i> hours	References
3 % H ₂ O ₂ + 4 ppm Fe ²⁺ (pH 2), 68 °C PBI	≈ 60 h : 0.17 %/h (105 kDa); 0.38 %/h (26 kDa)	[19]
3 % H ₂ O ₂ + 3 ppm Fe ²⁺ , 80 °C PBI and variants	12 h : 0.83 %/h (<i>m</i> PBI); 0.5 %/h (OPBI); 0.76 %/h (SOPBI-60); 0.71 %/h (CrL SOPBI-60); 5.18 %/h (SOPBI-92); 1.12 %/h (CrL SOPBI-92); dissolved (CrL SOPBI-154); 1.33 %/h (CrL SOPBI-154)	[24]
3 % H ₂ O ₂ + 4 ppm Fe ²⁺ , 68 °C PBI and cross-linked analogues	118 h : 0.32 %/h (PBI 23 kDa); 0.24 %/h (1.1 % CrL); 0.19 %/h (3.6 % CrL); 0.07 %/h (13 % CrL);	[17]
5 % H ₂ O ₂ , 60 °C PBI and blends	96 h : PBI 0.19 %/h (MW n/a); 0.08 %/h (treated in NaOH); 0.08 %/h blend, base excess (70 % PBI)	[18]
3 % H ₂ O ₂ + 4 ppm Fe ²⁺ , 68 °C, PBI and blends	120 h : 0.32 %/h (MW n/a); 0.13 %/h (30 % blend)	[18]
30 % H ₂ O ₂ + 20 ppm Fe ²⁺ , 68 °C, PBI	24 h : 0.36 %/h (MW n/a)	[25]
3 % H ₂ O ₂ + 4 ppm Fe ²⁺ , 68 °C PBI, its variants and blends	120 h : 0.18 %/h (MW n/a); 0.11 %/h (blend); 0.07 %/h (SO ₂ PBI blend); 0.02 %/h (F ₆ PBI blend)	[20]
3 % H ₂ O ₂ + 4 ppm Fe ²⁺ , 68 °C PBI of varied MWs	120 h : 0.30 %/h (24.7 kDa); after 300 h: 0.09 %/h (54.5 kDa)	[21]
3 % H ₂ O ₂ + 4 ppm Fe ²⁺ , 70 °C PBI and TMBP cross-linked	480 h : 0.10 %/h (10 % CrL); 0.09 %/h (15 % CrL); 0.07 %/h (20 % CrL)	[26]
30 % H ₂ O ₂ + 20 ppm Fe ²⁺ , 85 °C PBI and TMBP cross-linked	54 h : 1.33 %/h (PBI); 1.20 %/h (5 % CrL); 1.17 %/h (10 % CrL); 0.87 %/h (15 % CrL); 0.81 %/h (20 % CrL)	[26]
3 % H ₂ O ₂ + 4 ppm Fe ²⁺ , 68 °C PBI-Nafion blends	≈ 256 h : 0.05 %/h (66 kDa); 0.05 %/h (60 % Nafion); 0.06 %/h (88 % Nafion); 0.05 %/h (94 % Nafion); 0.02 %/h (100 % Nafion)	[27]
3 % H ₂ O ₂ + 4 ppm Fe ²⁺ , 68 °C Cross-linked PBI	440 h : 0.08 %/h (35 % CrL); 0.06 %/h (48 % CrL)	[28]
3 % H ₂ O ₂ + 4 ppm Fe ²⁺ , 68 °C PBI and thermally cured analogue	80 h : 0.13 %/h (48 kDa); 0.05 %/h (thermally cured)	[29]
3 % H ₂ O ₂ + 4 ppm Fe ²⁺ , 68 °C PBI and co-polymers	200 h : 0.13 %/h (33 kDa); 0.13 %/h (Co-20 %SO ₂ PBI); 0.12 %/h (Co-50 %SO ₂ PBI); 0.07 %/h (Co-80 %SO ₂ PBI); 0.05 %/h (SO ₂ PBI)	[30]
3 % H ₂ O ₂ + 4 ppm Fe ²⁺ , 68 °C PBI and variants	200 h : 0.12 %/h (33 kDa); 0.04 %/h (F ₆ PBI); 0.04 %/h (18.5 % CrL F ₆ PBI)	[31]
3 % H ₂ O ₂ + 4 ppm Fe ²⁺ , 68 °C PBI of varied MWs	280 h : 0.08 %/h (66 kDa); 0.03 %/h (0.2–0.8 M H ₃ PO ₄)	[22]

CrL cross-linked; TMBP 4,4'-diglycidyl(3,3',5,5'-tetramethylbiphenyl) epoxy resin

modified variants, covalently cross-linked membranes, and ionic blends. For the comparison of these results, a few remarks can be made. First of all the initial molecular weight of the polymer (in kDa) is decisive for the oxidative stability. During the Fenton test, the applied Fenton solution should be frequently renewed, typically on a daily basis. The thickness of the membrane samples is also of importance. It should be noted that not all these parameters are specified in the cited literature.

As seen from the table, great efforts are being made to improve the membrane durability by polymer chemistry. For example, synthetically introducing other heteroatoms or heterogroups such as $-O-$, $-SO_2-$, and $C(CF_3)_2-$ into the macromolecular chain has shown to significantly improve the polymer stability against the oxidative degradation. The oxidative resistance of the membrane can be further improved by ionically or covalently cross-linking the *m*PBI or its structurally modified variants.

22.3 Acid Loss

22.3.1 Mechanisms of Acid Loss

The major part of the proton conductivity in PBI-based HT-PEMFCs is attributed to free acid in the membrane. It has been shown that redistribution of phosphoric acid in HT-PEMFC MEAs is a rather quick process either from the membrane to the catalyst layer or vice versa [32]. It is this unbound portion of the acid that is particularly susceptible to loss since it is not bonded to the PBI backbone. Loss of the doping acid from a PBI membrane can take place via a number of mechanisms including evaporation, diffusion, capillary transportation, MEA compression, or washing out by condensed water at low temperature.

A particularly critical mechanism is washing or leaching out of the acid with liquid water, which is produced when the fuel cell temperature is below 100 °C, e.g., during a cold start or shutdown [12]. After immersion of a membrane

in liquid water or methanol the absorbed acid is easily lost while exposure to a flow of liquid water results in complete loss of all doping acid in a matter of hours [33].

In earlier years of the PAFC development, where a SiC matrix contained the phosphoric acid electrolyte, Mori et al. [34] observed changes in acid distribution during the PAFC operation. It seemed that the acid absorbed by the anode moved through the matrix to the cathode at which it was slowly carried out of the cell in the cathode gas. They suggested an electrode structure with low acid absorbency for the cathode and one with high acid absorbency for the anode, the latter functioning as an acid reservoir. Opposing this suggestion is the risk of anode flooding, particularly evident at high current densities due to a fraction of phosphoric acid anions being driven towards it without discharging. A resulting cation transference number (t^+) of 0.98 makes the acid management a critical issue for PAFCs. Generally there is a lack of fundamental and quantitative knowledge regarding the acid leaching mechanisms and their severity. This makes it a difficult task to propose a suitable accelerated stress test protocol for the purpose of evaluating this failure mode. Essentially, better understanding of the acid leaching phenomenon is required before appropriate tests can be derived, let alone purposefully derived AST protocols.

22.3.2 Acid Loss by Evaporation

The usual method applied for the acid leaching evaluation is to analyze the anodic and cathodic off-gasses for traces of vaporized acid. This is typically done by collecting the acid in water bubbler flasks. However, this does not necessarily provide a realistic picture of the severity, since only a single mechanism for the proposed acid loss is considered, i.e., the evaporation. Furthermore, it is apparent that not all of the escaped acid in the gas phase is carried all the way out with the fuel cell exhaust due to recondensation before collection. This conjecture is based on

Table 22.4 Estimates of phosphoric acid vapor pressure and acid evaporation rates in cathode air assuming $\lambda_{\text{air}} = 2$ at 0.2 A/cm² and full saturation. Total pressure set to 1 bar.

Temperature [°C]	P ₄ O ₁₀ in vapor of boiling acid [wt%]	Vapor pressure of H ₃ PO ₄ [μ bar or ppm]	Saturated H ₃ PO ₄ in cathode flow [μ g/(m ² s)]
150	0.00016	0.41	2.1
160	0.00028	0.71	3.6
170	0.00048	1.23	6.2
180	0.00084	2.13	11
190	0.0015	3.71	19
200	0.0025	6.45	33

Estimates are based on extrapolation from phosphoric acid vapor pressure data at higher temperatures [35]

common sense and is supported by the observation of corrosion of fuel cell components, e.g., bipolar plates. Thus, it is likely that acid loss by evaporation is frequently underestimated.

Brown and Whitt [35] measured the vapor pressure over boiling phosphoric acid. Most attention was given to the component water, but from approximately 220 °C to higher temperatures the weight percent of phosphoric acid, given as P₄O₁₀, increases in the vapor. Based on these values, the phosphoric acid vapor pressure at lower temperatures can be estimated by extrapolation when assuming an exponential temperature dependence. The estimate can be seen in Table 22.4. Assuming lambda of 2 for air and lambda of 1.2 for hydrogen, the air flow into the cell is approximately 4 times larger than the hydrogen flow. The ratio between the exit flows is over 20, being significantly larger because most of the hydrogen is consumed. The reduction of the total flow during the passage should bring the acid vapor closer to saturation. However, the exact numbers are difficult to assess because they also depend on the liberated water vapor. In any case the capability for transporting acid must be higher for the cathode flow if the applied fuel is pure hydrogen. With reformat or diluted hydrogen the loss rates should be more comparable.

Yu et al. [36] implicatively attributes the disparate acid evaporation rates between the cathode and anode side to a steam distillation mechanism that markedly promotes cathode side acid evaporation at temperatures above 160 °C. It is suggested that this proposed acid evaporation mechanism intensifies not only with

temperature but also with current density due to the enhanced rate of water generation. Yu et al. justified the proposed mechanism by the enhancement of the water vapor pressure in phosphoric acid, as studied by Fontana [37]. This is in accordance with phosphoric acid polymerizing at low water activities, thereby reducing the number of ortho-phosphoric acid molecules and consequently their vapor pressure. If the water activity rises due to increased production at high current density, the process is reversed and the vapor pressure of the ortho-phosphoric acid is increased.

Another suggested manner of acid loss within the gas exhaust is by acid aerosol formation. Mori et al. [34] first proposed such mist or drop formation as the primary way of acid transportation in the PAFC off-gas. Notice, however, that this assumption is made to explain the acid loss against the fact that the acid equilibrium vapor pressure is extremely low at temperatures below 300 °C [35].

The estimated evaporation rates given in Table 22.4 are in fact significantly higher than most of the measured data, as shown in Fig. 22.1 and Table 22.5. There may be at least three reasons for this. Firstly, the estimate is made on results from one study only and should as such be considered as a rough estimate. Secondly, the loss rates are calculated based on full saturation which is a risky assumption to make considering the short residence time of the air in the cathode channels. Thirdly, recondensation must be expected all the way from the membrane area through the gas diffusion layers, flow channels, manifolds, and tubing. Over time, saturation of

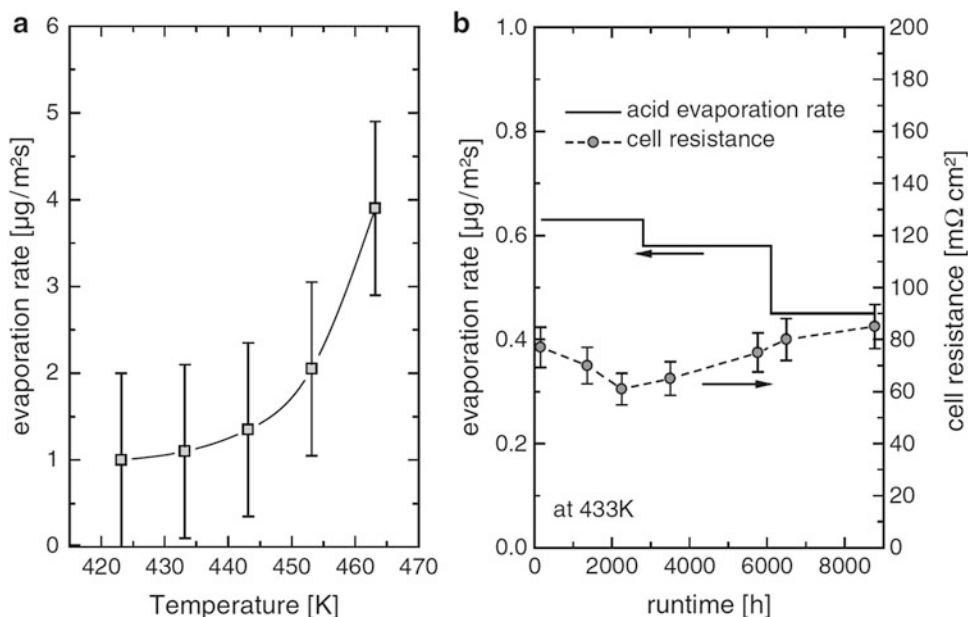


Fig. 22.1 (a) BoL phosphoric acid evaporation rates from Celtec® MEAs as a function of temperature. (b) Phosphoric acid evaporation rate from a Celtec® MEA operated at 160 °C over a period of 1 year (left axis) and

the cell resistance measured by 1 kHz AC impedance spectroscopy (right axis). In both figures the rates are measured via external acid collection. The figures are reproduced from [38] with permission of Springer

Table 22.5 Summary of acid evaporation rate measurements by different groups

Acid evaporation measurements	Acid losses [$\mu\text{g}/(\text{m}^2 \text{ s})$]	References
Direct cast <i>m</i> PBI membranes, 160 °C, 640 h, with a load cycle of OCV (2 min), 0.2 A/cm ² (30 min) and 0.6 A/cm ² (30 min):	Cathodic: 4.5×10^{-2} Initial anodic: 2.4×10^{-2}	[39]
ABPBI, 160 °C, 1000 h, 0.2 A/cm ² :	Cathodic, after 180 h: 0.21 Anodic, after 180 h: 0.21 (Anode: nothing after 600 h)	[40]
Direct cast 2OH-PBI, 160 °C, 8000 h:	Total: 0.5	[10]
Direct cast <i>p</i> PBI, 0.2 A/cm ² 80 °C, 900 h (+100 h break-in at 120 °C): 160 °C, 2500 h: 190 °C, 800 h:	Cathodic: 8.0×10^{-3} Anodic: 5.0×10^{-3} Cathodic: 1.9×10^{-2} Anodic: 1.7×10^{-3} Cathodic: 0.306 Anodic: 1.0×10^{-3}	[36] ^a
Direct cast 2OH-PBI, 0.2 A/cm ² 80 °C, 1300 h (+100 h break-in at 160 °C): 160 °C, 1700 h: 190 °C, 800 h:	Cathodic: 2.1×10^{-2} Anodic: 3.0×10^{-3} Cathodic: 2×10^{-2} Anodic: 4×10^{-3} Cathodic: 0.222 Anodic: 4.0×10^{-3}	[36] ^a
PBI, 150 °C, 450 h, 0.2 A/cm ² Acid doping level of 6.5: Acid doping level of 7.8:	Total: 7.4×10^{-7} Total: 1.4×10^{-6}	[41]
Three cells stack, PBI, 125 °C, 185 h, 0.2 A/cm ² :	Cathodic: 3.4 Anodic: 1.1	[42]
Advent TPS® membrane, ^b 150 °C, 360 h, 0.2 A/cm ² : Advent TPS® membrane, ^b 6 wt% Al ₂ O ₃ in electrode, 150 °C, 360 h, 0.2 A/cm ²	Total: 5.9 Total: 4.6	[43]

^aThis reference contains unincorporated measurements for dynamic testing: load cycling, thermal cycling, start–stop

^bPhosphoric acid-doped pyridine-based membranes (see Chap. 5)

these areas may lead to less recondensation allowing for a higher fraction of the lost acid to actually be collected outside the system. It should be mentioned that the evaporation rate is believed to be highest at the BoL, mainly due to a steadily established equilibrium and a maximum excess of the acid in the MEAs at this particular time of operation [38]. It should also be mentioned that these data are obtained based on the polyphosphoric acid (PPA) membranes (Direct cast, see Chap. 10) whose acid doping level is typically in a range of 20–40 mol phosphoric acid per mol polymer repeat unit, significantly higher than that of the post-doped membranes (see Chap. 9).

22.3.3 Phosphoric Acid Transfer in MEAs

The acid transfer within MEAs, though with no measurable loss out of the fuel cell, is another critical issue for the performance degradation. Akita et al. [44] evaluated the doping acid stability by the Soxhlet extraction method, i.e., holding an acid-doped membrane in a glass filter and extracting the doping acid with an 1 M methanol solution. They reported an acid loss of 65–70 % from membranes with an acid doping level of 1–5 mol phosphoric acid per mol PBI repeat unit. The stability improves when using organic phosphonic acids with a larger molecular size.

Acid movement due to the MEA compression may occur mainly in connection with thermal or load cycling, single cell or stack assembly, or during the hot pressing step of MEA fabrication. By use of titration analysis, Yu et al. [36] found an acid loss of 29 % after MEA hot pressing and heat treatment of direct cast membranes with acid doping levels as high as 26 mol phosphoric acid per mol PBI repeat unit. The heat treatment was applied to simulate operation, i.e. 24 h exposure in an oven at 160 °C.

It should be noted that part of the acid transport from the membrane into the catalyst layers of the electrodes is necessary for the MEA preparation. Different techniques are used to introduce the phosphoric acid into the catalyst layers:

by redistribution of acid from the doped PBI membrane [41], by direct acid addition to the electrodes [45], or both [46]. Studies have shown that it is not a critical issue how the acid is introduced since redistribution of the free acid occurs as soon as the fuel cell is assembled [32]. By use of electron probe microanalysis, Oono et al. [47] investigated the acid redistribution and loss from MEAs operated at 150 °C and 0.2 A/cm² for durations of up to 18,000 h. For 12,000 h of operation, their results indicated a preliminary acid redistribution from the membrane into the catalyst layers. Acid depleted areas of the catalysts were identified after 15,000 h. The finding does not seem to support the idea that the acid management for HT-PEMFCs using acid-doped PBI membranes is as important as it is for PAFCs.

The acid in the catalyst layer is retained by capillary forces and by the hydrophobicity of the microporous layer while the acid in the membrane is held by the acid–base interaction as well as physical absorption. A recent study showed that a stable interface between the membrane and the catalyst layer can be sustained as long as the proton conducting acid phase is established. Electrodes with no polymeric binder were constructed with improved performance and good stability [48].

Recent efforts have been made to develop techniques to quantify the acid transfer and redistribution in MEAs using synchrotron-based X-ray tomographic microscopy [49], synchrotron X-ray radiography [45], and neutron imaging [46]. More insights on the acid mobility and stability are expected with established use of these techniques.

22.4 Catalyst Degradation

Higher operational temperatures of HT-PEMFCs as compared to LT-PEMFCs impose more challenges with catalyst degradation. This issue coupled with the presence of free acid in the membrane obviously aggravates both carbon corrosion and platinum dissolution, which in turn triggers significant agglomeration of the

noble metal nanoparticles. Zhang et al. [50] and Shao et al. [51] have provided detailed reviews of catalyst degradation mechanisms in LT-PEMFCs. Zhang et al. [52] have made an excellent review of catalysts and support materials in which relevant degradation mechanisms and mitigation strategies for LT-PEMFCs and PAFCs, to some extent, are related to that for HT-PEMFCs.

The catalyst degradation mechanisms that are evident for HT-PEMFCs are largely the same as those for LT-PEMFCs and PAFCs. Early research on carbon supported platinum nanoparticles in PAFCs showed little potential dependence of the platinum surface area loss in the range of up to 0.75 V. This indicates catalyst degradation via coalescence by crystal migration of platinum adatoms on the carbon surface. Because of faster diffusion at higher temperatures, this mechanism might have higher influence on PAFCs and HT-PEMFCs than on LT-PEMFCs. For potentials above 0.8 V, the platinum surface area loss showed strong dependence on the electrode potential in phosphoric acid. This suggests an increased influence from the Ostwald ripening mechanism by dissolution and redeposition [53, 54], as schematically illustrated in Fig. 22.2. In case of platinum alloy catalysts (Pt-M/C), the dissolution of non-precious alloying elements in the acid

environment is of more concern than that of the platinum itself, for example in case of PtCo/C [55] or Pt₃Ni/C [56].

22.4.1 Platinum Dissolution

An earlier effort was made to determine the platinum dissolution in concentrated phosphoric acid under nitrogen atmosphere in a potential range from 0.8 to 0.95 V at temperatures of 176 and 196 °C [58]. Using electrodes of platinum supported on acetylene black (0.6 mg-Pt/cm²), Honji et al. [53] investigated the platinum dissolution after a 100 h exposure to 98 wt% phosphoric acid at 205 °C, showing a rapid dissolution increase for potentials higher than about 0.8 V. At 0.9 V, being the highest potential investigated in this study, approximately 80 % of the platinum was lost from the electrode during the time span of the study. Aragane et al. [59, 60] found a consistent increase in the platinum dissolution rate for a PAFC as the cell voltage increased from 0.6 to 1.0 V. Wang et al. [61] studied the platinum dissolution in perchloric acid to mimic the acidity of a perfluorosulfonic acid membrane electrolyte. They showed dramatic increases in the dissolved platinum concentration with enhanced potentials from 0.65 to 1.1 V. This is in agreement with

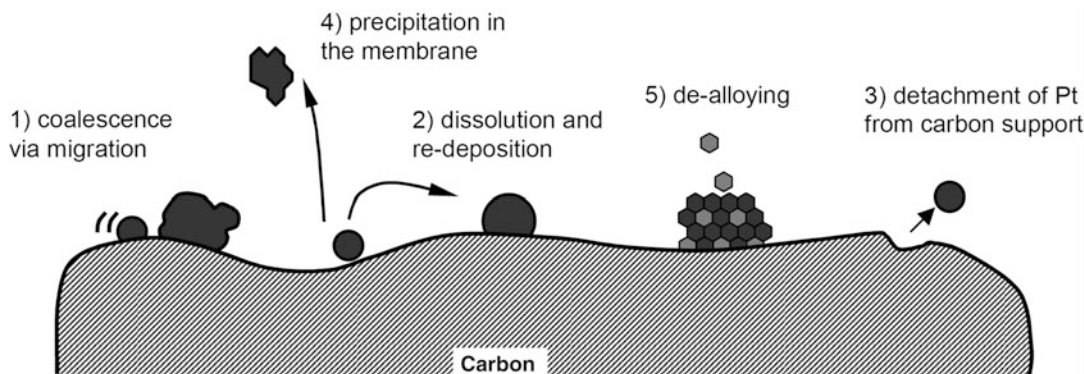


Fig. 22.2 Major mechanisms for platinum degradation in PEMFCs. (1) Coalescence via migration of Pt nanoparticles, (2) particle growth via the Ostwald ripening (dissolution and redeposition), (3) detachment of Pt

nanoparticles from the carbon support due to corrosion, (4) dissolution and precipitation in the membrane, and (5) de-alloying of Pt-alloy catalysts. Reproduced from [57] with permission of The Electrochemical Society

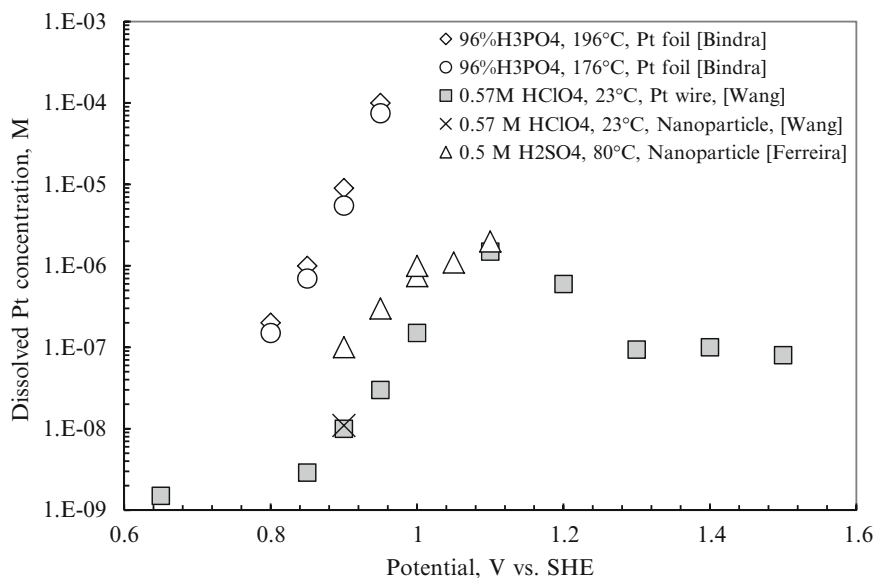


Fig. 22.3 Equilibrium concentrations of dissolved platinum in phosphoric acid, perchloric acid, and sulfuric acid as a function of potential. Data from Bindra et al. [58], Wang et al. [61], and Ferreira et al. [63]

the Pourbaix diagram of platinum in the region of 1.0–1.2 V and pH 0–2 [62]. A somewhat elaborated Pourbaix diagram is reproduced by Borup et al. [6]. Some of the fundamental results of equilibrium platinum concentrations as measured by different groups are summarized in Fig. 22.3.

As reviewed by Ahluwalia et al. [64], it is generally accepted in literature that the passivation by platinum oxides may limit the metal solubility. This can explain the peak solubility observed by Wang et al. [61] at 1.1 V, as shown in Fig. 22.3. Aragane et al. [60] estimated the dissolution rate by calculation, assuming that diffusion is the rate limiting step. This estimation showed an enhanced dissolution rate with both potential and temperature. However, the effect of temperature decreases with increasing potentials, as shown in Fig. 22.4 [58] where it can also be seen that the metal dissolution rate in hot phosphoric acid is decreasing strongly as the potential decreases. According to this calculation at 160 °C, the metal dissolution rate decreases by more than 100 million times when the cell voltage is decreased from the virtual cell open circuit voltage (1.0 V) to 0.6 V. Besides the potential

and temperature, parameters that may influence the platinum solubility include the high acidity, oxidative atmosphere, platinum particle size and potential sweep rate and/or pattern [64–66].

During the Ostwald ripening process, smaller platinum nanoparticles dissolve first into the acid or the ionomer phase. Platinum may subsequently be transported as ions within the catalyst layer or through the electrolyte in direction from cathode to anode. In connection with PAFC operation, Hyde et al. [67] seem to be the first who suggested this directional migration of platinum in fuel cells. Aragane et al. [59, 60] verified this by investigating the effect of potential on the platinum distribution in PAFCs. They found that exposure to 190 °C for 1500 h at open circuit voltage (≈ 1 V) led to a high platinum dissolution from the cathode with an equal amount of redeposition in the matrix very close to the cathode. A decrease in voltage led to decreased Pt dissolution with nothing observed below 0.6 V.

Similar to the case for PAFCs, the platinum deposition within the polymer electrolyte of LT-PEMFCs has been reviewed by Zhang et al. [8]. Yasuda et al. [68] observed the platinum deposition when maintaining an MEA at a

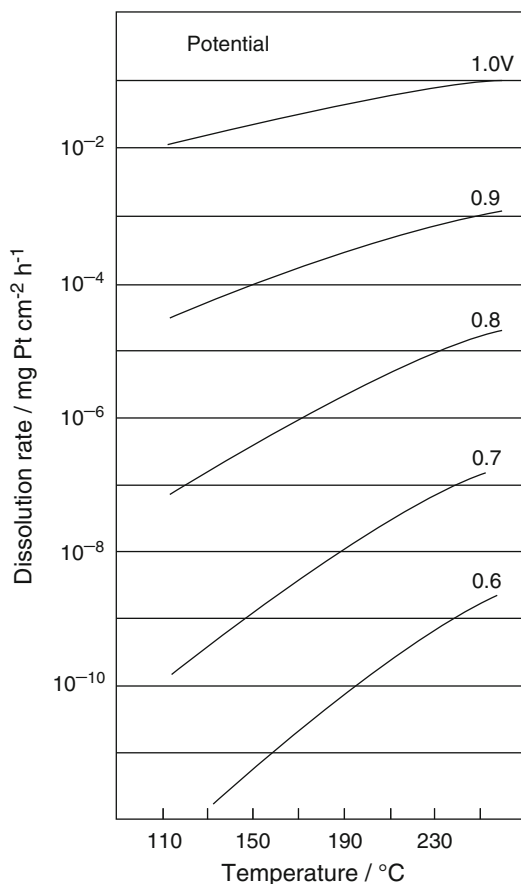


Fig. 22.4 Theoretically estimated platinum dissolution rates for various potentials as a function of temperature [60]. Estimates were based on solubility data from Bindra et al. [58]. Reproduced with permission of Springer

potential of 1.0 V. In the absence of hydrogen in the anode compartment, platinum was transported across the membrane and deposited on the anode layer. However, when hydrogen was present in the anode compartment, an accelerated platinum reduction took place in the membrane nearer to the cathode catalyst layer. When both hydrogen and oxygen were present in their respective compartments, the accelerated platinum reduction was less pronounced, ascribed to the lower hydrogen concentration in the membrane [2]. To the authors' knowledge, platinum deposition within the polymer electrolyte has yet to be conclusively reported in the case of HT-PEMFCs. However, as this degradation mechanism is evident both for PAFCs and

LT-PEMFCs, it seems reasonable to assume that a similar degradation mode takes place within HT-PEMFC MEAs.

22.4.2 Carbon Support Corrosion

In acid electrolytes the mechanism of carbon support corrosion is generally thought to proceed via a three-step process involving four electrons [52, 69]. The first step is carbon oxidation followed by formation of carbon surface oxide intermediates as revealed by voltammetric [70, 71] and spectrometric [72–74] studies. The last step must then involve hydrolysis of the carbon surface oxide, leading to formation of carbon dioxide, which is the thermodynamically favorable product at potentials higher than 0.207 V [52]. The cathode potential is normally far above this value and is therefore a driving force for carbon corrosion, though the sluggish kinetics makes it feasible to use carbon as support materials for catalysts. Clearly, the kinetics are influenced by temperature, making the carbon corrosion a more severe issue for HT-PEMFCs as compared to LT-PEMFCs. Under operation at the open circuit voltage and 180 °C for 224 h, Qi et al. [75] found that the cathodic platinum particle size increased by five times whereas the anodic catalyst particle size remained unchanged. The growth can be attributed to the Ostwald ripening as well as particle agglomeration and coalescence, which are accelerated by carbon corrosion.

During start-up and shutdown of a PEMFC, the local cathode potential can be even higher than the open circuit potential for a short period of time, which significantly speeds up the carbon corrosion [38]. A major consequence of carbon corrosion is the detachment of platinum, triggering the agglomeration of nanoparticles. Another consequence is the reduced hydrophilicity of the catalyst layer. Although hydrophilicity/hydrophobicity is not critical in relation to water management as in the LT-PEMFCs, it is still relevant in HT-PEMFCs for controlling the phosphoric acid distribution.

Significant work was carried out on carbon corrosion under operating conditions in PAFCs [76] as well as in PEMFCs [77]. The literature indicates that high surface area carbon blacks used as PEMFC catalyst support materials are quite susceptible to corrosion. For carbon supports with various platinum loadings, Stevens et al. [4] showed significantly enhanced carbon corrosion when temperature increased from 125 to 195 °C. Furthermore, Oh et al. [78] quantitatively related the first 30 min of carbon corrosion in an HT-PEMFC to that in a LT-PEMFC at potentials between 1.0 and 1.4 V. The LT-PEMFC was tested at 70 °C with fully humidified oxygen whereas the HT-PEMFC was tested at 150 °C using non-humidified oxygen. The results showed little difference in the carbon corrosion rate for potentials up to 1.1 V. At potentials higher than 1.1 V, however, the carbon corrosion rate for the HT-PEMFC increased dramatically in comparison to the LT-PEMFC. This indicates that such an increase in temperature has higher influence on the carbon corrosion than what can be offset by a decrease in humidity.

Oono et al. [79] investigated the temperature effect on the HT-PEMFC degradation in a temperature range from 150 to 190 °C. They attributed the initial performance loss, which was severely intensified with the temperature, to carbon corrosion and platinum particle

agglomeration. After a durability test at 150 °C for up to 18,000 h with a current density of 0.2 A/cm², the same group [47] observed visible thinning of the catalyst layers and growth of the platinum catalyst particles, interestingly, for both anode and cathode. Another study was made by Schmidt et al. [80] focusing on the corrosion stability of supported catalysts in PBI-based cells by alternately purging the fuel stream between hydrogen and air. This operation was found to drive the cathode potential to cycle between 0.95 and 0.2 V. During the cycling, carbon dioxide formation was found to correlate well with the catalyst support loss, which resulted in a fuel cell performance drop, particularly seen as an increased mass transport overpotential.

A suitable strategy to minimize the carbon corrosion issue is to use carbon materials which have higher graphite contents and therefore fewer structural defects at which the oxidation initiates [81]. Heat-treatment of carbon blacks at elevated temperature is known to be able to impart the graphitic character to the carbon black [77, 82, 83]. As seen from Fig. 22.5, graphitization of the carbon blacks improved the stability and catalyst durability, though at the expense of a significant decrease in the specific surface area of the support material. The specific surface area loss was found to be primarily due to the elimination of pores less than

Fig. 22.5 Corrosion current as function of heat treatment temperatures for Vulcan XC-72 and E350G carbon black supports for different potentials in hot phosphoric acid. [AA] are unpublished data by the author group and [BB] by Landsman et al. [82]

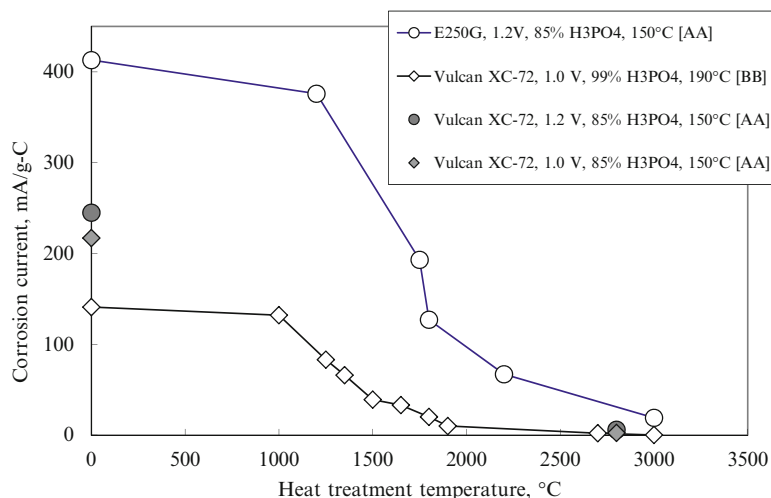


Table 22.6 Corrosion behavior of different carbon materials as re-made from Mader et al. [10] with permission of Springer

Carbon	Weight loss [%] T = 100 min	Weight loss [%] T = 800 min	BET surface area [m ² /g]	Carbon type
TIMCAL HSAG 100	2	12	130	Synthetic graphite
TIMCAL HSAG 300	4	13	280	Synthetic graphite
TIMCAL Ensaco 350G	13	73	770	Furnace black
Degussa HiBlack 40B	4	22	125	Furnace black
Degussa Printex L6	8	50	250	Furnace black
Vulcan XC72	9	35	250	Furnace black
Ketjen black	14	45	800	Furnace black
Shawinigan acetylene black	3	12	75	Thermal black

2.5 nm, which may not be available for the catalyst loading anyway.

Mader et al. [10] investigated the stability of different types of carbon for the PBI system at 180 °C and 1.0 V. Assuming the 4-electron reaction, they converted corrosion currents to weight losses as summarized in Table 22.6. It may be realized that the conventional carbon black materials corrode faster with increasing surface area. In this study, a similar trend was not evident for the high surface area graphites. A detrimental reduction of catalyst dispersion may be avoided by using such synthetic graphites.

22.4.3 Catalyst Focused Protocols

For fuel cell tests focusing on catalyst evaluation, the mass or area specific activity is determined as a steady state cathodic current of oxygen reduction respectively normalized to the initial mass or electrochemically active surface area (ECSA) of the catalyst. The DOE 2020 target is a mass activity of 0.44 A/mg-Pt. For the durability evaluation focusing on platinum catalysts, a potential cycling between 0.6 and 1.0 V is typically used under H₂/N₂ atmospheres of 1 bar. A scan rate of 50 mV/s is suggested, corresponding to 16 s per cycle. For the suggested number of 30,000 cycles, the test stretches over about a week. The DOE 2010 targets with use of this protocol are

less than 40 % loss of either the mass activity or the ECSA.

It is understood that in the cycling potential range, platinum particles experience the dissolution and redeposition that leads to decrease of surface area and therefore an activity reduction. Diagnostic measurements include the ECSA determination (under H₂/N₂) and polarization curve recording (by switching to H₂/air mode) on a regular basis. A new technique was recently developed by Engl et al. [84] for determination of the ECSA of HT-PEMFCs by CO stripping combined with real-time CO₂ exhaust gas analysis. A calibration curve for absolute ECSA determination via CO stripping was established.

For the durability evaluation focusing on the catalyst support, potentials higher than the open circuit voltage are typically applied either by cycling or by potentiostatic hold. When cycling in a potential regime that is higher than the normal open circuit voltage of the cell, the purpose of the test is usually to mimic the degradation associated with start-stop cycles. With high constant potential tests, it is the intention that the carbon supports suffer from severe corrosion while the platinum surface is kept oxidized without undergoing much dissolution and redeposition. For a potential hold at 1.2 V, the typical duration of the test is 400 h. Similar to the catalyst focussed protocol, regular measurements of the ECSA and polarization curves have been

Table 22.7 Summary of DOE catalyst evaluation protocols for LT-PEM

	Test conditions	Diagnostic metrics	End of test targets
Catalyst focused potential cycling protocol ^a	Triangular sweep cycle between 0.6–1.0 V with 50 mV/s under H ₂ /N ₂ <ul style="list-style-type: none"> Atmospheric pressure 80°C 100 % Relative humidity 	<ul style="list-style-type: none"> H₂/air polarization after 0, 1k, 5k, 10k, and 30k cycles (from 0 to ≥1.5 A/cm²) ECSA after 0, 10, 100, 1k, 3k, 10k, 20k, and 30k cycles (CV 0.05–0.6 V with 20 mV/s) Testing period 30 k cycles 	<ul style="list-style-type: none"> <30 mV voltage loss at 0.8 A/cm² <40 % mass activity loss <40 % loss of ECSA
Support focused potential hold protocol ^{a,b}	Potential holds at 1.2 V under H ₂ /N ₂ <ul style="list-style-type: none"> Atmospheric pressure 80°C 100 % Relative humidity 	<ul style="list-style-type: none"> H₂/air polarization every 24 h (from 0 to ≥1.5 A/cm²) ECSA every 24 h (CV 0.05–0.6 V with 20 mV/s) Testing period of 400 h 	<ul style="list-style-type: none"> <30 mV voltage loss at 1.5 A/cm² <40 % mass activity loss^c <40 % loss of initial ECSA

^aUSCAR Fuel Cell Tech Team, Cell component accelerated stress test and polarization curve protocols for PEM fuel cells (Revised May 26, 2010), see http://www1.eere.energy.gov/hydrogenandfuelcells/pdfs/component_durability_may_2010.pdf

^bAn alternative support protocol is a triangular sweep cycle between 1.0–1.5 V with 500 mV/s under H₂/N₂ atmosphere for a total number of 5000 cycles. Similar targets have been suggested. See U.S. DRIVE Fuel Cell Tech Team, FCTT AST polarization curve protocols for PEMFCs (Latest revision: January 14, 2013), <http://www.uscar.org/guest/teams/17/Fuel-Cell-Tech-Team>

^cThe 2020 DOE target for support stability is <10 % mass activity loss, http://energy.gov/sites/prod/files/2014/12/f19/fcto_myrrdd_fuel_cells.pdf

proposed during the test period. Also in consistent with the catalyst focussed protocol, the DOE 2010 targets with use of this test are less than 40 % loss of either the mass activity or ECSA. The test conditions proposed by DOE for electrode evaluations as per 2010 are summarised in Table 22.7. Notice that these suggested tests are purposefully derived towards LT-PEMFCs and are often modified slightly for evaluating HT-PEMFC electrodes since some specified conditions, e.g., temperature and humidity, cannot be considered relevant for the operation of the latter type of fuel cell.

22.4.4 Durable Catalysts and Supports

Significant efforts are being made to improve the durability of the support and supported catalysts for HT-PEMFCs. Liu et al. [85] introduced ZrO₂ into the carbon support in preparing 40 wt% Pt catalysts for PBI cells. After 3000 cycles between 0.6 and 1.2 V, the ZrO₂/C-supported catalyst showed a decay rate of 6 μV/cycle and

12 μV/cycle for respective current densities of 0.1 and 1 A/cm², compared to 9 and 28 μV/cycle for a Pt/C-based cathode. Recently, Perchthaler et al. [86] prepared catalysts using tungsten-based materials including carbide and oxides, showing lower degradation rates compared to the high specific surface area carbons. The catalysts were evaluated in a 20-cell HT-PEM stack for 1000 h operated with air and reformat hydrogen at 160 °C. Addition of a small amount of Al₂O₃ (up to 6 wt%) to the catalyst layer was found to form a conductive phase of dihydrophosphate, which enhanced the phosphoric acid stability as well as the electrochemical surface area of the catalysts [43].

Cleemann et al. [83] showed strong dependence of the fuel cell performance degradation on the catalyst supports. Graphitized carbon black and multi-walled carbon nanotubes as catalyst supports showed improvement in the catalyst and fuel cell durability. Further wrapping the carbon nanotubes by a polymer, e.g., PBI [87] or pyridine-containing polybenzimidazole (PyPBI) was found to improve the utilization efficiency and durability. The

Table 22.8 Acid uptake (sum of cathode and anode) of different bipolar plate materials at the EoL relative to the phosphoric acid content of the system at the BoL [93], with permission of International Electrochemistry Society

Bipolar plate material	PA _{EoL} [wt%]	Duration [h]
Phenolic resin-based graphite composite 1	23	ca. 300
Phenolic resin-based graphite composite 2	12	ca. 1600
Pyrolytically surface treated and sealed graphite	1	ca. 1600
Gold coated stainless steel	Below detection limit	ca. 1600

polymer acts as an efficient dispersant and produces a stable complex serving as a glue for immobilizing Pt nanoparticles onto the surface of multi-walled carbon nanotubes (MWCNTs) [88]. An eight times higher mass activity [89] and a four times better durability [90] were claimed by Berber and co-workers. Even with carbon blacks, impregnation with PYPBI before the platinum loading was found to facilitate the immobilization of the proton conducting path onto the surface of the electrocatalyst when further doped with poly(vinylphosphonic acid) (PVPA) instead of phosphoric acid [91].

22.5 Other Stack Components

22.5.1 Bipolar Plates

An important aspect of the development of fuel cell stacks is to make them more compact, and a key to that is to develop thinner bipolar plates preferably from metal. Especially low temperature automotive PEMFC stacks have reached impressive power densities with metallic bipolar plates. However, because of the free phosphoric acid and the elevated temperature, research and demonstration of HT-PEMFCs has so far been done almost exclusively with plates of graphite and its composite materials.

A corrosion study on the austenitic 316 L, 317 L, and 904 L stainless steels was conducted in 98 % phosphoric acid at 170 °C showing passivation regardless of the applied purge gas. When polarized at 0.1 V (hydrogen) and 0.7 V (air) in a phosphoric acid fuel cell environment,

corrosion currents at the level of mA/cm² were observed. Compared to carbon composite samples under identical conditions, 904 L showed lower currents while 316 L and 317 L showed much higher currents [92]. Harnig et al. [93] reported a study that determined the acid uptake in bipolar plate materials from MEAs using PBI membranes at 180 °C. At the EoL, the acid taken up by the bipolar plates was removed by boiling twice in water for a period of 30 min. Subsequently, the acid content was determined by titration. The acid uptake was presented relative to that in the system at the BoL as shown in Table 22.8. The high acid uptake by the composite materials was due to inherent surface porosities (<10 μm deep) that extended during the testing concurrent with corrosion of both binder and carbon phase, enhancing the acid wicking capability and increasing the hydrophilicity. In addition, the geometries of flow fields have also been shown to be of significance. A performance decay rate of 14 μV/h¹ within a period of 1000 h was reported for a cell with a spiral flow field, this being five times lower than that of another cell with a serpentine flow field [94].

22.5.2 Gas Diffusion Layers

The state-of-the-art GDL materials applied for HT-PEMFCs are much the same as the ones used for LT-PEMFCs. It seems that most of the published information is concerned with performance optimization, e.g., optimal porosity and PTFE loading. Very scarce HT-PEMFC GDL relevant information is available in terms of degradation or designated ASTs.

22.6 Lifetime Demonstration

22.6.1 Steady State Operation

Continuous steady state operation with a constant moderate load at a typical temperature of 150–160 °C is a mild mode for PBI cells. Longer lifetimes at these conditions are achieved due to (1) lack of liquid water formation, which minimizes acid washing out, (2) a maintained low voltage, which mitigates degradation of both carbon supports and catalysts. The lifetime seems very much dependent on temperature during continuous steady state operation. Extensive research has been performed particularly on PPA processed membranes (see Chap. 10). Briefly

speaking, operation times of up to 18,000 h at 150–160 °C have been shown with estimated degradation rates of 5–10 $\mu\text{V/h}$ [47, 95–97]. Table 22.9 summarizes some durability results under constant load conditions.

Focusing on polymer membranes, Yang et al. [98] studied effects of molecular weights from 30 to 94 kDa. With increased molecular weights, the polymer membranes showed enhanced chemical stability towards radical attacks under the Fenton test, reduced volume swelling upon the acid doping, and improved mechanical strength at acid doping levels of as high as about 11 mol phosphoric acid per mol polymer repeat unit. Fuel cell tests with hydrogen and air at 160 °C showed high open circuit

Table 22.9 Overall degradation rate of PBI cells under steady state operation with dry hydrogen and air (otherwise specified) at typically 150–160 °C

Lifetime test	Degradation rate	References
>2000 h at 180–200 °C and >5000 h at 150 °C:	<5 $\mu\text{V/h}$	[99]
<i>para</i> -PBI (pPBI) sol-gel membranes, at 160 °C:	4.9–6.3 $\mu\text{V/h}$ at 0.2 A/cm^2 43 $\mu\text{V/h}$ at 0.4 A/cm^2	[36, 100]
Ca. 18,000 h at 160 °C:	5–6 $\mu\text{V/h}$	[95, 96]
AB-PBI, 6000 h at 160 °C:	ca. 25 $\mu\text{V/h}$	[40, 101]
1200 h, 20 W stack with PTFE-based electrodes:	No visible degradation	[102]
>2400 h, 160 °C, 0.3 A/cm^2 :	2.4–6.4 $\mu\text{V/h}$ (copolymers)	[30]
>1500 h, 0.3 A/cm^2 at 160 °C:	1.5 $\mu\text{V/h}$ for PBI–78 kDa/10.8PA	[98]
>2000 h at 160 °C, thermally cured membranes:	0.2 A/cm^2 , 5–6 $\mu\text{V/h}$ 0.6 A/cm^2 , 43 $\mu\text{V/h}$	[29]
>6000 h	4.9–6.3 $\mu\text{V/h}$ 180 °C, 19 $\mu\text{V/h}$ (ASR increase only 30 $\text{m}\Omega\text{cm}^2$)	[103]
>2000 h, PBI & PBI-O-PhT + Zr (Acac) ₄ composite, 160 °C, 0.4 A/cm^2 :	No visible degradation	[104]
>8000 h, 160 °C, 0.2 A/cm^2 :	6–8 $\mu\text{V/h}$	[103]
780 h at 0.2 A/cm^2 , 160 °C:	~25 $\mu\text{V/h}$ (30–50 % Pt ECSA loss, 20 % membrane resistance increase, 14 times hydrogen crossover increase)	[105]
0.4 A/cm^2 ; 160 °C, reformat/air:	658 h for a 24 cell 500 W_e stack, 200–520 $\mu\text{V/h}$ 1105 h for a single cell, 41–149 $\mu\text{V/h}$	[106]
1000 h test, the spiral flow:	14 $\mu\text{V/h}$ (five times lower than the serpentine cell)	[94]
PyPBI, 180 °C, 0.2 A/cm^2 :	5.2 $\mu\text{V/h}$ (Acid loss: anode 0.6 and cathode: 15.9 $\text{ng}/(\text{cm}^2\text{h})$)	[107]
17,860 h, 150 °C, 0.2 A/cm^2 :	<4 $\mu\text{V/h}$	[47]
17,500 h, cross-linked AB-PBI, 150 °C, 0.2 A/cm^2 :	<2 $\mu\text{V/h}$	[97]
12 cell (320 cm^2) stack, 3400 h, 160–180 °C, 0.2 A/cm^2 , 33 % H_2 + 1 % CO:	first 2000 h: 24 $\mu\text{V/h}$ (followed by increased but varied cell degradation)	[108]

Table 22.10 Dynamic lifetime tests of PBI cells

Lifetime test	Decay rate	References
H ₂ /Air, 150 °C, daily on/off 7/17 h; 860 cycles, 3.5 years, 25 % loss in first 60 cycles:	ca. 300 μV/cycle or 40 μV/h	[99, 109]
H ₂ /Air, 160 °C, daily on/off 12/12 h, 260 cycles, 6500 h:	300 μV/cycle or 11 μV/h	[95, 96]
OCV for 2 min; 0.2 A/cm ² for 30 min; 0.6 A/cm ² for 30 min:	20 μV/h (OCV); 12 μV/h (0.2 A/cm ²); 19 μV/h (0.6 A/cm ²)	[39]
4000 h and 157 start-up/shutdowns; 180 °C, 0.2 A/cm ² :	480 μV/cycle or 19 μV/h ¹	[80]

voltage and power density and a low degradation rate of 1.5 μV/h at a constant load of 0.3 A/cm².

A significant piece of work was made by Oono and co-workers [47, 97]. At 150 °C and 0.2 A/cm² they performed a series test for a period of over 17,500 h with both *m*PBI and AB-PBI membranes. They found a gradual cell voltage decline until 14,000 h, after which a more rapid decrease occurred. It is assumed that the active area decrease due to catalyst agglomeration was the main reason for the initial gradual degradation and that membrane thinning, as well as acid migration, was responsible for the latter. Regions of the catalyst layers that were depleted of phosphoric acid were identified, which resulted in a reduction in the active area, causing the accelerated drop in the cell voltage after about 14,000 h of operation (Table 22.9).

22.6.2 Dynamic Test

During dynamic tests with thermal, load, and shutdown–start-up cycling, the amount and the vapor pressure of the water product varies and formation of liquid water might be involved. In addition, the shutdown–start-up or/and temperature cycling cause thermal and mechanical stresses to the membranes and cell components as well as volume expansions and contractions of the acid in the MEAs. Another important mechanism of the cell degradation involved in these dynamic tests is the corrosion of carbon supports and growth of noble metal catalysts [10]. Some dynamic test results are summarized in Table 22.10.

A thermal cycling test on a hydrogen-air cell with a daily shutdown and restart was performed under a constant cell voltage of 0.5 V by the

authors group [99, 109]. Over the first 60 daily cycles, a performance loss rate of 1.4 mA cm⁻² per cycle was observed. This performance loss is significant compared with that for steady state operation. In the following period, over more than 3 years and up to 850 cycles, a more or less stabilized performance was observed. A performance loss rate ca. 0.14 mAcm⁻² per cycle, corresponding approximately to a voltage drop rate of 300 μV per cycle or 40 μV under a constant current mode/h was observed over the whole test period.

Based on Celtec[®]-P1000 MEAs, Schmidt et al. [95, 96] reported a similar daily start-up–shutdown cycling test (12 h of operation at 160 °C followed by 12 h of shutdown). After a period of 6500 h with 260 cycles under mild conditions (160 °C and H₂/air), an average voltage drop of 300 μV per cycle was observed, corresponding to a performance loss of ca. 11 μV/h.

Staudt [39] reported another load test, by using the so-called *filled* PBI membranes, with an off time (open circuit voltage) for 2 min and an on time at 0.2 A/cm² for 30 min and at 0.6 A/cm² for 30 min. Little performance degradation was observed in the first 600 h. The performance loss was estimated to be about 20 μV/h at the open circuit voltage, 12 μV/h at 0.2 A/cm², and 19 μV/h at 0.6 A/cm², respectively, based on which a lifetime of 14,000 h was projected.

22.6.3 Effect of Fuel Impurities

The CO poisoning effect on the fuel cell performance is well known though it is significantly minimized at elevated temperatures [110–112]; though the information of the poisoning effect on

long-term durability is limited. Schmidt et al. [95] studied the effect of a realistic reformate containing 60 % H₂, 2 % CO, 5 ppm H₂S, 21 % H₂O, and CO₂ at 180 °C (see Chap. 10, Fig. 10.19). The fuel cell was operated at 0.2 A/cm² for a total of 3500 h including 3200 h of operation with H₂S containing reformate. An overall degradation rate of approximately 20 μV/h was observed, similar to that of MEAs operating with pure hydrogen. In other words, 100 % tolerance of the MEA; even when 5 ppm H₂S and 2 % CO in the anode feed were supplied continuously. On the other hand, significant effects of the fuel contaminations were reported by Mocoteguy et al. [106]. Lehnert et al. [108] constructed a 12 cell (320 cm²) stack and performed a 3400 h test at 160–180 °C with 33 % H₂, 1 % CO and different inert gases. During the first 2000 h, the stack showed an average degradation rate of 24 μV/h. In the following period, however, the degradation rate was increased and developed differently for most of the cells.

22.7 Conclusive Remarks

Durability is recognized as the most critical issue to address before commercialization of the PEMFC technology, including phosphoric acid-doped PBI cells. Major factors that are reducing the durability of PBI cells include dissolution and growth of platinum nanoparticles, corrosion of carbon supports, polymer oxidation, and membrane thinning. Operation parameters, e.g., fuel impurities, temperature, load levels, and thermal and load cycling—particularly start-ups and shutdowns—influence the durability of the cells. Higher operational temperatures impose more challenges for the material durability as the carbon corrosion, platinum dissolution, and polymer oxidation are all aggravated. The presence of phosphoric acid and its maintenance add an additional issue to the HT-PEMFC.

In this chapter the understanding of degradation mechanisms and their interaction with fuel cell durability is summarized. Oxidative degradation of the polybenzimidazoles seems to occur

at the weak link of the benzenoid rings bearing nitrogen atoms. Possible attack by the peroxide radicals inside fuel cells is assumed and has been extensively investigated by means of accelerated aging test with the Fenton agent. Significant degradation of the polymers is identified and modification of the polymer macrostructures, covalently crosslinking and ionically blending of the polymers have been shown to improve the materials durability. However, the translation of these degradation results to the fuel cell durability is by no means straightforward. This is particularly true since the effect of phosphoric acid has not been considered in most of the Fenton studies.

Acid transfer within the MEAs and its loss out of the cell are of critical concern. Via an evaporation mechanism the acid loss seems to be at a level of up to a few μg/(m² s) of the electrode area. Acid transfer within the MEAs, not necessarily resulting in acid loss out of a cell, seems more critical for the fuel cell performance degradation.

Carbon corrosion and platinum dissolution in the acidic electrolyte at elevated temperatures are well recognized from the early years of research on PAFCs and are definitely relevant to HT-PEMFCs based on the acid-doped PBI membranes. Both mechanisms are enhanced at higher temperatures and higher electrode potentials. This should be taken into account when platinum alloy catalysts are considered for the HT-PEMFC. More efforts are also needed to develop resistant support materials based on either structured carbons or non-carbon alternatives.

The stability of bipolar plates and gas diffusion layers are assumed to be of significance, but only limited information is available.

The long-term durability of HT-PEMFCs is encouraging. More than 18,000 h with an average degradation rate of around 5 μV/h have been reproducibly demonstrated under steady state operation. This is nearly halfway of the DOE targets for CHP systems for stationary applications. Other applications such as portable and APU units require significantly different testing protocols particularly with cycling operations. Degradation rates of about a few

hundred microvolts pr. cycle have been reported for start-up–shutdown cycling experiments. More evaluation on lifetime with cycling would help to define what is required of the HT-PEM MEAs in order to fulfill their specific needs.

In brief, the durability of the PBI-based technology has encouragingly showed that the HT-PEMFC is a viable option for replacing or supplementing conventional power systems; however, significant efforts are needed and are also being made to further improve the key materials, components, and the technology as a whole. In this regard, it would be beneficial if standardized ASTs were to be purposefully derived towards the testing of HT-PEM components, thus taking into account the few, but all-important, parameters that distinguish this fuel cell type from others.

Acknowledgments This work was financially supported by ForskEl program (DuRaPEM III no.2013-1-12064 and SmartMEA no.2014-1-12218) and Innovation Fund Denmark (4M Centre 0603-00527B).

References

- Xie J, Wood DL, Wayne DM et al (2005) Durability of PEFCs at high humidity conditions. *J Electrochem Soc* 152:A104–A113
- Yasuda K, Taniguchi A, Akita T et al (2006) Platinum dissolution and deposition in the polymer electrolyte membrane of a PEM fuel cell as studied by potential cycling. *Phys Chem Chem Phys* 8:746–752
- Knights SD, Colbow KM, St-Pierre J et al (2004) Aging mechanisms and lifetime of PEFC and DMFC. *J Power Sources* 127:127–134
- Stevens DA, Dahn JR (2005) Thermal degradation of the support in carbon-supported platinum electrocatalysts for PEM fuel cells. *Carbon* 43:179–188
- Taniguchi A, Akita T, Yasuda K et al (2004) Analysis of electrocatalyst degradation in PEMFC caused by cell reversal during fuel starvation. *J Power Sources* 130:42–49
- Borup R, Meyers J, Pivovar B et al (2007) Scientific aspects of polymer electrolyte fuel cell durability and degradation. *Chem Rev* 107:3904–3951
- Wu J, Yuan XZ, Martina JJ et al (2008) A review of PEM fuel cell durability: degradation mechanisms and mitigation strategies. *J Power Sources* 184:104–119
- Zhang SS, Yuan XZ, Wang HJ et al (2009) A review of accelerated stress tests of MEA durability in PEM fuel cells. *Int J Hydrogen Energy* 34:388–404
- Shao YY, Yin GP, Wang ZB et al (2007) Proton exchange membrane fuel cell from low temperature to high temperature: material challenges. *J Power Sources* 167:235–242
- Mader J, Xiao L, Schmidt TJ et al (2008) Polybenzimidazole/acid complexes as high-temperature membranes. Springer, Heidelberg, pp 63–124
- <http://energy.gov/eere/fuelcells/downloads/fuel-cell-technologies-office-multi-year-research-development-and-22>
- Li QF, Jensen JO, Savinell RF et al (2009) High temperature proton exchange membranes based on polybenzimidazoles for fuel cells. *Prog Polym Sci* 34:449–477
- Maier W, Arlt T, Wannek C et al (2010) In-situ synchrotron X-ray radiography on high temperature polymer electrolyte fuel cells. *Electrochem Commun* 12:1436–1438
- Gaudiana R, Conley RT (1969) Weak-link versus active carbon degradation routes in the oxidation of aromatic heterocyclic systems. *J Polym Sci B* 7:793
- Samms SR, Wasmus S, Savinell RF (1996) Thermal stability of proton conducting acid doped polybenzimidazole in simulated fuel cell environments. *J Electrochem Soc* 143:1225–1232
- Musto P, Karasz FE, Macknight WJ (1993) Fourier transform infra-red spectroscopy on the thermo-oxidative degradation of polybenzimidazole and of a polybenzimidazole/polyetherimide blend. *Polymer* 34:2934
- Li QF, Pan C, Jensen JO et al (2007) Cross-linked polybenzimidazole membranes for fuel cells. *Chem Mater* 19:350–352
- Kerres J, Schönberger F, Chromik A et al (2008) Partially fluorinated arylene polyethers and their ternary blend membranes with PBI and H₃PO₄. Part I. Synthesis and characterisation of polymers and binary blend membranes. *Fuel Cells* 8:175–187
- Lobato J, Cañizares P, Rodrigo MA et al (2007) Improved polybenzimidazole films for H₃PO₄-doped PBI-based high temperature PEMFC. *J Membr Sci* 306:47–55
- Li QF, Rudbeck HC, Chromik A et al (2010) Properties, degradation and high temperature fuel cell test of different types of PBI and PBI blend membranes. *J Membr Sci* 347:260–270
- Liao JH, Li Q, Rudbeck HC et al (2011) Oxidative degradation of polybenzimidazole membranes as electrolytes for high temperature proton exchange membrane fuel cells. *Fuel Cells* 11:745–755
- Liao J, Yang J, Li Q et al (2013) Oxidative degradation of acid doped polybenzimidazole membranes and fuel cell durability in the presence of ferrous ions. *J Power Sources* 238:516–522

23. Chang Z, Pu H, Wan D et al (2010) Effects of adjacent groups of benzimidazole on antioxidation of polybenzimidazoles. *Polym Degrad Stab* 95:2648–2653
24. Xu HJ, Chen KC, Guo XX et al (2007) Synthesis of novel sulfonated polybenzimidazole and preparation of cross-linked membranes for fuel cell application. *Polymer* 48:5556–5564
25. Chang ZH, Pu HT, Wan DC et al (2009) Chemical oxidative degradation of Polybenzimidazole in simulated environment of fuel cells. *Polym Degrad Stab* 94:1206–1212
26. Han M, Zhang G, Liu Z et al (2011) Cross-linked polybenzimidazole with enhanced stability for high temperature proton exchange membrane fuel cells. *J Mater Chem* 21:2187–2193
27. Aili D, Hansen MK, Pan C et al (2011) Phosphoric acid doped membranes based on Nafion[®], PBI and their blends—membrane preparation, characterization and steam electrolysis testing. *Int J Hydrogen Energy* 36:6985–6993
28. Aili D, Li Q, Christensen E et al (2011) Crosslinking of polybenzimidazole membranes by divinylsulfone post-treatment for high-temperature proton exchange membrane fuel cell applications. *Polym Int* 60:1201–1207
29. Aili D, Cleemann LN, Li Q et al (2012) Thermal curing of PBI membranes for high temperature PEM fuel cells. *J Mater Chem* 22:5444–5453
30. Yang J, Li Q, Cleemann LN et al (2012) Synthesis and properties of poly(aryl sulfone benzimidazole) and its copolymers for high temperature membrane electrolytes for fuel cells. *J Mater Chem* 22:11185–11195
31. Yang J, Li Q, Cleemann LN et al (2013) Crosslinked hexafluoropropylidene polybenzimidazole membranes with chloromethyl polysulfone for fuel cell applications. *Adv Energy Mater* 3:662–630
32. Wannek C, Konradi I, Mergel J et al (2009) Redistribution of phosphoric acid in membrane electrode assemblies for high-temperature polymer electrolyte fuel cells. *Int J Hydrogen Energy* 34:9479–9485
33. Li QF, He RH, Berg RW et al (2004) Water uptake and acid doping of polybenzimidazoles as electrolyte membranes for fuel cells. *Solid State Ion* 168:177–185
34. Mori T, Honji A, Kahara T et al (1988) Acid absorbancy of an electrode and its cell performance history. *J Electrochem Soc* 135:1104–1109
35. Brown EH, Whitt CD (1952) Vapor pressure of phosphoric acid. *Ind Eng Chem* 44:615–618
36. Yu S, Xiao L, Benicewicz BC (2008) Durability studies of PBI-based high temperature PEMFCs. *Fuel Cells* 8:165–174
37. Fontana B (1951) The vapor pressure of water over phosphoric acids. *J Am Chem Soc* 73:3348–3350
38. Büchi FN, Inaba M, Schmidt TJ (2009) *Polymer electrolyte fuel cell durability*. Springer, New York
39. Staudt R (2006) Development of polybenzimidazole-based high temperature membrane and electrode assemblies for stationary applications. Annual Progress Report 2006
40. Wannek C, Kohnen B, Oetien HF et al (2008) Durability of ABPBI-based MEAs for high temperature PEMFCs at different operating conditions. *Fuel Cells* 8:87–95
41. Oono Y, Sounai A, Hori M (2009) Influence of the phosphoric acid-doping level in a polybenzimidazole membrane on the cell performance of high-temperature proton exchange membrane fuel cells. *J Power Sources* 189:943–949
42. Pinar FJ, Cañizares P, Rodrigo MA et al (2011) Scale-up of a high temperature polymer electrolyte membrane fuel cell based on polybenzimidazole. *J Power Sources* 196:4306–4313
43. Oh HS, Cho Y, Lee WH et al (2013) Modification of electrodes using Al₂O₃ to reduce phosphoric acid loss and increase the performance of high-temperature proton exchange membrane fuel cells. *J Mater Chem A* 1:2578–2581
44. Akita H, Ichikawa M, Nosaki K et al (2000) Solid polymer electrolytes. US Patent 6,124,060
45. Arlt T, Maier W, Totzke C et al (2014) Synchrotron X-ray radioscopic in situ study of high-temperature polymer electrolyte fuel cells—effect of operation conditions on structure of membrane. *J Power Sources* 246:290–298
46. Boillat P, Biesdorf J, Oberholzer P et al (2014) Evaluation of neutron imaging for measuring phosphoric acid distribution in high temperature PEFCs. *J Electrochem Soc* 161:F192–F198
47. Oono Y, Sounai A, Hori M (2012) Long-term cell degradation mechanism in high-temperature proton exchange membrane fuel cells. *J Power Sources* 210:366–373
48. Martin S, Li Q, Steenberg T et al (2014) Binderless electrodes for high-temperature polymer electrolyte membrane fuel cells. *J Power Sources* 272:559–566
49. Eberhardt SH, Marone F, Stampanoni M et al (2014) Quantifying phosphoric acid in high-temperature polymer electrolyte fuel cell components by X-ray tomographic microscopy. *J Synchrotron Radiat* 21:1319–1326
50. Zhang S, Yuan X-Z, Hin JNC et al (2009) A review of platinum-based catalyst layer degradation in proton exchange membrane fuel cells. *J Power Sources* 194:588–600
51. Shao YY, Yin GP, Gao YZ (2007) Understanding and approaches for the durability issues of Pt-based catalysts for PEM fuel cell. *J Power Sources* 171:558–566
52. Zhang J (2008) *PEM fuel cell electrocatalysts and catalyst layers: fundamentals and applications*. Springer, London
53. Honji A, Mori T, Tamura K et al (1988) Agglomeration of platinum particles supported on carbon in phosphoric acid. *J Electrochem Soc* 135:355–359

54. Tseung ACC, Dhara SC (1975) Loss of surface-area by platinum and supported platinum electrocatalyst. *Electrochim Acta* 20:681–683
55. Yu P, Pemberton M, Plasse P (2005) PtCo/C cathode catalyst for improved durability in PEMFCs. *J Power Sources* 144:11–20
56. Colon-Mercado HR, Kim H, Popov BN (2004) Durability study of Pt₃Ni₁ catalysts as cathode in PEM fuel cells. *Electrochem Commun* 6:795–799
57. Inaba M (2009) Durability of electrocatalysts in polymer electrolyte fuel cells. *ECS Trans* 25:573–581
58. Bindra P, Clouser SJ, Yeager E (1979) Platinum dissolution in concentrated phosphoric acid. *J Electrochem Soc* 126:1631–1632
59. Aragane J, Murahashi T, Odaka T (1988) Change of Pt distribution in the active components of phosphoric acid fuel cell. *J Electrochem Soc* 135:844–850
60. Aragane J, Urushibata H, Murahashi T (1996) Effect of operational potential on performance decay rate in a phosphoric acid fuel cell. *J Appl Electrochem* 26:147–152
61. Wang XP, Kumar R, Myers DJ (2006) Effect of voltage on platinum dissolution relevance to polymer electrolyte fuel cells. *Electrochem Solid-State Lett* 9:A225–A227
62. Pourbaix M (1974) Atlas of electrochemical equilibria in aqueous solutions', Texas, Section 13.6, Platinum. In: Van Muylder J, De Zoubov N, Pourbaix M (eds) published by National Association of Corrosion Engineers, p 378–383
63. Ferreira PJ, la O GJ, Shao-Horn Y et al (2005) Instability of Pt/C electrocatalysts in proton exchange membrane fuel cells—a mechanistic investigation. *J Electrochem Soc* 152:A2256–A2271
64. Ahluwalia RK, Arisetty S, Wang X et al (2013) Thermodynamics and kinetics of platinum dissolution from carbon-supported electrocatalysts in aqueous media under potentiostatic and potentiodynamic conditions. *J Electrochem Soc* 160:F447–F455
65. Mitsushima S, Koizumi Y, Uzuka S et al (2008) Dissolution of platinum in acidic media. *Electrochim Acta* 54:455–460
66. Matsumoto M, Miyazaki T, Imai H (2011) Oxygen-enhanced dissolution of platinum in acidic electrochemical environments. *J Phys Chem C* 115:11163–11169
67. Hyde PJ, Maggiore CJ, Srinivasan S (1984) Use of a nuclear microprobe in the study of fuel cell electrodes. *J Electroanal Chem* 168:383–394
68. Yasuda K, Taniguchi A, Akita T et al (2006) Characteristics of a platinum black catalyst layer with regard to platinum dissolution phenomena in a membrane electrode assembly. *J Electrochem Soc* 153:A1599–A1603
69. Roen LM, Paik CH, Jarvic TD (2004) Electrocatalytic corrosion of carbon support in PEMFC cathodes. *Electrochem Solid-State Lett* 7:A19–A22
70. Loutfy RO (1986) Electrochemical characterization of carbon black. *Carbon* 24:127–130
71. Kinoshita K, Bett JAS (1973) Potentiodynamic analysis of surface oxides on carbon blacks. *Carbon* 11:403–411
72. Antonucci PL, Pino L, Giordano N et al (1989) A comparative analysis of structural and surface effects in the electrochemical corrosion of carbons. *Mater Chem Phys* 21:495–506
73. Rositani F, Antonucci PL, Minutoli M et al (1987) Infrared analysis of carbon blacks. *Carbon* 25:325–332
74. Kangasniemi KH, Condit DA, Jarvi TD (2004) Characterization of Vulcan electrochemically oxidized under simulated PEM fuel cell conditions. *J Electrochem Soc* 151:E125–E132
75. Qi ZG, Buelte S (2006) Effect of open circuit voltage on performance and degradation of high temperature PBI-H₃PO₄ fuel cells. *J Power Sources* 161:1126–1132
76. Kinoshita K, Bett J (1973) Electrochemical oxidation of carbon-black in concentrated phosphoric acid at 135°C. *Carbon* 11:237–247
77. Mathias MF, Makharia R, Gasteiger HA et al (2005) *J Electrochem Soc Interface* 14:24–35
78. Oh H-S, Lee J-H, Kim H (2012) Electrochemical carbon corrosion in high temperature proton exchange membrane fuel cells. *Int J Hydrogen Energy* 37:10844–10849
79. Oono Y, Fukuda T, Sounai A et al (2010) Influence of operating temperature on cell performance and endurance of high temperature proton exchange membrane fuel cells. *J Power Sources* 195:1007–1014
80. Hartnig C, Schmidt TJ (2011) Simulated start-stop as a rapid aging tool for polymer electrolyte fuel cell electrodes. *J Power Sources* 196:5564–5572
81. Ferreira-Aparicio P, Folgado MA, Daza L (2009) High surface area graphite as alternative support for proton exchange membrane fuel cell catalysts. *J Power Sources* 192:57–62
82. Landsman DA, Luczak FJ (2003) Catalyst studies and coating technologies. In: Vielstich W, Lamm A, Gasteiger HA (eds) *Handbook of fuel cells*, vol 3. Wiley, London, pp 811–831
83. Cleemann LN, Buazar F, Li Q et al (2013) Catalyst degradation in high temperature proton exchange membrane fuel cells based on acid doped polybenzimidazole membranes. *Fuel Cells* 13:822–831
84. Engl T, Waltar KE, Gubler L et al (2014) Second cycle is dead: advanced electrode diagnostics for high-temperature polymer electrolyte fuel cells. *J Electrochem Soc* 161:F500–F505
85. Liu G, Zhang HM, Zhai YF et al (2007) Pt₄ZrO₂/C cathode catalyst for improved durability in high temperature PEMFC based on H₃PO₄ doped PBI. *Electrochem Commun* 9:135–141

86. Perchthaler M, Ossiander T, Juhart V et al (2013) Tungsten materials as durable catalyst supports for fuel cell electrodes. *J Power Sources* 243:472–480
87. Okamoto M, Fujigaya T, Nakashima N (2009) Design of an assembly of poly(benzimidazole), carbon nanotubes, and Pt nanoparticles for a fuel-cell electrocatalyst with an ideal interfacial nanostructure. *Small* 5:735–740
88. Fujigaya T, Okamoto M, Nakashima N (2009) Design of an assembly of pyridine-containing polybenzimidazole, carbon nanotubes and Pt nanoparticles for a fuel cell electrocatalyst with a high electrochemically active surface area. *Carbon* 47:3227–3232
89. Hafez IH, Berber MR, Fujigaya T et al (2014) Enhancement of platinum mass activity on the surface of polymer-wrapped carbon nanotube-based fuel cell electrocatalysts. *Sci Rep* 4:8
90. Berber MR, Hafez IH, Fujigaya T et al (2014) Durability analysis of polymer-coated pristine carbon nanotube-based fuel cell electrocatalysts under non-humidified conditions. *J Mater Chem A* 2:19053–19059
91. Berber MR, Fujigaya T, Nakashima N (2014) High-temperature polymer electrolyte fuel cell using poly(vinylphosphonic acid) as an electrolyte shows a remarkable durability. *ChemCatChem* 6:567–571
92. Wang HL, Turner JA (2008) Austenitic stainless steels in high temperature phosphoric acid. *J Power Sources* 180:803–807
93. Hartmig C, Schmidt TJ (2011) On a new degradation mode for high-temperature polymer electrolyte fuel cells: how bipolar plate degradation affects cell performance. *Electrochim Acta* 56:4237–4242
94. Liu F, Kvesic M, Wippermann K et al (2013) Effect of spiral flow field design on performance and durability of HT-PEFCs. *J Electrochem Soc* 160: F892–F897
95. Schmidt TJ, Baurmeister J (2006) Durability and reliability in high-temperature reformed hydrogen PEFCs. *ECS Trans* 3:861–869
96. Schmidt TJ, Baurmeister J (2008) Properties of high-temperature PEFC Celtec (R)-P 1000 MEAs in start/stop operation mode. *J Power Sources* 176 (2):428–434
97. Oono Y, Sounai A, Hori M (2013) Prolongation of lifetime of high temperature proton exchange membrane fuel cells. *J Power Sources* 241:87–93
98. Yang JS, Cleemann LN, Steenberg T et al (2014) High molecular weight polybenzimidazole membranes for high temperature PEMFC. *Fuel Cells* 14:7–15
99. Li Q, He R, Jensen JO et al (2004) PBI-based polymer membranes for high temperature fuel cells—preparation, characterizations and fuel cell demonstrations. *Fuel Cells* 4:147–159
100. Xiao L, Zhang H, Scanlon E et al (2005) High-temperature polybenzimidazole fuel cell membranes via a sol-gel process. *Chem Mater* 17:5328–5333
101. Stolten D, Wannek C, Dohle H, Blum L, Mergel J, Peters R (2007) Strategy, status and outlook for HTPEFC development for APU application (Abstract 162). *Fuel Cell Seminar 2007*, San Antonio, 15–19 Oct 2007
102. Lee H-J, Kim BG, Lee DH et al (2011) Demonstration of a 20 W class high-temperature polymer electrolyte fuel cell stack with novel fabrication of a membrane electrode assembly. *Int J Hydrogen Energy* 36:5521–5526
103. Galbiati S, Baricci A, Casalegno A et al (2013) Degradation in phosphoric acid doped polymer fuel cells: a 6000 h parametric investigation. *Int J Hydrogen Energy* 38:6469–6480
104. Kondratenko MS, Ponomarev II, Gallyamov MO et al (2013) Novel composite Zr/PBI-O-PhT membranes for HT-PEFC applications. *Beilstein J Nanotechnol* 4:481–492
105. Modestov AD, Tarasevich MR, Filimonov VY et al (2009) Degradation of high temperature MEA with PBI-H₃PO₄ membrane in a life test. *Electrochim Acta* 54:7121–7127
106. Mocoteguy P, Ludwig B, Scholta J et al (2009) Long term testing in continuous mode of HT-PEMFC based H₃PO₄/PBI Celtec-P MEAs for μ -CHP applications. *Fuel Cells* 9:325–348
107. Molle MA, Chen X, Ploehn HJ et al (2014) High polymer content 3,5-pyridine-polybenzimidazole copolymer membranes with improved compressive properties. *Fuel Cells* 14:16–25
108. Janßen H, Supra J, Lüke L et al (2013) Development of HT-PEFC stacks in the kW range. *Int J Hydrogen Energy* 38:4705–4713
109. Li Q (2005) High temperature proton exchange membranes for fuel cells. Department of Chemistry, Technical University of Denmark, Kgs Lyngby
110. Qian G, Benicewicz BC (2011) Fuel impurity effects on high temperature PBI based fuel cell membranes. In: Gasteiger HA, Weber A, Narayanan SR, Jones D, Strasser P, Swider Lyons K et al (eds) *Polymer electrolyte fuel cells* 11. Electrochemical Society, Pennington, pp 1441–1448
111. Das SK, Reis A, Berry KJ (2009) Experimental evaluation of CO poisoning on the performance of a high temperature proton exchange membrane fuel cell. *J Power Sources* 193:691–698
112. Li QF, He RH, Gao JA et al (2003) The CO poisoning effect in PEMFCs operational at temperatures up to 200 °C. *J Electrochem Soc* 150: A1599–A1605

High Temperature Polymer Electrolyte Fuel Cell Systems for Aircraft Applications

23

Wendelin Waiblinger, Josef Kallo, Johannes Schirmer,
and K. Andreas Friedrich

Abbreviations

a_p	Power specific fuel cell area ($\text{m}^2 \text{kW}^{-1}$)
m_c	Conversion factor (38.4) ($\text{kgs mol}^{-1} \text{h}^{-1}$)
m_{fcvar}	Area specific variable fuel cell stack mass factor (kg m^{-2})
m_{sys}	Power specific system mass factor (kg kW^{-1})
\dot{m}_{fuel}	Fuel consumption (kg h^{-1})
\bar{M}	Mean aircraft mass during flight (kg)
M_{fc}	Mass of the fuel cell system (kg)
M_{fix}	Fixed mass of the fuel cell stack (kg)
M_{fuel}	Fuel on board at the beginning of flight (kg)
M_{max}	Available mass for the fuel and the fuel cell system (kg)
MTOW	Maximum takeoff weight (kg)
\bar{P}_{SLF}	Mean power for propulsion during flight (kW)
t_{op}	Flight endurance (h)
λ_a	Anode stoichiometry (–)
λ_c	Cathode stoichiometry (–)

23.1 Introduction

The high electrical efficiency of fuel cells and their operation using renewable fuels are the main drivers for various energy conversion applications, namely stationary power plant, vehicle propulsion, and space applications. Interestingly, the aircraft sector is also becoming increasingly interested in fuel cell technology. In comparison to the mass markets related to transportation, namely passenger cars and buses, with their respective substantial financial resources and research on fuel cell systems and related material development, research on and the application of fuel cells in the aircraft industry in the last two decades have been minor. Surprisingly, this special application requires a variety of novel functionalities that fuel cell systems can address. Furthermore, the aircraft market permits higher specific costs and can directly profit from the developments in the automotive industry.

In a commercial aircraft, fuel cell systems can replace current Auxiliary Power Units (APUs) or minimize the installed power-unit on the main engine shaft (e.g., Airbus A320-A340 or Boeing B737-B787), fulfilling the need for electric energy on board during a wide variety of flight and ground phases [1–5]. On the way to a more electrical aircraft without air bleed and with reduced hydraulic systems, fuel cells can provide an efficient method to facilitate reliable and

W. Waiblinger • J. Kallo (✉) • J. Schirmer
K.A. Friedrich
Institute of Engineering Thermodynamics,
German Aerospace Center, Pfaffenwaldring 38-40,
Stuttgart 70569, Germany
e-mail: Josef.kallo@dlr.de

controllable electric power generation. Furthermore, regarding safety in flight, the nitrogen-enriched cathode off-gas (equivalent to oxygen-depleted air) of a fuel cell can be used as an inert gas for the kerosene tanks. The low oxygen concentration prevents the development of flammable mixtures during all flight phases. In addition, the water collected by drying the oxygen depleted air can be used for sanitation and lavatory purposes. The amount of water produced during flight offers a major gravimetric advantage because it results in a lower takeoff and climb mass.

In addition, there is an increasing interest in fuel cell systems for General Aviation aircraft and Unmanned Airborne Vehicles (UAV) [6–10]. Using a fuel cell system as the main power source for propulsion and by fueling the aircraft with “green” hydrogen produced from excess renewable energy, complete CO₂-free and particle-free flight can be realized. An airplane with 6–8 seats, a 3000 kg maximum take-off weight (MTOW), a 500 kg payload, a range of 880 km, and a cruise speed of 150 KTS (278 km/h) can feasibly be produced in 5–8 years. However, electric fuel cell-propelled aircraft with more than 50 passenger seats remains a vision. In contrast, UAVs with 20–23 m wingspans, a MTOW of 1300 kg, and cruising speeds of 130 km/h appear attractive for achieving long-endurance flight. Continuous flight times of 36 h appear realistic with a payload of approximately 150 kg.

23.2 Specific Aircraft Considerations

To utilize the benefits of fuel cells in these applications, it is crucial to realize high electrical system efficiencies along with high power densities. Therefore, a complete system evaluation is necessary, considering all flight phases. Every component of the system, e.g., the fuel storage subsystem, the fuel cell itself, its thermal management periphery, and the safety and control subsystems, have to be evaluated with regard to weight savings. A more detailed overview of a

possible system layout is given in the following sections. The typical flight envelopes, both in commercial and in General Aviation/UAV airplanes, imply reliable operation at very low (down to $-47\text{ }^{\circ}\text{C}$) and very high (up to $55\text{ }^{\circ}\text{C}$) ambient temperatures. This may be a substantial challenge that fuel cells might not be able to meet. However, in most aircraft applications, specific procedures based on checklists as well as start-up procedures are common before a plane is operated. An external energy source, mainly a ground power unit (GPU), can be used in a prestart process. To achieve an adequate operating temperature, a conditioning time of up to 60 min is typical and reasonable. After start-up, a slightly insulated system can work at very low ambient temperatures by self-sustaining its temperature level. At an elevated ambient temperature (up to $55\text{ }^{\circ}\text{C}$), a high temperature polymer electrolyte fuel cell (HT-PEFC) system (with an operating temperature of $170\text{ }^{\circ}\text{C}$) has an advantage compared to a low-temperature PEFC (operated at a maximum of $80\text{ }^{\circ}\text{C}$) due to more effective heat rejection. Furthermore, on ground, convective heat management systems can be used to enhance heat rejection. In flight, a sophisticated cooling architecture using heat radiation sinks and low drag convective heat exchangers is necessary. By simple calculations based on the Stefan-Boltzmann law, there is a three times higher cooling potential due to heat radiation at $170\text{ }^{\circ}\text{C}$ compared to $80\text{ }^{\circ}\text{C}$. For the realization of a heat radiation sink, the metal skin of the airplane can be used. For future carbon fiber aircraft structures, the maximum desired skin temperature should not exceed $70\text{ }^{\circ}\text{C}$ to ensure its long-term use. For this purpose, a second thermal management subsystem design with a convective heat exchanger would be necessary. Comparing the convective cooling potentials in flight at high altitudes, low air density, and low ambient temperatures, the cooling power is higher by a factor of 1.5 for the higher working temperature of a HT-PEFC. A convective heat exchanger with air intake and flow channels, unfortunately, adds an additional drag, deteriorating the aerodynamics of the aircraft. A custom assessment is therefore crucial for each aircraft design and

mission. A further design parameter influencing technology selection is the need for an oxygen-depleted air (ODA) system in the aircraft. To reject the heat produced in the stack by the electrochemical reaction using cathode gases, a high air stoichiometry of 4–12 is needed. To achieve a sufficiently low oxygen concentration in the cathode exhaust air and to reliably fulfill the <12 vol.% O₂ requirements of the FAA (Federal Aviation Administration) [11], a cathode air stoichiometry lower than 1.9 is needed. Therefore, a cooling system using a liquid heat transport fluid appears to be necessary. Further aspects of a liquid-cooled system related to system efficiency will be discussed later.

As previously mentioned, during flight, the air density changes significantly. The air pressure at 0 MSL (mean sea level) is approximately 1 bar, and at 10,000 m MSL, the air pressure is 260 mbar. Due to water-free proton transport in the HT-PEFC electrolyte, a constant conductivity of the membrane can be expected for low air densities. Figure 23.1a shows a lab test measurement of an HT-PEFC 70 cell stack (49 cm²) at varying ambient pressures from 1 bar to 660 mbar. The decrease in performance at low pressure is moderate compared to a low temperature PEFC, which experiences pronounced drying of the membrane, with an approximately

20 % power density decrease at 660 mbar. The ohmic resistance at high current densities remains constant, and the loss in performance is related to the oxygen partial pressure. The somewhat greater decrease in Fig. 23.1a at 660 mbar was due to an experimental air flow limitation. The operation of an HT-PEFC system from Serenergy A/S in the motorglider Antares DLR-H2 is shown in Fig. 23.1b at low altitudes (circular symbols) and at 2500 m (square symbols). It can be observed that, in general, the assumption of pressure independence was confirmed in these flights, but a somewhat lower performance at higher current densities at 2500 m is interpreted as the result of insufficient air supply.

The main benefit of HT-PEFCs for aircraft applications is their power independence on ambient pressure. The use of liquid-cooled HT-PEFC technology for aircraft applications would be highly advantageous. In the following sections, we focus on advanced liquid-cooled systems and discuss our experience with the design of a 20 kW_{el} HT-PEFC system from Serenergy A/S, who cooperates with DLR in developing aircraft applications, mainly aiming at long endurance and superior gravimetric performance of the aircraft propulsion system.

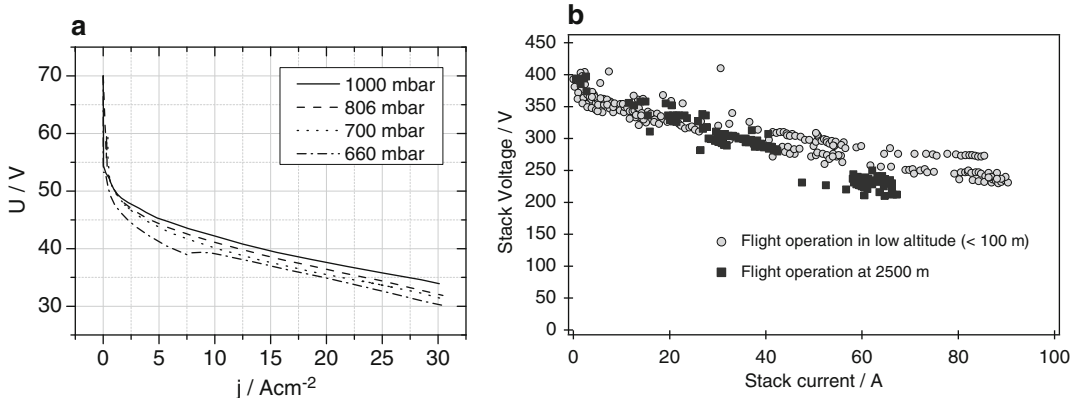


Fig. 23.1 (a) Voltage behavior of an air-cooled HT-PEFC system with variations in the ambient pressure in a low-pressure chamber, where the cathode

stoichiometry $\lambda_c = 3\text{--}6$; (b) Operation of air-cooled Serenergy fuel cell systems in the Antares DLR-H2 at low altitudes and at 2500 m

23.3 Basic Considerations on Fuels and Fuel Cell Technology in Aviation

When maximum flight endurance is the objective, the choice of fuel is most important. Fuel storage and supply systems, fuel pretreatment, fuel processing as well as the choice of fuel cell technology is strongly dependent on the fuel considered. Basically, all required system components have to be evaluated in this context. Compared to all other fuels, hydrogen can be fed to the fuel cell without pretreatment, making it suitable for a simple system design. Because of its low mass density, hydrogen is stored either under high pressure or in cryogenic tanks. Both storage methods add additional weight to the actual fuel system. Alternatively, hydrocarbons, such as alkanes or alcohols, can act as hydrogen carriers, with a gravimetric energy density that is higher than hydrogen if the tank or storage system is considered. In contrast, additional weight and system complexity is required for extracting hydrogen from hydrocarbons.

The fuel to be chosen in the context of endurance depends not only on the gravimetric energy density of the storage system but also on the characteristics of each individual subsequent fuel processing step. In particular, the reforming

temperature, the specific enthalpy for hydrogen production, and the steam-to-carbon ratio (S/C) are to be considered. A comparison of some exemplary fuels that can be used as chemical hydrogen storage is shown in Table 23.1.

In contrast to pure hydrogen, hydrocarbons are converted in a reforming process, generating a hydrogen-rich reformat gas that can be fed to the fuel cell. Steam reforming, in principle, is an endothermic process that requires an external heat supply. Compared to autothermal reforming, the reformat gas is not diluted with nitrogen.

23.3.1 Temperature of the Reforming Process

Reforming temperatures yielding maximum hydrogen and minimum CO output, in practice, depend on the fuel, process management and hardware, e.g., the catalyst. Typical temperature ranges are depicted in Table 23.2. Low reforming temperatures are favored for several reasons. When heat for reforming is supplied via combustion, the temperature of the burner off-gas is limited because of the materials of the hardware and because of heat loss via radiation. The temperature difference and, accordingly, the heat

Table 23.1 Comparison of mass- and energy density related parameters of potential fuels for fuel cell applications in aviation

Fuel	Formula	Mass density kg/m ³	LHV MJ/kg	C content wt. %	H ₂ content (fuel) wt. %	H ₂ content (fuel + tank) wt. %
Hydrogen	H ₂	0.09 (g)	120.0	0.0	100	6 (420 bar) [12]
						7.4 (cryogen) [13]
Methane	CH ₄	0.72	47.8	75.0	25.0	10 (200 bar) [12]
Methanol	CH ₃ OH	8100.0	20.0	37.5	12.5	12 (liquid)
Ethanol	C ₂ H ₅ OH	9010.0	26.9	52.1	13.0	12.5 (liquid)
Dimethyl ether	CH ₃ OCH ₃	1.69 (g)	28.6	52.1	13.0	8 (liquid, 4 bar) [14]
		693 (l)				

Table 23.2 Comparison of hydrocarbons as chemical hydrogen storage and steam reforming related parameters

Fuel	Steam reforming	Temperature/°C	$\Delta H^0/\text{kJmol}^{-1}_{\text{H}_2}$	$\lambda_{a,\text{min}}$	S/C
Methane	CH ₄ + 2H ₂ O → CO ₂ + 4H ₂	700–1000 [15]	+41.2	1.34	4–5
Methanol	CH ₃ OH + H ₂ O → CO ₂ + 3H ₂	200–300 [16]	+16.5	1.14	1.3–1.5
Ethanol	C ₂ H ₅ OH + 3H ₂ O → 2CO ₂ + 6H ₂	500–750 [17]	+28.9	1.24	3.0
	CH ₃ OCH ₃ + 3H ₂ O → 2CO ₂ + 6H ₂	200–450 [18]	+20.3	1.169	2.5

exchanger surface or size of the reformer is dependent on the temperature of the reforming process. Another reason is the heat-up time of the system and the thermal stress during start-up and shutdown. In more modern aircraft, large parts of the structure are designed using CFRP or GFRP materials. The long-term temperature tolerance of these materials is less than 70 °C, which requires attention to the insulation of hot spots inside the system. Low process temperatures allow a wider choice of materials that can be applied in the reactor design, and in the case of methanol steam reforming (MSR), even light-weight aluminum alloys can be considered.

23.3.2 Heat Integration and System Efficiency

The reforming process requires heat, which is delivered by a burner that can either be fed with fuel from the tank or with recycled anode waste gas from the fuel cell [19]. Supplying the reformer with heat solely from the combustion of recycled anode waste gas is the basis for an efficient fuel cell reformer process. The anode stoichiometry ($\lambda_{a,min}$) required to satisfy the heat demand is determined by the specific enthalpy of the reforming reaction (ΔH^0) for each fuel (see Table 23.2). The efficiency of heat transfer from the burner gas and the reformer is not included in this theoretical value because it depends on the individual hardware design.

23.3.3 Fuel Quality and Water

Hydrogen mole fractions at equilibrium range between 0.75 and 0.8 on a dry basis, depending on the fuel (see Table 23.2). Carbon monoxide (CO), a by-product from the reforming process, is a catalyst poison in PEM fuel cells. Addressing CO requires either complex cleaning processes or fuel cells with elevated temperatures that can tolerate CO levels of up to 1.5×10^4 ppm. A surplus of water effectively suppresses the amount of CO in the reformat gas. With respect to weight, water for steam reforming can be

recycled from cathode off-gases to a certain extent depending on the fuel. Hence, S/C is a relevant criterion and should be as low as possible because it affects the condensing temperature downstream of the fuel cell. On the other hand, it requires heat for evaporation upstream of the reformer and therefore has a dual effect on the system mass.

Concerning the gravimetric hydrogen density, alcohols show the highest values in Table 23.1. It should be noted that the tank considered for dimethyl ether (DME) still offers a potential for weight optimization. Alcohols store approximately twice as much hydrogen per weight unit compared to pure compressed hydrogen. Methanol can be reformed at the lowest temperature, requires the least enthalpy for hydrogen production from steam reforming and can be processed with an S/C of 1.5. Assuming full heat recovery from the anode waste gas, the heat for reforming can be produced with an anode stoichiometry being below the demand of the fuel cell operated with reformat gas.

Considering the importance of safety in the aviation industry, systems that are the least complex, more robust and reliable prevail. HT-PEFC technology is promising in this context. First, due to its tolerance to CO, it offers a less complex system design without reformat cleaning steps. Therefore, it paves the way to using hydrocarbons with high gravimetric energy densities as on-board fuel. Second, the elevated temperature enables heat integration within a combined and compact reformer HT-PEFC system and additionally facilitates the layout of system cooling. Third, there is no water management required that depends on parameters such as ambient pressure and humidity, which vary with altitude. In contrast, the low current density and the sensitivity versus the differential pressure between the anode and the cathode [20] as well as degradation issues remain challenges to overcome in the future [21].

For comparison, the endurance of an exemplary aircraft with either methanol or pressurized hydrogen (400 bar) as fuel can be estimated by assuming a fixed available weight of 540 kg for both the fuel cell and the tank. The fuel cell mass

Table 23.3 Comparison of flight endurance with HT-PEFC systems supplied either with pure hydrogen stored in a high-pressure tank or reformat gas from the on-board reforming of methanol

Fuel	Available mass (kg)	Fuel cell mass	Energy in the tank (kWh)	Fuel cell efficiency	Endurance (h)
Pure hydrogen	540	160	760	0.5	19
Methanol		240	1592	0.45	36

replaces the fuel mass and vice versa. The required power for straight level flight (SLF) is assumed to be 20 kW (see Table 23.3).

23.4 Development of an HT-PEFC System for Aircraft Propulsion

Within a follow up project of the Antares DLR H2, a power supply unit of an electric motor glider is being developed with an HT-PEFC system that is directly coupled with a methanol reforming unit. The aircraft is designed with a wingspan of 23 m and an MTOW of 1500 kg. There are four pods positioned under the wings. The fuel cell systems are integrated into the inner pods on the left- and right-hand sides of the fuselage. For cooling and cathode supply, there is an air inlet in each pod facing in the direction of flight. Each fuel cell system on either side is divided into four modules.

23.4.1 HT-PEFC Cooling Concept

Considering that simplicity is an important criterion in aviation, air cooling of the fuel cell system seems to be an appropriate solution. Despite benefits such as the availability of the coolant, its dual function and light weight, issues with varying parameters such as pressure, density and temperature must be addressed. The absolute pressure at an altitude of 10,000 m MSL is approximately 260 mbar, and the air density is 0.21 kg/m^3 . Liquid cooling can be realized in a closed loop, which makes it independent of altitude. If the coolant exit temperature of the stack is controlled at $165 \text{ }^\circ\text{C}$ and if air is supplied to the stack at $20 \text{ }^\circ\text{C}$, the volume flow must be two

orders of magnitude higher compared to a liquid thermofluid supplied at $160 \text{ }^\circ\text{C}$. Liquid cooling therefore allows narrower channel geometries and, accordingly, better heat transfer. In contrast to air, liquid thermofluids offer a four times higher heat conductivity, requiring less surface area for cooling because of the higher heat transfer coefficient. In the context of using reformat gas, an even temperature distribution in the HT-PEFC is crucial. A liquid-cooled stack is the basis for efficient heat integration with the reformer system. Accordingly, a compact design of the fuel cell stack and the evaporator is enabled. Furthermore liquids are pressurized more efficiently compared to gas, resulting in less auxiliary power consumption.

23.4.2 HT-PEFC System Layout with Reformat Supply from Methanol Steam Reforming

Each of the modules consists of a liquid-cooled HT-PEFC stack supplied from an individual steam reforming unit. The anode waste gas is recycled to a catalytic burner to supply heat for reforming. Fuel is mixed with water to a molar ratio of 1.5. At ambient pressure, the bubble point of the methanol water mixture is $75 \text{ }^\circ\text{C}$, and the dew point is $89 \text{ }^\circ\text{C}$. Heat from the HT-PEFC can be supplied via the cooling media at temperatures of $160 \text{ }^\circ\text{C}$, which are sufficient for evaporation and superheating. Before entering the reformer, the temperature of the fuel water mixture is increased further by the flue gas from the reformer heating. The anode of the HT-PEFC is directly fed with reformat gas from the reformer while the cathode is supplied with air from the environment. A liquid-cooling

loop is used to control the temperature of the fuel cell stack and to simultaneously evaporate the fuel. Additional excess heat is expelled via an air-cooled radiator (Fig. 23.2).

By deploying the process engineering simulation tool Aspen Plus, the enthalpy streams of the coupled fuel cell and reforming process can be made visible. Figure 23.3 shows the distribution

of the methanol enthalpy stream at the maximum power output of one out of two fuel cell systems. The evaporation of the methanol water mixture amounts to at least double the heat required for the reforming process itself. In the simulation, the second superheating step to over 200 °C occurs inside the reforming reactor. Thus, this enthalpy increase is allocated to the reforming

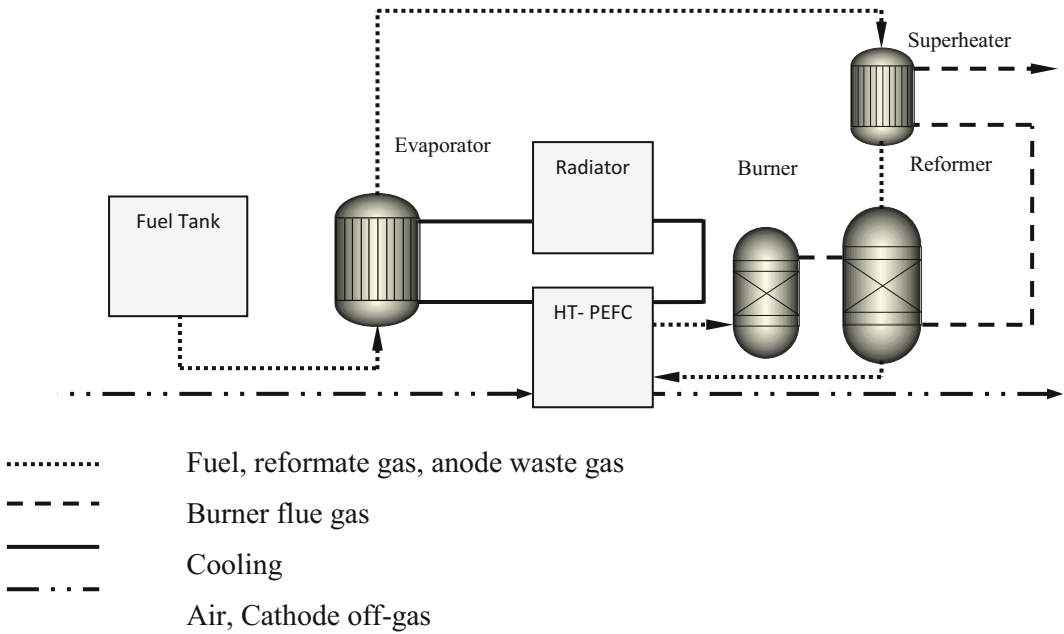
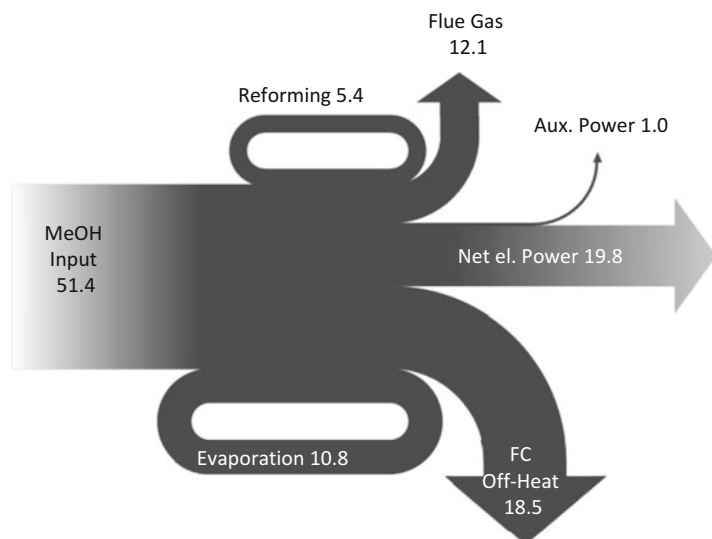


Fig. 23.2 Process scheme of the HT-PEFC system directly supplied by the MSR process

Fig. 23.3 Simulation results of the coupled HT-PEFC/reformer system in the form of a Sankey diagram showing enthalpy flows in kW at full load



reaction. Two-thirds of the heat demand can be supplied by the fuel cell off-heat, and the remaining third has to be contributed by the combustion of anode waste gas. The larger share of the fuel cell off-heat is not used and is dissipated via the radiator. This means that to a certain extent, a higher S/C ratio is possible because there is sufficient available heat from the fuel cell. Alternatively, the cooling loop can be engaged for wing de-icing and for cabin heating. In addition, the flue gas from the burner is expelled at a high temperature. This shows that potential remains for future concepts with, e.g., fuels requiring more energy for evaporation upstream of the reforming process.

23.4.3 Dimensioning the HT-PEFC Stack for Maximum Flight Endurance

During the design phase of the aircraft, the masses for both the fuel (M_{fuel}) and the fuel cell systems (M_{fc}) are planned to be a maximum of 540 kg (M_{max}). This means that all weight savings on the hardware side is a gain in fuel capacity (23.1).

$$M_{\text{max}} = M_{\text{fc}} + M_{\text{fuel}} \quad (23.1)$$

What fuel cell system size provides the greatest flight endurance? A large fuel cell stack can

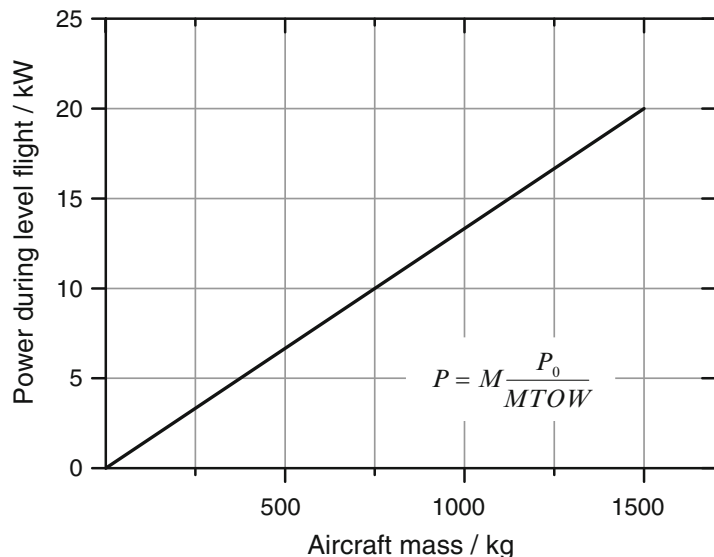
provide the required power for aircraft propulsion at low current densities, high fuel cell efficiency, and, accordingly, low fuel consumption. However, due to its weight, the fuel capacity is reduced. In comparison, a smaller stack enables an increased fuel capacity, but the stack is operating at higher current densities and is therefore less fuel efficient. Thus, the objective is to determine an ideal size for the fuel cell system that enables the maximum endurance (t_{op}). Therefore, a specific current density with a pronounced endurance optimum is determined. The power for propulsion depends on the flight mode considered, altitude, temperature, and weather conditions. Based on experience with the flying platform Antares DLR H2, this is estimated to be in the range of 20–30 kW for straight and level flight (SLF).

23.4.4 Determining Mean Power for Propulsion During Flight

Because fuel is consumed over time, the total weight of the aircraft is constantly decreased during operation, and accordingly, the required power decreases. The correlation between the required power and the aircraft mass is linear (Fig. 23.4).

The mean aircraft mass (\bar{M}) can be estimated as the arithmetic mean between the airplane's

Fig. 23.4 Correlation between propulsion power required during SLF and mass of the conceptual aircraft in the case of 20 kW at MTOW



maximum takeoff weight (MTOW) and the aircraft’s mass when all of the fuel mass is consumed at the end of flight. The mean power during flight (\bar{P}_{SLF}) is determined by (23.2).

$$\bar{P}_{\text{SLF}} = P_0 \left(1 + \frac{M_{\text{fc}} - M_{\text{max}}}{2\text{MTOW}} \right) \quad (23.2)$$

The mass of the fuel cell system is divided into three parts. First, there is the area specific mass factor (m_{fcvar}). Second, there is the power specific mass factor of the system (m_{sys}) including the reforming process. Finally, there is the fixed mass of the stack (M_{fix}). These values are based on hardware development that was performed in cooperation with Serenergy A/S, Denmark. The total area of the fuel cell depends on the operation point, e.g., the mean current density, and can be expressed by the power specific area (a_p) times the power (\bar{P}_{SLF}).

The mass of the fuel cell system is calculated according to (23.3).

$$M_{\text{fc}} = \bar{P}_{\text{SLF}}(a_p m_{\text{fcvar}} + m_{\text{sys}}) + M_{\text{fix}} \quad (23.3)$$

The mean power during flight can be expressed according to (23.4).

$$\bar{P}_{\text{SLF}} = P_0 \frac{(2\text{MTOW} + (M_{\text{fix}} - M_{\text{max}}))}{(2\text{MTOW} - P_0(a_p m_{\text{fcvar}} + m_{\text{sys}}))} \quad (23.4)$$

23.4.5 Determining Flight Endurance

The endurance (t_{op}) is determined by the fuel mass over the fuel consumption (\dot{m}_{fuel}) ((23.5) and (23.6)).

$$t_{\text{op}} = \frac{M_{\text{fuel}}}{\dot{m}_{\text{fuel}}} \quad (23.5)$$

$$M_{\text{fuel}} = M_{\text{max}} - P_{\text{SLF}}(a_p m_{\text{fcvar}} + m_{\text{sys}}) + M_{\text{fix}} \quad (23.6)$$

The flight endurance assuming full conversion of methanol according to Faraday is calculated according to (23.7).

$$t_{\text{op}} = \frac{zF(M_{\text{max}} - (\bar{P}_{\text{SLF}}(a_p m_{\text{fcvar}} + m_{\text{sys}}) + M_{\text{fix}}))}{j a_p \lambda_a m_c \bar{P}_{\text{SLF}}} \quad (23.7)$$

The endurance plot (Fig. 23.5) is used to determine the current density for the maximum endurance, and with Fig. 23.6, the fuel cell area is determined. For higher P_0 , the specific area at the point of maximum endurance decreases as the current density increases. The effect of CO exhibits a linear area increase within the investigated range. Under optimal conditions with no CO in the anode feed and with the required power for SLF being as low as 20 kW,

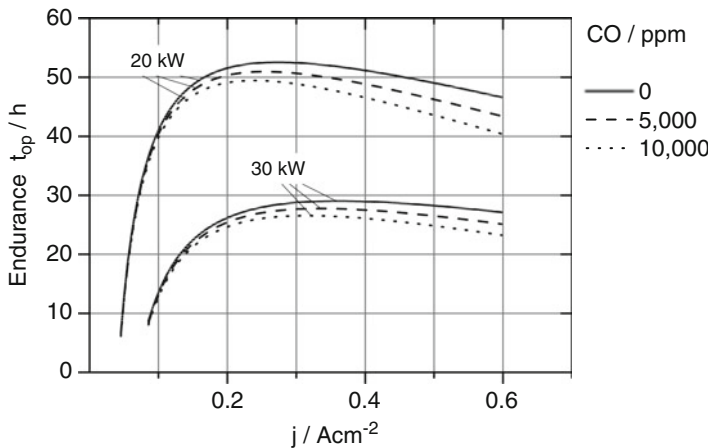


Fig. 23.5 The flight endurance as a function of current density with variations in P_0 between 20 and 30 kW and CO concentrations in the anode feed between 0 and

10,000 ppm. The total mass of the fuel and the fuel cell system $M_{\text{max}} = 540$ kg. The anode stoichiometry $\lambda_a = 1.25$

the theoretical endurance is 52.6 h, whereas for the considered worst-case scenario, it is 26.6 h.

There are two fuel cell systems, connected in parallel. The electric motor used as the aircraft propulsion system is an AC brushless external rotor type. It can be operated within a voltage range between 210 and 330 V. If the upper limit of the cell voltage is set to 0.7 V, the total number of cells should be 834. Although MEAs can be customized from an economical perspective, an off-the-shelf product is favored. An MEA with 165 cm², which is commercially available, is adequate for cases 2, 3, and 4 in Table 23.4. The required power during takeoff is also estimated based on operational experience with the aircraft Antares DLR H2 and is believed to be 40 kW. Within the lower voltage limit of the motor, this power can be reached with 960 cells

at 10,000 ppm CO. Furthermore, a battery is considered as a support during takeoff and as an additional energy reserve and safety backup. With a total of 72 battery cells and a cell voltage of 300 V at 100 % state of charge (SOC), the aircraft can even take-off on battery power alone.

For safety reasons in terms of backup power, 960 fuel cells are used in total. All 480 cells on either side are subdivided into four modules, which are connected in series. Hence, there are no DC/DC converters required. This helps to reduce weight and minimize the risk of parts failing, which can cause a total system breakdown. In addition, issues with EMC originating from voltage conversion can be circumvented. However, some challenges must be addressed. All individual fuel processing units must be operating simultaneously. During idle, the

Fig. 23.6 Experimental results from a single-cell MEA-type BASF Celtec P1100W. Power specific area $a_p/m^2 kW^{-1}$ at 160 °C operating temperature and at 1 atm. Stoichiometry at the anode $\lambda_a = 1.25$ and cathode $\lambda_c = 2.5$. Variation of CO level between 0 and 10,000 ppm

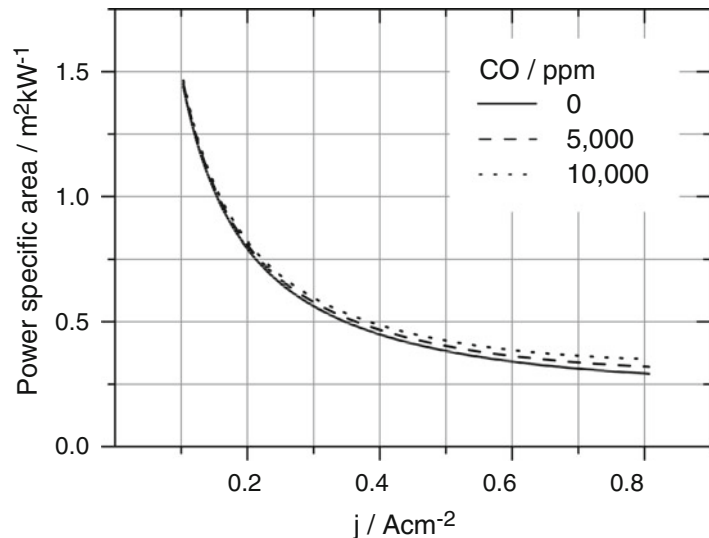


Table 23.4 Results of the endurance optimization for different power requirements and CO concentrations

Case	CO conc./ppm	P_0/kW	$j/A cm^{-2}$	Area $a_p/cm^2 kW^{-1}$	Area per cell/cm ²	t_{op}/h
1	0	20	0.271	6062	145	52.6
2	5000	20	0.256	6508	156	51.0
3	10,000	20	0.236	7110	171	49.5
4	0	30	0.362	4825	174	29.1
5	5000	30	0.337	5271	190	27.8
6	10,000	30	0.317	5697	205	26.6

The ideal area per cell is calculated considering 834 cells

voltage must be reduced to avoid overvoltage. This is for two reasons: to save the HT-PEFC system from degradation at open-circuit voltage (OCV) [22] and to protect power supply of the electric motor. This is performed by engaging the electric heating in the cooling loop that is used during start-up.

23.5 System Integration into the Wing Pod

As shown in Fig. 23.7, there are four modules with 120 cells connected in series. This configuration is utilized for three reasons: redundancy, package requirements, and mechanical concerns. Because the stack design is based on frictional connections between the MEAs and the bipolar plates, G-loads during operation in directions normal to the stack can lead to displacements and can cause internal or external leakage. With increasing aspect ratio and mass, the mechanical stress within the stack will increase. Therefore, the mechanical characteristics of graphite-based bipolar plates are to be considered. In addition, the eigenfrequency has to be determined and compared with the excitation frequencies from the propeller. From a weight perspective, the number of cells in one stack is also limited due to the increasing diameter of the manifold, which is supplied from one side only to avoid additional piping.

Each module is supplied from an individual reforming unit (Fig. 23.7), which includes an evaporator and an anode waste gas burner. By splitting these units according to the stack size, a very compact package can be realized. Compared to one central fuel processing unit, the evaporation is directly coupled to the hot coolant outlet stream from the fuel cell. Additionally, the fluid flows are well integrated into the fuel cell reformer units without the need for external piping across the wing pod. The anode inlet is connected to the reformer outlet; therefore, supply interruptions caused by condensing water in pipes can be avoided. Air enters the wing pod from the front, passing through the radiator of the cooling loop. To ensure an appropriate cathode inlet temperature, especially at higher altitudes, a cathode air preheater is integrated into the cooling loop.

23.5.1 Start-up Procedure Before Flight

For starting up the fuel cell system, electric heaters inside the cooling media are chosen. The required power during start-up is provided either from an external supply or from the battery pack in the hybrid variant, making the aircraft more autonomous. A total energy of approximately 6 kWh is theoretically required to heat up the system mass from 0 to 130 °C. The installed heating power is limited because the

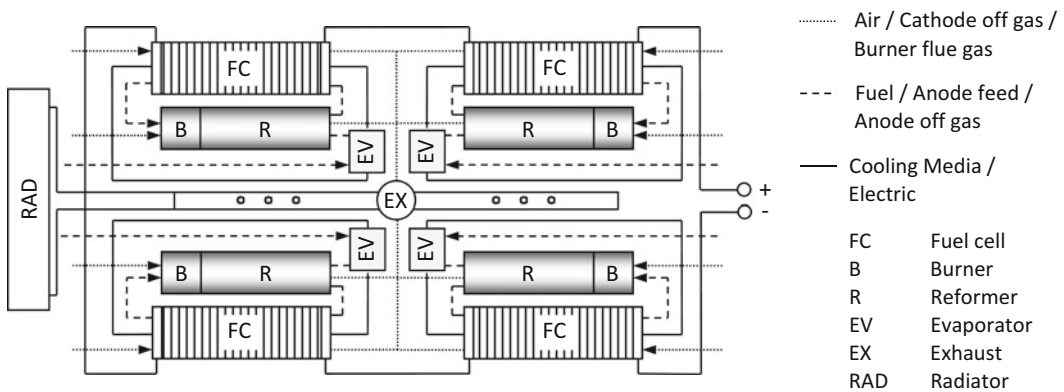


Fig. 23.7 Modular layout of the fuel cell architecture

thermal stress caused by temperature differences over the stack is limited to a certain range. In addition, the cooling media flow is limited because of the pressure drop over the stack, particularly at low temperatures. High pressures can cause mechanical failure of the gaskets and leakage with fatal effects on the HT-PEFC MEAs. While the cooling loop is electrically heated, the reforming unit is heated via the combustion of fuel. This two-way-heating concept enables the start-up procedure to be performed within less than an hour. The mass flow rate of the cooling media is limited due to high pressure drops in the stack at ambient temperature. By further cooling media screening, the start-up time possibly can be further reduced. Once the fuel cell stack has reached its operable temperature, the reforming process can be started. Electric power from the fuel cell is used to further heat the cooling loop, and the anode waste gas can take over the burner supply such that the external power supply is not required from this point on.

23.5.2 Shutdown Procedure After Landing

During the normal landing procedure, no electric power is required; therefore, the fuel cell system is in idle state. After landing, power is required to maneuver the aircraft to its final parking position. Subsequently, the shutdown process starts by slowly ramping the load back to idle. Then, electric bleeders are engaged to avoid overvoltage. The electric motor for aircraft propulsion is shut off at this point. While the fuel cell stack is cooled, the reformer must still be operated to avoid anode starvation until the electric bleeders are finally shut off.

During emergency shutdown, the load may be disengaged at full load. This steep load change requires the fuel supply to rapidly adapt. Until the fuel supply is adjusted, there is unconsumed reformate passing the burner. This causes a temperature peak in the burner and in the reformer compartment. Because the exhaust gas passes a condensing step, a full conversion of all combustibles must be ensured.

23.5.3 Dynamic Requirements During Flight Operation

During normal flight operations, the power setting remains unchanged; thus, the system is expected to be operating for a long time at a constant load point comparable to steady-state operation in non-mobile applications. Therefore, the on-board reforming process, despite its slow thermal reaction times, is well suited for normal flight operations. More dynamic sequences, such as climbing to higher altitudes, can be addressed by an additional power boost from the battery hybrid. For taxiing, there must be sufficient power available to overcome the starting torque of the wheels. This is desirable within a short sequence to integrate into the ground traffic, depending on the airport and traffic density. Here, the direct hybrid concept adds flexibility to the aircraft. In the case of a rejected landing (go-around), the immediate availability of full power is vital. This safety aspect is another strong argument in favor of realizing a hybrid system.

23.5.4 Outlook Toward HT-PEFC/Battery Hybridization

A direct hybrid can be realized as described by Nishizawa et al. [23]. Instead of a DC/DC converter, diodes are applied, balancing the supply current from the fuel cell system or the battery. The individual contribution share depends on the voltage of both sources. Assuming a constant reformate gas quality and an appropriate heat management system, the voltage of the fuel cell depends on the load, whereas the voltage of the battery system depends mostly on the SOC but also on the load. Recharging the batteries during flight can be implemented within the direct hybrid architecture (Fig. 23.8).

The voltage of the batteries is to be designed such that the HT-PEFC is supported at a cell voltage low enough to enable full fuel cell operation during normal flight. The cooperation between fuel cell and batteries is shown in

Fig. 23.8 Principle sketch of the direct hybrid configuration for aviation applications

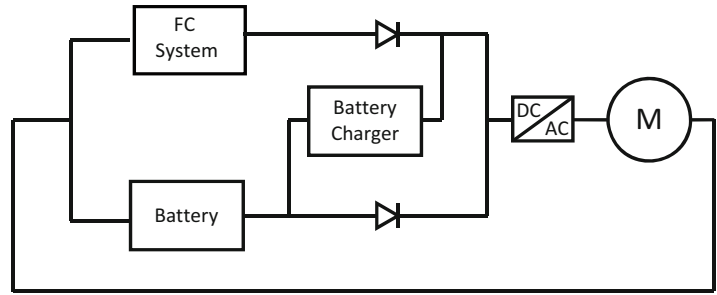


Fig. 23.9 Simulation results for current contributions in a direct hybrid with four 120 HT-PEFC cell stacks and 72 Li-ion batteries. HT-PEFC operating temperature of 160 °C, CO content in the reformat of 5000 ppm. Variation of the state of charge (SOC) between 10 and 100 %

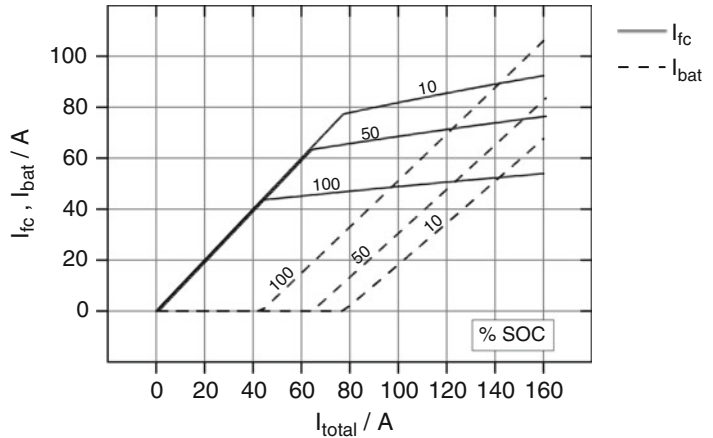


Fig. 23.9 for a hybrid layout with 480 HT-PEFC MEAs and 72 SAFT VL41M Li-ion batteries.

23.5.5 Outlook Toward Water Recycling

The reforming process requires water, which if not recovered from the exhaust gas, has to be carried along with the fuel. This ballast reduces the endurance, and hence, a solution for integrating on-board water recovery must be considered in terms of weight and volume.

Because waste gas from the anode is directly converted in the burner, all excess water from steam reforming is shuttled herein. The final molar water share in the exhaust gas depends on the air stoichiometry of the burner (λ_b). Cathode off-gas and the burner flue gas are mixed in the exhaust in the center of the wing pod. To provide sufficient water for steam reforming at an S/C of 1.5, a share of 0.43 of the water in the

exhaust stream must be recovered. Assuming a cathode stoichiometry (λ_c) of 3, the condensing temperature varies between 45 and 37 °C, with λ_b between 2 and 10, respectively. Keeping λ_b constant at 5 and varying λ_c in the range of 2–4, the required condensing temperature ranges between 47 and 38 °C (Fig. 23.10).

23.6 Conclusions

A first step toward HT-PEFC as a power source for propulsion in aviation has been demonstrated with the flying platform Antares DLR H2. The follow-up project aims on maximum flight endurance. Despite its low current density, HT-PEFC technology has a number of advantages that make it attractive to aviation. Methanol as a hydrogen carrier has shown the greatest number of promising characteristics in this context after fuel screening. A compact

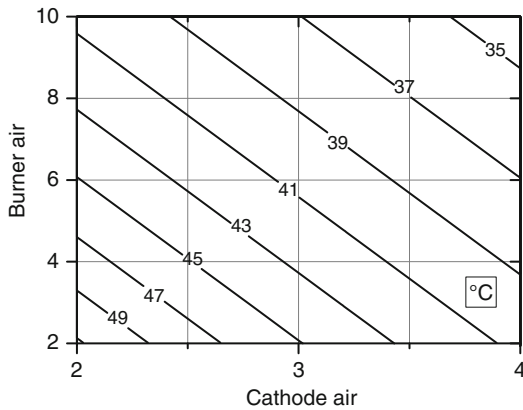


Fig. 23.10 Contour diagram of condensing temperatures versus cathode and burner air stoichiometry required for recycling to supply the reforming process at $S/C = 1.5$

modular system layout with methanol steam reforming units upstream of the liquid-cooled HT-PEFC has been established. Using heat integration, a conversion efficiency of methanol to electric power of greater than 45 % can be achieved. With an appropriate dimensioning of the fuel cell system, the flight endurance is expected to be between 25 and 50 h. Power peaks during takeoff, ground operation or critical flight situations are planned to be optionally addressed by engaging a direct fuel cell battery hybrid. Batteries are an important aspect in terms of safety. The dimensioning of the battery system requires an additional optimization in terms of maximizing endurance in the future. A remaining challenge is the online water recycling from cathode off-gas and burner flue gas inside the aircraft. Pressurized reforming concepts together with enhanced heat transfer may help further reduce weight in future designs.

References

- Renouard-Vallet G, Kallo J, Friedrich AK et al (2011) Fuel cells for aircraft applications. *ECS Trans* 30:271–280
- Friedrich KA, Kallo J, Schirmer J (2009) Fuel cell systems for aircraft application. *ECS Trans* 25:193–202
- Keim M, Kallo J, Friedrich KA et al (2013) Multi-functional fuel cell system in an aircraft environment: an investigation focusing on fuel tank inerting and water generation. *Aerosp Sci Technol* 29:330–338
- Pratt JW, Klebanoff LE, Munoz-Ramos K et al (2013) Proton exchange membrane fuel cells for electrical power generation on-board commercial airplanes. *Appl Energy* 101:776–796
- Renouard-Vallet G, Saballus M, Schmithals G (2010) Improving the environmental impact of civil aircraft by fuel cell technology: concepts and technological progress. *Energy Environ Sci* 3:1458–1468
- González-Espasandín Ó, Leo TJ, Navarro-Arévalo E (2014) Fuel cells: a real option for unmanned aerial vehicles propulsion. *Sci World J. Article ID 497642*, 12 pp
- Kim K, Kim T, Lee K et al (2011) Fuel cell system with sodium borohydride as hydrogen source for unmanned aerial vehicles. *J Power Sources* 196:9069–9075
- Lapeña-Rey N, Mosquera J, Bataller E et al (2010) First fuel-cell manned aircraft. *J Aircr* 47:1825–1835
- Lee B, Park P, Kim K et al (2014) The flight test and power simulations of an UAV powered by solar cells, a fuel cell and batteries. *J Mech Sci Technol* 28:399–405
- Rathke P, Kallo J, Schirmer J et al (2013) Antares DLR-H2—flying test bed for development of aircraft fuel cell systems. *ECS Trans* 51:229–241
- Fuel tank flammability reduction means, Advisory circular AC No. 25.981-2A (2008), p 28
- Luxfer® Gas Cylinders (2014) <http://www.luxfercylinders.com/products/alternative-fuel-cylinders>. Accessed 7 July 2014
- Aceves SM, Espinosa-Loza F et al (2010) High-density automotive hydrogen storage with cryogenic capable pressure vessels. *Int J Hydrog Energy* 35:1219–1226
- Stako (2008) LPG Tanks, Product brochure, personally transferred 2014
- Rostrup-Nielsen J, Christiansen LJ (2011) Routes to syngas. *Concepts in syngas manufacture*. Imperial College Press, London, pp 3–71
- Iulianelli A, Ribeirinha P et al (2013) Methanol steam reforming for hydrogen generation via conventional and membrane reactors: a review. *Renew Sustain Energy Rev* 29:355–368
- Wang F (2012) Hydrogen production from steam reforming of ethanol over an Ir/ceria-based catalyst: catalyst ageing analysis and performance improvement upon ceria doping. Dissertation, University Claude Bernard Lyon 1
- Semelsberger TA, Borup RL (2006) Dimethyl ether (DME) as an alternative fuel. *J Power Sources* 156:497–511
- Heinzel A, Roes J (2005) Increasing the electric efficiency of a fuel cell system by recirculating the anodeic offgas. *J Power Sources* 145:312–318

20. Bendzulla A (2010) Von der Komponente zum Stack: Entwicklung und Auslegung von HT-PEFC-Stacks der 5 kW-Klassen. Dissertation, RWTH Universtiy Aachen
21. Hartnig C, Schmidt TJ (2011) On a new degradation mode for high-temperature polymer electrolyte fuel cells: how bipolar plate degradation affects cell performance. *Elechtrochim Acta* 56:4237–4242
22. Qi Z, Buelte S (2006) Effect of open circuit voltage on performance and degradation of high temperature PBI-H₃PO₄ fuel cells. *J Power Sources* 161:1126–1132
23. Nishizawa A, Kallo J et al (2013) Fuel cell and Li-ion battery direct hybridization system for aircraft applications. *J Power Sources* 222:294–300

Kayley Fishel, Guoqing Qian, Glenn Eisman,
and Brian C. Benicewicz

24.1 Introduction

The concept of using electrochemical reactions with polymer-based proton exchange membranes to separate, purify, and compress hydrogen was an unobvious outcome of the effort to develop power generation solutions for satellites and spacecraft in the United States in the 1950s. With the development of membrane-based fuel cell technology by General Electric in the 1960s and 1970s [1, 2], applications in hydrogen and related alkali ion-intensive processes [3] were a natural fallout of their programs. Included in the list of such applications besides fuel cells were the chlor-alkali membrane process, water electrolysis, oxygen concentrators, and electrochemical hydrogen pumping/concentrators (EHP). Furthermore, the development of Nafion[®] (registered trademark of DuPont) ion exchange membranes was also an outcome of this period and remains the primary membrane separator for all of the above applications to date though this is being challenged by a new class of materials

capitalizing on high-temperature membranes, the topic of this chapter.

Electrochemical hydrogen pumping was first reported by Maget [4] while developing the SPE (Solid Polymer Electrolyte, the original description of the membrane and electrode technology prior to “PEM” terminology) family of electrochemical processes. Specifically it was found that a proton generated during the oxidation of hydrogen at the anode would recombine into “new” molecular hydrogen at the cathode after the proton was driven through the membrane by an applied potential (Fig. 24.1). For this process to work, other reaction chemistries at the cathode had to be eliminated, e.g., the oxygen or halide reduction reactions. Though this was a unique application of hydrogen oxidation-reduction chemistry, the hydrogen pump process never materialized as a useful concept and remained an intellectual and academic curiosity until recently. Applications and concepts which have emerged include hydrogen pumping, hydrogen separations, as well as adiabatic hydrogen compression. It has only been in recent years that practical applications have been, or are now under development for industrial and alternative energy applications. Furthermore, this technique has been found to be a useful electrochemical analytical tool for studying electrode performance in such devices as fuel cells and water electrolyzers [5].

K. Fishel • G. Qian • B.C. Benicewicz (✉)
Department of Chemistry and Biochemistry, University
of South Carolina, 541 Main Street, Horizon 1 Room 232,
Columbia, SC 29208, USA
e-mail: benice@sc.edu

G. Eisman
H2Pump LLC, 11 Northway Lane North, Latham, NY
12110, USA

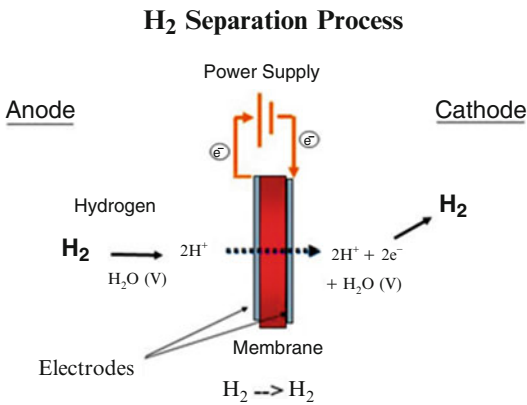
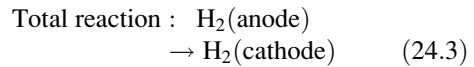
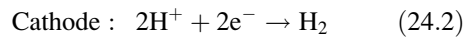
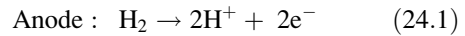


Fig. 24.1 Hydrogen membrane-based electrolysis

Recently, with the development of new high-temperature proton exchange membranes, as well as the increased interest in hydrogen-related technology and applications, there has been a resurgence of interest in EHP. Companies have formed to apply the process in both industrial and emerging hydrogen applications. There has also been an increase in the technical literature and conference presentations, and government (state and federal) agencies have included this technology in recent solicitations. These activities are partly due to membranes such as polybenzimidazoles (PBI), which have become available. This chapter will focus on the development of the high-temperature membrane-based electrochemical hydrogen pumping process.

24.2 Electrochemistry

The basic working principle of the electrochemical hydrogen pump process is that hydrogen molecules enter the anodic compartment of an electrochemical cell and are oxidized to protons and electrons within the catalyst layer of the electrode. The protons are driven through the ion exchange membrane while the electrons pass through the external circuit to the cathode as a result of the applied voltage to the electrodes. The protons and electrons then recombine at the cathode electrode to (re-)form molecular hydrogen. The overall chemical reactions are described by (24.1–24.3).



The cell voltage between the anode and cathode is given by (24.4). The Nernst potential E_{Nernst} is given by the Nernst equation (24.5), where E° is the standard potential of a hydrogen reaction, R is the gas constant, T is the temperature in Kelvin, F is Faraday's constant, p_{cathode} and p_{anode} are the partial pressures of hydrogen at the anode and cathode, respectively.

$$E = E_{\text{Nernst}} - E_{\text{polarization}} - E_{\text{ohmic}} \quad (24.4)$$

$$E_{\text{Nernst}} = E^\circ - \frac{RT}{2F} \ln \frac{p_{\text{cathode}}}{p_{\text{anode}}} \quad (24.5)$$

The polarization overpotential ($E_{\text{polarization}}$) is the sum of the polarization overpotentials at the anode and cathode and given by the Butler–Volmer equation. At low overpotentials, the polarization overpotential can be approximated by (24.6), where R is the gas constant, T is the temperature in Kelvin, F is the Faraday's constant, i is the current density, and i_0 is the exchange current density.

$$E_{\text{polarization}} = \frac{RT}{2F} \frac{i}{i_0} \quad (24.6)$$

The ohmic overpotential E_{ohmic} is the potential loss due to cell ohmic resistances and given by Ohm's law (24.7), where i is the current density, R_{ohmic} is the cell ohmic resistance, which includes membrane resistance, electrode resistance and cell hardware resistance.

$$E_{\text{ohmic}} = iR_{\text{ohmic}} \quad (24.7)$$

24.3 Low- and High-Temperature Devices

Just as the type of electrolyte membrane influences operational conditions and performance in fuel cells, the ion exchange membrane

used in hydrogen pumping applications affects the design and efficiency. Both low-temperature and high-temperature devices have been used or are under development for hydrogen separation and purification using this technique. In the low-temperature devices, the perfluorosulfonic acid family of membranes, e.g., Nafion[®], are ion exchange membranes with sulfonic acid groups directly bonded to the polymer. Devices containing these types of membranes operate at low temperatures (typically ~50–80 °C). Furthermore, the membranes need to be hydrated to support proton conduction [6]. A disadvantage of these membranes is the tendency of water to collect in the electrode layers and flow fields of the plates resulting in an undesirable “flooded” state. The result is a decrease in performance due to the reduced electrode active area. Among others, an additional disadvantage of the low-temperature cells is that the tolerance to selected impurities, e.g., carbon monoxide, at the electrode is low resulting in a (reversible) degradation process. This limits the utility of such devices in hydrogen separation and purification applications. Some of these obstacles in low-temperature devices can be overcome by using membranes that are able to operate at higher temperatures. Early high-temperature-based hydrogen purification was initially shown feasible using traditional phosphoric acid fuel cell (PAFC) technology [7]. High hydrogen recovery, high hydrogen purities, and tolerance to traditional fuel cell impurities were demonstrated using PAFC stack technology. In the 1990s, phosphoric acid-doped polymer membranes that offered similar increased tolerance to gas impurities were explored [8]. Operating at high temperatures (>100 °C) with phosphoric acid as the electrolyte requires a polymer membrane that is both thermally stable and chemically resistant. Since polybenzimidazoles (PBIs) demonstrate both of these qualities and have shown excellent stability under these conditions when used in fuel cells, PBI was a candidate for use in hydrogen pumping applications. Operating at these high temperatures also increases the platinum catalyst tolerance to carbon monoxide and other impurities, and thus becomes an enabling feature

in some applications. An additional advantage of high-temperature operation is that flooding of the electrodes with water is minimized, as water exists only in the gas phase at normal operating conditions. The chemistry of the polymer membrane influences the pump efficiency just as it influences the performance of a fuel cell. Various chemistries of PBI have been studied in hydrogen pumps to understand how the chemistry affects electrical efficiency, power consumption, durability of the membrane electrode assemblies, and gas purification.

24.4 High-Temperature Membrane Hydrogen Pumping

24.4.1 Para-PBI

Poly(2,2'-(*p*-phenylene)5,5'-bibenzimidazole) (para-PBI) has been tested by various research groups for high-temperature hydrogen pumping. In 2007, Perry et al. [9] reported the use of a para-PBI membrane prepared through the polyphosphoric acid process or PPA process [10] to be used as the polymer electrolyte membrane in an electrochemical hydrogen pump. Further information on the PPA process can be found in Chap. 10. Studies were performed using various gas mixtures, and operations were performed with and without external humidification in order to understand the power requirements, membrane electrode assembly (MEA) durability, and purification and electrochemical efficiencies. These para-PBI polymers had inherent viscosities (η) between 2.7 and 3.7 dL g⁻¹ and acid doping levels of 34.9–39.1 mol phosphoric acid (PA) per mole polymer repeat unit (PRU) [9]. Tests were initially performed with pure hydrogen and without external humidification at the anode. Polarization curves of the hydrogen pump are shown in Fig. 24.2.

The curves exhibited a linear relationship between voltage and current, which demonstrated reversibility, up to at least 1 A cm⁻². At a typical operating current density of 0.2 A cm⁻², electrochemical hydrogen pumping required relatively low voltages, i.e.,

Fig. 24.2 Polarization curves (scan rate 1.4 mA s^{-1}) of an electrochemical pump operating on pure hydrogen at 160°C , constant flow rate 94 mL min^{-1} . Reproduced from [9] with permission of Elsevier

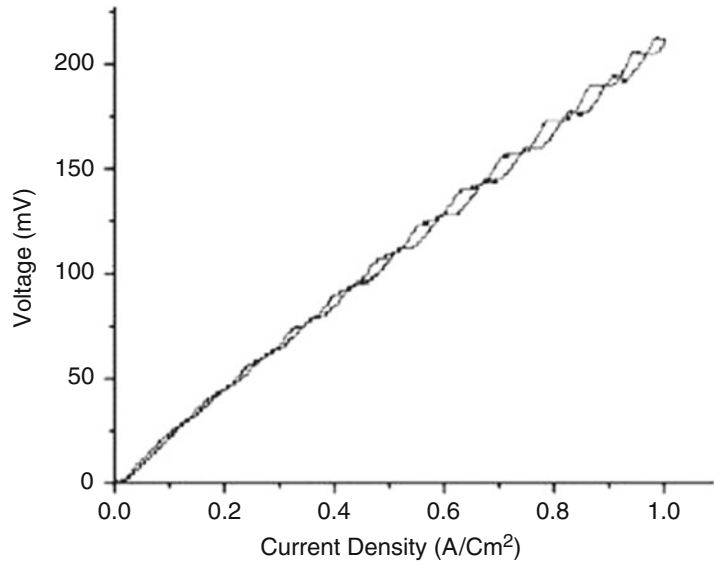
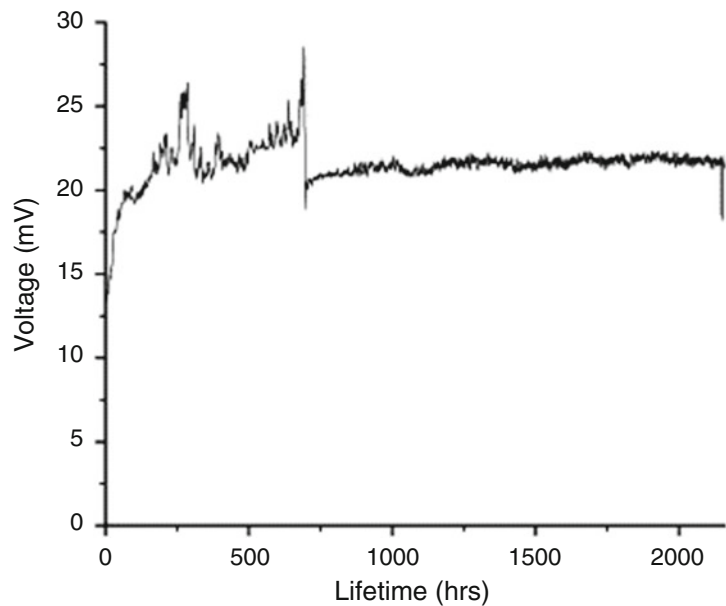


Fig. 24.3 Long-term operation of a hydrogen pump at 0.2 A cm^{-2} , 1.2 stoichiometric flow of pure hydrogen, 160°C . Reproduced from [9] with permission of Elsevier



45 mV at 160°C . The current efficiency of the electrochemical pump was conducted by measuring the cathodic outlet hydrogen flow at varying current densities. The relatively high current efficiencies, greater than 83 % from 0 to 2 A cm^{-2} , were achieved, showing high efficiencies under non-humidified conditions. The durability of the electrochemical pump was investigated at constant current density of

0.2 A cm^{-2} at 160°C operating on pure hydrogen with no external humidification and the voltage was found to be relatively constant at 22 mV for over 2000 h of operation as shown in Fig. 24.3.

The effects of relative humidity were then studied by cycling the relative humidity between 0 and 3 % at 160°C . There were no large changes seen in the voltage by changing the relative

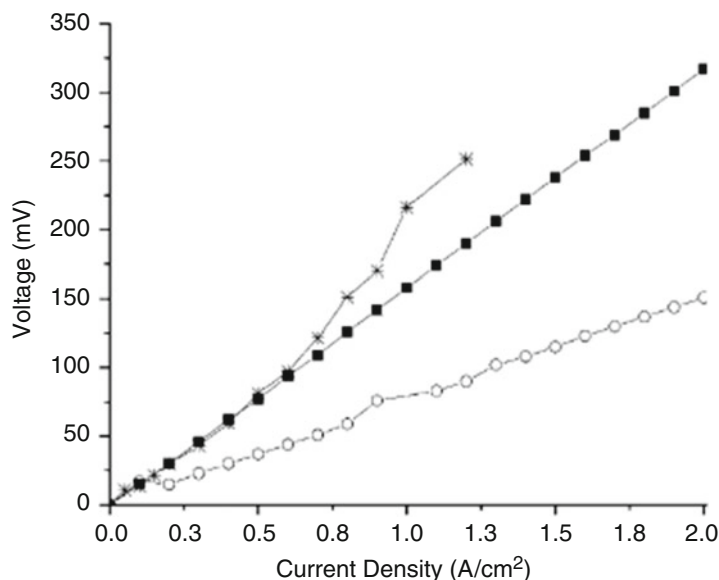


Fig. 24.4 Polarization curves for non-humidified conditions (*solid squares*) at 1653 h and humidified conditions (*unfilled squares*) at 2144 h. The crosshairs symbolize a humidified Nafion membrane operated at 70 °C for comparison [11]. The hydrogen inlet feed stream was adjusted to maintain 1.2 stoichiometric flows

at each current density for the humidified polarization curve. A constant flow of $\sim 75 \text{ mL min}^{-1}$ of hydrogen was supplied up to a current density of 0.8 A cm^{-2} and then the current steps were continued at 1.2 stoichiometric flow operation for the non-humidified polarization curve. Reproduced from [9] with permission of Elsevier

humidity; the average voltage for non-humidified conditions was approximately 33 mV and approximately 18 mV under humidified conditions. Performance was found to be improved at 3 % relative humidity when tested at 160 °C. This cell containing a para-PBI/PA membrane was reported to have a lifetime of over 4000 h with relatively stable voltages even under the stressful conditions of alternating between humidification and non-humidification. Power requirements were tested for both humidified systems and non-humidified systems by running polarization curves at 160 °C during each cycle. Figure 24.4 shows the polarization curves for the humidified and non-humidified operations and includes Nafion® (at 70 °C) for comparison.

It can be seen that both tests performed using para-PBI exhibit a near linear relationship. Voltages at 0.2 A cm^{-2} were 30 mV for the non-humidified cell and 18 mV for the humidified cell. Tests were also performed to evaluate the ability of the pump to run on gas streams contaminated with CO and CO₂ and to

evaluate the purity of the hydrogen produced at the cathode when operated at 160 °C. A gas stream of 35.8 % H₂, 11.9 % CO₂, 1906 ppm CO, and 11 % N₂ was used at the anode and the gas at the cathodic outlet was tested. Carbon monoxide concentrations were reduced to 11–13 ppm and carbon dioxide was reduced to 0.19–0.37 %, showing that these pumps can operate without high-purity hydrogen.

Kim et al. [12] later studied the effect of platinum catalyst loadings on the efficiencies of a H₂/CO₂ gas mixture (20/80 v/v) in cells containing membranes composed of para-PBI prepared through the PPA Process. Having the ability to reduce the amount of platinum used for catalysis in hydrogen pumping could significantly reduce material costs. Electrodes containing 1.1 and 0.2 mg cm⁻² were used at the anode and cathode to produce four different combinations of platinum loadings (1.1 mg cm⁻² at anode and cathode, 0.2 mg cm⁻² at anode and cathode, 1.1 mg cm⁻² at anode and 0.2 mg cm⁻² at cathode, and 0.2 mg cm⁻² at anode and

Fig. 24.5 Polarization curves for a hydrogen pump using different levels of Pt catalyst. (PHP = 1.1 mg cm^{-2} at anode and cathode, PHP-C = 1.1 mg cm^{-2} at anode and 0.2 mg cm^{-2} at cathode, PHP-A = 0.2 mg cm^{-2} at anode and 1.1 mg cm^{-2} at cathode, PHP-CA = 0.2 mg cm^{-2} at anode and cathode). H_2/CO_2 gas mixture (20/80 v/v). Reproduced from [12] with permission of Elsevier

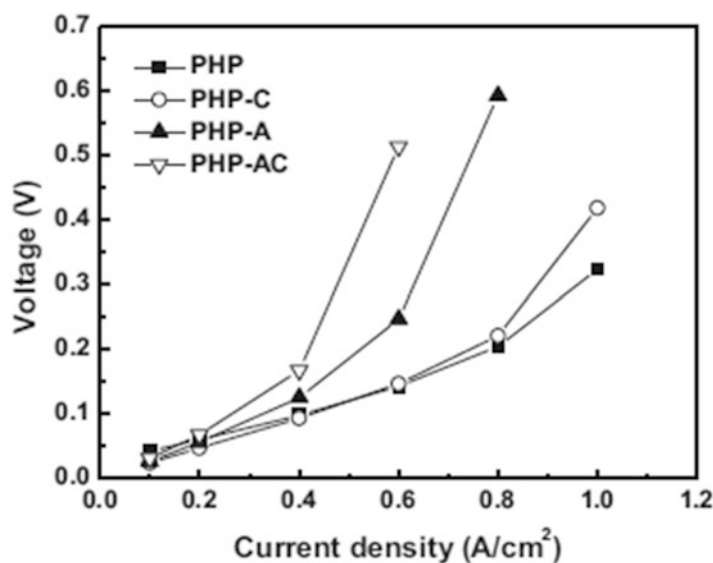


Table 24.1 Input and output of gases that were purified through hydrogen pumping using a Celtec-P membrane at 160°C

Gas	Input (%)	Output
H_2	50.5	99.896 %
CO	4.4	6.5 ppm
CO_2	39	1010 ppm
CH_4	6.1	18.7 ppm

1.1 mg cm^{-2} at cathode) to study the effect of the total platinum loading and the effect of a decrease in platinum loading at both the anode and cathode. Figure 24.5 shows the polarization curves of the various platinum loadings on the anodes and cathodes.

Compared to the MEA containing 1.1 mg cm^{-2} of platinum at both the anode and cathode, the MEA with lower platinum loading at the cathode (0.2 mg cm^{-2} at the cathode and 1.1 mg cm^{-2} at the anode) showed similar cell voltages up to 0.8 A cm^{-2} while the MEAs that contained lower platinum loading at the anode-side showed significantly higher cell voltages during H_2/CO_2 separation. These results indicate that the large overpotential seen in hydrogen purification using a H_2/CO_2 gas mixture is due mainly to the hydrogen oxidation reaction at the anode; therefore, the platinum loading at the cathode can be reduced without significant loss in performance.

Petek et al. [13] investigated a commercial Celtec-P-1000 MEA in a hydrogen pump at temperatures in the $120\text{--}180^\circ\text{C}$ range with detailed investigations at 150°C . They analyzed pumping characteristics using pure hydrogen, a simulated SMR-WGS (steam methane reforming-water gas shift) mixture of 70 % hydrogen, 3 % carbon monoxide, 20 % carbon dioxide, and 7 % methane, and a diluted hydrogen mixture containing as low as 5 % hydrogen. Hydrogen was separated quite efficiently from the SMR-WGS mixture with an estimated power requirement of 5 kW h kg^{-1} , which is much lower than the estimates for conventional PSA (pressure swing absorption) technologies. An adsorption limited current of approximately 0.3 A cm^{-2} was observed for the very dilute hydrogen containing mixtures with 5 % hydrogen.

H2Pump LLC tested various gas mixtures in a hydrogen pump with a Celtec-P membrane [14]. When using a gas mixture containing 50.5 % H_2 , 4.4 % CO, 39 % CO_2 , and 6.1 % CH_4 at 160°C , hydrogen was able to be purified to almost 99.9 % (Table 24.1).

Further testing was performed on a gas mixture containing 1.12 % CO, 43.8 % CO_2 , with a H_2 balance using a Celtec-P membrane at 160°C at 0.2 A cm^{-2} . The carbon monoxide was found to be ~ 1 ppm at the outlet. These findings show

Fig. 24.6 Purification ratios for carbon dioxide and carbon monoxide at various current densities using a Celtec-P membrane at 160 °C

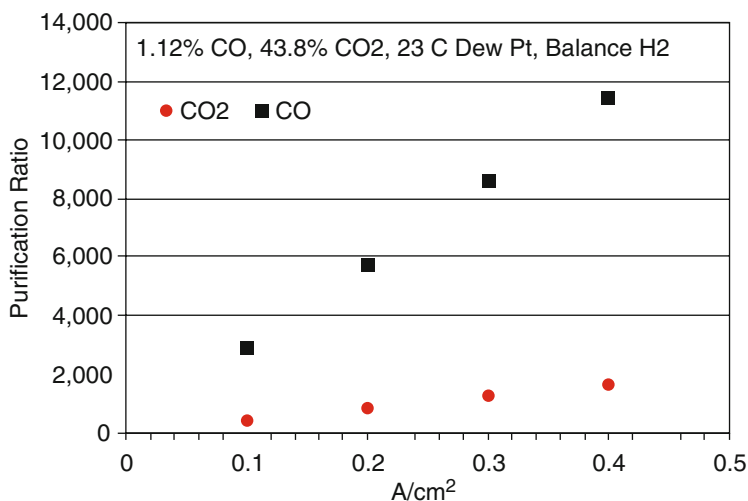
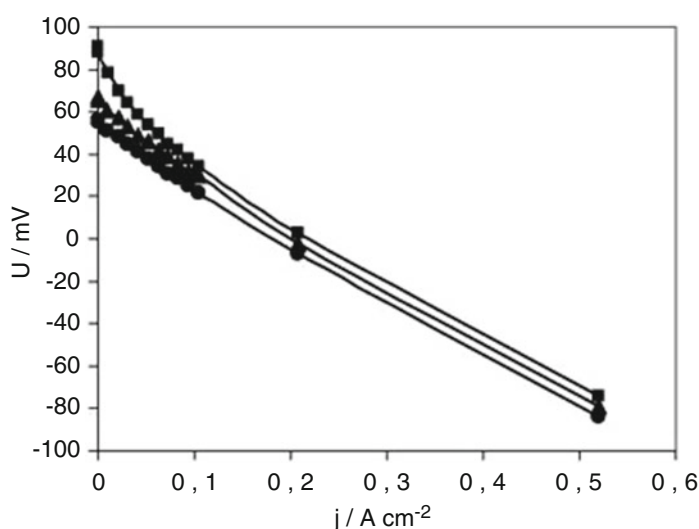


Fig. 24.7 Polarization curves measured at 160 °C for changing cathode gas pressures (*square* = 0 bar, *triangle* = 90 mbar, *circle* = 120 mbar) Reproduced from [5] with permission of Elsevier



the excellent purity that can be achieved using a para-PBI membrane in a hydrogen pumping device (Fig. 24.6).

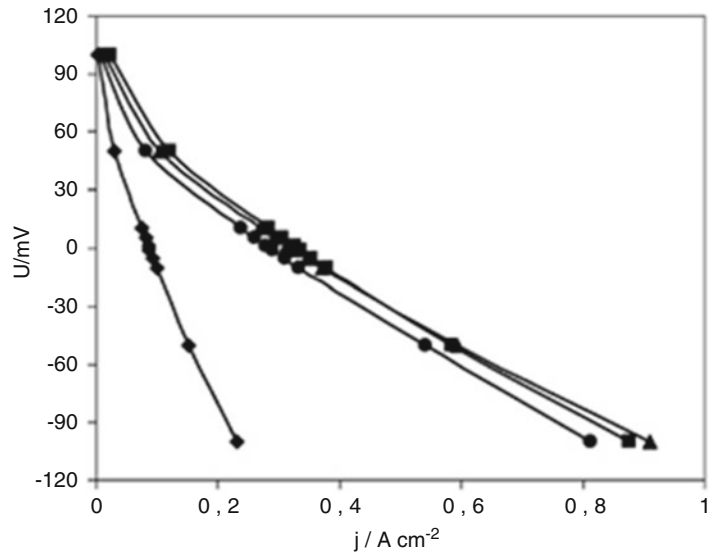
24.4.2 Other PBIs

Huth et al. [5] performed hydrogen pumping tests on a PBI membrane to study proton transport and anode kinetics. Unfortunately, the source of the material, type of PBI, and membrane acid doping level were not specified. Polarization curves can be seen in Fig. 24.7 and showed a nearly linear behavior over the entire potential range

indicating that membrane resistance dominates the overall cell resistance in this region.

The effects of temperature when the partial pressure of hydrogen was held at 3 bar were studied. When temperature increased, a larger change in current was seen with changing voltage showing an increase in conductivity (Fig. 24.8). Huth et al. [5] went on to perform many further experiments to study the proton transport mechanism and anode kinetics and found that the anodic hydrogen oxidation reaction follows the Volmer–Tafel mechanism with the Volmer reaction being the rate-limiting step.

Fig. 24.8 Polarization curves of the proton pump at various temperatures with a hydrogen partial pressure of 3 bar (*diamond* = 40 °C, *circle* = 80 °C, *triangle* = 120 °C, *square* = 160 °C). Reproduced from [5] with permission of Elsevier



Thomassen et al. [15] also evaluated a PBI-based membrane for EHP applications. Again, the membrane source, type of PBI, and membrane acid doping were not specified. Reformate gas mixtures containing varying amounts of hydrogen, carbon dioxide, carbon monoxide, nitrogen, and methane were used in a hydrogen pump cell with good results. Current efficiencies up to 90 % were reported at high current densities, and the cells were operated at a differential pressure of 0.65 bar. Significant reductions in gas impurities were measured under stable operating conditions.

24.5 Low-Temperature Hydrogen Pumping

Although the focus of this book is predominantly on polymer membranes for use in high-temperature devices, a few examples of polymer membranes used in low-temperature hydrogen pumping have been included in this chapter for comparison.

24.5.1 Perfluorosulfonic Acid-Based Membranes

Perfluorosulfonic acid-based membranes are some of the most commonly studied membranes in hydrogen pumping. Lee et al. [16] studied

hydrogen purification at low temperatures using a Nafion[®] 115 membrane using a hydrogen/nitrogen/carbon dioxide mixture. Testing was performed at various temperatures and operating pressures with hydrogen inlet compositions ranging from 10 to 90 %. Detailed results from a 50 % hydrogen mixture are shown in Fig. 24.9. Hydrogen purity was then measured as a function of current density when testing was performed at various temperatures (Fig. 24.10).

As expected, hydrogen purity increased with increasing current density. Hydrogen purities of >90 % were easily achieved at a wide range of temperatures, pressures, and current densities. Abdulla et al. [17] conducted an excellent and detailed study on the efficiency of hydrogen pumping using a Nafion[®] 115 membrane in both a single stage and multistage design. Further studies on perfluorosulfonic acid-based membranes can be found in the additional references [11, 18–21].

24.5.2 Poly(Ether Ether Ketone)-Based Membranes

Poly(ether ether ketone)-based membranes (PEEK) have also been studied in low-temperature hydrogen pumping as more cost effective alternatives to perfluorosulfonic

Fig. 24.9 Polarization curves for various cell temperatures and pressures (hydrogen inlet composition 50 %) Reproduced from [16] with permission of Elsevier

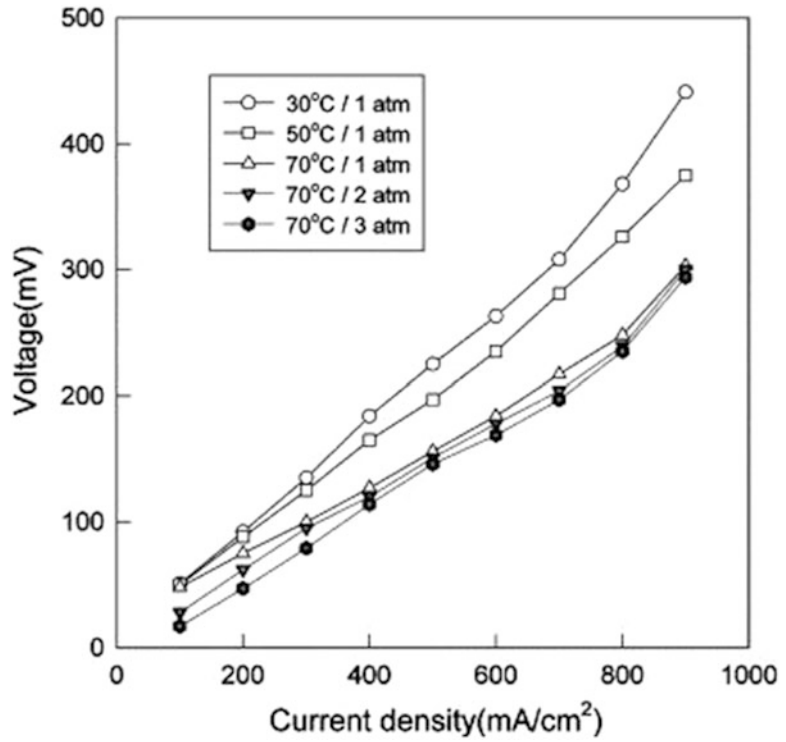


Fig. 24.10 Hydrogen purity vs. current density at various cell temperatures and operating pressures (hydrogen inlet composition 50 %). Reproduced from [16] with permission of Elsevier

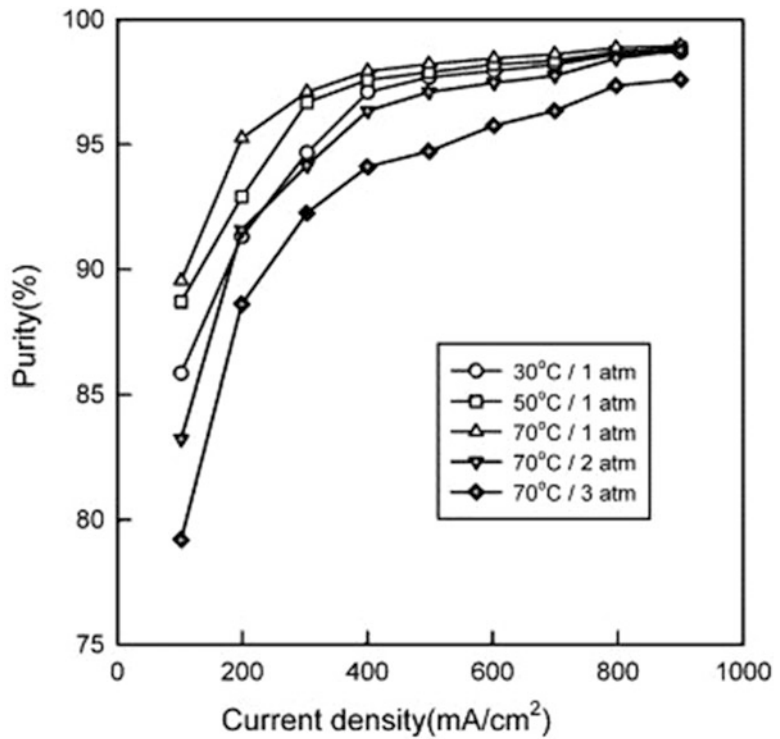
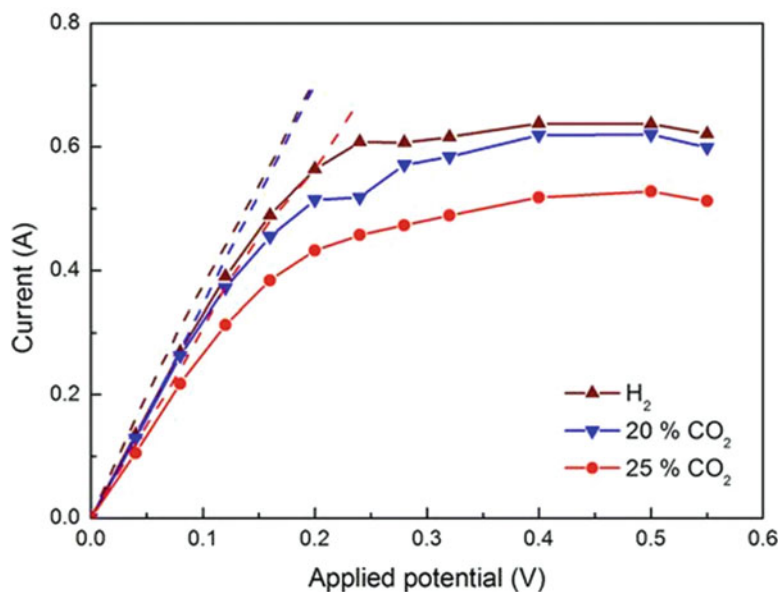


Fig. 24.11 Current as a function of applied potential with varying amounts of CO₂ at 80 °C and 16 mL inlet. Reproduced from [16] with permission of the American Chemical Society



acid-based membranes. Wu et al. [22] synthesized a sulfonated PEEK (SPEEK) membrane with a semi-interpenetrating network of cross-linked polystyrene sulfonic acid (sIPN) and performed hydrogen pumping tests. Current was measured as a function of applied potential at varying CO₂ levels (Fig. 24.11). It can be seen that the current quickly increases until the limiting current is reached which was indicative of a mass transport resistance. Polarization curves for the sIPN membrane with various anode feeds can be seen in Fig. 24.12 (active area 1.9 cm⁻²).

24.6 Applications

The application of electrochemical hydrogen pumping technology is relatively recent and has been predominately limited to four areas: (1) industrial hydrogen recycling, (2) fuel cell applications (anode tail-gas recirculation for reuse in fuel cells or related fuel cell systems), (3) electroanalytical methods, and (4) hydrogen compression. Of the four, only the first three topic areas have seen significant development efforts although electrochemical compression is experiencing a higher degree of R&D activity due to the current interest in hydrogen vehicle

refueling. Developed in the 1960s, the use of this technology has been slow to emerge. This is partly due to the fact that the EHP stack technology parallels fuel cell development and commercialization activities.

24.6.1 Electrochemical Industrial Hydrogen Recycling

The recycling of hydrogen using electrochemical methods in industrial applications has been a recent focus of a number of companies, the most predominant one being H2Pump LLC (Latham, NY) [23]. In this application, hydrogen is recovered from hydrogen-intensive industrial processes, purified, and then made available for reuse on-site. Applications include metallurgical processes such as stainless steel annealing, brazing, powder metal sintering, as well as semiconductor production, to name a few. Chemical processes that generate hydrogen are also opportunities for this technology. There are a number of challenges that must be overcome if EHP methods are to be realized in industrial settings. Regardless of the stack technology, it must be scalable to be able to handle large volumes of process gas, able to operate reliably

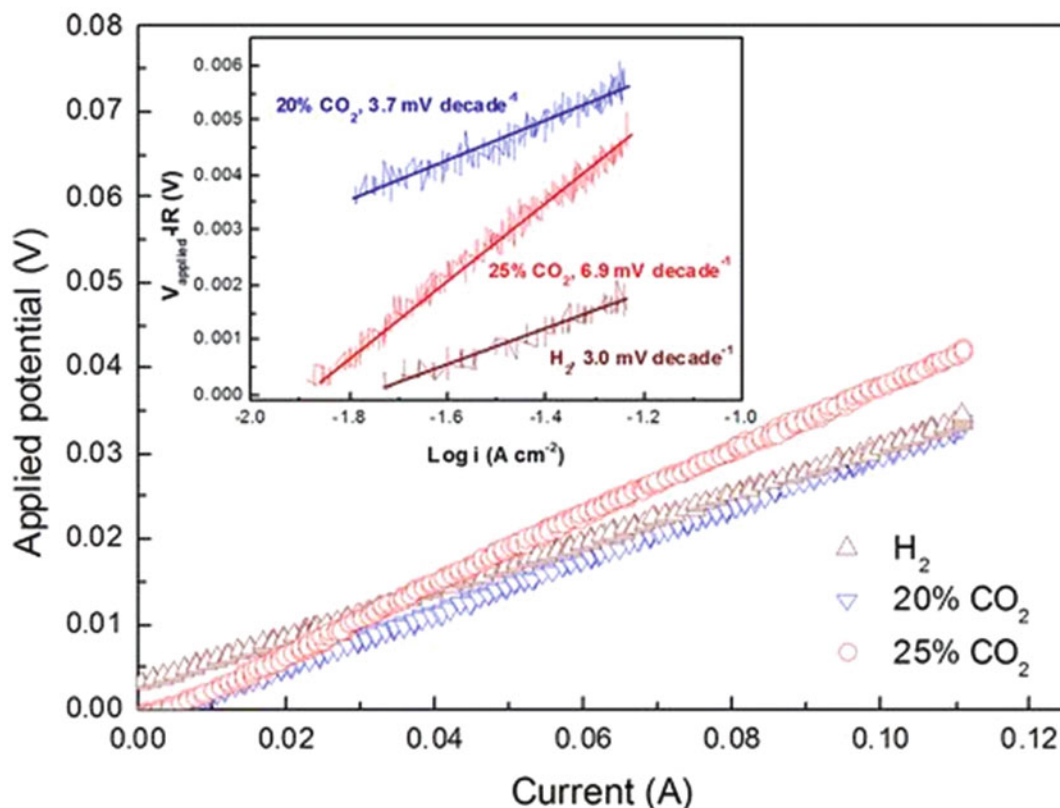


Fig. 24.12 Polarization curve and Tafel Plots. Reproduced from [22] with permission of the American Chemical Society

in the presence of a host of impurities from the industrial process, and be able to generate pressurized product hydrogen. The pressure requirement to drive the “pumped” hydrogen through a final clean up stage, typically a dryer, as well as to feed it back into the feedstock manifold of the site. As a result, a “system” to manage the different unit operations is required as a function of the operating profile of a given application. Such systems have been developed and Fig. 24.13 shows a fully integrated unit that is capable of pumping 100 kg of hydrogen per day.

24.6.2 Fuel Cell Applications

There are two potential uses of an EHP in combination with fuel cells. In the first, anode tail-gas recirculation, hydrogen is extracted from the fuel

cell stack anode exhaust. Once recovered, it is then fed back to the original source of the hydrogen thereby improving the overall fuel efficiency of the system. In the second, excess hydrogen from the reformer is captured and recovered for either recirculation or for use in other fuel cell subsystems. In addition, recovered hydrogen from either of these two sources within fuel cell systems can be used for its heating or chemical value, or for providing a source of hydrogen for motive refueling needs. Hydrogen pumps have been used by Bloom Energy Corporation to reach technological and cost goals in planar solid oxide fuel cells (PSOFC). In this application, a hydrogen pump can be used for hydrogen recycling or external hydrogen delivery. The hydrogen pump test duration lasted 2000 h and showed less than a 5 % performance degradation on hydrogen production [24].



Fig. 24.13 H2Pump LLC hydrogen pumping unit

24.6.3 Electroanalytical Methods

With a strong emphasis on the development of electrochemical membrane processes, e.g., water electrolysis and fuel cells, electrode performance must be well characterized electrochemically. Use of a hydrogen pump concept can provide insight into anode and/or cathode electrode electrochemical characteristics. Furthermore, the method can also be utilized to determine the back diffusion of hydrogen through the membrane [5, 25].

24.6.4 Compression

EHP technology is of interest as it can be used in place of a mechanical compressor to generate pressurized hydrogen. Although it is membrane and hardware dependent, very high pressures have been reported using EHP technology, at least at the lab scale. The advantages include (1) energy is consumed only to compress

hydrogen, (2) unlike a mechanical compressor, a pressure head is not required, (3) the capital costs of the core EHP system are lower than mechanical methods, (4) high turn down ratio characteristics, and (5) the energy requirements are comparable to the mechanical compressor as measured by the kW h kg^{-1} of hydrogen which is pumped and compressed. A significant development challenge includes managing high differential pressures across the membrane, thereby requiring sufficient mechanical strength of the membrane separators, gaskets, and related stack hardware. In addition, the forces encountered on the end-plates of a stack can be significant. Due to the logarithmic nature of the Nernst potential, the energy requirements are approximately $6\text{--}10 \text{ kW h kg}^{-1}$, similar to that required by a mechanical compressor. Pressures in the vicinity of 345 bar have been recently reported [26] for Nafion[®] membrane systems whereas 22 bar has been reported for PBI high-temperature membrane pumps [14].

24.6.5 Hydrogen Purification

Regardless of the source of the hydrogen, the technique can be used for bulk purification of hydrogen as long as the impurities that have to be removed from the hydrogen do not impact the electrochemical membrane process or the ancillary subsystems.

24.6.6 Limitations of the Technology

There are a number of limitations of this technology which also indicates opportunities for further development. These are presented in Table 24.2.

24.6.7 Comparison to Fuel Cells: Lifetime/MEA Stability

Although the electrochemical pump stack module is similar to stacks used in membrane fuel cells, there are significant differences. These include the future prospect of not having to use

Table 24.2 Technological limitations

Metric	Impact	Consequences
Performance	Electrode stability	Decreased performance and/or higher energy requirements
	Membrane and electrode poisoning	Reliability
	Low anode hydrogen concentrations	
	Membrane flooding and/or drying	
Pressure limitation	Membrane and hardware mechanical stability	Catastrophic failure
Cost	Utilization of precious metals	Economics
	Membranes	

precious metals, lower catalyst loadings, different flow fields, the lack of oxygen in the cathode, and low voltages for the hydrogen oxidation and reduction processes. The latter two are of great importance as the primary degradation mechanism in low-temperature membrane fuel cells is related to hydrogen peroxide radical attack of the membrane and ionomer in the electrode layers. The lack of oxygen in an EHP process creates distinct lifetime and performance advantages over fuel cells. Furthermore, as the voltages required to “drive” the oxidation and reduction reactions are by definition zero (except for a small overvoltage), the carbon supports of the catalysts are not at risk of oxidation.

24.7 Conclusions

High-temperature hydrogen separation using PBI-based membranes has been demonstrated to produce high purity hydrogen, even without significant optimization of the cell design, gasketing, and sealing strategies. A particular advantage of high-temperature operation is the increased tolerance to impurities that may be present in reformation processes or in industrial process streams. This is a critical aspect of high-temperature EHP and expands the utility of such devices for practical applications. Early work in this field has confirmed the scalability of the device to industrially relevant volumes with power requirements that are considerably lower than widely used existing technologies. Further development of devices with higher purity gas

production and higher pressures will be assisted by additional hardware designs. It is expected that longer lifetimes will be realized as compared to fuel cells by the removal of the oxidative degradation processes found in fuel cell cathodes. There appear to be many opportunities for membrane development, as well as, stack and system designs that are tailored to meet the needs of both current industrial and future hydrogen markets.

References

1. Grubb W, Niedrach L (1960) Batteries with solid ion exchange membrane electrolytes, II low temperature hydrogen-oxygen fuel cells. *J Electrochem Soc* 107:131–135
2. Niedrach L, Grubb W (1963) Ion exchange membrane fuel cells. *Fuel cells*. Academic, New York, pp 253–298
3. Yeo R (1982) Solubility parameter of perfluoro-sulfonated polymers. In: *ACS Symposium Series 180. Perfluorinated ionomers*. American Chemical Society, Washington DC, pp 65–77
4. Maget H (1970) Process for gas purification. US Patent 3,489,670
5. Huth A, Schaar B, Oekermann T (2009) A proton pump concept for the investigation of proton transport and anode kinetics in proton exchange membrane fuel cells. *Electrochim Acta* 54:2774–2780
6. Eisman G (1986) The physical and mechanical properties of a new perfluorosulfonic acid ionomer for fuel cell applications. Presented at the 169th Electrochemical Society Meeting, vol 86–13. *The Electrochemical Society Proceedings*, Boston, pp 156–161
7. Farooque M, Kush A, Abens S (1990) Novel electrochemical hydrogen separation device using phosphoric acid cell. *Sep Sci Technol* 25:1361–1373
8. Molle M, Schmidt T, Benicewicz B (2012) Polybenzimidazole fuel cell technology: theory,

- performance, and applications. Encyclopedia of sustainability, science and technology. Springer, New York, pp 391–431
9. Perry K, Eisman G, Benicewicz B (2008) Electrochemical hydrogen pumping using a high-temperature polybenzimidazole (PBI) membrane. *J Power Sources* 177:478–484
 10. Xiao L, Zhang H, Scanlon E et al (2005) High-temperature polybenzimidazole membranes via a sol-gel process. *Chem Mater* 38:5929–5936
 11. Strobel R, Oszcipok M, Fasil M et al (2002) The compression of hydrogen in an electrochemical cell based on a PE fuel cell design. *J Power Sources* 105:208–215
 12. Kim S, Lee B, Ahn S et al (2013) Characterizations of polybenzimidazole based electrochemical hydrogen pumps with various Pt loadings for H₂/CO₂ gas separation. *Int J Hydrog Energy* 38:14816–14823
 13. Petek T, Wainright J, Savinell R (2012) High temperature electrochemical hydrogen pump cell using a PBI membrane at high current densities. *ECS Trans* 50:2153–2162
 14. Eisman G, Share D, Carlstrom C (2012) Process intensification of hydrogen unit operations using an electrochemical device. www.hydrogen.energy.gov/pdfs/progress12/ii_c_2_eisman_2012.pdf. Accessed 24 Aug 2014
 15. Thomassen M, Sheridan E, Krello J (2010) Electrochemical hydrogen separation and compression using polybenzimidazole (PBI) fuel cell technology. *J Nat Gas Sci Eng* 2:229–234
 16. Lee H, Choi H, Choi K et al (2004) Hydrogen separation using electrochemical method. *J Power Sources* 132:92–98
 17. Abdulla A, Laney K, Padilla M et al (2011) Efficiency of hydrogen recovery from reformat with a polymer electrolyte hydrogen pump. *AIChE J* 57:1767–1779
 18. Brunetti A, Barbieri G, Drioli E (2006) A PEMFC and H₂ membrane purification integrated plant. *Desalination* 199:156–158
 19. Gardner C, Ternan M (2007) Electrochemical separation of hydrogen from reformat using PEM fuel cell technology. *J Power Sources* 171:835–841
 20. Barbir F, Gorgun H (2007) Electrochemical hydrogen pump for recirculation of hydrogen in a fuel cell stack. *J Appl Electrochem* 37:359–365
 21. Sedlak J, Austin J, LaConti A (1981) Hydrogen recovery and purification using the solid polymer electrolyte electrolysis cell. *Int J Hydrog Energy* 6:45–51
 22. Wu X, He G, Yu L et al (2014) Electrochemical hydrogen pump with SPEEK/CrPSSA semi-interpenetrating polymer network proton exchange membrane for H₂/CO₂ separation. *ACS Sustain Chem Eng* 2:75–79
 23. Eisman G (2012) Recycling hydrogen with a novel electrochemical process. *Ind Heat* 10:45–47
 24. Mitlitsky F (2009) Low-cost co-production of hydrogen and electricity. Annual Merit Review. www.hydrogen.energy.gov/pdfs/review09/fc_46_mitlitsky.pdf. Accessed 20 Aug 2014
 25. Thomas S, Ren X, Zelenay P et al (1999) Direct methanol fuel cells: cathode evaluation and optimization. In: Gottesfeld S, Fuller T (eds) Proton conducting membrane fuel cells II. The Electrochemical Society, Pennington
 26. Canada National Research Council (2003) Hydrogen compression milestone promises major benefits for the fuel cell industry. http://www.nrc-cnrc.gc.ca/eng/achievements/highlights/2003/hydrogen_compression.html. Accessed 15 Aug 2014

Index

A

- Acid-base chemistry
 - acid dissociation, 40, 42, 48
 - acid doping (doped), 47, 48, 51, 53
 - acidity constant, 39
 - base doping (doped), 48, 50, 54
 - chemical shift (NMR), 45
 - Grotthuss mechanism, 37–39, 43, 46–48, 53
 - hydrogen bond, 37–39, 44, 45, 47, 48, 50, 53
 - hydrogen bond donor (acceptor), 38, 40, 42, 43
 - ionic liquid, 39, 40, 44, 46, 47
 - ionicity, 39, 42–45, 47, 53
 - polarizability, 42, 43
 - protic, 42–47
 - proton transfer, 37–40, 42, 44–48, 50, 53
 - vehicle mechanism, 37, 53
 - Walden rule, 46, 47
- Acid doping
 - acid-base, 47, 48, 50
 - acid doping levels, 112–116, 122, 130, 152, 159, 160, 162, 200, 206, 210, 220, 221, 223, 226, 228, 229, 233, 239, 240, 243, 244, 262, 268, 292, 337, 347, 391, 495, 503, 529, 533
 - adsorption isotherms, 184–186
 - adsorption model, 179–183
 - affinity, 198
 - equilibrium, 113–116
 - hydration, 114
 - hydrogen bond, 113
 - level, 59, 63
 - modified BET-isotherm, 180–183
 - Raman spectroscopy, 186–190
 - swelling, 67, 159, 328
- Acid loss
 - evaporation, 345, 347
 - leaching, 339, 347
 - vapor pressure, 340
- Area-specific resistance (ASR), 133, 503
- Auxiliary power unit (APU), 331, 333, 341, 427, 428, 430, 488, 505

B

- Binder
 - bipolar plate, 428–430
 - catalyst plastic pyramid, 429
 - plastic pyramid, 429
 - thermoplastic, 428
 - thermosetting, 522
- Bipolar plates
 - acid uptake, 434–437
 - binder, 428–430
 - function, 426, 427
 - gold coated, 502
 - graphite composite, 426, 433
 - manufacturing, 428–430
 - requirements, 427
 - stainless steels, 502
- Blends
 - acid-base concept, 59–87
 - acid-excess, 50, 74
 - base excess, 62, 63, 65, 86, 491
 - covalent cross-linking, 60, 79, 82
 - Fenton test, 67, 95, 208
 - ionic cross-linking, 161
 - phosphoric acid uptake, 6
 - thermal stability, 75, 76

C

- Carbon
 - bipolar plate, 320, 347, 426, 428
 - catalyst support, 309
 - composite membrane, 290, 291
 - corrosion current, 305
 - nanotubes, 74, 118, 290, 291, 430, 431, 501
 - potential dependence, 496
 - protocols, 382, 501
 - stabilized carbon, 307
 - startup-shutdown, 382
 - support, 27, 306, 307, 309, 310, 319, 334, 338, 339, 341, 347–349, 361, 362, 379, 381, 395, 496, 498–500, 502, 504, 505, 539
 - synthetic graphites, 428, 430, 436, 437, 500
- Carbon monoxide
 - coverage, 304, 399
 - poisoning, 152, 235, 365, 390–392, 465, 504

- Catalyst. *See also* Platinum catalyst
agglomeration, 495
alloys, 297, 306, 307, 310, 333, 342, 349
coalescence, 496
CO stripping, 300–302, 500
degradation, 338, 340, 344, 349, 381, 495, 496
electrochemical surface area (ECSA), 298,
310, 335, 338, 349, 501
hydrogen underpotential deposition, 300
loading, 239, 297, 318, 337, 358, 362,
373, 390, 499, 531, 539
migration, 496
nanoparticles, 495, 496
platinum, 2, 190, 342, 362, 401, 409,
499, 500, 529, 531
- Catalyst binder
AB-PBI, 197
polyvinylidene fluoride (PVDF), 335, 429,
434, 436, 437
poly(2,5-benzimidazole) (AB-PBI), 334–336
polytetrafluoroethylene (PTFE), 335
- Catalyst degradation
acid loss, 339, 340
carbon corrosion, 498–500
dissolution rates, 497, 498
electrochemical surface area (ECSA), 501
Ostwald ripening (mechanism), 497
redistribution, 495
sintering, 487
solubility, 497
- Catalyst layer
design, 342–344
hydrophilic, 347
hydrophobic, 318, 335, 336
ionomer, 29
- Composite membranes
clay, 277
coupling agent, 259, 260
fillers, 6–20
lithium chloride, 261
Nafion/PTFE, 251, 252
PBI/PTFE, 259–261, 263, 266
poly(vinyl alcohol) (PVA), 252
porous film, 252, 268, 269
porous polytetrafluoroethylene (PTFE), 251–271
reinforcement, 253–255, 257, 259
silica, 246, 248
- Conductivity
activation energy, 135
definitions and equations, 132, 133
four probe, 133, 134
in-plane, 432–434
measurements, 133–135
mixed, 133, 134
Pouillet's law, 133
temperature dependence, 135
through-plane, 434
- Copolymers, 93–100, 102–105, 107, 109, 112,
114–116, 119
- Corrosion, 302–306, 319, 498–500
carbon, 302–306, 319
- Cross-linking
covalent, 60, 62, 74–76, 79, 82–84, 104, 106, 107, 119
ionic, 60, 62, 63, 65, 67–69, 73–76, 79, 84, 86
- D**
- Direct methanol fuel cell (DMFC), 142, 251, 291, 318
methanol crossover, 252
- Doping
acid, 4, 67, 92, 97, 99, 107, 111–113, 162,
220, 228, 261, 284, 291, 328, 490, 503, 533
acid doping level, 59, 63, 112–116, 122, 132,
152, 159, 160, 162, 200, 206, 220, 221,
224, 226, 228, 229, 233, 239, 240, 243,
244, 262, 292, 337, 347, 391, 494, 495,
503, 529, 533
acid uptake, 106, 113, 131, 196
adsorption isotherms, 183–187, 189
amphoteric, 198
base, 62, 86
base doping level, 50
conductivity, 240
degradation, 240
phosphoric acid, 28, 48, 51, 92, 97, 109,
120, 151, 169, 189, 190, 195, 196, 200,
202, 207, 209, 227, 230, 262, 263, 268,
275, 278, 285, 291, 292, 328, 333, 347,
354, 361, 362, 391, 434, 490, 495, 505, 529
- Durability
acid loss, 209, 340
beginning of life, 487
degradation rates, 203, 235, 333, 379, 381,
502, 505
end of life (EOL)
long-term, 487
impurity effect, 504
post-mortem, 366–367
startup-shutdown, 504, 505
steady state, 118, 122, 381, 502
target, 331–333, 337, 341, 488
thinning, 487, 489, 499, 505
- Dynamic lifetime test
loading cycling, 503
protocols, 504
startup-shutdown, 503
- E**
- Electrochemical hydrogen pumping
compression, 538
effect of humidity, 530
hydrogen purity, 534, 535, 538
lifetime, 538, 539
perfluorosulfonic acid, 534
polybenzimidazoles, 528, 529
poly(ether ether ketone), 534
- Electrochemical impedance spectroscopy
diagnostics, 389
Nyquist plots, 135, 357, 479

Electrochemical methods

- cyclic voltammetry (CV), 361–363
- linear sweep voltammetry (LSV), 360

Electro-osmotic drag, 140–144
water, 2, 144, 206–207

F

Fenton test. *See also* Oxidative stability

- Fenton agent, 490, 505
- ferrous ions, 95, 203, 490
- hydrogen peroxide, 102, 146, 202, 490

Fuel cell

- activation loss, 358
- blends, 86
- compression, 138, 538
- durability, 162, 209–210, 276
- IR-correction, 356
- mass transport, 356
- ohmic loss, 356
- open circuit voltage, 141, 251, 292
- polarization curves, 7, 355, 356, 478, 483
- Tafel plot, 537
- test procedure, 222, 229, 365

Fuels

- dimethyl ether, 514, 515
- hydrogen, 2, 459, 537
- methane, 391, 514
- methanol, 459, 462, 465
- on-board, 515
- reforming, 459, 468, 477, 514

G

Gas diffusion

- electrode, 134, 208, 262, 320, 322, 323, 388, 392, 394–396, 411
- gas diffusion layer (GDL), 209, 233, 275, 311, 315–317, 320, 323, 324, 332, 353, 354, 391, 392, 396, 403, 426, 434, 493, 502, 505
- permeability, 207

Gasket

- elastomer, 427, 438
- function, 426
- plastic pyramid, 429
- requirement, 427

Grothaus mechanism, 48, 290

H

Homopolymer, 92–94, 96

Hydrocarbon membranes

- sulfonated, 11–14, 16–18

Hydrogen bond(ing), 37–39, 44, 45, 47, 48, 50, 53, 113, 138, 228, 239, 253, 254, 256, 258, 259, 348

Hydrogen evolution reaction (HER), 300, 311

Hydrogen oxidation reaction (HOR), 297, 298, 303, 304, 310, 311, 532, 533

I

Ionicity, 39, 42–45, 47, 53

Ionic liquid, 39, 40, 44, 46, 47, 286

M

MEA

Mechanical properties

- ASTM standard, 137, 438
- comparession, 138
- creep, 138
- dynamic mechanical analysis (DMA), 139, 140
- elongation, 137
- hardness shore A, 438
- indentation, 138
- tear strength, 438
- tensile stress, 137
- Young's (Elastic) modulus, 137

Membrane

- casting, 153, 197, 201, 203, 208
- conductivity, 10, 205, 282, 284, 285, 347, 390, 391, 396, 397, 481
- crossover, 360, 399
- degradation, 72, 209, 338, 340, 488
- doping, 327, 398
- gas diffusivity, 207
- mechanical, 60, 221, 268

Membrane electrode assembly (MEA), 26, 27, 29–35, 69,

- 87, 91, 109, 117, 118, 120–123, 128, 197, 203, 233–236, 251, 263–266, 268, 276, 297, 298, 308, 309, 311, 315–324, 326–328, 332–349, 388, 392, 397, 398, 401, 407, 409, 413, 414, 425–427, 436, 437, 441, 442, 446, 448, 450, 451, 457, 465, 467–469, 478, 489, 492, 494, 495, 497, 504, 505, 520, 529, 532, 538–539
- accelerated stress test (AST), 380
- Butler–Volmer equation, 355
- compression (contact pressure), 367–378
- EIS, 357–360, 364
- long-term test, 378
- ohmic resistance, 27, 31, 34, 297, 338, 342, 346, 349, 368
- open circuit voltage, 30, 33, 265, 504
- structure design, 341–345, 347, 348
- Tafel slope, 333, 336

Membrane modifications

- composites, 196, 207–209
- crosslinking, 196, 208–209
- grafting, 208

Methanol

- combustion heating, 462, 469–471
- cross-over, 6, 11, 18, 35
- oxidation, 6, 143
- permeation, 143, 144
- reformers, 91, 123, 459–462, 464, 467, 469, 474–476, 514–518

Molecular weight

- gel permeation chromatography, (*see also* Size exclusion chromatography (SEC)), 66, 67, 69, 73, 95, 130
- light scattering, 127–129
- Mark–Houwink–Sakurada, 154, 241
- single-point method, 154
- viscosity, 128–129

O

- Oxidative degradation
 - chain scission, 490
 - Fenton agent, 489
 - peroxide radicals, 489
 - phosphoric acid, 505
 - thermal, 489
 - weight loss, 490
- Oxidative stability, 66, 80, 94–96, 100, 102, 107, 121, 144–147, 489, 490
- Oxygen reduction reaction (ORR)
 - acid adsorption, 300, 333
 - catalyst, 303, 333, 334
 - kinetics, 297, 303, 333, 342
 - mechanism, 336
 - oxygen solubility, 404

P

- Perfluorosulfonic acid
 - composite, 6–23
 - inorganic fillers, 6
 - modified, 23–27, 35
 - phosphoric acid doping, 328
 - short side chain, 18, 27–34
- Permeability
 - gas, 140–141, 146, 196, 207, 239, 336, 347, 369
 - hydrogen, 141–142, 207, 209
 - hydrogen stripping, 142
 - oxygen, 141
- Phosphoric acid
 - acid–base chemistry, 3, 37–54
 - acidity, 51, 171, 179
 - acid retention, 276
 - anhydride, 135, 170
 - conductivity, 170, 174–175, 190, 204, 205
 - evaporation, 116, 494
 - fuel cell (PAFC), 2, 4, 169, 179, 268, 318–320, 322, 327, 328, 333, 335, 336, 344, 345, 348, 388, 389, 396–403, 414, 495, 497, 505, 529
 - leaching, 248, 249
 - protolytic equilibria, 171–173
 - vapour pressure, 173–174
 - viscosity, 175–176
 - Walden plot, 179
- Phosphoric acid fuel cell (PAFC), 492
- Platinum alloys
 - core-shell, 342
 - Pt-Al, 333
 - Pt-Co, 334, 342, 349
 - Pt-Cr, 333, 342
 - Pt-Fe, 333
 - Pt-Ni, 333, 342, 349
 - Pt-Ru, 333
 - Pt-V, 333
- Platinum catalysts
 - agglomeration, 318, 338, 339, 341, 344, 345, 347, 349
 - carbon corrosion, 498, 505
 - coalescence, 345
 - dissolution, 320, 487, 488, 495, 496, 498, 505
 - migration, 345
 - nanoparticles, 297, 334, 338, 497, 505
 - ostwald ripening, 298
 - redistribution, 308
- Polyacid membranes, 51
- Polybenzimidazole
 - membrane fabrication, 156
 - solubility, 195
- Polybenzimidazole blends
 - acid–base, 490
 - acidic polymers, 62
 - chemical stability, 60
 - conductivity, 60, 217, 290, 491
 - doping, 28, 48, 170, 204, 205
 - thermal stability, 66, 202
- Polybenzimidazole membranes
 - acid doping, 239
 - chemical stability, 67, 286
 - conductivity, 217, 290, 491
 - electro-osmotic drag, 140
 - gas permeability, 141, 146, 347
 - gas solubility, 141, 390
 - mechanical strength, 203, 207
 - structure and morphology, 201
 - thermal stability, 202
- Polybenzimidazole modification
 - blend, 6, 74, 95
 - composite, 60, 246, 248, 277, 279, 282, 290–292
 - crosslinking, 267
 - grafting, 62
 - hybrid, 284
 - N-substitution, 161, 208
 - pendant groups, 201
- Polybenzimidazole solutions
 - conformation, 255
 - filtration, 136
 - lithium chloride, 253
 - radius of gyration, 255–257
 - solubility, 128
 - static light scattering, 255, 256
 - viscosity, 254
- Polybenzimidazole synthesis
 - degree of polymerization, 127
 - main chain modifications, 156
 - microwave assisted synthesis, 154
 - molecular weights, 127, 128, 152, 154, 155
 - polymer repeat unit, 59, 195
 - solubility, 128, 223
 - solvent free, 152
 - tailored basicity, 242
- Polymer
 - decomposition temperature, 111, 208
 - glass transition temperature, 27, 29
 - homopolymer, 224, 230, 233
 - molecular weight distribution (MWD), 490
 - stability, 492

- Polyphosphoric acid (PPA)
content, 115
copolymers, 230
PBI variants, 156
phosphoric acid contents, 132, 138, 195, 200, 203, 207, 208, 219, 337, 340, 341, 349, 405, 502
polyphosphoric acid process, 529
solvent, 153, 196, 217
- Protic ionic liquid, 44, 46, 47
- Proton conductivity
acid-base, 37–54
Grothuss mechanism, 38, 206
hydrogen bonds, 40–43
permanent, 239, 240
proton transfer, 37, 48
vehicle mechanism, 29
- Pyridine containing polymers
acid uptake, 111
aromatic polyethers, 62, 91–123
cross-linked, 72, 104–111
fuel cells, 91, 95, 96, 117, 119, 122
membrane electrode assembly, 128
side group functionalized, 96–104
synthesis, 91–96
- R**
- Relative humidity
control, 147–148
definition, 147–148
dew point method, 147
mechanical properties, 33, 67, 113
proton conductivity, 243, 244, 279, 284
- S**
- Simulation
Monte Carlo method, 344
polymer chain, 219
three-dimensional kinetic, 338
- Size exclusion chromatography (SEC), 130–131
- Sol-gel method
PPA process, 217, 218
SiO₂ fillers, 25
- Solid acid, 53
- Solubility
hydrogen, 399, 404
methanol, 141
- Solvents
dimethylsulfoxide (DMSO), 98
methanesulfonic acid (MSA), 196
N,N-dimethylacetamide (DMAc), 136, 156
N,N-dimethylformamide (DMF), 156, 196
N-methyl-2-pyrrolidone (NMP), 136, 156, 196
- Stability
oxidative, 66, 80, 94–96, 100, 102, 107, 121, 144–147, 489, 490
PBI, 67, 286, 287
thermal, 3, 14, 44, 60, 65, 66, 69, 71, 75, 86, 93, 95, 98, 99, 103–105, 144, 151, 152, 160, 162, 200, 202–203, 239, 241, 276, 278, 284, 286, 287, 291, 336, 428, 431
- Stacks
air-Cool, 452, 456, 460
construction materials, 450
design, 441, 447, 449, 455, 460, 521
- Sulfonated PBI, 131
- Swelling
acid doping, 67
linear, 132
van der Waals volume, 67
volume, 65, 67, 200, 208, 503
water uptake, 198, 328
- System diagnostics
air-cooled, 460–462
CO effect, 2, 390, 532
CO₂ effect, 2, 532
efficiency, 468, 475
impedance, 465, 466, 481
liquid cooled systems, 462–465
system control, 463
system idling, 483
water uptake, 131
- T**
- Targets
bipolar plate, 426, 427
catalyst loading, 337
catalyst support, 334
cost, 331, 332
DOE, 505
durability, 333
gasket, 426, 427
membrane, 276
- Thermal stability
differential (DTA), 65, 71
thermogravimetric analysis (TGA), 60, 71, 75, 76, 79
- V**
- Viscosity
dynamic shear viscosity, 255, 256
elastomer, 438
helix test, 438
inherent, 129, 152, 197, 203, 204, 217, 219–221, 231, 242, 529
intrinsic, 128, 129, 154, 197, 241, 242, 254
Mark-Houwink equation, 203, 241
PBI, 254
specific, 128, 154
- W**
- Walden plot, 44, 46, 47
Walden rule, 46
Water uptake, 15, 199